

T. Pradeep
Publications 2023

Contents

1. Publications	8 - 464
2. Editorials	466 - 474
3. Selected media reports	476 - 480
4. Patents/Technology	481 - 483

Journal Papers Published in 2023

Publications from our group

- (1) Chakraborty, A.; Stanley, M. M.; Mondal, B.; Nonappa; Bodiuzzaman, M.; Chakraborty, P.; Kannan, M. P.; Pradeep, T. Tunable Reactivity of Silver Nanoclusters: A Facile Route to Synthesize a Range of Bimetallic Nanostructures. *Nanoscale* **2023**, *15* (6), 2690–2699. (DOI: 10.1039/D2NR06350F).
- (2) Jose, A.; Jana, A.; Gupte, T.; Nair, A. S.; Unni, K.; Nagar, A.; Kini, A. R.; Spoorthi, B. K.; Jana, S. K.; Pathak, B.; Pradeep, T. Vertically Aligned Nanoplates of Atomically Precise Co₆S₈ Cluster for Practical Arsenic Sensing. *ACS Mater. Lett.* **2023**, *5* (3), 893–899. (DOI: 10.1021/acsmaterialslett.3c00085).
- (3) Vishwakarma, G.; Malla, B. K.; Reddy, K. S. S. V. P.; Ghosh, J.; Chowdhury, S.; Yamijala, S. S. R. K. C.; Reddy, S. K.; Kumar, R.; Pradeep, T. Induced Migration of CO₂ from Hydrate Cages to Amorphous Solid Water under Ultrahigh Vacuum and Cryogenic Conditions. *J. Phys. Chem. Lett.* **2023**, *14* (11), 2823–2829. (DOI: 10.1021/acs.jpcllett.3c00373).
- (4) Jana, A.; Spoorthi, B. K.; Nair, A. S.; Nagar, A.; Pathak, B.; Base, T.; Pradeep, T. A Luminescent Cu₄ Cluster Film Grown by Electrospray Deposition: A Nitroaromatic Vapour Sensor. *Nanoscale* **2023**, *15* (18), 8141–8147. (DOI: 10.1039/D3NR00416C).
- (5) Roy, J.; Mondal, B.; Vishwakarma, G.; Nonappa; Vasanthi Sridharan, N.; Krishnamurthi, P.; Pradeep, T. Dissociative Reactions of [Au₂₅(SR)₁₈][−] at Copper Oxide Nanoparticles and Formation of Aggregated Nanostructures. *Nanoscale* **2023**, *15* (18), 8225–8234. (DOI: 10.1039/D3NR00897E).
- (6) Sugi, K. S.; Sandra, A. P.; Nonappa; Ghosh, D.; Mohanty, J. S.; Paulthangam Kannan, M.; Sooraj, B. S.; Srikrishnarka, P.; Roy, J.; Dar, W. A.; Pradeep, T. Secondary Ligand-Induced Orthogonal Self-Assembly of Silver Nanoclusters into Superstructures with Enhanced NIR Emission. *Nanoscale* **2023**, *15* (28), 11927–11934. (DOI: 10.1039/D3NR02561F).
- (7) Jana, A.; Kini, A. R.; Pradeep, T. Atomically Precise Clusters: Chemical Evolution of Molecular Matter at the Nanoscale. *ACM* **2023**, *3* (1), 56–65. (DOI: 10.51167/acm00040).

- (8) Vishwakarma, G.; Malla, B. K.; Chowdhury, S.; Khandare, S. P.; Pradeep, T. Existence of Acetaldehyde Clathrate Hydrate and Its Dissociation Leading to Cubic Ice under Ultrahigh Vacuum and Cryogenic Conditions. *J. Phys. Chem. Lett.* **2023**, *14* (23), 5328–5334. (DOI: 10.1021/acs.jpcllett.3c01181).
- (9) Ghosh, J.; Vishwakarma, G.; Kumar, R.; Pradeep, T. Formation and Transformation of Clathrate Hydrates under Interstellar Conditions. *Acc. Chem. Res.* **2023**, *56* (16), 2241–2252. (DOI: 10.1021/acs.accounts.3c00317).
- (10) Jana, A.; Dar, W. A.; Jana, S. K.; Poonia, A. K.; Yadav, V.; Roy, J.; Chandra, S.; Adarsh, K. N. V. D.; Ras, R. H. A.; Pradeep, T. Photoconversion of Ag₃₁ to Ag₄₂ Initiated by Solvated Electrons. *Chem. Mater.* **2023**, *35* (17), 7020–7031. (DOI: 10.1021/acs.chemmater.3c01293).
- (11) Srikrishnarka, P.; Kumaran, D.; Kini, A. R.; Kumar, V.; Nagar, A.; Islam, M. R.; Nagarajan, R.; Pradeep, T. Observing Real-Time Adhesion of Microparticles on Glass Surfaces. *Langmuir* **2023**, *39* (48), 17071–17079. (DOI: 10.1021/acs.langmuir.3c01856).
- (12) Mondal, B.; Jana, A.; Roy, J.; Mata, A. C.; Nair, A. S.; Mahendranath, A.; Roy, S.; Pathak, B.; Ajayan, P. M.; Pradeep, T. Structure and Electrocatalytic Performance of Cocrystallized Ternary Molybdenum Oxosulfide Clusters for Efficient Water Splitting. *ACS Mater. Lett.* **2023**, *5* (12), 3306–3315. (DOI: 10.1021/acsmaterialslett.3c00957).
- (13) Bose, P.; Kumaranchira Ramankutty, K.; Chakraborty, P.; Khatun, E.; Pradeep, T. A Concise Guide to Chemical Reactions of Atomically Precise Noble Metal Nanoclusters. *Nanoscale* **2024**. (DOI: 10.1039/D3NR05128E).
- (14) Malla, B. K.; Vishwakarma, G.; Chowdhury, S.; Pradeep, T. Vacuum Ultraviolet Photolysis of Condensed Methyl Chloride in Interstellar Model Conditions and Trapping of Intermediates at Intergrain Interfaces. *J. Phys. Chem. C* **2023**, *127* (50), 24149–24157. (DOI: 10.1021/acs.jpcc.3c05889).

Publications with other groups

- (1) Chandra, S.; Sciortino, A.; Das, S.; Ahmed, F.; Jana, A.; Roy, J.; Li, D.; Liljeström, V.; Jiang, H.; Johansson, L.-S.; Chen, X.; Nonappa; Cannas, M.; Pradeep, T.; Peng, B.; Ras, R. H. A.; Sun, Z.; Ikkala, O.; Messina, F. Gold Au(I)_6 Clusters with Ligand-Derived Atomic Steric Locking: Multifunctional Optoelectrical Properties and Quantum Coherence. *Adv. Opt. Mater.* **2023**, *11* (8), 2202649. (DOI: 10.1002/adom.202202649).
- (2) Roy, P.; Deb, D.; Suganya, A.; Roy, B.; Pradeep, T.; Saha, T. Endangered Indigenous Rice Varieties as a Source of B Vitamins for the Undernourished Population. *Cereal Chem.* **2023**, *100* (4), 887–894. (DOI: 10.1002/cche.10668).
- (3) Patel, D. K.; Sooraj, B. S.; Kirakci, K.; Macháček, J.; Kučeráková, M.; Bould, J.; Dušek, M.; Frey, M.; Neumann, C.; Ghosh, S.; Turchanin, A.; Pradeep, T.; Base, T. Macropolyhedral Syn-B18H22, the “Forgotten” Isomer. *J. Am. Chem. Soc.* **2023**, *145* (32), 17975–17986. (DOI: 10.1021/jacs.3c05530).

Editorials

- (1) Michalak, A. M.; Xia, J.; Brdjanovic, D.; Mbiyozo, A.-N.; Sedlak, D.; Pradeep, T.; Lall, U.; Rao, N.; Gupta, J. The Frontiers of Water and Sanitation. *Nat. Water* **2023**, *1* (1), 10–18. (DOI: 10.1038/s44221-022-00020-1).

Journal Papers

Publications from our group


Cite this: *Nanoscale*, 2023, **15**, 2690

Tunable reactivity of silver nanoclusters: a facile route to synthesize a range of bimetallic nanostructures†

Amrita Chakraborty,^a Megha Maria Stanley,^a Biswajit Mondal,^a Nonappa,^b Mohammad Bodiuzzaman,^a Papri Chakraborty,^a M. P. Kannan^a and Thalappil Pradeep^a✉

Quantized energy levels and unique optoelectronic properties of atomically precise noble metal nanoclusters (NCs) have made them important in materials science, catalysis, sensors, and biomedicine. Recent studies on the profound chemical interactions of such NCs within themselves and with ultrasmall plasmonic nanoparticles (NPs) indicate that depending on the size, shape, and composition of the second reactant, NCs can either take part in colloidal assembly without any chemical modifications or lead to products with atoms exchanged. Anisotropic NPs are a unique class of plasmonic nanomaterials as their sharp edges and protrusions show higher chemical reactivity compared to flat surfaces, often leading to site-specific growth of foreign metals and metal oxide shells. Here, using chemical interactions between gold nanotriangles (AuNTs) and Ag NCs of different compositions, we show for the first time that metal atom etching, alloying/atom exchange, and colloidal assembly can all happen at a particular length scale. Specifically, Ag₂₅(DMBT)₁₈ NCs (denoted as **1**), upon reacting with AuNTs of ~57 nm edge length, etch gold atoms from their sharp tips and edges. Simultaneously, the two nanosystems exchange metal atoms, resulting in Ag-doped AuNTs and Au_xAg_{24-x}(DMBT)₁₈ (x = 1, 2). However, another Ag NC with the same metallic core, but a different ligand shell, namely, Ag₂₅H₂₂(DPPE)₈ (denoted as **2**), creates dendritic shells made of Ag, surrounding these AuNTs under the same reaction conditions. Furthermore, we show that in the case of a more reactive thiol-protected Ag NC, namely, Ag₄₄(pMBA)₃₀ (denoted as **3**), gold etching is faster from the edges and tips, which drastically alters the identities of both the reactants. Interestingly, when the AuNTs are protected by pMBA, **3** systematically assembles on AuNTs through H-bonding, resulting in an AuNT core–Ag NC shell nanocomposite. Thus, while shedding light on various factors affecting the reactivity of Ag NCs towards AuNTs, the present study proposes a single strategy to obtain a number of bimetallic nanosystems of targeted morphology and functionality.

Received 13th November 2022,

Accepted 3rd January 2023

DOI: 10.1039/d2nr06350f

rsc.li/nanoscale

Introduction

Noble metal NCs of precise compositions and structures, composed of a few to tens of metal atoms, show molecule-like optical properties.^{1,2} In the last decade, the synthesis of a large variety of NCs, their structural determination using single-crystal X-ray diffraction (XRD) studies, and the structure–property correlation of their physical and chemical behaviors have

been the principal aspects of research in the area, with a recent emphasis on bimetallic NCs.^{3–6} Lately, the chemical properties of noble metal NCs are gaining attention due to their large surface to volume ratio and low coordination of surface atoms which are important for applications such as catalysis^{7,8} and bioimaging.⁹ Besides forming adducts with small molecules such as cyclodextrins,^{10,11} crown ethers,¹² fullerenes,¹³ and cucurbiturils,¹⁴ NCs also take part in binary colloidal assemblies with 1D plasmonic NPs. For instance, pMBA capped Ag and Au NCs, when anchored to the surface of TeNWs, led them to arrange in a crossed-bilayer assembly at the liquid–air interface.¹⁵ H-bonding interactions among the anchored NCs of the two layers result in precise orientations. The same NCs take part in H-bonding-mediated assemblies with pMBA-protected ultrasmall gold nanorods (AuNRs) encapsulating the latter in multilayer cages.¹⁶ In such assemblies,

^aDepartment of Chemistry, DST Unit of Nanoscience (DST UNS) and Thematic Unit of Excellence (TUE), Indian Institute of Technology Madras, Chennai 600 036, India. E-mail: pradeep@iitm.ac.in

^bFaculty of Engineering and Natural Sciences, Tampere University, FI-33101 Tampere, Finland

†Electronic supplementary information (ESI) available. See DOI: <https://doi.org/10.1039/d2nr06350f>

the identities of NCs and anisotropic nanoparticles were retained. On the other hand, studies on thiol- and phosphine-protected noble metal NCs have shown that NCs of two different types of metals, when mixed under ambient conditions, spontaneously exchanged metal atoms and ligands in solution, leading to intercluster alloying.¹⁷ A similar reaction between two NCs,¹⁸ or NC and metal thiolates,¹⁹ made of isotopically pure silver atoms resulted in isotopically mixed NCs. Bürgi and co-workers have shown that doping a different metal to Au NCs is possible by using metallic foils of Ag, Cu and Cd as the source of heteroatoms.²⁰ In a recent report, ultrasmall plasmonic Ag NPs were also found to be the source of atomic Ag while reacting with Au NCs, resulting in mono-disperse Au–Ag alloy NPs and Ag-doped Au NCs.²¹

These results indicate that the interaction of NCs with other nanosystems can range from weaker to strong interactive forces, either retaining¹⁶ or altering their chemical properties.²¹ Plasmonic NPs of anisotropic morphology, such as nanorods, nanobipyramids, and nanostars, show differential reactivity along their sharp protrusions, edges, and tips as compared to their flat surfaces.^{22–24} Site-specific chemical reactivity leads to the preferential end-to-end assembly of AuNRs,²⁵ the tip-specific growth of non-metallic shells,^{24,26,27} and the site-selective growth of foreign metals.^{28–30} Thus, the chemical reactivity of noble metal NCs with anisotropic plasmonic NPs is an exciting field that is yet to be explored. A study by Yuan *et al.* showed that the highest curvature caused the tips of triangular gold nanoprisms to show the highest chemical reactivity followed by those of bipyramids and AuNRs.³¹

Therefore, we chose planar gold nanotriangles (AuNTs) as the anisotropic NPs and allowed them to interact with different Ag NCs under ambient conditions. A thorough characterization of the intermediate and product NPs reveal that the reaction with a thiolate-protected Ag NC, namely, Ag₂₅(DMBT)₁₈ (abbreviated here as **1**), causes controlled etching of atoms from the sharp vertices and edges of AuNTs. Simultaneously, the two nanosystems exchanged metal atoms, leading to Au_xAg_{25–x}(DMBT)₁₈ and blunt AuNTs with limited Ag doping to the surface. This unique reactivity suggests that the differential surface curvature of AuNTs makes the Au atoms at the sharp tips and edges behave like loosely bound atoms, and the flat surfaces behave like a gold foil and the heavy metallic body remains unaffected, resembling bulk gold.

We have further shown that by tuning the composition of the NC and the AuNT–Ag NC interface, the outcome of such reactions can change drastically. For example, a similar interaction of AuNTs with Ag₂₅H₂₂(DPPE)₈ (abbreviated here as **2**) produced a dendritic nanoshell of Ag surrounding the AuNTs, whereas their reaction with Ag₄₄(pMBA)₃₀ (abbreviated here as **3**) leads to uncontrolled etching of Au atoms from the tips and edges of AuNTs. Interestingly, suitable modification of the AuNT–Ag NC interface results in a geometrically precise core–shell bimetallic nanocomposite. Thus, their chemical interaction with NCs has the potential to produce atom-etched, atom-exchanged, and core–shell products from a single nanostructure by slightly tuning the reactants and reaction parameters.

Experimental

Materials and methods

Chemicals and materials. Tetrachloroauric acid trihydrate (HAuCl₄·3H₂O, ≥99.9%), hexadecyltrimethylammonium chloride (CTAC, 25 wt% in water), sodium borohydride (NaBH₄, ≥99%), 2,4-dimethylbenzenethiol (DMBT), 1,2-bis(diphenylphosphino)ethane (DPPE, 97%), tetraphenylbromide (PPh₄Br), 4-mercaptobenzoic acid (pMBA, 97%), sodium iodide (NaI, ≥99.5%), cesium hydroxide (CsOH, >99%) and L-ascorbic acid (AA, ≥99%) were purchased from Sigma Aldrich. Silver nitrate (AgNO₃, 99%) and sodium hydroxide (NaOH) pellets were obtained from Rankem, India. All analytical grade solvents, *e.g.*, *N,N*-dimethylformamide (DMF), dichloromethane (DCM), dimethyl sulfoxide (DMSO) and methanol (MeOH), were purchased from Rankem chemicals. All chemicals were used as received without further purification. Glassware was washed with aqua regia, sonicated three times with water for 3 min each, rinsed with distilled water, and dried before use. Distilled water was used for all syntheses.

Synthesis of gold nanotriangles (AuNTs). The seed-mediated method reported by Scarabelli *et al.* was followed to synthesize gold nanotriangles.³² To prepare the seed, 25 µL of 0.05 M HAuCl₄ solution was added to 4.7 mL of 0.1 M CTAC solution with slow stirring. Subsequently, 0.01 M NaBH₄ solution was prepared in ice-cold water and 300 µL of this was injected into the reaction mixture under vigorous stirring. The seed solution was kept at 28 °C for 2 h, which was diluted 10 times using 0.1 M CTAC prior to its addition to the growth solution. For a 40 mL batch of AuNTs, the following two growth solutions were prepared.

Growth solution A. To 8 mL of DI water, 1.6 mL of 0.1 M CTAC, 40 µL of 0.05 M HAuCl₄ and 15 µL of a 0.01 M NaI solution were added sequentially under manual stirring.

Growth solution B. 500 µL of 0.05 M HAuCl₄ solution was added to 40 mL of 0.05 M CTAC, followed by 300 µL of 0.01 M NaI solution, all under manual stirring.

After the preparation of these solutions, 40 µL and 400 µL of 0.1 M AA were added to the growth solutions A and B, respectively. The reaction mixtures were manually shaken until the solution became colorless, indicating the reduction of Au(III) to Au(I). Immediately, 100 µL of the diluted seed was added to growth solution A with mild shaking. Within 1 s of this, 3.2 mL of growth solution A was added to growth solution B. The mixture was kept still for a minimum period of 1 h after the initial manual shaking for about 5 s. The appearance of a dark blue color indicated the formation of nanotriangles.

Purification of the as-synthesized batch. To eliminate spherical NPs formed along with the AuNTs, a flocculation method was followed, *i.e.*, a suitable amount of aqueous CTAC stock solution (25 wt%) was added to the as-synthesized AuNTs (in 5 mL batches) to achieve the final CTAC concentrations of 150, 175 and 200 mM, respectively. The mixtures were kept undisturbed overnight at 28 °C. As a result, AuNTs with better size and shape uniformity were precipitated in all

three cases while the impurities remained dispersed in the supernatant. The yield was optimum in the case of 175 mM final CTAC concentration. After decanting the supernatant, the pellets were dispersed in DI water with mild sonication, which resulted in a solution of greenish blue color.

Synthesis of 1. NC 1 was synthesized according to a previously reported method.³³ Briefly, 38 mg of AgNO₃ was dissolved in 2 mL of MeOH and 17 mL of DCM was added to it. Under stirring conditions, 90 μ L of 2,4-dimethylbenzenethiol (DMBT) was added to this solution. After 20 min of stirring, 6 mg of tetraphenylbromide (PPh₄Br) was added followed by the addition of a freshly prepared solution of 15 mg of sodium borohydride (NaBH₄) in 0.5 mL of ice-cold water. The reaction was carried out for 6 h and kept in a refrigerator (4 °C) overnight. The solvent was evaporated under reduced pressure and the product was cleaned several times with excess MeOH. The cleaned clusters were characterized by optical absorption spectroscopy and electrospray ionization mass spectrometry.

Synthesis of 2. NC 2 was synthesized following the procedure reported recently.³⁴ Briefly, 20 mg of AgNO₃ was dissolved in 5 mL of MeOH. 75 mg of DPPE dissolved in 7 mL of DCM was added to it under stirring at room temperature. Stirring was continued for 20 minutes. Meanwhile, 35 mg of NaBH₄ was dissolved in 1 mL of ice-cold DI water. This was added to the reaction mixture in one shot. With the addition of NaBH₄, the colorless solution turned light yellow. It was crucial to carry out the synthetic procedure in the dark to avoid any undesired oxidation of Ag. After roughly 30 minutes of continuous stirring, when the reaction mixture turned orange, the product was extracted and purified to obtain clean NCs.

Synthesis of 3. As reported by Desiredy *et al.*,³⁵ NC 3 was synthesized by adding 128 mg of AgNO₃ and 173 mg of MBA to a mixture of DMSO and water (volume ratio 4 : 7) under stirring conditions. To this, an aqueous solution of CsOH (50%) was added dropwise until the solution became clear. 283 mg of NaBH₄ was dissolved in 9 mL of ice-cold DI water, a 1 mL aliquot of which was added dropwise to this greenish yellow clear solution at an interval of 9 minutes with continuous stirring. After this, the reaction mixture was kept under stirring conditions for 1 h to complete the reaction. As a result, the solution turned wine red, confirming the formation of 3. This crude cluster was purified in a few steps. First, it was centrifuged at 5000 rpm for 5 min to remove any NPs formed during the synthesis. Excess DMF was added to the supernatant and it was centrifuged at 5000 rpm for 1 min. To the precipitate containing 3, equal volumes of DMF and toluene were added along with citric acid. This protonated the carboxylic acid groups present in the cluster. This was centrifuged again at 5000 rpm for 1 min and the procedure was repeated once more to ensure complete protonation of the acid groups. Finally, the purified NC was dissolved in ultrapure DMF.

Reaction between AuNTs and 1. Purified AuNTs were subjected to centrifugation (6000 rpm for 10 min) to remove excess CTAC. 90% of the colorless supernatant was decanted

and the AuNTs settled at the bottom were redispersed in the same amount of DI water. This process was repeated once more and the pellet was finally redispersed in DMF. The concentration of the AuNT solution was maintained such that the optical density (O.D.) at the SPR maximum (~640 nm) was 1. To 500 μ L of this AuNTs, 40 μ L of purified NC 1 was added dropwise with moderate stirring at room temperature. The amount of NC added and the time of the reaction were varied for comparative studies.

Reaction between AuNTs and 2. In a similar way as described above, to 500 μ L of AuNTs (as above), 50 μ L of 1.2 μ g mL⁻¹ NC 2 were added under stirring conditions. The reaction was continued at room temperature.

Reaction between AuNTs and 3. This reaction was carried out in two ways with bare AuNTs, which was similar to the method described in the case of 1, and with *p*MBA-protected AuNTs (abbreviated as AuNT@*p*MBA). For the latter, washed AuNTs were dispersed in 500 μ L of DMF as stated above. Meanwhile, solid *p*MBA was dissolved in DMF to achieve a final concentration of 0.1 mM. 500 μ L of this was added to AuNTs and the mixture was vortexed for 10 min. After 3 h, this solution was centrifuged for 6 min at 6000 rpm and the supernatant was decanted to remove excess CTAC and unbound *p*MBA, if any. The pellet thus obtained was AuNT@*p*MBA. NC 3 was added to AuNT@*p*MBA (of O.D. 1 at 640 nm) with mild stirring, and the mixture was kept undisturbed at room temperature.

Instrumentation. UV-vis absorption spectra of all the samples were recorded using a PerkinElmer Lambda 25 spectrometer. A quartz cuvette of path length 10 mm was used for all measurements. TEM imaging was performed using a JEOL 3010 instrument at 200 kV acceleration voltage. For transmission electron tomographic reconstruction, the specimen was tilted between $\pm 69^\circ$ angles with 2° increment and a tilt series of 2D projections were acquired with the SerialEM software package in low dose mode using a JEOL 3200 TEM operating at 300 kV with an omega filter. The acquired stack of images was subjected to a series of pre-processing, coarse alignment, and final alignment using the IMOD software package. 3D reconstruction was obtained with a custom-made maximum entropy method (MEM) program on MacPro.³⁶ STEM images were collected using a JEOL JEM 2800 microscope at 200 kV acceleration voltage. Mass spectrometric analysis was performed using a Waters Synapt G2Si high-definition mass spectrometer equipped with electrospray ionization (ESI). X-ray diffraction (XRD) patterns were recorded with a Bruker AXS D8 Discover diffractometer using Cu K α (λ = 1.54 Å) radiation. Samples were scanned between the 5° and 90° range of 2θ and the peaks were matched with the JCPDS (Joint Committee on Powder Diffraction Standards) database. To identify the chemical oxidation states of the elements, XPS was performed using an ESCA probe TPD spectrometer (Omicron Nanotechnology) with a polychromatic Al K α ($h\nu$ = 1486.6 eV) X-ray source with a step size of 0.1 eV per second. The binding energies (B.E) of all the elements were calibrated with respect to C 1s (284.8 eV).

Results and discussion

Interaction of AuNTs with a moderately reactive Ag NC

Equilateral AuNTs were synthesized following the synthetic methods reported by Scarabelli *et al.*,³² Fig. 1a presents the TEM image of AuNTs obtained after purification by the flocculation method (Fig. S1† presents the detailed characterization). A statistical analysis of 100 AuNTs reveals that the mean particle size (distance from the tip to the opposite side) of the as-synthesized AuNTs was 57.8 ± 3.6 nm (Fig. 1b). For better insight, 3D tomographic images of these AuNTs were reconstructed from the respective tilt series of TEM images. Fig. 1c and ESI Video S1† show the 3D views of AuNTs which clearly exhibit their planar triangular morphology with sharp edges and tips. Parallely, we synthesized an Ag NC that is known to exchange metal atoms with other NCs in solution,³⁷ *i.e.*, NC 1. The synthesis of 1 was confirmed from its characteristic absorption spectrum, *i.e.*, a broad peak at ~ 675 nm, an intense peak at ~ 490 nm and 2 other peaks at around 336 nm and 396 nm (top panel of Fig. 1d), and ESI mass spectrum (MS) (Fig. 3a). Pristine AuNTs, protected by a labile layer of cetyl trimethyl ammonium chloride (CTAC), were dispersed in aqueous medium. After removing excess CTAC by centrifugation, the pellet of AuNTs was dispersed in DMF, which was the same solvent as 1. A dilute solution of NC 1 was added dropwise to AuNTs under stirring conditions until the color of the medium changed from blue (characteristic color of pure AuNTs) to greenish-brown. The reaction was allowed to continue for 72 h and the product (denoted as AuNT@1) was separated by centrifugation for analysis. A comparison of the absorption spectra of pristine AuNTs, 1, and AuNT@1 presented in Fig. 1d shows that the LSPR of the AuNTs at ~ 630 nm undergoes a blue shift in the latter, which can be

attributed to the reduction in the aspect ratio of the AuNTs, as often observed in the case of conventional oxidative etching.³¹ Peaks between 350 nm and 450 nm come from unreacted 1 adsorbed on the surface of the AuNTs. The increased width of all the peaks denotes electronic coupling between the two systems. The broad peak around 800 nm is presumably due to the quantum mechanical effect as explained by Lahtinen *et al.* in the case of Au₂₅₀ trimers.³⁸ The TEM image of the reacted AuNTs in Fig. 1e confirms that the morphology of the AuNTs was significantly altered upon reaction. The particles retained their triangular shape, but the edges were rounded and the tips were blunt. The particle size distribution of AuNT@1 in Fig. 1f indicates that the average size of the NTs has been reduced by 12 nm and the size-polydispersity has increased. Fig. 1g (also ESI Video S2†) presents the electron tomographic 3D reconstruction of AuNT@1 particles that gives a better insight on the overall pebble-like morphology. We must clarify that the label, AuNT@1, does not imply that 1 is covering AuNTs. We also note that gold atoms can migrate from the sharp tips of AuNTs to their flat surfaces when dispersed in DI water.³⁹ However, the TEM images of AuNTs dispersed in DMF show that even after a week there was no alteration in the geometry of the AuNTs (Fig. S2†).

To study the gradual change of AuNTs during the reaction, the reaction product was extracted at different time intervals and their TEM and STEM images were examined carefully. In Fig. 2a, the TEM image of AuNT@1 after 24 hours of the reaction showed a hint of bulging along the flat sides of the particles. This image implies that metallophilic attraction led 1 to attach to the AuNTs, preferentially on their planar surfaces, which exerted stronger van der Waals force compared to their edges. Such adducts were also formed at the intermediate stages of the reaction between polydisperse AgNPs and Au

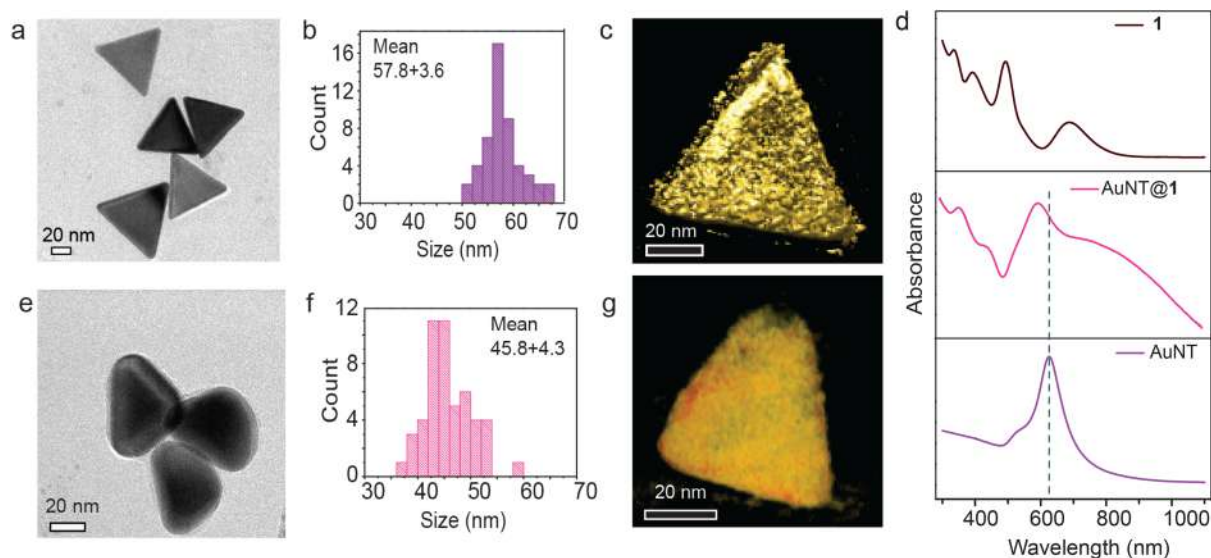


Fig. 1 Characterization of AuNTs before and after the reaction with 1: (a) TEM image of parent AuNTs and (b) the corresponding particle size distribution, (c) 3D tomographic reconstruction of a single AuNT, (d) comparative absorption spectra of 1, AuNT@1, and AuNTs, (e) TEM image of AuNT@1, (f) the corresponding particle size distribution and (g) 3D tomographic reconstruction of a single AuNT@1.

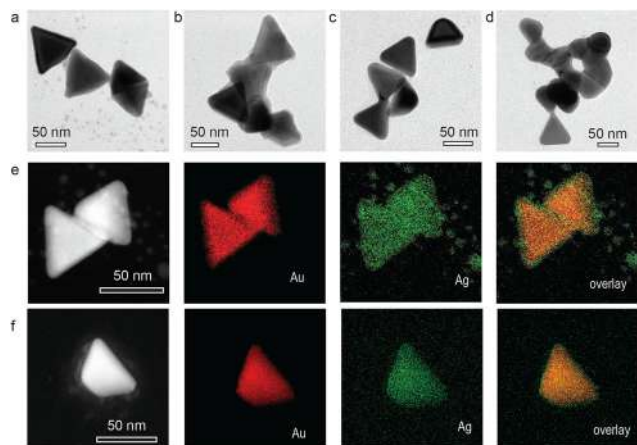


Fig. 2 Time-dependent analysis of AuNT@1: TEM images of the reaction product after (a) 1 day, (b) 3 days, (c) 6 days and (d) 10 days. (e) STEM EDS elemental mapping of AuNT@1 after 3 days of the reaction, and (f) after 6 days of the reaction.

NCs, as observed by Bose *et al.*²¹ In the present study, after 72 h of the reaction, more cluster moieties got adsorbed on AuNTs forming AuNT-1 adducts, as shown in Fig. 2b. At this stage, the tips of the nanotriangles started to lose their sharpness, suggesting the etching of Au atoms from the highly curved and least protected (by CTAC) surfaces of the AuNTs upon reaction. Fig. 2c presents the TEM image of AuNT@1 after 6 days, which shows that the AuNTs became blunt. In the case of the oxidative etching of anisotropic Au NPs, we have seen that the rate of reshaping decreases significantly with time as the surface curvature increases.³¹ Accordingly, the TEM image of AuNT@1 taken after 10 days of reaction (Fig. 2d) suggests that, after a certain point, the reshaping of AuNTs was ceased. Although a prolonged reaction time removed CTAC from the surface of AuNTs, causing them to fuse with each other, most of the reacted AuNTs still carried the signature of their triangular morphology. The rate of the reaction and end results were hardly affected by an increase in the NC concentration in the reaction medium (Fig. S3†).

STEM EDS elemental mapping of the reacted particles was also performed at the two significant stages of the transformation. Fig. 2e represents a dark-field STEM image of AuNT@1 and the corresponding EDS elemental mapping after 72 h of the reaction. At this intermediate stage, a thin non-uniform Ag shell surrounding the sharp AuNTs can be observed along with some unreacted NC in the vicinity. The STEM image of such a single particle collected after 6 days of reaction (Fig. 2f) shows that besides the vertices, the edges of the particles also lost their sharpness, thereby destroying the planar geometry of the parent AuNTs. Besides, the particle seemed to be free from any loosely bound NC. However, the corresponding EDS elemental mapping shows that Ag was evenly distributed on the surface of the reacted AuNTs, but no trace of S was found, suggesting the absence of DMBT. This observation confirms that there was no reacted or unreacted NC adsorbed on the

AuNT surface, rather elemental Ag was doped to the AuNTs in a metal exchange reaction.

We then performed powder XRD analysis, which showed no change in the lattice spacing of the AuNTs upon reaction (Fig. S4†). Together, these two studies indicate that Ag atoms were doped to the AuNTs, but the doping of Ag atoms was limited to the surface and didn't result in alloying of the whole body of nanotriangles.

Plasmonic nanoparticles such as AuNTs are not atomically precise. Even the best synthetic batch of AuNTs do not all contain the same number of Au atoms. Hence, chances are that the number of Ag atoms doped to AuNTs will vary. Mass spectrometric analysis of the change of AuNTs is beyond the limit of commercially available mass spectrometers. Hence, a definite value of Ag atoms doped per AuNT is hard to determine. However, NCs are ultrasmall, atomically precise structures. Hence, the reacted NC was analyzed using ESI MS in order to comprehend the mechanistic pathway. Precisely, after 72 h of the reaction, the solution was centrifuged to spin down the AuNT@1 particles and the supernatant was analyzed. The ESI MS of **1** before and after reaction are shown in Fig. 3a. The intense peak at $m/z \sim 5167$ in both the cases is attributed to the molecular ion peak with a molecular formula of $[\text{Ag}_{25}(\text{DMBT})_{18}]^-$. In case of the reacted NC, the appearance of a new peak at $m/z \sim 5256$ indicates that an Ag atom of some of the NCs was replaced with an Au atom. Another weak signal found at $m/z \sim 5345$ corresponds to the replacement of 2 Ag atoms of **1** by 2 Au atoms, keeping the nuclearity constant, namely, $[\text{Ag}_{25-x}\text{Au}_x(\text{DMBT})_{18}]^-$ ($x = 1, 2$). This is direct evidence of atom exchange between AuNTs and **1**, resembling a chemical reaction. Along with the atom exchange products, we observed two intense peaks at $m/z \sim 4923$ and ~ 4679 , which are due to the loss of one and two (Ag-DMBT) units, respectively from the parent NC. However, these (Ag-DMBT)_n-deficient NC moieties showed no trace of Au doping, suggesting that atom-etched NC moieties did not take part in atom exchange

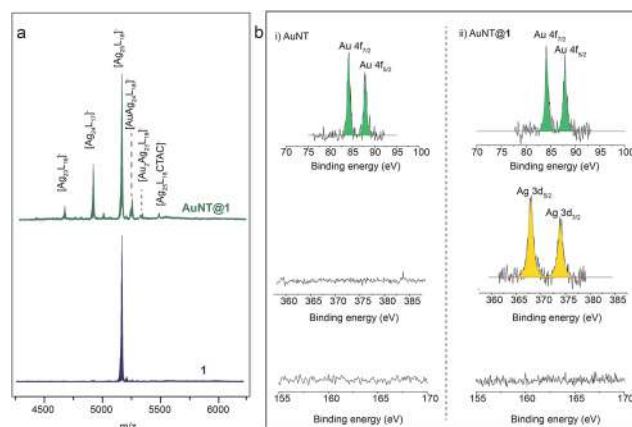


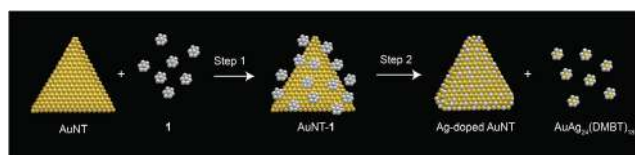
Fig. 3 (a) ESI MS study of **1** before and after the reaction with AuNTs, (b) comparative XPS analysis showing the emergence of an Ag peak in AuNT@1, but no signal was seen around 162 eV denoting the absence of S.

with AuNTs and *vice versa*. These may also be a result of the fragmentation of **1** during the reaction. The X-ray photoelectron spectroscopic study of parent AuNTs and AuNT@**1** reveals the presence of Ag in the latter; however, no trace of S was found (Fig. 3b). The above results reconfirm that metallic Ag was incorporated to AuNTs in its elemental form and not in the form of the adsorbed Ag-DMBT unit or unreacted **1** as that would produce a signal for S as well. Based on these observations and the previous studies of chemical interactions between nanosystems, we propose a mechanism of the reaction between bare AuNTs and **1**. Krishnadas *et al.* have shown that the reaction between Au and Ag NCs leads to atom exchange products even up to the complete conversion of one metal cluster to the other, one atom at a time.³⁷ Even small AgNPs, due to the high surface to volume ratio, are known to show profound reactivity towards Au NCs. Such reactivity between plasmonic NPs and NCs decreased significantly upon increasing the size of AgNPs from 4 nm to 8 nm.²¹ Hence, considering their dimension, AuNTs are not expected to take part in atom exchange with Ag NCs to a significant extent. However, due to their non-spherical morphology, Au atoms along their edges and tips took part in the reaction.

As expected from the previous reports of chemical reactions among nanosystems, an AuNT-**1** adduct was formed in step 1 of the reaction due to the metallophilic attraction between the reactants. Now, Au atoms at the sharp edges and vertices of AuNTs were under-coordinated, and hence, more exposed to the reactant NC (here, **1**). In step 2, loosely bound Au atoms leached out from the vertices and edges of the sharp AuNTs converting the latter into blunt pebble-like triangular NPs. On the other hand, some of the NCs lost Ag-DMBT units from their inherent composition. Such a partial decomposition of NCs to form metal thiolates was observed earlier in the presence of a foreign metal ion.⁴⁰ In a parallel pathway, the AuNTs and undecomposed **1** moieties exchange metal atoms, producing Ag@AuNTs and $[\text{Ag}_{25-x}\text{Au}_x(\text{DMBT})_{18}]^-$ ($x = 1, 2$). Thus, the reaction simultaneously produces Au-doped Ag NCs and Ag-doped AuNPs as the end products. Scheme 1 shows the overall reaction between AuNTs and **1**. Notably, although ligand exchange is quite a common phenomenon of NC reactivity,⁴¹ in this case we observed only metal atom transfer to the AuNTs and no ligand exchange.

Effect of the shell of the NC

The physical and chemical properties of noble metal NCs are guided by their atomic composition, the nature of the ligand, and the structure of the metallic core.¹ Therefore, to have a



Scheme 1 Two-step reaction between AuNTs and **1**.

complete understanding of the chemical reactivity of NCs with anisotropic NPs, it is crucial to study the effect of these parameters. In order to investigate the effect of the ligand shell in the present reaction, we synthesized another Ag NC of the same metallic core as **1**, but the protecting shell is made of a phosphine ligand instead of a thiol.³⁴ This NC, namely, **2** was soluble in methanol, whereas AuNTs were dispersed in DI water. The clear blue aqueous dispersion of AuNTs turned turbid instantly as **2** was added to it with moderate stirring. This indicates that the DPPE ligands came out of the NC, partially or fully, into the reaction medium. The absorption spectrum of the reaction product, namely, AuNT@**2** showed no significant shift in the LSPR peak position even after 6 days of the reaction (Fig. 4a). TEM images collected after 1 day (Fig. 4b) and 6 days (Fig. 4c) of the reaction showed that the reaction with **2** did not affect the size and aspect ratio of AuNTs in aqueous medium. In the EDS elemental analysis of AuNT@**2**, an intense signal for Au and Ag was obtained, but no trace of P was found (Fig. S5†). This was possibly because in aqueous medium, the ligand of **2** precipitated, decomposing the NC too soon to effectively react with AuNTs and alter their morphology. However, the naked core of **2** acted as a source of Ag(0) that was doped to the surface of AuNTs. As a result, even after days of the reaction, the vertices and edges of AuNTs were sharp, retaining their planar geometry. The inset of Fig. 4c presents the respective particle size distribution, which closely matches that of the average size of parent AuNTs.

Effect of solvent on the reaction product

The solvent often plays a crucial role in weak chemical interactions among nano-systems. DMF has been widely used as the medium of nanoscale reactions in earlier studies¹⁷ and in case of the reaction between AuNTs and **1**. Interestingly, in

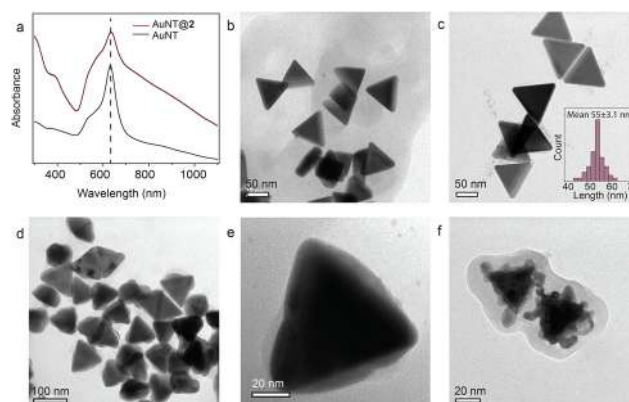


Fig. 4 Characterization of AuNT@**2**: (a) comparative absorption spectra of AuNTs before and after the reaction with **2** in water (vertically translated for a clear view) and (b) TEM images of AuNT@**2** after 1 day and (c) after 6 days, with the corresponding particle size distribution in the inset. (d) TEM image of AuNT@**2**-DMF, (e) magnified view of a single AuNT@**2**-DMF particle, and (f) TEM image of AuNT@**2**-DMF upon reacting with an excess amount of **2**.

DMF, **2** reacts with AuNTs in a very different way than in aqueous medium. The reaction product, abbreviated as AuNT@2-DMF, showed a non-uniform over-growth on the flat surfaces of AuNTs, as evident from their TEM images (Fig. 4d and e). Respective EDS analysis of this structure showed traces of Ag, indicating the doping of Ag to AuNTs. With increasing NC concentration (2.5 times), the thickness of irregularly deposited Ag was increased. An additional thin layer of Ag was also observed surrounding these hybrid structures in the respective TEM image (Fig. 4f). The absence of P in the TEM EDS studies of these structures (Fig. S6†) proves that the nodules are made of elemental Ag, and not of unreacted or partially decomposed **2**. Since the metallic core of **2** was the same as **1**, and the solvent was the same in both the cases, this difference in reactivity was directly related to the different surface ligands of the NCs. Phosphine-protected Au NCs are known to undergo ligand exchange by reaction with thiols or metal thiolates,⁴² which implies that phosphines are much more labile as ligands compared to thiols. In **2**, the core is protected by labile hydride and DPPE ligands, making them highly reactive. However, crystallization of **1** has been possible,³³ showing their greater stability. This is aligned with our observation that under the reaction conditions (especially the solvent), NC **2** decomposed and Ag atoms were doped to the AuNTs, while NC **1** exchanged Ag-DMBT units with them. Furthermore, while water stabilizes elemental Ag, and thereby hinders the chemical interaction between the two nano-systems, less polar solvents such as DMF facilitate it.

Effect of the atomcity of the NC core

In the previous studies of intercluster reactions, Au₂₅(PET) is known to exchange metal atoms with Ag NCs of different atomcity to different extents.¹⁷ Therefore, we synthesized **3** following an established protocol.³⁵ The synthesis was verified by the characteristic absorption features (Fig. 5a) and ESI MS of the NC (Fig. S7a†) before it was added to AuNTs dispersed in DMF with continuous stirring. Initially, the color of the NC disappeared instantly upon addition, suggesting a fast chemical interaction. Dropwise addition of **3** continued until the

characteristic wine-red color of **3** was persistent in the reaction mixture. By comparing the absorption spectra of **3**, the reaction product (denoted as AuNT@**3**) and AuNTs, we observed that the LSPR peak of AuNTs was blue-shifted and significantly broadened while the signature peaks of the NC were not distinctly visible (Fig. 5a). TEM images of AuNT@**3** after 0, 1, 3 and 6 days are presented in Fig. 5b–e, which show that in the case of **3**, Au atoms continued to etch from the tips of AuNTs until the triangular morphology of the particles was lost completely. Due to this fast and uncontrolled reaction, the molecular ion peak of **3** disappeared and the corresponding Au-doped Ag NC was not detected in ESI MS analysis (Fig. S7a†). Instead, red-luminescent by-products were obtained (Fig. S7b and c†), which presumably were mixed metal thiolates, that are known to show aggregation-induced luminescence.⁴³

Effect of the surface ligand of the AuNTs

The as-synthesized AuNTs were stabilized by CTAC through a non-covalent interaction. From flat sides to edges to the vertices of AuNTs, as the curvature of the surface increases, the extent of surface coverage by CTAC molecules is lower. This makes the Au atoms at the sharp tips more accessible to the reactant NCs, which came out from the AuNTs during the course of the reaction with **1** and **3**. Now, AuNPs can be easily and efficiently functionalized with different thiol molecules by Au–S bond formation.⁴⁴ In a previous report, we have seen that pMBA-functionalization of AuNRs allowed them to act as a template for the systematic multi-layer assembly of **3** surrounding them.¹⁶ Here, in order to explore the role of the AuNT–Ag NC interface on their chemical interaction, the CTAC layer of AuNTs was replaced with the respective ligands (DMBT and pMBA) *via* the ligand exchange method (see the Experimental methods section) prior to the reaction with **1** and **3**. Choosing the same ligand as that of the reactant NC was important to avoid the formation of complex by-products. The functionalization was verified by TEM EDS elemental analysis and Raman spectroscopic studies (Fig. S8 and S9†). TEM images revealed that even after 10 days of the reaction with **1**, DMBT-protected AuNTs suffered little or no morphological changes (Fig. S8c†), presumably because DMBT molecules hindered the necessary collision between the surface Au atoms and Ag NCs. The ESI MS spectra of the reacted NC showed no additional peak in this case, suggesting that the surface protection refrained the AuNTs to take part in atom exchange chemistry with **1**. However, in the case of pMBA functionalization, AuNTs interacted with **3** in a very different way. **3** is known to take part in the inter- and intrasystem H-bonding through their ligand shell.⁴⁵ Since the pMBA molecules bind to the AuNTs *via* the Au–S covalent bond, their –COOH groups were available for H-bond formation. As expected from their interaction with pMBA-protected AuNRs reported previously,¹⁶ **3** took part in the H-bonding mediated assembly to produce a multilayer shell surrounding the AuNTs, completely encapsulating individual AuNT@pMBA. Fig. 6a shows the proposed scheme. The TEM image of the resulting nanostructure, named, AuNT@pMBA@**3**, reveals their core-shell geometry (Fig. 6b),

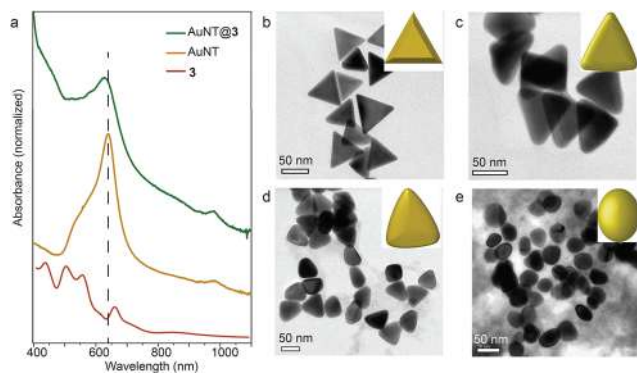


Fig. 5 Characterization of AuNT@**3**: (a) UV-vis absorption spectra of **3**, AuNTs and AuNT@**3**, and TEM images of AuNT@**3** after (b) 0 day, (c) 1 day, (d) 3 days and (e) 6 days of the reaction.

where the shell follows the morphology of the underlying AuNTs. However, the thickness of the shells was not strictly uniform. AuNT@pMBA that was well-isolated from the neighboring particles, allowed more layers of 3 NCs to grow surrounding it (Fig. 6c), as compared to the aggregated ones (Fig. 6b). Thus, while in every other case the chemical interaction with Ag NCs led to atom exchange or removal or both, here the two nanosystems assembled through H-bonds between the ligand shells. The absorption spectrum of the product composite contained the signature peaks of both AuNTs and 3 (Fig. 6d), suggesting that the parent NC retained their identity in this hybrid nanostructure.

A red shift of the LSPR peak as compared with that of AuNT@pMBA suggests an increase in the effective edge-length due to the coupling with 3 in the core-shell structure. The FESEM image of AuNT@pMBA@3 and the corresponding EDS elemental analysis are presented in Fig. S10.† The line profile (Fig. S10b†) shows the distribution of elemental Au, Ag and S along a single particle. Fig. S10c and S10d† (corresponding to points denoted as 1 and 2, respectively) show that at the centre, the particle contains ~62% Au and ~20% Ag, whereas the edge contained ~22% Au and ~52% Ag. However, the amount of S at point 2 is lesser than expected from the composition of 3, which can be attributed to beam-induced damage

caused to the NC shell. While AuNT@1, AuNT@2 and AuNT@3 showed insignificant morphological or compositional changes, the TEM image of AuNT@pMBA@3 collected after 2 months (Fig. 6e) shows that the AuNTs retained their morphology perfectly in the composite, while the uniform shell was turned into 'islands' or 'nodules'. This can be because the pMBA ligands attached to the surface of AuNTs prevented the stronger chemical interaction between 3 and the underlying AuNTs, keeping the morphology of the encapsulated AuNTs intact. However, ultrafine NCs such as 3, consisting of a few metal atoms, possess an extremely high surface energy, and are prone to aggregation. Studies have shown that Ag NCs, anchored to the surfaces such as graphite,⁴⁶ TeNWs,⁴⁷ etc., start to diffuse, presumably to reduce the interfacial energy (between the NC and the planar surface). During such mobility, the NCs encounter adjacent NC moieties, and coalesce to produce aggregates. This result is particularly interesting as significant effort has been made into growing Au,⁴⁸ Ag,⁵⁰ or Au-Ag bimetallic islands⁴⁹ on anisotropic Au NPs previously to achieve promising candidates for SERS-based studies. However, there are limited reports on the wet chemical synthesis in this direction. Our present strategy of a straightforward colloidal assembly produces an AuNT core-Ag island nanostructure spontaneously with time.

Conclusions

In conclusion, we have shown that due to differential surface energies, gold atoms at the tips, flat surfaces, and core of a single anisotropic nanoparticle, namely, AuNT, interact with atomically precise Ag NCs to various extents. Parallely, the low-coordinated atoms are etched from the sharp tips of the AuNTs, and Ag atoms are doped to their surface, while the core of the AuNTs is unaltered. Moreover, a series of anisotropic Au core-Ag shell nanostructures were achieved by tuning the compositions of the Ag NC, solvent, and AuNT-Ag NC interface. Thus, our present study reflects the versatile nature of nanoscale reactivity and explores its sensitivity towards some of the factors such as the surface curvature, solvent, and surface protective layer, leaving a scope to explore further. For example, the effect of size of the nanotriangle on such reactivity with silver nanoclusters will be an interesting follow-up study. Such bimetallic anisotropic core-shell and alloy nanostructures play promising roles in diverse applications and therefore, a common strategy to synthesize them at room temperature has immense importance in the field of materials science. Thus, while exploring the chemical properties of noble metal NCs, the present study shows their utility in creating advanced nanostructures of desired functionalities.

Conflicts of interest

The authors declare no conflicts of interest.

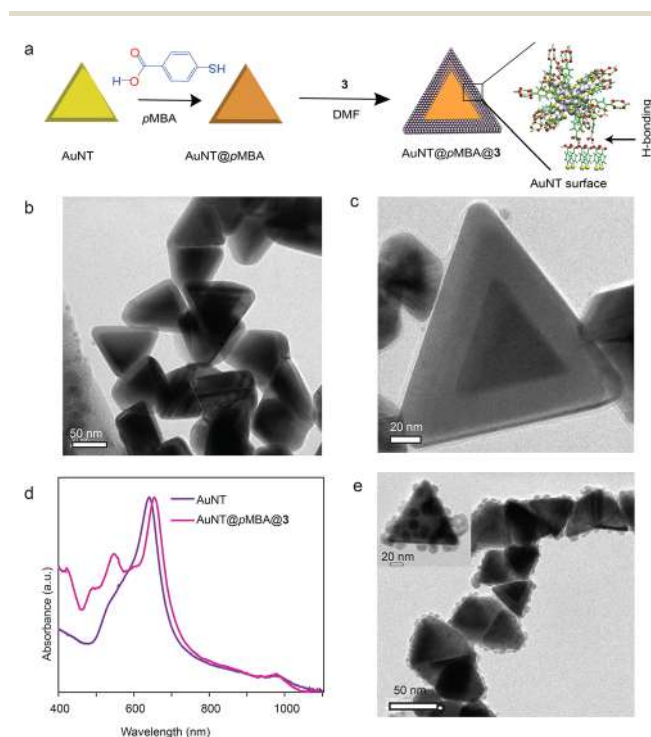


Fig. 6 Interaction between AuNT@pMBA and 3: (a) schematic representation of the H-bond mediated assembly of 3 on the AuNT@pMBA template, (b) TEM image of AuNT@pMBA@3 after 24 h, (c) that of a single AuNT@pMBA@3 clearly showing the core-shell composite structure, (d) UV-vis absorption spectra of AuNT and AuNT@pMBA@3, and (e) TEM image of AuNT@pMBA@3 after 2 months, the inset shows that of a single particle.

Acknowledgements

We thank the Department of Science and Technology, Government of India for constantly supporting our research program. A. C. thanks CSIR for her senior research fellowship. M. M. S. thanks Department of Chemistry, Stella Maris College, Chennai and INSA-IASc-NASI Summer Research Fellowship. We also thank the Academy of Finland for project funding (BioBase, No. 352900), Photonics Research and Innovation (PREIN) flagship and Nanomicroscopy Centre at Aalto University for access to instrumentation facilities. M. P. K. thanks MRF and B. M., M. B., P. C., and S. B. thank IIT Madras for their research fellowships.

References

- I. Chakraborty and T. Pradeep, *Chem. Rev.*, 2017, **117**, 8208–8271.
- Atomically Precise Metal Nanoclusters*, ed. T. Pradeep, Elsevier, Amsterdam, 2023.
- Z. Wang, R. Senanayake, C. M. Aikens, W.-M. Chen, C.-H. Tung and D. Sun, *Nanoscale*, 2016, **8**, 18905–18911.
- B.-L. Han, Z. Wang, R. K. Gupta, L. Feng, S. Wang, M. Kurmoo, Z.-Y. Gao, S. Schein, C.-H. Tung and D. Sun, *ACS Nano*, 2021, **15**, 8733–8741.
- Y. Yang, T. Jia, Y.-Z. Han, Z.-A. Nan, S.-F. Yuan, F.-L. Yang and D. Sun, *Angew. Chem., Int. Ed.*, 2019, **58**, 12280–12285.
- L. Tang, A. Ma, C. Zhang, X. Liu, R. Jin and S. Wang, *Angew. Chem., Int. Ed.*, 2021, **60**, 17969–17973.
- Y. Du, H. Sheng, D. Astruc and M. Zhu, *Chem. Rev.*, 2020, **120**, 526–622.
- S. Yamazoe, K. Koyasu and T. Tsukuda, *Acc. Chem. Res.*, 2014, **47**, 816–824.
- Nonappa, *Beilstein J. Nanotechnol.*, 2020, **11**, 533–546.
- A. Mathew, G. Natarajan, L. Lehtovaara, H. Häkkinen, R. M. Kumar, V. Subramanian, A. Jaleel and T. Pradeep, *ACS Nano*, 2014, **8**, 139–152.
- A. Nag, P. Chakraborty, G. Paramasivam, M. Bodiuzzaman, G. Natarajan and T. Pradeep, *J. Am. Chem. Soc.*, 2018, **140**, 13590–13593.
- P. Chakraborty, A. Nag, K. S. Sugi, T. Ahuja, B. Varghese and T. Pradeep, *ACS Mater. Lett.*, 2019, **1**, 534–540.
- P. Chakraborty, A. Nag, B. Mondal, E. Khatun, G. Paramasivam and T. Pradeep, *J. Phys. Chem. C*, 2020, **124**, 14891–14900.
- T. Jiang, G. Qu, J. Wang, X. Ma and H. Tian, *Chem. Sci.*, 2020, **11**, 3531–3537.
- A. Som, I. Chakraborty, T. A. Maark, S. Bhat and T. Pradeep, *Adv. Mater.*, 2016, **28**, 2827–2833.
- A. Chakraborty, A. C. Fernandez, A. Som, B. Mondal, G. Natarajan, G. Paramasivam, T. Lahtinen, H. Häkkinen, Nonappa and T. Pradeep, *Angew. Chem., Int. Ed.*, 2018, **57**, 6522–6526.
- K. R. Krishnadas, A. Baksi, A. Ghosh, G. Natarajan, A. Som and T. Pradeep, *Acc. Chem. Res.*, 2017, **50**, 1988–1996.
- P. Chakraborty, A. Nag, G. Natarajan, N. Bandyopadhyay, G. Paramasivam, M. K. Panwar, J. Chakrabarti and T. Pradeep, *Sci. Adv.*, 2019, **5**, eaau7555.
- L. Tang, X. Kang, X. Wang, X. Zhang, X. Yuan and S. Wang, *Inorg. Chem.*, 2021, **60**, 3037–3045.
- R. Kazan, U. Müller and T. Bürgi, *Nanoscale*, 2019, **11**, 2938–2945.
- P. Bose, P. Chakraborty, J. S. Mohanty, Nonappa, A. Ray Chowdhuri, E. Khatun, T. Ahuja, A. Mahendranath and T. Pradeep, *Nanoscale*, 2020, **12**, 22116–22128.
- X. Zhuo, X. Zhu, Q. Li, Z. Yang and J. Wang, *ACS Nano*, 2015, **9**, 7523–7535.
- W. Zhang, J. Liu, W. Niu, H. Yan, X. Lu and B. Liu, *ACS Appl. Mater. Interfaces*, 2018, **10**, 14850–14856.
- B. Wu, D. Liu, S. Mubeen, T. T. Chuong, M. Moskovits and G. D. Stucky, *J. Am. Chem. Soc.*, 2016, **138**, 1114–1117.
- J. Wu, Y. Xu, D. Li, X. Ma and H. Tian, *Chem. Commun.*, 2017, **53**, 4577–4580.
- H. Jia, A. Du, H. Zhang, J. Yang, R. Jiang, J. Wang and C.-y. Zhang, *J. Am. Chem. Soc.*, 2019, **141**, 5083–5086.
- A. Kim, S. Zhou, L. Yao, S. Ni, B. Luo, C. E. Sing and Q. Chen, *J. Am. Chem. Soc.*, 2019, **141**, 11796–11800.
- F. Wang, S. Cheng, Z. Bao and J. Wang, *Angew. Chem., Int. Ed.*, 2013, **52**, 10344–10348.
- X. Zhu, H. Jia, X.-M. Zhu, S. Cheng, X. Zhuo, F. Qin, Z. Yang and J. Wang, *Adv. Funct. Mater.*, 2017, **27**, 1700016.
- Y. Li, H. Lin, W. Zhou, L. Sun, D. Samanta and C. A. Mirkin, *Sci. Adv.*, 2021, **7**, eabf1410.
- H. Yuan, K. P. F. Janssen, T. Franklin, G. Lu, L. Su, X. Gu, H. Uji-i, M. B. J. Roeloffs and J. Hofkens, *RSC Adv.*, 2015, **5**, 6829–6833.
- L. Scarabelli, M. Coronado-Puchau, J. J. Giner-Casares, J. Langer and L. M. Liz-Marzán, *ACS Nano*, 2014, **8**, 5833–5842.
- C. P. Joshi, M. S. Bootharaju, M. J. Alhilaly and O. M. Bakr, *J. Am. Chem. Soc.*, 2015, **137**, 11578–11581.
- M. Jash, A. C. Reber, A. Ghosh, D. Sarkar, M. Bodiuzzaman, P. Basuri, A. Baksi, S. N. Khanna and T. Pradeep, *Nanoscale*, 2018, **10**, 15714–15722.
- A. Desiredy, B. E. Conn, J. Guo, B. Yoon, R. N. Barnett, B. M. Monahan, K. Kirschbaum, W. P. Griffith, R. L. Whetten, U. Landman and T. P. Bigioni, *Nature*, 2013, **501**, 399–402.
- P. Engelhardt, in *Electron Microscopy: Methods and Protocols*, ed. J. Kuo, Humana Press, Totowa, NJ, 2007, pp. 365–385, DOI: [10.1007/978-1-59745-294-6_18](https://doi.org/10.1007/978-1-59745-294-6_18).
- K. R. Krishnadas, D. Ghosh, A. Ghosh, G. Natarajan and T. Pradeep, *J. Phys. Chem. C*, 2017, **121**, 23224–23232.
- T. Lahtinen, E. Hulkko, K. Sokołowska, T.-R. Tero, V. Saarnio, J. Lindgren, M. Pettersson, H. Häkkinen and L. Lehtovaara, *Nanoscale*, 2016, **8**, 18665–18674.
- F. Qin, T. Zhao, R. Jiang, N. Jiang, Q. Ruan, J. Wang, L.-D. Sun, C.-H. Yan and H.-Q. Lin, *Adv. Opt. Mater.*, 2016, **4**, 76–85.
- M. A. Habeeb Muhammed and T. Pradeep, *Chem. Phys. Lett.*, 2007, **449**, 186–190.

- 41 Y. Wang and T. Bürgi, *Nanoscale Adv.*, 2021, **3**, 2710–2727.
- 42 G. H. Woehrle, L. O. Brown and J. E. Hutchison, *J. Am. Chem. Soc.*, 2005, **127**, 2172–2183.
- 43 D. Bain, S. Maity and A. Patra, *Chem. Commun.*, 2020, **56**, 9292–9295.
- 44 M. R. Dewi, G. Laufersky and T. Nann, *RSC Adv.*, 2014, **4**, 34217–34220.
- 45 B. Yoon, W. D. Luedtke, R. N. Barnett, J. Gao, A. Desireddy, B. E. Conn, T. Bigioni and U. Landman, *Nat. Mater.*, 2014, **13**, 807–811.
- 46 I. M. Goldby, L. Kuipers, B. von Issendorff and R. E. Palmer, *Appl. Phys. Lett.*, 1996, **69**, 2819–2821.
- 47 A. Som, A. K. Samal, T. Udayabhaskararao, M. S. Bootharaju and T. Pradeep, *Chem. Mater.*, 2014, **26**, 3049–3056.
- 48 G. Wang, Y. Liu, C. Gao, L. Guo, M. Chi, K. Ijio, M. Maeda and Y. Yin, *Chem*, 2017, **3**, 678–690.
- 49 Q. Fan, K. Liu, J. Feng, F. Wang, Z. Liu, M. Liu, Y. Yin and C. Gao, *Adv. Funct. Mater.*, 2018, **28**, 1803199.
- 50 L. Chen, R. Li and P. Yang, Plasmonic nanoprobe based on the shape transition of Au/Ag core-shell nanorods to dumbbells for sensitive Hg-ion detection, *RSC Advances*, 2019, **9**, 17783–17790.

Supplementary Information

Tunable reactivity of silver nanoclusters: Facile route to synthesize a range of bimetallic nanostructures

Amrita Chakraborty,^a Megha Maria Stanley,^a Biswajit Mondal,^a Nonappa,^b Md Bodiuzzaman,^a Papri Chakraborty,^a M. P. Kannan,^a and Thalappil Pradeep^{a,*}

Affiliations:

^aDST Unit of Nanoscience and Thematic Unit of Excellence, Department of Chemistry, Indian Institute of Technology Madras, Chennai 600036, India.

^bFaculty of Engineering and Natural Sciences, Tampere University, FI-33101, Tampere, Finland.

Table of contents

SI No.	Title	Page No.
Fig. S1	Detailed characterization of AuNT	2
Fig. S2	TEM image of AuNTs dispersed in DMF	3
Fig. S3	Effect of the NC concentration on the reaction	3
Figure S4	Comparative powder XRD of AuNT and AuNT@1	4
Fig. S5	TEM EDS analysis of AuNT@2 in water	4
Fig. S6	TEM EDS analysis of AuNT@2 in DMF	4
Fig. S7	Characterization of reacted 3	5
Fig. S8	Characterization of AuNT@DMBT and AuNT@DMBT@1	5
Fig. S9	Characterization of AuNT@pMBA	6
Fig. S10	TEM EDS of AuNT@pMBA@3 nanocomposite and TEM image of the same after 5 months	6
Video S1	Tomographic reconstruction of AuNT	Attached

Video S2	Tomographic reconstruction of AuNT@1	Attached
----------	--------------------------------------	----------

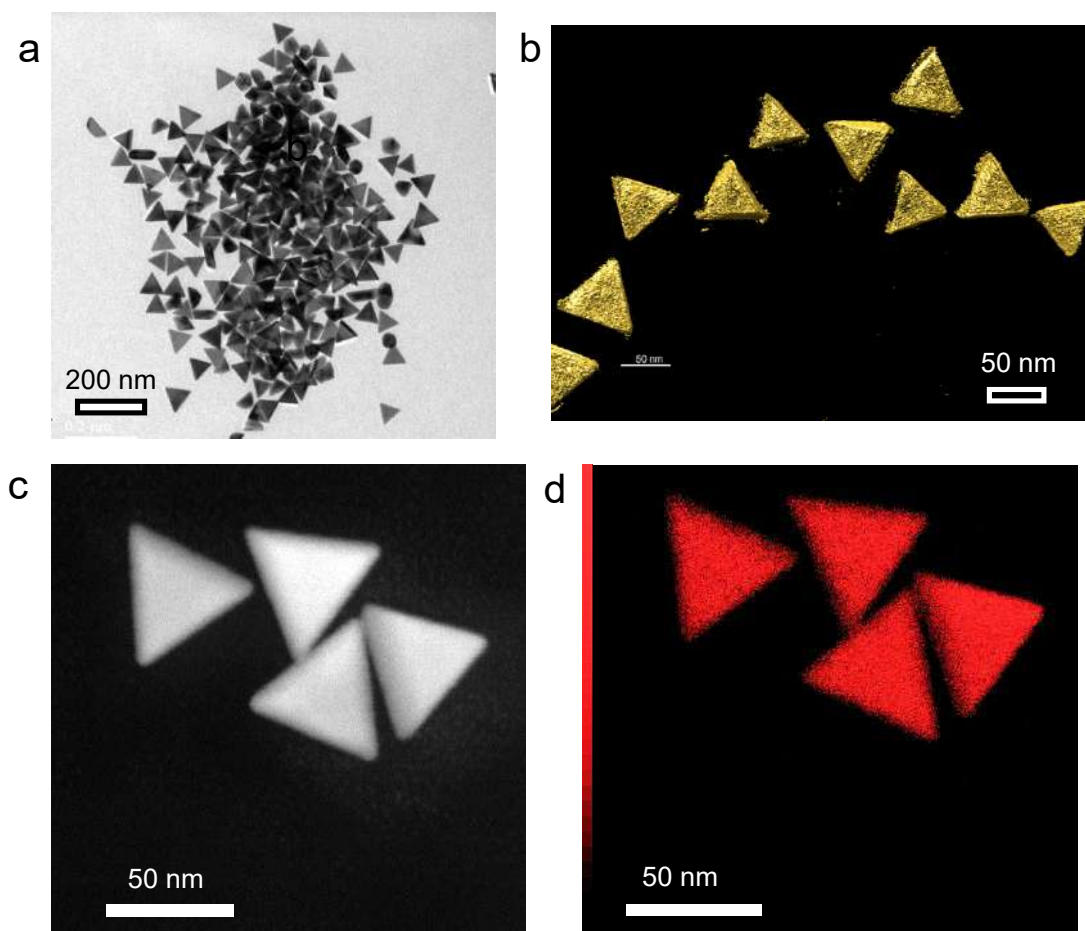


Fig. S1 Characterization of AuNT: a) TEM image, b) 3D tomographic reconstruction, c) dark-field STEM image, and d) corresponding EDS elemental mapping (Au is shown in red).

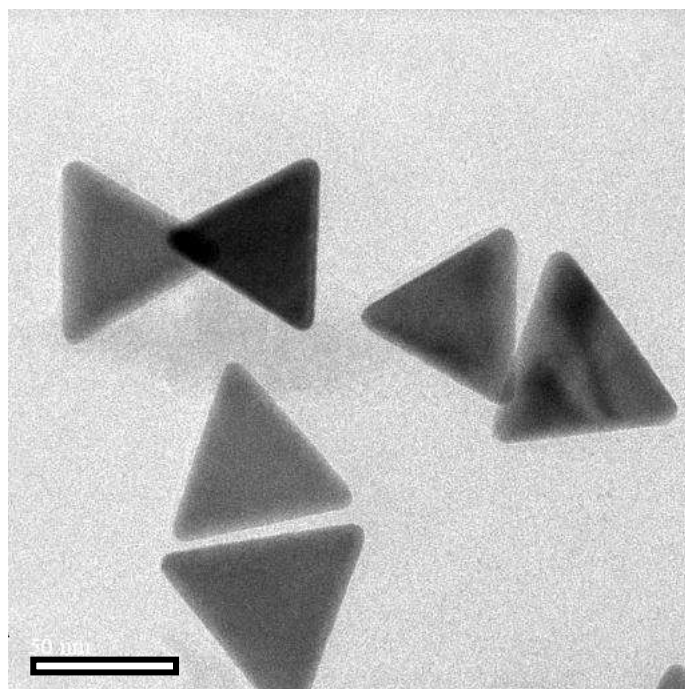


Fig. S2 TEM image of AuNTs dispersed in DMF after a week. Scale bar 50 nm.

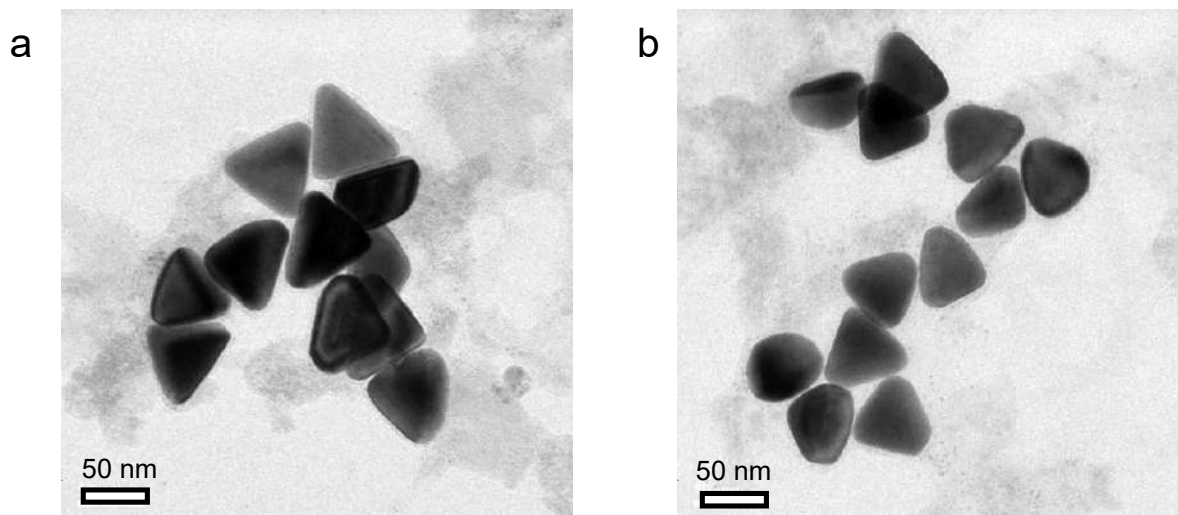


Fig. S3 TEM image of AuNT@**1** upon addition of a) 40 μ L, and b) 200 μ L **1** showing minor effect of NC concentration on the product.

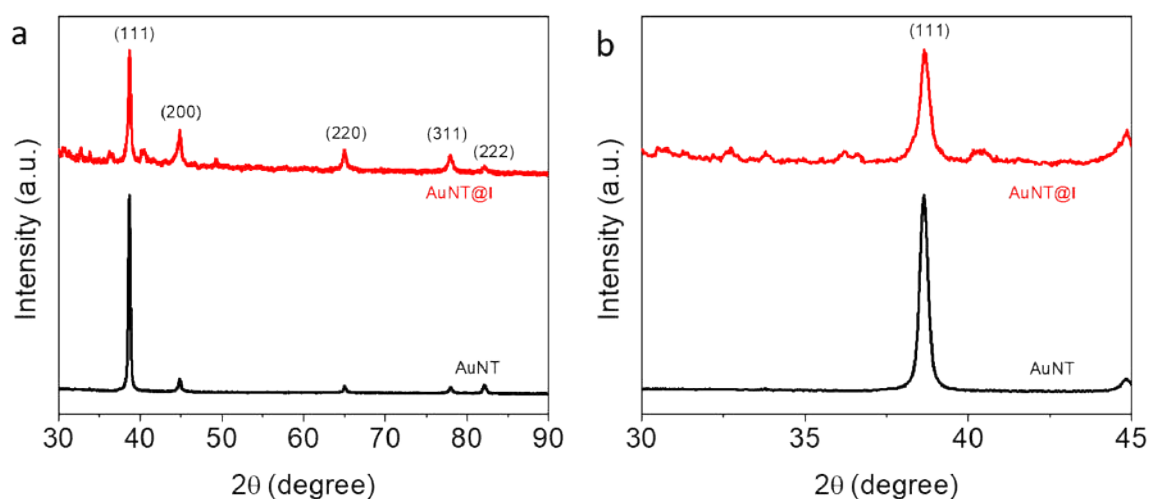


Fig. S4. Comparative powder XRD of AuNT and AuNT@1 (a) and magnified view of the peaks corresponding to the (111) lattice plane (b), showing no change in the peak position.

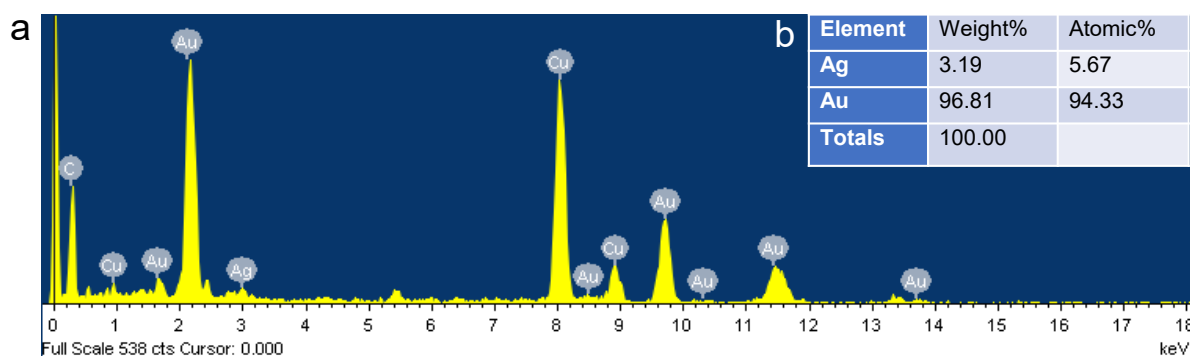


Fig. S5 TEM EDS analysis of AuNT@2 in water: EDS spectrum (a) and corresponding elemental quantification (b).

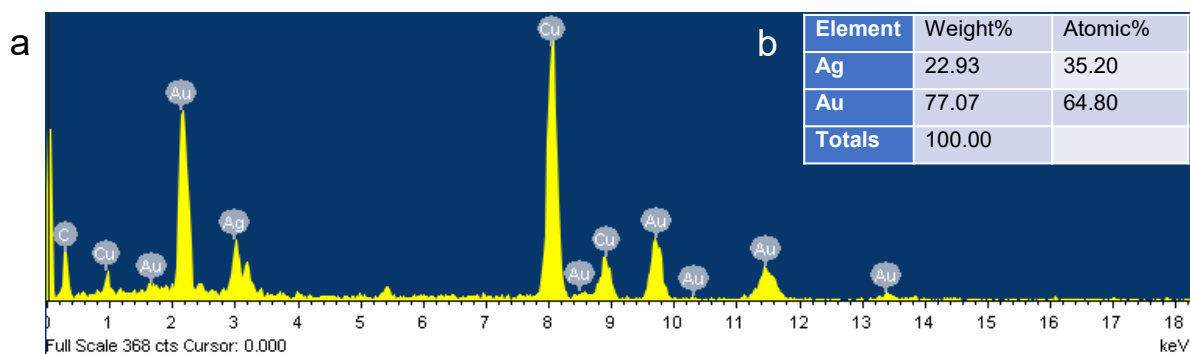


Fig. S6 TEM EDS analysis of AuNT@2 in DMF: EDS spectrum (a) and corresponding elemental quantification (b).

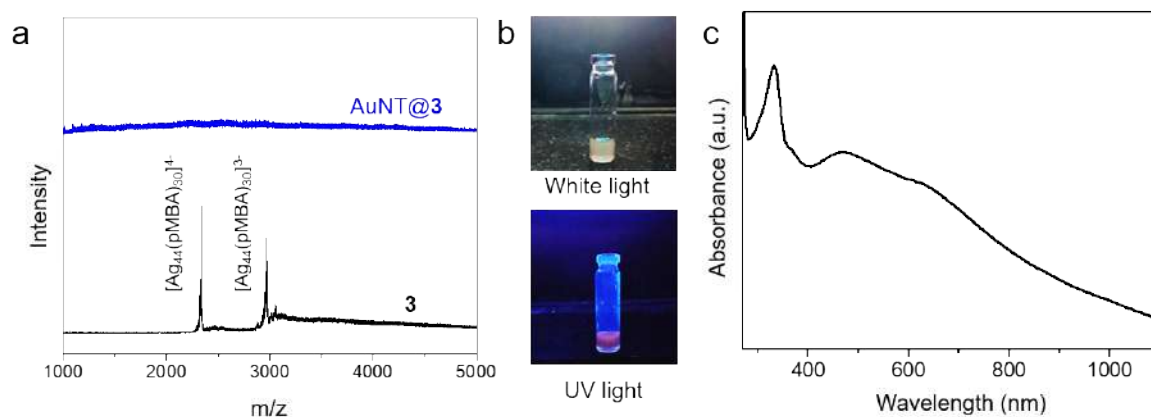


Fig. S7 Characterization of reacted **3**: (a) ESI MS spectra of parent NC and that reacted with AuNTs showing that the two molecular ion peaks of the NC disappear upon reaction. (b) photograph of the reaction mixture showing luminescent by-product and (c) corresponding UV-vis absorption spectrum.

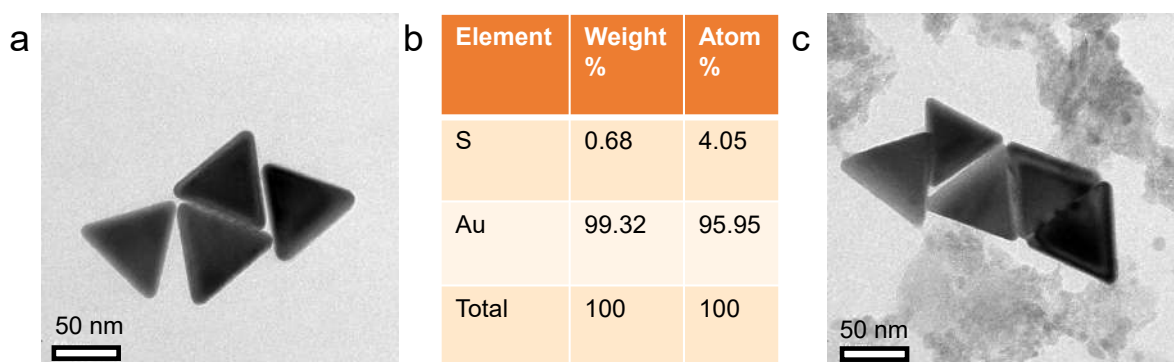


Fig. S8 Characterization of AuNT@DMBT and AuNT@DMBT@1: (a) TEM image of AuNT@DMBT, (b) TEM EDS elemental analysis of AuNT@DMBT showing the presence of S on the nanoparticles, and (c) TEM image of AuNT@DMBT@1 which shows no morphological changes.

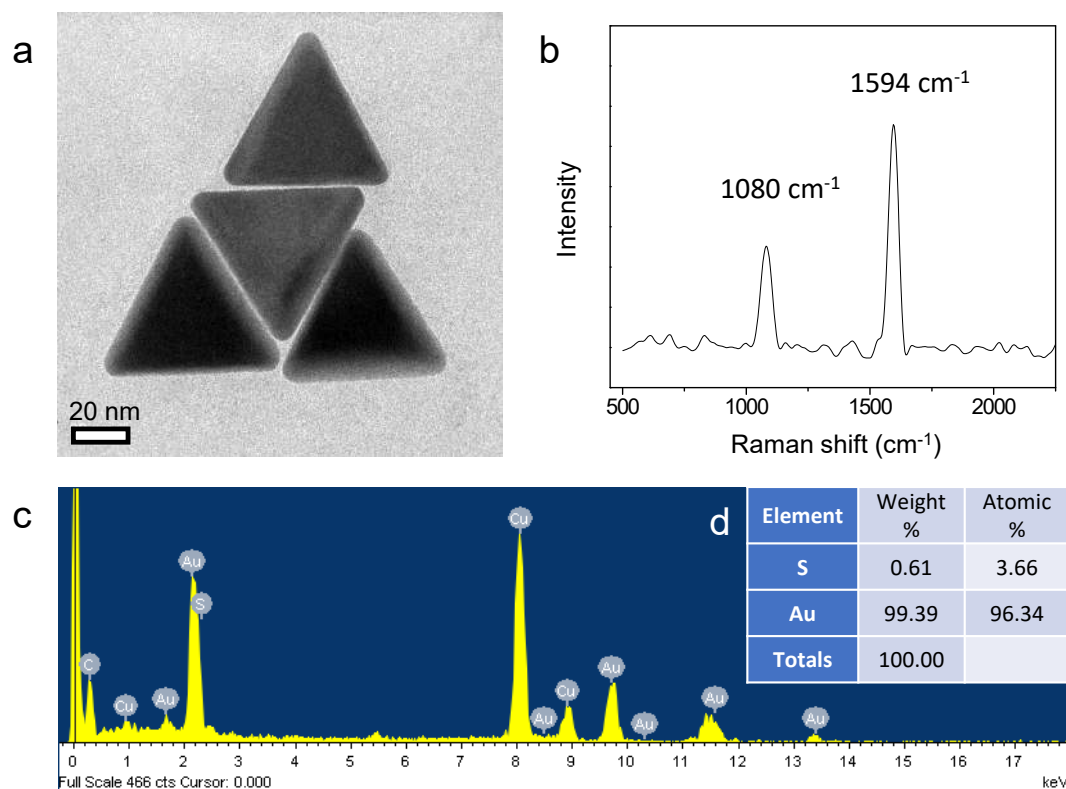


Fig. S9 Characterization of AuNT@pMBA: (a) TEM image of the particles showing no change in the size and shape as compared to the parent AuNTs. (b) Raman spectrum of AuNT@pMBA showing two peaks at 1080 cm^{-1} and 1594 cm^{-1} , the characteristic features of pMBA molecule, (c) TEM EDS spectrum and (d) corresponding elemental quantification showing the traces of S along the particles.

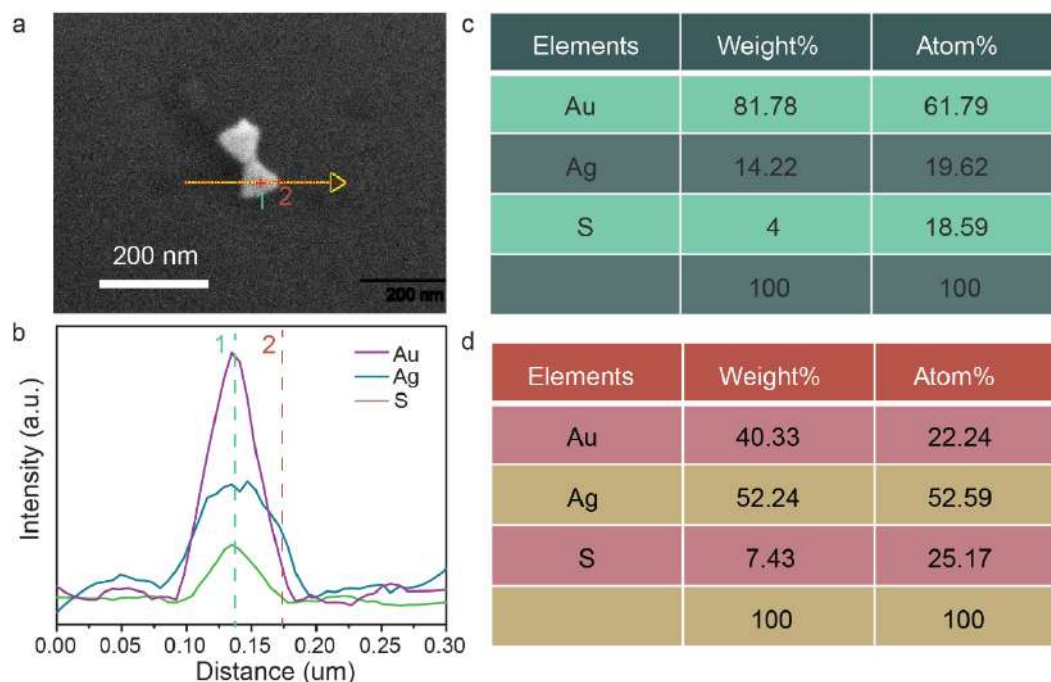


Fig. S10 (a) FESEM image of AuNT@pMBA@3, (b) EDS line profile drawn along the yellow arrow in Figure (a) showing the distribution of Au, Ag, and S along a particle, (c) elemental quantification at the centre of the particle (position 1) and (d) that at the edge (position 2).

Video S1 and S2 are attached separately.

Vertically Aligned Nanoplates of Atomically Precise Co_6S_8 Cluster for Practical Arsenic Sensing

Anagha Jose, Arijit Jana, Tanvi Gupte, Akhil S. Nair, Keerthana Unni, Ankit Nagar, Amoghavarsha R. Kini, B. K. Spoorthi, Sourav Kanti Jana, Biswarup Pathak,* and Thalappil Pradeep*



Cite This: *ACS Materials Lett.* 2023, 5, 893–899



Read Online

ACCESS |



Metrics & More

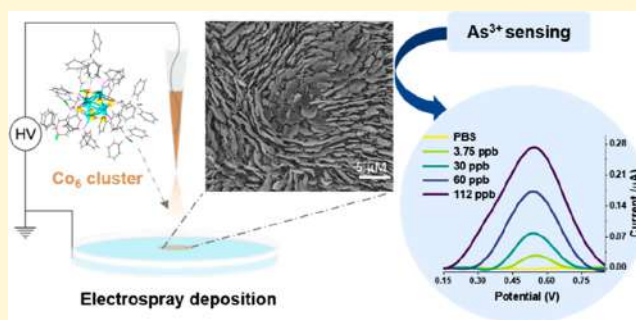


Article Recommendations



Supporting Information

ABSTRACT: Two-dimensional nanostructures with atomically precise building blocks have potential applications in catalysis and sensing. However, structural instability and surface reactivity limit their practical use. In this work, we demonstrate the formation of vertically aligned nanoplates of the $[\text{Co}_6\text{S}_8\text{DPPE}_6\text{Cl}_6]$ cluster (Co_6 in short), protected by 1,2-bis(diphenylphosphino)ethane, using ambient electrospray deposition (ESD). Charged microdroplets of Co_6 formed by ESD on a water surface created such nanostructures. Preferential arrangement of clusters in the nanoplates with enhanced surface area results in sensitive and selective electrochemical response toward arsenite down to 5 parts per billion, in tap water. Density functional theory calculations reveal the preferential binding of arsenite with Co_6 . Our work points to a practical application of atomically precise clusters of large societal relevance.



INTRODUCTION

Atomically precise clusters of noble metals, metal oxides, and chalcogenides are expanding the boundaries of materials chemistry.^{1–8} Quantized electronic structures due to atomic confinement leading to new photophysical, chemical, catalytic, and magnetic properties of these materials have resulted in several advancements.^{9–16} One of the obvious areas of their impact is in sensors due to the possibility of a large number of accessible surface sites and the ability to tune the sensitivity of analytes to their varying electronic structure.¹⁷ As a result, optical and fluorescence sensors to detect chemical, biochemical, and elemental species have been reported.^{18–22} However, the use of such sensors in practical applications has been lacking either due to the reduced stability of such systems, selectivity toward analytes, limits of analysis, or cost.²³ Therefore, atomically precise clusters, synthesized from inexpensive precursors and with superior stability, are essential for expanding the utility of these materials.

Arsenic in drinking water affects over 120 million people worldwide, and its grip is expanding continuously due to the excessive use of groundwater, fertilizers, and agrochemicals.^{24,25} A practical arsenic sensor in water without the need for preconcentration and sophisticated instrumentation is very much in need. Key to developing such practical electrochemical devices for arsenic is the development of stable,

selective, sensitive, and affordable electrodes.^{26,27} Increased sensitivity requires the electrode to be composed of specific chemical species with morphologies or superstructural microcrystalline assemblies, enhancing the specific surface areas.^{28–30} In view of the sensitivity of cobalt-based systems for arsenic sensing,³¹ we decided to explore the atomically precise Co_6 cluster system to develop a practical sensor. We have developed a method of ambient electrospray deposition (ESD) of the Co_6 cluster system leading to their 2D nanostructures with unique morphologies.^{32–34} In this work, we present a practical electrochemical arsenic sensor based on the resulting structures for arsenite detection down to 5 parts per billion (ppb) in tap water implementable in field applications. As the safe limit of arsenic in drinking water is 10 ppb, and the detection is demonstrated in tap water, practical application of such materials is possible. Cost per analysis is estimated to be less than \$1 per measurement.

Received: January 27, 2023

Accepted: February 17, 2023

Published: February 22, 2023



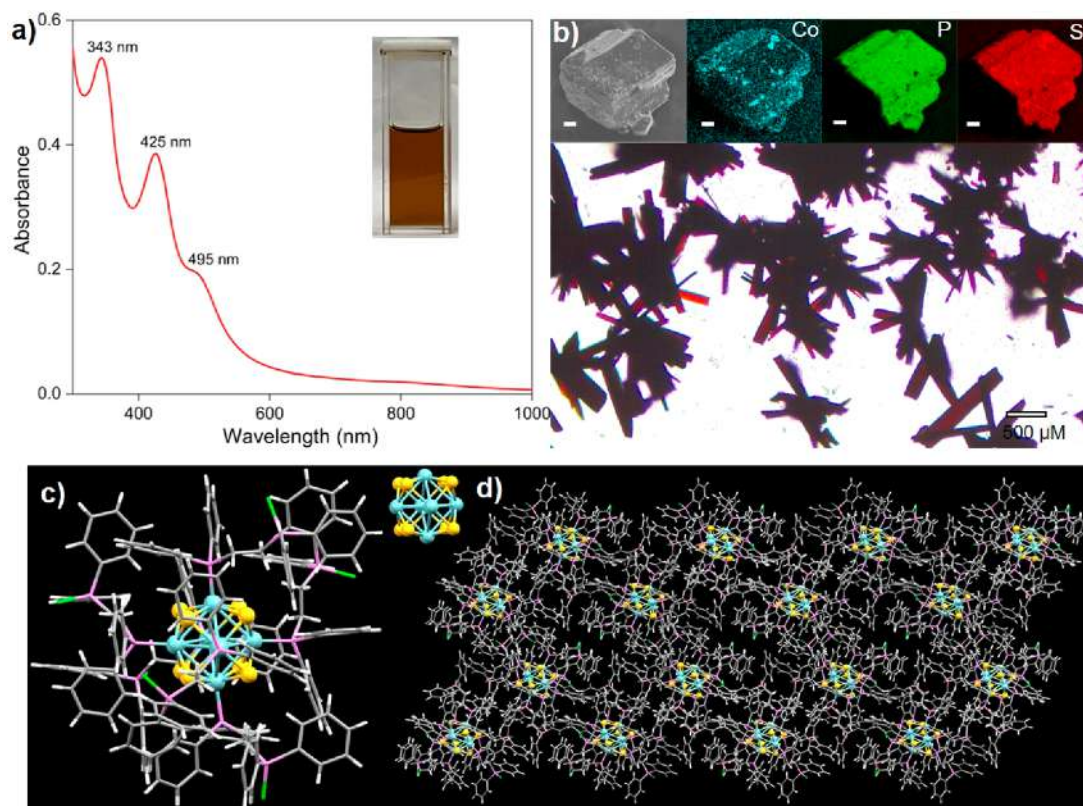


Figure 1. (a) UV–vis absorption spectrum of Co_6 in DCM (inset shows the photograph of the respective solution). (b) Optical microscopic image of the crystals (inset shows the FESEM micrograph of a crystal and the respective elemental mapping; scale bar corresponds to 500 nm). (c) Molecular structure of the cluster including ligands (inset shows the Co_6S_8 core, with an octacapped octahedron geometry). (d) Large area supramolecular packing of $[\text{Co}_6\text{S}_8\text{DPPE}_6\text{Cl}_6]$ in the b plane. Atomic color codes for c and d: cyan = cobalt, yellow = sulfur, pink = phosphorus, green = chlorine, gray = carbon, and white = hydrogen.

RESULTS AND DISCUSSION

The Co_6 cluster was synthesized using a reported protocol³⁵ with a different ligand, namely, 1,2-bis(diphenylphosphino)ethane (DPPE; detailed synthetic procedure is given in the SI). The as-synthesized cluster in dichloromethane (DCM) was brownish in color and exhibited well-defined optical absorption peaks in a characteristic pattern emphasizing its molecular nature (Figure 1a). The stability of the cluster was monitored using time-dependent UV–vis in solution, and no change was seen up to 60 days under ambient conditions (Figure S1). We have observed almost identical absorption features in multiple solvents (Figure S2). Cuboidal single crystals of the cluster were grown in 7 days from a saturated DCM solution upon layering with hexane at 4 °C (Figure 1b). Field emission scanning electron microscopic (FESEM) images of the crystal (shown in the inset of Figure 1b) correlate with the optical micrograph. Energy-dispersive spectroscopy (EDS; Figure S3) and elemental mapping of the crystals (shown in the inset of Figure 1b) confirm the presence of Co, S, P, and Cl in them. Single crystal X-ray diffraction (SCXRD) measurements gave the structural framework of the cluster shown in Figure 1c. It exhibited a monoclinic unit cell with the space group of $P2_1/c$ (detailed crystallographic information is given in Table S1 and S2). The core of the cluster is arranged in an octahedral fashion with six Co atoms, having an average Co–Co bond length of ~ 2.8 Å. Each triangular face of the Co_6 octahedron is further protected by eight isolated S atoms, resulting in an octacapped octahedral geometry (shown in the inset of Figure 1c). The average Co–S bond length is ~ 2.2 Å and each S sits

~ 1.5 Å away from the centroid of the respective Co_3 faces (shown in Figure S4). A bond length analysis shows strong metal–metal and metal–sulfide interactions, which provide rigidity to the kernel of the cluster.

Six bidentate DPPE ligands protect the cluster; one phosphine end of DPPE is directly bonded to the cobalt, and the other end binds with the chlorine resulting in average Co–P and P–Cl bond lengths of 2.12 and 2.48 Å, respectively. Supramolecular packing of the cluster reveals that four clusters are packed inside the unit cell (Figure S5). Large area packing shows the AB...AB kind of packing of the clusters (Figure 1d) through CH- π , CH-Cl, CH-P, and Cl- π interactions (Figure S6). High resolution electrospray ionization mass spectrometry (HRESI-MS) of the cluster showed a peak at m/z 3213.96 in the positive ion mode, in the singly charged state, which corresponds to the composition of the cluster $[\text{Co}_6\text{S}_8(\text{DPPE})_6\text{Cl}_6]$ as revealed by SCXRD (Figure S7). The presence of these elements has been further verified using X-ray photoelectron spectroscopy (XPS; Figure S8). Experimental X-ray diffraction patterns obtained from the crystalline samples of Co_6 cluster were in good agreement with the simulated data (shown in Figure S9). The strong appearance of 6.21, 6.42, 6.6, 7.19, 8.15, 11.6, and 14.83 diffraction peaks in the 5 – 15° 2θ range correspond to (012), (110), (102), (11–2), (004), (122) and (116) lattice planes, respectively. However, several features were not clearly visible due to their poor intensities. Some intensity variations were also seen. Thermogravimetric (TG) and differential thermogravimetric (DTG) analysis of microcrystalline Co_6 was carried out for the

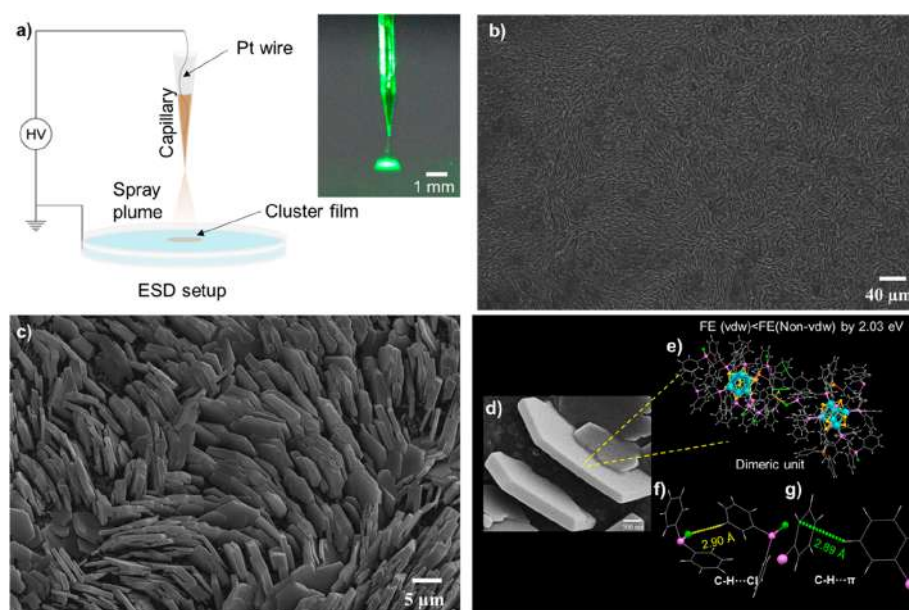


Figure 2. (a) Schematic representation of our home-built electro-spray setup. Inset shows a photographic image of the nanospray plume generated from the tip of the capillary. The plume is visualized using a green laser, which scatters from it. (b) Large area and (c) magnified FESEM micrographs of the vertically aligned nanoplates. (d) An expanded image of microcrystalline hexagonal nanoplates. (e) Intercluster interaction leading to such a superstructure. (f, g) Ligand-centered short contact interactions between two clusters.

heating range from 25 to 700 °C. No mass loss was observed up to 400 °C, suggesting superior thermal stability in the solid state (Figure S10).

Time-dependent density functional theory (TD-DFT) calculations (see details in SI) were carried out to obtain an atomistic understanding of the optical properties of $[\text{Co}_6\text{S}_8(\text{DPPE})_6\text{Cl}_6]$.³⁶ The obtained theoretical absorption spectrum is in agreement with the experimental spectrum (Figure S11a). The frontier molecular orbital (FMO) analysis revealed the contribution of the molecular orbitals corresponding to 321, 427, and 498 nm (Figure S11b). Projected density of states (PDOS) analysis indicates that the occupied states have major contributions from Co(d) states and P(sp) states, whereas the unoccupied states are mainly occupied by S(sp) and Cl(sp) states centered at the ligands encapsulating the Co_6 kernel (Figure S11c). This is further supported by the Kohn–Sham orbital analysis (Figure S11d). However, we note that the HOMO and LUMO states have a higher contribution from the ligands than the Co_6 kernel indicating the significant role of ligands in governing the electronic properties of the cluster (Figure S12).

We created self-assembled superstructures of the cluster using the ESD technique. A schematic of our home-built ESD setup is shown in Figure 2a. The cluster solution in DCM was sprayed as solvated microdroplets through a glass capillary tip (diameter 30–35 μm) by applying a positive potential of 2.75–3 kV (photograph of spray plume is shown in the inset of Figure 2a) at a flow rate of 30 $\mu\text{L h}^{-1}$. After 30 min of continuous deposition of such charged microdroplets onto an ultrapure water substrate, a brownish thin film resulted, floating on it. From our previous report, the spray current measured between the tip and the substrate was 40 nA.³² The obtained film was carefully transferred to a suitable substrate (glass slide or aluminum foil) for further studies. An optical micrograph of the film (shown in Figure S13) demonstrates its transparent nature. Surprisingly, the FESEM micrograph (Figure 2b and S14) reveals an assembly of vertically aligned

nanoplates with a thickness of 200 ± 100 nm and an edge length of 600 ± 200 nm. Atomic force microscopy (AFM) analysis of the assembly of vertically aligned nanoplates gave more insights into the morphology. The nanoplates were found to have a thickness of 200 ± 100 nm with a width of 450 ± 200 nm (Figure S15). An expanded view of the image suggests the vertical alignment of most of the platelets (Figure 2c). FESEM images collected from different cluster batches demonstrated the reproducibility of these nanostructures (Figure S16). We note that the oriented assembly of nanoclusters leading to specific morphology, such as nano-sheets, fibers, *etc.*, was observed earlier.^{37–40}

UV–vis absorption studies of the dissolved ESD film showed well-defined absorption features matching with the as-synthesized cluster (Figure S17a). ESI-MS of the ESD film showed a peak at m/z 3213.96 in the positive ion mode which matches well with the molecular composition of the Co_6 cluster (Figure S17b). Solid-state IR studies were carried out on both the drop-casted cluster and the ESD film, and both were in good agreement (Figure S18). These results concluded that the cluster remains intact upon ESD. To ensure the uniqueness of the ESD technique, we drop-casted the same cluster solution (in DCM) onto a water surface. FESEM images of the films formed reveal no specific morphology, inferring that nanoplates are specific to the deposition technique (Figure S19). The formation of nanoplates using ESD is also substrate specific, and we have confirmed it by taking different substrates such as conducting carbon cloth, glycerol, and ethylene glycol (Figures S20, S21, and S22). This signifies that the use of a liquid hydrophilic substrate is essential to create such nanostructures. This oriented microcrystalline assembly could be a result of specific intramolecular interactions. To further understand such interactions, we have carried out periodic DFT calculations.⁴¹ We have considered a dimer constituted by two $[\text{Co}_6\text{S}_8(\text{DPPE})_6\text{Cl}_6]$ units and analyzed the energetics of its formation from two monomer units for studying the role of intercluster interactions with and

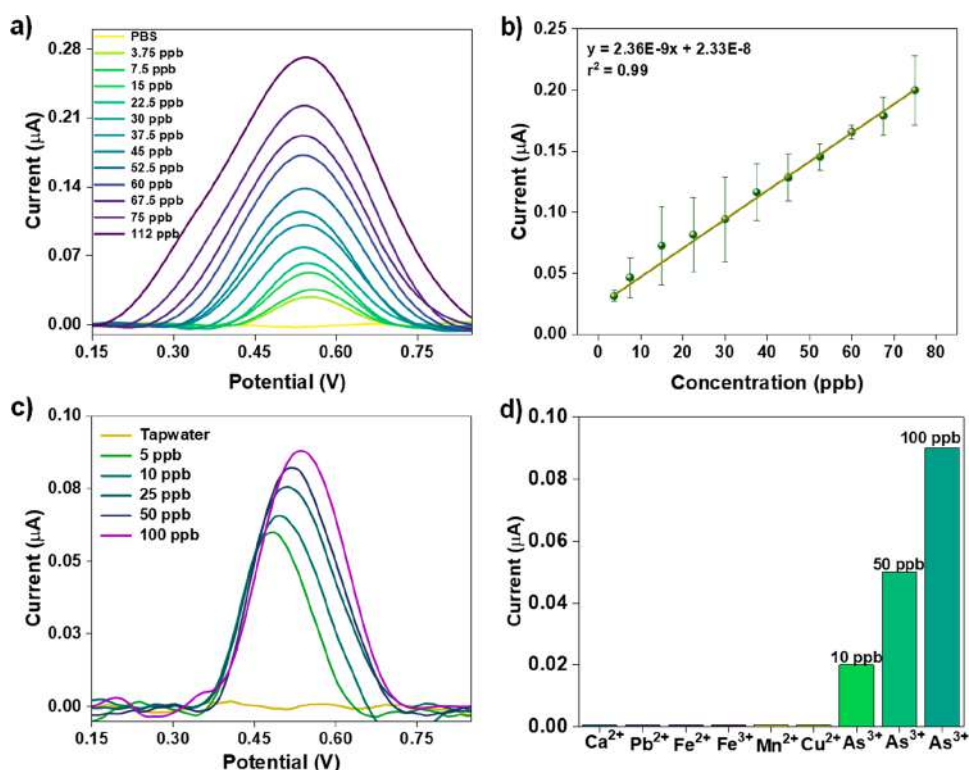


Figure 3. (a) Baseline corrected voltammetric profiles of the ESD-modified Co₆ GC electrode in response to various concentrations (3.75–112 ppb) of As³⁺ in a buffer solution. (b) Linearity analysis of voltammetric response for different concentrations of As³⁺. Error bars represent interelectrode variability. (c) Baseline corrected voltammetric profiles for various concentrations (5–100 ppb) of As³⁺ in tap water. (d) Interfering ion studies with different metal ions (100 ppb each of Ca²⁺, Pb²⁺, Fe²⁺, Fe³⁺, Mn²⁺, and Cu²⁺ added sequentially) and the response of arsenic in the presence of all of the metal ions.

without van der Waals (vdW) considerations.⁴² The calculated dimer formation energy when vdW interactions are taken into account is found to be less than the non-vdW scenario by 2.03 eV (optimized structure is in Figure 2e). This indicates that the noncovalent interactions such as CH \cdots Cl and CH \cdots π mediated by the phenyl rings of ligands provide structural stability of the superstructure (Figure 2fg).

These oriented nanoplates were cast on a glassy carbon (GC) electrode using 5 wt % nafion, and the deposited film contained intact nanoplates (Figure S23). Electrochemical arsenic (As³⁺) sensing experiments were carried out using voltammetry. The experimental details are presented in the SI. Different concentrations of As³⁺ were prepared by dissolving NaAsO₂ in phosphate-buffered saline (PBS, pH \sim 7). The electrode showed an excellent current response to As³⁺ in PBS as shown in Figure 3a, over a wide concentration window of 4 to 112 ppb. The electrode system is stable for multiple measurements, and all of the concentration-dependent measurements shown in Figures 3a and S24 were performed using a single electrode. The increase in current upon increasing the concentration is due to enhanced electrocatalytic oxidation of arsenite onto the exposed nanoplates. Control experiments were also performed for bare GC electrode and as-synthesized Co₆ cluster (Figures S25 and S26). No significant current response was observed for these experiments. Vertically aligned nanoplates with specific exposed planes and consequent cluster sites probably act as catalytically active surfaces for As³⁺ binding.

We have investigated the suitable binding of As(OH)₃ with the Co₆ cluster using DFT calculations, which reveals that As(OH)₃ exhibits a strong affinity to the cluster with a binding

energy of -0.63 eV in correspondence with the experimental observation (Figure S27). It may be noted that arsenite exists as the neutral As(OH)₃ species at pH 7. This is further supported by the charge density difference (CDD) analysis of As(OH)₃ binding to the Co₆ cluster (Figure S28). Detailed structural analysis uncovers that the phosphine end of the ligand bonded with cobalt has a high affinity with As³⁺. Although the free phosphine end interacts with As³⁺, the cavity made by the flexible arms of DPPE interacts with the $-\text{OH}$ of As(OH)₃ (shown in Figure S29a). Bader charge analysis of the Co₆S₈P₆ unit reveals that all P atoms bonded with the Co are negatively charged, which favors electrostatic interaction with the positively charged arsenic (Figure S29b).

The sensor behaves linearly in the concentration window relevant to drinking water. The sensitivity was calculated to be 3.496×10^{-9} $\mu\text{A/ppb/mm}^2$, and the estimated limit of detection (LOD) was 0.66 ppb, which is far below the guideline value of arsenic in drinking water (10 ppb), as recommended by the World Health Organization (WHO).^{43,44} A theoretical LOD of 0.825 ppb using CoOx on a glassy carbon electrode in PBS at pH 7 was reported previously.³¹ Similar experiments were conducted in tap water with the gradual addition of As³⁺ over a concentration window of 5–100 ppb (Figure 3c). As may be inferred from this data set, measurements below 10 ppb can be done easily in field conditions. Interference studies with different metal ions, commonly present in arsenic-contaminated water, were performed in tap water (Figure 3d) and PBS (Figure S30). The concentration of all of the metal ions (Ca²⁺, Mn²⁺, Fe²⁺, Fe³⁺, Cu²⁺, and Pb²⁺) was maintained at 100 ppb each during the studies. Later, we analyzed three arsenic concentrations

(10, 50, and 100 ppb) which were added sequentially in the presence of these ions at 100 ppb each. The electrode responds specifically to As^{3+} both in tap water and in PBS. The recyclability of the working electrode for arsenic detection was verified by performing cyclic voltammetry (CV) in PBS for 40 cycles with a fixed arsenite concentration of 100 ppb (Figure S31). The composition of the nanoplates after electrochemical arsenic sensing experiments was verified by UV-vis measurement (Figure S32). The tests conducted individually and collectively show the specificity and practical utility of the sensor.

The analysis can be performed without the need for preconcentration, additional reagents, and sample processing, which enables rapid measurements. From a practical perspective, the amount of cobalt cluster in an electrode is approximately 0.5 ng. With the cost of the binder and other consumables, the materials cost per electrode is expected to be less than \$0.5. As the electrode can be reused, costs can come down further. Therefore, each analysis can be done below a cost of \$1.

In conclusion, we present a practical arsenic sensing method built using an atomically precise Co_6 cluster working down to 5 ppb in tap water. A new cobalt cluster, $[\text{Co}_6\text{S}_8\text{DPPE}_6\text{Cl}_6]$, was synthesized using ambient conditions and characterized using SCXRD and other spectroscopic studies. The sensing platform was prepared by ESD of the cluster on the water surface resulting in vertically aligned crystalline nanoplates. The interactions of charged microdroplets of cluster ions with the water surface resulted in the preferential organization of these nanoplates, enhancing the surface area and selectivity leading to an excellent response to As^{3+} . We obtained a LOD of 0.66 ppb, which is well below the guideline value of arsenic in drinking water (10 ppb) as recommended by WHO. Ease of availability, selectivity, sensitivity, and cost-effectiveness made it a good candidate for practical arsenic sensing. We note that affordable arsenic sensing below 10 ppb in water can have far reaching implications for global health.

■ ASSOCIATED CONTENT

SI Supporting Information

The Supporting Information is available free of charge at <https://pubs.acs.org/doi/10.1021/acsmaterialslett.3c00085>.

Experimental details, instrumentation, theoretical calculations, crystal data, characterization of the cluster by UV-vis, ESI-MS, SEM, XPS, PXRD, and TGA; characterization of ESD film by UV-vis, ESI-MS, AFM, SEM, and FTIR; CV of control experiments of arsenic sensing (PDF)

Crystallographic information (CIF)

■ AUTHOR INFORMATION

Corresponding Authors

Thalappil Pradeep – Department of Chemistry, DST Unit of Nanoscience (DST UNS) and Thematic Unit of Excellence (TUE), Indian Institute of Technology Madras, Chennai 600036, India; International Centre for Clean Water, Chennai 600113, India; orcid.org/0000-0003-3174-534X; Email: pradeep@iitm.ac.in

Biswarup Pathak – Department of Chemistry, Indian Institute of Technology Indore (IIT Indore), Indore 453552, India; orcid.org/0000-0002-9972-9947; Email: biswarup@iiti.ac.in

Authors

Anagha Jose – Department of Chemistry, DST Unit of Nanoscience (DST UNS) and Thematic Unit of Excellence (TUE), Indian Institute of Technology Madras, Chennai 600036, India

Arijit Jana – Department of Chemistry, DST Unit of Nanoscience (DST UNS) and Thematic Unit of Excellence (TUE), Indian Institute of Technology Madras, Chennai 600036, India

Tanvi Gupte – Department of Chemistry, DST Unit of Nanoscience (DST UNS) and Thematic Unit of Excellence (TUE), Indian Institute of Technology Madras, Chennai 600036, India; orcid.org/0000-0002-0518-8482

Akhil S. Nair – Department of Chemistry, Indian Institute of Technology Indore (IIT Indore), Indore 453552, India; orcid.org/0000-0001-5723-3970

Keerthana Unni – Department of Chemistry, DST Unit of Nanoscience (DST UNS) and Thematic Unit of Excellence (TUE), Indian Institute of Technology Madras, Chennai 600036, India

Ankit Nagar – Department of Chemistry, DST Unit of Nanoscience (DST UNS) and Thematic Unit of Excellence (TUE), Indian Institute of Technology Madras, Chennai 600036, India

Amoghavarsha R. Kini – Department of Chemistry, DST Unit of Nanoscience (DST UNS) and Thematic Unit of Excellence (TUE), Indian Institute of Technology Madras, Chennai 600036, India

B. K. Spoorthi – Department of Chemistry, DST Unit of Nanoscience (DST UNS) and Thematic Unit of Excellence (TUE), Indian Institute of Technology Madras, Chennai 600036, India

Sourav Kanti Jana – Department of Chemistry, DST Unit of Nanoscience (DST UNS) and Thematic Unit of Excellence (TUE), Indian Institute of Technology Madras, Chennai 600036, India; orcid.org/0000-0001-5772-7022

Complete contact information is available at:

<https://pubs.acs.org/doi/10.1021/acsmaterialslett.3c00085>

Author Contributions

A. Jose performed synthesis, crystallization, and other experimental studies. A. Jana, K.U., and B.K.S. performed electrospray deposition studies. T.G., A. Jose, and A. Jana performed electrochemical sensing studies. A.S.N. performed theoretical calculations under the guidance of B.P. A.N. performed FESEM studies. A.R.K. performed crystallization and X-ray photoelectron spectroscopic studies. S.K.J. was involved in the discussion of experimental data. A. Jose wrote the first draft of the manuscript with inputs from T.P. and A. Jana, and all coauthors contributed to finalizing it. T.P. conceptualized the work and finalized the manuscript. CRediT: Anagha Jose conceptualization, investigation, writing-original draft; Keerthana Unni investigation.

Notes

The authors declare no competing financial interest.

■ ACKNOWLEDGMENTS

We thank the Sophisticated Analytical Instruments Facility, IIT Madras, and Sudhadevi Antharjanam for the SC-XRD measurements. A.J. thanks MHRD for the PMRF research grant. T.P. acknowledges funding from the Centre of Excellence on Molecular Materials and Functions under the

Institution of Eminence scheme of IIT Madras. We thank the Department of Science and Technology, Government of India, for continuous support of our research program.

REFERENCES

- (1) Chakraborty, I.; Pradeep, T. Atomically Precise Clusters of Noble Metals: Emerging Link between Atoms and Nanoparticles. *Chem. Rev.* **2017**, *117*, 8208–8271.
- (2) Kang, X.; Li, Y.; Zhu, M.; Jin, R. Atomically Precise Alloy Nanoclusters: Syntheses, Structures, and Properties. *Chem. Soc. Rev.* **2020**, *49*, 6443–6514.
- (3) Murray, R. W. Nanoelectrochemistry: Metal Nanoparticles, Nanoelectrodes, and Nanopores. *Chem. Rev.* **2008**, *108*, 2688–2720.
- (4) Zhu, Y.; Lin, Q.; Zhong, Y.; Tahini, H. A.; Shao, Z.; Wang, H. Metal Oxide-Based Materials as an Emerging Family of Hydrogen Evolution Electrocatalysts. *Energy Environ. Sci.* **2020**, *13*, 3361–3392.
- (5) Chen, X.; Mao, S. S. Titanium Dioxide Nanomaterials: Synthesis, Properties, Modifications and Applications. *Chem. Rev.* **2007**, *107*, 2891–2959.
- (6) Roy, X.; Lee, C. H.; Crowther, A. C.; Schenck, C. L.; Besara, T.; Lalancette, R. A.; Siegrist, T.; Stephens, P. W.; Brus, L. E.; Kim, P.; Steigerwald, M. L.; Nuckolls, C. Nanoscale Atoms in Solid-State Chemistry. *Science*. **2013**, *341*, 157–160.
- (7) Gadjeva, N. A.; Champsaur, A. M.; Steigerwald, M. L.; Roy, X.; Nuckolls, C. Dimensional Control of Assembling Metal Chalcogenide Clusters. *Eur. J. Inorg. Chem.* **2020**, *2020*, 1245–1254.
- (8) Gholipour-Ranjbar, H.; Fang, H.; Guan, J.; Peters, D.; Seifert, A.; Jena, P.; Laskin, J. Designing New Metal Chalcogenide Nanoclusters through Atom-by-Atom Substitution. *Small* **2021**, *17*, 2002927.
- (9) Jin, R. Atomically Precise Metal Nanoclusters: Stable Sizes and Optical Properties. *Nanoscale* **2015**, *7*, 1549–1565.
- (10) Hulkko, E.; Lopez-Acevedo, O.; Koivisto, J.; Levi-Kalishman, Y.; Kornberg, R. D.; Pettersson, M.; Häkkinen, H. Electronic and Vibrational Signatures of the Au₁₀₂(p-MBA)₄₄ Cluster. *J. Am. Chem. Soc.* **2011**, *133*, 3752–3755.
- (11) Du, X.; Jin, R. Atomically Precise Metal Nanoclusters for Catalysis. *ACS Nano* **2019**, *13*, 7383–7387.
- (12) Jain, P. K.; Huang, X.; El-Sayed, I. H.; El-Sayed, M. A. Noble Metals on the Nanoscale: Optical and Photothermal Properties and Some Applications in Imaging, Sensing, Biology, and Medicine. *Acc. Chem. Res.* **2008**, *41*, 1578–1586.
- (13) Ye, R.; Hurlburt, T. J.; Sabyrov, K.; Alayoglu, S.; Somorjai, G. A. Molecular Catalysis Science: Perspective on Unifying the Fields of Catalysis. *Proc. Natl. Acad. Sci. U. S. A.* **2016**, *113*, 5159–5166.
- (14) Zhu, M.; Aikens, C. M.; Hendrich, M. P.; Gupta, R.; Qian, H.; Schatz, G. C.; Jin, R. Reversible Switching of Magnetism in Thiolate-Protected Au₂₅ Superatoms. *J. Am. Chem. Soc.* **2009**, *131*, 2490–2492.
- (15) Kang, X.; Zhu, M. Tailoring the Photoluminescence of Atomically Precise Nanoclusters. *Chem. Soc. Rev.* **2019**, *48*, 2422–2457.
- (16) Wang, X.; Zhao, L.; Li, X.; Liu, Y.; Wang, Y.; Yao, Q.; Xie, J.; Xue, Q.; Yan, Z.; Yuan, X.; Xing, W. Atomic-Precision Pt₆ Nanoclusters for Enhanced Hydrogen Electro-Oxidation. *Nat. Commun.* **2022**, *13*, 1–10.
- (17) Du, Y.; Sheng, H.; Astruc, D.; Zhu, M. Atomically Precise Noble Metal Nanoclusters as Efficient Catalysts: A Bridge between Structure and Properties. *Chem. Rev.* **2020**, *120*, 526–622.
- (18) Chen, X.; Zhou, Y.; Peng, X.; Yoon, J. Fluorescent and Colorimetric Probes for Detection of Thiols. *Chem. Soc. Rev.* **2010**, *39*, 2120–2135.
- (19) Guan, G.; Zhang, S. Y.; Cai, Y.; Liu, S.; Bharathi, M. S.; Low, M.; Yu, Y.; Xie, J.; Zheng, Y.; Zhang, Y. W.; Han, M. Y. Convenient Purification of Gold Clusters by Co-Precipitation for Improved Sensing of Hydrogen Peroxide, Mercury Ions and Pesticides. *Chem. Commun.* **2014**, *50*, 5703–5705.
- (20) March, G.; Nguyen, T. D.; Piro, B. Modified Electrodes Used for Electrochemical Detection of Metal Ions in Environmental Analysis. *Biosensors* **2015**, *5*, 241–275.
- (21) Mathew, A.; Pradeep, T. Noble Metal Clusters: Applications in Energy, Environment, and Biology. *Part. Part. Syst. Charact.* **2014**, *31*, 1017–1053.
- (22) Yarov, K. E.; Mir, W. J.; Song, X.; Gutiérrez-Arzaluz, L.; Naphade, R.; Nematulloev, S.; Chen, C.; Huang, R.-W.; Shao, B.; Hasanov, B. E.; Han, Y.; Mohammed, O. F.; Bakr, O. M. Mn⁴⁺-Doped Fluoride Nanocrystals Enable High-Resolution Red-Emitting X-Ray Imaging Screens. *ACS Materials Lett.* **2022**, *4*, 2273–2281.
- (23) Male, K. B.; Hrapovic, S.; Santini, J. M.; Luong, J. H. T. Biosensor for Arsenite Using Arsenite Oxidase and Multivalled Carbon Nanotube Modified Electrodes. *Anal. Chem.* **2007**, *79*, 7831–7837.
- (24) Ravenscroft, P. *Predicting the Global Extent of Arsenic Pollution of Groundwater and Its Potential Impact on Human Health*; UNICEF: New York, 2007.
- (25) Podgorski, J.; Berg, M. Global Threat of Arsenic in Groundwater. *Science*. **2020**, *368*, 845–850.
- (26) Yang, M.; Chen, X.; Jiang, T. J.; Guo, Z.; Liu, J. H.; Huang, X. J. Electrochemical Detection of Trace Arsenic(III) by Nanocomposite of Nanorod-Like α -MnO₂ Decorated with ~5 nm Au Nanoparticles: Considering the Change of Arsenic Speciation. *Anal. Chem.* **2016**, *88*, 9720–9728.
- (27) Jana, S. K.; Chaudhari, K.; Islam, M. R.; Natarajan, G.; Ahuja, T.; Som, A.; Paramasivam, G.; Raghavendra, A.; Sudhakar, C.; Pradeep, T. Selective and Practical Graphene-Based Arsenite Sensor at 10 ppb. *ACS Appl. Nano Mater.* **2022**, *5*, 11876–11888.
- (28) Gupte, T.; Jana, S. K.; Mohanty, J. S.; Srikrishnarka, P.; Mukherjee, S.; Ahuja, T.; Sudhakar, C.; Thomas, T.; Pradeep, T. Highly Sensitive As₃⁺ Detection Using Electrodeposited Nanostructured MnOx and Phase Evolution of the Active Material during Sensing. *ACS Appl. Mater. Interfaces* **2019**, *11*, 28154–28163.
- (29) Jiang, T. J.; Guo, Z.; Liu, J. H.; Huang, X. J. Gold Electrode Modified with Ultrathin SnO₂ Nanosheets with High Reactive Exposed Surface for Electrochemical Sensing of As(III). *Electrochim. Acta* **2016**, *191*, 142–148.
- (30) Kwak, K.; Lee, D. Electrochemistry of Atomically Precise Metal Nanoclusters. *Acc. Chem. Res.* **2019**, *52*, 12–22.
- (31) Salimi, A.; Mamkhezri, H.; Hallaj, R.; Soltanian, S. Electrochemical Detection of Trace Amount of Arsenic(III) at Glassy Carbon Electrode Modified with Cobalt Oxide Nanoparticles. *Sensors Actuators, B Chem.* **2008**, *129*, 246–254.
- (32) Sarkar, D.; Mahapatra, A.; Som, A.; Kumar, R.; Nagar, A.; Baidya, A.; Pradeep, T. Patterned Nanobrush Nature Mimics with Unprecedented Water-Harvesting Efficiency. *Adv. Mater. Interfaces* **2018**, *5*, 1800667.
- (33) Jana, A.; Jana, S. K.; Sarkar, D.; Ahuja, T.; Basuri, P.; Mondal, B.; Bose, S.; Ghosh, J.; Pradeep, T. Electrospray Deposition-Induced Ambient Phase Transition in Copper Sulphide Nanostructures. *J. Mater. Chem. A* **2019**, *7*, 6387–6394.
- (34) Ray Chowdhuri, A.; Spoorthi, B. K.; Mondal, B.; Bose, P.; Bose, S.; Pradeep, T. Ambient Microdroplet Annealing of Nanoparticles. *Chem. Sci.* **2021**, *12*, 6370–6377.
- (35) Stuczynski, S. M.; Kwon, Y. U.; Steigerwald, M. L. The Use of Phosphine Chalcogenides in the Preparation of Cobalt Chalcogenides. *J. Organomet. Chem.* **1993**, *449*, 167–172.
- (36) Frisch, M. J.; Trucks, G. W.; Schlegel, H. B.; Scuseria, G. E.; Robb, M. A.; Cheeseman, J. R.; Scalmani, G.; Barone, V.; Mennucci, B.; Petersson, G. A.; Nakatsuji, H.; et al. *Gaussian 09*, Revision D.01; Gaussian, Inc.: Wallingford, CT, 2009.
- (37) Som, A.; Griffo, A.; Chakraborty, I.; Hähl, H.; Mondal, B.; Chakraborty, A.; Jacobs, K.; Laaksonen, P.; Ikkala, O.; Pradeep, T.; Nonappa. Strong and Elastic Membranes via Hydrogen Bonding Directed Self-Assembly of Atomically Precise Nanoclusters. *Small* **2022**, *18*, 2201707.
- (38) Xie, Z.; Sun, P.; Wang, Z.; Li, H.; Yu, L.; Sun, D.; Chen, M.; Bi, Y.; Xin, X.; Hao, J. Metal–Organic Gels from Silver Nanoclusters with

Aggregation-Induced Emission and Fluorescence-to-Phosphorescence Switching. *Angew. Chemie - Int. Ed.* **2020**, *59*, 9922–9927.

(39) Wu, Z.; Dong, C.; Li, Y.; Hao, H.; Zhang, H.; Lu, Z.; Yang, B. Self-Assembly of Au15 into Single-Cluster-Thick Sheets at the Interface of Two Miscible High-Boiling Solvents. *Angew. Chemie - Int. Ed.* **2013**, *52*, 9952–9955.

(40) Wu, Z.; Liu, J.; Li, Y.; Cheng, Z.; Li, T.; Zhang, H.; Lu, Z.; Yang, B. Self-Assembly of Nanoclusters into Mono-, Few-, and Multilayered Sheets via Dipole-Induced Asymmetric van Der Waals Attraction. *ACS Nano* **2015**, *9*, 6315–6323.

(41) Kresse, G.; Hafner, J. Ab Initio Molecular-Dynamics Simulation of the Liquid-Metal–Amorphous-Semiconductor Transition in Germanium. *Phys. Rev. B: Condens. Matter Mater. Phys.* **1994**, *49*, 14251.

(42) Grimme, S. *J. Comput. Chem.* **2006**, *27*, 1787–1799.

(43) WHO. *Guidelines for Drinking-Water Quality*; WHO, 2011; pp 315–318.

(44) U.S. EPA. Technical Factsheet: Final Rule for Arsenic in Drinking Water; U.S. EPA, 2001; pp 1–6.

Recommended by ACS

Defect Engineered Dendritic Fibrous Nanosilica as Prospective Alloy Anode for the Fabrication of High-Energy Li-Ion Capacitors with Ultralong Durability

Manohar Akshay, Vanchiappan Aravindan, *et al.*

FEBRUARY 01, 2023
ACS MATERIALS LETTERS

READ 

Single Cu Atom Doping on Au₁₁ Nanocluster: Its Implication toward Selectivity in C–C Coupling Reaction

Sayani Mukherjee, Sukhendu Mandal, *et al.*

FEBRUARY 16, 2023
CHEMISTRY OF MATERIALS

READ 

Phosphine-Protected Atomically Precise Silver–Gold Alloy Nanoclusters and Their Luminescent Superstructures

Madhuri Jash, Thalappil Pradeep, *et al.*

DECEMBER 27, 2022
CHEMISTRY OF MATERIALS

READ 

ZnS Nanospheres Coated with ZnSe/MoSe₂ Shells as Dual Heterojunctions with Wide Spectral Responses for the Photoreduction of Cr(VI)

Longyu Qiu, Yongsheng Yu, *et al.*

DECEMBER 28, 2022
ACS APPLIED NANO MATERIALS

READ 

Get More Suggestions >

Vertically Aligned Nanoplates of Atomically Precise Co₆S₈ Cluster for Practical Arsenic Sensing

Anagha Jose^a, Arijit Jana^a, Tanvi Gupte^a, Akhil S. Nair^b, Keerthana Unni^a, Ankit Nagar^a, Amoghavarsha R. Kini^a, B. K. Spoorthi^a, Sourav Kanti Jana^a, Biswarup Pathak^{b*}, Thalappil Pradeep^{a,c*}

^aDepartment of Chemistry, DST Unit of Nanoscience (DST UNS) and Thematic Unit of Excellence (TUE), Indian Institute of Technology Madras, Chennai 600036, India. Email: pradeep@iitm.ac.in

^bDepartment of Chemistry, Indian Institute of Technology Indore (IIT Indore), Indore 453552, India. Email: biswarup@iiti.ac.in

^cInternational Centre for Clean Water, 2nd Floor, B-Block, IIT Madras Research Park, Kanagam Road, Taramani, Chennai 600113, India.

Table of contents

Items	Description	Page no
1.	Experimental section	3
2.	Instrumentation	4
3.	Theoretical calculation	5
Table S1	Crystal data and structure refinement for the Co ₆ nanocluster	8
Table S2	Atomic coordinates and equivalent isotropic displacement parameters for the Co ₆ nanocluster	13
Figure S1	Time-dependent UV-vis absorption spectra of the Co ₆ nanocluster indicating its stability	14
Figure S2	UV-vis absorption spectra of the Co ₆ nanocluster in different solvents	15
Figure S3	Point EDS spectrum of the Co ₆ nanocluster crystal	15
Figure S4	Atomic arrangements of the Co ₆ nanocluster	16
Figure S5	Unit cell molecular packing of the Co ₆ nanocluster along different axis	16
Figure S6	Different types of intercluster interactions	16
Figure S7	The full range ESI-MS spectrum of the Co ₆ nanocluster	17

Figure S8	XPS spectra of the Co ₆ nanocluster along with appropriate peak fitting	17
Figure S9	Comparison between experimental and simulated PXRD patterns	18
Figure S10	Thermogravimetric (TG) and differential thermogravimetric (DTG) analysis of the microcrystalline Co ₆ nanocluster	18
Figure S11	Time-dependent density functional theory (TD-DFT) calculations	19
Figure S12	Electron density maps of Frontier molecular orbitals (FMOs) of the nanocluster	19
Figure S13	Optical microscopic images of ESD film	20
Figure S14	A large area FESEM	20
Figure S15	AFM micrographs of vertically aligned nanoplatelets	20
Figure S16	FESEM micrographs of three different films	21
Figure S17	UV-vis absorption spectra before and after electrospray deposition and ESI MS of the ESD film	21
Figure S18	FT-IR spectra of the Co ₆ nanocluster in comparison with the ESD film	21
Figure S19	FESEM micrographs of the Co ₆ sample drop casted on water	22
Figure S20	FESEM images of the Co ₆ sample ESD on carbon cloth	22
Figure S21	FESEM images of the Co ₆ electrosprayed sample on glycerol	22
Figure S22	FESEM images of the Co ₆ electrosprayed sample on ethylene glycol	23
Figure S23	FESEM image of the EDS-Co ₆ nanofilm modified glassy carbon electrode	23
Figure S24	Cyclic voltammograms of the ESD-Co ₆ modified GC electrode in PBS	24
Figure S25	Cyclic voltammograms of bare GC electrode in PBS	24
Figure S26	Cyclic voltammograms of the Co ₆ nanocluster-modified GC electrode in PBS	25
Figure S27	Relative energy profile of the interaction between As(OH) ₃ and the Co ₆ cluster	26
Figure S28	Charge density difference (CDD) analysis of As(OH) ₃ binding to the Co ₆ cluster	26

Figure S29	Interactions between As(OH) ₃ and the Co ₆ nanocluster and Badger charge analysis	27
Figure S30	Interfering ions study with different metal ions in PBS	27
Figure S31	Baseline corrected voltammetric profiles of recyclability of ESD-Co ₆ modified GC electrode in PBS	28
Figure S32	UV-vis absorption spectra of ESD-film dissolved in DCM after 40 cycles of arsenic sensing experiments	28
Figure S33	Schematic diagram of the reaction vessel during the synthesis of the [Co ₆ S ₈ DPPE ₆ Cl ₆] nanocluster	30

1. Experimental section

Chemicals used

The borosilicate glass capillary was purchased from Sutter instruments, USA. All the materials were commercially available and were used without further purification. Cobaltous chloride ($\text{CoCl}_2 \cdot 6\text{H}_2\text{O}$, 97%) was purchased from Fisher Scientific. Sodium sulfide nonahydrate ($\text{Na}_2\text{S} \cdot 9\text{H}_2\text{O}$, 98%) was purchased from SRL. 1,2-bis(diphenylphosphino)ethane (97%) was purchased from Spectrochem. Sodium arsenite (NaAsO_2) was purchased from S. D. Fine Chem. Ltd. HPLC grade dichloromethane (DCM), dimethylformamide (DMF), and methanol (MeOH) were purchased from Rankem. CDCl_3 (99.99 % purity) was purchased from Sigma-Aldrich. All solvents and chemicals were used as such without further purification.

Synthesis of Co_6 cluster

The Co_6 cluster was synthesized at room temperature (25 °C) upon dissolving 0.016 g (0.124 mmol) of $\text{CoCl}_2 \cdot 6\text{H}_2\text{O}$ in 2 mL of DMF. 0.2 g (0.5 mmol) of DPPE in 3 mL of DMF was added to the dissolved CoCl_2 solution and stirred (1000 rpm) for 10 min. After that, 0.15 g $\text{Na}_2\text{S} \cdot 9\text{H}_2\text{O}$ dissolved in 1 mL of methanol was added gradually to the stirred solution. In the course of the reaction, the bluish solution changes to dark brown with a greenish intermediate (shown in Figure S36). The final solution was kept for stirring for two days at room temperature. Purified cluster was dissolved in multiple solvents for further studies. The yield of the cluster is 85% in terms of cobalt precursors.

Electrospray deposition

A home-built electrospray set-up was used for preparing the thin film. The electrospray source was made by pulling a borosilicate glass capillary of 1.5 mm outer diameter (OD) and 0.86 mm inner diameter (ID), using a micropipette puller instrument. It was cut into two pieces having an ID of 30-35 μm . Freshly prepared Co_6 cluster in DCM was filled inside the capillary using a micro-injector pipette tip. A spray plume was produced from the tip of the capillary by applying a DC potential of 2.75 to 3 kV between a platinum wire placed inside the capillary and the ground. The capillary tip was kept at a distance of 6 to 8 mm over the water substrate during the ESD process.

Preparation of working electrode

The working electrode was made by carefully transferring the ESD-nanofilm onto a glassy carbon electrode. To reduce the structural damage of the nanoplates, we transferred it to a 3: 1 (v/v) nafion: DMF mixture and it was sonicated for 1 min to make a brownish dispersion. This dispersion was drop cast on a glassy carbon electrode and dried in vacuum for 1 h (the active

surface area was $\approx 7 \text{ mm}^2$). Prior to each measurement, argon bubbling (exposure time = 10 min) was performed to remove dissolved oxygen. All the measurements were performed at room temperature (25 °C).

2. Instrumentation

UV–vis absorption spectra of the cluster in their respective solution were recorded using a PerkinElmer Lambda 25 spectrophotometer in the wavelength range of 200–1100 nm. The slit width used for the measurement is 1 nm. Mass spectrometric measurements were performed using Waters Synapt G2-Si high-resolution mass spectrometer instrument equipped with time of flight (TOF) detector. Samples were measured using electrospray ionization (ESI) in the positive mode. An optimised instrumental condition (capillary voltage = 3 kV, source temperature = 100 °C, desolvation temperature = 150 °C, cone voltage = 0 V, source offset = 0 V, flow rate = 20 $\mu\text{L}/\text{min}$, desolvation gas flow = 400 L/h) was used to record the spectrum. FT-IR spectra were measured using a JASCO-4100 spectrometer. A thin pallet of sample embedded with KBr was used for the measurement. X-ray photoelectron spectroscopy (XPS) measurements were done using an Omicron ESCA Probe spectrometer equipped with a polychromatic Al K α X-ray source ($h\nu = 1486.7 \text{ eV}$). The sample dissolved in DCM was drop-casted on an XPS sample stub and dried under ambient conditions. The pass energy for survey scans was kept at 50 eV and changed to 20 eV for specific regions for the measurements. Binding energies (BE) of the core levels were calibrated with C 1s BE set at 285 eV. Multinuclear NMR spectra were measured using a 500 MHz Bruker instrument (using CDCl_3 solvents). TGA and DTG measurements were analyzed in the temperature range of 25 to 700 °C using a NETZSCH STA 449 F3 Jupiter instrument. About $\sim 5 \text{ mg}$ of crystalline sample was loaded in an alumina crucible for the measurement. Nitrogen was used as the environment with a flow rate of 10 °C/min

Optical microscopic images of the crystals and ESD film were observed using Leica Microscope. Surface morphology and elemental analysis were performed by FESEM–EDX (Thermo Scientific Verios G4 UC). Backscattered electrons and secondary electrons were used for imaging the surface at an accelerating voltage of 10 kV under high vacuum conditions. Surface morphology analysis of the ESD-film was performed by an Atomic Force Microscopy (AFM) system (Park Systems XE-100) in the non-contact mode.

Single crystal XRD

Single-crystal X-ray diffraction data were recorded at 296 K using Bruker D8 VENTURE instrument. It equipped with a Mo K α X-ray source with the wavelength 0.71073 Å. A PHOTON 100 CMOS detector has been used to record the diffraction spots of multiple frames. A suitable crystal was mounted on a Kapton polymer loop with the help of paratone oil. The programme APEX3-SAINT (Bruker, 2016) was used for integrating the frames. A multi-scan absorption correction was done using the programme SADABS (Bruker, 2016). The structure was solved by SHELXT-2014 (Sheldrick, 2014) and refined by full-matrix least squares techniques using SHELXL-2018 (Sheldrick, 2018) computer programme. Hydrogen atoms were fixed at calculated positions and refined as riding model with C-H = 0.93 Å and Uiso(H) = 1.2 Ueq(C). Mercury 2020.2.0 software has been used for the visualization of the structure.

Electrochemical sensing

All the electrochemical measurements were performed using a CH 600A (CH Instruments) electrochemical workstation. Arsenic sensing was carried out by cyclic voltammetry (CV) technique using NaAsO₂ dissolved in phosphate-buffered saline (PBS, pH ~ 7). The measurements were done with the following optimised parameters: scan rate of 50 mVs⁻¹, sensitivity of 2 × 10⁻⁶, and potential range of -0.5 to 1 V. A conventional three-electrode cell was used with Ag/AgCl as the reference electrode and a Pt wire as a counter electrode. The working electrode was made by dispersing ESD nanofilm with 5.wt% Nafion binder. A few μ L amount of this slurry was drop casted on a polished glassy carbon electrode (active surface area \approx 7 mm²) for preparing the working electrode. Prior to each measurement, argon bubbling (exposure time = 10 min) was performed to remove the dissolved oxygen. All the measurements were performed at room temperature (25 °C).

3.Theoretical calculations

The periodic DFT calculations were done using Vienna Ab-Initio Simulation Package (VASP) by using Generalized gradient approximation of Perdew–Burke–Ernzerhof (PBE) functional.^{1,2} Projector augmented wave (PAW) method is used for treating ion electron interactions.³ The ionic relaxations have been carried out using a Conjugate gradient algorithm with convergence criteria of 10⁻⁴ eV for minimum energy and 0.05 eV Å⁻¹ for Hellmann-Feynman forces on atoms. Due to the large size of the unit cells of the compounds, the Brillouin zone was sampled at the Gamma point (1×1×1). For the projected density of states (PDOS) calculation, a higher (2×2×2) K-mesh is used. The atomic charges are calculated using Bader charge analysis.⁴ For

identifying the intercluster interactions, calculations of dimer and monomer clusters units are carried out with and without applying van der Waals correction using DFT-D3 method.⁵

The molecular DFT calculations were done using Gaussian 09 D.01 program.⁶ B3LYP functional with Pople's 6-31G* basis set was used for non-metal elements and LANL2DZ-ECP (effective core potential) was employed for Co atoms, respectively.^{7, 8} The TD-DFT calculations considered 300 singlet-to-singlet excitation energies. Since a full ligand simulation with DPPE ligands is computationally expensive, we simplified the -Ph groups to -Me at the positions far from the Co₆ kernel while retaining the -Ph groups positioned close to the kernel. This allows us to reduce the computational cost without adapting a crude approximation of complete ligand simplification strategy. Kohn-Sham orbital analysis has been performed for identifying the orbital contribution in molecular orbitals and corresponding energies by using multi wave function 3.6 program.⁹

Table S1. Crystal data and structure refinement for Co₆ nanocluster.

Identification code	Co ₆	
Empirical formula	C156 H144 Cl6 Co6 P12 S8	
Formula weight	3213.10	
Temperature	296(2) K	
Wavelength	0.71073 Å	
Crystal system	Monoclinic	
Space group	P 21/c	
Unit cell dimensions	a = 20.4453(7) Å	α = 90°.
	b = 18.7380(6) Å	β = 102.515(2)°.
	c = 44.5513(15) Å	γ = 90°.
Volume	16662.2(10) Å ³	
Z	4	
Density (calculated)	1.281 mg/m ³	
Absorption coefficient	0.941 mm ⁻¹	
F(000)	6608	
Crystal size	0.200 x 0.150 x 0.130 mm ³	
Theta range for data collection	2.401 to 20.000°.	
Index ranges	-19<=h<=19, -18<=k<=18, -42<=l<=42	
Reflections collected	165604	
Independent reflections	15508 [R(int) = 0.1709]	
Completeness to theta = 20.000°	99.8 %	
Absorption correction	Semi-empirical from equivalents	
Max. and min. transmission	0.7446 and 0.5706	
Refinement method	Full-matrix least-squares on F ²	
Data / restraints / parameters	15508 / 1092 / 1693	
Goodness-of-fit on F ²	1.077	
Final R indices [I>2sigma(I)]	R1 = 0.0935, wR2 = 0.2479	
R indices (all data)	R1 = 0.1514, wR2 = 0.3071	
Extinction coefficient	n/a	
Largest diff. peak and hole	0.822 and -1.053 e.Å ⁻³	

Table S2. Atomic coordinates ($\times 10^4$) and equivalent isotropic displacement parameters ($\text{\AA}^2 \times 10^3$) for Co_6 nanocluster. $U(\text{eq})$ is defined as one third of the trace of the orthogonalized U_{ij} tensor.

	x	y	z	$U(\text{eq})$
Co(1)	2822(1)	8672(1)	3246(1)	48(1)
Co(2)	2003(1)	8082(1)	3633(1)	52(1)
Co(3)	2986(1)	6995(1)	3822(1)	56(1)
Co(4)	3807(1)	7599(1)	3448(1)	51(1)
Co(5)	2440(1)	7217(1)	3186(1)	47(1)
Co(6)	3341(1)	8468(1)	3887(1)	57(1)
Cl(1)	2981(4)	9868(4)	1855(2)	163(3)
Cl(2)	-4(3)	6884(3)	1911(1)	113(2)
Cl(3)	3268(6)	11459(5)	4690(2)	226(4)
Cl(4)	157(4)	8589(7)	4683(2)	218(4)
Cl(5)	4045(6)	3651(5)	4192(2)	223(4)
Cl(6)	7085(9)	8165(10)	4104(5)	380(8)
C(1)	1581(7)	5707(7)	3001(3)	53(3)
C(2)	939(8)	5583(8)	3040(4)	72(5)
C(3)	784(8)	4940(10)	3159(5)	89(6)
C(4)	1244(9)	4408(9)	3223(4)	80(5)
C(5)	1869(9)	4508(8)	3193(4)	74(5)
C(6)	2051(8)	5168(8)	3076(4)	66(4)
C(7)	2160(7)	6178(7)	2540(3)	46(3)
C(8)	1778(8)	5798(10)	2307(4)	78(5)
C(9)	2021(10)	5486(10)	2083(4)	91(6)
C(10)	2680(11)	5580(10)	2074(5)	94(6)
C(11)	3094(10)	5973(9)	2290(5)	89(6)
C(12)	2818(8)	6267(9)	2522(4)	73(5)
C(13)	1030(6)	6926(7)	2646(3)	52(3)
C(14)	1093(7)	7519(8)	2422(3)	56(4)
C(15)	-246(8)	8089(8)	2358(4)	67(4)
C(16)	-53(9)	8639(9)	2564(4)	82(5)
C(17)	-525(11)	8971(10)	2696(5)	102(6)
C(18)	-1188(11)	8730(13)	2613(6)	118(8)
C(19)	-1396(10)	8193(12)	2407(6)	109(7)
C(20)	-911(9)	7859(10)	2281(4)	84(5)

C(21)	534(8)	8441(9)	1915(4)	71(4)
C(22)	914(9)	9025(9)	2064(5)	94(6)
C(23)	1072(10)	9566(12)	1874(6)	114(7)
C(24)	829(13)	9536(15)	1565(7)	132(9)
C(25)	446(13)	8977(14)	1418(6)	121(7)
C(26)	336(11)	8436(11)	1605(5)	102(6)
C(27)	3759(8)	8459(10)	2057(4)	71(4)
C(28)	3855(9)	7795(10)	2214(5)	84(5)
C(29)	4443(9)	7430(12)	2231(5)	100(6)
C(30)	4918(9)	7679(12)	2095(5)	98(6)
C(31)	4833(10)	8312(13)	1940(5)	112(7)
C(32)	4258(9)	8706(11)	1930(5)	101(6)
C(33)	2388(8)	8340(10)	1742(4)	69(4)
C(34)	2188(9)	7685(10)	1829(5)	92(5)
C(35)	1792(11)	7252(13)	1602(6)	121(7)
C(36)	1586(13)	7484(16)	1315(7)	139(10)
C(37)	1812(14)	8120(15)	1234(6)	133(9)
C(38)	2206(10)	8561(11)	1439(4)	92(5)
C(39)	2731(7)	8923(8)	2366(3)	62(3)
C(40)	3208(7)	9346(7)	2609(3)	56(3)
C(41)	3491(8)	10273(7)	3136(4)	64(4)
C(42)	4109(8)	10335(8)	3083(4)	71(5)
C(43)	4542(9)	10868(9)	3215(6)	101(7)
C(44)	4327(11)	11304(11)	3418(5)	110(7)
C(45)	3713(10)	11266(9)	3491(5)	93(6)
C(46)	3290(8)	10725(8)	3338(4)	77(5)
C(47)	2145(7)	10109(7)	2795(4)	56(4)
C(48)	1519(8)	9946(8)	2844(4)	72(5)
C(49)	986(9)	10345(9)	2726(5)	91(6)
C(50)	1071(9)	10949(9)	2568(5)	88(6)
C(51)	1693(10)	11130(10)	2510(5)	102(7)
C(52)	2220(9)	10711(9)	2621(4)	86(6)
C(53)	4687(9)	9435(11)	4197(4)	79(4)
C(54)	5205(10)	8995(12)	4342(6)	112(7)
C(55)	5844(12)	9102(16)	4318(7)	148(9)
C(56)	6000(11)	9676(17)	4150(6)	137(10)
C(57)	5467(11)	10108(14)	4006(5)	115(7)
C(58)	4828(9)	9995(11)	4026(4)	89(5)

C(59)	3952(9)	8995(11)	4632(4)	81(4)
C(60)	3828(12)	8334(13)	4733(5)	125(8)
C(61)	3955(14)	8160(16)	5040(6)	156(11)
C(62)	4180(14)	8694(19)	5248(6)	164(12)
C(63)	4301(13)	9360(16)	5159(5)	137(9)
C(64)	4147(13)	9499(14)	4853(5)	135(9)
C(65)	3439(9)	10107(9)	4203(4)	81(4)
C(66)	2781(9)	10163(10)	4305(5)	92(5)
C(67)	2412(11)	11551(10)	4036(6)	105(5)
C(68)	2058(11)	11265(10)	3762(6)	107(6)
C(69)	1877(10)	11679(13)	3502(7)	122(7)
C(70)	2061(10)	12389(12)	3508(6)	107(6)
C(71)	2425(12)	12695(14)	3764(7)	134(8)
C(72)	2588(11)	12277(11)	4023(6)	112(7)
C(73)	1796(14)	11056(14)	4479(6)	148(6)
C(74)	1244(13)	10704(16)	4308(7)	165(6)
C(75)	582(14)	10728(16)	4352(7)	181(7)
C(76)	545(16)	11122(18)	4611(7)	192(8)
C(77)	1067(14)	11492(17)	4800(7)	181(7)
C(78)	1680(14)	11479(15)	4720(6)	166(7)
C(79)	574(7)	9016(8)	3667(4)	66(4)
C(80)	787(9)	9566(9)	3522(5)	83(5)
C(81)	419(10)	10191(10)	3455(5)	108(7)
C(82)	-206(11)	10252(12)	3533(6)	120(8)
C(83)	-430(11)	9693(13)	3684(6)	124(8)
C(84)	-42(9)	9100(10)	3750(5)	94(6)
C(85)	434(7)	7550(8)	3563(4)	64(4)
C(86)	48(9)	7674(9)	3281(5)	84(5)
C(87)	-410(9)	7195(10)	3128(5)	90(6)
C(88)	-484(10)	6562(10)	3265(5)	99(6)
C(89)	-101(10)	6406(10)	3541(5)	106(7)
C(90)	341(9)	6893(10)	3686(5)	98(6)
C(91)	1039(8)	8039(8)	4155(4)	69(4)
C(92)	1360(9)	8641(11)	4381(4)	97(5)
C(93)	1521(14)	9300(15)	4978(6)	133(7)
C(94)	2192(13)	9388(14)	5012(5)	128(8)
C(95)	2492(15)	9957(17)	5206(6)	153(10)
C(96)	2152(18)	10330(19)	5384(8)	183(13)

C(97)	1497(18)	10220(20)	5368(8)	211(17)
C(98)	1153(15)	9701(18)	5152(6)	184(14)
C(99)	1442(14)	7805(16)	4912(6)	150(6)
C(100)	1095(15)	7395(15)	5094(6)	168(7)
C(101)	1417(16)	6799(16)	5265(7)	181(7)
C(102)	2058(16)	6549(18)	5256(7)	183(8)
C(103)	2397(16)	6971(15)	5086(7)	174(7)
C(104)	2096(14)	7567(15)	4918(6)	154(6)
C(105)	2120(9)	5811(9)	4141(4)	82(4)
C(106)	1711(9)	5313(10)	3963(5)	99(5)
C(107)	1088(10)	5125(11)	4007(5)	113(5)
C(108)	853(11)	5452(11)	4240(5)	120(6)
C(109)	1249(10)	5963(12)	4422(5)	116(5)
C(110)	1869(9)	6145(11)	4364(4)	99(5)
C(111)	3433(11)	5981(12)	4480(4)	102(6)
C(112)	3308(15)	5457(15)	4676(6)	157(10)
C(113)	3730(20)	5430(20)	4971(8)	198(16)
C(114)	4238(19)	5890(20)	5052(7)	191(15)
C(115)	4330(20)	6410(20)	4872(7)	230(20)
C(116)	3935(14)	6440(14)	4596(6)	155(11)
C(117)	3191(9)	5229(8)	3923(4)	82(5)
C(118)	3925(9)	5192(10)	3936(5)	97(5)
C(119)	3837(10)	4044(10)	3474(6)	101(5)
C(120)	3651(11)	3339(12)	3407(6)	115(6)
C(121)	3386(13)	3094(13)	3104(7)	127(8)
C(122)	3315(11)	3580(13)	2882(6)	116(7)
C(123)	3454(10)	4291(12)	2946(6)	113(6)
C(124)	3725(11)	4495(12)	3263(6)	107(6)
C(125)	5100(13)	4401(14)	3879(6)	141(5)
C(126)	5577(13)	3990(16)	4089(6)	173(7)
C(127)	6264(13)	3997(18)	4102(7)	185(7)
C(128)	6434(16)	4553(17)	3929(7)	186(8)
C(129)	6032(13)	4968(17)	3706(7)	172(7)
C(130)	5322(13)	4894(16)	3688(7)	159(6)
C(131)	4998(8)	6811(9)	3114(4)	69(4)
C(132)	4588(9)	6268(10)	3030(5)	89(6)
C(133)	4769(10)	5702(11)	2859(6)	118(8)
C(134)	5321(10)	5730(10)	2753(5)	92(6)

C(135)	5737(9)	6302(11)	2823(5)	99(6)
C(136)	5555(9)	6870(11)	2989(5)	98(6)
C(137)	5128(8)	8285(9)	3218(4)	70(4)
C(138)	4987(8)	8451(9)	2901(5)	79(5)
C(139)	5232(10)	9033(10)	2774(5)	103(6)
C(140)	5658(10)	9505(10)	2953(5)	87(6)
C(141)	5758(12)	9415(12)	3249(6)	116(7)
C(142)	5541(10)	8800(10)	3408(5)	94(6)
C(143)	5445(8)	7316(10)	3729(4)	86(5)
C(144)	6156(13)	7180(20)	3712(7)	218(9)
C(145)	6390(30)	6960(30)	4390(12)	272(8)
C(146)	6150(20)	6340(30)	4221(10)	278(9)
C(147)	5880(20)	6220(30)	4481(11)	286(9)
C(148)	5910(20)	6420(30)	4795(12)	294(10)
C(149)	6280(20)	7050(30)	4888(11)	283(10)
C(150)	6570(20)	7360(20)	4657(11)	274(9)
C(151)	7580(20)	6960(30)	3982(9)	329(9)
C(152)	7460(20)	6280(30)	3846(9)	336(11)
C(153)	8070(20)	5910(30)	3853(10)	337(11)
C(154)	8630(30)	6330(30)	4004(10)	347(12)
C(155)	8840(20)	7020(30)	4134(11)	333(11)
C(156)	8190(20)	7330(30)	4120(10)	329(11)
P(1)	1838(2)	6535(2)	2851(1)	47(1)
P(2)	335(2)	7703(2)	2150(1)	69(1)
P(3)	2971(2)	8917(3)	2005(1)	69(1)
P(4)	2900(2)	9558(2)	2953(1)	52(1)
P(5)	2581(4)	11069(3)	4386(2)	116(2)
P(6)	3827(2)	9219(3)	4228(1)	70(1)
P(7)	1089(3)	8568(4)	4740(2)	120(2)
P(8)	1049(2)	8192(2)	3751(1)	61(1)
P(9)	2948(2)	6049(2)	4088(1)	71(1)
P(10)	4216(3)	4295(3)	3872(2)	116(2)
P(11)	4810(2)	7506(2)	3372(1)	62(1)
P(12)	6750(5)	7273(9)	4076(3)	236(5)
S(1)	3181(2)	7805(2)	2980(1)	50(1)
S(2)	3858(2)	8771(2)	3519(1)	51(1)
S(3)	1796(2)	8199(2)	3119(1)	50(1)
S(4)	2491(2)	9149(2)	3647(1)	59(1)

S(5)	2631(2)	7852(2)	4098(1)	64(1)
S(6)	1944(2)	6912(2)	3557(1)	56(1)
S(7)	3999(2)	7496(2)	3961(1)	64(1)
S(8)	3301(2)	6533(2)	3415(1)	59(1)

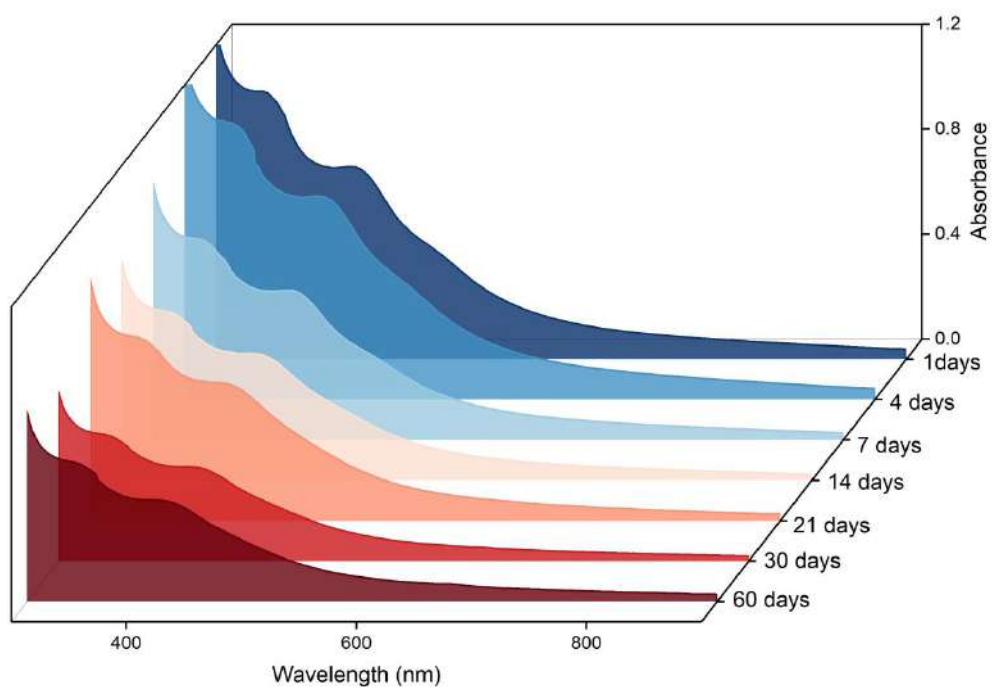


Figure S1. Time-dependent UV-vis absorption spectra of the Co₆ nanocluster in DCM, indicating its stability up to 60 days in ambient conditions.

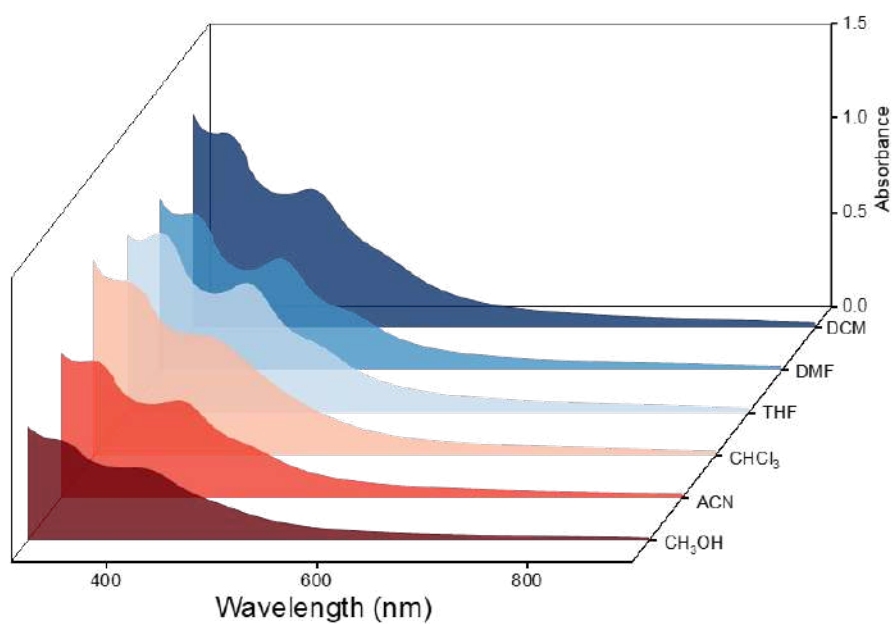


Figure S2. UV-vis absorption spectra of the Co₆ nanocluster measured in different solvents. Identical peak patterns and positions were observed in all the solvents.

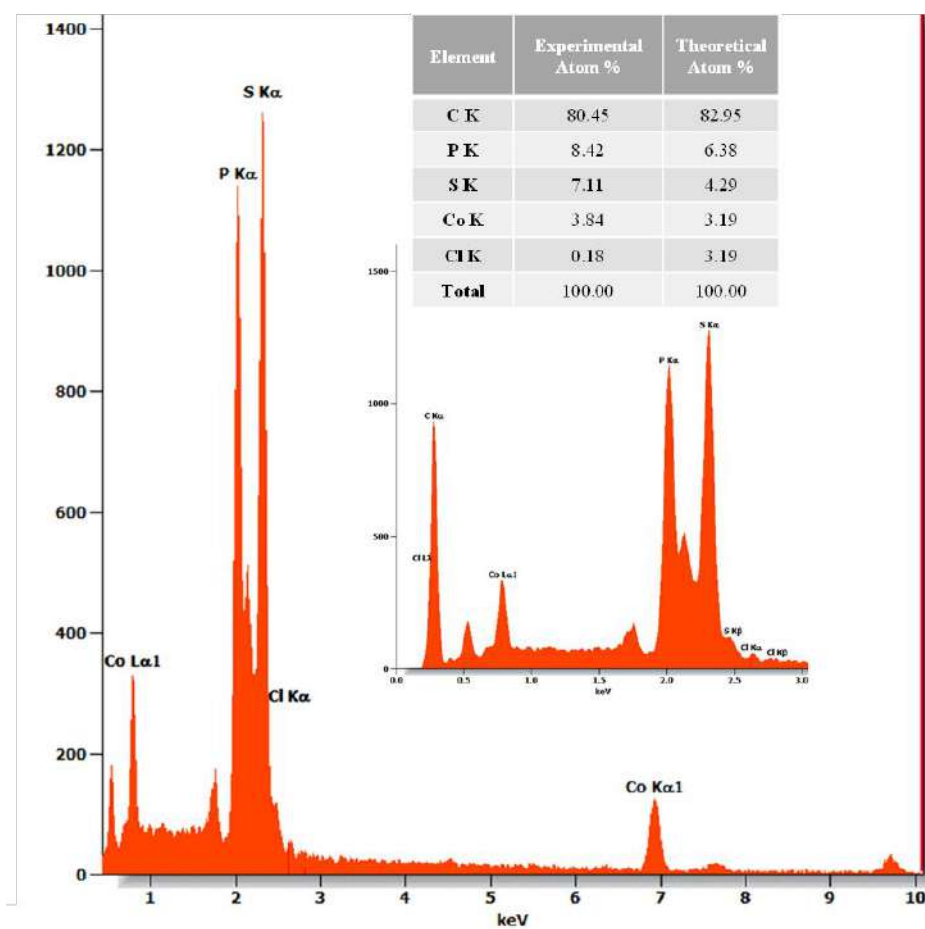


Figure S3. Point EDS spectrum of the Co₆ nanocrystal. Inset shows the elemental composition.

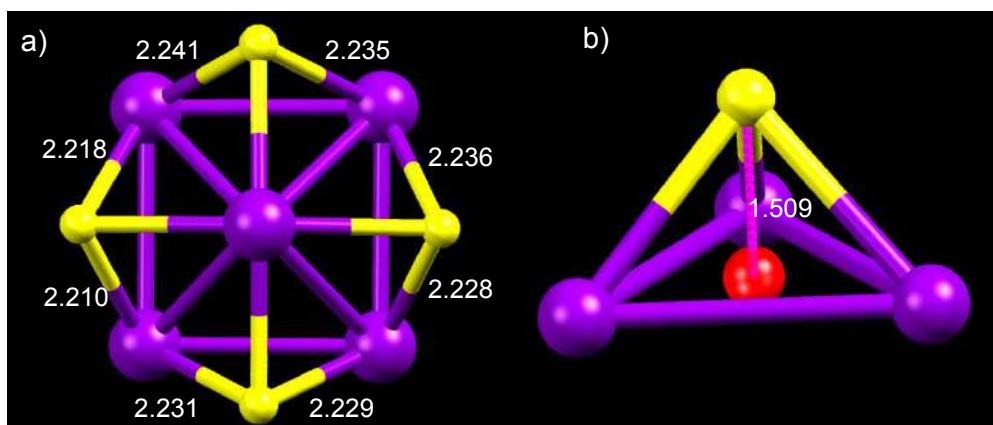


Figure S4. a) Front view of the Co_5S_4 unit with marked Co-S bonds. b) The distance between the centroid of triangular facet to sulphur.

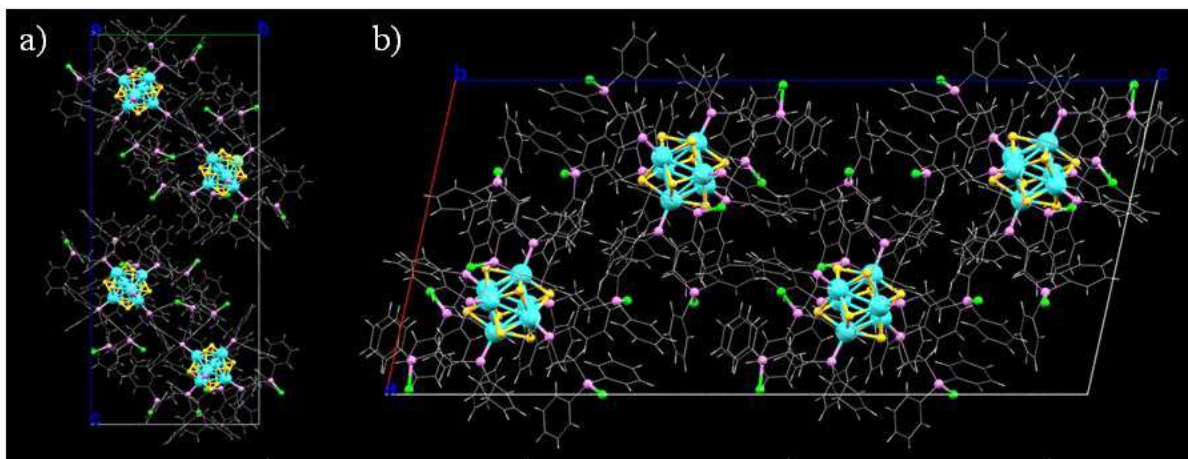


Figure S5. Unit cell molecular packing of the Co_6 nanocluster along a) a, and b) b axis.

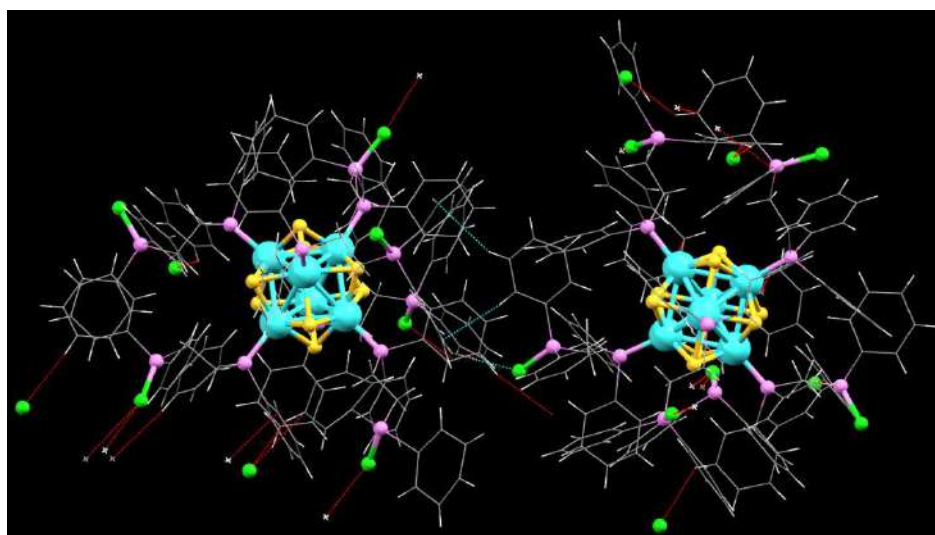


Figure S6. Different types of intercluster interactions responsible for intermolecular packing inside the crystal.

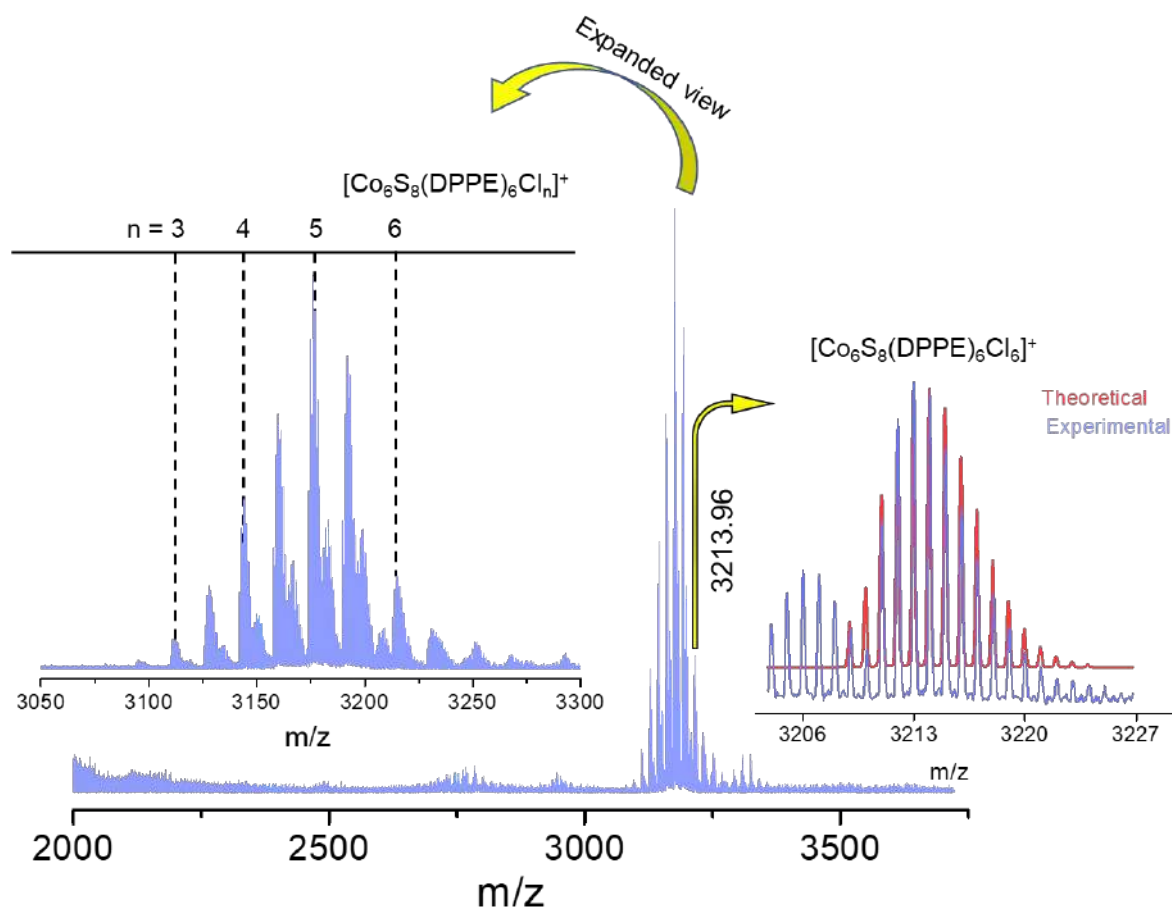


Figure S7. a) The full range ESI-MS spectrum in positive ion mode. The inset shows the exact matching of the isotopic distribution of the experimental with theoretical data.

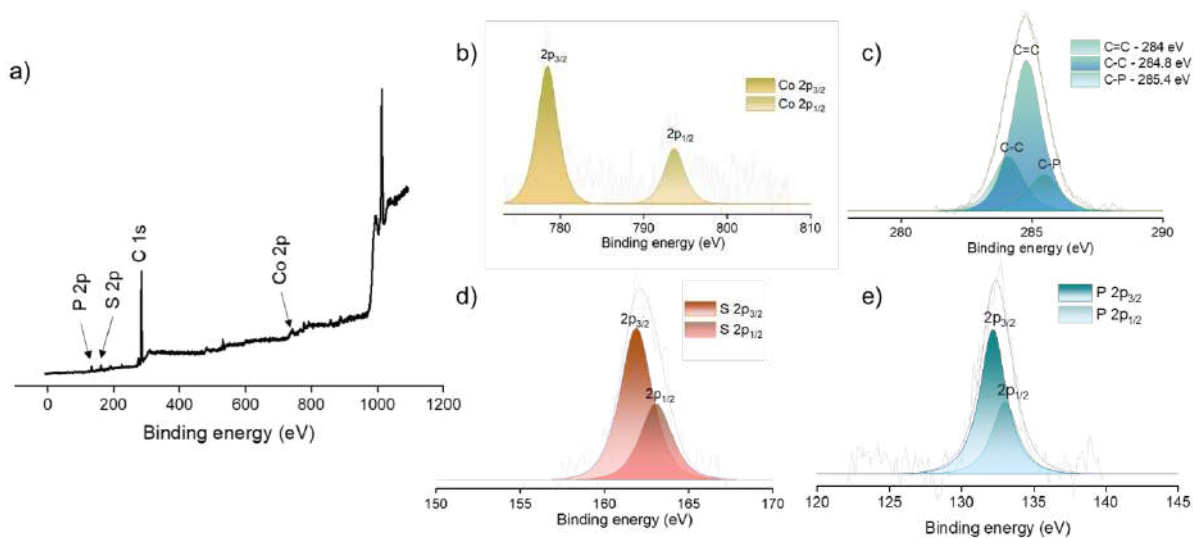


Figure S8. a) XPS survey spectrum of the Co_6 nanocluster showed the spectral signature of respective elements. Spectral fitting of b) Co 2p, c) C 1s, d) S 2p and e) P 2p regions.

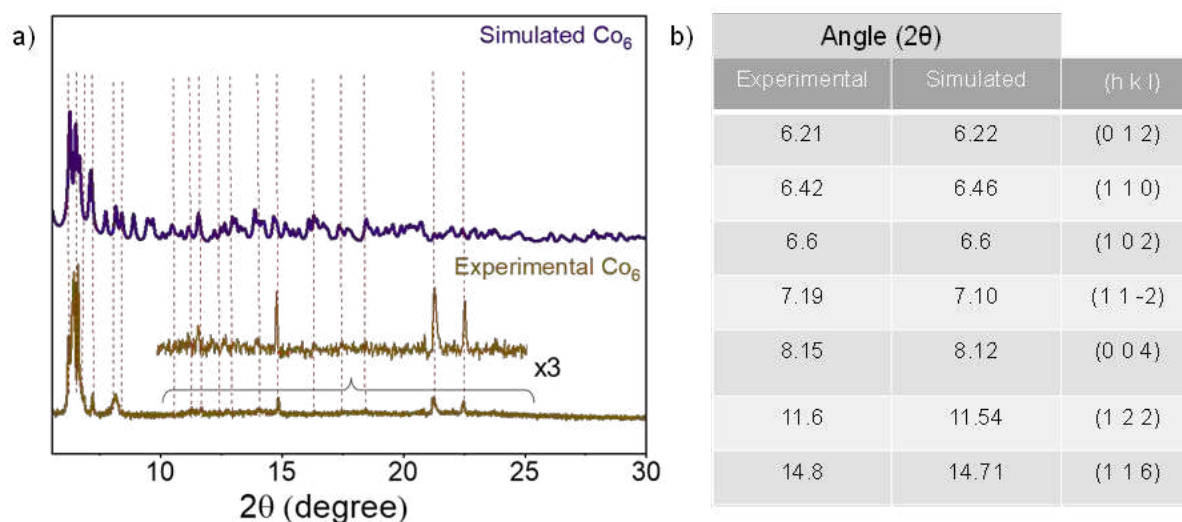


Figure S9. a) Comparison between the experimental and simulated PXRD patterns obtained from single crystals. Experimental spectrum in the 10° - 25° 2θ range is also expanded to see the features clearly. b) Analysis of the corresponding lattice planes.

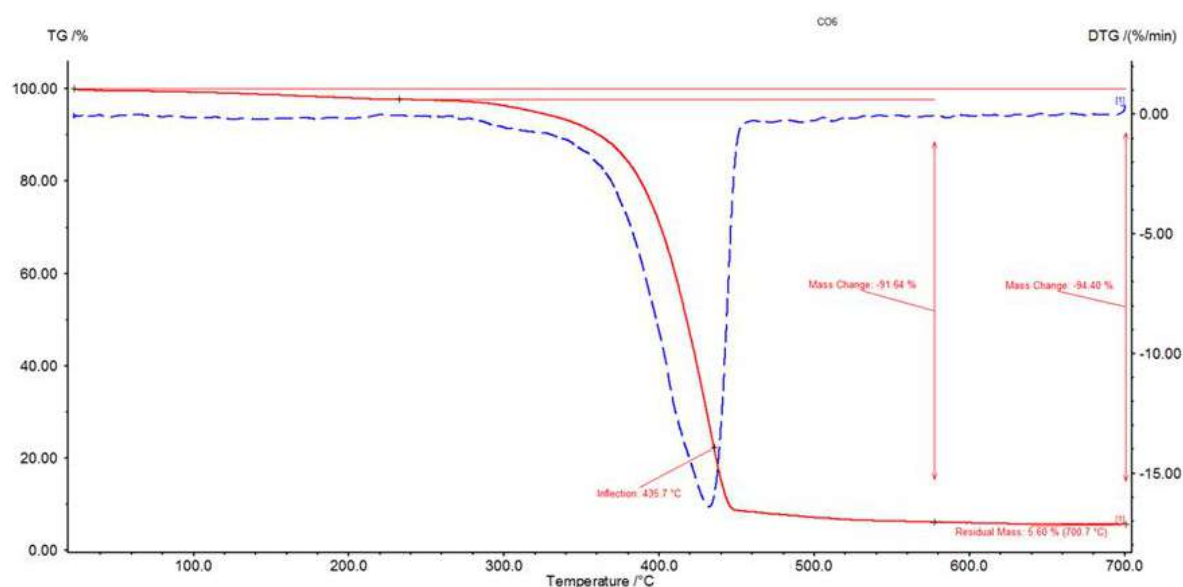


Figure S10. Thermogravimetric (TG) and differential thermogravimetric (DTG) analysis of the microcrystalline Co₆ nanocluster in the heating range of 25 - 700 °C. Solid line (red) indicate the TG and dotted line (blue) indicate the DTG profiles.

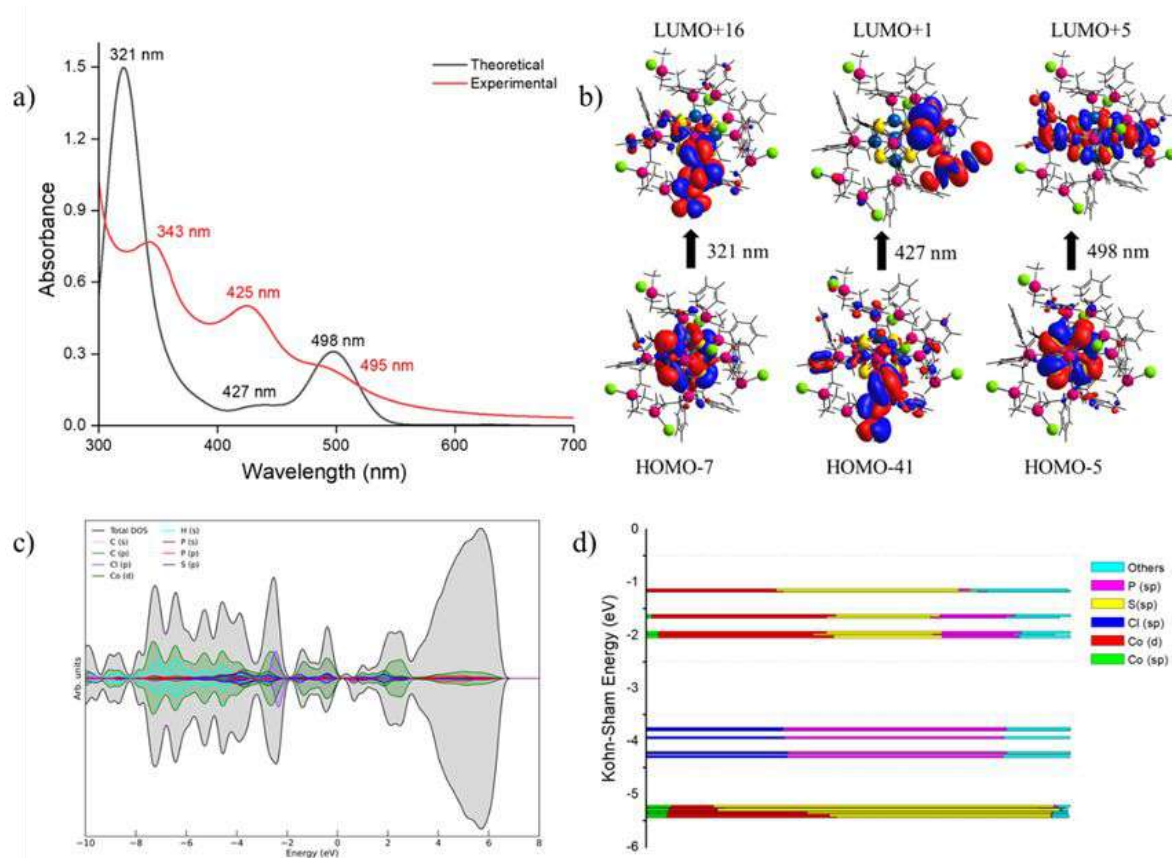


Figure S11. a) Comparison between the experimental and theoretical absorbance spectra of the Co₆ nanocluster. b) Electron density maps of the respective transitions at 321, 427, and 498 nm. c). Projected density of states (PDOS) analysis d). Kohn-Sham orbital contribution analysis.

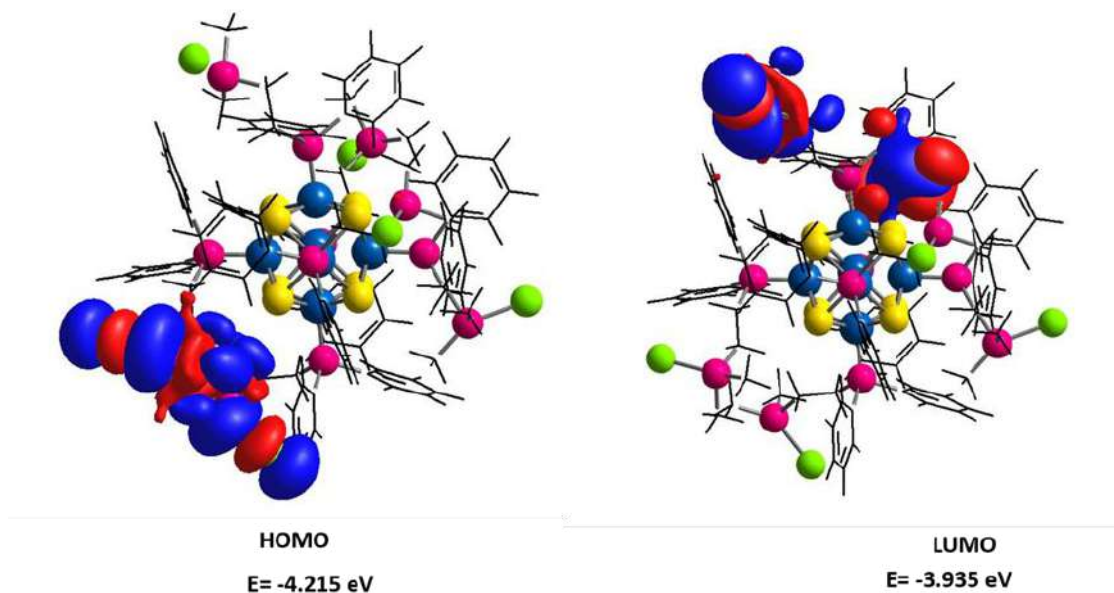


Figure S12. Electron density maps of Frontier molecular orbitals (FMOs) of the Co₆ nanocluster.

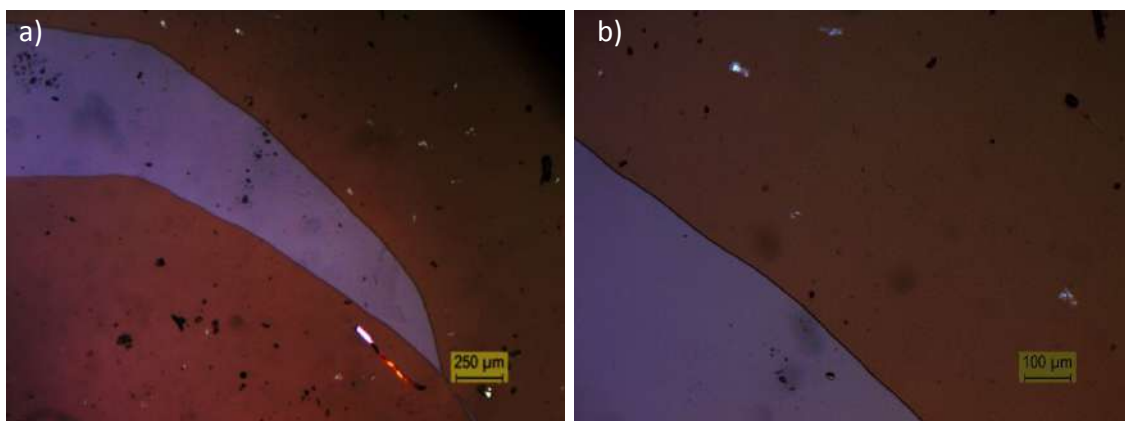


Figure S13. Optical microscopic images of the ESD film at different magnifications.

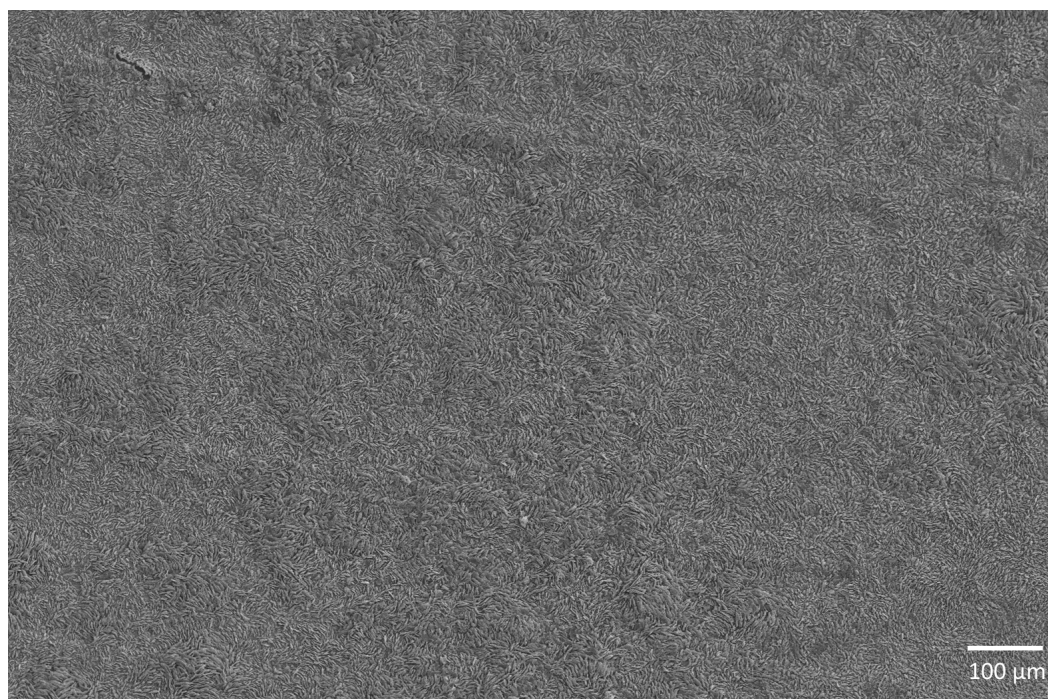


Figure S14. A large area FESEM micrograph demonstrated the uniform nature of the vertically aligned nanoplates.

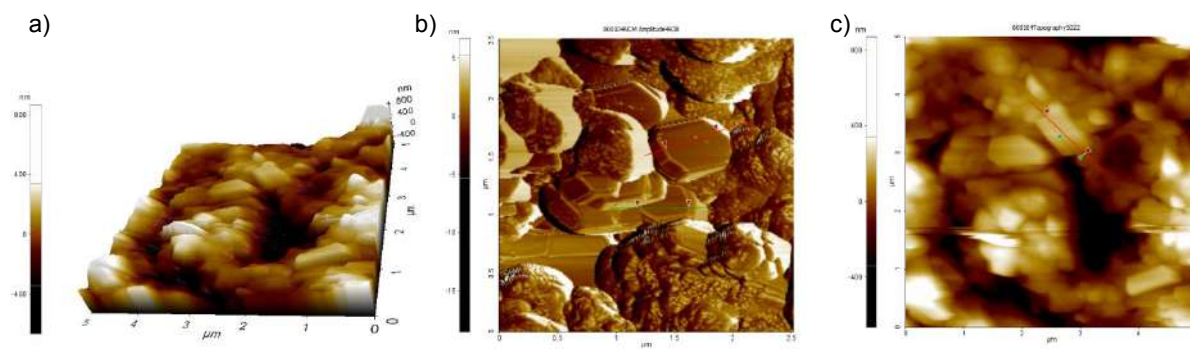


Figure S15. a) Large area, and b, c) magnified AFM micrographs of the vertically aligned nanoplates.



Figure S16. FESEM micrographs of three different films demonstrating reproducible nature of such nanostructures.

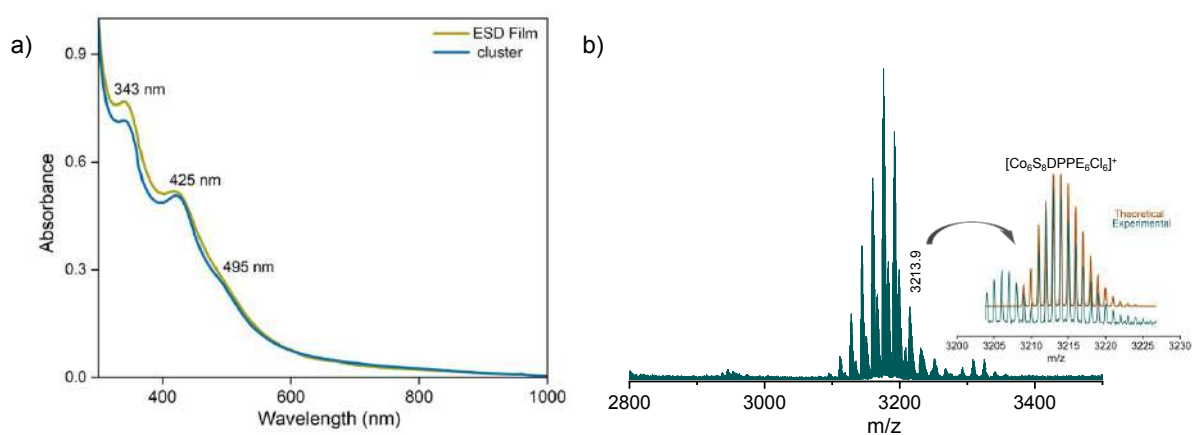


Figure S17. a) UV-vis absorption spectra before and after electrospray deposition. ESD film was dissolved in DCM for the measurement. b) ESI-MS spectrum in positive ion mode of the ESD film. Inset shows the exact matching of the isotopic distribution of the experimental and theoretical data.

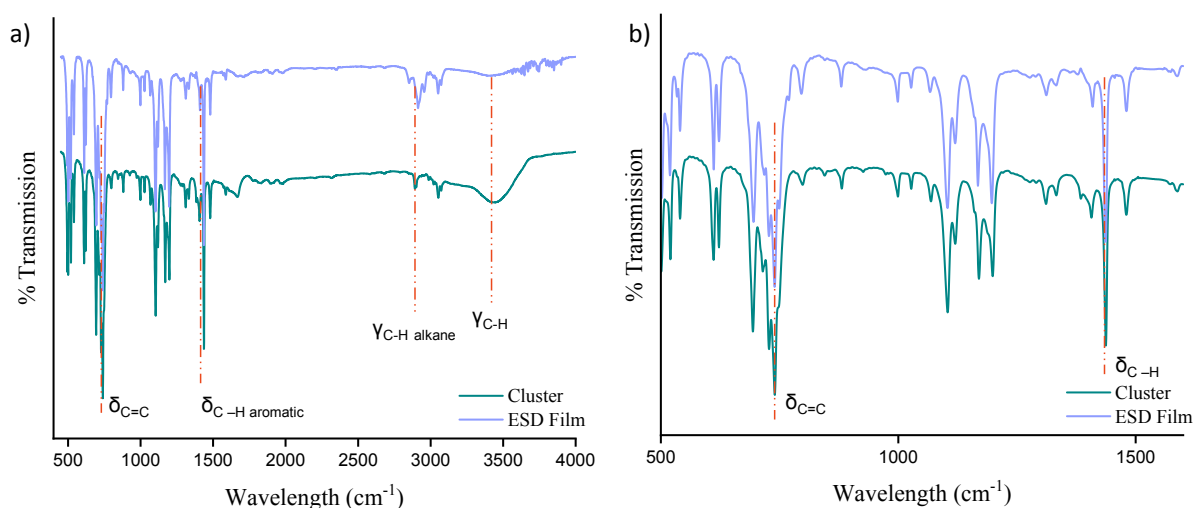


Figure S18. a) The full range FT-IR spectra of the Co₆ nanocluster in comparison with ESD film. b) Expanded view of two different spectral regions indicate nearly identical vibrational spectral features.

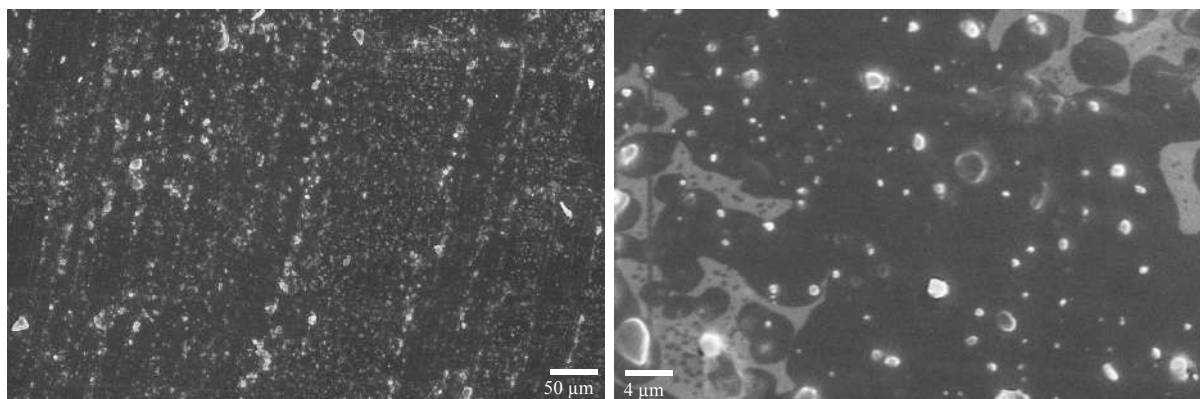


Figure S19. FESEM micrographs of the Co₆ sample drop casted on water at different magnifications. No specific nanostructure was observed upon such drop casting.

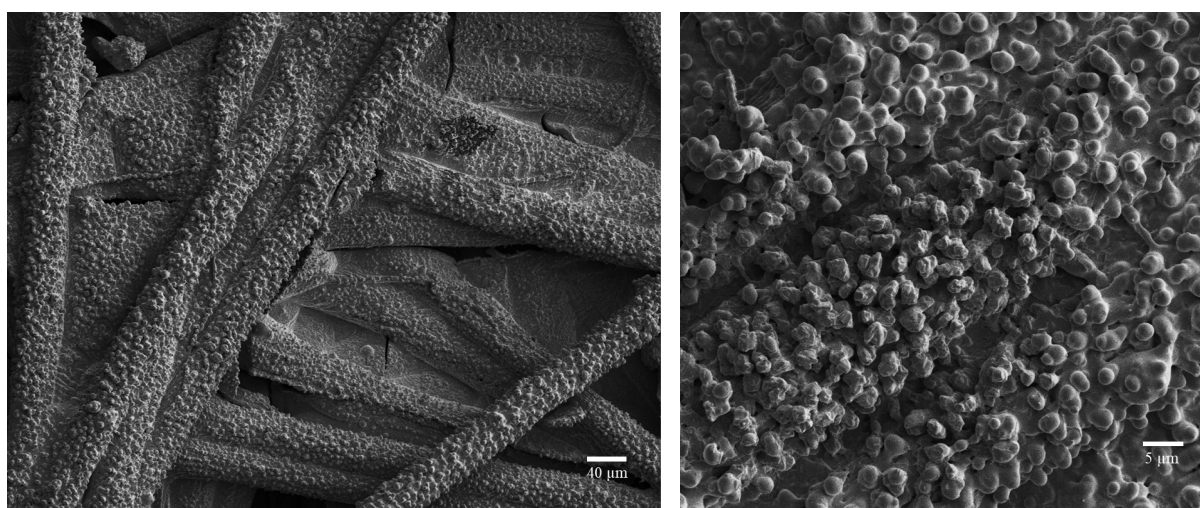


Figure S20. FESEM images of the carbon cloth at different magnifications after electro spray deposition of the Co₆ nanocluster. No specific aligned nanostructure was observed.

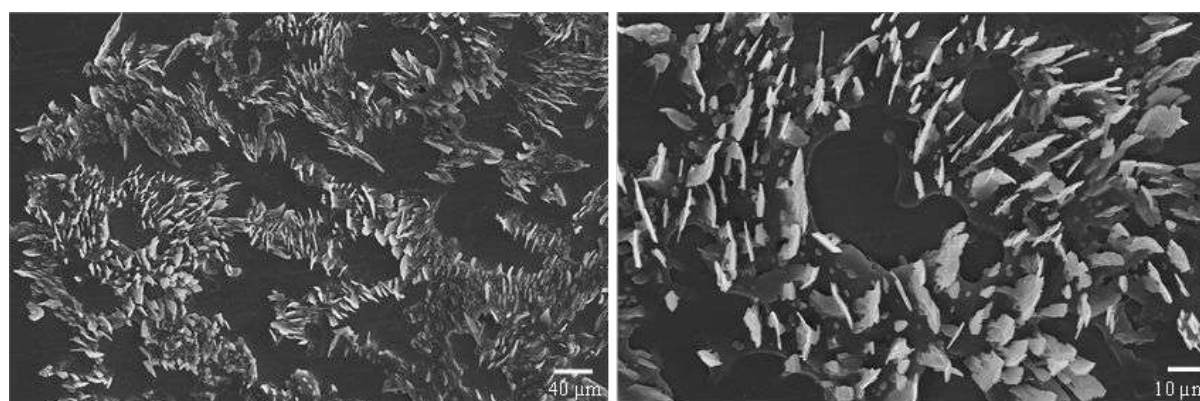


Figure S21. FESEM images of the Co₆ electro sprayed sample on glycerol.

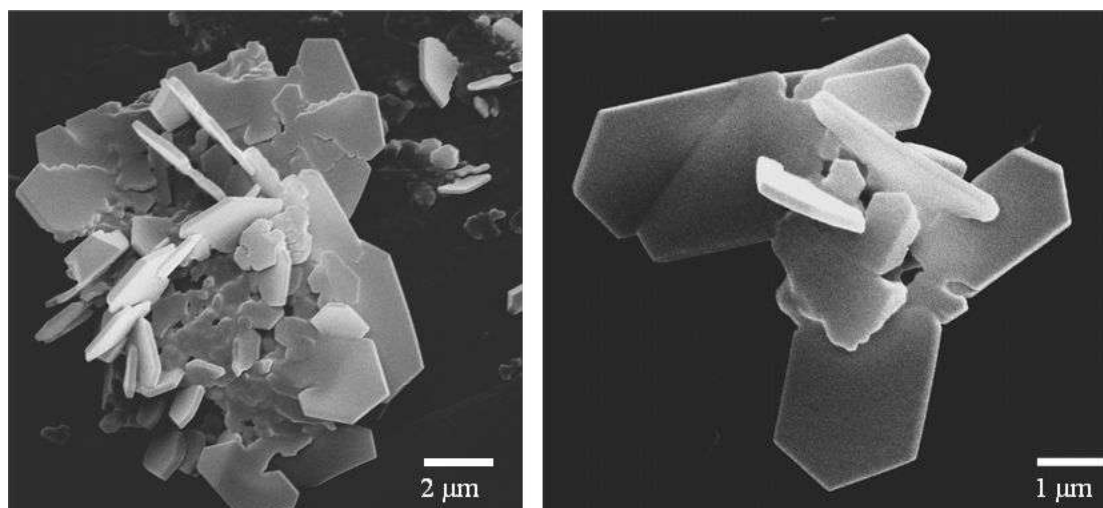


Figure S22. FESEM images of the Co₆ electrospayed sample on ethylene glycol.

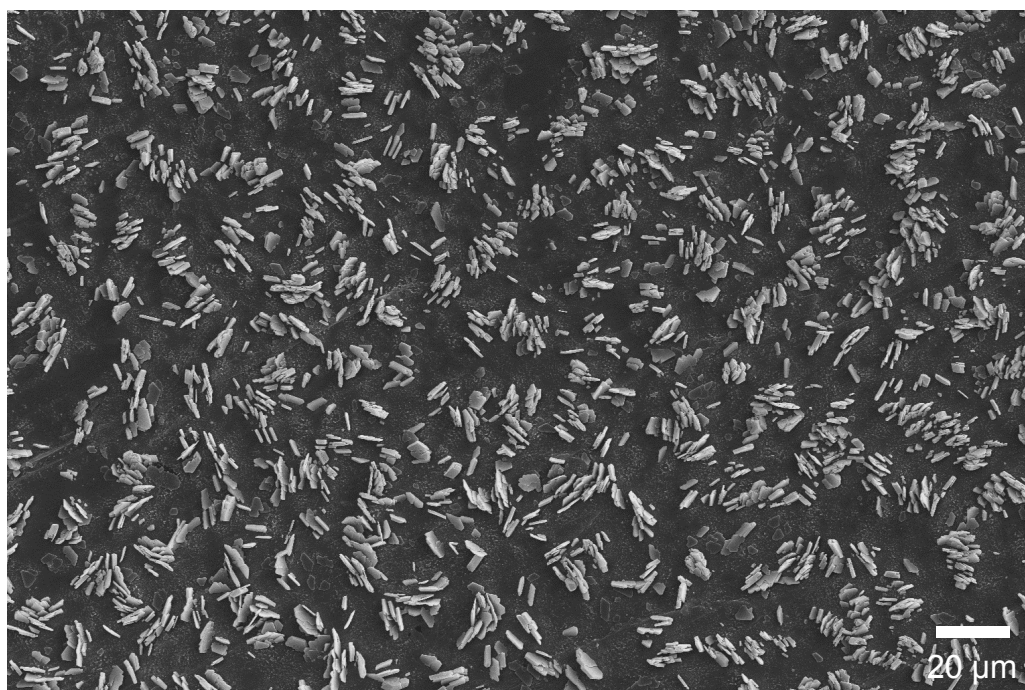


Figure S23. FESEM image of ESD-Co₆ film modified glassy carbon electrode.

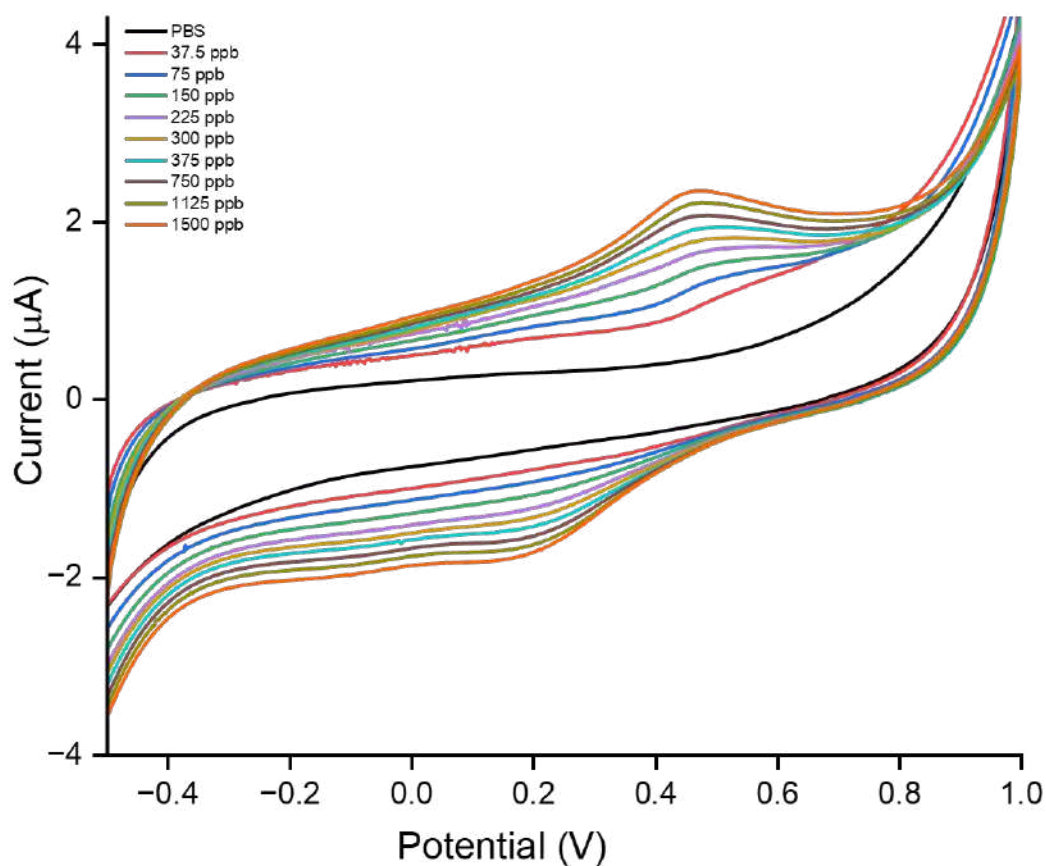


Figure S24. Cyclic voltammograms of ESD- Co_6 modified GC electrode in a buffer solution of pH 7 at a scan rate of 50 mVs^{-1} for various concentrations (37.5–1500 ppb) of As^{3+} .

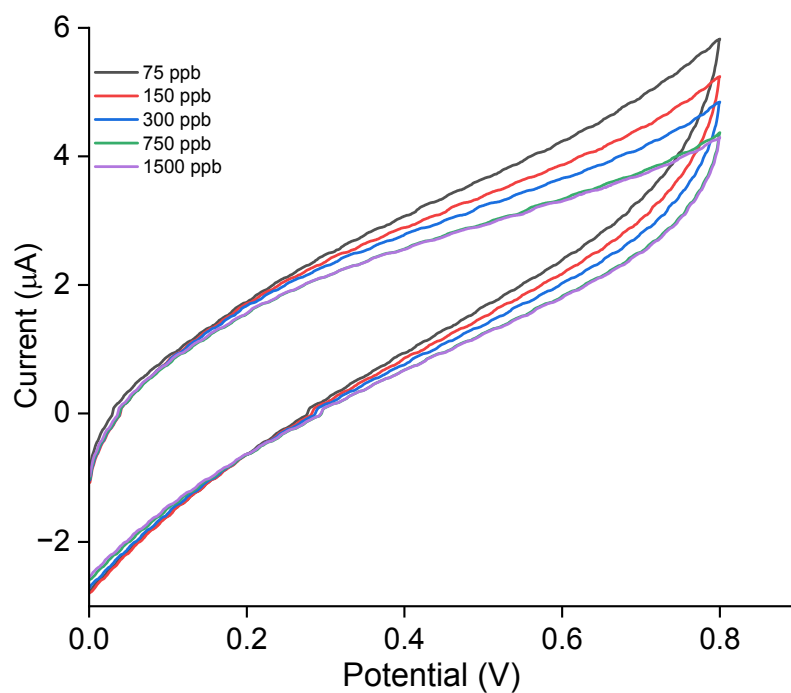


Figure S25. Cyclic voltammograms of bare GC electrode in a buffer solution of pH 7 at a scan rate of 50 mVs^{-1} for various concentrations (75–1500 ppb) of As^{3+} .

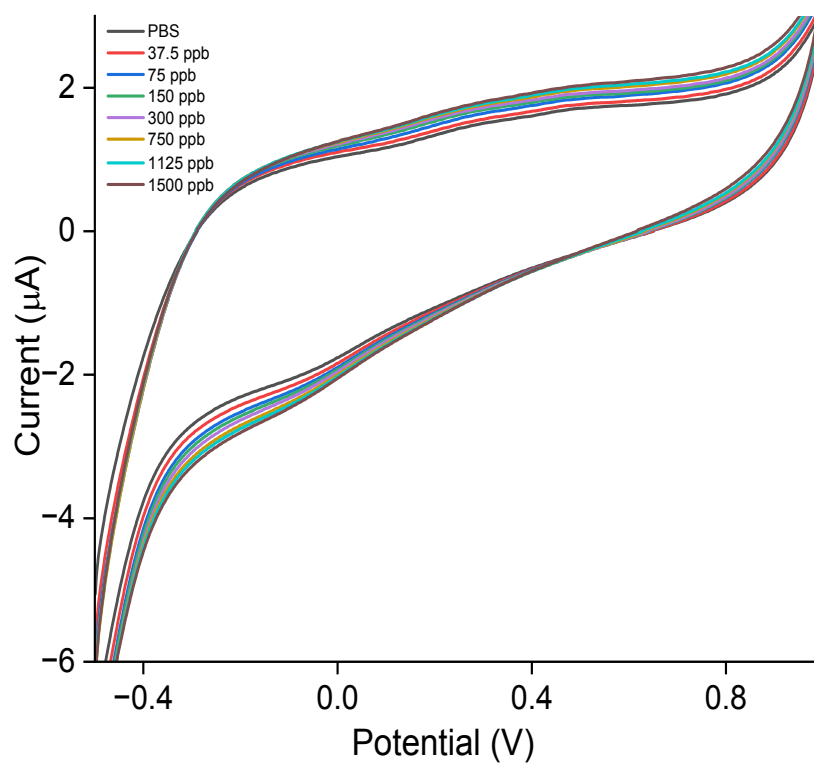


Figure S26. Cyclic voltammograms of Co₆ nanocluster modified GC electrode in a buffer solution of pH 7 at a scan rate of 50 mVs⁻¹ for various concentrations (37.5–1500 ppb) of As³⁺.

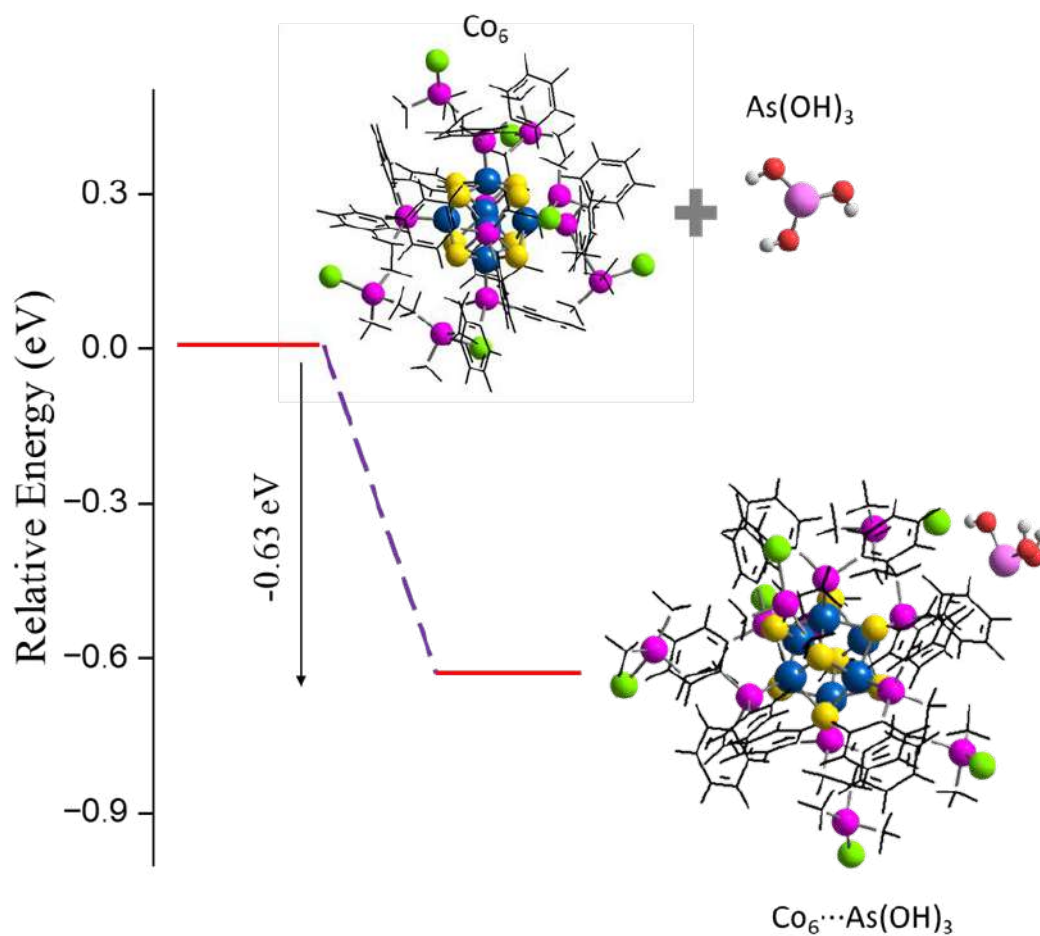


Figure S27. Relative energy profile of the interaction between As(OH)_3 and the Co_6 nanocluster.

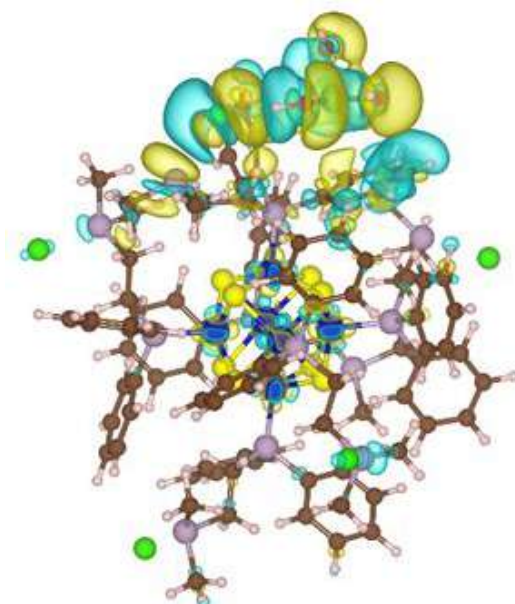


Figure S28. Charge density difference (CDD) analysis of As(OH)_3 binding to the Co_6 cluster. The color code is, blue: Co, yellow: S, green: Cl, lavender: P, brown: C, pink: H. The positive and negative isosurfaces constructed at $0.001 \text{ eV}/\text{\AA}^3$ are represented by cyan and yellow isosurfaces.

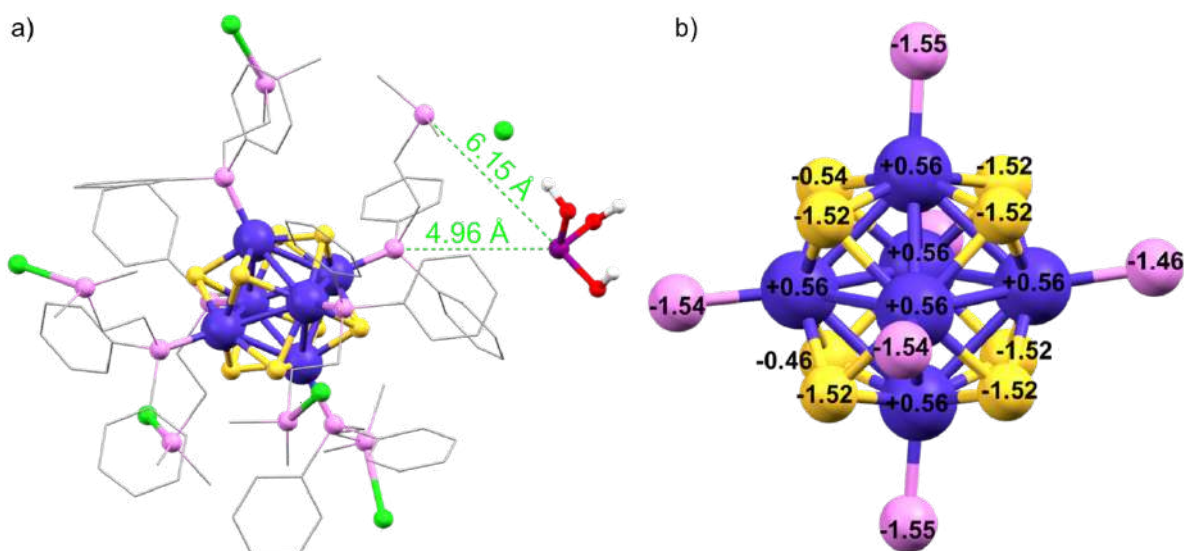


Figure S29. a) Interactions between As(OH)₃ and the Co₆ nanocluster. B) Bader charge analysis of the Co₆S₈P₆ unit.

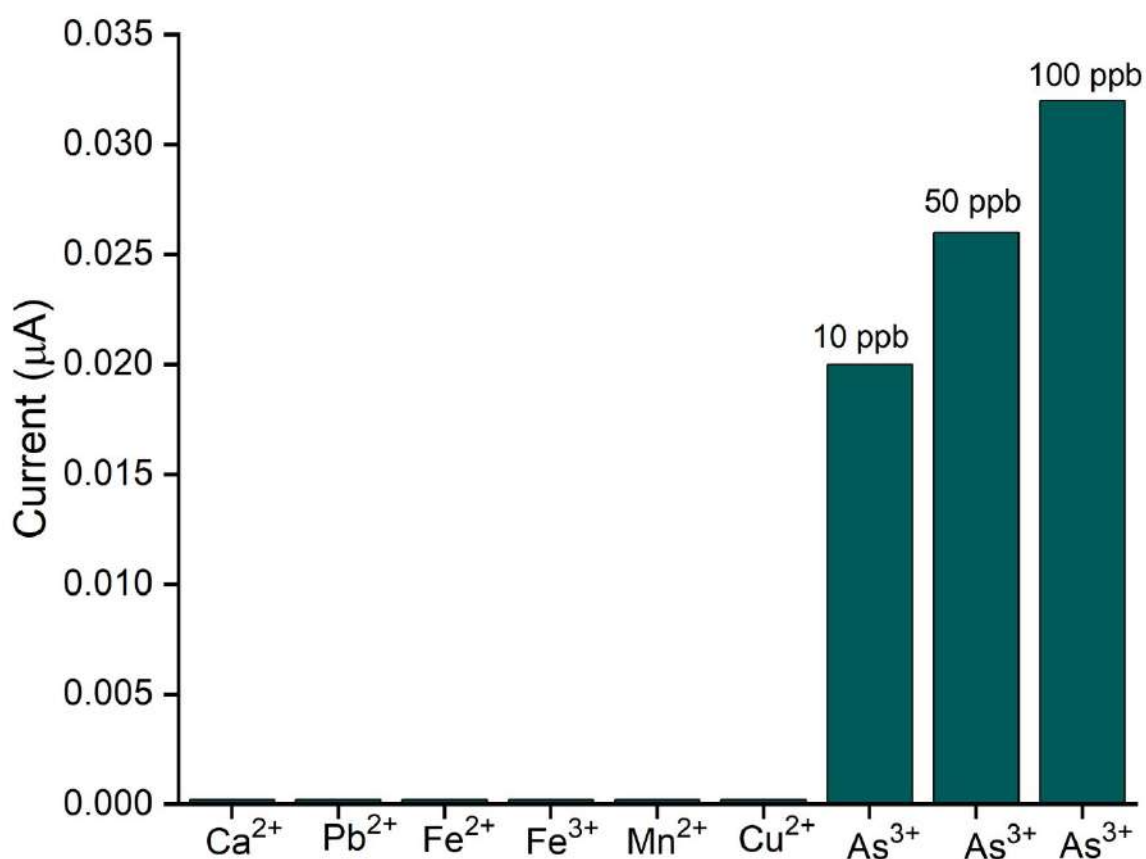


Figure S30. Interfering ions study with different metal ions (100 ppb Ca²⁺, Fe²⁺, Fe³⁺, Pb²⁺, Mn²⁺, and Cu²⁺ added sequentially) and the response of arsenic in presence of all the metal ions in PBS.

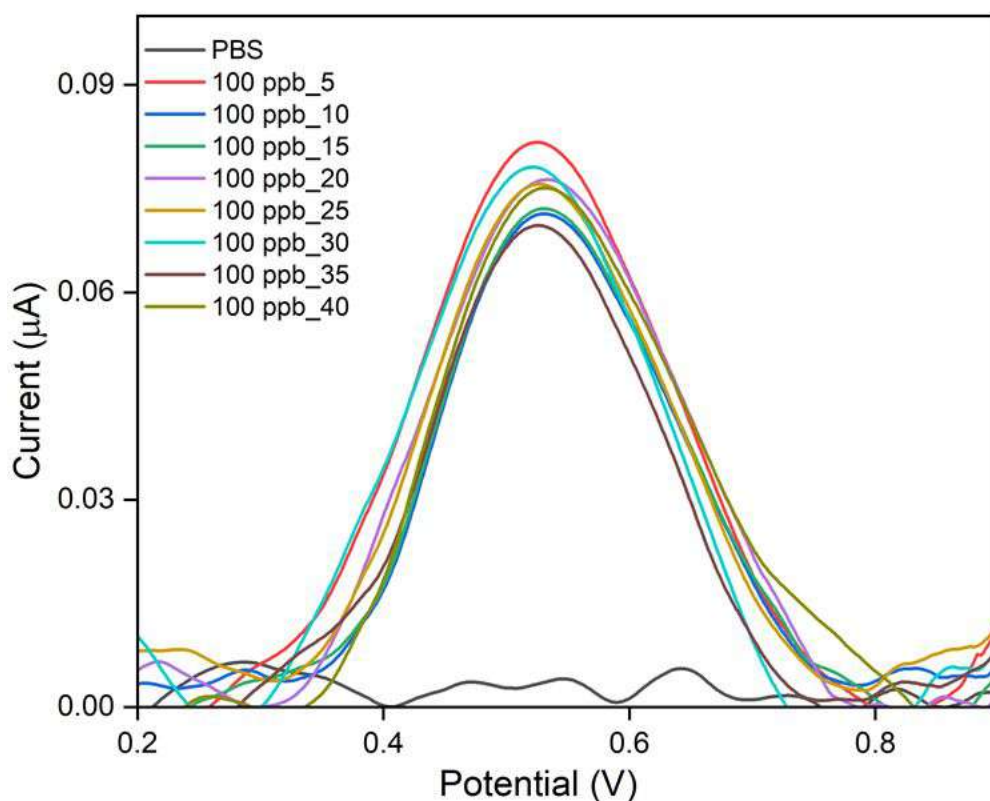


Figure S31. Baseline corrected voltammetric profiles of recyclability of ESD- Co_6 modified GC electrode in phosphate buffer solution of pH 7 up to 40 cycles at a scan rate of 50 mVs^{-1} for a fixed concentration (100 ppb) of As^{3+} .

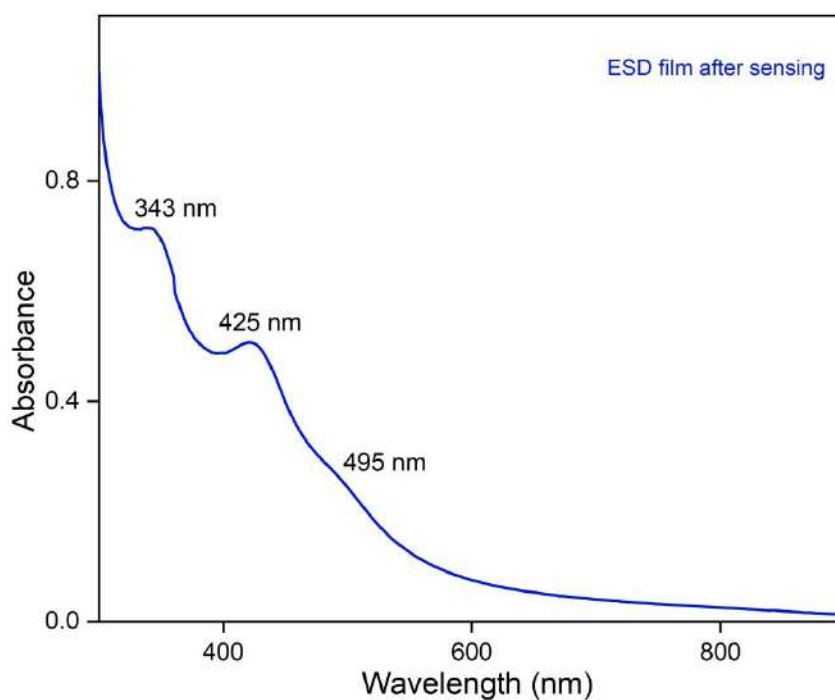


Figure S32. UV-vis absorption spectra of the ESD-film dissolved in DCM after 40 cycles of arsenic sensing experiments. The appearance of identical absorption bands indicating the essential structural integrity of the cluster after sensing.

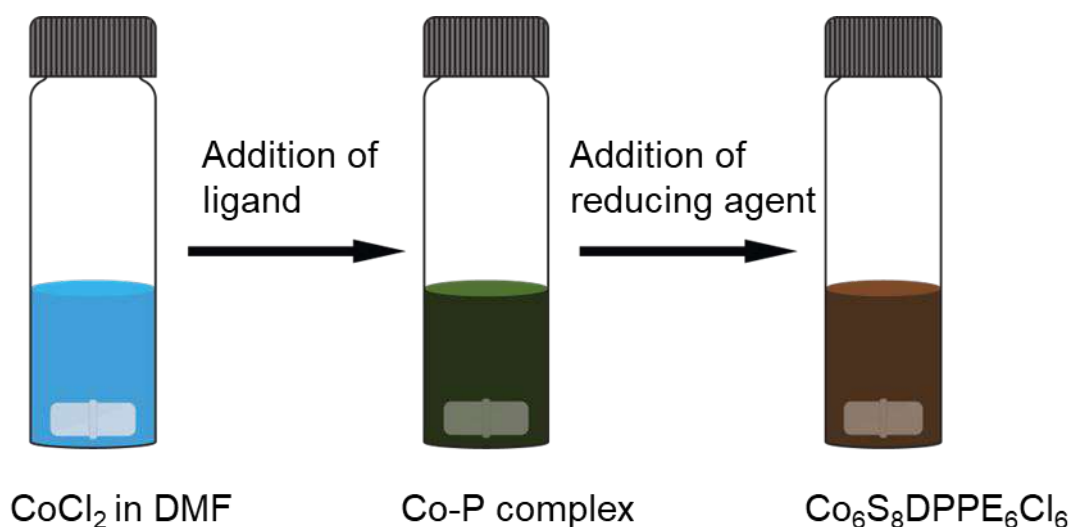


Figure S33. Schematic diagram of the reaction vessel during the synthesis of the $[\text{Co}_6\text{S}_8\text{DPPE}_6\text{Cl}_6]$ nanocluster.

Calculation of LOD

The theoretical limit of detection (LOD) was calculated using the following formula:¹⁰

$$\text{LOD} = \frac{3 \times \sigma}{M}$$

Where σ is the standard deviation of the blank sample and M is the slope of the linear fit.

Therefore,

$$\text{LOD} = \frac{3 \times 3.9225 \times 10^{-10}}{1.77 \times 10^{-7}} = 0.66 \text{ ppb}$$

References

1. Kresse, G.; Hafner, J. Ab Initio Molecular-Dynamics Simulation of the Liquid-Metal–Amorphous-Semiconductor Transition in Germanium. *Phys. Rev. B: Condens. Matter Mater. Phys.* **1994**, 49, 14251.
2. G. Kresse and J. Hafner, *Phys. Rev. B*, **1994**, 49, 14251–14269.
3. Perdew, J. P.; Chevary, J. A.; Vosko, S. H.; Jackson, K. A.; Pederson, M. R.; Singh, D. J.; Fiolhais, C. Atoms, molecules, solids, and surfaces: Applications of the generalized gradient approximation for exchange and correlation. *Phys. Rev. B: Condens. Matter Mater. Phys.* **1992**, 46, 6671.
4. Tang, W., Sanville, E., Henkelman, G. A grid-based Bader analysis algorithm without lattice bias, *J. Phys.: Compute Mater.* **2009**, 21 084204.
5. S. Grimme, *J. Comput. Chem.*, **2006**, 27, 1787–1799.

6. Frisch, M. J.; Trucks, G. W.; Schlegel, H. B.; Scuseria, G. E.; Robb, M. A.; Cheeseman, J. R.; Scalmani, G.; Barone, V.; Mennucci, B.; Petersson, G. A.; Nakatsuji, H.; et al. Gaussian 09, Revision D.01; *Gaussian, Inc.: Wallingford, CT*, **2009**.
7. Becke, A. D. Density-Functional Thermochemistry. III. The Role of Exact Exchange. *J. Chem. Phys.* **1993**, 98, 5648-5652.
8. McLean, A. D.; Chandler, G. S. Contracted Gaussian Basis Sets for Molecular Calculations. I. Second Row Atoms, Z=11-18. *J. Chem. Phys.* **1980**, 72, 5639 –5648.
9. Lu, T.; Chen, F. Multiwfn: A Multifunctional Wavefunction Analyzer. *J. Comput. Chem.* **2012**, 33, 580-592.
10. Miller, J. N. Basic Statistical Methods for Analytical Chemistry. Part 2. Calibration and Regression Methods. A Review. *Analyst* **1991**, 116 (1), 3.

Induced Migration of CO₂ from Hydrate Cages to Amorphous Solid Water under Ultrahigh Vacuum and Cryogenic Conditions

Gaurav Vishwakarma, Bijesh K. Malla, K. S. S. V. Prasad Reddy, Jyotirmoy Ghosh, Soham Chowdhury, Sharma S. R. K. C. Yamijala, Sandeep K. Reddy,* Rajnish Kumar,* and Thalappil Pradeep*



Cite This: *J. Phys. Chem. Lett.* 2023, 14, 2823–2829



Read Online

ACCESS |



Metrics & More

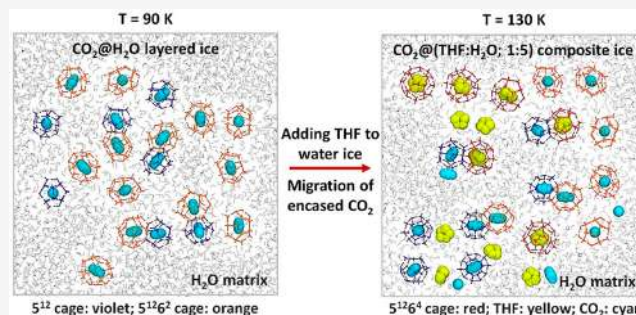


Article Recommendations



Supporting Information

ABSTRACT: Restricted migration of reactive species limits chemical transformations within interstellar and cometary ices. We report the migration of CO₂ from clathrate hydrate (CH) cages to amorphous solid water (ASW) in the presence of tetrahydrofuran (THF) under ultrahigh vacuum (UHV) and cryogenic conditions. Thermal annealing of sequentially deposited CO₂ and H₂O ice, CO₂@H₂O, to 90 K resulted in the partitioning of CO₂ in 5¹² and 5¹²6² CH cages (CO₂@5¹², CO₂@5¹²6²). However, upon preparing a composite ice film composed of CO₂@5¹², CO₂@5¹²6² and THF distributed in the water matrix at 90 K, and annealing the mixture for 6 h at 130 K produced mixed CO₂–THF CH, where THF occupied the 5¹²6⁴ cages (THF@5¹²6⁴) exclusively while CO₂ in 5¹²6² cages (CO₂@5¹²6²) got transferred to the ASW matrix and CO₂ in the 5¹² cages (CO₂@5¹²) remained as is. This cage–matrix exchange may create a more conducive environment for chemical transformations in interstellar environments.



The existence of clathrate hydrates (CHs) under high and ultrahigh vacuum (UHV) and cryogenic conditions is now well established.^{1–17} While CH of CO₂ at 120 K in a vacuum of 10^{–6} to 10^{–7} Torr has been known since 1991,¹² the formation of CHs of CH₄,^{6,18} C₂H₆,¹⁴ CO₂,^{6,18} acetone,¹⁵ formaldehyde,¹⁶ and tetrahydrofuran (THF)¹³ in UHV has been observed in the past few years in the range of 10–130 K. CHs are crystalline host–guest inclusion compounds and have drawn wide interest due to their scientific and technological implications.^{19–21} CHs often coexist along with water ice and are mainly classified into structures I (sI, consisting of two small 5¹² and six large 5¹²6² cages per unit cell) and II (sII, consisting of 16 small 5¹² and eight large 5¹²6⁴ cages per unit cell). While CO₂ is known to be encased in small 5¹² and large 5¹²6² cages, THF due to its larger van der Waals radius occupies the large 5¹²6⁴ cage exclusively.^{2,9,13,22} In UHV, spectroscopic signatures of molecules in different hydrate cages (5¹², 5¹²6², and 5¹²6⁴) were reported,^{6,13–16} although these structures have not been confirmed by X-ray diffraction experiments. However, in a high vacuum, in situ synchrotron X-ray diffraction experiments have been used to establish the existence of CHs of CH₄ and CO₂.⁸ Various CHs could exist along with the water matrix, although their extended crystalline phase has not been observed, in UHV. The presence of CH nuclei in the nanometric domain suggests the coexistence of various phases such as CH, amorphous ice, and dilute solutions of molecules under UHV and cryogenic conditions.¹⁴

The dynamics of host and guest molecules in CHs have been studied, revealing the reorientation of water and diffusion of guest molecules.^{23–29} Moudrakovski et al.,²⁷ by choosing two sets of guest pairs, THF–CO₂ and isobutane–CO₂, have shown that the coupled motions of water and CO₂ are faster in the former case when THF and CO₂ occupy the large (5¹²6⁴) and small (5¹²) cages of sII hydrate, respectively. They have also shown that such molecular dynamics are the result of synergistic guest A–host water–guest B (CO₂–H₂O–THF) hydrogen-bonding interactions. Also, using molecular dynamics simulations performed at elevated temperatures (310, 315, and 320 K) and at a pressure of 100 MPa, Liang et al.³⁰ reported mechanisms of CO₂ migration within CO₂ CHs and suggested that for the diffusion of CO₂ molecules through five-membered water rings of the 5¹² cage, at least one water vacancy is required, and for CO₂ molecules to pass through the six-membered water rings of the 5¹²6² cage, only a slight distortion of the local ring structure is sufficient. Such molecular migrations suggest that host–guest interaction in molecular solids can create a conducive environment for

Received: February 9, 2023

Accepted: March 10, 2023

Published: March 13, 2023



chemical transformations. However, similar observations (for vapor-deposited ice film) under UHV and at extremely low temperatures as reported in this work have not been explored. Chemical evolution in interstellar ices depends mostly on the migration of reacting atoms and molecules at cryogenic temperatures. CH formation/dissociation in such conditions may provide mobility to the molecular species enabling chemical transformation. Also, the interstellar medium is expected to be more complex because a variety of clathrate-forming molecules exist along with water. Various single and mixed CHs may form along with pure solids of CO₂ and other molecular species, including CH₄, CO, CH₃OH, and NH₃ that exist there. Thus, preparing mixed CH and studying guest migration under UHV and cryogenic conditions may have implications for astrophysical and prebiotic science. While CO₂⁶ and THF¹³ CHs are reported to form in UHV, during thermal annealing, these CH cages are likely to undergo molecular exchange leading to the structural evolution of cages. In this study, we have used a custom-built UHV setup,³¹ illustrated in Figure 1, to investigate the evolution of clathrate cages of CO₂ during the formation of THF CH under UHV and cryogenic temperatures.

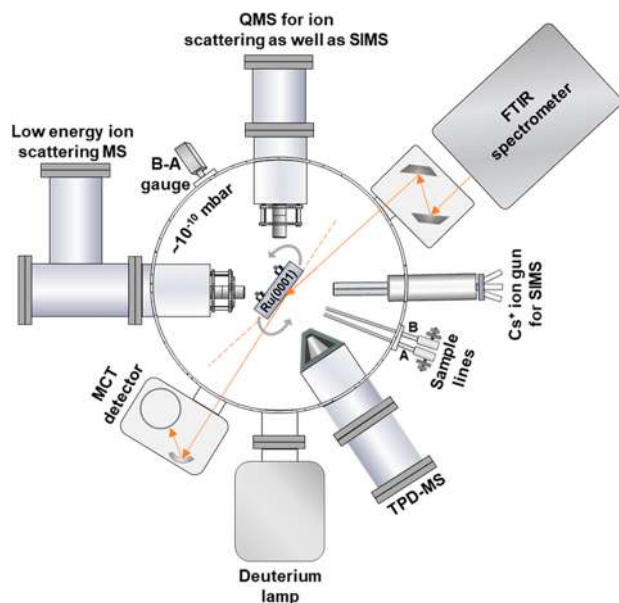


Figure 1. Schematic diagram of the experimental setup. In the schematic, the surface is oriented to do RAIR measurements.

To understand the evolution of clathrate cages of CO₂, we first prepared CO₂@S¹² and CO₂@S¹²6². Figures 2A,B show the temperature-dependent RAIR spectra of 300 ML CO₂@H₂O (150@150 ML) layered film in the C=O antisymmetric stretching region in the 90–150 K window. Spectra in a broader temperature window of 10–150 K are shown in Figure S1. Figures 2A,B show two IR peaks at 2348 and 2341 cm⁻¹ at 90 K, which are assigned to the CO₂ encased in small S¹² (CO₂@S¹²) and large S¹²6² (CO₂@S¹²6²) cages of sI, respectively. The observed frequencies are comparable to the previous reports (2346, 2337 cm⁻¹),^{1,2} where CH was grown by molecular deposition of water–guest gaseous mixtures in a vacuum at cryogenic temperatures. The frequency separation for the CO₂@S¹² and CO₂@S¹²6² cages in this study is ~7 cm⁻¹, which is comparable to ~9 cm⁻¹ of the previous report.¹ Notably, at 90 K, the peaks at 2348 and 2341 cm⁻¹ have full

width at half-maximum (FWHM) values of 3.4 and 6.7 cm⁻¹, respectively (shown in Figure S2), which are comparable to the FWHM values of 4 cm⁻¹ (for CO₂@S¹² cages) and 8 cm⁻¹ (for CO₂@S¹²6² cages) of the previous report.² Furthermore, we have confirmed the formation of CO₂@S¹² and CO₂@S¹²6² cages using quantum chemical simulations (see later). Based on the above observations, the 2348 and 2341 cm⁻¹ peaks are assigned to CO₂@S¹² and CO₂@S¹²6² cages, respectively. This partitioning of CO₂ in different CH cages at 90 K without the “help guest” molecules (THF, ethylene oxide, etc.) is seen for the first time in UHV.^{1,2,9} However, upon annealing the sample above 90 K (also presented as contour plot in Figure 2B), the intensities of both the peaks (2348 and 2341 cm⁻¹) decreased proportionally before vanishing completely at 150 K due to the dissociation of the CH.

In one of our previous studies,⁶ we had reported that in a codeposited mixture of CO₂ and H₂O ice at 10 K under UHV, CO₂ primarily occupies S¹² cages (2346 cm⁻¹) of sI along with a fraction of untrapped CO₂ (2353 cm⁻¹) that exists in the pores of the amorphous water matrix. However, in this study, a peak at ~2382 cm⁻¹ was observed for the sequentially deposited CO₂@H₂O layered film at 10 K (Figure S1). This peak is assigned to the multilayer CO₂ ice film (compared to the spectrum of 150 ML of pure CO₂ film, Figure S3). The peak at 2382 cm⁻¹ in the C=O antisymmetric stretching region did not change significantly during annealing the sample up to 80 K (Figure S1). However, at 90 K, the temperature at which pure CO₂ desorbs, most of the CO₂ diffuses through the water matrix and desorbs, leaving only a small fraction of it in the ice matrix that were later encaged in CH cages. The annealing temperature and associated mobility of CO₂ (mainly induced due to UHV environment) are crucial for forming the CH structure at 90 K. A shift in the C=O antisymmetric stretching region from ~2382 cm⁻¹ at a lower temperature to a doublet (2348 and 2341 cm⁻¹) at 90 K suggests CO₂ diffusion into the water matrix and interaction with water. This frequency shift was noted to be abrupt between 80 and 90 K (Figure S1).

We conducted a time-dependent RAIR experiment using a 300 ML CO₂@H₂O layered film at 80 K to further understand this abrupt frequency change, or, in other words, diffusion of CO₂ into the water matrix and subsequent CH formation. The corresponding IR spectra at 80 K in the C=O antisymmetric stretching region are shown in Figures 2C,D. At 0 min, a peak at ~2382 cm⁻¹ was observed and was assigned to the multilayer film of CO₂.⁶ Upon annealing the sample at the same temperature under UHV for several hours, the peak at 2382 cm⁻¹ changes its shape and position with time due to the diffusion and desorption of CO₂ through the ice matrix. In other words, this band's evolution and shift are directly related to the thickness of the multilayer CO₂ film.³² In addition, to confirm this, IR spectra of pure CO₂ ice of different thicknesses (2–150 ML) in the C=O antisymmetric stretching region at 10 K were collected as shown in Figure S4. The IR spectra in Figure S4 suggest that the intermediate spectra in Figures 2C,D are because of the different (reduced) thicknesses of the CO₂ film. This is because, at 80 K, in the CO₂@H₂O (150@150 ML) layered film, CO₂ molecules diffuse into water matrix. The shift and shape change in the C=O antisymmetric stretching region were observed until ~3 h (see the contour plot, Figure 2D). Finally, the 2382 cm⁻¹ peak was shifted to 2348 and 2341 cm⁻¹ and remained there until the end of the experiment (6 h). These observations suggest that CO₂ in the

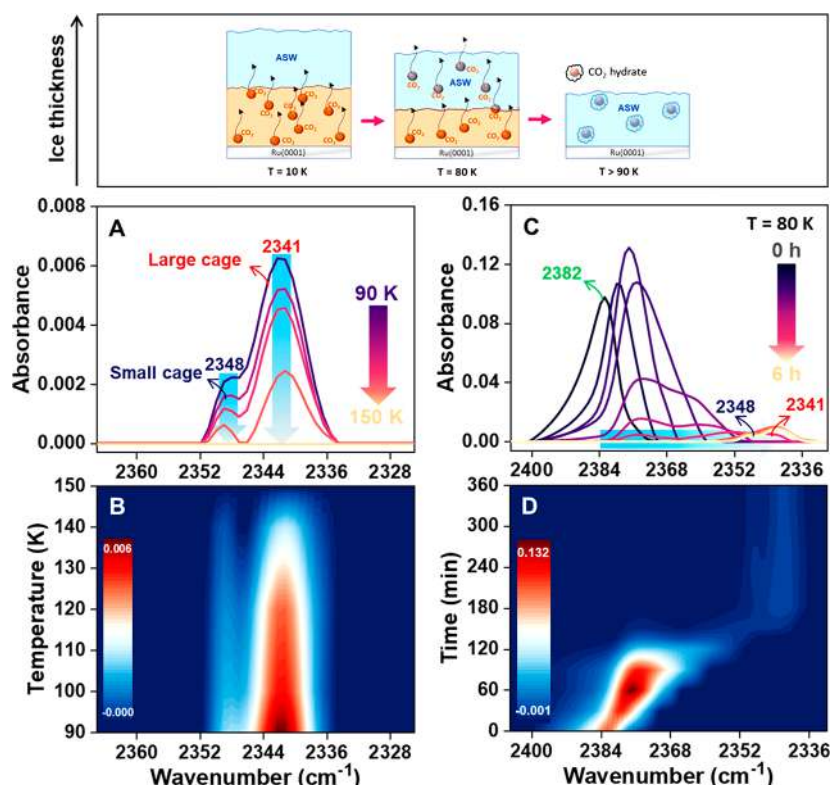


Figure 2. (A, B) Temperature-dependent RAIR spectra of 300 ML CO₂@H₂O (150@150 ML) layered film in the 90–150 K window in the C=O antisymmetric stretching region. (C, D) Time-dependent RAIR spectra of 300 ML CO₂@H₂O (150@150 ML) layered film at 80 K in the C=O antisymmetric stretching region. The peak at 2382 cm⁻¹ (at 0 min) evolved with time and finally resulted in the twin peaks at 2348 and 2341 cm⁻¹ after 3 h. The ice samples were created by vapor deposition at 10 K and further annealed to the set temperatures at an annealing rate of 2 K min⁻¹. Thermal annealing of the as-prepared sample and corresponding physical changes in ice matrix are schematically illustrated in the top panel.

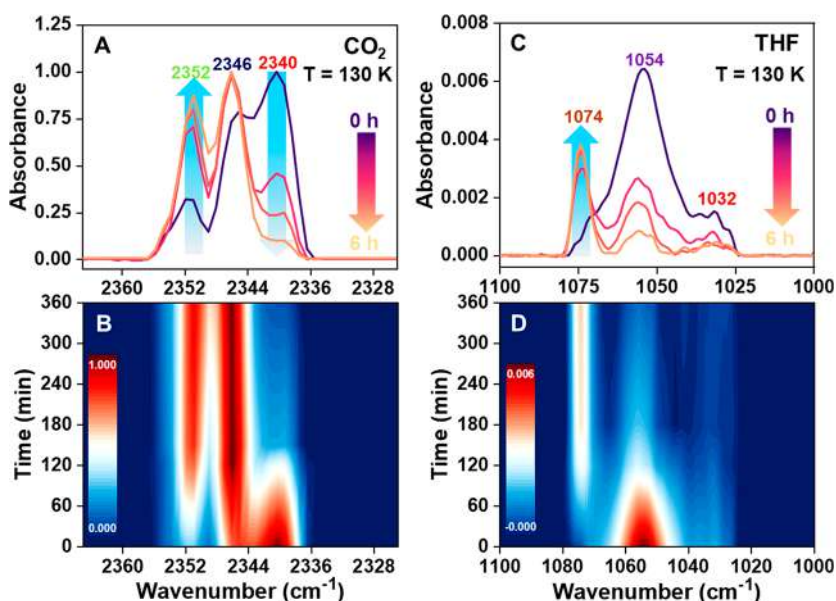


Figure 3. (A, B) Normalized time-dependent RAIR spectra of 300 ML CO₂@(THF+H₂O; 1:5) ice film at 130 K in the C=O antisymmetric stretching region of CO₂. (C, D) Time-dependent RAIR spectra of the same system in the C–O antisymmetric stretching region of THF. The ice sample was created by vapor deposition at 10 K and further annealed to 130 K at an annealing rate of 2 K min⁻¹.

layered CO₂@H₂O film near its desorption temperature diffuses through the water matrix (illustrated schematically in the top panel of Figure 2), and the enhanced mobility of CO₂ leads to its insertion into the different CH cages formed simultaneously at ~90 K.

To examine the host–guest dynamics under UHV at cryogenic temperatures, we have chosen two guests, CO₂ and THF, and prepared 300 ML of CO₂@(THF+H₂O; 1:5) composite film at 10 K. See the Experimental Section for details of sample preparation. The resulting ice sample was

annealed to 130 K and held there for 6 h to create mixed CO₂–THF CH. However, during annealing (of the sample from 10 to 130 K), initially CO₂ diffuses into the THF+H₂O (1:5) ice matrix, and at ~90 K it forms classical sI hydrate forming the CO₂@5¹² and CO₂@5¹²6² cages (2348 and 2341 cm⁻¹, as shown in Figure 2). Figure 3 presents the time-dependent RAIR spectra of 300 ML of CO₂@(THF+H₂O; 1:5) composite film at 130 K in the C=O antisymmetric stretching region (A, B) of solid CO₂ and C–O antisymmetric stretching region (C, D) of solid THF. At 0 h, the spectra in Figures 3A,B show three peaks at 2352, 2346, and 2340 cm⁻¹ in the C=O antisymmetric stretching region that are assigned to CO₂ in amorphous ice matrix, CO₂@5¹², and CO₂@5¹²6² cages, respectively.^{1,6} However, upon annealing the sample at 130 K for 6 h, the peak at 2340 cm⁻¹ decreases and that at 2352 cm⁻¹ increases, while that at 2346 cm⁻¹ remains unaltered. This means that the CO₂ in the CO₂@5¹²6² cages are being transported to the matrix of ASW and CO₂@5¹² cages remain mostly unperturbed in the course of time. Simultaneously, in the C–O antisymmetric stretching region of THF in Figures 3C,D, a new peak arises at 1074 cm⁻¹ while the peaks at 1054 and ~1032 cm⁻¹ decrease within a similar time scale. The peak at 1074 cm⁻¹ is the characteristic peak for THF encased in 5¹²6⁴ CH (THF@5¹²6⁴) cages, whereas the peaks at 1054 and ~1032 cm⁻¹ are assigned to THF trapped in amorphous water pores.^{2,7,13,33} Therefore, at 130 K with time, the encased CO₂ is leaving the CO₂@5¹²6² cages (reduction in the intensity of the 2340 cm⁻¹ peak) while THF is forming the 5¹²6⁴ cages (emergence of the 1074 cm⁻¹ peak); also, the CO₂ molecules that vacated the 5¹²6² cages moved to the amorphous water matrix (this was confirmed by the emergence of the 2352 cm⁻¹ peak). Hence, the formation of THF CH enhanced the mobility of CO₂ molecules into the water matrix. Also, the empty clathrate cages (CO₂@5¹²6² cage in the current case) are inherently unstable, and partial dissociation of the same (which will further enhance the mobility of water molecules) might synergistically help the formation of pure THF CH (or a mixed CO₂–THF CH) at 130 K. This is because the thermodynamic stability of THF CH is superior compared to CO₂ CH.³⁴ Additionally, the formation of CO₂@5¹² and THF@5¹²6⁴ cages was confirmed by calculating the vibrational frequencies of guests in the respective cages, and the obtained results are discussed below.

In addition, we have performed two control experiments to examine the role of THF CH and temperature on the migration of CO₂ in the water matrix under UHV. In the first experiment, we created 300 ML of CO₂@(THF+H₂O; 1:5) composite ice film at 10 K. The resulting sample was annealed to 120 K and held there for 6 h; the results are shown in Figure S5. During annealing at 120 K, neither the 1074 cm⁻¹ peak (in the C–O antisymmetric stretching region of THF) nor the 2352 cm⁻¹ peak (in the C=O antisymmetric stretching region of CO₂) appears, contrary to the results shown in Figures 3A,C. This suggests that at 120 K, neither THF CH forms nor CO₂ migrates into the water matrix. In the second experiment, we created pure CO₂ CH by annealing the CO₂@H₂O layered film (as discussed in Figure 2) at ~90 K. Then the sample was further annealed to 130 K and held there for 6 h; the result is shown in Figure S6. We observed that the peaks at 2348 and 2341 cm⁻¹ in the C=O antisymmetric stretching region decreased proportionally due to the dissociation of CH and desorption of CO₂ at 130 K. However, a decrease in the peak at 2341 cm⁻¹ (due to CO₂@5¹²6²) alone and the appearance

of peak at 2352 cm⁻¹ (CO₂ in ASW) were not observed. This suggests that in the absence of THF CH, CO₂ does not migrate into the water matrix. Therefore, these two control experiments suggest that the THF CH formation in a water matrix containing CO₂ CH is crucial for the mobility of CO₂ under UHV and at 130 K.

In addition, the mobility of H₂O molecules during CH formation/dissociation was monitored for CO₂@H₂O and CO₂@(THF+H₂O; 1:5) films in the O–H stretching region at 130 K; the results are shown in Figure S7. We observed that after 6 h the change in the shape of the O–H stretching region was not significant for pure CO₂ CH (Figure S7A) as it was observed for mixed CH of CO₂ with THF (Figure S7B). The change in shape of the O–H stretching band depicts the ordering/reorientation of water molecules in the ice matrix;³⁵ a similar result has been observed in our previous reports.^{13,36,37} The higher mobility of water in the case of the CO₂@(THF+H₂O; 1:5) composite ice film is reasonable because at 130 K the following events occur: (1) formation of THF CH, (2) dissociation of CO₂ CH (CO₂@5¹²6² cages), and (3) migration of CO₂ molecules into the water matrix.

Fleyfel and Devlin² have reported the epitaxial growth of sI CO₂ hydrate on ethylene oxide hydrate and sII CO₂ hydrate on THF hydrate under vacuum. For epitaxial growth, the resulting CH structure of CO₂ depends on the type of “help guest” and its base structure. However, in the current study, the results presented in Figure 2 clearly demonstrate the partitioning of CO₂ in CO₂@5¹² and CO₂@5¹²6² cages of sI at 90 K without the help guest. In UHV, such a result has not been reported earlier. In addition, when we introduced THF in the CO₂@H₂O film, CO₂@(THF+H₂O; 1:5), and annealed the resulting ice, we observed a unusual situation where at 130 K the water matrix contains THF as well as CO₂@5¹² and CO₂@5¹²6² cages. Moudrakovski et al.²⁷ have presented evidence for cage-to-cage transport of CO₂, when THF and CO₂ were guests in the 5¹²6⁴ and 5¹² cages of sII hydrate, respectively. They have suggested that this is because of the synergistic hydrogen-bonding interactions of THF and CO₂ with the water lattice that promoted the injection of Bjerrum defects, which in turn enabled faster water reorientation. In present study at 130 K, after initial THF CH (THF@5¹²6⁴ cage) formation, caged THF can undergo hydrogen-bonding interaction with CO₂ of both the CO₂@5¹² and CO₂@5¹²6² cages. However, the results presented in Figure 3A demonstrate the migration of CO₂ from CO₂@5¹²6² cages alone. Here, we have two possibilities: (1) As suggested by Liang et al.³⁰ that for CO₂ molecules to move from the 5¹²6² cage, only a slight distortion of the local ring structure is sufficient, compared to the case of the 5¹² cage, where one water vacancy is required. This suggests that the interaction of THF with water of the 5¹²6² cage may provide the required distortion to the local ring structure for CO₂ migration from the CO₂@5¹²6² cages. A similar experimental result has been reported by Devlin and Monreal.³⁸ In mixed CO₂–THF sII CH, they observed³⁸ that over a 5 h period, CO₂ moves from the CO₂@5¹²6² cage and additional CO₂@5¹² cage arises at 116 K. (2) It is possible that caged THF may interact with the CO₂ of both the 5¹² and 5¹²6² cages, enabling the migration to CO₂ of both the cages to the water matrix as suggested by Moudrakovski et al.²⁷ This suggests that primarily CO₂ molecules from both the cages are migrating; in other words, CH cages are dissociating. However, in the presence of THF@5¹²6⁴ cages, the 5¹² cages are being occupied by CO₂. Further

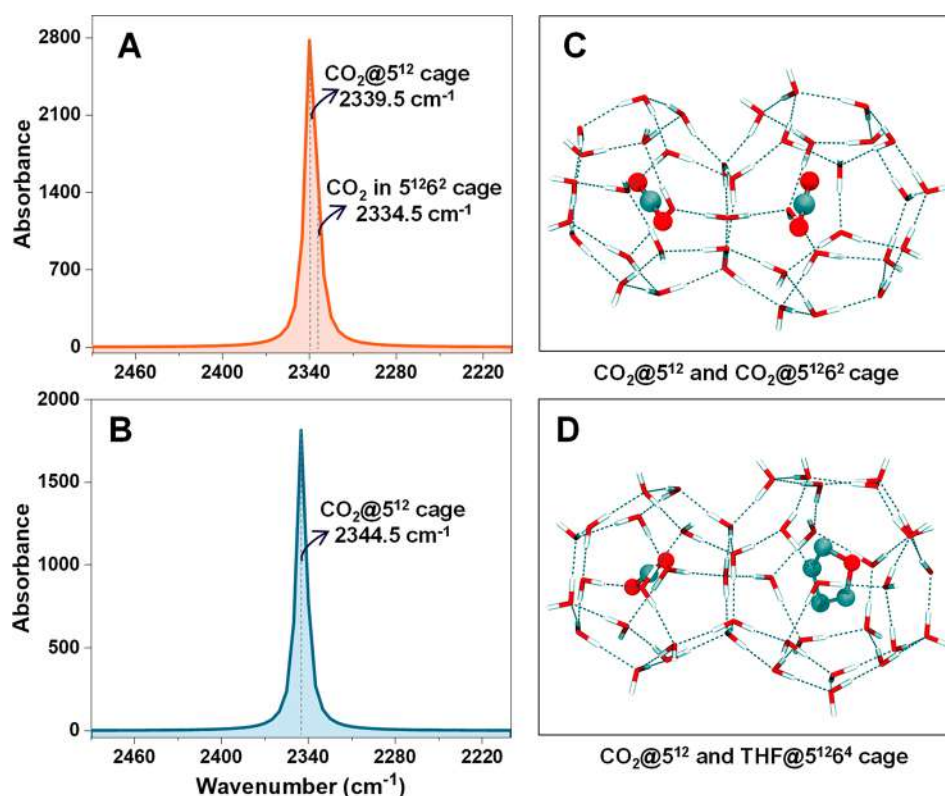


Figure 4. Computed IR spectra in the C=O antisymmetric stretching region of CO₂. (A) When CO₂ was sequentially added in one small 5¹² and one large 5¹²6² cage of sI. (B) When CO₂ and THF were sequentially added in one small 5¹² and one large 5¹²6⁴ cage of the sII, the result is shown only for encased CO₂ in the 5¹² cage. IR spectra were generated from fully optimized CH structures along with the guest molecules; the optimized structures of CH cages are shown in (C) and (D).

experimental and computational studies are required to decipher the exact mechanism of CO₂ migration in the presence of THF under UHV conditions.

If we compare the IR peaks for the CO₂@5¹² cage in water matrix with and without THF, they are at 2346 and 2348 cm⁻¹, respectively. This suggests that there is a structural change^{2,22} in the presence of THF. At lower temperature, when THF is not mobile, the diffusing CO₂ forms sI hydrate, and with increase in temperature when THF is mobile, formation of sII hydrate was observed. It should be noted that the IR spectral resolution employed in the work was 2 cm⁻¹. The change in vibrational frequency of the CO₂@5¹² cage in presence and absence of THF is computed, and the results are discussed below.

We confirmed the formation of pure CO₂ CH (CO₂@5¹² and CO₂@5¹²6²) and mixed CH of CO₂ with THF (CO₂@5¹² and THF@5¹²6⁴) using quantum chemical calculations. The optimized geometries and corresponding vibrational frequencies for different CH structures in the C=O antisymmetric stretching region of CO₂ are shown in Figure 4. For pure CO₂ CH, the relevant computed vibrational frequencies for CO₂@5¹² and CO₂@5¹²6² cages are 2339.5 and 2334.5 cm⁻¹, respectively, as shown in Figure 4A. The frequency shift between two peaks (of CO₂@5¹² and CO₂@5¹²6² cages) obtained in computational and experimental studies are ~5 and ~7 cm⁻¹, respectively (Table S1). Thus, the computationally determined vibrational frequencies in the C=O antisymmetric stretching region during hydrate formation closely match with the experimental values shown in Figure 2A. Similarly, for mixed CH of CO₂ with THF, the computed vibrational frequencies for CO₂@5¹² and THF@5¹²6⁴ cages are

2344.5 cm⁻¹ (in the C=O antisymmetric stretching region of CO₂) and 1087 cm⁻¹ (in the C–O antisymmetric stretching region of THF). These computed results agree well with the experimental results shown in Figures 3A,C and are listed in Table S2. The computed IR spectrum for the CO₂–THF is shown in Figure 4B. If we compare the computed vibrational frequencies for the CO₂@5¹² cage with and without THF in an adjacent cage, they are at 2344.5 and 2339.5 cm⁻¹, respectively. This suggest that THF is indeed playing a crucial role in structural evolution of CO₂ CH. Here, all the calculations were done by considering the small and large cages of CH structures adjoining each other. The coordinates of the optimized geometries of pure CO₂ CH (CO₂@5¹² and CO₂@5¹²6² cages) and mixed CH of CO₂–THF (CO₂@5¹² and THF@5¹²6⁴ cages) are given in Tables S3 and S4.

The CO₂ dynamics in the presence of polar THF discussed in this work can be extended for several other guest molecules to understand the molecular mobility and structural evolution of CH cages in such molecular solids under UHV and cryogenic conditions. Such molecular mobility could lead to new reaction pathways for chemical transformation. For example, when CO₂ (or other guest molecule) is encased, these CO₂ molecules are perhaps not available for any reaction. However, if these molecules come out of cages under certain circumstances as the present work suggests, new chemical pathways are possible, which would lead to new possibilities of chemical evolution.

In this study, we observed the migration of CO₂ from 5¹²6² CH cages to the bulk of ASW in the presence of THF at 130 K in UHV. Continuous evolution of CH structures and the

corresponding changes in the ice matrix imply rapid structural dynamics and flexibility of the ice matrix, possibly similar to liquid-like order at 130 K, in UHV. This CH cage-to-matrix exchange of molecules suggests an active environment in these molecular solids that enables mobility of the species for chemical transformations, specially with additional activation. The structural evolution in mixed CHs implies mechanical changes in the system, although the time scale of this process has not been examined. It occurs faster than the time needed for spectral measurements (<2 s) so that all the species are captured in one spectrum.

■ ASSOCIATED CONTENT

SI Supporting Information

The Supporting Information is available free of charge at <https://pubs.acs.org/doi/10.1021/acs.jpclett.3c00373>.

Experimental Section (including experimental setup, materials and reagents, sample preparation, experimental procedure, RAIRS setup, and computational details); temperature-dependent/time-dependent RAIR spectra of pure CO₂, CO₂@H₂O, and CO₂@(THF+H₂O; 1:5) films; comparison of the experimental and computational vibrational frequencies (Tables S1 and S2) and Cartesian coordinates (Tables S3 and S4) for pure CO₂ CH and mixed CH of CO₂ and THF (PDF)

■ AUTHOR INFORMATION

Corresponding Authors

Thalappil Pradeep – DST Unit of Nanoscience (DST UNS) and Thematic Unit of Excellence (TUE), Department of Chemistry, Indian Institute of Technology Madras, Chennai 600036, India; International Centre for Clean Water, IIT Madras Research Park, Chennai 600113, India; orcid.org/0000-0003-3174-534X; Email: pradeep@iitm.ac.in

Rajnish Kumar – Department of Chemical Engineering, Indian Institute of Technology Madras, Chennai 600036, India; International Centre for Clean Water, IIT Madras Research Park, Chennai 600113, India; orcid.org/0000-0002-4172-2638; Email: rajnish@iitm.ac.in

Sandeep K. Reddy – Centre for Computational and Data Science, Indian Institute of Technology Kharagpur, Kharagpur, West Bengal 721302, India; orcid.org/0000-0002-1458-6853; Email: skreddy@iitkgp.ac.in

Authors

Gaurav Vishwakarma – DST Unit of Nanoscience (DST UNS) and Thematic Unit of Excellence (TUE), Department of Chemistry, Indian Institute of Technology Madras, Chennai 600036, India

Bijesh K. Malla – DST Unit of Nanoscience (DST UNS) and Thematic Unit of Excellence (TUE), Department of Chemistry, Indian Institute of Technology Madras, Chennai 600036, India

K. S. S. V. Prasad Reddy – Department of Chemistry, Indian Institute of Technology Madras, Chennai 600036, India

Jyotirmoy Ghosh – Department of Chemistry, Purdue University, West Lafayette, Indiana 47907, United States

Soham Chowdhury – DST Unit of Nanoscience (DST UNS) and Thematic Unit of Excellence (TUE), Department of Chemistry, Indian Institute of Technology Madras, Chennai 600036, India

Sharma S. R. K. C. Yamijala – Department of Chemistry and Centre for Atomistic Modelling and Materials Design, Centre for Quantum Information, Communication, and Computing, and Centre for Molecular Materials and Functions, Indian Institute of Technology Madras, Chennai 600036, India; orcid.org/0000-0003-1773-9226

Complete contact information is available at: <https://pubs.acs.org/doi/10.1021/acs.jpclett.3c00373>

Author Contributions

G.V. and T.P. designed the research; G.V., B.K.M., and S.C. performed the experiments; K.S.S.V.P.R., S.S.R.K.Y., and S.K.R. performed the quantum chemical calculations; G.V., B.K.M., K.S.S.V., J.G., S.C., S.S.R.K.Y., S.K.R., R.K., and T.P. analyzed data; and G.V., B.K.M., R.K., and T.P. wrote the paper.

Notes

The authors declare no competing financial interest.

■ ACKNOWLEDGMENTS

We acknowledge the Science and Engineering Research Board (SERB), Department of Science and Technology (DST), Government of India, for research funding. T.P. and R. K. acknowledge funding from the Centre of Excellence on Molecular Materials and Functions under the Institution of Eminence scheme of IIT Madras. S.K.R. acknowledges the ISIRD award, IIT Kharagpur for the financial support and the National Supercomputing Mission (NSM) for providing computing resources of “PARAM Shakti” at IIT Kharagpur, which is implemented by C-DAC and supported by the Ministry of Electronics and Information Technology (MeitY) and Department of Science and Technology (DST), Government of India. S.S.R.K.C.Y. acknowledges the financial support of IIT Madras through its new faculty support grants NFSG (IP2021/0972CY/NFSC008973), NFIG (RF2021/0577CY/NFIG 008973), and DST-SERB (SRG/2021/001455). G.V. and S.C. thank IITM for their research fellowship. B.K.M. thanks the University Grants Commission (UGC) for his research fellowship.

■ REFERENCES

- (1) Fleyfel, F.; Devlin, J. P. FT-IR Spectra of 90 K Films of Simple, Mixed, and Double Clathrate Hydrates of Trimethylene Oxide, Methyl Chloride, Carbon Dioxide, Tetrahydrofuran, and Ethylene Oxide Containing Decoupled D₂O. *J. Phys. Chem.* **1988**, 92 (3), 631–635.
- (2) Fleyfel, F.; Devlin, J. P. Carbon Dioxide Clathrate Hydrate Epitaxial Growth: Spectroscopic Evidence for Formation of the Simple Type-II Carbon Dioxide Hydrate. *J. Phys. Chem.* **1991**, 95 (9), 3811–3815.
- (3) Hallbrucker, A. A Clathrate Hydrate of Nitric Oxide. *Angew. Chemie Int. Ed.* **1994**, 33 (6), 691–693.
- (4) Hallbrucker, A.; Mayer, E. Unexpectedly Stable Nitrogen, Oxygen, Carbon Monoxide and Argon Clathrate Hydrates from Vapour-Deposited Amorphous Solid Water: An X-Ray and Two-Step Differential Scanning Calorimetry Study. *J. Chem. Soc. Faraday Trans.* **1990**, 86 (22), 3785–3792.
- (5) Mayer, E.; Hallbrucker, A. Unexpectedly Stable Nitrogen and Oxygen Clathrate Hydrates from Vapour Deposited Amorphous Solid Water. *Chem. Commun.* **1989**, No. 12, 749–751.
- (6) Ghosh, J.; Methikkalam, R. R. J.; Bhuin, R. G.; Ragupathy, G.; Choudhary, N.; Kumar, R.; Pradeep, T. Clathrate Hydrates in Interstellar Environment. *Proc. Natl. Acad. Sci. U. S. A.* **2019**, 116 (5), 1526–1531.

- (7) Monreal, I. A.; Devlin, J. P.; Maşlakcı, Z.; Cicek, M. B.; Uras-Aytemiz, N. Controlling Nonclassical Content of Clathrate Hydrates through the Choice of Molecular Guests and Temperature. *J. Phys. Chem. A* **2011**, *115* (23), 5822–5832.
- (8) Bauer, R. P. C.; Ravichandran, A.; Tse, J. S.; Appathurai, N.; King, G.; Moreno, B.; Desgreniers, S.; Sammynaiken, R. In Situ X-Ray Diffraction Study on Hydrate Formation at Low Temperature in a High Vacuum. *J. Phys. Chem. C* **2021**, *125* (48), 26892–26900.
- (9) Netsu, R.; Ikeda-Fukazawa, T. Formation of Carbon Dioxide Clathrate Hydrate from Amorphous Ice with Warming. *Chem. Phys. Lett.* **2019**, *716*, 22–27.
- (10) Ripmeester, J. A.; Ding, L.; Klug, D. D. A Clathrate Hydrate of Formaldehyde. *J. Phys. Chem.* **1996**, *100* (32), 13330–13332.
- (11) Richardson, H. H.; Wooldridge, P. J.; Devlin, J. P. FT-IR Spectra of Vacuum Deposited Clathrate Hydrates of Oxirane H₂S, THF, and Ethane. *J. Chem. Phys.* **1985**, *83* (9), 4387–4394.
- (12) Blake, D.; Allamandola, L.; Sandford, S.; Hudgins, D.; Freund, F. Clathrate Hydrate Formation in Amorphous Cometary Ice Analogs in Vacuo. *Science* **1991**, *254* (5031), 548–551.
- (13) Ghosh, J.; Bhuin, R. G.; Ragupathy, G.; Pradeep, T. Spontaneous Formation of Tetrahydrofuran Hydrate in Ultrahigh Vacuum. *J. Phys. Chem. C* **2019**, *123*, 16300–16307.
- (14) Malla, B. K.; Vishwakarma, G.; Chowdhury, S.; Selvarajan, P.; Pradeep, T. Formation of Ethane Clathrate Hydrate in Ultrahigh Vacuum by Thermal Annealing. *J. Phys. Chem. C* **2022**, *126*, 17983.
- (15) Ghosh, J.; Bhuin, R. G.; Vishwakarma, G.; Pradeep, T. Formation of Cubic Ice via Clathrate Hydrate, Prepared in Ultrahigh Vacuum under Cryogenic Conditions. *J. Phys. Chem. Lett.* **2020**, *11* (1), 26–32.
- (16) Ghosh, J.; Vishwakarma, G.; Das, S.; Pradeep, T. Facile Crystallization of Ice I_h via Formaldehyde Hydrate in Ultrahigh Vacuum under Cryogenic Conditions. *J. Phys. Chem. C* **2021**, *125* (8), 4532–4539.
- (17) Dartois, E. CO Clathrate Hydrate: Near to Mid-IR Spectroscopic Signatures. *Icarus* **2011**, *212* (2), 950–956.
- (18) Ghosh, J.; Methikkalam, R. R. J.; Bhuin, R. G.; Ragupathy, G.; Choudhary, N.; Kumar, R.; Pradeep, T. Reply to Choukroun et Al.: IR and TPD Data Suggest the Formation of Clathrate Hydrates in Laboratory Experiments Simulating ISM. *Proc. Natl. Acad. Sci. U. S. A.* **2019**, *116*, 14409–14410.
- (19) Sloan, E. D. Fundamental Principles and Applications of Natural Gas Hydrates. *Nature* **2003**, *426*, 353–359.
- (20) Walsh, M. R.; Koh, C. A.; Sloan, D. E.; Sum, A. K.; Wu, D. T. Microsecond Simulations of Spontaneous Methane Hydrate Nucleation and Growth. *Science* (80-.). **2009**, *326* (5956), 1095–1098.
- (21) Park, Y.; Kim, D. Y.; Lee, J. W.; Huh, D. G.; Park, K. P.; Lee, J.; Lee, H. Sequestering Carbon Dioxide into Complex Structures of Naturally Occurring Gas Hydrates. *Proc. Natl. Acad. Sci. U. S. A.* **2006**, *103* (34), 12690–12694.
- (22) Kumar, R.; Lang, S.; Englezos, P.; Ripmeester, J. Application of the ATR-IR Spectroscopic Technique to the Characterization of Hydrates Formed by CO₂, CO₂/H₂ and CO₂/H₂/C₃H₈. *J. Phys. Chem. A* **2009**, *113* (22), 6308–6313.
- (23) Davidson, D. W.; Ripmeester, J. A. NMR, NQR, and Dielectric Properties of Clathrates. In *Inclusion Compounds*; Atwood, J. L., Davies, J. E. D., MacNicol, D. D., Eds.; Academic Press: 1984; Vol. 3, pp 69–123.
- (24) Ripmeester, J. A.; Ratcliffe, C. I. Solid State NMR Studies of Inclusion Compounds. In *Inclusion Compounds*; Atwood, J. L., Davies, J. E. D., MacNicol, D. D., Eds.; Oxford University Press: Oxford, 1991; Vol. 5, pp 37–85.
- (25) Kirschgen, T. M.; Zeidler, M. D.; Geil, B.; Fujara, F. A Deuteron NMR Study of the Tetrahydrofuran Clathrate Hydrate Part II:† Coupling of Rotational and Translational Dynamics of Water. *Phys. Chem. Chem. Phys.* **2003**, *5* (23), 5247–5252.
- (26) Davies, S. R.; Sloan, E. D.; Sum, A. K.; Koh, C. A. In Situ Studies of the Mass Transfer Mechanism across a Methane Hydrate Film Using High-Resolution Confocal Raman Spectroscopy. *J. Phys. Chem. C* **2010**, *114* (2), 1173–1180.
- (27) Moudrakovski, I. L.; Udachin, K. A.; Alavi, S.; Ratcliffe, C. I.; Ripmeester, J. A. Facilitating Guest Transport in Clathrate Hydrates by Tuning Guest-Host Interactions. *J. Chem. Phys.* **2015**, *142* (7), 074705.
- (28) Alavi, S.; Ripmeester, J. A. Hydrogen-Gas Migration through Clathrate Hydrate Cages. *Angew. Chemie - Int. Ed.* **2007**, *46* (32), 6102–6105.
- (29) Takeya, S.; Ripmeester, J. A. Dissociation Behavior of Clathrate Hydrates to Ice and Dependence on Guest Molecules. *Angew. Chemie - Int. Ed.* **2008**, *47* (7), 1276–1279.
- (30) Liang, S.; Liang, D.; Wu, N.; Yi, L.; Hu, G. Molecular Mechanisms of Gas Diffusion in CO₂ Hydrates. *J. Phys. Chem. C* **2016**, *120* (30), 16298–16304.
- (31) Bag, S.; Bhuin, R. G.; Methikkalam, R. R. J.; Pradeep, T.; Kephart, L.; Walker, J.; Kuchta, K.; Martin, D.; Wei, J. Development of Ultralow Energy (1–10 eV) Ion Scattering Spectrometry Coupled with Reflection Absorption Infrared Spectroscopy and Temperature Programmed Desorption for the Investigation of Molecular Solids. *Rev. Sci. Instrum.* **2014**, *85* (1), No. 014103.
- (32) Escribano, R. M.; Caro, G. M. M.; Cruz-Diaz, G. A.; Rodríguez-Lazcano, Y.; Maté, B. Crystallization of CO₂ Ice and the Absence of Amorphous CO₂ Ice in Space. *Proc. Natl. Acad. Sci. U. S. A.* **2013**, *110* (32), 12899–12904.
- (33) Monreal, I. A.; Cwiklik, L.; Jagoda-Cwiklik, B.; Devlin, J. P. Classical to Nonclassical Transition of Ether-HCN Clathrate Hydrates at Low Temperature. *J. Phys. Chem. Lett.* **2010**, *1* (1), 290–294.
- (34) Babu, P.; Linga, P.; Kumar, R.; Englezos, P. A Review of the Hydrate Based Gas Separation (HBGS) Process For carbon Dioxide Pre-Combustion Capture. *Energy* **2015**, *85*, 261–279.
- (35) Backus, E. H. G.; Grecea, M. L.; Kleyn, A. W.; Bonn, M. Surface Crystallization of Amorphous Solid Water. *Phys. Rev. Lett.* **2004**, *92* (23), 236101.
- (36) Vishwakarma, G.; Ghosh, J.; Pradeep, T. Desorption-Induced Evolution of Cubic and Hexagonal Ices in an Ultrahigh Vacuum and Cryogenic Temperatures. *Phys. Chem. Chem. Phys.* **2021**, *23* (41), 24052–24060.
- (37) Vishwakarma, G.; Malla, B. K.; Methikkalam, R. R. J.; Pradeep, T. Rapid Crystallization of Amorphous Solid Water by Porosity Induction. *Phys. Chem. Chem. Phys.* **2022**, *24* (42), 26200–26210.
- (38) Devlin, J. P.; Monreal, I. A. Instant Conversion of Air to a Clathrate Hydrate: CO₂ Hydrates Directly from Moist Air and Moist CO₂ (G). *J. Phys. Chem. A* **2010**, *114*, 13129–13133.

Supporting Information

Induced Migration of CO₂ from Hydrate Cages to Amorphous Solid Water under Ultrahigh Vacuum and Cryogenic Conditions

Gaurav Vishwakarma¹, Bijesh K. Malla¹, K. S. S. V. Prasad Reddy², Jyotirmoy Ghosh³, Soham Chowdhury¹, Sharma S. R. K. C. Yamijala^{2,4}, Sandeep K. Reddy^{5}, Rajnish Kumar^{6,7*}, and Thalappil Pradeep^{1,7*}*

¹DST Unit of Nanoscience (DST UNS) and Thematic Unit of Excellence (TUE), Department of Chemistry, Indian Institute of Technology Madras, Chennai 600036, India,

²Department of Chemistry, Indian Institute of Technology Madras, Chennai, 600036 India,

³Department of Chemistry, Purdue University, 560 Oval Drive, West Lafayette, IN, 47907 USA,

⁴Centre for Atomistic Modelling and Materials Design, Centre for Quantum Information, Communication, and Computing, and Centre for Molecular Materials and Functions, Indian Institute of Technology Madras, Chennai 600036, India,

⁵Centre for Computational and Data Science, Indian Institute of Technology Kharagpur, Kharagpur, West Bengal, 721302 India,

⁶Department of Chemical Engineering, Indian Institute of Technology Madras, Chennai 600036, India,

⁷International Centre for Clean Water, IIT Madras Research Park, Chennai 600113, India

Corresponding author

*Email: pradeep@iitm.ac.in, rajnish@iitm.ac.in, skreddy@iitkgp.ac.in

This PDF file includes:

Experimental section (pages S2-S4)

Figure S1 to S7 (pages S5-S11)

Table 1 to 4 (pages S12-S22)

Experimental Section

Experimental setup

All the experiments were conducted in an ultrahigh vacuum chamber (illustrated in Figure 1), described in detail elsewhere.¹ The vacuum chamber is equipped with reflection absorption infrared spectroscopy (RAIRS), temperature-programmed desorption (TPD) mass spectrometry, secondary ion mass spectrometry (SIMS), low energy ion scattering (LEIS) mass spectrometry, and a UV lamp. At room temperature, the base pressure of the chamber was $\sim 5 \times 10^{-10}$ mbar and it was maintained by three oil-free turbomolecular pumps backed by several diaphragm pumps (Pfeiffer vacuum). Vacuum was monitored by a Bayard-Alpert (BA) gauge (PBR 260, Pfeiffer Vacuum) and controlled by a MaxiGauge controller (Pfeiffer, Model TPG 256 A).

A Ru(0001) single crystal surface (15 mm diameter and 1 mm thick) was used as the substrate to grow the thin ice films. The substrate was mounted on a copper holder and connected to the cold tip of the closed-cycle He cryostat (Coldedge Technologies). The substrate temperature could be varied by a resistive heater (25 Ω) from 8-1000 K, and measured with a K-type thermocouple and a platinum sensor with a temperature accuracy/uncertainty of 0.5 K. Temperature (ramping) was controlled and monitored with a temperature controller, Lakeshore, Model 336.

Materials and reagents

CO₂ gas (99.99%) was purchased from Indogas and used without further purification. THF (99.8%) was purchased from Thermo Fisher Scientific India Pvt. Ltd., and Millipore water (H₂O of 18.2 M Ω resistivity) was kept in a vacuum-sealed test tube and was further purified by several freeze-pump-thaw cycles.

Sample Preparation

Before each experiment, the Ru(0001) substrate was heated to 400 K multiple times to ensure the cleanness of the surface, adequate for the present experiments. Thin films of ices were created by vapor deposition at 10 K. Molecular deposition was controlled through two high-precision all-metal leak valves attached to the UHV chamber, and the inlet lines were directed to the middle of the substrate. Out of two sample lines (shown in Figure 1), one (inlet line A) was used exclusively for CO₂ or THF and the other (inlet line B) was used exclusively for H₂O vapor deposition. During vapor deposition, the purity (and ratio of the ice mixture) of CO₂, H₂O and THF were further confirmed by the presence of their distinctive molecular ion peaks in the mass spectrum using a residual gas analyzer. The vapor deposition coverage was expressed in monolayers (ML), assuming that 1.33×10^{-6} mbar s = 1 ML, which was estimated to contain $\sim 1.1 \times 10^{15}$ molecules cm⁻², as followed in our earlier studies.²⁻⁴

Experimental Procedure

For forming pure CO₂ CH (CO₂@5¹² and CO₂@5¹²6²), a layered film was prepared by sequentially depositing 150 ML of CO₂ followed by 150 ML of H₂O (hereafter referred as

CO₂@H₂O) on Ru(0001) at 10 K. After CO₂ deposition, we waited for an adequate period to get back the base pressure in the chamber. For the deposition of 150 ML of CO₂ (or H₂O,) the UHV chamber was backfilled at a total pressure of $\sim 5 \times 10^{-7}$ mbar for 5 min, assuming the same sticking coefficient for both the species. The chamber pressure and deposition time were varied accordingly for preparing the ice films of different thicknesses. Here, coverages were measured as the product of the dosing time and the increase in total chamber pressure for the dose. The as-prepared ice films at 10 K were annealed up to 150 K at an annealing rate of 2 K min⁻¹, and the IR spectra were collected at various temperatures. During annealing, at 90 K, CO₂ diffuses into amorphous ice matrix and forms CO₂@5¹² and CO₂@5¹²6² cages of sI.

The preparation of CH of CO₂ with THF (CO₂@5¹² and THF@5¹²6⁴) was conducted in three steps. First step involved the preparation of a composite film. For this, 100 ML of CO₂ film was prepared followed by co-deposition of 200 ML of THF+H₂O (1:5) film over it at 10 K. For this, the inlet line A was filled with CO₂ vapor and a thin layer of 100 ML of CO₂ was prepared on the substrate. After the deposition of CO₂, inlet line A was evacuated thoroughly, followed by filling it with THF vapor. H₂O vapor was supplied using inlet line B. THF and H₂O vapor were co-deposited in a 1:5 molar ratio to create 200 ML of mixed ice of THF+H₂O over 100 ML CO₂ film. The prepared composite ice was referred to as CO₂@(THF+H₂O; 1:5). In the second step, the resulting composite ice film at 10 K was annealed to 90 K to form CO₂@5¹² and CO₂@5¹²6² cages in the ice matrix containing small fraction of THF. In the third step, this composite ice film with CO₂@5¹², CO₂@5¹²6² and THF distributed in the water matrix was annealed to 130 K and held there for six hours to form mixed CO₂-THF CH. The annealing of ice sample at 130 K for 6 h was required to create THF CH as reported in our previous study⁵ which was performed under similar experimental conditions.

RAIRS Setup

The thermally processed ice films were investigated by a Bruker Vertex 70 FT-IR spectrometer in the 4000-550 cm⁻¹ range with a spectral resolution of 2 cm⁻¹. The spectrometer and the external MCT (mercury cadmium telluride) detector were attached to the chamber through a ZnSe (transparent to IR beam) viewport. The IR beam was taken out from the spectrometer and focused on the sample through gold-plated mirrors at an incident angle of $80 \pm 7^\circ$. The reflected IR beam from the sample was refocused to the detector. The IR beam path outside the vacuum chamber was purged with dry nitrogen to avoid absorption by atmospheric gases. Each spectrum was an average of 512 scans and it required ~ 7 min to complete the acquisition.

Computational Details

We generated the initial coordinates of the clathrates from the cubic cells of sI and sII CHs, as reported by Takeuchi et al.⁶ Here, the sI CH consists of both dodecahedron (5¹²) and tetrakaidecahedron (5¹²6²) cages, whereas the sII CH consists of both dodecahedron (5¹²) and hexadecahedron (5¹²6⁴) cages. In our simulations, to study the inter-cage first-neighbor effects, we considered the combined structures of 5¹² and 5¹²6², as well as 5¹² and 5¹²6⁴ cages. These geometries are obtained by extracting the coordinates of the adjacent 5¹² and 5¹²6²/5¹²6⁴ cages from an sI/sII CH. By incorporating the guest molecules in these adjacent cages, we generated different clathrate structures. In a 5¹² and 5¹²6² adjacent cage, the guest-cage interactions are

studied by inserting CO₂ molecules in both 5¹² and 5¹²6² cages. On the other hand, in the 5¹² and 5¹²6⁴ adjacent cage, the smaller 5¹² cage was filled with CO₂ and the larger 5¹²6⁴ cage was filled with THF. Initially, the guest molecules were placed at the centers of the cages but were allowed to relax during the simulations. The optimized geometries of the first-neighboring cages, namely, 5¹² and 5¹²6², as well as 5¹² and 5¹²6⁴ cages along with the guest molecules are given in Tables S3 and S4.

All simulations were performed using the Kohn-Sham Density Functional theory as implemented in the Gaussian16 software package.⁷ Since including the van der Waals interactions between the host and guest molecules is quite essential while simulating the clathrates, we used the dispersion corrected wb97xD⁸ hybrid functional along with the 6-31+g(d,p) basis set in our simulations. During geometry optimization, all atoms of the clathrate were allowed to relax, and vibrational analysis was conducted to ensure that the optimized clathrates represent the ground state structures, i.e., no imaginary frequency was observed for these optimized geometries. All the reported vibrational frequencies were scaled with a scaling factor of 0.952 (which was obtained from the CCCBDB website).⁹

Supporting information 1:

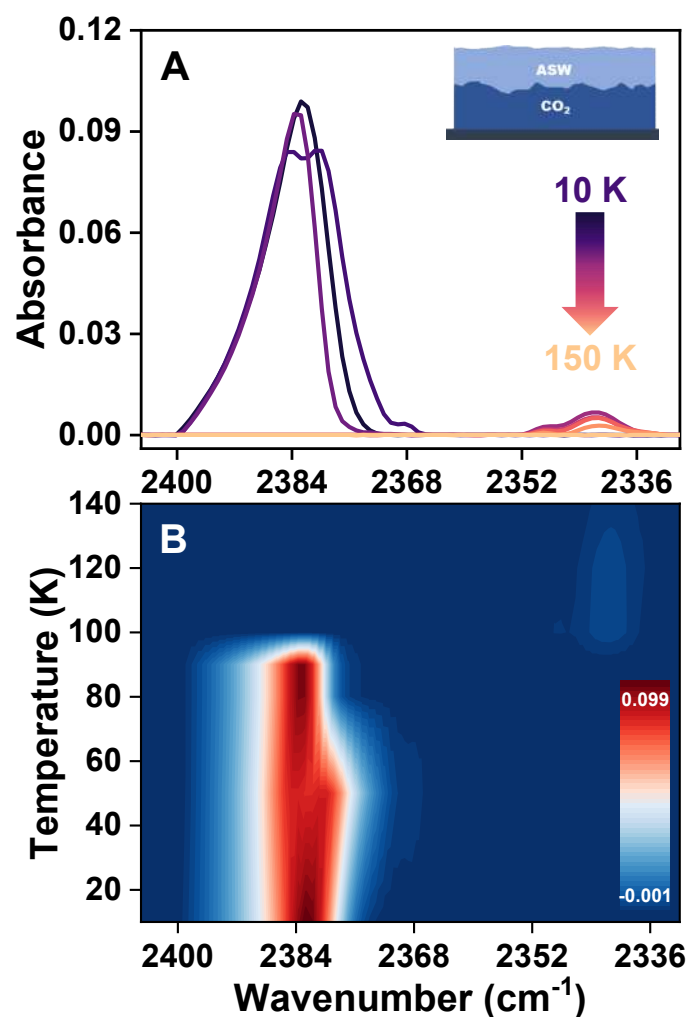


Figure S1. (A-B) Temperature-dependent RAIR spectra of 300 ML $\text{CO}_2@H_2O$ (150@150 ML) layered ice at 10-150 K in the C=O antisymmetric stretching region. The $\text{CO}_2@H_2O$ layered ice was created by vapor deposition at 10 K and further annealed to the set temperatures at an annealing rate of 2 K min^{-1} . Upon annealing the sample above 90 K, CO_2 molecule diffuses and desorbs through water matrix while a small fraction of CO_2 remains into amorphous solid water.

Supporting information 2:

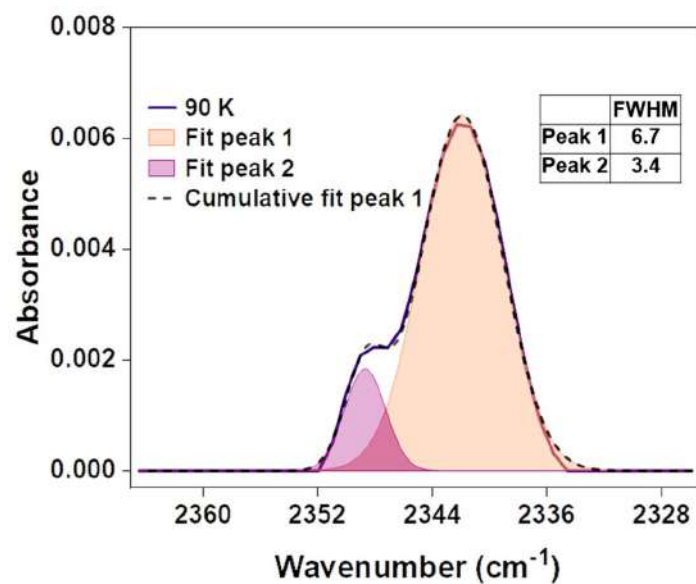


Figure S2. The IR spectrum in the Figure 2A in the C=O antisymmetric stretching region at 90 K was deconvoluted to calculate the FWHM for the peak at 2348 cm⁻¹ (for the CO₂ in the small 5¹² cages) and 2341 cm⁻¹ (for the CO₂ in the large 5¹²6² cages). The obtained FWHM values are 3.4 and 6.7 cm⁻¹, respectively.

Supporting information 3:

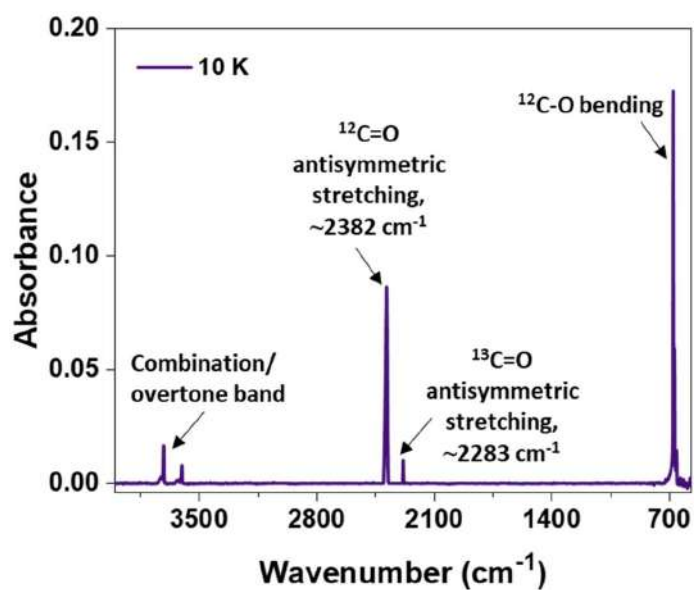


Figure S3. Full scale RAIR spectrum of 150 ML of CO₂ at 10 K. Ice sample was prepared by vapor deposition at 10 K.

Supporting information 4:

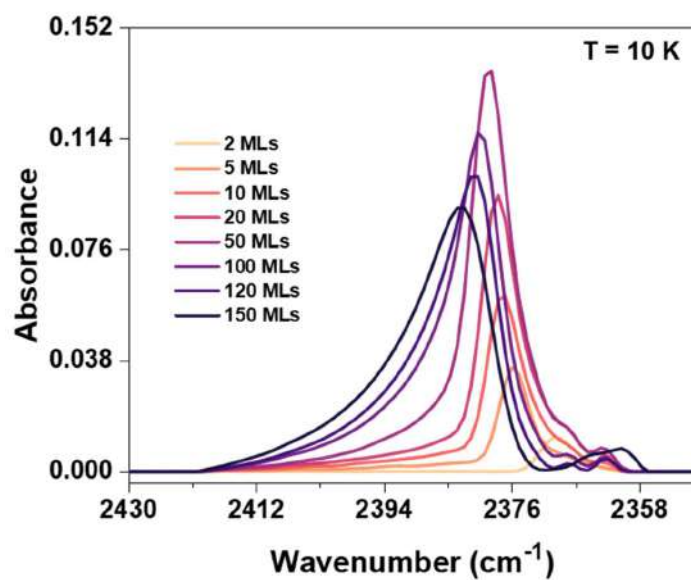


Figure S4. Thickness-dependent RAIR spectra of 2-150 ML of pure CO₂ in the C=O antisymmetric stretching region at 10 K. Ice sample was prepared by vapor deposition at 10 K. The shape and peak positions of IR spectra are highly sample-thickness dependent.

Supporting information 5:

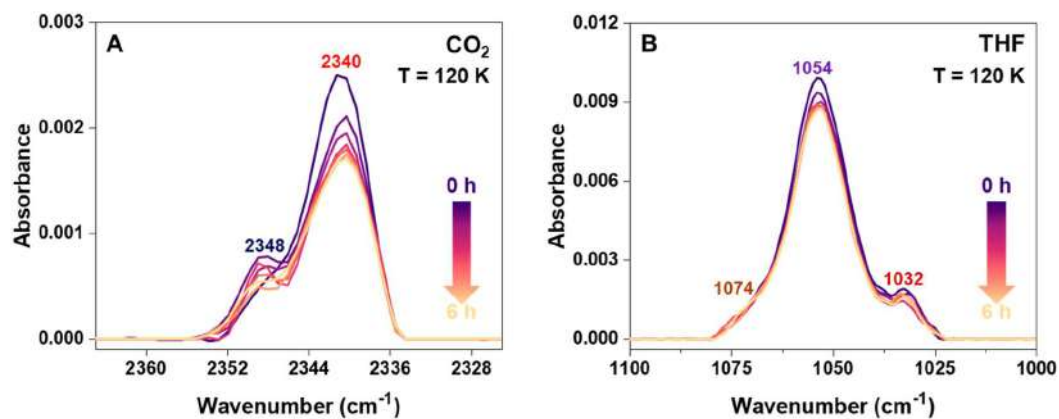


Figure S5. Time-dependent RAIR spectra of 300 ML CO₂@(THF+H₂O; 1:5) ice film at 120 K in (A) C=O antisymmetric stretching region of CO₂ and (B) C-O antisymmetric stretching region of solid THF. The ice sample was created by vapor deposition at 10 K and further annealed to 120 K at an annealing rate of 2 K min⁻¹. At 120 K with time, neither 1074 cm⁻¹ peak emerged nor the 2340 cm⁻¹ peak decreased contrary to the results in Figure 3. The obtained result suggests that formation of THF CH is crucial for CO₂ molecules migration.

Supporting information 6:

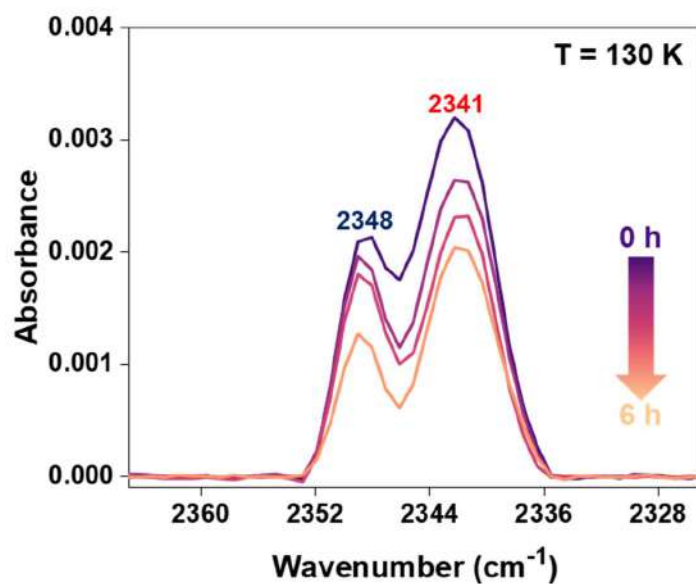


Figure S6. Time-dependent RAIR spectra of 300 ML CO₂@H₂O ice at 130 K in the C=O antisymmetric stretching region. The ice sample was created by vapor deposition at 10 K and further annealed to 130 K at an annealing rate of 2 K min⁻¹. During annealing at 130 K for several hours both the peaks at 2348 and 2341 cm⁻¹ decreased proportionally due to the CO₂ CH dissociation at elevated temperatures.

Supporting information 7:

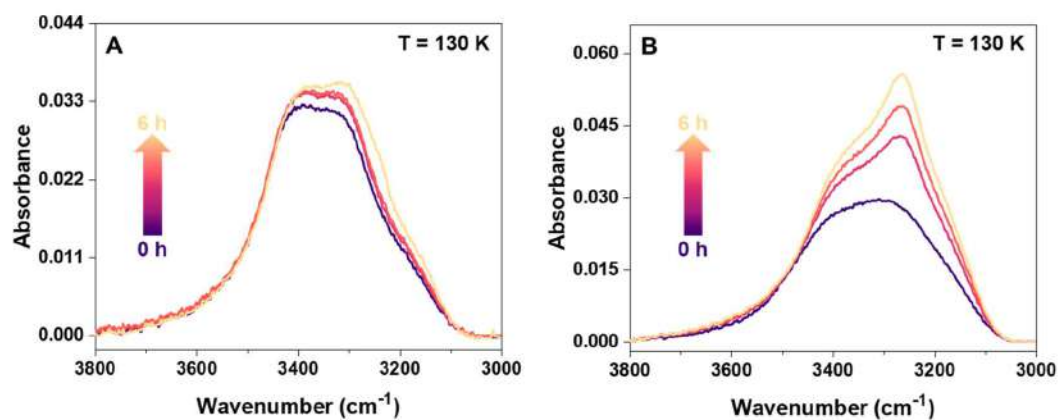


Figure S7. Time-dependent RAIR spectra for (A) CO₂@H₂O layered ice and (B) CO₂@(THF+H₂O; 1:5) ice films in the O-H stretching region at 130 K. The ice samples were created by vapor deposition at 10 K and further annealed to 130 K at an annealing rate of 2 K min⁻¹. The change in shape of the O-H stretching band is prominent in latter case compared to the former. Such a change in shape of the O-H stretching band depicts the reorientation of water molecules in the ice matrix.

Table S1. Comparison of the computational and experimental vibrational frequency of pure CO₂ CH in the C=O antisymmetric stretching region.

CO ₂ CH structure I	5 ¹² and 5 ¹² 6 ² cage	Frequency shift between the two cages
Experimental vibrational frequency	2348 cm ⁻¹ (5 ¹² cage)	7 cm ⁻¹
	2341 cm ⁻¹ (5 ¹² 6 ² cage)	
Computational vibrational frequency	2339.5 cm ⁻¹ (5 ¹² cage)	5 cm ⁻¹
	2334.5 cm ⁻¹ (5 ¹² 6 ² cage)	

Table S2. Comparison of the experimental and computational vibrational frequency of mixed CO₂ and THF CHs in the C=O antisymmetric stretching of CO₂ and in the C-O antisymmetric stretching region of THF.

Mixed CO ₂ and THF CH	Experimental vibrational frequency	Computed vibrational frequency
CO ₂ in 5 ¹² cage	2346 cm ⁻¹	2344.5 cm ⁻¹
THF in 5 ¹² 6 ⁴ cage	1074 cm ⁻¹	1087 cm ⁻¹

Table S3. Cartesian coordinates of CO₂ CH of adjacent 5¹² and 5¹²6² cages.

H	5.72169700	1.93119900	-1.53170400
H	-0.32862600	4.42413700	-0.10451600
H	2.04103200	0.63354100	-3.50724000
H	3.55246400	-2.77257700	2.21505500
H	5.55315400	2.40022200	2.24285500
H	6.65321000	0.93197000	-0.73842000
H	5.20352900	4.20305600	-1.75310500
H	1.94949100	2.11438800	2.82509700
H	6.01758300	-2.88685500	-0.56925100
H	5.07466000	-2.40184500	2.03657400
H	0.10650400	2.95519600	-0.11272800

H	2.40467400	-1.59235200	-3.03895500
H	1.97110900	-4.55181700	1.95935500
H	3.81890400	3.48495700	-1.69615600
H	5.39478100	1.08149900	3.10063000
H	5.61656500	-2.42321900	-1.99533600
H	3.77552400	-0.80732400	-3.07955600
H	2.66317200	0.82283300	3.40187300
H	1.26770400	-3.29376900	1.36006700
H	4.73222100	3.57996800	0.46910500
H	8.26958800	0.60746500	0.92791900
H	6.84528900	0.86484800	1.57426600
H	1.43360000	3.90723400	1.33161400
H	4.07169900	-3.93294000	-1.17726300
H	2.85909500	-4.07569400	-0.18586600
H	1.51349100	-3.80790200	-3.58618400
H	-0.03982100	0.76165900	-2.99000400
H	3.79808800	3.77850200	1.69564900
H	6.94424900	-1.31165600	0.99312000
H	-0.76182900	1.07996400	-0.96517100
H	2.21473900	-3.67049900	-2.17101700
H	5.84420500	-0.09485600	-2.49936000
H	6.05881200	-0.90525200	-3.83254700
H	1.64870900	3.84094100	-1.55286300
H	1.98702400	2.91239100	-2.75932300
H	-0.41404300	-2.40958900	0.08565400
H	4.20267900	-0.94797200	3.39982700
H	4.27742600	-0.20581100	4.78224100
O	4.75926200	3.44542000	-1.36315600
O	6.04521300	1.63851200	2.63481200

O	6.31705700	1.16116400	-1.62428400
O	0.46968400	3.87906400	-0.09733800
O	5.61887000	-3.19433800	-1.40053700
O	2.80653000	-0.70301300	-3.01306900
O	1.46507400	1.42244000	-3.70295400
O	4.33061400	-2.39560000	2.66509800
O	1.80209100	1.21854200	3.17623100
O	2.14342200	-3.72556600	1.50105500
O	4.72868400	3.65576600	1.44102500
O	7.34689300	0.34859800	0.85701800
O	2.00255600	3.82727800	2.13404800
O	6.63397200	-2.24664600	1.06156800
O	3.16403400	-4.30389000	-1.08131600
O	1.62806100	-3.20642000	-2.84651700
O	5.54381900	-0.89346600	-3.02240000
O	2.29385000	3.69755800	-2.26859500
O	4.17774200	-0.05303300	3.83934200
H	1.69705400	4.49184500	2.75668000
H	1.44873500	1.53254400	-4.65691700
H	7.35661800	-2.75264500	1.44157300
O	-2.61214100	3.62234100	-0.00029200
H	-3.11720500	3.60236600	0.85390900
H	-2.09470800	2.79131700	0.00921200
O	-3.15703700	-3.12516300	-2.25419800
H	-3.53195400	-3.39963600	-1.40396600
H	-2.24292300	-2.84166500	-2.05929700
O	-3.90980000	3.23379800	2.31477200
H	-4.82999500	2.95180900	2.15110900
H	-3.45949500	2.40872000	2.57908400

O	-4.36692400	-3.92267400	0.22945500
H	-3.74772300	-3.78121400	0.97548900
H	-4.60432300	-4.85342400	0.22930300
O	-3.05889900	1.12032900	-3.47999200
H	-3.50003600	1.80569500	-2.95097100
H	-3.66192800	0.34128800	-3.50678900
O	-6.30149200	-0.73299600	2.66697500
H	-6.36866300	-1.24331800	1.80763700
H	-7.16134900	-0.79929000	3.09143300
O	-0.76787200	0.36904300	-2.46823400
H	-1.62821200	0.64672100	-2.89421200
O	-4.05121900	-1.55274700	3.84448000
H	-4.93360300	-1.28150700	3.48502900
H	-4.11625300	-1.54884300	4.80260400
O	-6.57142800	2.20733000	-1.13721000
H	-5.72278800	2.60724400	-1.45708000
H	-7.25899800	2.86095800	-1.28807300
O	-0.22126200	0.02479500	1.98266800
H	-0.09357900	-0.91098300	1.73087300
H	0.57464700	0.36935600	2.45928000
O	-6.86084500	-0.42569500	-1.74606400
H	-6.76947800	0.53503100	-1.55011300
H	-7.67331900	-0.53333300	-2.24698400
O	-0.26765200	-2.56449200	1.05288500
H	-1.11637700	-2.85353400	1.42798300
O	-4.25608200	3.25702200	-1.97852700
H	-3.63216600	3.42690400	-1.20430500
H	-4.22328200	4.03895500	-2.53565200
O	-0.59887600	-2.19623300	-1.59950400

H	0.15623600	-2.60979800	-2.06772000
H	-0.64022200	-1.26853400	-1.92654000
O	-2.76469400	0.73575600	2.68408400
H	-1.82698700	0.50201900	2.53429600
H	-3.13847300	0.01324500	3.20659400
O	-6.42512100	-2.05161600	0.43550400
H	-5.72632100	-2.70956300	0.26670100
H	-6.56942900	-1.52400700	-0.37377500
O	-2.68580600	-3.42681400	2.37932300
H	-2.50492000	-4.13993600	2.99763400
H	-3.13198400	-2.72254800	2.90224100
O	-6.39545400	2.04290200	1.73430100
H	-6.26898100	1.13019600	2.03584100
H	-6.40423500	2.00824200	0.76410800
O	-4.61238300	-1.08881100	-3.39712900
H	-4.10916300	-1.84830600	-3.03234000
H	-5.37992700	-0.95187000	-2.82225500
O	-0.80774600	1.56810400	-0.10803200
H	-0.57748700	0.95572300	0.62884100
C	-3.54966100	-0.22139700	0.06794800
O	-4.15979100	0.72026300	-0.23789500
O	-2.96211400	-1.18954000	0.34361800
C	2.46306800	0.04718500	-0.16120100
O	2.55910800	1.18003900	-0.41096900
O	2.36690100	-1.08043000	0.11553800

Table S4. Cartesian coordinates of mixed CO₂ and THF CH with CO₂@5¹² and THF@5¹²6⁴ cage.

H	1.12509500	3.89385900	1.51521000
H	1.46501500	4.22418400	0.03818700
O	0.72073000	4.08162500	0.65131700
H	4.79711600	-3.88473400	0.48395700
H	3.76102400	-4.22757900	-0.62220600
O	4.71226900	-4.08434600	-0.46599400
H	6.65274500	-0.56929000	0.65303700
H	6.61463400	-1.00865500	-0.83375600
O	7.00599300	-0.35115900	-0.22723700
H	6.80650700	-2.95769800	-2.16746700
H	5.45908700	-2.94005700	-1.38479200
O	6.08249400	-2.37566600	-1.92148200
H	5.14337000	3.53369800	3.63263700
H	4.64274200	2.07047200	3.36031300
O	4.55115800	3.02763700	3.06951800
H	-0.33689400	-2.02050000	-2.15635900
O	-1.11947900	-1.55966000	-1.74916300
H	5.84294200	-2.05423800	2.32679600
H	7.14753700	-1.34591800	2.80486100
O	6.30458400	-1.18370000	2.37227100
H	5.29321100	-0.03448800	3.33945800
H	3.97390400	0.13055000	4.18220100
O	4.79296400	0.58681900	3.90049600
H	5.31964800	1.01700100	-3.57263300
H	5.94654200	2.09211400	-2.64659100
O	5.42885100	1.97814600	-3.46216900
H	6.91635100	1.19442200	-0.69446600
H	7.74217000	2.47488900	-1.08335300
O	6.84490500	2.14147300	-1.00362500

H	5.35584000	-1.37317000	-3.11782700
O	5.02062700	-0.78354300	-3.83222000
O	-1.23841100	2.35327700	0.11334500
H	0.02056100	-4.43520700	1.91765600
H	-0.02983700	-3.02353500	1.26087400
O	0.58917500	-3.78244600	1.49605500
H	2.45773500	-2.18165100	3.68013800
H	1.84553300	-3.23858900	2.66638700
O	2.60537300	-3.04867300	3.24996600
H	4.95079600	3.40695600	1.31535600
H	5.72688800	3.16151700	-0.03855600
O	5.09512900	3.75146200	0.41637100
O	2.42054100	-0.64968300	4.57842700
H	5.27611800	-4.27982800	2.75538700
H	4.02610000	-3.32704500	2.65533400
O	4.94209700	-3.51529900	2.27831100
H	0.84692700	1.74931800	-4.91359800
H	1.77821500	2.12857000	-3.70969700
O	1.05452600	1.49539100	-4.01020100
H	-1.15571100	-1.76526400	-0.05437000
O	-1.12939100	-1.92625500	0.91874500
H	1.71539000	-5.43321400	-0.96751300
H	1.44465000	-4.29300800	0.06290100
O	1.95423200	-4.52898100	-0.74685600
H	1.06108900	1.96419800	3.62253200
H	-0.03633400	0.88774700	3.28663000
O	0.67783600	1.12178300	3.92136100
H	3.77398600	4.21559900	-0.42845900
O	2.97518300	4.51759900	-0.94034500

H	1.44125900	-2.31676600	-3.31724200
H	1.36310200	-3.41836100	-2.17875100
O	0.84046100	-2.93107700	-2.83510800
H	1.69779100	4.24584200	3.80427700
H	2.86348000	3.42674900	3.15511800
O	1.88739100	3.55109600	3.16835500
H	3.20151700	-0.93661100	-3.98392600
H	1.83730500	-0.17821600	-4.07821000
O	2.25002400	-1.05755100	-4.14735800
H	3.86487100	2.72605600	-3.40279100
H	2.91560400	3.58795300	-2.49478300
O	2.95569300	3.09800000	-3.33657100
H	-1.11696500	1.95052400	-0.77091000
H	1.71638400	0.01446100	4.29280200
H	2.26888100	-0.80793400	5.51436800
H	3.10914700	5.45260000	-1.11749700
H	5.41550800	-1.09587300	-4.65075100
O	-6.92841500	-2.21719100	-0.19994500
H	-7.07253800	-1.64952700	-1.00305400
H	-6.16733900	-2.79482600	-0.37782100
O	-1.25815500	0.52773000	2.11727100
H	-1.23681200	1.17183200	1.37367500
H	-1.20646200	-0.36639600	1.71427200
O	-7.23648300	-0.59374500	-2.26373000
H	-7.33335300	0.32607300	-1.94615200
H	-6.46037700	-0.61006200	-2.85809900
H	-0.50143300	2.99890900	0.25313300
O	-4.78527900	-1.70689300	3.12294400
H	-5.68593000	-1.48577400	2.83616700

H	-4.36202000	-0.85588600	3.37275900
O	-4.96010700	3.34851200	-1.86536700
H	-4.46006500	3.45151500	-0.99465200
H	-5.19091100	4.23712200	-2.14928300
O	-3.23640800	-3.31336300	1.61494700
H	-3.82772500	-2.77697800	2.19690000
H	-3.77197000	-3.56796100	0.84435400
O	-3.50861800	1.79550200	-3.51397200
H	-4.04770600	2.39395400	-2.93972000
H	-3.56108300	2.15052000	-4.40521900
O	-7.55295100	1.57482300	1.71675600
H	-7.50273300	0.59666000	1.86048700
H	-8.44099500	1.84599400	1.96183800
O	-3.22157100	-2.81461000	-2.76542200
H	-2.45532600	-2.32421900	-2.36124100
H	-2.84959700	-3.33892200	-3.48004300
O	-5.23028200	2.78852000	2.54527000
H	-6.07706400	2.37504600	2.26835400
H	-5.44725400	3.46916700	3.18688900
H	-1.08329500	-0.60730600	-1.98664800
O	-7.36639600	-1.09094700	2.06508500
H	-7.20010200	-1.53868300	1.17655400
H	-8.07335100	-1.58418100	2.48880900
H	-1.97847200	-2.40330800	1.15273500
O	-4.88713200	-0.70532100	-3.74275000
H	-4.34153500	-1.43563300	-3.40583300
H	-4.36741200	0.10413600	-3.61686200
O	-3.67608200	3.59125600	0.34997600
H	-2.79389500	3.16297900	0.32783400

H	-4.15777500	3.27372400	1.13536000
O	-1.08070300	1.11274700	-2.35056200
H	-0.32382000	1.31344900	-2.94381500
H	-1.89693200	1.37560300	-2.82078900
O	-7.35637800	1.95698900	-1.15119400
H	-6.54692600	2.44292500	-1.38034600
H	-7.34023400	1.83551100	-0.18812300
O	-3.59193300	0.69742400	3.63982300
H	-2.75459000	0.69092100	3.13883900
H	-4.12716200	1.41618500	3.26754800
O	-4.70643700	-3.88399200	-0.74563100
H	-4.18540100	-3.52931200	-1.50154300
H	-4.96713700	-4.77799800	-0.97965500
C	-4.45710900	-0.19086400	0.04396100
O	-3.79719900	-0.92737400	-0.57028400
O	-5.09953400	0.56650400	0.64892900
O	3.77685800	-0.85021500	-0.58678000
C	2.54233800	1.06869600	0.12242400
C	2.21826700	-0.15541400	0.99948000
C	3.53144900	0.51354700	-0.92792100
C	2.62024200	-1.31326900	0.09313900
H	1.64220100	1.45973500	-0.35914100
H	2.98050900	1.88406200	0.70279400
H	2.83871000	-0.16070800	1.90100000
H	1.17105400	-0.19631500	1.30583100
H	4.49385600	1.02883400	-0.93069900
H	3.10713100	0.57019400	-1.93860200
H	2.88911700	-2.22432800	0.63073700
H	1.82044500	-1.54574800	-0.62852800

References

- (1) Bag, S.; Bhuin, R. G.; Methikkalam, R. R. J.; Pradeep, T.; Kephart, L.; Walker, J.; Kuchta, K.; Martin, D.; Wei, J. Development of Ultralow Energy (1-10 eV) Ion Scattering Spectrometry Coupled with Reflection Absorption Infrared Spectroscopy and Temperature Programmed Desorption for the Investigation of Molecular Solids. *Rev. Sci. Instrum.* **2014**, *85* (1), 014103.
- (2) Ghosh, J.; Methikkalam, R. R. J.; Bhuin, R. G.; Ragupathy, G.; Choudhary, N.; Kumar, R.; Pradeep, T. Clathrate Hydrates in Interstellar Environment. *Proc. Natl. Acad. Sci. U. S. A.* **2019**, *116* (5), 1526–1531.
- (3) Ghosh, J.; Bhuin, R. G.; Vishwakarma, G.; Pradeep, T. Formation of Cubic Ice via Clathrate Hydrate, Prepared in Ultrahigh Vacuum under Cryogenic Conditions. *J. Phys. Chem. Lett.* **2020**, *11* (1), 26–32.
- (4) Kim, Y.; Moon, E.; Shin, S.; Kang, H.; Kim, Y.; Moon, E.; Shin, S.; Kang, H. Acidic Water Monolayer on Ruthenium(0001). *Angew. Chemie Int. Ed.* **2012**, *51* (51), 12806–12809.
- (5) Ghosh, J.; Bhuin, R. G.; Ragupathy, G.; Pradeep, T. Spontaneous Formation of Tetrahydrofuran Hydrate in Ultrahigh Vacuum. *J. Phys. Chem. C* **2019**, *123*, 16300–16307.
- (6) Takeuchi, F.; Hiratsuka, M.; Ohmura, R.; Alavi, S.; Sum, A. K.; Yasuoka, K. Water Proton Configurations in Structures I, II, and H Clathrate Hydrate Unit Cells. *J. Chem. Phys.* **2013**, *138* (12), 124504.
- (7) Frisch, M. J., Trucks, G. W., Schlegel, H. B., Scuseria, G. E., Robb, M. A., Cheeseman, J. R., ... & Fox, D. J. (2016). Gaussian 16 Revision C. 01. 2016; Gaussian Inc. Wallingford CT, 421.
- (8) Chai, J. Da; Head-Gordon, M. Long-Range Corrected Hybrid Density Functionals with Damped Atom-Atom Dispersion Corrections. *Phys. Chem. Chem. Phys.* **2008**, *10* (44), 6615–6620.
- (9) Johnson III, R. D. NIST 101. Computational Chemistry Comparison and Benchmark Database, NIST; 1999.



Cite this: *Nanoscale*, 2023, **15**, 8141

Received 28th January 2023,
Accepted 26th March 2023

DOI: 10.1039/d3nr00416c

rsc.li/nanoscale

A luminescent Cu₄ cluster film grown by electro-spray deposition: a nitroaromatic vapour sensor†

Arijit Jana,^a B. K. Spoorthi,^a Akhil S. Nair,^b Ankit Nagar,^a Biswarup Pathak,^b Tomas Base^c and Thalappil Pradeep^a

We present the fabrication and use of a film of a carborane-thiol-protected tetranuclear copper cluster with characteristic orange luminescence using ambient electrospray deposition (ESD). Charged microdroplets of the clusters produced by an electrospray tip deposit the clusters at an air–water interface to form a film. Different microscopic and spectroscopic techniques characterized the porous surface structure of the film. Visible and rapid quenching of the emission of the film upon exposure to 2-nitrotoluene (2-NT) vapours under ambient conditions was observed. Density functional theory (DFT) calculations established the favourable binding sites of 2-NT with the cluster. Desorption of 2-NT upon heating recovered the original luminescence, demonstrating the reusability of the sensor. Stable emission upon exposure to different organic solvents and its quenching upon exposure to 2,4-dinitrotoluene and picric acid showed selectivity of the film to nitroaromatic species.

Selective and observable detection of nitroaromatic precursors, widely used for the synthesis of explosives, has received special attention due to increased concerns of security.^{1–3} Direct detection of such chemical entities using instrumental methods, such as mass spectrometry,⁴ surface-enhanced Raman spectroscopy,⁵ and sophisticated sensor arrays,⁶ requires expensive infrastructure and/or complicated sampling protocols. On the other hand, optical detection with organic and inorganic sensing materials, such as π electron-rich aromatic compounds,⁷ metal–organic frameworks,⁸ dendrimers,⁹ polymers,¹⁰ quantum dots,¹¹ and gold mesoflowers,¹² has been explored for reliable detection. Optical detection primar-

ily relies on visible changes of luminescence in terms of the emission brightness or colour of such materials upon exposure to the sensing materials. Atomically precise metal nanoclusters with tunable luminescence characteristics are versatile additions to this application.^{13–15} Such nanomaterials have specific multicolour luminescence properties due to electronic transitions within closely spaced quantized electronic energy levels.^{16–18} Modulation of luminescence by applying external stimuli, such as temperature,^{19,20} pressure,²¹ and electric potential,²² suggests a possibility to have sensing responses with molecules, particularly electron-deficient nitroaromatic compounds.²³

Detection of nitroaromatics in the gas/vapour phase is challenging compared to their detection in the condensed state, primarily due to their low volatility and a lack of efficient intermolecular interactions.^{24,25} Therefore, the preparation of luminescent vapour sensors with highly sensitive exposed surface area is an essential goal towards easy, fast and reliable sensors. However, fabrication of an active two-dimensional (2D) surface composed of ultra-small nanoclusters is challenging due to their reduced stability, inherent reactivity, unregulated aggregation behaviour and the lack of large order inter-cluster interactions.^{26,27} To overcome such challenges, we introduced the ESD technique, which generates solvated charged microdroplets of cluster ions in air by applying an electric potential.^{28,29} Soft landing of ions onto a transient water surface resulted in a sensitive 2D nanocluster assembled film. The ESD technique favours fast and soft aggregation of clusters at the air–water interface without using long chain ligands,³⁰ metal ions,³¹ mixed solvent systems,³² thermal annealing,³³ and gel forming agents.³⁴ In our earlier experiments, we had shown the advantages of this technique for the preparation of various nanomaterials, including metallic nanobrushes,³⁵ nanopyramids and platelets,³⁶ vertically aligned nanoplates,³⁷ annealed nanoparticle superstructures,³⁸ and other surface exposed nanostructures.³⁹

Here, we have fabricated a robust surface-activated film of a Cu₄@ICBT cluster, covered with an *ortho*-carborane 12-iodo

^aDepartment of Chemistry, DST Unit of Nanoscience (DST UNS) and Thematic Unit of Excellence (TUE), Indian Institute of Technology Madras, Chennai 600036, India. E-mail: pradeep@iitm.ac.in

^bDepartment of Chemistry, Indian Institute of Technology Indore (IIT Indore), Indore 453552, India. E-mail: biswarup@iiti.ac.in

^cDepartment of Synthesis, Institute of Inorganic Chemistry, The Czech Academy of Science 1001, Husinec – Rez, 25068, Czech Republic. E-mail: tbase@iic.acs.cz

† Electronic supplementary information (ESI) available. See DOI: <https://doi.org/10.1039/d3nr00416c>

9-thiol ligand, through the ESD technique. The atomic structure of the cluster shows a nearly square planar Cu_4 core protected by four carborane ligands along with three iodine atoms (shown in Fig. 1a).⁴⁰ $\text{Cu}_4\text{@ICBT}$ was synthesized by a ligand exchange-induced structure transformation (LEIST) reaction starting from the Cu_{18} nanocluster.⁴¹ LEIST synthesis reactions were used for preparing various gold⁴² and silver⁴³ nanoclusters. Synthetic details and structural characterization of the cluster were described previously⁴⁰ and the essential details are presented in Fig. S1 in the ESI.† ESD experiments were performed using a home-built setup. Fig. 1b shows the schematic representation of the ESD setup.

Details of the deposition process are presented in the ESI.† In brief, charged microdroplets of cluster ions were generated upon applying a high voltage (2.5–3 kV) through a platinum

(Pt) wire to a 0.5 mM solution of the cluster using a glass capillary (tip diameter, 25–30 μm) (shown in Fig. S2†). The deposition of ions was performed on water, which was grounded to neutralize the charge. After 30 min of deposition, we observed a white-coloured thin film floating on the water surface (shown in the inset of Fig. 1b and c), and this film was transferred onto either a clean glass slide or an Al foil for further experiments. The floating nature of the film is due to the hydrophobic nature of carboranes,⁴⁴ and the surface charge of the deposited ions is responsible for interparticle interactions, which resulted in the formation of a stable film.

Next, the surface structure of the ESD film was characterized using optical and electron microscopic techniques. Optical micrographs showed a sheet-like translucent appearance and the film was crumpled at multiple locations (Fig. 1c,

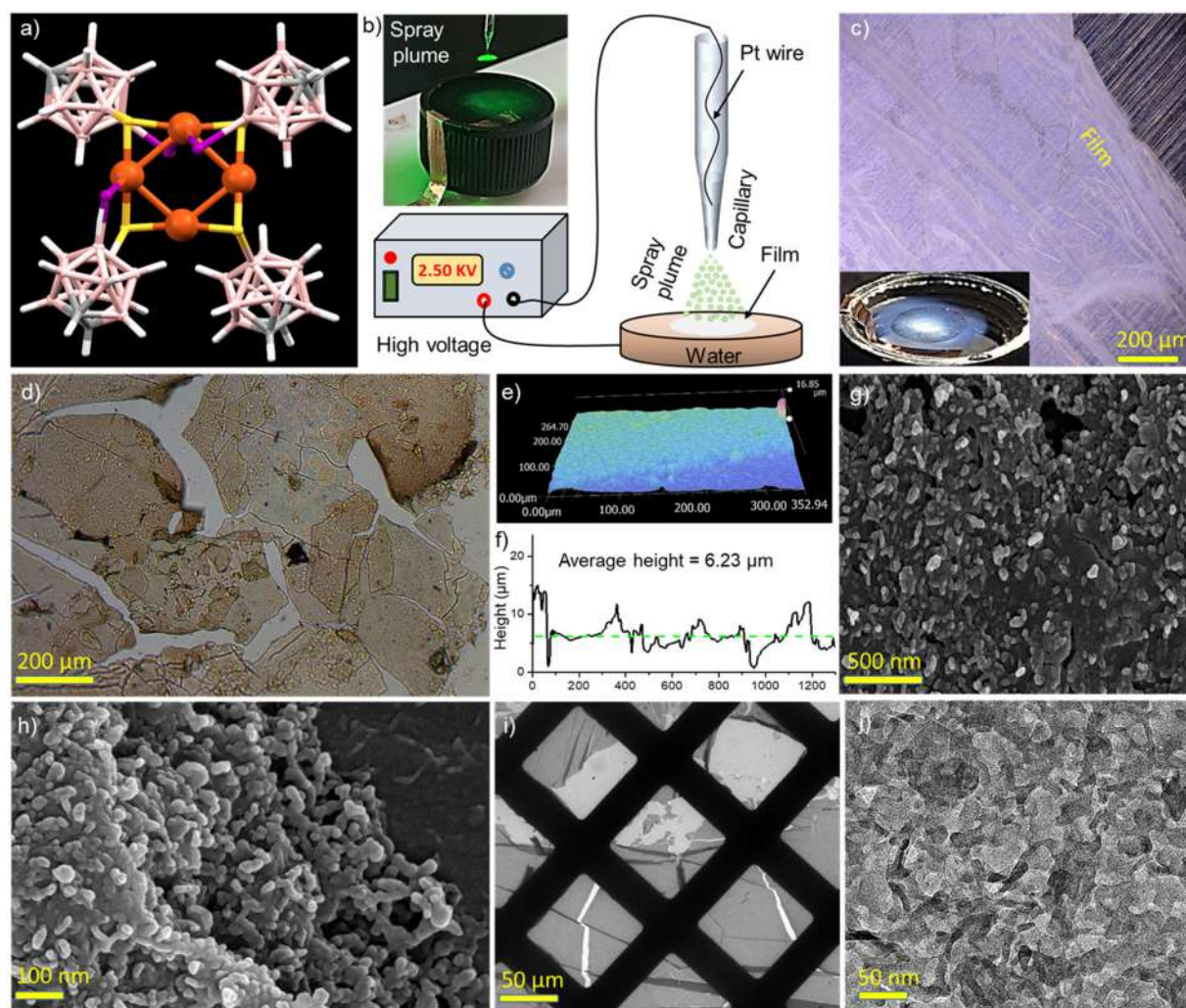


Fig. 1 (a) Molecular structure of the $\text{Cu}_4\text{@ICBT}$ cluster (atomic color code: orange = copper, yellow = sulphur, pink = boron, grey = carbon, violet = iodine and white = hydrogen). (b) Schematic representation of the ESD setup, (the inset shows the photograph of the spray plume during ESD, illuminated with a green laser). Electrospray deposition occurs on the surface of water, kept in a plastic cap, and the solution was grounded electrically. Optical micrographs of the film in (c) reflection and (d) transmission modes, respectively (the inset of (c) shows the floated film on the water surface). (e) 3D surface topology of the film indicating its roughness and (f) cross-section analysis. (g and h) FESEM micrographs and (i and j) TEM micrographs of the film at different magnifications.

stability of the clusters present in the ESD film after a complete adsorption and desorption cycle was monitored through MS studies by dissolving it in acetone. The appearance of the characteristic peak at m/z 1334.16 suggests the structural stability of the cluster after 2-NT adsorption and desorption processes (Fig. S8†).

To understand the kinetics of the adsorption and desorption processes, we measured the time-dependency of the emission features (shown in Fig. S9†), and we observed ~ 3 and 4.5-fold intensity reduction after 2 and 4 minutes of 2-NT exposure, respectively. The PL quenching of the film upon its exposure to 2-NT was exponential with no emission at all observed after ~ 15 min (Fig. 3b). The desorption of 2-NT by heating to 50 °C showed linear dependency and full luminescence recovery in ~ 60 min. The desorption process is slower than the adsorption process, which suggests a relatively strong interaction between the molecules of 2-NT and the film. Such types of adsorption and desorption processes indicate rapid adsorption and systematic desorption of 2-NT from the ESD film. Alternating exposure of the film to 2-NT vapours and thermal heating (Fig. 3c) demonstrated perfect reversibility of the adsorption–desorption process and PL measurements proved quantitative recovery of the luminescence properties.

Infrared (IR) and XPS measurements were performed to confirm the binding of 2-NT to the ESD film. IR spectra (shown in Fig. 3d and S10†) reveal the appearance of two new

vibrational peaks at 1347 and 1520 cm^{-1} due to N–O stretching modes, indicating the adsorption of 2-NT by the film. These features were absent for the parent film. Other characteristic vibrational peaks for C–H (3051 cm^{-1}) and B–H (2610 cm^{-1}) stretching modes, cage breathing mode (872 cm^{-1}), and BBB/BBC bending mode (975 cm^{-1}) of carboranes suggest the structural integrity of the cluster after 2-NT adsorption. Furthermore, the XPS study reveals the appearance of all the respective elements of the cluster, *i.e.*, Cu, S, C, B, and I, in the survey spectrum (Fig. S11†). We have observed two new peaks of N 1s and O 1s at the binding energy values of 405.3 and 531.9 eV, respectively.

The adsorption capacity of a microcrystalline $\text{Cu}_4\text{@ICBT}$ sample to 2-NT was tested using a uniform microcrystalline powder of the cluster. An optical micrograph reveals that the sample has rhombohedral microcrystals with dimensions of 20–25 μm length and 5–8 μm width (Fig. S12†). After dispersing these particles in DCM, we dropped them on a glass slide to make a thin film. In the subsequent step, this film of microcrystals was exposed to 2-NT (Fig. S12†). Time-dependent PL measurements showed nearly identical emission intensity even after 6 h of exposure. These results prove that the microcrystals themselves are incapable of 2-NT adsorption and detection, whereas the 2D film, prepared by ESD, with an exposed surface with characteristic morphologies promotes effective 2-NT adsorption.

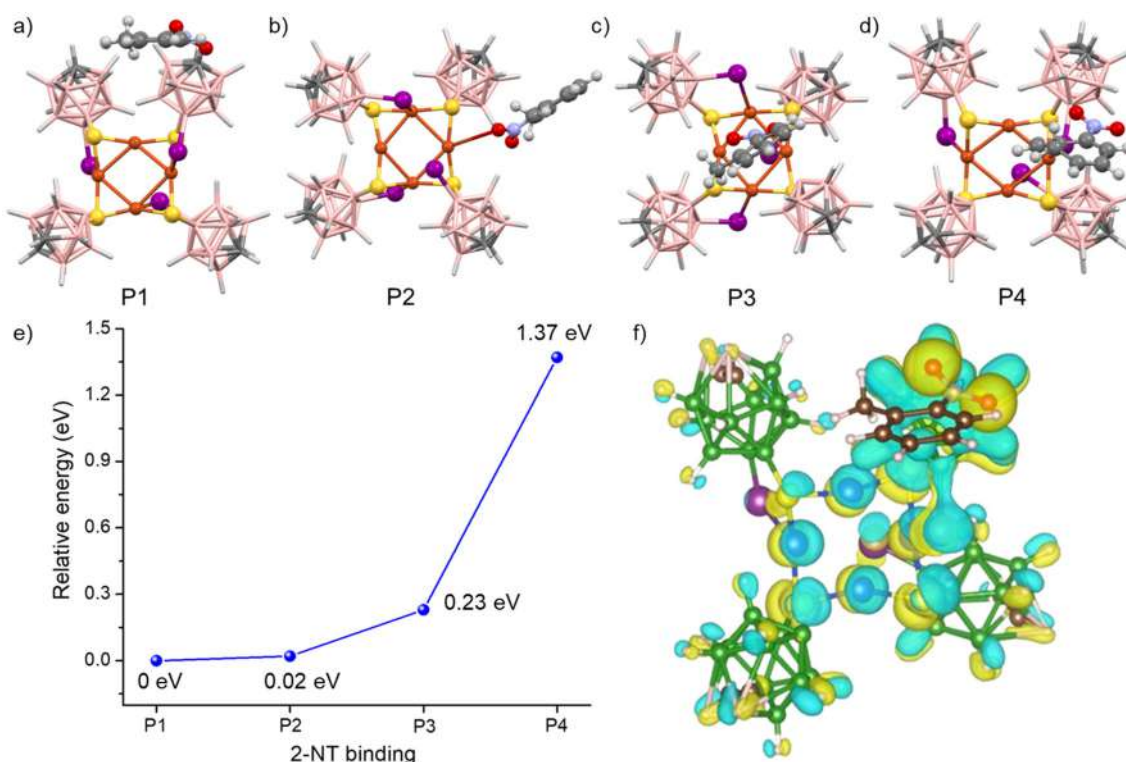


Fig. 4 (a–d) Structural representations of different binding configurations of 2-NT at different positions of the cluster. (e) Relative energy diagram of the binding of 2-NT with the respective position of $\text{Cu}_4\text{@ICBT}$. (f) Charge density difference (CDD) analysis of 2-NT binding with the cluster. Atomic color code used for the CDD plot is blue–copper, yellow–sulphur, green–boron, grey–carbon, and pink–hydrogen. The yellow and cyan electron density isosurfaces are plotted at a value of 0.005 $\text{eV } \text{\AA}^{-3}$.

Density functional theory (DFT) calculations using the Vienna *Ab initio* Simulation Package (VASP) were used to simulate the binding of 2-NT to the cluster.⁴⁵ The Cu₄@ICBT structure optimized using the Perdew–Burke–Ernzerhof (PBE) functional within the generalized gradient approximation (GGA) is given in Fig. S13.†⁴⁶ Details of the theoretical calculations are presented in the ESI.† This was followed by simulations of 2-NT binding at the Cu₄@ICBT optimized structure. Four positions, *i.e.*, (P1) parallel to carboranes, (P2) perpendicular to carboranes through the –NO₂ end, (P3) perpendicular to the Cu₄S₄ kernel, and (P4) parallel to the Cu₄S₄ kernel, were identified as most probable binding configurations (shown in Fig. 4a–d). DFT calculations proved that the P1 and P2 positions to be the most favourable binding positions having the lowest relative energies (RE) of 0 and 0.02 eV, respectively, whereas the P3 and P4 positions showed higher relative energy values of 0.23 and 1.37 eV. For the P1 binding configuration, the optimized geometry shows four intermolecular van der Waals interactions, *i.e.*, CH...HB, NO...B, NO...C, and NO...HC between the nitro group of the 2-NT molecule and a nearby carborane unit with distances of 2.39, 3.51, 3.21 and 2.43 Å, respectively (shown in Fig. S14†). For the P2 configuration, two strong interactions, *i.e.*, BH...N and BH...ON with the distances of 2.72 and 2.54 Å, respectively, showed favourable interactions between the two moieties (Fig. S15†). A similar type of strong intermolecular interactions between 2-NT with the cluster was not observed for any of the other configurations. Charge density difference (CDD) analysis shows that there is a delocalization of electron density between 2-NT and the cluster, resulting in feasible adsorption. Excited state charge transfer between the delocalized electron density of the LUMO of the cluster and 2-NT is assumed to be the driving force behind the emission quenching, upon its adsorption.

Freshly prepared films were independently exposed to various organic solvents to check the selectivity. The combined PL data (shown in Fig. S16–S26† and Fig. 5) showed comparable emission intensity of the film after its exposure to DCM, chloroform, methanol, ethanol, hexane, cyclohexane, benzene, toluene, acetonitrile, THF, and ethyl acetate vapours. However, complete luminescence quenching of the film was observed upon its exposure to two other nitroaromatics, 2,4-dinitrotoluene and picric acid (Fig. S27 and S28†), which proves the interesting selectivity of the film towards species with nitro functionality. Due to the lower vapour pressure, 2,4-dinitrotoluene and picric acid took ~30–35 min for complete luminescence quenching. Interactions between the nitro groups with the cluster are probably the reason behind luminescence quenching, which was also confirmed by DFT calculations.

In conclusion, this work demonstrated the fabrication of a film of atomically precise cluster functioning as a selective and reversible nitroaromatic vapour sensor using a molecularly flat carborane-thiol-protected tetranuclear copper nanocluster. The film was grown under an ambient condition through the ESD technique, depositing charged microdroplets of the clusters on water. Different microscopic techniques demonstrated the flexible nature of the film with surface porosity. Visible orange

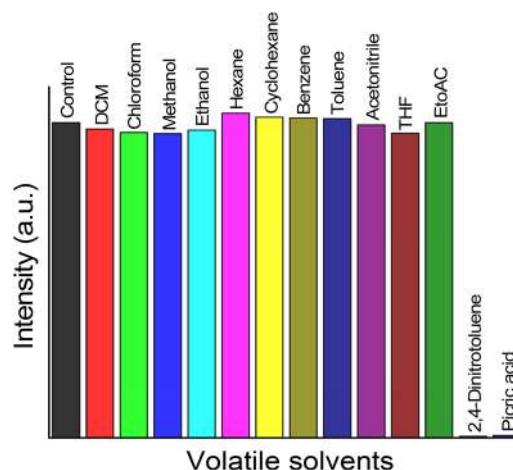


Fig. 5 Bar diagram shows the selectivity of the Cu₄@ICBT film to the exposed vapours (exposure time 2 h each) of various organic solvents and other nitro aromatic compounds, *i.e.*, 2,4-dinitrotoluene and picric acid. Luminescence quenching was observed only for nitroaromatics.

luminescence of the cluster was retained after the formation of the film. The as-grown film acts as a luminescence vapour sensor for detecting various nitroaromatics with excellent selectivity and full recovery of its luminescence by heating to only 50 °C. Theoretical calculations revealed favourable van der Waals interactions between the peripheral carboranes and the nitro moiety of the nitroaromatic species as responsible for luminescence quenching. Such a type of selective luminescence recognition has great potential for efficient visible detection of the precursors of explosives based on nitroaromatics. The extent of the sensitivity of the cluster-based sensor needs to be evaluated.

Conflicts of interest

There are no conflicts to declare.

Acknowledgements

The authors acknowledge the Department of Science and Technology (DST), Government of India, and the Ministry of Education, Youth and Sports of Czech Republic for financial support to the bilateral research projects DST/INT/Czech/P-16/2020 and LTA19152, respectively. A. J. acknowledges the financial support from IIT Madras. The authors acknowledge Papri Chakraborty and Jayoti Roy for their assistance with the mass spectrometry measurements. T. P. acknowledges funding from the Centre of Excellence (COE) on Molecular Materials and Functions under the Institution of Eminence scheme of IIT Madras. This work is a part of an India-Czech collaboration established by T. Pradeep and T. Base to explore the potential of carborane and metal clusters.

References

- 1 X. Sun, Y. Wang and Y. Lei, *Chem. Soc. Rev.*, 2015, **44**, 8019–8061.
- 2 S. Shanmugaraju and P. S. Mukherjee, *Chem. Commun.*, 2015, **51**, 16014–16032.
- 3 R. Paolesse, S. Nardis, D. Monti, M. Stefanelli and C. Di Natale, *Chem. Rev.*, 2017, **117**, 2517–2583.
- 4 P. Sulzer, A. Mauracher, S. Denifl, F. Zappa, S. Ptasinska, M. Beikircher, A. Bacher, N. Wendt, A. Aleem, F. Rondino, S. Matejcek, M. Probst, T. D. Mäk and P. Scheier, *Anal. Chem.*, 2007, **79**, 6585–6591.
- 5 A. Chou, E. Jaatinen, R. Buividas, G. Seniutinas, S. Juodkazis, E. L. Izake and P. M. Fredericks, *Nanoscale*, 2012, **4**, 7419–7424.
- 6 T. H. Kim, B. Y. Lee, J. Jaworski, K. Yokoyama, W. J. Chung, E. Wang, S. Hong, A. Majumdar and S. W. Lee, *ACS Nano*, 2011, **5**, 2824–2830.
- 7 A. Chowdhury and P. S. Mukherjee, *J. Org. Chem.*, 2015, **80**, 4064–4075.
- 8 D. Banerjee, Z. Hu and J. Li, *Dalton Trans.*, 2014, **43**, 10668–10685.
- 9 Y. Zhang, M. Xu, B. R. Bunes, N. Wu, D. E. Gross, J. S. Moore and L. Zang, *ACS Appl. Mater. Interfaces*, 2015, **7**, 7471–7475.
- 10 K. K. Kartha, S. S. Babu, S. Srinivasan and A. Ajayaghosh, *J. Am. Chem. Soc.*, 2012, **134**, 4834–4841.
- 11 L. Lin, M. Rong, S. Lu, X. Song, Y. Zhong, J. Yan, Y. Wang and X. Chen, *Nanoscale*, 2015, **7**, 1872–1878.
- 12 A. Mathew, P. R. Sajanlal and T. Pradeep, *Angew. Chem.*, 2012, **124**, 9734–9738.
- 13 R. Jin, C. Zeng, M. Zhou and Y. Chen, *Chem. Rev.*, 2016, **116**, 10346–10413.
- 14 I. Chakraborty and T. Pradeep, *Chem. Rev.*, 2017, **117**, 8208–8271.
- 15 A. Mathew and T. Pradeep, *Part. Part. Syst. Charact.*, 2014, **31**, 1017–1053.
- 16 X. Kang and M. Zhu, *Chem. Soc. Rev.*, 2019, **48**, 2422–2457.
- 17 *Atomically Precise Metal Nanoclusters*, ed. T. Pradeep, Elsevier, Amsterdam, 2023.
- 18 J. Troyano, F. Zamora and S. Delgado, *Chem. Soc. Rev.*, 2021, **50**, 4606–4628.
- 19 S. Perruchas, C. Tard, X. F. Le Goff, A. Fargues, A. Garcia, S. Kahlal, J. Y. Saillard, T. Gacoin and J. P. Boilot, *Inorg. Chem.*, 2011, **50**, 10682–10692.
- 20 I. Roppolo, E. Celasco, A. Fargues, A. Garcia, A. Revaux, G. Dantelle, F. Maroun, T. Gacoin, J. P. Boilot, M. Sangermano and S. Perruchas, *J. Mater. Chem.*, 2011, **21**, 19106–19113.
- 21 Z. Wu, J. Liu, Y. Gao, H. Liu, T. Li, H. Zou, Z. Wang, K. Zhang, Y. Wang, H. Zhang and B. Yang, *J. Am. Chem. Soc.*, 2015, **137**, 12906–12913.
- 22 M. Xie, C. Han, Q. Liang, J. Zhang, G. Xie and H. Xu, *Sci. Adv.*, 2019, **5**, 1–9.
- 23 W. A. Dar, A. Jana, K. S. Sugi, G. Paramasivam, M. Bodiuzzaman, E. Khatun, A. Som, A. Mahendranath, A. Chakraborty and T. Pradeep, *Chem. Mater.*, 2022, **34**, 4703–4711.
- 24 M. E. Germain and M. J. Knapp, *Chem. Soc. Rev.*, 2009, **38**, 2543–2555.
- 25 Y. Wang, A. La, Y. Ding, Y. Liu and Y. Lei, *Adv. Funct. Mater.*, 2012, **22**, 3547–3555.
- 26 Z. Luo Jr., A. W. Castleman and S. N. Khanna, *Chem. Rev.*, 2016, **116**, 14456–14492.
- 27 Q. Yao, Z. Wu, Z. Liu, Y. Lin, X. Yuan and J. Xie, *Chem. Sci.*, 2021, **12**, 99–127.
- 28 J. Cyriac, T. Pradeep, H. Kang, R. Souda and R. G. Cooks, *Chem. Rev.*, 2012, **112**, 5356–5411.
- 29 S. Rauschenbach, F. L. Stadler, E. Lunedei, N. Malinowski, S. Koltsov, G. Costantini and K. Kern, *Small*, 2006, **2**, 540–547.
- 30 Z. Wu, J. Liu, Y. Li, Z. Cheng, T. Li, H. Zhang, Z. Lu and B. Yang, *ACS Nano*, 2015, **9**, 6315–6323.
- 31 S. Chandra, Nonappa, G. Beaune, A. Som, S. Zhou, J. Lahtinen, H. Jiang, J. V. I. Timonen, O. Ikkala and R. H. A. Ras, *Adv. Opt. Mater.*, 2019, **7**, 1900620.
- 32 (a) M. Jash, A. Jana, A. K. Poonia, E. Khatun, P. Chakraborty, A. Nagar, T. Ahuja, K. V. Adarsh and T. Pradeep, *Chem. Mater.*, 2023, **35**, 313–326; (b) Z. Xie, P. Sun, Z. Wang, H. Li, L. Yu, D. Sun, M. Chen, Y. Bi, X. Xin and J. Hao, *Angew. Chem., Int. Ed.*, 2020, **59**, 9922–9927.
- 33 Z. Wu, C. Dong, Y. Li, H. Hao, H. Zhang, Z. Lu and B. Yang, *Angew. Chem., Int. Ed.*, 2013, **52**, 9952–9955.
- 34 V. Hynninen, S. Chandra, S. Das, M. Amini, Y. Dai, S. Lepikko, P. Mohammadi, S. Hietala, R. H. A. Ras, Z. Sun, O. Ikkala and Nonappa, *Small*, 2021, **17**, 2005205.
- 35 D. Sarkar, M. K. Mahitha, A. Som, A. Li, M. Wlekinski, R. G. Cooks and T. Pradeep, *Adv. Mater.*, 2016, **28**, 2223–2228.
- 36 A. Jana, S. K. Jana, D. Sarkar, T. Ahuja, P. Basuri, B. Mondal, S. Bose, J. Ghosh and T. Pradeep, *J. Mater. Chem. A*, 2019, **7**, 6387–6394.
- 37 A. Jose, A. Jana, T. Gupte, A. S. Nair, K. Unni, A. Nagar, A. R. Kini, B. K. Spoorthi, S. K. Jana, B. Pathak and T. Pradeep, *ACS Mater. Lett.*, 2023, **5**, 893–899.
- 38 A. R. Chowdhuri, B. K. Spoorthi, B. Mondal, P. Bose, S. Bose and T. Pradeep, *Chem. Sci.*, 2021, **12**, 6370–6377.
- 39 J. Ghosh and R. G. Cooks, *TrAC, Trends Anal. Chem.*, 2023, **161**, 117010.
- 40 A. Jana, M. Jash, W. A. Dar, J. Roy, P. Chakraborty, G. Paramasivam, S. Lebedkin, K. Kirakci, S. Manna, S. Antharjanam, J. Machacek, M. Kucerakova, S. Ghosh, K. Lang, M. M. Kappes, T. Base and T. Pradeep, *Chem. Sci.*, 2023, **14**, 1613–1626.
- 41 J. Li, H. Z. Ma, G. E. Reid, A. J. Edwards, Y. Hong, J. M. White, R. J. Mulder and R. A. J. O'Hair, *Chem. – Eur. J.*, 2018, **24**, 2070–2074.
- 42 (a) N. Yan, N. Xia and Z. Wu, *Small*, 2020, **200609**, 1–9; (b) X. Kang, H. Chong and M. Zhu, *Nanoscale*, 2018, **10**, 10758–10834.
- 43 (a) X. Kang and M. Zhu, *Chem. Mater.*, 2019, **31**, 9939–9969; (b) M. S. Bootharaju, V. M. Burlakov, T. M. D. Besong,

- C. P. Joshi, L. G. Abdulhalim, D. M. Black, R. L. Whetten, A. Goriely and O. M. Bakr, *Chem. Mater.*, 2015, **27**, 4289–4297; (c) A. Jana, P. M. Unnikrishnan, A. K. Poonia, J. Roy, M. Jash, G. Paramasivam, J. Machacek, K. N. V. D. Adarsh, T. Base and T. Pradeep, *Inorg. Chem.*, 2022, **61**, 8593–8603.
- 44 S. Fujii, *Med. Chem. Commun.*, 2016, **7**, 1082–1092.
- 45 G. Kresse and J. Hafner, *Phys. Rev. B: Condens. Matter Mater. Phys.*, 1994, **49**, 14251–14269.
- 46 G. Kresse and D. Joubert, *Phys. Rev. B: Condens. Matter Mater. Phys.*, 1999, **59**, 1758–1775.

Supplementary Information

A Luminescent Cu₄ Cluster Film Grown by Electrospray Deposition: A Nitroaromatic Vapour Sensor

Arijit Jana^a, B. K. Spoorthi,^a Akhil S. Nair,^b Ankit Nagar,^a Biswarup Pathak,^{b*} Tomas Base^{c*} and Thalappil Pradeep^{a*}

^aDepartment of Chemistry, DST Unit of Nanoscience (DST UNS) and Thematic Unit of Excellence (TUE), Indian Institute of Technology Madras, Chennai 600036, India. E-mail: pradeep@iitm.ac.in

^bDepartment of Chemistry, Indian Institute of Technology Indore (IIT Indore), Indore 453552, India. Email: biswarup@iiti.ac.in

^cInstitute of Inorganic Chemistry, The Czech Academy of Science 1001 Husinec – Rez, 25068, Czech Republic. E-mail: tbase@iic.acs.cz

Table of Contents:

Sl. No	Title	Page no
1.	Experimental section	3,4
2.	Theoretical calculation	4
3.	Instrumentation	4,5
Fig. S1	Synthesis and characterization of Cu ₁₈ using UV-vis absorption and mass spectrometric studies. Synthesis and characterization of Cu ₄	6
Fig. S2	Optical microscopic images of the electrospray tips	7
Fig. S3	Optical microscopic image of the ESD-film	7
Fig. S4	FE-SEM micrographs showed the time dependent growth of film during ESD process	8
Fig. S5	TEM micrographs of different films	8
Fig. S6	Thin film XRD spectrum of the Cu ₄ @ICBT film	9
Fig. S7	XPS spectra of as prepared Cu ₄ @ICBT film	9
Fig. S8	High-resolution ESI-MS spectrum in positive ion mode of the ESD-film after 2-NT adsorption and desorption cycle.	10
Fig. S9	Adsorption and desorption PL spectral profile of film	10
Fig. S10	Full range IR spectra of the film before and after 2-NT adsorption	11
Fig. S11	XPS spectra of the Cu ₄ @ICBT film after 2-NT vapor exposure	11
Fig. S12	Sensing ability of 2-NT using rhombus microcrystalline sample	12
Fig. S13	DFT optimized structure of Cu ₄ @ICBT nanocluster	12
Fig. S14	Short contact interactions of 2-NT with cluster in P1 configuration	13
Fig. S15	Short contact interactions of 2-NT with cluster in P2 configuration	13
Fig. S16	PL spectra of the film before and after DCM exposure	14
Fig. S17	PL spectra of the film before and after chloroform exposure	14
Fig. S18	PL spectra of the film before and after methanol exposure	15
Fig. S19	PL spectra of the film before and after ethanol exposure	15
Fig. S20	PL spectra of the film before and after hexane exposure	16
Fig. S21	PL spectra of the film before and after cyclohexane exposure	16

Fig. S22	PL spectra of the film before and after benzene exposure	17
Fig. S23	PL spectra of the film before and after toluene exposure	17
Fig. S24	PL spectra of the film before and after acetonitrile exposure	18
Fig. S25	PL spectra of the film before and after THF exposure	18
Fig. S26	PL spectra of the film before and after ethylacetate exposure	19
Fig. S27	PL spectra of the film before and after 2, 4-dinitrotoluene exposure	19
Fig. S28	PL spectra of the film before and after picric acid exposure	20
	References	20

Experimental section

a) Material and chemicals

The borosilicate glass capillary (inner diameter 0.86 mm, outer diameter 1.5 mm) was purchased from Sutter instruments, USA. Platinum electrodes (99.98 % pure) of 0.2 mm diameter was bought from Sigma Aldrich, India. The *ortho*-carborane 12-iodo 9-thiol ligand was synthesized following the earlier literature, after purchasing *ortho*-carborane from Katchem s.r.o. (Czech Republic).^{1, 2} Copper iodide (CuI) and sodium borohydride (NaBH₄, 99%) were purchased from Sigma Aldrich chemicals. 1, 2-bis(diphenylphosphino)-ethane (DPPE) was bought from Rankem chemicals. Milli-Q water was used for the purification of the cluster and electrospray deposition process. 2-nitrotoluene, 2,4-dinitrotoluene, and picric acid were purchased from Sd Fine Chem Ltd., HiMedia Lab. Pvt. Ltd., and MOLYCHEM, respectively. HPLC-grade solvents such as dichloromethane, chloroform, acetonitrile, methanol, ethanol, cyclohexane, toluene, benzene, THF, ethylacetate, and acetone were purchased from Rankem chemicals and Finar chemicals. All the chemicals are commercially available and used without further purification.

b) Synthesis of Cu₁₈ nanocluster

The [Cu₁₈(DPPE)₆H₁₆]²⁺ nanocluster have been synthesized by following literature report.³ In brief, 95 mg copper iodide was mixed with 120 mg 1, 2-bis(diphenylphosphino)-ethane (DPPE) ligand in an argon closed Schleck tube. 20 ml acetonitrile was added with it. After 20 min stirring, a white suspension formed due to formation of copper phosphine complex. 187 mg NaBH₄ was added to the reaction mixture directly for the reduction. After 5 h reaction as formed orange color suspension confirms the formation of Cu₁₈ nanocluster (shown in Fig. S1). Centrifugation of the suspended product followed by repetitive washing using methanol and acetonitrile leads to the purified product. Purified cluster extracted in DCM was used for Cu₄@ICBT synthesis. The Cu₁₈ has a broad UV-vis absorption spectrum and the characteristic mass spectrum (presented in Fig. S1c, d) confirms the cluster. The yield of the product is 70 % in terms of copper.

c) Synthesis of Cu₄@ICBT nanocluster

The Cu₄@ICBT was synthesized following a ligand exchange induced structural transformation (LEIST) reaction starting from Cu₁₈. Purified Cu₁₈ cluster (50 mg) in 15 ml DCM was reacted with 40 mg of *ortho*-carborane 12-iodo 9-thiol (I₉) ligand. After 2 h of reaction Cu₄@ICBT formed as a snow-white precipitates having characteristic orange emission under UV lamp (shown in Fig. S1f, g). The precipitates are extracted through ultracentrifugation. Repetitive washing using DCM and methanol removes the excess ligands. The purified cluster was dissolved in acetone for ESD process. The yield of the product is 80 % in terms of Cu₁₈.

d) Preparation of microcrystalline sample

To prepare the uniform microcrystalline powder, we have dissolved 30 mg freshly prepared cluster in 10 ml acetone. 7 ml DCM mixed with it and put for crystallization at room temperature

(25 °C). After 24, a yellowish precipitates formed bottom of the crystallization vial. After centrifugation at 1000 rpm, we have drop casted the precipitates on a glass slide for further studies. The length of these rhombus shaped microcrystal is 20-25 μm and width 5-8 μm (shown in Fig. S11b).

Theoretical calculation

The DFT calculations are carried out using Vienna Ab-Initio Simulation Package (VASP) employing GGA-PBE method.⁴ Projector augmented wave (PAW) method is used for treating ion electron interactions.⁵ A convergence criteria of 10^{-4} eV for minimum energy and 0.05 eV \AA^{-1} for Hellmann-Feynman forces on atoms are used for the calculations. The Brillouin zone was sampled at the Gamma point (1 \times 1 \times 1). All calculations are performed with spin polarization. The dispersion interactions were accounted for by using the DFT-D3 method.⁶ The charge density difference ($\Delta\rho$) of 2-NT binding at $\text{Cu}_4\text{@ICBT}$, is calculated by the following equation:

$$\Delta\rho = \rho_{\text{Cu}_4\text{@ICBT}+2\text{-NT}} - \rho_{\text{Cu}_4\text{@ICBT}} - \rho_{2\text{-NT}}$$

Where, $\rho_{\text{Cu}_4\text{@ICBT}+2\text{-NT}}$, $\rho_{\text{Cu}_4\text{@ICBT}}$ and $\rho_{2\text{-NT}}$ represent the charge density of 2-NT adsorbed $\text{Cu}_4\text{@ICBT}$, $\text{Cu}_4\text{@ICBT}$ and 2-NT, respectively at the DFT optimized geometry.

Instrumentation

a) Electrospray deposition

Electrospray deposition experiments were performed using a home built setup. A schematic representation of the ESD setup is presented in the Fig. 1b. Charged microdroplets of $\text{Cu}_4\text{@ICBT}$ ions were generated from a capillary tip. These tips were made by pulling the borosilicate glass capillary using a flaming micropipette puller instrument (model P-97, Sutter instrument). The diameter of the ESD tip is 25-30 μm (shown in Fig. S2). All the ESD tips were checked using an optical microscope to generate uniform microdroplets. 4-5 mg purified sample dissolved in 1 ml acetone was used for ESD process. Cluster solution was inserted inside the capillary using a microinjector pipette. A high voltage DC potential of 2.5-3 kV was applied to the solution through a platinum wire electrode (diameter 0.2 mm). Spray emitter was placed manually above the collector with tip to collector distance of 10-15 mm. After potential applied as formed spray plume consist of charged microdroplets, were directed towards ground water bath having 5-6 ml Milli-Q water inside it. A photograph of such deposition is shown in the inset of Fig. 1b.

b) Microscopic characterization

Optical microscopic images were collected using a LEICA optical microscope equipped with LAS V4.8 software in transmission mode. Optical microscopic images in the reflected mode were collected using Keyence VHX-950F digital microscope. Scanning electron microscopic (SEM) images are recorded using Verios G4 UC, Thermo Scientific field emission scanning electron microscope (FESEM). After transferring the sample on a clean aluminum foil, gold sputtering was performed to increase the conductivity of the film. All the FE SEM images were collected in high

vacuum at an operating voltage of 10-15 kV. Transmission electron microscopy (TEM) was measured using a JEOL-3010 transmission electron microscope at operating voltage of 200 kV. A Gatan 794 multiscan CCD camera was used for image collection.

c) Spectroscopic characterization

UV-vis absorption spectra were measured using Perkin Elmer Lambda 365 UV-vis spectrometer in the wavelength region of 200 to 1100 nm. Photoluminescence spectra were measured using Jobin Yvon Nanolog fluorescence spectrometer with a bandpass of 3 nm for the measurements. A CCD detector was used to record the emission intensity in the range of 300-850 nm. Film transferred on a clean glass slide was used to record the spectrum in reflectance mode. FT-IR spectra of the samples were recorded using JASCO-4100 spectrometer in attenuated total reflection (ATR) mode. Mass spectrometric studies were performed in positive ion mode using a Waters Synapt G2Si-HDMS instrument. The instrument is equipped with an electrospray source, quadrupole ion trap, ion mobility cell and time of flight (TOF) detector. Electrosprayed film was dissolved in acetone to record the spectrum. Formic acid was added to enhance the ionization. The sample was electrosprayed at a flow rate of 10 μ L/min with capillary voltage 3 kV, cone voltage 0 kV, spray current 100 nA, source temperature 80 $^{\circ}$ C, desolvation temperature 100 $^{\circ}$ C and desolvation gas flow of 300 L/h for the measurement. X-ray photoelectron (XPS) spectra were measured using ESCA probe TPD (Omicron Nanotechnology) equipped with Mg K α X-ray source ($h\nu$ =1253.6 eV). X-ray flux was adjusted to reduce the beam induced damage. At least three spectra were collected and average was taken for selected binding energy. The spectra were calibrated using the binding energy of C 1s peak at 284.8 eV. Powder X-ray diffraction of the film was measured using a D8 Advance Bruker instrument, using Cu K α X-ray source ($h\nu$ = 8047.8 eV).

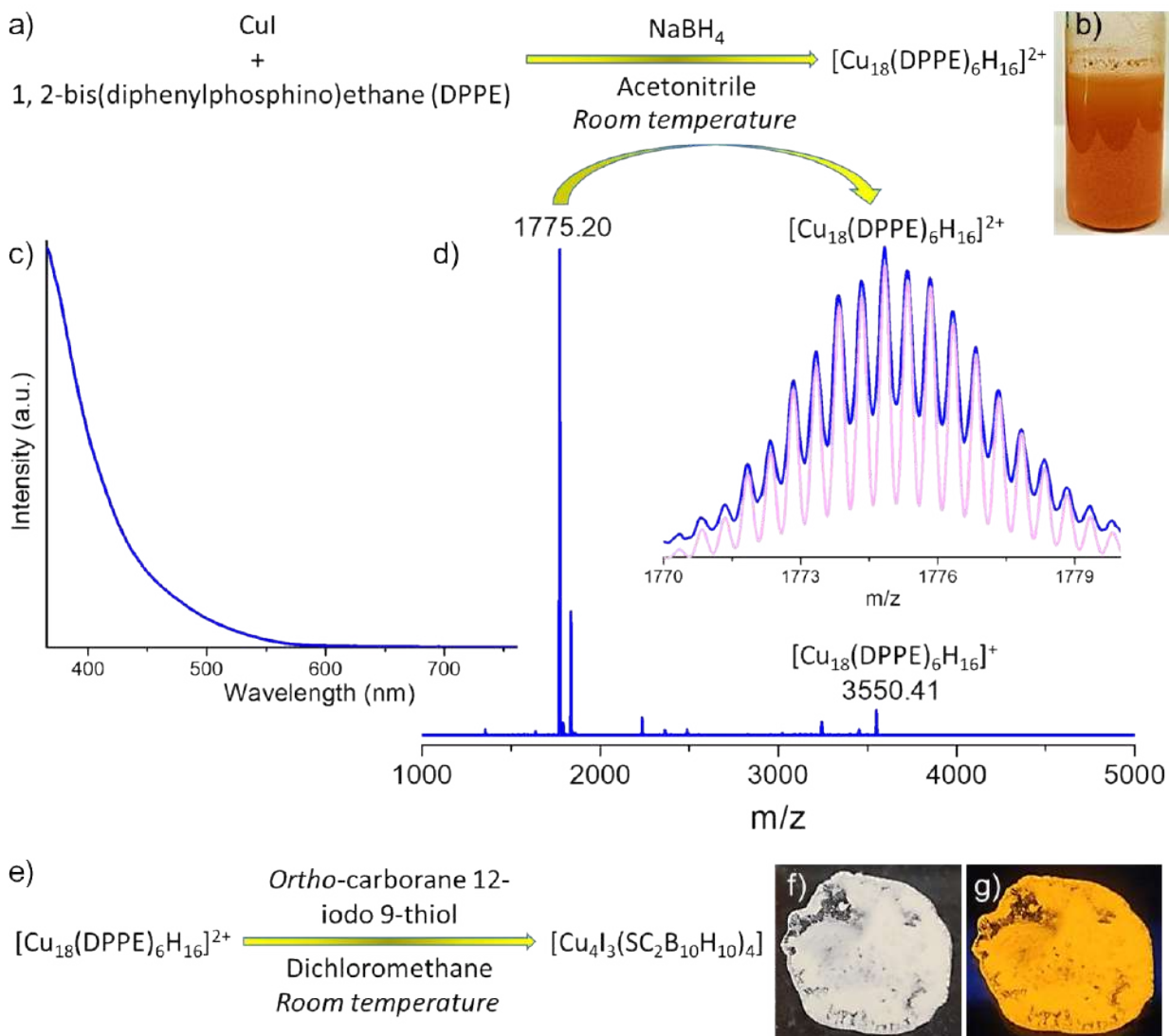


Fig. S1 a) Scheme of the synthesis of Cu_{18} through reduction reaction. b) Optical photograph of as prepared Cu_{18} . c) UV-vis absorption spectrum of the cluster. d) Mass spectrum of the cluster in positive ion mode. Both monopositive and dipositive species were observed in the spectrum. Inset shows exact matching of the isotopic distribution of the experimental (blue) with theoretical (pink) spectrum. e) Scheme of the synthesis of $\text{Cu}_4@\text{ICBT}$ through LEIST reaction. Photographs of purified $\text{Cu}_4@\text{ICBT}$ f) under daylight and g) under UV light. Visible orange emission was observed.

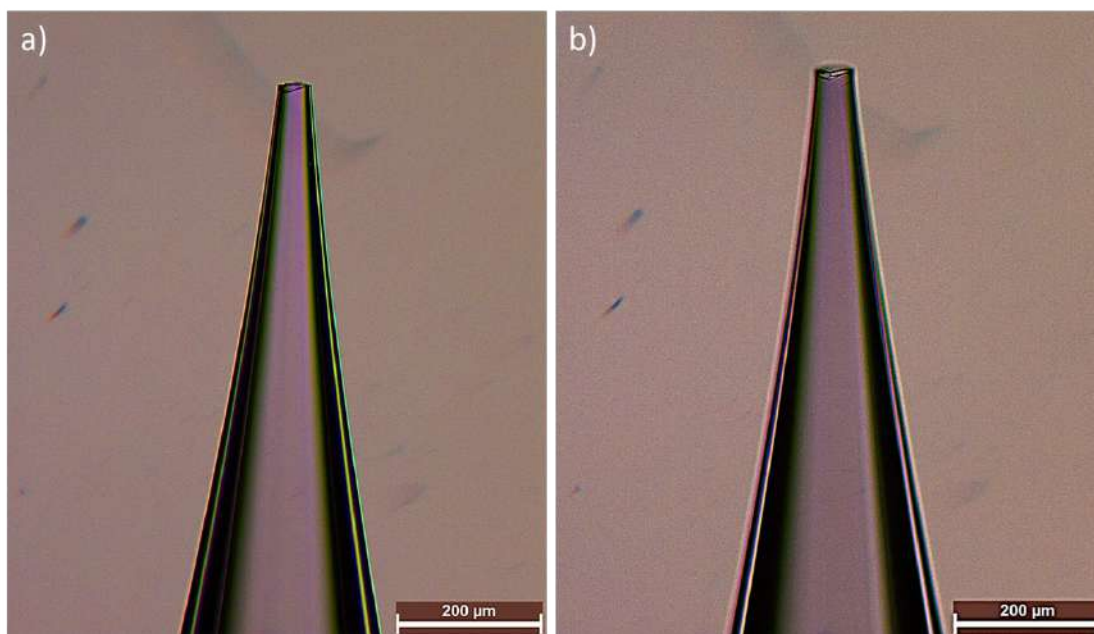


Fig. S2. a, b) Optical microscopic images of the electrospay tips, made by pulling the borosilicate glass capillary. Tip diameter is 25-30 μm .

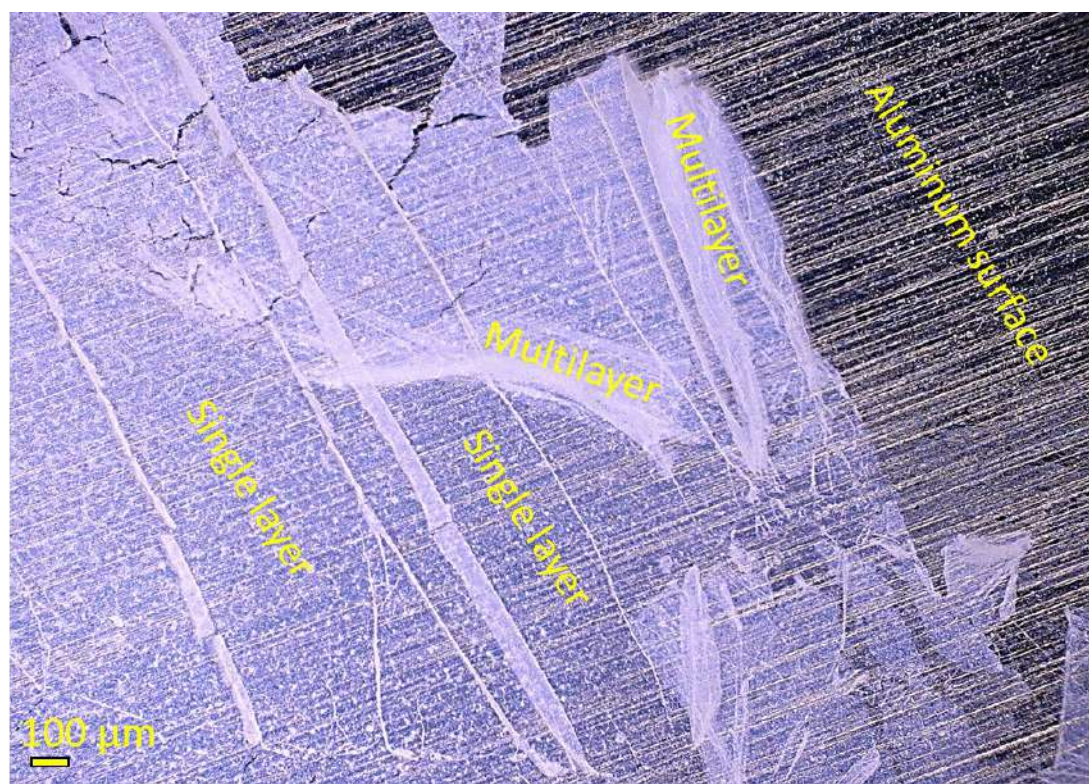


Fig. S3 Optical microscopic image of the ESD-film.

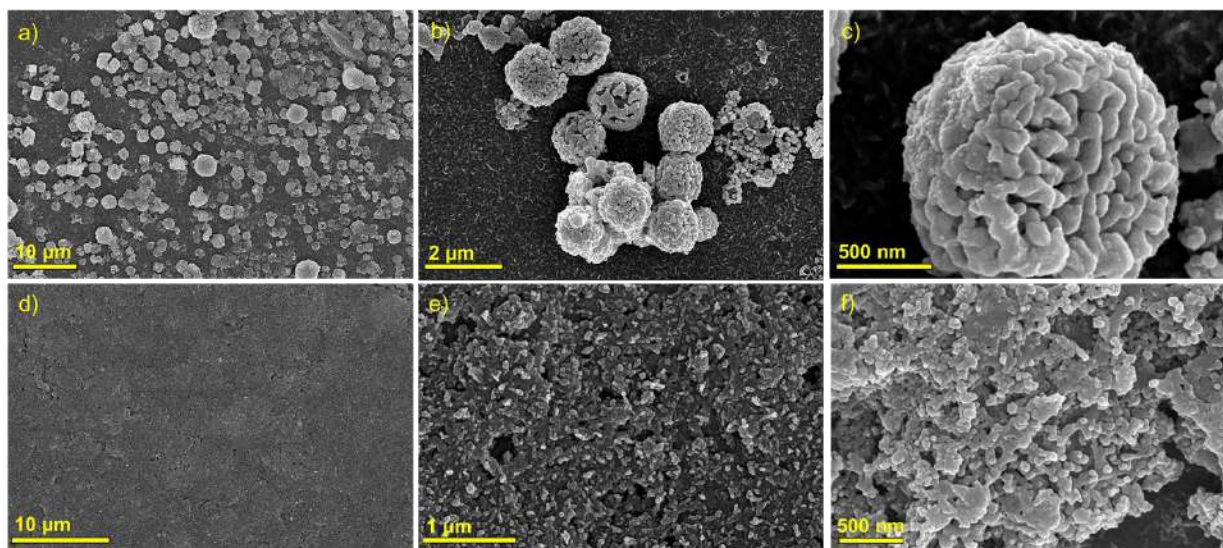


Fig. S4 FESEM micrographs showed the time dependent growth of film during ESD process, a-c) micrographs with increasing magnification after 10-15 min of ESD process, which showed the formation of spherical aggregate. d-f) micrographs of the film with increasing magnification after 30 min of ESD process.

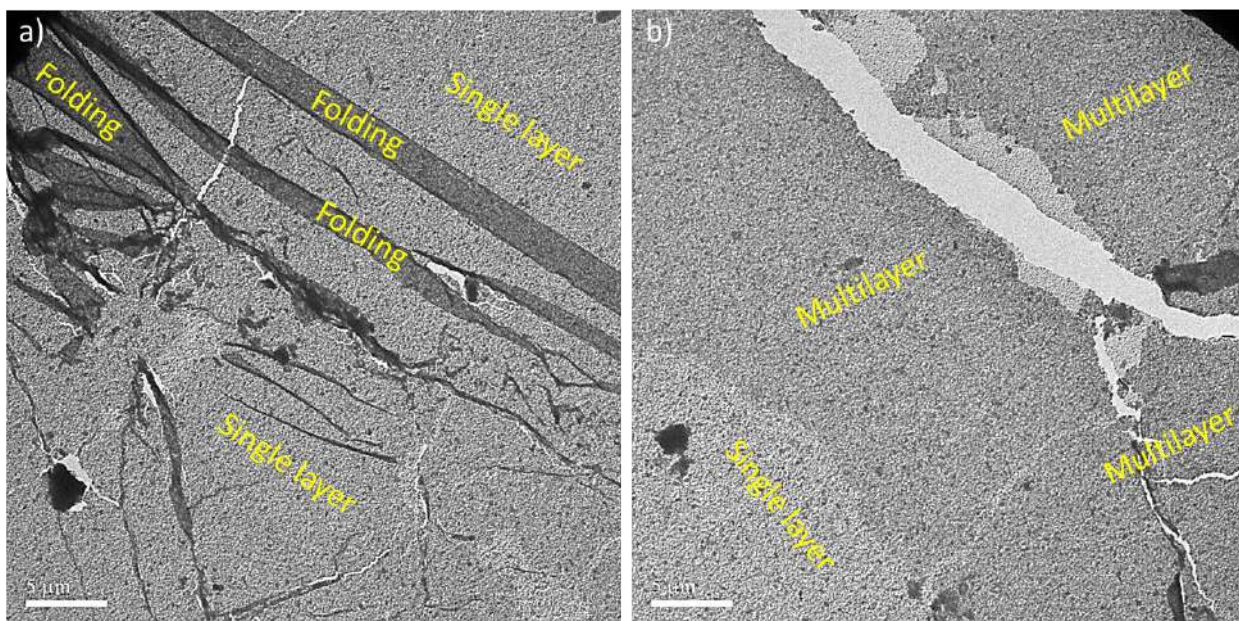


Fig. S5 a, b) TEM micrographs of different films.

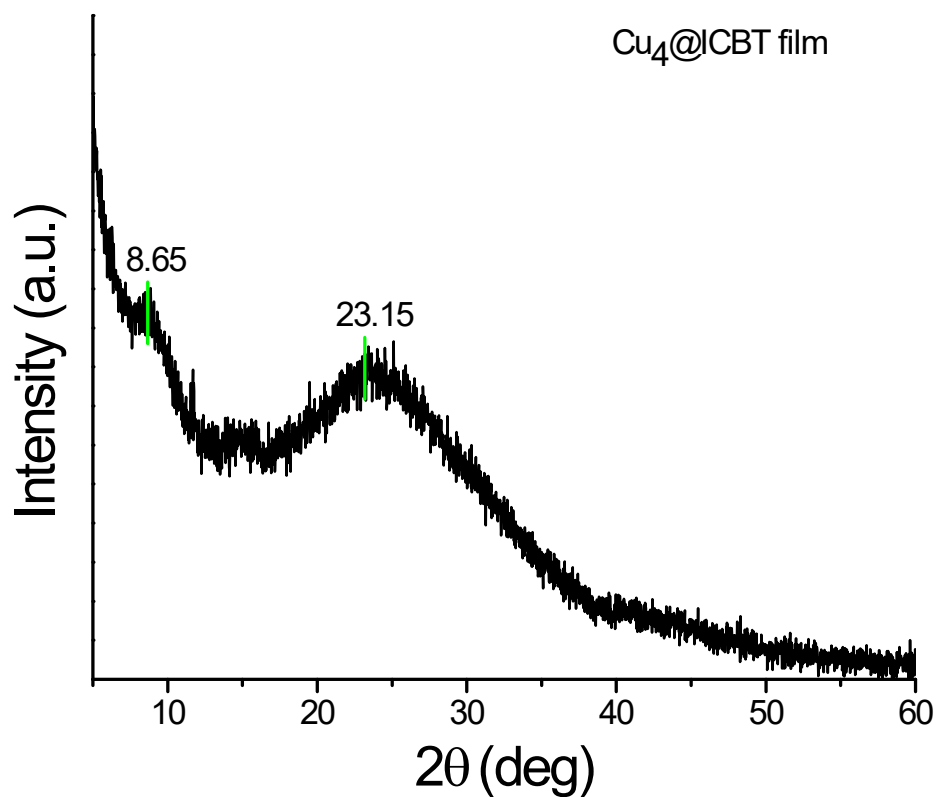


Fig. S6 Thin film XRD spectrum of the $\text{Cu}_4\text{@ICBT}$ film having two broad diffraction features.

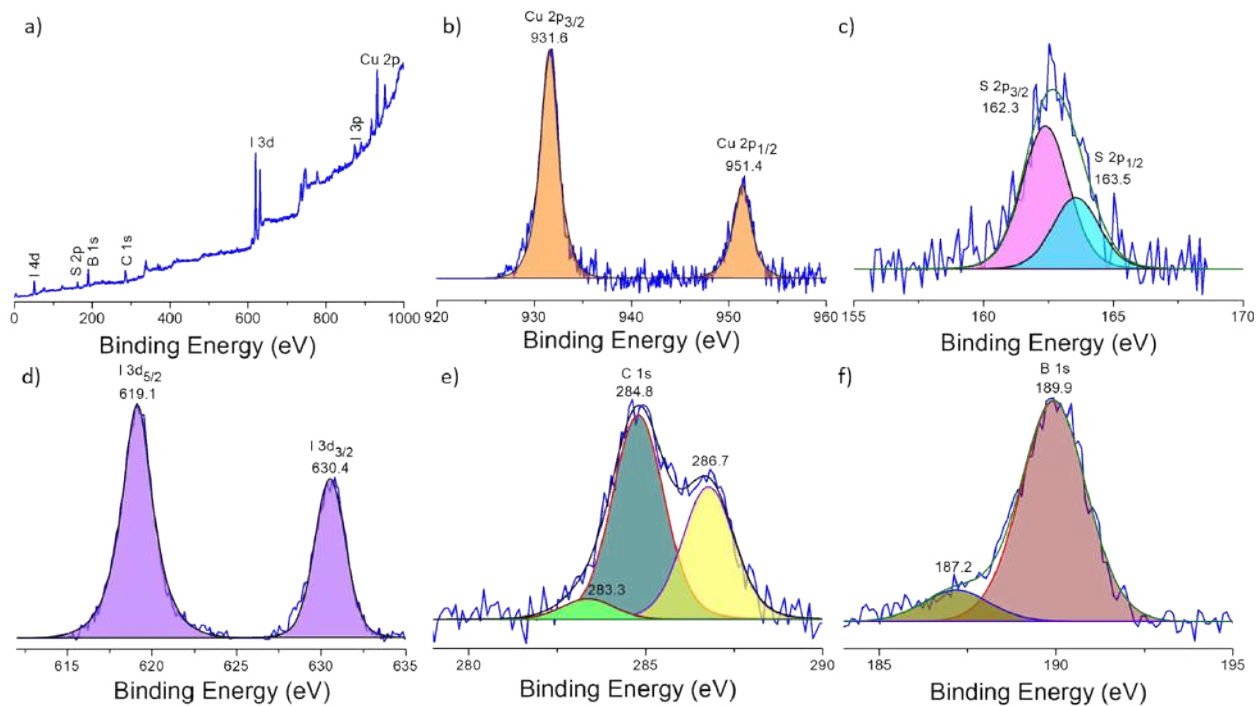


Fig. S7 a) XPS survey spectrum of $\text{Cu}_4\text{@ICBT}$ film. Selected peak fittings of b) Cu 2p, c) S 2p, d) I 3d, e) C 1s and f) B 1s spectral regions.

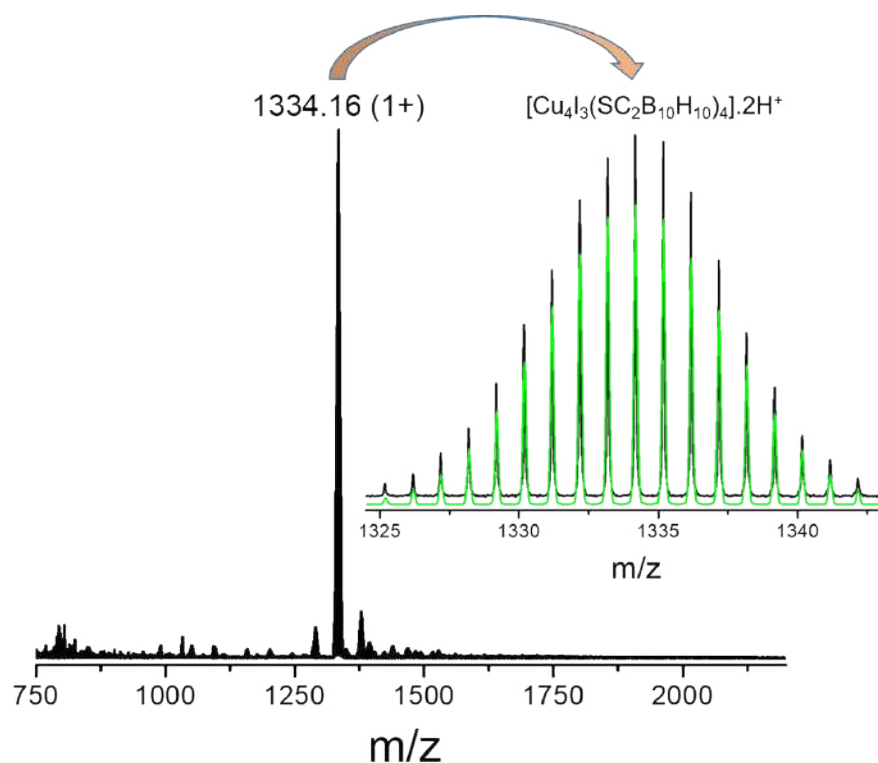


Fig. S8 High-resolution ESI-MS spectrum in positive ion mode of the ESD-film after 2-NT adsorption and desorption cycle. Isotopic distribution of the experimental spectrum (black color) at m/z 1334.16 matches well with the simulated spectrum (green color)

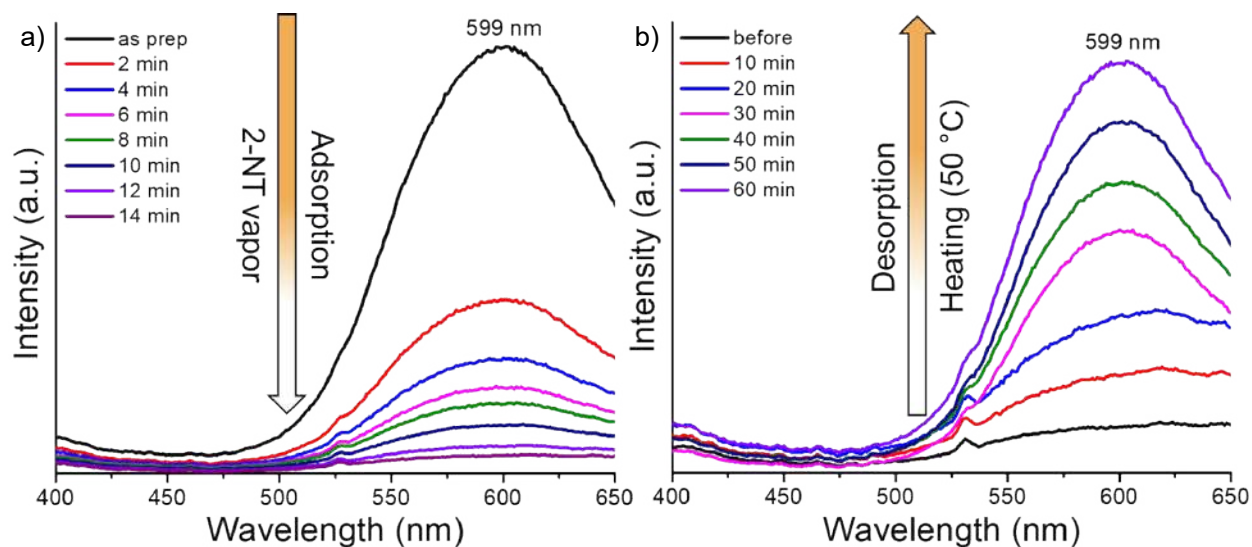


Fig. S9 Photoluminescence spectral profile of 2-NT a) adsorption and b) desorption by the Cu_4 @ICBT film.

d and S3†). Scratches on the aluminium substrate were visible through the film, indicating its translucent character. The surface topography reveals a relatively rough surface of the film (Fig. 1e) with an average thickness of 6.23 μm . We have used a scanning electron microscope to get additional information on its morphology. FESEM micrographs demonstrated (Fig. 1g and h) that the basal plane is covered by several fibrous knots. To understand the growth of the film, we measured the images after various deposition times, which revealed the formation of porous spherical aggregates after 10–15 min of deposition. As-formed spherical particles resulted in a compact film upon subsequent deposition process (Fig. S4†). The rough surfaces of the spherical aggregates with multiple tangles interact with each other and form the resulting film, which also has similar knots on its surface. Transmission electron micrographs (shown in Fig. 1i, j and S5†) confirm the sheet-like nanostructures with multiple knots. Thin film XRD (shown in Fig. S6†) reveals two broad diffraction peaks at 2θ values of 8.65° and 23.15° , suggesting the weak crystallinity of the film.

The molecular structure of the cluster in the film was verified using high-resolution electrospray ionization mass spectrometry (HRESI-MS). The MS spectrum of an acetone solution of the film (Fig. 2a) shows a characteristic peak at m/z 1334.02 with a monocationic charge. Experimental isotopic distribution of the mass having a molecular composition of $[\text{Cu}_4\text{S}_4\text{I}_3(\text{C}_2\text{B}_{10}\text{H}_{11})_4]\cdot 2\text{H}^+$ matches well with the calculated one (shown in the inset of Fig. 2a) and the parent cluster.⁴⁰ X-ray

photoelectron spectroscopy (XPS) confirms the elemental composition (presence of Cu, S, C, B and I) in the film (Fig. S7†). Peak fittings of the Cu 2p region having two peaks at binding energies of 931.6 and 951.4 eV for $2p_{3/2}$ and $2p_{1/2}$ indicate a nearly zero oxidation state for copper (Fig. 2b). The UV-vis spectra of the film showed a single absorption band with a maximum of 267 nm, which is identical to that of the as-prepared cluster (Fig. 2c). All these data verified the essential structural stability of the cluster after the ESD process.

The as-grown ESD film emits bright orange luminescence under a 365 nm UV lamp. The solid state photoluminescence spectra of the film show a characteristic emission band centred at 599 nm under excitation at 330 nm (shown in Fig. 2d). The excitation and emission spectra compare well with the spectra of the parent cluster.⁴⁰ The Stokes shift of ~ 3.7 eV represents a large gap between the absorption and emission bands. Based on the molecular structure of the cluster with characteristic luminescence, we expected the material to function as a potential sensor of volatile organic compounds and thus we exposed the film to different organic solvents and nitroaromatics. While the characteristic orange luminescence remained unchanged after the film's exposure to vapours of various organic solvents, we observed a relatively quick quenching of the emission as a result of the film exposure to nitroaromatics (2-NT) with a vapour concentration of 0.024% at 25 $^\circ\text{C}$ (vapour pressure: 0.185 mm Hg). It took typically a few minutes to completely quench the emission. PL measurements show the complete disappearance of the 599 nm emission band after exposure to 2-NT (Fig. 3a) and its full recovery upon heating to 50 $^\circ\text{C}$. The PL spectrum with a strong emission band confirmed the recovery (Fig. 3a). The

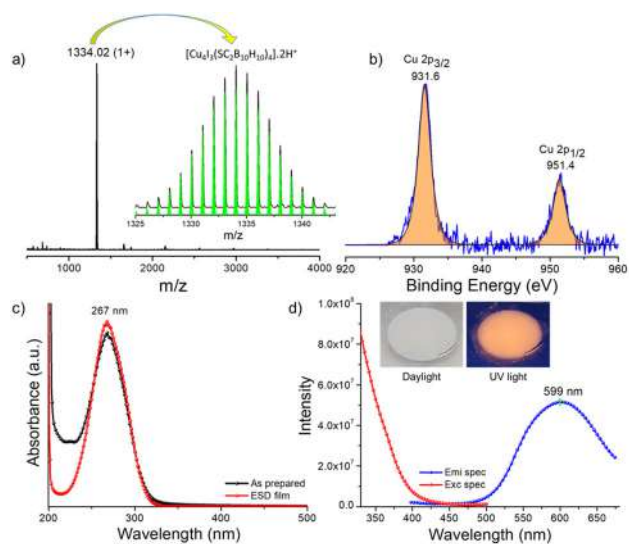


Fig. 2 (a) Positive ion-mode ESI-mass spectrum of a solution of the $\text{Cu}_4\text{@ICBT}$ film in acetone. 0.1 (M) formic acid was added to increase the ionization efficiency. The inset shows the isotopic distribution of the experimental spectrum in comparison with the theoretical one. The spectrum is compared with the parent cluster. (b) Selected area XPS spectrum of the Cu 2p region. (c) UV-vis absorption spectra of the ESD film dissolved in acetone in comparison with the as-prepared cluster. (d) Photoluminescence excitation and emission spectra of the film. The inset shows the photograph of the ESD film under daylight (left) and UV light (right).

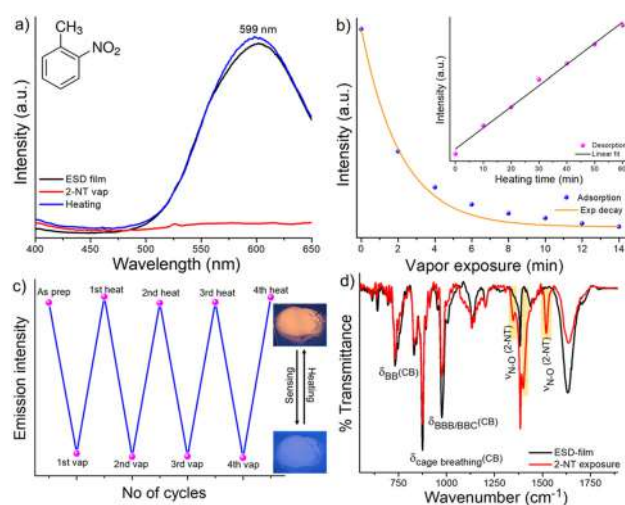


Fig. 3 (a) PL emission spectra of the film after 2-NT vapour exposure resulted in quenching the emission and thermal desorption (upon heating at 50 $^\circ\text{C}$) resulted in the regeneration of luminescence. (b) Adsorption and desorption patterns of 2-NT from the film. (c) 2-NT vapour adsorption and desorption up to the 4th cycle, indicating the re-usability of the film. (d) Expanded FT-IR spectral region of the 2-NT-exposed film in comparison with the as-grown film. New features are highlighted.

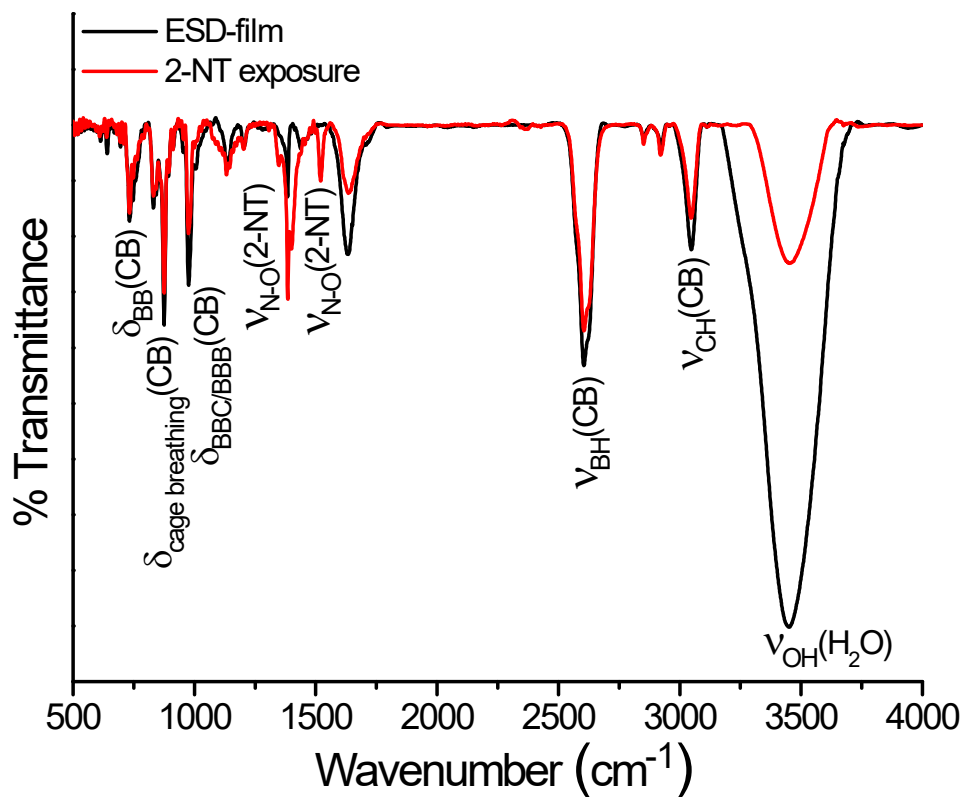


Fig. S10 Full range IR spectra of the film before and after 2-NT adsorption.

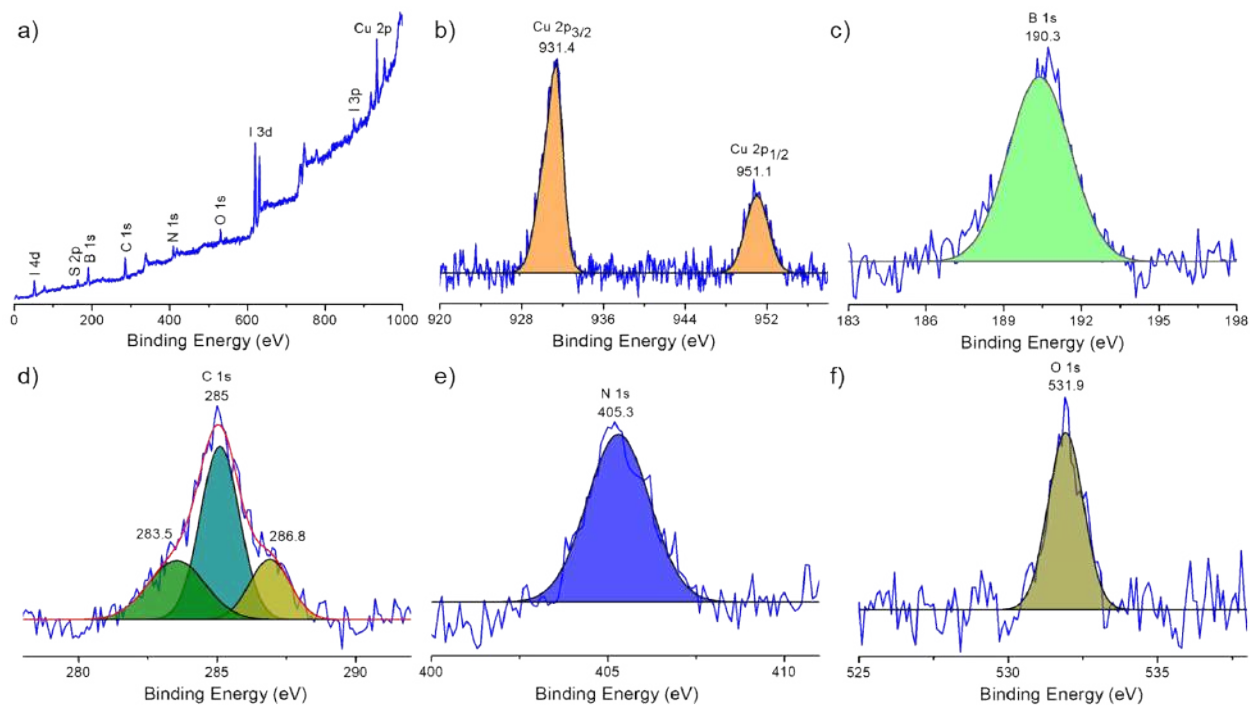


Fig. S11 XPS spectra of the Cu₄@ICBT film after 2-NT vapor exposure. a) Survey spectrum and selected peak fittings of b) Cu 2p, c) B 1s, d) C 1s, e) N 1s and f) O 1s spectral regions.

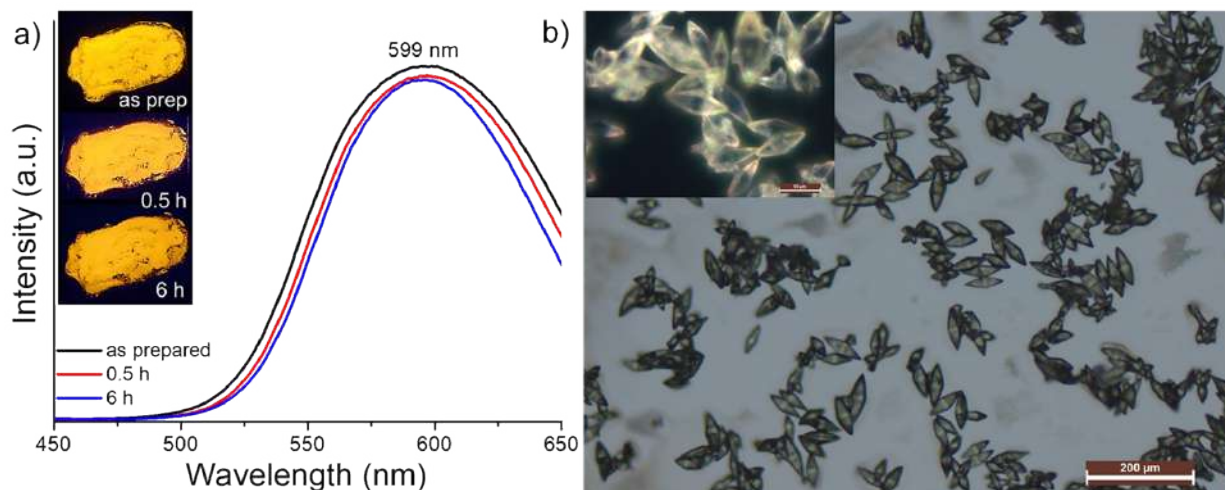


Fig. S12 a) Photoluminescence spectra shows no significant emission quenching of rhombus microcrystals upon exposure of 2-NT. Inset shows bright orange emission after 6 h 2-NT exposure. b) Optical microscopic image of the uniform rhombus microcrystals.

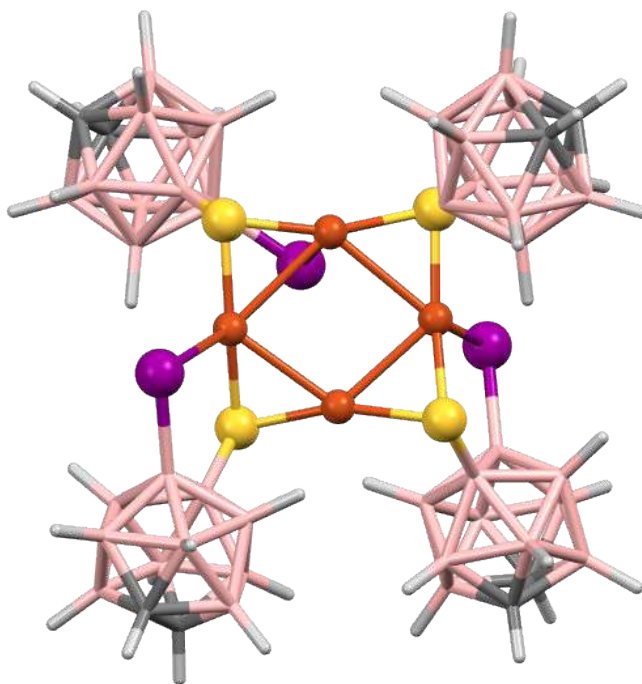


Fig. S13 DFT optimized structure of Cu₄@ICBT nanocluster having a square planar Cu₄ kernel protected by four carborane ligands. Atomic color code: orange = copper, yellow = sulphur, pink = boron, grey = carbon, violet = iodine and white = hydrogen.

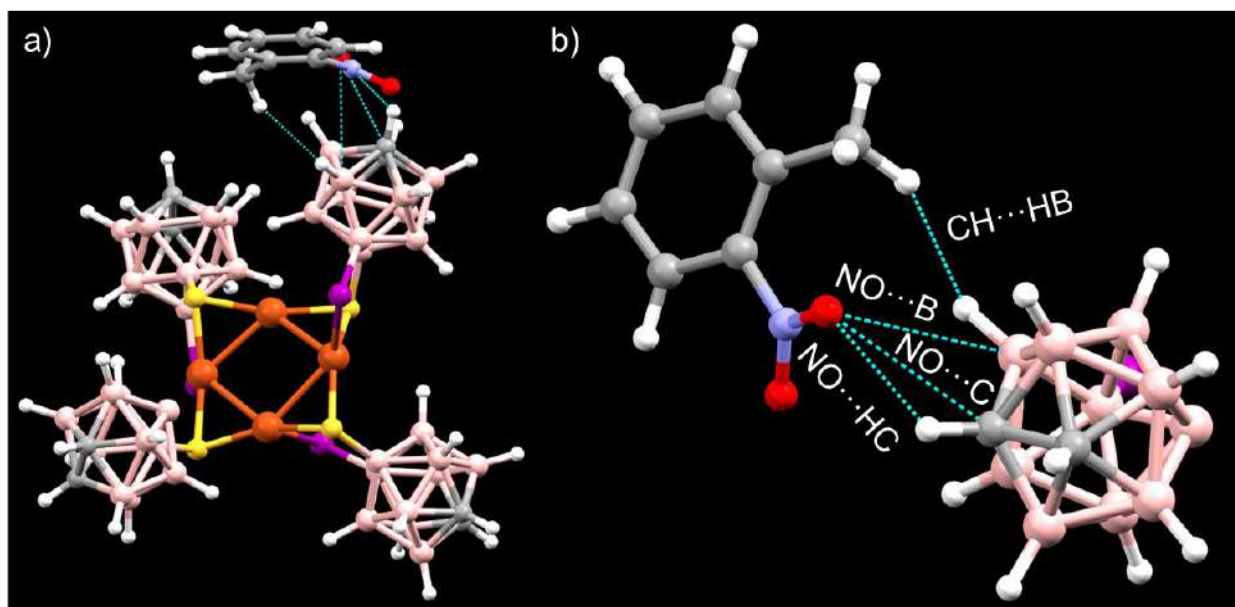


Fig. S14 a) Short contact van der Waals interactions of 2-NT with cluster in P1 configuration. b) Expanded view of these interactions.

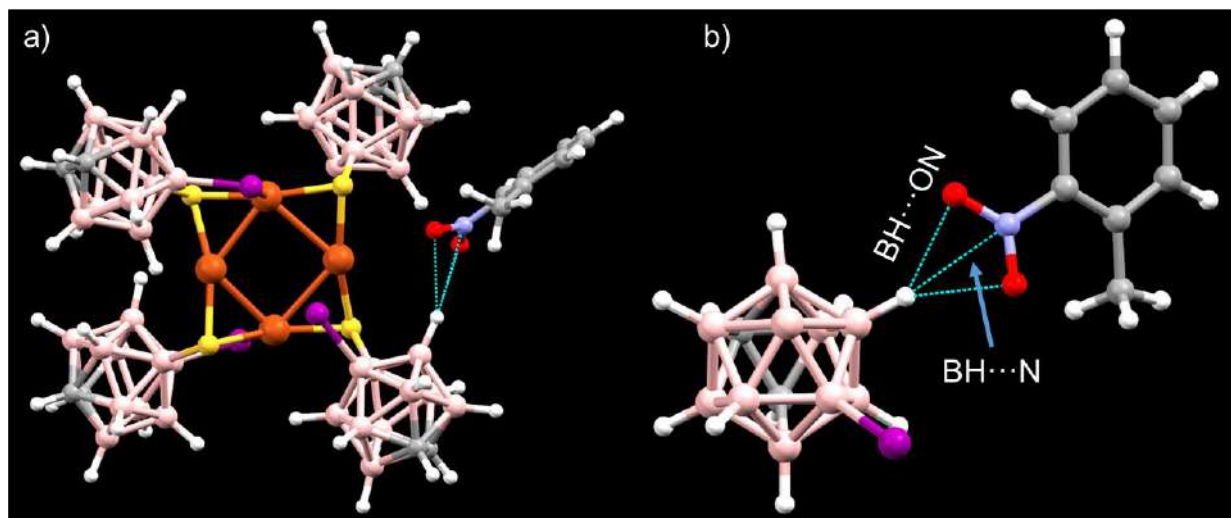


Fig. S15 a) Short contact van der Waals interactions of 2-NT with cluster in P2 configuration. b) Expanded view of these interactions.

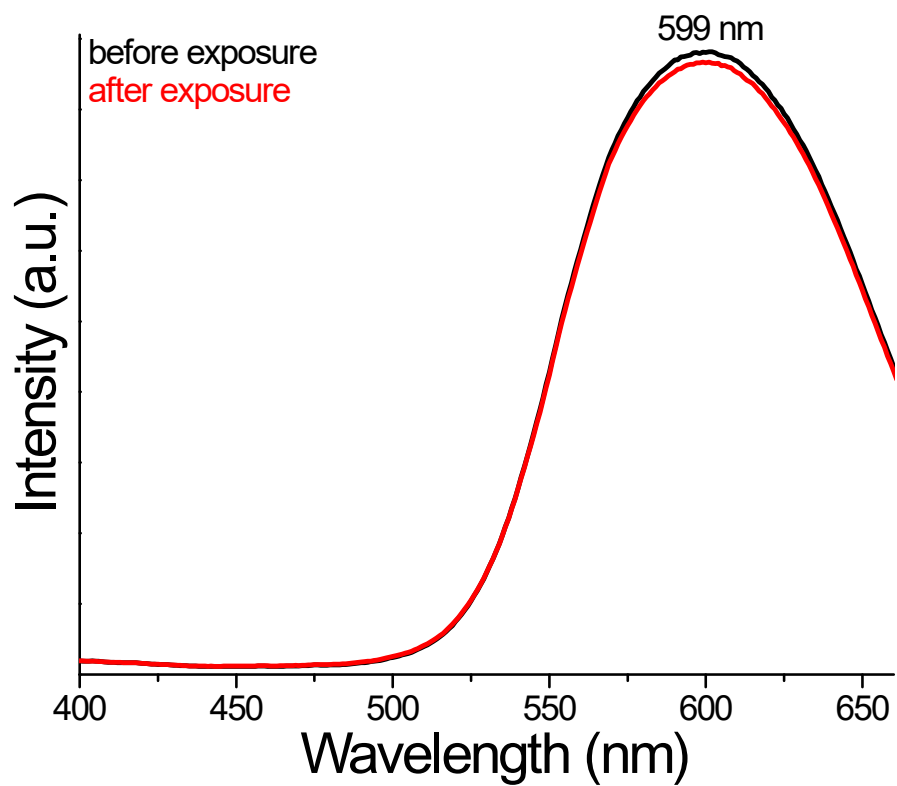


Fig. S16 PL spectra of the film before and after DCM exposure.

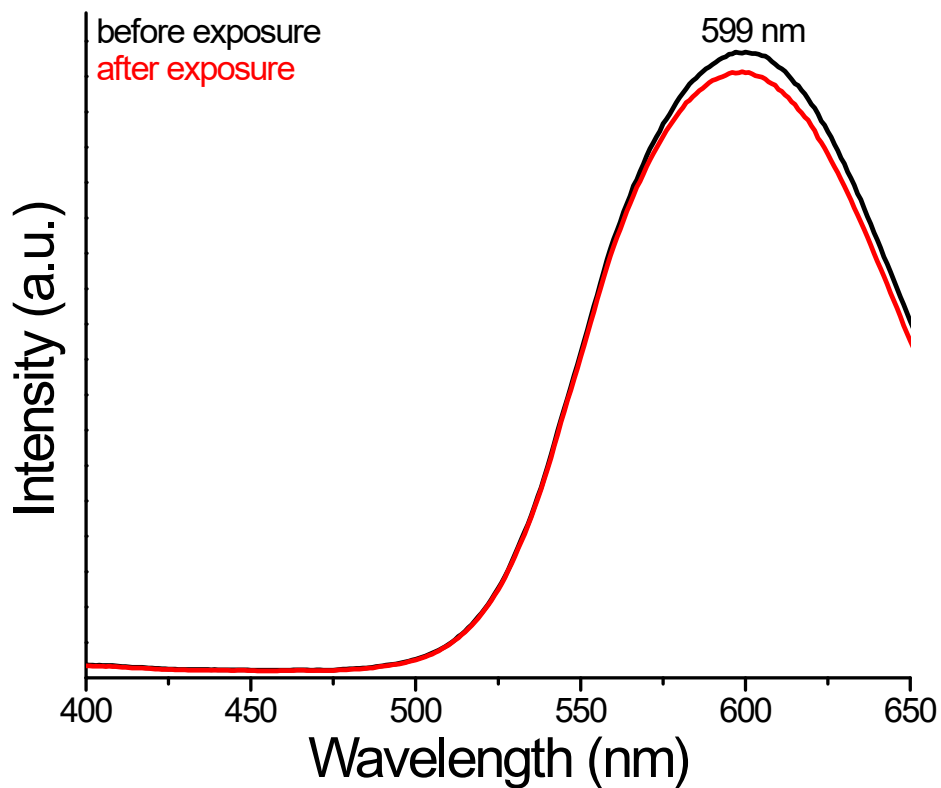


Fig. S17 PL spectra of the film before and after chloroform exposure.

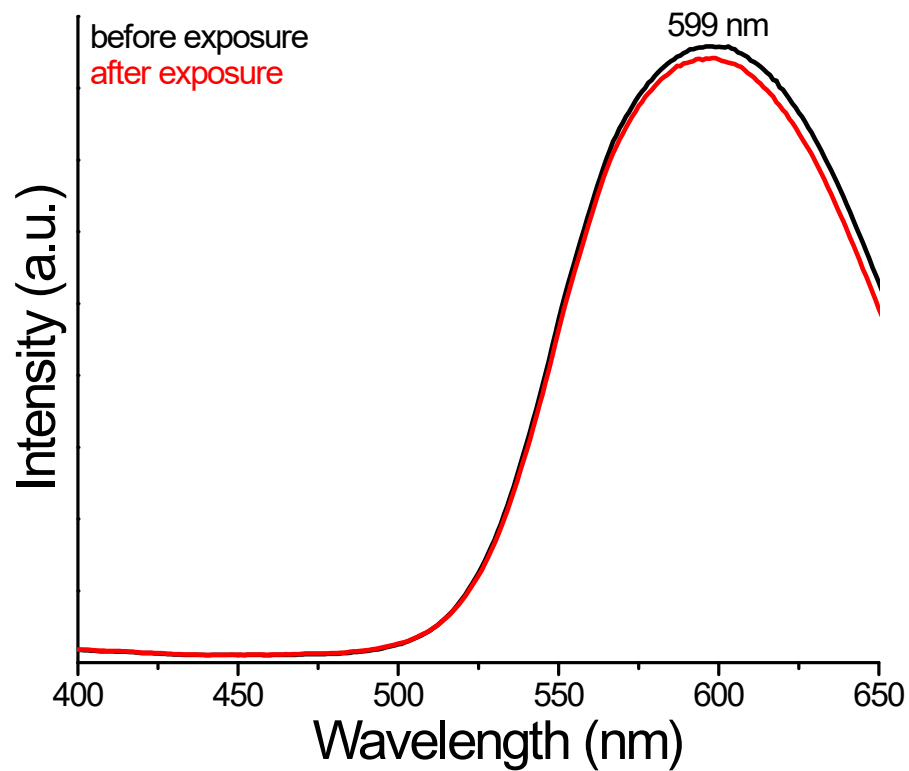


Fig. S18 PL spectra of the film before and after methanol exposure.

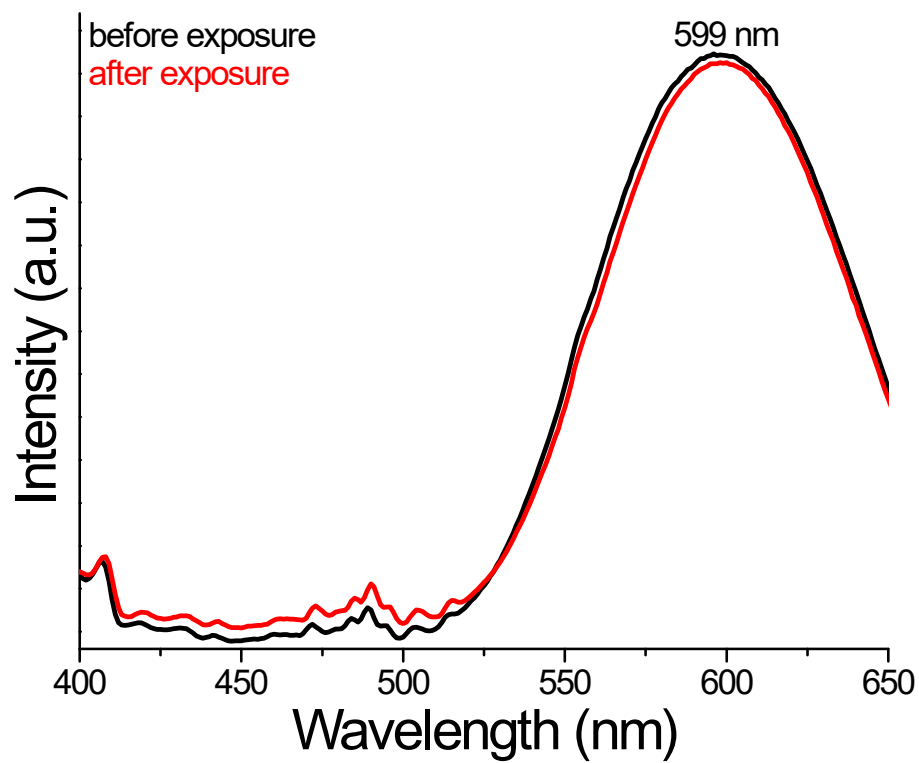


Fig. S19 PL spectra of the film before and after ethanol exposure.

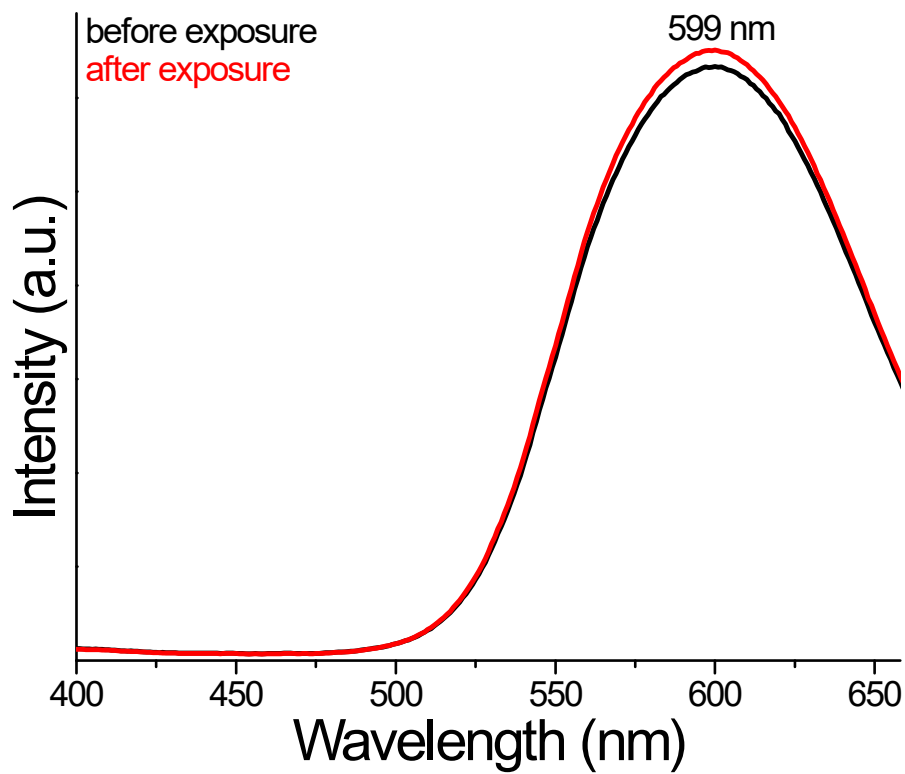


Fig. S20 PL spectra of the film before and after hexane exposure.

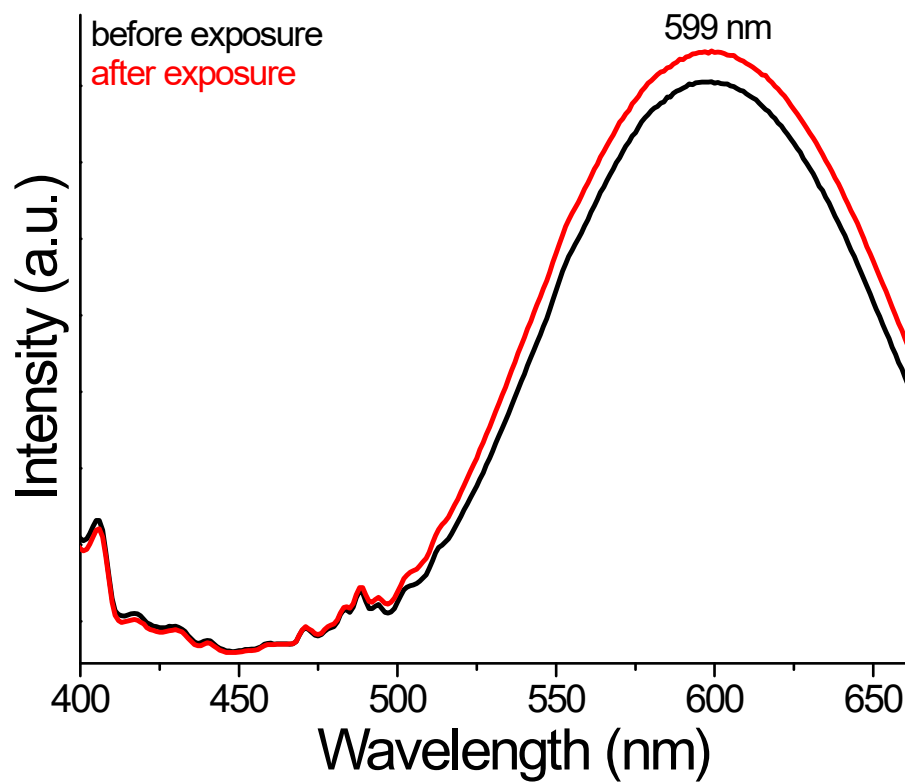


Fig. S21 PL spectra of the film before and after cyclohexane exposure.

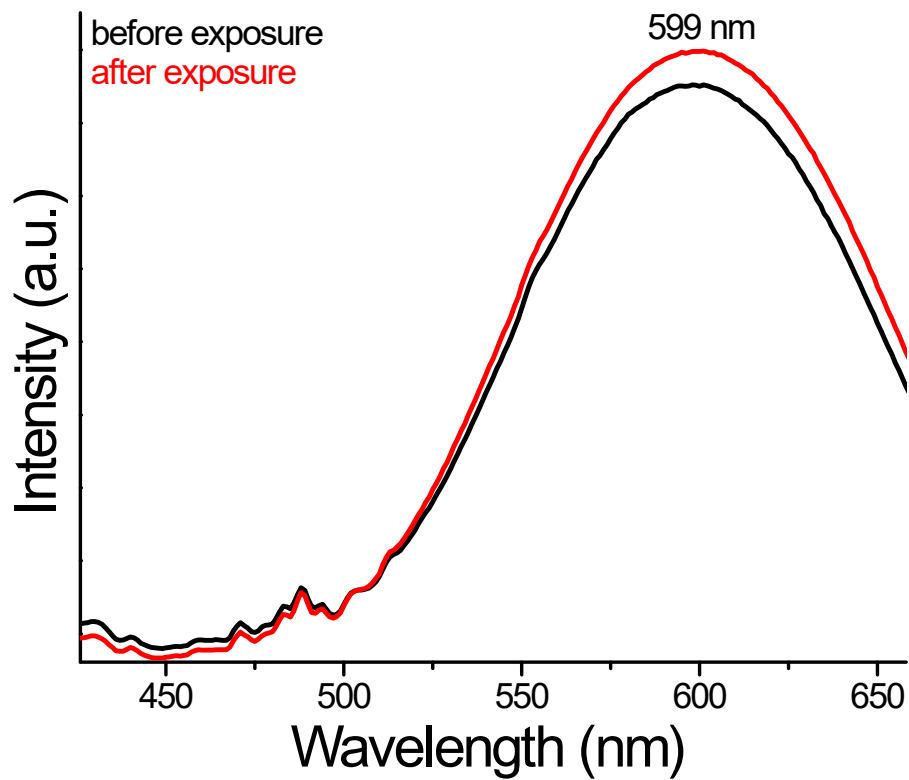


Fig. S22 PL spectra of the film before and after benzene exposure.

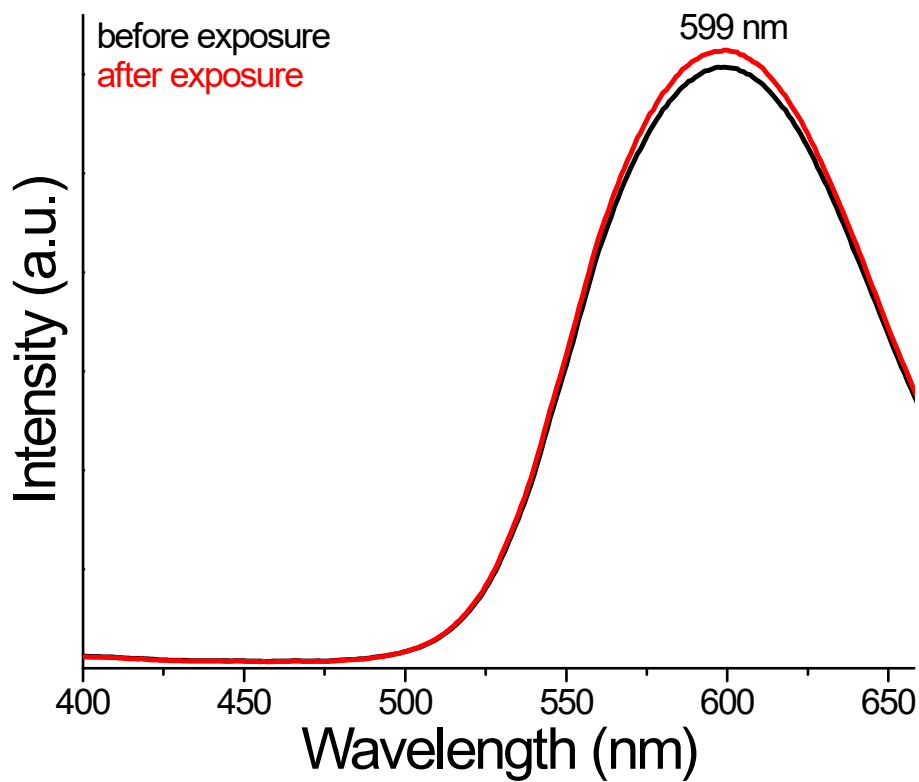


Fig. S23 PL spectra of the film before and after toluene exposure.

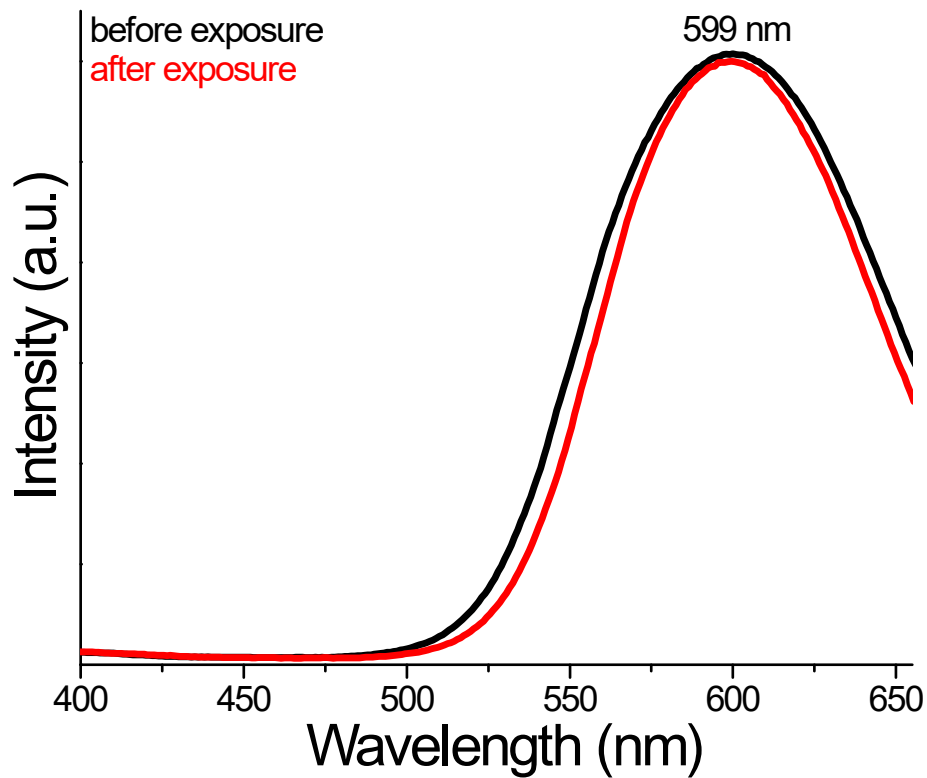


Fig. S24 PL spectra of the film before and after acetonitrile exposure.

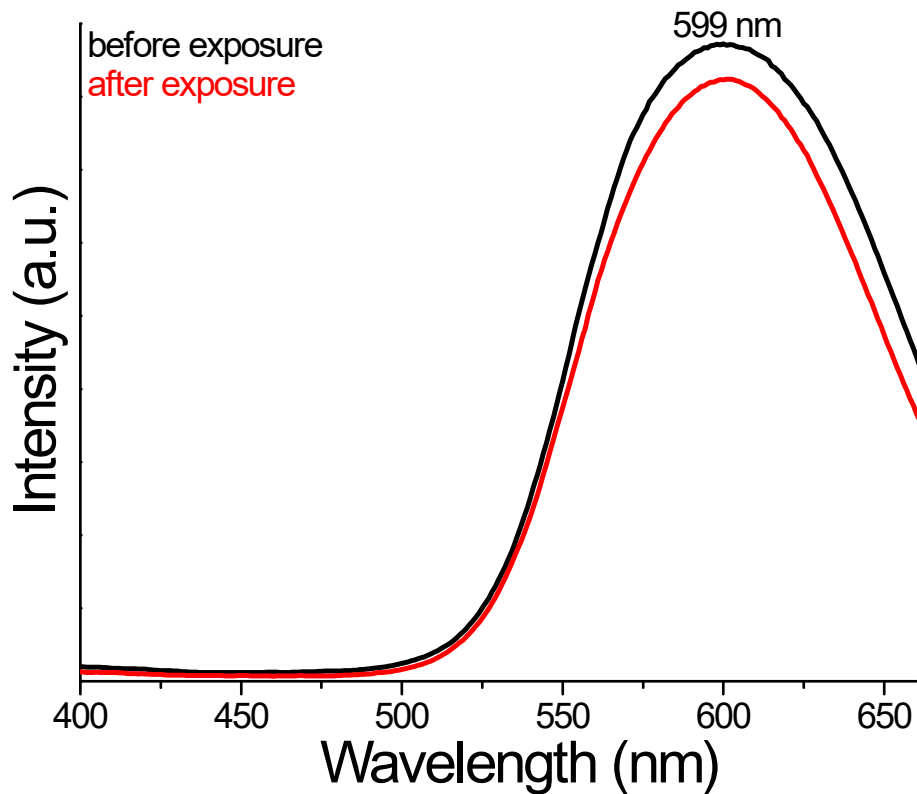


Fig. S25 PL spectra of the film before and after THF exposure.

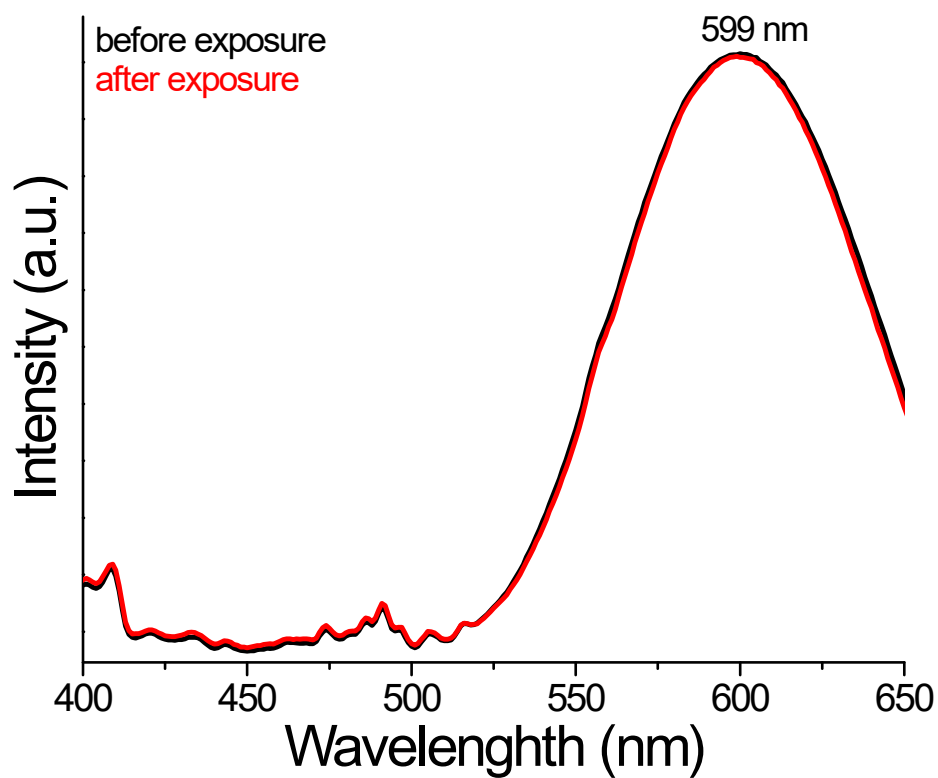


Fig. S26 PL spectra of the film before and after ethylacetate exposure.

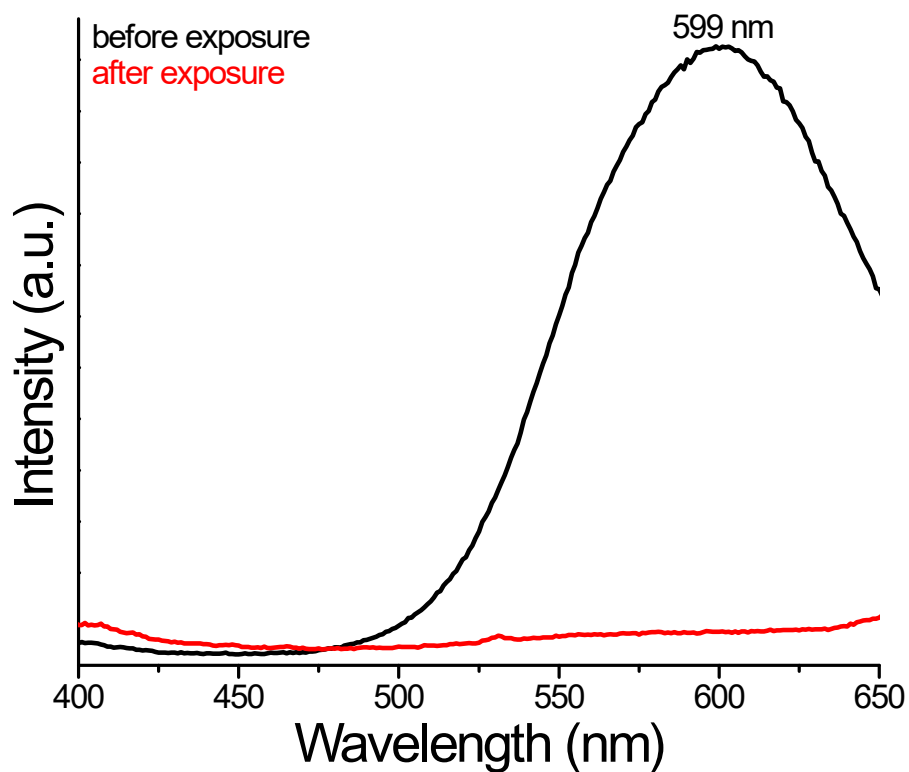


Fig. S27 PL spectra of the film before and after 2, 4-dinitrotoluene exposure.

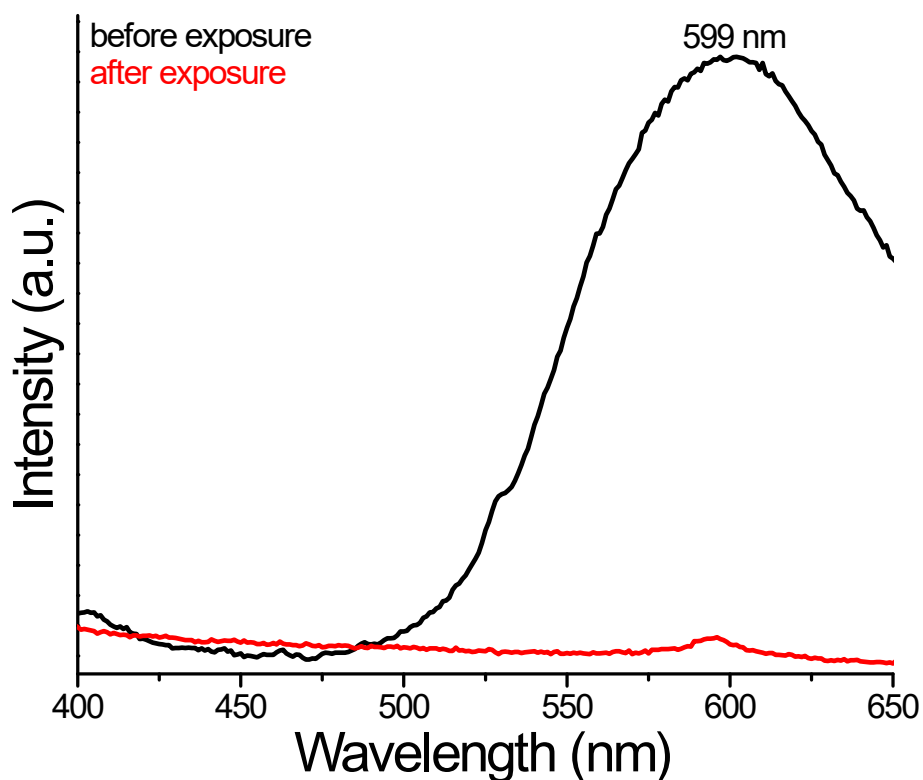


Fig. S28 PL spectra of the film before and after picric acid exposure.

References

- 1 J. Plešek, S. Hermanek, *Collect. Czech Chem. Commun.*, 1981, **46**, 687-692.
- 2 J. Plešek, Z. Janoušek, S. Hermanek, *Czech Chem. Commun.*, 1978, **43**, 1332-1338.
- 3 J. Li, H. Z. Ma, G. E. Reid, A. J. Edwards, Y. Hong, J. M. White, R. J. Mulder and R. A. J. O'Hair, *Chem. - A Eur. J.*, 2018, **24**, 2070–2074.
- 4 G. Kresse and J. Hafner, *Phys. Rev. B*, 1994, **49**, 14251–14269.
- 5 G. Kresse and D. Joubert, *Phys. Rev. B - Condens. Matter Mater. Phys.*, 1999, **59**, 1758–1775.
- 6 S. Grimme, *J. Comput. Chem.*, 2006, **27**, 1787–1799.



Cite this: DOI: 10.1039/d3nr00897e

Dissociative reactions of $[\text{Au}_{25}(\text{SR})_{18}]^{-}$ at copper oxide nanoparticles and formation of aggregated nanostructures†

Jayoti Roy,^a Biswajit Mondal,^{‡a} Gaurav Vishwakarma,^a Nonappa,^b Nishanthi Vasanthi Sridharan,^{†a} Pattabiraman Krishnamurthi^a and Thalappil Pradeep^{†a,c}

Reactions between nanoclusters (NCs) have been studied widely in the recent past, but such processes between NCs and metal–oxide nanoparticles (NPs), belonging to two different size ranges, have not been explored earlier. For the first time, we demonstrate the spontaneous reactions between an atomically precise NC, $[\text{Au}_{25}(\text{PET})_{18}]^{-}$ (PET = 2-phenylethanethiolate), and polydispersed copper oxide nanoparticles with an average diameter of 50 nm under ambient conditions. These interparticle reactions result in the formation of alloy NCs and copper-doped NC fragments, which assemble to form nanospheres at the end of the reaction. High-resolution electrospray ionization mass spectrometry (ESI MS), transmission electron microscopy (HR-TEM), electron tomography, and X-ray photoelectron spectroscopy (XPS) studies were performed to understand the structures formed. The results from our study show that interparticle reactions can be extended to a range of chemical systems, leading to diverse alloy NCs and self-assembled colloidal superstructures.

Received 25th February 2023,

Accepted 30th March 2023

DOI: 10.1039/d3nr00897e

rsc.li/nanoscale

Introduction

Understanding chemical transformations in terms of breaking and making of bonds is the central theme of chemical science. Nanoclusters (NCs) are a unique class of nanoparticles that are gaining enormous importance due to their precise structures, specific compositions, and unique properties, similar to those of molecules. Thiolate- and alkynyl-protected atomically precise NCs of noble metals are true molecules and their science is expanding rapidly. Such NCs are $[\text{Au}_{16}(\text{SR})_{12}]^{q-}$ ($q = 4$, SR = captopril; and $q = 0$, SR = adamantanethiol), $[\text{Au}_{18}(\text{SR})_{14}]^{q-}$ ($q = 3, 4, 5$), $[\text{Ag}_{25}(\text{SR})_{18}]^{-}$, $[\text{Au}_{25}(\text{SR})_{18}]^{-/+}$, $[\text{Ag}_{29}(\text{SR})_{12}(\text{PR})_4]^{-3}$, $[\text{Au}_{38}(\text{SR})_{24}]^0$, $[\text{Ag}_{44}(\text{SR})_{30}]^{q-}$ ($q = 3, 4$),

$[\text{Ag}_{46}(\text{SR})_{24}(\text{PR})_8](\text{NO}_3)_2$, $[\text{Ag}_{40}(\text{SR})_{24}(\text{PR})_8](\text{NO}_3)_2$, $[\text{Au}_{110}(\text{SR})_{48}]^{q-}$ ($q = 2, 3$), $[\text{Au}_{110}(\text{C}\equiv\text{CR})_{48}]^{q-}$ ($q = 2, 3$), $[\text{Au}_{137}(\text{SR})_{56}]^{q+}$ ($q = 2, 3$), $[\text{Au}_{144}(\text{SR})_{60}]^{q+}$ ($q = 2, 3$), etc., where SR, PR, and $\text{C}\equiv\text{CR}$ are thiolate, phosphine, and alkynyl ligands, respectively.^{1–15} Apart from their important optical,^{13,16–19} catalytic,^{13,20–24} and luminescence^{25–32} properties and associated applications,^{33–37} they also exhibit interesting chemical phenomena. Particularly, the size- and structure-conserving chemical reactions in which core atoms undergo exchange between clusters of different kinds are important to mention.^{38,39} Interparticle reactions between these nanoparticles need to be understood in the framework of established principles of chemistry along with an atomic level understanding of the mechanisms involved. Exploration of such reactions requires precise entities such as model nanosystems mentioned earlier and molecular tools. Reactions of similar kind often have led to the creation of new molecular entities apart from simple alloy clusters. Expanding this chemistry further has resulted in tri- and tetra-metallic clusters.^{40,41}

Ligand exchange^{42–45} and metal exchange^{46,47} reactions of NCs have established that NCs can react just as molecules. $[\text{Au}_{25}(\text{SR})_{18}]^{-}$ and $[\text{Ag}_{44}(\text{SR})_{30}]^{4-}$ react spontaneously to form alloy NCs as the product.⁴⁸ Similarly, a reaction between $[\text{Au}_{25}(\text{SR})_{18}]^{-}$ and $[\text{Ag}_{25}(\text{SR})_{18}]^{-}$ was also studied in solution, where monomers and dimers of both the clusters were involved in intercluster reactions.^{49,50} Reports of interparticle

^aDST Unit of Nanoscience (DST UNS) & Thematic Unit of Excellence (TUE), Department of Chemistry, Indian Institute of Technology Madras, Chennai 600036, India

^bFaculty of Engineering and Natural Sciences, Tampere University, FI-33720 Tampere, Finland

^cInternational Centre for Clean Water, 2nd Floor, B-Block, IIT Madras Research Park, Kanagam Road, Taramani, Chennai 600113, India. E-mail: pradeep@iitm.ac.in

†Electronic supplementary information (ESI) available: Concentration calculations of the employed materials, UV-vis study, time-dependent MS studies, HRTEM micrographs, and FTIR and DLS studies. See DOI: <https://doi.org/10.1039/d3nr00897e>

‡Present address: Institute of Nanotechnology, Karlsruhe Institute of Technology, 76344 Karlsruhe, Germany.

reactions suggest that a possible route for these reactions is through the exchange of metal or metal–ligand fragments, through interparticle dimers. Monolayers of ligands protecting the surface of the NCs are dynamic, and the metal–ligand interface plays an important role in controlling the reactions.

Apart from the chemistry between clusters, cluster–bulk chemistry, for instance, the reaction of $[\text{Au}_{25}(\text{SR})_{18}]^-$ and $[\text{Au}_{38}(\text{SR})_{24}]^-$ NCs with bulk Ag–metal, has also been reported.⁵¹ This kind of exchange is elegantly seen in isotopic exchange experiments of $[^{107}\text{Ag}_{25}(\text{SR})_{18}]^-$ and $[^{109}\text{Ag}_{25}(\text{SR})_{18}]^-$ with bulk Ag–powder and related experiments.⁵² Similar atom exchange chemistry has also been seen in the reaction between clusters and metal ions, such as $[\text{Au}_{25}(\text{SR})_{18}]^-$ and Pt^{4+} , Pd^{4+} , Hg^{2+} , and Cd^{2+} leading to $[\text{MAu}_{24}(\text{SR})_{18}]^-$ (where $\text{M} = \text{Pt/Pd/Hg/Cd}$).⁹ In similar processes, the metal ions participating in the reactions get reduced by the clusters, which are charged in the native state. Recently, NCs have been used as attractive nanoscale building blocks to fabricate 3D superstructures *via* colloidal self-assembly.^{9,53,54} Exploring self-assemblies of NPs has been a hot topic in nanotechnology for the past few years and it remains relevant due to the tunable collective properties as well as the remarkable applications of the superstructures in a wide range of fields. The inter-nano-cluster interactions play a vital role in the novel properties of metal nanoparticle assemblies.²² Reactions between various sized nanoparticles in homogeneous solutions constitute an emerging area in the field of NCs with great potential for the controlled formation of transition metal nanoalloys and self-assembled superstructures.⁵⁵

Multidimensional close-packed nanocluster-based molecular aggregates have been achieved using evaporation-induced assembly, interfacial assembly, binary solvent-induced assembly, the antisolvent approach, dip coating, and the Langmuir–Blodgett method.^{56–58} Still, achieving a combination of precision and reproducibility of self-assembled large-area NP superstructures remains a grand challenge. Metal NPs too exhibit polydispersity, a tendency toward uncontrolled aggregation, and a lack of directional inter-nanoparticle interactions. Additionally, rather than the anticipated homogeneous or precise product, delayed diffusion of colloidal particles and nonspecific binding may cause a variety of undesired architectures.

In this context, we decided to explore the redox chemistry between noble metal NCs, such as $[\text{M}_{25}(\text{SR})_{18}]^-$ ($\text{M} = \text{Au}, \text{Ag}$) with metal oxide and sulfide nanoparticles, such as MO_x (*e.g.*, CuO , Cu_2O , NiO , PbO , *etc.*) and Ag_2S . As this corresponds to a large chemical diversity, we decided to focus on one reaction in the present paper, namely that between $[\text{Au}_{25}(\text{SR})_{18}]^-$ and CuO NPs. These experiments suggest that chemical reactions between the systems are strongly dependent upon the concentration of the reactants. Our results suggest that simple atom exchange occurs in the low concentration limit of metal oxides. Interestingly, at a higher concentration, the clusters undergo oxidative decomposition. This results in mixed metal–thiolates, which subsequently form nanoaggregates.

Experimental section

Reagents and materials

Chloroauric acid trihydrate ($\text{HAuCl}_4 \cdot 3\text{H}_2\text{O}$), 2-phenylethane thiol (PET), tetraoctylammonium bromide (TOAB), sodium borohydride (NaBH_4), and copper acetate dihydrate $[\text{Cu}(\text{CO}_2\text{CH}_3)_2 \cdot 2\text{H}_2\text{O}]$ were procured from Sigma-Aldrich. Solvents, such as tetrahydrofuran (THF), dichloromethane (DCM), and methanol (MeOH) were purchased from Finar Limited and were of HPLC grade. Milli-Q water was used during the synthesis of NC and NP. All chemicals were utilised without further purification.

Synthesis

Synthesis of $[\text{Au}_{25}(\text{PET})_{18}]^-$. $[\text{Au}_{25}(\text{PET})_{18}]^-$ (*i.e.*, abbreviated as $[\text{Au}_{25}]$) NC was synthesized using an established literature procedure.^{59,60} About 40 mg of $\text{HAuCl}_4 \cdot \text{H}_2\text{O}$ was dissolved in 7.5 mL of THF and the solution was mixed with 65 mg of TOABr. The resulting solution was stirred for around 10–15 min to get an orange-red solution. To this solution, the PET ligand ($\sim 68 \mu\text{L}$) was added by maintaining an $\text{Au}:\text{PET}$ molar ratio of 1 : 5 and the system was stirred continuously for another hour. The Au–thiolate complex was formed which was reduced by a solution of 39 mg of NaBH_4 in 2.5 mL ice-cold water. The color of the solution changed instantly from yellow to brown. The solution was stirred continuously for another 5 hours for the complete conversion of diverse NCs to $[\text{Au}_{25}]$. Finally, the as-synthesized cluster was vacuum dried using a rotavapor and washed several times with excess MeOH to get rid of free thiol and thiolate. Finally, the $[\text{Au}_{25}]$ NCs were extracted in acetone and the solution was centrifuged. The supernatant solution containing $[\text{Au}_{25}]$ was collected. It was vacuum dried and the residue was dissolved in DCM to prepare a stock solution. 25 μL of the stock solution ($\sim 1.35 \text{ nM}$) was used during the reaction.

Synthesis of copper oxide nanoparticles (CuO NPs). Pure metallic copper oxide nanoparticles (*i.e.*, abbreviated as CuO NPs) were prepared by the thermochemical reduction method according to a previously published method.⁶¹ In a typical synthesis, 1 g of copper acetate dihydrate was dissolved in 12.5 mL of deionized water. The solution was stirred for one hour until the salt was dissolved completely. The resulting reaction mixture was heated in a muffle furnace at 500 °C for one hour under atmospheric conditions. A dark blackish-brown precipitate was formed after one hour. The reaction mixture was cooled at room temperature and washed with a 2 : 3 MeOH–water solution. Finally, the CuO NPs were washed with MeOH. The pure bare CuO NPs were dried under 60 °C for 30 minutes. 1 mg of the as-synthesized NPs was dispersed in 1 mL of DCM to prepare the dispersed solution of 1 mg mL^{-1} .

Instrumentation

UV-vis studies were performed using a PerkinElmer Lambda 25 UV-vis spectrometer in the range of 1100–200 nm at a scan rate of 240 nm per minute. All ESI MS studies were performed

in the negative ion mode using a Waters Synapt G2-Si high-definition mass spectrometer (HDMS). During measurements, capillary voltage, cone voltage, and source offset were maintained at 3 kV, 120–150 V and 80–120 V, respectively to obtain well-resolved mass spectra. The source temperature and desolvation temperature were maintained at 100 and 150 °C, respectively. The desolvation gas flow was maintained at 450 L h⁻¹ during the measurements. ESI MS, in a time-dependent manner, was employed to study the progress of the reaction between NPs and NC. 1 mL solution was taken out from the reaction vessel each time and centrifuged at 10 000 revolutions per minute (rpm) for complete removal of bigger particles and aggregates. TEM images of the samples were obtained with a JEOL 3010 instrument at an operating voltage of 200 kV with an ultrahigh resolution (UHR) polepiece. 3 µL of each sample solution was drop cast over a TEM grid (specifically carbon-coated Ni grid) and dried under an ambient atmosphere before imaging. The 2D projections for electron tomography were collected using transmission electron microscopy (TEM) operating at an accelerating voltage of 300 kV on a JEOL 3200FSC. Image acquisition was done using SerialEM software. A Malvern Zetasizer Nano ZSP instrument was utilized to study particle size distributions in solution, using dynamic light scattering (DLS). The XPS measurements were performed using an ESCA Probe TPD spectrometer of Omicron Nanotechnology. Polychromatic Al K α was used as the X-ray source ($h\nu = 1486.6$ eV). After the reaction, the NPs were directly drop cast on the sample stub. A constant analyzer energy of 20 eV was used for the measurements. Binding energy (BE) was calibrated with C 1s at 284.8 eV. All the XPS spectra were deconvoluted using the Casa XPS software. Fourier transform infrared (FTIR) spectra were measured with a PerkinElmer Spectrum 2 spectrometer with a UATR attachment. Each spectrum was collected in the wavenumber range of 400–4000 cm⁻¹.

Results and discussion

Characterization of the starting materials

Bare CuO NPs and [Au₂₅] NCs were initially selected as model systems to explore the interparticle reaction between CuO NPs and atomically precise gold NCs because of their excellent stability individually. Atomic precision of [Au₂₅] NCs was confirmed by UV-vis and ESI MS measurements. The characteristic peaks of [Au₂₅] NCs at 675 nm and 450 nm were observed in the UV-vis spectrum (Fig. S1†). Negative ion mode ESI MS measurements showed the monoanionic molecular ion peak of [Au₂₅] at m/z 7393 (Fig. S2†). The experimental isotopic distribution of the nanocluster composition of [Au₂₅] is in good agreement with the calculated one, as shown in Fig. S2†.

TEM micrographs of the as-synthesized [Au₂₅] NC are shown in Fig. S3(A(i and ii)).† A honeycomb-like arrangement consisting of NCs was observed under the electron microscope. The observed morphology of NCs could be due to the interactions among PET ligands during the evaporation of the

solvent.^{53,62,63} The CuO NPs were synthesized using the protocol discussed in the Experimental section. The TEM micrographs of the as-synthesized CuO NPs are shown in Fig. S3(B(i)).† An inter-planar distance of 0.27 nm and the EDS elemental composition further confirm the formation of CuO NPs (Fig. S3(B)).†^{61,64}

Reaction between CuO NPs and [Au₂₅] NCs

The reaction between CuO NPs and the [Au₂₅] NCs was demonstrated by mixing a known volume of DCM solution of [Au₂₅] and a dispersion of CuO NPs, also in DCM, at fixed concentrations (w/v) under stirring conditions (see the Experimental section and the ESI†). Molecular changes in the cluster were confirmed by UV-vis spectroscopy (Fig. S1†) by separating the NCs from NPs using high speed centrifugation of the solution. The red shift in the absorbance peaks of Au₂₅ after the reaction with NPs may be attributed to the exchange of surface atoms with Cu (see Fig. S1†) and the process seems to attain rapid thermodynamic equilibrium. Cu (1.28 Å) has a smaller atomic radius than gold (1.44 Å), and the Cu–Au bond (bond dissociation energy, EBD = 227.1 ± 1.2 kJ mol⁻¹) is slightly stronger than the Au–Au bond (EBD = 226.2 ± 0.5 kJ mol⁻¹).⁶⁵ Thus, Cu doping to [Au₂₅] NCs is possible and it significantly alters the optical properties of the parent NC. Relative lower energy shift in the optical absorption spectrum (as shown in the inset of Fig. S1†) can be attributed to the reduction in the HOMO–LUMO gap of the parent NC due to the formation of Cu-doped NCs. This also indicated that all or most of the Cu-doped NCs are expected to have a core–shell structure.⁶⁶ Experimental studies of the NC and NP reactions revealed that coinage metal doping alters the optical properties and oxidation states of the NC in solution.

We attempted to understand the chemical changes during the reaction using time-dependent mass spectrometric studies. To monitor the progress of the reaction, the reaction mixture was analysed after a certain time interval with ESI MS measurements. As described in the Experimental section, after a constant time interval ($\Delta t = 30$ min), the solution was centrifuged and the blackish brown supernatant was subjected to mass spectrometric studies. All the mass spectrometric parameters were kept constant throughout the experiment to analyse the compositional variation of the reaction mixture with time. As shown in Fig. 1(A) and Fig. S4, S5,† a peak of monoanionic [Au₂₄Cu₁(PET)₁₈]⁻ (m/z 7260) (the difference in mass from the parent [Au₂₅], Δm , is = 131 = [m_{Au} – m_{Cu}] = [196.9 – 63.5]) (abbreviated as [Au₂₄Cu₁]), [Au₂₃Cu₂(PET)₁₈]⁻ (m/z 7129) (abbreviated as [Au₂₃Cu₂]) (here, $\Delta m = 262 = [m_{\text{Au}} - 2m_{\text{Cu}}]$) along with a few other peaks (m/z 2100–5000) corresponding to other intermediate species appeared with time. Fluctuating intensity trends of [Au₂₄Cu₁] and [Au₂₃Cu₂] were observed during the course of the reaction (Fig. 1(A)(a–d and a'–d')). The parent [Au₂₅] NC (m/z 7393) showed a continuous reduction in the signal intensity during the reaction (peak at m/z 7393 in Fig. 1(A(i–v))). The exact number of copper atoms doping into the gold NC was confirmed from the exact matching of experimental isotopic distribution with the calculated

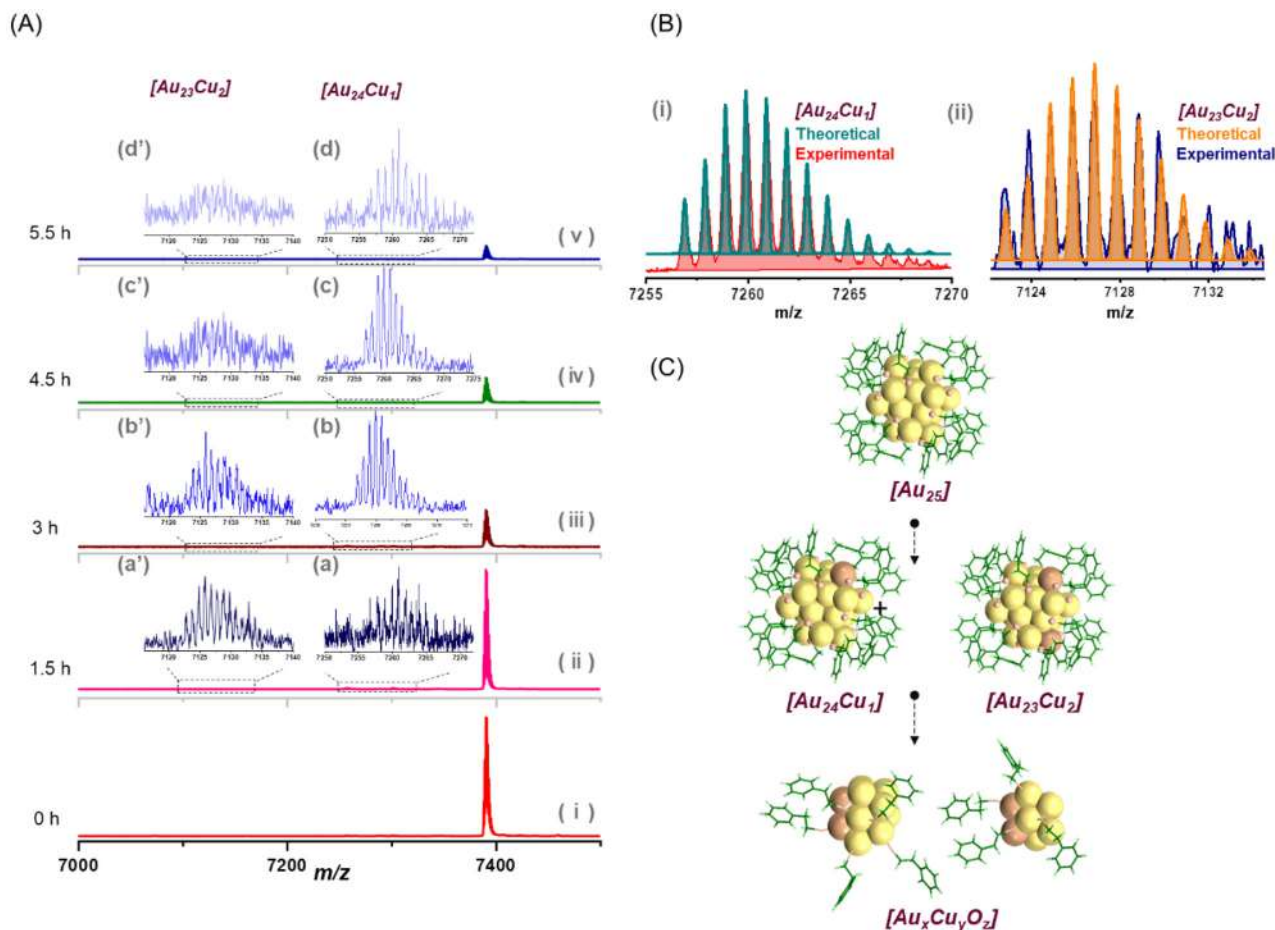


Fig. 1 (A(i–v)) Time-dependent ESI MS spectra of the NC solution in the mass range of m/z 7000–7500. During the reaction, the time-dependent evolution of copper-doped NC species, $[\text{Au}_{24}\text{Cu}_1]$ and $[\text{Au}_{23}\text{Cu}_2]$ are observed in the mass spectral region of m/z 7250–7272 (a–d) and m/z 7116–7140 (a'–d'), respectively. (B) High-resolution isotopic distribution of the mass spectrum of $[\text{Au}_{24}\text{Cu}_1]$ (i) and $[\text{Au}_{23}\text{Cu}_2]$ (ii) with their calculated ones (green and orange, respectively). The experimental mass spectra in (B) were obtained from the 3 h-spectral data (1(A)(iii)) to fit with the theoretical ones. (C) Schematic representation of the reaction at $[\text{Au}_{25}]$ NCs in the course of time.

mass spectrum (as shown in Fig. 1(B)(i and ii)). The experimental mass spectra of the specific m/z range in Fig. 1(B) were recorded from the MS data after 3 h of reaction (Fig. 1(A)(iii)) to fit with the respective theoretically calculated mass. The variation of ion abundances of copper-doped $[\text{Au}_{25}]$ NCs can be correlated with the formation of other intermediates in the m/z range of 2100–5000. The time-dependent ion intensity variation of $[\text{Au}_{24}\text{Cu}_1]$ and $[\text{Au}_{23}\text{Cu}_2]$ NCs is shown in Fig. S4(B).† The formation of monoanionic metal-thiolate intermediates, such as $[\text{Au}_8(\text{PET})_9]^-$ (m/z 2820), $[\text{Au}_8(\text{PET})_{12}\text{O}_2]^-$ (m/z 3256), $[\text{Au}_{10}(\text{PET})_{10}\text{O}_2]^-$ (m/z 3378), $[\text{Au}_{10}(\text{PET})_{10}]^-$ (m/z 3396), $[\text{Au}_9\text{Cu}_2(\text{PET})_{11}]^-$ (m/z 3411), and $[\text{Au}_{11}(\text{PET})_{10}(\text{O}_2)_2]^-$ (m/z 3601) was seen in the course of reaction (see Fig. S5 and S6†). As we did not observe any NC fragments containing O or O_3 , such fragments can also be attributed to S or S_2 instead of O_2 and $(\text{O}_2)_2$ addition. It is difficult to differentiate one such NC fragment containing O_2 instead of S (O_2 and S have the same mass) by looking into the high-resolution isotopic distribution. So, the molecular compositions with O_2 can be varied

with S. Moreover, it has been reported that after losing all 'staple' Au-PET units, $[\text{Au}_{25}]$ NC forms Au_xS_y fragment ions during its gas-phase fragmentation.¹⁵ When the NCs were accommodated on the surface of CuO NPs during the reaction, atomic exchanges took place between the NPs and the NCs. As a result of this interparticle interaction between NCs and NPs, Cu-doped $[\text{Au}_{25}]$ and other Cu and O-doped smaller Au-NC fragments were formed. Because of the accessible sites of $[\text{Au}_{25}]$ NC,⁶⁷ Cu and O atoms of NPs can interact with Au-S staples on the surface of the NC. The interactions between Cu- and O-atoms of CuO NPs with the $[\text{Au}_{25}]$ NC during the solution phase reaction resulted in the decomposition of the parent $[\text{Au}_{25}]$ NC.⁶⁸

These reactions are found to be highly dependent on the concentration (w/v) of the dispersed solution of CuO NPs. Lower the concentration of the NPs, the slower is the kinetics of the reaction. For example, for a very low concentration of CuO NPs (1/5th (w/v) of the prepared stock solution), only singly copper-doped $[\text{Au}_{25}]$ NCs were formed (see Fig. S7†).

The thiolate fragments indicated that the process may lead to the assembly of small clusters, mediated by thiolates. We find that all the fragments, including the alloy NCs formed during the reaction, finally coalesce to form nano-assemblies, as observed in TEM images (see Fig. 2). In Fig. 2, we observed that the size of the parent CuO NPs decreases from ~ 50 nm to <10 nm during the interparticle reaction with $[\text{Au}_{25}]$ NCs (also see Fig. S8†). The bare parent CuO NPs tend to be intermingled with the NCs, as shown in Fig. S8(A)†. In Fig. 2(B), TEM images showed the formation of three-dimensional nanosphere (NS)-shaped assemblies after six hours of reaction. At this stage of the reaction, the size of homogeneous NSs was expanded to a diameter regime of 200–400 nm. Large area TEM (Fig. 2(B)) and scanning transmission electron microscopy (STEM) (Fig. S9(A)†) micrographs showed the formation of well-shaped NSs.

Differential centrifugation was performed to separate the self-assembled superstructures, *i.e.*, NSs from parent NPs and NCs. Initially, NPs were separated from the rest of the solution; later, NSs were precipitated out from the solution. Elemental compositions of the NPs, NSs, and NCs were analyzed by EDS (Fig. S10–S13†). Fig. S11 and S12† show the TEM micrographs of isolated NSs (as the precipitate) and reacted NCs (as the supernatant) after centrifuging the reaction mixture at 9000 rpm. The precipitate (see Fig. 3(A(i–v))) and supernatant (see Fig. 3(B(ii–v))) obtained after centrifugation were used for STEM and EDS elemental mapping.

EDS mapping confirmed the presence of gold, copper, sulfur, and oxygen as elemental composition in the structures (Fig. 3(A(ii–v))). It is important to note that as shown in Fig. 3(B(ii–v)), gold, copper and sulfur are present throughout the NC aggregates, suggesting that the copper was doped into the NC. The elemental maps suggest that oxygen is concentrated in the nanospheres and not in the NC aggregates. This would mean that NCs are doped predominantly with Cu and no additional chemical changes have occurred. However, in the

CuO particles, the incorporation of Au and S has occurred. As the only source of S is NCs, they have undergone partial degradation.

To gain insights into the morphology of assembled nanostructures, and thus to have a better understanding of the assembly of NC–NP fragments, TEM tomographic reconstruction was performed. Fig. 3(C(i–iii)) shows the TEM micrographs at three different tilt angles. For 3D reconstruction of the structure, a series of 2D projections were collected by tilting the sample from $+69^\circ$ to -69° with an increment angle of 2° . 3D reconstruction suggests sphere-like assembly. It must be noted that due to possible drying effects, the spherical superstructures were partially deformed (Fig. 3D, see ESI Video V1† for tilt series of aligned 2D projections). The 3D reconstructed image and the cross-sectional view suggest densely packed nanoparticles throughout the spherical superstructure with slight differences in the core and peripheral regions (Fig. 3D, see ESI Video V2† for 3D reconstruction of the nanosphere). Importantly, nanoparticles were distributed throughout the sphere, though without a regular order or packing pattern.

To examine the changes in the chemical environment upon reaction between NPs and NCs, an XPS study was performed. XPS revealed a change in the oxidation state of elements as a result of the reaction. In Fig. 4, the Au 4f region shows a blue shift in the binding energy (BE) corresponding to the oxidation of Au (due to Au–Cu bond) upon reaction with CuO NPs. The Cu $2p_{3/2}$ peak of reacted CuO was shifted to lower BE after the reaction, due to the reduction of a fraction of Cu(II) to Cu(I). Additionally, reduction in the strong satellite peaks corresponding to Cu(II) (prominent in parent NPs), can be noticed after the reaction. These observations suggest a mixed oxidation state of Cu after the reaction.

Similarly, S 2p BEs were compared before and after the reaction. The peak at 162 eV corresponds to $2p_{3/2}$ of S, attributed to the Au–S bonds. The appearance of a new peak at 167.2 eV

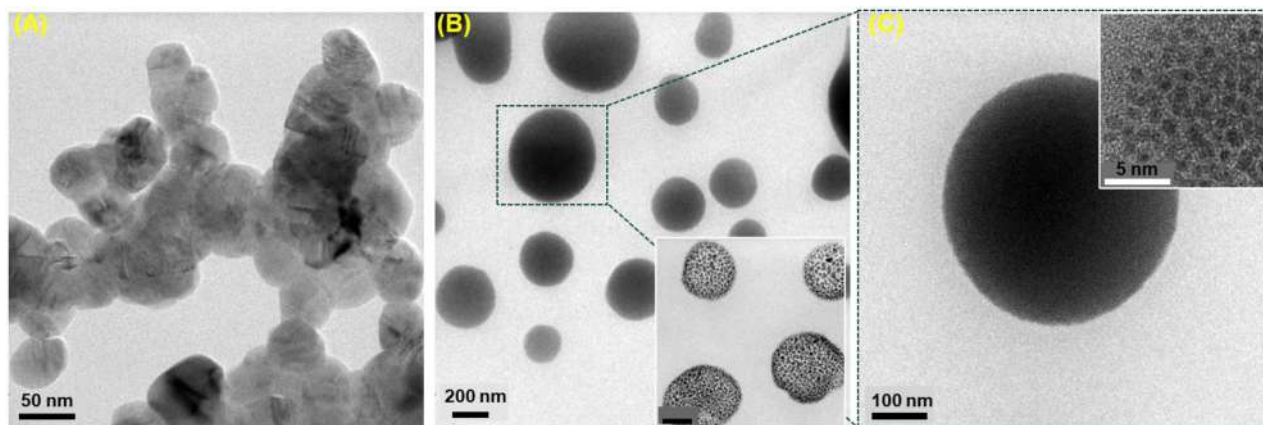


Fig. 2 TEM images (left to right) showing bare CuO NPs before (A) and after (B) reaction with Au_{25} NCs. CuO NPs with an average size of ~ 50 nm (A) and assembly formed post reaction (B). A second kind of assembly was observed in the inset of (B). Other than NSs, unreacted and reacted NPs were observed under TEM which are presented in the ESI.† In (C), higher magnification TEM image of a single nanosphere. Inset shows the HR-TEM from a selected area.

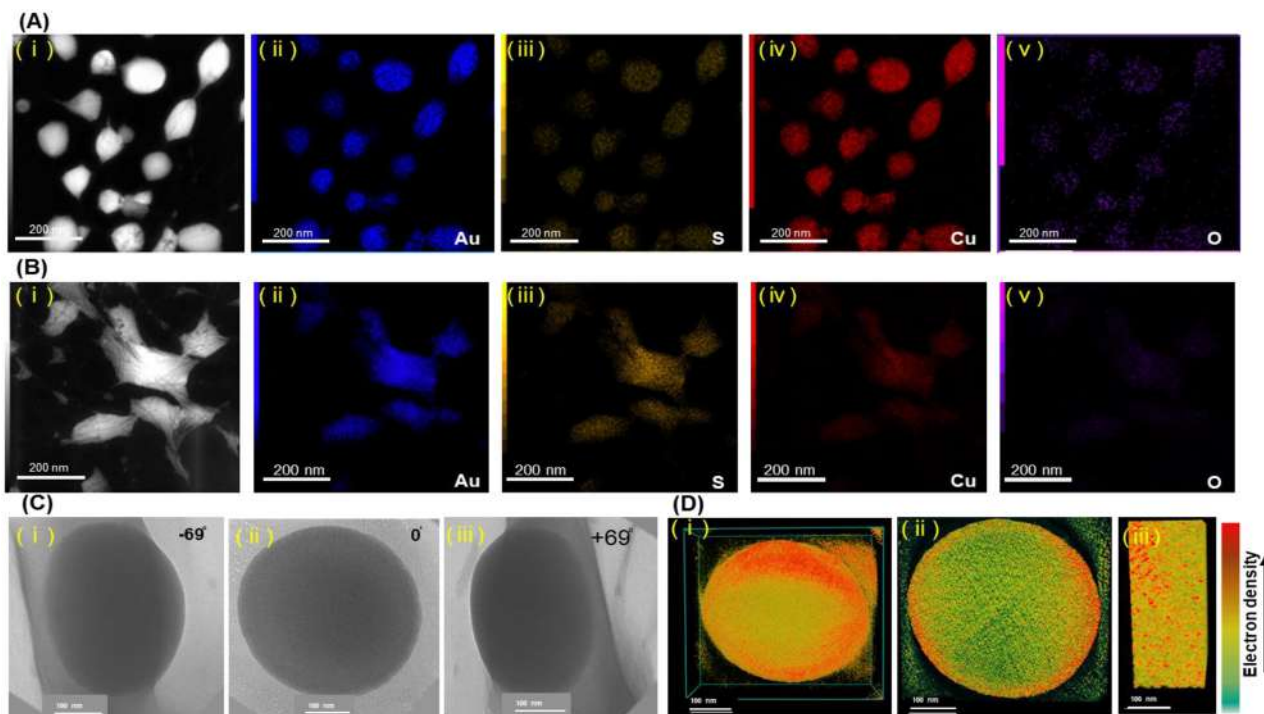


Fig. 3 (A and B) DF STEM images of nanosphere and reacted nanoclusters, respectively and corresponding EDS elemental mapping for Au, S, Cu and O. (C) 2D TEM projection of a spherical superstructure at different tilt angles. (D) TEM tomographic reconstruction of C, cross-sectional view, and a portion showing densely packed nanoparticles.

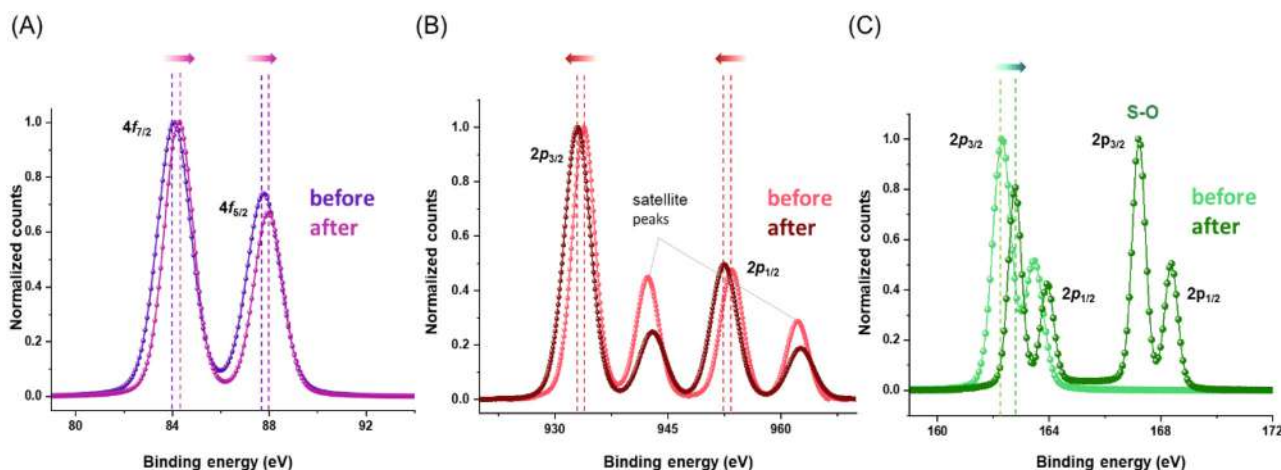


Fig. 4 XPS spectra of (A) Au 4f, (B) Cu 2p, and (C) S 2p regions, before and after the reaction.

in the XPS study of reacted NPs indicates the formation of a new S–O bond as a result of the reaction of NPs with NC. So, it is revealed that strong electrostatic and coordination interactions between Au–S of NCs and Cu–O atoms of NPs enhance the NC–NP interactions and atomic exchange during the reaction.

To understand the molecular interactions responsible for the formation of nanoaggregates after the reaction, FTIR measurements of the supernatant (see Fig. S14(ii)†) after reac-

tion were carried out. The resultant FTIR data were compared with [Au₂₅] NC (Fig. S14(i)), TOAB (Fig. S14(iii)), and PET (Fig. S14(iv)).† New IR frequencies (ν) were observed due to new C–O and S–O bonds and also due to intermolecular hydrogen bonding (H-bonding) as a result of the reaction. The spectra are shown in Fig. S14.† In Fig. S14,† the progression bands in the range of 1900–1700 cm^{−1} in [Au₂₅] vanished completely after the reaction, indicating the loss of crystallinity and degradation of NC during the course of the reaction. The

formation of C–O and S–O bonds indicate atom transfer between precursors during the reaction. As a corollary, these non-covalent and covalent interactions play a vital role in the formation of molecular nanoaggregates and NSs.

DLS has been utilized to reveal the size evolution of nanostructures in solution as a function of reaction time. Time-dependent DLS measurements (see Fig. 5) of the reaction showed a gradual increment in the hydrodynamic radius (R_H) of the NSs after 2 h of the reaction. Additionally, DLS measurements revealed that the average radius of the NS aggregates gradually increased between 2 to 5 h continuously. Furthermore, the average R_H of NSs remained constant (*i.e.*, average R_H during 5 h of the reaction) with a further increase in the reaction time (~ 6 h). Hence, this proves the formation of NSs in the solution phase with excellent colloidal stability.

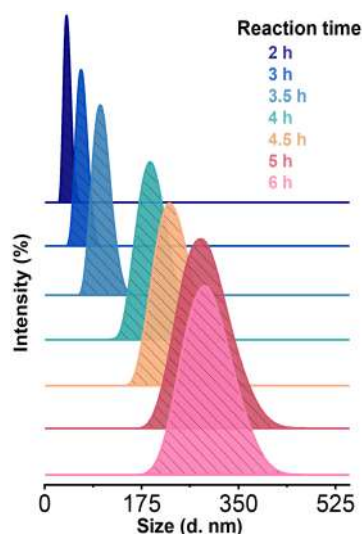
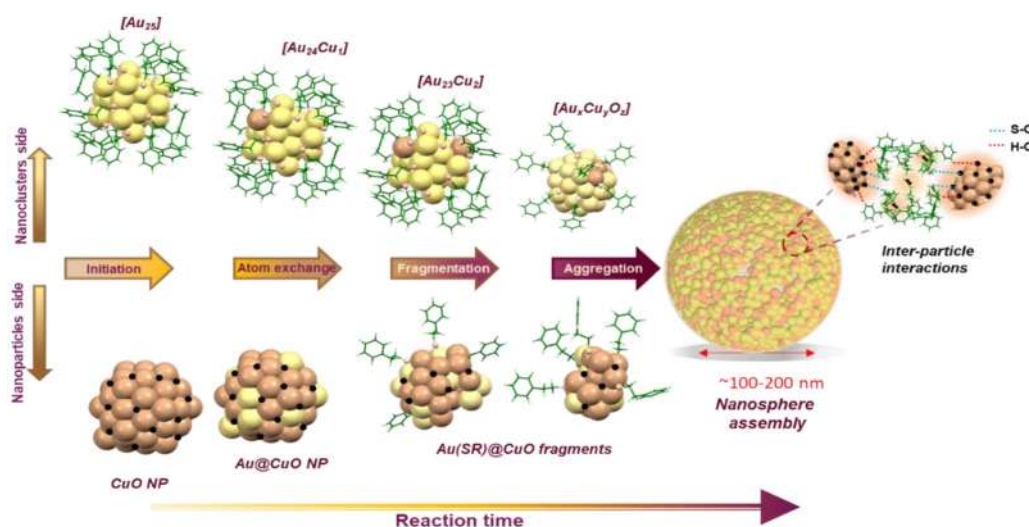


Fig. 5 Time-dependent monitoring of the reaction by DLS.

A similar DLS experiment was demonstrated to probe into the disassembly of nanoaggregates (see Fig. S15†). Solvent plays an important role in growth of nanoparticles, their assembly, and disassembly. Interactions between the nanoparticle surface and solvent molecules or between the solvent molecules and ligands considerably influence the particle size and morphology. Methanol was gradually added to the reaction medium (*i.e.*, DCM solution) at the end (after six hours) of the reaction, and DLS was performed. In a highly polar dispersion medium, charged thiolate complex ions (which were earlier assembled to form NSs) are more soluble. As a result, particles are prevented from aggregation, and disassembly of NSs was observed. As shown in Fig. S15,† the average R_H of NSs was ~ 301 nm after 6 h of reaction. However, after 10 μ l of MeOH addition, R_H increased. But, with further increment in MeOH (50–100 μ l), the R_H started decreasing. More disaggregation was observed by introducing more (~ 250 –500 μ l) MeOH to the reaction mixture. As a result, the peak at ~ 300 nm decreased while an intense new peak at ~ 98 nm, appeared (see Fig. S15†). The disassembly of NS after the addition of MeOH was further confirmed by TEM imaging (Fig. S16†).

Mechanism of formation of NSs

We suggest that the polymerization of Cu-doped Au-NC fragments with the smaller-sized alloy-NP fragments *via* direct assembly leads to the formation of supramolecular architectures. During the initial stage of this process, along with the generation of smaller thiolate-protected copper-doped gold NCs, smaller NPs were also formed, which, in turn, arranged systematically due to the covalent and non-covalent interactions leading to the spherical entity in the final stage (see Scheme 1). This self-assembly is mainly driven by hydrogen bonding, van der Waals interactions, C–H \cdots π / π – π interactions,⁶⁹ metallophilic (as seen in Fig. 1–3) and covalent bonding (*i.e.*, S–O, C–O) (as noticed in Fig. 4 and Fig. S14†), and amphiphilic interactions (as observed in Fig. 5, and



Scheme 1 Structural evolution of nanosphere formation during the reaction between NC and NP.

Fig. S15†) between the NP and NC fragments. These interactions within NP assemblies may produce novel properties, such as efficient charge transport, enhanced conductivity, *etc.*, due to the synergistic effects between thiolated NP fragments. Also, shape complementarity of ligands on reacted particle fragments could be responsible for the strong attractive forces to form the nanoassembly.

Based on the spectrometric, microscopic, and spectroscopic investigations, we propose that the formation of the vesicle-like nano-assembly during interparticle reactions relies on the following aspects: (i) formation of S–O and C–O bonds between surface ligands of reacted NCs and CuO NPs (see Fig. S14(ii)†); (ii) the $\text{CH}\cdots\pi/\pi\cdots\pi$ and $\text{H}\cdots\text{H}$ interactions between thiolates of doped NPs and NCs and (iii) polymerization of Cu-doped NC and NP fragments. The overall mechanistic pathway of the reaction between CuO NPs and $[\text{Au}_{25}]$ NCs is shown in Scheme 2. The mechanistic pathway to form aggregated nanostructures consists of two steps. In the initial step of the reaction (*i.e.*, path A of Scheme 2), atomic exchange and redox reaction take place between NCs and NPs. Negishi *et al.* have studied the effect of Cu-doping on the electronic structure, geometric structure, and stability of Au_{25} in detail.⁶⁶ Most likely, in a single Cu-doped Au_{25} nanocluster, preferentially, a Cu atom occupies the center of the Au_{13} metal core due to the smaller atomic radius of Cu (1.28 Å) than gold (1.44 Å). The second Cu atom in the $\text{Cu}_2\text{Au}_{23}$ nanocluster can exist on the icosahedral surface or the staple position.⁶⁶ As per our XPS study, we understood that during the chemical reaction, a fraction of Au atoms underwent oxidation. In contrast, reduction occurred for some Cu atoms of the nanoparticles. The core Au atom of Au_{25} may be removed as Au^{1+} , and Cu^{2+} gets reduced to Cu^0 and occupy the central position of the nanocluster. Moreover, doping processes enhanced the formation of Cu and O-doped NC fragments and Au-thiolate doped NP fragments as noticed in the ESI MS study. The doped fragments of NC and NPs coalesced together to produce NS-like assemblies in the final step (*i.e.*, step B of Scheme 2) of the reaction.

The NC-based assembly plays a key role in customizing advanced functional materials *via* collective and synergetic properties between neighboring building blocks. It is crucial to develop a workflow to witness interparticle interaction-driven self-assemblies between NCs and NPs in the sub-nano-

meter regime to understand the chemistry of heterometallic superstructures. Moreover, recent achievements in interparticle interaction also manifest in the controlled formation of various superstructures, such as NC-mediated precision nanowire assemblies, NP-templated cluster assemblies or superlattice arrangement.^{57,70,71} The chemistry presented here suggests that the NC behaves similarly to molecules. It was demonstrated that NCs undergo oxidation, reduction (observed in UV-vis, XPS studies), decomposition (indicated in MS-based studies), and aggregation (noticed in TEM, and STEM micrographs), similar to the molecular systems. The redox chemistry occurs between systems with largely varying dimensions from 1 nm to 100 nm leading to aggregated structures of micrometer dimensions. This controlled chemical evolution from chemical reaction between clusters and NPs may be useful in making complex architectures. Such nanostructures composed of multiple metal ions with mixed properties may become useful in applications such as catalysis and magnetism.

Conclusions

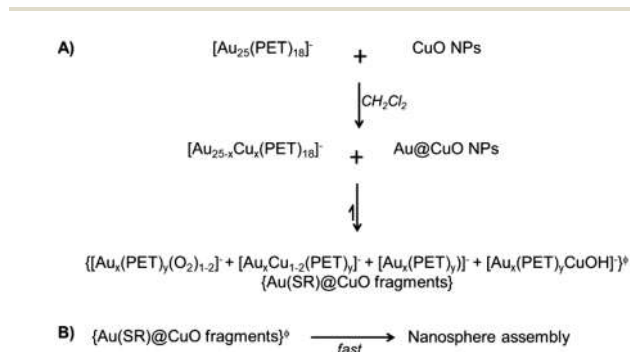
Polydispersed CuO NPs and PET-protected $[\text{Au}_{25}]$ NCs were used in our study to explore the consequence of possible atom transfer processes between NCs and NPs. Upon increasing the concentration of the oxide NPs, sphere-shaped nanoaggregates were formed along with Cu-doped NCs. The atom exchange rate enhanced the formation of smaller PET-protected multi-metallic cluster fragments which eventually coalesce to form macro-scale spherical aggregates. We monitored the reaction in a time-dependent fashion. The NSs formed were disassembled with increasing solvent polarity. Our study demonstrates the spontaneity of atom transfer when NCs are brought in contact with metal-oxide NPs. Such NC–NP reactions can provide an entirely new method of generating multimetallic and uniform complex architectures. This method may be extended to other metal-chalcogenide systems such as CuS, CuSe and CuTe and oxides such as MnO, ZnO, and NiO to expand the properties of the products.

Author contributions

T. P. proposed the project. J. R. performed the experiments. J. R. performed mass spectrometric, UV-vis, and DLS measurements. J. R. and B. M. carried out TEM studies. J. R. and G. V. carried out XPS studies. J. R., N. V. S., and P. K., prepared the samples. N. performed STEM imaging, EDS analysis, and electron tomography reconstruction. J. R. wrote the first draft of the manuscript, and the final version of the manuscript was prepared through the contributions of all authors. All authors have given approval to the final version of the manuscript.

Conflicts of interest

There are no conflicts to declare.



Scheme 2 Mechanistic pathway of the reaction.

Acknowledgements

We thank the Department of Science and Technology, Government of India, for supporting our research programme. J. R. and G. V. thank IIT Madras for the doctoral research fellowships. B. M. thanks IIT Madras for the postdoctoral fellowship. N. V. S. thanks the Pradeep Research Group for a summer project opportunity. T. P. acknowledges funding from the Centre of Excellence on Molecular Materials and Functions under the Institution of Eminence scheme of IIT Madras. N. acknowledges the Academy of Finland project funding (no. 352900), the Photonics Research and Innovation (PREIN) flagship and facilities at the OtaNano-Nanomicroscopy Center (Aalto-NMC).

References

- Q. Yao, X. Yuan, V. Fung, Y. Yu, D. T. Leong, D. E. Jiang and J. Xie, *Nat. Commun.*, 2017, **8**, 1–11.
- S. Gaur, J. T. Miller, D. Stellwagen, A. Sanampudi, C. S. S. R. Kumar and J. J. Spivey, *Phys. Chem. Chem. Phys.*, 2012, **14**, 1627–1634.
- Y. Negishi, K. Nobusada and T. Tsukuda, *J. Am. Chem. Soc.*, 2005, **127**, 5261–5270.
- X. Kang, H. Chong and M. Zhu, *Nanoscale*, 2018, **10**, 10758.
- C. P. Joshi, M. S. Bootharaju, M. J. Alhilaly and O. M. Bakr, *J. Am. Chem. Soc.*, 2015, **137**, 11578–11581.
- L. G. AbdulHalim, M. S. Bootharaju, Q. Tang, S. Del Gobbo, R. G. AbdulHalim, M. Eddaoudi, D. Jiang, O. M. Bakr, L. G. AbdulHalim, M. S. Bootharaju, Q. Tang, S. Del Gobbo, R. G. AbdulHalim, M. Eddaoudi, D. Jiang and O. M. Bakr, *J. Am. Chem. Soc.*, 2015, **137**, 11970–11975.
- M. Bodiuzzaman, A. Ghosh, K. S. Sugi, A. Nag, E. Khatun, B. Varghese, G. Paramasivam, S. Antharjanam, G. Natarajan and T. Pradeep, *Angew. Chem., Int. Ed.*, 2019, **58**, 189–194.
- H. Yang, Y. Wang, H. Huang, L. Gell, L. Lehtovaara, S. Malola, H. Häkkinen and N. Zheng, *Nat. Commun.*, 2013, **4**, 1–8.
- W. Fei, S. Antonello, T. Dainese, A. Dolmella, M. Lahtinen, K. Rissanen, A. Venzo and F. Maran, *J. Am. Chem. Soc.*, 2019, **141**, 16033–16045.
- J. Q. Wang, S. Shi, R. L. He, S. F. Yuan, G. Y. Yang, G. J. Liang and Q. M. Wang, *J. Am. Chem. Soc.*, 2020, **142**, 18086–18092.
- N. Yan, N. Xia, L. Liao, M. Zhu, F. Jin, R. Jin and Z. Wu, *Sci. Adv.*, 2018, **4**, 7259–7271.
- W. Jiang, Y. Bai, Q. Li, X. Yao, H. Zhang, Y. Song, X. Meng, H. Yu and M. Zhu, *Inorg. Chem.*, 2020, **59**, 5394–5404.
- V. R. Jupally, A. C. Dharmaratne, D. Crasto, A. J. Huckaba, C. Kumara, P. R. Nimmala, N. Kothalawala, J. H. Delcamp and A. Dass, *Chem. Commun.*, 2014, **50**, 9895–9898.
- C. A. Fields-Zinna, J. S. Sampson, M. C. Crowe, J. B. Tracy, J. F. Parker, A. M. deNey, D. C. Muddiman and R. W. Murray, *J. Am. Chem. Soc.*, 2009, **131**, 13844–13851.
- L. A. Angel, L. T. Majors, A. C. Dharmaratne and A. Dass, *ACS Nano*, 2010, **4**, 4691–4700.
- Y. Zeng, S. Havenridge, M. Gharib, A. Baksi, K. L. D. M. Weerawardene, A. R. Ziefuß, C. Strelow, C. Rehbock, A. Mews, S. Barcikowski, M. M. Kappes, W. J. Parak, C. M. Aikens and I. Chakraborty, *J. Am. Chem. Soc.*, 2021, **143**, 9405–9414.
- S. Chen, W.-H. H. Fang, L. Zhang and J. Zhang, *Angew. Chem., Int. Ed.*, 2018, **57**, 11252–11256.
- C. P. Joshi, M. S. Bootharaju, M. J. Alhilaly and O. M. Bakr, *J. Am. Chem. Soc.*, 2015, **137**, 11578–11581.
- A. Mathew, G. Natarajan, L. Lehtovaara, H. Hä, R. M. Kumar, V. Subramanian, A. Jaleel and T. Pradeep, *ACS Nano*, 2014, **8**, 139–152.
- A. Sagadevan, A. Ghosh, P. Maity, O. F. Mohammed, O. M. Bakr and M. Rueping, *J. Am. Chem. Soc.*, 2022, **144**, 12052–12061.
- M. Daté, H. Imai, S. Tsubota and M. Haruta, *Catal. Today*, 2007, **122**, 222–225.
- J. V. Rival, P. Mymoona, K. M. Lakshmi, Nonappa, T. Pradeep and E. S. Shibu, *Small*, 2021, **17**, 2005718.
- J. Ahmed, P. Trinh, A. M. Mugweru and A. K. Ganguli, *Solid State Sci.*, 2011, **13**, 855–861.
- A. K. Das, S. Mukherjee, S. R. Sreehari, A. S. Nair, S. Bhandary, D. Chopra, D. Sanyal, B. Pathak and S. Mandal, *ACS Nano*, 2020, **14**, 16681–16688.
- A. Nag, P. Chakraborty, M. Bodiuzzaman, T. Ahuja, S. Antharjanam and T. Pradeep, *Nanoscale*, 2018, **10**, 9851–9855.
- Z. Wu, J. Liu, Y. Gao, H. Liu, T. Li, H. Zou, Z. Wang, K. Zhang, Y. Wang, H. Zhang and B. Yang, *J. Am. Chem. Soc.*, 2015, **137**, 12906–12913.
- R. Kazan, B. Zhang and T. Bürgi, *Dalton Trans.*, 2017, **46**, 7708–7713.
- M. A. H. Muhammed, P. K. Verma, S. K. Pal, A. Retnakumari, M. Koyakutty, S. Nair and T. Pradeep, *Chem. – Eur. J.*, 2010, **16**, 10103–10112.
- E. S. Shibu, M. A. H. Muhammed, T. Tsukuda and T. Pradeep, *J. Phys. Chem. C*, 2008, **112**, 12168–12176.
- P. L. Xavier, K. Chaudhari, P. K. Verma, S. K. Pal and T. Pradeep, *Nanoscale*, 2010, **2**, 2769–2776.
- Y. Chen, M. Zhou, Q. Li, H. Gronlund and R. Jin, *Chem. Sci.*, 2020, **11**, 8176–8183.
- S. Maity, D. Bain and A. Patra, *J. Phys. Chem. C*, 2019, **123**, 2506–2515.
- Q. Yao, Z. Wu, Z. Liu, Y. Lin, X. Yuan and J. Xie, *Chem. Sci.*, 2021, **12**, 99–127.
- G. N. Parsons and R. D. Clark, *Chem. Mater.*, 2020, **32**, 4920–4953.
- M. H. Naveen, R. Khan and J. H. Bang, *Chem. Mater.*, 2021, **33**, 7595–7612.
- S. Hossain, Y. Niihori, L. V. Nair, B. Kumar, W. Kurashige and Y. Negishi, *Acc. Chem. Res.*, 2018, **51**, 3114–3124.
- Y. Song, Y. Li, M. Zhou, X. Liu, H. Li, H. Wang, Y. Shen, M. Zhu and R. Jin, *Sci. Adv.*, 2021, **7**, eabd2091.

- 38 S. Wang, Y. Song, S. Jin, X. Liu, J. Zhang, Y. Pei, X. Meng, M. Chen, P. Li and M. Zhu, *J. Am. Chem. Soc.*, 2015, **137**, 4018–4021.
- 39 L. Wang, K. Shen, M. Chen and Y. Zhu, *Nanoscale*, 2019, **11**, 13767–13772.
- 40 E. Khatun, P. Chakraborty, B. R. Jacob, G. Paramasivam, M. Bodiuzzaman, A. Dar and T. Pradeep, *Chem. Mater.*, 2020, **32**(1), 611–619.
- 41 E. Khatun and T. Pradeep, *ACS Omega*, 2021, **6**, 1–16.
- 42 S. Knoppe and T. Bürgi, *Phys. Chem. Chem. Phys.*, 2013, **15**, 15816–15820.
- 43 Z. Huang, Y. Ishida, K. Narita and T. Yonezawa, *J. Phys. Chem. C*, 2018, **122**, 18142–18150.
- 44 S. Knoppe, A. C. Dharmaratne, E. Schreiner, A. Dass and T. Bürgi, *J. Am. Chem. Soc.*, 2010, **132**, 16783–16789.
- 45 Y. Niihori, S. Hossain, B. Kumar, L. V. Nair, W. Kurashige and Y. Negishi, *APL Mater.*, 2017, **5**, 053201.
- 46 S. Wang, L. Xiong, G. Sun, L. Tang, J. Zhang, Y. Pei and M. Zhu, *Nanoscale Adv.*, 2020, **2**, 664–668.
- 47 B. Zhang, O. V. Safonova, S. Pollitt, G. Salassa, A. Sels, R. Kazan, Y. Wang, G. Rupprechter, N. Barrabés and T. Bürgi, *Phys. Chem. Chem. Phys.*, 2018, **20**, 5312–5318.
- 48 K. R. Krishnadas, A. Ghosh, A. Baksi, I. Chakraborty, G. Natarajan and T. Pradeep, *J. Am. Chem. Soc.*, 2016, **138**, 140–148.
- 49 K. R. Krishnadas, A. Baksi, A. Ghosh, G. Natarajan and T. Pradeep, *Nat. Commun.*, 2016, **7**, 1–9.
- 50 M. Neumaier, A. Baksi, P. Weis, E. K. Schneider, P. Chakraborty, H. Hahn, T. Pradeep and M. M. Kappes, *J. Am. Chem. Soc.*, 2021, **143**, 6969–6980.
- 51 R. Kazan, U. Müller and T. Bürgi, *Nanoscale*, 2019, **11**, 2938–2945.
- 52 P. Chakraborty, A. Nag, G. Natarajan, N. Bandyopadhyay, G. Paramasivam, M. K. Panwar, M. Kumar Panwar, J. Chakrabarti and T. Pradeep, *Sci. Adv.*, 2019, **5**, eaau7555.
- 53 Nonappa, T. Lahtinen, J. S. Haataja, T. R. Tero, H. Häkkinen and O. Ikkala, *Angew. Chem., Int. Ed.*, 2016, **55**, 16035–16038.
- 54 A. Som, A. Griffo, I. Chakraborty, H. Hähl, B. Mondal, A. Chakraborty, K. Jacobs, P. Laaksonen, O. Ikkala, T. Pradeep, A. Som, O. Ikkala, A. Griffo, P. Laaksonen, H. Hähl, K. Jacobs, I. Chakraborty, B. Mondal, A. Chakraborty and T. Pradeep, *Small*, 2022, **18**, 2201707.
- 55 Y. Zhou and H. C. Zeng, *Small*, 2016, **12**, 2652–2664.
- 56 A. Dong, J. Chen, P. M. Vora, J. M. Kikkawa and C. B. Murray, *Nature*, 2010, **466**, 474–477.
- 57 A. Som, A. Griffo, I. Chakraborty, H. Hähl, B. Mondal, A. Chakraborty, K. Jacobs, P. Laaksonen, O. Ikkala, T. Pradeep, A. Som, O. Ikkala, A. Griffo, P. Laaksonen, H. Hähl, K. Jacobs, I. Chakraborty, B. Mondal, A. Chakraborty and T. Pradeep, *Small*, 2022, **18**, 2201707.
- 58 J. Pang, S. Xiong, F. Jaeckel, Z. Sun, D. Dunphy and C. J. Brinker, *J. Am. Chem. Soc.*, 2008, **130**, 3284–3285.
- 59 A. Baksi, P. Chakraborty, S. Bhat, G. Natarajan and T. Pradeep, *Chem. Commun.*, 2016, **52**, 8397–8400.
- 60 X. Kang, H. Chong and M. Zhu, *Nanoscale*, 2018, **10**, 10758–10834.
- 61 J. Naktiyok and A. K. Özer, *Niğde Ömer Halisdemir Üniversitesi Mühendislik Bilimleri Dergisi*, 2019, **8**(2), 1292–1298, DOI: [10.28948/ngumuh.598177](https://doi.org/10.28948/ngumuh.598177).
- 62 J. Wei, H. Wang, Y. Deng, Z. Sun, L. Shi, B. Tu, M. Luqman and D. Zhao, *J. Am. Chem. Soc.*, 2011, **133**, 20369–20377.
- 63 J. A. Kephart, C. G. Romero, C. C. Tseng, K. J. Anderton, M. Yankowitz, W. Kaminsky and A. Velian, *Chem. Sci.*, 2020, **11**, 10744–10751.
- 64 O. P. Keabadile, A. O. Aremu, S. E. Elugoke and O. E. Fayemi, *Nanomaterials*, 2020, **10**, 2502–2520.
- 65 Y. R. Luo, *Compr. Handb. Chem. Bond Energies*, 2007, pp. 1–1656.
- 66 Y. Negishi, K. Munakata, W. Ohgake and K. Nobusada, *J. Phys. Chem. Lett.*, 2012, **3**, 2209–2214.
- 67 G. Natarajan, A. Mathew, Y. Negishi, R. L. Whetten and T. Pradeep, *J. Phys. Chem. C*, 2015, **119**, 27768–27785.
- 68 S. Bhat, R. P. Narayanan, A. Baksi, P. Chakraborty, G. Paramasivam, R. Rajan, J. Methikkalam, A. Nag, G. Natarajan and T. Pradeep, *J. Phys. Chem. C*, 2018, **122**(34), 19455–19462.
- 69 Nonappa and O. Ikkala, *Adv. Funct. Mater.*, 2018, **28**, 1704328.
- 70 A. Chakraborty, A. C. Fernandez, A. Som, B. Mondal, G. Natarajan, G. Paramasivam, T. Lahtinen, H. Häkkinen, Nonappa and T. Pradeep, *Angew. Chem., Int. Ed.*, 2018, **57**, 6522–6526.
- 71 P. Bose, P. Chakraborty, J. S. Mohanty, Nonappa, A. Ray Chowdhuri, E. Khatun, T. Ahuja, A. Mahendranath and T. Pradeep, *Nanoscale*, 2020, **12**, 22116–22128.

Electronic Supplementary Information

Dissociative reaction of $[\text{Au}_{25}(\text{SR})_{18}]^-$ at copper oxide nanoparticles and formation of aggregated nanostructures

Jayoti Roy,^a Biswajit Mondal,^a Gaurav Vishwakarma,^a Nonappa,^b Nishanthi Vasanthi Sridharan,^a Pattabiraman Krishnamurthi,^a Thalappil Pradeep^{*a,c}

^aDST Unit of Nanoscience (DST UNS) & Thematic Unit of Excellence (TUE), Department of Chemistry, Indian Institute of Technology Madras, Chennai 600036, India.

^bFaculty of Engineering and Natural Sciences, Tampere University, FI-33720 Tampere, Finland.

^cInternational Centre for Clean Water, 2nd Floor, B-Block, IIT Madras Research Park, Kanagam Road, Taramani, Chennai 600113, India.

Table of contents

Name	Description	Page no.
	Calculations of precursor concentration	S3
Fig. S1	UV-vis of NC after and before the reaction	S4
Fig. S2	ESI MS of $[\text{Au}_{25}]$	S5
Fig. S3	HRTEM images of $[\text{Au}_{25}]$ and CuO NPs	S6
Fig. S4	ESI MS of NCs fragments and table of assigned chemical compositions	S7
Fig. S5	Evolution and ion abundances of $[\text{Au}_{24}\text{Cu}_1]$ and $[\text{Au}_{23}\text{Cu}_2]$	S8
Fig. S6	High-resolution isotopic distributions of smaller NC fragments with their calculated ones	S9
Fig. S7	Time-dependent ESI MS of reaction with reduced quantity of CuO NPs	S10
Fig. S8	TEM micrographs of bare CuO NPs after the reaction	S10
Fig. S9	STEM micrographs of nano-assemblies and the EDS spectrum	S11

Fig. S10	STEM image and EDS elemental mapping of reacted NPs	S11
Fig. S11	TEM micrographs of NSs	S12
Fig. S12	TEM photographs of NCs	S12
Fig. S13	EDS spectrum of supernatant containing NCs and isolated NSs	S13
Fig. S14	FT-IR analysis of [Au ₂₅] NC, supernatant of the reaction, TOABr and PET	S13
Fig. S15	DLS study and TEM images of disassembly of NSs	S14
Fig. S16	TEM images of completely disassembled NSs	S15
Video V1	Tilt series of Fig. 3(C)	Attached
Video V2	3D construction of Fig. 3(D)	Attached

Calculation of number of particles/ml for:

a) [Au₂₅(PET)₁₈]⁻ cluster

Molecular weight = 7391

$$\text{Mass of 1 [Au}_{25}\text{] NC (m)} = \frac{7391 \times 10^3}{6.023 \times 10^{23}} \text{ mg} = 1.227 \times 10^{-17} \text{ mg}$$

$$\text{Mass of [Au}_{25}\text{] NC in 1 ml of stock solution considered in the experiments (W)} = \frac{1 \text{ mg}}{100 \text{ ml}}$$

$$\begin{aligned} \text{No of [Au}_{25}\text{] NC in 1 ml of stock solution/1ml} &= (W/m) \\ &= \left(\frac{0.01}{1.227 \times 10^{-17}} \right) \text{ No/ml} \\ &= (8.15 \times 10^{15}) \text{ No/ml} \end{aligned}$$

$$\begin{aligned} \text{Molarity of NCs in the stock solution} &= \left(\frac{N}{N_A} \right) \\ &= \frac{8.15 \times 10^{15}}{6.023 \times 10^{23}} \text{ M} \\ &= 1.35 \text{ nM} \end{aligned}$$

Amount of stock solution was used during reaction – 25 µL.

b) CuO nanoparticles

Average size of CuO NPs (HRTEM) = 2R = 50 nm

$$\begin{aligned} \text{Volume of 1 CuO NP (sphere), } V &= \left(\frac{4}{3} \right) \pi R^3 \text{ nm}^3 \\ &= 65416.6 \text{ nm}^3 \end{aligned}$$

$$\begin{aligned} \text{Density of CuO NP, } \rho &= 6.31 \text{ g/ cm}^3 \\ &= (0.631 \times 10^{-17}) \text{ mg/nm}^3 \end{aligned}$$

$$\begin{aligned} \text{Mass of 1 CuO NP, } m &= V \times \rho \\ &= (65416.6 \times 0.631 \times 10^{-17}) \text{ mg} \\ &= 4.13 \times 10^{-13} \text{ mg} \end{aligned}$$

Weight of CuO NPs (dry weight of the sample), W = 1.6 mg/ml

$$\begin{aligned} \text{No of NPs in the solution, } N &= \left(\frac{W}{m} \right) \\ &= 4.019 \times 10^{12} \text{ number/ml} \end{aligned}$$

$$\begin{aligned} \text{Molarity of the CuO NPs in solution} &= \left(\frac{N}{N_A} \right) \\ &= 6.67 \times 10^{-3} \text{ nM} \end{aligned}$$

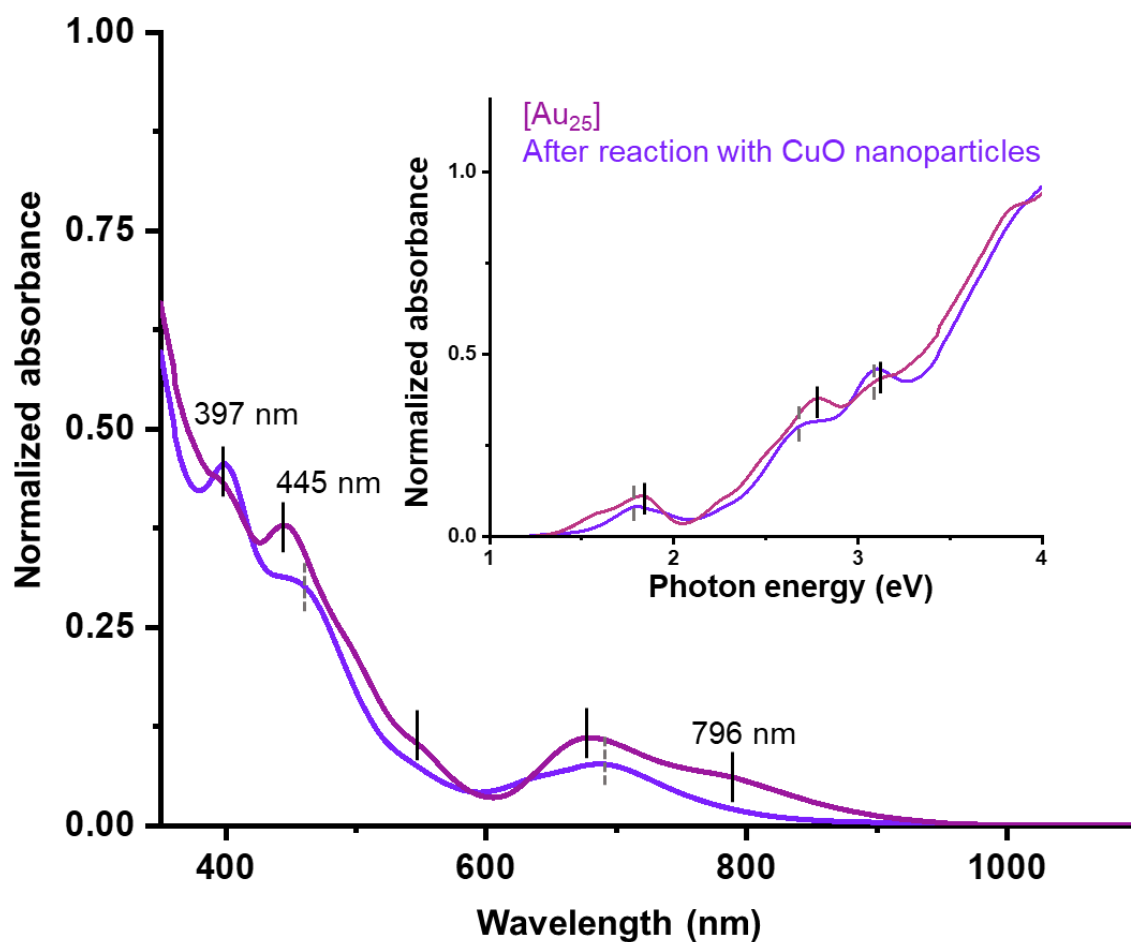


Fig. S1 UV-vis spectra of [Au₂₅] before and after the reaction. Inset shows the absorption spectra in terms of photon energy (eV) of [Au₂₅] before and after of the reaction.

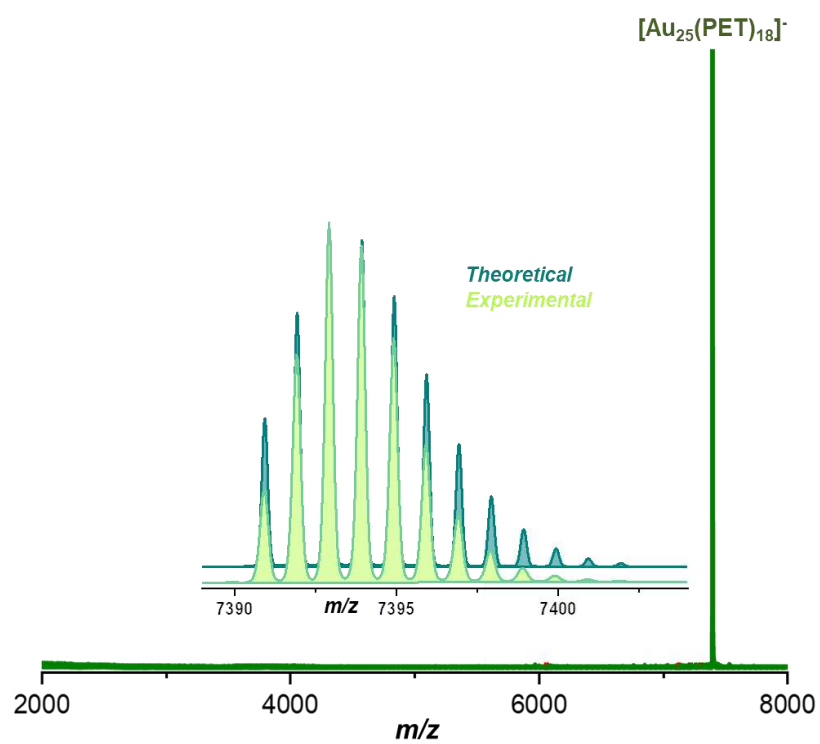


Fig. S2 ESI MS of $[\text{Au}_{25}]$ in DCM in the negative mode. The overlay plot of the experimental (light green) and calculated (dark green) isotopic distributions of $[\text{Au}_{25}]$.

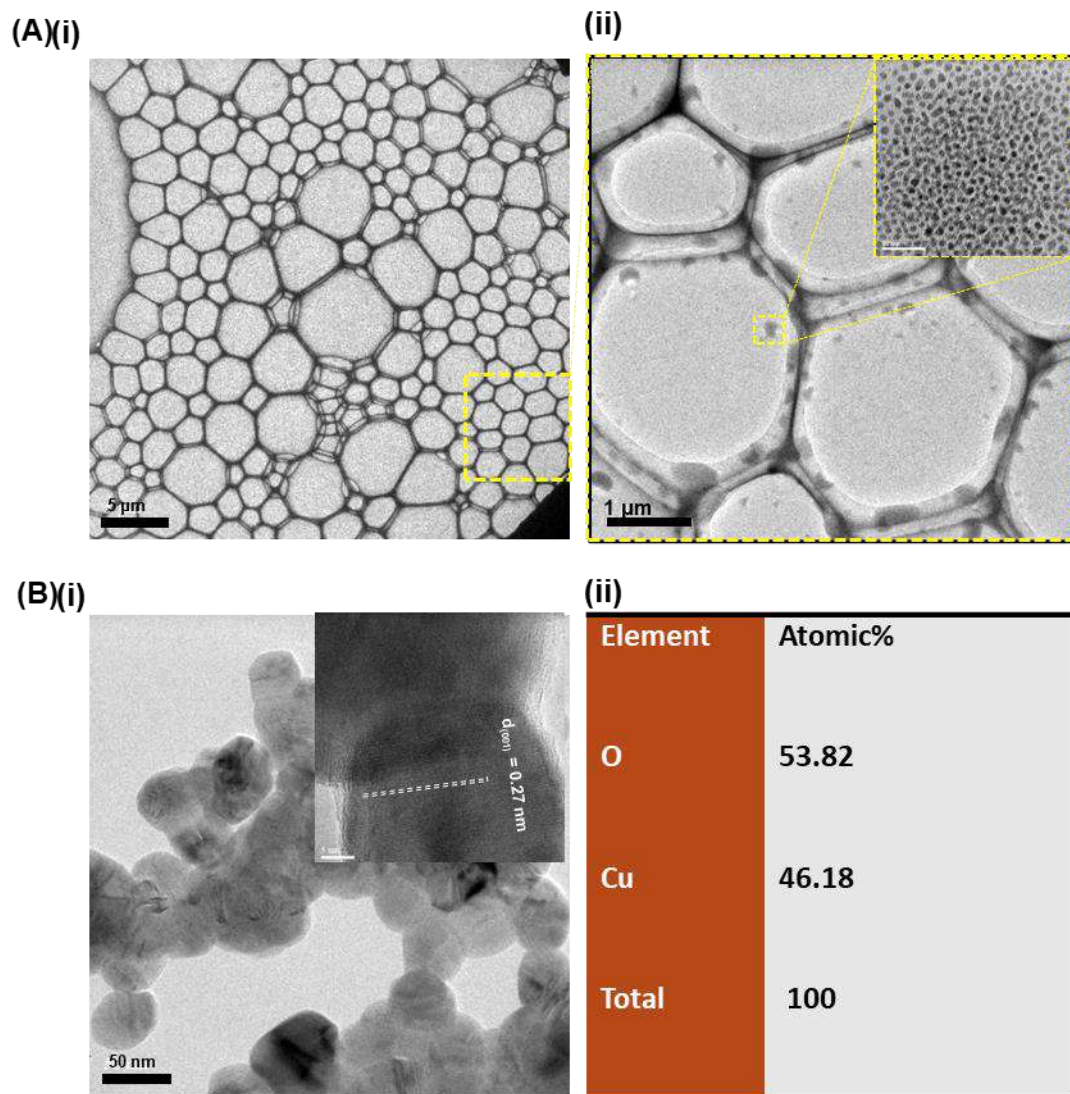


Fig. S3 (A(i-ii)) TEM micrographs of drop casted $[\text{Au}_{25}]$ NC. In inset of (A(ii)) shows the discrete NCs (slight beam-induced aggregation and damage are also observed). (B(i)) TEM image of bare parent CuO NPs. Inset shows the lattice spacing of crystalline NPs. (B(ii)) EDS elemental compositions of parent NPs.

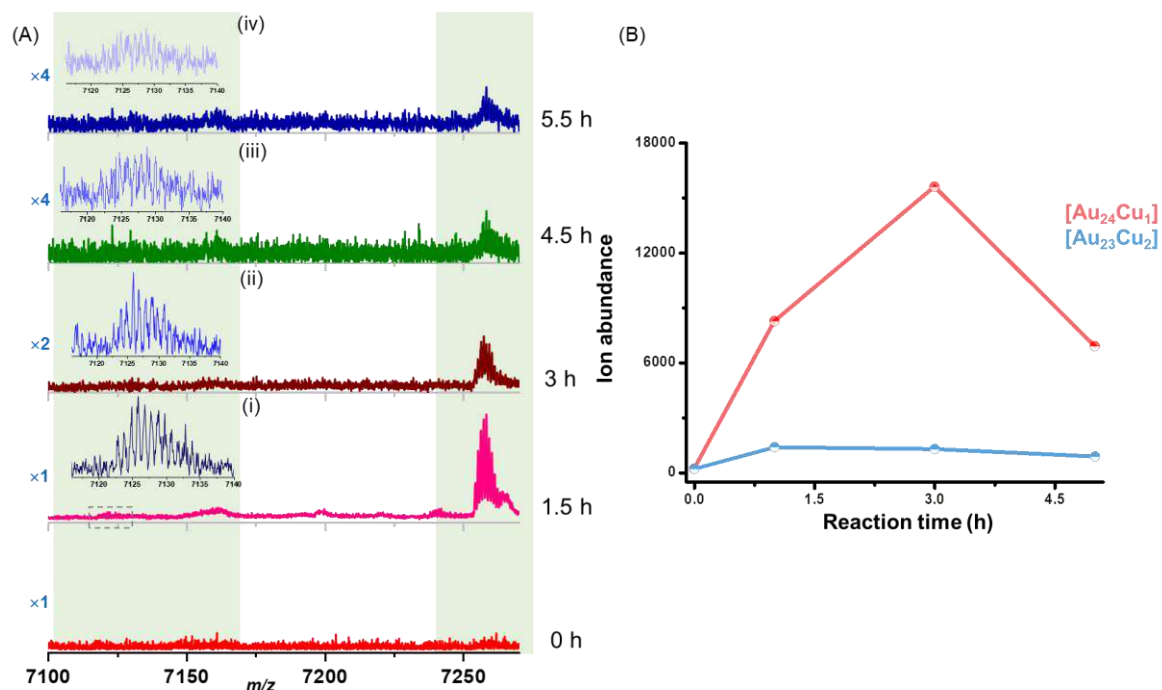


Fig. S4 ESI MS spectra (A) of the evolution of $[\text{Au}_{24}\text{Cu}_1]$ and $[\text{Au}_{23}\text{Cu}_2]$ NCs during the reaction and their ion abundance plot (B) as a function of reaction time.

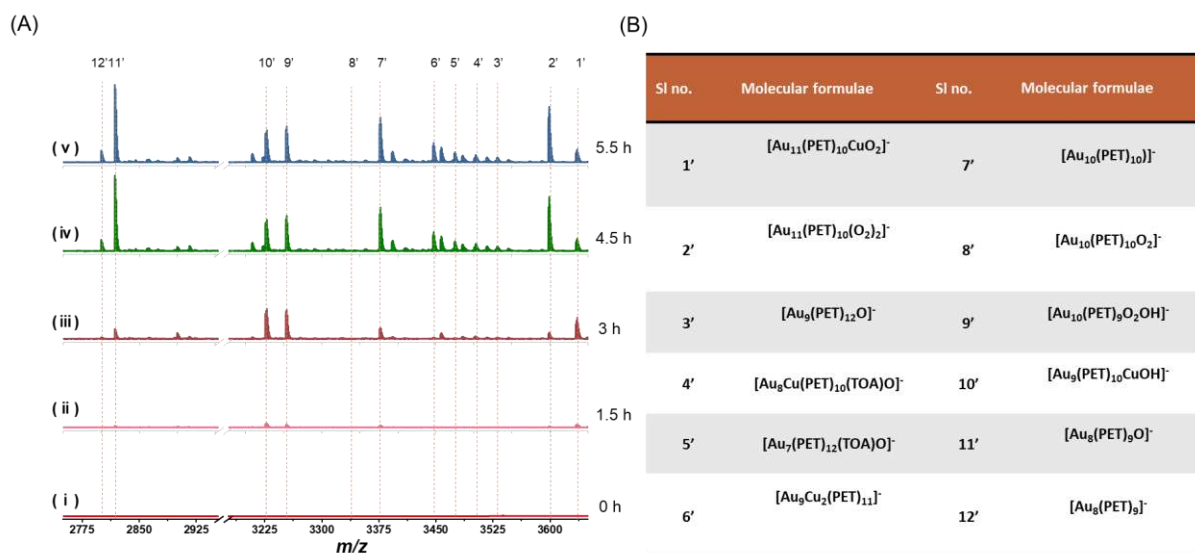


Fig. S5 ESI MS of smaller NCs fragments generated with time and (B) table of chemical compositions of the fragments.

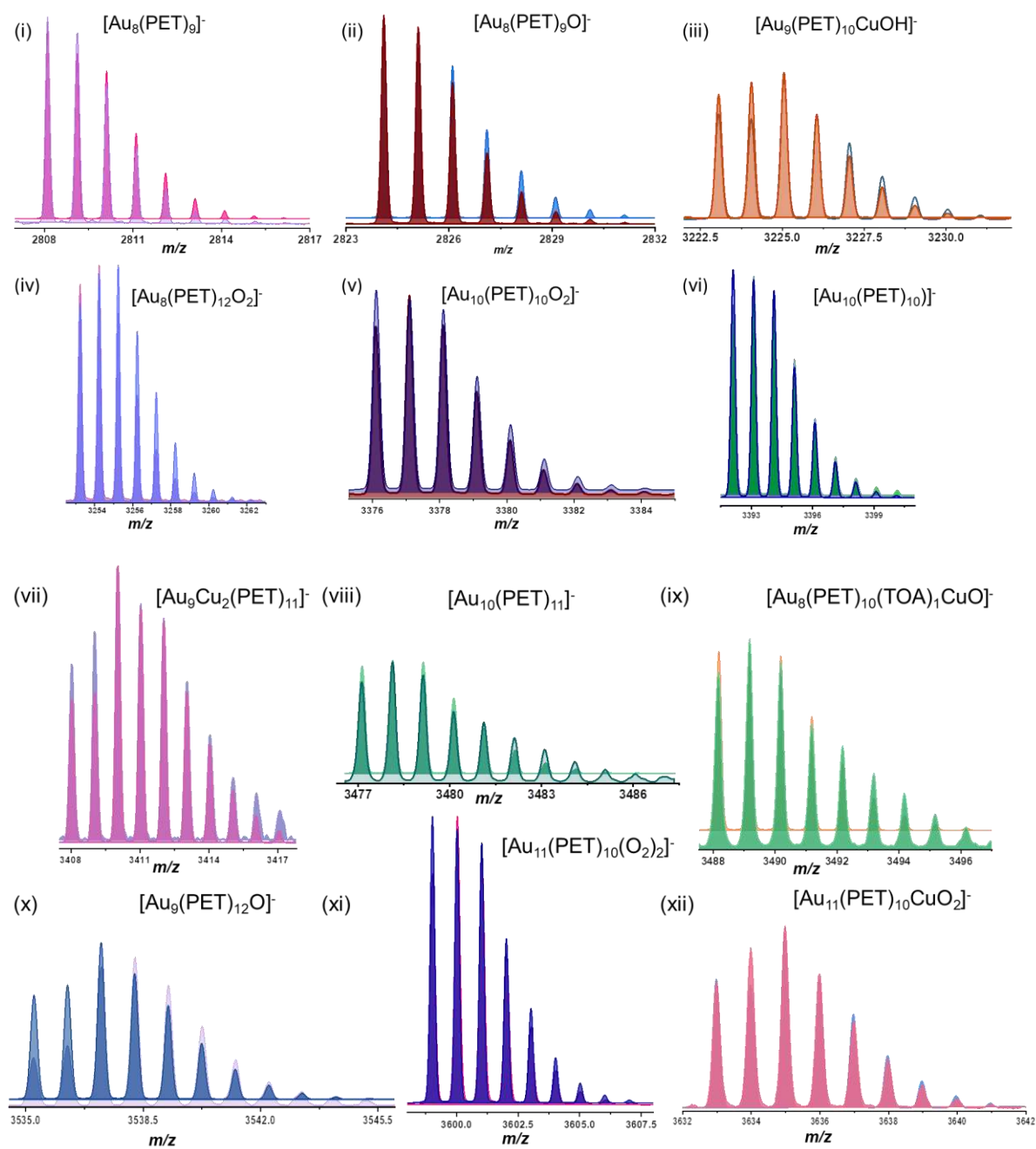


Fig. S6 Experimental high-resolution isotopic distribution of smaller NC fragments with their calculated isotopic distributions.

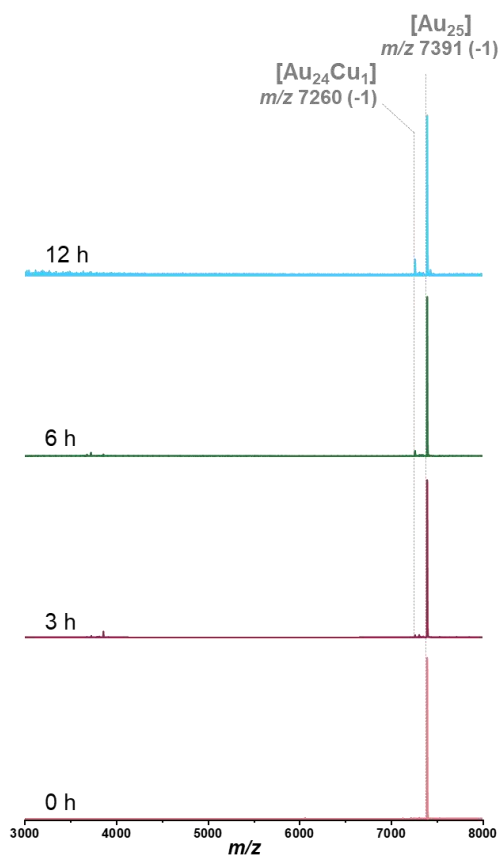


Fig. S7 Time-dependent ESI MS of reaction between $[Au_{25}]$ and very diluted CuO NPs solutions.

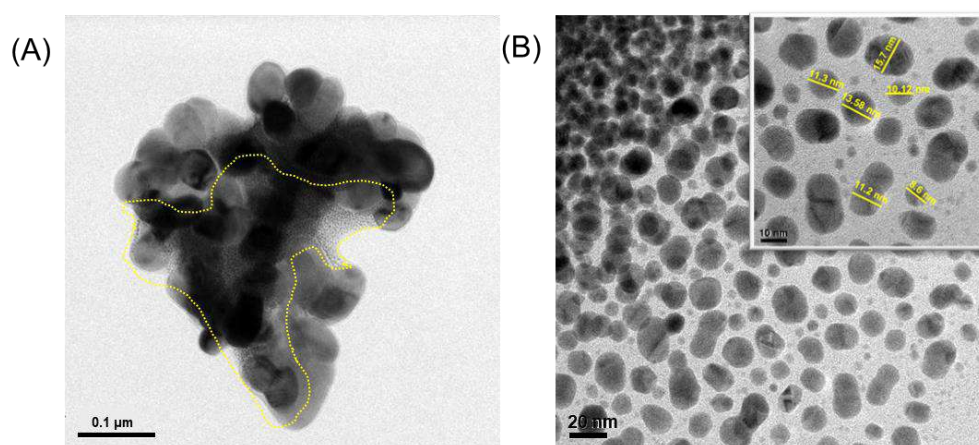


Fig. S8 TEM micrographs show bare CuO NPs after the reaction. In (A) and (B), the bare NPs are intermingled with NC (area under dotted line), and smaller size bare NPs are shown, respectively.

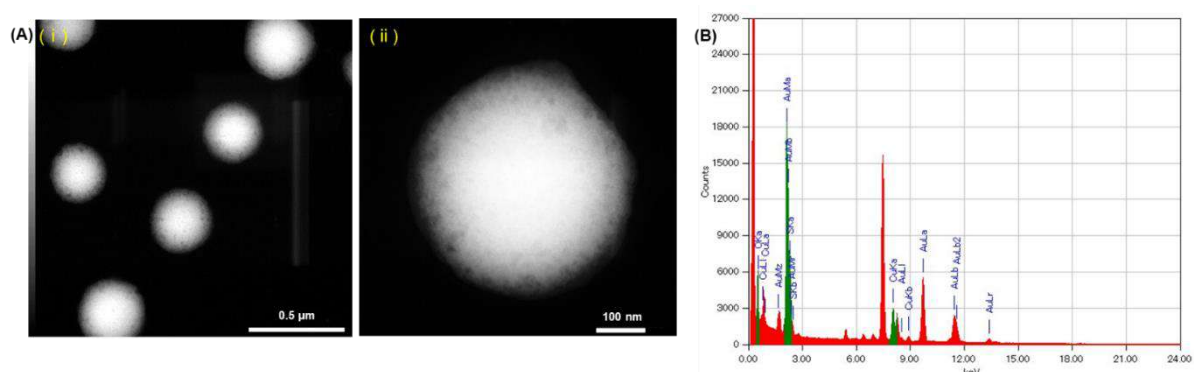


Fig. S9 (A(i-ii)) STEM micrographs of nano-assemblies and (B) EDS spectrum collected from (A(ii)) Showing the elemental compositions.

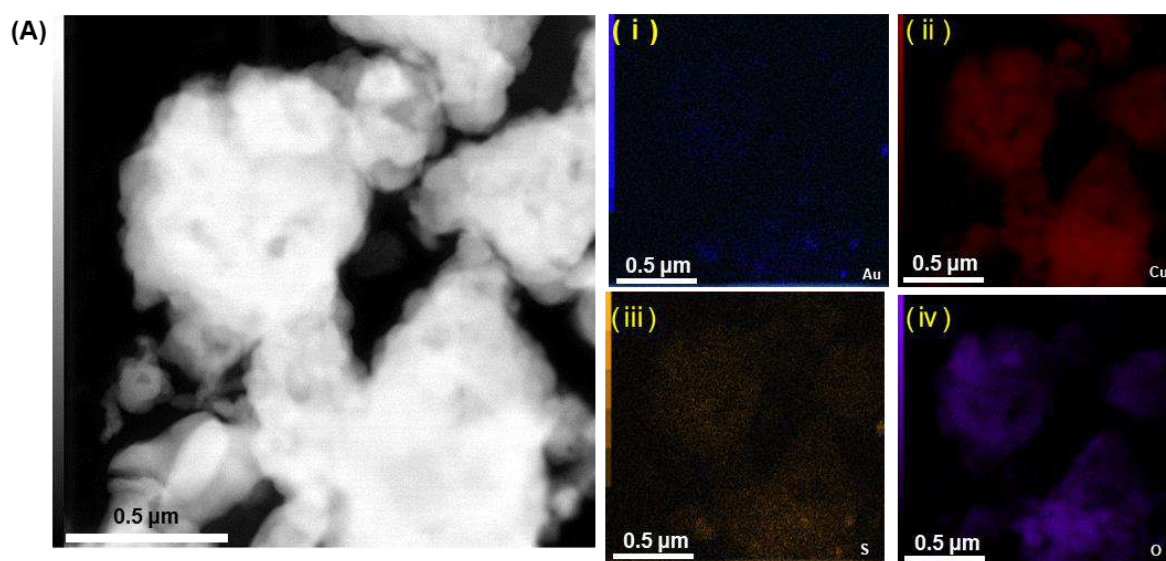


Fig. S10 (A) STEM image and EDS elemental mapping of NPs after the reaction.

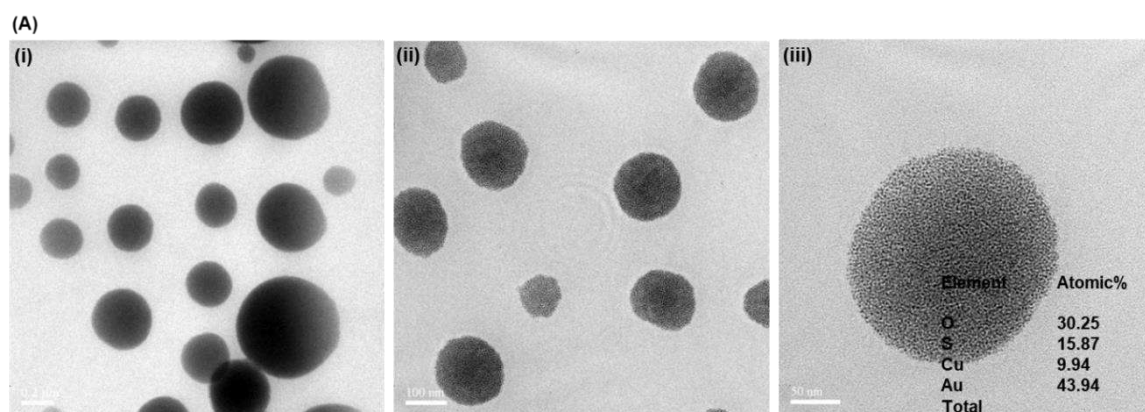


Fig. S11 TEM micrographs of NCs present in the supernatant and respective elemental compositions (in inset).

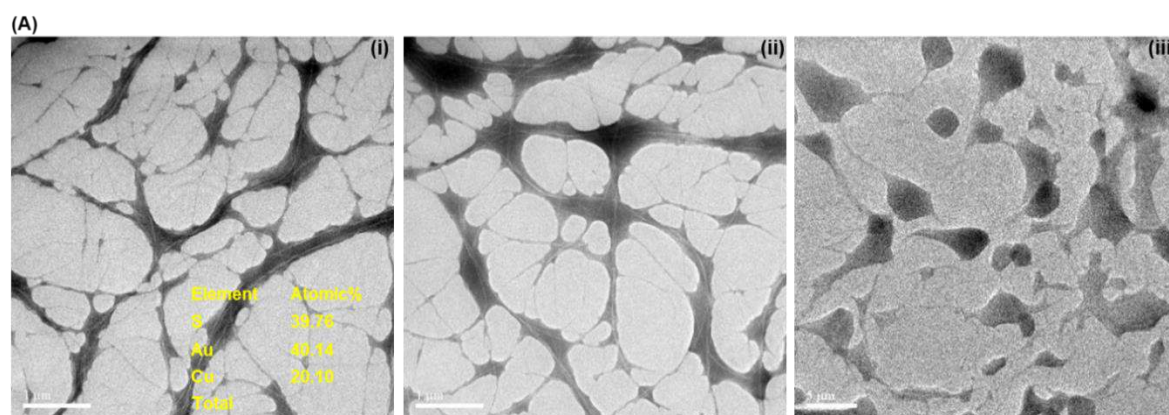


Fig. S12 TEM photographs of NCs present in the supernatant and respective elemental composition (in inset of (i)).

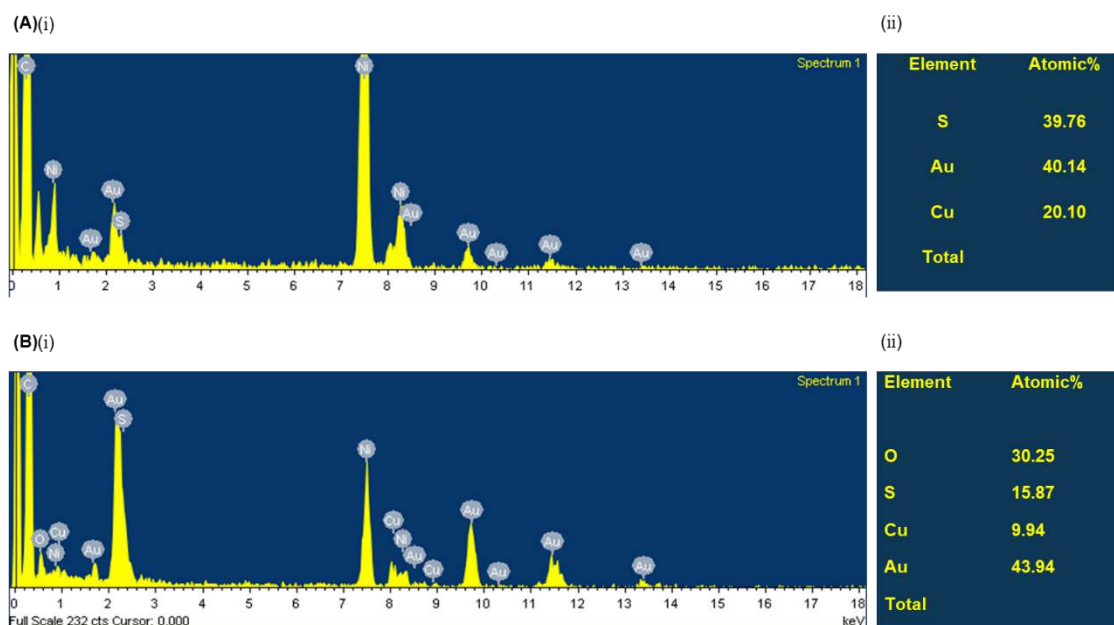


Fig. S13 Elemental compositions from EDS spectrum of – (A(i-ii)) supernatant containing NCs, and (B(i-ii)) isolated NSs. The Ni signal is coming from the grid (carbon coated Ni grid is used for the imaging).

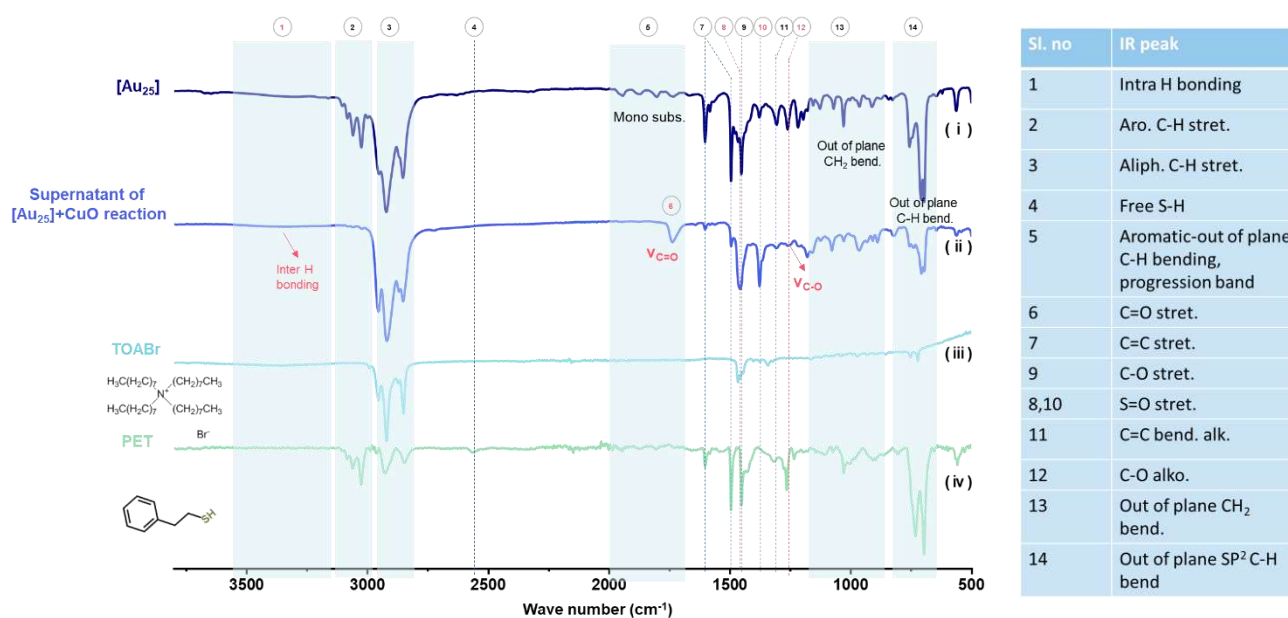


Fig. S14 FTIR analysis of (i) $[Au_{25}]$ NC, (ii) supernatant of the reaction, (iii) TOABr and (iv) PET (frequencies marked with red indicate new peaks appeared due to the reaction).

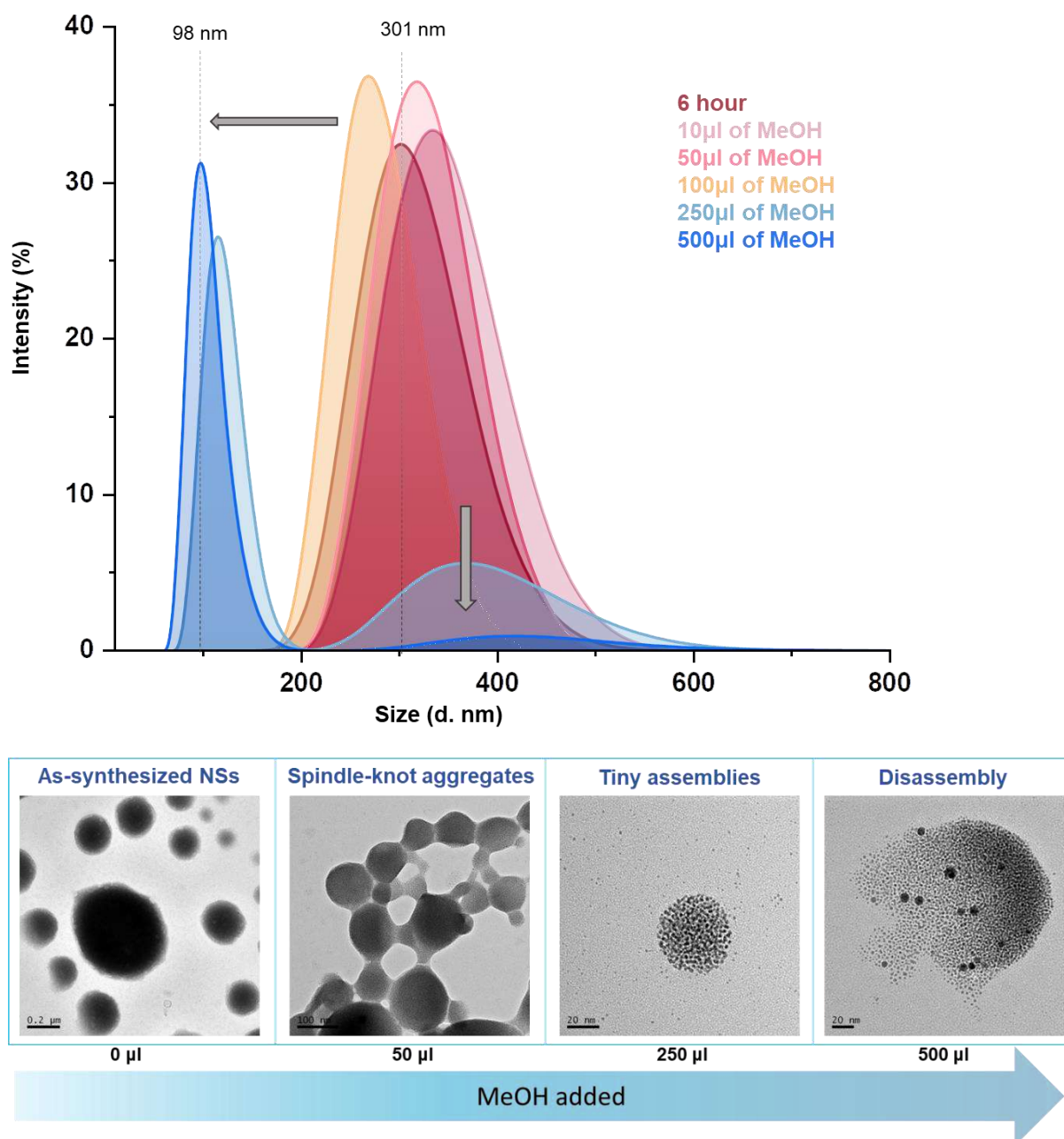


Fig. S15 DLS study and TEM images showing gradual disassembly, from NSs to smaller aggregates.

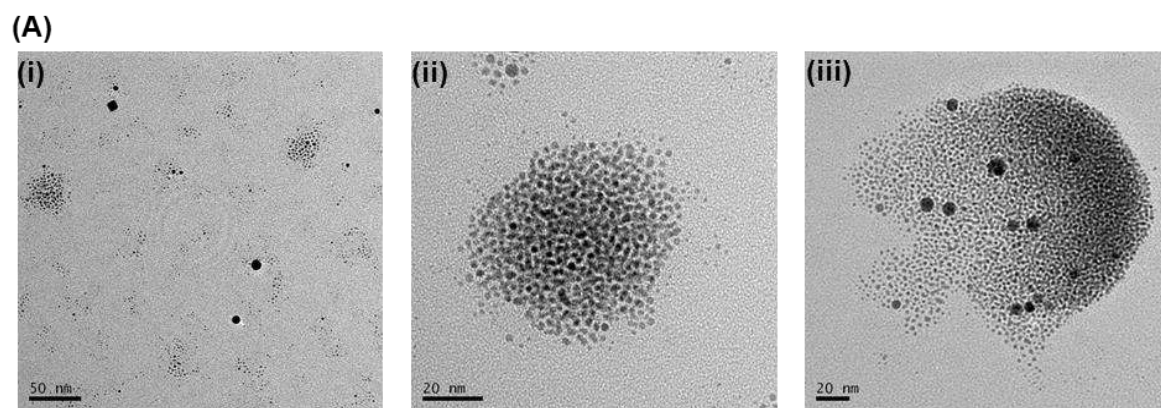
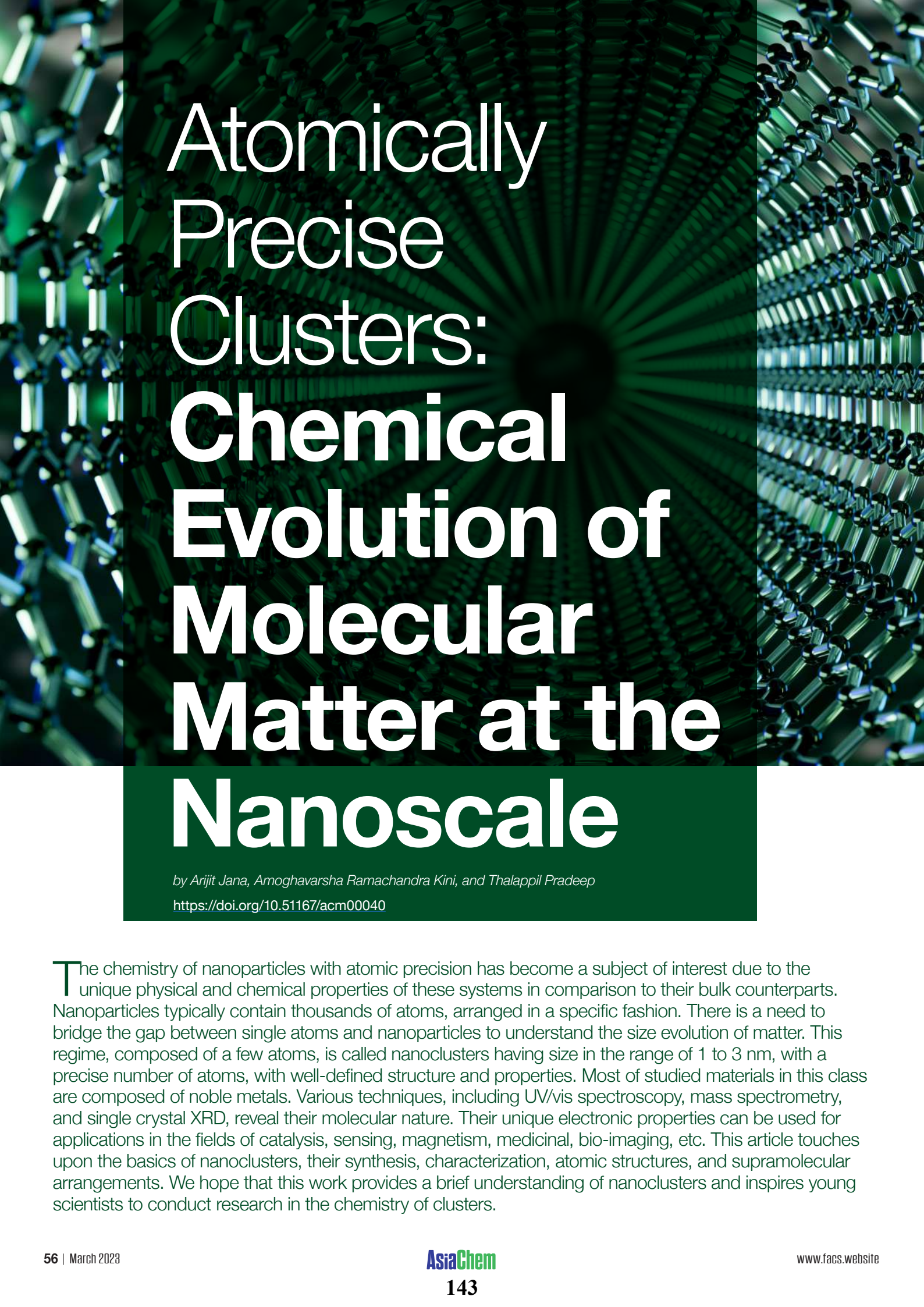


Fig. S16 TEM images of disassembled NSs after addition of 500 μl of MeOH.



Atomically Precise Clusters: Chemical Evolution of Molecular Matter at the Nanoscale

by Arijit Jana, Amoghavarsha Ramachandra Kini, and Thalappil Pradeep

<https://doi.org/10.51167/acm00040>

The chemistry of nanoparticles with atomic precision has become a subject of interest due to the unique physical and chemical properties of these systems in comparison to their bulk counterparts. Nanoparticles typically contain thousands of atoms, arranged in a specific fashion. There is a need to bridge the gap between single atoms and nanoparticles to understand the size evolution of matter. This regime, composed of a few atoms, is called nanoclusters having size in the range of 1 to 3 nm, with a precise number of atoms, with well-defined structure and properties. Most of studied materials in this class are composed of noble metals. Various techniques, including UV/vis spectroscopy, mass spectrometry, and single crystal XRD, reveal their molecular nature. Their unique electronic properties can be used for applications in the fields of catalysis, sensing, magnetism, medicinal, bio-imaging, etc. This article touches upon the basics of nanoclusters, their synthesis, characterization, atomic structures, and supramolecular arrangements. We hope that this work provides a brief understanding of nanoclusters and inspires young scientists to conduct research in the chemistry of clusters.

Introduction to nanoclusters

There's plenty of room at the bottom, Prof. Richard Feynman

Size-selected particles containing metal atoms are gaining increasing interest both in fundamental science and applications due to their tunable electronic structures and associated atom-specific functional properties. Traditional nanoparticles of metals with the dimension of 5-100 nm have continuous energy bands due to the overlap of valence and conduction bands. They exhibit surface plasmon resonance (SPR) features, in the absorption spectrum due to the oscillation of a large number of conduction band electrons. On the other hand, particles with dimensions <3 nm exhibit discrete electronic energy levels and manifest molecule-like multiple absorption features (Figure 1a, b). Other chemical properties of such ultrasmall particles depend on the shape, size, and composition of the particles. Even a single atom alteration can have a drastic effect on their physiochemical properties. Such ultrasmall particles with atomic precision are denoted by various names such as nanoclusters, clusters, aspicules, or nanomolecules. There are a number of review articles in the literature to know more about these systems.¹⁻³

The synthesis of monolayer-protected nanoclusters mostly relies on metal thiolate reduction in a mixed solvent using suitable reducing agents, such as sodium borohydride, sodium cyanoborohydride, tertbutyl ammonium borane complex, hydrazine, etc.⁴ A controlled synthetic conditions with specific temperature, pressure, solvent system and speed of stirring are involved in regulating the nuclearity of the cluster. Sometimes post-synthetic phase stability through excess ligand etching, thermal treatment, and size-focusing methods are used to convert poly-dispersed mixtures to monodispersed particles. The resulting samples show molecule-like characteristic optical signatures and undergo inter-cluster reactions like molecules, resulting in product nanoclusters. Ligand-exchange induced structural transformation (LEIST) is another synthetic method used for converting one cluster to another using excess ligands.^{5,6} In general, phosphine and hydride-protected labile clusters are converted to thiolated clusters with higher thermodynamic stability. A few other methods, such as solid-state synthesis, photo reduction, microwave-assisted synthesis, hydrothermal and radiolytic reductions, were used to synthesize different nanoclusters.^{1,2,4}

Transmission electron microscopic (TEM) investigations were performed to understand the atomic structure of such particles. Early TEM investigations of clusters revealed the presence of transient metal aggregates surrounded by an amorphous layer of ligands. Structural fluctuations of the ultrasmall metal core under the electron beam limits the quality of image acquisition. However, using a low-dose electron beam, measurement at cryogenic conditions, and advanced instrumentation resulted in good atomic imaging of a few nanoclusters. Palmer et al.

observed rapid fluctuation of low symmetric chiral isomers of Au₅₅ nanoclusters through time-lapse sequences of images collected using aberration-corrected scanning-TEM (STEM) (Figure 1c).⁷ Recently, we have developed a methodology for atomic-scale imaging of crushed crystals of Ag₂₅ and Ag₂₉ clusters using a conventional transmission electron microscope at room temperature.⁸ TEM micrographs show a layer-by-layer assembly of Ag₂₉ clusters having an interlayer distance of 1.71, 1.97, and 2.42 nm, corresponding to (200), (111), and (110) lattice planes, respectively. Such a methodology can be extended for the structural investigation of unknown clusters.

Mass spectrometry (MS) is one of the principal techniques used to characterize nanoclusters. Two soft ionization techniques, electrospray ionization (ESI) and matrix-assisted laser desorption ionization (MALDI) were used to detect such molecular species in the gas phase. The negative ion-mode ESI-MS spectrum of a well-known cluster, i.e., Ag₂₉ is presented in Figure 1e.⁹ The isotopic purity of the cluster was understood by matching the experimental spectrum with the theoretical one. Along with the characteristic MS pattern, various other studies, such as collision-energy dependent fragmentation, ion-mobility separation, collision induced dissociation (CID) and surface-induced dissociation (SID), provides additional insight into their atomic structure. Intercluster reaction in solution resulted in new alloy clusters through the exchange of metal atoms, which was monitored through mass spectrometric studies.¹⁰⁻¹² Dynamic nature of the surface ligand promotes the exchange reaction, and new clusters were formed with mixed ligands. Theoretical investigations of intercluster reaction concluded that adduct dimeric species were formed in the intermediate step. Exact kinetic modeling of such reactions reveal such reactions occurs in three steps, a) formation of a dimeric species through interparticle interactions, b) atom exchange in dimeric species, and c) dissociation of dimers.¹³ Kinetic simulation shows consecutive reactions starting from mother species which resulted in higher-order heterometal-doped sister species. Time-dependent ion intensities of the newly formed species measured through MS correlate well with kinetic modeling. The intercluster reactions between bimetallic and monometallic clusters leading to trimetallic clusters were also monitored through time-dependent MS studies.¹⁴ Exchange of inner kernel metal atoms of the cluster by keeping the structure intact was first observed through MS studies.¹⁵ Interparticle reactions between isotopically labeled [Ag₂₅(SR)₁₈] clusters i.e., ¹⁰⁷Ag₂₅(SR)₁₈ and ¹⁰⁹Ag₂₅(SR)₁₈, show a rapid exchange of silver isotopes upon forming a transient dimer species.

The separation of isomeric clusters and their supra-molecular adducts were also executed through ion-mobility MS studies. Isomers of glutathione-protected Ag₁₁ cluster were distinguished in the gas phase as they have varying drift times in the ion mobility cell.¹⁶ Combined CID and SID studies of such isomers show different fragmentation patterns, which suggested the existence of structural isomers. Another study demonstrated the formation of



Arijit Jana

Arijit Jana received his B.Sc. in Chemistry from the Ramakrishna Mission Vidyamandira and M.Sc. from IIT Madras. He is currently a PhD student at IIT Madras under Prof. Thalappil Pradeep. His research interests are on atomically precise metal nanoclusters, cluster-assembled framework solids and ambient electrospray deposition.



Amoghavarsha Ramachandra Kini

Amoghavarsha completed his B.Sc. and M.Sc. degrees in Chemistry from the University of Mysore. He is currently a PhD student at IIT Madras under Prof. Thalappil Pradeep. His research focus is on multimetallic alloy nanoclusters.



Thalappil Pradeep

Thalappil Pradeep is Institute professor and Deepak Parekh Institute chair professor in the Department of Chemistry at IIT Madras. He is also the professor-in-charge of the International Centre for Clean Water (ICCW). He earned his PhD degree from the Indian Institute of Science. Pradeep had post-doctoral training at the University of California, Berkeley and Purdue University, West Lafayette. Major research fields in his group are in the areas of atomically precise nanoclusters, mass spectrometry, ice chemistry and water purification using nanotechnology.



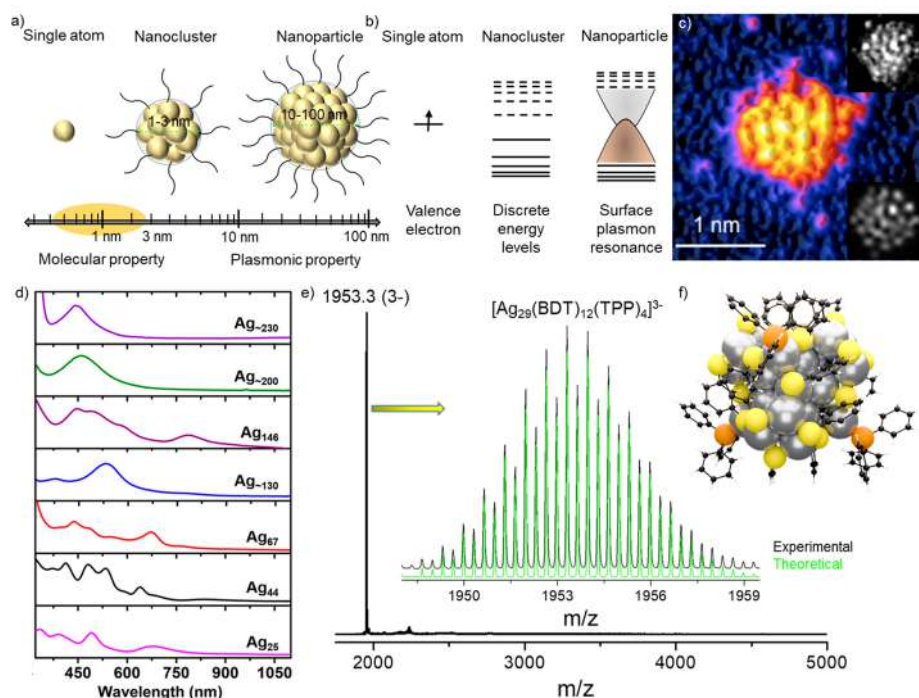


Figure 1: a) Schematic representation and b) energy level diagram of nanoclusters having a metal core protected by surface ligands and its comparison with nanoparticles. c) HAADF-STEM micrograph of Au_{55} nanocluster. Inset (top) real time frame and (down) simulated atomic imaging. d) Steady-state UV-vis absorption spectra of different silver nanoclusters with increasing nuclearity from the molecular to plasmonic regime. e) Full range mass spectrum of Ag_{29} in the negative ion mode. Inset shows the isotopically resolved experimental and simulated spectra. f) Atomic structural model of the same cluster. Reproduced with permission from Ref ^{7, 9, 37}

supramolecular adduct of cluster-fullerene aggregate promoted by weak intermolecular π - π , and CH- π interactions.¹⁷ The MS spectrum shows the formation of hybrid species with a varying number of fullerene attachments with $\text{Ag}_{29}(\text{BDT})_{12}$ cluster (where, $\text{BDT} = 1,3$ benzene dithiol). Furthermore, CID fragmentation studies of mass-selected adduct species reveal systematic detachments of fullerene moieties from the cluster. Host-guest complexation between the Ag_{29} cluster with cyclodextrins shows cis-trans isomerization of cyclodextrins over the surface of the cluster.¹⁸ Different collision cross section (CCS) values of these isotopologues imply such isomerization promoted by weak intermolecular interactions. The symmetry of the cluster bonded with active surface ligands and the chemical nature of the guest species regulate the nature of these supramolecular isomers.

Atomistic understanding of structure

Single crystal x-ray diffraction (SC-XRD) studies successfully resolved the atomic structure of such materials. Single crystals are grown from a supersaturated solutions using antisolvent layering or vapor diffusion techniques.¹⁹ Electrocyclization of Au_{25} cluster using a small applied potential resulted in large-sized uniform crystals.²⁰ Till date, ~500 gold and silver clusters with

various nuclearity were structurally understood through SC-XRD. In 2007, Kornberg et al. solved the first gold nanocluster, i.e., Au_{102} protected by 44 para-mercaptobenzoic acid ligands, at a resolution of 1 Å.²¹ This nanocluster has 49 atoms with a decahedron inner core having an Au-Au distance of 2.8–3.1 Å, clasped with extra gold atoms in an unanticipated fashion. Later, several nanoclusters were structurally resolved through single-crystal XRD. In general, the atomic arrangement was illustrated to be composed of an inner layer of metal atoms, called an inner kernel/core, enclosed by an outer layer of metal atoms, further protected by ligands. The inner kernel with tetrahedral (Td), octahedral (Oh), cubic, icosahedral, square antiprismatic, and distorted structures were observed for various gold and silver nanoclusters. The outer layer remains open or becomes distorted for some clusters due

to steric accommodation of ligands, metal-ligand interfacial movement, and binding stability of metal atoms. Electron diffraction of the microcrystalline sample is also used to structurally determine such atomically defined particles. Azubel et al. resolved the atomic structure of the Au_{68} cluster using a low-dose aberration-corrected transmission electron microscope.²² Recently, neutron diffraction and scattering studies were performed to resolve the atomic structure with a satisfactory resolution.²³ Especially the position of atoms with less electron density, such as hydrides, sulfides, carbides, and chlorides is precisely located using this technique. Deep learning coupled with various diffraction methods is also involved in structure determination in the field.²⁴

Several nanoclusters were reported to have fused inner kernel structures. The fusion of icosahedral (M_{12}) or central-icosahedral (M_{13}) units through the vertex, edge, and face-sharing modes create di, tri, tetra, and pentameric series. In 2007, Shichibu et al. synthesized an Au_{25} nanocluster protected by n-alkane thiol, formed by the fusion of two icosahedral units by sharing one vertex.²⁵ This nanocluster looks like a rod-shaped molecule, contrary to the well-known structure of Au_{25} , which has a central icosahedral core surrounded by six Au_2SR_3 surface staples arranged in an octahedral fashion. This structure extends to three icosahedral units arranged in a straight line forming a linear tri-icosahedral unit with 37 gold atoms.²⁶ The optical absorption spectra show a gradual reduction of the band gap of 1.96, 1.73, and 0.83 eV for Au_{13} , Au_{25} , and Au_{37} , respectively, which suggest constant evolution of energy levels upon structural fusion of icosahedral units. Last year, Wang et al. synthesized a rod-shaped silver nanocluster, i.e., Ag_{61} having four icosahedral units connected linearly through vertex sharing.²⁷ UV-vis spectrum shows a strong absorption peak at the near-infrared region due to one-dimensional electronic coupling between the icosahedral units.

The fusion of cores through vertex sharing gives beautiful structures evident from the cyclic arrangement of three icosahedral units in $M_{37/38}$ ($M = \text{Au}/\text{Ag}$, an alloy nanocluster with the formula $\text{Au}_{18}\text{Ag}_{19/20}$) has a cyclic arrangement of five Au_{13} through vertex sharing. The fusion of the icosahedral core can also happen through face sharing, as reported for the Au_{38} nanocluster. This cluster has bi-icosahedral Au_{23} cores fused through a triangular face. The fusion of cores through edge-sharing was theoretically investigated by Hakkinen et al. for several nanoclusters, including $\text{Au}_{40}(\text{SH})_{24}$, $\text{Au}_{57}(\text{SH})_{32}$, $\text{Au}_{74}(\text{SH})_{40}$, and $\text{Au}_{108}(\text{SH})_{56}$.²⁹ Here, the icosahedral cores share an edge with a 90° rotation

'Each of us have things and thoughts and descriptions of an amazing universe in our possession that kings in the 17th century would have gone to war to possess'

Prof. Kary Mullis

from each other. Using the theoretical models set for clusters mentioned above, they could predict the structure of a new cluster, $\text{Au}_{54}(\text{SR})_{30}$.³⁰

The tetrahedral core consists of four metal atoms that show interesting fused arrangements for a higher-order assembled kernel. Zeng et al. reported the double-stranded growth of tetrahedral cores in a series of clusters with a general formula of $\text{Au}_{8n+4}(\text{TBBT})_{4n+8}$ (with n ranging from 2 to 6 and TBBT is 4-tert-butylbenzenethiolate ligand). The clusters they reported are $\text{Au}_{20}(\text{TBBT})_{16}$, $\text{Au}_{28}(\text{TBBT})_{20}$, $\text{Au}_{36}(\text{TBBT})_{24}$, $\text{Au}_{44}(\text{TBBT})_{28}$, and $\text{Au}_{52}(\text{TBBT})_{32}$, having 2, 4, 6, 8, and 10 tetrahedral units, respectively.³¹ The Au_{20} is formed by vertex sharing of two tetrahedra. This structure was extended to Au_{28} with two strands of vertex-sharing tetrahedra, each arranged in a double helical fashion. This structure extends in the same manner from Au_{28} to Au_{52} in two strands in a double helical manner, where Au_{52} contains two strands of five vertexes sharing an icosahedron each. Tetrahedral cores have also been reported to form cyclic arrangements in Au_{22} , Au_{28} , Au_{34} , and Au_{40} nanoclusters having 1, 2, 3, and 4 bi-tetrahedral units with 7 Au atoms, respectively. The cubic core has eight metal atoms fused in a series of clusters, i.e., Ag_{14} , Ag_{38} , and Ag_{63} , having 1, 4, and 8 fused cubes, respectively.

A handful of nanoclusters with large nuclearity, i.e., M_mL_n , $m = 150\text{--}1000$, were structurally resolved. A few examples are $[\text{Au}_{156}(\text{C}\equiv\text{CR})_{60}]^{32}$, $[\text{Au}_{191}(\text{SPh}^t\text{Bu})_{66}]^{33}$, $[\text{Au}_{246}(\text{SR})_{80}]^{34}$, $[\text{Ag}_{307}\text{Cl}_{62}(\text{SPh}^t\text{Bu})_{110}]^{35}$ and $[\text{Ag}_{374}(\text{SR})_{113}\text{Br}_2\text{Cl}_{21}]^{36}$. The structural anatomy of these clusters reveal that they have multilayered core-shell arrangements of metal atoms, and a ligand shell uniformly protects the outer layer. For example, Au_{156} has a concentric Au_{126} core composed of Au_{46} - Au_{50} - Au_{30} layered geometry having length and width of 2.38 and 2.04 nm, respectively. The unidirectional Au_{46} inner kernel is composed of one icosahedron (Au_{12}), two fused flattened icosahedra (Au_{11}), and two terminal pentagonal pyramids (Au_6) connected in a linear fashion. The Au_{46} inner kernel is further protected by a drum-like Au_{50} tube and covered by a belt-shaped third shell of 30 gold atoms. The outermost shell consists of 30 gold atoms connected with 60 alkynyl ligands. UV-vis absorption spectrum of these clusters exhibits a single plasmonic absorption feature centered at ~ 500 nm. A series of silver nanoclusters, having 25, 44, 67, 130, 146, 200, and 230 atoms, manifest such variation of ground state absorption features upon gradually increasing atomicity (Figure 1d).³⁷ These large clusters are the missing link between molecular and metallic nanoparticles.

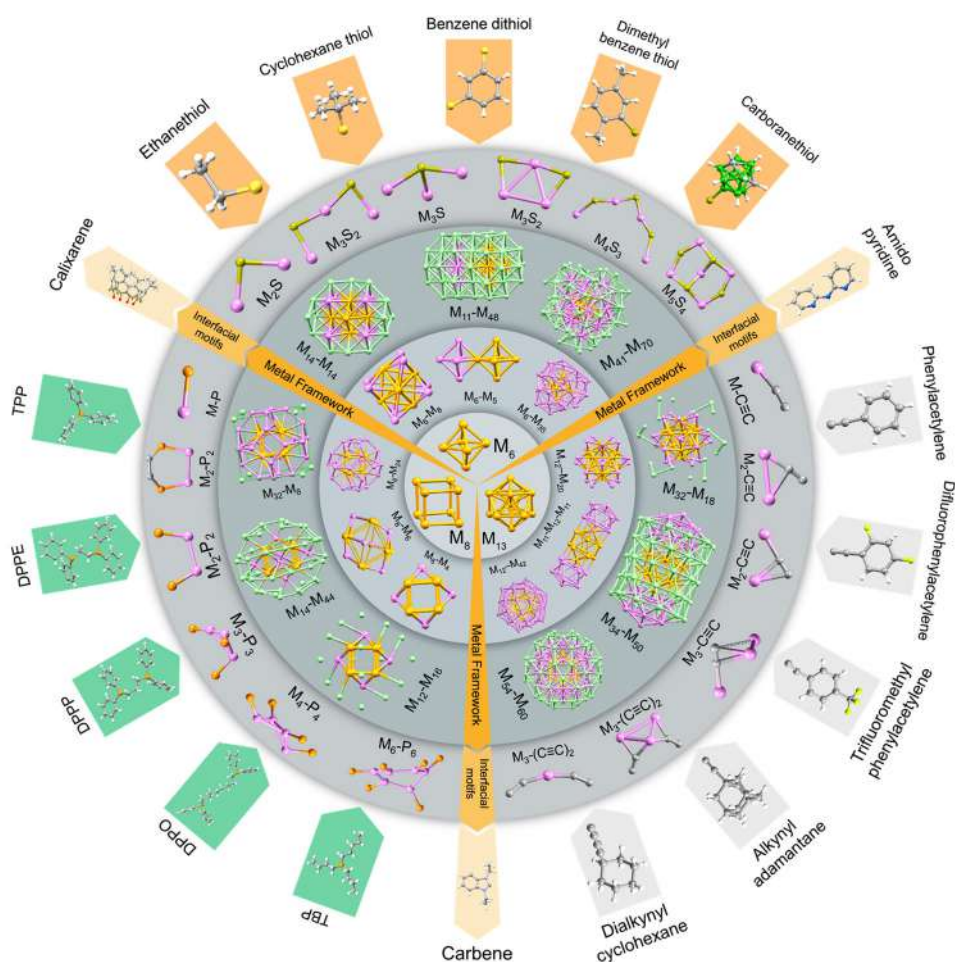


Figure 2: Illustration of the structural model of monolayer protected metal nanoclusters having different types of multilayered core-shell geometry, interfacial motifs and surface ligands. Reproduced with permission from Ref 27, 32, 46, 50, 51, 65

Ligands play an essential role, not just by shielding the metal core but also they determine the chemical properties of the cluster. The instability of bare clusters due to their excessive surface reactivity limits their study in the condensed phases. They have been synthesized in the gas phase under ultrahigh vacuum, and various properties of bare clusters were studied in the same condition. The ligands, i.e., thiols, phosphines, alkynes, carbenes, calixarene, and amido-pyridines are used for synthesizing metal clusters.¹⁻³ For thiol-based ligands, different metal-sulfide linkages bridge the metal core and peripheral ligands. A few such staple motifs are a) monomeric ($-\text{M}-\text{S}-\text{M}-$, $-\text{M}_3-\text{S}_3$), b) dimeric ($-\text{M}-\text{S}-\text{M}-\text{S}-\text{M}-$), c) trimeric ($-\text{M}-\text{S}-\text{M}-\text{S}-\text{M}-\text{S}-\text{M}-$) and d) tetrameric (M_4S_4) units present for a thiolated metal cluster. Positional isomerism of the thiol group present in the ligand can regulate the nuclearity of nanoclusters. Chen et al. observed size tuning of gold clusters from $\text{Au}_{130}(\text{p-MBT})_{50}$, $\text{Au}_{104}(\text{m-MBT})_{41}$, to $\text{Au}_{40}(\text{o-MBT})_{24}$ (where MBT is methylbenzene thiol) upon changing the ligand from para, meta to ortho-MBT.³⁸ This type of decreasing trend in atomicity is due to the increasing steric hindrance of the secondary methyl group in the ligands.

The binding of phosphine ligands through metal-phosphine bonds also resulted in clusters. Sometimes phosphine ligands act as secondary ligands weakly bonded with the outer cluster shell. Alkyne ligands are bonded with the cluster through $\text{C}\equiv\text{C}$ end and through linear, L and V-shaped staple motifs via σ and π -bonding. Electronic distribution through π -conjugation results in different absorption, emission and catalytic activity of alkynyl protected nanoclusters. Figure 2 summarizes different types of kernel structure, interfacial motifs and ligand shell present in clusters.

Intercluster assembly

Understanding the supramolecular assembly of clusters within a single crystal is important to correlate their various solid-state properties, such as conductivity, luminescence, chirality, mechanical, and catalytic properties. Generally, clusters are packed in a layer-by-layer (AB...AB, ABC...ABC) fashion in the lattice. For example, the crystal has a well-known Au_{25} cluster-packed a face center cubic (fcc) structure.³⁹ On the other hand, the silver analogue, Ag_{25} is packed in a AB...AB mode along the b and c axis.⁴⁰ A recent report by Jin et al. demonstrated

DNA helix-like packing of heterodimeric $\text{Au}_{29}(\text{SAdm})_{18}$ nanocluster (where SAdm = Adamantane thiolate).⁴¹ Structural fusion of two clusters i.e., $\text{Au}_{30}(\text{SR})_{18}$ and $\text{Au}_{28}(\text{SR})_{20}$ resulted in such heterodimeric nature. Anisotropic interactions between two enantiomers through specific pairs of ligands contributed to this double helical assembly. Higher-order tetra helical arrangement was also observed.

Just as organic molecules and other natural objects, nanoclusters act as chiral atomic entities. The chirality of such nanomaterials originates due to a) chiral ligand, b) helical staple motifs, c) chiral kernel structure, and d) intercluster packing. Generally, the outer ligand shell induces chirality to the core metal atoms.⁴² Separating optically pure isomers of individual nanoclusters from the solution is challenging due to their sizeable macromolecular structure and rapid inter-conversion rate. Sun et al. demonstrated spontaneous resolution of racemic Ag_{14} clusters through re-crystallization in acetonitrile solvent.⁴³ Homocluster crystallization is favored through hydrogen bonding interactions between surface ligands and solvent molecules. Another report by Mak et al. shows enantiomeric self-assembly of Ag_{30} upon re-crystallization in dimethyl acetamide (DMAC) solvent.⁴⁴ Chirality of the nanocluster arises from the spiral arrangement of the ligands directed by unusual B–H $\cdots\pi$ and

C–H $\cdots\pi$ bonding interactions among the carborane cages and the benzene rings. Noncovalent weak interactions of DMAC with the ligand shell of the clusters favor crystallization of R and L-isomers together. The use of external chiral ligands sometime helps to crystallize specific isomers. Nakashima et al. separated chiral isomers of $[\text{Ag}_{29}(\text{BDT})_{12}(\text{TPP})_4]$ nanocluster using a chiral high-performance liquid chromatography (HPLC) column.⁴⁵ Separated isomers show mirror image circular dichroism (CD) spectra, which imply their optical purity. Theoretical calculations reveal chiral column helps the chirality induction of Ag_{29} through the interactions with the outer interior of staple motifs. Another report from our group showed a propeller-shaped structure with six rotary arms in a Ag_{21} nanocluster, primarily protected by meta-carborane 9-thiol ligands.⁴⁶ The staggered arrangements of six peripheral carboranes determine the rotary nature of the cluster. Therefore, efficient tuning of the ligand shell will result in various structural frameworks.

Sometimes two or more different ways of intercluster packing were observed for a particular cluster, known as polymorphism. We have observed polymorphism on Ag_{29} nanocluster with cubic and trigonal crystal systems.⁴⁷ Crystallization of the cluster in the DMF solution through the slow evaporation method generates cubic crystals. In

contrast, vapour diffusion of methanol into the DMF solution resulted in trigonal crystals (shown in Figure 3). The stronger CH $\cdots\pi$ and H $\cdots\text{H}$ van der Waals interactions between the secondary triphenylphosphine ligands resulted in the cubic form compared to the trigonal system. Both crystals look similar to the naked eye, however rigidity of cubic crystals augmented stronger luminescence compared to trigonal crystals. Another report shows ligand-induced isomorphism of $\text{Au}_{28}(\text{SR})_{20}$ nanoclusters protected by cyclohexyl-thiol (CHT) and 4-tert-butylphenyl thiol (TBPT), respectively.⁴⁸ Despite having similar inner kernel structures, the outer $\text{Au}_8(\text{SR})_{12}$ staples are arranged in two trimeric and two monomeric units for $\text{Au}_{28}@\text{CHT}$, whereas through four dimeric units for the $\text{Au}_{28}@\text{TBPT}$ cluster. Such variation of the outer shell induced isomerization of the cluster influenced their catalytic activities.

A single crystal grown by a purified nanocluster leads to the assembly of specific particles in the lattice. In some cases, solvent molecules or counter ions were crystallized along with the nanocluster. Cocrystals are formed by crystallizing two clusters inside the unit cell through favorable intermolecular interactions.⁴⁹ In 2018, Zheng et al. prepared the first thiolate-protected cocrystal, i.e., $(\text{AuAg})_{45}(\text{SR})_{27}(\text{PPh}_3)_6$ and $(\text{AuAg})_{267}(\text{SR})_{80}$ by the reduction of metal thiolate.⁵⁰ The trigonal prismatic smaller $(\text{AuAg})_{45}$ cluster (particle dimension of 1.1 nm) is packed with the spherical larger cluster having a particle dimension of 2.5 nm. These diversified particles, in terms of their shape and size packed themselves in the crystal through ligand-centred CH $\cdots\pi$ interactions. Supramolecular packing of the cocrystal demonstrated a hexagonal arrangement of each particle. We synthesized dimethyl benzene thiol (DMBT) and triphenylphosphine-protected Ag_{40} and Ag_{46} cocrystals with the same outer shell but different inner core structures.⁵¹ During crystallization, these particles were not distinguishable due to the identical arrangement of the outer shell i.e., $[\text{Ag}_{32}(\text{DMBT})_{24}(\text{TPP})_8]$. Mass spectrometric studies of a few such crystals dissolved in suitable solvents further verified the presence of both these clusters in the crystal. Another report from our group showed the intercluster reaction between triphenylphosphine and hydride-protected Ag_{18} and tert-butylthiol (TBT) protected Ag_{12} nanoclusters resulting in Ag_{16} and Ag_{17} clusters, primarily protected by TBT ligands. Subsequent crystallization of as-synthesized clusters resulted in a cocrystal of $\text{Ag}_{16}:\text{Ag}_{17}$ having 2:1 occupancies in the crystal.⁵² The indistinguishable metal-chalcogenolate outer shell having an Ag_{16}S_8 unit possess simultaneous crystallization of the clusters. Until now, ~10 cocrystals have been structurally resolved using X-ray crystallography.^{53,54}

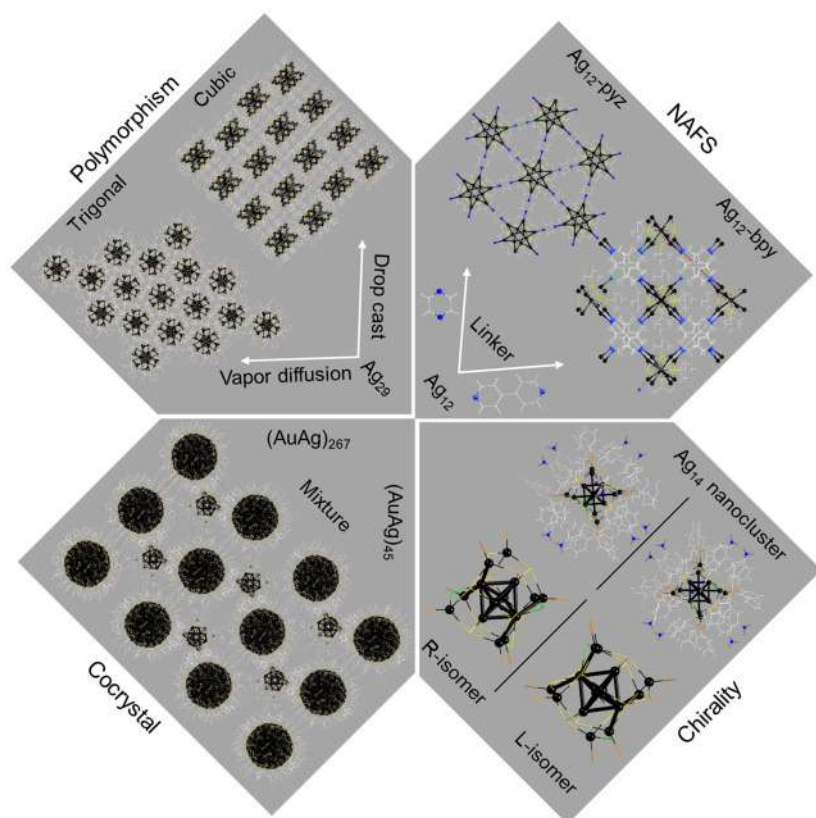


Figure 3: Structural representation of intercluster packing resulted polymorphic crystals, cocrystals, chirality and nanocluster assembled framework solids. Reproduced with permission from Ref ^{43, 47, 50, 57}

Assembly of nanoclusters using suitable organic linkers forms a porous framework structure, known as nanocluster assembled framework solid (NAFS). They are structurally similar to traditional metal-organic frameworks (MOFs). Instead of a single metal atom as a node for MOFs, a cluster core of aggregated metal atoms act as a node for such materials. Multidentate N-donor ligands, such as bipyridine (bpy), pyrazine (pyz), 1,2-bis(4-pyridyl)ethane (bpe), 1,2-di(pyridine-4-yl)diazene (dpd), tris(4-pyridylphenyl)-amine (tpa), 5,10,15,20-tetra(4-pyridyl) porphyrin (tpp), etc., are used as linkers for various NAFS. Such linkers promoted large-order intercluster assembly, which incorporates the stability of the framework and creates unique materials combining the optical and electronic properties of cluster and organic linkers. Mak et al. synthesized the first NAFS having an Ag_{12} cluster node interconnected by 4,4'-bpy linkers.⁵⁵ The resulting NAFS show superior stability for up to a year compared to clusters, which degraded within 30 min in ambient conditions. A structural framework having multiple nanochannels of these materials promotes the adoption of volatile organic molecules. Drastic variation of the electronic properties was observed in this NAFS compared to the bare cluster. Mak et al. demonstrated the site-specific assembly of superatomic Ag_{14} cluster through bidentate N-donor pyridyl ligands.⁵⁶ Eight open vertices of the cluster promote differently ordered assemblies. Steric availability of the ligands is the most influencing factor behind higher-ordered framework assembly. Another interesting NAFS, i.e., Ag_{12} -pyz reported from our group with pyz linkers, shows a distinct variation of the cluster structure compared to Ag_{12} -bpy through metal-metal and metal-sulfide rearrangements promoted by the linkers.⁵⁷ SCXRD reveals a graphene-like hexagonal layered assembly of the NAFS. Successful exfoliation of each layer from the parent crystals through ultra-sonication enables us to image each layer through transmission electron microscopy. Crosslinking between framework structures resulted in a hybrid flexible membrane as shown by Zang et al.⁵⁸ Accessible amino groups present in the linkers covalently crosslinked with acrylate monomers through photoinduced polymerization propagated along the membranes provided them with superior photoemission characteristics.

Emerging properties

Technology plays a key role in sustaining the modern world, and there is a continuous effort to make smaller devices for portability and versatility without compromising performance efficiency. Nanoclusters and their superstructural assembly have emerging potential with fascinating properties, such

as luminescence, chiroptical behaviour, conductivity, photoconductivity, etc. Here, we provide a brief account of research towards studying various properties of nanoclusters in the past few years.

Photoluminescence:

Photoluminescence (PL) is an interesting property observed for several nanoclusters due to the radiative relaxation of the excited states between closely spaced electronic

The Science of today is the technology of tomorrow,

Prof. Edward Teller.

energy levels. PL properties have potential applications in the field of sensing, bioimaging, and optoelectronic devices.¹⁻³ Although most clusters are red emitting (depicted in Figure 4a), the emission wavelength of clusters usually varies from greenish-yellow ($\lambda = 450$ nm) to near-infrared ($\lambda = 1500$ nm) region. For example, ortho-carborane 1,2 dithiol protected Ag_{14} cluster has red luminescence centered at λ_{max} 626 nm using excitation at 370 and 450 nm (shown in Figure 4b). Generally, silver nanoclusters are better fluorophore than gold clusters in terms of emission brightness, quantum yield, colour tunability and photostability. The structural framework of the metal atoms, metal-ligand interface, electronic nature of the surface ligands and surrounding environment determines the emission characteristics of such materials.⁵⁹ Isomerization also have significant effect on PL properties. Jin et al. demonstrated that $\text{Au}_{28}(\text{CHT})_{20}$ shows ~15-fold higher emission than $\text{Au}_{28}(\text{TBBT})_{20}$, where CHT is cyclohexane thiol and TBBT is p-tert-butylbenzenethiol.⁶⁰ The absorption spectra of both these clusters are similar having a HOMO-LUMO gap of around 1.7 eV; however, PL emission properties are different. Despite having a similar Au_{14} kernel, the arrangement of the outer staple motifs determines the relaxation dynamics. Femtosecond transient absorption studies further reveals that surface staple motifs to kernel centre charge transfer is responsible for such a behavior.

Sometimes aggregation resulted in enhanced emission of clusters, popularly known as aggregation-induced emission (AIE) or aggregation-induced enhanced emission (AIEE).⁶¹ Zhu et al. observed 13 times bright emission (QY of 0.9 to 11.7%) of $[\text{Ag}_{29}(\text{BDT})_{12}(\text{TPP})_4]$ upon gradual addition of TPP ligands into the DMF solution of the cluster.⁶² Restriction of the dynamic dissociation process of TPP ligands promotes PL enhancement by reducing the non-radiative transition processes. Mass spectrometric

studies also verified such dynamic dissociation of the cluster. We have also observed similar luminescence phenomena of the same cluster by changing the secondary ligands from monophosphines to diphosphines.⁶³ Increasing the chain length of such bidentate ligands enhances the emission ~30-fold through a ligand-to-metal charge transfer (LMCT) mechanism. Crystallization is another type of aggregation that also results in enhanced emission. The first crystallization-induced emission enhancement (CIEE) behavior was observed in a bimetallic $[\text{Au}_4\text{Ag}_{13}(\text{dppm})_3(\text{SR})_9]$ nanocluster, which becomes strongly emitting upon forming crystals.⁶⁴ The cluster is non-emitting in solution and weakly emitting in amorphous conditions. Restriction of intramolecular motions in the crystalline state through C-H... π interaction enhances the radiative transition. We observed similar behavior in a silver cluster, i.e., $[\text{Ag}_{22}(\text{2,5-DMBT})_{12}(\text{DPPE})_4\text{Cl}_4]^{2+}$ having a distorted Ag_{10} core protected by an Ag_{12} shell.⁶⁵ PL profile of CIE behavior is shown in Figure 4c. This superatomic cluster with four magic electrons promotes intermolecular interactions through short contact C-H... π , and π ... π interactions which favor its CIE nature.

PL properties of the nanoclusters generally increase upon reducing the surrounding temperature. Restricting intramolecular motion in cryogenic conditions increases the excited state's radiative relaxation. Sun et al. observed similar phenomena of gradual increase of emission intensities of gold and silver nanoclusters, i.e., Au_8 , Au_{13} , Ag_{44} , Ag_{50} , Ag_{64} , Ag_{73} , Ag_{80} , and Ag_{90} , upon reducing the temperature.⁵⁹ We have also observed a similar phenomenon of carborane-thiol protected Ag_{14} nanocluster (Figure 4d), which shows > 25-fold enhanced emission upon reducing the temperature from 298 to 77 K (Figure 4e).⁶⁶ The reduction of intensity might not always be linear with temperature. A large buckyball-type Ag_{180} cluster shows nonlinear PL enhancement upon reducing the temperature from 293 to 193 K in its crystalline state with 30 nm blue-shifting of emission maxima.⁶⁷ Further reducing the temperature from 193 to 93 K shows linear enhancement of emission intensity.

Gu et al. observed pressure-induced emission enhancement of gold nanoclusters by applying hydrostatic pressure through a diamond anvil cell (DAC) (shown in Figure 4f).⁶⁸ They have performed in situ optical spectroscopic measurements using $[\text{Au}_{21}(\text{SR})_{12}(\text{dppm})_2]^+$ and $[\text{Au}_{28}(\text{SR})_{20}]$ having mono and bi cuboctahedral structure and $[\text{Au}_{24}(\text{SR})_{20}]$ and $[\text{Au}_{14}\text{Cd}(\text{SR})_{12}]$ having bi-tetrahedral metal kernel, respectively. Redshifting of the absorption spectra upon gradually increasing pressure was

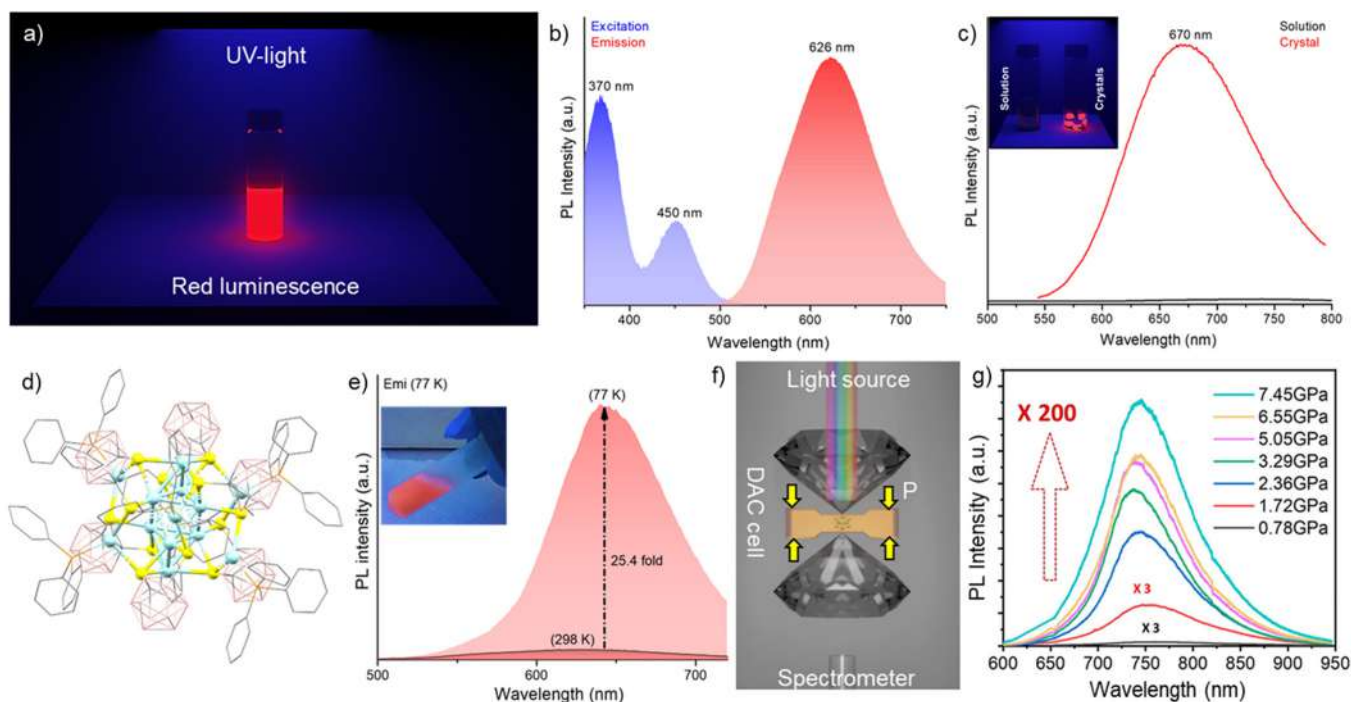


Figure 4: a) A schematic depiction of a nanocluster solution emitting red color under UV light. b) Excitation and emission spectral profile of a red emitting Ag_{14} nanocluster. c) Crystallization-induced-emission spectra of Ag_{22} nanocluster. Inset shows the illustration of of luminescence of solution at 77 K. and single crystals. d) Molecular structure of Ag_{14} nanocluster. e) Temperature-dependent PL profile of the same cluster (inset shows a photograph at 77 K). f) A schematic representation of DAC used for hydrostatic pressure-dependent optical measurements. g) Pressure-sequence PL spectra of $[\text{Au}_{14}\text{Cd}(\text{SR})_{12}]$ cluster shows 200-fold emission enhancement. Reproduced with permission from Ref ^{65, 66, 68}

observed for all the clusters. DFT calculation shows induced electron delocalization over ligands upon squeezing the cluster, narrowing the spacing of energy levels. PL investigation reveals emission enhancement for all these clusters and ~200-fold highest emission enhancement at ~7 GPa for the $[\text{Au}_{14}\text{Cd}(\text{SR})_{12}]$ cluster (Figure 4g). Such emission enhancement is due to the reduction of excited state structural distortion, which eventually enhances the near-band-edge transition dipole. Another report by Zang et al. displays the piezochromic behavior of Ag_{50} cluster crystals.⁶⁹ Reversible color tuning of the crystals from orange-red to dark red upon increasing the pressure from 1 atm to 7.5 GPa, correlated well with the reduction of the optical band gap.

NAFS also behave as tunable luminescence materials. The bare Ag_{12} nanocluster is red emitting ($\lambda_{\text{max}} = 620 \text{ nm}$), however, $\text{Ag}_{12}@\text{4,4'-bpy}$ NAFS is green emitting ($\lambda_{\text{max}} = 507 \text{ nm}$) in its crystalline state.⁵⁵ A 60-fold enhancement of PL quantum yield (0.2 % to 12.1 %) upon forming a framework structure signifies the role of an ordered arrangement of chromophores. The emission colors of this NAFS was shifted from green to orange-yellow in the presence of volatile organic compounds (VOCs) such as ethanol, acetonitrile, chloroform, and 2-cyanoethanol, etc. The emission intensity of this material increases linearly upon increasing the vapor pressure of ethanol from 0 to 1.33 kPa,

showing the linear response, which further implies the tangible incorporation of ethanol molecules in the cavity. The alteration of electronic structure upon encapsulation of such VOCs is due to the formation of inclusion complexes through $\pi\cdots\pi$, and hydrogen bonding interactions with adjacent layers. Single crystals of such inclusion complexes further verified the inclusion of VOCs in the lattice. Ultrafast multicolor luminescence switching has enormous potential in optical sensors, luminescence signaling devices, and other optoelectronic applications.

Conductivity

Miniaturization of electronic devices has been evident recently due to the growth of single-atom transistors, memory devices, etc. Nanoclusters are a great option for making nanoscale conducting fibers, crystals, and other superstructures, which can be used for various nano-dimensional electronic applications like photoconductivity, sensors, field effect transistors (FETs), and many more. First, we will discuss the photoconductive behavior of a randomly assembled fibrous network of Ag_{88} nanocluster.⁷⁰ The comparative photoconductivity of two nearly isostructural Ag_{88} clusters i.e., $\text{Ag}_{88}\text{-A}$ and $\text{Ag}_{88}\text{-B}$, primarily protected by thiacaixarene ligands. Authors have prepared a one-dimensional nanotubes to study their photoconductive behavior in electrochemical conditions (0.2 M aqueous Na_2SO_4) through a three-electrode setup. Linear

sweep voltammetric (LSV) profile showed that $\text{Ag}_{88}\text{-B}$ has a better photocurrent response ($0.20 \mu\text{A}/\text{cm}^2$) than the first one, having a photocurrent response of $0.12 \mu\text{A}/\text{cm}^2$. Intercluster assembly reveals that $\text{Ag}_{88}\text{-A}$ assembled in a face-to-face fashion, while $\text{Ag}_{88}\text{-B}$ arranged as face-to-side through intercluster noncovalent interactions of tert-butyl groups. The structural asymmetry of the $\text{Ag}_{88}\text{-B}$ cluster with specific packing promotes higher electron mobility than the other one.

Li et al. demonstrated the hierarchical assembly of Au_{21} nanoclusters in crystals by changing the counter ions (i.e., AgCl_2^- and Cl^-) during crystallization.⁷¹ The two counter ions reside near the diphenyl ligands through anion- π and aryl C-H \cdots Cl interactions. The Au_{21} nanoclusters are assembled linearly along the diagonal of (100) and (010) planes for $\text{Au}_{21}@\text{AgCl}_2^-$ and $\text{Au}_{21}@\text{Cl}^-$ clusters, respectively. The different crystal packing of the two Au_{21} nanoclusters and the different counterions resulted in a difference in the conductivity of these two clusters, which was measured and characterized by measuring the I-V curves for the clusters. The average electrical conductivity (σ) of $\text{Au}_{21}@\text{AgCl}_2^-$ was $\sim 1.44 \times 10^{-8} \text{ S/m}$ and for $\text{Au}_{21}@\text{Cl}^-$ it was $\sim 2.38 \times 10^{-6} \text{ S/m}$, averaged over 6 to 7 crystals. The conductivity in a material like a crystal or an assembly of nanoparticles depends on the interparticle distance, i.e., higher conductivity is observed at lower

interparticle distances (a general rule is that there will be ~ 1 order of magnitude change in conductivity for every 1 Å change in interparticle distance). The center-to-center distances between the adjacent clusters in crystals with AgCl_2^- and Cl^- counterions are 16.80 and 16.39 Å, suggesting that the clusters are closer together in $\text{Au}_{21}@\text{Cl}^-$ and hence the conductivity of this cluster crystal should be higher than $\text{Au}_{21}@\text{AgCl}_2^-$ cluster, which is also supported by the σ values of the clusters. Here the interparticle distance differs only by a small magnitude, but the conductivity increases by two orders of magnitude; hence the interparticle distance cannot be the only factor affecting the change in conductivity of these clusters. Further studies are needed to understand the mechanism of electron transport through crystals.

Clusters can also be used for FET applications by transporting electricity along specific crystal axes. Yuan et al. demonstrated such a behavior of an alloy cluster with a composition of $\text{Au}_{21.3}\text{Ag}_{12.7}\text{L}_{20}$ (where L is 1-ethynyladamantane).⁷² This cluster crystallizes in two forms depending on the solvent system. When the clusters are crystallized in the chloroform-methanol system, they form

a monomeric unit, and when crystallized in the dichloromethane-methanol system, they form a one-dimensional polymer-like assembly into the crystal (shown in Figure 5a) through Ag–L–Au–L–Ag linkages. Authors have fabricated FET devices using Si wafers, coating them with 300 nm SiO_2 and depositing four terminal electrodes onto them. The crystals were painted at suitable positions with silver paste to create contacts with the electrodes. Using this device, they studied the one-directional conductivity through crystals along the a and c axis. Electrical conductivity was measured by the slope of the linear I–V curve along the a and c-axis, as shown in Figure 5b. The crystal's conductivity along the c-axis was found to be $1.49 \times 10^{-5} \text{ Sm}^{-1}$ which is 1800 times more than the conductivity along the a-axis (shown in Figure 5c). In the crystal, there is anisotropy, where the clusters are connected along the c-axis but are not in contact and insulated by the bulky adamantane ligands along the a-axis. The anisotropy in the crystal and the DFT predicted electronic structure hinted at the anisotropic semiconducting property of the cluster crystals. This study has opened new opportunities to engineer ligands to create crystals of clusters with unidirectional conductivity.

All the work mentioned above are on the bulk properties of nanocluster assemblies or crystals. However, Feng et al. have recently reported the measurement of conductance of a single cluster using a MCBJ (mechanically controlled break junction) device.⁷³ In MCBJ, a skinny ductile metal wire is pulled to create a nanoscale gap contact of a single molecule, placed over a flexible base (shown in Figure 5e). The polymer base is then bent in a controlled manner so that the metal wire breaks and the contact is broken. After breaking, the gap between the two metal wires is adjusted to the separation distance equal to the cluster length, enabling the cluster to fit into this gap and create a contact between the broken metal wires. The electrical contact is made when there is an alignment of the molecular orbital of the cluster and the Fermi levels of the metal electrodes, and the change in potential when this contact is made is called the inflection point voltage or transition voltage (shown in Figure 5f).

Authors have studied the conductance of Ag_{25} , Ag_{43} , Ag_{44} , Ag_{63} , Ag_{78} , Ag_{141} , Ag_{136} and Ag_{374} clusters using MCBJ technique (shown in Figure 5d). The conductivity plots of all the clusters are shown in Figure 5g,

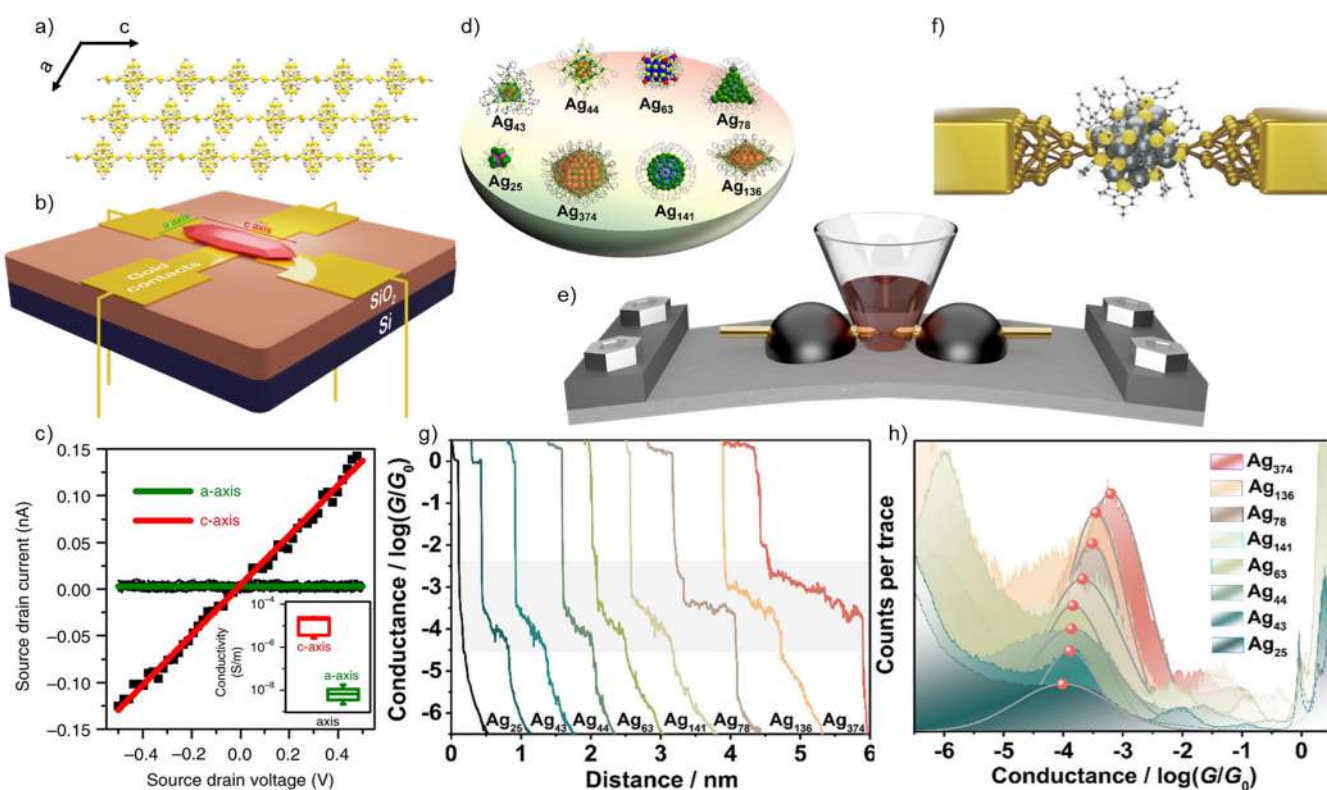


Figure 5: a) Intercluster packing of a bimetallic Au-Ag alloy cluster. b) Schematic representation of conductivity measurements of a single crystal of the same cluster. c) I–V plot of the crystal along different axial directions. d) Structural representation of various clusters involved for single particle conductivity measurements. e) Schematic representation of MCBJ device with a liquid cell. f) atomic dimension of gold electrodes holding a single cluster. g) Conductance traces of nanoclusters with different sizes as a function of distance between the gold electrodes. h) 1D conductance histograms of different nanocluster junctions. Reproduced with permission from Ref ^{72, 73}

h. The conductance in such small particles is through the tunneling of electrons through the molecule, which decreases with the increase in the length of the molecule according to the equation $G = Ae^{-\beta d}$, where G is conductance, A is the pre-exponential factor, β is tunneling decay constant and d is the length of the molecule. The β is size independent and depends on the tunneling barrier. Generally, the conductivity of clusters decreases exponentially with the increase in their length. However, the HOMO-LUMO gap decreases fairly rapidly with the increase in the size of clusters, and the β will become size-dependent. This arising dependency of β on the size of the cluster will likely eliminate the decay of conductance with the increasing size of the cluster. These results show that as the size of the cluster increases, the conductivity increases, which is contradictory to the observations made for other simple molecules. Normally tunneling of electrons through the vacuum requires a greater potential ($> 1.0V$) between electrodes separated by a distance. However, when a silver cluster occupies the junction, the potential for tunneling reduces to $\sim 1.0V$, which indicates a lower tunneling barrier for electrons through the clusters. It is also notable that the cluster metal core is involved in the conduction, not the ligand. This is evident because even though different ligands protect the silver clusters used here, the inflection point voltage for all the clusters is the same.

Conclusion and future perspective

This review summarizes the advancements in atomically precise clusters, especially for gold and silver, and the effect of confinement on their properties. The structural framework of such materials is presented in terms of their bonding and intermolecular interactions. We have discussed various types of the core structure of clusters and their subsequent expansion leading to the core-shell geometry of larger clusters. Surface ligands are essential in determining atomicity and for simultaneously determining clusters' physiochemical properties. Extended structural assembly of clusters in single crystals resulted in chirality, polymorphism, and framework solids, which has enabled us to understand more about such materials recently.

After the pioneering work of synthesizing colloidal gold nanoparticles in 1980 by Brust et al., extensive research over the last three decades witnessed significant progress in atomically precise materials. Many gold and silver nanoclusters with varying atomicity were synthesized and characterized through TEM, mass spectrometry, and other studies. Structural aspects of clusters were resolved through single crystal XRD, and electron diffraction and atom-specific chemical properties were correlated with structural aspects. Stability of ultrasmall particles is a primary concern for their practical applications. Use of bulky three-dimensional ligands (especially carborane thiols and alkynes) resulted

in new clusters with better stability than their organic counterparts. Encapsulation using inorganic templates such as glass matrix, MOFs, and two-dimensional chalcogenides enables enhanced stability with composite properties. Other metal-based nanoclusters, especially Cu, Ni, Co, Pd, and Ru remain to be explored in detail due to their instability issues. The interaction of clusters with living organisms such as viruses and bacteria will be a new dimension to be explored. The species formed by the interaction of clusters and viruses can be studied using high-resolution megadalton mass spectrometry, which will provide information about the nature of interactions between these systems and will help us to implement clusters in medicine. Single particle conductivity and photoluminescence characteristics will open up new possibilities in ultrafast photoswitches, quantum computing, bioimaging, and other photonic applications. Machine learning and computer simulation of large clusters and their aggregates and crystals will help us understand their properties efficiently.

Acknowledgement

Authors acknowledge the support from Department of Science and Technology (DST), Govt. of India. T.P. acknowledges funding from the Centre of Excellence on Molecular Materials and Functions under the Institution of Eminence scheme of IIT Madras.

References

- Jin, R.; Zeng, C.; Zhou, M.; Chen, Y. (2016). Atomically Precise Colloidal Metal Nanoclusters and Nanoparticles: Fundamentals and Opportunities. *Chem. Rev.* 116, 10346–10413.
- Chakraborty, I.; Pradeep, T. (2017). Atomically Precise Clusters of Noble Metals: Emerging Link between Atoms and Nanoparticles. *Chem. Rev.* 117, 8208–8271.
- Jena, P.; Sun, Q. (2018) Super Atomic Clusters: Design Rules and Potential for Building Blocks of Materials. *Chem. Rev.* 118, 5755–5870.
- Udayabhaskararao, T.; Pradeep, T. (2013) New Protocols for the Synthesis of Stable Ag and Au Nanocluster Molecules. *J. Phys. Chem. Lett.* 4, 1553–1564.
- Kang, X.; Zhu, M. (2019) Transformation of Atomically Precise Nanoclusters by Ligand-Exchange. *Chem. Mater.* 31 (24), 9939–9969.
- Jana, A.; Chakraborty, P.; Dar, W. A.; Chandra, S.; Khatun, E.; Kannan, M. P.; Ras, R. H. A.; Pradeep, T. (2020) Dual Emitting Ag₃₅ Nanocluster Protected by 2-Pyrene Imine Thiol. *Chem. Commun.* 56, 12550–12553.
- Wang, Z. W.; Palmer, R. E. (2012) Experimental Evidence for Fluctuating, Chiral-Type Au₅₅ Clusters by Direct Atomic Imaging. *Nano Lett.* 12 (11), 5510–5514.
- Mahendranath, A.; Mondal, B.; Sugi, K. S.; Pradeep, T. (2022) Direct Imaging of Lattice Planes in Atomically Precise Noble Metal Cluster Crystals Using a Conventional Transmission Electron Microscope. *Chem. Commun.* 58 (12), 1906–1909.
- AbdulHalim, L. G.; Bootharaju, M. S.; Tang, Q.; Del Gobbo, S.; AbdulHalim, R. G.; Eddaoudi, M.; Jiang, D. E.; Bakr, O. M. (2015) Ag₂₉(BDT)₁₂(TPP)₄: A Tetravalent Nanocluster. *J. Am. Chem. Soc.* 137, 11970–11975.
- Krishnadas, K. R.; Ghosh, A.; Baksi, A.; Chakraborty, I.; Natarajan, G.; Pradeep, T. (2016) Intercluster Reactions between Au₂₅(SR)₁₈ and Ag₄₄(SR)₃₀. *J. Am. Chem. Soc.* 138 (1), 140–148.
- Krishnadas, K. R.; Baksi, A.; Ghosh, A.; Natarajan, G.; Pradeep, T. (2016) Structure-Conserving Spontaneous Transformations between Nanoparticles. *Nat. Commun.* 7, 1–9.
- Krishnadas, K. R.; Baksi, A.; Ghosh, A.; Natarajan, G.; Som, A.; Pradeep, T. (2017) Interparticle Reactions: An Emerging Direction in Nanomaterials Chemistry. *Acc. Chem. Res.* 50 (8), 1988–1996.
- Neumaier, M.; Baksi, A.; Weis, P.; Schneider, E. K.; Chakraborty, P.; Hahn, H.; Pradeep, T.; Kappes, M. M. (2021) Kinetics of Intercluster Reactions between Atomically Precise Noble Metal Clusters [Ag₂₅(DMBT)₁₈]- and [Au₂₅(PET)₁₈]- in Room Temperature Solutions. *J. Am. Chem. Soc.* 143 (18), 6969–6980.
- Khatun, E.; Chakraborty, P.; Jacob, B. R.; Paramasivam, G.; Bodiuzzaman, M.; Dar, W. A.; Pradeep, T. (2020) Intercluster Reactions Resulting in Silver-Rich Trimetallic Nanoclusters. *Chem. Mater.* 32 (1), 611–619.
- Chakraborty, P.; Nag, A.; Natarajan, G.; Bandyopadhyay, N.; Paramasivam, G.; Panwar, M. K.; Chakrabarti, J.; Pradeep, T. (2019) Rapid Isotopic Exchange in Nanoparticles. *Sci. Adv.* 5, 2–10.
- Baksi, A.; Harvey, S. R.; Natarajan, G.; Wysocki, V. H.; Pradeep, T. (2016) Possible Isomers in Ligand Protected Ag₁₁ Cluster Ions Identified by Ion Mobility Mass Spectrometry and Fragmented by Surface Induced Dissociation. *Chem. Commun.* 52 (19), 3805–3808.
- Chakraborty, P.; Nag, A.; Paramasivam, G.; Natarajan, G.; Pradeep, T. (2018) Fullerene-Functionalized Monolayer-Protected Silver Clusters: [Ag₂₉(BDT)₁₂(C₆₀)_n]³⁻ n= 1-9. *ACS Nano* 12, 2415–2425.
- Nag, A.; Chakraborty, P.; Paramasivam, G.; Bodiuzzaman, M.; Natarajan, G.; Pradeep, T. (2018) Isomerism in Supramolecular Adducts of Atomically Precise Nanoparticles. *J. Am. Chem. Soc.* 140 (42), 13590–13593.
- Jana, A.; Pradeep, T. (2023) Nanocluster assembled solids. Chapter 3, Elsevier, 49–82.
- Antonello, S.; Dainese, T.; Pan, F.; Rissanen, K.; Maran, F. (2017) Electrocrystallization of Monolayer-Protected Gold Clusters: Opening the Door to Quality, Quantity, and New Structures. *J. Am. Chem. Soc.* 139, 4168–4174.
- Jadzinsky, P. D.; Calero, G.; Ackerson, C. J.; Bushnell, D. A.; Kornberg, R. D. (2007) Structure of a Thiol Monolayer-Protected Gold Nanoparticle at 1.1 Å Resolution. *Science* 318, 430–434.
- Azubel, M.; Koivisto, J.; Malola, S.; Bushnell, D.; Hura, G. L.; Koh, A. L.; Tsunoyama, H.; Tsukuda, T.; Pettersson, M.; Häkkinen, H.; Kornberg, R. D. (2014) Electron Microscopy of Gold Nanoparticles

- at Atomic Resolution. *Science* 345 (6199), 909–912.
23. Liu, X.; Yan, H.; Chen, Y.; Yang, Y.; Porcar, L.; Radulescu, A.; Guldin, S.; Jin, R.; Stellacci, F.; Luo, Z. (2022) Quantifying the Solution Structure of Metal Nanoclusters Using Small-Angle Neutron Scattering. *Angew. Chemie Int. Ed.* 61, 1–7.
 24. Wang, S.; Liu, T.; Jiang, D. E. (2021) Locating Hydrides in Ligand-Protected Copper Nanoclusters by Deep Learning. *ACS Appl. Mater. Interfaces* 13 (45), 53468–53474.
 25. Shichibu, Y.; Negishi, Y.; Watanabe, T.; Chaki, N. K.; Kawaguchi, H.; Tsukuda, T. (2007) Biicosahedral Gold Clusters [Au₂₅(PPh₃)₁₀(SCnH_{2n+1})₅Cl]₂⁺ (n = 2–18): A Stepping Stone to Cluster-Assembled Materials. *J. Phys. Chem. Lett.* 111 (22), 7845–7847.
 26. Jin, R.; Liu, C.; Zhao, S.; Das, A.; Xing, H.; Gayathri, C.; Xing, Y.; Rosi, N. L.; Gil, R. R.; Jin, R. (2015) Tri-Icosahedral Gold Nanocluster [Au₃₇(PPh₃)₁₀(SC₂H₄Ph)₁₀X]₂⁺: Linear Assembly of Icosahedral Building Blocks. *ACS Nano* 9 (8), 8530–8536.
 27. Yuan, S. F.; Xu, C. Q.; Liu, W. D.; Zhang, J. X.; Li, J.; Wang, Q. M. (2021) Rod-Shaped Silver Supercluster Unveiling Strong Electron Coupling between Substituent Icosahedral Units. *J. Am. Chem. Soc.* 143 (31), 12261–12267.
 28. Song, Y.; Fu, F.; JunZhang; Chai, J.; Kang, X.; Li, P.; Li, S.; Zhou, H.; Zhu, M. (2015) The Magic Au₆₀ Nanocluster: A New Cluster-Assembled Material with Five Au₁₃ Building Blocks. *Angew. Chemie - Int. Ed.* 54, 8430–8434.
 29. Malola, S.; Lehtovaara, L.; Knoppe, S.; Hu, K. J.; Palmer, R. E.; Bürgi, T.; Häkkinen, H. (2012) Au₄₀(SR)₂₄ Cluster as a Chiral Dimer of 8-Electron Superatoms: Structure and Optical Properties. *J. Am. Chem. Soc.* 134 (48), 19560–19563.
 30. Malola, S.; Lehtovaara, L.; Häkkinen, H. (2014) A DFT Study of Linear Gold-Thiolate Superclusters Absorbing in the Therapeutic NIR Window. *J. Phys. Chem. Lett.* 5 (8), 1329–1334.
 31. Du, X.; Chai, J.; Yang, S.; Li, Y.; Higaki, T.; Li, S.; Jin, R. (2019) Fusion Growth Patterns in Atomically Precise Metal Nanoclusters. *Nanoscale* 11 (41), 19158–19165.
 32. Hu, F.; Guan, Z. J.; Yang, G.; Wang, J. Q.; Li, J. J.; Yuan, S. F.; Liang, G. J.; Wang, Q. M. (2021) Molecular Gold Nanocluster Au₁₅₆ Showing Metallic Electron Dynamics. *J. Am. Chem. Soc.* 143 (41), 17059–17067.
 33. Sakthivel, N. A.; Shabanezhad, M.; Sementa, L.; Yoon, B.; Stener, M.; Whetten, R. L.; Ramakrishna, G.; Fortunelli, A.; Landman, U.; Dass, A. (2020) The Missing Link: Au₁₉₁(SPh-TBu)₆₆ Janus Nanoparticle with Molecular and Bulk-Metal-like Properties. *J. Am. Chem. Soc.* 142 (37), 15799–15814.
 34. Zhou, M.; Zeng, C.; Song, Y.; Padelford, J. W.; Wang, G.; Sfeir, M. Y.; Higaki, T.; Jin, R. (2017) On the Non-Metallicity of 2.2 nm Au₂₄₆(SR)₈₀ Nanoclusters. *Angew. Chemie - Int. Ed.* 56 (51), 16257–16261.
 35. Ma, M. X.; Ma, X. L.; Liang, G. M.; Shen, X. T.; Ni, Q. L.; Gui, L. C.; Wang, X. J.; Huang, S. Y.; Li, S. M. (2021) A Nanocluster [Ag₃₀₇Cl₆₂(SPh₂Bu)₁₁₀]: Chloride Intercalation, Specific Electronic State, and Superstability. *J. Am. Chem. Soc.* 143, 13731–13737.
 36. Zhou, Q.; Kaappa, S.; Malola, S.; Lu, H.; Guan, D.; Li, Y.; Wang, H.; Xie, Z.; Ma, Z.; Häkkinen, H.; Zheng, N.; Yang, X.; Zheng, L. (2018) Real-Space Imaging with Pattern Recognition of a Ligand-Protected Ag₃₇₄ Nanocluster at Sub-Molecular Resolution. *Nat. Commun.* 9, 1–8.
 37. Song, Y.; Lambright, K.; Zhou, M.; Kirschbaum, K.; Xiang, J.; Xia, A.; Zhu, M.; Jin, R. (2018) Large-Scale Synthesis, Crystal Structure, and Optical Properties of the Ag₁₄₆Br₂(SR)₈₀ Nanocluster. *ACS Nano* 12, 9318–9325.
 38. Chen, Y.; Zeng, C.; Kauffman, D. R.; Jin, R. (2015) Tuning the Magic Size of Atomically Precise Gold Nanoclusters via Isomeric Methylbenzenethiols. *Nano Lett.* 15 (5), 3603–3609.
 39. Kang, X.; Chong, H.; Zhu, M. (2018) Au₂₅(SR)₁₈: The Captain of the Great Nanocluster Ship. *Nanoscale* 10 (23), 10758–10834.
 40. Joshi, C. P.; Bootharaju, M. S.; Alhilaly, M. J.; Bakr, O. M. (2015) [Ag₂₅(SR)₁₈]- The “Golden” Silver Nanoparticle Silver Nanoparticle. *J. Am. Chem. Soc.* 137 (36), 11578–11581.
 41. Li, Y.; Zhou, M.; Song, Y.; Higaki, T.; Wang, H.; Jin, R. (2021) Double-Helical Assembly of Heterodimeric Nanoclusters into Supercrystals. *Nature* 594, 380–384.
 42. Zhu, Y.; Guo, J.; Qiu, X.; Zhao, S.; Tang, Z. (2021) Optical Activity of Chiral Metal Nanoclusters. *Accounts Mater. Res.* 2 (1), 21–35.
 43. Liang, X. Q.; Li, Y. Z.; Wang, Z.; Zhang, S. S.; Liu, Y. C.; Cao, Z. Z.; Feng, L.; Gao, Z. Y.; Xue, Q. W.; Tung, C. H.; Sun, D. (2021) Revealing the Chirality Origin and Homochirality Crystallization of Ag₁₄ Nanocluster at the Molecular Level. *Nat. Commun.* 12 (1), 1–10.
 44. Huang, J. H.; Wang, Z. Y.; Zang, S. Q.; Mak, T. C. W. (2020) Spontaneous Resolution of Chiral Multi-Thiolate-Protected Ag₃₀ Nanoclusters. *ACS Cent. Sci.* 6 (11), 1971–1976.
 45. Yoshida, H.; Ehara, M.; Priyakumar, U. D.; Kawai, T.; Nakashima, T. (2020) Enantioseparation and Chiral Induction in Ag₂₉ Nanoclusters with Intrinsic Chirality. *Chem. Sci.* 11 (9), 2394–2400.
 46. Jana, A.; Unnikrishnan, P. M.; Poonia, A. K.; Roy, J.; Jash, M.; Paramasivam, G.; Machacek, J.; Adarsh, K. N. V. D.; Base, T.; Pradeep, T. (2022) Carboranethiol-Protected Propeller-Shaped Photoresponsive Silver Nanomolecule. *Inorg. Chem.* 61 (23), 8593–8603.
 47. Nag, A.; Chakraborty, P.; Bodiuzzaman, M.; Ahuja, T.; Antharjanam, S.; Pradeep, T. (2018) Polymorphism of Ag₂₉(BDT)₁₂(TPP)₄₃- Cluster: Interactions of Secondary Ligands and Their Effect on Solid State Luminescence. *Nanoscale* 10 (21), 9851–9855.
 48. Chen, Y.; Liu, C.; Tang, Q.; Zeng, C.; Higaki, T.; Das, A.; Jiang, D. (2016) Isomerism in Au₂₈(SR)₂₀ Nanocluster and Stable Structures. *J. Am. Chem. Soc.* 138, 1482–1485.
 49. Bodiuzzaman, M.; Dar, W. A.; Pradeep, T. (2021) Cocrystals of Atomically Precise Noble Metal Nanoclusters. *Small* 17 (27), 1–15.
 50. Yan, J.; Malola, S.; Hu, C.; Peng, J.; Dittich, B.; Teo, B. K.; Häkkinen, H.; Zheng, L.; Zheng, N. (2018) Co-Crystallization of Atomically Precise Metal Nanoparticles Driven by Magic Atomic and Electronic Shells. *Nat. Commun.* 9 (1), 1–8.
 51. Bodiuzzaman, M.; Ghosh, A.; Sugi, K. S.; Nag, A.; Khatun, E. (2019) Camouflaging Structural Diversity : Co-Crystallization of Two Different Nanoparticles Having Different Cores but the Same Shell. *Angew. Chemie - Int. Ed.* 58, 189–194.
 52. Dar, W. A.; Bodiuzzaman, M.; Ghosh, D.; Paramasivam, G.; Khatun, E.; Sugi, K. S.; Pradeep, T. (2019) Interparticle Reactions between Silver Nanoclusters Leading to Product Cocrystals by Selective Cocrystallization. *ACS Nano* 13, 13365–13373.
 53. Kang, X.; Zhu, M. (2020) Cocrystallization of Atomically Precise Nanoclusters. *ACS Mater. Lett.* 2 (10), 1303–1314.
 54. Liu, J. Y.; Alkan, F.; Wang, Z.; Zhang, Z. Y.; Kurmo, M.; Yan, Z.; Zhao, Q. Q.; Aikens, C. M.; Tung, C. H.; Sun, D. (2019) Different Silver Nanoparticles in One Crystal: Ag₂₁₀(IPrPhS)₇₁(Ph₃P)₅Cl and Ag₂₁₁(IPrPhS)₇₁(Ph₃P)₆Cl. *Angew. Chemie - Int. Ed.* 58, 195–199.
 55. Huang, R. W.; Wei, Y. S.; Dong, X. Y.; Wu, X. H.; Du, C. X.; Zang, S. Q.; Mak, T. C. W. (2017) Hypersensitive Dual-Function Luminescence Switching of a Silver-Chalcogenolate Cluster-Based Metal-Organic Framework. *Nat. Chem.* 9 (7), 689–697.
 56. Wang, Z.; Wang, M.; Li, Y.; Luo, P.; Jia, T.; Huang, R.; Zang, S.; Mak, T. C. W. (2018) Atomically Precise Site-Specific Tailoring and Directional Assembly of Supramolecular Silver Nanoclusters. *J. Am. Chem. Soc.* 140, 1069–1076.
 57. Dar, W. A.; Jana, A.; Sugi, K. S.; Paramasivam, G.; Bodiuzzaman, M.; Khatun, E.; Som, A.; Mahendranath, A.; Chakraborty, A.; Pradeep, T. (2022) Molecular Engineering of Atomically Precise Silver Clusters into 2D and 3D Framework Solids. *Chem. Mater.* 34 (10), 4703–4711.
 58. Wang, Y. M.; Zhang, Q. W.; Wang, Q. Y.; Li, H. Y.; Dong, X. Y.; Wang, S.; Zang, S. Q. (2019) Fabrication of Silver Chalcogenolate Cluster Hybrid Membranes with Enhanced Structural Stability and Luminescence Efficiency. *Chem. Commun.* 55 (97), 14677–14680.
 59. Kang, X.; Zhu, M. (2019) Tailoring the Photoluminescence of Atomically Precise Nanoclusters. *Chem. Soc. Rev.* 48, 2422–2457.
 60. Chen, Y.; Zhou, M.; Li, Q.; Gronlund, H.; Jin, R. (2020) Isomerization-Induced Enhancement of Luminescence in Au₂₈(SR)₂₀ nanoclusters. *Chem. Sci.* 11, 8176–8183.
 61. Goswami, N.; Yao, Q.; Luo, Z.; Li, J.; Chen, T.; Xie, J. (2016) Luminescent Metal Nanoclusters with Aggregation-Induced Emission. *J. Phys. Chem. Lett.* 7, 962–975.
 62. Kang, X.; Wang, S.; Zhu, M. (2018) Observation of a New Type of Aggregation-Induced Emission in Nanoclusters. *Chem. Sci.* 9, 3062–3068.
 63. Khatun, E.; Ghosh, A.; Chakraborty, P.; Singh, P.; Bodiuzzaman, M.; Ganesan, P.; Natarajan, G.; Ghosh, J.; Pal, S. K.; Pradeep, T. (2018) A Thirty-Fold Photoluminescence Enhancement Induced by Secondary Ligands in Monolayer Protected Silver Clusters. *Nanoscale* 10 (42), 20033–20042.
 64. Chen, T.; Yang, S.; Chai, J.; Song, Y.; Fan, J.; Rao, B.; Sheng, H.; Yu, H.; Zhu, M. (2017) Crystallization-Induced Emission Enhancement: A Novel Fluorescent Au-Ag Bimetallic Nanocluster with Precise Atomic Structure. *Sci. Adv.* 3, 1–8.
 65. Khatun, E.; Bodiuzzaman, M.; Sugi, K. S.; Chakraborty, P.; Paramasivam, G.; Dar, W. A.; Ahuja, T.; Antharjanam, S.; Pradeep, T. (2019) Confining an Ag₁₀ Core in an Ag₁₂ Shell: A Four-Electron Superatom with Enhanced Photoluminescence upon Crystallization. *ACS Nano* 13 (5), 5753–5759.
 66. Jana, A.; Jash, M.; Poonia, A. K.; Paramasivam, G.; Islam, M. R.; Chakraborty, P.; Antharjanam, S.; Machacek, J.; Ghosh, S.; Adarsh, K. N. V. D.; Base, T.; Pradeep, T. (2021) Light-Activated Intercluster Conversion of an Atomically Precise Silver Nanocluster. *ACS Nano* 15 (10), 15781–15793.
 67. Wang, Z.; Su, H.; Tan, Y.; Schein, S.; Lin, S.; Liu, W.; Wang, S.; Wang, W.; Tung, C.; Sun, D.; Zheng, L. (2017) Assembly of Silver Trigons into a Buckyball-like Ag₁₈₀ Nanocage. *Proc. Natl. Acad. Sci. U. S. A.* 114(46), 12132–12137.
 68. Li, Q.; Mosquera, M. A.; Jones, L. O.; Parakh, A.; Chai, J.; Jin, R.; Schatz, G. C.; Gu, X. W. (2020) Pressure-Induced Optical Transitions in Metal Nanoclusters. *ACS Nano* 14, 11888–11896.
 69. Sun, Q.-Q.; Li, Q.; Li, H.-Y.; Zhang, M.-M.; Sun, M.-E.; Li, S.; Quan, Z.; Zang, S.-Q. (2021) Thermochromism and Piezochromism of an Atomically Precise High-Nuclearity Silver Sulfide Nanocluster. *Chem. Commun.* 57, 2372–2375.
 70. Wang, Z.; Su, H. F.; Gong, Y. W.; Qu, Q. P.; Bi, Y. F.; Tung, C. H.; Sun, D.; Zheng, L. S. (2020) A Hierarchically Assembled 88-Nuclei Silver-Thiacalix[4]Arene Nanocluster. *Nat. Commun.* 11, 1–8.
 71. Li, Q.; Russell, J. C.; Luo, T. Y.; Roy, X.; Rosi, N. L.; Zhu, Y.; Jin, R. (2018) Modulating the Hierarchical Fibrous Assembly of Au Nanoparticles with Atomic Precision. *Nat. Commun.* 9, 1–7.
 72. Yuan, P.; Zhang, R.; Selenius, E.; Ruan, P.; Yao, Y.; Zhou, Y.; Malola, S.; Häkkinen, H.; Teo, B. K.; Cao, Y.; Zheng, N. (2020). Solvent-Mediated Assembly of Atom-Precise Gold–Silver Nanoclusters to Semiconducting One-Dimensional Materials. *Nat. Commun.* 11, 1–8.
 73. Feng, A.; Hou, S.; Yan, J.; Wu, Q.; Tang, Y.; Yang, Y.; Shi, J.; Xiao, Z.; Lambert, C. J.; Zheng, N.; Hong, W. (2022). Conductance Growth of Single-Cluster Junctions with Increasing Sizes. *J. Am. Chem. Soc.* 144 (34), 15680–15688.

Existence of Acetaldehyde Clathrate Hydrate and Its Dissociation Leading to Cubic Ice under Ultrahigh Vacuum and Cryogenic Conditions

Gaurav Vishwakarma, Bijesh K. Malla, Soham Chowdhury, Sakshi Pradip Khandare, and Thalappil Pradeep*



Cite This: *J. Phys. Chem. Lett.* 2023, 14, 5328–5334



Read Online

ACCESS |



Metrics & More

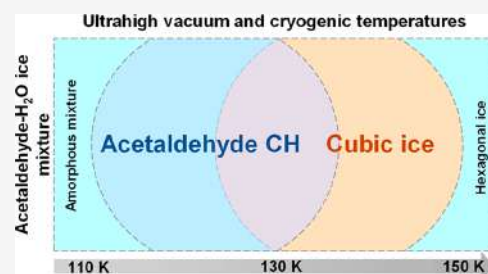


Article Recommendations



Supporting Information

ABSTRACT: Acetaldehyde in a dilute aqueous solution gets hydrated to produce a geminal diol under atmospheric conditions. The acetaldehyde–water ice system under high pressure also converts to a geminal diol, and therefore, its stable clathrate hydrate (CH) phase, which in most systems forms at high pressures, is unknown. In the present study, we showed that acetaldehyde CH exists in ultrahigh vacuum (10^{-10} mbar) under cryogenic conditions (below 140 K) and continues to exist at 115 K for periods well over 1 day. Decomposition of acetaldehyde CH at 130–135 K produces water ice in its cubic crystalline form. The mechanism and kinetics involved in the process have also been studied. Reflection absorption infrared spectroscopy and temperature-programmed desorption mass spectrometry were utilized to confirm the CH formation. Our study establishes the possibility of a stable CH phase for acetaldehyde in interstellar and cometary environments.



The existence of the clathrate hydrates (CHs) of several simple molecules in ultrahigh vacuum (UHV) and cryogenic conditions is now well established; examples include CH_4 ,¹ CO_2 ,^{1,2} C_2H_6 ,³ acetone,⁴ formaldehyde,⁵ and THF.^{2,6} Some of these CHs dissociate leading to cubic ice (ice I_c),⁴ while others form hexagonal ice (ice I_h),⁵ although CH to crystalline ice transformation under high-pressure conditions was known even earlier.^{7–12} Exploration of CH phases in vacuum conditions continues with various simple molecules.¹³ An important possibility is the occurrence of unique CH phases for certain molecules, hitherto unknown.

CHs are a class of host–guest compounds wherein water within its hydrogen-bonded cages hosts guest molecules such as CH_4 , CO_2 , H_2S , etc.¹⁴ Depending on the molecular size and chemical behavior of guest molecules, these CHs are known to exist mainly in two structures, namely structure I (sI) and structure II (sII). Such structures exist at moderately low temperatures and high pressures. However, until now, a stable CH phase of acetaldehyde has not been observed.^{15,16} This is because acetaldehyde in dilute aqueous solution and in the solid state converts to a geminal diol under atmospheric pressure.^{15,17} The hydration of acetaldehyde to a geminal diol was confirmed by calorimetric and spectrophotometric methods.^{17–19} Even incorporating a “help guest” to stabilize the acetaldehyde CH was found to be ineffective, as it became a geminal diol under high pressure. However, the geminal diol formed was subsequently transformed to its CH phase under a high pressure of 120 bar at 253.¹⁶ In view of this thermodynamically stable geminal diol, the existence of

acetaldehyde CH has not been observed so far. We thought it instructive to explore the existence of acetaldehyde CH in UHV and cryogenic conditions.

Water ice is pervasive in terrestrial and extraterrestrial environments and exists in various amorphous and crystalline forms.^{20,21} Among the all-crystalline forms, ice I_h is the most stable and prevalent crystalline form of ice under Earth’s conditions.²² However, the preparation and study of ice I_c have drawn close attention of the scientific community due to its importance to extraterrestrial environments, Earth’s atmosphere, cryopreservation, and climate change.^{9,23–26} Among the main established routes for forming ice I_c ,²⁶ studying its formation via CH dissociation under UHV and cryogenic conditions will be of importance for cometary and interstellar environments.^{4,27,28}

In the following, we present a systematic study of the transformation of acetaldehyde in its water ice mixture to its CH phase at 115 K. This transformation was studied by reflection absorption infrared spectroscopy (RAIRS) and temperature-programmed desorption mass spectrometry (TPD-MS). Further, the dissociation of acetaldehyde CH at

Received: May 1, 2023

Accepted: June 1, 2023

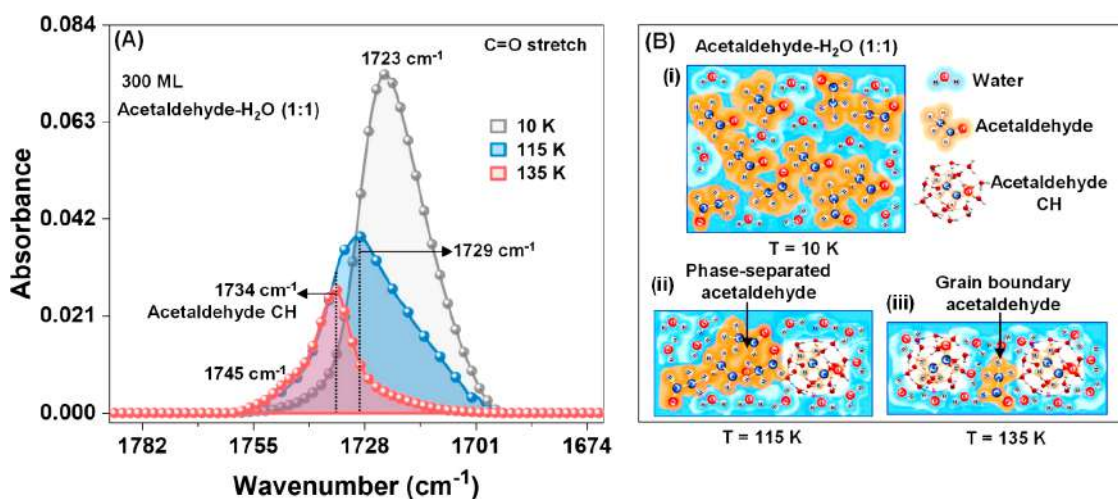


Figure 1. Formation of acetaldehyde CH under UHV conditions, as observed using the C=O stretching region. (A) Temperature-dependent RAIR spectra of 300 ML of acetaldehyde–H₂O (1:2) film in the C=O stretching region. The peaks at 1729 and 1734 cm⁻¹ are marked by vertical dashed lines. The ice mixture was codeposited on a Ru(0001) substrate at 10 K and annealed at a rate of 2 K·min⁻¹ to the set temperatures. (B) Schematic representation of stepwise evolution of ice mixture upon thermal annealing. Change in the thickness of the composite film is a result of acetaldehyde desorption, as implied in (i–iii).

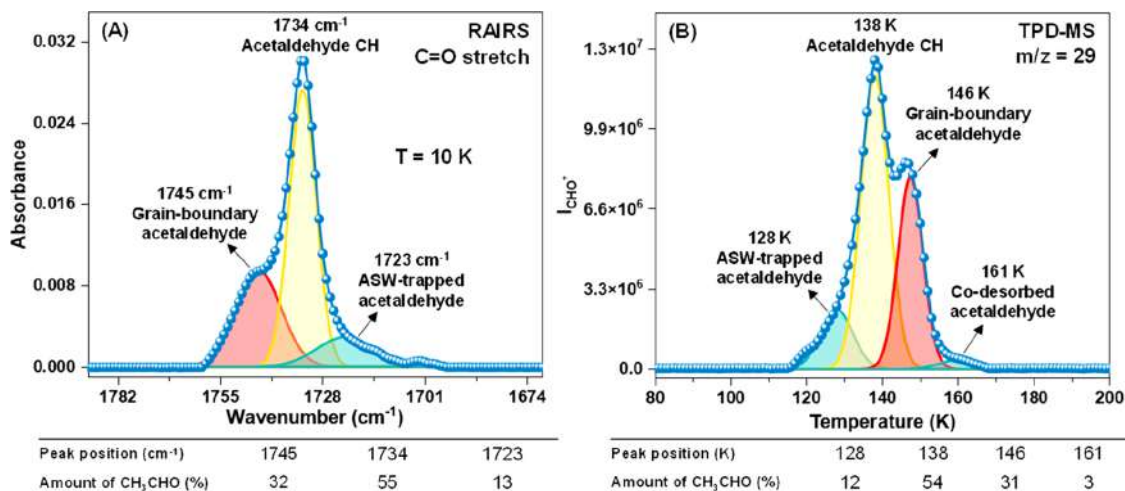


Figure 2. (A) RAIR spectrum of 300 ML of acetaldehyde–H₂O (1:2) film at 10 K in the C=O stretching region, after forming CH. For this measurement, the ice mixture was prepared by codeposition on a Ru(0001) substrate at 10 K and annealed at a rate of 2 K·min⁻¹ to 137 K to form acetaldehyde CH. The resulting ice at 137 K was cooled to 10 K, and the RAIR spectrum was measured. The C=O stretching band was deconvoluted to estimate the fractions of different phases of acetaldehyde in the H₂O matrix. (B) TPD-MS spectrum of the same system. After RAIRS data acquisition at 10 K, the TPD-MS spectrum was collected by annealing the substrate at a rate of 30 K·min⁻¹ to 200 K. In the spectrum, the intensity of CHO⁺ (*m/z* = 29) is plotted as a function of substrate temperature. The TPD spectrum in the temperature window of 80–200 K was deconvoluted to estimate the different fractions of acetaldehyde in the H₂O matrix. The tables at the bottom of Figures (A) and (B) present the fractions of acetaldehyde in different phases obtained from the corresponding RAIR and TPD-MS spectra.

130–135 K and subsequent formation of ice I_c were studied. The associated kinetics parameters and activation energy for the conversion of “the CH phase to ice I_c” were estimated.

Acetaldehyde CH was prepared by thermal annealing of an acetaldehyde–H₂O (1:2) ice mixture under UHV. Figure 1A shows the temperature-dependent RAIR spectra of 300 ML of acetaldehyde–H₂O (1:2) film in the C=O stretching region. The spectrum collected just after vapor deposition of the ice mixture at 10 K shows a peak at 1723 cm⁻¹, which is attributed to the interaction of acetaldehyde with water ice. When the ice mixture was annealed from 10 to 115 K, a peak at 1729 cm⁻¹ along with a shoulder at 1734 cm⁻¹ appeared (marked by vertical dashed lines). The peak at 1729 cm⁻¹ is due to the pure solid acetaldehyde, which was confirmed by comparing it

with the RAIR spectrum of pure acetaldehyde, shown in Figure S1. This suggests that acetaldehyde got phase separated in the water matrix during annealing.²⁹ However, the shoulder at 1734 cm⁻¹ is an entirely new IR feature and is attributed to acetaldehyde CH. The basis of this assignment is some previous studies,^{1,4,5,30,31} which suggest that the vibrational frequency of the guest molecules trapped in CH cages usually falls in between their condensed (1729 cm⁻¹) and vapor (1746 cm⁻¹)^{32,33} phase frequencies. Therefore, the peak at 1734 cm⁻¹ in the C=O stretching region may be assigned to acetaldehyde CH. This assignment is further supported by the following observation. Upon further annealing the ice mixture to 135 K, the peak at 1723 cm⁻¹ vanished due to the desorption of phase-separated acetaldehyde from ice matrix, while the peak

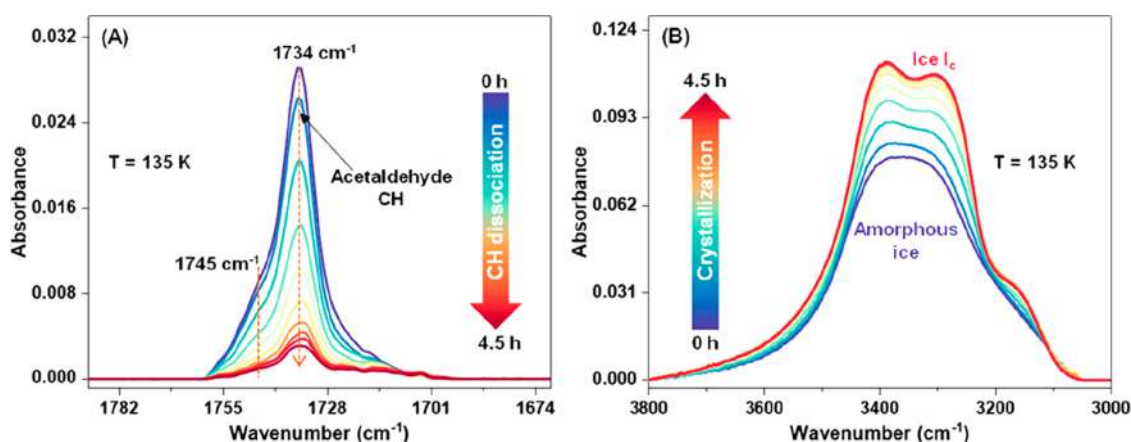


Figure 3. Ice I_c formation via acetaldehyde CH. RAIR spectra of 300 ML of acetaldehyde– H_2O (1:2) film at 135 K in the (A) C=O and (B) O–H stretching regions. The ice mixture was codeposited on a Ru(0001) substrate at 10 K and annealed at a rate of $2\text{ K}\cdot\text{min}^{-1}$ to 135 K. Upon isothermal annealing at 135 K, the peak at 1734 cm^{-1} diminishes with time due to the dissociation of acetaldehyde CH, which resulted in ice I_c .

at 1734 cm^{-1} remained because of the trapping of acetaldehyde in CH cages.^{1,4,5} Notably, at higher temperatures, a small, broad peak at 1745 cm^{-1} appeared (along with 1734 cm^{-1}), which was assigned to grain-boundary acetaldehyde,³⁴ in other words, acetaldehyde that was trapped into intergrain regions. The primary reason for this assignment is that the vibrational feature at 1745 cm^{-1} is broad (due to a random distribution of acetaldehyde in the grain boundaries) and is very close to the gas phase vibrational feature (1746 cm^{-1})^{32,33} of acetaldehyde. Figure 1B illustrates schematically the stepwise physical change that occurs upon annealing the acetaldehyde– H_2O (1:2) ice mixture from 10 to 135 K. Further, the stability of acetaldehyde CH was investigated in a separate time-dependent RAIRS experiment performed at 115 K for 27 h. The result presented in Figure S2A suggests that the acetaldehyde CH phase is not only stable at 115 K under UHV but also does not convert to the geminal diol.

To get a clearer picture and further confirm the CH formation, we have carried out a TPD experiment, and the outcome was correlated with the RAIRS results of the same sample. For this, we have prepared a 300 ML acetaldehyde– H_2O (1:2) film at 10 K and annealed it to 137 K at a rate of $2\text{ K}\cdot\text{min}^{-1}$ to form acetaldehyde CH, free of phase-separated acetaldehyde (which would have desorbed during annealing as shown in Figure 1A). The prepared sample was cooled back to 10 K. Just after cooling back to 10 K, the RAIR spectrum was collected as shown in Figure 2A, which shows three peaks at 1745 cm^{-1} (broad), 1734 cm^{-1} (sharp), and $\sim 1723\text{ cm}^{-1}$ (weak and broad) in the C=O stretching region, attributed to the grain-boundary acetaldehyde (32% of the total acetaldehyde present in ice matrix at this condition), acetaldehyde CH (55%), and a dilute mixture of acetaldehyde in water ice (13%), respectively. The table (below Figure 2A) shows the fractions of acetaldehyde in different phases, and they were obtained by deconvoluting the RAIR spectrum presented in Figure 2A. After IR spectral acquisition at 10 K, the sample was annealed at a rate of $30\text{ K}\cdot\text{min}^{-1}$ to 200 K, and the TPD spectrum was collected as shown in Figure 2B. The thermal desorption trace of acetaldehyde was obtained by plotting the intensity of CHO^+ ($m/z = 29$) as a function of temperature. Figure 2B shows four desorption peaks at 128, 138, 146, and 161 K, which are attributed to the desorption of (1) acetaldehyde that is present in amorphous ice pores (12%), (2) acetaldehyde that was trapped in CH cages (54%), (3)

grain-boundary acetaldehyde (31%), and (4) a small fraction of acetaldehyde that desorbs along with water (3%), respectively. Moreover, the TPD spectrum of pure acetaldehyde shows a desorption peak at $\sim 110\text{ K}$, as shown in Figure S2B. In Figure 2B, the peak at 128 K is due to the premelting of ice that releases some (12%) of acetaldehyde present in the pores of ASW. The total fractions of acetaldehyde trapped in ASW matrix ($12 + 3 = 15\%$) obtained from TPD experiment are comparable to that of 13% estimated from the RAIR spectrum shown in Figure 2A. The assignment of the peak at 146 K as due to grain-boundary acetaldehyde is because it coincides with the amorphous to crystalline transition of ice. When amorphous ice converts to crystalline ice above 140 K, due to the rearrangement of water molecules, the molecular species trapped in the amorphous pores/grain boundaries leave the ice matrix abruptly in an event known as a “molecular volcano”, resulting in a sharp desorption peak of the corresponding species.^{35,36} The peak at 146 K is sharp, which further supports our assignment. The remaining peak at 138 K was assigned to the desorption of acetaldehyde that is trapped in CH cages. This assignment was confirmed by comparing the estimated fractions of acetaldehyde trapped in CH cages obtained from the RAIRS and TPD measurements (see the Tables listed in Figure 2). A good agreement of the fractions of acetaldehyde of different phases estimated from the RAIRS and TPD measurements of the same sample further justified our assignments. Thus, for the first time, we report the formation of stable CH of acetaldehyde prepared under UHV and cryogenic conditions.

CHs are known to dissociate to different crystalline structures.^{4,5,7,8} To explore this possibility, we have carried out a time-dependent RAIRS experiment with 300 ML of acetaldehyde– H_2O (1:2) film at 135 K. The results obtained in the (A) C=O and (B) O–H stretching regions are shown in Figure 3A,B, respectively. Figure 3A shows that after keeping the ice sample at 135 K for 4.5 h, the acetaldehyde CH peak at 1734 cm^{-1} (along with 1745 cm^{-1}) in the C=O stretching region decreases due to CH dissociation. In a similar time scale, the O–H stretching band shown in Figure 3B shows a profound change due to the dissociation of acetaldehyde CH. At 0 h, the broad feature in the O–H stretching region, which is characteristic of amorphous ice, undergoes splitting within 4.5 h. The splitting of the O–H stretching band in the IR spectra is associated with the crystallization of the water ice

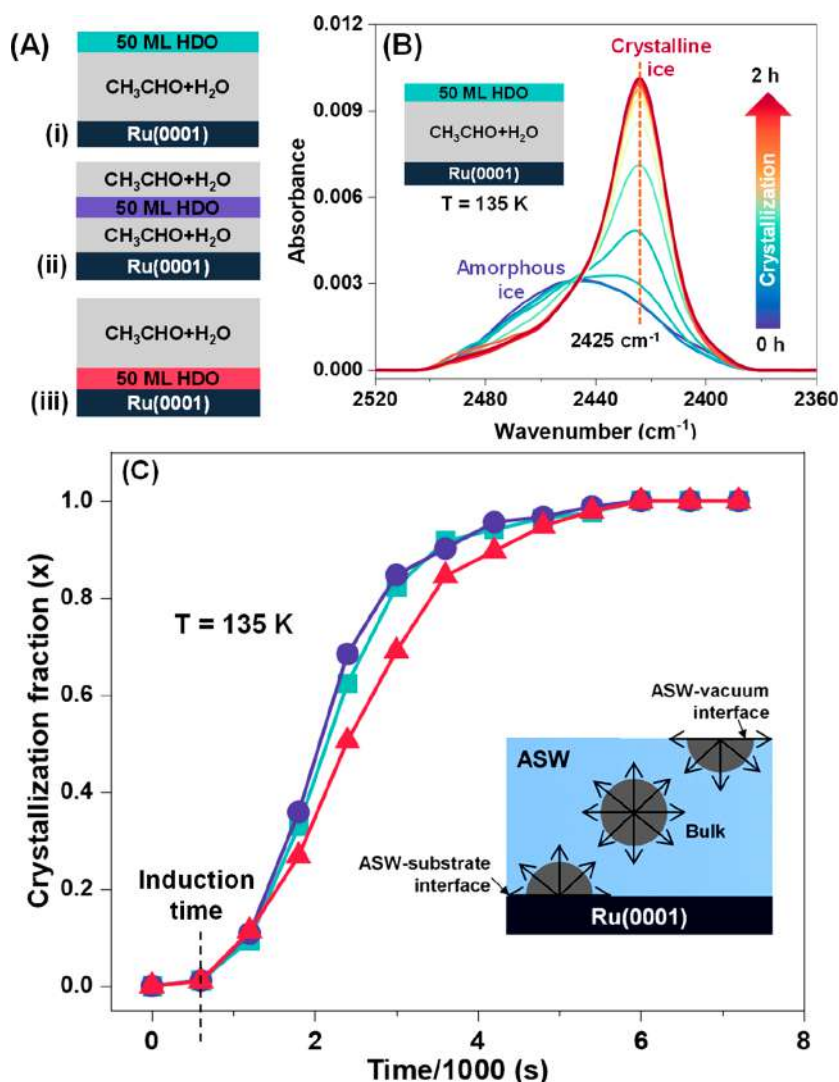


Figure 4. Isothermal RAIRS measurement of the crystallization fraction of a 50 ML HDO layer embedded in 200 ML acetaldehyde–H₂O (1:10) film at 135 K. (A) Structure of composite ice film containing a 50 ML HDO layer at specific positions in a 200 ML acetaldehyde–H₂O (1:10) film, namely, at the top (green layer), in the bulk (blue layer), and at the bottom (red layer). Acetaldehyde–H₂O (1:10) film is indicated by gray layers. (B) Changes in the O–D stretching band of 50 ML HDO, at 135 K with time, shown for the composite film with the HDO layer at the top. (C) Crystallization fraction versus time curves for the 50 ML HDO layer embedded at various positions in the 200 ML acetaldehyde–H₂O (1:10) film. The CF was calculated from a vertical cut at 2425 cm^{−1} in the O–D stretching band of the isothermal RAIR spectra shown in B and Figure S5. The inset of C shows the possibilities of the onset of ASW crystallization, which may initiate at interfaces or in the bulk.

film.^{4,37–39} The spectrum after 4.5 h is attributed to the formation of ice I_c. This assignment was confirmed by comparing the spectrum with the IR spectrum of our previous work⁴ (shown in Figure S3) where cubic ice was prepared using acetone CH. It was confirmed by reflection high energy electron diffraction (RHEED). The RAIR spectra in the O–H stretching region (Figure S3) confirmed the formation of ice I_c after the dissociation of acetaldehyde CH at 135 K. However, 150 ML of pure ASW does not undergo crystallization at 130–135 K in similar experimental conditions. Results of isothermal annealing of ASW are shown in Figure S4. We conclude that acetaldehyde CH at 135 K under UHV dissociates to form cubic crystalline ice.

To understand the mechanism of CH dissociation and subsequent crystalline ice formation during isothermal experiments, we have carried out an experiment using the “selective placement method”.^{39,40} For this, in three different experiments (see the Experimental Section for details of sample

preparation), we placed a 50 ML HDO (5% D₂O in H₂O) probe layer in 200 ML acetaldehyde–H₂O (1:10) films at specific positions as shown in Figure 4A and evaluated the crystallization fraction by monitoring the evolution in the O–D stretching band of the HDO layer (shown in Figures 4B and S5) at 135 K as a function of crystallization time. Figure 4C shows the change in the crystallization fraction of the 50 ML HDO layer placed at different positions in the 200 ML acetaldehyde–H₂O (1:10) film at the top (green curve), middle (blue curve), and bottom (red curve). Crystallization fractions were calculated from a vertical cut at 2425 cm^{−1} in the O–D stretching band shown in Figures 4B and S5; the first spectrum in each case is from completely amorphous film and the final spectrum is from the completely crystalline film, while the intermediate spectra are a linear combination of amorphous and crystalline spectra. Figure 4C shows that the HDO probe layer placed in the bulk (blue curve) and at the ice–vacuum interface (green curve) crystallized almost at the

Table 1. Kinetics Parameters Estimated Using the Avrami Equation at Various Temperatures

Temperature	130 K	132 K	135 K	137 K
ln (<i>k</i>)	9.2 ± 0.7	8.5 ± 0.7	7.9 ± 0.9	6.3 ± 1.9
<i>n</i>	2.64 ± 0.10	2.13 ± 0.09	1.96 ± 0.12	1.89 ± 0.27

same speed. This suggests that the crystallization initiates at random nucleation sites in bulk and propagates in all directions; that is why the HDO probe layer placed at the bulk and ice–vacuum interface crystallizes at the same speed. This, in turn, implies that the acetaldehyde CHs are distributed all over the ice matrix, and during isothermal annealing, CH dissociates at random places (independent of site, namely in bulk or at interfaces) and induces ASW crystallization. However, the HDO layer placed at the bottom (red curve) of the acetaldehyde–H₂O (1:10) film crystallizes last and with slower kinetics. The reason for this is that the fraction of acetaldehyde CH present in the HDO layer placed at the bottom will be less compared to the other two cases. This is because, during thermal annealing, the possibility of acetaldehyde diffusion and subsequent CH formation in the HDO layer is least among the cases shown in Figure 4A. In conclusion, under UHV and cryogenic conditions, acetaldehyde CH was found to be distributed throughout the ASW matrix in the form of small domains (instead of an extended crystalline phase), and its dissociation leads to the crystallization of ASW which initiates in the bulk, at random locations.

Notably, in Figure 4C, each curve has an induction time of ~10 min. In other words, ASW crystallization starts after 10 min of isothermal annealing of the sample at 135 K. However, acetaldehyde CH dissociation (reduction in the intensity of 1734 cm⁻¹) at 135 K starts from 0 min as shown in Figure S6. That means, at first, CH dissociation takes place followed by the onset of ASW crystallization. It confirms our interpretation of the 138 and 146 K peaks in TPD-MS data (shown in Figure 2B) as due to the desorption of acetaldehyde trapped in CH cages and grain boundaries, respectively. This is explained by the fact that at ~138 K CH dissociates leading to the desorption of acetaldehyde, and this initiates the crystallization of ASW. During ASW crystallization, water molecules undergo rearrangement, which will lead to the desorption of acetaldehyde that exists in grain boundaries of the ASW matrix at temperatures >140 K.

Our claim of acetaldehyde CH formation and subsequent crystallization of ASW to ice I_c was further confirmed in several control experiments. (1) A temperature-dependent RAIRS experiment with acetaldehyde–D₂O (1:2) film was carried out, and the results are shown in Figure S7. Figure S7 shows that acetaldehyde forms CH with D₂O, and its subsequent dissociation leads to the formation of ice I_c. (2) A temperature-dependent RAIRS experiment with sequentially deposited acetaldehyde@H₂O film also resulted in acetaldehyde CH followed by ice I_c at higher temperatures (Figure S8). Further, considering the cometary environment where such guest molecules are less abundant, we have performed a time-dependent RAIRS experiment with dilute mixtures of acetaldehyde–H₂O (1:20 and 1:40) at 135 K. The results from these two experiments (Figures S9 and S10) show the formation of acetaldehyde CH and subsequent ice I_c.

Kinetic parameters of ice I_c crystallization via acetaldehyde CH were evaluated using the Avrami equation by conducting time-dependent RAIRS experiments with 300 ML of

acetaldehyde–H₂O (1:10) film in the temperature range of 130–135 K (Figure S11).^{41,42} The methods utilized for the estimation of various kinetic parameters for ice I_c crystallization are the same as discussed in our previous papers^{4,5,38,39} and are briefly described in the Supporting Information. Table 1 summarizes the estimated crystallization rate constant (*k*) and Avrami exponent (*n*) at various temperatures evaluated from the time-dependent RAIR spectra shown in Figure S11. At higher temperatures, because of fast CH dissociation, the rate of crystallization will be faster. The estimated values of *n* (2.64–1.89) shown in Table 1 are consistent with the *n* values of our previous study of ice I_c formation via CH dissociation.⁴ The values of *n* suggest that the crystallization kinetics is diffusion-controlled with particles growing into a predominantly spherical geometry.^{4,43–45} Further, the activation energy (*E_a*) of crystallization was estimated (see the details in Supporting Information). The estimated value was 56.6 kJ mol⁻¹ and is comparable to the previously reported^{40,46–49} activation energy values (60–77 kJ mol⁻¹) for the crystallization of pure ASW. This implies that even at low temperatures, the CH dissociation causes enough mobility for the water molecules to overcome the kinetic barrier of crystallization.

In conclusion, we report the existence of elusive acetaldehyde CH under UHV and cryogenic temperatures. We found that acetaldehyde in its ice mixture with water forms CH at 115 K, and the CH phase remains beyond 27 h without converting to a geminal diol. The conversion of acetaldehyde CH to ice I_c (at 130–135 K) and the associated mechanism and kinetics were also studied. Ice I_c via acetaldehyde CH could be one of the routes for the formation of this phase in comets, as ice I_c and CH are reported to exist in such environments.^{27,28,50} While our study established the possibility of several similar molecules in the CH phase, it also points to the existence of such molecular solids in comets, planets, and interstellar environment. The consequence of the CH in deciding the molecular composition of such environments needs further investigation.

■ ASSOCIATED CONTENT

Supporting Information

The Supporting Information is available free of charge at <https://pubs.acs.org/doi/10.1021/acs.jpclett.3c01181>.

Experimental Section (including apparatus, materials and reagents, sample preparation, experimental procedure, RAIRS and TPD-MS setup), temperature- and time-dependent RAIR spectra of pure acetaldehyde and acetaldehyde–H₂O films, time-dependent RAIR spectra of acetaldehyde–H₂O films (in different ratios) at different temperatures, TPD-MS spectra of pure acetaldehyde, crystallization kinetics (PDF)

■ AUTHOR INFORMATION

Corresponding Author

Thalappil Pradeep – DST Unit of Nanoscience (DST UNS) and Thematic Unit of Excellence (TUE), Department of

Chemistry, Indian Institute of Technology Madras, Chennai 600036, India; International Centre for Clean Water, IIT Madras Research Park, Chennai 600113, India;

orcid.org/0000-0003-3174-534X; Email: pradeep@iitm.ac.in

Authors

Gaurav Vishwakarma – DST Unit of Nanoscience (DST UNS) and Thematic Unit of Excellence (TUE), Department of Chemistry, Indian Institute of Technology Madras, Chennai 600036, India

Bijesh K. Malla – DST Unit of Nanoscience (DST UNS) and Thematic Unit of Excellence (TUE), Department of Chemistry, Indian Institute of Technology Madras, Chennai 600036, India

Soham Chowdhury – DST Unit of Nanoscience (DST UNS) and Thematic Unit of Excellence (TUE), Department of Chemistry, Indian Institute of Technology Madras, Chennai 600036, India

Sakshi Pradip Khandare – DST Unit of Nanoscience (DST UNS) and Thematic Unit of Excellence (TUE), Department of Chemistry, Indian Institute of Technology Madras, Chennai 600036, India

Complete contact information is available at:

<https://pubs.acs.org/10.1021/acs.jpclett.3c01181>

Author Contributions

T.P. and G.V. designed the research. T.P. supervised its progress. G.V., B.K.M., S.C., and S.P.K. have performed the experiments. G.V., B.K.M., S.C., S.P.K., and T.P. have analyzed the results. The first draft of manuscript is written by G.V. The final version of manuscript was written with the contributions of all authors.

Notes

The authors declare no competing financial interest.

ACKNOWLEDGMENTS

We acknowledge the Science and Engineering Research Board (SERB), Department of Science and Technology (DST), Government of India for research funding. T.P. acknowledges funding from the Centre of Excellence on Molecular Materials and Functions under the Institution of Eminence scheme of IIT Madras. G.V. and S.C. thank IITM for their research fellowships. B.K.M. thanks the Council of Scientific & Industrial Research (CSIR) for his research fellowship.

REFERENCES

- (1) Ghosh, J.; Methikkalam, R. R. J.; Bhui, R. G.; Ragupathy, G.; Choudhary, N.; Kumar, R.; Pradeep, T. Clathrate Hydrates in Interstellar Environment. *Proc. Natl. Acad. Sci. U. S. A.* **2019**, *116*, 1526–1531.
- (2) Vishwakarma, G.; Malla, B. K.; Reddy, K. S. S. V. P.; Ghosh, J.; Chowdhury, S.; Yamijala, S. S. R. K. C.; Reddy, S. K.; Kumar, R.; Pradeep, T. Induced Migration of CO₂ from Hydrate Cages to Amorphous Solid Water under Ultrahigh Vacuum and Cryogenic Conditions. *J. Phys. Chem. Lett.* **2023**, *14*, 2823–2829.
- (3) Malla, B. K.; Vishwakarma, G.; Chowdhury, S.; Selvarajan, P.; Pradeep, T. Formation of Ethane Clathrate Hydrate in Ultrahigh Vacuum by Thermal Annealing. *J. Phys. Chem. C* **2022**, *126*, 17983–17989.
- (4) Ghosh, J.; Bhui, R. G.; Vishwakarma, G.; Pradeep, T. Formation of Cubic Ice via Clathrate Hydrate, Prepared in Ultrahigh Vacuum under Cryogenic Conditions. *J. Phys. Chem. Lett.* **2020**, *11*, 26–32.
- (5) Ghosh, J.; Vishwakarma, G.; Das, S.; Pradeep, T. Facile Crystallization of Ice I_h via Formaldehyde Hydrate in Ultrahigh Vacuum under Cryogenic Conditions. *J. Phys. Chem. C* **2021**, *125*, 4532–4539.
- (6) Ghosh, J.; Bhui, R. G.; Ragupathy, G.; Pradeep, T. Spontaneous Formation of Tetrahydrofuran Hydrate in Ultrahigh Vacuum. *J. Phys. Chem. C* **2019**, *123*, 16300–16307.
- (7) Kuhs, W. F.; Genov, G.; Staykova, D. K.; Hansen, T. Ice Perfection and Onset of Anomalous Preservation of Gas Hydrates. *Phys. Chem. Chem. Phys.* **2004**, *6*, 4917–4920.
- (8) Falenty, A.; Kuhs, W. F. Self-Preservation of CO₂ Gas Hydrates-Surface Microstructure and Ice Perfection. *J. Phys. Chem. B* **2009**, *113*, 15975–15988.
- (9) Komatsu, K.; Machida, S.; Noritake, F.; Hattori, T.; Sano-Furukawa, A.; Yamane, R.; Yamashita, K.; Kagi, H. Ice Ic without Stacking Disorder by Evacuating Hydrogen from Hydrogen Hydrate. *Nat. Commun.* **2020**, *11*, 464.
- (10) Falenty, A.; Hansen, T. C.; Kuhs, W. F. Cubic Ice Formation and Annealing during CO₂ Clathrate Hydrate Decomposition at Low Temperatures; Hokkaido Univ Press: Sapporo, 2010.
- (11) Takeya, S.; Uchida, T.; Nagao, J.; Ohmura, R.; Shimada, W.; Kamata, Y.; Ebinuma, T.; Narita, H. Particle Size Effect of CH₄ Hydrate for Self-Preservation. *Chem. Eng. Sci.* **2005**, *60*, 1383–1387.
- (12) Falenty, A.; Hansen, T. C.; Kuhs, W. F. Formation and Properties of Ice XVI Obtained by Emptying a Type SII Clathrate Hydrate. *Nature* **2014**, *516*, 231–233.
- (13) Bauer, R. P. C.; Ravichandran, A.; Tse, J. S.; Appathurai, N.; King, G.; Moreno, B.; Desgreniers, S.; Sammynaiken, R. In Situ X-Ray Diffraction Study on Hydrate Formation at Low Temperature in a High Vacuum. *J. Phys. Chem. C* **2021**, *125*, 26892–26900.
- (14) Sloan, E. D. Fundamental Principles and Applications of Natural Gas Hydrates. *Nature* **2003**, *426*, 353–359.
- (15) Davidson, D. W.; Gough, S. R.; Ripmeester, J. A. Dielectric and Nuclear Magnetic Resonance Characterization of Unstable Clathrate Hydrates of Acetaldehyde and Propionaldehyde. *Can. J. Chem.* **1976**, *54*, 3085–3088.
- (16) Kang, H.; Ahn, Y. H.; Koh, D. Y.; Lee, H. Thermodynamic and Spectroscopic Identification of Aldehyde Hydrates. *Korean J. Chem. Eng.* **2016**, *33*, 1897–1902.
- (17) Bell, R. P.; Clunie, J. C. The Hydration of Acetaldehyde in Aqueous Solution. *Trans. Faraday Soc.* **1952**, *48*, 439–442.
- (18) Matsushima, M. The Hydration of Some Organic Compounds in an Aqueous Solution. I. Studies of Aliphatic Aldehydes by Raman-Effect Observation. *Bull. Chem. Soc. Jpn.* **1963**, *36*, 954–960.
- (19) Kurz, J. L. The Hydration of Acetaldehyde. I. Equilibrium Thermodynamic Parameters. *J. Am. Chem. Soc.* **1967**, *89*, 3524–3528.
- (20) Petrenko, V.; Whitworth, R. *Physics of Ice*; Oxford University Press, 2002.
- (21) Jenniskens, P.; Blake, D. F. Crystallization of Amorphous Water Ice in the Solar System. *Astrophys. J.* **1996**, *473*, 1104–1113.
- (22) Lobban, C.; Finney, J. L.; Kuhs, W. F. The Structure of a New Phase of Ice. *Nature* **1998**, *391*, 268–270.
- (23) del Rosso, L.; Celli, M.; Grazzi, F.; Catti, M.; Hansen, T. C.; Fortes, A. D.; Ulivi, L. Cubic Ice Ic without Stacking Defects Obtained from Ice XVII. *Nat. Mater.* **2020**, *19*, 663–668.
- (24) Davies, M. B.; Fitzner, M.; Michaelides, A. Routes to Cubic Ice through Heterogeneous Nucleation. *Proc. Natl. Acad. Sci. U. S. A.* **2021**, *118*, e2025245118.
- (25) Huang, X.; Wang, L.; Liu, K.; Liao, L.; Sun, H.; Wang, J.; Tian, X.; Xu, Z.; Wang, W.; Liu, L.; Jiang, Y.; Chen, J.; Wang, E.; Bai, X. Tracking Cubic Ice at Molecular Resolution. *Nature* **2023**, *617*, 86–91.
- (26) Kuhs, W. F.; Sippel, C.; Falenty, A.; Hansen, T. C. Extent and Relevance of Stacking Disorder in “Ice Ic. *Proc. Natl. Acad. Sci. U. S. A.* **2012**, *109*, 21259–21264.
- (27) Luspai-Kuti, A.; Mousis, O.; Hässig, M.; Fuselier, S. A.; Lunine, J. I.; Marty, B.; Mandt, K. E.; Wurz, P.; Rubin, M. The Presence of Clathrates in Comet 67P/Churyumov-Gerasimenko. *Sci. Adv.* **2016**, *2*, No. e1501781.

- (28) Prialnik, D.; Bar-Nun, A. Crystallization of Amorphous Ice as the Cause of Comet P/Halley's Outburst at 14 AU. *Astron. Astrophys.* **1992**, 258, L9–L12.
- (29) Bhuin, R. G.; Methikkalam, R. R. J.; Sivaraman, B.; Pradeep, T. Interaction of Acetonitrile with Water-Ice: An Infrared Spectroscopic Study. *J. Phys. Chem. C* **2015**, 119, 11524–11532.
- (30) Buch, V.; Devlin, J. P.; Monreal, I. A.; Jagoda-Cwiklik, B.; Uras-Aytemiz, N.; Cwiklik, L. Clathrate Hydrates with Hydrogen-Bonding Guests. *Phys. Chem. Chem. Phys.* **2009**, 11, 10245–10265.
- (31) Subramanian, S.; Sloan, E. D. Trends in Vibrational Frequencies of Guests Trapped in Clathrate Hydrate Cages. *J. Phys. Chem. B* **2002**, 106, 4348–4355.
- (32) Ito, F. Matrix-Isolation Infrared Study of Acetaldehyde: Host-Dependent Vibrational Features. *J. Mol. Spectrosc.* **2022**, 384, 111593.
- (33) Ding, Y.; Peng, W. Y.; Strand, C. L.; Hanson, R. K. Quantitative Measurements of Broad-Band Mid-Infrared Absorption Spectra of Formaldehyde, Acetaldehyde, and Acetone at Combustion-Relevant Temperatures near 5.7 Mm. *J. Quant. Spectrosc. Radiat. Transfer* **2020**, 248, 106981.
- (34) Kondo, T.; Kato, H. S.; Kawai, M.; Bonn, M. The Distinct Vibrational Signature of Grain-Boundary Water in Nano-Crystalline Ice Films. *Chem. Phys. Lett.* **2007**, 448, 121–126.
- (35) May, R. A.; Smith, R. S.; Kay, B. D. The Release of Trapped Gases from Amorphous Solid Water Films. I. "Top-down" Crystallization-Induced Crack Propagation Probed Using the Molecular Volcano. *J. Chem. Phys.* **2013**, 138, 104501.
- (36) May, R. A.; Smith, R. S.; Kay, B. D. Probing the Interaction of Amorphous Solid Water on a Hydrophobic Surface: Dewetting and Crystallization Kinetics of ASW on Carbon Tetrachloride. *Phys. Chem. Chem. Phys.* **2011**, 13, 19848–19855.
- (37) Backus, E. H. G.; Grecea, M. L.; Kleyn, A. W.; Bonn, M. Surface Crystallization of Amorphous Solid Water. *Phys. Rev. Lett.* **2004**, 92, 236101.
- (38) Vishwakarma, G.; Ghosh, J.; Pradeep, T. Desorption-Induced Evolution of Cubic and Hexagonal Ices in an Ultrahigh Vacuum and Cryogenic Temperatures. *Phys. Chem. Chem. Phys.* **2021**, 23, 24052–24060.
- (39) Vishwakarma, G.; Malla, B. K.; Methikkalam, R. R. J.; Pradeep, T. Rapid Crystallization of Amorphous Solid Water by Porosity Induction. *Phys. Chem. Chem. Phys.* **2022**, 24, 26200–26210.
- (40) Lee, D. H.; Kang, H. Acid-Promoted Crystallization of Amorphous Solid Water. *J. Phys. Chem. C* **2018**, 122, 24164–24170.
- (41) Avrami, M. Kinetics of Phase Change. I: General Theory. *J. Chem. Phys.* **1939**, 7, 1103–1112.
- (42) Avrami, M. Kinetics of Phase Change. II Transformation-Time Relations for Random Distribution of Nuclei. *J. Chem. Phys.* **1940**, 8, 212–224.
- (43) Hage, W.; Hallbrucker, A.; Mayer, E.; Johari, G. P. Crystallization Kinetics of Water below 150 K. *J. Chem. Phys.* **1994**, 100, 2743–2747.
- (44) Rao, C. N. R.; Rao, K. J. *Phase Transitions in Solids: An Approach to the Study of the Chemistry and Physics of Solids*; McGraw-Hill: New York, 1978.
- (45) Doremus, R. H. *Rates of Phase Transformations*; Academic Press: New York, 1985.
- (46) Kondo, T.; Kato, H. S.; Bonn, M.; Kawai, M. Deposition and Crystallization Studies of Thin Amorphous Solid Water Films on Ru(0001) and on CO-Precovered Ru(0001). *J. Chem. Phys.* **2007**, 127, 094703.
- (47) Safarik, D. J.; Mullins, C. B. The Nucleation Rate of Crystalline Ice in Amorphous Solid Water. *J. Chem. Phys.* **2004**, 121, 6003–6010.
- (48) Smith, R. S.; Matthiesen, J.; Knox, J.; Kay, B. D. Crystallization Kinetics and Excess Free Energy of H₂O and D₂O Nanoscale Films of Amorphous Solid Water. *J. Phys. Chem. A* **2011**, 115, 5908–5917.
- (49) Yuan, C.; Smith, R. S.; Kay, B. D. Communication: Distinguishing between Bulk and Interface-Enhanced Crystallization in Nanoscale Films of Amorphous Solid Water. *J. Chem. Phys.* **2017**, 146, 031102.
- (50) Gronkowski, P. The Search for a Cometary Outbursts Mechanism: A Comparison of Various Theories. *Astron. Nachrichten* **2007**, 328, 126–136.

Supporting information

Existence of Acetaldehyde Clathrate Hydrate and Its Dissociation Leading to Cubic Ice under Ultrahigh Vacuum and Cryogenic Conditions

Gaurav Vishwakarma¹, Bijesh K. Malla¹, Soham Chowdhury¹, Sakshi Pradip Khandare¹, and Thalappil Pradeep^{1,2}*

¹DST Unit of Nanoscience (DST UNS) and Thematic Unit of Excellence (TUE), Department of Chemistry, Indian Institute of Technology Madras, Chennai 600036, India.

²International Centre for Clean Water, IIT Madras Research Park, Chennai 600113, India.

Corresponding author

*Email: pradeep@iitm.ac.in

This PDF file includes:

Experimental section (pages S2-S4)

Figure S1 to S10 (pages S5-S9)

Crystallization kinetics (pages S10-S12)

References (pages S13-S15)

Experimental Section

Apparatus. All the experiments were performed in a UHV chamber with a base pressure $\sim 5 \times 10^{-10}$ mbar, described in detail elsewhere.¹ Briefly, the vacuum chamber is equipped with reflection absorption infrared spectroscopy (RAIRS), temperature-programmed desorption mass spectrometry (TPD-MS), secondary ion mass spectrometry (SIMS), low energy ion scattering (LEIS) mass spectrometry, and a UV lamp.² The vacuum of the chamber was maintained by three oil-free turbomolecular pumps backed by several diaphragm pumps. A Ru(0001) single crystal surface (1.5 cm diameter and 1 mm thick) was used as the substrate to grow thin ice films. The substrate is mounted on a copper holder and connected at the tip of a closed-cycle helium cryostat. The substrate is fitted with a resistive heater (25 Ω) and can be maintained at any temperature between 8 and 1000 K. The temperature of the substrate is measured with a K-type thermocouple and a platinum sensor with a temperature accuracy/uncertainty of 0.5 K.

Materials and Reagents. As received acetaldehyde (anhydrous, $\geq 99.5\%$, Sigma-Aldrich), D₂O (99.9%, Sigma-Aldrich), and Millipore water (H₂O of 18.2 M Ω resistivity) were taken in a vacuum-sealed test tube and further purified in several freeze-pump-thaw cycles.

Sample Preparation. Thin films of ice were created by vapor deposition on precooled Ru(0001) substrate at 10 K. During vapor deposition, the purity of H₂O, D₂O, and acetaldehyde was further confirmed by the presence of their distinctive molecular ion peaks in the mass spectrum using a residual gas analyzer. The molecular deposition was controlled through two high-precision all-metal leak valves attached to the UHV chamber. Out of two inlet lines, one was used exclusively for H₂O/D₂O, and the other was used exclusively for acetaldehyde. The vapor deposition coverage was expressed in monolayers (ML), assuming 1.33×10^{-6} mbar s = 1 ML, which was estimated to contain $\sim 1.1 \times 10^{15}$ molecules cm⁻², as adopted in other reports.^{3,4}

Experimental Procedure. Before each experiment, the Ru(0001) substrate was heated to 400 K multiple times to ensure the cleanness of the surface, adequate for the present experiments. Thin films of 300 ML of the acetaldehyde-H₂O mixture were created at 10 K by backfilling the vacuum chamber at a total pressure of $\sim 5 \times 10^{-7}$ mbar for 10 minutes. Different ratios of acetaldehyde and H₂O/D₂O (1:2, 1:10, 1:20, and 1:40) were prepared at 10 K by keeping the total pressure constant and varying the inlet pressure of acetaldehyde and water accordingly. For instance, for co-deposition of acetaldehyde and H₂O (hereafter referred as acetaldehyde-H₂O) at 1:2 ratio, the inlet pressure of acetaldehyde was kept at $\sim 2.5 \times 10^{-7}$ mbar, and that of H₂O was at $\sim 2.5 \times 10^{-7}$ mbar, considering ion-gauge sensitivity factors for water and acetaldehyde as ~ 1.0 and ~ 2.0 , respectively.⁵ For sequential deposition of 300 ML of acetaldehyde and H₂O (hereafter referred to as acetaldehyde@H₂O), 150 ML of acetaldehyde was deposited first on the Ru(0001) substrate, followed by 150 ML of H₂O over it. For ‘selective placement method’ experiment, we have prepared three different composite films of 250 ML thickness with acetaldehyde, H₂O and HDO, namely; (1) 200 ML acetaldehyde-H₂O (1:10)@50 ML HDO, (2) 100 ML acetaldehyde-H₂O (1:10)@50 ML HDO@100 ML acetaldehyde-H₂O (1:10), and (3) 50 ML HDO@200 ML acetaldehyde-H₂O (1:10). The acetaldehyde-H₂O mixtures are of 1:10 composition. In these samples, the HDO film was prepared by exposing the vapor of a liquid mixture containing 5% D₂O and 95% H₂O (which is known to produce 10% HDO and 90% H₂O with a tiny fraction of D₂O) on the substrate.⁶ The first composite film, 200 ML acetaldehyde-H₂O (1:10)@50 ML HDO was prepared by first co-depositing 200 ML of acetaldehyde and H₂O in 1:10 ratio on Ru(0001) at 10 K, followed by the deposition of 50 ML of HDO film over it. In a similar manner, the other two samples were also prepared. For temperature and time-dependent experiments, the as-prepared thin films at 10 K were annealed at a rate of 2 K·min⁻¹ to the set temperatures. After maintaining the ice samples at a particular temperature, they were examined by RAIRS and TPD-MS.

RAIRS and TPD-MS Setup. RAIRS and TPD-MS were utilized to monitor the thermal processing of vapor-deposited ice samples as adopted in our previous studies.^{2,4,7} RAIRS data were collected in the 4000-550 cm^{-1} range with a spectral resolution of 2 cm^{-1} using a Bruker FT-IR spectrometer, Vertex 70. The IR beam was focused on the ice sample at an incident angle of $80^\circ \pm 7^\circ$ through a ZnSe viewport. The reflected IR beam from the sample was re-focused to a liquid N₂-cooled mercury cadmium telluride (MCT) detector. The IR beam outside the vacuum chamber was purged with dry N₂ to avoid absorption by atmospheric carbon dioxide. Each RAIR spectrum was averaged over 512 scans to ensure a better signal-to-noise ratio. TPD mass spectra were acquired using an Extrel quadrupole mass spectrometer in an out-of-sight configuration. Thermal desorption of acetaldehyde and water were recorded by monitoring $m/z = 29$ and 18 peaks, respectively.

Supporting information 1:

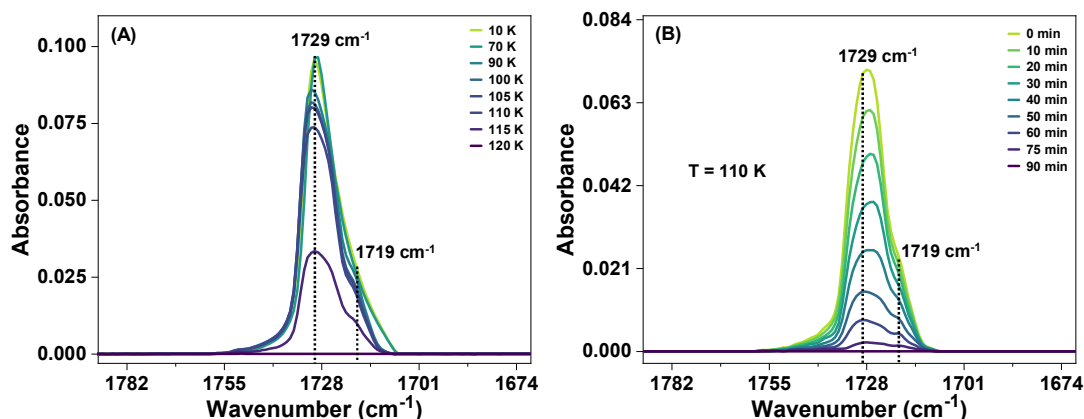


Figure S1. (A) Temperature-dependent RAIR spectra of 75 ML of pure acetaldehyde in the C=O stretching region. Acetaldehyde film was prepared at 10 K and annealed at a rate of 2 K min⁻¹ resulting in complete desorption of acetaldehyde film from the substrate. The broad peak at 1729 cm⁻¹ in the C=O stretching region at 10 K was assigned to the amorphous acetaldehyde film. This peak did not change during annealing of sample up to 80 K. However, at 90 K, due to the crystallization of the acetaldehyde film, the peak at 1729 cm⁻¹ was split into two, at 1729 and 1719 cm⁻¹. (B) Time-dependent RAIR spectra of 75 ML of pure acetaldehyde film at 110 K in the C=O stretching region. During isothermal annealing, acetaldehyde desorbed from the substrate within 90 min without any significant spectral change. Thus, once the two-peak structure is formed, it does not change with time.

Supporting information 2:

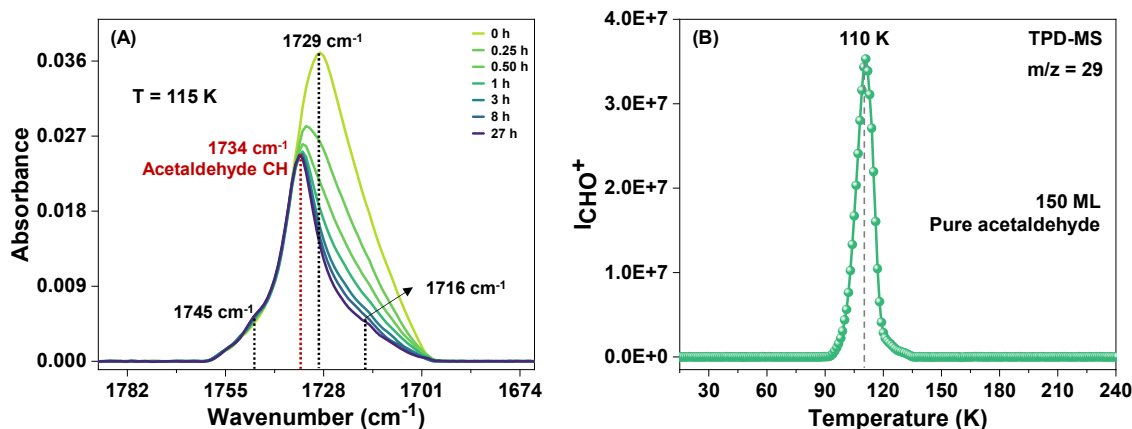


Figure S2. (A) Time-dependent RAIR spectra of 300 ML of acetaldehyde-H₂O (1:2) film at 115 K in the C=O stretching region. The ice mixture was co-deposited on Ru(0001) substrate at 10 K and annealed at a rate of 2 K.min⁻¹ to 115 K. At 115 K with time, the peak at 1729 cm⁻¹ (attributed to phase-separated acetaldehyde) is decreasing due to the desorption of phase-separated acetaldehyde. However, the peak at 1734 cm⁻¹ (attributed to acetaldehyde CH) remained due to the trapping of acetaldehyde in CH cages. At 115 K, between 1 to 27 h, we did not observe much change in the intensity of the peak at 1734 cm⁻¹, which confirms the stability of acetaldehyde CH under UHV. (B) TPD spectrum of 150 ML of pure acetaldehyde. The ramping rate applied for this experiment was 30 K.min⁻¹. Here, the intensity of HCO⁺ (m/z = 29) is plotted as a function of substrate temperature.

Supporting information 3:

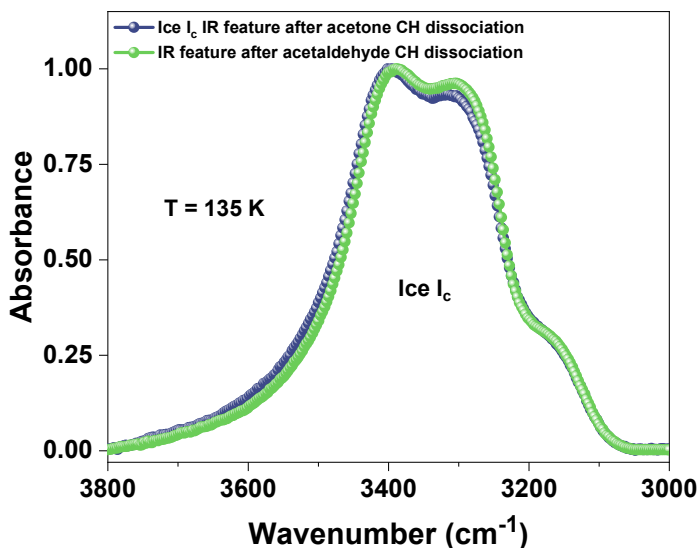


Figure S3. Comparison of O-H stretching bands of crystalline H₂O film obtained after acetone CH dissociation (blue trace) and the resultant ice system left after the dissociation of acetaldehyde CH at 135 K (green trace). Both these experiments were carried out separately. Here, the similarity of the O-H stretching bands of these two systems suggests that the dissociation of acetaldehyde CH produces ice I_c. Notably, the formation of ice I_c via acetone CH was studied by RAIRS and confirmed by reflection high-energy electron diffraction (RHEED).

Supporting information 4:

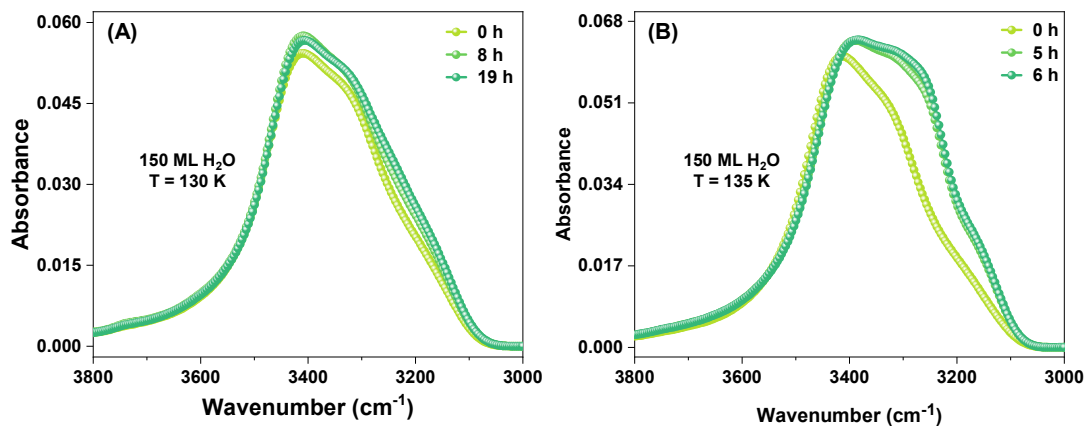


Figure S4. Time-dependent RAIR spectra of 150 ML of solid H₂O film at (a) 130 K, and (b) 135 K in the O-H stretching region. The water vapor was deposited at 10 K on Ru(0001) substrate. The ice films were annealed at a rate of 2 K.min⁻¹ to the set temperatures.

Supporting information 5:

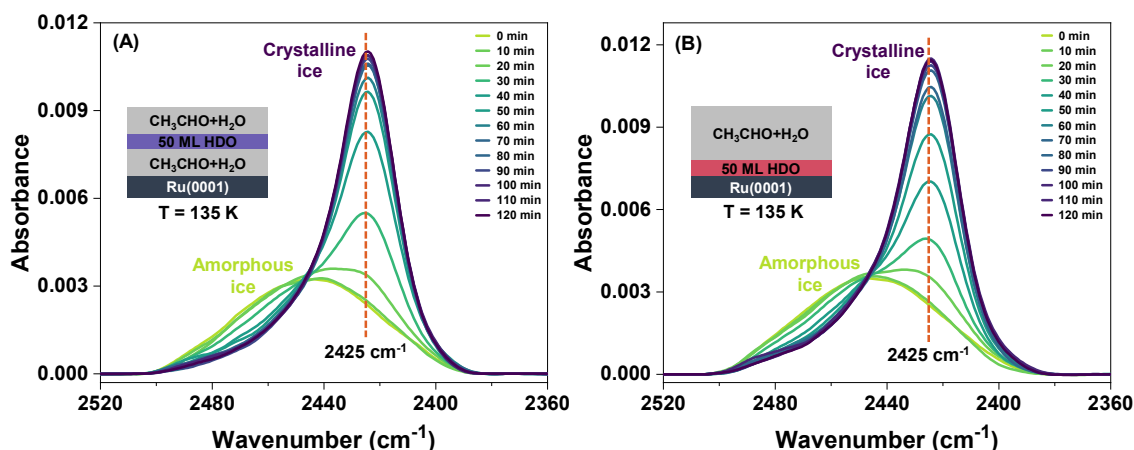


Figure S5. Isothermal RAIR spectra at 135 K in the O-D stretching region of 250 ML of composite ice film containing 200 ML acetaldehyde-H₂O (1:10) film with 50 ML HDO (5% D₂O in H₂O) layer placed at various positions, (A) in the middle of 200 ML acetaldehyde-H₂O film, and (B) at the bottom of 200 ML acetaldehyde-H₂O film. The vertical cut at 2425 cm⁻¹ was used to calculate the crystallization fraction of the probe HDO layer.

Supporting information 6:

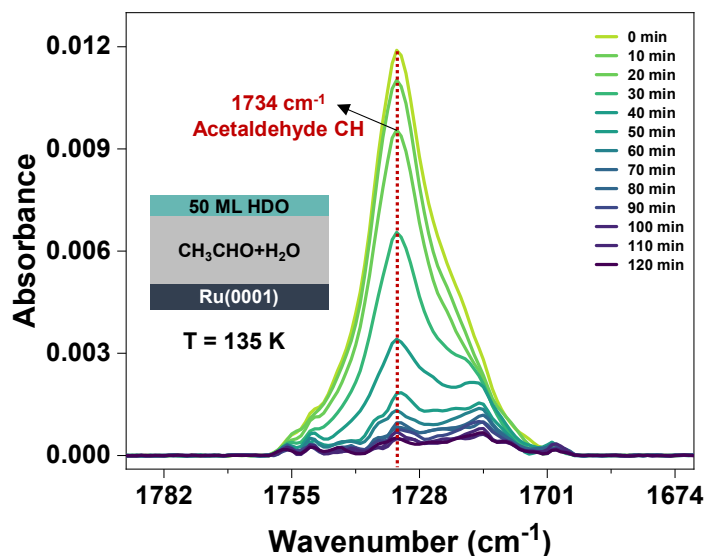


Figure S6. Isothermal RAIR spectra at 135 K in the C=O stretching region of 250 ML of composite ice film containing 200 ML acetaldehyde-H₂O (1:10) film with 50 ML HDO (5% D₂O in H₂O) layer placed at the top of 200 ML acetaldehyde-H₂O film. The peak at 1734 cm⁻¹ (attributed to acetaldehyde CH) in the C=O stretching region is decreasing from 0 min itself due to the dissociation of acetaldehyde CH.

Supporting information 7:

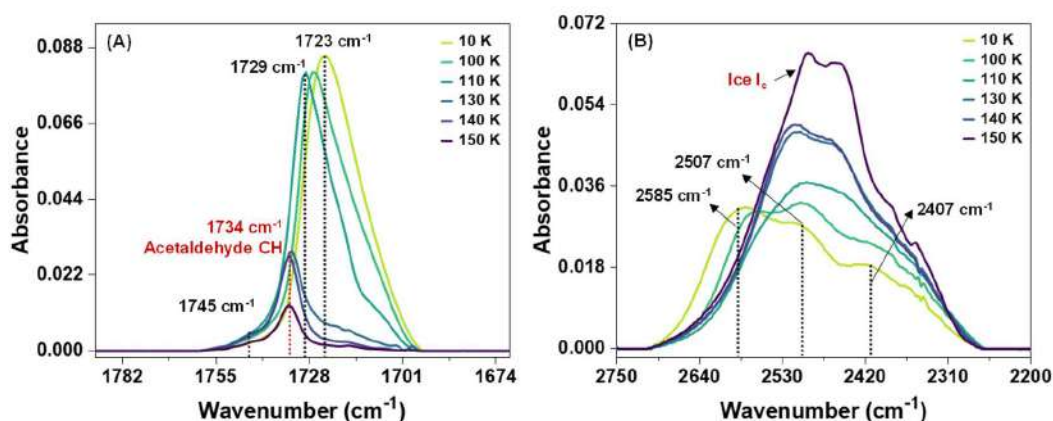


Figure S7. (A) Temperature-dependent RAIR spectra of 300 ML of acetaldehyde-D₂O (1:2) film in the (A) C=O stretching and (B) O-D stretching regions. The ice mixture was co-deposited on Ru(0001) substrate at 10 K and annealed at a rate of 2 K.min⁻¹ to the set temperatures. Acetaldehyde forms CH with D₂O during the thermal annealing of the ice mixture. However, upon its dissociation above 140 K, it converts to D₂O ice I_c.

Supporting information 8:

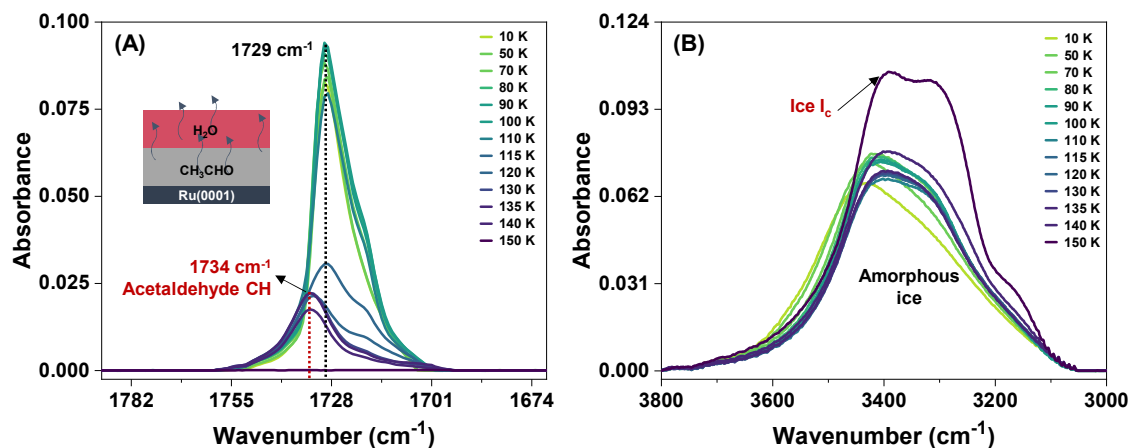


Figure S8. Temperature-dependent RAIR spectra of 225 ML of acetaldehyde@H₂O (75@150 ML) film in the (A) C=O stretching and (B) O-H stretching regions. The ice sample was prepared by first depositing 75 ML of acetaldehyde on Ru(0001) substrate at 10 K, followed by 150 ML of H₂O over it. The prepared ice sample at 10 K was annealed at a rate of 2 K.min⁻¹ to the set temperatures. Above the desorption temperature of acetaldehyde (>110 K), most of the acetaldehyde diffuses and desorbs through the water matrix, while a small fraction of acetaldehyde is trapped in hydrate cages (confirmed by the appearance of 1734 cm⁻¹ peak). However, upon acetaldehyde CH dissociation above 140 K, it converts to ice I_c.

Supporting information 9:

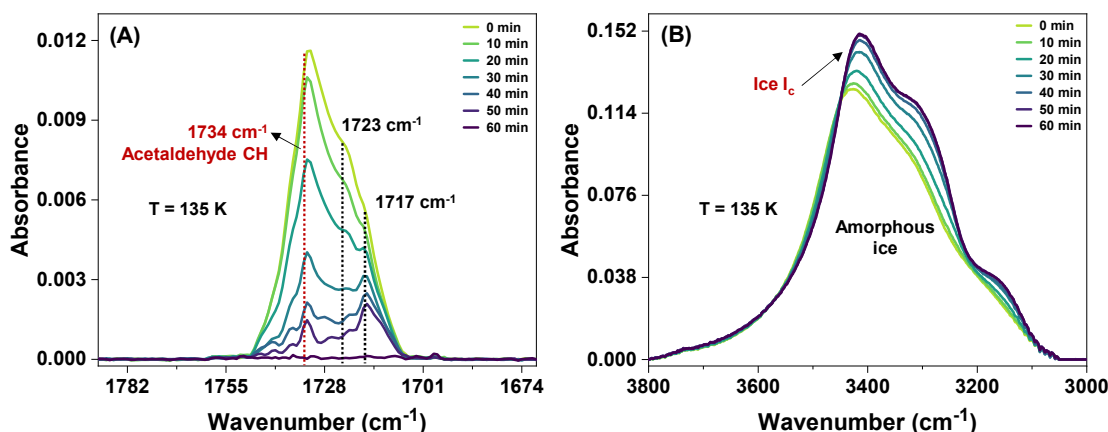


Figure S9. Time-dependent RAIR spectra of 300 ML of acetaldehyde-H₂O (1:20) at 135 K in the (A) C=O stretching and (B) O-H stretching regions. The ice mixture was co-deposited on Ru(0001) substrate at 10 K and annealed at a rate of 2 K.min⁻¹ to the set temperatures. At 135 K (0 min), three peaks at 1734, 1723, and 1717 cm⁻¹ were observed. The peak at 1734 cm⁻¹ was assigned to acetaldehyde CH, whereas the peaks at 1723 and 1717 cm⁻¹ were due to a dilute mixture of acetaldehyde in the water matrix. However, upon acetaldehyde CH dissociation during the isothermal annealing of the ice mixture at 135 K for 60 min, it converts to ice I_c.

Supporting information 10:

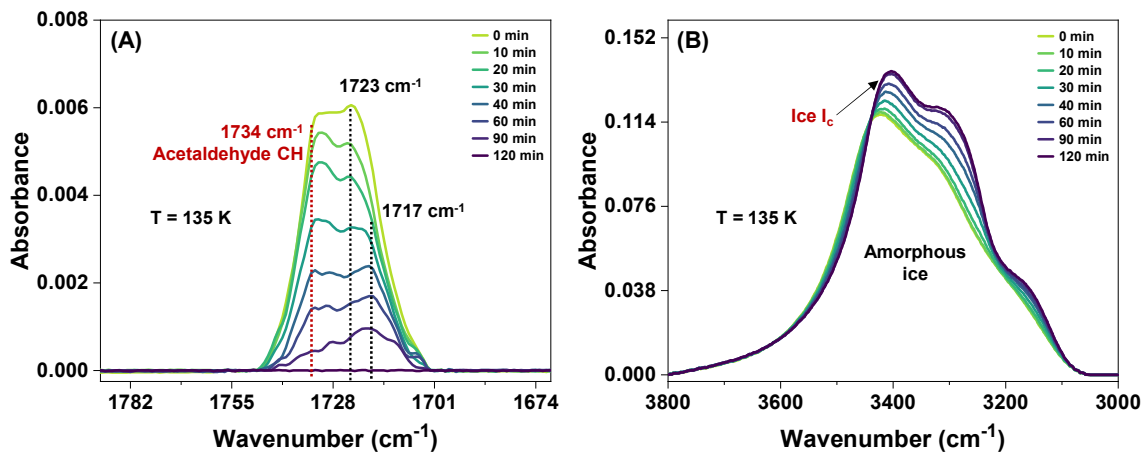


Figure S10. Time-dependent RAIR spectra of 300 ML of acetaldehyde-H₂O (1:40) at 135 K in the (A) C=O stretching and (B) O-H stretching regions. The ice mixture was co-deposited on Ru(0001) substrate at 10 K and annealed at a rate of 2 K.min⁻¹ to the set temperatures. At 135 K (0 min), three peaks at 1734, 1723, and 1717 cm⁻¹ were observed. The peak at 1734 cm⁻¹ was assigned to acetaldehyde CH, whereas the peaks at 1723 and 1717 cm⁻¹ were due to a dilute mixture of acetaldehyde in the water matrix. However, upon acetaldehyde CH dissociation during the isothermal annealing of the ice mixture at 135 K for 120 min, it converts to ice I_c.

Crystallization kinetics

The crystallization kinetics of ice I_c formation was determined using isothermal time-dependent RAIR spectra of 300 ML of acetaldehyde- H_2O (1:10) films, as shown in Figure S11. Here, by monitoring the evolution in O-H stretching band at the corresponding temperatures, 130, 132, 135, and 137 K, the associated crystallization kinetics were evaluated.^{6–13} Figure S12

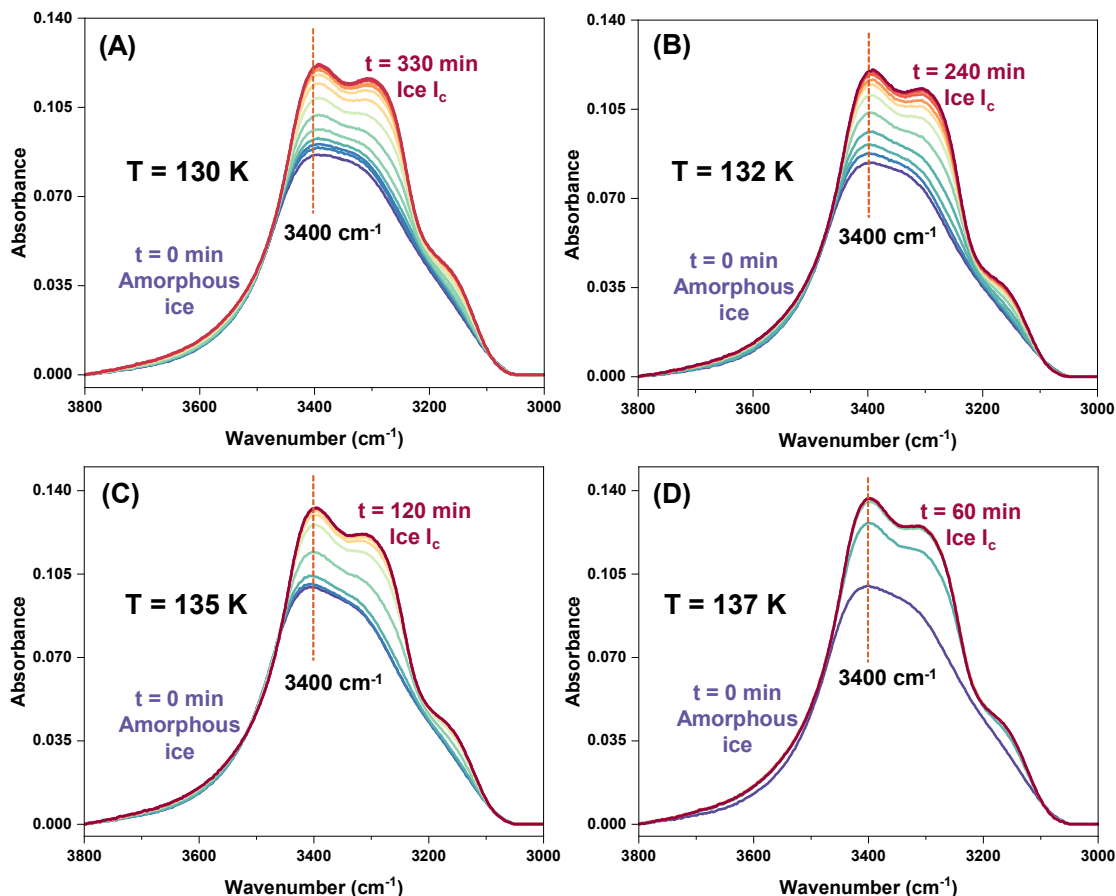


Figure S11. Isothermal time-dependent RAIR spectra of 300 ML of acetaldehyde- H_2O (1:10) in the O-H stretching region at (A) 130 K, (B) 132 K, (C) 135 K, and (D) 137 K. The ice samples were prepared by co-deposition on Ru(0001) substrate at 10 K and annealed at a rate of 2 K.min⁻¹ to the set temperatures. In each case, the first spectrum is due to the amorphous ice, and the last spectrum is due to crystalline ice, while the intermediate spectra are a linear combination of amorphous and crystalline spectra. Crystallization fractions were calculated from a vertical cut at 3400 cm⁻¹ in the O-H stretching band, as shown in Figures A, B, C, and D.

shows the isothermal time-dependent RAIR spectra of 300 ML of acetaldehyde- H_2O (1:10) films in the O-H stretching region at (A) 130 K, (B) 132 K, (C) 135 K, and (D) 137 K. In all the spectra shown in Figure S11, the first spectrum in each case is considered from a completely amorphous film which is a relatively broad peak and the last spectrum is from a completely crystalline film. During the ice I_c formation the peak shifts to a lower frequency, splits, and

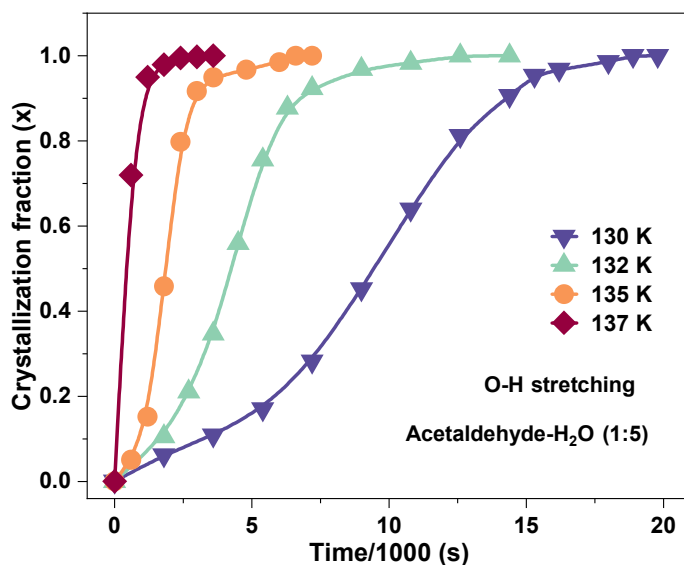


Figure S13. Crystallization fraction versus time curves for 300 ML of acetaldehyde-H₂O (1:10) film obtained from isothermal RAIR measurements at 130, 132, 135, and 137 K as shown in Figure S11. The Crystallization fraction was calculated from a vertical cut at 3400 cm⁻¹ in the O-H stretching band, as shown in Figure S11.

increases in intensity.^{7,14} All the spectra shown in Figure S11 have isosbestic point^{8,9,14} which suggests that the intermediate spectra are a linear combination of amorphous and crystalline spectra. Therefore, the fraction crystallized with time can be calculated from a vertical cut at 3400 cm⁻¹ in the O-H stretching band (shown by the dashed vertical line). Eq. (1) was used to convert the absorbance data to crystallization fraction, $x(t)$

$$x(t) = \frac{\Delta A(1)}{\Delta A(2)} \quad (1)$$

where $\Delta A(1)$ is the difference in the absorbance at a particular time t and that at time zero ($t = 0$), and $\Delta A(2)$ is the difference in absorbance of a completely crystallized film (when there is no spectral change with time) and that of a completely amorphous film (at $t = 0$) at the given temperature.

Figure S12 shows the crystallization fraction versus time curves obtained from the isothermal RAIRS measurements shown in Figure S11. The change of the curve shape from sigmoidal (at a lower T , 130 K) to exponential (at a higher T , 137 K) suggests that the crystallization kinetics increases with increasing temperature. Further, the Kinetics parameters shown in Table 1 in the main paper are estimated by fitting the crystallization fraction, $x(t)$, to the Avrami equation.^{15,16} The Avrami equation is given by,

$$x(t) = 1 - \exp(-k.t)^n \quad (2)$$

where k is the rate constant, t is time, and n is Avrami exponent. For all temperatures, n can hold integer values between 1 to 4 and predicts the nature of the crystallization process.^{17–19} Equation 2 can be rearranged in a linear form.

$$\ln(-\ln[1-x(t)]) = n \ln(t) + n \ln k \quad (3)$$

Figure S13A shows a plot between $\ln(-\ln[1-x(t)])$ versus $\ln(t)$ for different temperatures and was evaluated using eqn (3). The kinetics parameters, k and n for different temperatures were obtained from the linearly fitted lines and listed in Table 1. The obtained values of k suggest that with an increase in temperature, the rate of ice I_c formation increases. Also, the estimated values of n (2.64–1.89) shown in Table 1 reflect that the crystallization kinetics is diffusion-controlled with particles growing into a predominantly spherical geometry as the theory of

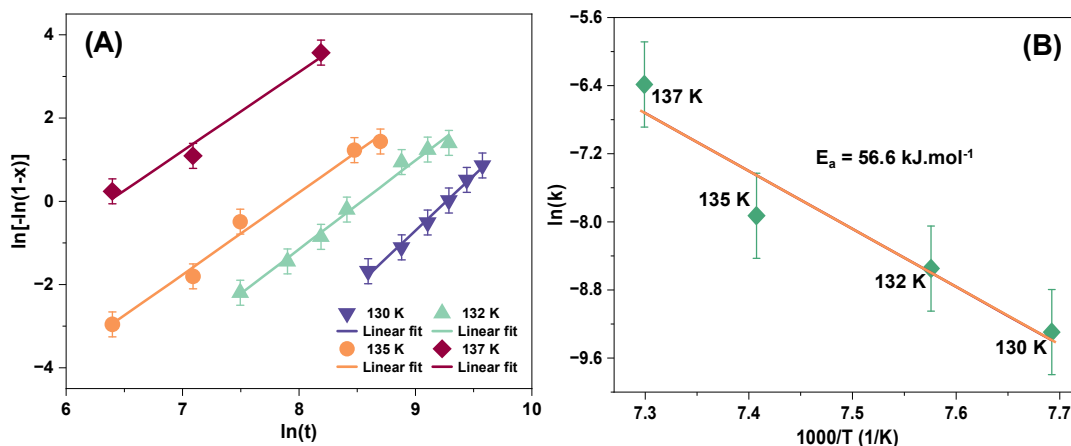


Figure S14. (A) A plot of the linearized form of the Avrami equation. Plots of $\ln[-\ln(1-x)]$ versus $\ln(t)$ at different temperatures of 130, 132, 135, and 137 K were evaluated using the O-H stretching bands. The obtained data points were fitted using the Avrami equation. (B) Arrhenius plot of $\ln k$ versus $(1/T)$ was achieved from the analysis of the slope and intercept of the linearly fitted lines of Figure S13A for different temperatures. The activation energy (E_a) of ice crystallization was calculated from the slope of the linearly fitted straight line of Figure B.

phase transformation by nucleation and growth would suggest.^{17–19} Finally, the activation energy (E_a) of ice I_c formation via acetaldehyde CH was estimated from the analysis of the slope and intercept of the linearly fitted lines of the plot shown in S13A. Figure S13B shows an Arrhenius plot of $\ln k$ versus $(1/T)$. The activation energy (E_a) of ice I_c crystallization was estimated to be 56.6 kJ.mol^{-1} and is comparable to previously reported^{6,8,20–22} activation energy values ($60\text{--}77 \text{ kJ mol}^{-1}$) for the crystallization of pure ASW.

References

- (1) Bag, S.; Bhuin, R. G.; Methikkalam, R. R. J.; Pradeep, T.; Kephart, L.; Walker, J.; Kuchta, K.; Martin, D.; Wei, J. Development of Ultralow Energy (1-10 eV) Ion Scattering Spectrometry Coupled with Reflection Absorption Infrared Spectroscopy and Temperature Programmed Desorption for the Investigation of Molecular Solids. *Rev. Sci. Instrum.* **2014**, *85*, 014103.
- (2) Vishwakarma, G.; Malla, B. K.; Reddy, K. S. S. V. P.; Ghosh, J.; Chowdhury, S.; Yamijala, S. S. R. K. C.; Reddy, S. K.; Kumar, R.; Pradeep, T. Induced Migration of CO₂ from Hydrate Cages to Amorphous Solid Water under Ultrahigh Vacuum and Cryogenic Conditions. *J. Phys. Chem. Lett.* **2023**, *14*, 2823–2829.
- (3) Kimmel, G. A.; Petrik, N. G.; Dohnálek, Z.; Kay, B. D. Crystalline Ice Growth on Pt(111): Observation of a Hydrophobic Water Monolayer. *Phys. Rev. Lett.* **2005**, *95*, 166102.
- (4) Ghosh, J.; Methikkalam, R. R. J.; Bhuin, R. G.; Ragupathy, G.; Choudhary, N.; Kumar, R.; Pradeep, T. Clathrate Hydrates in Interstellar Environment. *Proc. Natl. Acad. Sci. U. S. A.* **2019**, *116*, 1526–1531.
- (5) Bartmess, J. E.; Georgiadis, R. M. Empirical Methods for Determination of Ionization Gauge Relative Sensitivities for Different Gases. *Vacuum* **1983**, *33*, 149–153.
- (6) Lee, D. H.; Kang, H. Acid-Promoted Crystallization of Amorphous Solid Water. *J. Phys. Chem. C* **2018**, *122*, 24164–24170.
- (7) Ghosh, J.; Bhuin, R. G.; Vishwakarma, G.; Pradeep, T. Formation of Cubic Ice via Clathrate Hydrate, Prepared in Ultrahigh Vacuum under Cryogenic Conditions. *J. Phys. Chem. Lett.* **2020**, *11*, 26–32.
- (8) Smith, R. S.; Matthiesen, J.; Knox, J.; Kay, B. D. Crystallization Kinetics and Excess Free Energy of H₂O and D₂O Nanoscale Films of Amorphous Solid Water. *J. Phys. Chem. A* **2011**, *115*, 5908–5917.
- (9) Smith, R. S.; Petrik, N. G.; Kimmel, G. A.; Kay, B. D. Thermal and Nonthermal Physiochemical Processes in Nanoscale Films of Amorphous Solid Water. *Acc. Chem. Res.* **2012**, *45*, 33–42.
- (10) Ghosh, J.; Vishwakarma, G.; Das, S.; Pradeep, T. Facile Crystallization of Ice I_h via

- Formaldehyde Hydrate in Ultrahigh Vacuum under Cryogenic Conditions. *J. Phys. Chem. C* **2021**, *125*, 4532–4539.
- (11) Vishwakarma, G.; Ghosh, J.; Pradeep, T. Desorption-Induced Evolution of Cubic and Hexagonal Ices in an Ultrahigh Vacuum and Cryogenic Temperatures. *Phys. Chem. Chem. Phys.* **2021**, *23*, 24052–24060.
 - (12) Vishwakarma, G.; Malla, B. K.; Rajan, R.; Methikkalam, J.; Pradeep, T. Rapid Crystallization of Amorphous Solid Water by Porosity Induction. *Phys. Chem. Chem. Phys.* **2022**, *24*, 26200–26210.
 - (13) Backus, E. H. G.; Grecea, M. L.; Kleyn, A. W.; Bonn, M. Surface Crystallization of Amorphous Solid Water. *Phys. Rev. Lett.* **2004**, *92*, 236101.
 - (14) Yuan, C.; Smith, R. S.; Kay, B. D. Surface and Bulk Crystallization of Amorphous Solid Water Films: Confirmation of “Top-down” Crystallization. *Surf. Sci.* **2016**, *652*, 350–354.
 - (15) Avrami, M. Kinetics of Phase Change. I: General Theory. *J. Chem. Phys.* **1939**, *7*, 1103–1112.
 - (16) Avrami, M. Kinetics of Phase Change. II Transformation-Time Relations for Random Distribution of Nuclei. *J. Chem. Phys.* **1940**, *8*, 212–224.
 - (17) Hage, W.; Hallbrucker, A.; Mayer, E.; Johari, G. P. Crystallization Kinetics of Water below 150 K. *J. Chem. Phys.* **1994**, *100*, 2743–2747.
 - (18) Rao, C. N. R.; Rao, K. J. *Phase Transitions in Solids : An Approach to the Study of the Chemistry and Physics of Solids*, McGraw-Hill, New York, 1978.
 - (19) Doremus, R. H. *Rates of Phase Transformations*, Academic Press, New York, 1985.
 - (20) Kondo, T.; Kato, H. S.; Bonn, M.; Kawai, M. Deposition and Crystallization Studies of Thin Amorphous Solid Water Films on Ru(0001) and on CO-Precovered Ru(0001). *J. Chem. Phys.* **2007**, *127*, 094703.
 - (21) Safarik, D. J.; Mullins, C. B. The Nucleation Rate of Crystalline Ice in Amorphous Solid Water. *J. Chem. Phys.* **2004**, *121*, 6003–6010.
 - (22) Yuan, C.; Smith, R. S.; Kay, B. D. Communication: Distinguishing between Bulk and Interface-Enhanced Crystallization in Nanoscale Films of Amorphous Solid Water. *J.*

Chem. Phys. **2017**, *146*, 031102.



Cite this: DOI: 10.1039/d3nr02561f

Secondary ligand-induced orthogonal self-assembly of silver nanoclusters into superstructures with enhanced NIR emission†

Korath Shivan Sugi,^{a,b} Amritha P. Sandra,^{a,b} Nonappa,^c Debasmita Ghosh,^{a,b} Jyoti Sarita Mohanty,^{a,b} Murugesan Paulthangam Kannan,^{a,b} B. S. Sooraj,^{a,b} Pillalamarri Srikrishnarka,^{a,b} Jayoti Roy,^{a,b} Wakeel Ahmed Dar^{a,b} and Thalappil Pradeep^{a,b}✉

Orthogonal self-assembly is one of the crucial strategies for forming complex and hierarchical structures in biological systems. However, creating such ordered complex structures using synthetic nanoparticles is a challenging task and requires a high degree of control over structure and multiple non-covalent interactions. In this context, nanoarchitectonics serves as an emerging tool to fabricate complex functional materials. Here, we present a secondary ligand-induced orthogonal self-assembly of atomically precise silver nanoclusters into complex superstructures. Specifically, we use Ag₁₄NCs protected with naphthalene thiol and 1,6-bis(diphenylphosphino)hexane ligands. Controlled addition of 1,6-bis(diphenylphosphino)hexane, the secondary ligand resulted in a self-assembled supracolloidal structure including helical fibers, spheres, and nanosheets. The self-assembly process is tunable by controlling the molar ratio of the ligand. The resulting superstructures exhibit enhanced NIR emission due to restricted intramolecular motion. This demonstrates that by tuning supramolecular interactions, hierarchical nanostructures with desired properties similar to biomolecules can be obtained from atomically precise building blocks.

Received 31st May 2023,
Accepted 14th June 2023
DOI: 10.1039/d3nr02561f
rsc.li/nanoscale

Introduction

Self-assembly of molecular building units into complex functional and structural biological superstructures is omnipresent in nature.^{1–3} Orthogonal self-assembly is one of the important features of biological systems.^{4–8} In orthogonal self-assembly, multiple but non-interfering non-covalent interactions play a crucial role in the formation of complex structures. Examples include the double helical structure of DNA, protein folding, and cell membranes.^{2,3,9} Extensive research has been con-

ducted to synthesize/mimic such biological architectures using molecular-level building blocks, supramolecular polymers, and metal–ligand complexes using orthogonal self-assembly.^{6,7,10–13} Hierarchical structures of metallacycles and metallacages are fabricated by exploiting the orthogonal metal–ligand coordination and other noncovalent interactions.⁹ Sun *et al.* demonstrated that alanine-based chiral metallacycles could self-assemble into nanospheres at low concentrations and chiral metallo gels at high concentrations utilizing the noncovalent interactions.¹² Recently, nano architectures from nanomaterials are fabricated using the nanoarchitectonics concept.^{14–16}

Despite numerous efforts using molecular and macromolecular building blocks, orthogonal self-assembly of synthetic metal nanoparticles has been a challenge. This is attributed to non-uniform size, uncontrolled ligand density, and aggregation tendencies. In recent years, atomically precise metal nanoclusters (NCs)^{17,18} have gained attention as functional materials due to their small size, well-defined structure, and unique physical properties.¹⁹ They are considered as potential luminophores due to their unique optical properties.^{20,21} They are also known to self-assemble into hierarchical structures reminiscent of biological systems.^{22,23} Several strategies are employed to assemble NCs into dimers and higher hierarchi-

^aDST Unit of Nanoscience (DST UNS) and Thematic Unit of Excellence (TUE), Department of Chemistry, Indian Institute of Technology Madras, Chennai 600 036, India. E-mail: pradeep@iitm.ac.in

^bInternational Centre for Clean Water, Chennai 600113, India

^cFaculty of Engineering and Natural Sciences, Tampere University, FI-33720 Tampere, Finland

†Electronic supplementary information (ESI) available: Collision-induced dissociation mass spectra, SEM image and EDS mapping, XPS, ³¹P NMR of Ag₁₄ nanoclusters, TEM images showing the structural evolution of Ag₁₄ nanoclusters with the addition of different molar ratios of DPPH ligands, TEM images of NCA-1.0, STEM images of NCA-1.0, UV-vis spectrum and ESI MS of NCA-1.0 redispersed in DMF, TEM images of the DPPH-NT mixture, and schematic illustration of supramolecular interactions in Ag₁₄ nanoclusters. See DOI: <https://doi.org/10.1039/d3nr02561f>

cal structures, which show self-assembly-induced luminescence, mechanical performance, and biological activities.^{22,24–27} The most common strategies involve the functionalization of protecting ligands and introducing new linkers such as organic molecules, ions, counterions, solvents, and phase transfer agents that can induce self-assembly in NCs.^{28,29} Well-defined cluster assembled solids (CASS) have been assembled by exploiting the noncovalent interactions-mediated inter-cluster assembly.³⁰ Apart from their ease of handling, hierarchical/supramolecular architectures of atomically precise NCs retain the intrinsic properties of individual NCs and at the same time display emerging or collective properties.^{31,32}

In this context, a facile and novel route is demonstrated here to self-assemble NCs into supramolecular architectures reminiscent of biomolecules. We have synthesized Ag₁₄ nanoclusters co-protected by naphthalene thiolate and 1,6-bis(diphenylphosphino)hexane (DPPH). These NCs exhibited distinct optical properties compared to analogous Ag₁₄ NCs protected with different ligands.^{33–36} By controlled addition of DPPH as a bidentate secondary ligand, the Ag₁₄ NCs initially assemble into thin sheets. The sheets further assemble into spherical superstructures and rope-like wraps. Mass spectrometric investigations of supramolecular structures reveal the formation of NC-DPPH adducts. Such supramolecular architectures of NCs show enhanced near-infrared (NIR) emission due to the restricted intramolecular motion (RIM). We believe that such assemblies are directed by the supramolecular interactions between bidentate DPPH ligands and naphthalene thiol (NT) ligands, also the long chain of DPPH acts as a bridge between two NCs resulting in an orthogonal assembly. This method could pave the way to create hierarchical NC architectures with desired properties, which can further offer new avenues to programmable self-assembly of NCs with controllable properties.

Experimental section

Materials

Silver nitrate (AgNO₃) was purchased from RANKEM. 1-Naphthalenethiol (NT), 1,6-bis(diphenylphosphino)hexane (DPPH), tetraphenylphosphonium chloride (PPh₄Cl), triethylamine (TEA), and sodium borohydride (NaBH₄) were purchased from Sigma Aldrich. All other solvents such as methanol, hexane, dichloromethane (DCM), trichloromethane (TCM), and *N,N*-dimethylformamide (DMF) were of analytical grade.

Characterization

PerkinElmer Lambda 25 spectrometer was used to record the UV-Vis absorption spectrum of the nanocluster samples. Photoluminescence measurements were carried out using a Horiba Jobin Yvon NanoLog instrument. Mass spectrometric measurements were performed using a Waters Synapt G2 Si instrument (details in ESI†). The X-ray photoelectron spectroscopy (XPS) measurements of nanocluster samples were

carried out with an Omicron ESCA Probe Spectrometer. Nuclear magnetic resonance (NMR) spectra (³¹P) of the nanocluster samples were recorded using a 500 MHz Bruker Avance III spectrometer. Dynamic light scattering (DLS) measurements were performed using a Malvern Zetasizer ZSP instrument. High-resolution transmission electron microscopy (HRTEM) was performed with a JEOL 3010. Scanning electron microscope (SEM) images and energy dispersive X-ray analysis (EDAX) were collected using an FEI QUANTA-200 SEM. Scanning transmission electron microscope (STEM) imaging was performed using JEOL JEM-2800 high throughput electron microscope equipped with a Schottky type field emission gun operated at 200 kV with simultaneous bright field (BF) and dark field (DF) STEM imaging. For elemental mapping energy dispersive X-ray mapping and spectra were collected using dual silicon drift detectors. The tilt series for electron tomographic reconstruction of the nanocluster assembled architectures were collected using the JEM 3200FSC microscope operated at 300 keV (see electronic ESI† for details).

Synthesis of Ag₁₄(NT)₇(DPPH)₂Cl₂ nanoclusters

The Ag₁₄(NT)₇(DPPH)₂Cl₂ NCs were synthesized by dissolving 20 mg of silver nitrate in 3 mL of methanol. To this solution, 11 mL of DCM was added. A 10 μL of 1-NT was added and the reaction is carried out at 0 °C. After the addition of NT, the color of the solution changed to turbid yellow indicating the formation of silver thiolates. After 5 minutes, 6.8 mg of DPPH (in 0.5 mL DCM) and 6 mg of PPh₄Cl (in 0.5 mL DCM) were added. After 30 minutes, 45 mg of NaBH₄ in 1 mL ice-cold (DI) water and 50 μL of TEA were added. The color of the solution changed to dark brown after the addition of NaBH₄. After five hours of continuous stirring, the crude cluster was kept in the fridge overnight for size focusing. The resultant material was centrifuged and the precipitate was washed several times with methanol, hexane, and DMF and dispersed in DCM or TCM for characterization.

Secondary ligand-induced nanoarchitectures of Ag₁₄ nanoclusters

Approximately 10 mg of Ag₁₄(NT)₇(DPPH)₂Cl₂ NCs were dissolved in 10 mL of TCM. To this NC solution, the DPPH ligand was added with the molar ratio of DPPH/NC ranging from 0.5 to 10.

Results and discussion

Characterization of Ag₁₄ nanoclusters

Naphthalene thiol-protected Ag₁₄NCs were synthesized and characterized according to the methods described in the experimental section. The quantized electronic structure of the NCs is evident from the optical absorption spectral peaks centered at 340, 490, and 690 nm (Fig. 1A). They also display intense NIR emission at 1035 nm when excited at 340 nm (inset of Fig. 1A). The ESI MS in the positive mode resulted in a peak centered at *m/z* 3605, which was assigned as [Ag₁₄(NT)₇(DPPH)₂Cl₂] (Fig. 1B). Experimental and theoretical

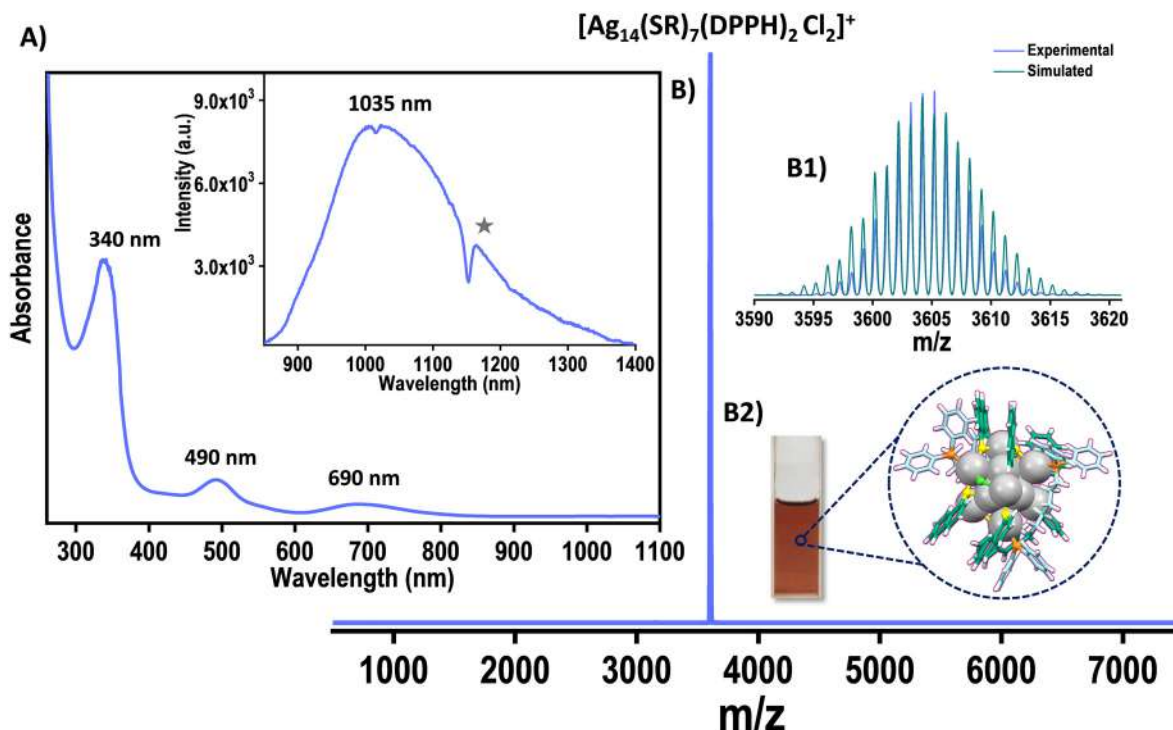


Fig. 1 (A) UV-Vis spectrum of Ag_{14} NCs. Inset of A shows the emission at 340 nm excitation of Ag_{14} NCs (star symbol (*) denotes the solvent-induced structuration).³⁷ (B) The ESI MS of Ag_{14} NCs. (B1) The experimental and simulated spectra match well. (B2) Photograph of the Ag_{14} NC solution. Color codes: grey, Ag; blue/sea green, C; yellow, S; orange, P; green, Cl; white, H.

isotopic distribution matched well and revealed that the Ag_{14} NCs are monovalent (Fig. 1B1).

Collision-induced dissociation (CID) study of $[\text{Ag}_{14}(\text{NT})_7(\text{DPPH})_2\text{Cl}_2]^+$ further reaffirms the assigned molecular formula (Fig. S1†). A systematic loss of DPPH and NT ligand (L) was observed with an increase in collision energy (CE). Initially, one DPPH was lost, and with further increase in the CE, the second DPPH unit was lost, followed by other primary ligands. The composition of Ag_{14} NC was further confirmed by elemental analysis which confirms the presence of Ag, S, Cl, and P. Their atomic percentages matched well with the assigned formula (Fig. S2†). Besides, elemental characterization was also performed using X-ray photoelectron spectroscopy (XPS). Peaks corresponding to Ag $3d_{5/2}$, S $2p_{3/2}$, P $2p_{3/2}$, and Cl $2p_{3/2}$ appeared at ~ 368.5 , ~ 162.9 , ~ 131.8 , and ~ 198.3 eV, respectively (Fig. S3†).

The ^{31}P NMR spectrum of DPPH alone shows major signals at 32.7 and -17.1 ppm (Fig. S4†), which can be attributed to oxidized species such as DPPHO_2 and uncoordinated DPPH ligands.³⁸ The ^{31}P NMR spectrum of Ag_{14} NCs shows two doublets due to the coupling of ^{31}P with ^{109}Ag and ^{107}Ag , which implies the coordination of the DPPH ligand to silver.^{39,40}

Ligand engineering induced tailoring of the optical properties

The UV-vis spectrum of the NT-protected Ag_{14} NCs is compared with that of the other two Ag_{14} NCs reported in the literature.^{33,34} A drastic change in optical properties was

observed for NT-protected Ag_{14} NCs (Fig. 2). The UV-vis spectrum of $\text{Ag}_{14}(3,4\text{-DFBT})_{12}\text{TPP}_8$ (3,4-DFBT = 3,4 difluorobenzene-thiol, TPP = triphenylphosphine) displays two major absorption bands at 368 and 530 nm whereas, $\text{Ag}_{14}(1,2\text{-BDT})_6\text{TPP}_8$ (1,2-BDT = 1,2 benzenedithiol, TPP = triphenylphosphine) shows peaks at 425, 600, and 860 nm. The $[\text{Ag}_{14}(\text{NT})_7(\text{DPPH})_2\text{Cl}_2]$ NC shows molecular peaks at 340, 490, and 690 nm. The $\text{Ag}_{14}(3,4\text{-DFBT})_{12}\text{TPP}_8$ NCs display dual emis-

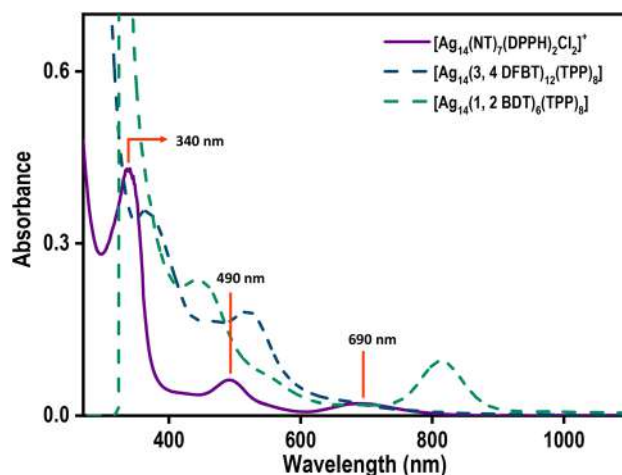


Fig. 2 The UV-vis spectra of $[\text{Ag}_{14}(\text{NT})_7(\text{DPPH})_2\text{Cl}_2]^+$ (violet trace), $\text{Ag}_{14}(3,4\text{-DFBT})_{12}\text{TPP}_8$ (dark blue trace), and $\text{Ag}_{14}(1,2\text{-BDT})_6\text{TPP}_8$ (sea green trace).

sion peaks around 536 nm and 420 nm. Such dual emission was also observed in the case of $\text{Ag}_{14}(\text{1,2-BDT})_6\text{TPP}_8$ NCs. The NT-protected Ag_{14} NCs, in contrast, show NIR emission at 1035 nm. This observation signifies the pivotal role of ligands in tailoring the optoelectronic properties of NCs.

Secondary ligand-induced assembly of Ag_{14} NCs

NCs are assembled into hierarchical structures using strategies that involve introducing organic molecules, ions, counterions, solvents, and phase transfer agents. The secondary ligand induced transformation and self-assembly of nanoclusters are studied in detail.^{41–43} Considering the long-chain length of the bidentate DPPH ligand, we were motivated to introduce different ratios of DPPH ligands to induce self-assembly in Ag_{14} NCs.

Different concentrations of DPPH were introduced into the Ag_{14} NCs, and their corresponding UV-vis spectra were monitored (Fig. 3). The resulting NC architectures (NCA) are labelled as NCA-0.5, NCA-1.0, NCA-3.0, NCA-5.0, and NCA-10.0 with 0.5, 1.0, 3.0, 5.0, and 10.0 mole ratio of DPPH (with respect to the cluster), respectively. Up to a 1.0 mole ratio, the molecular features of Ag_{14} NCs were intact, with further increasing the concentration of DPPH, the NC solution becomes colorless. The corresponding UV-vis spectrum reveals the disappearance of major molecular features centered at 490 and 690 nm of the NCs. The peak at 340 nm is red shifted to 390 nm. We assume that this could be due to the degradation of NCs. The disappearance of NC features with increased DPPH ligands concentration illustrates that the NCs decompose or transform in this operation. The TEM images of Ag_{14} NCs with different concentrations of DPPH revealed the formation of supramolecular hierarchical structures (Fig. S5†). The NCA-0.5 shows a sheet-like assembly, and NCA-1.0 forms right-handed (P-type) super-helical bundles (Fig. S6 and S7†) or coiled coil-like structures^{44,45} alongside spherical structures

of $\sim 200\text{--}300$ nm (Fig. S8†). The EDS mapping of NCA 1.0 shows the presence of Ag, S, Cl, P and C which further suggests the aggregation of NCs (Fig. S9, S10, and S11†). With further increase in the concentration of DPPH, we have observed sheets and aggregates, which could be due to the decomposition or transformation of NCs; as also evident from the ^{31}P NMR data (Fig. S12 and S13†). The NCA-1.0 was analyzed in greater detail. The magnified images of spheres and helical bundles, similar to intermediate filaments such as keratin suggest that they comprise atomically precise Ag_{14} NCs (Fig. 4). Resolving the three-dimensional (3D) structures using electron tomography (ET) reconstruction reaffirms the spherical nature of superstructures (Fig. 4D and E). The cross-sectional view of the sphere reveals a solid interior due to the Ag_{14} NC assembly (Fig. 4F). Such NC assemblies could be formed by the inter-cluster supramolecular interactions between the NT ligands and secondary DPPH ligands.

Dynamic light scattering (DLS) studies unveil the size evolution of the nanostructures formed during the controlled addition of DPPH ligands (Fig. 4G). The average size of Ag_{14} NCs was found to be 3.2 ± 0.36 nm; NCA-0.5 shows an average size of 245 ± 2 nm. The NCA-1.0 superstructures show an average size of 375 ± 5 nm. With further increasing the concentration of DPPH, the size reduces, suggesting small aggregates and dissolved species.

To gain more insight into the NC assembled superstructures, we have performed ESI MS. Along with the parent NC ion (X^+), several new peaks were observed in the ESI MS of NCA-1.0 in the m/z range of 3900–4600 (Fig. 5). Detailed analysis of the peaks reveals that they are NC-DPPH adducts, the composition of the adducts are $[\text{X}_3\text{Y}_3]^{3+}$ ($\text{Y} = \text{DPPH}$), (m/z 4059), $[\text{X}_2\text{Y}_3]^{2+}$ (m/z 4287) along with other fragmentation peaks (Fig. 5). Higher NC-DPPH adducts were not observed, which could be due to their lower ionization efficiency. The compositions and the charge states of the adducts were determined by analyzing the m/z values and isotopic patterns of the peaks. In the isotopic distribution of $[\text{X}_3\text{Y}_3]^{3+}$, the difference between the peaks is m/z 0.33, which confirmed a charge state of 3+ (Fig. 5A2). The experimental isotopic distribution matches well with the theoretical isotopic distribution of $[\text{X}_3\text{Y}_3]^{3+}$, which further reaffirms the assigned composition. The difference between peaks in the isotopic distribution of $[\text{X}_2\text{Y}_3]^{2+}$ is m/z 0.5, which suggests a charge state of 2+ (Fig. 5A3). Along with these adducts there are several other low intensity peaks which could be due to weak gas phase adducts of X and Y. Due to low intensity, we could not perform CID measurements on the DPPH-mediated trimers and dimers of Ag_{14} NCs. To understand the role of DPPH in directing the hierarchical structures, NCA-1.0 was redispersed in DMF as DPPH is insoluble in DMF and analysed using UV-vis spectroscopy and ESI MS (Fig. S14†). The ESI MS in DMF didn't show any NC adducts which further confirms the role of DPPH in the NC assembly (Fig. S14†). We have also performed TEM measurements of the DPPH-NT mixture, which revealed that they also form thin sheets (Fig. S15†). The formation of sheet-like structures further reaffirms the supramolecular inter-

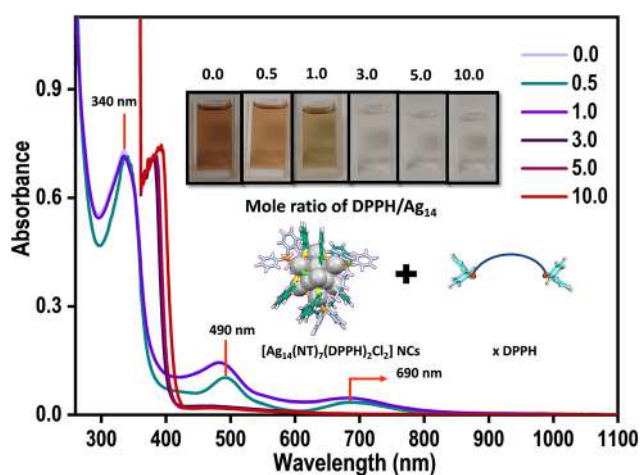


Fig. 3 Variation of UV-vis spectra trend of $[\text{Ag}_{14}(\text{NT})_7(\text{DPPH})_2\text{Cl}_2]^+$ NCs with the addition of different mole ratios of DPPH ligand. Inset shows the corresponding photographs of the NCs solutions.

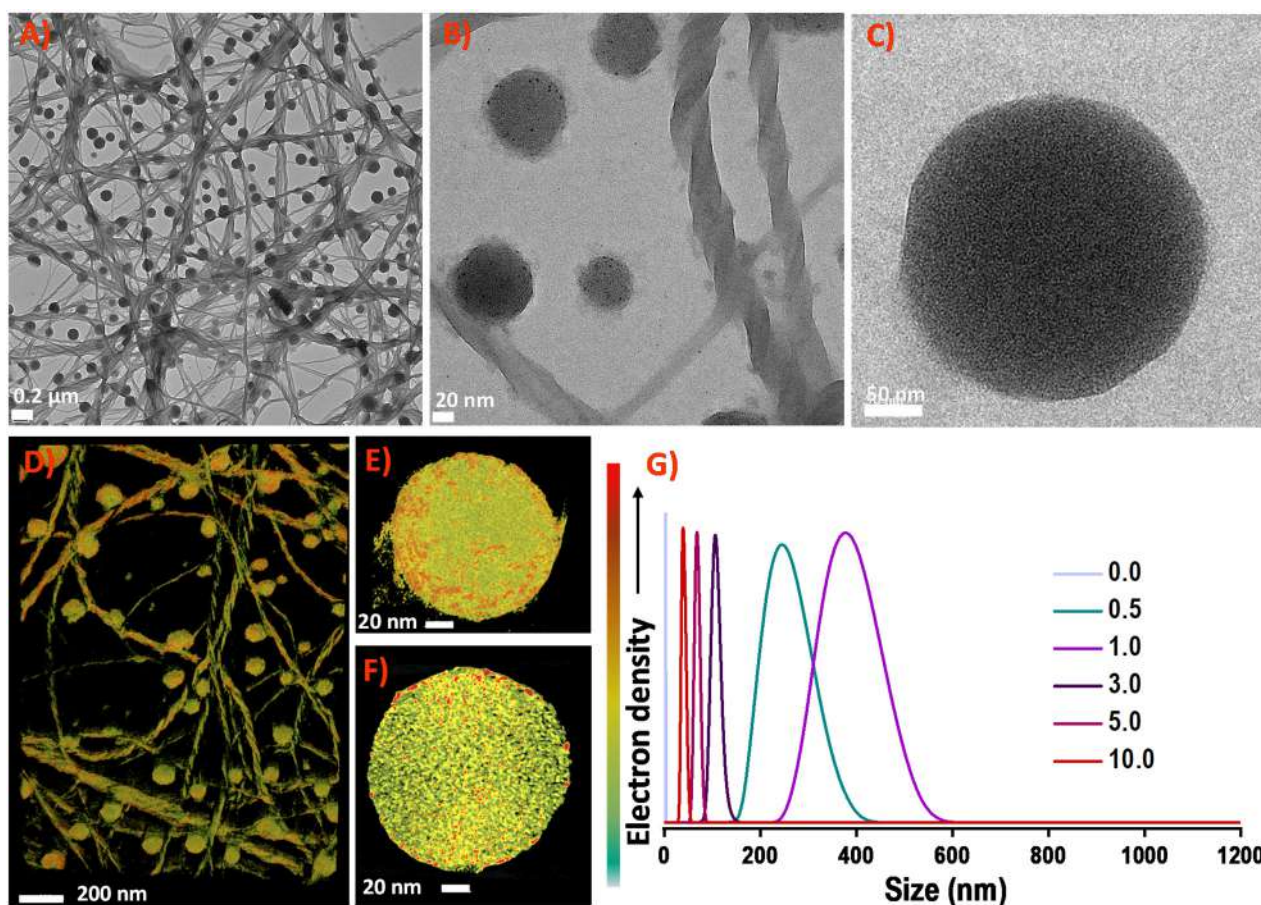


Fig. 4 TEM images showing the self-assembled superhelices and spheres NCA-1.0. Magnified TEM images are shown in A–C. (D) Electron tomography (ET) reconstruction of NCA-1.0. (E) and (F) are the 3D reconstructed structure of the Ag_{14} NC assembled sphere and its cross-sectional view. (G) DLS measurements show variation in size of $[\text{Ag}_{14}(\text{NT})_7(\text{DPPH})_2\text{Cl}_2]^+$ NCs with the addition of different molar ratios of DPPH ligands.

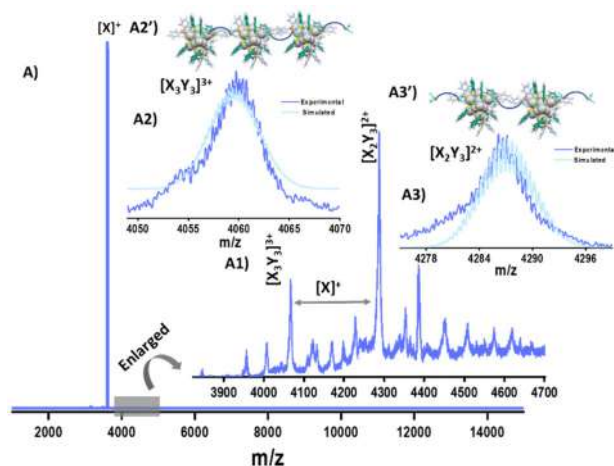


Fig. 5 (A) ESI MS showing the supramolecular adducts in NCA-1.0. (A1) Enlarged view of the same. (A2) The experimental and theoretical isotopic patterns of $[\text{X}_3\text{Y}_3]^{3+}$. (A2') Schematic representation of $[\text{X}_3\text{Y}_3]^{3+}$. (A3) The experimental and theoretical isotopic patterns of $[\text{X}_2\text{Y}_3]^{2+}$. (A3') Schematic representation of $[\text{X}_2\text{Y}_3]^{2+}$. (X = $[\text{Ag}_{14}(\text{NT})_7(\text{DPPH})_2\text{Cl}_2]^+$; Y = DPPH). Color codes: grey, Ag; blue/sea green, C; yellow, S; orange, P; green, Cl; white, H.

actions between the primary NT ligands and secondary DPPH ligands.

Mechanism for the formation of supramolecular architectures

We speculate that the optimum concentration of DPPH directs orthogonal self-assembly, which leads to the formation of two different supramolecular architectures in the same system. Specific non-covalent intermolecular interactions could direct the formation of such interpenetrating networks. Orthogonal self-assembly^{6,11,13} is an essential strategy in biological systems, where complex structures are generated by highly specific non-covalent interactions between constituents such as proteins, amphiphiles, and biopolymers.¹⁰ In supramolecular chemistry, specific non-covalent interactions are exploited to achieve such orthogonal self-assembly.⁴⁶ The naphthalene diimide chromophores⁴⁷ are known to organize into supramolecular helices.⁴⁸ Substitutions on naphthalene had resulted in helical tubes,⁴⁹ twisted ribbons or helices with preferred handedness.⁵⁰

Based on microscopic and spectroscopic investigations, we propose that the orthogonal self-assembly process of Ag_{14} NCs

relies on (i) bidentate nature of DPPH ligand, (ii) $\pi\cdots\pi$ stacking of the NT ligands in Ag_{14} NCs, (iii) $\text{CH}\cdots\pi$ interactions between NT and DPPH ligands (Fig. S16[†]), and (iv) $\text{H}\cdots\text{H}$ interactions between NT ligands (Scheme 1). Such covalent and non-covalent interactions together lead to the formation of the microspheres and sheets/films of Ag_{14} NCs (Scheme 1A1) whereas, a lower degree of self-assembly in the z-axis results in the formation of superhelices which tends to bundle to form rope-like NC assemblies (Scheme 1A2). Compared to other ligand-protected Ag_{14} nanoclusters such as $\text{Ag}_{14}(\text{3,4-DFBT})_{12}\text{TPP}_8$,³⁴ $\text{Ag}_{14}(\text{1,2-BDT})_6\text{TPP}_8$,³³ and $\text{Ag}_{14}(\text{pntp})_{10}(\text{dpph})_4\text{Cl}_2$,⁵¹ $[\text{Ag}_{14}(\text{NT})_7(\text{DPPH})_2\text{Cl}_2]^+$ NCs are ligand deficient. Therefore, their surface structure can afford a few more ligands without stripping the thiolates and phosphines. The NT and DPPH ligands and their $\pi\cdots\pi$ and $\text{CH}\cdots\pi$ interactions play a crucial role in directing such orthogonal self-assembled nanostructures.

Enhanced emission

The optical features of Ag_{14} NCs were retained up to NCA-1.0 which suggests that the NC property is retained in hierarchical structures. This prompted us to investigate their emission properties. A significant enhancement in the emission of Ag_{14} NCs assembled superstructures was observed (Fig. 6).

A three-fold enhancement in PL emission was observed in the case of NCA-1.0 than its parent Ag_{14} NCs. With increasing the concentration of DPPH (3.0, 5.0, and 10.0), the PL intensity reduces significantly. Increment in the emission of Ag_{14} NCs in solution by the addition of DPPH is attributed to the restricted motion of the ligands through ordered self-assembly. Atomically precise NCs are known to display aggregation-induced emission (AIE) due to restrictions in the intermolecular rotation (RIR).⁵² The ordered assembly of surface motifs in aggregation-induced nanostructures reduces vibrational relaxation enhancing emission.⁵³ The inter-nanocluster $\text{CH}\cdots\pi$ interactions are also known to restrict the intramolecular rotations/vibrations and amplify the PL emission of NCs.⁵⁴ We hypothesize that inter-nanocluster $\text{CH}\cdots\pi$ and $\pi\cdots\pi$

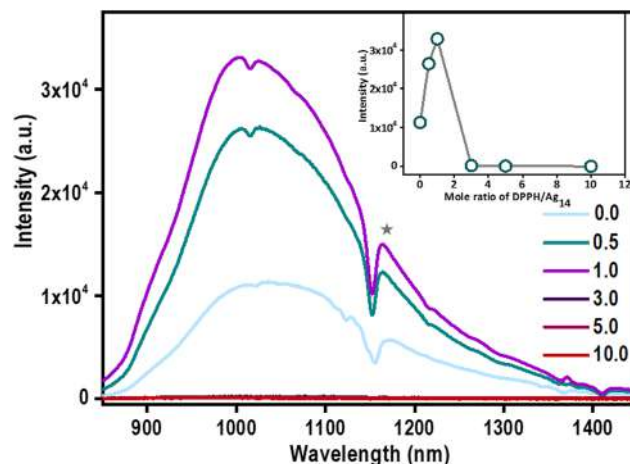


Fig. 6 Variation of PL trend of $[\text{Ag}_{14}(\text{NT})_7(\text{DPPH})_2\text{Cl}_2]^+$ NCs with the addition of different mole ratios of DPPH ligand (the star denotes the solvent-induced structuration). Inset shows the variation of PL intensity at 1035 nm with a different mole ratio of DPPH ligand.

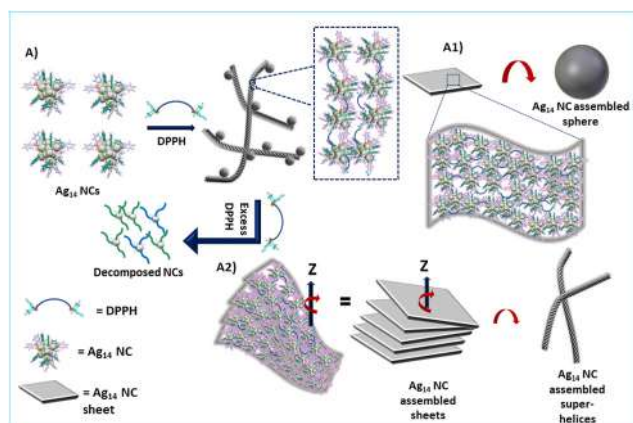
interactions that direct the ordered assembly of the NCs together restrict the molecular rotations and enhances the emission.

Conclusions

In this work, we demonstrate a novel facile route for creating supramolecular architectures of atomically precise NCs. The controlled addition of bidentate secondary ligand DPPH directs the orthogonal self-assembly of NCs reminiscent of biological systems. The mass spectrometric investigations reveal that the supramolecular architectures are formed by the assembly of NC-DPPH adducts. The distinct non-covalent interactions of surface motifs with excess secondary bidentate ligands play a pivotal role in such orthogonal self-assembly of NCs. The self-assembled structures show an enhanced NIR emission due to restricted intramolecular motion (RIM). To the best of our knowledge, this is the first example of secondary-ligand induced orthogonal self-assembly of atomically precise NCs. We envision the application of orthogonal self-assembly approaches to create self-assembled structures from atomically precise NCs that offer complex hierarchical architectures of NCs.

Author contributions

K.S.S and A.P.S performed synthesis, and other experimental studies. Nonappa performed electron tomography, HRTEM and STEM studies. D.G and J.R performed mass spectrometric studies. J.S.M performed the TEM measurements. M.P.K performed XPS studies. B.S.S performed NMR studies. P.S performed SEM measurements. W.A.D was involved in the discussion of experimental data. K.S.S wrote the first draft of the manuscript and all co-authors have given approval to the final



Scheme 1 Schematic illustration showing the mechanism of DPPH-induced orthogonal self-assembly of Ag_{14} NCs into superhelices and spheres.

version of the manuscript. T.P conceptualized and finalized the manuscript.

Conflicts of interest

There are no conflicts to declare.

Acknowledgements

We thank the Department of Science and Technology, Government of India, for constantly supporting our research program on nanomaterials. K. S. S thanks the University Grants Commission (UGC), Govt. of India, for her research fellowship. P. S., J. R., and D. G. thanks IIT Madras for their research fellowship. W. A. D thanks SERB-DST for the award of a National Postdoctoral Fellowship (NPDF). B. S. S thanks CSIR for his research fellowship. We thank Dr Ganesan Paramasivam for his help and suggestions in this work. We acknowledge the Academy of Finland for project funding (No. 352900), Photonics Research and Innovation (PREIN) flagship, Nanomicroscopy Center at Aalto University and Tampere Microscopy Centre at Tampere University for instrumentation facilities.

References

- 1 J. D. Watson and F. H. C. Crick, *Nature*, 1953, **171**, 737–738.
- 2 T. Xiao, X.-Q. Sun and L. Wang, in *Handbook of Macrocyclic Supramolecular Assembly*, ed. Y. Liu, Y. Chen and H.-Y. Zhang, Springer Singapore, Singapore, 2019, pp. 1–28, DOI: [10.1007/978-981-13-1744-6_54-1](https://doi.org/10.1007/978-981-13-1744-6_54-1).
- 3 T. Leigh and P. Fernandez-Trillo, *Nat. Rev. Chem.*, 2020, **4**, 291–310.
- 4 C. K. McLaughlin, G. D. Hamblin and H. F. Sleiman, *Chem. Soc. Rev.*, 2011, **40**, 5647–5656.
- 5 P. Yakovchuk, E. Protozanova and M. D. Frank-Kamenetskii, *Nucleic Acids Res.*, 2006, **34**, 564–574.
- 6 M. L. Saha, S. De, S. Pramanik and M. Schmittel, *Chem. Soc. Rev.*, 2013, **42**, 6860–6909.
- 7 X.-Y. Hu, T. Xiao, C. Lin, F. Huang and L. Wang, *Acc. Chem. Res.*, 2014, **47**, 2041–2051.
- 8 T. Xiao, X.-Q. Sun and L. Wang, *Handbook of Macrocyclic Supramolecular Assembly*, 2020, pp. 1317–1344.
- 9 S. Datta, M. L. Saha and P. J. Stang, *Acc. Chem. Res.*, 2018, **51**, 2047–2063.
- 10 J. Boekhoven, A. M. Brizard, M. C. A. Stuart, L. Florusse, G. Raffy, A. Del Guerzo and J. H. van Esch, *Chem. Sci.*, 2016, **7**, 6021–6031.
- 11 P. Wei, X. Yan and F. Huang, *Chem. Soc. Rev.*, 2015, **44**, 815–832.
- 12 Y. Sun, S. Li, Z. Zhou, M. L. Saha, S. Datta, M. Zhang, X. Yan, D. Tian, H. Wang, L. Wang, X. Li, M. Liu, H. Li and P. J. Stang, *J. Am. Chem. Soc.*, 2018, **140**, 3257–3263.
- 13 S. Datta, S. K. Misra, M. L. Saha, N. Lahiri, J. Louie, D. Pan and P. J. Stang, *Proc. Natl. Acad. Sci. U. S. A.*, 2018, **115**, 8087–8092.
- 14 K. Ariga, T. Mori, T. Kitao and T. Uemura, *Adv. Mater.*, 2020, **32**, 1905657.
- 15 V. Karthick, L. Kumar Shrestha, V. G. Kumar, P. Pranjali, D. Kumar, A. Pal and K. Ariga, *Nanoscale*, 2022, **14**(30), 10630–10647.
- 16 K. Ariga, *Nanoscale*, 2022, **14**(30), 10610–10629.
- 17 R. Jin, C. Zeng, M. Zhou and Y. Chen, *Chem. Rev.*, 2016, **116**, 10346–10413.
- 18 I. Chakraborty and T. Pradeep, *Chem. Rev.*, 2017, **117**, 8208–8271.
- 19 J. V. Rival, P. Mymoona, K. M. Lakshmi, Nonappa, T. Pradeep and E. S. Shibu, *Small*, 2021, **17**, 2005718.
- 20 H. Zhang, Z. Zhao, P. R. McGonigal, R. Ye, S. Liu, J. W. Y. Lam, R. T. K. Kwok, W. Z. Yuan, J. Xie, A. L. Rogach and B. Z. Tang, *Mater. Today*, 2020, **32**, 275–292.
- 21 Nonappa, *Beilstein J. Nanotechnol.*, 2020, **11**, 533–546.
- 22 C. Zeng, Y. Chen, K. Kirschbaum, K. J. Lambright and R. Jin, *Science*, 2016, **354**, 1580–1584.
- 23 Y. Li, M. Zhou, Y. Song, T. Higaki, H. Wang and R. Jin, *Nature*, 2021, **594**, 380–384.
- 24 Q. Li, J. C. Russell, T.-Y. Luo, X. Roy, N. L. Rosi, Y. Zhu and R. Jin, *Nat. Commun.*, 2018, **9**, 3871.
- 25 S. Chandra, Nonappa, G. Beaune, A. Som, S. Zhou, J. Lahtinen, H. Jiang, J. V. I. Timonen, O. Ikkala and R. H. A. Ras, *Adv. Opt. Mater.*, 2019, **7**, 1900620.
- 26 Y. Bi, Z. Wang, T. Liu, D. Sun, N. Godbert, H. Li, J. Hao and X. Xin, *ACS Nano*, 2021, **15**, 15910–15919.
- 27 J. Shen, Q. Xiao, P. Sun, J. Feng, X. Xin, Y. Yu and W. Qi, *ACS Nano*, 2021, **15**, 4947–4955.
- 28 A. Ebina, S. Hossain, H. Horihata, S. Ozaki, S. Kato, T. Kawawaki and Y. Negishi, *Nanomaterials*, 2020, **10**, 1105.
- 29 Z. Wu, Q. Yao, S. Zang and J. Xie, *ACS Mater. Lett.*, 2019, **1**, 237–248.
- 30 X. Kang and M. Zhu, *Coord. Chem. Rev.*, 2019, **394**, 1–38.
- 31 A. Som, A. Griffo, I. Chakraborty, H. Hähl, B. Mondal, A. Chakraborty, K. Jacobs, P. Laaksonen, O. Ikkala, T. Pradeep and Nonappa, *Small*, 2022, **18**, 2201707.
- 32 P. Sun, Z. Wang, Y. Bi, D. Sun, T. Zhao, F. Zhao, W. Wang and X. Xin, *ACS Appl. Nano Mater.*, 2020, **3**, 2038–2046.
- 33 M. Bodiuzzaman, E. Khatun, K. S. Sugi, G. Paramasivam, W. A. Dar, S. Antharjanam and T. Pradeep, *J. Phys. Chem. C*, 2020, **124**, 23426–23432.
- 34 H. Yang, J. Lei, B. Wu, Y. Wang, M. Zhou, A. Xia, L. Zheng and N. Zheng, *Chem. Commun.*, 2013, **49**, 300–302.
- 35 A. Jana, M. Jash, A. K. Poonia, G. Paramasivam, M. R. Islam, P. Chakraborty, S. Antharjanam, J. Machacek, S. Ghosh, K. N. V. D. Adarsh, T. Base and T. Pradeep, *ACS Nano*, 2021, **15**, 15781–15793.
- 36 Z.-Y. Wang, M.-Q. Wang, Y.-L. Li, P. Luo, T.-T. Jia, R.-W. Huang, S.-Q. Zang and T. C. W. Mak, *J. Am. Chem. Soc.*, 2018, **140**, 1069–1076.

- 37 Q. Li, D. Zhou, J. Chai, W. Y. So, T. Cai, M. Li, L. A. Peteanu, O. Chen, M. Cotlet, X. Wendy Gu, H. Zhu and R. Jin, *Nat. Commun.*, 2020, **11**, 2897.
- 38 T. Imamoto, T. Oshiki, T. Onozawa, T. Kusumoto and K. Sato, *J. Am. Chem. Soc.*, 1990, **112**, 5244–5252.
- 39 S. Bestgen, O. Fuhr, B. Breitung, V. S. Kiran Chakravadhanula, G. Guthausen, F. Hennrich, W. Yu, M. M. Kappes, P. W. Roesky and D. Fenske, *Chem. Sci.*, 2017, **8**, 2235–2240.
- 40 M.-C. Brandys and R. J. Puddephatt, *J. Am. Chem. Soc.*, 2002, **124**, 3946–3950.
- 41 X. Kang, S. Wang and M. Zhu, *Chem. Sci.*, 2018, **9**, 3062–3068.
- 42 E. Khatun, A. Ghosh, P. Chakraborty, P. Singh, M. Bodiuzzaman, P. Ganesan, G. Nataranjan, J. Ghosh, S. K. Pal and T. Pradeep, *Nanoscale*, 2018, **10**, 20033–20042.
- 43 M. S. Bootharaju, S. Lee, G. Deng, H. Chang, W. Baek and T. Hyeon, *J. Chem. Phys.*, 2021, **155**, 014307.
- 44 L. Pauling and R. B. Corey, *Nature*, 1953, **171**, 59–61.
- 45 F. H. Crick, *Nature*, 1952, **170**, 882–883.
- 46 A. J. Savyasachi, O. Kotova, S. Shanmugaraju, S. J. Bradberry, G. M. Ó'Máille and T. Gunnlaugsson, *Chem*, 2017, **3**, 764–811.
- 47 M. R. Molla, A. Das and S. Ghosh, *Chem. – Eur. J.*, 2010, **16**, 10084–10093.
- 48 S. M. Wagalgave, S. D. Padghan, M. D. Burud, M. A. Kobaisi, D. D. La, R. S. Bhosale, S. V. Bhosale and S. V. Bhosale, *Sci. Rep.*, 2019, **9**, 12825.
- 49 G. D. Pantoş, P. Pengo and J. K. M. Sanders, *Angew. Chem., Int. Ed.*, 2007, **46**, 194–197.
- 50 M. Al Kobaisi, S. V. Bhosale, K. Latham, A. M. Raynor and S. V. Bhosale, *Chem. Rev.*, 2016, **116**, 11685–11796.
- 51 X. Q. Liang, Y. Z. Li, Z. Wang, S. S. Zhang, Y. C. Liu, Z. Z. Cao, L. Feng, Z. Y. Gao, Q. W. Xue, C. H. Tung and D. Sun, *Nat. Commun.*, 2021, **12**, 4966.
- 52 X. Kang and M. Zhu, *Chem. Soc. Rev.*, 2019, **48**, 2422–2457.
- 53 Z. Luo, X. Yuan, Y. Yu, Q. Zhang, D. T. Leong, J. Y. Lee and J. Xie, *J. Am. Chem. Soc.*, 2012, **134**, 16662–16670.
- 54 T. Chen, S. Yang, J. Chai, Y. Song, J. Fan, B. Rao, H. Sheng, H. Yu and M. Zhu, *Sci. Adv.*, 2017, **3**, e1700956.

Electronic supplementary information

Secondary ligand-induced orthogonal self-assembly of silver nanoclusters into superstructures with enhanced NIR emission

Korath Shivan Sugi,^a Amritha P Sandra,^a Nonappa,^b Debasmita Ghosh,^a Jyoti Sarita Mohanty,^a Murugesan Paulthangam Kannan,^a B. S. Sooraj,^a Pillalamarri Srikrishnarka,^a Jayoti Roy,^a Wakeel Ahmed Dar,^a and Thalappil Pradeep^{*a}

^a *DST Unit of Nanoscience (DST UNS) and Thematic Unit of Excellence (TUE), Department of Chemistry, Indian Institute of Technology Madras, Chennai 600 036; India; International Centre for Clean Water, Chennai 600113, India*

^b *Faculty of Engineering and Natural Sciences, Tampere University, FI-33720 Tampere, Finland*

**E-mail: pradeep@iitm.ac.in*

Table of contents

SL. No.	Description	Page No.
	Serial EM and electron tomography reconstruction	2
	ESI MS conditions	2
Fig. S1	Collision-induced dissociation mass spectra of the Ag ₁₄ nanoclusters	3
Fig. S2	SEM image and EDS mapping of Ag ₁₄ nanoclusters	4
Fig. S3	XPS of Ag ₁₄ nanoclusters	4
Fig. S4	³¹ P NMR of Ag ₁₄ nanoclusters	5
Fig. S5	TEM images showing the structural evolution of Ag ₁₄ nanoclusters with the addition of different molar ratios of DPPH ligand	6
Fig. S6	Large area TEM images of NCA-1.0	7
Fig. S7	Large area HRTEM images of NCA 1.0	8

Fig. S8	STEM images of NCA-1.0	9
Fig. S9	STEM-EDS mapping of NCA-1.0	9
Fig. S10	STEM-EDS mapping of spherical structures in NCA-1.0	10
Fig. S11	EDX spectrum of NCA-1.0	10
Fig. S12	The ^{31}P NMR spectra of NCA 0.5 and NCA 1.0.	11
Fig. S13	The ^{31}P NMR spectra of NCA 3.0, NCA 5.0, and NCA 10.0.	11
Fig. S14	UV-vis spectrum and ESI MS of NCA-1.0 redispersed in DMF	12
Fig. S15	TEM images of the DPPH-NT mixture	12
Fig. S16	Schematic illustration of supramolecular interactions in Ag_{14} nanoclusters	13

Serial EM and electron tomography reconstruction: The image acquisition was performed using a JEOL JEM-3200FSC field emission TEM operated at 300 kV with an Omega-type zero-loss filter. The tilt series of 2D projections (between $\pm 69^\circ$ angles with 2° increment steps) were recorded using SerialEM software.¹⁻³ The pre-alignment and final alignment were performed using IMOD software.⁴ Finally, the maximum entropy method (MEM),⁵ was used with a custom-made program with a regularization parameter value of $\lambda = 1.0\text{e}^{-3}$ for reconstruction and colored tomograms were prepared using Chimera software.

ESI MS conditions

Sample concentration: 10 $\mu\text{g/mL}$

Solvent: DCM/TCM/DMF

Flow rate: 30 $\mu\text{L/min}$

Capillary voltage: 2 kV

Source temperature: 50°C

Sampling cone: 0

Source offset: 0

Desolvation temperature: 65°C

Desolvation gas flow: 400.0 L/h

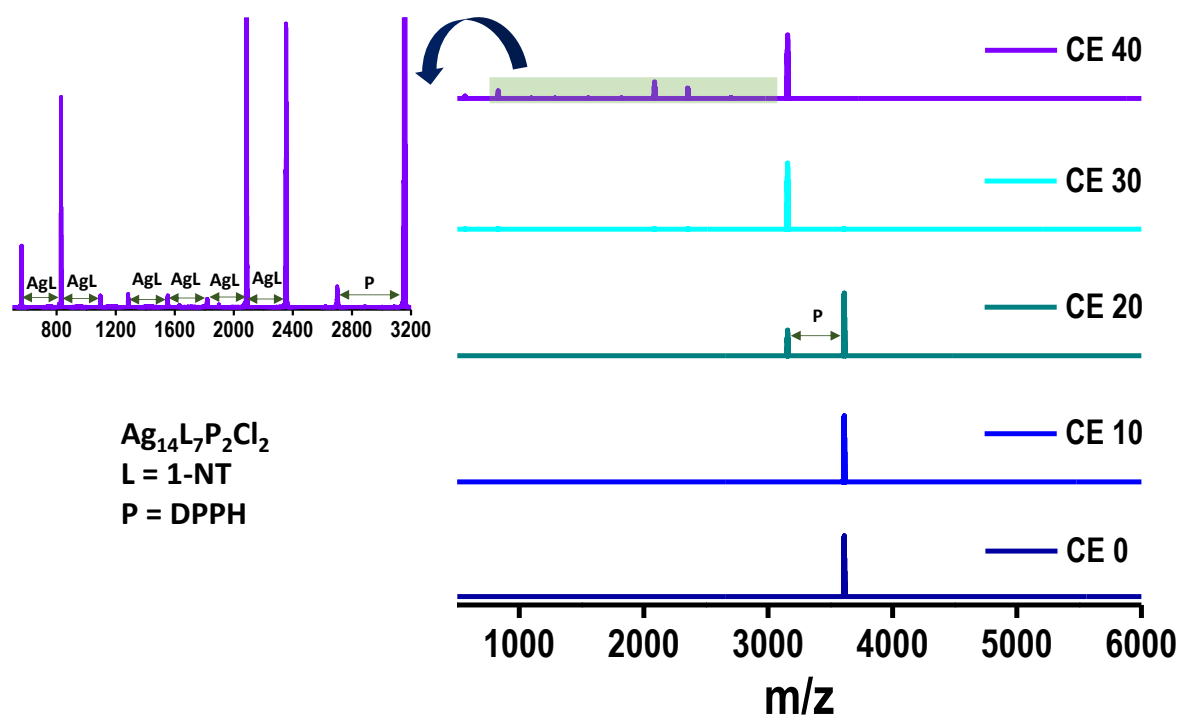


Fig. S1 A) Collision-induced dissociation (CID) mass spectra of the peak which is assigned as $[Ag_{14}(NT)_7(DPPH)_2Cl_2]^+$. The systematic loss of two DPPH ligands upon the increase in collision energy was observed along with the loss of some Ag-L.

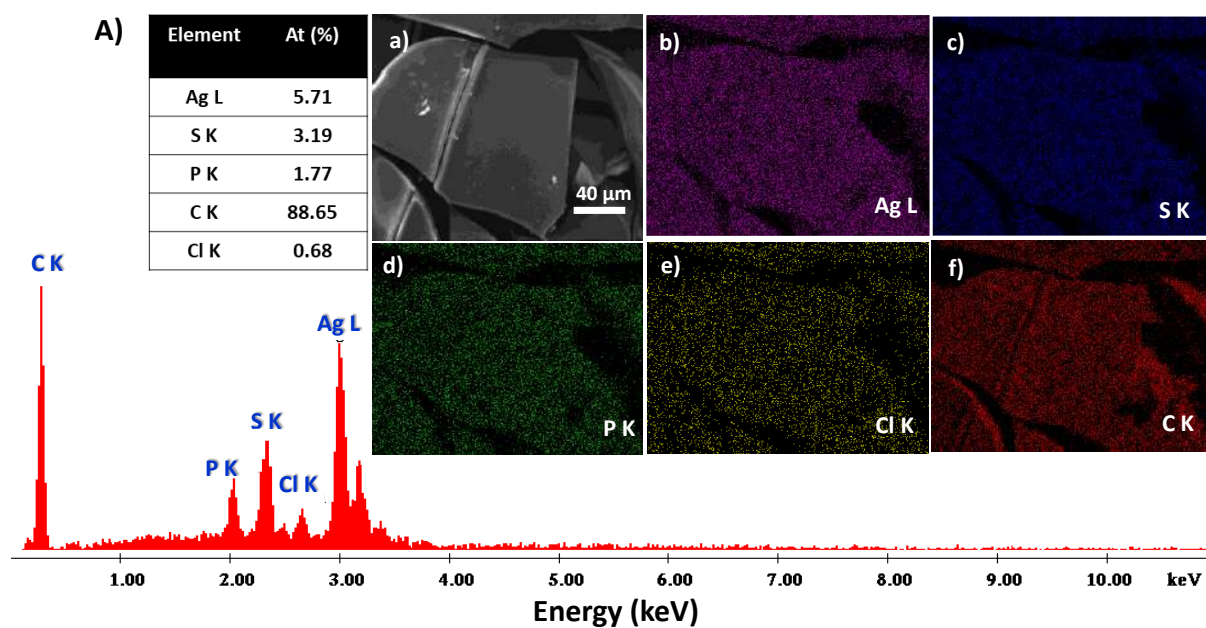


Fig. S2 A) SEM image and EDS mapping of b) Ag L, c) S K, d) P K, e) Cl K, and f) C K.

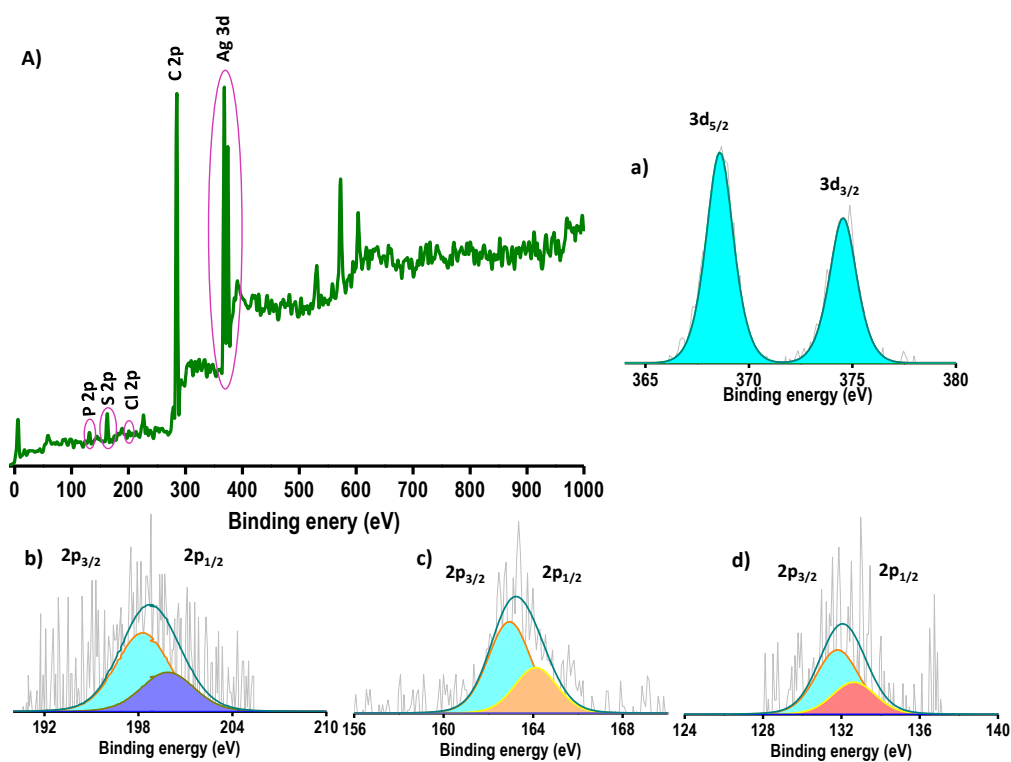


Fig. S3 A) XPS survey spectrum of $[\text{Ag}_{14}(\text{NT})_7(\text{DPPH})_2\text{Cl}_2]^+$. Expanded area of a) Ag 3d, b) Cl 2p, c) S 2p, and d) P 2p.

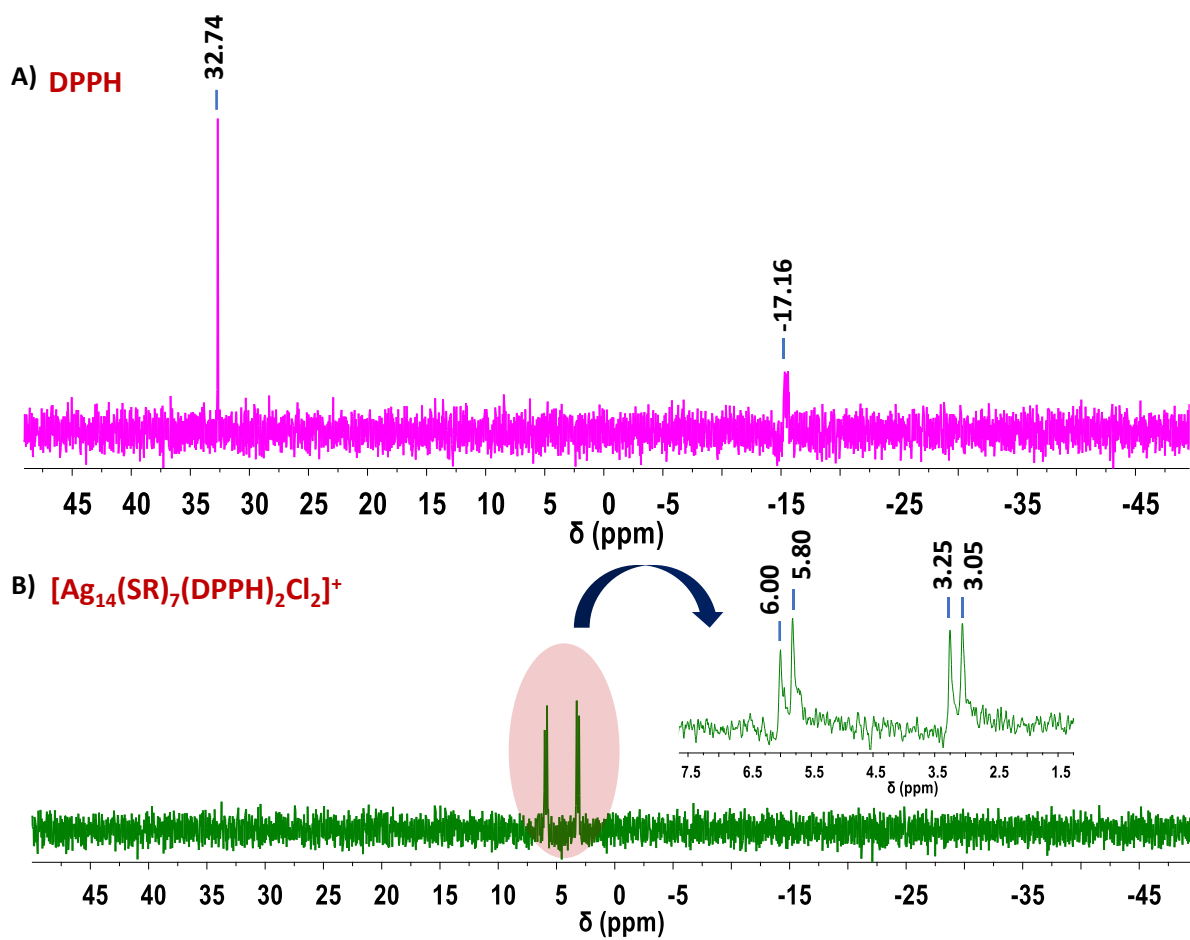


Fig. S4 The ^{31}P NMR spectra of A) DPPH and B) $[\text{Ag}_{14}(\text{NT})_7(\text{DPPH})_2\text{Cl}_2]^+$ NCs confirm the formation of Ag-P bonds.

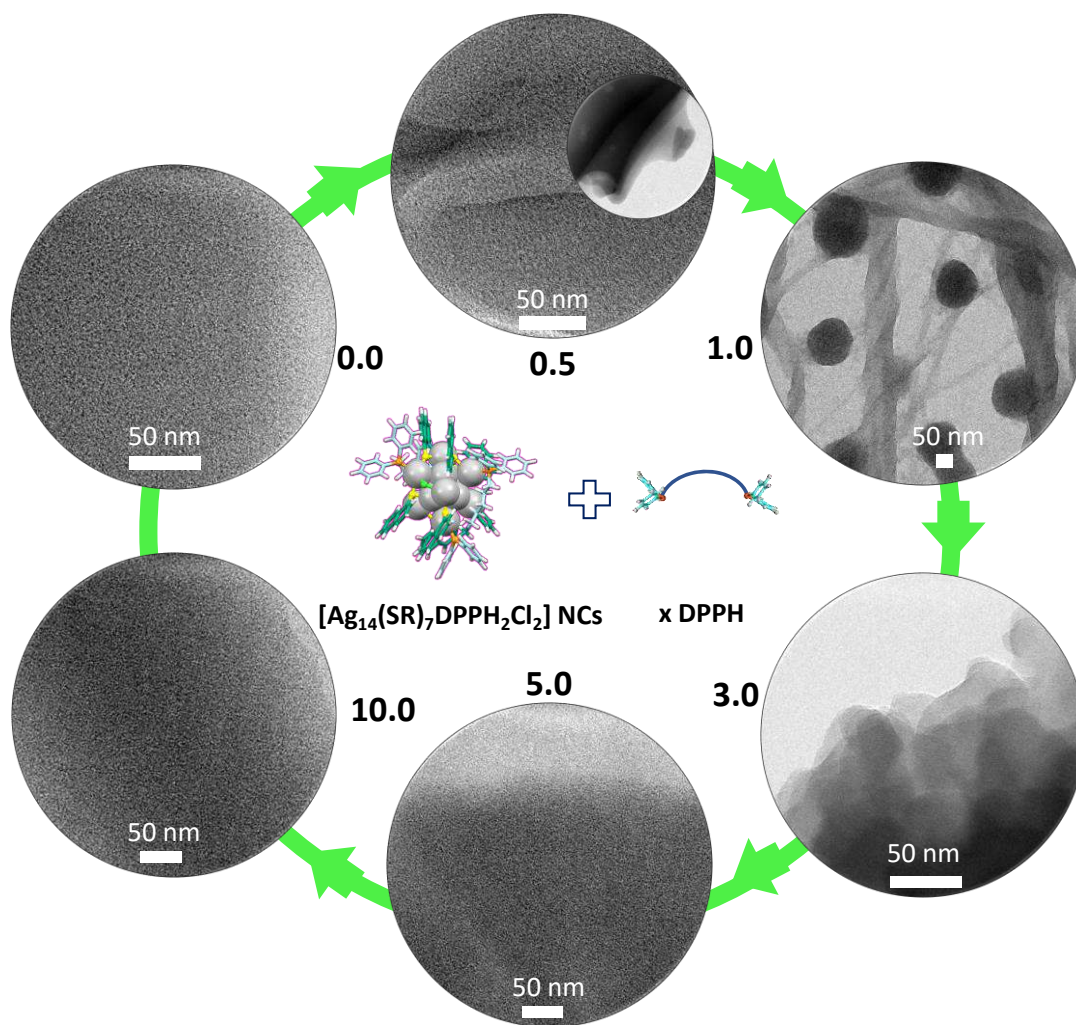


Fig. S5 TEM images showing the structural evolution of $[\text{Ag}_{14}(\text{NT})_7(\text{DPPH})_2\text{Cl}_2]^+$ NCs with the addition of different molar ratios of DPPH ligand.

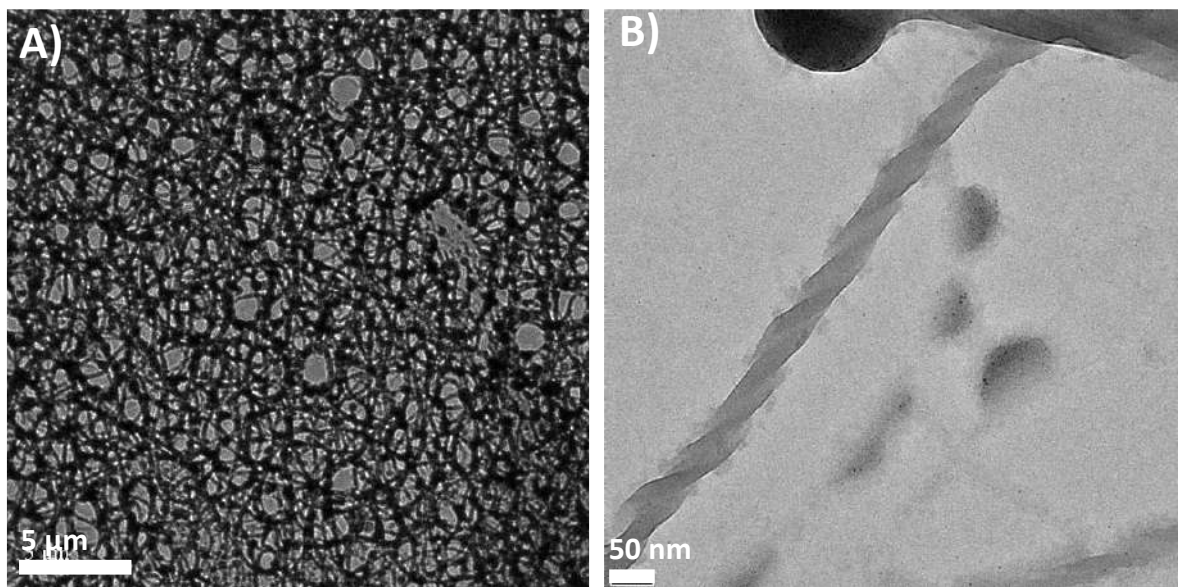


Fig. S6 A) Large area TEM images of NCA-1.0. B) Expanded view of super helical structures.

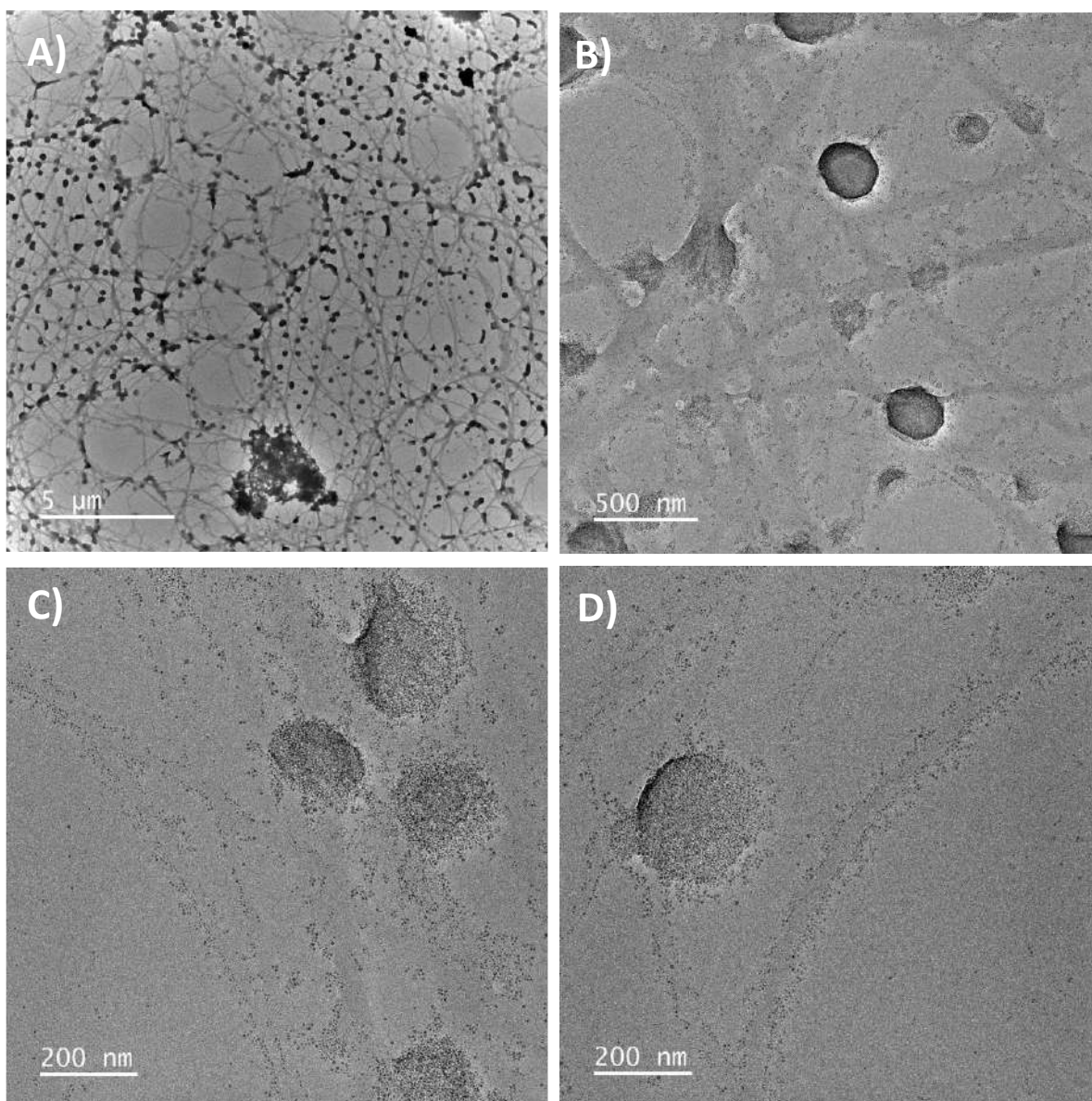


Fig. S7 A) Large area HRTEM images of NCA-1.0. B), C), and D) are the expanded view which confirms the presence of nanoclusters in the helical and spherical structures.

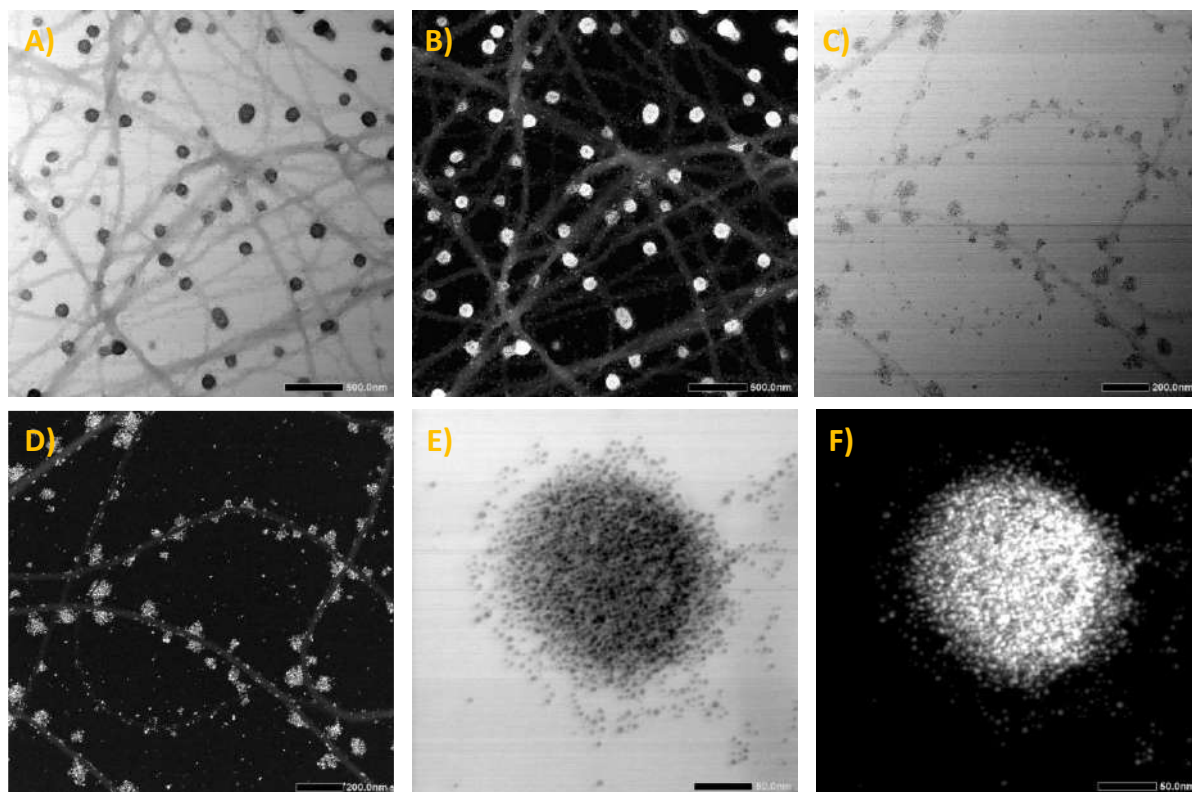


Fig. S8 Bright field (BF) and dark field (DF) STEM images of different regions of the NCA-1.0 sample.

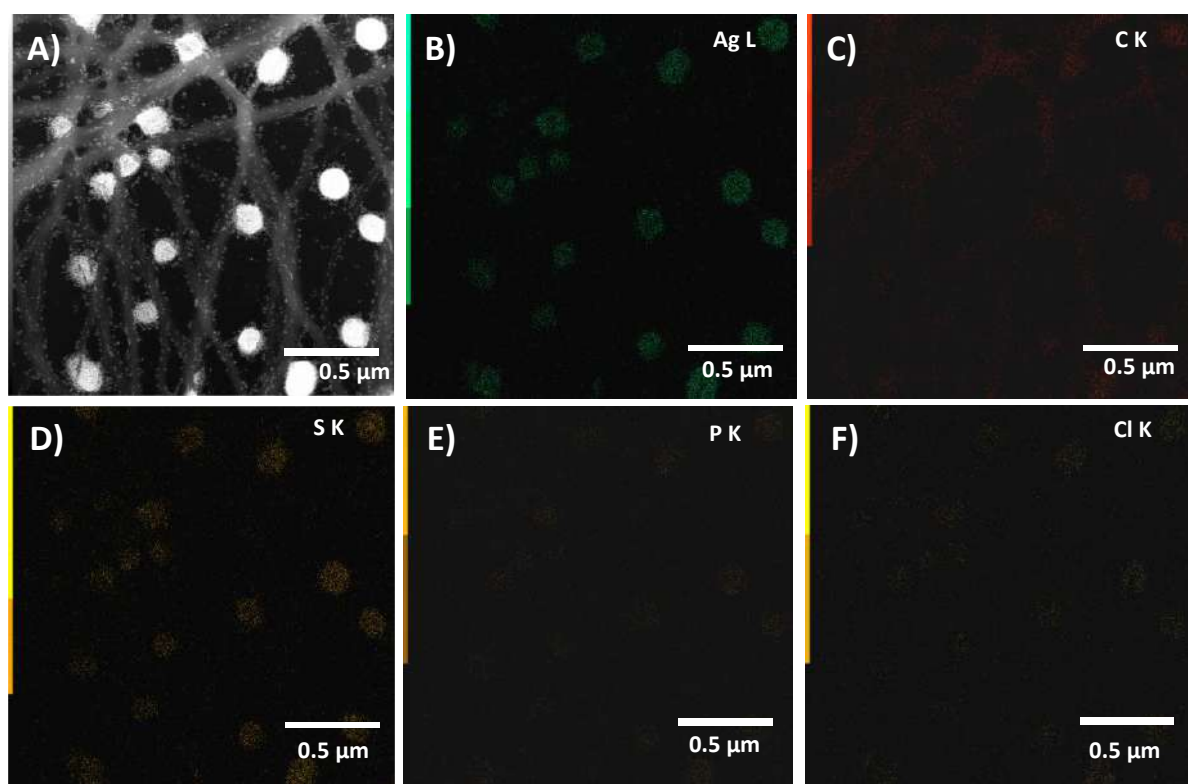


Fig. S9 STEM-EDS mapping of Ag, C, S, P, and Cl of NCA-1.0.

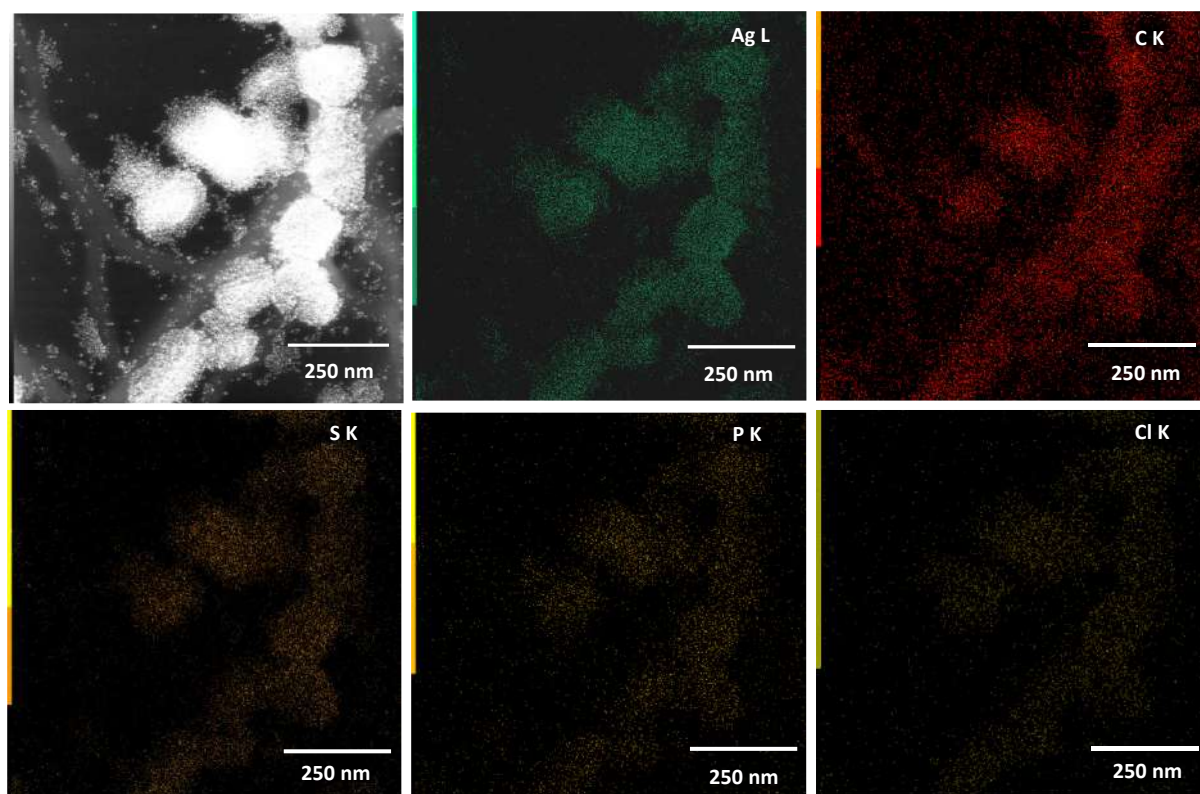


Fig. S10 STEM-EDS mapping of Ag, C, S, P, and Cl in spherical structures of NCA-1.0.

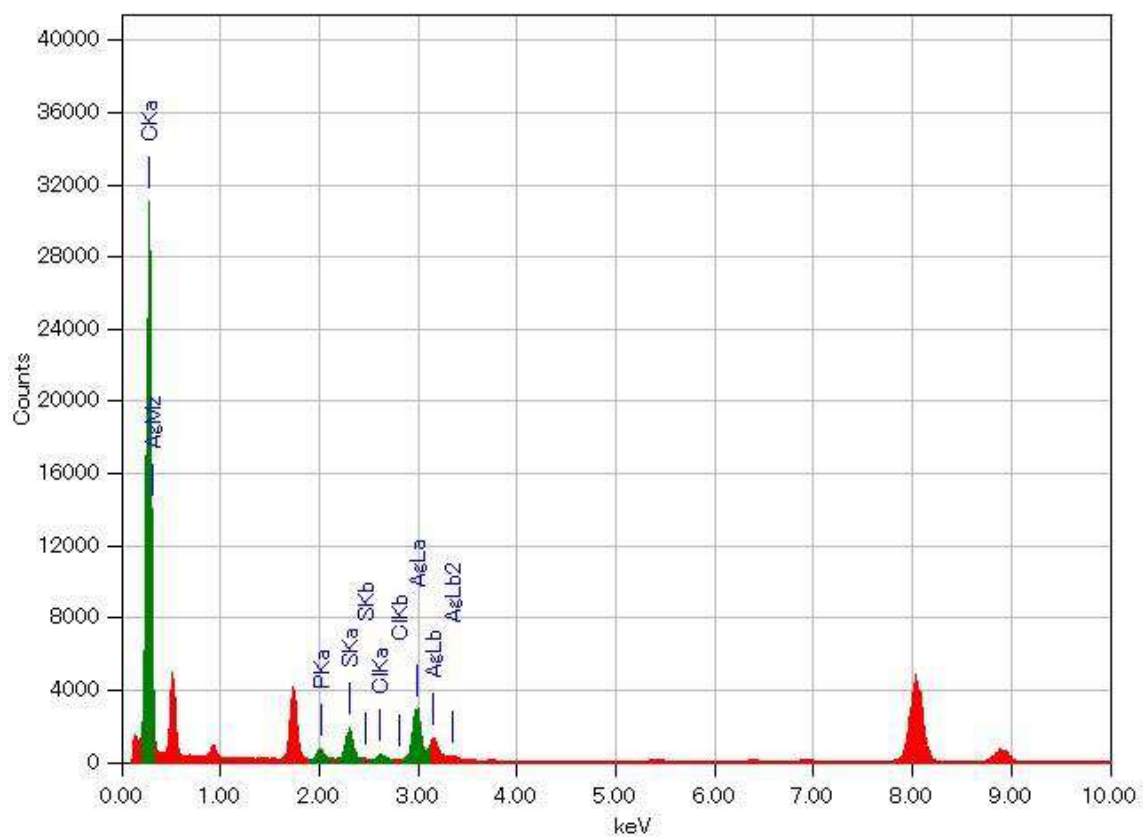


Fig. S11 EDX spectrum of NCA-1.0.

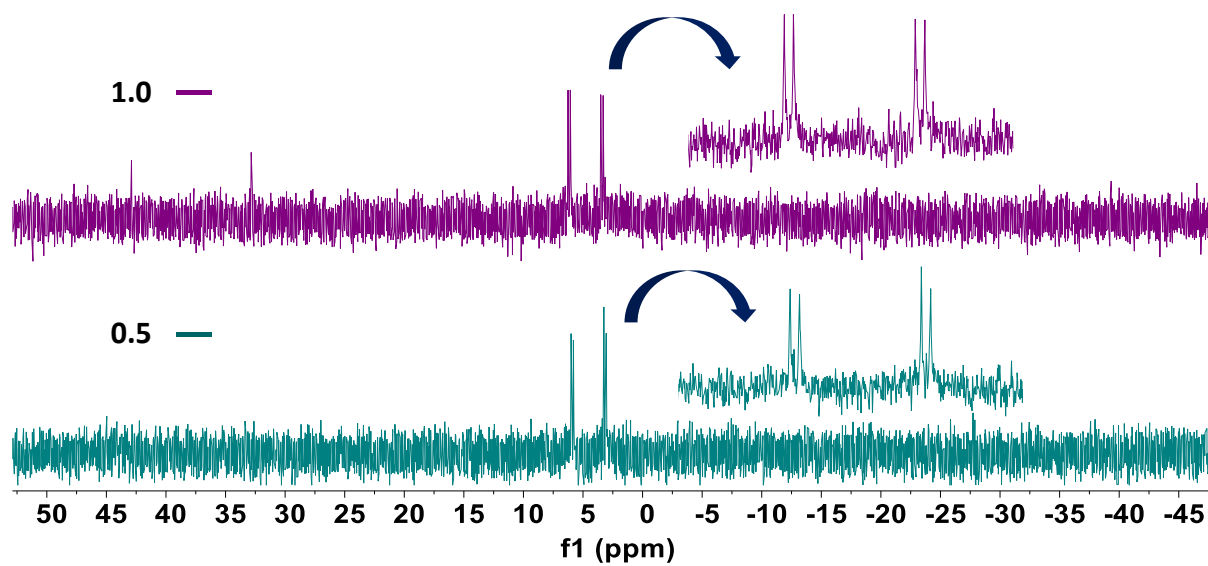


Fig. S12 The ^{31}P NMR spectra of NCA 0.5 and NCA 1.0.

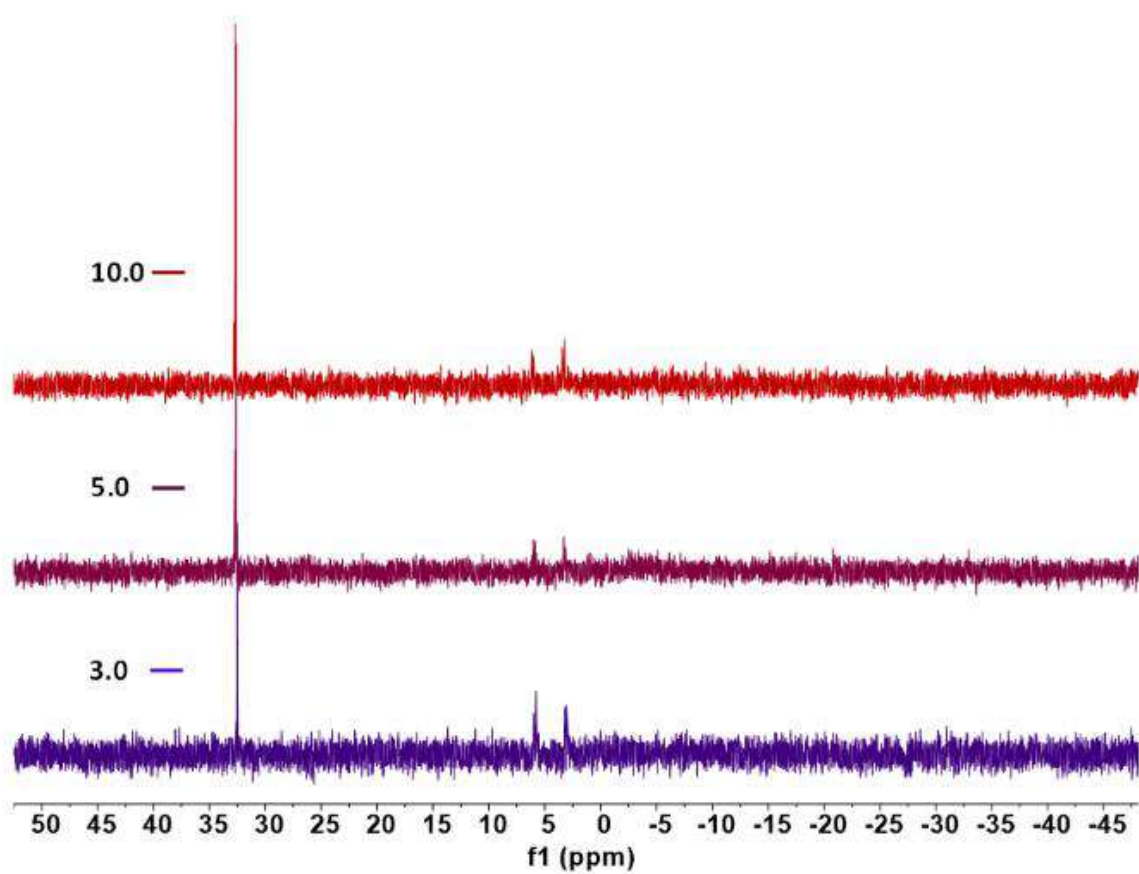


Fig. S13 The ^{31}P NMR spectra of NCA 3.0, NCA 5.0, and NCA 10.0.

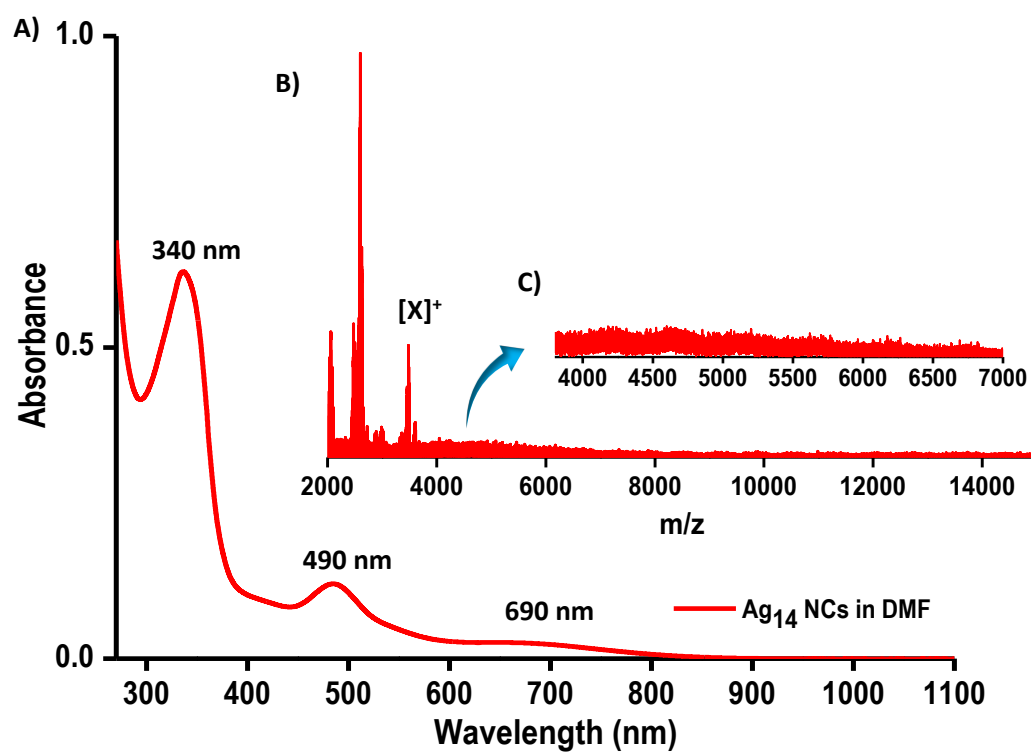


Fig. S14 A) UV-vis spectrum of NCA-1.0 redispersed in DMF. B) The corresponding ESI MS. C) Enlarged view.

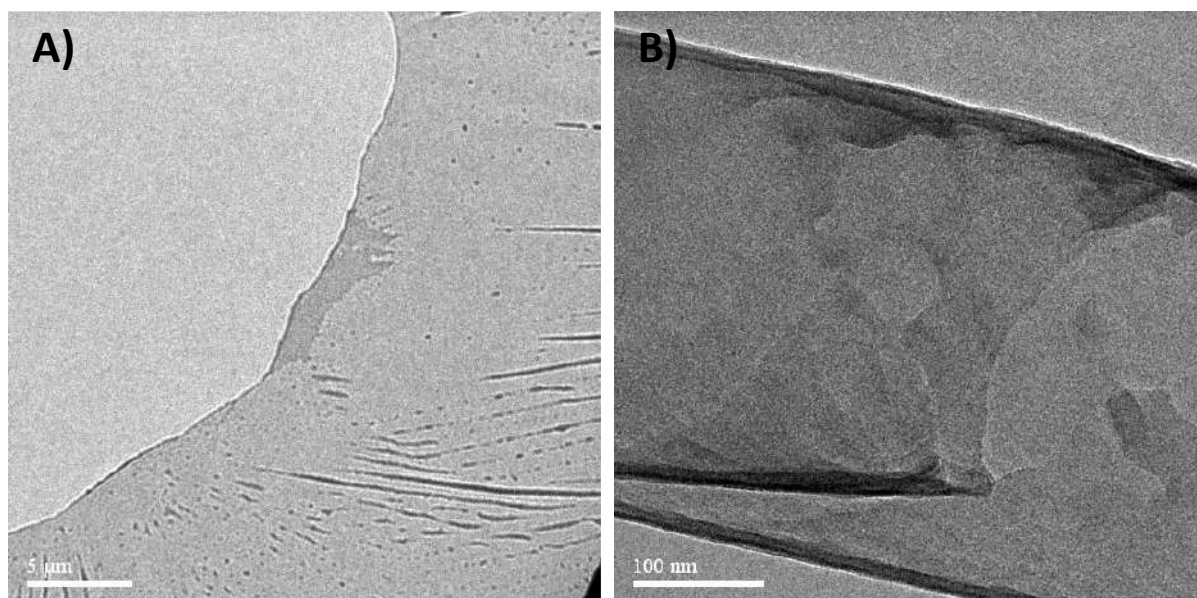


Fig. S15 A) and B) is the TEM images of the DPPH-NT mixture.

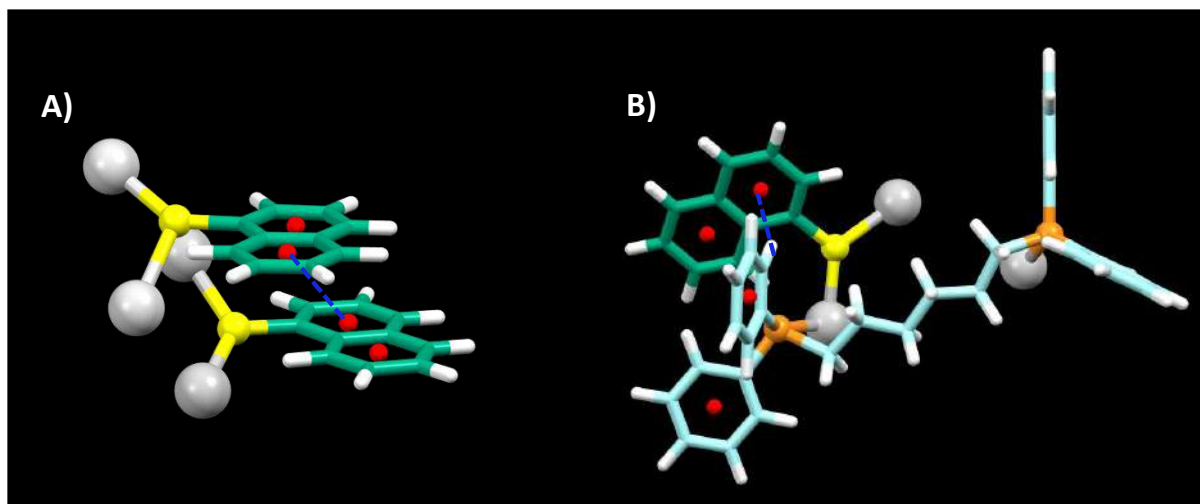


Fig. S16 Schematic illustration of possible supramolecular interactions in Ag₁₄ NC assemblies. A) $\pi \dots \pi$ interactions between NT ligands. B) CH $\dots\pi$ interactions between NT and DPPH ligands.

References

1. D. N. Mastronarde, *Microscopy and Microanalysis*, 2003, **9**, 1182-1183.
2. D. N. Mastronarde, *Journal of Structural Biology*, 2005, **152**, 36-51.
3. N. Nonappa and P. Engelhardt, *Imaging & Microscopy*, 2019, **21**, 22-24.
4. J. R. Kremer, D. N. Mastronarde and J. R. McIntosh, *J Struct Biol*, 1996, **116**, 71-76.
5. P. Engelhardt, in *Encyclopedia of Analytical Chemistry*, DOI: <https://doi.org/10.1002/9780470027318.a1405>.

Formation and Transformation of Clathrate Hydrates under Interstellar Conditions

Jyotirmoy Ghosh, Gaurav Vishwakarma, Rajnish Kumar,* and Thalappil Pradeep*



Cite This: <https://doi.org/10.1021/acs.accounts.3c00317>



Read Online

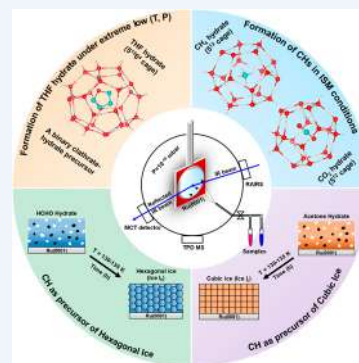
ACCESS |

Metrics & More

Article Recommendations

CONSPECTUS: Continuing efforts by many research groups have led to the discovery of ~240 species in the interstellar medium (ISM). Observatory- and laboratory-based astrochemical experiments have led to the discovery of these species, including several complex organic molecules (COMs). Interstellar molecular clouds, consisting of water-rich icy grains, have been recognized as the primordial sources of COMs even at extremely low temperatures (~10 K). Therefore, it is paramount to understand the chemical processes of this region, which may contribute to the chemical evolution and formation of new planetary systems and the origin of life.

This Account discusses our effort to discover clathrate hydrates (CHs) of several molecules and their structural varieties, transformations, and kinetics in a simulated interstellar environment. CHs are nonstoichiometric crystalline host–guest complexes in which water molecules form cages of different sizes to entrap guest molecules. CHs are abundant on earth and require moderate temperatures and high pressures for their formation. Our focus has been to form CHs at extremely low pressure and temperature as in the ISM, although their existence under such conditions has been a long-standing question since water and guest molecules (CH_4 , CO_2 , CO , etc.) exist in space. In multiple studies conducted at $\sim 10^{-10}$ mbar, we showed that CH_4 , CO_2 , and C_2H_6 hydrates could be formed at 30, 10, and 60 K, respectively. Well-defined IR spectroscopic features supported by quantum chemical simulations and temperature-programmed desorption mass spectrometric analyses confirmed the existence of the S^{12} (for CH_4 and CO_2) and $S^{12}6^2$ (for C_2H_6) CH cages. Mild thermal activation for long periods under ultrahigh vacuum (UHV) allowed efficient molecular diffusion, which is crucial for forming CHs. We also explored the formation of THF hydrate (a promoter/stabilizer for binary CHs), and a spontaneous method was found for its formation under UHV. In a subsequent study, we observed a binary THF- CO_2 hydrate and its thermal processing at 130 K leading to the transportation of CO_2 from the hydrate cages to the matrix of amorphous water. The findings imply that such systems possess a dynamic setting that facilitates the movement of molecules, potentially accounting for the chemical changes observed in the ISM. Furthermore, an intriguing fundamental phenomenon is the consequences of these CHs and their dynamics. We showed that preformed acetone and formaldehyde hydrates dissociate to form cubic (I_c) and hexagonal (I_h) ices at 130–135 K, respectively. These unique processes could be the mechanistic routes for the formation of various ices in astrophysical environments. Other than adding a new entry, namely, CHs, to the list of species found in ISM, its existence opens new directions to astrochemistry, observational astronomy, and astrobiology. Our work provides a molecular-level understanding of the formation pathways of CHs and their transformation to crystalline ices, which sheds light on the chemical evolution of simple molecules to COMs in ISM. Furthermore, CHs can be potential candidates for studies involving radiation, ionization, and electron impact to initiate chemical transformations between the host and guest species and may be critical in understanding the origin of life.



KEY REFERENCES

- Ghosh, J.; Methikkalam, R. R. J.; Bhuin, R. G.; Ragupathy, G.; Choudhary, N.; Kumar, R.; Pradeep, T. Clathrate Hydrates in Interstellar Environment. *Proc. Natl. Acad. Sci. U.S.A.* **2019**, *116*, 1526–1531.¹ This work reported the experimental evidence of CH_4 and CO_2 clathrate hydrates (CHs) at extremely low pressure (10^{-10} mbar) under cryogenic conditions, relevant to the interstellar medium (ISM).
- Ghosh, J.; Bhuin, R. G.; Vishwakarma, G.; Pradeep, T. Formation of Cubic Ice via Clathrate Hydrate, Prepared

in Ultrahigh Vacuum under Cryogenic Conditions. *J. Phys. Chem. Lett.* **2020**, *11*, 26–32.² This work reported a unique crystallization process of cubic ice (ice I_c) involving the dissociation of preformed acetone hydrate in UHV.

Received: June 3, 2023



ACS Publications

© XXXX American Chemical Society

A

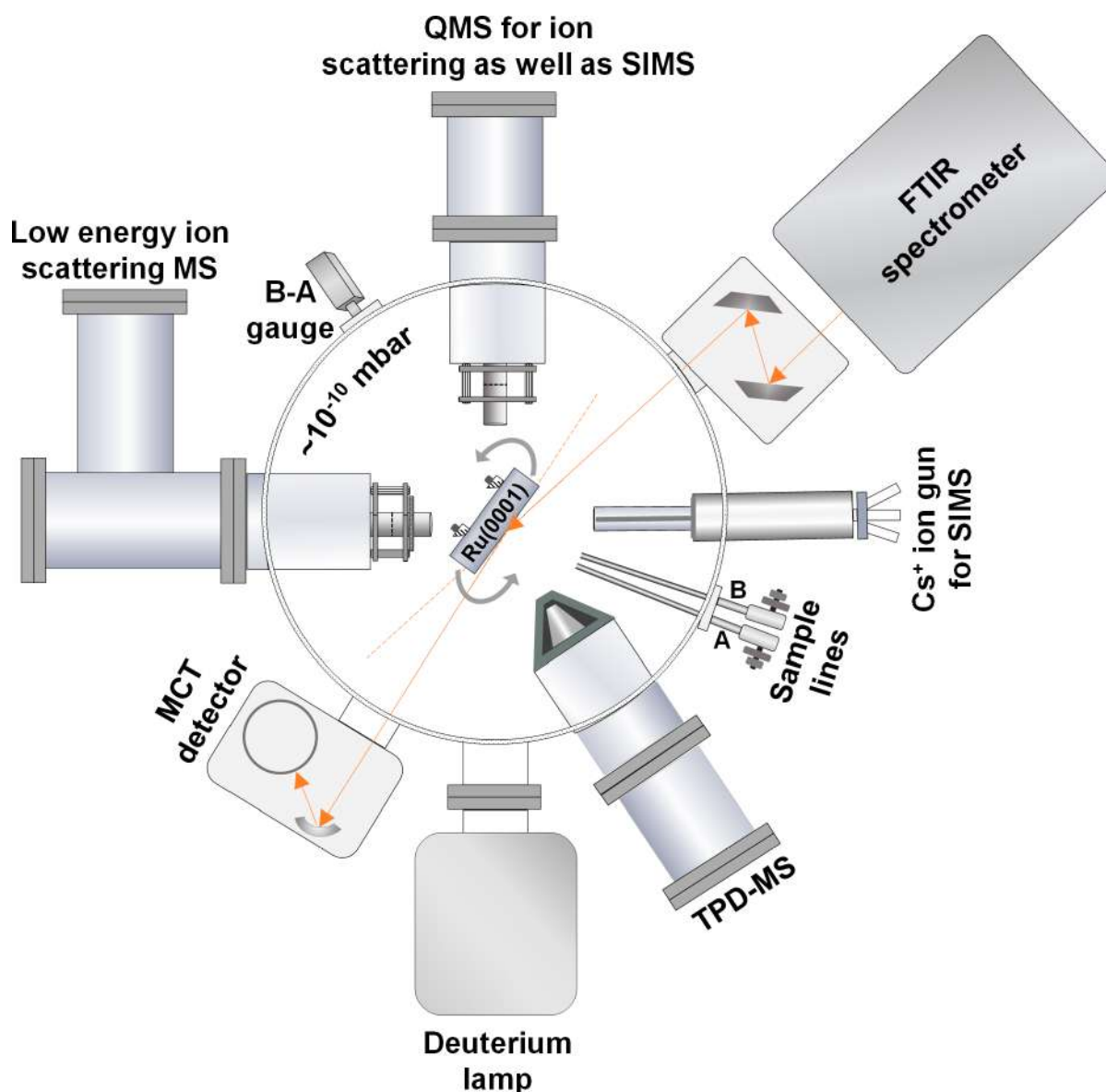


Figure 1. Schematic representation of a custom-built UHV instrument. The current representation depicts the orientation of the substrate suitable for RAIRS measurements. Here, several minor components are not shown for clarity. Adapted with permission from ref 57. Copyright 2023 American Chemical Society.

- Ghosh, J.; Vishwakarma, G.; Das, S.; Pradeep, T. Facile Crystallization of Ice I_h via Formaldehyde Hydrate in Ultrahigh Vacuum under Cryogenic Conditions. *J. Phys. Chem. C* **2021**, 125, 4532–4539.³ This work showed that a stable hexagonal crystalline ice (ice I_h) can be obtained based on the dissociation of formaldehyde hydrate in UHV.
- Ghosh, J.; Bhuin, R. G.; Ragupathy, G.; Pradeep, T. Spontaneous Formation of Tetrahydrofuran Hydrate in Ultrahigh Vacuum. *J. Phys. Chem. C* **2019**, 123, 16300–16307.⁴ This work demonstrated the formation of tetrahydrofuran (THF) hydrate in UHV, which was a diffusion-controlled process, revealed by the isothermal kinetic measurements.

1. INTRODUCTION

The interstellar medium (ISM) is not empty but contains diffuse clouds, composed of gaseous species, particulate matter, and dust particles.^{5,6} To date, ~240 different molecules have

been found in these clouds, making ISM exceedingly diverse and a host to rich chemistry.⁷ Molecular H_2 is the most abundant species found in ISM along with common terrestrial molecular species, molecular ions, radicals, complex organic molecules (COMs), and polycyclic aromatic hydrocarbons (PAHs).⁵ ISM is extremely cold (~ 10 K); therefore, most of these gaseous species get accreted onto the dust surfaces to form icy grain mantles. Ice in the ISM context refers to all condensed molecular solids. Such interstellar icy dust particles are considered to be the birthplace of COMs even at such low temperatures; therefore, it is important to study the associated chemistry.^{5,6} Several studies^{8–10} involving absorption IR spectroscopy were used to characterize the compositions of interstellar ice, and water is found to be the major constituent, followed by CO_2 , CO , CH_3OH , NH_3 , and CH_4 .⁶ This interstellar ice is known to have two different phases, namely, water-rich and water-poor analogs.⁶ The water-rich phase consists of mostly water and CO_2 , alongside small amounts of

NH_3 and CH_4 ices, whereas the water-poor phase contains mostly CO , CO_2 , and CH_3OH .⁶ In interstellar environments, the coexistence of all of these molecules along with water in the condensed phase presents a perfect recipe for clathrate hydrates (CHs), a unique molecular species yet to be detected in ISM, and this Account addresses that gap.

CHs are nonstoichiometric crystalline host–guest complexes, where water molecules form a cage-like structure to entrap different guest species to gain stabilization by the host–guest interaction.^{11,12} Their structures are dependent on the nature of guest species, and the most commonly occurring structures are referred to as structure I (sI), structure II (sII), and structure H (sH).^{11,12} CHs are also abundant on earth and generally found in permafrost regions, ocean floors, and outer continental shelves as marine sediments.^{11,13} CHs are known to serve as important materials as a sustainable source of energy^{14,15} and for the storage of natural gases with huge entrapment capability,^{14,16} CO_2 sequestration,^{17,18} and seawater desalination.¹⁹ It is also important to understand the nucleation and decomposition behaviors of CHs for flow assurance in subsea pipelines²⁰ and global climate change,¹⁸ respectively.

In general, high pressure and moderate to low temperature are the stabilizing conditions for the nucleation and growth of CHs.¹¹ However, CHs can also form at low pressures and temperatures as per the P – T phase diagram, and their existence was predicted in the outer solar system²¹ and on the surfaces of Mars and Titan.^{22,23} In the 1980s, CHs were first formed experimentally under vacuum (1.33×10^{-7} mbar) by the codeposition of an appropriate water:oxirane vapor mixture followed by annealing to 120 K.²⁴ Subsequently, other studies were followed, involving a similar vapor deposition method with small proton-acceptor guest species, which stabilizes the CH structure.^{25–28} Ice nanocrystal arrays were also shown to be converted to CH arrays.^{29,30} Under relatively higher vacuum ($\sim 10^{-6}$ mbar), several other CHs were studied such as those of NO ,³¹ N_2 ,^{32,33} O_2 ,^{32,33} CO ,³³ and Ar.³³

There has been speculation about the existence of CHs in comets and other planetary atmospheres due to prevalent temperature and pressure. However, there was no experimental evidence of the formation of CHs in UHV and cryogenic conditions relevant to the interstellar environment before our studies. In this Account, we discuss our experimental effort toward the formation of CHs in a simulated interstellar environment and the associated chemistry, kinetics, and transformation of such structures. This discussion begins with the description of a custom-built UHV instrument for studying CHs, in which an interstellar condition was mimicked. In the next section, we discuss the formation of CH_4 , C_2H_6 , and CO_2 hydrates under UHV ($\sim 10^{-10}$ mbar) in the 10–60 K range and their characterization by IR spectroscopy, quantum chemical calculations, and mass spectrometry. Then, we demonstrate that the CHs can be converted to different forms of crystalline ice (cubic and hexagonal ice) upon their dissociation. We have provided spectroscopic and electron diffraction evidence in support of the observation of these different crystalline forms of ice. In a later section, we discuss a spontaneous method of forming THF hydrate in UHV, which can promote the formation of binary CHs (a type of CH where two different guest species are trapped in two separate CH cages). Furthermore, we show that it is indeed possible for a binary THF- CO_2 hydrate to form under UHV, which shows the transportation of CO_2 from

CHs to an amorphous solid water (ASW) matrix upon annealing at certain temperatures, suggesting the dynamic nature of these interstellar ice systems, which is a prerequisite for more complex chemistries to occur at such low temperatures. Finally, a conclusion is drawn about the future directions of this emerging field.

2. INSTRUMENTATION AND METHOD

2.1. Experimental Setup

Herein, the experimental details and description of the custom-built UHV instrument for studying CHs are presented, as shown in Figure 1. More details about the instrument can be found in recent papers.^{34–38} The instrument has a cylindrical UHV chamber fitted with turbomolecular pumps backed by oil-free diaphragm pumps. Ionization gauges of the Bayard–Alpert type were used in the UHV range. The base pressure below $\sim 5 \times 10^{-10}$ mbar was achieved after the bake-out. A closed-cycle helium cryostat cooled the Ru(0001) substrate over which ice layers were grown. An electrically resistive heater (25 Ω) was used to heat the substrate, and three temperature sensors such as silicon diode, a thermocouple, and a Pt resistor were used for temperature measurements.

2.2. RAIRS Instrumentation

Our reflection absorption infrared spectroscopy (RAIRS) setup used an IR beam focused on the substrate at an $80 \pm 7^\circ$ incident angle, and the reflected beam was refocused to a liquid-nitrogen-cooled MCT external detector through gold-coated mirrors. All of the RAIRS instrumental components outside UHV were purged continuously with dry nitrogen gas to avoid the spectral background from water and CO_2 . In all of the experiments, 2 cm^{-1} resolution was used with 512 scans in the mid-infrared region (4000–400 cm^{-1}).

2.3. TPD-MS Instrumentation

The TPD-MS module from Extrel CMS was attached to the experimental chamber, and it consists of an electron impact source, mass analyzer, and detector. The ionized gaseous species were focused on the mass analyzer by using a stack of Einzel lenses. For TPD-MS, the temperature ramping was controlled with a Lakeshore temperature controller. A thermocouple sensor was used during the experiments in combination with a Pt sensor. The outputs of both sensors from the temperature controller were given to the mass controller and were recorded by the Merlin software along with selected mass intensities.

2.4. General Experimental Protocol

The general experimental procedure of forming CHs is either codeposition or the sequential deposition of water and CH-forming gases. A high-precision leak valve was used to control the deposition pressure, where water and other gaseous guests were deposited by using two separate inlet lines. Millipore water (18.2 M Ω) was used by purifying with freeze–pump–thaw cycles to deposit 300 monolayers (MLs) of ice; therefore, the substrate does not affect the formation of CH. The monolayer (ML) coverage was calculated by assuming that 1.33×10^{-6} mbar s = 1 ML.^{39,35}

For the deposition of 300 MLs of 1:1 mixed ice, the chamber was backfilled starting from a base pressure of $\sim 5 \times 10^{-10}$ mbar to a total pressure of $\sim 5 \times 10^{-7}$ mbar (the pressure of the specific gas as well as water was 2.5×10^{-7} mbar, individually) and deposited for 10 min. Moreover, a residual gas analyzer was used during the deposition of these molecules,

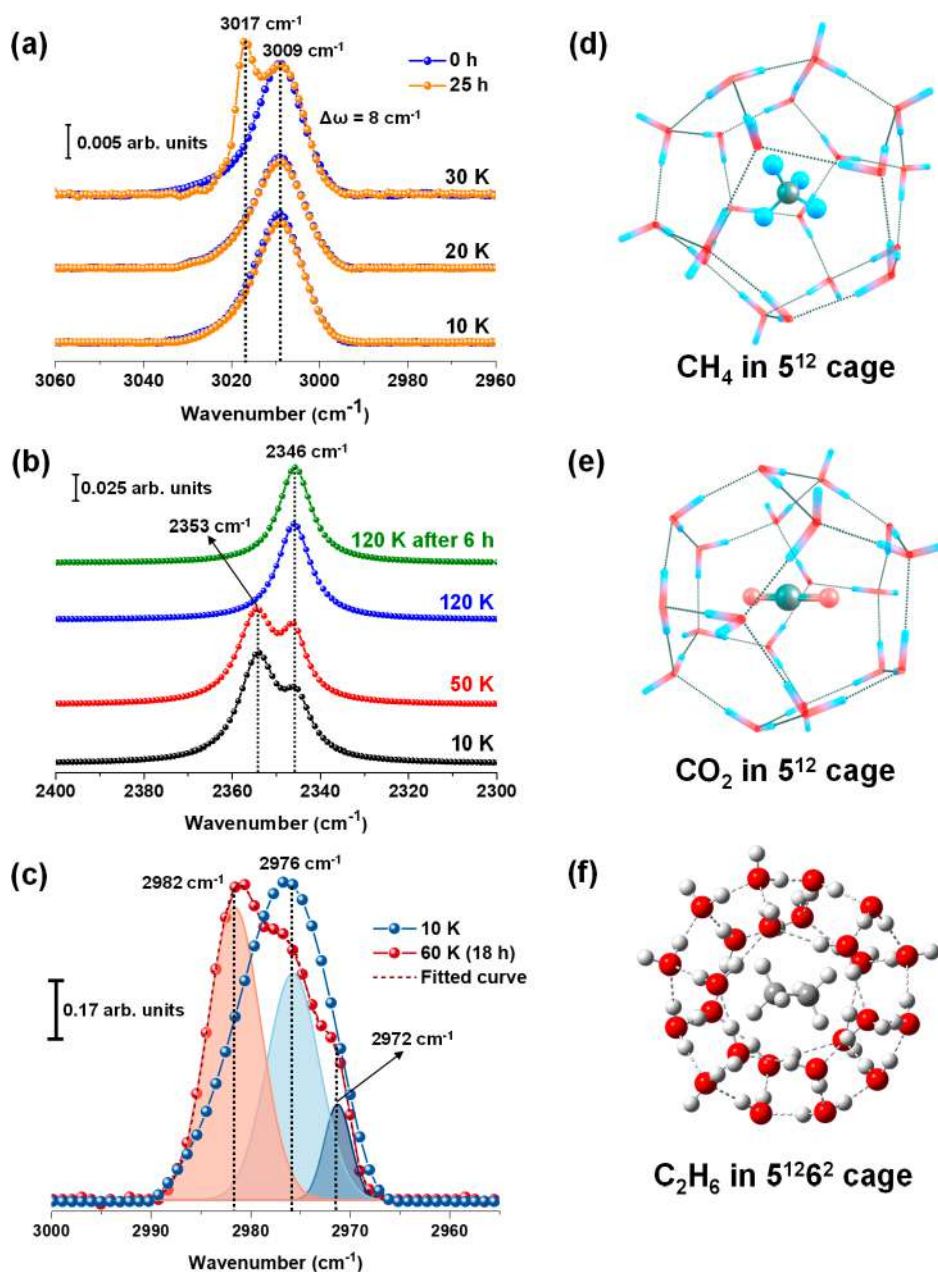


Figure 2. Formation of CHs is studied by RAIR spectroscopy and quantum chemical calculations. RAIR spectra of 300 MLs (1:1) codeposited ice systems, namely, (a) $\text{CH}_4 + \text{H}_2\text{O}$, (b) $\text{CO}_2 + \text{H}_2\text{O}$, and (c) $\text{C}_2\text{H}_6 + \text{H}_2\text{O}$ at different temperatures and annealing times, as indicated. Here, only the C–H and C=O antisymmetric stretching regions are shown for hydrocarbons and CO_2 , respectively. DFT-optimized structures of hydrate cages are shown for (d) CH_4 hydrate, (e) CO_2 hydrate, and (f) C_2H_6 hydrate. Adapted with permission from ref 1. Copyright 2019 the authors. Published by the National Academy of Sciences under Creative Commons Attribution-NonCommercial-NoDerivatives License 4.0 (CC BY-NC-ND) and adapted with permission from ref 43. Copyright 2022 American Chemical Society.

and the MS intensities of these species were utilized to determine the molecular ratio. The mixed ice was heated at 2 K min^{-1} to the desired temperature. RAIR spectra were obtained to monitor CH formation. Identical experimental conditions were maintained throughout the spectral measurement.

3. CLATHRATE HYDRATES UNDER INTERSTELLAR CONDITIONS

3.1. IR Spectroscopic Evidence

We started our quest for CHs in the ISM with CH_4 hydrate, the most common gas hydrate found on earth. At first, 300

MLs of 1:1 CH_4 and water were codeposited at 10 K. Time-dependent RAIR spectra were recorded in the C–H antisymmetric stretching region of CH_4 at 10, 20, and 30 K for different annealing times (0 and 25 h) as shown in Figure 2a. The spectra showed an IR feature of solid CH_4 at 3009 cm^{-1} , which remained constant at 10 and 20 K even after 25 h.¹ However, a new peak at 3017 cm^{-1} appeared after 25 h of annealing at 30 K, which was blue-shifted in comparison to the spectral band for solid CH_4 (3009 cm^{-1}).¹ This new peak (3017 cm^{-1}) was assigned to CH_4 hydrate, and the experimental blue shift of 8 cm^{-1} was due to the entrapment of CH_4 in the hydrate cage.¹ Previous study⁴⁰ had suggested that the trapped guest molecules in CH cages have more

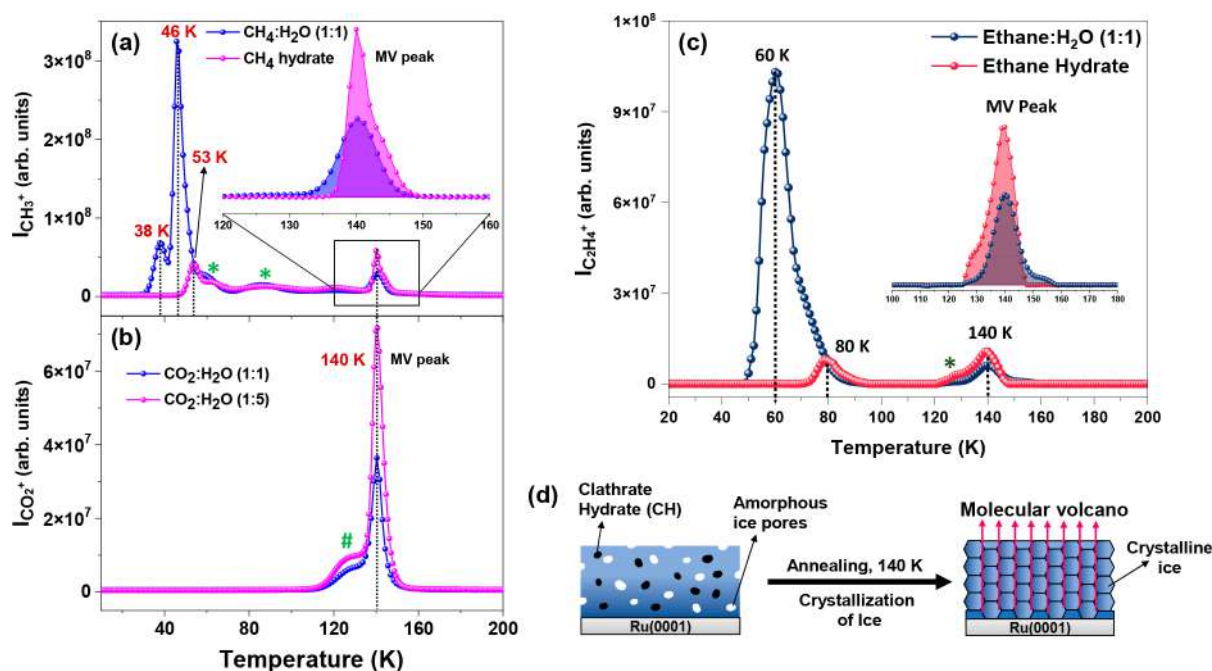


Figure 3. TPD mass spectra of 300 MLs of codeposited ice systems at different ratios (heating rate = 30 K min^{-1}). Here, the intensities of CH_3^+ ($m/z = 15$), CO_2^+ ($m/z = 44$), and C_2H_4^+ ($m/z = 28$) are plotted with the substrate temperature. (a) Desorption of CH_4 before (blue trace) and after hydrate formation (magenta trace). (b) Desorption of CO_2 after hydrate formation at different ratios, as indicated. (c) Desorption of C_2H_6 before (dark-blue trace) and after (red trace) hydrate formation. (d) Schematic representation of molecular volcano (MV) upon crystallization of ice. MV peaks are shown in the insets. Adapted with permission from ref 1. Copyright 2019 the authors. Published by the National Academy of Sciences under a Creative Commons Attribution-NonCommercial-NoDerivatives License 4.0 (CC BY-NC-ND) and adapted with permission from ref 43. Copyright 2022 American Chemical Society.

vibrational freedom and behave like gaseous species; therefore, their vibrational frequency stays in between their gaseous- and condensed-phase frequencies. Another study⁴¹ also showed a blue-shifted IR feature due to CH_4 trapped in a hydrate cage. The prolonged annealing (25 h) at 30 K, near the desorption temperature of CH_4 , was crucial to forming the hydrate cage.¹ Primarily due to the application of UHV at these temperatures, CH_4 molecules gained enhanced mobility, which led to the mixing of CH_4 and codeposited water, which results in enhanced interaction and CH_4 insertion into the hydrate cages.¹ A time-dependent RAIR study of pure condensed CH_4 in the absence of water at 25 K did not show the peak at 3017 cm^{-1} , which confirmed its assignment to CH_4 hydrate. In addition, quantum chemical calculations using density functional theory (DFT) also confirmed the formation of CH_4 hydrate. It revealed the preferential formation of stable, small 5^{12} cages (Figure 2d) under the simulated condition.¹ The calculated vibrational shift with the formation of CHs nearly matches the experimentally obtained spectral shift (8 cm^{-1}). A microsecond molecular dynamics (MD) simulation study⁴² of CH_4 hydrate nucleation predicted the preferential formation of smaller 5^{12} cages during the initial stages of nucleation, which supports our result.

The existence of CHs in ISM was further supported by the experimental evidence of two other hydrates, namely, CO_2 ¹ and C_2H_6 hydrates.⁴³ An earlier report²⁸ suggested that CO_2 hydrate can be formed at $1.33 \times 10^{-6} \text{ mbar}$ and 120 K. Figure 2b shows the RAIR spectra of 300 MLs of a $\text{CO}_2:\text{H}_2\text{O}$ (1:5) codeposited mixture in the C=O antisymmetric stretching region. The peak at 2346 cm^{-1} was attributed to CO_2 hydrate, entrapped in the 5^{12} cage as suggested by the DFT calculations (Figure 2e).¹ The other peak at 2353 cm^{-1} was due to the

remaining untrapped solid CO_2 , which exists outside the hydrate cages in the amorphous ice matrix.¹ The 2346 cm^{-1} peak was the characteristic feature of CO_2 hydrate as reported before.²⁸ The gradual decrease in intensity for the 2353 cm^{-1} peak and the simultaneous emergence of the 2346 cm^{-1} peak with temperature suggested that annealing helps in better mixing of ice and CO_2 , which favors the formation of CO_2 hydrate. The results suggested that CO_2 hydrate can be formed at 10 K, and it is quite stable at 120 K for 6 h. This is attributed to the stronger interaction of CO_2 with water than with CH_4 , although both are weak.^{1,44} The formation of C_2H_6 hydrate in ISM was also explored.⁴³ As per an earlier study,²⁵ C_2H_6 hydrate can be formed at 10^{-7} mbar and 90 K but only in the presence of oxirane, which helped in the nucleation of ethane-oxirane mixed hydrate. Figure 2c shows the RAIR spectra of a 300 MLs $\text{C}_2\text{H}_6:\text{H}_2\text{O}$ (1:1) codeposited mixture in the C–H antisymmetric stretching region at different temperatures.⁴³ Three distinct peaks appeared at 60 K, positioned at 2972, 2976, and 2982 cm^{-1} corresponding to the crystalline, amorphous, and CH forms of C_2H_6 , respectively.⁴³ The 2982 cm^{-1} peak is the characteristic IR feature of C_2H_6 hydrate as observed in earlier reports.^{25,45} Again, the blue-shifted nature of the 2982 cm^{-1} peak as compared to the amorphous and crystalline IR features of C_2H_6 indicates its assignment to C_2H_6 hydrate. A comparison of DFT-calculated vibrational and experimental shifts suggested that C_2H_6 is trapped in the $5^{12}6^2$ cage as shown in Figure 2f.⁴³

3.2. Mass Spectrometric Evidence

Temperature-programmed desorption-mass spectrometry (TPD-MS) also supported the formation of CHs in ISM. TPD-MS is an MS-based analytical technique routinely utilized in surface science and laboratory astrochemical experiments.

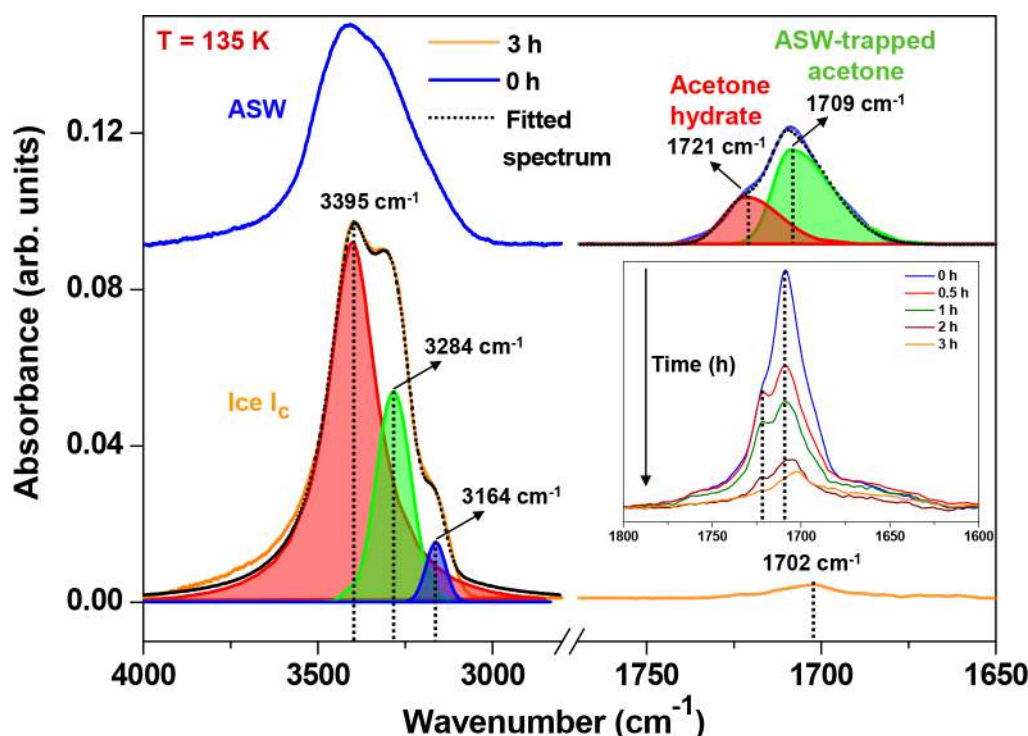


Figure 4. RAIR spectra of 300 MLs of acetone:H₂O (1:1) in the O–H and C=O stretching regions at 135 K. The inset shows the change in the C=O stretching band due to the dissociation of acetone hydrate with time. Here, the blue and orange traces are attributed to amorphous solid water (ASW) and cubic crystalline ice (ice I_c). The spectral change of the O–H band is due to ice crystallization, and different features were resolved upon deconvolution. Adapted with permission from ref 2. Copyright 2020 American Chemical Society.

Here, the continuous desorption of adsorbed species from the substrate upon thermal stimulation is analyzed by a mass spectrometer, and the resultant mass intensities are plotted as a function of the substrate temperature. Porous amorphous ice can entrap guest molecules, which are released during the crystallization of ice at 140 K due to the collapse of these pores.⁴⁶ This results in an abrupt release of the trapped species, which produces a “molecular volcano (MV)”.⁴⁶ Figure 3a represents the comparative TPD spectra before and after the formation of CH₄ hydrate, which were monitored using the intensity of the CH₃⁺ peak ($m/z = 15$).¹ CH₄ hydrate was formed by annealing a codeposited mixture at 30 K for 25 h as mentioned before. The other peaks at 38 and 46 K correspond to multilayer CH₄ and CH₄ trapped in the ASW pores, respectively. The intensity of the MV peak before the formation of the hydrate is due to the trapped CH₄ in ASW, whereas the intensity of the MV peak was enhanced upon the formation of the hydrate due to the simultaneous release of trapped CH₄ from ASW pores as well as from the hydrate cages (Figure 3a).¹ Note that the amounts of gases deposited are the same in both cases. The slight distortion in the MV peak is attributed to the modification of ASW pores due to CH formation (Figure 3a). Figure 3b shows the TPD spectra of 300 MLs of CO₂ + H₂O at two ratios, 1:1 and 1:5, and they were annealed at 120 K for the complete formation of CO₂ hydrate.¹ Then the samples were cooled back to 10 K, and TPD spectra were recorded. The peak at 140 K corresponds to the MV of CO₂, and its intensity increased as the ratio of CO₂ to H₂O was changed from 1:1 to 1:5. Experiments suggested that the extent of formation of CO₂ hydrate was greater for the diluted water and CO₂ mixture, and it agreed well with the IR spectral interpretation.^{1,44}

Figure 3c shows the TPD profiles for C₂H₆ hydrate before and after formation.⁴³ Two sets of TPD-MS experiments were performed; in the first, we deposited 300 MLs of an C₂H₆:H₂O (1:1) ice mixture at 10 K and heated it to 200 K at a ramping rate of 30 K min^{−1}. The desorption of C₂H₆ was monitored by the intensity of the C₂H₄⁺ peak ($m/z = 28$). The peaks at 60 and 140 K were attributed to the desorption of multilayer C₂H₆ from ASW pores and the MV peak, respectively.⁴³ In the second experiment, a C₂H₆:H₂O (1:1) ice mixture was annealed at 60 K for 18 h to create C₂H₆ hydrate. After the hydrate was formed, the sample was cooled to 10 K and the TPD spectrum was recorded (red trace), which showed two peaks at 80 and 140 K. The peak at 80 K was assigned to the desorption of trapped C₂H₆ (amorphous or crystalline) from the ASW matrix. The peak was shifted from 60 to 80 K primarily due to the formation of CH as well as a more compact ice network as a result of prolonged annealing.⁴³ The MV peak of C₂H₆ hydrate showed a higher intensity compared to the MV peak before hydrate formation. The enhanced intensity of the MV peak for the hydrate was due to the release of trapped C₂H₆ from the ASW pores and the dissociation of the CH cage, as explained before. Note that the peak marked by an asterisk around 125 K was due to the desorption of C₂H₆ due to the predissociation of hydrate cages.⁴³

4. TRANSFORMATIONS OF CLATHRATE HYDRATES

4.1. Formation of Cubic Ice (Ice I_c) from CH

The dissociation behavior⁴⁷ of CHs is also important to understand since it leads to different crystalline phases of ice. An earlier study⁴⁸ suggested that emptying neon from its hydrate cages led to the formation of ice XVI, a new crystalline phase of ice. The dissociation of CO₂ hydrates led to cubic ice

(ice I_c).⁴⁹ In our study,² we showed that acetone hydrates could be prepared by codepositing acetone:H₂O (1:1) mixtures and annealing them to 135 K. However, keeping acetone hydrate at 135 K for 3 h led to its dissociation, which resulted in ice I_c .² Figure 4 shows the RAIR spectra of the codeposited film at 135 K (blue trace; 0 h) and after 3 h (orange trace; 3 h).² The inset shows the C=O stretching band, and at 0 h, it shows two features at 1721 and 1709 cm⁻¹ which were attributed to acetone hydrate^{50,51} and ASW-trapped acetone,⁵² respectively. The peak intensity was reduced with time and resulted in a peak at 1702 cm⁻¹, which was assigned to a dilute mixture of acetone and water (1:20). The profound change in the O–H stretching band with time indicates the change in the overall structure of ice due to the dissociation of acetone hydrate.² In Figure 4, the broad O–H stretching band (blue trace) is a characteristic feature of ASW, which eventually became sharp and developed three shoulder features after 3 h (orange trace). Ice crystallization is generally associated with the splitting and sharpening of the O–H stretching band, and it was deconvoluted to three distinct features at 3164, 3284, and 3395 cm⁻¹, corresponding to the ν_1 in-phase band, the ν_3 TO band, and the overlapped ν_3 LO and ν_1 out-of-phase bands of ice I_c .⁵³ Isotopic experiments with an acetone:D₂O (1:1) system also led to the formation of cubic D₂O ice due to the dissociation of acetone hydrate (not shown).² Note that, in similar studies at 130 K, the ice I_c conversion took 9 h, whereas the ice I_c was not observed at 120 K, even after 48 h. The thermal motion of acetone molecules is likely to be responsible for the formation of acetone hydrate and subsequently ice I_c .² In a similar study, the dissociation of acetaldehyde hydrate leads to the formation of ice I_c .⁵⁴

We have also provided more direct structural evidence to support the claim of forming ice I_c via hydrate dissociation.² Figure 5 shows the time-dependent reflection high-energy electron diffraction (RHEED) images of acetone:H₂O (1:1) at different temperatures.² In Figure 5a, the RHEED image does not show any pattern, indicating the amorphous nature of the mixture. However, several diffraction rings were observed after 5 h (Figure 5b).² Here, most of the acetone molecules desorb from the mixture, as indicated by the IR spectra. Note that these diffraction patterns originate from the ice I_c and match the earlier diffraction studies of ice I_c .^{55,56} Time-dependent RHEED studies at 130 K showed an ice I_c pattern after 12 h (Figure 5d). However, the diffraction patterns were not observed at 120 K, even after 24 h (Figure 5e,f). These observations support the RAIR spectral interpretation, which suggests that ice I_c was formed only through the dissociation of acetone hydrate.²

4.2. Formation of Hexagonal Ice (Ice I_h) from CH

Among several polymorphs of ice, hexagonal ice (ice I_h) is the most common, and it occurs naturally on earth. However, the formation of ice I_h from CH precursors was not studied. We found that formaldehyde hydrate dissociated to form ice I_h under UHV at 130–135 K.³ Figure 6a,b shows the time-dependent RAIR spectra of the codeposited formaldehyde:H₂O (1:1) film at 135 K in the C=O and O–H stretching regions, respectively. The IR feature at 1733 cm⁻¹ is attributed to the C=O stretching band of formaldehyde hydrate (Figure 6a).³ This assignment was performed by comparing formaldehyde vapor (1746 cm⁻¹) and condensed phase (1723 cm⁻¹) frequencies. The hydrate phase frequencies fall in

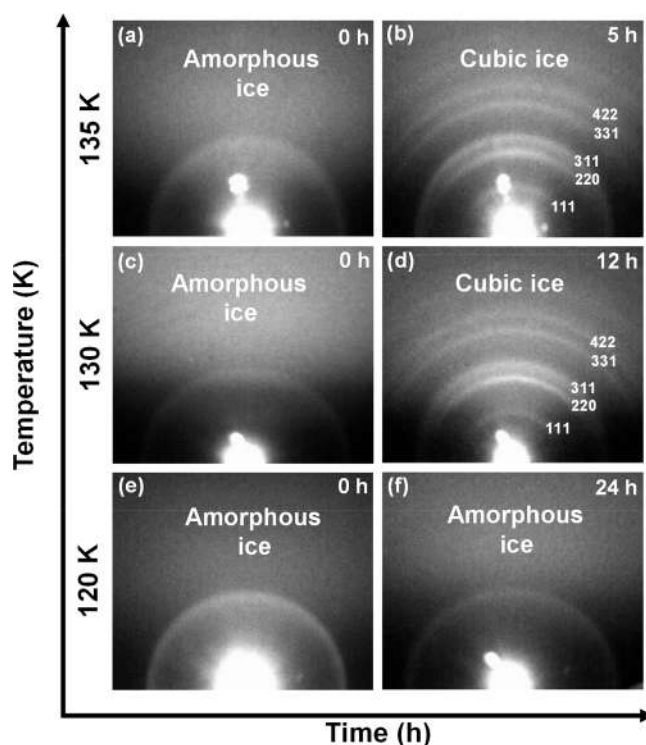


Figure 5. Time-dependent RHEED images of 300 MLs of acetone:H₂O (1:1) at 120, 130, and 135 K and different annealing times, as indicated. After codeposition, the mixtures were annealed at 2 K min⁻¹ to reach the required temperatures. Adapted with permission from ref 2. Copyright 2020 American Chemical Society.

between them.³ Besides, the O–H stretching region showed a profound change after 5 h with the disappearance of the formaldehyde hydrate IR peak. This O–H stretching band (blue trace) is the characteristic feature of ice I_h as confirmed by comparing pure crystalline ice I_h spectra, recorded independently. The control study also suggested that water by itself cannot form ice I_h at 135 K in the absence of formaldehyde hydrate since its usual crystallization temperature is 150–155 K under UHV. The existence of formaldehyde and water in space suggests the possibility to form hydrates and their subsequent transformation to ice I_h , which constitutes a mechanistic route for its formation in ISM.³

5. STRUCTURAL DYNAMICS OF CLATHRATE HYDRATES

The structural dynamics in CHs are important to study, which reveals that the reorientation of water and the diffusion of guest molecules are the driving forces for these structures. Furthermore, the presence of a second guest species provides extra thermodynamic stability to the hydrate framework, and they are termed binary CHs. THF hydrate is known to be a stabilizer for such binary CHs.⁴ THF being a larger molecule occupies the larger cages ($S^{12}6^4$), whereas the other guest species occupy the smaller ones (S^{12}). Here, we have studied the formation of THF hydrate by codepositing a THF:H₂O mixture (1:5) and annealing it to 130 K.⁴ Figure 7a,b shows the time-dependent spectra of the same system in the asymmetric C–O and O–H stretching regions. The peaks at 1034 and 1053 cm⁻¹ were assigned to THF trapped in different sites of ASW, whereas the other peak at 1074 cm⁻¹ is the characteristic feature of THF hydrate.⁴ Continuous

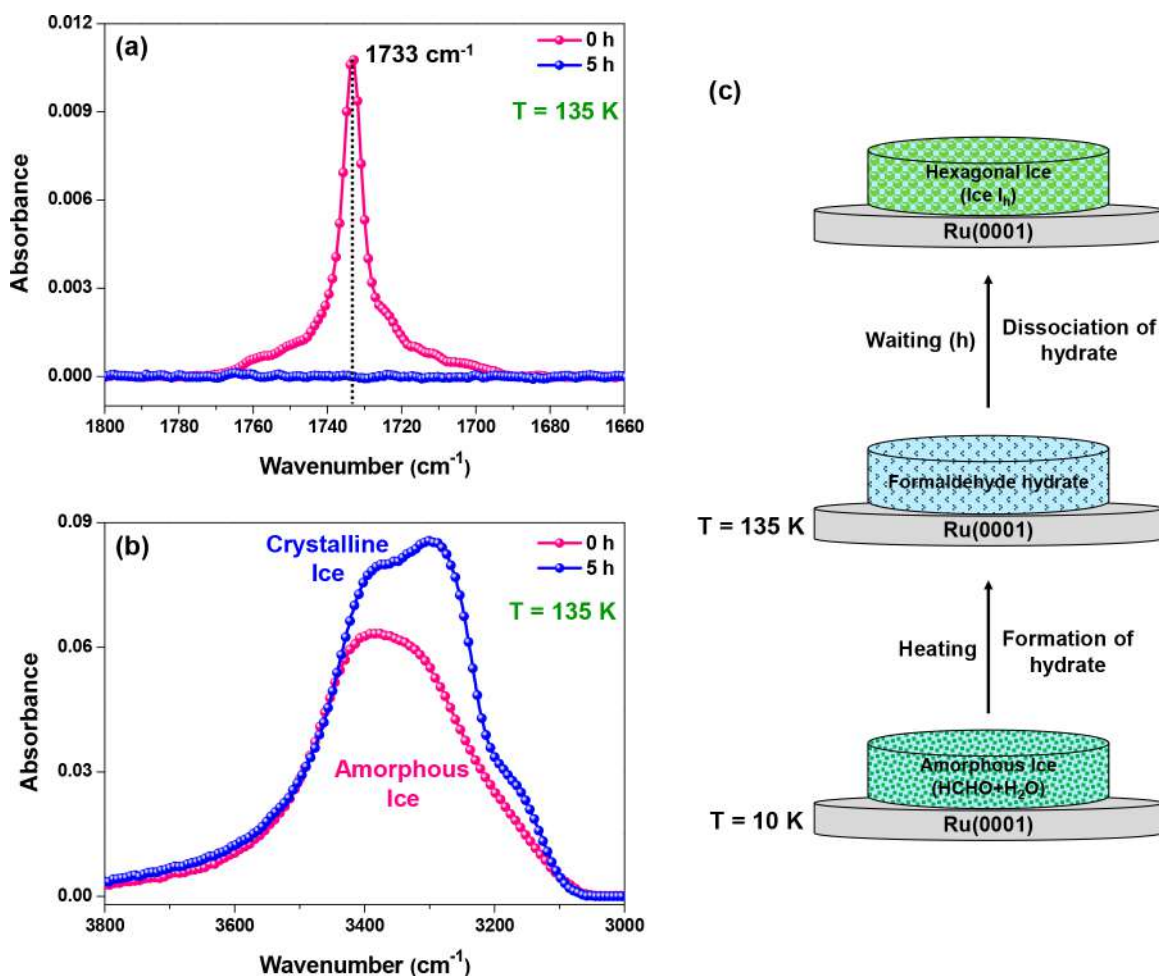


Figure 6. Time-dependent RAIR spectra of 300 MLs of formaldehyde:H₂O (1:1) at 135 K in the (a) C=O and (b) O–H stretching regions. (c) The schematic illustration shows the formation of formaldehyde hydrate and its dissociation, which leads to the formation of hexagonal ice (ice I_h). Adapted with permission from ref 3. Copyright 2021 American Chemical Society.

annealing (6 h) of the system increased the intensity of the THF hydrate peak and decreased the intensity of the other two peaks. The 1074 cm⁻¹ peak serves as a convenient indicator of THF hydrate since it lies well above the IR peak positions of other likely condensed phases of THF. In Figure 7b, the O–H stretching band is also red-shifted with time, which was an indication of ice crystallization. Results suggested that the gradual transformation of THF hydrate also changes the structure of ice from amorphous to crystalline.⁴ Furthermore, the crystallization kinetics suggested that the formation of THF hydrate was a diffusion-controlled process.⁴ In addition, this study has the potential to explore a certain number of binary CHs. To explore this possibility, we conducted a study with a CO₂@(THF + H₂O; 1:5) composite ice film, where a THF + water mixture was sequentially deposited on a predeposited CO₂ film and this system was annealed at 130 K for 6 h.⁵⁷ Figure 7c,d shows the corresponding time-dependent RAIR spectra in the C=O and C–O antisymmetric stretching regions of CO₂ and THF, respectively. The IR peaks at 2352, 2346, and 2340 cm⁻¹ were assigned to CO₂ in the ASW matrix and 5¹² and 5¹²6² cages, respectively.^{1,26,57} Continuous annealing decreased the intensity of the 2346 cm⁻¹ peak and increased that of the 2352 cm⁻¹ peak, whereas the intensity of the 2340 cm⁻¹ peak remained constant. It suggested that CO₂ was transported from 5¹²6² cages to the

ASW matrix and that CO₂ in 5¹² cages remained mostly unperturbed.⁵⁷ In Figure 7c, a new peak arose at 1074 cm⁻¹ while the peaks at 1054 and 1032 cm⁻¹ decreased with time, as shown in Figure 7c,d. The peak at 1074 cm⁻¹ was the characteristic peak for THF hydrate encased in 5¹²6⁴ cages, whereas the peaks at 1054 and 1032 cm⁻¹ were assigned to THF trapped in ASW pores.^{4,27,50} The formation of stable binary THF-CO₂ hydrate is a possibility, which is confirmed by the IR features of individual guest species (2346 and 1074 cm⁻¹ of CO₂ and THF), and computationally optimized structures also supported this observation.⁵⁷ The higher mobility of CO₂ in comparison to THF favors the formation of the CO₂ hydrate, kinetically. However, upon annealing at higher temperatures for a longer time, the formation of THF hydrate is triggered. The larger size of THF makes it a preferred guest over CO₂ in large (5¹²6⁴) cages. This leads to partial dissociation of CO₂ cages and rearrangement of the hydrate structure resulting in the increase in CO₂ in the ASW matrix, as shown schematically in Figure 7e.⁵⁷

From the foregoing, it is evident that several CHs can be formed under UHV if subjected to certain key experimental conditions such as the annealing temperature, time, and stoichiometric ratio. The extreme low-temperature conditions in ISM result in a mass transfer limitation, primarily due to limited natural convection (and mixing of species), which may

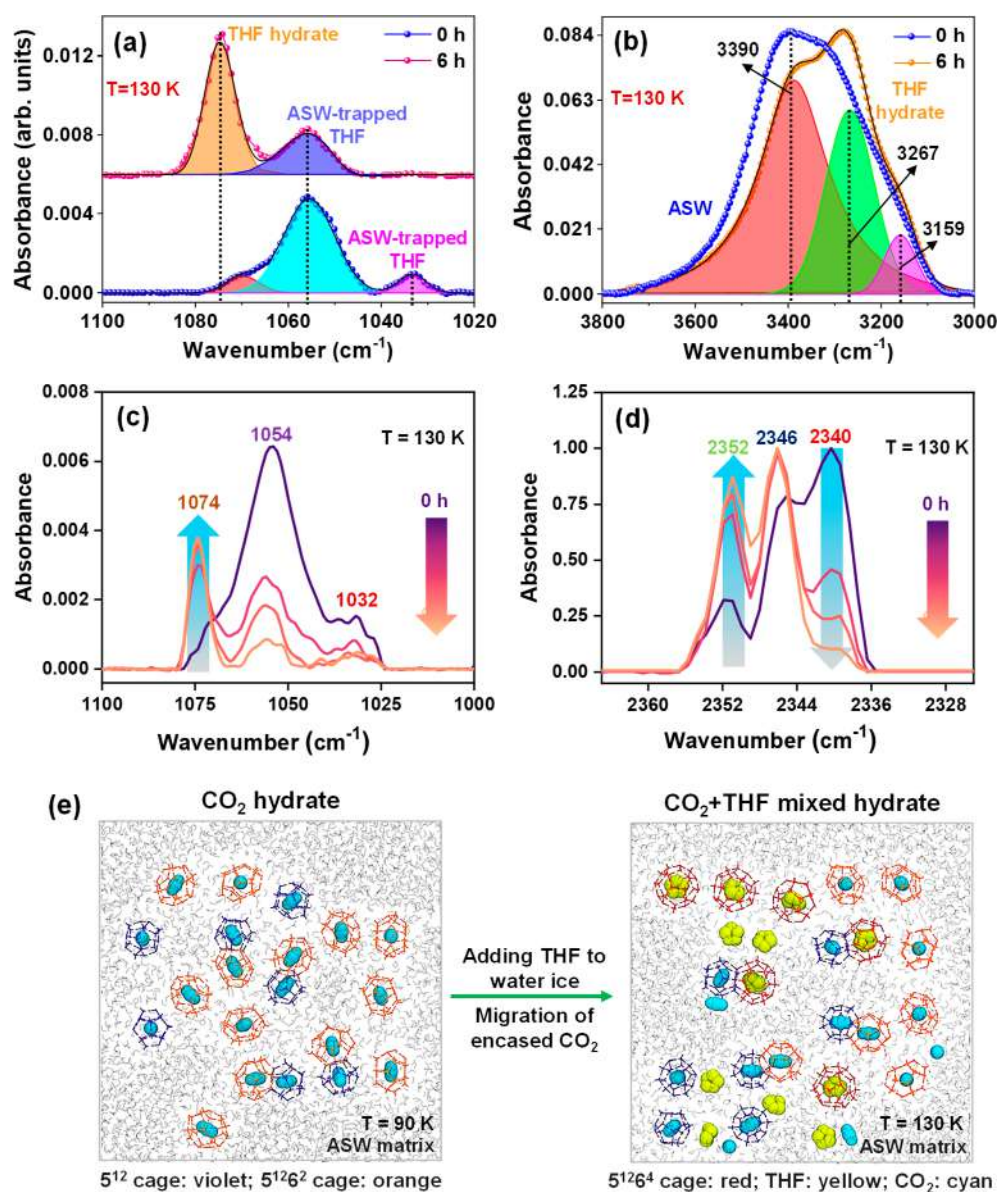


Figure 7. Time-dependent RAIR spectra of 300 MLs of THF:H₂O (1:1) in the (a) asymmetric C–O and (b) O–H stretching regions and of CO₂@(THF + H₂O; 1:5) at 130 K in the (c) asymmetric C–O and (d) C=O antisymmetric stretching regions at 130 K. (e) The schematic illustration shows the formation of the THF-CO₂ hydrate and the migration of CO₂ from 5¹²6² cages to the ASW matrix upon its dissociation by annealing at 130 K. Color code used: 5¹² cage, violet; 5¹²6² cage, orange; 5¹²6⁴ cage, red; THF, yellow; and CO₂, cyan. Adapted with permission from ref 4. Copyright 2019 American Chemical Society and adapted with permission from ref 57. Copyright 2023 American Chemical Society.

hinder the nucleation process of CHs. Achieving sufficient molecular mobility is key to forming the hydrates, which is obtained by prolonged annealing of the system near their respective desorption temperatures, irrespective of the type of guest. As per our understanding based on the experimental results, the mechanism of CH formation involves the solvation or mixing of guest molecules with water molecules as the first step. It is followed by the formation of hydrate cages around the solvated guest molecules in a stochastic manner. On the other hand, the formation of different crystalline forms of ice upon dissociation of hydrate is possibly due to the orientational defects (Bjerrum defects).^{57–59} The guest–host hydrogen bonding causes defects within the water network (host), which again depends on the type of guest molecules present in the hydrate cages. However, these defect-induced structural changes are only partially understood, and computational

studies involving MD simulations on the formation and dissociation behavior of CHs may provide additional insights.

6. PHOTOCHEMICAL EFFECTS ON CLATHRATE HYDRATES

Light irradiation is known to initiate photochemistry in ISM ices, which is suggested to be a path to chemical complexity in space.⁶ These experiments involve single, binary, or multi-component ice mixtures with a range of radiation (MeV electrons/protons to high-energy UV photons).⁶ Upon radiation exposure, water–ice dissociates to produce highly reactive radicals and initiates radical chemistry.⁶ However, high diffusion barriers of radicals in ice present restricted photochemistry.⁶ On the contrary, CHs were shown to act as a host for unique hydrogen transfer reactions involving radicals.^{60,61} Furthermore, the CH cages were demonstrated to store⁶² and

stabilize the free radicals⁶³ under high-pressure conditions. Given this, the photochemistry of CHs would be interesting under UHV and cryogenic conditions, where the guest molecule AB could dissociate to form A and B radicals. Depending on the size and kinetic energy, the fate of these radicals may vary such as recombination, stabilization upon entrapment, movement to the adjacent cage, and reaction with AB, A, or B.^{60–62}

So far, ice photochemical experiments resulted in racemic mixtures of the photolyzed products and not the homochiral form found on earth, which remains an unsolved puzzle in chemistry. The entrapped species in CH cages may interact with radiation asymmetrically to produce either left- or right-handed molecules. The proposed study can shed light on the origin of enantiomeric excess on earth.

7. FUTURE PERSPECTIVES

In this Account, the investigation of different CHs and their several important aspects such as nucleation conditions, mechanism, stability, and transformation to other ice structures are presented in the context of interstellar processes. The results suggested that the temperature and annealing time are crucial parameters in deciding the formation and structural changes of CHs. The key outcome of these studies is that it provides conclusive evidence that several CHs are formed at extremely low pressures and temperatures, conditions analogous to the ISM. This finding may open several possibilities for future explorations. While the formation of CHs of simple molecules such as methane, ethane, and carbon dioxide in interstellar-like environments is already established in the current study, many other guest molecules such as H₂, CO, N₂, O₂, NH₃, and C₂H₂ are known to form CHs, which are also found in space or the ISM along with water in solid form. Therefore, we believe that this Account will provide a direction to investigate several other CHs under suitable conditions. Furthermore, the fate of CHs upon their dissociation could be an exciting area to explore since CHs can transform into different polymorphs of ice, as highlighted in this Account. The nucleation mechanism, stability, and structure of several polymorphs of ice are intriguing. Formation and detailed studies of binary CHs under interstellar-like conditions would be another direction. Our studies have provided an early hint that binary CHs could be formed in the presence of appropriate stabilizers such as THF. In addition, these binary CHs can be utilized as precursors for interguest chemical interactions under extreme conditions of ISM such as UV and particle impact.

Apart from these possibilities, the ultimate goal of the astrochemistry community is to understand the origin of life. Understanding the chemical evolution of simple molecules to COMs has been a long-standing question. CHs can be an ideal precursor to trap several simple guest species that can undergo chemical reactions. The presence of cosmic radiation could be the driving force in such exotic environments. More experimental studies in this direction are necessary for a complete understanding of the phenomena involved. The utilization of the direct structural interpretation of CHs through extensive diffraction data^{2,64} under such extreme conditions will provide important insights. There is also a need to understand the dynamics of the formation of CHs in UHV starting from ice mixtures, which will require detailed computational studies. Despite these challenges, we hope that the present investigations have provided new insights into

the fascinating area of CHs and suggest exciting new directions for the future.

AUTHOR INFORMATION

Corresponding Authors

Rajnish Kumar – Department of Chemical Engineering, Indian Institute of Technology Madras, Chennai 600036, India; orcid.org/0000-0002-4172-2638; Email: rajnish@iitm.ac.in

Thalappil Pradeep – Department of Chemistry, DST Unit of Nanoscience (DST UNS) and Thematic Unit of Excellence (TUE), Indian Institute of Technology Madras, Chennai 600036, India; orcid.org/0000-0003-3174-534X; Email: pradeep@iitm.ac.in

Authors

Jyotirmoy Ghosh – Department of Chemistry, DST Unit of Nanoscience (DST UNS) and Thematic Unit of Excellence (TUE), Indian Institute of Technology Madras, Chennai 600036, India

Gaurav Vishwakarma – Department of Chemistry, DST Unit of Nanoscience (DST UNS) and Thematic Unit of Excellence (TUE), Indian Institute of Technology Madras, Chennai 600036, India

Complete contact information is available at:
<https://pubs.acs.org/10.1021/acs.accounts.3c00317>

Notes

The authors declare no competing financial interest.

Biographies

Jyotirmoy Ghosh earned his Ph.D. in physical chemistry from the Indian Institute of Technology Madras in 2020 under the guidance of Prof. Thalappil Pradeep. He is currently a postdoctoral research associate at Purdue University, USA. His Ph.D. research has been focused on the investigations of clathrate hydrates and ice systems of interstellar relevance under UHV and cryogenic conditions.

Gaurav Vishwakarma is a Ph.D. student at the Indian Institute of Technology Madras under the guidance of Prof. Thalappil Pradeep. His research focuses on the investigations of clathrate hydrates and ice systems under UHV and cryogenic conditions.

Rajnish Kumar is a professor at the Indian Institute of Technology Madras. His research interests are in the formation of gas hydrates and their applications in energy storage, transportation, CO₂ capture, water treatment, and desalination.

Thalappil Pradeep is an institute professor and the Deepak Parekh Institute Chair Professor at the Indian Institute of Technology Madras. He works on nanomaterials, water purification, and the chemistry of molecular solids such as ice. He has developed state-of-the-art instrumentation for such studies.

ACKNOWLEDGMENTS

J.G. and G.V. thank the University Grants Commission (UGC) and IIT Madras for their research fellowships. The authors thank the Science and Engineering Research Board (SERB) and the Department of Science and Technology (DST), Government of India, for research funding. T.P. acknowledges funding from the Centre of Excellence on Molecular Materials and Functions under the Institution of Eminence scheme of IIT Madras.

REFERENCES

- (1) Ghosh, J.; Methikkalam, R. R. J.; Bhuin, R. G.; Ragupathy, G.; Choudhary, N.; Kumar, R.; Pradeep, T. Clathrate Hydrates in Interstellar Environment. *Proc. Natl. Acad. Sci. U. S. A.* **2019**, *116*, 1526–1531.
- (2) Ghosh, J.; Bhuin, R. G.; Vishwakarma, G.; Pradeep, T. Formation of Cubic Ice via Clathrate Hydrate, Prepared in Ultrahigh Vacuum under Cryogenic Conditions. *J. Phys. Chem. Lett.* **2020**, *11*, 26–32.
- (3) Ghosh, J.; Vishwakarma, G.; Das, S.; Pradeep, T. Facile Crystallization of Ice I_h via Formaldehyde Hydrate in Ultrahigh Vacuum under Cryogenic Conditions. *J. Phys. Chem. C* **2021**, *125*, 4532–4539.
- (4) Ghosh, J.; Bhuin, R. G.; Ragupathy, G.; Pradeep, T. Spontaneous Formation of Tetrahydrofuran Hydrate in Ultrahigh Vacuum. *J. Phys. Chem. C* **2019**, *123*, 16300–16307.
- (5) Herbst, E. The Chemistry of Interstellar Space. *Chem. Soc. Rev.* **2001**, *30*, 168–176.
- (6) Öberg, K. I. Photochemistry and Astrochemistry: Photochemical Pathways to Interstellar Complex Organic Molecules. *Chem. Rev.* **2016**, *116*, 9631–9663.
- (7) McGuire, B. A. 2021 Census of Interstellar, Circumstellar, Extragalactic, Protoplanetary Disk, and Exoplanetary Molecules. *Astrophys. J. Suppl. Ser.* **2022**, *259*, 30.
- (8) Gibb, E. L.; Whittet, D. C. B.; Boogert, A. C. A.; Tielens, A. G. M. Interstellar Ice: The Infrared Space Observatory Legacy. *Astrophys. J. Suppl. Ser.* **2004**, *151*, 35.
- (9) Öberg, K. I.; Boogert, A. C. A.; Pontoppidan, K. M.; van den Broek, S.; van Dishoeck, E. F.; Bottinelli, S.; Blake, G. A.; Evans, N. J. The Spitzer Ice Legacy: Ice Evolution from Cores to Protostars. *Astrophys. J.* **2011**, *740*, 109.
- (10) Boogert, A. C. A.; Gerakines, P. A.; Whittet, D. C. B. Observations of the Icy Universe. *Annu. Rev. Astron. Astrophys.* **2015**, *53*, 541–581.
- (11) Sloan, E. D. Fundamental Principles and Applications of Natural Gas Hydrates. *Nature* **2003**, *426*, 353–359.
- (12) Ripmeester, J. A.; Tse, J. S.; Ratcliffe, C. I.; Powell, B. M. A New Clathrate Hydrate Structure. *Nature* **1987**, *325*, 135–136.
- (13) Makogon, Y. F. A Gas Hydrate Formation in the Gas Saturated Layers under Low Temperature. *Gas Ind.* **1965**, *5*, 14–15.
- (14) Chong, Z. R.; Yang, S. H. B.; Babu, P.; Linga, P.; Li, X.-S. Review of Natural Gas Hydrates as an Energy Resource: Prospects and Challenges. *Appl. Energy* **2016**, *162*, 1633–1652.
- (15) Khurana, M.; Yin, Z.; Linga, P. A Review of Clathrate Hydrate Nucleation. *ACS Sustain. Chem. Eng.* **2017**, *5*, 11176–11203.
- (16) Yin, Z.; Zheng, J.; Kim, H.; Seo, Y.; Linga, P. Hydrates for Cold Energy Storage and Transport: A Review. *Adv. Appl. Energy* **2021**, *2*, No. 100022.
- (17) Rufford, T. E.; Smart, S.; Watson, G. C. Y.; Graham, B. F.; Boxall, J.; Diniz da Costa, J. C.; May, E. F. The Removal of CO_2 and N_2 from Natural Gas: A Review of Conventional and Emerging Process Technologies. *J. Pet. Sci. Eng.* **2012**, *94–95*, 123–154.
- (18) Hughes, T. J.; Honari, A.; Graham, B. F.; Chauhan, A. S.; Johns, M. L.; May, E. F. CO_2 Sequestration for Enhanced Gas Recovery: New Measurements of Supercritical CO_2 – CH_4 Dispersion in Porous Media and a Review of Recent Research. *Int. J. Greenh. Gas Control* **2012**, *9*, 457–468.
- (19) Kang, K. C.; Linga, P.; Park, K.; Choi, S.-J.; Lee, J. D. Seawater Desalination by Gas Hydrate Process and Removal Characteristics of Dissolved Ions (Na^+ , K^+ , Mg^{2+} , Ca^{2+} , B^{3+} , Cl^- , SO_4^{2-}). *Desalination* **2014**, *353*, 84–90.
- (20) Hassanpouryouzband, A.; Joonaki, E.; Farahani, M. V.; Takeya, S.; Ruppel, C.; Yang, J.; English, N. J.; Schicks, J. M.; Edlmann, K.; Mehrabian, H.; Aman, Z. M.; Tohidi, B. Gas Hydrates in Sustainable Chemistry. *Chem. Soc. Rev.* **2020**, *49*, 5225–5309.
- (21) Miller, S. L. The Occurrence of Gas Hydrates in the Solar System*. *Proc. Natl. Acad. Sci. U. S. A.* **1961**, *47*, 1798–1808.
- (22) Miller, S. L.; Smythe, W. D. Carbon Dioxide Clathrate in the Martian Ice Cap. *Science* **1970**, *170*, 531–533.
- (23) Tobie, G.; Lunine, J. I.; Sotin, C. Episodic Outgassing as the Origin of Atmospheric Methane on Titan. *Nature* **2006**, *440*, 61–64.
- (24) Bertie, J. E.; Devlin, J. P. Infrared Spectroscopic Proof of the Formation of the Structure I Hydrate of Oxirane from Annealed Low-temperature Condensate. *J. Chem. Phys.* **1983**, *78*, 6340–6341.
- (25) Richardson, H. H.; Wooldridge, P. J.; Devlin, J. P. FT-IR Spectra of Vacuum Deposited Clathrate Hydrates of Oxirane H_2S , THF, and Ethane. *J. Chem. Phys.* **1985**, *83*, 4387–4394.
- (26) Fleyfel, F.; Devlin, J. P. FT-IR Spectra of 90 K Films of Simple, Mixed, and Double Clathrate Hydrates of Trimethylene Oxide, Methyl Chloride, Carbon Dioxide, Tetrahydrofuran, and Ethylene Oxide Containing Decoupled D_2O . *J. Phys. Chem.* **1988**, *92*, 631–635.
- (27) Fleyfel, F.; Devlin, J. P. Carbon Dioxide Clathrate Hydrate Epitaxial Growth: Spectroscopic Evidence for Formation of the Simple Type-II Carbon Dioxide Hydrate. *J. Phys. Chem.* **1991**, *95*, 3811–3815.
- (28) Blake, D.; Allamandola, L.; Sandford, S.; Hudgins, D.; Freund, F. Clathrate Hydrate Formation in Amorphous Cometary Ice Analogs in Vacuo. *Science* **1991**, *254*, 548–551.
- (29) Hernandez, J.; Uras, N.; Devlin, J. P. Coated Ice Nanocrystals from Water–Adsorbate Vapor Mixtures: Formation of Ether– CO_2 Clathrate Hydrate Nanocrystals at 120 K. *J. Phys. Chem. B* **1998**, *102*, 4526–4535.
- (30) Delzeit, L.; Devlin, J. P.; Buch, V. Structural Relaxation Rates near the Ice Surface: Basis for Separation of the Surface and Subsurface Spectra. *J. Chem. Phys.* **1997**, *107*, 3726–3729.
- (31) Hallbrucker, A. A Clathrate Hydrate of Nitric Oxide. *Angew. Chem., Int. Ed. Engl.* **1994**, *33*, 691–693.
- (32) Mayer, E.; Hallbrucker, A. Unexpectedly Stable Nitrogen and Oxygen Clathrate Hydrates from Vapour Deposited Amorphous Solid Water. *J. Chem. Soc. Chem. Commun.* **1989**, No. 12, 749–751.
- (33) Hallbrucker, A.; Mayer, E. Unexpectedly Stable Nitrogen, Oxygen, Carbon Monoxide and Argon Clathrate Hydrates from Vapour-Deposited Amorphous Solid Water: An X-Ray and Two-Step Differential Scanning Calorimetry Study. *J. Chem. Soc. Faraday Trans.* **1990**, *86*, 3785–3792.
- (34) Bag, S.; Bhuin, R. G.; Methikkalam, R. R. J.; Pradeep, T.; Kephart, L.; Walker, J.; Kuchta, K.; Martin, D.; Wei, J. Development of Ultralow Energy (1–10 eV) Ion Scattering Spectrometry Coupled with Reflection Absorption Infrared Spectroscopy and Temperature Programmed Desorption for the Investigation of Molecular Solids. *Rev. Sci. Instrum.* **2014**, *85*, No. 014103.
- (35) Ghosh, J.; Hariharan, A. K.; Bhuin, R. G.; Methikkalam, R. R. J.; Pradeep, T. Propane and Propane–Water Interactions: A Study at Cryogenic Temperatures. *Phys. Chem. Chem. Phys.* **2018**, *20*, 1838–1847.
- (36) Methikkalam, R. R. J.; Bhuin, R. G.; Ghosh, J.; Sivaraman, B.; Pradeep, T. Interaction of Acetonitrile with Alcohols at Cryogenic Temperatures. *J. Phys. Chem. C* **2017**, *121*, 2822–2835.
- (37) Methikkalam, R. R. J.; Ghosh, J.; Bhuin, R. G.; Bag, S.; Ragupathy, G.; Pradeep, T. Iron Assisted Formation of CO_2 over Condensed CO and Its Relevance to Interstellar Chemistry. *Phys. Chem. Chem. Phys.* **2020**, *22*, 8491–8498.
- (38) Vishwakarma, G.; Ghosh, J.; Pradeep, T. Desorption-Induced Evolution of Cubic and Hexagonal Ices in an Ultrahigh Vacuum and Cryogenic Temperatures. *Phys. Chem. Chem. Phys.* **2021**, *23*, 24052–24060.
- (39) Moon, E.-S.; Kang, H.; Oba, Y.; Watanabe, N.; Kouchi, A. Direct Evidence for Ammonium Ion Formation in Ice Through Ultraviolet-Induced Acid–Base Reaction of NH_3 With H_3O^+ . *Astrophys. J.* **2010**, *713*, 906.
- (40) Buch, V.; Devlin, J. P.; Monreal, I. A.; Jagoda-Cwiklik, B.; Uras-Aytemiz, N.; Cwiklik, L. Clathrate Hydrates with Hydrogen-Bonding Guests. *Phys. Chem. Chem. Phys.* **2009**, *11*, 10245–10265.
- (41) Dartois, E.; Deboffle, D.; Bouziti, M. Methane Clathrate Hydrate Infrared Spectrum - II. Near-Infrared Overtones, Combination Modes and Cages Assignments. *Astron. Astrophys.* **2010**, *514*, A49.

- (42) Walsh, M. R.; Koh, C. A.; Sloan, E. D.; Sum, A. K.; Wu, D. T. Microsecond Simulations of Spontaneous Methane Hydrate Nucleation and Growth. *Science* **2009**, *326*, 1095–1098.
- (43) Malla, B. K.; Vishwakarma, G.; Chowdhury, S.; Selvarajan, P.; Pradeep, T. Formation of Ethane Clathrate Hydrate in Ultrahigh Vacuum by Thermal Annealing. *J. Phys. Chem. C* **2022**, *126*, 17983–17989.
- (44) Ghosh, J.; Methikkalam, R. R. J.; Bhui, R. G.; Ragupathy, G.; Choudhary, N.; Kumar, R.; Pradeep, T. Reply to Choukroun et al.: IR and TPD Data Suggest the Formation of Clathrate Hydrates in Laboratory Experiments Simulating ISM. *Proc. Natl. Acad. Sci. U. S. A.* **2019**, *116*, 14409–14410.
- (45) Dartois, E.; Langlet, F. Ethane Clathrate Hydrate Infrared Signatures for Solar System Remote Sensing. *Icarus* **2021**, *357*, No. 114255.
- (46) Smith, R. S.; Petrik, N. G.; Kimmel, G. A.; Kay, B. D. Thermal and Nonthermal Physiochemical Processes in Nanoscale Films of Amorphous Solid Water. *Acc. Chem. Res.* **2012**, *45*, 33–42.
- (47) Takeya, S.; Ripmeester, J. A. Dissociation Behavior of Clathrate Hydrates to Ice and Dependence on Guest Molecules. *Angew. Chem., Int. Ed.* **2008**, *47*, 1276–1279.
- (48) Falenty, A.; Hansen, T. C.; Kuhs, W. F. Formation and Properties of Ice XVI Obtained by Emptying a Type SII Clathrate Hydrate. *Nature* **2014**, *516*, 231–233.
- (49) Falenty, A.; Kuhs, W. F. Self-Preservation of CO₂ Gas Hydrates—Surface Microstructure and Ice Perfection. *J. Phys. Chem. B* **2009**, *113*, 15975–15988.
- (50) Monreal, I. A.; Devlin, J. P.; Maşlakçı, Z.; Çiçek, M. B.; Uras-Aytemiz, N. Controlling Nonclassical Content of Clathrate Hydrates Through the Choice of Molecular Guests and Temperature. *J. Phys. Chem. A* **2011**, *115*, 5822–5832.
- (51) Consani, K. Infrared Bands of Acetone in Solid Argon and the Structure II Clathrate 2-Acetylene/Acetone/17-Water. *J. Phys. Chem.* **1987**, *91*, 5586–5588.
- (52) Shin, S.; Kang, H.; Kim, J. S.; Kang, H. Phase Transitions of Amorphous Solid Acetone in Confined Geometry Investigated by Reflection Absorption Infrared Spectroscopy. *J. Phys. Chem. B* **2014**, *118*, 13349–13356.
- (53) Hagen, W.; Tielens, A. G. G. M.; Greenberg, J. M. The Infrared Spectra of Amorphous Solid Water and Ice I_c between 10 and 140 K. *Chem. Phys.* **1981**, *56*, 367–379.
- (54) Vishwakarma, G.; Malla, B. K.; Chowdhury, S.; Khandare, S. P.; Pradeep, T. Existence of Acetaldehyde Clathrate Hydrate and Its Dissociation Leading to Cubic Ice under Ultrahigh Vacuum and Cryogenic Conditions. *J. Phys. Chem. Lett.* **2023**, *14*, 5328–5334.
- (55) Lisgarten, N. D.; Blackman, M. The Cubic Form of Ice. *Nature* **1956**, *178*, 39–40.
- (56) Kouchi, A.; Kuroda, T. Amorphization of Cubic Ice by Ultraviolet Irradiation. *Nature* **1990**, *344*, 134–135.
- (57) Vishwakarma, G.; Malla, B. K.; Reddy, K. S. S. V. P.; Ghosh, J.; Chowdhury, S.; Yamijala, S. S. R. K. C.; Reddy, S. K.; Kumar, R.; Pradeep, T. Induced Migration of CO₂ from Hydrate Cages to Amorphous Solid Water under Ultrahigh Vacuum and Cryogenic Conditions. *J. Phys. Chem. Lett.* **2023**, *14*, 2823–2829.
- (58) Wooldridge, P. J.; Richardson, H. H.; Devlin, J. P. Mobile Bjerrum Defects: A Criterion for Ice-like Crystal Growth. *J. Chem. Phys.* **1987**, *87*, 4126–4131.
- (59) Moudrakovski, I. L.; Udachin, K. A.; Alavi, S.; Ratcliffe, C. I.; Ripmeester, J. A. Facilitating Guest Transport in Clathrate Hydrates by Tuning Guest-Host Interactions. *J. Chem. Phys.* **2015**, *142*, No. 074705.
- (60) Ohgaki, K.; Nakatsuji, K.; Takeya, K.; Tani, A.; Sugahara, T. Hydrogen Transfer from Guest Molecule to Radical in Adjacent Hydrate-Cages. *Phys. Chem. Chem. Phys.* **2008**, *10*, 80–82.
- (61) Sugahara, T.; Kobayashi, Y.; Tani, A.; Inoue, T.; Ohgaki, K. Intermolecular Hydrogen Transfer between Guest Species in Small and Large Cages of Methane + Propane Mixed Gas Hydrates. *J. Phys. Chem. A* **2012**, *116*, 2405–2408.
- (62) Goldberg, P. Free Radicals and Reactive Molecules in Clathrate Cavities. *Science* **1963**, *142*, 378–379.
- (63) Takeya, K.; Tani, A.; Yada, T.; Ikeya, M.; Ohgaki, K. Electron Spin Resonance Study on γ -Ray-Induced Methyl Radicals in Methane Hydrates. *Jpn. J. Appl. Phys.* **2004**, *43*, 353.
- (64) Bauer, R. P. C.; Ravichandran, A.; Tse, J. S.; Appathurai, N.; King, G.; Moreno, B.; Desgreniers, S.; Sammynaiken, R. In Situ X-Ray Diffraction Study on Hydrate Formation at Low Temperature in a High Vacuum. *J. Phys. Chem. C* **2021**, *125*, 26892–26900.

Photoconversion of Ag₃₁ to Ag₄₂ Initiated by Solvated Electrons

Arijit Jana, Wakeel Ahmed Dar, Sourav Kanti Jana, Ajay Kumar Poonia, Vivek Yadav, Jayoti Roy, Sourov Chandra, Kumaran Nair Valsala Devi Adarsh,* Robin H. A. Ras,* and Thalappil Pradeep*



Cite This: <https://doi.org/10.1021/acs.chemmater.3c01293>



Read Online

ACCESS |



Metrics & More



Article Recommendations



Supporting Information

ABSTRACT: Light-matter interactions, especially in atomically precise nanomaterials, belong to an unexplored realm of research with potential benefits for the synthesis of materials. Here, we present an interesting light-activated expansion process of an Ag₃₁ nanocluster to an Ag₄₂ analogue, both clusters being protected with 6-(dibutylamino)-1,3,5-triazine-2, 4-dithiol (shortly, TRZ-H₂) ligands. The conversion process was initially monitored through UV-vis, revealing that the violet-colored Ag₃₁ got converted to greenish Ag₄₂, exhibiting their characteristic absorption features. High-resolution mass spectrometric studies confirmed that the as-synthesized [Ag₃₁(TRZ)₁₀] with coexisting di- and monoanionic charged species in dichloromethane solution got converted to [Ag₄₂(TRZ)₁₃] with a dipositive charge state. Electrochemical studies revealed the photoresponsive nature of Ag₃₁, and light illumination resulted in transient intermediate clusters covered with solvated electrons, which contributed to the core expansion. Ag₃₁ is NIR-emitting, while Ag₄₂ is red-emitting. The ultrafast transient absorption studies reveal that Ag₄₂ has strikingly short excited-state carrier dynamics than Ag₃₁. The stable excited-state carriers for Ag₃₁ upon photoexcitation also underline the unique electronic characteristics responsible for such light-activated structural evolution.



INTRODUCTION

Atomically precise metal nanoclusters (NCs) with a kernel of metal atoms, protected by various ligands, connecting the gap between traditional nanoparticles and single atoms, have emerged as a new class of functional nanomaterials with unique optical and physicochemical properties.^{1–6} Such type of ultrasmall nanoparticles with a core dimension <3 nm displayed exotic optical properties, such as molecule-like multiple absorption and emission due to the electronic transitions between their discrete energy levels.^{7–9} A wide range of silver NCs with varying nuclearities, such as Ag₆, Ag₁₄, Ag₁₆, Ag₂₁, Ag₂₅, Ag₂₉, Ag₃₅, Ag₄₀–Ag₄₆, Ag₆₁, Ag₆₇, Ag₁₄₆, Ag₃₇₄, and so forth, with protecting ligands were synthesized, and some of them have been structurally characterized using single-crystal X-ray diffraction studies.^{1–3,10–21} Atomic arrangements of such nanomaterials, associated energy levels, and surface reactivity promote their potential applications in the fields of catalysis, molecular recognition, biomedical imaging, and optoelectronic devices.^{22–29} The stability of silver NCs mainly depends on the outer coverage of surface ligands. The bare NCs without ligands are highly reactive, and they react to themselves or with species in the surrounding environments and form larger particles or adduct species.³⁰ Different surface ligands, such as thiol, imine thiol, selenol, phosphine, carboxylic acid, calixarene, alkynyl, and so forth, create clusters with higher stability than bare NCs.^{31–40} Generally, thiolated silver NCs are more stable than

phosphine, hydride, and alkyne-protected ones.^{1–3} We have introduced a new bidentate thiol ligand for silver clusters, i.e., 6-(dibutylamino)-1, 3, 5-triazine-2, 4-dithiol (shortly, TRZ-H₂) having two butyl chains connected through a nitrogen atom and a triazine ring. Steric bulk created by two butyl chains attached to the triazine ring makes this ligand more attractive than their bidentate thiol analogues such as benzene-dithiol.¹⁵ The electron-withdrawing ability of three nitrogens present in the triazine ring makes it less electron-dense than benzene. The enhanced polarizability of the heterocycle rather than benzene makes the π – π^* electronic transition of the triazine ligand different from the benzene analogues.^{41,42} Recently, we have demonstrated the multifunctional optoelectronic and quantum coherence behavior of an ultrasmall Au₆ NC protected by the same ligand.⁴³

The past decade has witnessed the synthesis of various silver NCs and an understanding of their structure–property correlations. These nanomaterials spontaneously change their nuclearity, size, and shape upon change in parameters such as temperature, pressure, solvents, external metal ions, and so

Received: May 26, 2023

Revised: August 15, 2023

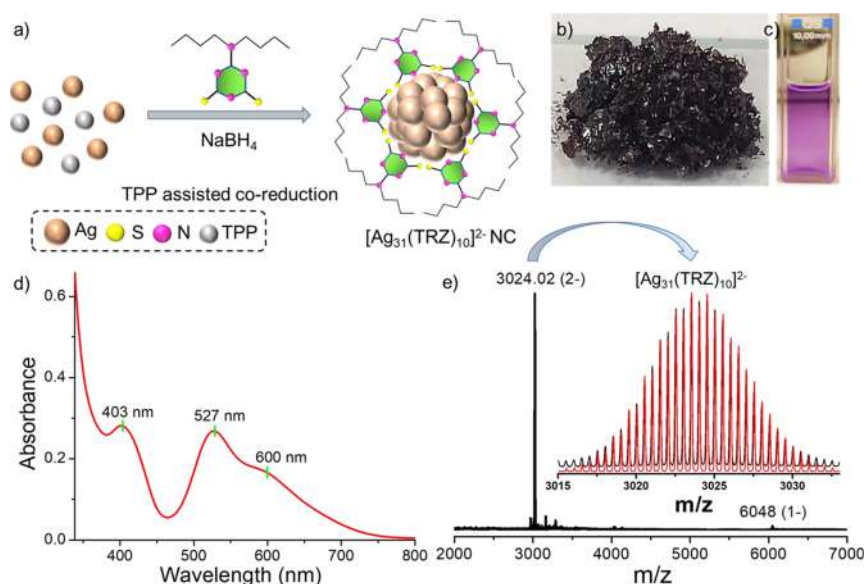


Figure 1. (a) Schematic representation of the synthesis of Ag_{31} using the triphenylphosphine-assisted coreduction reaction. Photographs of (b) 200 mg powder of Ag_{31} and (c) violet-colored Ag_{31} in DCM. (d) UV-vis absorption spectrum of the cluster. (e) Full range ESI-MS spectrum in the negative-ion mode. An intense dianionic peak at m/z 3024.02 and a monoanionic peak at 6048.01 indicate the presence of both the charge states of the cluster. The inset shows the isotopic distribution of the experimental (black) and theoretical (red) spectra.

forth.^{44–48} For example, enhanced emission at a low temperature was observed for silver NCs due to the modulation of their optical band gap.^{49,50} Zang and co-workers observed a visible color change in a single crystal of silver-sulfide NC due to its structural strain at high pressure.⁵¹ Along with a visible color change, bathochromic shifting of the emission maxima with luminescence enhancement was also observed for different silver NCs.^{52,53} Interconversion of silver NCs promoted by solvents and counterions is also manifested in their surface sensitivity.^{54,55} Recently, we have illustrated metal–metal and metal–sulfide structural rearrangements of silver NCs promoted by external bidentate organic linkers resulting in functional metal–organic framework solids.⁵⁶ Compared to other stimuli, the effect of light exposure to silver NCs is not well explored. However, silver nanoparticles and nanostructures are known for their light sensitivity.^{57–59} Photoinduced structural effects of various silver nanostructures lead to their applications in plasmon-assisted polymerization, photodriven chemical transformations, photochromic effects, surface-enhanced Raman scattering, and so forth.^{60–64} Interactions between electromagnetic radiation and surface-bound free electrons are responsible for such type of photochemical effects. In this context, a detailed understanding of the interaction between newly synthesized silver NCs and light is an actively pursued research frontier.

In the present work, we present the synthesis of a TRZ- H_2 protected silver NC, i.e., $[\text{Ag}_{31}(\text{TRZ})_{10}]$ (shortly Ag_{31}) using triphenylphosphine-assisted metal thiolate coreduction reaction. This is the first report of a silver NC protected by triazine dithiol ligand. Due to the specific metal core and surface ligand arrangements, it shows a characteristic UV–visible absorption feature having three absorption maxima at 403, 527, and 600 nm. High-resolution mass spectrometry (MS) and other spectroscopic and microscopic studies confirm the atomic arrangement of the cluster. Thermogravimetric analysis shows the thermal stability of the cluster in the solid state, and time-dependent UV–vis shows the stability of the cluster in solution. Interestingly, we have observed that the violet-

colored Ag_{31} got converted to greenish Ag_{42} upon white light illumination. MS investigations reveal the formation of a new cluster, i.e., $[\text{Ag}_{42}(\text{TRZ})_{13}]$, with higher nuclearity. The photoluminescence (PL) studies show that NIR-emitting Ag_{31} got converted to red-emitting Ag_{42} . The formation of mixed intermediate clusters with photogenerated electrons by light exposure is probably the reason behind such a structural expansion. Ultrafast transient absorption studies further reveal the unique characteristics of the excited-state carriers in these clusters. This work demonstrates the potential of light-activated conversion of ligand-protected NCs with specific optical and photophysical characteristics. Although there is a large body of data on these clusters, their single crystals were not obtained to determine their structures.

EXPERIMENTAL SECTION

Chemicals. Silver nitrate (AgNO_3) was purchased from Rankem Chemicals. Sodium borohydride (NaBH_4 , 98%) and triphenylphosphine (TPP) were bought from Aldrich Chemicals. The ligand, TRZ- H_2 , was purchased from TCI America. Sodium sulfate and tetrabutylammonium hexafluorophosphate (TBAF) were purchased from Fisher Scientific and Aldrich, respectively. Solvent grade dichloromethane (DCM), chloroform (CHCl_3), *n*-hexane, *N,N*-dimethylformamide, and methanol were bought from Rankem chemicals and Finar, India. Milli-Q water was used for the synthesis and purification of clusters. Deuterated solvent, CDCl_3 (99.8 atom % D), was purchased from Sigma Aldrich. All chemicals are commercially available and were used as such without further purification.

Synthesis of Ag_{31} NC. Ag_{31} was synthesized at room temperature using a triphenylphosphine-assisted silver-thiolate coreduction reaction. In brief, 20 mg of AgNO_3 (0.12 mM) was dissolved in 5 mL of methanol. 25 mg of TRZ- H_2 (0.09 mM) was dissolved in 9 mL of DCM and added to the stirring condition. After 15 min of reaction, 75 mg of TPP (0.28 mM) dissolved in 2 mL of DCM was added to the reaction mixture. After 10 min of reaction, 12–13 mg of NaBH_4 dissolved in 1 mL of Milli-Q water was added. After adding NaBH_4 , a dark reddish solution was formed, which eventually was converted to a bluish-violet solution after an overnight reaction. After 12 h of reaction, mixed solvents were removed at reduced pressure. The crude

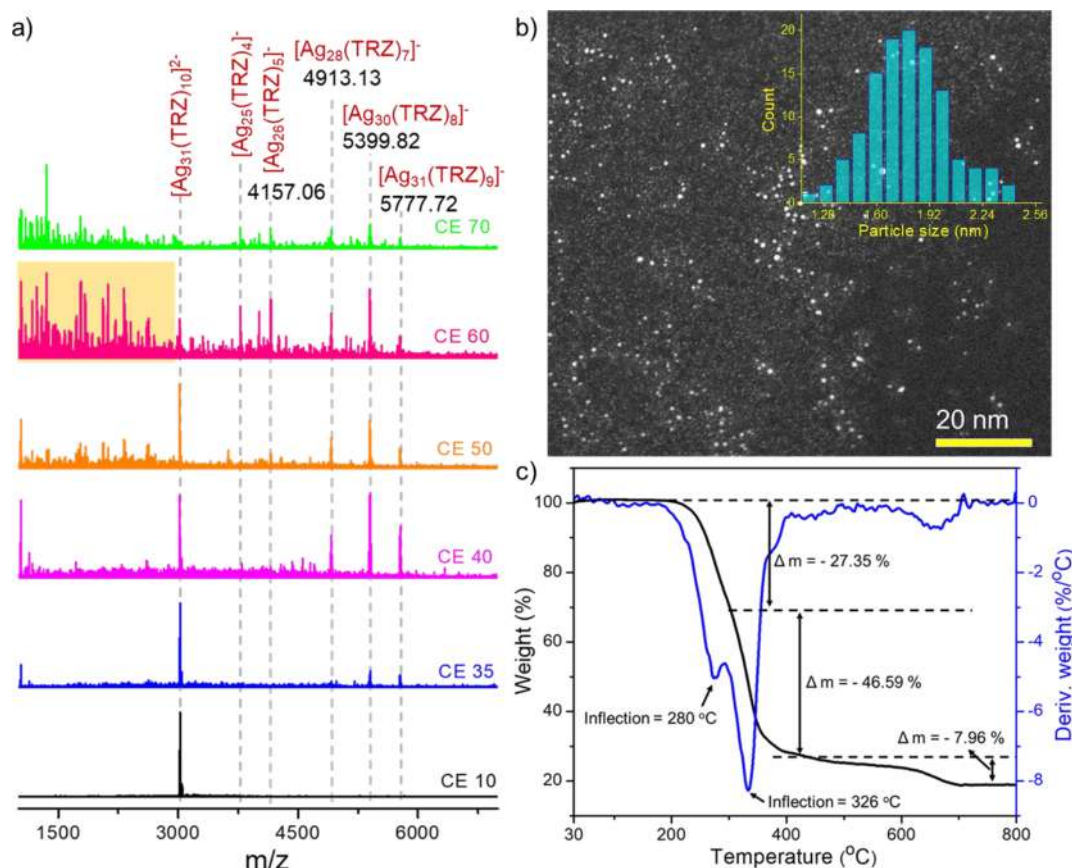


Figure 2. (a) Collision energy-dependent MS/MS fragmentation spectra of Ag_{31} shows the losses of TRZ and silver fragments from the parent cluster. An expanded view of the highlighted region is shown in the [Supporting Information](#). (b) Scanning transmission electron microscopic image of the Ag_{31} NC. The inset shows the particle size distribution profile with an average diameter of 1.8 ± 0.21 nm. (c) Thermogravimetric analysis and differential thermal analysis of Ag_{31} indicating its thermal stability up to 280 °C.

oily product was cleaned five to six times using methanol and hexane in ultrasonic condition to make pure dark violet-colored powder. The yield of the product was 75% in terms of silver.

Light-Triggered Conversion. The Ag_{31} powder (3 mg) was dissolved in 3 mL of DCM or chloroform in a clean glass bottle to study the light-illuminated conversion process. A white light source (xenon arc lamp with a power of 100–200 W) from Newport, India was used for irradiation. Continuous exposure to light leads to such intercluster conversion, which was initially monitored by the visible change in the color of the solution. To further verify the conversion, UV–vis absorption and MS studies were performed. The yield of the interconverted Ag_{42} cluster is 30–35% in terms of the Ag_{31} cluster.

RESULTS AND DISCUSSION

Synthesis and Characterization of Ag_{31} . We have synthesized TRZ-protected Ag_{31} at room temperature (25 °C) by triphenylphosphine-assisted coreduction of silver thiolate precursor using NaBH_4 as the reducing agent. [Figure 1a](#) shows the schematic representation of the synthesis. A detailed synthesis protocol of Ag_{31} is presented in the Experimental Section. The formation of Ag_{31} was monitored using time-dependent UV–vis ([Figure S1](#)), which shows the appearance of characteristic absorption bands after 6 h of reaction and which eventually becomes more prominent after the overnight reaction. The purified cluster was used for further studies. Photographs in [Figure 1b,c](#) depict the violet-colored cluster in the solid state and in DCM solution, respectively. UV–vis absorption characterized the Ag_{31} , representing discrete spectral bands at 403, 527, and 600 nm ([Figure 1d](#)). The

characteristic spectral feature is the fingerprint of the NC. To understand the effect of TPP in the synthesis, we performed a reaction with equal amounts of metal and thiolate precursors without TPP. The product formed due to the reduction without TPP is red, unlike violet-colored Ag_{31} with TPP. UV–vis absorption spectrum is also not similar in both the cases (shown in [Figure S2](#)). Furthermore, we successfully scaled up the synthesis (5-fold) of Ag_{31} through TPP-assisted reduction reaction, which was verified through UV–vis studies ([Figure S3](#)).

The molecular composition of the Ag_{31} was substantiated using high-resolution electrospray ionization mass spectrometry (HR-ESI-MS) studies. Additional details of instrumentation and sample preparation are presented in the [Supporting Information](#). [Figure 1e](#) shows the negative-ion mode ESI-MS spectrum of the cluster with an intense ion peak at m/z 3024.02 and a relatively weak peak at m/z 6048.01. A peak-to-peak separation of isotopic distribution is 0.5 for m/z 3024.02 and 1 for m/z 6048.01 peaks, confirming that the charge states of the ions were 2 and 1, respectively. The total mass of 6048.01 matches with the composition of $[\text{Ag}_{31}(\text{TRZ})_{10}]$, coexisting with the di- and monoanionic charge state species. The isotopic envelope matches well with the theoretical spectrum (shown in the inset of [Figure 1e](#)). We did not observe any peak in the spectrum collected in the positive-ion mode ([Figure S4](#)), manifesting the lack of additional cationic species. Upon additional MS measurements using cesium acetate as the ionizing agent, we observed the emergence of

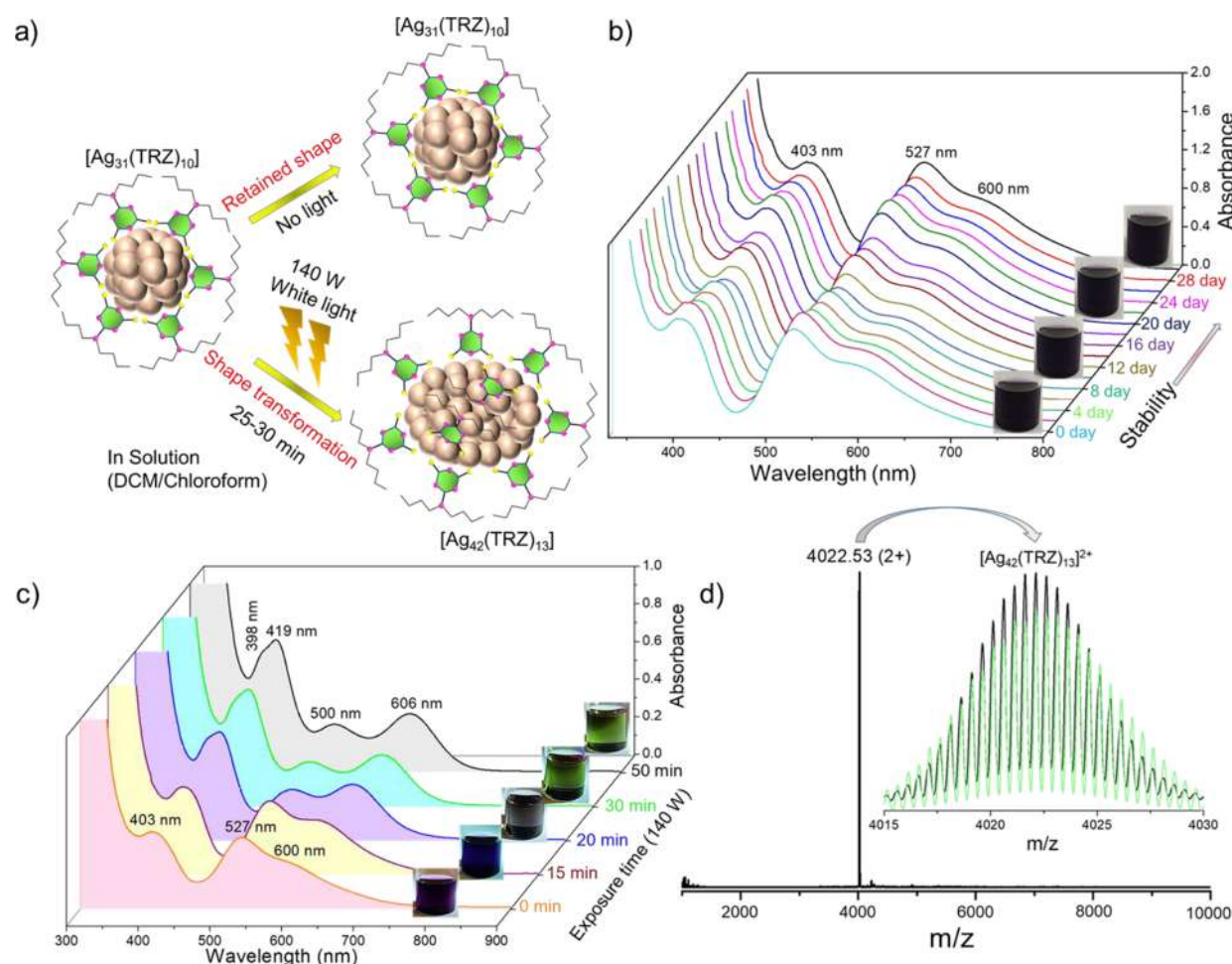


Figure 3. (a) Schematic representation shows light-irradiated conversion of Ag_{31} to Ag_{42} in DCM solution, whereas Ag_{31} remains intact without light irradiation. (b) Time-dependent UV–vis absorption spectra of Ag_{31} show stability for a month without light exposure. (c) UV–vis absorption spectra during the conversion process. The inset shows the photographs of the respective solutions at different time points. Upon further exposure for 120 min, no change was noticed. (d) Positive-ion mode ESI-MS spectrum of as formed Ag_{42} after 30 min of light illumination. Complete conversion of the parent cluster is noticed.

both mono- and dianionic species of the cluster (Figure S5). Furthermore, a peak at 3094.41 (charge state 2−) corresponding to Cs^+ attachment with the trianionic cluster, i.e., $[\text{Ag}_{31}(\text{TRZ})_{10}]^{3-}$, was detected. Collectively, these findings provide evidence for the coexistence of multianionic charge states of the cluster, with a dianionic cluster as the major species in solution.

To gain additional insight into the molecular composition of the cluster, we have performed collision energy-dependent fragmentation studies upon isolating the parent dianionic species at m/z 3024.02 (shown in Figure 2a). No fragmentation of the parent peak was observed up to CE 10 (in an instrument unit). Upon further increasing the collision energy from CE 10 to 35, we observed two new peaks with a monoanionic charge state at m/z 5777.72 and 5399.82. The mass losses of 270 and 648 amu represent the fragmentation of TRZ and $\text{Ag}(\text{TRZ})_2$, respectively, from the parent $[\text{Ag}_{31}(\text{TRZ})_{10}]$ NC. Therefore, the two peaks at 5777.72 and 5399.82 are assigned to the molecular formulae, $[\text{Ag}_{31}(\text{TRZ})_9]^-$ and $[\text{Ag}_{30}(\text{TRZ})_8]^-$, respectively. Upon further increasing the collision energy to CE 70, a few additional peaks were observed at m/z 4913.13, 4157.06, and 3779.24. These new fragments are assigned as $[\text{Ag}_{28}(\text{TRZ})_7]^-$, $[\text{Ag}_{26}(\text{TRZ})_5]^-$, and $[\text{Ag}_{25}(\text{TRZ})_4]^-$. We have also observed several new

fragmented peaks along with these prominent peaks at CE 60. The major fragmented peaks at m/z 3019.84, 2633.04, 2351.79, 2320.04, 2120.32, 2061.42, 1836.29, 1779.93, 1350.52, 1232.74, and 1031.01 are assigned to the compositions, $[\text{Ag}_{14}\text{S}_5(\text{TRZ})_5]^-$, $[\text{Ag}_{11}\text{S}_3(\text{TRZ})_5]^-$, $[\text{Ag}_9\text{S}(\text{TRZ})_5]^-$, $[\text{Ag}_9(\text{TRZ})_5]^-$, $[\text{Ag}_9\text{S}_2(\text{TRZ})_4\text{H}_5]^-$, $[\text{Ag}_{11}\text{S}_2(\text{TRZ})_3]^-$, $[\text{Ag}_{12}(\text{TRZ})_2\text{H}_2]^-$, $[\text{Ag}_9(\text{TRZ})_3]^-$, $[\text{Ag}_5(\text{TRZ})_3\text{H}]^-$, $[\text{Ag}_8\text{S}_3(\text{TRZ})_4]^-$, and $[\text{Ag}_7(\text{TRZ})_6]^-$, respectively (shown in Figures S6 and S7). Altogether, the losses of different Ag and TRZ fragments during collision-induced dissociation studies confirmed the molecular composition of Ag_{31} .

The Ag_{31} cluster was further characterized by scanning transmission electron microscopy (STEM). The STEM micrograph in Figure 2b shows ultrasmall particles with a dimension of <2 nm. The ^1H NMR chemical shifts at 3.54, 1.56, 1.32, and 0.89 ppm of the free ligands were shifted to 3.39, 1.43, 1.17, and 0.81 ppm in the cluster (Figures S8 and S9). The broad spectral features of the Ag_{31} cluster are due to the large electron density of the silver core. Fourier transform infrared (FT-IR) spectroscopy also depicts the binding of the TRZ ligand on the cluster. Figure S10 shows the comparative IR spectra of the free TRZ- H_2 ligand and the Ag_{31} cluster. The C–H stretching peak at 2950 cm^{-1} remains at the same

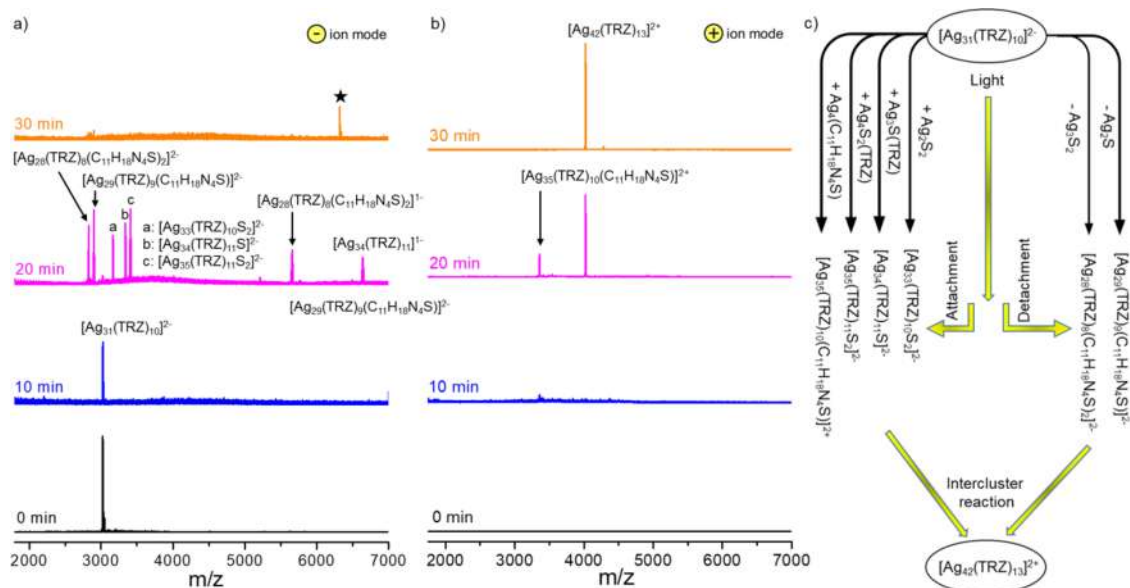


Figure 4. Time-dependent MS spectra showing the formation of intermediate NCs in (a) negative- and (b) positive-ion modes during the conversion of Ag_{31} to Ag_{42} . * indicates some complex species. (c) Schematic illustration of the intermediate species formed during the conversion process.

position for the cluster, which suggests that the butyl chains remain unaffected. The $C=N$ stretching peaks at 1599 and 1536 cm^{-1} for the TRZ- H_2 ligand were shifted to 1513 and 1478 cm^{-1} due to the close proximity of triazine moiety. The sharpness of the $C-N$ stretching band was reduced, while the peak remained at the same position (1126 cm^{-1}). X-ray photoelectron spectroscopy (XPS) was performed on the Ag_{31} cluster, and the data are shown in Figure S11. The survey scan shows the presence of the respective elements, i.e., Ag, S, C, and N, originating from the metal and ligands. We could not successfully prepare single crystals suitable for X-ray diffraction. The as-prepared violet powder shows weak X-ray diffraction features due to poor crystallinity (Figure S12). To investigate the thermal stability of the cluster, we measured its thermogravimetric (TG) profile. TG measurement shows thermal stability of the cluster without having any mass losses up to $\sim 200\text{ }^\circ\text{C}$ (shown in Figure 2c).

Light-Triggered Intercluster Conversion. Despite ambient stability and thermal robustness, we observed the conversion of Ag_{31} to other clusters upon photoirradiation, which is visible by the change in the color of the solution. Figure 3a shows the schematic representation of the light-illuminated conversion of Ag_{31} to Ag_{42} , whereas no conversion was observed for the same cluster without light irradiation. We monitored the UV-vis absorption spectra of the cluster in DCM for an interval of 2 days and observed identical absorbance features after 30 days without any light irradiation (Figure 3b). Ambient stability of the cluster was also observed in chloroform solution (Figure S13). However, white light irradiation (Xe arc lamp, 140 W) results in a visible change of color from violet to green after 30 min of irradiation (Figure 3c). UV-vis absorption measurement showed that the green product has absorption bands centered at 398, 419, 500, and 606 nm in a characteristic pattern, which indicates the formation of a new cluster. Time-dependent UV-vis measurements showed three characteristic bands at 403, 527, and 600 nm up to 15 min of light irradiation, which suggests that Ag_{31} remains intact in the solution. Further 20–25 min of

irradiation resulted in a grayish intermediate solution, which was converted to a green-colored solution within 5–10 min. The absorption features of the gray and green solutions are nearly similar. After continuous light exposure up to 60 min, absorption features remained the same, confirming that the green solution is the final product in the conversion process.

The molecular composition of the end product and the intermediate species formed during such a conversion process were monitored using HR-ESI-MS studies. Time-dependent MS studies showed the appearance of the peak at $m/z\ 3024.02$ (charge state 2−) after 15 min of light exposure (Figure 4a,b), which suggests the presence of Ag_{31} cluster in solution up to 15 min. Additional peaks were not observed in the positive-ion mode. The MS data of the grayish intermediate species (formed after 20–25 min of light exposure) show two new peaks at $m/z\ 3358.79$ and 4022.53 in the positive-ion mode with a charge state of 2+. These peaks are assigned to $[Ag_{35}(TRZ)_{10}(C_{11}H_{18}N_4S)_2]^{2+}$ and $[Ag_{42}(TRZ)_{13}]^{2+}$. There are multiple new peaks at $m/z\ 2830.10$, 2899.97 , 3164.34 , 3337.20 , and 3407.16 with 2− charge state, which are assigned as $[Ag_{28}(TRZ)_8(C_{11}H_{18}N_4S)_2]^{2-}$, $[Ag_{29}(TRZ)_9(C_{11}H_{18}N_4S)_2]^{2-}$, $[Ag_{33}(TRZ)_{10}S_2]^{2-}$, $[Ag_{34}(TRZ)_{11}S]^{2-}$, and $[Ag_{35}(TRZ)_{11}S_2]^{2-}$, respectively. The green-colored end product has a single peak at $m/z\ 4022.53$, with dipositive charge state with the composition as $[Ag_{42}(TRZ)_{13}]^{2+}$, and theoretical isotopic distribution matches well with the experimental spectrum (Figure 3d). No other species were observed throughout the MS spectrum. Also, data collected in the negative-ion mode show no peaks, which suggests the complete conversion of Ag_{31} to Ag_{42} (Figure S14). Therefore, light illumination resulted in clusters with lower and higher nuclearities, and the intercluster reaction between these species (summarized in Figure 4c) resulted in Ag_{42} as an end product. Light-induced growth was observed for a gold NC upon reorganization of the fragmented species arising from light exposure.⁶⁵

Collision energy-dependent fragmentation studies were performed to understand the structural skeleton of the Ag_{42}

NC (Figure 5). On increasing the CE from 0 to 50, no fragmentation of the parent cluster was observed. Further

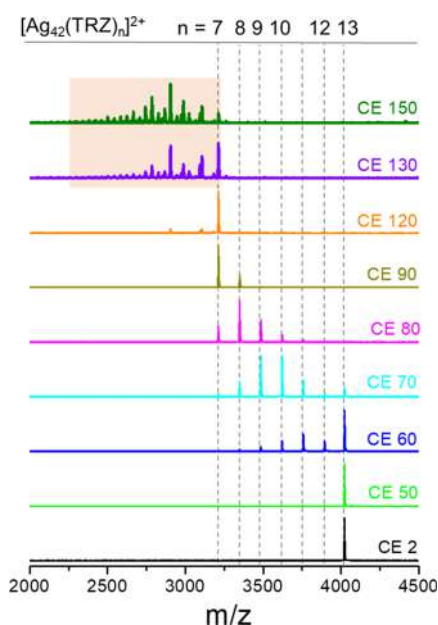


Figure 5. Collision energy-dependent MS/MS fragmentation spectra of Ag_{42} . Sequential TRZ detachment of up to six ligands was observed upon increasing the collision energy. An expanded view of the highlighted region with peak assignments is shown in the Supporting Information.

increasing the collision energy to CE 60, we observed the appearance of five new peaks at m/z 3887.46, 3752.33, 3617.35, 3482.42, and 3347.53 with a dipositive charge state. The sequential mass losses of m/z 270 indicate loss of TRZ ligands from the cluster. Upon further increasing CE to 120, we observed losses of six TRZ fragments from the cluster. Increasing the CE beyond 120 leads to the fragmentation of the metal core of the cluster. Detailed analyses of the molecular composition of these fragments in the lower mass range are presented in Figure S15. Fragmentation of TRZ ligands were also observed.

We have observed a similar type of light-activated conversion in chloroform solution, confirmed through UV-vis absorption and MS studies (shown in Figure S16). The identical absorption features (shown in Figure S17) up to 24 days in DCM and chloroform solutions, respectively, indicate the stability of Ag_{42} in ambient conditions. XPS and IR studies further confirm the binding of the TRZ ligands. The XPS survey spectrum shows the presence of the expected elements, i.e., Ag, S, C, and N in Ag_{42} (Figure S18). The binding energy of 368.4 and 374.4 eV represents the $3d_{5/2}$ and $3d_{3/2}$ of metallic silver (0). Spectral fitting of the C 1s region shows three peaks at 285.1, 286.1, and 287.6 eV due to C–C, C–N, and C=N bonding of TRZ ligands. Deconvolution of the N 1s region shows two peaks at 398.7 and 400.1 eV due to C–N and C=N bonding, respectively. FT-IR studies (shown in Figure S19) further confirm the binding of TRZ ligands with the cluster. TEM investigation reveals the appearance of ultrasmall Ag_{42} , having an average particle diameter of 1.93 ± 0.12 nm (shown in Figure S20).

The intercluster conversion kinetics depends on the lamp power and concentration of the cluster. We have studied the conversion process using different lamp powers, i.e., 100, 140,

and 180 W having the same concentration (1 mg/mL). Comparative UV-vis measurements (shown in Figure S21) reveal a slowdown (~ 40 min) of the conversion kinetics under the lamp power of 100 W, whereas the conversion took ~ 20 min under the 180 W lamp. Similarly, we measured the conversion kinetics at 140 W at varying cluster concentrations of 1, 3, and 5 mg/mL (shown in Figure S22). The conversion took 30 min for 1 mg/mL and 50 and 70 min for 3 and 5 mg/mL concentrations, respectively. The reduction of the absorbance of Ag_{42} in comparison to Ag_{31} also suggests the reduction of the number of particles upon such a photo-conversion process. Furthermore, we have studied the effect of light activation in the solid state. A cluster film was prepared on a glass slide upon drop casting 3 mg of Ag_{31} upon dissolution in DCM. Time-dependent UV-vis absorption studies of the light-exposed thin film showed identical spectral bands up to 210 min of light exposure (lamp power 140 W) (Figure S23). Therefore, this light-activated intercluster conversion is a solution-state phenomenon. The interactions between clusters through long butyl chains on each TRZ ligand promote the dissociation and aggregation reaction pathways. The present finding provides new insight into the ligand's effect on light-induced intercluster conversion. Our earlier studies demonstrated the light-induced conversion of *ortho*-carborane 1, 2-dithiol, and triphenylphosphine coprotected silver NC in DCM solution.⁶⁶ The presence of long butyl chains and nitrogen with multiple binding sites on TRZ ligands facilitates short-range intercluster interactions in solution, playing a significant role in increasing the nuclearity of the cluster.

To understand the electronic stability, we have calculated the valence electrons of these clusters using the electron counting formula as $(N\nu - M - Z)$, where N = number of metal atoms, ν = atomic valence of the metal atom, M = number of ligands, and Z = overall charge.^{67–69} $[\text{Ag}_{31}(\text{TRZ})_{10}]^{2-}$ and $[\text{Ag}_{31}(\text{TRZ})_{10}]^{1-}$ have an electron count of 13e ($31 - 20 + 2$) and 12e ($31 - 20 + 1$), respectively. This cluster showed photosensitive behaviors, probably due to the lack of a close shell superatomic electronic configuration. On the other hand, the valence electron for the $[\text{Ag}_{42}(\text{TRZ})_{13}]^{2+}$ cluster is 14e ($42 - 26 - 2$).

Understanding the Intercluster Conversion through Photoelectrochemical Studies. To understand the photo-activated conversion process, we have measured the open-circuit potential (OCP) of Ag_{31} solution (in DCM) during light illumination conditions. This experiment refers to previously studied measurements (by Bard et al.) of single nanoparticle collisions by OCP and other electrochemical techniques.^{70–73} We used 0.2 M TBAF as the electrolyte during the measurement to enhance ionic conductivity of the solution. The OCP measurements of Ag_{31} solution (concentration of 1 mg/mL) show a gradual rise in potential after light exposure. Continuous light exposure up to ~ 3000 s shows three different kinetics during this conversion process (Figure 6a). The rate of potential enhancement is 6.56×10^{-4} V/s for an interval of ~ 130 s, and this indicates the initial conversion step. This rapid potential enhancement compared to other steps is due to the enhanced Brownian motion of the Ag_{31} cluster. The second and third kinetics took ~ 1250 and ~ 1400 s, with the rate of OCP enhancement being 7.58×10^{-5} and 1.98×10^{-5} V/s, respectively. Electrons generated from the negatively charged Ag_{31} are probably responsible for this light-activated enhancement of potential. As these electrons are

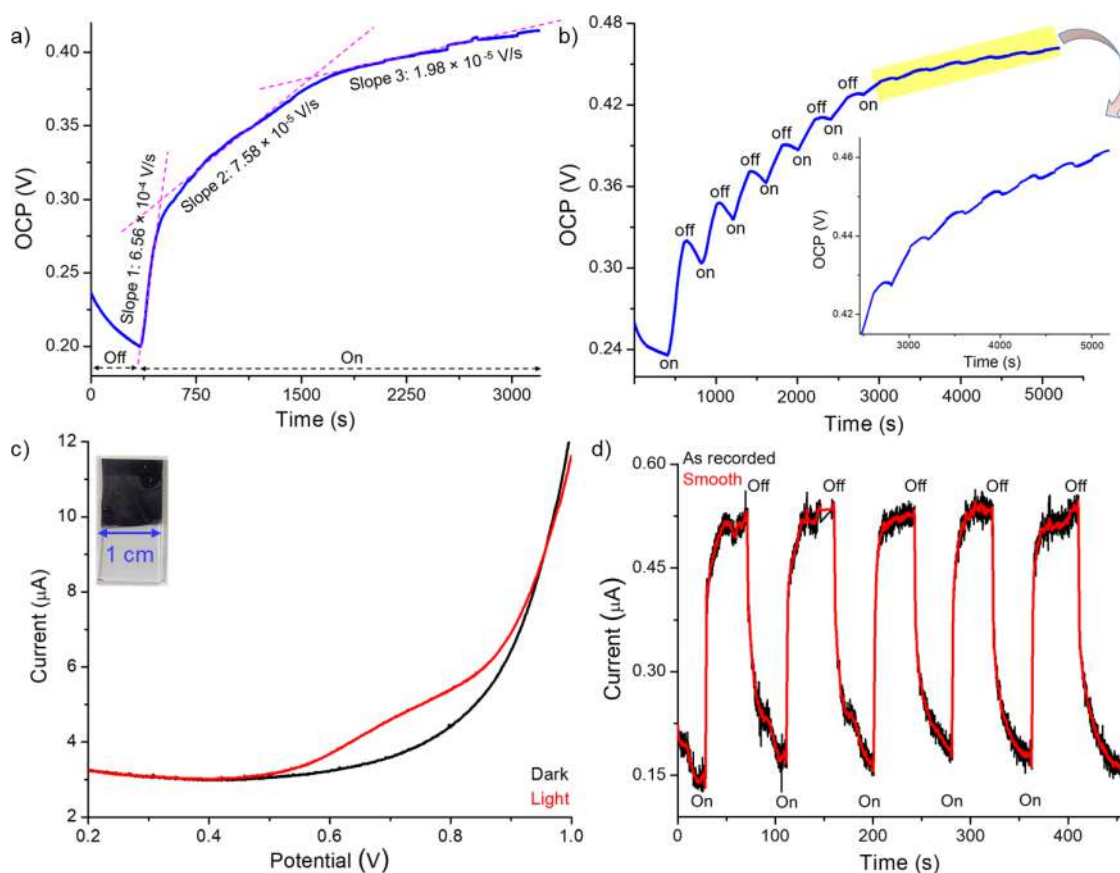


Figure 6. (a) OCP measurement of Ag_{31} in the presence of 0.2 M TBAF solution in DCM (conc. 1 mg/mL) during continuous light illumination (140 W). (b) OCP profile of Ag_{31} during a sequential light on and off cycle. Light exposure time is 200 s in each step. (c) Electrochemical LSV current–voltage (I – V) characteristics of Ag_{31} in the presence of 0.01 M Na_2SO_4 solution. The inset shows a photograph of an ITO electrode coated with Ag_{31} . (d) Chronoamperometric measurement of the Ag_{31} film at 0.72 V demonstrated a reversible photocurrent response.

generated in their respective solutions, we believe that they are solvated. Propagating solvated electrons upon photoexcitation was also observed for various gold and silver nanoparticles.^{74–76} To understand the role of the cluster, a control OCP measurement was performed using the same electrolyte solution without cluster, and there was no change in OCP response under the photoillumination condition (Figure S24). Independent OCP measurements using cluster concentrations of 1, 2, and 3 mg/mL show similar first kinetic step (~ 130 s) for all concentrations, whereas the time taken for the second kinetic step increases from ~ 1250 s for 1 mg/mL to 2000 and 3000 s for 2 and 3 mg/mL clusters, respectively (shown in Figure S25). All these measurements suggest that the second conversion step is the rate-determining step for this conversion process. Increasing concentration took more time to complete the conversion, which is correlated with the concentration-dependent UV–vis absorption studies (shown in Figure S22). Rather than continuous exposure of light, a stepwise light exposure cycle (time interval for each on–off step is 200 s) shows a gradual reduction of the OCP photoresponse (shown in Figure 6b). After ~ 3000 s of stepwise light exposure, photosensitivity reduces significantly since the formed Ag_{42} is less photoactive than Ag_{31} . The newly formed intermediate clusters, monitored through MS studies, along with the solvated electrons are responsible for making the Ag_{42} cluster. An independent cyclic voltammetry measurement also shows the emergence of photogenerated electrons for Ag_{31} cluster in DCM solution (concentration of 1 mg/mL with 0.2 M TBAF)

(Figure S26a). On the other hand, the presynthesized Ag_{42} cluster remains photosilent in similar electrochemical conditions (shown in Figure S26b).

Considering the light sensitivity of Ag_{31} cluster, electrochemical photocurrent measurements in the solid state were performed upon preparing a thin layer of clusters on an indium tin oxide (ITO) working electrode (active surface area 1 cm^2). Photocurrent measurements were performed using 0.01 M aqueous Na_2SO_4 electrolyte in the presence of Pt wire as a counter electrode and Ag/AgCl as a reference electrode. Linear sweep voltammetry (LSV) measurements for Ag_{31} (Figure 6c) showed a positive photocurrent response in the potential range of 0.5–0.9 V upon light illumination. Furthermore, chronoamperometric measurement shows a positive photocurrent response of $\sim 0.38\text{ }\mu\text{A}$ at a bias voltage of 0.72 V. The photocurrent response was reversible up to five cycles (Figure 6d). Bare ITO electrodes did not impart any photocurrent response in the same condition (Figure S27). Photogenerated electrons of Ag_{31} were transferred to the ITO electrode, which exhibited a photocurrent in the solid state. Intercluster collisions between these charged species are interrupted in the solid state. However, dynamic motions in solution and subsequent intercluster collision are responsible for such intercluster conversion.

Effect on Optical Emission. We have measured the emission properties of both the clusters in their respective solutions in DCM. Ag_{31} shows no visible luminescence under 365 nm UV light, as shown in the inset of Figure 7a. PL

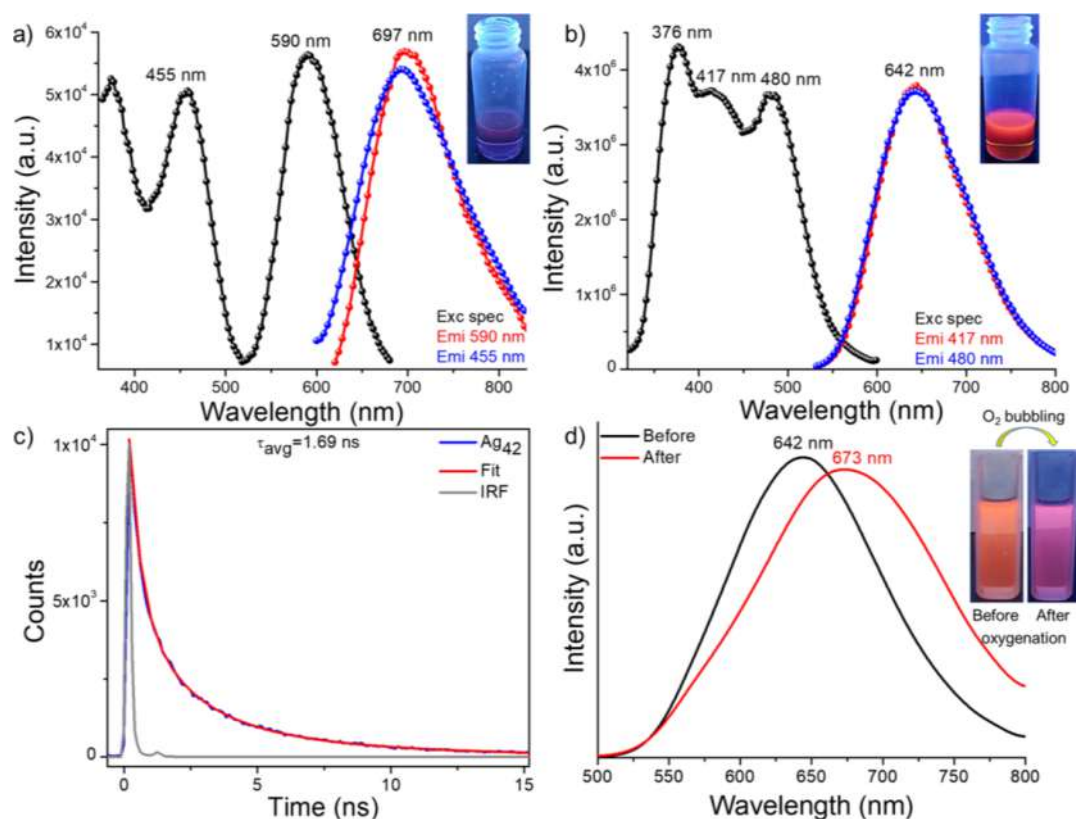


Figure 7. (a) PL excitation and emission spectra of Ag_{31} show a weak NIR-I emission. The inset shows the respective cluster under UV light. (b) PL excitation and emission spectra of Ag_{42} show bright red luminescence. The inset shows an image of the cluster under UV light. (c) Fluorescence decay profile of Ag_{42} . (d) Emission spectra of Ag_{42} before and after oxygenation. The excitation wavelength is 480 nm. The inset shows images of the Ag_{42} cluster under UV light.

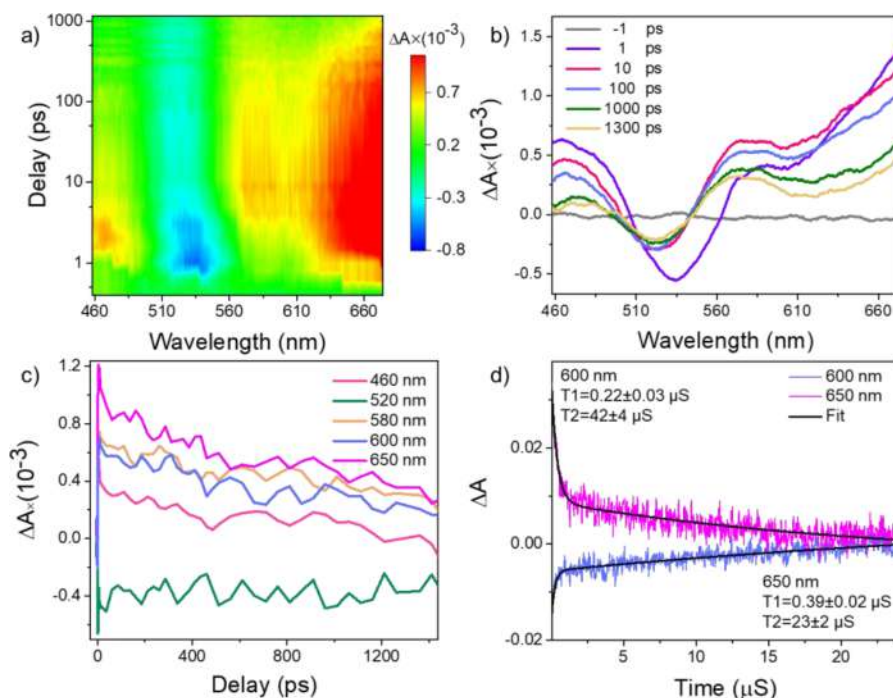


Figure 8. (a) Contour plot of the fs-TA spectrum of Ag_{31} NC, where the pump excitation was at 400 nm. (b) Spectral evolution TA as a function of time delay. (c) Kinetic decay traces of ESA and GSPB signals. (d) Nanosecond time evolution spectral profile measured by laser flash photolysis.

spectral measurement shows a weak emission at 697 nm in the NIR-I window, using excitations at 455 and 590 nm. On the other hand, the Ag_{42} has a bright red luminescence under a 365

nm UV lamp (shown in the inset of Figure 7b). The emission maximum was centered at 642 nm upon photoexcitation at 376, 417, and 480 nm. The emissive lifetime of 1.69 ns in its

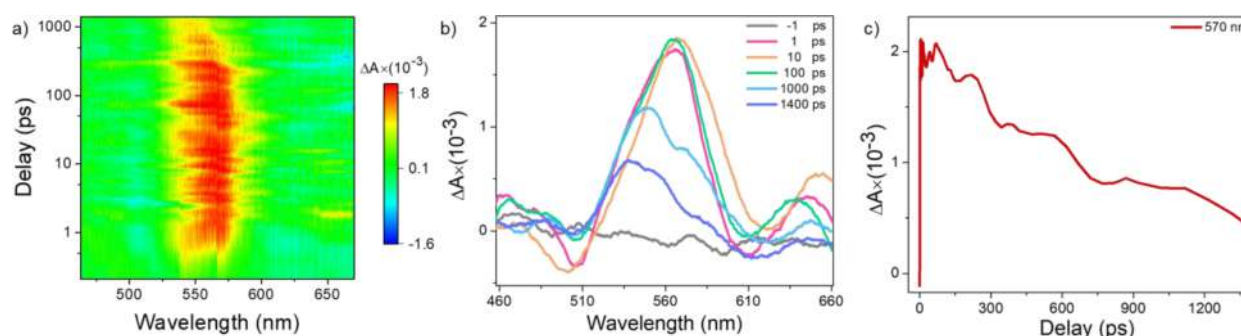


Figure 9. (a) fs-TA contour map of Ag_{42} , where the pump excitation was at 400 nm. (b) Time evolution of the TA spectra of Ag_{42} . (c) Selected kinetic decay traces for the 570 nm ESA features.

DCM solution (Figure 7c) suggests fluorescence emission originating from the singlet excited state. The expansion of the emissive band gap (0.15 eV) and enhancement of the emission intensity for the Ag_{42} cluster are probably due to the enhanced symmetry of the ligand distribution around the cluster core, which promotes enhanced interfacial charge transfer.

Although there is no significant visible color change of the cluster in its solid state, we observed double emission bands centered at 649 and 740 nm, where 740 nm is the primary emission band (Figure S28). Intercluster interaction in the solid state is probably the reason behind these low-energy emission features. After oxygen bubbling, there is no significant emission quenching, confirming that the emission originated from a singlet state. However, we observed a visible color change from orange to purple after oxygen bubbling (30–35 min). PL measurement (Figure 7d) shows a 642 nm peak that shifted to 673 nm after oxygen exposure. Although the singlet excited state is not quenched by oxygen, the interactions between the Ag_{42} cluster and oxygen lead to the stabilization of the excited state. Identical UV–vis absorption features (shown in Figure S29) of the oxygenated sample suggest the structural stability of the Ag_{42} cluster.

Comparative Excited-State Electron Dynamics. We conducted femtosecond transient absorption (fs-TA) and nanosecond laser flash-photolysis (ns-LFP) studies to visualize the excited-state carrier dynamics of these clusters. In our measurements, we excited the sample in DCM solution with a 120 fs laser pulse at 400 nm, and the resulting change in the system was monitored by time-delayed broad band pulses of 460–670 nm range. Specific instrumentation details can be found in the Supporting Information. The fs-TA signals of Ag_{31} are plotted in Figure 8. The contour maps of Ag_{31} consist of ground state photobleaching (GSPB) bands at 520 and 610 nm, along with three excited-state absorption (ESA) features (yellow and red colors represent a positive signal) at 470, 580, and 650 nm (Figure 8a).

For better quantification, the spectral cross-section at the selected time delay is shown in Figure 8b. The figure shows that the primary photobleach is at 520 nm, which is the position of optical absorption (527 nm) manifested in the form of a negative signal. However, the 610 nm GSPB band is visible only in the downhill region in the ESA band. These photobleach signals arise due to the phase-space filling of excited-state carriers formed by pump excitation, and ESA is due to the transitions of these carriers into elevated excited-energy states. Here, it is interesting to see that among all these features, photobleach (in the region of 520 and 610 nm) and ESA (470 and 670 nm) have the same type of time evolution

but relatively different and correlated electron dynamics compared to the ESA of 580 nm (Figure 8c). The features of 520, 620, 470, and 670 nm build up immediately after photoexcitation within the same time period of 0.5 ps and then exhibit an early decay.

On the other hand, ESA of 580 nm rises slowly and builds up in the decay duration. This behavior suggests that an ESA of 580 nm arises after the early decay of all other features. For quantification of this ultrashort-time behavior, the temporal profile for the early time is shown Figure S30. By fitting the decay with of the single exponential function, we found the decay constant of 3.6 ± 0.3 and 3.5 ± 0.5 ps. This type of ultrafast electronic behavior was also observed for the gold and silver NCs and assigned to the internal conversion from ($\text{LUMO}+n$) to LUMO states.^{77–79} These studies suggest that the observed electron dynamics of the excited state can be linked to two different processes. The first fast relaxation is due to internal conversion, and the subsequent slow component is due to the relaxation within the ground state. Further, the excited-state carriers do not relax completely, suggesting a long lifetime. Therefore, to determine the decay kinetics of relaxation to the ground state, ns-LFP of Ag_{31} was performed (Figure 8d), revealing a microsecond-long lifetime for the cluster.

TA spectral features of Ag_{42} are plotted in Figure 9, where we see weak GSPB bands at 510 and 606 nm and prominent excited-state absorption bands at 465, 560, and 650 nm. Although the spectral features of both the clusters are nearly similar, their lifetimes are contrastingly different. Temporal evolution of TA in Figure 9c reveals a ns lifetime compared to the μs lifetime for the parent Ag_{31} .

CONCLUSIONS

In conclusion, we present the first triazine dithiol-protected silver NC, i.e., Ag_{31} , using a triphenylphosphine-assisted metal thiolate coreduction reaction. The UV–vis absorption bands in a characteristic pattern represent the discrete electronic energy levels of the NC. MS measurements and collision energy-dependent fragmentation studies confirm the molecular composition of the cluster with mono- and dianionic charge states. Thermally stable Ag_{31} shows light-triggered size expansion in its solution. The visible color change from violet to green and the changes in the UV–vis spectral features reveal such a light-activated process. MS studies confirm the formation of $[\text{Ag}_{42}(\text{TRZ})_{13}]^{2+}$ as an end product through intercluster reactions between intermediate clusters with lower and higher nuclearities. The PL spectral measurements showed that the Ag_{31} is weakly NIR emissive, with an emission

maximum at 697 nm, whereas the Ag₄₂ is intensely red emissive (maximum at 642 nm). The photoconducting Ag₃₁ shows light-irradiated enhancement of OCP in photoelectrochemical conditions. The formation of light-activated solvated electrons might be triggering this conversion process. The femtosecond and nanosecond ultrafast TA studies reveal that the stable excited-state carriers of Ag₃₁ (lifetime in the μ s range) got converted to Ag₄₂, having unstable carriers with ns lifetime. Altogether, these studies showed an unusual size evolution of a silver nanocluster triggered by light.

■ ASSOCIATED CONTENT

SI Supporting Information

The Supporting Information is available free of charge at <https://pubs.acs.org/doi/10.1021/acs.chemmater.3c01293>.

Instrumentation details, supplementary UV–vis, PL, MS spectra, NMR, IR, XPS, and TEM characterization of Ag₃₁ and Ag₄₂ nanoclusters, and details of intercluster conversion measured through UV–vis and photoelectrochemical measurements (PDF)

■ AUTHOR INFORMATION

Corresponding Authors

Kumaran Nair Valsala Devi Adarsh – Department of Physics, Indian Institute of Science Education and Research Bhopal, Bhopal 462066, India; orcid.org/0000-0002-6337-6545; Email: adarsh@iiserb.ac.in

Robin H. A. Ras – Department of Applied Physics, School of Science, Aalto University, 02150 Espoo, Finland; orcid.org/0000-0002-2076-242X; Email: robin.ras@aalto.fi

Thalappil Pradeep – DST Unit of Nanoscience (DST UNS) and Thematic Unit of Excellence (TUE), Department of Chemistry, Indian Institute of Technology Madras, Chennai 600036, India; orcid.org/0000-0003-3174-534X; Email: pradeep@iitm.ac.in

Authors

Arijit Jana – DST Unit of Nanoscience (DST UNS) and Thematic Unit of Excellence (TUE), Department of Chemistry, Indian Institute of Technology Madras, Chennai 600036, India

Wakeel Ahmed Dar – DST Unit of Nanoscience (DST UNS) and Thematic Unit of Excellence (TUE), Department of Chemistry, Indian Institute of Technology Madras, Chennai 600036, India

Sourav Kanti Jana – DST Unit of Nanoscience (DST UNS) and Thematic Unit of Excellence (TUE), Department of Chemistry, Indian Institute of Technology Madras, Chennai 600036, India; orcid.org/0000-0001-5772-7022

Ajay Kumar Poonia – Department of Physics, Indian Institute of Science Education and Research Bhopal, Bhopal 462066, India; orcid.org/0000-0002-5551-7299

Vivek Yadav – DST Unit of Nanoscience (DST UNS) and Thematic Unit of Excellence (TUE), Department of Chemistry, Indian Institute of Technology Madras, Chennai 600036, India

Jayoti Roy – DST Unit of Nanoscience (DST UNS) and Thematic Unit of Excellence (TUE), Department of Chemistry, Indian Institute of Technology Madras, Chennai 600036, India

Sourav Chandra – Department of Applied Physics, School of Science, Aalto University, 02150 Espoo, Finland; orcid.org/0000-0003-0129-4242

Complete contact information is available at: <https://pubs.acs.org/doi/10.1021/acs.chemmater.3c01293>

Notes

The authors declare no competing financial interest.

■ ACKNOWLEDGMENTS

The authors acknowledge the support of the Department of Science and Technology (DST), Govt. of India. A.J. thanks the IIT Madras for his research fellowship. We thank the Sophisticated Analytical Instruments Facility (SAIF), IIT Madras, for thermogravimetric measurements. T.P. acknowledges funding from the Centre of Excellence on Molecular Materials and Functions under the Institution of Eminence scheme of IIT Madras. K.N.V.D.A. gratefully acknowledges the Science and Engineering Research Board (SERB) for the grant CRG/2019/002808. This work was also supported by the Academy of Finland Center of Excellence Program (2022–2029) in Life-Inspired Hybrid Materials (LIBER) project number 346109.

■ DEDICATION

This article is dedicated to Prof. K. Vidyasagar on the occasion of his 65th birthday.

■ REFERENCES

- (1) Jin, R.; Zeng, C.; Zhou, M.; Chen, Y. Atomically Precise Colloidal Metal Nanoclusters and Nanoparticles: Fundamentals and Opportunities. *Chem. Rev.* **2016**, *116*, 10346–10413.
- (2) Chakraborty, I.; Pradeep, T. Atomically Precise Clusters of Noble Metals: Emerging Link between Atoms and Nanoparticles. *Chem. Rev.* **2017**, *117*, 8208–8271.
- (3) Pradeep, T., Ed.; *Atomically Precise Metal Nanoclusters*; Elsevier: Amsterdam, 2023; pp 1–643.
- (4) Jana, A.; Kini, A. R.; Pradeep, T. Atomically Precise Clusters: Chemical Evolution of Molecular Matter at the Nanoscale. *AsiaChem Mag.* **2023**, *3*, 56–65.
- (5) Jena, P.; Sun, Q. Super Atomic Clusters: Design Rules and Potential for Building Blocks of Materials. *Chem. Rev.* **2018**, *118*, 5755–5870.
- (6) Luo, X. M.; Li, Y. K.; Dong, X. Y.; Zang, S. Q. Platonic and Archimedean Solids in Discrete Metal-Containing Clusters. *Chem. Soc. Rev.* **2023**, *52*, 383–444.
- (7) Chen, T.; Lin, H.; Cao, Y.; Yao, Q.; Xie, J. Interactions of Metal Nanoclusters with Light: Fundamentals and Applications. *Adv. Mater.* **2022**, *34*, No. 2103918.
- (8) Kang, X.; Zhu, M. Tailoring the Photoluminescence of Atomically Precise Nanoclusters. *Chem. Soc. Rev.* **2019**, *48*, 2422–2457.
- (9) Luo, Z.; Castleman, A. W.; Khanna, S. N. Reactivity of Metal Clusters. *Chem. Rev.* **2016**, *116*, 14456–14492.
- (10) Han, Z.; Dong, X.; Luo, P.; Li, S.; Wang, Z.; Zang, S.; Mak, T. C. W. Ultrastable Atomically Precise Chiral Silver Clusters with More than 95% Quantum Efficiency. *Sci. Adv.* **2020**, *6*, No. eaay0107.
- (11) Yang, H.; Lei, J.; Wu, B.; Wang, Y.; Zhou, M.; Xia, A.; Zheng, L.; Zheng, N. Crystal Structure of a Luminescent Thiolated Ag Nanocluster with an Octahedral Ag₆⁴⁺ Core. *Chem. Commun.* **2013**, *49*, 300–302.
- (12) Cerretani, C.; Kanazawa, H.; Vosch, T.; Kondo, J. Crystal Structure of a NIR-Emitting DNA-Stabilized Ag₁₆ Nanocluster. *Angew. Chem., Int. Ed.* **2019**, *58*, 17153–17157.

- (13) Jana, A.; Unnikrishnan, P. M.; Poonia, A. K.; Roy, J.; Jash, M.; Paramasivam, G.; Machacek, J.; Adarsh, K. N. V. D.; Base, T.; Pradeep, T. Carboranethiol-Protected Propeller-Shaped Photoresponsive Silver Nanomolecule. *Inorg. Chem.* **2022**, *61*, 8593–8603.
- (14) Joshi, C. P.; Bootharaju, M. S.; Alhilaly, M. J.; Bakr, O. M. $[\text{Ag}_{25}(\text{SR})_{18}]^-$: The “Golden” Silver Nanoparticle. *J. Am. Chem. Soc.* **2015**, *137*, 11578–11581.
- (15) AbdulHalim, L. G.; Bootharaju, M. S.; Tang, Q.; Del Gobbo, S.; AbdulHalim, R. G.; Eddaoudi, M.; Jiang, D. E.; Bakr, O. M. $\text{Ag}_{29}(\text{BDT})_{12}(\text{TPP})_4$: A Tetravalent Nanocluster. *J. Am. Chem. Soc.* **2015**, *137*, 11970–11975.
- (16) Guan, Z. J.; Zeng, J. L.; Nan, Z. A.; Wan, X. K.; Lin, Y. M.; Wang, Q. M. Thiacalix[4]Arene: New Protection for Metal Nanoclusters. *Sci. Adv.* **2016**, *2*, No. e1600323.
- (17) Bodiuzzaman, M.; Ghosh, A.; Sugi, K. S.; Nag, A.; Khatun, E.; Varghese, B.; Paramasivam, G.; Antharjanam, S.; Natarajan, G.; Pradeep, T. Camouflaging Structural Diversity: Co-Crystallization of Two Different Nanoparticles Having Different Cores but the Same Shell. *Angew. Chem., Int. Ed.* **2019**, *58*, 189–194.
- (18) Yuan, S. F.; Xu, C. Q.; Liu, W. D.; Zhang, J. X.; Li, J.; Wang, Q. M. Rod-Shaped Silver Supercluster Unveiling Strong Electron Coupling between Substituent Icosahedral Units. *J. Am. Chem. Soc.* **2021**, *143*, 12261–12267.
- (19) Alhilaly, M. J.; Bootharaju, M. S.; Joshi, C. P.; Besong, T. M.; Emwas, A. H.; Juarez-Mosqueda, R.; Kaappa, S.; Malola, S.; Adil, K.; Shkurenko, A.; Häkkinen, H.; Eddaoudi, M.; Bakr, O. M. $[\text{Ag}_{67}(\text{SPhMe}_2)_{32}(\text{PPh}_3)_8]^{3+}$: Synthesis, Total Structure, and Optical Properties of a Large Box-Shaped Silver Nanocluster. *J. Am. Chem. Soc.* **2016**, *138*, 14727–14732.
- (20) Song, Y.; Lambright, K.; Zhou, M.; Kirschbaum, K.; Xiang, J.; Xia, A.; Zhu, M.; Jin, R. Large-Scale Synthesis, Crystal Structure, and Optical Properties of the $\text{Ag}_{146}\text{Br}_2(\text{SR})_{80}$ Nanocluster. *ACS Nano* **2018**, *12*, 9318–9325.
- (21) Yang, H.; Wang, Y.; Chen, X.; Zhao, X.; Gu, L.; Huang, H.; Yan, J.; Xu, C.; Li, G.; Wu, J.; Edwards, A. J.; Dittich, B.; Tang, Z.; Wang, D.; Zheng, N. Plasmonic Twinned Silver Nanoparticles with Molecular Precision. *Nat. Commun.* **2016**, *7*, 12809.
- (22) Liu, Y.; Chai, J.; Cai, X.; Chen, M.; Jin, R.; Ding, W.; Zhu, Y. Central Doping of a Foreign Atom into the Silver Cluster for Catalytic Conversion of CO_2 toward C–C Bond Formation. *Angew. Chem., Int. Ed.* **2018**, *57*, 9775–9779.
- (23) Pramanik, S.; Bhalla, V.; Kumar, M. Hexaphenylbenzene-Stabilized Luminescent Silver Nanoclusters: A Potential Catalytic System for the Cycloaddition of Terminal Alkynes with Isocyanides. *ACS Appl. Mater. Interfaces* **2015**, *7*, 22786–22795.
- (24) (a) Wu, Y.; Wang, D.; Li, Y. Nanocrystals from Solutions: Catalysts. *Chem. Soc. Rev.* **2014**, *43*, 2112–2124. (b) Jin, R.; Li, G.; Sharma, S.; Li, Y.; Du, X. Toward Active-Site Tailoring in Heterogeneous Catalysis by Atomically Precise Metal Nanoclusters with Crystallographic Structures. *Chem. Rev.* **2021**, *121*, 567–648.
- (25) Zhang, C.; Guo, Z.; Chen, G.; Zeng, G.; Yan, M.; Niu, Q.; Liu, L.; Zuo, Y.; Huang, Z.; Tan, Q. Green-Emitting Fluorescence Ag Clusters: Facile Synthesis and Sensors for Hg^{2+} Detection. *New J. Chem.* **2016**, *40*, 1175–1181.
- (26) Fan, C.; Lv, X.; Liu, F.; Feng, L.; Liu, M.; Cai, Y.; Liu, H.; Wang, J.; Yang, Y.; Wang, H. Silver Nanoclusters Encapsulated into Metal–Organic Frameworks with Enhanced Fluorescence and Specific Ion Accumulation toward the Microdot Array-Based Fluorimetric Analysis of Copper in Blood. *ACS Sens.* **2018**, *3*, 441–450.
- (27) Neacșu, V. A.; Cerretani, C.; Llisberg, M. B.; Swasey, S. M.; Gwinn, E. G.; Copp, S. M.; Vosch, T. Unusually Large Fluorescence Quantum Yield for a Near-Infrared Emitting DNA-Stabilized Silver Nanocluster. *Chem. Commun.* **2020**, *56*, 6384–6387.
- (28) Díez, I.; Pusa, M.; Kulmala, S.; Jiang, H.; Walther, A.; Goldmann, A. S.; Müller, A. H. E.; Ikkala, O.; Ras, R. H. A. Color Tunability and Electrochemiluminescence of Silver Nanoclusters. *Angew. Chem., Int. Ed. Engl.* **2009**, *48*, 2122–2125.
- (29) Chen, L.; Black, A.; Parak, W. J.; Klinke, C.; Chakraborty, I. Metal Nanocluster-based Devices: Challenges and Opportunities. *Aggregate* **2022**, *3*, No. e132.
- (30) Jash, M.; Methikkalam, R. R. J.; Bodiuzzaman, M.; Paramasivam, G.; Pradeep, T. Reaction between Ag_{17}^+ and Acetylene Outside the Mass Spectrometer: Dehydrogenation in the Gas Phase. *Chem. Commun.* **2020**, *56*, 15623–15626.
- (31) Liu, J. W.; Wang, Z.; Chai, Y. M.; Kurmoo, M.; Zhao, Q. Q.; Wang, X. P.; Tung, C. H.; Sun, D. Core Modulation of 70-Nuclei Core-Shell Silver Nanoclusters. *Angew. Chem., Int. Ed.* **2019**, *58*, 6276–6279.
- (32) Desireddy, A.; Conn, B. E.; Guo, J.; Yoon, B.; Barnett, R. N.; Monahan, B. M.; Kirschbaum, K.; Griffith, W. P.; Whetten, R. L.; Landman, U.; Bigioni, T. P. Ultrastable Silver Nanoparticles. *Nature* **2013**, *501*, 399–402.
- (33) Bootharaju, M. S.; Joshi, C. P.; Alhilaly, M. J.; Bakr, O. M. Switching a Nanocluster Core from Hollow to Nonhollow. *Chem. Mater.* **2016**, *28*, 3292–3297.
- (34) Jana, A.; Chakraborty, P.; Dar, W. A.; Chandra, S.; Khatun, E.; Kannan, M. P.; Ras, R. H. A.; Pradeep, T. Dual Emitting Ag_{35} Nanocluster Protected by 2-Pyrene Imine Thiol. *Chem. Commun.* **2020**, *56*, 12550–12553.
- (35) Chakraborty, I.; Kurashige, W.; Kanehira, K.; Gell, L.; Häkkinen, H.; Negishi, Y.; Pradeep, T. $\text{Ag}_{44}(\text{SeR})_{30}$: A Hollow Cage Silver Cluster with Selenolate Protection. *J. Phys. Chem. Lett.* **2013**, *4*, 3351–3355.
- (36) Bootharaju, M. S.; Dey, R.; Gevers, L. E.; Hedhili, M. N.; Basset, J. M.; Bakr, O. M. A New Class of Atomically Precise, Hydride-Rich Silver Nanoclusters Co-Protected by Phosphines. *J. Am. Chem. Soc.* **2016**, *138*, 13770–13773.
- (37) Liu, K. G.; Hu, M. L.; Jiang, D. E.; Gao, X. M.; Liu, T. All-Carboxylate-Protected Superautomic Silver Nanocluster with an Unprecedented Rhombohedral Ag_8 Core. *J. Am. Chem. Soc.* **2020**, *142*, 16905–16909.
- (38) Wang, Z.; Alkan, F.; Aikens, C. M.; Kurmoo, M.; Zhang, Z. Y.; Song, K. P.; Tung, C. H.; Sun, D. An Ultrastable 155-Nuclei Silver Nanocluster Protected by Thiacalix[4]Arene and Cyclohexanethiol for Photothermal Conversion. *Angew. Chem., Int. Ed.* **2022**, *61*, No. e202206742.
- (39) Zhang, M. M.; Dong, X. Y.; Wang, Z. Y.; Luo, X. M.; Huang, J. H.; Zang, S. Q.; Mak, T. C. W. Alkynyl-Stabilized Superautomic Silver Clusters Showing Circularly Polarized Luminescence. *J. Am. Chem. Soc.* **2021**, *143*, 6048–6053.
- (40) Lei, Z.; Wan, X.-K.; Yuan, S.-F.; Guan, Z.-J.; Wang, Q.-M. Alkynyl Approach toward the Protection of Metal Nanoclusters. *Acc. Chem. Res.* **2018**, *51*, 2465–2474.
- (41) Su, S. J.; Sasabe, H.; Pu, Y. J.; Nakayama, K. I.; Kido, J. Tuning Energy Levels of Electron-Transport Materials by Nitrogen Orientation for Electrophosphorescent Devices with an Ideal Operating Voltage. *Adv. Mater.* **2010**, *22*, 3311–3316.
- (42) Wang, W.; Hobza, P. Theoretical Study on the Complexes of Benzene with Isoelectronic Nitrogen-Containing Heterocycles. *ChemPhysChem* **2008**, *9*, 1003–1009.
- (43) Chandra, S.; Sciortino, A.; Das, S.; Ahmed, F.; Jana, A.; Roy, J.; Li, D.; Liljeström, V.; Jiang, H.; Johansson, L.-S.; Chen, X.; Nonappa, Cannas, M.; Pradeep, T.; Peng, B.; Ras, R. H. A.; Sun, Z.; Ikkala, O.; Mess, F. Gold Au(I)_6 Clusters with Ligand-Derived Atomic Steric Locking: Multifunctional Optoelectrical Properties and Quantum Coherence. *Adv. Opt. Mater.* **2023**, *11*, No. 2202649.
- (44) Wang, Z.; Su, H. F.; Tan, Y. Z.; Schein, S.; Lin, S. C.; Liu, W.; Wang, S. A.; Wang, W. G.; Tung, C. H.; Sun, D.; Zheng, L. S. Assembly of Silver Trigons into a Buckyball-like Ag_{180} Nanocage. *Proc. Natl. Acad. Sci. U. S. A.* **2017**, *114*, 12132–12137.
- (45) Li, Q.; Mosquera, M. A.; Jones, L. O.; Parakh, A.; Chai, J.; Jin, R.; Schatz, G. C.; Gu, X. W. Pressure-Induced Optical Transitions in Metal Nanoclusters. *ACS Nano* **2020**, *14*, 11888–11896.
- (46) Yuan, S. F.; Guan, Z. J.; Liu, W. D.; Wang, Q. M. Solvent-Triggered Reversible Interconversion of All-Nitrogen-Donor-Pro

tected Silver Nanoclusters and Their Responsive Optical Properties. *Nat. Commun.* **2019**, *10*, 4032.

(47) Chevrier, D. M.; Conn, B. E.; Li, B.; Jiang, D. E.; Bigioni, T. P.; Chatt, A.; Zhang, P. Interactions between Ultrastable $\text{Na}_4\text{Ag}_{44}(\text{SR})_{30}$ Nanoclusters and Coordinating Solvents: Uncovering the Atomic-Scale Mechanism. *ACS Nano* **2020**, *14*, 8433–8441.

(48) Hou, Y.; Wang, Y.; Xu, T.; Wang, Z.; Tian, W.; Sun, D.; Yu, X.; Xing, P.; Shen, J.; Xin, X.; Hao, J. Synergistic Multiple Bonds Induced Dynamic Self-Assembly of Silver Nanoclusters into Lamellar Frameworks with Tailored Luminescence. *Chem. Mater.* **2022**, *34*, 8013–8021.

(49) Wang, Z.; Zhu, Y. J.; Li, Y. Z.; Zhuang, G. L.; Song, K. P.; Gao, Z. Y.; Dou, J. M.; Kurmoo, M.; Tung, C. H.; Sun, D. Nuclearity Enlargement from $[\text{PW}_9\text{O}_{34}@\text{Ag}_{51}]$ to $[(\text{PW}_9\text{O}_{34})_2@\text{Ag}_{72}]$ and 2D and 3D Network Formation Driven by Bipyridines. *Nat. Commun.* **2022**, *13*, 1802.

(50) Li, B.; Huang, R. W.; Qin, J. H.; Zang, S. Q.; Gao, G. G.; Hou, H. W.; Mak, T. C. W. Thermochromic Luminescent Nest-Like Silver Thiolate Cluster. *Chem. –Eur. J.* **2014**, *20*, 12416–12420.

(51) Sun, Q.-Q.; Li, Q.; Li, H.-Y.; Zhang, M.-M.; Sun, M.-E.; Li, S.; Quan, Z.; Zang, S.-Q. Thermochromism and Piezochromism of an Atomically Precise High-Nuclearity Silver Sulfide Nanocluster. *Chem. Commun.* **2021**, *57*, 2372–2375.

(52) Zhang, S. S.; Alkan, F.; Su, H. F.; Aikens, C. M.; Tung, C. H.; Sun, D. An Atomically Precise Silver Nanocluster Co-Protected by Inorganic and Organic Ligands. *J. Am. Chem. Soc.* **2019**, *141*, 4460–4467.

(53) Su, Y. M.; Cao, Z. Z.; Feng, L.; Xue, Q. W.; Tung, C. H.; Gao, Z. Y.; Sun, D. Thermally Hypsochromic or Bathochromic Emissions? The Silver Nuclei Does Matter. *Small* **2022**, *18*, No. 2104524.

(54) Bootharaju, M. S.; Burlakov, V. M.; Besong, T. M. D.; Joshi, C. P.; Abdulhalim, L. G.; Black, D. M.; Whetten, R. L.; Goriely, A.; Bakr, O. M. Reversible Size Control of Silver Nanoclusters via Ligand-Exchange. *Chem. Mater.* **2015**, *27*, 4289–4297.

(55) Wei, X.; Chu, K.; Adsetts, J. R.; Li, H.; Kang, X.; Ding, Z.; Zhu, M. Nanocluster Transformation Induced by SbF_6^- Anions toward Boosting Photochemical Activities. *J. Am. Chem. Soc.* **2022**, *144*, 20421–20433.

(56) Dar, W. A.; Jana, A.; Sugi, K. S.; Paramasivam, G.; Bodiuzzaman, M.; Khatun, E.; Som, A.; Mahendranath, A.; Chakraborty, A.; Pradeep, T. Molecular Engineering of Atomically Precise Silver Clusters into 2D and 3D Framework Solids. *Chem. Mater.* **2022**, *34*, 4703–4711.

(57) Stamplecoskie, K. G.; Scaiano, J. C. Light Emitting Diode Irradiation Can Control the Morphology and Optical Properties of Silver Nanoparticles. *J. Am. Chem. Soc.* **2010**, *132*, 1825–1827.

(58) Callegari, A.; Tonti, D.; Chergui, M. Photochemically Grown Silver Nanoparticles with Wavelength-Controlled Size and Shape. *Nano Lett.* **2003**, *3*, 1565–1568.

(59) Lu, D.; Liu, Q.; Zhang, T.; Cai, Y.; Yin, Y.; Jiang, G. Stable Silver Isotope Fractionation in the Natural Transformation Process of Silver Nanoparticles. *Nat. Nanotechnol.* **2016**, *11*, 682–686.

(60) Raza, S.; Kakhodazadeh, S.; Christensen, T.; Di Vece, M.; Wubs, M.; Mortensen, N. A.; Stenger, N. Multipole Plasmons and Their Disappearance in Few-Nanometre Silver Nanoparticles. *Nat. Commun.* **2015**, *6*, 8788.

(61) Stamplecoskie, K. G.; Pacioni, N. L.; Larson, D.; Scaiano, J. C. Plasmon-Mediated Photopolymerization Maps Plasmon Fields for Silver Nanoparticles. *J. Am. Chem. Soc.* **2011**, *133*, 9160–9163.

(62) Stefancu, A.; Gargiulo, J.; Laufersky, G.; Auguié, B.; Chiş, V.; Le Ru, E. C.; Liu, M.; Leopold, N.; Cortés, E. Interface-Dependent Selectivity in Plasmon-Driven Chemical Reactions. *ACS Nano* **2023**, *17*, 3119–3127.

(63) Naoi, K.; Ohko, Y.; Tatsuma, T. TiO_2 Films Loaded with Silver Nanoparticles: Control of Multicolor Photochromic Behavior. *J. Am. Chem. Soc.* **2004**, *126*, 3664–3668.

(64) Li, W.; Guo, Y.; Zhang, P. SERS-Active Silver Nanoparticles Prepared by a Simple and Green Method. *J. Phys. Chem. C* **2010**, *114*, 6413–6417.

(65) Tang, L.; Kang, X.; Wang, S.; Zhu, M. Light-Induced Size-Growth of Atomically Precise Nanoclusters. *Langmuir* **2019**, *35*, 12350–12355.

(66) Jana, A.; Jash, M.; Poonia, A. K.; Paramasivam, G.; Islam, M. R.; Chakraborty, P.; Antharjanam, S.; Machacek, J.; Ghosh, S.; Adarsh, K. N. V. D.; Base, T.; Pradeep, T. Light-Activated Intercluster Conversion of an Atomically Precise Silver Nanocluster. *ACS Nano* **2021**, *15*, 15781–15793.

(67) Walter, M.; Akola, J.; Lopez-Acevedo, O.; Jadzinsky, P. D.; Calero, G.; Ackerson, C. J.; Whetten, R. L.; Grönbeck, H.; Häkkinen, H. A Unified View of Ligand-Protected Gold Clusters as Superatom Complexes. *Proc. Natl. Acad. Sci. U. S. A.* **2008**, *105*, 9157–9162.

(68) Weerawardene, K. L. D. M.; Häkkinen, H.; Aikens, C. M. Connections between Theory and Experiment for Gold and Silver Nanoclusters. *Annu. Rev. Phys. Chem.* **2018**, *69*, 205–229.

(69) Liang, T.; Ren, L. U. Some Studies Concerning Rotating Axes and Polyatomic Molecules. *Phys. Rev.* **1935**, *47*, 552.

(70) Zhou, H.; Park, J. H.; Fan, F. R. F.; Bard, A. J. Observation of Single Metal Nanoparticle Collisions by Open Circuit (Mixed) Potential Changes at an Ultramicroelectrode. *J. Am. Chem. Soc.* **2012**, *134*, 13212–13215.

(71) Xiao, Y.; Fan, F. R. F.; Zhou, J.; Bard, A. J. Current Transients in Single Nanoparticle Collision Events. *J. Am. Chem. Soc.* **2008**, *130*, 16669–16677.

(72) Xiao, X.; Bard, A. J. Observing Single Nanoparticle Collisions at an Ultramicroelectrode by Electrocatalytic Amplification. *J. Am. Chem. Soc.* **2007**, *129*, 9610–9612.

(73) Zhou, H.; Fan, F. R. F.; Bard, A. J. Observation of Discrete Au Nanoparticle Collisions by Electrocatalytic Amplification Using Pt Ultramicroelectrode Surface Modification. *J. Phys. Chem. Lett.* **2010**, *1*, 2671–2674.

(74) Al-Zubeidi, A.; Ostovar, B.; Carlin, C. C.; Li, B. C.; Lee, S. A.; Chiang, W.-Y.; Gross, N.; Dutta, S.; Misiura, A.; Searles, E. K.; Chakraborty, A.; Roberts, S. T.; Dionne, J. A.; Rossky, P. J.; Landes, C. F.; Link, S. Mechanism for Plasmon-Generated Solvated Electrons. *Proc. Natl. Acad. Sci. U. S. A.* **2023**, *120*, No. e2217035120.

(75) Nakanishi, H.; Bishop, K. J. M.; Kowalczyk, B.; Nitzan, A.; Weiss, E. A.; Tretiakov, K. V.; Apodaca, M. M.; Klajn, R.; Stoddart, J. F.; Grzybowski, B. A. Photoconductance and Inverse Photoconductance in Films of Functionalized Metal Nanoparticles. *Nature* **2009**, *460*, 371–375.

(76) Bernardi, M.; Mustafa, J.; Neaton, J. B.; Louie, S. G. Theory and Computation of Hot Carriers Generated by Surface Plasmon Polaritons in Noble Metals. *Nat. Commun.* **2015**, *6*, 7044.

(77) Higaki, T.; Liu, C.; Zhou, M.; Luo, T. Y.; Rosi, N. L.; Jin, R. Tailoring the Structure of 58-Electron Gold Nanoclusters: $\text{Au}_{103}\text{S}_2(\text{S-Nap})_{41}$ and Its Implications. *J. Am. Chem. Soc.* **2017**, *139*, 9994–10001.

(78) Zhou, M.; Jin, R.; Sfeir, M. Y.; Chen, Y.; Song, Y.; Jin, R. Electron Localization in Rod-Shaped Triicosahedral Gold Nanocluster. *Proc. Natl. Acad. Sci. U. S. A.* **2017**, *114*, E4697–E4705.

(79) Li, Q.; Zhou, M.; So, W. Y.; Huang, J.; Li, M.; Kauffman, D. R.; Cotlet, M.; Higaki, T.; Peteanu, L. A.; Shao, Z.; Jin, R. A Monocuboctahedral Series of Gold Nanoclusters: Photoluminescence Origin, Large Enhancement, Wide Tunability, and Structure-Property Correlation. *J. Am. Chem. Soc.* **2019**, *141*, 5314–5325.

Supporting Information

Photoconversion of Ag₃₁ to Ag₄₂ Initiated by Solvated Electrons

Arijit Jana^a, Wakeel Ahmed Dar^a, Sourav Kanti Jana^a, Ajay Kumar Poonia^b, Vivek Yadav^a, Jayoti Roy^a, Sourov Chandra^c, Kumaran Nair Valsala Devi Adarsh^{b*}, Robin H. A. Ras^{c*}, Thalappil Pradeep^{a*}

^a DST Unit of Nanoscience (DST UNS) and Thematic Unit of Excellence (TUE), Department of Chemistry, Indian Institute of Technology Madras, Chennai – 600036, India

^b Department of Physics, Indian Institute of Science Education and Research Bhopal, Bhopal – 462066, India

^c Department of Applied Physics, Aalto University, School of Science, Puumiehenkuja 2, 02150, Espoo, Finland

Table of contents

Items	Descriptions	Page No
1	Instrumentation	3-5
Figure S1	Time-dependent UV-vis absorption spectra show the formation of Ag ₃₁ cluster during the progression of TPP-assisted metal-thiolate reduction reaction	6
Figure S2	UV-vis absorption spectra of the product formed without TPP	6
Figure S3	Nearly identical UV-vis absorption spectra show a five-fold scale-up of the synthesis of Ag ₃₁ using TPP-assisted metal thiolate reduction reaction	7
Figure S4	The positive ion mode ESI-MS spectrum of the as prepared Ag ₃₁ shows no prominent peaks in the spectrum	7
Figure S5	Negative ion mode ESI-MS spectrum of Ag ₃₁ nanocluster after the addition of cesium acetate	8
Figure S6	The expanded view of the higher mass range in the MS/MS spectrum of Ag ₃₁ at CE 60 along with the composition of the fragments	8
Figure S7	The expanded view of the lower mass range in the MS/MS spectrum of Ag ₃₁ at CE 60 along with the composition of the fragments	9
Figure S8	Full range ¹ H NMR spectrum of Ag ₃₁ in comparison to TRZ-H ₂ ligand	9
Figure S9	An expanded ¹ H NMR spectrum of Ag ₃₁ in comparison to TRZ-H ₂ ligand	10
Figure S10	FT-IR spectrum of Ag ₃₁ along with TRZ-H ₂ ligand	11
Figure S11	XPS spectrum of Ag ₃₁ shows the presence of respective elements	12
Figure S12	Powder X-ray diffraction spectrum of Ag ₃₁ powder	12
Figure S13	UV-vis absorption spectra with identical absorption features indicate the stability of Ag ₃₁ nanocluster in CHCl ₃ solution	13
Figure S14	Mass spectra of light-triggered products in a) DCM and b) chloroform solvent in negative ion mode	13
Figure S15	Expanded view of the lower range collision energy-dependent fragmentation spectra of Ag ₄₂	14

Figure S16	a) UV-vis absorption spectra shows the light-triggered interconversion of Ag ₃₁ dissolved in chloroform. b) ESI-MS data of the light-triggered product shows the formation of Ag ₄₂ nanocluster as a predominant end product	14
Figure S17	Time dependent UV-vis absorption spectra of Ag ₄₂ with identical spectral feature in a) DCM and b) chloroform, which demonstrated its stability	15
Figure S18	a) XPS survey scan of Ag ₄₂ indicating the presence of all the elements. Selected area spectral fittings of b) Ag 3d, c) S 2p, d) C 1s and e) N 1s regions	15
Figure S19	Comparative FT-IR spectra of Ag ₄₂ cluster and TRZ-H ₂ ligand	16
Figure S20	TEM micrograph of Ag ₄₂ cluster	16
Figure S21	Lamp power dependent conversion of Ag ₃₁ to Ag ₄₂ in its DCM solution at a fixed concentration	17
Figure S22	Concentration-dependent conversion of Ag ₃₁ to Ag ₄₂ in its DCM solution at a fixed lamp power	17
Figure S23	UV-vis absorption spectra of Ag ₃₁ after light irradiation in solid state	18
Figure S24	Open circuit potential (OCP) measurement of 0.2 M TBAF solution in dark and light illumination using Pt wire as a working electrode and Ag/AgCl as reference electrode	18
Figure S25	Open circuit potential (OCP) measurements of Ag ₃₁ at different concentrations	19
Figure S26	Cyclic voltammograms of a) Ag ₃₁ , b) Ag ₄₂ clusters before and after light irradiation (lamp power 140 W) in 0.2 M TBAF solution in DCM	19
Figure S27	Chronoamperometric photocurrent response of a bare ITO electrode under electrochemical conditions (electrolyte used 0.5 M aqueous Na ₂ SO ₄)	20
Figure S28	Comparative PL emission spectra of Ag ₄₂ by 480 nm excitation in DCM solution as well as in the solid state	20
Figure S29	Comparative UV-vis absorption spectra of Ag ₄₂ in DCM solution before and after oxygen bubbling	21
Figure S30	Early time scale temporal spectral profiles with associated fittings for Ag ₃₁ nanocluster	21
	References	22

Instrumentation

UV-vis absorption spectroscopy: UV-vis absorption spectra were measured in transmission mode using Perkin Elmer Lambda 365 UV-vis spectrometer using a bandpass filter of 1 nm.

Photoluminescence spectroscopy: Photoluminescence spectra were measured using a Jobin Yvon Nanolog fluorescence spectrometer using a slit width of 3 nm and a resolution bandwidth of 5 nm. The Nanolog instrument has a 450 W xenon-arc lamp source, double monochromator with kinetic gratings, associated reflective optics, and CCD detector. Samples were dissolved in DCM (~3 ml) was placed in a 1 cm quartz cuvette to measure the spectrum.

Scanning transmission electron microscopy: STEM images of Ag₃₁ nanocluster were captured using a double Cs-corrected JEM-2200FS transmission electron microscope. The measurement was performed at an accelerating voltage of 200 kV. The sample was prepared by drop-casting Ag₃₁ cluster in DCM over the ultrathin carbon-coated copper grid.

Transmission electron microscopy: TEM imaging of Ag₄₂ nanocluster was performed using a JEOL 3010 high resolution transmission electron microscope operated at 200 kV. A Gatan multistage CCD camera was used to record the micrograph.

Mass spectrometry: Mass spectra of all the clusters were measured using Waters Synapt G2Si HDMS instrument. The instrument is equipped with an electrospray ionization source, mass-selected ion trap, ion mobility cells, and time of flight mass analyzer. An optimized operating conditions such as flow rate 15-20 μ L/min, capillary voltage 2-3 kV, cone voltage 20 V, source offset 10 V, desolvation gas flow 400 L/min and source temperature 80-100 $^{\circ}$ C were used for the measurements. Collision-induced dissociation (CID) studies were performed upon colliding the selected molecular ion with argon gas inside the trap cell of the instrument. Gradually increasing the collision energy (CE 0 to 70 for Ag₃₁ and CE 0 to 150 for Ag₄₂) leads to the fragmentation of the species. All the measurements used low concentrations (~ 1 μ g/ml) of cluster samples.

Infrared spectroscopy: FT-IR spectra were measured using a JASCO-4100 FT-IR spectrometer after preparing potassium bromide (KBr) pellets of the respective samples.

X-ray photoelectron spectroscopy: XPS data were measured using an ESCA probe TPD equipped with a polychromatic Mg K α X-ray source ($h\nu$ = 1253.6 eV). The binding energy of the spectral regions of different elements was calibrated with respect to C 1s (285.0 eV).

NMR spectroscopy: NMR spectra were measured using a Bruker 500 MHz NMR instrument. Samples were dissolved in CDCl_3 to record the spectrum. Data were analyzed using MestRe-Nova software.

Powder X-ray diffraction: Powder X-ray diffraction was measured by a D8 Advance Bruker instrument using $\text{Cu K}\alpha$ as the X-ray source ($h\nu = 8047.8 \text{ eV}$).

Thermogravimetric analysis: Thermogravimetric measurements were performed using NETZSCH STA 449 F3 Jupiter TGA instrument equipped with Proteus-6.1.0 software. 4.82 mg Ag_{31} powder was used for the measurement. The study was performed in a temperature range of 30 to 800 °C under an argon atmosphere (gas flow rate 20 mL/min) with a heating rate of 10 °C/min.

For Ag_{31} cluster, TG measurement shows no significant mass losses upto 200 °C (shown in Figure 2c). Further heating leads to 27 % mass loss at 280 °C due to the detachments of six TRZ ligands and 46 % loss at 326 °C due to the dissociation of $[\text{Ag}_{11}\text{S}(\text{TRZ})_2]$ fragment.

Electrochemical studies: The electrochemical behavior of the light-triggered conversion process of Ag_{31} cluster in DCM solution was studied using a CHI-600A potentiostat. 0.2 M tetrabutylammonium hexafluorophosphate (TBAF) solution was used as an electrolyte throughout the experiments. We have performed these experiments in a two-electrode setup, where a clean Pt wire (diameter 2 mm) acts as a working electrode and Ag/AgCl is used as a reference electrode. All the experiments were performed at room temperature (22 °C). Electrochemical photocurrent measurements in the solid state were performed in a three-electrode setup using a Bio-Logic SP-200 potentiostat. 3 mg cluster dissolved in 1 ml DCM was drop cast on a clean ITO glass slide (an active surface area of 1 cm^2) to prepare the working electrode. A platinum electrode (diameter 2 mm) was used as a counter electrode, and Ag/AgCl electrode acted as a reference electrode. 0.01 M Na_2SO_4 in water was used as an electrolytic solution for the photocurrent measurements. A white light source (xenon arc lamp) from Newport, India, was used as a white light source throughout the experiments.

TCSPC measurement: Time-resolved photoluminescence lifetime measurements were performed using a HORIBA Delta flex TCSPC spectrometer. The instrument was coupled with a ps pulse diode laser (pulse width of 85 ps) with an excitation wavelength centered at 405 nm. A HORIBA PPD-850 detector was used to record the decay profile.

Femtosecond transient absorption studies: The femtosecond TA measurements were performed using an ultrafast short laser pulse (pulse width 120 fs) centered at 800 nm. The pulse was generated by spectra physics Maitai oscillator with a few hundred nJ energy. The output beam was sent to Ti: sapphire optical amplifier to produce high energy pulses (pulse energy 4 mJ, width 120 fs, repetition rate 1 kHz). The output beam is further split into two parts: the first high-energy beam produces the second harmonic using β -barium borate crystal. The obtained 400 nm pulses are used to excite the sample with an intensity of 250 $\mu\text{J}/\text{cm}^2$. The second part of the beam was used to generate the white light continuum probe pulses (450-800 nm) by CaF_2 crystal. The computer-controlled motion controller creates the delay between pump and probe pulses. The absorbance changes in the probe beam are due to the pump being calculated using the equation-

$$\Delta A = \log [I_{ex}(s)/I_0(s)] - [I_{ex}(r)/I_0(r)]$$

Where, r and s correspond to the reference and sample, I_{ex} and I_0 are transmitted intensities of probe pulse after excitation and in the ground state, respectively. The intensity of the transmitted pulse is measured with the help of MS 2004.

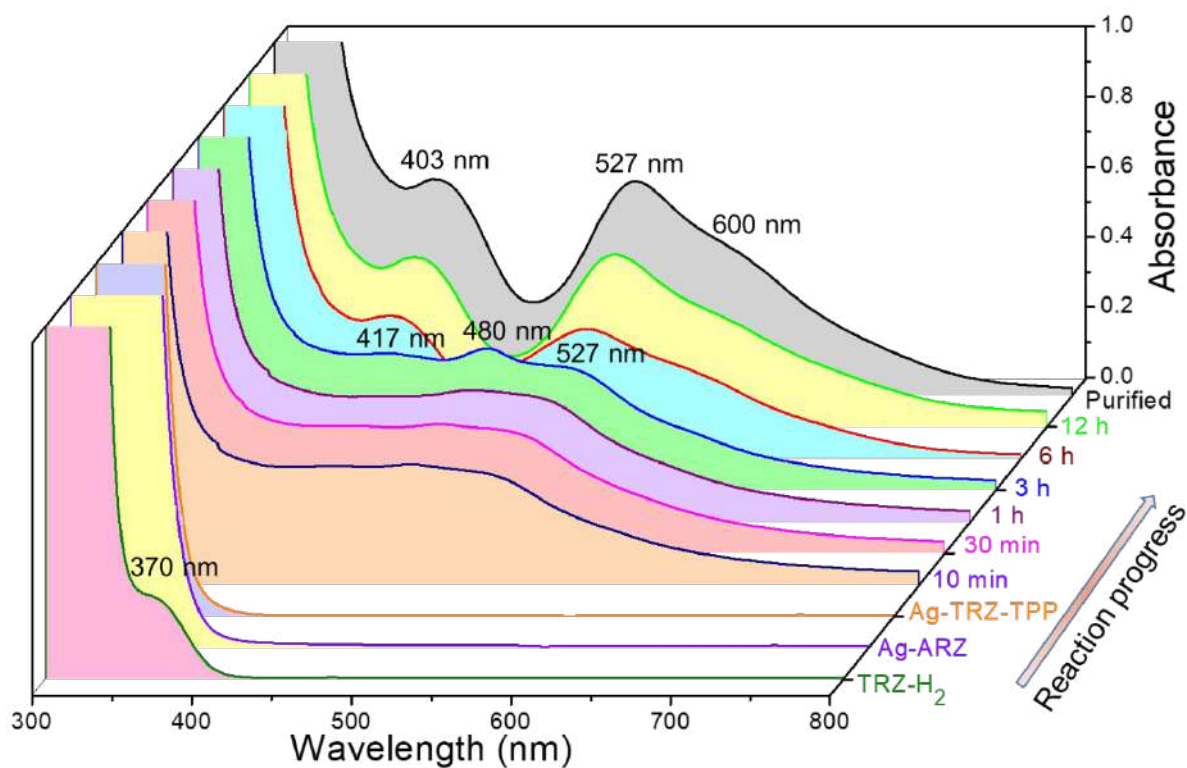


Figure S1. Time-dependent UV-vis absorption spectra show the formation of Ag_{31} cluster during the progression of TPP-assisted metal-thiolate reduction reaction.

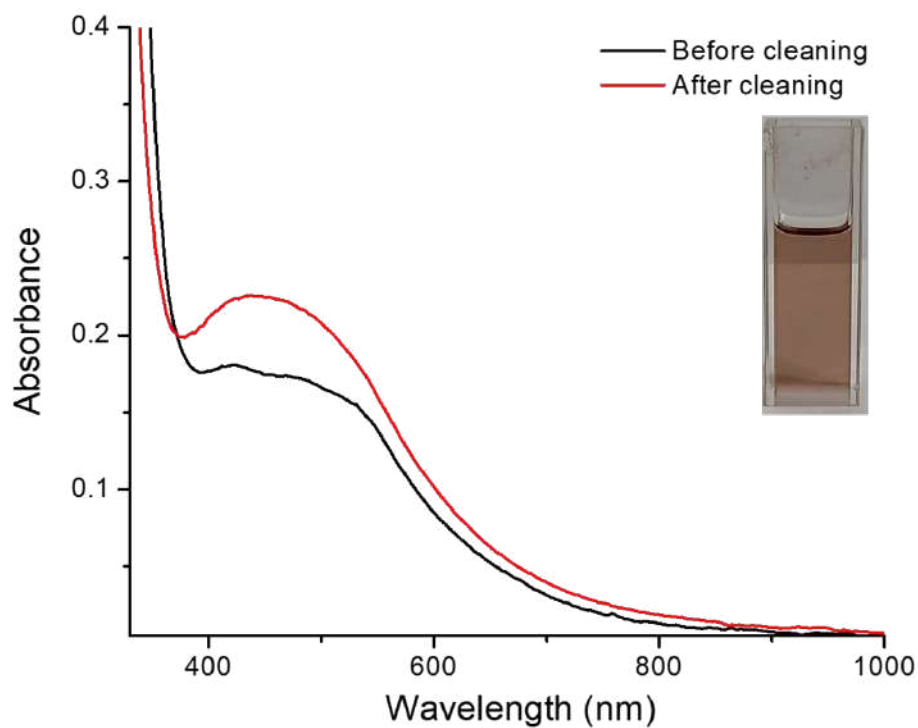


Figure S2. UV-vis absorption spectra of the product formed without TPP. All other precursors and reaction conditions are similar for the synthesis. Inset shows a photograph of the product in DCM.

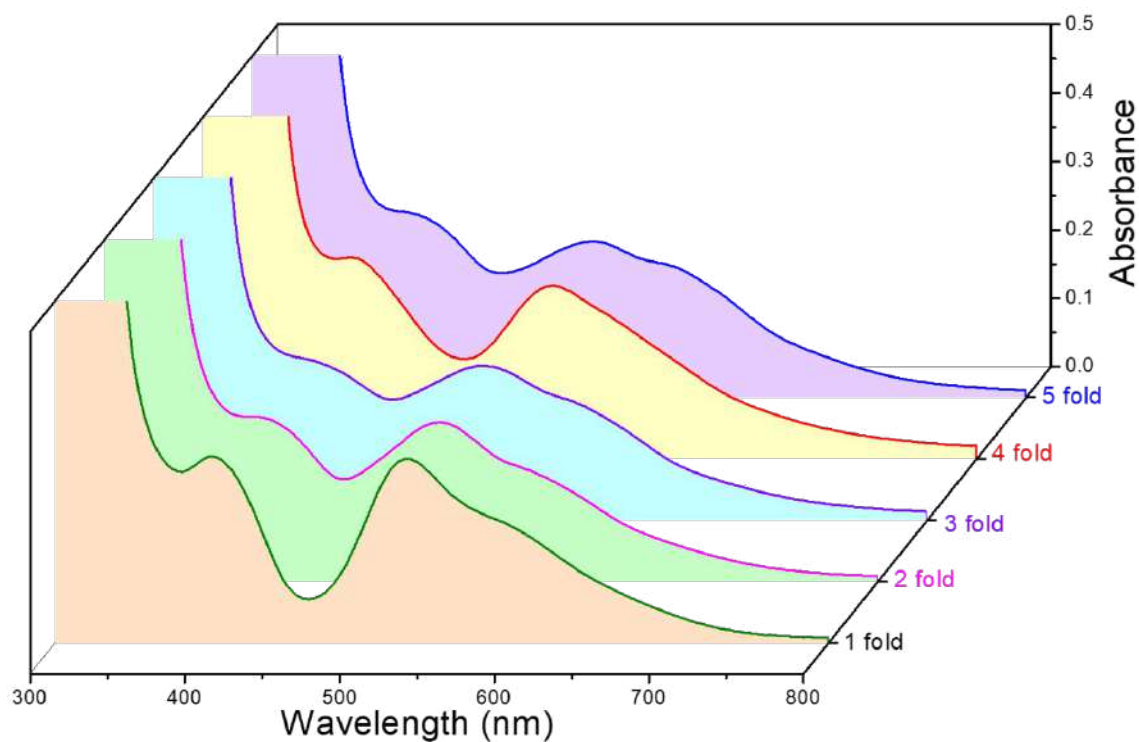


Figure S3. Nearly identical UV-vis absorption spectra show a five-fold scale-up of the synthesis of Ag_{31} using TPP-assisted metal thiolate reduction reaction.

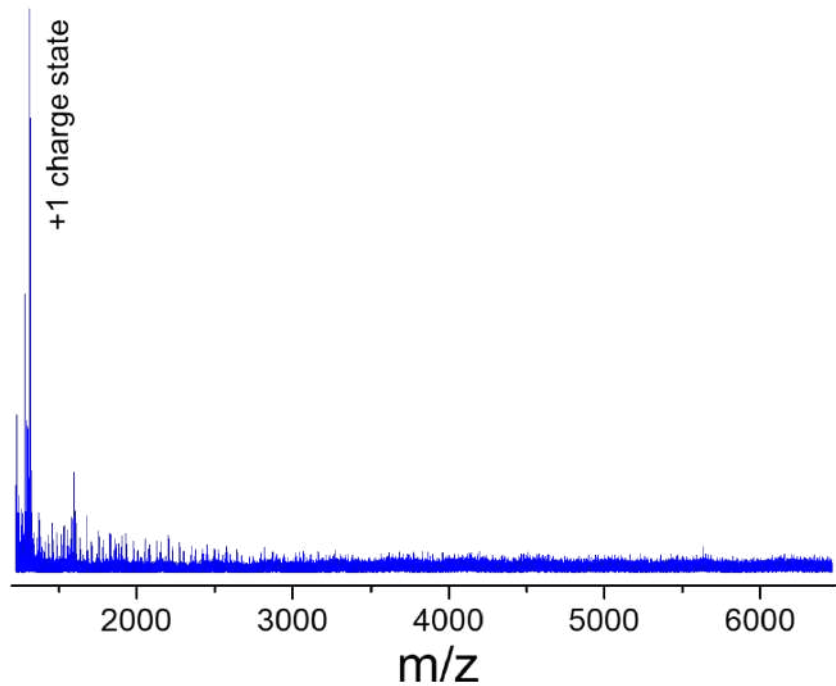


Figure S4. The positive ion mode ESI-MS spectrum of the as prepared Ag_{31} shows no prominent peaks in the spectrum.

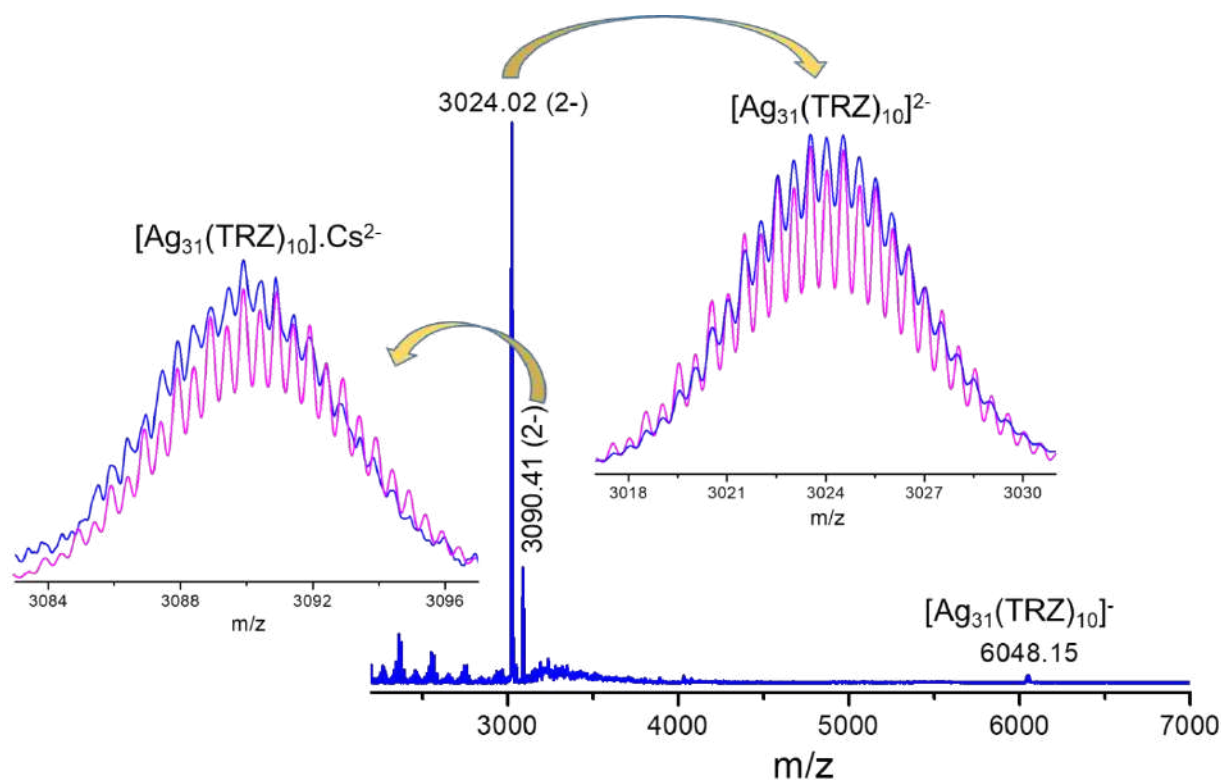


Figure S5. Negative ion mode ESI-MS spectrum of Ag_{31} nanocluster after the addition of cesium acetate. The inset depicts a comparison of the isotopic distribution of the experimental and theoretical spectra.

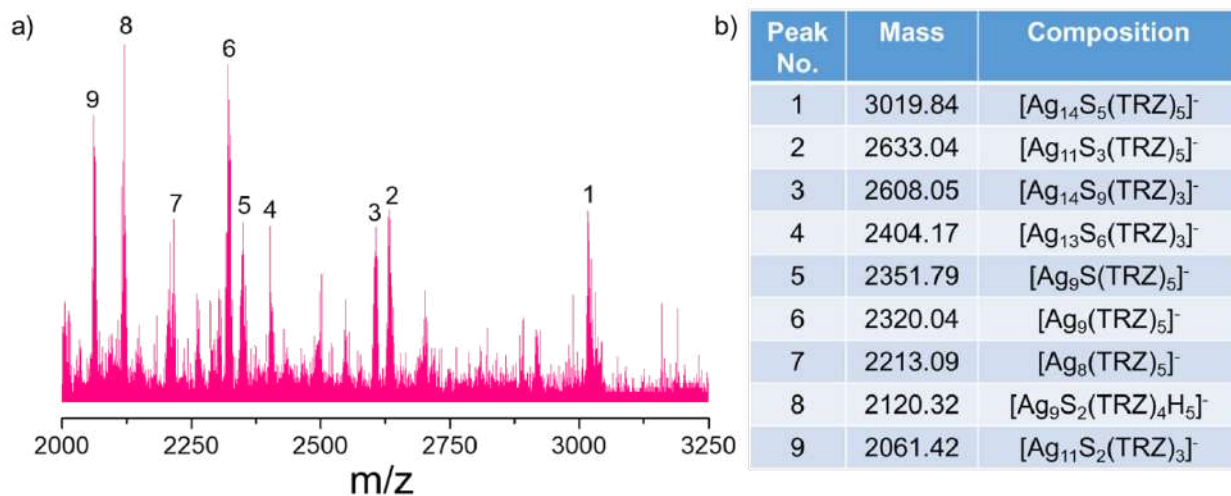


Figure S6. a) Expanded view of the higher mass range in the MS/MS spectrum of Ag_{31} at CE 60. b) Analysis of the molecular composition of the fragments.

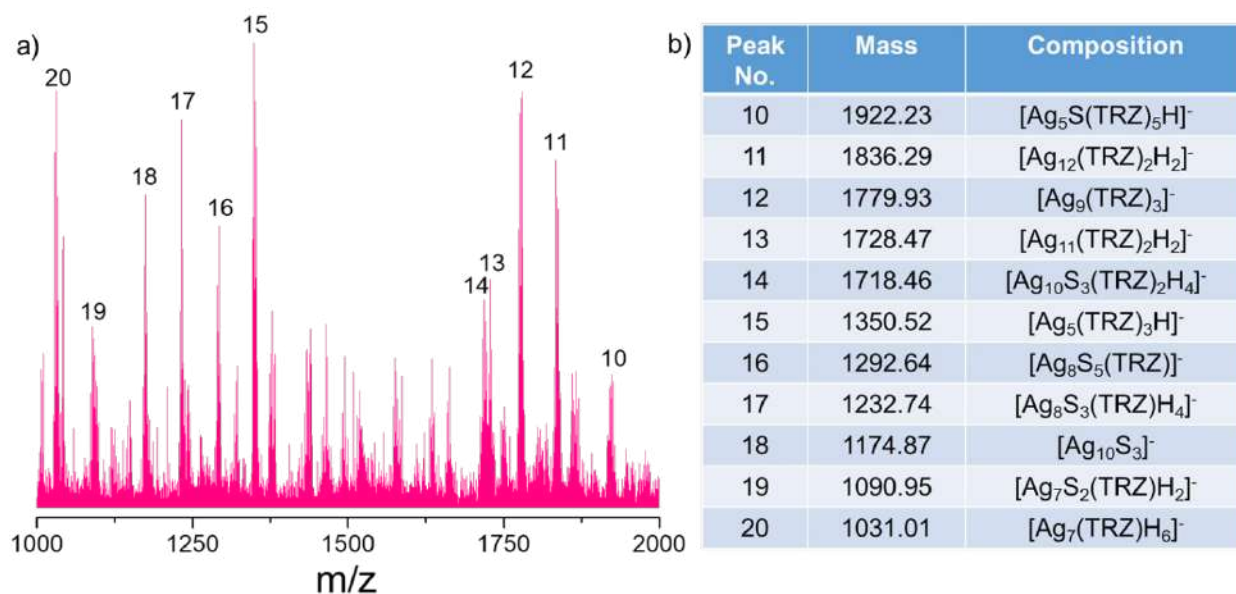


Figure S7. a) Expanded view of the lower mass range in the MS/MS spectrum of Ag_{31} at CE 60. b) Analysis of the molecular composition of the fragments.

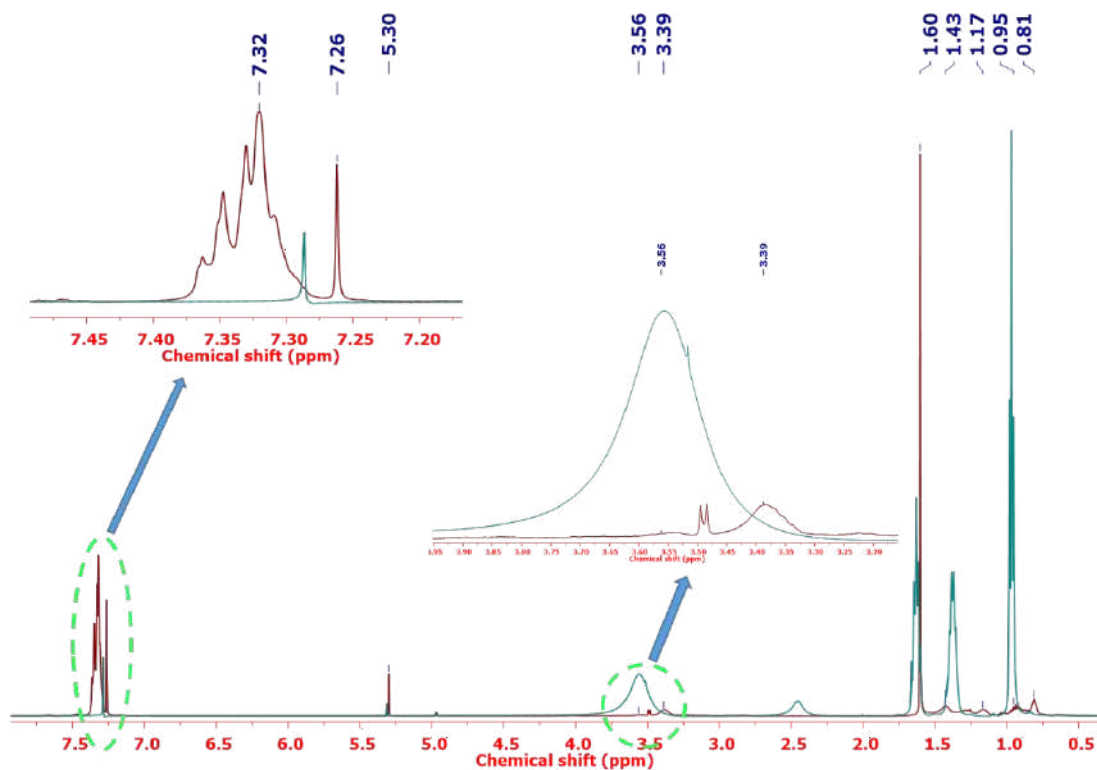


Figure S8. Full range ^1H NMR spectrum of Ag_{31} in comparison to TRZ-H_2 ligand. The trace impurity peak at 7.32 (m), 7.26 (s), 5.30 (s) ppm are due to TPP, CHCl_3 and dichloromethane, respectively. Color code: orange = Ag_{31} cluster, blue = TRZ-H_2 ligand.

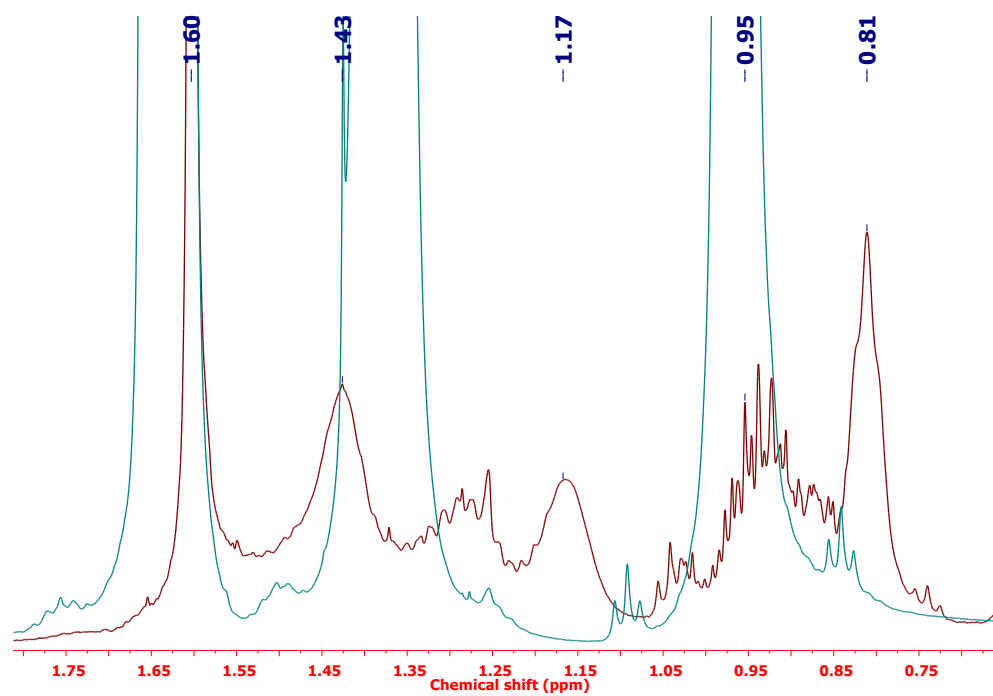


Figure S9. An expanded (0.5-1.75 ppm) ^1H NMR spectrum of Ag_{31} in comparison to TRZ- H_2 ligand. Color code: orange = Ag_{31} , blue = TRZ- H_2 ligand.

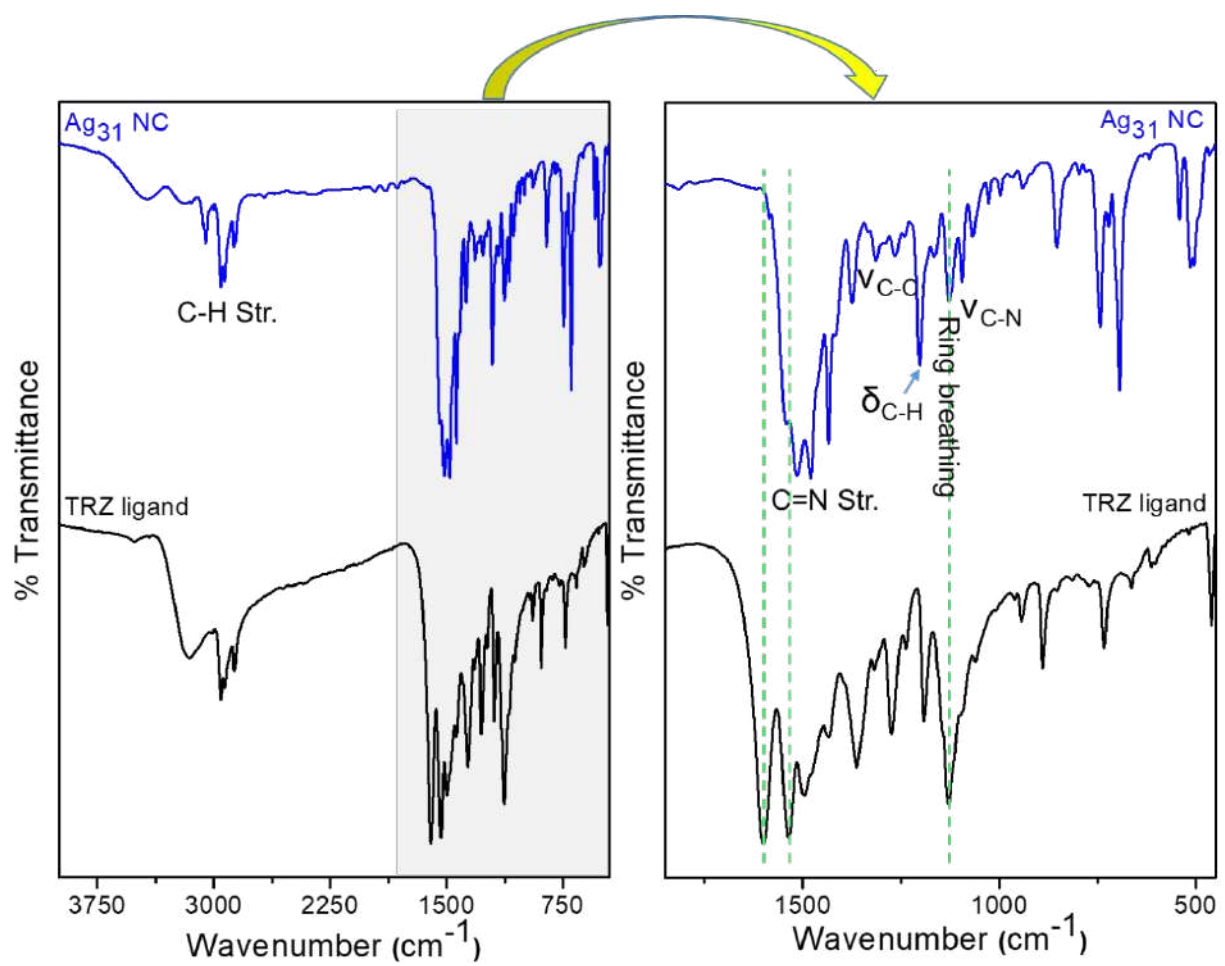


Figure S10. FT-IR spectra of Ag_{31} along with TRZ- H_2 ligand. Peaks of interest are marked.

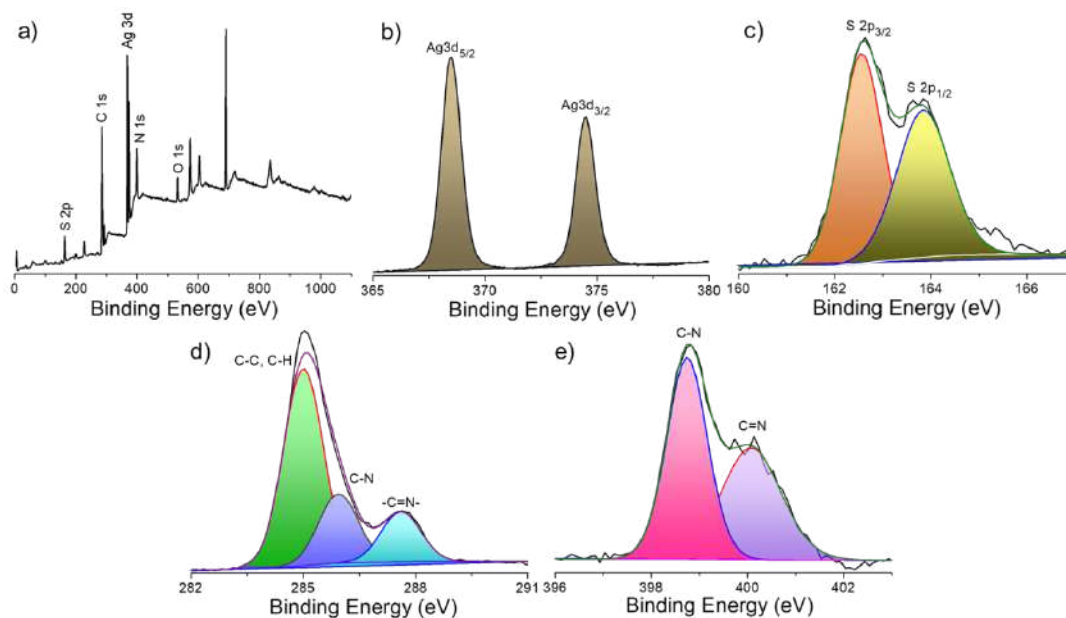


Figure S11. a) XPS survey spectrum of Ag_{31} shows the presence of expected elements. b-e) Selected area scans showed the respective elements. The binding energies of $\text{Ag } 3d_{5/2}$ and $3d_{3/2}$ are 368.5 and 374.4 eV, respectively, indicative of metal-like $\text{Ag}(0)$ states.^{1,2} Spectral fittings of the C 1s region shows three binding energies at 285.0, 285.9, and 287.5 eV due to C-C, C-N, and C=N regions, respectively. We have also observed two fitted regions of N 1s at 398.7 and 400.0 eV for C-N and C=N bonding, respectively.³

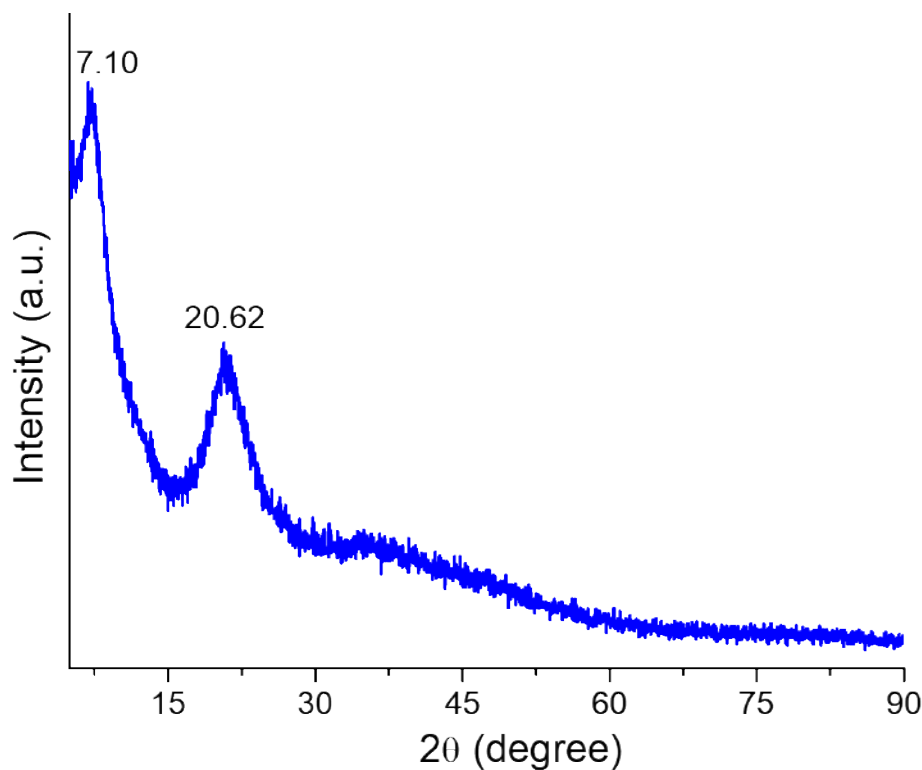


Figure S12. Powder X-ray diffraction spectrum of Ag_{31} shows weak diffraction peaks due to the lack of crystallinity.

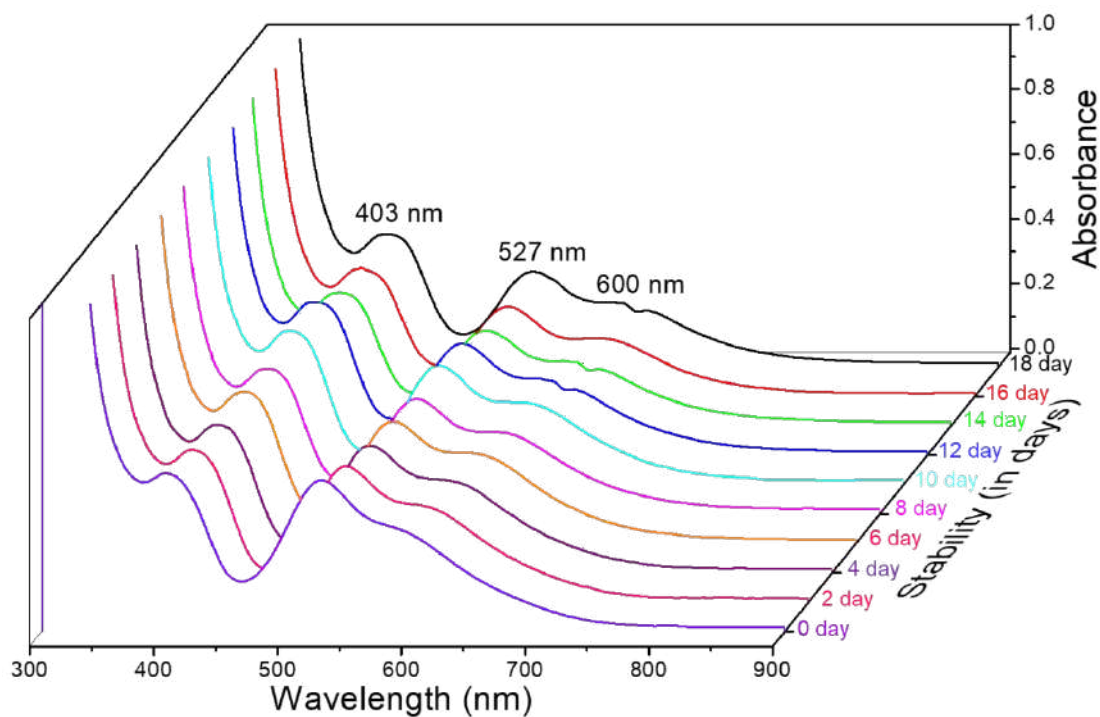


Figure S13. UV-vis absorption spectra with identical absorption features indicate the stability of Ag_{31} in CHCl_3 solution.

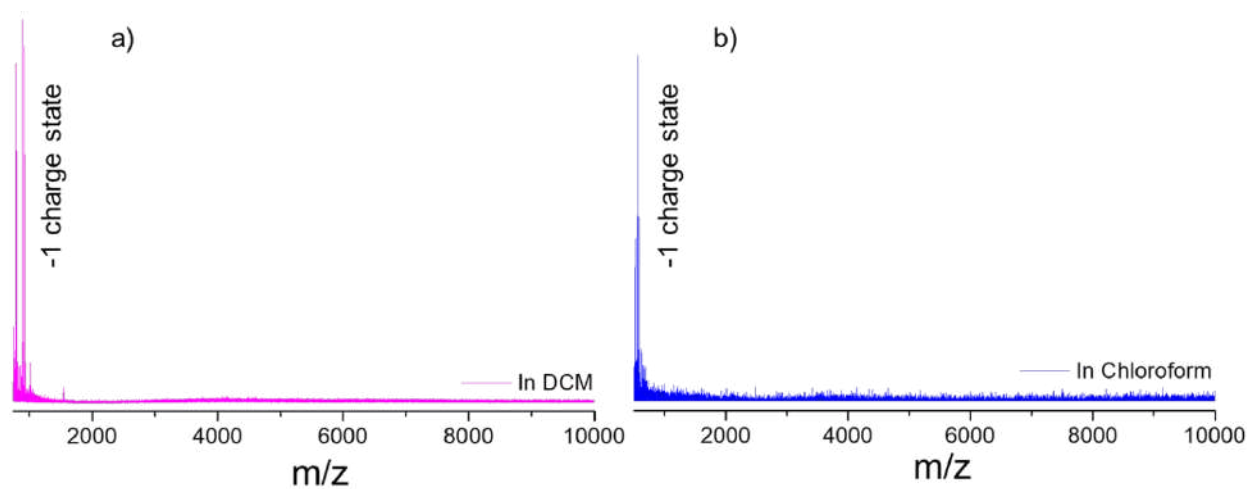


Figure S14. Mass spectra of light-triggered products in a) DCM and b) chloroform solvent in negative ion mode. Features of Ag_{31} and other clusters were not observed. Mononegative charge state peaks are due to complexes.

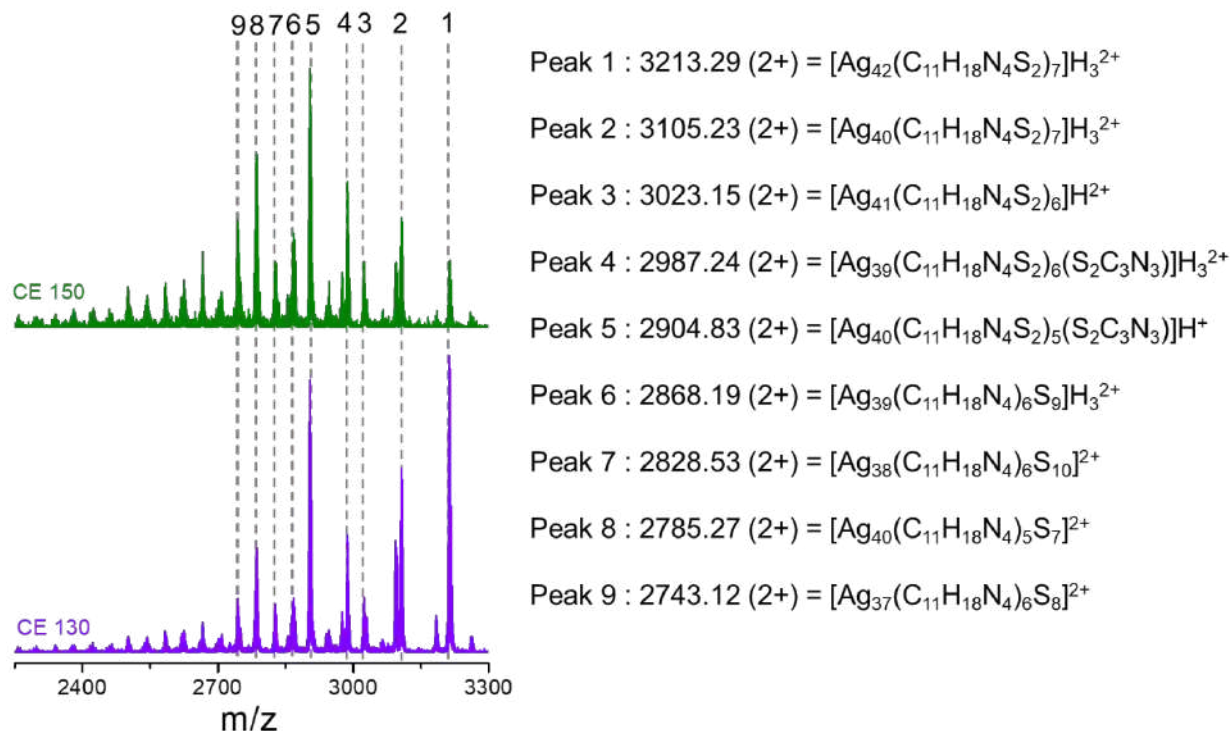


Figure S15. Expanded views of the lower range collision energy-dependent fragmentation spectra of Ag_{42} . Molecular composition of the respective ion peaks are shown here.

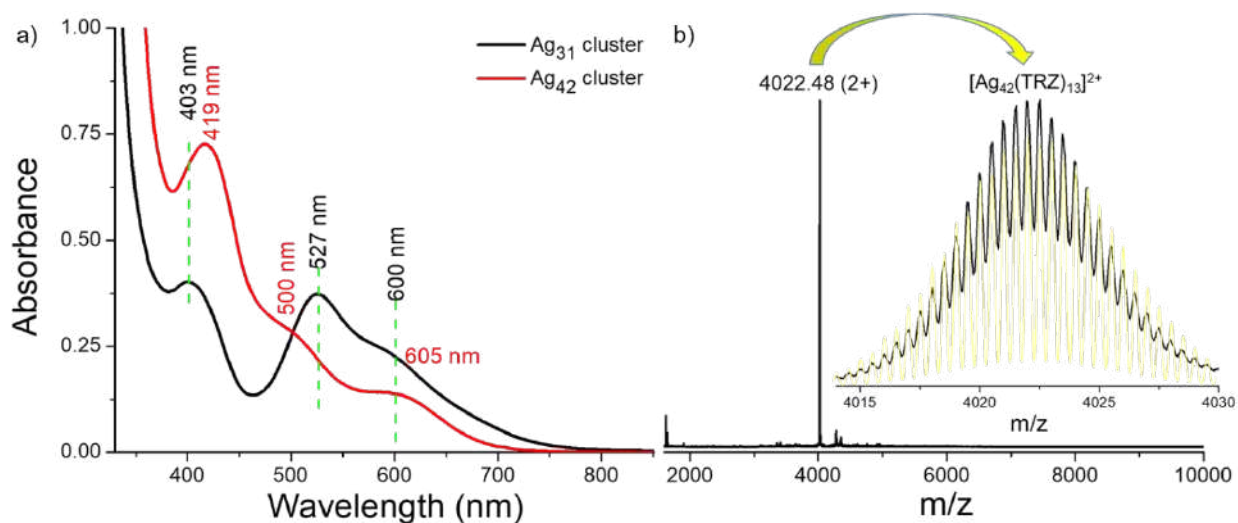


Figure S16. a) UV-vis absorption spectra shows the light-triggered interconversion of Ag_{31} dissolved in chloroform. b) ESI-MS data of the light-triggered product shows the formation of Ag_{42} nanocluster as a predominant end product. Inset shows the matching of the experimental (black) and theoretical (yellow) spectrum.

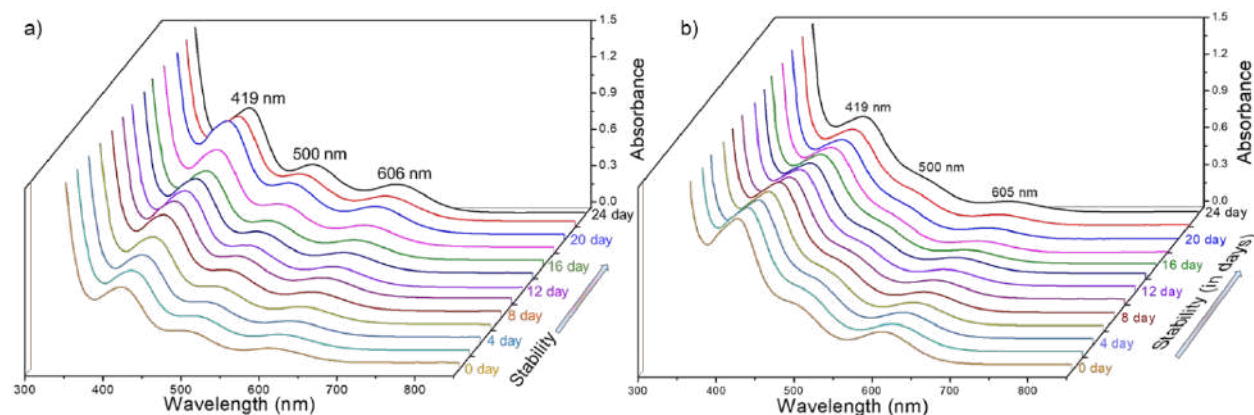


Figure S17. Time dependent UV-vis absorption spectra of Ag_{42} with identical spectral feature in a) DCM and b) chloroform, which demonstrated its stability.

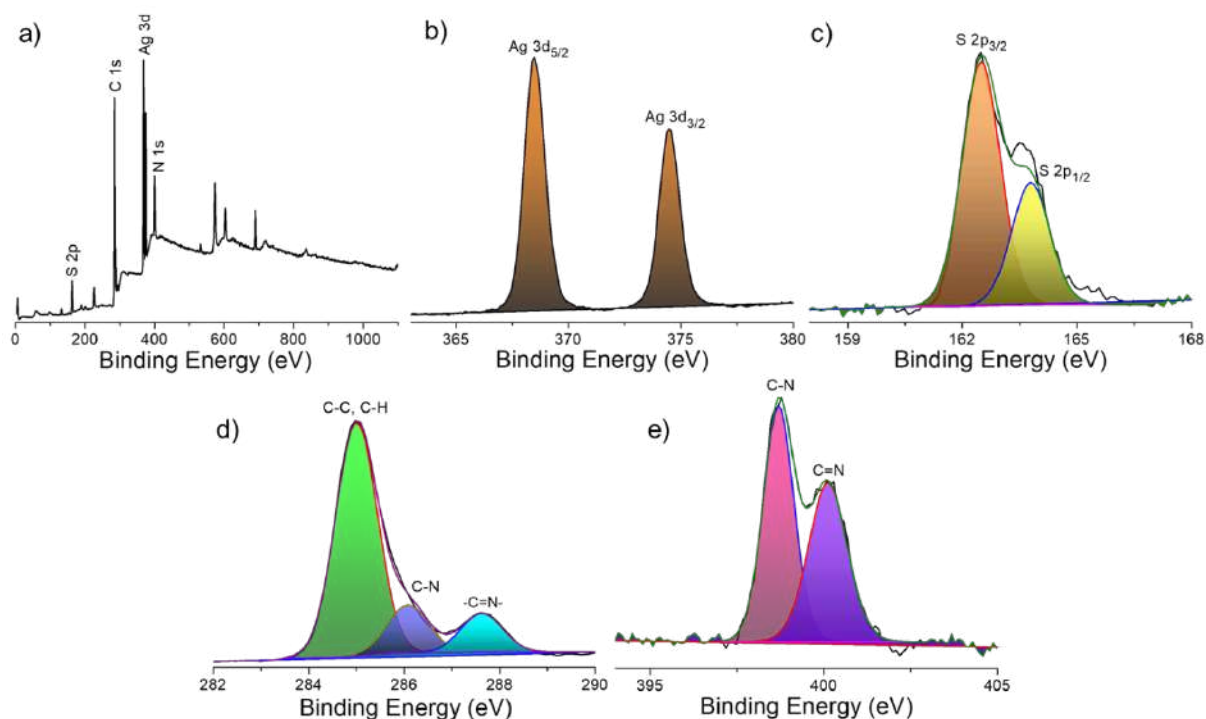


Figure S18. a) XPS survey scan of Ag_{42} indicating the presence of all the elements. Selected area spectral fittings of b) Ag 3d, c) S 2p, d) C 1s and e) N 1s regions.

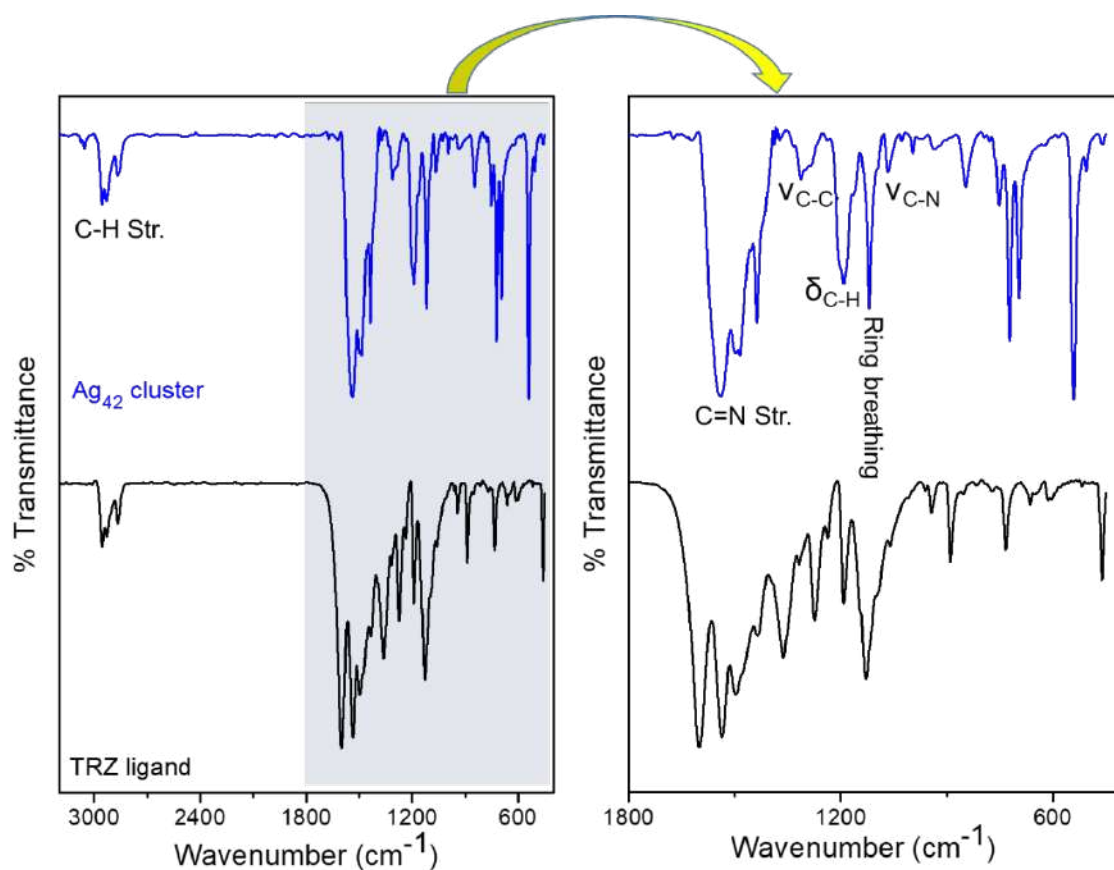


Figure S19. Comparative FT-IR spectra of Ag_{42} cluster and TRZ- H_2 ligand. Peaks of interest are marked.

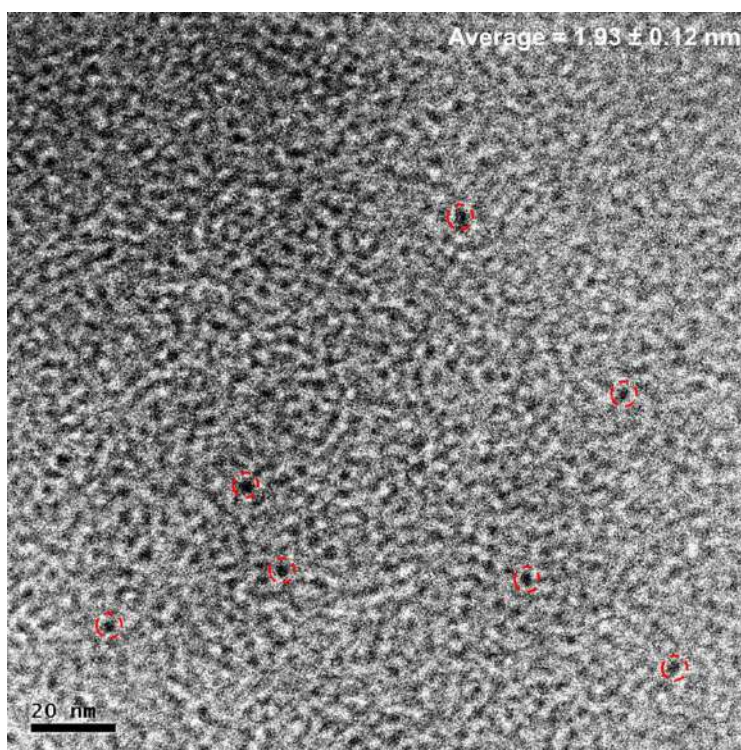


Figure S20. TEM micrograph of the Ag_{42} cluster. Ultrasmall cluster particles are marked in red.

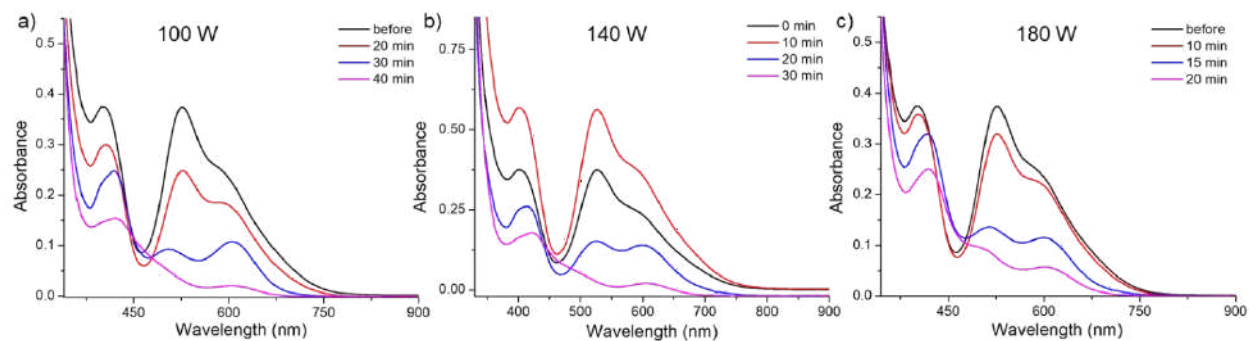


Figure S21. a-c) Lamp power-dependent conversion of Ag_{31} to Ag_{42} in its DCM solution. Cluster concentration was 1 mg/ml for each measurement.

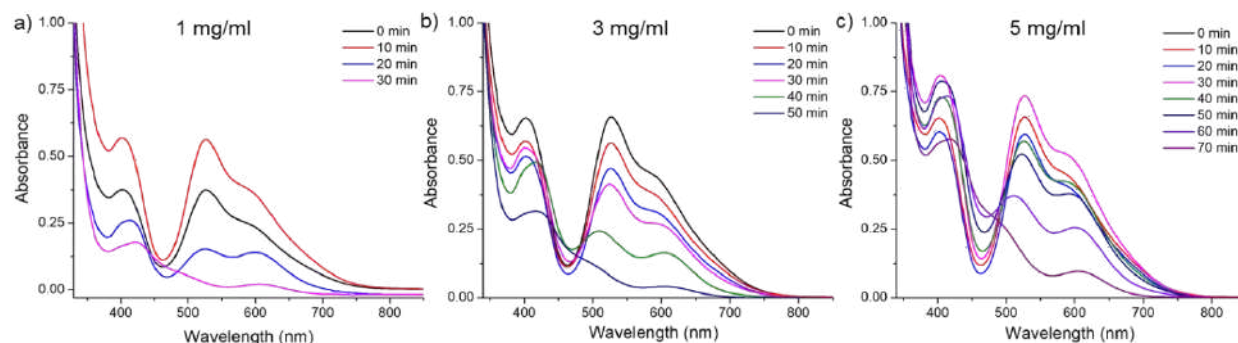


Figure S22. Concentration-dependent conversion of Ag_{31} to Ag_{42} in its DCM solution. Lamp power was 140 W for all the experiments.

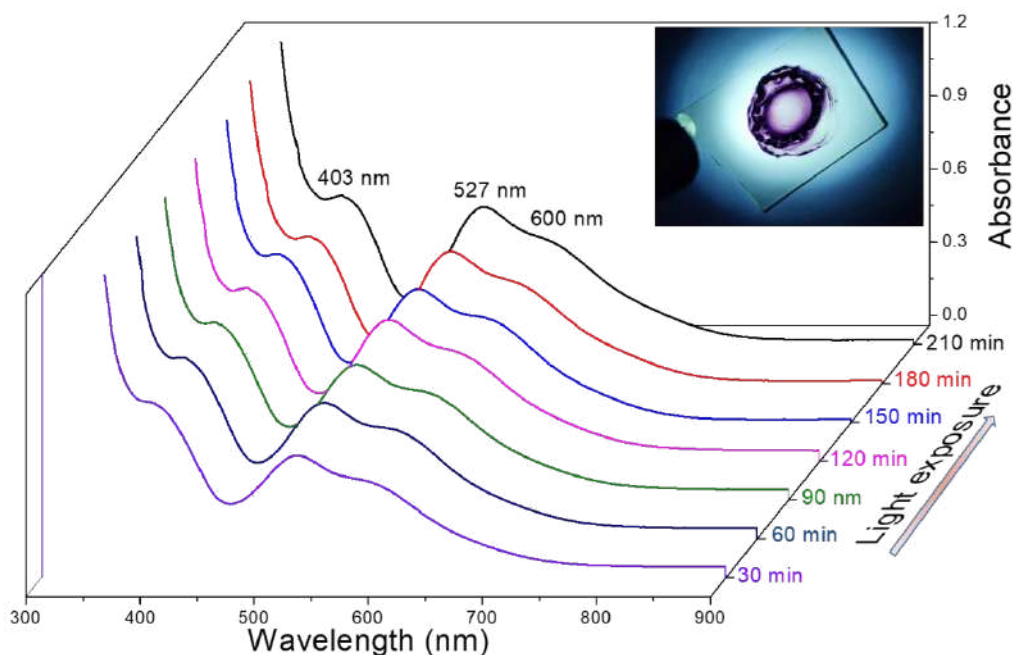


Figure S23. UV-vis absorption spectra of Ag_{31} after light irradiation in solid state. All the measurements were performed using a xenon arc lamp (lamp power = 140 W). Inset shows the photograph of a thin film during the process of light illumination.

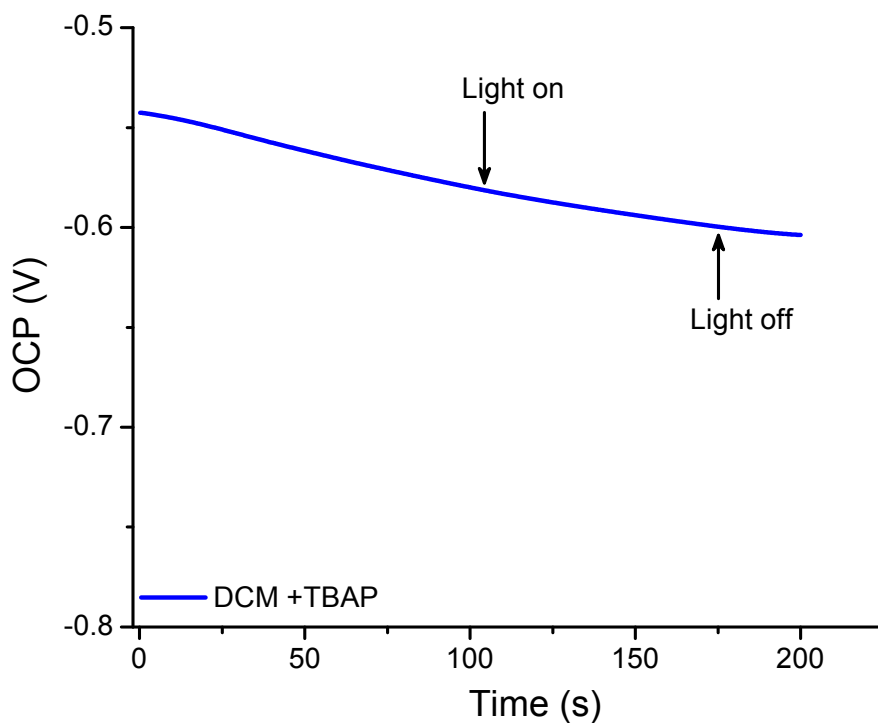


Figure S24. Open circuit potential (OCP) measurement of 0.2 M TBAF in DCM solution in dark and light illumination (140 W) using Pt wire as a working electrode and Ag/AgCl as reference electrode.

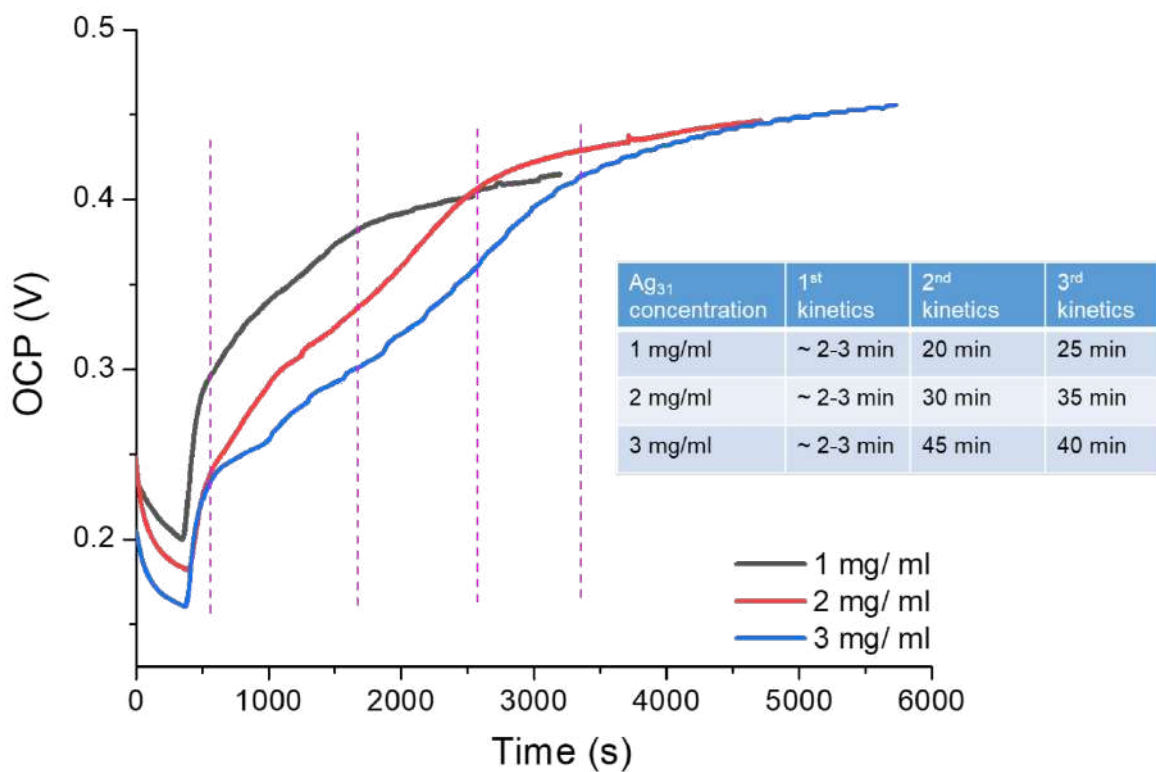


Figure S25. Open circuit potential (OCP) measurements of Ag₃₁ at different concentrations. Electrolyte used was 0.2 M TBAF in dichloromethane and lamp power was 140 W.

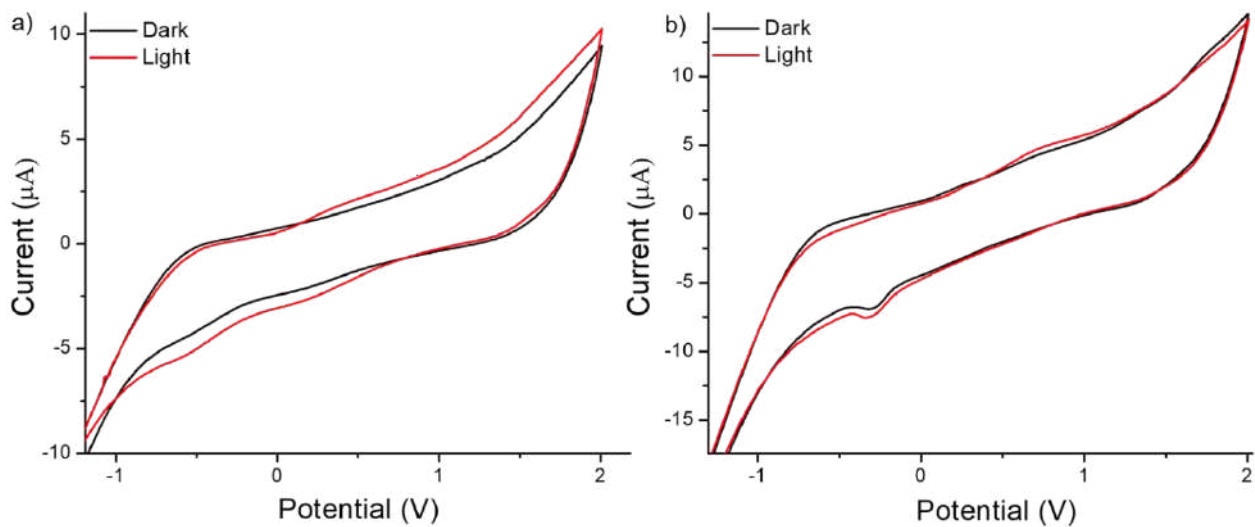


Figure S26. Cyclic voltammograms of a) Ag₃₁, b) Ag₄₂ clusters before and after light irradiation (lamp power 140 W) in 0.2 M TBAF solution, in DCM.

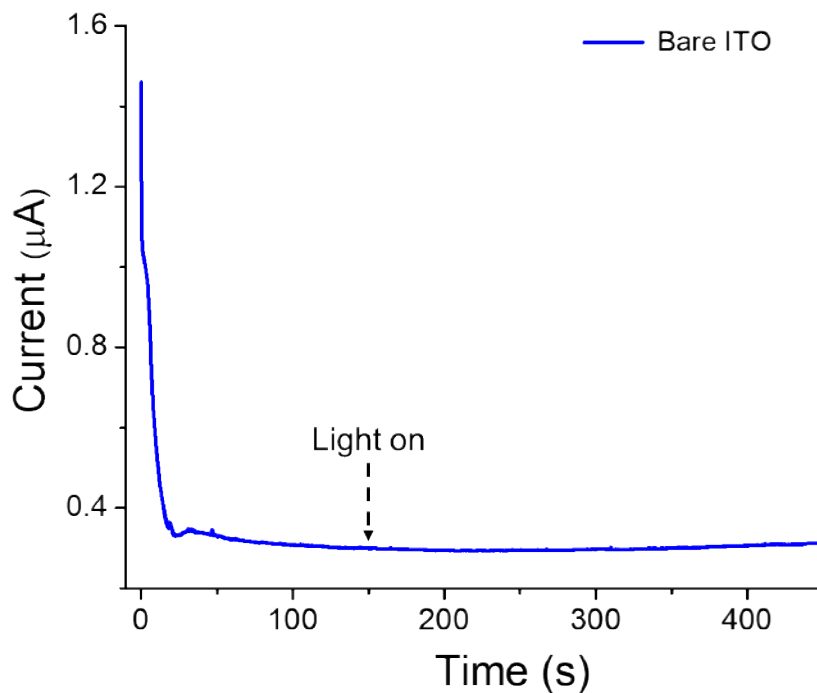


Figure S27. Chronoamperometric photocurrent response of a bare ITO electrode under electrochemical conditions (electrolyte used was 0.5 M aqueous Na_2SO_4 , lamp power 140 W).

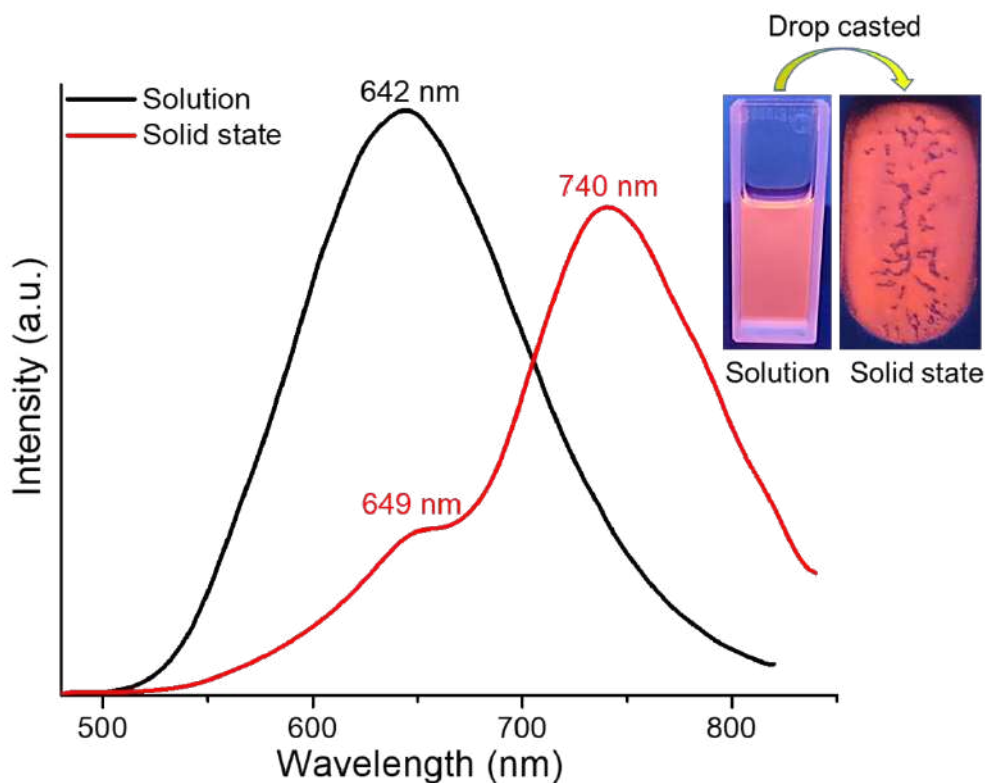


Figure S28. Comparative PL emission spectra of Ag_{42} nanocluster by 480 nm excitation in DCM solution as well as in the solid state. Inset showed the photographs of the respective clusters under 365 nm UV lamp.

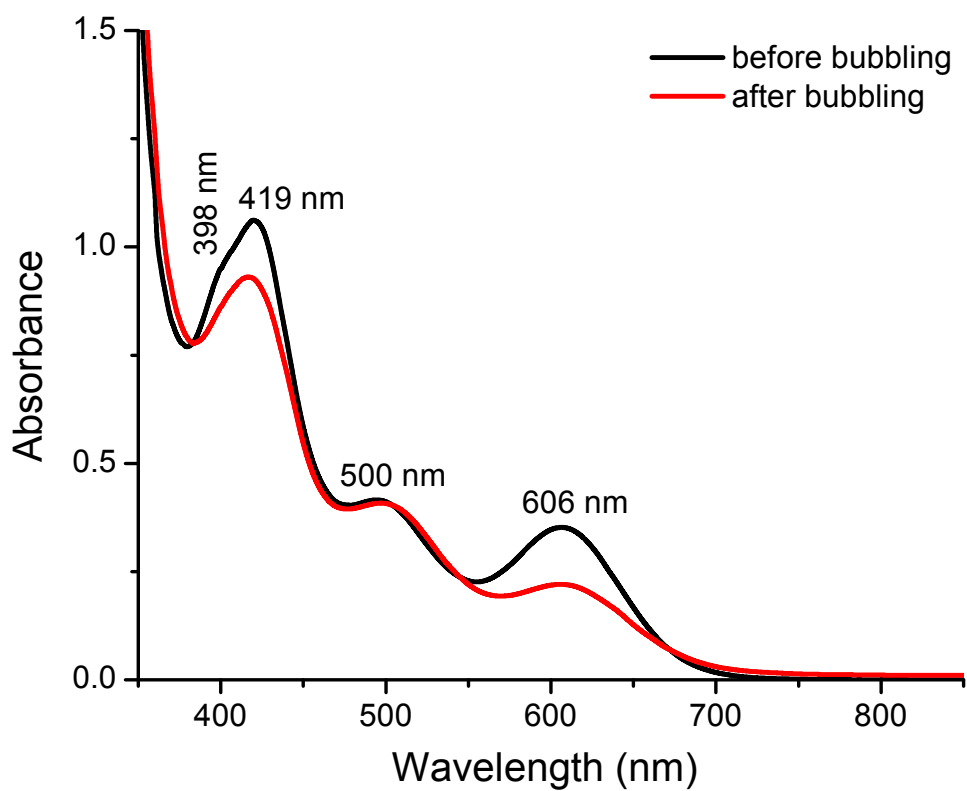


Figure S29. Comparative UV-vis absorption spectra of Ag_{42} in DCM solution before and after oxygen bubbling. Time of bubbling was 30-35 min.

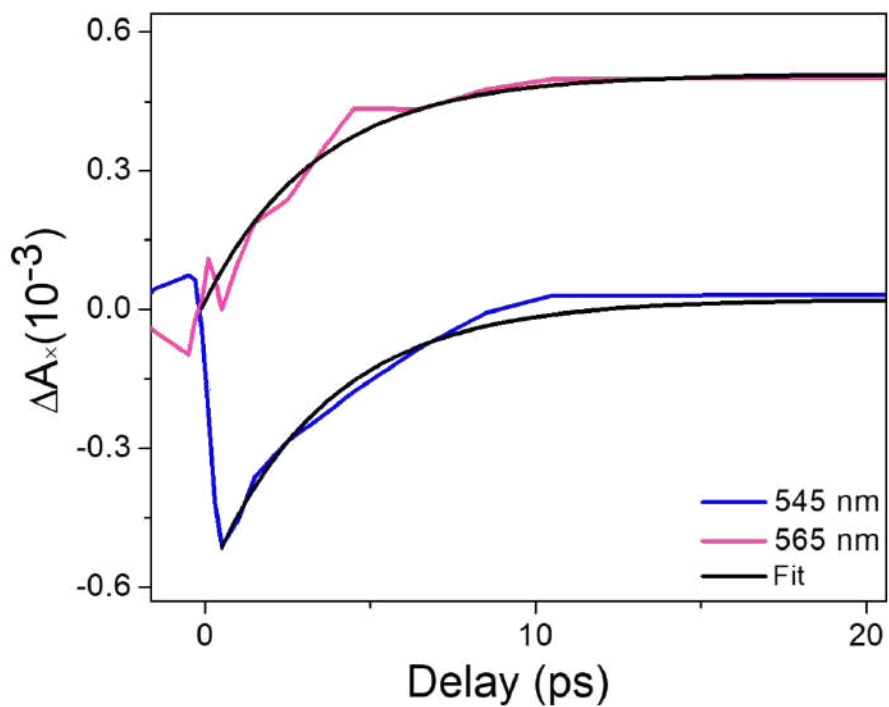


Figure S30. Early time scale temporal spectral profiles with associated fittings for Ag_{31} nanocluster.

References:

- (1) Wagstaffe, M.; Hussain, H.; Acres, M. J.; Jones, R.; Syres, K. L.; Thomas, A. G. Structure and Reactivity of a Model Oxide Supported Silver Nanocluster Catalyst Studied by near Ambient Pressure X-Ray Photoelectron Spectroscopy. *J. Phys. Chem. C* **2017**, *121* (39), 21383–21389.
- (2) Yang, L.; Jiang, X.; Ruan, W.; Yang, J.; Zhao, B.; Xu, W.; Lombardi, J. R. Charge-Transfer-Induced Surface-Enhanced Raman Scattering on Ag-TiO₂ Nanocomposites. *J. Phys. Chem. C* **2009**, *113* (36), 16226–16231.
- (3) Chandra, S.; Sciortino, A.; Das, S.; Ahmed, F.; Jana, A.; Roy, J.; Li, D.; Liljeström, V.; Jiang, H.; Johansson, L.-S.; Chen, X.; Nonappa; Cannas, M.; Pradeep, T.; Peng, B.; Ras, R. H. A.; Sun, Z.; Ikkala, O.; Mess, F. Gold Au(I)₆ Clusters with Ligand-Derived Atomic Steric Locking: Multifunctional Optoelectrical Properties and Quantum Coherence. *Adv. Opt. Mater.* **2023**, *2202649*, 1–8.

Observing Real-Time Adhesion of Microparticles on Glass Surfaces

Pillalamarri Srikrishnarka, Dhivyaraja Kumaran, Amoghavarsha Ramachandra Kini, Vishal Kumar, Ankit Nagar, Md Rabiul Islam, Ramamurthy Nagarajan,* and Thalappil Pradeep*



Cite This: <https://doi.org/10.1021/acs.langmuir.3c01856>



Read Online

ACCESS |



Metrics & More

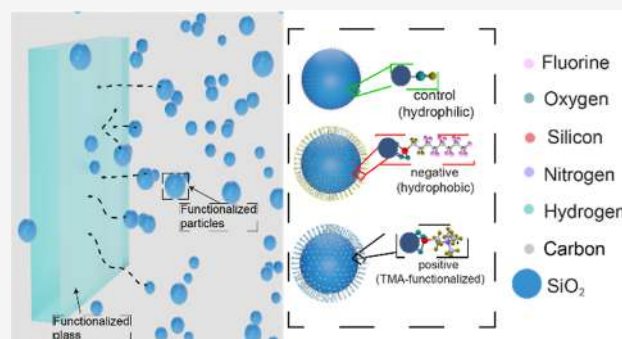


Article Recommendations



Supporting Information

ABSTRACT: Fouling on glass surfaces reduces the solar panel efficiency and increases water consumption for cleaning. Superhydrophobic coatings on glass enable self-cleaning by allowing water droplets to carry away dirt particles. Observing the interaction between charged particles and surfaces provides insights into effective cleaning. Using a high-speed camera and a long-distance objective, we analyzed the *in situ* deposition of variously functionalized and charged silica dust microparticles on chemically treated glass. The ambient charges for the control, hydrophobic, and positively charged particles were approximately -0.5 , -0.13 , and $+0.5$ nC, respectively. We found that a positively charged particle of 2.3 ± 1.2 μm diameter adhered to hydroxylated glass in ~ 0.054 s, compared to 0.40 and 0.45 s for quaternary ammonium- and fluorosilane-functionalized hydrophobic glass. Experiments suggest that quaternary ammonium-functionalized glass surfaces are about 77.8% more resistant to soiling than bare surfaces.



INTRODUCTION

Dust buildup on photovoltaic (PV) panels and façades is a severe problem since it negatively impacts light transmission and performance, including energy conversion efficiency. Also, large volumes of water are used in cleaning these surfaces. Dust travels long distances ranging from a few meters to thousands of kilometers, impacting the local environment and human health.¹ According to Elminir et al., dust deposited on horizontally installed PV panels in arid environments was ~ 15.84 g m⁻², resulting in a 52.5% decrease in light transmission.² Panat and Varanasi observed that with 50 g m⁻² dust deposition, there was $\sim 50\%$ loss in a solar panel's power output at a lab scale, under simulated harsh soiling.³ A global economic loss of between 3.3 and 5.5 billion USD is caused by an average power loss of 3 to 4%.⁴ A 1 MW solar farm requires close to 24,000 L of water or roughly 3–4 L per solar panel of ~ 400 W for cleaning. Moon et al. showed that even the most effective robotic cleaning system requires ~ 570 L of water to clean an area of 3000 m² (amounting to 5221 W) in an hour.⁵ Dust deposition on PV panels is dynamic, and it depends on the location. Such particles could be natural or anthropogenic in origin.^{6,7} These particles affect the quality of air,^{8,9} and consequently impact the local environment.

Inspired by nature, glass surfaces have been treated with transparent superhydrophobic coatings such as fluorosilane^{10–13} and nonfluorinated silane^{14–16} to remove dust particles passively. Recently, Dhar et al. reported a transparent superhydrophobic coating using dipentaerythritol pentaacrylate reacted with branched polyethylenimine which was

spray-coated on glass to impart hydrophobicity.¹⁷ Due to this superhydrophobic coating, a water flow removed the deposited model dust particles.¹⁷ Zhang and Seegar fabricated a new group of nanostructures based on silicone nanofilaments.¹⁸ These filaments were grown on glass and immersed in a toluene solution, and their growth was controlled by regulating water concentration during the condensation of trichlorosilane. These filaments were treated with O₂ plasma and modified with 1H, 1H, 2H, and 2H-perfluoro-decyl trichlorosilane. This transformed it into a superhydrophobic surface with excellent transparency. Ganesh et al. fabricated a superhydrophobic coating on glass using electrospinning to remove dirt without compromising transparency.^{19–21} Active cleaning methods are being investigated to curb excessive water use and to transition to sustainable cleaning systems.²² Some of the useful techniques include superhydrophobic coatings on glass surfaces, electrostatic cleaning, straightforward brushing, and ultrasonic cleaning. With the assistance of hydrophilic curved rings on a hydrophobic backdrop, Sun and Böhringer produced an active self-cleaning system capable of eliminating all types of dust particles from the surface. Here, mechanical vibrations were utilized to remove dust particles in the

Received: July 4, 2023

Revised: October 26, 2023

Accepted: October 27, 2023

presence of water as they trickled down the surface.²³ Vagra and Wiesner utilized a centrifugal force of ~ 65.9 nN to dislodge silica particles in the size range of ~ 15 to $30\ \mu\text{m}$ from a glass surface.²⁴ Recently, Kawamoto and co-workers installed parallel electrodes on the surface of PV panels connected to a high-voltage AC supply. When the panel was tilted and the electrodes were switched between positive and negative potentials alternatively at regular intervals, the resulting electrostatic forces made the dust particles fall, cleaning the surface without water.²⁵ A similar approach was followed by Panat and Varanasi, where they observed high removal efficiency even using a DC voltage and successfully recovered $\sim 95\%$ of the lost power after cleaning.³ Wang et al. fabricated a superhydrophobic antireflective coating on the PV module, which self-cleaned under artificial rain, providing a new approach to clean large-scale PV farms due to its cost-effectiveness and scalability.²⁶ The methods mentioned above remove particles with a size $>30\ \mu\text{m}$, but the removal efficiency decreases for fine and ultrafine particles. Upon adhesion, these particles will further aggregate and degrade the overall performance of the solar panels. Therefore, avoiding particle adherence as well as removing them early is important from multiple perspectives.

Superhydrophobic surfaces have varied applications including oil/water separation,²⁷ eco-friendly clothing, etc. For example, a cotton fabric was coated with appropriate molecular coatings for hydrophobicity.²⁸ This fabric²⁸ was superhydrophobic and superoleophilic with an oil/water separation efficiency of 98.49% even after 18 cycles. A multifunctional fabric which is superhydrophobic with properties such as thermal stability even at $180\ ^\circ\text{C}$, pH stability, resistance to organic solvents, and abrasion resistance was fabricated using a polyethylene terephthalate (PET) fabric with hierarchical structures by in situ polymerization of pyrrole over it.²⁹ Further treatment of this fabric with pentaerythritol tetraacrylate, 3-aminopropyltriethoxysilane, and octadecyl acrylate imparted multifunctionality to this fabric. Superhydrophobic fabrics also help build wearable sensors, especially for monitoring sweat rate and its composition.^{30,31} Recently, Liu et al. fabricated a sweat sensor based on polyacrylate sodium/MXene which was further sandwiched between two superhydrophobic textile layers for monitoring sweat vapor with high sensitivity and rapid response time.³² The superhydrophobic fabric enabled excellent breathability for the permeation of water vapor and prevented the sensor from external water droplets and internal sensible sweat.

In this paper, we present a study of the interaction between microscopic model dust particles and functionalized glass surfaces in real time. The particles were tracked using the image sequence obtained from a high-speed camera, and we found that hydrophobic glass foul less than the hydrophilic ones. Particles tend to deposit faster on hydrophilic glass than on hydrophobic or amine-functionalized glass. Surface energy and charge could increase the time needed for particle adhesion. The methodology presented could help evaluate dust adhesion on glass and help in assessing the ease of cleaning for a specific type of glass. To the best of our knowledge, there has been no report on such time-resolved observations of particle adhesion on surfaces.

MATERIALS AND METHODS

Materials. Ethanol (absolute AR) and hexane were purchased from Fisher Scientific UK, and sulfuric acid (AR) (H_2SO_4) was

purchased from RANKEM, India. 1H, 1H, 2H, 2H- perfluorooctyltriethoxysilane (98%) (PTFS) and hydrogen peroxide (H_2O_2) were purchased from Sigma-Aldrich, India. *N*-Trimethoxysilylpropyl-*N*,*N*,*N*-trimethylammonium chloride (TMA) was purchased from TCL Chemicals India Pvt. Ltd. Microscopic glass slides ($75 \times 25 \times 1.3$) mm^2 were from BLUE STAR, India, and spherical silica particles (SS-T-2.5, $1\text{--}5\ \mu\text{m}$) were from Sinoenergy Corporation, China. Millipore-produced deionized (DI) water was used throughout the experiments, and all the reagents were used without further purification.

Methods. Functionalization of Glass. The glass slides were cleaned before further surface functionalization. A three-step process was followed for cleaning these glass slides; initially, the glass slides were cut to dimensions of $28 \times 25\ \text{mm}^2$ using a diamond cutter. The cut-glass slides were sonicated for 15 min in soap solution. After washing, they were sonicated in ethanol for another 15 min. Finally, they were immersed in piranha solution [$1:4$ (v/v) 30% H_2O_2 and 30% H_2SO_4] for 2 h. Following this, glass slides were rinsed with DI water and finally dried by using dry nitrogen (N_2) gas. To transform these hydrophilic glass slides into hydrophobic ones, the glass slides were immersed in 1 mM PTFS hexane solution for 12 h. These slides were rinsed with hexane to remove any unbound PTFS and the hydrophobic glass slides so formed were dried under N_2 gas. To impart positive charges on the glass, the hydrophilic glass slides were immersed in a 1 mM ethanol solution of TMA for 12 h. Slides were rinsed with ethanol to remove any unbound TMA and dried using N_2 gas.

Functionalization of Particles. About 10 g of silica particles was added to a soap solution and sonicated for 15 min, following which, they were vacuum-filtered and washed twice with DI water. These particles were further added to an ethanol solution, sonicated for 15 min, and vacuum-filtered. The filtered particles were transferred to a piranha solution for 2 h. Finally, the particles were rinsed with DI water, vacuum-filtered one more time, and dried in an oven at $75\ ^\circ\text{C}$ overnight. From these dried particles, about 3 g was later transferred to 1 mM PTFS in hexane and kept for 12 h to impart hydrophobicity. They were vacuum-filtered, dried overnight, and transferred to polypropylene (PP) bottles for later use. Similarly, another 3 g of the dried particles was transferred to 1 mM TMA ethanol solution for 12 h to impart the amine functionality.³³ These particles were washed with ethanol, dried, and transferred to a PP bottle. The remaining hydrophilic silica particles were transferred to a PP bottle for further use.

Ambient Dust Deposition. To visualize the ambient dust deposited on different glasses, functionalized glasses were vertically placed at the top of a ~ 20 m high building within the academic zone of the Indian Institute of Technology (IIT) Madras, Chennai, India. The glass slides were placed during the summer months, and at the end of each day, the slides were visualized under an optical microscope to note the ambient particle deposition.

Model Dust Deposition. For investigating the model dust deposition on functionalized glass, the experiment was conducted in an acrylic chamber. The silica particles were fluidized by using a medical-grade nebulizer operating at a fixed flow rate of $0.4\ \text{mL min}^{-1}$. The flow of these particles was stopped after 5 s, following which the glass slides were removed and the particle distribution on the surface was plotted.

Feret Diameter Measurement. To measure the diameter of the particle and calculate the size distribution, the Feret diameter was measured by using a custom MATLAB function. Briefly, the image of interest was chosen from which a specific region was selected by cropping the unwanted parts. The color image was then transformed into a binary image, and "fill holes" functionality was used to fill any gaps. Then the Feret diameter was measured using the "Feret diameter" function in MATLAB. Then each diameter was multiplied with a scale of $0.7\ \mu\text{m pixel}^{-1}$ and the distribution was plotted as a histogram. The corresponding code is presented as Annexure-1.

In Situ Particle–Surface Interactions. To investigate particle–surface interactions, a glass slide was placed vertically inside a transparent acrylic chamber of dimensions $10 \times 10 \times 10\ \text{cm}^3$, having an inlet and outlet for the flow of silica particles. The glass was placed

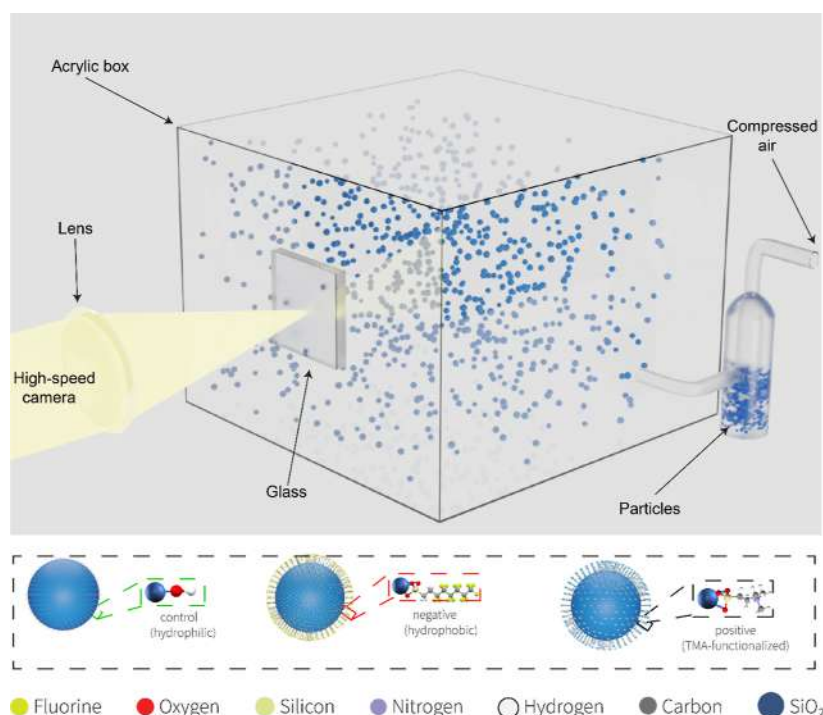


Figure 1. Schematic representation of the experimental setup and molecular models of functionalized silica particles are shown in the inset below. Fluidized microparticles of different functionalities impacting the glass slide randomly are imaged by a high-speed camera.

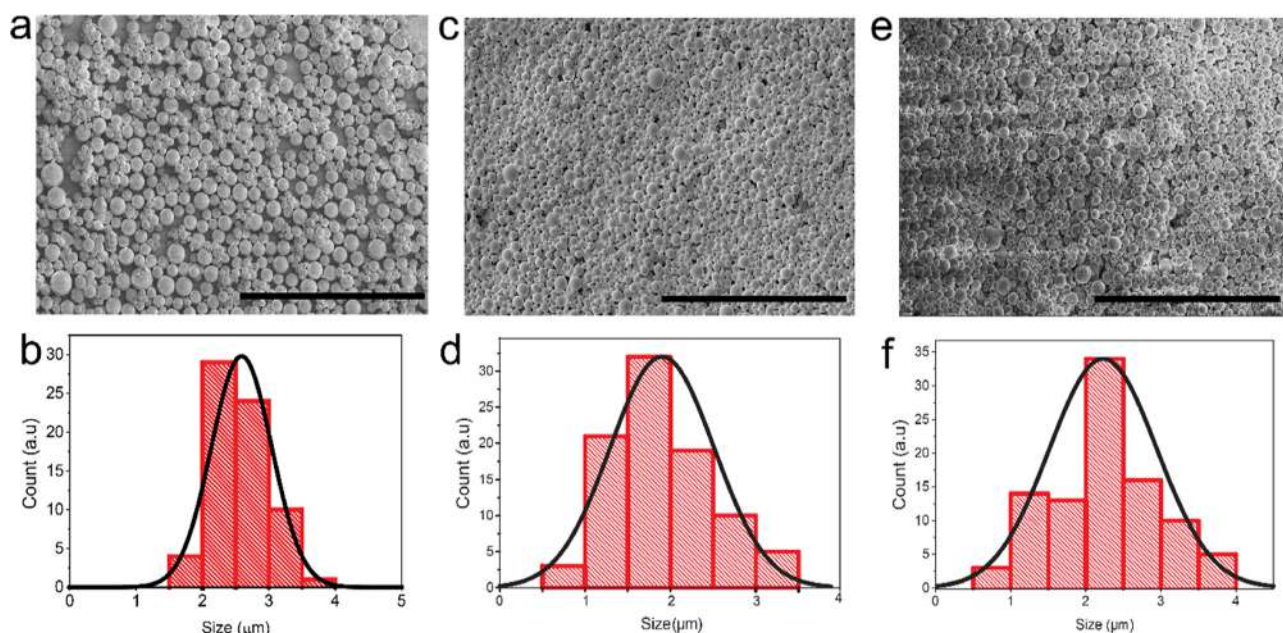


Figure 2. (a,c,e) Scanning electron micrographs of bare, hydrophobic (PTFS), and positively charged (TMA)-treated silica particles with a scale bar of 20 μm . (b,d,f) Corresponding size distribution of the silica particles measured from SEM.

vertically at the center of the acrylic chamber. This acrylic chamber was placed on a Labjack (Holmarc), which was further placed on an optical rail (Thorlabs). These were then placed on an optical table with vibration isolation. A schematic of the acrylic chamber hosting the glass slide and particles is shown in Figure 1. Silica particles were fluidized using precleaned compressed air obtained from a medical-grade nebulizer with a flow rate of 0.4 mL min^{-1} . A gas trap with a flat base was used to contain the silica particles. Gas was let in from the top of the trap to fluidize the particles, and from the side, these particles were transported inside the acrylic chamber as shown in Figure 1. A high-speed camera (Phantom V1212, 1000 frames per s)

was coupled with a long-working distance objective (KEYENCE ZHX 1000 \times) viewed at 1000 \times magnification. A frame size of 536×496 pixels with a resolution of $\sim 0.7 \mu\text{m pixel}^{-1}$ was obtained from calibration images. A continuous 300 W Xe arc lamp was coupled to the zoom lens in the coaxial illumination mode to illuminate the foreground and increase the sharpness of the particles deposited on the glass slide. The background was illuminated by using a Veritas Constellation 120E LED strobe light, operating in continuous mode at 120 W. The acrylic chamber was placed in such a way that the focal point of the lens was exactly on the glass facing the particles. The experiments were conducted at 18 $^{\circ}\text{C}$ and at 35%RH. The low

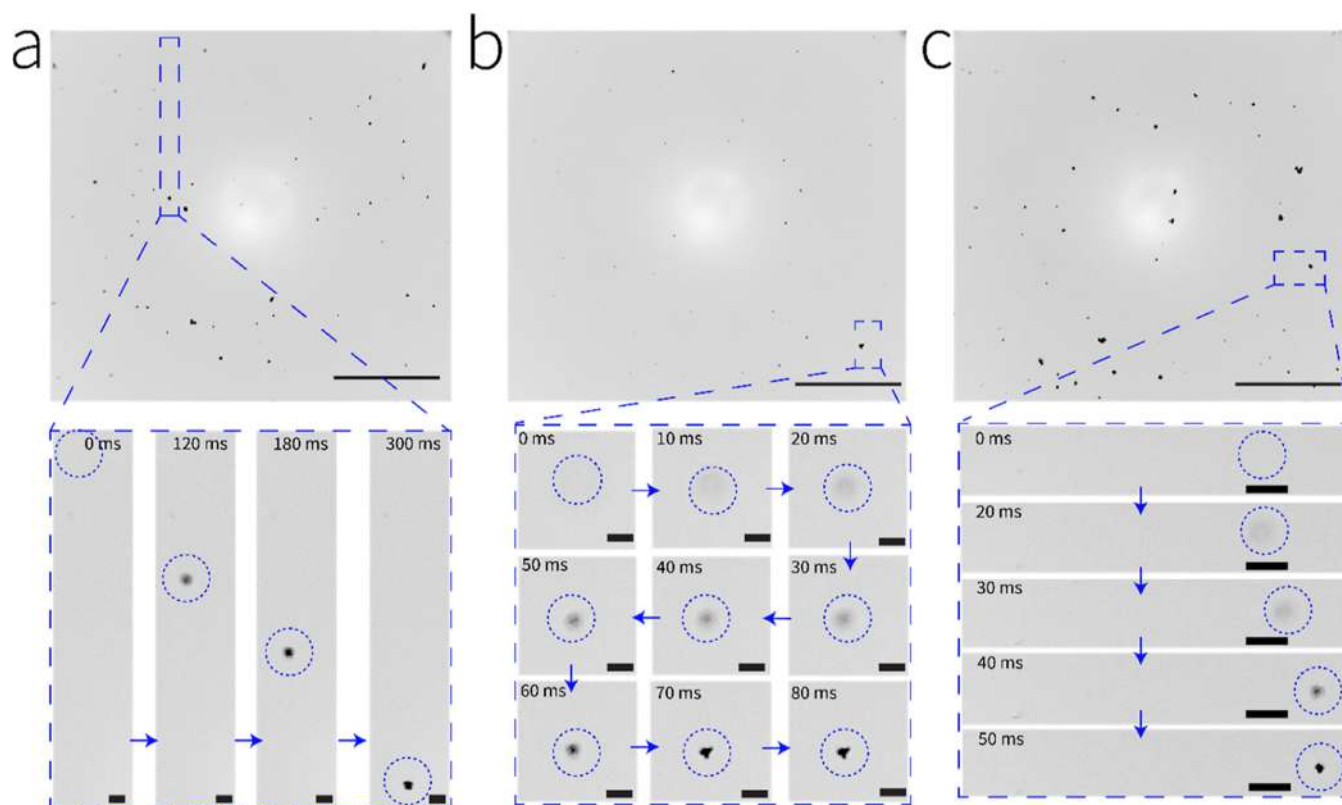


Figure 3. Digital photographs were taken from a high-speed camera. The interaction of positive, control, and negatively charged particles on hydrophilic glass is shown in (a, b, and c, respectively). The scale bar corresponds to 100 μm . In all the magnified images in the bottom frames, the scale bar corresponds to 10 μm . Dotted circles correspond to the particles of interest.

temperature was needed to protect the high-speed camera, strobe light, and Xe arc lamp from overheating.

CHARACTERIZATION

Silica particles were characterized with a Thermo Scientific Verios G4 UC FESEM, with retractable detectors operating at 2 kV. The samples were gold sputtered using a CRESSINGTON sputter coater operating for a period of 80 s. Glass slides after exposure to silica particles were viewed with a Leica polarization microscope for particle counting. The Feret diameter was noted by using MATLAB 20 software. The functionalized silica particles and glass slides were characterized using a Thermo Scientific Spectrum one FTIR instrument operated in the total attenuated reflection (ATR) mode to confirm the presence of the hydrophobic and amine moieties. The coatings on the glass after multiple cycles of modification and washing of the glass slides were confirmed with X-ray photoelectron spectroscopy (XPS). This analysis was carried out by using an Omicron ESCA probe TPD with Al $K\alpha$ as the X-ray source (1486.86 eV). Survey scans were performed at a pass energy of 50 eV and a step size of 0.5 eV, ranging from 0 to 1100 eV binding energy, to identify all the elements in the samples. Detailed scans were conducted for the elements of interest at a pass energy of 20 eV and a step size of 0.08 eV. In order to obtain the best resolution of the peaks, detailed scans for the elements of interest were run at least three times each. Contact angle measurements were performed by using the sessile droplet method, with water being used as the solvent (with a volume of 3 μL) using a Holmarc contact angle meter. To measure the ambient charge of the particles,

about 10 mg of the particles was added to a Faraday cup that was connected to a Keithley 6514 electrometer.

RESULTS AND DISCUSSION

Fabrication of Model Dust and Functionalized Glass.

For creating model dust particles, spherical silica particles (size $2.5 \pm 1.2 \mu\text{m}$ as seen in Figure 2c) were functionalized with PTFE to impart hydrophobicity and TMA to impart positive charges. The particles are spherical as seen in Figure 2a and have a size of $2.5 \pm 1.5 \mu\text{m}$ as shown in Figure 2b. Scanning electron micrographs of the negatively and positively charged particles are shown in Figure 2c,e. The size of negatively and positively charged particles was 2.3 ± 1.2 and $2.4 \pm 0.6 \mu\text{m}$, respectively, as shown in Figure 2d,f. There were no artifacts and surface deformations observed and the particles remained spherical even after chemical functionalization.

FTIR analysis was performed to confirm these moieties on silica particles, and a comparison of the data is shown in Figure S1. The peaks at 1138 and 1190 cm^{-1} confirm the presence of CF_3 and CF_2 vibrations in the hydrophobic silica. A peak at 1214 cm^{-1} is attributed to C–N stretching, confirming the anchoring of the amine moieties. A summary of the FTIR peaks is presented in Table S1.

About 100 mg of untreated, hydrophobic, and TMA-functionalized silica particles were added to a Faraday cup which was in turn connected to a Keithley 6510 electrometer. Figure S2 shows the ambient charge of particles as soon as they were added to the Faraday cup. Bare silica particles had a charge of -0.5 nC , hydrophobic silica particles had a charge of -0.13 nC , and TMA-functionalized particles had a charge of $+0.5 \text{ nC}$ due to the presence of the amine group. This

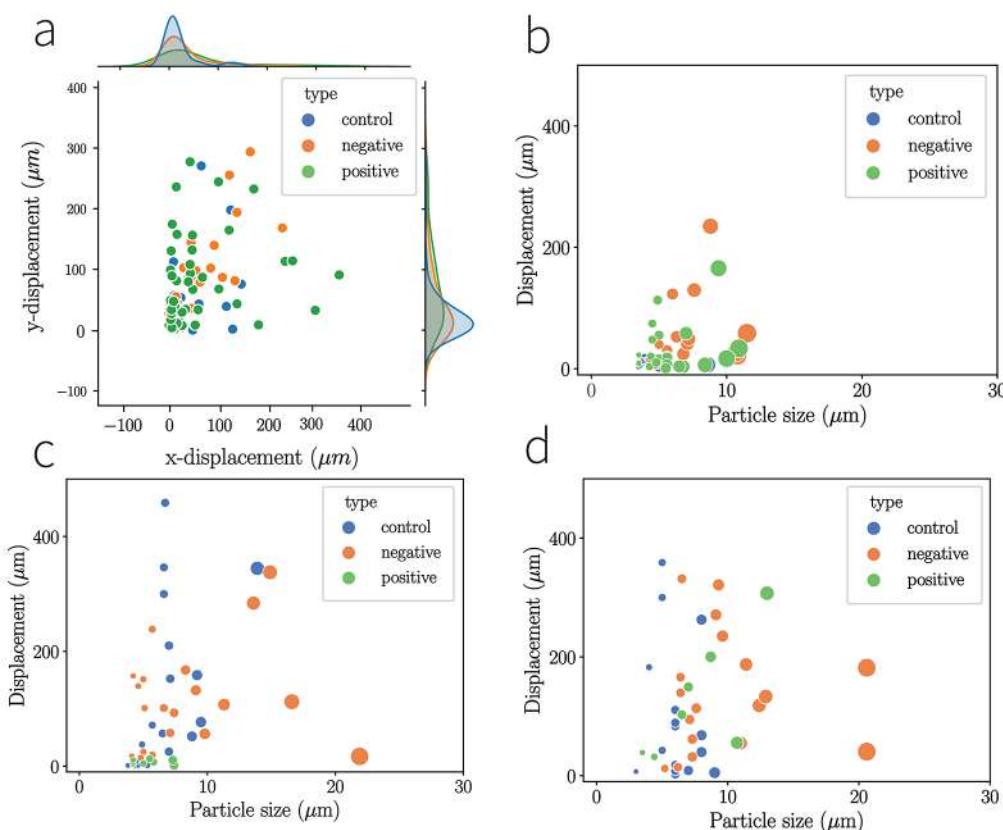


Figure 4. (a) Particle displacements along the x and y axis on hydrophilic, hydrophobic, and amine-functionalized glass. (b–d) Corresponding size of the particle and distance traveled before adhering to (b) hydrophilic, (c) hydrophobic, and (d) TMA-functionalized glass.

amounted to $\sim -7.5 \times 10^{-10}$, -8.5×10^{-10} , and 7.5×10^{-10} nC per particle for bare, hydrophobic, and amine-functionalized particles, respectively, assuming a particle size of $2.5 \mu\text{m}$ (see later for microscopic analysis). Molecular models of bare, hydrophobic, and amine-functionalized silica are also shown in Figure S2. Bare particles, hydrophobic particles, and TMA-functionalized particles will be termed control, negative, and positively charged particles, respectively, in this article.

The optical images containing a droplet in contact with the surface during the water contact angle measurements are shown in Figure S3. Hydrophilic glass had a contact angle of 25° , while the hydrophobic glass had a contact angle of 102° , and TMA-functionalized glass was slightly hydrophobic in nature, with a contact angle hovering around 88° . The surface energy of the treated surfaces was calculated based on the water contact angle using the equation below

$$\frac{\cos \theta + 1}{2} = \gamma_A (e^{-\beta(\gamma_B - \gamma_A)^2})$$

where θ is the water contact angle, γ_A the surface energy of the solid substrate, γ_B surface energy of water, and β is $0.0001057 (\text{m}^2 \text{mJ}^{-1})^2$.³⁴ The surface energy for hydrophilic glass was calculated to be $\sim 0.9 \text{ mN/m}$, for TMA-treated glass $\sim 0.5 \text{ mN/m}$, and for hydrophobic glass $\sim 0.4 \text{ mN/m}$.

To confirm the coating on glass, XPS analysis was performed, and the corresponding spectra are shown in Figures S4 and S5. All the samples exhibited the expected presence of C, Si, and O as seen in the survey spectra of hydrophobic glass (Figure S4) and TMA-treated glass (Figure S5). For hydrophobic glass, there were five peaks correspond-

ing to C (284.5 eV), C–C (283.9 eV), C–O (288 eV), CF_2 (290.9 eV), and CF_3 (293.3 eV) as seen in Figure S4b. Two peaks were observed in the detailed Si scans for the hydrophobic glass. The peak at $\sim 102.8 \text{ eV}$ corresponds to the silane and that at $\sim 103.5 \text{ eV}$ was assigned to SiO_2 as shown in Figure S4c. In Figure S4d, two types of oxygens were present in abundance and could be assigned to the different bonding modes of O in glass. Finally, Figure S4e shows a detailed F scan; a single peak was present at 687.63 V and was assigned to F in the $-\text{CF}_2-$ moieties. This confirms the hydrophobic coating on glass. The XPS survey spectrum of TMA-treated glass is shown in Figure S5a; the detailed C spectrum in Figure S5b shows adventitious C (284.5 eV) and C–O (286.6 eV) and another peak at 288.6 eV was assigned to the C–N bond. The detailed Si spectrum shown in Figure S5c shows two peaks at ~ 102.8 and 103.5 eV due to silane and SiO_2 , respectively. The O 1s region shown in Figure S5d has two peaks assigned to different bonding modes in glass. Finally, the TMA-treated glass has a peak at $\sim 399.6 \text{ eV}$ that is assigned to the C–N bond.

A digital photograph from the camera is shown in Figure S6a. From this, a small region is selected as seen in Figure S6b. From the image sequences from time-dependent imaging, the region of interest (ROI) was selected and cropped. The photographs in which particles enter the frame were chosen and cropped to comprehend particle motion as they attach to the surface. These cropped images were further analyzed using the “trackpy” module in Python to estimate the movements in the x - and y -axes.

Images of glass slides after particle deposition are shown in Figure 3, wherein Figure 3a represents the hydrophilic glass when positively charged particles adhered to it after 16 s. An ROI in Figure 3a (shown by the dashed rectangle) was chosen where the particle (indicated by the dotted circle) traveled from the top and was attached to the surface. Corresponding pictures are displayed in Figure 3a. The blurring of the particle in the first three images (the first image shows a clean region before the particle appears) shows that the particle was traveling from a depth and as it got adhered, it came into focus. In the image, just as the particle appears in the ROI, i.e., first appearance of a diffused region, a time of 0 ms is assigned. At the end of 180 ms, the particle is moving and slowly coming to focus and finally adheres to the hydrophilic glass at ~ 300 ms, and no further change is observed. A video depicting the particle adhesion on glass is shown in Video S1. In Figure 3b, interaction of control particles on a hydrophilic glass substrate was captured, and the inset shows a control particle adhering to the surface without any motion in the x - y direction. The control particle adheres much faster, taking ~ 80 ms to adhere to the glass and no further change is seen. Similarly, Figure 3c shows the interaction of negatively charged particles with the hydrophilic glass slides; the inset shows a positively charged particle moving toward the surface as it focuses on the site of adhesion. Furthermore, the negatively charged particle takes ~ 50 ms to adhere to the glass. A video showing a particle traveling from the depth and adhering to the glass is shown in Video S2.

The interactions of positively charged particles with hydrophobic glass are shown in Figure S7a and the ROI, representing a particle (shown in a dotted circle) that reached the surface from a certain depth. It took ~ 30 ms to adhere to the surface. We observed that the control particle takes a parabolic path to adhere to the hydrophobic glass, as seen in the inset of Figure S7b. The blurriness of the particle as it travels from the depth is prominent at the frame of 120 ms, as shown in the inset, and finally, it comes to focus as it adheres to the surface at the end of ~ 200 ms. The interaction of negatively charged particles with the hydrophobic glass is shown in Figure S7c and the inset magnifies the region where the particle adheres to the surface. In the case of the negatively charged particle, we also observed a motion in the x and y directions while traveling from a depth. It took ~ 86 ms for it to adhere to the surface.

The interaction between positively charged particles with TMA-functionalized glass is shown in Figure S8a, where a positively charged particle was seen to move along the y direction and adhere to the surface. In this sequence of images, we observed that the particle in focus suddenly moves to a different location, finally adhering to a different location, and it takes ~ 480 ms for adhesion. The interaction of the control particle with the TMA-functionalized surface is shown in Figure S8b and the inset shows a particle initially moving toward the surface as it deblurs. Direct adhesion on the surface was observed for negatively charged particles interacting with the TMA-functionalized glass, as seen in Figure S8c (inset).

Due to the boundary layer phenomenon, as the particles are approaching the surface, they would have the least velocity, and the electrostatic forces of attraction/repulsion would dominate. A summary of the particle displacements along different functionalized glasses is shown in Figure 4a. Time-resolved high-speed optical imaging revealed that most particles were displaced by ~ 40 and ~ 80 μm in the x and y

directions before adhering to the surface. The average displacement of control particles was minimal compared to others.

Some outliers showed displacements of up to 140 and 300 μm along the x and y axes, respectively. Based on the above observations, it is apparent that lesser particle movement along the x and y axes is due to "faster" adherence to surfaces with high surface energy. The negatively charged particle of size ~ 10 μm traveled the longest distance of ~ 230 μm , before colliding with the glass substrate and adhering to the hydrophilic surface, as shown in Figure 4b. Due to the high surface energy of hydrophilic glass, particles witnessed lesser displacement.

Also, we suspect that the positively charged particles had lesser displacement due to electrostatic attraction with the oppositely charged functionalities present on the glass substrate. All positively charged particles traversed less than ~ 13 μm before colliding with the hydrophobic glass (Figure 4c). In the case of control and negatively charged particles, the distribution of displacements across the particle size regime was random and no systematic correlation was observed (Figure 4c,d). This could be due to the particle-substrate electrostatic repulsion and steric hindrance offered by the surface groups, which resulted in longer displacements, irrespective of the nature of the charge on the particles. This was evident when the particles adhered to the surface, as shown in Figure S9. All the particles readily adhered to the hydrophilic glass slide, with positively charged particles taking ~ 0.054 s to adhere. There was an increase in the time for adhesion to the hydrophobic and TMA-functionalized glass. Particle adhesion took the longest, ~ 0.45 s, on a TMA-functionalized glass surface. Further experiments are needed to determine the effects of the surface charge and surface energy on the particle-substrate interaction.

Ex situ deposition of particles on glass after 19 s of exposure to model dust particles gave a distribution, as shown in Figure S10. In the case of hydrophilic glass with $-\text{OH}$ functionalization, control particles displayed ~ 1.8 -fold and ~ 3 -fold higher deposition compared to positively charged and negatively charged particles. In the case of TMA-functionalized glass, control particles exhibited ~ 3.5 -fold and ~ 2.3 -fold higher deposition compared to positively charged and negatively charged particles, respectively. In the case of hydrophobic glass with PTFE-functionalization, control particles showed ~ 1.6 -fold higher deposition than negatively charged particles. However, the highest fouling was by positively charged particles. We suspect that the highest fouling was due to an opposite surface charge between the positively charged particles and hydrophobic glass. This implies that surface functionalization of the glass substrate results in lesser particle deposition or fouling. The highest fouling was observed with the hydrophilic glass slide having $-\text{OH}$ functionalization. Further studies are needed to study the influence of surface charge and energy dependencies on the fouling of glass by real dust.

Exposure to Ambient Dust. To investigate the impact of surface functionalization on ambient dust deposition, chemically treated glass slides were placed at a height of ~ 20 m from the floor of our laboratory building within the IIT Madras campus and were viewed with an optical microscope at the end of 4 days. Particle size was measured using the Feret diameter feature in ImageJ and the size distribution is shown in Figure S11. At the end of the fourth day, particle deposition increased,

as seen for hydrophilic glass slides. Dust particles of 60 μm in size were observed at the end of 4 days. Hydrophobic glass slides fouled less compared to hydrophilic glass with a maximum particle size of 100 μm . TMA-functionalized glass fouled the least even at the end of 4 days. Lower surface energy and long-chain moieties on the surface of the glass could reduce fouling. Prolonged exposure to ambient dust would provide further quantifiable data on the overall reduction in fouling based on surface functionalization. However, this is further dependent on many experimental conditions, and the outcomes will be dependent on local factors such as humidity, temperature, particulate matter concentration, and wind velocity.

Ease of Cleaning the Surface. We placed fine sand particles on hydrophilic, hydrophobic, and TMA-treated glass, on which water droplets were placed. We observed that the droplet was spread on hydrophilic glass (Figure S12a) but it retained the shape in the case of functionalized glass as shown in Figure S12b,c. The surface functionalization did reduce the surface energy, which enabled the droplet to retain the droplet form. There was significant pinning of droplets when the slides were tilted as seen in Figure S12d–f.

CONCLUSIONS

Ambient dust exposure on chemically functionalized glass surfaces showed that TMA-functionalized and hydrophobic glass surfaces fouled the least compared to the hydrophilic glass. An experimental setup was designed to observe particle adhesion on model glass surfaces in situ. Particle motion along these surfaces was tracked successfully with a high-speed camera. The hydrophilic glass surface fouled more readily due to particle deposition. Deposition on such a surface was immediate (within 0.05 s), and the least lateral motion of the particles (2.3 μm) was observed. Also, positively charged particles adhered on a hydroxylated glass in ~ 0.054 s as opposed to 0.40 and 0.45 s needed for adhesion on a TMA-functionalized and a hydrophobic glass, respectively. These observations could shed light on the interaction of microscopic particles on surfaces. In addition, varying the %RH while performing the experiments can induce condensation on the glass, affecting particle adhesion, and we suspect easier particle adhesion on the glass. The presence of droplets on the glass could lead to the formation of a coffee ring of dust particles upon drying. By combining surface functionalization with the electrostatic surface cleaning method shown by Panat and Varanasi, we expect that the overall DC potential needed for cleaning the soiled surfaces could be reduced greatly. By reducing the surface energy, the centrifugal force needed to dislodge particles on glass could be reduced. In the future, we plan to study the effect of carbon chain length on the adhesion time of the particles. In situ particle deposition coupled with charge measurement is being planned and would provide exact information about the surface charge and surface energy.

ASSOCIATED CONTENT

Supporting Information

The Supporting Information is available free of charge at <https://pubs.acs.org/doi/10.1021/acs.langmuir.3c01856>.

FTIR spectra of bare, amine, and hydrophobic silica; ambient charge of particles; water contact angle measurements; optical image from the high-speed camera before processing; digital photographs of particle

interactions on amine and hydrophobic glass; heat-map representing the time taken for the particles to adhere to different types of glass; and particle size distribution of deposited particles on different types of glass (PDF)

MATLAB code used to calculate the ferret diameter (PDF)

Video depicting particle adhesion on glass (MP4)

Video showing a particle traveling from the depth and adhering to the glass (MP4)

AUTHOR INFORMATION

Corresponding Authors

Ramamurthy Nagarajan – Department of Chemical Engineering, Indian Institute of Technology Madras, Chennai 600036, India; Email: nag@iitm.ac.in

Thalappil Pradeep – DST Unit of Nanoscience and Thematic Unit of Excellence, Department of Chemistry, Indian Institute of Technology Madras, Chennai 600036, India; orcid.org/0000-0003-3174-534X; Email: pradeep@iitm.ac.in

Authors

Pillalamarri Srikrishnarka – DST Unit of Nanoscience and Thematic Unit of Excellence, Department of Chemistry, Indian Institute of Technology Madras, Chennai 600036, India; Department of Chemical Engineering, Indian Institute of Technology Madras, Chennai 600036, India; orcid.org/0000-0001-5187-6879

Dhivyaraja Kumaran – Department of Applied Mechanics, Indian Institute of Technology Madras, Chennai 600036, India

Amoghavarsha Ramachandra Kini – DST Unit of Nanoscience and Thematic Unit of Excellence, Department of Chemistry, Indian Institute of Technology Madras, Chennai 600036, India

Vishal Kumar – DST Unit of Nanoscience and Thematic Unit of Excellence, Department of Chemistry, Indian Institute of Technology Madras, Chennai 600036, India; Department of Chemical Engineering, Indian Institute of Technology Madras, Chennai 600036, India; orcid.org/0000-0002-2374-0568

Ankit Nagar – DST Unit of Nanoscience and Thematic Unit of Excellence, Department of Chemistry, Indian Institute of Technology Madras, Chennai 600036, India

Md Rabiul Islam – DST Unit of Nanoscience and Thematic Unit of Excellence, Department of Chemistry, Indian Institute of Technology Madras, Chennai 600036, India; orcid.org/0000-0001-6454-4013

Complete contact information is available at: <https://pubs.acs.org/doi/10.1021/acs.langmuir.3c01856>

Author Contributions

T.P., R.N., and P.S. designed the research. T.P. and R.N. supervised the progress, and P.S. and D.K. performed experiments using the high-speed camera. V.K. measured the ambient charge of the particles; A.M.K., A.K., and M.R.I. assisted in analyzing the results and making figures. The final version of the manuscript was written with the contributions of all authors.

Notes

The authors declare no competing financial interest.

ACKNOWLEDGMENTS

The authors thank Prof. Mahesh Panchagnula for allowing us to use his high-speed camera. The authors acknowledge Prof. Pijush Ghosh for contact angle measurements. The authors thank the “Dust free glass” project funded by Saint Gobain Research India Ltd. We thank Dr. B. S. Srinivas Prasad for his valuable suggestions throughout the project. T.P. acknowledges funding from the Centre of Excellence on Molecular Materials and Functions under the Institute of Eminence scheme of IIT Madras. P.S. would like to thank Paulami Bose for assisting in drawing the molecular structures. P.S., D.K., V.K., and A.K. thank IIT Madras for their research fellowship. A.M.K. and M.R.I. thank the Council of Science and Industrial Research (CSIR), Government of India for their research fellowship.

REFERENCES

- (1) van der Does, M.; Knippertz, P.; Zschenderlein, P.; Giles Harrison, R.; Stuut, J.-B. W. The Mysterious Long-Range Transport of Giant Mineral Dust Particles. *Sci. Adv.* **2018**, *4* (12), No. eaau2768.
- (2) Elminir, H. K.; Ghitass, A. E.; Hamid, R. H.; El-Hussainy, F.; Beheary, M. M.; Abdel-Moneim, K. M. Effect of Dust on the Transparent Cover of Solar Collectors. *Energy Convers. Manage.* **2006**, *47* (18–19), 3192–3203.
- (3) Panat, S.; Varanasi, K. K. Electrostatic Dust Removal Using Adsorbed Moisture-Assisted Charge Induction for Sustainable Operation of Solar Panels. *Sci. Adv.* **2022**, *8* (10), No. eabm0078.
- (4) Sarver, T.; Al-Qaraghuli, A.; Kazmerski, L. L. A Comprehensive Review of the Impact of Dust on the Use of Solar Energy: History, Investigations, Results, Literature, and Mitigation Approaches. *Renewable Sustainable Energy Rev.* **2013**, *22*, 698–733.
- (5) Moon, S. M.; Shin, C. Y.; Huh, J.; Oh, K. W.; Hong, D. Window Cleaning System with Water Circulation for Building Façade Maintenance Robot and Its Efficiency Analysis. *Int. J. Precis. Eng. Manuf. - Green Technol.* **2015**, *2* (1), 65–72.
- (6) Moffet, R. C.; Desyaterik, Y.; Hopkins, R. J.; Tivanski, A. V.; Gilles, M. K.; Wang, Y.; Shutthanandan, V.; Molina, L. T.; Abraham, R. G.; Johnson, K. S.; Mugica, V.; Molina, M. J.; Laskin, A.; Prather, K. A. Characterization of Aerosols Containing Zn, Pb, and Cl from an Industrial Region of Mexico City. *Environ. Sci. Technol.* **2008**, *42* (19), 7091–7097.
- (7) Chen, H.; Laskin, A.; Baltrusaitis, J.; Gorski, C. A.; Scherer, M. M.; Grassian, V. H. Coal Fly Ash as a Source of Iron in Atmospheric Dust. *Environ. Sci. Technol.* **2012**, *46* (4), 2112–2120.
- (8) McGaughey, G. R.; Desai, N. R.; Allen, D. T.; Seila, R. L.; Lonneman, W. A.; Fraser, M. P.; Harley, R. A.; Pollack, A. K.; Ivy, J. M.; Price, J. H. Analysis of Motor Vehicle Emissions in a Houston Tunnel during the Texas Air Quality Study 2000. *Atmos. Environ.* **2004**, *38* (20), 3363–3372.
- (9) Huang, L.; Zhu, Y.; Wang, Q.; Zhu, A.; Liu, Z.; Wang, Y.; Allen, D. T.; Li, L. Assessment of the Effects of Straw Burning Bans in China: Emissions, Air Quality, and Health Impacts. *Sci. Total Environ.* **2021**, *789*, 147935.
- (10) Ke, C.; Zhang, C.; Wu, X.; Jiang, Y. Highly Transparent and Robust Superhydrophobic Coatings Fabricated via a Facile Sol-Gel Process. *Thin Solid Films* **2021**, *723*, 138583.
- (11) Liu, Y.; Tan, X.; Li, X.; Xiao, T.; Jiang, L.; Nie, S.; Song, J.; Chen, X. Eco-Friendly Fabrication of Transparent Superhydrophobic Coating with Excellent Mechanical Robustness, Chemical Stability, and Long-Term Outdoor Durability. *Langmuir* **2022**, *38* (42), 12881–12893.
- (12) Yu, S.; Guo, Z.; Liu, W. Biomimetic Transparent and Superhydrophobic Coatings: From Nature and beyond Nature. *Chem. Commun.* **2015**, *51* (10), 1775–1794.
- (13) Helmer, D.; Keller, N.; Kotz, F.; Stolz, F.; Greiner, C.; Nargang, T. M.; Sachsenheimer, K.; Rapp, B. E. Transparent, Abrasion-Insensitive Superhydrophobic Coatings for Real-World Applications. *Sci. Rep.* **2017**, *7* (1), 15078.
- (14) Wu, Y.; Tan, X.; Wang, Y.; Tao, F.; Yu, M.; Chen, X. Nonfluorinated, Transparent, and Antireflective Hydrophobic Coating with Self-Cleaning Function. *Colloids Surf., A* **2022**, *634*, 127919.
- (15) Allahdini, A.; Jafari, R.; Momen, G. Transparent Non-Fluorinated Superhydrophobic Coating with Enhanced Anti-Icing Performance. *Prog. Org. Coat.* **2022**, *165*, 106758.
- (16) Jeevajoithi, K.; Subasri, R.; Soma Raju, K. R. C. Transparent, Non-Fluorinated, Hydrophobic Silica Coatings with Improved Mechanical Properties. *Ceram. Int.* **2013**, *39* (2), 2111–2116.
- (17) Dhar, M.; Kara, U. I.; Das, S.; Xu, Y.; Mandal, S.; Dupont, R. L.; Boerner, E. C.; Chen, B.; Yao, Y.; Wang, X.; Manna, U. Design of a Self-Cleanable Multilevel Anticounterfeiting Interface through Covalent Chemical Modulation. *Mater. Horiz.* **2023**, *10* (6), 2204–2214.
- (18) Zhang, J.; Seeger, S. Superoleophobic Coatings with Ultralow Sliding Angles Based on Silicone Nanofilaments. *Angew. Chem., Int. Ed.* **2011**, *50* (29), 6652–6656.
- (19) Ganesh, V. A.; Dinachali, S. S.; Nair, A. S.; Ramakrishna, S. Robust Superamphiphobic Film from Electrospun TiO₂ Nanostructures. *ACS Appl. Mater. Interfaces* **2013**, *5* (5), 1527–1532.
- (20) Ganesh, V. A.; Nair, A. S.; Raut, H. K.; Yuan Tan, T. T.; He, C.; Ramakrishna, S.; Xu, J. Superhydrophobic Fluorinated POSS-PVDF-HFP Nanocomposite Coating on Glass by Electrospinning. *J. Mater. Chem.* **2012**, *22* (35), 18479–18485.
- (21) Ganesh, V. A.; Dinachali, S. S.; Raut, H. K.; Walsh, T. M.; Nair, A. S.; Ramakrishna, S. Electrospun SiO₂ Nanofibers as a Template to Fabricate a Robust and Transparent Superamphiphobic Coating. *RSC Adv.* **2013**, *3* (12), 3819–3824.
- (22) Bouaddi, S.; Fernández-García, A.; Sansom, C.; Sarasua, J. A.; Wolfertstetter, F.; Bouzekri, H.; Sutter, F.; Azpitarte, I. A Review of Conventional and Innovative Sustainable Methods for Cleaning Reflectors in Concentrating Solar Power Plants. *Sustainability* **2018**, *10* (11), 3937.
- (23) Sun, D.; Böhringer, K. F. An Active Self-Cleaning Surface System for Photovoltaic Modules Using Anisotropic Ratchet Conveyors and Mechanical Vibration. *Microsyst. Nanoeng.* **2020**, *6* (1), 87.
- (24) Varga, H. F.; Wiesner, M. R. Relationship between Atomic Force Microscopy and Centrifugation Measurements for Dust Fractions Implicated in Solar Panel Soiling. *Environ. Sci. Technol.* **2022**, *56* (13), 9604–9612.
- (25) Kawamoto, H. Electrostatic Cleaning Equipment for Dust Removal from Soiled Solar Panels. *J. Electrostat.* **2019**, *98*, 11–16.
- (26) Wang, P.; Wang, H.; Li, J.; Ni, L.; Wang, L.; Xie, J. A Superhydrophobic Film of Photovoltaic Modules and Self-Cleaning Performance. *Sol. Energy* **2021**, *226*, 92–99.
- (27) Zhang, Y.; Gong, X. Smart and Durable pH-Responsive Superhydrophobic Fabrics with Switchable Surface Wettability for High-Efficiency and Complex Oil/Water Separation. *Giant* **2023**, *14*, 100157.
- (28) Yu, H.; Wu, M.; Duan, G.; Gong, X. One-Step Fabrication of Eco-Friendly Superhydrophobic Fabrics for High-Efficiency Oil/Water Separation and Oil Spill Cleanup. *Nanoscale* **2022**, *14* (4), 1296–1309.
- (29) Xiong, Z.; Yu, H.; Gong, X. Designing Photothermal Superhydrophobic PET Fabrics via In Situ Polymerization and 1,4-Conjugation Addition Reaction. *Langmuir* **2022**, *38* (28), 8708–8718.
- (30) Liu, Y.; Sheng, Z.; Huang, J.; Liu, W.; Ding, H.; Peng, J.; Zhong, B.; Sun, Y.; Ouyang, X.; Cheng, H.; Wang, X. Moisture-Resistant MXene-Sodium Alginate Sponges with Sustained Superhydrophobicity for Monitoring Human Activities. *Chem. Eng. J.* **2022**, *432*, 134370.
- (31) Wang, X.; Liu, Y.; Cheng, H.; Ouyang, X. Surface Wettability for Skin-Interfaced Sensors and Devices. *Adv. Funct. Mater.* **2022**, *32* (27), 2200260.
- (32) Liu, Y.; Li, X.; Yang, H.; Zhang, P.; Wang, P.; Sun, Y.; Yang, F.; Liu, W.; Li, Y.; Tian, Y.; Qian, S.; Chen, S.; Cheng, H.; Wang, X. Skin-Interfaced Superhydrophobic Insensitive Sweat Sensors for Evaluating

Body Thermoregulation and Skin Barrier Functions. *ACS Nano* **2023**, *17* (6), 5588–5599.

(33) Thomas Iii, S. W.; Vella, S. J.; Dickey, M. D.; Kaufman, G. K.; Whitesides, G. M. Controlling the Kinetics of Contact Electrification with Patterned Surfaces. *J. Am. Chem. Soc.* **2009**, *131* (25), 8746–8747.

(34) Gindl, M.; Sinn, G.; Gindl, W.; Reiterer, A.; Tschegg, S. A Comparison of Different Methods to Calculate the Surface Free Energy of Wood Using Contact Angle Measurements. *Colloids Surf., A* **2001**, *181* (1–3), 279–287.

Structure and Electrocatalytic Performance of Cocrystallized Ternary Molybdenum Oxosulfide Clusters for Efficient Water Splitting

Biswajit Mondal,[▽] Arijit Jana,[▽] Jayoti Roy,[▽] Astrid Campos Mata, Akhil S. Nair, Ananthu Mahendranath, Soumyabrata Roy, Biswarup Pathak,* Pulickel M. Ajayan,* and Thalappil Pradeep*



Cite This: *ACS Materials Lett.* 2023, 5, 3306–3315



Read Online

ACCESS |



Metrics & More

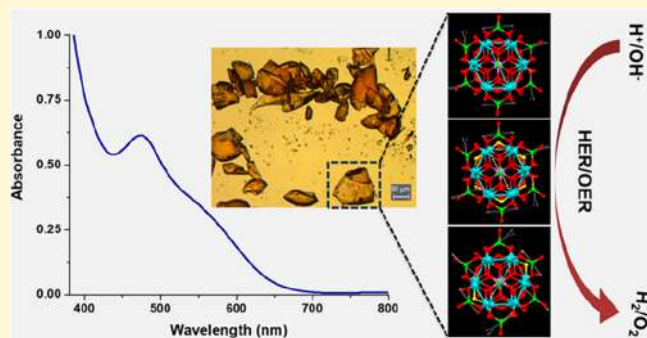


Article Recommendations



Supporting Information

ABSTRACT: Polyoxometalates (POMs) belong to a class of metal oxanion clusters that hold enormous promise for a wide range of catalytic reactions, due to their structural diversity and the presence of redox-active metal centers and heteroatomic sites within the framework. In this study, we successfully determined the structures of the first cocrystallized ternary molybdenum oxo-sulfide clusters: $\text{Mo}_{12}\text{NaO}_{54}\text{P}_8\text{C}_{48}\text{H}_{40}$, $\text{Mo}_{12}\text{NaS}_2\text{O}_{52}\text{P}_8\text{C}_{48}\text{H}_{40}$, and $\text{Mo}_{12}\text{NaS}_6\text{O}_{48}\text{P}_8\text{C}_{48}\text{H}_{40}$, which are abbreviated as Mo_{12} , $\text{Mo}_{12}@\text{S}_2$, and $\text{Mo}_{12}@\text{S}_6$, respectively. Together, they are referred to as $\text{Mo}_{12}\text{-TC}$. These clusters exhibit nearly identical exterior structures, making them indistinguishable, leading to their cocrystallization in a single unit cell with 50%, 25%, and 25% occupancy for Mo_{12} , $\text{Mo}_{12}@\text{S}_2$, and $\text{Mo}_{12}@\text{S}_6$, respectively, and could not be separated easily. To confirm their molecular formulae and occupancy within a crystal, we conducted single-crystal X-ray diffraction (SCXRD) and high-resolution electrospray ionization–mass spectrometry (ESI-MS) studies. The clusters exhibit a dumbbell-like shape, with each terminal of the dumbbell comprising a hexagonal Mo_6 basal plane shielded by multiple oxo, and oxosulfide moieties for Mo_{12} and $\text{Mo}_{12}@\text{S}_2/\text{Mo}_{12}@\text{S}_6$ clusters, respectively. Additionally, the clusters are protected by a ligand shell consisting of vertically aligned phenylphosphonic acid (PPA). $\text{Mo}_{12}\text{-TC}$ demonstrates promising activity for electrochemical hydrogen and oxygen evolution reactions (HER and OER). $\text{Mo}_{12}\text{-TC}$ exhibits overpotentials of 0.262 and 0.413 V vs RHE to reach HER current densities (in H_2SO_4) of 10 and 100 mA cm^{-2} , respectively, and overpotentials of 0.45 and 0.787 V vs RHE to reach OER current densities (in KOH) of 10 and 100 mA cm^{-2} , respectively, stable up to 5000 cycles. Density functional theory (DFT) calculations further elucidate their electrocatalytic potential, revealing the presence of active sites within these molecular frameworks.



A diverse group of anionic polynuclear metal-oxo clusters (POMs), with a general formula $[\text{M}_m\text{O}_y]^{4-}$ (where M represents principally metals, such as Mo, W, V, and Nb), act as catalysts in a wide range of chemical transformations.^{1–3} The continued interest in this field stems from the remarkable physical and chemical properties exhibited by these clusters, which arise from their flexible composition, structure, size, charge distribution, photochemistry, and redox chemistry.^{4–9} The multidimensional assembly of these molecular cluster materials has led to the formation of various nanostructural and microstructural solids.^{10,11} As conventional POM chemistry expands, it intersects with a range of scientific disciplines, including materials science, catalysis, nanotechnology, surface science, biology, magnetism,

sensors, supramolecular materials, colloid science, memory devices, and molecular materials, thereby adding new dimensions to the field.^{12–27}

Pristine POMs have certain drawbacks, such as low conductivity and tendency for aggregation, degradation, and leaching, which limit their applications. However, a funda-

Received: August 20, 2023

Revised: November 2, 2023

Accepted: November 8, 2023

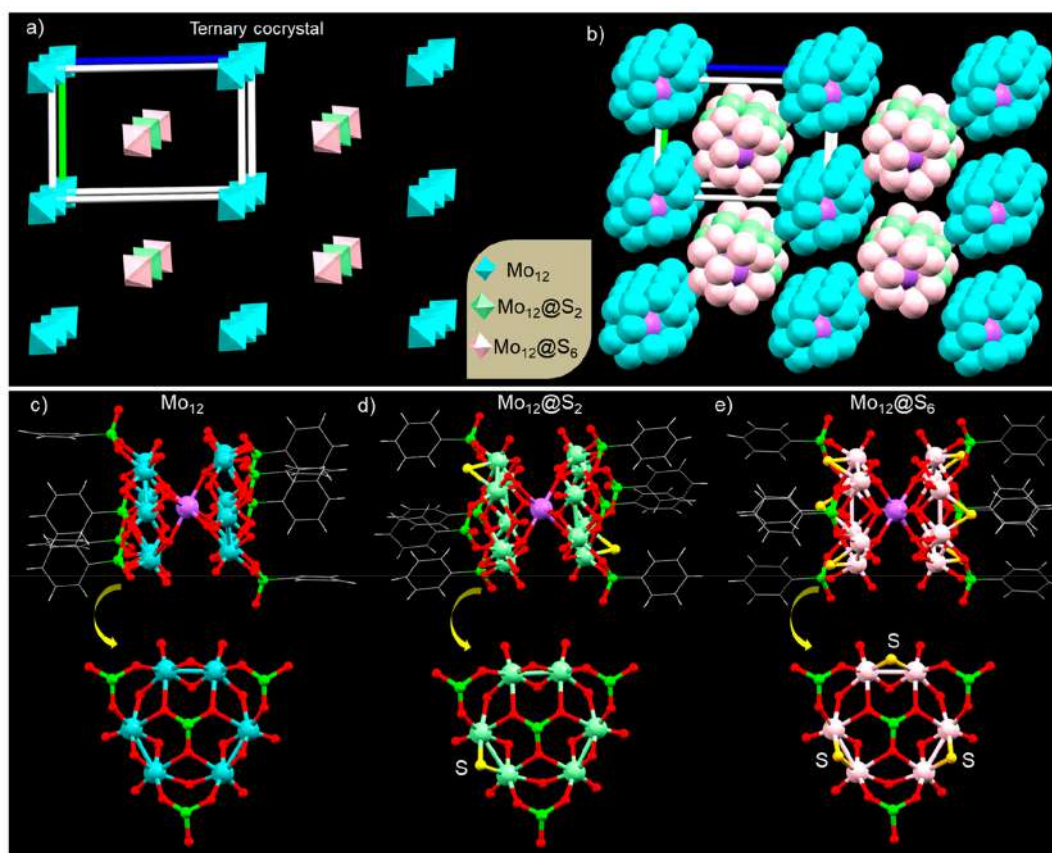


Figure 1. Single-crystal structures of the Mo₁₂-TC. (a) Schematic representation of the (2 × 2 × 2) unit cell of the ternary cocrystallized solid having the respective clusters. (b) Structural arrangement of the inner NaMo₁₂ units in the same lattice. The total molecular structures of (c) Mo₁₂, (d) Mo₁₂@S₂, and (e) Mo₁₂@S₆ clusters including PPA ligands. [Color labels: sky blue, pink, and light green = Mo; yellow = S; red = O, green = P, purple = Na; gray = C, white = H.]

mental characteristic of POMs is their ease of functionalization through the introduction of metal ions and other ligands.²⁸ This process of functionalization is widely employed to modify existing properties or introduce new ones, which is particularly valuable in catalysis, molecular magnetism, electrochemistry, dye-sensitized solar cells, and electrochemical water splitting.^{2,3,28} Derivatization involves the incorporation of specific metallic centers into the polyoxometalate frameworks.^{29,30} Alternatively, functionalization can be achieved by substituting oxo ligands with others, such as cyclopentadienyl derivatives, nitrogen-containing ligands, or sulfides. Introducing soft donating centers, such as S atoms, into the POM framework offers the potential for the emergence of novel properties. Since both O and S are constituents of group 6A within the periodic table, their chemical properties are very similar and substitution reactions between them are prone to occur.³¹ S-coordinated transition-metal-based POMs are efficient catalysts, due to their ability to facilitate electron and proton transfer, which is crucial for electrocatalytic and photoelectrocatalytic processes like HER and OER.^{32–40} Recently, capsules-like oxosulfur-based Mo-nanostructures encapsulated Ru nanoparticle was designed by Chen et al., which shows exceptional OER and HER dual activity and stability.⁴¹ These systems exhibit excellent electrochemical properties characterized by a rapid and highly reversible redox activity. Amiin et al. reported a cost-effective, operationally stable, multifunctional, and highly efficient vertically aligned MoS₂ electrocatalyst encapsulated with N-doped carbon frameworks.⁴²

In the past five years, there have been discoveries of new types of cluster cocrystals. These solids consist of multiple clusters arranged in a lattice structure, resulting in new properties.^{43,44} Several materials containing noble-metal clusters, particularly silver and copper clusters, have been structurally characterized during this period.^{45–48} Indistinguishable arrangements of the surface ligands and ligand-specific interparticle interactions resulted in these solids. From the perspective of transition-metal clusters, Roy et al. have synthesized various binary cocrystallized solids by combining superatomic Co₆ and Cr₆ clusters with molecular C₆₀ and C₇₀ clusters.^{49–51} These cocrystallized materials have demonstrated superconductive phonon and electron transport, polarized optical emission, and magnetic ordering behaviors, due to the electronic coupling of oppositely charged ionic species.^{52–55} POMs also formed cocrystallized materials with proteins, peptides, polycyclic aromatic hydrocarbons, carbon nanotubes, and silver clusters, resulting in functional materials.^{56–61}

By controlling the assembly of polyoxometallate clusters within a cocrystallized solid, it becomes possible to customize their properties, thus creating new opportunities to explore their potential applications. Despite this, the utilization of such cocrystallized solids in applications, particularly electrochemical water splitting, has been limited. In this work, we focused on the collective functional properties of cocrystallized molybdenum oxo-sulfide clusters. Through a conventional ambient wet chemical synthesis, we successfully synthesized mixed oxo-sulfide clusters of molybdenum. The resulting

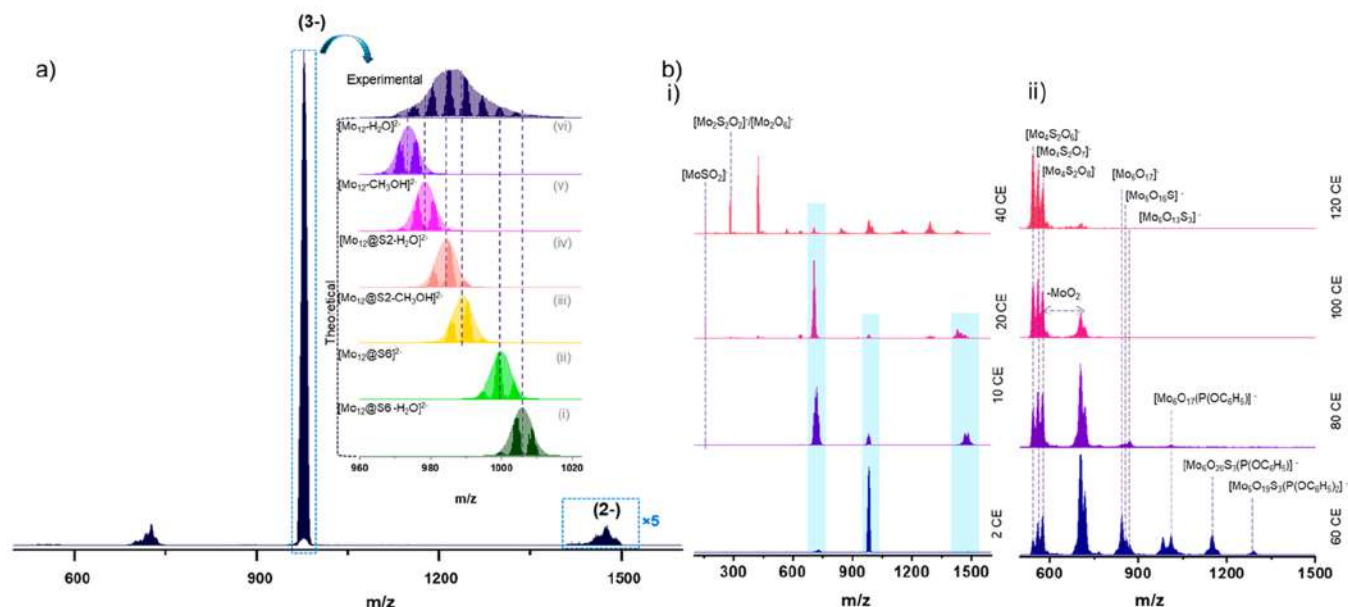


Figure 3. (a) High-resolution ESI-MS spectrum of the Mo₁₂-TC having an intense peak at m/z 989 and a mild peak at m/z 1484 in trianionic and dianionic charge states, respectively. Inset shows the exact matching of the experimental spectrum with the theoretical spectrum of the molecular compositions of cocrystallized clusters. (b) CE-dependent MS/MS fragmentation pattern of the major parent peak (m/z 989).

eight, and out of eight, seven are connected with O/S and one with a Mo atom (Figures 1c–e).

The binding of PPA ligands with the Mo atoms through Mo–O bonding is shown in Figure S7 in the Supporting Information. Each Mo₆ unit is connected with four PPA ligands, whereas the central PPA is connected with three oxygens arranged in a tripodal fashion and each oxygen is further bonded with a nonbonded Mo₂ unit in μ_2 mode. The other three PPA units are present at the periphery of the Mo₆ unit. Two O atoms of these three PPA ligands are connected with the Mo₆ unit, and the remaining one is free. The connected two O atoms are attached with Mo. Comparative P–O bond distances of different PPA ligands are presented in Table S4 in the Supporting Information. The average distance between central phosphorus and peripheral phosphorus is 4.68 Å, and the average distance between centroids of the central phenyl ring with the peripheral phenyl rings is \sim 4.84 Å (shown in Figure S7).

Supramolecular packing of these clusters along the different crystallographic axes is shown in Figures 2a and 2b, and the corresponding structures of ligands are also shown (Figures 2c and 2d). Careful analysis reveals that these clusters are packed in a layer-by-layer fashion along both the a - and b -axes. Careful analysis reveals that there are three types of intermolecular interactions (CH \cdots π , CH \cdots HC, and O \cdots O; see Figure S8 in the Supporting Information). To visualize the layered intermolecular packing, we have directly imaged the single crystals using conventional transmission electron microscopy (TEM), following the technique developed in our group.⁶² Although clusters are beam-sensitive, they could be imaged under appropriate conditions, as shown previously.⁶³ TEM micrographs of the ground cocrystals show different atomic layers with interlayer spacings of 1.30 and 1.13 nm (shown in Figures 2e and 2f) corresponding to lattice planes of (010) and (101), respectively, which are consistent with the interlayer spacing of Mo₁₂ crystallites resolved from SCXRD (shown in Figure 2g and 2h).

The molecular composition of Mo₁₂-TC was analyzed using high-resolution ESI-MS investigations in the negative ion mode, after dissolving a few crystals in methanol (Figure 3a). In the mass spectrum, two broad peaks were detected within the m/z range of 950–1040 (as major peak) and m/z 1440–1640, representing trianionic and dianionic charge states, respectively. The trianionic peak observed at m/z 950–1040 corresponds to the molecular species of the three-clusters i.e., Mo₁₂, Mo₁₂@S₂, Mo₁₂@S₆ found in the crystal structure. Theoretical mass calculations revealed that the crystal consisted of these clusters and a certain number of water and methanol molecules that were derived from the solvent system. Similar solvent-associated peaks were also observed in other metal nanoclusters.^{64–66} The broad isotopic distribution in the mass spectrum can be attributed to two factors: (1) molybdenum (Mo) has seven naturally stable isotopes, resulting in a wide isotopic distribution along with the contributions of naturally abundant isotopes from various atoms i.e., Na, O, S, C, P, and H present in the nanoclusters, and (2) the small mass differences ($\Delta m \approx 9$ –11) between individual nanoclusters in their trianionic state. Additionally, these nanoclusters ionize by getting attached to one or two solvent molecules (H₂O = 18 and MeOH = 32), which further contributes to the broad distribution of a specific charge state observed.

In order to gain a deeper understanding of the structure, the peaks within the m/z range 950–1040 were subjected to collision-induced dissociation (CID) by isolating them within the ion trap. This isolation step aimed to eliminate other ionic species present in the gas phase. The selected ions were then subjected to sequential fragmentation upon collision with argon gas. Upon sequential increase of CE up to 20, the trianionic species underwent fragmentation through CID, resulting in two distinct sets of peaks at m/z 1436–1510 and m/z 690–740, with the charge state of -1 and -2 , respectively (shown in Figure 3b). These peaks were attributed to the cleavage of the molybdenum nanoclusters, where

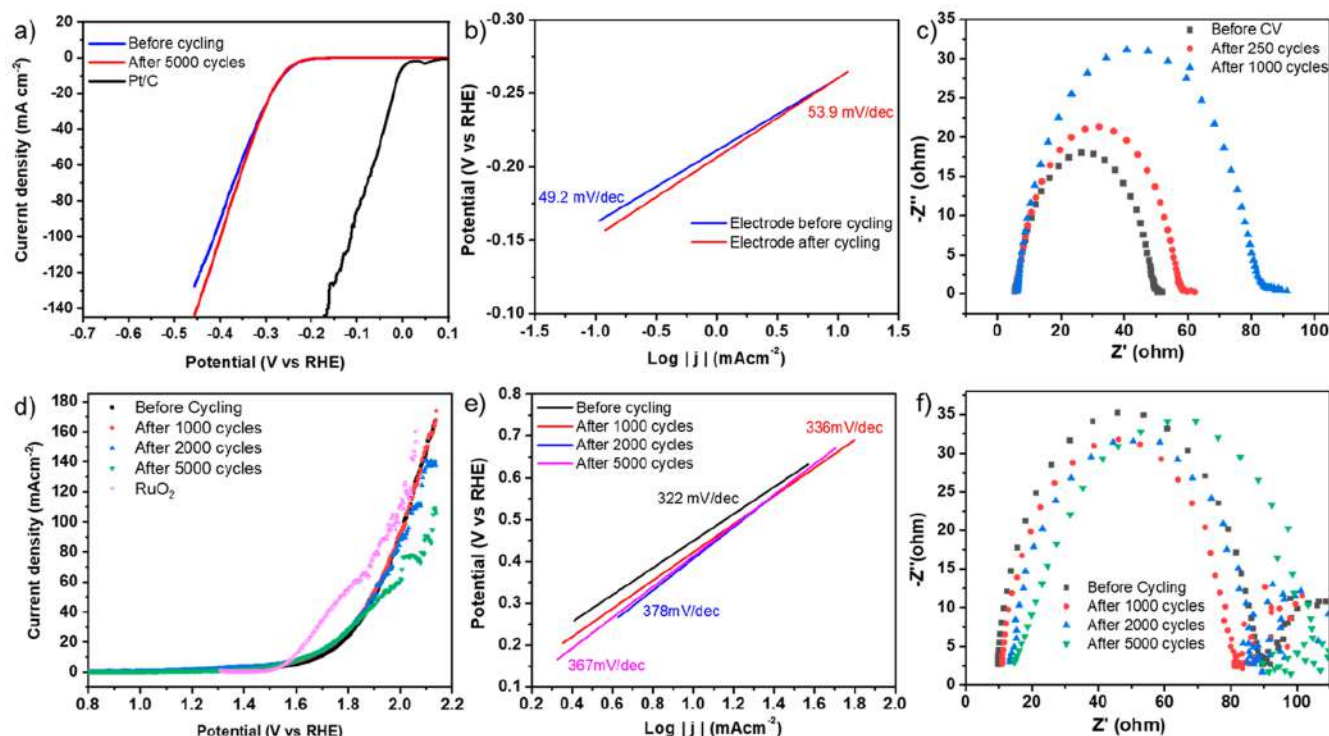


Figure 4. (a) Comparative LSV polarization curves of Mo₁₂-TC for HER before and after 5000 cycles. (b) Tafel plots of the polarization curves (before and after cycling). (c) EIS spectra showing R_{CT} during HER in 0.5 M H₂SO₄ at -0.256 V (vs RHE). (d) Comparative polarization curves of the Mo₁₂-TC catalyst clusters for the OER initially and after 1000, 2000, and 5000 cycles. (e) Tafel plots of the polarization curve (initially and after 1000, 2000, 5000 cycles) and (f) EIS spectra of cluster showing R_{CT} during the OER in 1.0 M KOH at 1.74 V (vs RHE).

fragments attached to Na were ionized as a monoanionic fragment, while the other half without Na was ionized as a dianionic fragment. As the applied collision energy reached the range of 10–20, H₂O and CH₃OH groups started to detach from the nanoclusters. The detachment confirmed the weak interaction between the solvent molecules and the parent nanoclusters.

At higher collisional energy (>20), two distinct pathways of fragmentation were observed. The first pathway involved the generation of fragment ions derived from sodiated fragment ions, while the second pathway involved fragments produced from the dianionic fragment ions. Both monoanionic and dianionic fragments simultaneously gave rise to constituent daughter ions as the collision energy was increased. Peripheral ligands attached to the nanoclusters, specifically PPA groups, were subsequently detached (occurring at an applied collisional energy of 60–80, as depicted in Figure 3b), followed by the fragmentation of the metal-oxo/sulfido kernels. This indicates direct binding of the PPA ligands at the peripheral sites of the nanoclusters. Fragmentation of the Mo–O–S core in the parent nanoclusters resulted in the formation of ions such as [Mo₆O₁₃S₃][−], [Mo₆O₁₆S][−], [Mo₆O₁₇][−], [Mo₄S₂O₈][−], [Mo₄S₂O₇][−], and [Mo₄S₂O₆][−] in the collision energy range of 100–120. Smaller fragment ions, including [MoSO₂][−], [Mo₂S₂O₂][−], and [Mo₂O₆][−] ions, were detected at a lower m/z range. The sequential fragmentation observed during CID further supports the structural integrity of the clusters. The binding of PPA ligands was additionally confirmed by using FT-IR, which exhibited characteristic vibrational peaks at 1395 and 950 cm^{−1} corresponding to the P–O stretching and cage

breathing modes, respectively (Figure S9 in the Supporting Information).

The catalytic HER performance of Mo₁₂-TC was evaluated in 0.5 M H₂SO₄ solution using a conventional three-electrode electrochemical setup. A graphite rod, a saturated calomel electrode (SCE), and the microcrystalline catalyst coated on glassy carbon (GC) electrode were used as the counter, reference, and working electrodes, respectively. Linear sweep voltammetry (LSV) polarization studies were performed to analyze the HER activity of the cluster at a scan rate of 5 mV s^{−1}, as presented in Figure 4a. The Mo₁₂-TC catalyst demonstrated promising HER activity that required an overpotential of 0.262 V to achieve a current density of 10 mA cm^{−2} and 0.413 V to reach a current density of 100 mA cm^{−2}. The stability of the cluster was assessed through an accelerated durability test between 0 and 0.4 V (vs RHE) at 100 mV s^{−1}. A small increase (2 mV) in overpotential (at 10 mA cm^{−2}) was observed after 5000 cycles, indicating that these cocrystallized materials are stable for long-term use without a significant loss in catalytic performance (Figure 4a). The Tafel analysis (shown in Figure 4b), indicative of the electron transfer rate and mechanism (rate determining step) at the electrode–electrolyte interface, yielded a Tafel slope of 49.2 mV dec^{−1} for this catalyst. We infer that the obtained fast electron transfer at the interface resulted in enhanced HER activity through the Volmer–Heyrovsky mechanism.⁶⁷ The small increase (4.7 mV dec^{−1}) in the Tafel slope after cycling confirms the catalytic stability of Mo₁₂-TC. The charge-transfer resistance (R_{CT}) values for the cluster were calculated from electrochemical impedance spectroscopy (EIS), measured at a potential of -0.256 V vs RHE. The result is shown in Figure 4c

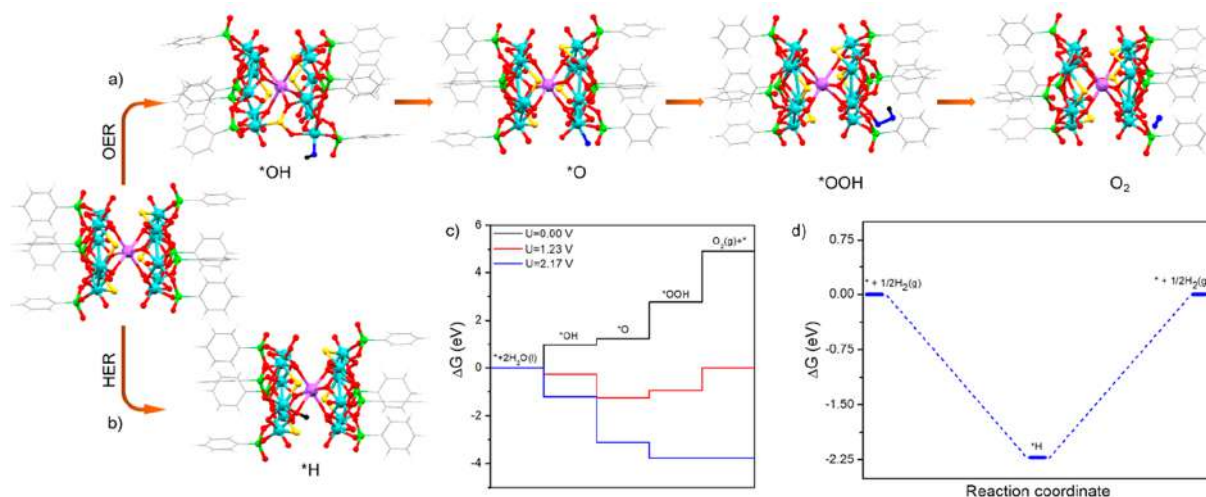


Figure 5. (a) Adsorption configurations of *OH, *O, and *OOH adduct intermediates and the O₂ end product of the Mo₁₂@S₄ cluster involved in the OER pathway. (b) Adsorption configuration of activated hydrogen species (*H) on the cluster. (c) Calculated OER free-energy profile for the cluster at different potentials. The free-energy profiles at 0 V (black), equilibrium potential of 1.23 V (red), and the limiting potential of 2.17 V (blue) are shown. (d) Free-energy profile of HER activity of the cluster. [Color labels: cyan = Mo; red = O, green = P, purple = Na, gray = C, white = H. The O and H atoms in the adsorption configurations of OER and HER intermediates are shown in blue and black, respectively.]

as a Nyquist plot, where the *x*- and *y*-axes are the real and negative imaginary parts of impedance, respectively. The Nyquist plots from the EIS spectra on the Mo₁₂-TC catalyst at different stages were fitted using equivalent Randles circuit models (as shown in Figures S10 and S11 in the Supporting Information) for accurately depicting the impedance behavior of the system and deconvoluting the components (series resistance, charge-transfer resistance, and constant phase elements) from the fitting parameters (as tabulated in Table S5 in the Supporting Information).

Figure 4c shows that *R*_{CT} does not change significantly after several cycles, with values of ~44.1, ~52.7, and ~76.8 Ω for the cluster, in the beginning, after 250 cycles, and after 1000 cycles. The observed changes could be attributed to the formation of passivating layers on the electrode or the formation of bubbles during the measurement. These layers could hinder the transport of electrons and flow of reactants to and from the electrode surface, impeding the overall electrochemical process.

Although the LSV after 5000 cycles of the accelerated degradation test (ADT) shows slightly higher current in the more negative potential range, in the onset region, where the EIS was recorded, the 5000 C LSV is slightly left-shifted (compared to the pristine catalyst LSV) leading to higher *R*_{CT} values, as observed in the EIS studies. This effect was more pronounced during the initial cycling stages (first 500/1000 ADT cycles), until a more stable current and polarization curve was obtained after structural stabilization.

The electrocatalytic OER performance of Mo₁₂-TC was investigated in an alkaline medium (1 M KOH) using a similar cell setup. The polarization curves measured at a scan rate of 5 mV s⁻¹ exhibit excellent activities for electrochemical OER with an onset potential (potential to reach a current density of 1 mA cm⁻²) of ~1.35 V (vs RHE) and overpotentials of 455, 545, 596, 635, and 787 mV at 10, 20, 30, 40, and 100 mA cm⁻², respectively (Figure 4d). The comparisons of the HER and OER catalytic performance of Mo₁₂-TC with the state-of-the-art Pt/C and RuO₂ catalysts are shown in Figures 4a and

4d, for reference. Figure 4d also depicts the LSVs after 1000, 2000, and 5000 cycles, showing no significant increase in overpotentials, indicating that these clusters are durable. The sudden shift (toward a more positive potential) in the OER LSV (beyond 1.9 V) after 5000 cycles is probably due to the accumulation and evolution of high amounts of bubbles on the nonporous electrode surface leading to poor electrode–electrolyte contact and materials falling off from the coated catalyst layer. Figure 4e shows the Tafel plots for the OER in the initial condition and after 1000, 2000, and 5000 cycles. The cluster exhibits a Tafel slope of 322 mV dec⁻¹, which increases slightly to 367 mV dec⁻¹ after 5000 cycles. EIS study shows the *R*_{CT} value to be ~78.7 Ω before cycling and ~70.8, ~72.8, ~91.2 Ω after 1000, 2000, and 5000 cycles, respectively, at 1.74 V (vs RHE, ~15 mA cm⁻²) (Figure 4f). The increase in *R*_{CT} values after several cycles can be attributed to marginal deactivation of the catalyst during OER. Moreover, to understand the post-electrocatalytic stability, as well the stability of the catalyst in different electrolytes, various spectroscopic and diffraction studies, such as UV-vis, attenuated total reflectance Fourier transform infrared (FTIR), X-ray photoelectron spectroscopy (XPS), X-ray diffraction (XRD) and Raman studies of the Mo₁₂-TC were performed, as provided in Figures S12–S14 and Tables S6 and S7 in the Supporting Information. Based on these combined studies broadly, the catalyst was found to be structurally and chemically stable under the catalytic conditions. Observed fluctuations in the XPS studies can arise from various surface oxidized species, adsorbed chemicals, electrolytes, and impurities and some expected changes in the elemental oxidation states on the surface during electrocatalysis. Further, we performed cyclic voltammetry (CV) studies at different scan rates on Mo₁₂-TC coated electrodes in the acidic medium (Figure S15 in the Supporting Information) to determine the double layer capacitance (*C*_{dl}). The *C*_{dl} value, comparable to the ECSA (electrochemical active surface area) of the catalyst, was obtained from the current density in the anodic and

cathodic sweeps, ΔJ ($|j_{\text{Cat}} - j_{\text{An}}|$), vs scan rate plot as 0.5 mF cm^{-2} .⁶⁸

Density functional theory (DFT) was employed to study the reaction mechanism of HER and OER over $\text{Mo}_{12}@\text{S}_4$ cluster using the Vienna Ab-Initio Simulation Package (VASP) with the Perdew–Burke–Ernzerhof (PBE) functional under generalized gradient approximation (GGA).^{69–71} To circumvent the computational cost, we have modeled a single molecular unit of $\text{Mo}_{12}@\text{S}_4$ cluster and considered it for further calculations. DFT optimized structures of Mo_{12} and $\text{Mo}_{12}@\text{S}_4$ are shown in Figure S16 in the Supporting Information and the electron density maps of the frontier molecular orbitals of the cluster are shown in Figures S17 and S18 in the Supporting Information. We simulated the OER using a four-electron transfer reaction mechanism involving $^*\text{O}$, $^*\text{OH}$, and $^*\text{OOH}$ (where the asterisk symbol (*) denotes the adsorbed species) intermediates (Figure 5a). The most stable binding modes of these intermediates were found to be one-fold binding (Figure 5a). The intermediates $^*\text{OH}$ and $^*\text{O}$ exhibited binding to the Mo site, while the lowest-energy geometry for $^*\text{OOH}$ exhibited binding to the O site of the cluster. Figure 5c shows the free-energy change of each intermediate steps involved in the reaction, which is calculated via the following equation:

$$\Delta G = \Delta E + \Delta \text{ZPE} - T\Delta S \quad (1)$$

where T is the temperature (298 K) and E , ZPE, and S are the total energy, zero-point energy, and the entropy of adsorbed hydrogen, respectively. The computed Gibbs free energy changes for $\text{H}_2\text{O} \rightarrow ^*\text{OH}$, $^*\text{OH} \rightarrow ^*\text{O}$, $^*\text{O} \rightarrow ^*\text{OOH}$ and $^*\text{OOH} \rightarrow \text{O}_2(\text{g})$ are 0.97, 0.26, 1.52, and 2.17 eV, respectively. The potential-determining step (PDS) of the reaction was found to be the transformation of $^*\text{OOH}$ into O_2 which could be attributed to the strong adsorption of $^*\text{OOH}$ at the O site, which reduces the feasibility of it undergoing further oxidation. The higher value for overpotential (0.94 eV) obtained from DFT calculations, with respect to the experiment, could be attributed to the single molecular unit approximation of the cluster as well as the absence of explicit solvent interactions and dynamic effects in the calculations, which may play a crucial role in determining the catalytic activity under experimental conditions. We have performed a comparative OER theoretical calculation using the Mo_{12} cluster (without any S atoms). The presence of S in the cluster not only facilitates the overall OER catalytic performance of the cluster but also reduces the overpotential of the reaction (see Figure S19 in the Supporting Information).

Similarly, we have studied the energetics of the HER event over the $\text{Mo}_{12}@\text{S}_4$. The free energy change (ΔG_{H^*}) of the formation of activated hydrogen species is -2.22 eV (Figure 5d). This supports the experimental observation that the cluster acts as an efficient HER catalyst. Figure 5b shows the adsorption configuration of active hydrogen ($^*\text{H}$) on the cluster.

In summary, we presented a new type of cocrystallized structurally similar molybdenum oxo-sulfide clusters. These clusters were synthesized under ambient conditions by the reduction of NaMoO_4 and $\text{Na}_2\text{S}_2\text{O}_4$ precursors in the presence of S. $\text{Mo}_{12}\text{-TC}$ was characterized using various characterization techniques (SCXRD, ESI-MS, FT-IR, etc.). SCXRD reveals that each unit cell consists of three clusters (Mo_{12} , $\text{Mo}_{12}@\text{S}_2$, and $\text{Mo}_{12}@\text{S}_6$) with 50%, 25%, and 25% occupancy, respectively. This POM has two oval-shaped Mo_6 -oxo/sulfide

units, which are connected with a Na atom through oxygen centers. High-resolution mass spectrometry showed the presence of these clusters in solution, and the CID-MS studies reveal the losses of MoOS , and MoO_2 fragments from the parent species, which further confirm the presence of oxygen and sulfur moieties in the structure. Furthermore, the intermolecular layers of these clusters present in the crystals were imaged directly using conventional transmission electron microscopy. The cocrystallized nanocluster catalyst performed excellently as inexpensive, efficient, and stable electrocatalysts for both HER and OER, requiring moderate overpotentials for reaching current densities of 100 mA cm^{-2} . The catalyst exhibits good electrocatalytic stability, retaining its activity and electron transfer kinetics after 5000 cycles. The mechanistic details of the clusters' water splitting activities were examined by DFT calculations, which identified the stable adsorption configurations: i.e., mixed oxo and sulfide sites for the OER, and Mo as energetically favorable sites for the HER activity.

■ ASSOCIATED CONTENT

Supporting Information

The Supporting Information is available free of charge at <https://pubs.acs.org/doi/10.1021/acsmaterialslett.3c00957>.

Details of chemical used, experimental section, instrumentation, X-ray crystallographic details, computational details, and additional experimental data (PDF)

Single-crystal X-ray data of nanocluster (CIF)

Single-crystal X-ray data of nanocluster (CIF)

Single-crystal X-ray data of nanocluster (CIF)

Single-crystal X-ray data of nanocluster (CIF)

Single-crystal X-ray data of nanocluster (CIF)

Single-crystal X-ray data of nanocluster (CIF)

Single-crystal X-ray data of nanocluster (CIF)

Single-crystal X-ray data of nanocluster (CIF)

Single-crystal X-ray data of nanocluster (CIF)

Single-crystal X-ray data of nanocluster (CIF)

■ AUTHOR INFORMATION

Corresponding Authors

Thalappil Pradeep – DST Unit of Nanoscience (DST UNS) & Thematic Unit of Excellence (TUE), Department of Chemistry, Indian Institute of Technology–Madras, Chennai 600036, India; International Centre for Clean Water, Chennai 600113, India; orcid.org/0000-0003-3174-534X; Email: pradeep@iitm.ac.in

Pulickel M. Ajayan – Department of Materials Science and NanoEngineering, Rice University, Houston, Texas 77005, United States; orcid.org/0000-0001-8323-7860; Email: ajayan@rice.edu

Biswarup Pathak – Department of Chemistry, Indian Institute of Technology Indore, Indore 453552, India; orcid.org/0000-0002-9972-9947; Email: biswarup@iiti.ac.in

Authors

Biswajit Mondal – DST Unit of Nanoscience (DST UNS) & Thematic Unit of Excellence (TUE), Department of Chemistry, Indian Institute of Technology–Madras, Chennai 600036, India

Arijit Jana – DST Unit of Nanoscience (DST UNS) & Thematic Unit of Excellence (TUE), Department of Chemistry, Indian Institute of Technology–Madras, Chennai 600036, India

Jayoti Roy – DST Unit of Nanoscience (DST UNS) & Thematic Unit of Excellence (TUE), Department of Chemistry, Indian Institute of Technology–Madras, Chennai 600036, India

Astrid Campos Mata – Department of Materials Science and NanoEngineering, Rice University, Houston, Texas 77005, United States

Akhil S. Nair – Department of Chemistry, Indian Institute of Technology Indore, Indore 453552, India; The NOMAD Laboratory at the FHI of the Max-Planck Gesellschaft and IRIS-Adlershof of the Humboldt-Universität zu Berlin, Berlin 14195, Germany; orcid.org/0000-0001-5723-3970

Ananthu Mahendranath – DST Unit of Nanoscience (DST UNS) & Thematic Unit of Excellence (TUE), Department of Chemistry, Indian Institute of Technology–Madras, Chennai 600036, India

Soumyabrata Roy – Department of Materials Science and NanoEngineering, Rice University, Houston, Texas 77005, United States

Complete contact information is available at:

<https://pubs.acs.org/10.1021/acsmaterialslett.3c00957>

Author Contributions

^VThese authors contributed equally in this project. B.M. planned and designed the whole project, with input from T.P.; he synthesized the clusters and did the initial characterization. He wrote the first draft of the manuscript. A.J. helped in crystallization of clusters and also contributed to the production of figures and writing of the manuscript. J.R. helped in synthesis of clusters and carried out the MS study; she also contributed to the analysis of MS data. A.C.M. and S.R. conducted electrocatalytic measurements and characterizations of the cluster electrodes, contributed in the manuscript drafting and revisions under the supervision of P.M.A. A.S.N. performed theoretical calculations under the guidance of B.P. A.M. contributed to the analysis of TEM micrographs of crystals. T.P. supervised the whole project and finalized the manuscript.

Notes

The authors declare no competing financial interest.

ACKNOWLEDGMENTS

We thank the Sophisticated Analytical Instruments Facility, IIT Madras, and Sudhadevi Antharjanam for the SC-XRD measurements. We thank Babu Varghese for the refinement of SC-XRD data. B.M. thanks IIT Madras for the fellowship. T.P. acknowledges funding from the Centre of Excellence on Molecular Materials and Functions under the Institution of Eminence scheme of IIT Madras. We thank the Department of Science and Technology, Government of India, for continuous support of our research program.

REFERENCES

- (1) Long, D. L.; Tsunashima, R.; Cronin, L. Polyoxometalates: Building Blocks for Functional Nanoscale Systems. *Angew. Chem. - Int. Ed.* **2010**, *49*, 1736–1758.
- (2) Wang, S. S.; Yang, G. Y. Recent Advances in Polyoxometalate-Catalyzed Reactions. *Chem. Rev.* **2015**, *115* (11), 4893–4962.
- (3) Azmani, K.; Besora, M.; Soriano-López, J.; Landolsi, M.; Teillout, A. L.; de Oliveira, P.; Mbomekallé, I. M.; Poblet, J. M.; Galán-Mascarós, J. R. Understanding Polyoxometalates as Water Oxidation Catalysts through Iron vs Cobalt Reactivity. *Chem. Sci.* **2021**, *12* (25), 8755–8766.
- (4) Papaconstantinou, E.; Hiskia, A. Photochemistry and Photocatalysis by Polyoxometalates. In *Polyoxometalate Molecular Science*; Springer, Dordrecht, The Netherlands, 2003; pp 381–416, DOI: [10.1007/978-94-010-0091-8_13](https://doi.org/10.1007/978-94-010-0091-8_13).
- (5) Ye, J. C.; Chen, J. J.; Yuan, R. M.; Deng, D. R.; Zheng, M. S.; Cronin, L.; Dong, Q. F. Strategies to Explore and Develop Reversible Redox Reactions of Li-S in Electrode Architectures Using Silver-Polyoxometalate Clusters. *J. Am. Chem. Soc.* **2018**, *140* (8), 3134–3138.
- (6) Lei, J.; Yang, J.-J.; Liu, T.; Yuan, R.-M.; Deng, D.-R.; Zheng, M.-S.; Chen, J.-J.; Cronin, L.; Dong, Q.-F. Tuning Redox Active Polyoxometalates for Efficient Electron-Coupled Proton-Buffer-Mediated Water Splitting. *Chem.-Eur. J.* **2019**, *25* (49), 11432–11436.
- (7) Streb, C.; Kastner, K.; Tucher, J. Polyoxometalates in Photocatalysis. In *Chemical Photocatalysis*; Walter de Gruyter GmbH, 2020; pp 363–378, DOI: [10.1515/9783110576764-015](https://doi.org/10.1515/9783110576764-015).
- (8) Streb, C. New Trends in Polyoxometalate Photoredox Chemistry: From Photosensitisation to Water Oxidation Catalysis. *Dalton Trans.* **2012**, *41* (6), 1651–1659.
- (9) Gumerova, N. I.; Rompel, A. Synthesis, Structures and Applications of Electron-Rich Polyoxometalates. *Nat. Rev. Chem.* **2018**, *2* (2), 1–20.
- (10) Yu, B.; Zhao, X.; Ni, J.; Yang, F. Multiscale Assembly of Polyoxometalates: From Clusters to Materials. *ChemPhysMater.* **2023**, *2* (1), 20–29.
- (11) Piot, M.; Abécassis, B.; Brouri, D.; Troufflard, C.; Proust, A.; Izzet, G. Control of the Hierarchical Self-Assembly of Polyoxometalate-Based Metallomacrocycles by Redox Trigger and Solvent Composition. *Proc. Natl. Acad. Sci. U.S.A.* **2018**, *115* (36), 8895–8900.
- (12) Ni, L.; Li, H.; Xu, H.; Shen, C.; Liu, R.; Xie, J.; Zhang, F.; Chen, C.; Zhao, H.; Zuo, T.; Diao, G. Self-Assembled Supramolecular Polyoxometalate Hybrid Architecture as a Multifunctional Oxidation Catalyst. *ACS Appl. Mater. Interfaces* **2019**, *11* (42), 38708–38718.
- (13) Stuckart, M.; Monakhov, K. Y. Polyoxometalates as Components of Supramolecular Assemblies. *Chem. Sci.* **2019**, *10* (16), 4364–4376.
- (14) Roy, S.; Crans, D. C.; Parac-Vogt, T. N. Editorial: Polyoxometalates in Catalysis, Biology, Energy and Materials Science. *Front. Chem.* **2019**, *7*, 646.
- (15) Gumerova, N. I.; Rompel, A. Interweaving Disciplines to Advance Chemistry: Applying Polyoxometalates in Biology. *Inorg. Chem.* **2021**, *60* (9), 6109–6114.
- (16) Busche, C.; Vilà-Nadal, L.; Yan, J.; Miras, H. N.; Long, D. L.; Georgiev, V. P.; Asenov, A.; Pedersen, R. H.; Gadegaard, N.; Mirza, M. M.; Paul, D. J.; Poblet, J. M.; Cronin, L. Design and Fabrication of Memory Devices Based on Nanoscale Polyoxometalate Clusters. *Nature* **2014**, *515* (7528), 545–549.
- (17) Veríssimo, M. I. S.; Evtuguin, D. V.; Gomes, M. T. S. R. Polyoxometalate Functionalized Sensors: A Review. *Front. Chem.* **2022**, *10*, 840657.
- (18) Chen, L.; Chen, W. L.; Wang, X. L.; Li, Y. G.; Su, Z. M.; Wang, E. B. Polyoxometalates in Dye-Sensitized Solar Cells. *Chem. Soc. Rev.* **2019**, *48* (1), 260–284.
- (19) Shi, D.; Zheng, R.; Liu, C.-S.; Chen, D. M.; Zhao, J.; Du, M. Dual-Functionalized Mixed Keggin- and Lindqvist-Type Cu₂₄-Based POM@MOF for Visible-Light-Driven H₂ and O₂ Evolution. *Inorg. Chem.* **2019**, *58* (11), 7229–7235.
- (20) Paille, G.; Gomez-Mingot, M.; Roch-Marchal, C.; Haouas, M.; Benseghir, Y.; Pino, T.; Ha-Thi, M. H.; Landrot, G.; Mialane, P.; Fontecave, M.; Dolbecq, A.; Mellot-Draznieks, C. Thin Films of Fully Noble Metal-Free POM@MOF for Photocatalytic Water Oxidation. *ACS Appl. Mater. Interfaces* **2019**, *11* (S1), 47837–47845.
- (21) Qin, J. S.; Du, D. Y.; Guan, W.; Bo, X. J.; Li, Y. F.; Guo, L. P.; Su, Z. M.; Wang, Y. Y.; Lan, Y. Q.; Zhou, H. C. Ultrastable Polymolybdate-Based Metal-Organic Frameworks as Highly Active Electrocatalysts for Hydrogen Generation from Water. *J. Am. Chem. Soc.* **2015**, *137* (22), 7169–7177.

- (22) Clemente-Juan, J. M.; Coronado, E.; Gaita-Ariño, A. Magnetic Polyoxometalates: From Molecular Magnetism to Molecular Spintronics and Quantum Computing. *Chem. Soc. Rev.* **2012**, *41* (22), 7464–7478.
- (23) Zheng, S. T.; Yang, G. Y. Recent Advances in Paramagnetic-TM-Substituted Polyoxometalates (TM = Mn, Fe, Co, Ni, Cu). *Chem. Soc. Rev.* **2012**, *41* (22), 7623–7646.
- (24) Duan, Y.; Clemente-Juan, J. M.; Giménez-Saiz, C.; Coronado, E. Large Magnetic Polyoxometalates Containing the Cobalt Cubane “[Co^{III}Co₃^{II}(OH)₃(H₂O)_{6-m}(PW₉O₃₄)]^{3-*m*} (*m* = 3 or 5) as a Subunit. *Front. Chem.* **2018**, *6*, 231.
- (25) Luo, Z.; Kögerler, P.; Cao, R.; Hill, C. L. Synthesis, Structure, and Magnetism of a Polyoxometalate with Coordinatively Unsaturated d-Electron-Transition Metal Centers. *Inorg. Chem.* **2009**, *48* (16), 7812–7817.
- (26) Čolović, M. B.; Lacković, M.; Lalatović, J.; Mougharbel, A. S.; Kortz, U.; Krstić, D. Z. Polyoxometalates in Biomedicine: Update and Overview. *Curr. Med. Chem.* **2020**, *27* (3), 362–379.
- (27) Bijelic, A.; Aureliano, M.; Rompel, A. Polyoxometalates as Potential Next-Generation Metalloids in the Combat Against Cancer. *Angew. Chem., Int. Ed.* **2019**, *58* (10), 2980–2999.
- (28) Dolbecq, A.; Dumas, E.; Mayer, C. R.; Mialane, P. Hybrid Organic-Inorganic Polyoxometalate Compounds: From Structural Diversity to Applications. *Chem. Rev.* **2010**, *110* (10), 6009–6048.
- (29) Liu, R.; Cao, K.; Clark, A. H.; Lu, P.; Anjass, M.; Biskupek, J.; Kaiser, U.; Zhang, G.; Streb, C. Top-down Synthesis of Polyoxometalate-like Sub-Nanometer Molybdenum-Oxo Clusters as High-Performance Electrocatalysts. *Chem. Sci.* **2020**, *11* (4), 1043–1051.
- (30) Weinstock, I. A.; Schreiber, R. E.; Neumann, R. Dioxxygen in Polyoxometalate Mediated Reactions. *Chem. Rev.* **2018**, *118* (5), 2680–2717.
- (31) Zhang, G.; Wang, X. Oxyulfid-Halbleiter Für Die Photokatalytische Wasserspaltung Mit Sichtbarem Licht. *Angew. Chem.* **2019**, *131* (44), 15726–15728.
- (32) Fielden, J.; Sumlin, J. M.; Han, N.; Geletii, Y. V.; Xiang, X.; Musaev, D. G.; Lian, T.; Hill, C. L. Water Splitting with Polyoxometalate-Treated Photoanodes: Enhancing Performance through Sensitizer Design. *Chem. Sci.* **2015**, *6* (10), 5531–5543.
- (33) Salazar Marcano, D. E.; Moussawi, M. A.; Anyushin, A. V.; Lentink, S.; Van Meervelt, L.; Ivanović-Burmazović, I.; Parac-Vogt, T. N. Versatile Post-Functionalisation Strategy for the Formation of Modular Organic-Inorganic Polyoxometalate Hybrids. *Chem. Sci.* **2022**, *13* (10), 2891–2899.
- (34) Roy, S.; Bagchi, D.; Vemuri, V.; Ch. Sarma, S.; Ahuja, V.; Rajaji, V.; Narayana, C.; Peter, S. C. Deconvolution of Phase-Size-Strain Effects in Metal Carbide Nanocrystals for Enhanced Hydrogen Evolution. *Nanoscale* **2020**, *12* (28), 15414–15425.
- (35) Roy, S.; Vemuri, V.; Maiti, S.; Manoj, K. S.; Subbarao, U.; Peter, C. Two Keggin-Based Isostructural POMOF Hybrids: Synthesis, Crystal Structure, and Catalytic Properties. *Inorg. Chem.* **2018**, *57* (19), 12078–12092.
- (36) Roy, S.; Mumbarradi, D.; Jain, A.; George, S. J.; Peter, S. C. Crystal Engineering in Supramolecular Polyoxometalate Hybrids through PH Controlled in Situ Ligand Hydrolysis. *Inorg. Chem.* **2018**, *57* (2), 590–601.
- (37) Roy, S.; Sarkar, S.; Pan, J.; Waghmare, U. V.; Dhanya, R.; Narayana, C.; Peter, S. C. Crystal Structure and Band Gap Engineering in Polyoxometalate-Based Inorganic–Organic Hybrids. *Inorg. Chem.* **2016**, *55* (7), 3364–3377.
- (38) Sarma, S. Ch.; Mishra, V.; Mary, K. A. A.; Roy, S.; Peter, S. C. Inverse Strain Effect in Atomic Scale—Enhanced Hydrogen Evolution Activity and Durability in Cu-Substituted Palladseite. *ACS Energy Lett.* **2018**, *3* (12), 3008–3014.
- (39) Khan, M. A.; Al-Attas, T.; Roy, S.; Rahman, M. M.; Ghaffour, N.; Thangadurai, V.; Larter, S.; Hu, J.; Ajayan, P. M.; Kibria, M. G. Seawater Electrolysis for Hydrogen Production: A Solution Looking for a Problem? *Energy Environ. Sci.* **2021**, *14* (9), 4831–4839.
- (40) Kumbhakar, P.; Parui, A.; Dhakar, S.; Paliwal, M.; Behera, R.; Gautam, A. R. S.; Roy, S.; Ajayan, P. M.; Sharma, S.; Singh, A. K.; Tiwary, C. S. Spontaneous Hydrogen Production Using Gadolinium Telluride. *iScience* **2023**, *26*, No. 106510.
- (41) Chen, D.; Yu, R.; Wu, D.; Zhao, H.; Wang, P.; Zhu, J.; Ji, P.; Pu, Z.; Chen, L.; Yu, J.; Mu, S. Anion-Modulated Molybdenum Oxide Enclosed Ruthenium Nano-Capsules with Almost the Same Water Splitting Capability in Acidic and Alkaline Media. *Nano Energy* **2022**, *100*, No. 107445.
- (42) Amiin, I. S.; Pu, Z.; Liu, X.; Owusu, K. A.; Monestel, H. G. R.; Boake, F. O.; Zhang, H.; Mu, S. Multifunctional Mo–N/C@MoS₂ Electrocatalysts for HER, OER, ORR, and Zn–Air Batteries. *Adv. Funct. Mater.* **2017**, *27* (44), 1702300.
- (43) Bodiuzzaman, M.; Dar, A.; Pradeep, T. Cocrystals of Atomically Precise Noble Metal Nanoclusters. *Small* **2021**, *17* (27), 2003981.
- (44) Wu, Z.; Yao, Q.; Zang, S.; Xie, J. Directed Self-Assembly of Ultrasmall Metal Nanoclusters. *ACS Mater. Lett.* **2019**, *1* (2), 237–248.
- (45) Chai, J.; Yang, S.; Lv, Y.; Chen, T.; Wang, S.; Yu, H.; Zhu, M. A Unique Pair: Ag₄₀ and Ag₄₆ Nanoclusters with the Same Surface but Different Cores for Structure-Property Correlation. *J. Am. Chem. Soc.* **2018**, *140* (46), 15582–15585.
- (46) Dar, W. A.; Bodiuzzaman, M.; Ghosh, D.; Paramasivam, G.; Khatun, E.; Sugi, K. S.; Pradeep, T. Interparticle Reactions between Silver Nanoclusters Leading to Product Cocrystals by Selective Cocrystallization. *ACS Nano* **2019**, *13* (11), 13365–13373.
- (47) Liu, J. Y.; Alkan, F.; Wang, Z.; Zhang, Z. Y.; Kurmoo, M.; Yan, Z.; Zhao, Q. Q.; Aikens, C. M.; Tung, C. H.; Sun, D. Different Silver Nanoparticles in One Crystal: Ag₂₁₀(ⁱPrPhS)₇₁(Ph₃P)₅Cl and Ag₂₁₁(ⁱPrPhS)₇₁(Ph₃P)₆Cl. *Angew. Chem.* **2019**, *58* (1), 195–199.
- (48) Huang, J. H.; Liu, L. Y.; Wang, Z. Y.; Zang, S. Q.; Mak, T. C. W. Modular Cocrystallization of Customized Carboranylthiolate-Protected Copper Nanoclusters via Host-Guest Interactions. *ACS Nano* **2022**, *16* (11), 18789–18794.
- (49) Roy, X.; Lee, C. H.; Crowther, A. C.; Schenck, C. L.; Besara, T.; Lalancette, R. A.; Siegrist, T.; Stephens, P. W.; Brus, L. E.; Kim, P.; Steigerwald, M. L.; Nuckolls, C. Nanoscale Atoms in Solid-State Chemistry. *Science (New York, N.Y.)* **2013**, *341* (6142), 157–160.
- (50) Yang, J.; Russell, J. C.; Tao, S.; Lessio, M.; Wang, F.; Hartnett, A. C.; Peurifoy, S. R.; Doud, E. A.; O'Brien, E. S.; Gadjieva, N.; Reichman, D. R.; Zhu, X.; Crowther, A. C.; Billinge, S. J. L.; Roy, X.; Steigerwald, M. L.; Nuckolls, C. Superatomic Solid Solutions. *Nat. Chem.* **2021**, *13* (6), 607–613.
- (51) Pinkard, A.; Champsaur, A. M.; Roy, X. Molecular Clusters: Nanoscale Building Blocks for Solid-State Materials. *Acc. Chem. Res.* **2018**, *51* (4), 919–929.
- (52) O'Brien, E. S.; Trinh, M. T.; Kann, R. L.; Chen, J.; Elbaz, G. A.; Masurkar, A.; Atallah, T. L.; Paley, M. V.; Patel, N.; Paley, D. W.; Kymissis, I.; Crowther, A. C.; Millis, A. J.; Reichman, D. R.; Zhu, X. Y.; Roy, X. Single-Crystal-to-Single-Crystal Intercalation of a Low-Bandgap Superatomic Crystal. *Nat. Chem.* **2017**, *9* (12), 1170–1174.
- (53) Ong, W. L.; O'Brien, E. S.; Dougherty, P. S. M.; Paley, D. W.; Higgs, C. F.; McGaughey, A. J. H.; Malen, J. A.; Roy, X. Orientational Order Controls Crystalline and Amorphous Thermal Transport in Superatomic Crystals. *Nat. Mater.* **2017**, *16* (1), 83–88.
- (54) Handa, T.; Shih, P.; Koay, C. S.; Nuckolls, C.; Roy, X.; Berkelbach, T. C.; Zhu, X. Anisotropically Fused Clusters Form a 2D Superatomic Sheet Exhibiting Polarized Light Emission. *J. Phys. Chem. C* **2023**, *127* (3), 1519–1526.
- (55) Lee, C. H.; Liu, L.; Beijer, C.; Turkiewicz, A.; Goko, T.; Arguello, C. J.; Frandsen, B. A.; Cheung, S. C.; Medina, T.; Munsie, T. J. S.; et al. Ferromagnetic Ordering in Superatomic Solids. *J. Am. Chem. Soc.* **2014**, *136* (48), 16926–16931.
- (56) Bijelic, A.; Rompel, A. The Use of Polyoxometalates in Protein Crystallography - An Attempt to Widen a Well-Known Bottleneck. *Coord. Chem. Rev.* **2015**, *299*, 22–38.
- (57) Soria-Carrera, H.; Atrí An-Blasco, E.; Martín-Rapun, R.; Mitchell, S. G. Polyoxometalate–Peptide Hybrid Materials: From Structure–Property Relationships to Applications. *Chem. Sci.* **2022**, *14* (1), 10–28.

- (58) Le Magueres, P.; Hubig, S. M.; Lindeman, S. V.; Veya, P.; Kochi, J. K. Novel Charge-Transfer Materials via Cocrystallization of Planar Aromatic Donors and Spherical Polyoxometalate Acceptors. *J. Am. Chem. Soc.* **2000**, *122* (41), 10073–10082.
- (59) Bosch-Navarro, C.; Matt, B.; Izzet, G.; Romero-Nieto, C.; Dorian, K.; Raya, A.; Molina, S. I.; Proust, A.; Guldi, D. M.; Marti-Gastaldo, C.; Coronado, E. Charge Transfer Interactions in Self-Assembled Single Walled Carbon Nanotubes/Dawson–Wells Polyoxometalate Hybrids. *Chem. Sci.* **2014**, *5* (11), 4346–4354.
- (60) Wang, Z.; Su, H. F.; Tung, C. H.; Sun, D.; Zheng, L. S. Deciphering Synergetic Core-Shell Transformation from $[\text{Mo}_6\text{O}_{22}@\text{Ag}_{44}]$ to $[\text{Mo}_8\text{O}_{28}@\text{Ag}_{50}]$. *Nat. Commun.* **2018**, *9* (1), 1–8.
- (61) Yonesato, K.; Yanai, D.; Yamazoe, S.; Yokogawa, D.; Kikuchi, T.; Yamaguchi, K.; Suzuki, K. Surface-Exposed Silver Nanoclusters inside Molecular Metal Oxide Cavities. *Nat. Chem.* **2023**, *15* (7), 940–947.
- (62) Mahendranath, A.; Mondal, B.; Sugi, K. S.; Pradeep, T. Direct Imaging of Lattice Planes in Atomically Precise Noble Metal Cluster Crystals Using a Conventional Transmission Electron Microscope. *Chem. Commun.* **2022**, *58* (12), 1906–1909.
- (63) Mahendranath, A.; Mondal, B.; Sugi, K. S.; Pradeep, T. Direct Imaging of Lattice Planes in Atomically Precise Noble Metal Cluster Crystals Using a Conventional Transmission Electron Microscope. *Chem. Commun.* **2022**, *58* (12), 1906–1909.
- (64) Jana, A.; Chakraborty, P.; Dar, W. A.; Chandra, S.; Khatun, E.; Kannan, M. P.; Ras, R. H. A.; Pradeep, T. Dual Emitting Ag_{35} Nanocluster Protected by 2-Pyrene Imine Thiol. *Chem. Commun.* **2020**, *56* (83), 12550–12553.
- (65) Jash, M.; Jana, A.; Poonia, A. K.; Khatun, E.; Chakraborty, P.; Nagar, A.; Ahuja, T.; Adarsh, K. V.; Pradeep, T. Phosphine-Protected Atomically Precise Silver-Gold Alloy Nanoclusters and Their Luminescent Superstructures. *Chem. Mater.* **2023**, *35* (1), 313–326.
- (66) Roy, J.; Chakraborty, P.; Paramasivam, G.; Natarajan, G.; Pradeep, T. Gas Phase Ion Chemistry of Titanium–Oxofullerene with Ligated Solvents. *Phys. Chem. Chem. Phys.* **2022**, *24* (4), 2332–2343.
- (67) Lasia, A. Mechanism and Kinetics of the Hydrogen Evolution Reaction. *Int. J. Hydrogen Energy* **2019**, *44* (36), 19484–19518.
- (68) Roy, S.; Bagchi, D.; Dheer, L.; Sarma, S. C.; Rajaji, V.; Narayana, C.; Waghmare, U. V.; Peter, S. C. Mechanistic Insights into the Promotional Effect of Ni Substitution in Non-Noble Metal Carbides for Highly Enhanced Water Splitting. *Appl. Catal. B: Environ.* **2021**, *298*, No. 120560.
- (69) Kresse, G.; Hafner, J. *Ab Initio* Molecular-Dynamics Simulation of the Liquid-Metal–Amorphous-Semiconductor Transition in Germanium. *Phys. Rev. B* **1994**, *49* (20), 14251.
- (70) Perdew, J. P.; Chevary, J. A.; Vosko, S. H.; Jackson, K. A.; Pederson, M. R.; Singh, D. J.; Fiolhais, C. Atoms, Molecules, Solids, and Surfaces: Applications of the Generalized Gradient Approximation for Exchange and Correlation. *Phys. Rev. B* **1992**, *46* (11), 6671.
- (71) Kresse, G.; Joubert, D. From Ultrasoft Pseudopotentials to the Projector Augmented-Wave Method. *Phys. Rev. B* **1999**, *59* (3), 1758.

Supporting Information

Structure and Electrocatalytic Performance of Co-crystallized Ternary Molybdenum Oxo-sulfide Clusters for Efficient Water Splitting

Biswajit Mondal^{1#}, Arijit Jana^{1#}, Jayoti Roy^{1#}, Astrid Campos Mata², Akhil S Nair³, Ananthu Mahendranath¹, Soumyabrata Roy², Biswarup Pathak^{4*}, Pulickel M. Ajayan^{2*} and Thalappil Pradeep^{1,5*}

¹DST Unit of Nanoscience (DST UNS) & Thematic Unit of Excellence (TUE), Department of Chemistry, Indian Institute of Technology Madras, Chennai 600036, India

²Department of Materials Science and NanoEngineering, Rice University, TX 77005, USA

³Department of Chemistry, Indian Institute of Technology Indore, Indore 453552, India. The NOMAD Laboratory at the FHI of the Max-Planck Gesellschaft and IRIS-Adlershof of the Humboldt-Universität zu Berlin, Germany.

⁴Department of Chemistry, Indian Institute of Technology Indore, Indore 453552, India

⁵International Centre for Clean Water, 2nd Floor, B-Block, IIT Madras Research Park, Kanagam Road, Taramani, Chennai 600113, India

Table of content

Number	Description	Page no.
1.	Experimental section	S3
2.	Instrumentation	S4
3.	Theoretical calculations	S5
Table S1	Crystal data and structural refinement	S6
Table S2	Atomic coordinates and equivalent isotropic displacement parameters	S7
Figure S1	Optical microscopic images of crystals	S9
Figure S2	Unit cell packing of NaMo ₁₂ unit of the cocrystal	S10
Figure S3	Structural framework of Mo ₁₂ , Mo ₁₂ @S ₂ , and Mo ₁₂ @S ₆ clusters without TPP ligands	S10
Figure S4	Space-filling structural model of NaMo ₁₂ unit for Mo ₁₂ cluster	S11
Figure S5	Short contact O···O interactions between two dumbbell-shaped molybdenum oxo-sulfide units for all clusters	S11
Figure S6	Mo-Mo bond distances and the respective Mo-Na-Mo bond angles	S11
Table S3	Comparative Mo-O/ Mo-S bond distances of [Mo ₆ S ₂ O ₁₀ (C ₆ H ₅ PO ₃) ₄] unit	S12

Table S4	Comparative P-O bond distances of different PPA ligands	S12
Figure S7	Interatomic distances of central P and peripheral P of PPA ligands and the distances between the centroids of the phenyl rings of the PPA ligands	S12
Figure S8	Intercluster packing showing different intermolecular interactions	S13
Figure S9	FT-IR spectrum of molybdenum oxo sulphide cocrystals with respective peak assignments	S13
Figure S10	Randles circuit and Nyquist plot fitting of the EIS spectra for HER	S14
Figure S11	Randles circuit and Nyquist plot fitting of the EIS spectra for OER	S14
Table S5	EIS (Nyquist plot) fitting parameters for HER and OER on Mo ₁₂ -TC catalyst	S15
Figure S12	Comparative UV-vis absorption and FTIR spectra of Mo ₁₂ clusters in presence of H ₂ SO ₄ and KOH	S15
Figure S13	Comparative (a) Raman spectra and (b) XRD patterns of Mo ₁₂ -TC at different electrochemical conditions	S16
Figure S14	Comparative XPS elemental spectra of Mo ₁₂ -TC under different electrochemical conditions.	S16
Table S6	Atomic % of the catalyst from XPS at different electrochemical conditions	S17
Table S7	Atomic % of the catalyst from XPS at different electrochemical conditions	S17
Figure S15	CV at different scan rates in H ₂ SO ₄ for the Mo ₁₂ -TC coated electrode and (b) $\Delta J (j_{Cat}-j_{An})$ vs. scan rate plot	S18
Figure S16	DFT optimized structure of Mo ₁₂ and Mo ₁₂ @S ₄ cluster. Selected bond length and angles of the cluster.	S18
Figure S17	Electron density maps of the frontier molecular orbitals of the cluster	S19
Figure S18	Total density of state (DOS) and projected DOS (PDOS) spectral profile of the cluster	S20
Figure S19	Structural representation of Mo ₁₂ cluster and its adsorption configurations of *OH, *O, and *OOH adduct intermediates and O ₂ end product involved in OER pathway for the same cluster.	S20
References		S21

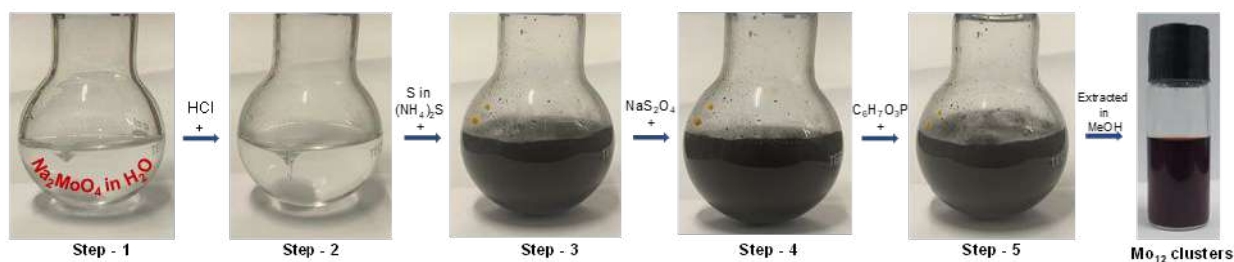
Experimental Section

Chemicals used

Sodium molybdate (Na_2MoO_4) was purchased from Merck. Sodium dithionite ($\text{Na}_2\text{S}_2\text{O}_4$) was bought from Merck. Sulphur powder was purchased from CDH. Phenylphosphonic acid was received from Spectrochem. 50% ammonium sulfide was brought from Sigma Aldrich. Hydrochloric acid was purchased from Merck. DI water was used for the synthesis. HPLC-grade solvents such as methanol were purchased from Rankem chemicals. All the chemicals are commercially available and used as such without any purification.

Synthesis of Mo_{12} clusters

In a typical synthesis, 0.86 g of Na_2MoO_4 was dissolved in 25 mL of DI water (step – 1). The pH of the solution was adjusted to ~ 3 by adding HCl (step – 2). Then, 0.4 g of S dissolved in 2 mL of 50% ammonium sulfide solution was added to aqueous solution of Na_2MoO_4 (step – 3). Upon addition of S, the color of the solution became dark brown. 0.133 g of $\text{Na}_2\text{S}_2\text{O}_4$ and 0.158 g of phenylphosphonic acid were added to the above reaction mixture and the reaction was continued overnight (step – 4, 5). Finally, it was centrifuged at 5000 rpm for 5 min to collect the precipitate. The cluster was extracted in methanol for further characterization and crystallization.



Schematic S1. Photographs of the reaction bottle showed the visual color changes during the synthesis of the Mo_{12} clusters.

Electrochemical studies

Electrochemical measurements for hydrogen evolution (HER) and oxygen evolution (OER) reactions were studied in a conventional three-electrode cell using an AUTOLAB electrochemical workstation. A graphite rod, a saturated calomel electrode (SCE), and the catalyst coated on glassy carbon (GC) electrode were used as the counter, reference, and working electrodes, respectively

for HER. A mercury/mercuric oxide (Hg/HgO) electrode was used as reference electrode for OER studies. All measured potentials were converted to the reversible hydrogen electrode (RHE) values. The GC electrode (0.071 cm²) was coated by catalyst ink (5 μ L of 4 mg of the cluster, 1 mg Vulcan C, 10 μ L of nafion 1%, 125 μ L of H₂O, and 125 isopropyl alcohol). HER studies were carried out under acidic conditions (0.5 M H₂SO₄) and OER studies under basic conditions (1M KOH).

Linear sweep voltammetry (LSV) experiments were conducted between -0.45 V to 0.2 V and 0.8V to 2.2 V, for HER and OER respectively, at scan rate of 5 mV s⁻¹. To evaluate the stability of our catalyst, accelerated degradation tests (ADT) using cyclic voltammetry (CV) studies we conducted between -0.356 V to -0.106 V (HER) and 1.29 V to 2.04 V (OER) for up to 5000 cycles, at scan rate of 50 mV s⁻¹. Electrochemical impedance spectroscopy (EIS) was performed for both HER and OER at a frequency range from 100 kHz to 0.1 Hz, at potential values of -0.256 V for HER and 1.74 V for OER.

Instrumentations

UV-Vis absorption spectroscopy

UV-Vis absorption spectra were measured using Perkin Elmer Lambda 365 UV-Vis spectrophotometer in the wavelength range of 1100 nm to 200 nm using a bandpass filter of 1 nm. Purified cluster after extracting in MeOH was used for the measurements.

Mass spectrometry

All high-resolution electrospray ionization mass spectrometry (ESI MS) studies were performed using a Waters Synapt G2-Si high-definition mass spectrometer (HDMS). All MS measurements were acquired in the negative ion mode. The capillary voltage, cone voltage, and source offset were kept at 2.75 kV, 50-60 V, and 30-40 V, respectively, throughout the ESI MS measurements to obtain a well-resolved mass spectrum of Mo-S NC. The source and desolvation temperatures were maintained at 100 and 150 $^{\circ}$ C, respectively. The desolvation gas flow was set at 500 l h⁻¹ during the measurements. For the collision-induced dissociation (CID) study in the instrument, the mass-selected ions were passed through the trap, ion-mobility, and transfer cells before entering the time-of-flight mass analyzer. The CID was performed only in the trap cell, while the other collision cells were kept off. No extra voltages were applied in the IMS and transfer cells to avoid

additional ions fragmentation. The collision energy (CE) in the trap varied between 0 and 200 CE (instrumental units) during CID MS study.

Transmission electron microscopy

Transmission electron micrographs were collected using JEOL 3010 at an operating voltage of 100 kV (to reduce beam-induced damage) with an ultrahigh-resolution (UHR) polepiece. This has a filament made up of LaB₆. The instrument works under a vacuum in the range 10⁻⁵ to 10⁻⁶ Pa. Gatan Orius SC200 CCD camera (2K x 2K) was used to collect the images. Before the imaging, a few single crystals were separated and ground with a mortar and pestle. Then, it was drop-cased on a carbon coated 300 mesh copper grid after suspending in MeOH.

Single crystal XRD

Single-crystal X-ray diffraction studies were performed at 296 K using Bruker D8 VENTURE instrument. The diffractometer is equipped with a Cu K α X-ray source with the wavelength 1.54178 Å. A PHOTON 100 CMOS detector has been used to record the diffraction spots of different frames. A suitable crystal was mounted on a Kapton polymer loop with the help of paratone oil. The program APEX3-SAINT (Bruker, 2016) was used for integrating the frames. A multi-scan absorption correction was done using the program SADABS (Bruker, 2016). The structure was solved by SHELXT-2014 (Sheldrick, 2014) and refined by full-matrix least squares techniques using SHELXL-2018 (Sheldrick, 2018) computer program. Hydrogen atoms were fixed at calculated positions and refined as riding model with C-H = 0.93 Å and Uiso(H) = 1.2 Ueq©. Mercury 2020.2.0 and VESTA software have been used for the visualization of the structure and electron density modelling.

Theoretical calculations

A single cluster unit of the Mo₁₂ structure is considered for the theoretical study. The periodic DFT calculations were done using Vienna Ab-Initio Simulation Package (VASP) by using Generalized gradient approximation of Perdew–Burke–Ernzerhof (PBE) functional.^{1–3} Projector augmented wave (PAW) method is used for treating ion-electron interactions.^{4,5} The ionic relaxations have been carried out using a conjugate gradient algorithm with convergence criteria of 10⁻⁴ eV for minimum energy and 0.05 eV Å⁻¹ for Hellmann-Feynman forces on atoms. Due to the large size of the unit cells of the compounds, the Brillouin zone was sampled at the Gamma point (1×1×1).

For the projected density of states (PDOS) calculation, a higher (2×2×2) K-mesh is used. For identifying the intercluster interactions, calculations of dimer and monomer clusters units are carried out with and without applying van der Waals correction using DFT-D3 method.

The molecular DFT calculations were done using Gaussian 09 D.01 program.⁶ B3LYP functional with Pople's 6-31G* basis set was used for non-metal elements and LANL2DZ-ECP (effective core potential) was employed for Co atoms, respectively.^{7, 8} The TD-DFT calculations considered 300 excited states.

Table S1. Crystal data and structure refinement

Identification code	NaMo12 cocrystal	
Empirical formula	Mo12 Na O54 P8 C48 H40	
Formula weight	2902.86	
Temperature	296(2) K	
Wavelength	1.54178 Å	
Crystal system	Monoclinic	
Space group	P2 ₁ /c	
Unit cell dimensions	a = 18.1456(7) Å	α = 90°.
	B = 13.8107(5) Å	β = 108.052(3)°.
	C = 20.6756(9) Å	γ = 90°.
Volume	4926.3(3) Å ³	
Z	2	
Density (calculated)	2.070 Mgm ⁻³	
Absorption coefficient	14.612 mm ⁻¹	
F(000)	2966	
Crystal size	0.150 x 0.100 x 0.100 mm ³	
Theta range for data collection	3.912 to 64.996°.	
Index ranges	-21 ≤ h ≤ 20, -15 ≤ k ≤ 16, -23 ≤ l ≤ 24	
Reflections collected	42462	
Independent reflections	8332 [R(int) = 0.1868]	
Completeness to theta = 64.996°	99.4 %	
Absorption correction	Semi-empirical from equivalents	
Max. and min. transmission	56 and 0.35	
Refinement method	Full-matrix least-squares on F ²	
Data / restraints / parameters	8332 / 661 / 666	

Goodness-of-fit on F^2	1.016
Final R indices [$I > 2\sigma(I)$]	$R1 = 0.0858$, $wR2 = 0.2228$
R indices (all data)	$R1 = 0.1659$, $wR2 = 0.3100$
Extinction coefficient	0.00031(5)
Largest diff. peak and hole	1.364 and -1.086 e.Å ⁻³

Table S2. Atomic coordinates ($\times 10^4$) and equivalent isotropic displacement parameters (Å² $\times 10^3$) for NaMo₁₂. U(eq) is defined as one third of the trace of the orthogonalized U_{ij} tensor.

	x	y	z	U(eq)
C(1)	6931(9)	3952(18)	3529(10)	106(5)
C(2)	6335(11)	4051(19)	3813(10)	115(5)
C(3)	5590(10)	3720(20)	3448(11)	119(5)
C(4)	5440(10)	3365(19)	2799(11)	117(5)
C(5)	6026(12)	3340(20)	2493(10)	121(6)
C(6)	6767(10)	3650(20)	2857(11)	116(5)
C(7)	7238(11)	674(15)	4393(15)	119(6)
C(8)	7064(12)	-308(15)	4362(15)	133(6)
C(9)	6340(13)	-624(14)	3967(16)	138(6)
C(10)	5773(12)	33(16)	3643(16)	135(6)
C(11)	5943(13)	1011(15)	3670(16)	139(6)
C(12)	6666(13)	1329(13)	4076(16)	134(6)
C(13)	7241(12)	4575(18)	1403(16)	137(6)
C(14)	7094(13)	3603(17)	1229(17)	149(7)
C(15)	6355(15)	3309(15)	815(17)	153(7)
C(16)	5788(14)	4004(19)	546(17)	155(7)
C(17)	5915(13)	4968(18)	763(18)	153(7)
C(18)	6645(15)	5256(15)	1182(17)	149(7)
C(19)	5786(15)	6390(30)	4608(17)	178(8)
C(20)	5552(18)	6320(30)	3905(17)	184(8)
C(21)	4770(20)	6150(30)	3551(13)	189(8)
C(22)	4271(14)	5870(30)	3908(17)	184(8)

C(23)	4517(18)	5910(30)	4616(17)	189(8)
C(24)	5300(20)	6050(30)	4963(13)	189(8)
O(1)	8309(7)	3392(9)	4405(7)	76(3)
O(2)	8323(7)	4599(10)	3478(7)	76(3)
O(3)	7879(7)	5124(9)	4482(7)	78(4)
O(4)	9170(7)	6108(9)	4308(6)	70(3)
O(5)	9766(7)	3746(9)	4229(6)	73(3)
O(6)	9127(7)	4480(9)	5565(7)	75(3)
O(8)	8464(10)	5231(11)	6500(8)	101(5)
O(9)	9027(9)	2953(11)	6427(8)	97(4)
O(10)	9541(7)	2634(9)	5257(6)	74(3)
O(11)	8130(10)	1915(11)	5283(8)	100(5)
O(12)	8662(8)	225(10)	5251(9)	95(4)
O(13)	8588(8)	1338(10)	4303(7)	83(4)
O(15)	10017(9)	1733(9)	4178(7)	90(4)
O(16)	10047(8)	3273(10)	2994(7)	82(4)
O(17)	8594(8)	4032(10)	2272(7)	88(4)
O(18)	9584(8)	5225(10)	3276(7)	79(3)
O(19)	8624(10)	5275(14)	1386(8)	112(5)
O(20)	8131(9)	5735(11)	2339(7)	97(5)
O(21)	9043(9)	7198(9)	3109(8)	88(4)
O(23)	8488(9)	7906(10)	4385(8)	93(4)
O(24)	7195(8)	6958(11)	4499(9)	103(5)
O(25)	8627(7)	6392(9)	5393(6)	76(3)
O(26)	7133(9)	5757(11)	5426(9)	105(5)
O(27)	6840(30)	7490(30)	5610(20)	149(14)
O(27')	6400(70)	7290(90)	5520(60)	160(20)
O(7)	7610(30)	3730(60)	5440(40)	82(12)
O(14)	8667(14)	2570(30)	3286(12)	78(6)
O(22)	7695(12)	6520(30)	3401(15)	77(6)
S(1)	7415(13)	3720(30)	5537(15)	83(5)
S(2)	8446(18)	2520(30)	3047(16)	84(7)
S(3)	7401(15)	6550(40)	3250(20)	82(7)
Mo(1)	8194(1)	5031(1)	5651(1)	79(1)
Mo(2)	8654(1)	3224(1)	5597(1)	78(1)
Mo(3)	9287(1)	2486(1)	4190(1)	76(1)

Mo(4)	9300(1)	3716(1)	3234(1)	76(1)
Mo(5)	8674(1)	6158(1)	3322(1)	79(1)
Mo(6)	8226(1)	6741(1)	4340(1)	80(1)
Na(1)	10000	5000	5000	78(3)
P(1)	8197(3)	1085(4)	4829(3)	84(2)
P(2)	8207(4)	4912(5)	1867(3)	92(2)
P(3)	6778(4)	6640(5)	5007(4)	107(2)
P(4)	7903(3)	4275(4)	4000(3)	76(1)
O(28)	8409(19)	7700(20)	6417(17)	106(10)
O(29)	8720(20)	8470(20)	2341(16)	105(10)
O(30)	8030(40)	9280(50)	2950(40)	250(30)
O(31)	10276(16)	5940(20)	2261(14)	140(10)
O(32)	7820(30)	1260(40)	2410(30)	93(16)
O(33)	9612(18)	-560(20)	4485(18)	101(9)
O(34)	9950(20)	-1040(30)	3410(20)	128(12)
O(35)	6210(30)	6360(40)	2330(20)	159(17)

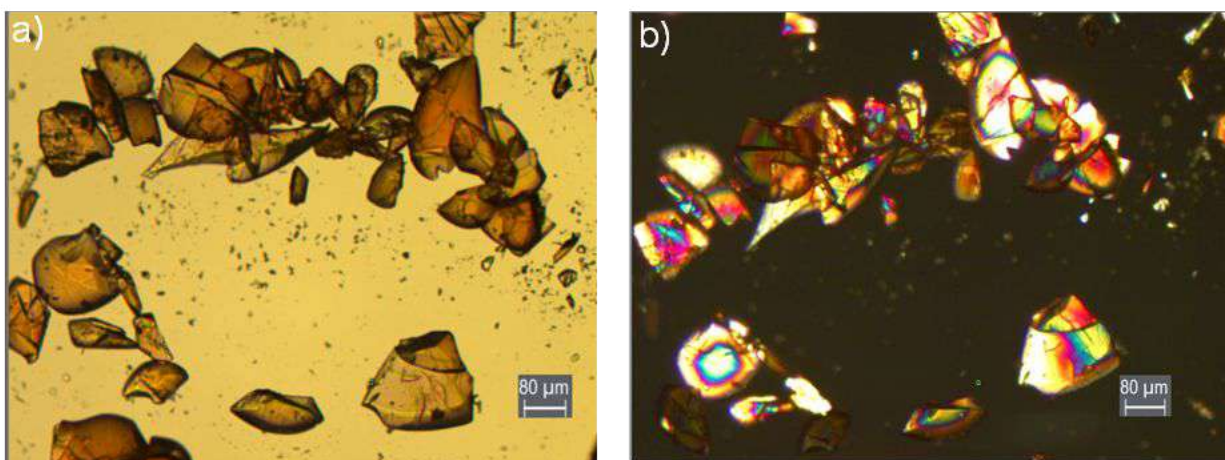


Figure S1. Optical microscopic images of crystals a) without and b) with polarizer.

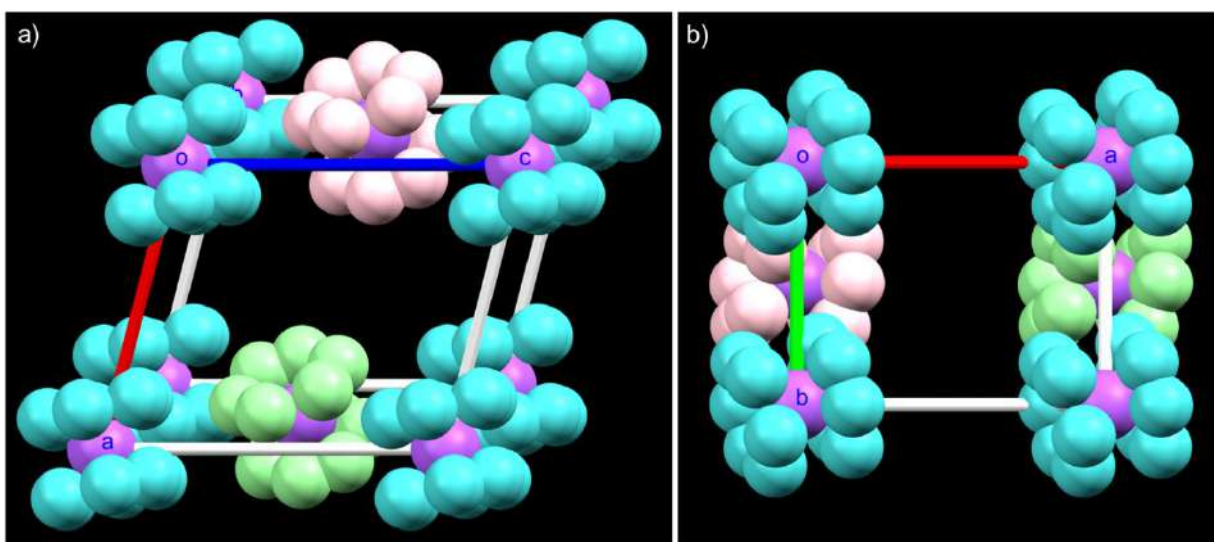


Figure S2. Unit cell packing of NaMo_{12} unit of the cocrystal along a) b and b) c crystallographic axis. Color labels: sky blue = Mo for Mo_{12} cluster, light green = Mo for $\text{Mo}_{12}@\text{S}_2$ cluster, pink = Mo for $\text{Mo}_{12}@\text{S}_6$ cluster, purple = sodium.

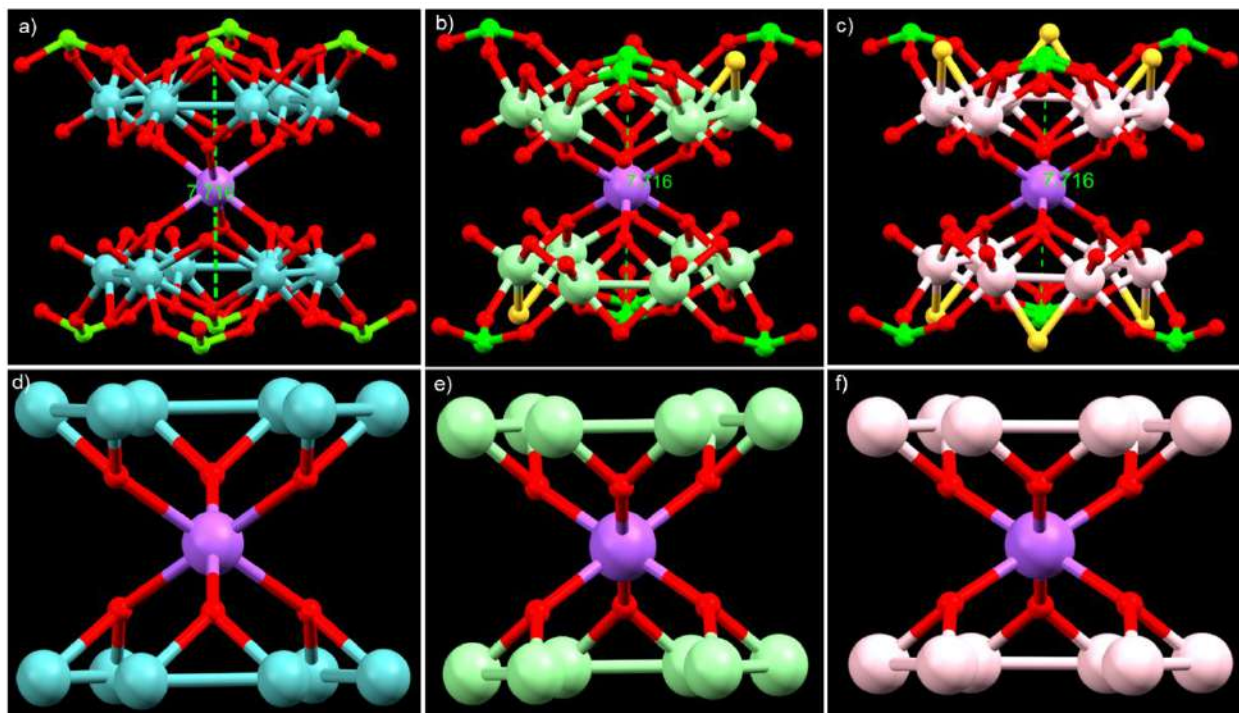


Figure S3. Structural model of the kernels of a) Mo_{12} , b) $\text{Mo}_{12}@\text{S}_2$, and c) $\text{Mo}_{12}@\text{S}_6$ clusters without PPA ligands. $\text{NaMo}_{12}\text{O}_6$ inner kernel framework of d) Mo_{12} , e) $\text{Mo}_{12}@\text{S}_2$ and f) $\text{Mo}_{12}@\text{S}_6$ clusters. Color code: sky blue, light green and pink = Mo; yellow = S; red = O, green = P, purple = Na.

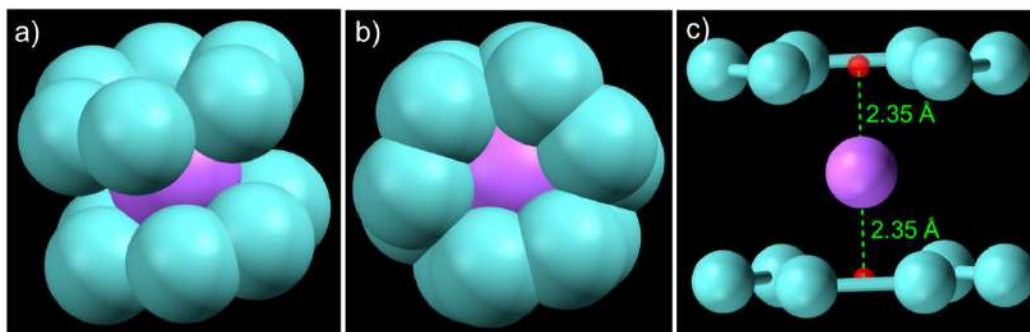


Figure S4. Space filling model of NaMo_{12} unit for Mo_{12} cluster along a) side view and b) top view. C) The distance between sodium and the centrod of Mo_6 unit.

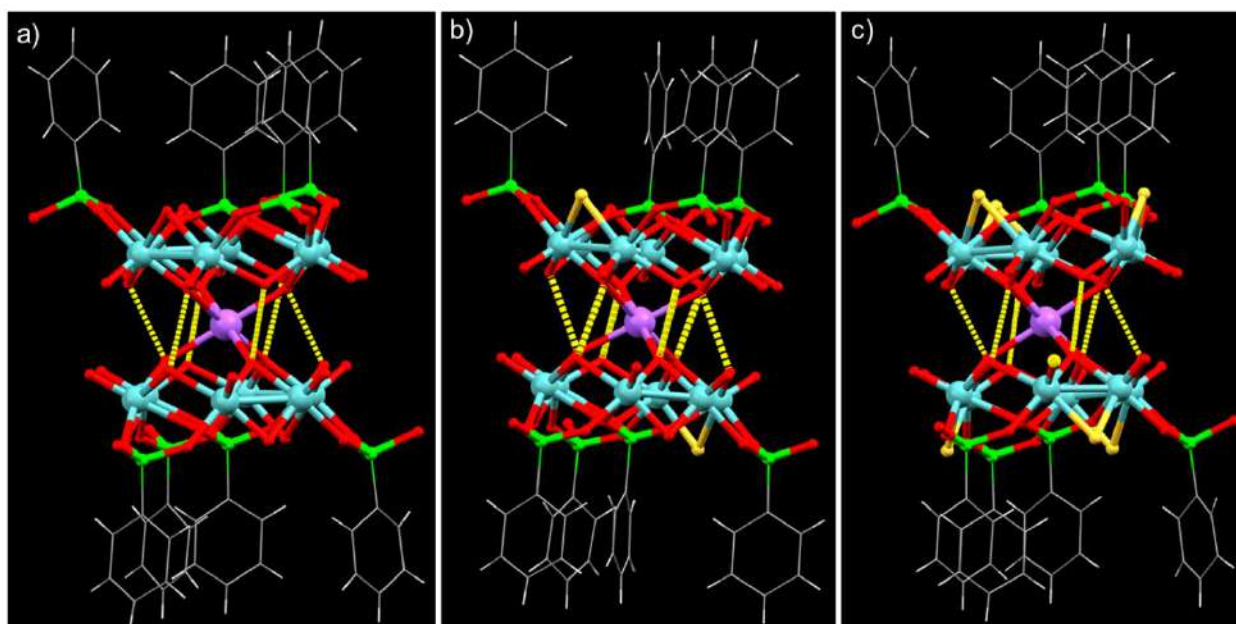


Figure S5. Short contact $\text{O}\cdots\text{O}$ interactions between two dumbbell-shaped units for a) Mo_{12} , b) $\text{Mo}_{12}@\text{S}_2$ and $\text{Mo}_{12}@\text{S}_6$ clusters.

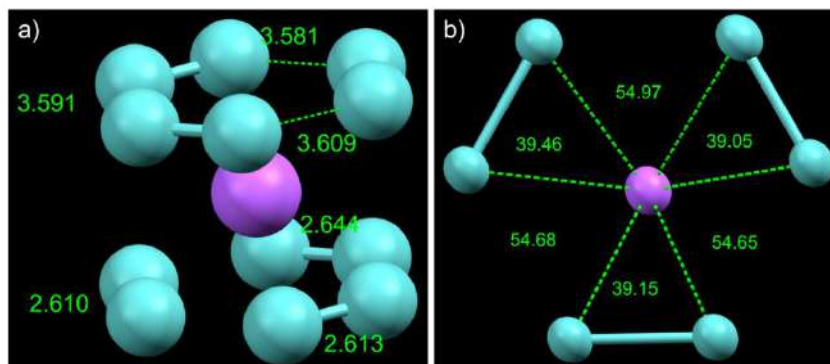


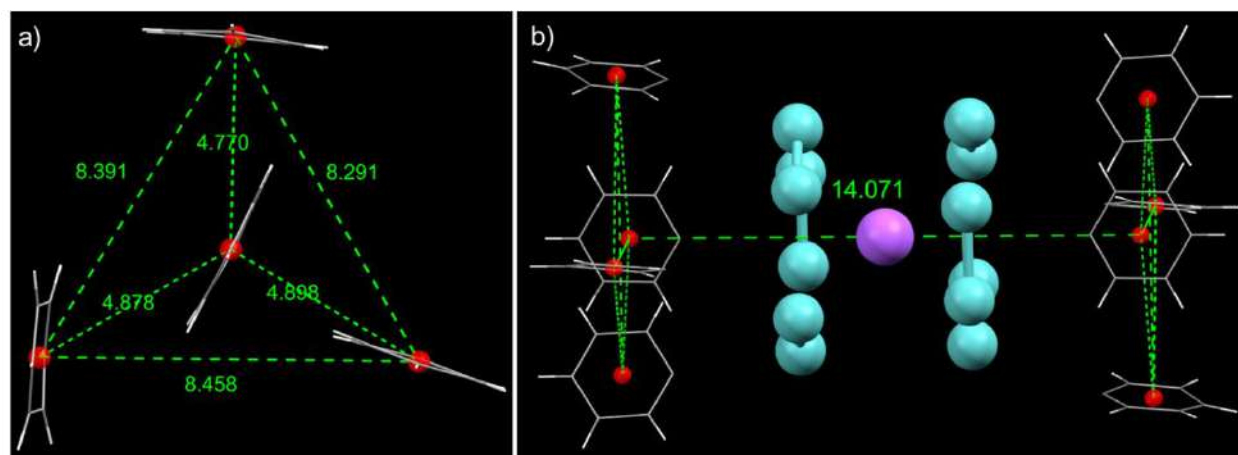
Figure S6. A) Mo-Mo bond distances of Mo_6 units, and b) the respective Mo-Na-Mo bond angles for Mo_{12} cluster.

Table S3. Comparative Mo-O/ Mo-S bond distances of $[\text{Mo}_6\text{S}_2\text{O}_{10}(\text{C}_6\text{H}_5\text{PO}_3)_4]$ unit.

Type of bonds	Mo-O distance (in Å)	Mo-S distance (in Å)
Mo-O (isolated O)	1.680, 1.690, 1.693, 1.695, 1.671, 1.699	
Mo-O (central P of PPA)	2.308, 2.364, 2.296, 2.333, 2.325, 2.360	
Mo-O /Mo-S (dangling O/S)	2.111, 2.118	2.119, 2.142, 2.125, 2.167
Mo-O (peripheral P of PPA)	2.049, 2.052, 2.088, 2.052, 2.091, 2.020	

Table S4. Comparative P-O bond distances of different PPA ligands bonded with the cluster.

PPA ligand	P-O bond distance (in Å)
Central PPA	1.533, 1.548, 1.567
Peripheral PPA (Unit 1)	1.519, 1.537, 1.619 (free)
Peripheral PPA (Unit 2)	1.510, 1.512, 1.558 (free)
Peripheral PPA (Unit 3)	1.519, 1.532, 1.510 (free)

**Figure S7.** A) Interatomic distances of central P and peripheral P of PPA ligands. B) The distance between the centroids of two apexes of the cluster. These distances are similar for all three clusters.

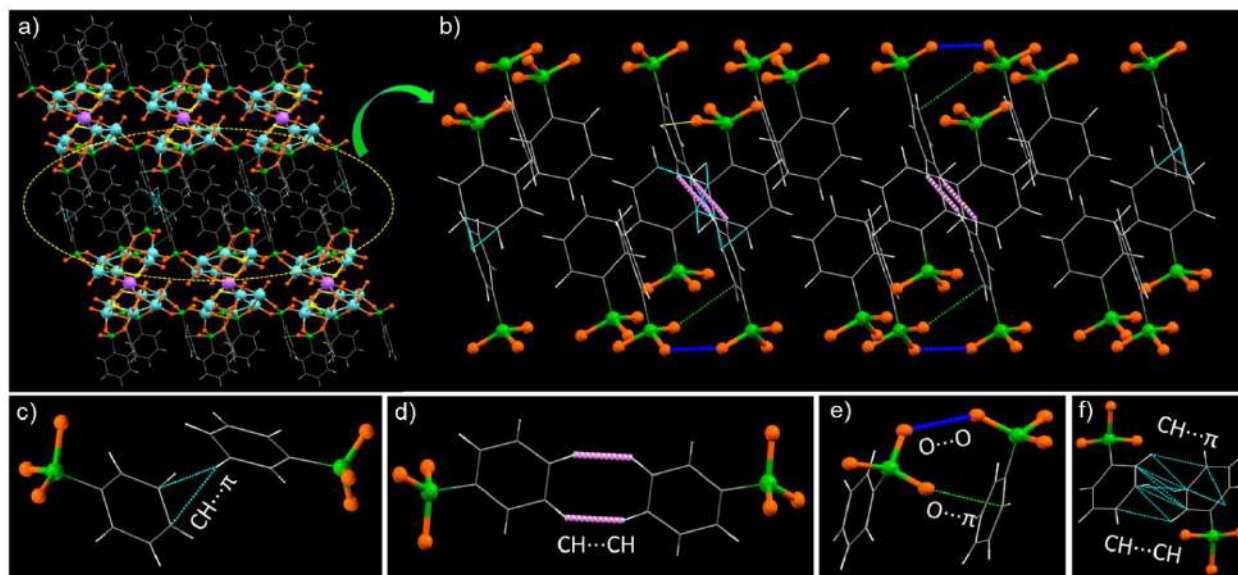


Figure S8. A) Intercluster packing shows different short contact interactions between peripheral benzene rings of the PPA ligands. B-f) Expanded view of these interactions with marked distances.

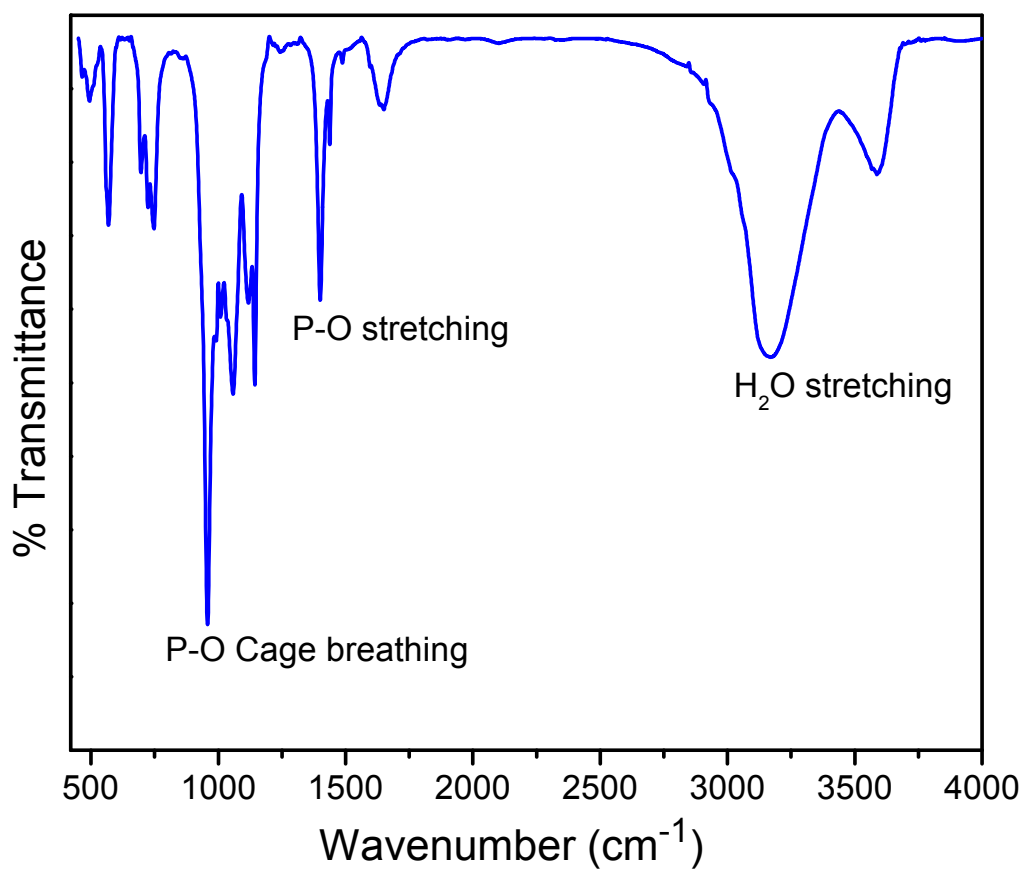


Figure S9. FT-IR spectrum of co-crystallized molybdenum oxo-sulfido clusters with respective peak assignments.

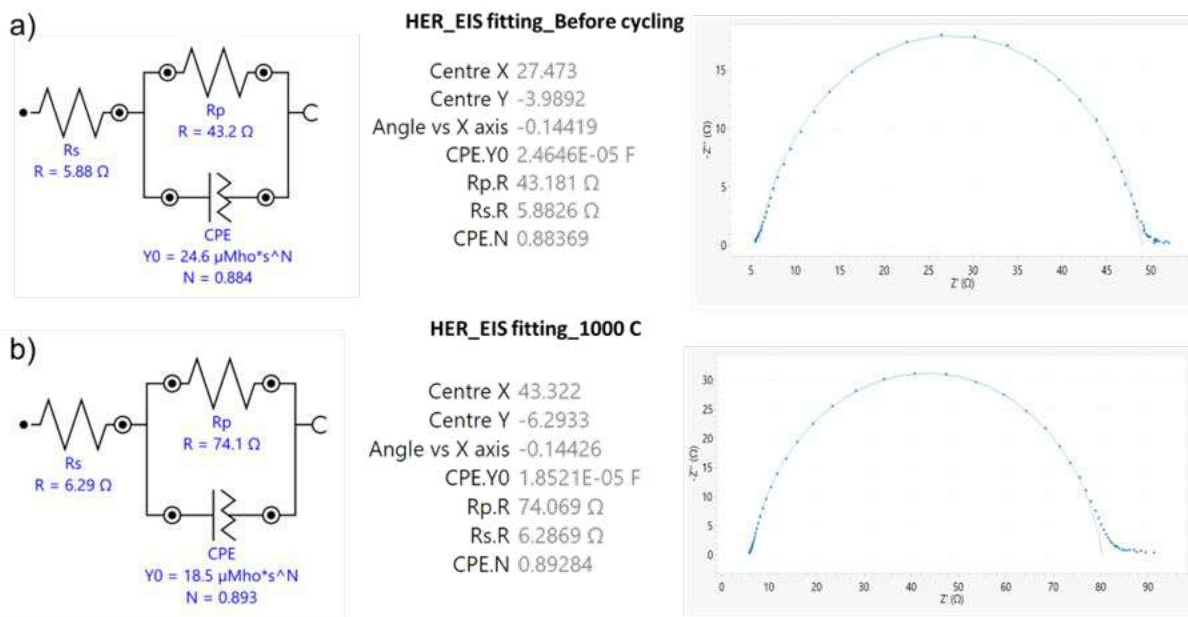


Figure S10. Randles circuit and Nyquist plot fitting of the EIS spectra for (a) HER on the pristine Mo₁₂-TC catalyst and (b) HER on the Mo₁₂-TC catalyst after 1000 cycles.

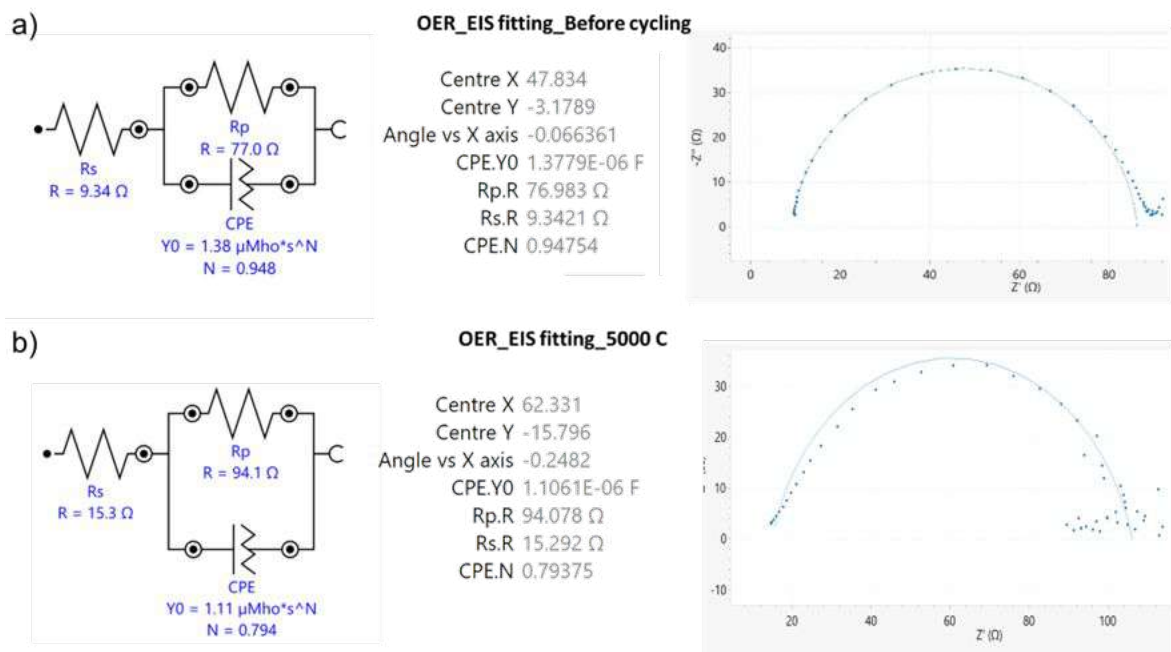


Figure S11. Randles circuit and Nyquist plot fitting of the EIS spectra for (a) OER on the pristine Mo₁₂-TC catalyst and (b) OER on the Mo₁₂-TC catalyst after 5000 cycles.

Table S5. EIS (Nyquist plot) fitting parameters for HER and OER on Mo₁₂-TC catalyst from the Randles equivalent circuits provided in Figure S10 and Figure S11. Rs stands for solution/series resistance, Rp denotes the charge transfer resistance or R_{CT} and CPE represents the constant phase element.

Condition	Rs (Ω)	Rp (Ω)	CPE.Y0 (F)	CPE.N
HER Before cycling	5.883	43.181	2.465e-5	0.884
HER After 250 cycles	6.206	50.332	2.417e-5	0.894
HER After 1000 cycles	6.287	74.069	1.852e-5	0.893
OER Before cycling	9.342	76.983	1.3783e-6	0.948
OER After 1000 cycles	10.469	70.816	1.408e-6	0.925
OER After 2000 cycles	12.651	76.464	1.325e-6	0.884
OER After 5000 cycles	15.292	94.078	1.106e-6	0.794

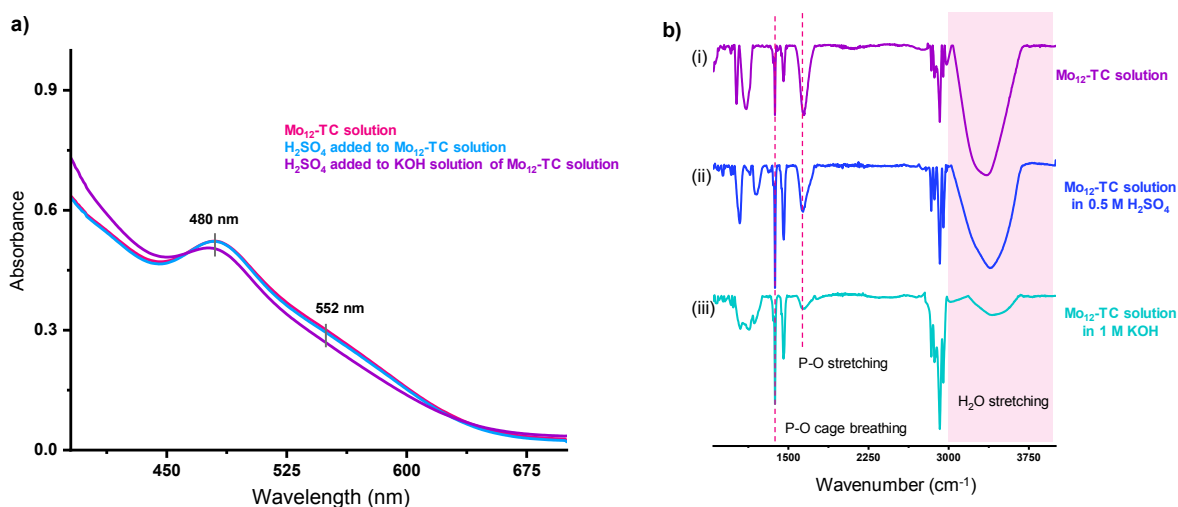


Figure S12. a) Comparative a) UV-vis absorption and b) FTIR spectra of Mo₁₂-TC, Mo₁₂-TC in 0.5 M H₂SO₄ (1:1 methanol: water), and Mo₁₂-TC in 1 M KOH (1:1 methanol: water) solutions. IR spectra were measured in Attenuated Total Reflectance Fourier Transform Infrared (ATR-FTIR) mode by placing the respective solutions on the ATR crystal.

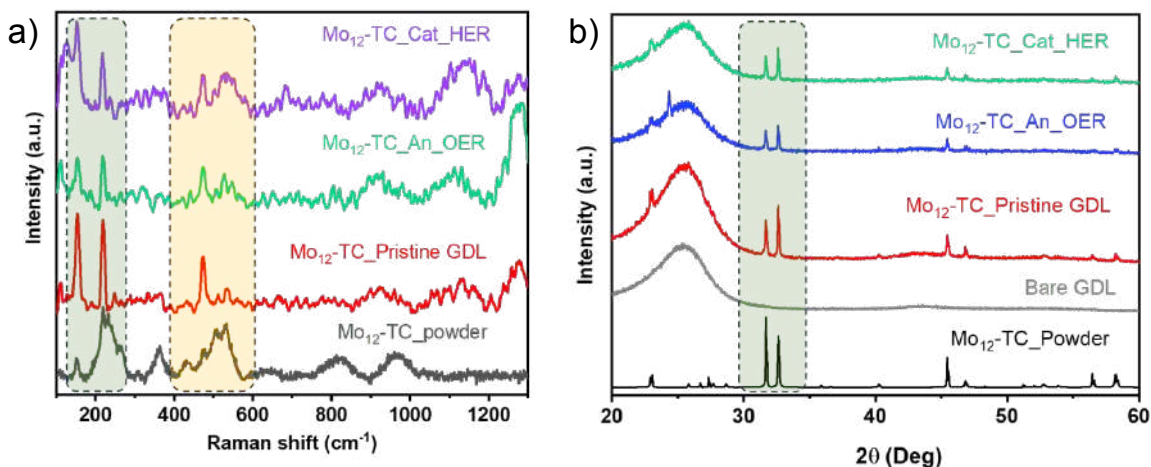


Figure S13. Comparative (a) Raman spectra and (b) XRD patterns of Mo₁₂-TC at different electrochemical conditions.

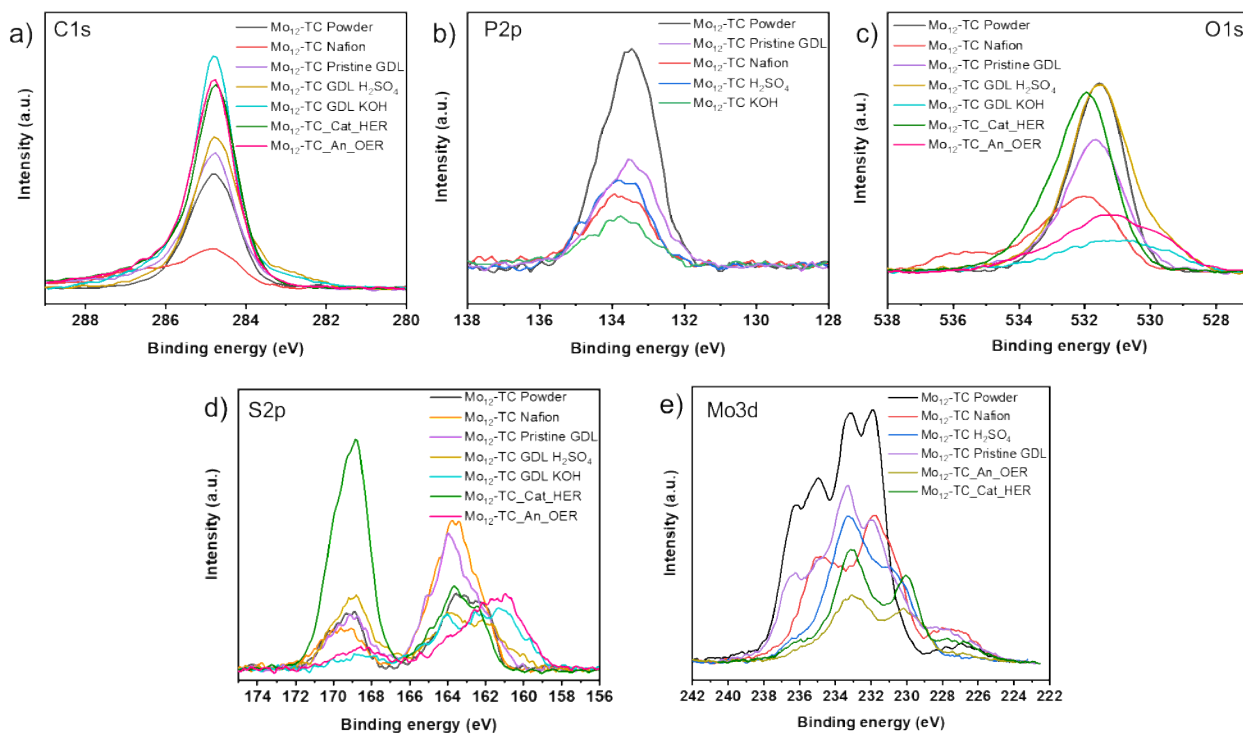


Figure S14. Comparative XPS elemental spectra of Mo₁₂-TC under different electrochemical conditions.

Table S6. Atomic % of the catalyst from XPS at different electrochemical conditions.

Sample	%C	%Mo	%O	%P	%S
Mo₁₂ Pristine electrode	58.97	5.51	26.18	2.25	5.51
Mo₁₂ HER	60.72	2.48	28.14	0.52	8.13
Mo₁₂ electrode H₂SO₄	50.38	6.36	34.96	3.4	4.9
Mo₁₂ OER	70.25	0.7	22.76	0.14	6.16
Mo₁₂ electrode KOH	82.05	0.81	11.4	0.92	4.82
Mo₁₂ Powder	45.5	8.43	36.23	4.39	5.46
Mo₁₂ Nafion	60.43	5.23	24.1	1.97	8.27
Mo₁₂ H₂SO₄	21.08	3.96	60	1.89	13.07
Mo₁₂ KOH	70.7	1.82	21.95	1.13	4.4

Table S7. Atomic % of the catalyst from XPS at different electrochemical conditions

Sample	%Mo	%P	%S
Mo₁₂ Pristine electrode	37.12	15.69	47.69
Mo₁₂ HER	22.79	4.58	72.63
Mo₁₂ electrode H₂SO₄	43.37	23.28	33.45
Mo₁₂ OER	10.04	1.93	88.03
Mo₁₂ electrode KOH	12.42	13.98	73.6
Mo₁₂ Powder	46.12	24	29.87
Mo₁₂ Nafion	33.81	12.73	53.45
Mo₁₂ H₂SO₄	20.91	10	69.09
Mo₁₂ KOH	24.7	15.41	59.89

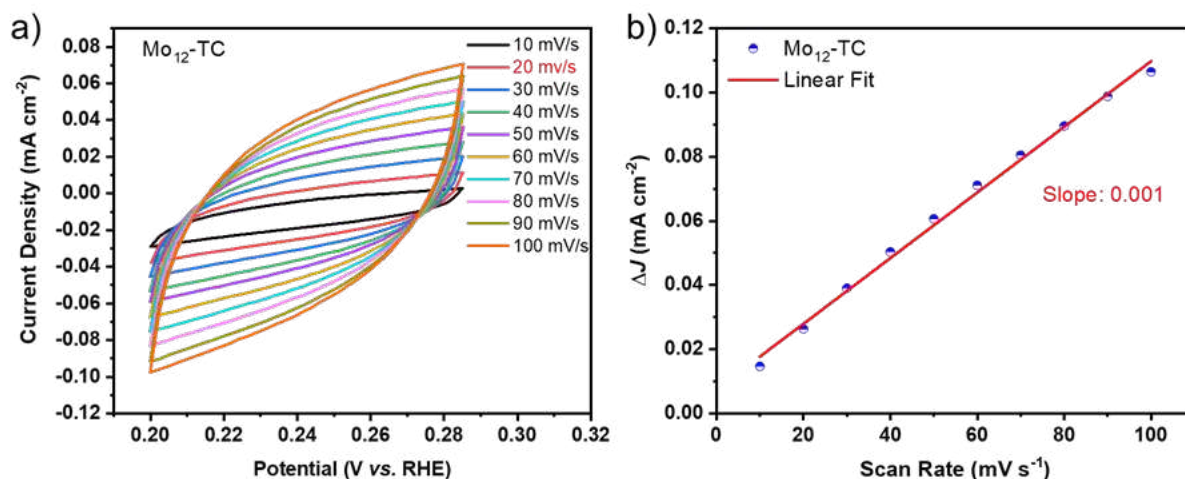


Figure S15. (a) CV at different scan rates in H₂SO₄ for the Mo₁₂-TC coated electrode and (b) ΔJ ($|j_{\text{Cat}} - j_{\text{An}}|$) vs. scan rate plot showing a slope of 0.001 corresponding to a C_{dl} of 0.5 mFcm⁻².

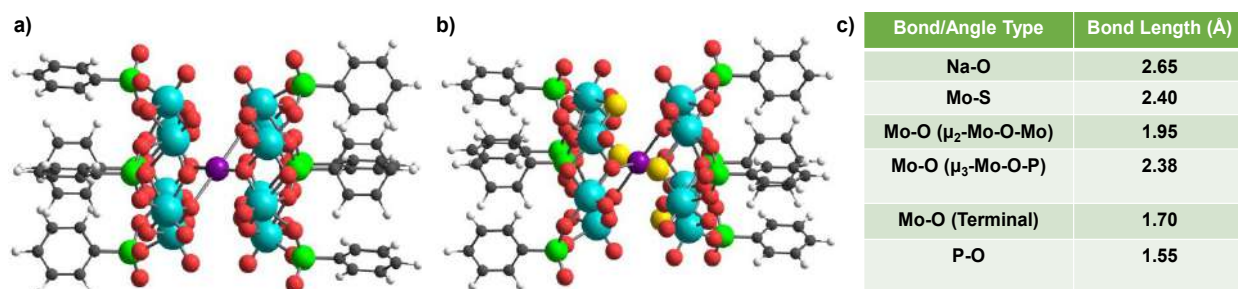


Figure S16. a) DFT optimized structure of a) Mo₁₂ and b) Mo₁₂@S₄ cluster. c) Selected bond length and angles of the cluster. Atomic color code: sky blue = Mo; yellow = S; red = O, green = P, purple = Na, black = C, white = hydrogen.

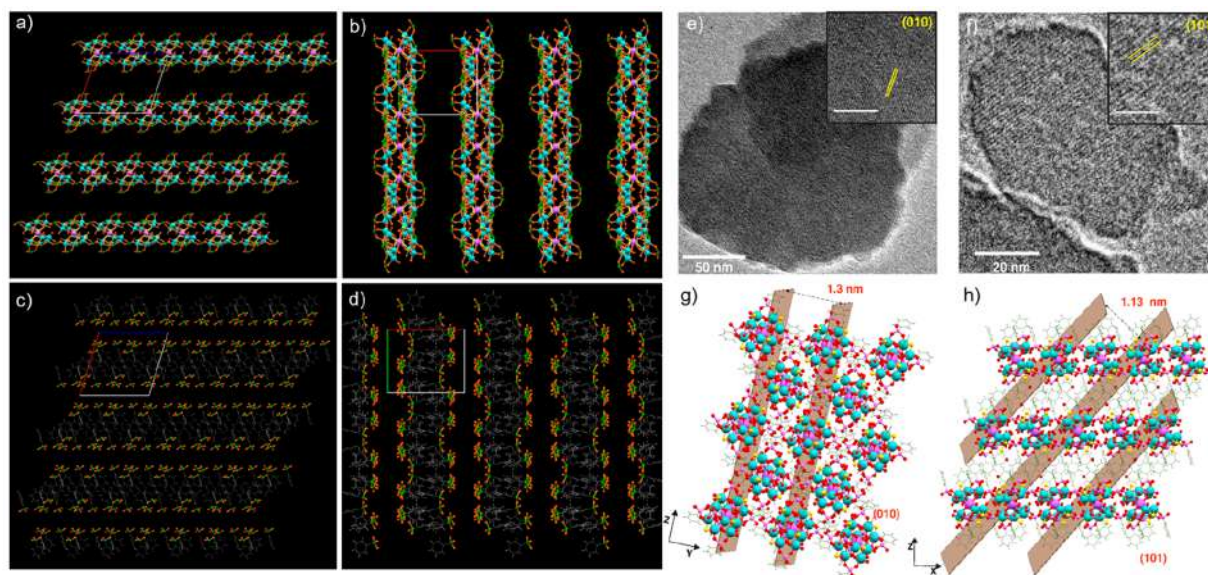


Figure 2. Supramolecular intercluster packing along the (a) *b* and (b) *c* crystallographic axes, and (c, d) corresponding packing of PPA ligands. (e, f) High-resolution TEM micrographs of the exfoliated layers of cocrystals. Inset show (010) and (101) lattice planes of the cocrystal, respectively. Intercluster packing along (g) (010) and (h) (101) lattice planes with marked interlayer spacings.

product consisted of three cocrystallized clusters (Mo_{12} , $\text{Mo}_{12}@\text{S}_2$, and $\text{Mo}_{12}@\text{S}_6$), as confirmed by single-crystal X-ray diffraction (SCXRD) and electron spray ionization–mass spectroscopy (ESI-MS) studies. Experimental and corroborative theoretical studies showed that these mixed clusters exhibit promising catalytic capabilities for electrochemical water splitting through active sites embedded within the molecular structures.

The following discussion pertains to the synthesis, structure, and characterization of cocrystallized clusters of Mo_{12} , $\text{Mo}_{12}@\text{S}_2$, and $\text{Mo}_{12}@\text{S}_6$. These clusters were prepared at room temperature through a one-step reduction process involving the precursors sodium molybdate (NaMoO_4) and sodium dithionite ($\text{Na}_2\text{S}_2\text{O}_4$). Upon introduction of a sulfur solution (obtained by dissolving solid sulfur in 50% ammonium sulfide solution) into aqueous NaMoO_4 , the color of the reaction mixture changed from colorless to brown. Addition of $\text{Na}_2\text{S}_2\text{O}_4$ resulted in a darker shade of brown, indicating the formation of these clusters. The concentration of the solutions and various experimental parameters are presented in the [Experimental Section](#) in the Supporting Information. The clusters were purified through centrifugation (see the [Experimental Section](#)). A schematic of the detailed synthetic procedure is presented in the [Experimental Section](#).

Single crystals were obtained after 30 days by the slow evaporation of the purified cluster in methanol at room temperature (25 °C). As-grown yellowish polyhedral crystals (shown in [Figure S1](#) in the Supporting Information) were used for X-ray diffraction (XRD) and other experimental studies. Mo_{12} -TC crystallized in a monoclinic crystal system with the space group $P2_1/c$ ([Table S1](#) in the Supporting Information). SCXRD study revealed that Mo_{12} -TC cocrystallized in a lattice, where eight Mo_{12} clusters were present in each corner of the unit cell, and the $\text{Mo}_{12}@\text{S}_2$ and $\text{Mo}_{12}@\text{S}_6$ clusters were present on the two opposite faces, having their occupancies of 50%, 25%, and 25%, respectively (shown in [Figure S2](#) in the Supporting Information). Expanded views ($2 \times 2 \times 2$) of the lattice framework are shown in [Figures 1a](#) and [1b](#). Further

analysis of these structures revealed that all three clusters have similar NaMo_{12} kernels protected by oxo- and sulfido-moieties. For Mo_{12} clusters, 54 oxo-linkages were observed; however, for $\text{Mo}_{12}@\text{S}_2$ and $\text{Mo}_{12}@\text{S}_6$ clusters, two sulfido-52 oxo, and six sulphido-48 oxo linkages were observed, respectively (shown in [Figures 1c](#), [1d](#), and [1e](#), as well as [Figure S3](#) in the Supporting Information). The primary distinctions in the structures of these three clusters involve the replacement of two (found in $\text{Mo}_{12}@\text{S}_2$) and six dangling S linkages (found in $\text{Mo}_{12}@\text{S}_6$) with dangling O linkages. Four vertically aligned PPA ligands are shielded on each side of the metal-oxo-sulfide framework.

The core of these clusters, i.e., the NaMo_{12} unit, consists of two hexagonal Mo_6 rings sandwiched with a Na atom connected through three oxo linkages (shown in [Figure S4](#) in the Supporting Information). The distance between sodium and the centroid of the hexagonal Mo_6 unit is 2.35 Å ([Figure S4](#)). There are six short O...O interactions between these two dumbbell-shaped $\text{Mo}_6\text{O}_{27}\text{P}_4$ units having an average distance of ~ 2.8 Å (shown in [Figure S5a](#) in the Supporting Information). These interactions are occurring between the μ_2 dangling oxygen of one unit with the μ_3 oxygen of the other unit. Such strong interactions are responsible for the structural rigidity of the two $\text{Mo}_6\text{O}_{27}\text{P}_4$ units. A similar type of ...O interaction was also observed for the other two clusters (see [Figures S5b](#) and [S5c](#) in the Supporting Information). Each Mo_6 unit of the cluster has three Mo_2 units, where the average Mo–Mo distance of the bonded Mo_2 unit is ~ 2.62 Å, and the Mo–Mo distance between nonbonded units is 3.59 Å ([Figure S6](#) in the Supporting Information). Each bonded Mo_2 unit is connected with sodium through an oxygen ([Figure S3](#) in the Supporting Information) and each nonbonded Mo_2 unit is connected with one dangling O/S atom and one O atom, which is further connected to the central PPA unit (see [Figures 1c–e](#)). Each Mo is bonded with an isolated O having an average distance of 1.68 Å ([Table S3](#) in the Supporting Information). The coordination mode of each Mo atom is

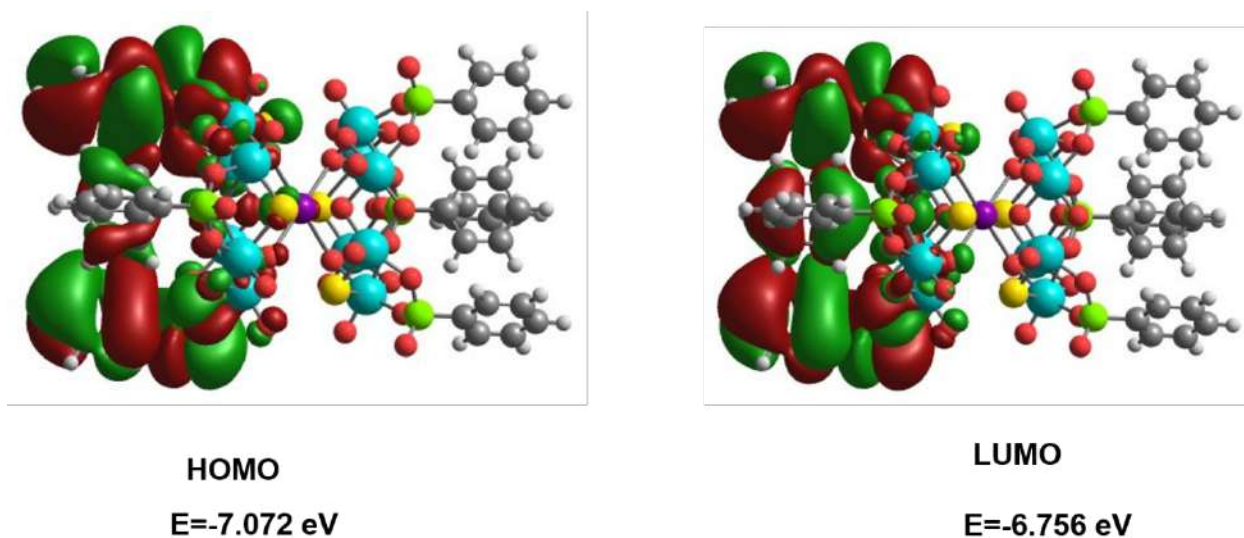


Figure S17. Electron density maps of the frontier molecular orbitals of the cluster. The energy of the respective orbitals are marked here. Green and dark red indicate positive and negative isosurfaces are plotted at 0.015 eV/\AA^3 . Atomic colors are the same with the earlier figures.

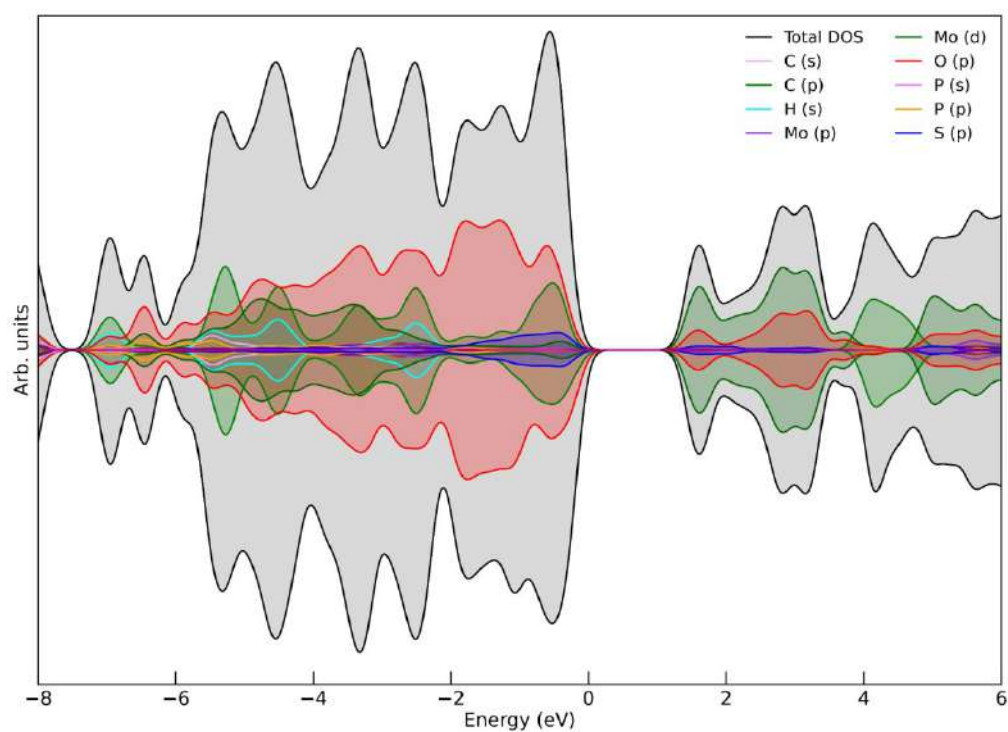


Figure S18. Total density of state (DOS) and projected density of states (PDOS) spectral profile of the respective elements of these clusters.

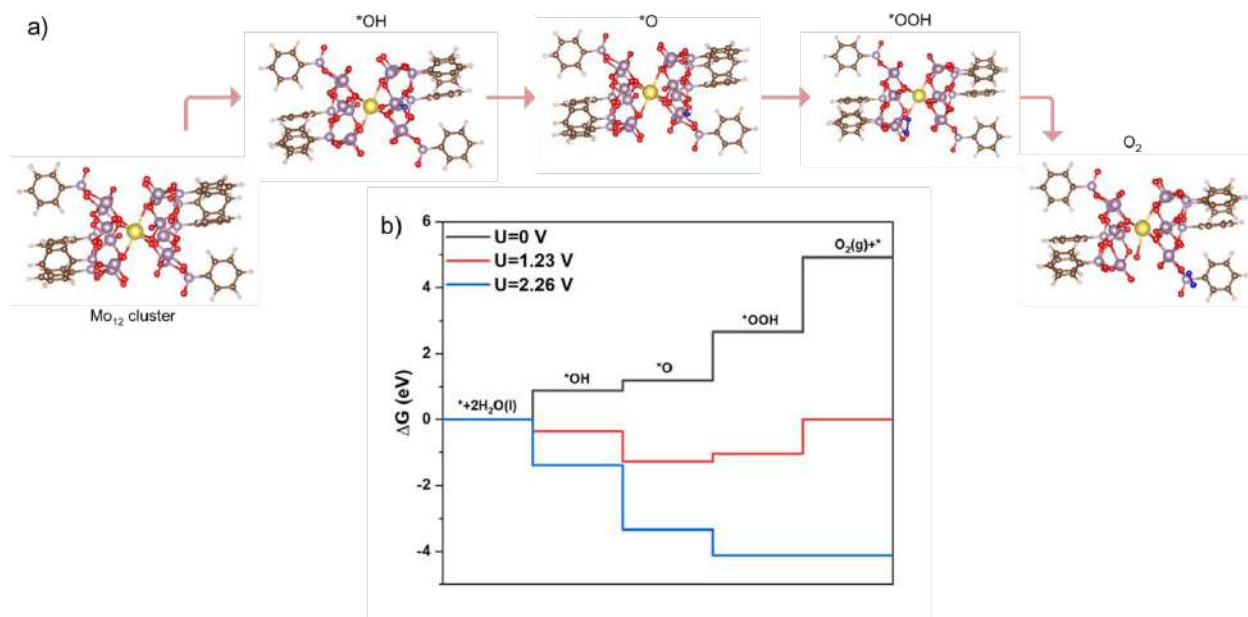


Figure S19. a) Structural representation of Mo₁₂ cluster and its adsorption configurations of *OH, *O, and *OOH adduct intermediates and O₂ end product involved in OER. Atomic color code: Mo: purple, Na: Golden yellow, O: red, C: brown, H: pink, adsorbed O: blue. b) Calculated OER free energy profile for the Mo₁₂ cluster at different potentials. The free energy profiles at 0 V (black), equilibrium potential of 1.23 V (red), and the limiting potential of 2.26 V (blue) are shown here.

References

- (1) Perdew, J. P.; Burke, K.; Ernzerhof, M. Generalized Gradient Approximation Made Simple. *Phys. Rev. Lett.* **1996**, 77 (18), 3865–3868.
- (2) Adamo, C.; Barone, V. Physically Motivated Density Functionals with Improved Performances: The Modified Perdew-Burke-Ernzerhof Model. *J. Chem. Phys.* **2002**, 116 (14), 5933–5940.
- (3) Adamo, C.; Barone, V. Toward Reliable Density Functional Methods without Adjustable Parameters: The PBE0 Model. *J. Chem. Phys.* **1999**, 110, 6158–6170.
- (4) Mortensen, J. J.; Hansen, L. B.; Jacobsen, K. W. Real-Space Grid Implementation of the Projector Augmented Wave Method. *Phys. Rev. B - Condens. Matter Mater. Phys.* **2005**, 71 (035109), 1–11.
- (5) Enkovaara, J.; Rostgaard, C.; Mortensen, J. J.; Chen, J.; Dułak, M.; Ferrighi, L.; Gavnholt, J.; Glinzvad, C.; Haikola, V.; Hansen, H. A.; Kristoffersen, H. H.; Kuisma, M.; Larsen, A. H.; Lehtovaara, L.; Ljungberg, M.; Lopez-Acevedo, O.; Moses, P. G.; Ojanen, J.; Olsen, T.; Petzold, V.; Romero, N. A.; Stausholm-Møller, J.; Strange, M.; Tritsarlis, G. A.; Vanin, M.; Walter, M.; Hammer, B.; Häkkinen, H.; Madsen, G. K. H.; Nieminen, R. M.; Nørskov, J. K.; Puska, M.; Rantala, T. T.; Schiøtz, J.; Thygesen, K. S.; Jacobsen, K. W. Electronic Structure Calculations with GPAW: A Real-Space Implementation of the Projector

Augmented-Wave Method. *J. Phys. Condens. Matter* **2010**, 22 (253202), 1–24.



Cite this: DOI: 10.1039/d3nr05128e

A concise guide to chemical reactions of atomically precise noble metal nanoclusters

Paulami Bose,[†] Krishnadas Kumaranchira Ramankutty,[†] Papri Chakraborty,[‡] Esma Khatun and Thalappil Pradeep^{*,†}

Nanoparticles (NPs) with atomic precision, known as nanoclusters (NCs), are an emerging field in materials science in view of their fascinating structure–property relationships. Ultrasmall noble metal NPs have molecule-like properties that make them fundamentally unique compared with their plasmonic counterparts and bulk materials. In this review, we present a comprehensive account of the chemistry of monolayer-protected atomically precise noble metal nanoclusters with a focus on the chemical reactions, their diversity, associated kinetics, and implications. To begin with, we briefly review the history of the evolution of such precision materials. Then the review explores the diverse chemistry of noble metal nanoclusters, including ligand exchange reactions, ligand-induced structural transformations, and reactions with metal ions, metal thiols, and halocarbons. Just as molecules do, these precision materials also undergo intercluster reactions in solution. Supramolecular forces between these systems facilitate the creation of well-defined hierarchical assemblies, composites, and hybrid materials. We conclude the review with a future perspective and scope of such chemistry.

Received 11th October 2023,
Accepted 11th November 2023

DOI: 10.1039/d3nr05128e

rsc.li/nanoscale

1. Introduction

Richard Feynman's historic Caltech address, *There's Plenty of Room at the Bottom*, in 1959, discussed the concept of nanotechnology which envisioned "maneuvering things atom by atom".¹ Development of atomically precise metal nanoclusters may be viewed as a direction to create materials atom by atom. The term 'metal cluster' was originally defined by Cotton in 1964 as "a finite group of metal atoms which are held together mainly or at least to a significant extent, by bonds directly between the metal atoms, even though some nonmetal atoms may also be intimately associated with the cluster" to refer to coordination compounds.^{2,3} This term was also used in the early literature to refer to plasmonic noble metal particles consisting of several hundreds or a few thousands of atoms, although the term 'metal nanocluster' is nowadays used more appropriately to refer to atomically precise, bare, or ligand-protected particles with a precise, molecule-like composition (M_xL_y ; $M =$

metal atom, $L =$ ligands such as thiolate, phosphine, *etc.*) and well-defined properties. Precision refers to structure as well, both in the molecular form in the gaseous, solution and solid states. Therefore, clusters in the context of this review may be defined as "a finite group of atoms with precise composition and structure, composed of two or more metal atoms held together by chemical bonds between them, and the structure formed stands protected or unprotected with ligands, with well-defined properties."

Electronic confinement of noble metals has been an important subject matter of research in the past few decades.^{4–6} As the particle size shrinks below ~ 3 nm to an intermediate size regime, bridging the dimensions of molecules and condensed matter, molecule-like properties arise in such materials.^{4,7} Such molecular materials are called atomically precise noble metal nanoclusters (NCs), which have precise composition, structure, and unique properties.^{7–11} $Au_{102}(p\text{-MBA})_{44}$ nanocluster ($p\text{-MBA} = \text{para-mercaptobenzoic acid}$) was the first reported single-crystal structure in the family of thiolate-protected atomically precise nanoclusters,¹² although clusters such as $Au_{11}I_3[P(C_6H_4-p-Cl)_3]_7$ (ref. 13) and $[Au_{13}(PPhMe_2)_{10}C_{12}]^{3+}$ (ref. 14) were known since 1970, with other ligands. Since then, more than 250 nanocluster crystal structures have been published.^{7,11,15} Many more noble metal nanoclusters with proteins,^{16–21} DNA,^{22–27} poly(amidoamine)-based dendrimers,^{28–31} and cyclodextrins^{32–34} are now known.¹¹ Today, atomic precision in assemblies is attainable in several materials, such as metals, metal oxides, semi-

DST Unit of Nanoscience & Thematic Unit of Excellence, HSB 148, Indian Institute of Technology Madras, Chennai-600036, Tamil Nadu, India.

E-mail: pradeep@iitm.ac.in

[†]Present address: School of Chemistry, Indian Institute of Science Education and Research Thiruvananthapuram, Vithura, Thiruvananthapuram-695551, Kerala, India.

[‡]Present address: Institute of Nanotechnology, Karlsruhe Institute of Technology, 76344 Eggenstein-Leopoldshafen, and Institute of Physical Chemistry, Karlsruhe Institute of Technology, 76131 Karlsruhe, Germany.

conductors, ionic compounds, and even rare gases.³⁵ Carbon clusters, such as Buckminsterfullerene or C_{60} , are some of the most popular clusters investigated so far.^{36,37} Molecular clusters such as $(H_2O)_{2,3,4,\dots}$ and $(CH_3OH)_n(H_2O)_m$, where $n, m = 1, 2, 3, \dots$, and zero-dimensional (0D) particles of perovskites, graphene, *etc.*, are also gaining interest.^{38,39} In our latest book we presented a comprehensive overview of noble metal nanoclusters and their properties, with a compendium of all reported clusters.¹⁵ However, in this review, we will be focusing on the thiolate and phosphine-protected nanoclusters in the context of their chemical reactions.

Noble metal nanoclusters exhibit well-defined physical, chemical, and electronic properties.^{7,11,12} Unique characteristic properties of nanoclusters include discrete electronic structures,^{40–47} corresponding HOMO–LUMO transitions,^{48–53} chemical reactivity,^{10,54–56,57–59} photoluminescence^{60–63} and intrinsic magnetism.^{64–69} Metal nanoclusters have attracted tremendous interest from the scientific community due to their potential applications in optoelectronics,^{70,71} sensing,^{63,72–74,75} bioimaging,^{63,76–79,80} catalysis,^{8,81–83,84} and others.^{7,11}

Today, the chemistry of well-defined monolayer-protected nanoclusters is an active area of research. We present this review as a mini guide to ligand-protected atomically precise metal nanoclusters and their diverse chemistry (schematically represented in Fig. 1). To begin with, we trace the origin and landmark developments in nanocluster science. The article presents

the recent research on ligand-induced chemistry, intercluster & interparticle reactions and their mechanism, thermodynamics, kinetics, and implications. Knowledge of the precise chemical reactivity of such nanoclusters gives a way to control their composition to form alloys and hybrid materials, and also for engineering their properties. Such new materials may find suitable roles in photophysical, catalytic, and optoelectronic applications. Chemical reactions between nanomaterials of various types provide new insights into the dynamics at the nanoscale. Reactivity at the nanoscale is of importance to chemistry in general, and to catalysis, functional materials, photophysics, nanomedicines, sensors, and clean water, in particular.

2. Atomically precise noble metal nanoclusters: the evolution

Size-dependent studies of colloidal silver particles in solution using radiolytic and electrochemical methods by Henglein *et al.* in the 1980s were among the earliest experiments using nanoscale noble metals.^{85–88} Haruta's discovery, in 1989, of the catalytic activity of finely divided, nanosized gold particles supported on oxide surfaces boosted research on noble metal NPs.⁸⁹ However, most of the early insights into atomically precise metal nanoclusters were derived from gas-phase investigations.

2.1. Insights from gas-phase studies

Gas-phase studies provided the first glimpses into the characteristics of metal nanoclusters. Nanoclusters of alkali, alkaline earth, and noble metals have been studied extensively since the 1980s. Gas-phase investigations of metal nanoclusters made extensive use of techniques like mass spectrometry, ion mobility spectrometry, photoelectron spectroscopy, vibrational spectroscopy, *etc.*^{90,91} Using mass spectrometry, Knight *et al.* characterized sodium Na_n ($n = 4–100$) metal nanoclusters in the gas phase.⁹² The most abundant peaks observed correspond to the nanoclusters with $n = 8, 20, 40, 58$, and 92 . According to the jellium model, the electrons in these nanoclusters are distributed into discrete electronic shells, just as in atoms. The numbers 8, 20, 40, 58, and 92 correspond to the total number of valence electrons ($3s^1$) in these nanoclusters, analogous to the valence shell electron configurations of noble gases. The nanoclusters whose valence shell electron counts fall in this series of 'magic' numbers are referred to as 'magic clusters'. The abundance of these nanoclusters in the mass spectra is attributed to their stability gained from the completion of electronic shell structures, just like noble gases. This is one of the reasons for the fact that 'every atom counts' in the case of atomically precise metal nanoclusters. Magic nanoclusters of metals such as aluminum were also observed. For example, Khanna *et al.*, showed that Al_{13}^- , which has a magic number of 40 electrons, exhibits special inertness towards gas-phase etching reactions.^{93,94} Such nanoclusters are also called 'superatoms', a term coined by Khanna *et al.* in 1995.⁹⁵ They also introduced the idea of using superatomic nanoclusters as building blocks for nanocluster-assembled

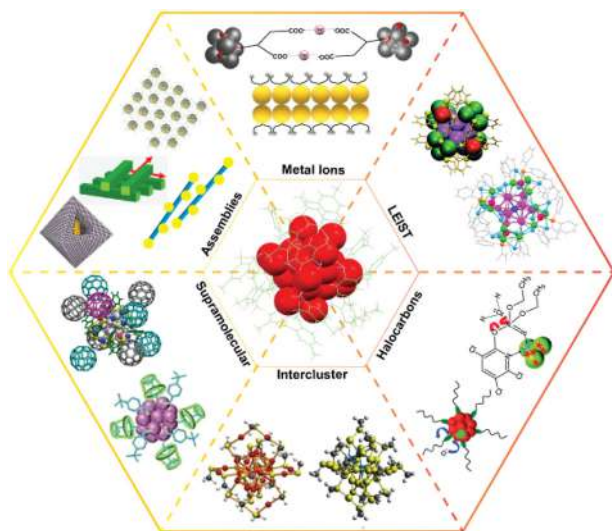


Fig. 1 Schematic illustration of the diverse chemistry of the ligand-protected atomically precise noble metal nanoclusters. Images under assemblies are adapted with permission from ref. 275, 281, 278 and 285. Copyright 2014 and 2018 John Wiley and Sons. Copyright 2014 American Chemical Society. Copyright 2020 The Royal Society of Chemistry. Images under halocarbons are adapted from ref. 258 and 257. Copyright 2013 Royal Society of Chemistry. Images under supramolecular are adapted from ref. 259 and 260. Copyright 2014 and 2018 American Chemical Society. Images under intercluster are adapted from ref. 55. Copyright 2016 Springer Nature Group. Images under LEIST are adapted from ref. 218 and 176. Copyright 2018 Royal Society of Chemistry. Copyright 2020 American Chemical Society.

materials. The stability of gas-phase metal nanoclusters, especially larger ones, depends on closed geometric shells as well as electronic shells. In the gas phase, the geometry of the nanocluster, rather than the electronic structure, determines the stability. Due to the overlap of electronic bands, there is a negligible change in electronic energy with the addition of each new atom to the nanocluster. For example, positively charged calcium nanoclusters in the gas phase such as Ca_{561} , Ca_{1412} , Ca_{2865} , *etc.*, exhibit mass spectral abundance which is ascribed to the successive addition of layers of atoms to form stable geometries.⁹⁶ Bare gold nanoclusters in the gas phase have been investigated since the 1980s. Kappes *et al.* used ion mobility (IM) measurements and trapped ion electron diffraction^{97–99} in conjunction with density functional theory (DFT) calculations in order to assign structures of Au_n^- ($n < 13$) nanoclusters⁹⁸ and also suggested that planar to three-dimensional transition in these nanoclusters occurs at $n = 11$.⁹⁸ The structure of unprotected noble metal nanoclusters deposited on surfaces has also been probed using techniques such as scanning tunneling microscopy.^{100,101}

2.2. Atomically precise metal nanoclusters in solution: phosphine- and thiolate-protected metal nanoclusters

Solution-phase nanochemistry of noble metals was accelerated after the discovery of the Brust–Schiffrin method reported in 1994,¹⁰² wherein thiolates were used as protecting ligands with limited information on the structure and composition of these particles.

The earliest examples of atomically precise metal cluster compounds studied in the solution phase were gold–phosphine coordination complexes, like $\text{Au}_{11}(\text{PPh}_3)_7(\text{SCN})_3$ and $\text{Au}_{11}\text{I}_3(\text{P}(\text{C}_6\text{H}_4\text{-}p\text{-Cl})_3)_7$. These compounds were synthesized in 1969 and 1970, respectively.^{13,103} $\text{Au}_{11}\text{X}_3[\text{PR}_3]_7$ is the first known crystal structure with an incomplete icosahedral core.¹³ In 1981, Briant *et al.* reported the first $[\text{Au}_{13}(\text{PPhMe}_2)_{10}\text{C}_{12}]^{3+}$ nanocluster consisting of a perfect icosahedral core.¹⁴ Bigger nanoclusters such as $[\text{Au}_{39}(\text{PPh}_3)_{14}\text{Cl}_6]\text{Cl}_2$ consisting of larger, atomically precise Au cores were reported in 1992.¹⁰⁴ Schmid *et al.* synthesized the well-known molecule, $\text{Au}_{55}[\text{P}(\text{C}_6\text{H}_5)_3]_{12}\text{Cl}_6$, in 1981, which attracted significant attention in the community.¹⁰⁵ The crystal structure of this nanocluster remained elusive; however, insights into its structure came from later studies.¹⁰⁶ Though techniques such as fast atom bombardment mass spectrometry (FABMS) were used to analyze compounds such as $[\text{Pt}_2(\text{AuPPh}_3)_{10}\text{Ag}_{13}\text{Cl}_7]$, *etc.*,¹⁰⁷ single-crystal X-ray diffraction was the major tool for probing their compositions and structures. Extensive reviews are available on the single-crystal structure of atomically precise nanoclusters.^{7,11,108}

Even though phosphine-protected noble metal nanoclusters have been known since the 1960s as mentioned above, the big leap in the field of solution-phase nanochemistry of noble metals occurred only after the pioneering efforts of the Whetten and Murray research groups on thiolate-protected noble metal particles. In 1996, Whetten *et al.* were the first to observe atomically precise compositions for thiolate-protected

gold particles using mass spectrometry. Particles with such compositions were referred to as ‘nanocrystal gold molecules’.¹⁰⁹ Murray *et al.* electrochemically observed a molecule-like electronic structure for many such particles. In 2005, Shichibu *et al.* synthesized glutathione (SG)-protected $\text{Au}_{25}(\text{SG})_{18}$ nanocluster *via* ligand exchange reaction of pre-formed Au-phosphine nanoclusters.^{110–112} In the same year, Tsukuda *et al.* mass spectrometrically observed a series of glutathione-protected gold nanoclusters with precise and molecule-like compositions, such as $\text{Au}_{10}(\text{SG})_{10}$, $\text{Au}_{15}(\text{SG})_{13}$, $\text{Au}_{18}(\text{SG})_{14}$, $\text{Au}_{22}(\text{SG})_{16}$, $\text{Au}_{22}(\text{SG})_{17}$, $\text{Au}_{25}(\text{SG})_{18}$, $\text{Au}_{29}(\text{SG})_{20}$, $\text{Au}_{33}(\text{SG})_{22}$, and $\text{Au}_{39}(\text{SG})_{24}$ which were separated by polyacrylamide gel electrophoresis (PAGE).¹¹³ In 2006, Häkkinen *et al.* proposed the ‘divide and protect’ structural model wherein these nanoclusters were viewed as consisting of a discrete metal core, protected by well-defined metal–ligand oligomeric units.¹¹⁴ In 2007, Whetten *et al.* unambiguously assigned the composition of the most popular nanocluster in this family, $\text{Au}_{25}(\text{PET})_{18}$ (PET = 2-phenylethanethiolate) (which was wrongly assigned as $\text{Au}_{38}(\text{PET})_{24}$ in earlier investigations) through electrospray ionization mass spectrometry (ESI MS). In 2007, Shichibu *et al.* synthesized a biicosahedral nanocluster, $[\text{Au}_{25}(\text{PPh}_3)_{10}(\text{SC}_n\text{H}_{2n+1})_5\text{Cl}_2]^{2+}$ ($n = 2–18$) by the chemical reaction between $[\text{Au}_{11}(\text{PPh}_3)_8\text{Cl}_2]^+$ and n -alkanethiol ($\text{C}_n\text{H}_{2n+1}\text{SH}$, $n = 2, 8, 10, 12, 14, 16$, and 18).¹¹⁵ This was the first Au_{25} nanocluster compound whose crystal structure was resolved. Apart from thiolate and phosphinate monolayers, anion templates, such as halides,¹¹⁶ sulfides,¹¹⁷ chalcogenides,¹¹⁸ and polyoxometalates,^{119,120} are becoming increasingly prominent in the preparation of high-nuclearity atomically precise Ag nanoclusters.¹²¹ Mass spectrometry, separation techniques such as electrophoresis, size-exclusion chromatography (SEC), and single-crystal X-ray diffraction have made tremendous contributions to the science of ligand-protected noble metal nanoclusters.^{91,122,123} Recently, microelectron diffraction has been used to resolve the structures of those nanoclusters for which crystallization was difficult.^{124,125} Computational methods have made significant contributions to our understanding of the structures and properties of these nanoclusters, complementing the experimental approaches.^{9,41,47,50,126–129}

2.3. Early insights into structures

The identification of atomically precise nanoclusters such as $\text{Au}_{25}(\text{PET})_{18}$ sparked extensive research into numerous nanoclusters and their properties; however, the structures of these early nanoclusters remained unknown for quite some time. Therefore, these particles were called ‘monolayer-protected nanoclusters’ (MPCs); the term was originally used to refer to their larger (consisting of a few hundred metal atoms), plasmonic counterparts wherein the protecting ligands were assumed to be arranged in a uniform, 2D fashion, as in the case of self-assembled monolayers (SAMs)¹³⁰ of ligands on metals. In 2007, Kornberg *et al.* were the first to resolve the crystal structure of a thiolate-protected gold nanocluster, namely $\text{Au}_{102}(\text{MBA})_{44}$ (MBA = *p*-mercaptobenzoic acid).¹³¹

Au₁₀₂(MBA)₄₄ provided significant new insights into the structure of the ligands on the NPs. Au₁₀₂(MBA)₄₄ consists of an Au₇₉ core protected by nineteen Au(SR)₂ and two Au₂(SR)₃ units, often referred to as staple units. In 2008, the crystal structure of Au₂₅(SR)₁₈, one of the most popular members of this family of nanoclusters,¹³² was resolved independently by Akola *et al.* and Heaven *et al.*, which showed that it consisted of an Au₁₃ icosahedron protected by six Au₂(SR)₃ oligomeric staples.^{133,134} These findings proved that the structural arrangement of protecting ligands on metal NPs can be completely different from that of SAMs. Recently, atomic precision has been achieved in a larger size regime of nanoclusters wherein plasmonic features start appearing. For example, structures of Au₂₇₉(SPh-*t*Bu)₈₄,^{135,136} Au₃₂₉(SR)₈₄,^{137,138} [Ag₃₇₄(SR)₁₁₃Br₂Cl₂],¹³⁹ Au₃₃₃(SR)₇₉,¹⁴⁰ and Au₂₄₆(SR)₈₀¹⁴¹ were reported by different groups. There are also attempts to accurately probe the composition of plasmonic NPs using mass spectrometry.^{142,143}

In the few past years, there have been immense advancements in analytic instrumentation, making it possible to study these precision materials in detail.^{26,91,144–146,147} High-resolution mass spectrometry (HR MS) coupled with soft ionization can precisely determine the composition of the core and ligands as well as the charge states of the nanocluster.^{55,148} Other advanced mass spectrometric (MS) techniques, like ion mobility MS (IM-MS)^{97,149–153} and tandem MS (MS/MS),^{19,154,155} are becoming increasingly powerful to understand the size, shape, and structural evolution. Single-crystal X-ray crystallography has made it possible to resolve the structures of several thiol (–SR)-capped nanoclusters, like Au₂₅(SR)₁₈,¹³⁴ Au₂₈(SR)₂₀,¹⁵⁶ Au₃₈(SR)₂₄,¹⁵⁷ Au₄₀(SR)₂₄,¹⁵⁸ Au₅₂(SR)₃₂,¹⁵⁹ Au₄₀(SR)₂₄,¹⁶⁰ Au₉₂(SR)₄₄,¹⁵⁹ Au₁₀₂(SR)₄₄,¹³¹ Au₁₃₃(SR)₅₂,¹⁶¹ Ag₄₄(SR)₃₀,¹⁶² Ag₂₅(SR)₁₈,¹⁶³ Ag₂₉(SR)₁₂,¹⁶⁴ and more. Furthermore, with the development of hyphenated techniques, other inherent nanocluster properties, such as electron affinity (EA), ionization energy (IE), electronic transitions, *etc.*, are being studied in greater detail.⁹¹ A few of the milestones in the development of noble metal cluster chemistry are briefly presented in Fig. 2.

2.4. Structural models

Various models have been proposed to understand the structure and stability of these nanoclusters.^{9,41,129} When the ‘divide and protect model’,¹¹⁴ which was one of the earliest, was put forward, no crystal structures were known for thiolate-protected noble metal nanoclusters. In 2008, Häkkinen *et al.* proposed the superatom complex (SAC), which was an extension of the superatom theory and was used in the case of gas-phase metal nanoclusters, to understand the stability of ligand-protected noble metal nanoclusters.¹³⁰ In 2013, Cheng *et al.* proposed the superatom network (SAN) model for some of the thiolate-protected noble metal nanoclusters.¹⁶⁵ They also proposed the superatom valence bond (SVB) model for non-spherical nanoclusters such as Au₃₈(SR)₂₄ for which the ordinary SAC model cannot be used for explaining the stability. In 2015, Natarajan *et al.* proposed a new structural model,

namely the Borromean ring model,¹⁶⁶ for thiolate-protected noble metal nanoclusters wherein these nanoclusters are viewed as a single structural unit, *i.e.*, interlocked oligomeric metal–ligand rings in contrast to the ‘divide and protect model’ wherein nanoclusters possess a discrete core and staple units. According to this model, Au₂₅(SR)₁₈, for example, is viewed as three interlocked Au₈(SR)₆ rings surrounding the central Au atom. For the first time, a systematic method of precise naming of alloy nanoclusters and mixed-ligand nanoclusters based on this model was proposed. In 2016, Xu *et al.* proposed another structural model, namely the grand unified model (GUM) that successfully comprehended the structures of all the gold nanoclusters known by then.¹⁶⁷ Here, these gold nanoclusters are viewed as built up from triangular and tetrahedral elementary building blocks. An interesting suggestion based on this model is that the evolution of the gold cores in these nanoclusters cannot be viewed simply as the addition of an Au atom alone, but rather as built from these elementary building blocks.

2.5. Properties of metal nanoclusters

Soon after the crystal structures of Au₁₀₂(SR)₄₄ and Au₂₅(SR)₁₈ were resolved, attempts to understand the structure–property relations in these nanoclusters also commenced. For example, distinct electronic absorption bands of Au₂₅(SR)₁₈ were assigned to various electronic transitions within the molecular orbitals derived from the metal atoms and the ligands.^{50,126} Several groups have studied the electrochemistry of various metal nanoclusters¹⁶⁸ and their alloys,^{169–171} such as Au₂₅(SR)₁₈, Au₃₈(SR)₂₄, Au₆₇(SR)₃₅, Au₁₀₂(SR)₄₄, Au₁₄₄(SR)₆₀, Au₃₃₃(SR)₇₉ Ag_xAu_{25–x}(SR)₁₈ (*x* = 1–5), M₂Au₃₆(SR)₂₄ (*M* = Pd, Pt), *etc.*, further establishing the molecule-like electronic structures of these nanoclusters.^{172,173} In 2008, distinct charge states of Au₂₅(SR)₁₈ were observed by a few research groups.^{66,130} Electron paramagnetic resonance (EPR) spectroscopy of Au₂₅(SR)₁₈ was also reported subsequently.⁶⁶ Photoluminescence in gold nanoclusters was first reported by Wilcoxon *et al.* in 1998¹⁷⁴ and subsequently by many other groups.^{50,111,126,128} Photoluminescence was observed from protein-protected noble metal nanoclusters as well.¹⁹ Nuclear magnetic resonance (NMR) spectra of Au₂₅(SR)₁₈ were reported by different groups.^{67,175,176} In 2010, the structure of Au₃₈(SR)₂₄, another popular member of the thiolate-protected gold nanoclusters, was theoretically predicted by Lopez-Acevedo *et al.*,⁴⁴ and its crystal structure was revealed in the same year by Qian *et al.*¹⁵⁷ Chirality in thiolate-protected noble metal nanoclusters was first reported by Schaaff and Whetten in 2000.¹⁷⁷ In 2012, the first separation of enantiomers of Au₃₈(SR)₂₄ was achieved using chiral HPLC by Dolamic *et al.*,¹⁷⁸ which was a significant step toward understanding the chirality of nanoclusters. In 2015, the structural isomerism in Au₃₈(SR)₂₄ was observed by Tian *et al.*¹⁷⁹ Infrared and Raman spectroscopy of these nanoclusters were reported by Dolamic *et al.* and Varnholt *et al.*, in 2013 and 2014, respectively, revealing the distinct vibrational features of the staples of these nanoclusters.^{180,181} Whereas most of these advance-

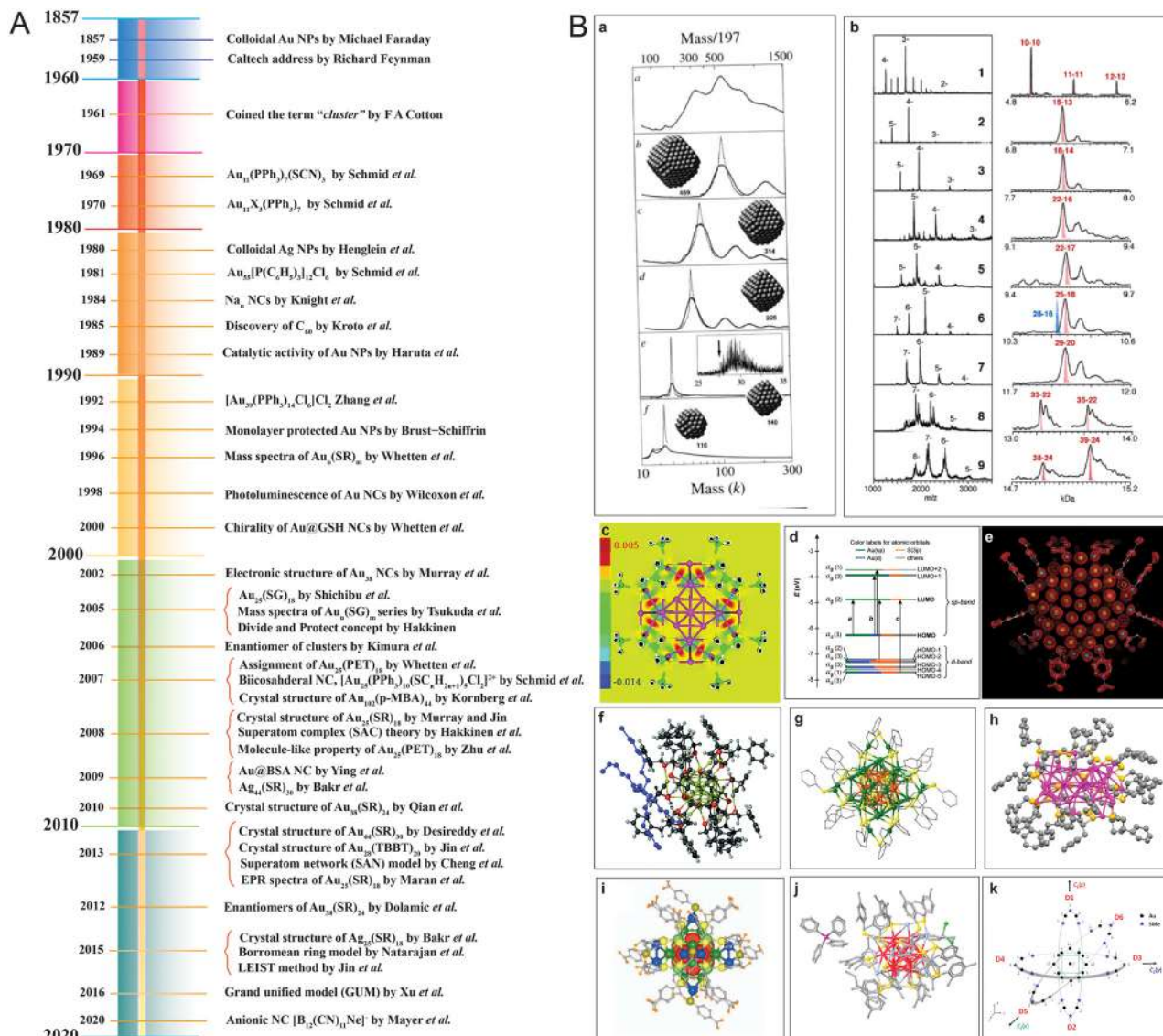


Fig. 2 (A) A representative timeline of the evolution of nanocluster science. (B) A few notable mentions from the nanocluster timeline, namely (a) mass spectra of Au_n(SR)_m, (b) mass spectra of Au_n(SG)_m series, (c) divide and protect concept as visualized from the difference in electron density due to bonds, (d) Kohn–Sham (KS) orbital energy level diagram of Au₂₅(SH)₁₈⁻, crystal structures of (e) Au₁₀₂(p-MBA)₄₄, (f) [N(C₆H₅)₄][Au₂₅(SH)₁₈], (g) Ag₄₄(4-FTP)₃₀(PPh₃)₄, (h) Au₃₈(SR)₂₄, (i) Na₄Au₄₄(MBA)₃₀, and (j) Ag₂₅(DMBT)₁₈, and (k) Borromean rings diagram of Au₂₅(SMe)₁₈ nanocluster. Adapted from ref. a,¹⁰⁹ b,¹¹³ c,¹¹⁴ d^{50,126} e,¹³¹ f,¹³⁴ g,²⁹¹ h,²⁹² i,¹⁶² j,¹⁶³ and k.¹⁶⁶ Copyright 1996 John Wiley and Sons. Copyright 2005, 2006, 2008, 2010, and 2015 American Chemical Society. Copyright 2007 American Association for the Advancement of Science. Copyright 2013 Springer Nature Group.

ments were centered around gold nanoclusters, the search for an atomically precise silver nanocluster was fruitful only in 2013 when Desiredy *et al.* reported the structure of Ag₄₄(SR)₃₀.¹⁶² Ag₂₅(SR)₁₈, which is structurally and compositionally analogous to Au₂₅(SR)₁₈, was discovered in 2015 by Joshi *et al.*¹⁶³ Clusters of other metals and alloy nanoclusters composed of two, three and four elements have been reported.^{10,182} Apart from thiolates, a wide variety of ligands, such as selenolates,^{183–187} tellurolates, alkynes,^{188,189} carbenes,¹⁹⁰ *etc.*, have also been used as protecting ligands for noble metal nanoclusters. For a comprehensive summary of the advancements in the field of thiolate-protected noble

metal nanoclusters, please consult several additional references.^{7,8,10–12,41,57,91,173,191–194}

3. Chemical reactivity of ligand-protected atomically precise metal clusters

The molecule-like nature of the physical properties of these nanoclusters is evident from the structural and spectroscopic studies discussed above. Recently, we have shown that these

nanoclusters exhibit molecule-like chemical reactivity as well. In the following sections, we discuss different aspects of their chemistry in detail.

3.1. Ligand exchange and ligand-induced transformations

Post-synthetic modification in particles is a versatile approach for the transformation in atomically precise nanoclusters in terms of compositional, morphological, and structural changes. Reactions of nanoclusters with structurally different ligands are another way to synthesize new nanoclusters. Substitution or exchange of ligands is one of the earliest reactions of such nanoclusters.¹⁹⁵

Over the past two decades, monolayer-protected metal nanoclusters reacting with various ligands have produced nanoclusters with novel physical and chemical properties.¹⁹⁶ Murray *et al.* performed the first of such ligand-exchange reactions with thiol-protected gold nanoclusters.¹⁹⁷ Murray *et al.* also studied the mechanism of these ligand-exchange reactions in detail using mass spectrometry, NMR spectroscopy, and electrochemistry.^{195,198} The rate of such reactions depends on the concentrations of both the nanocluster and the foreign ligand. The electron-donating and withdrawing nature of the functional groups on the ligands also governs the reaction rates. Using electrochemistry, Parker *et al.* showed that the electron-withdrawing ligands accelerate the exchange rate relative to electron-donating ligands.¹⁹⁹ Murray *et al.* observed that the ligand exchange is a second-order reaction.²⁰⁰ Rate of reaction is determined by the bonding of incoming and outgoing ligands with metal, much like an associative mechanism. However, the rate is independent of the size of the nanoclusters. For example, both $\text{Au}_{38}(\text{PET})_{24}$ and $\text{Au}_{140}(\text{PET})_{53}$ showed similar rate constants during ligand exchange using various *p*-substituted aryl thiols.²⁰¹ The understanding of site selectivity and specificity of ligands in exchange reactions significantly improved with the availability of single-crystal structures of nanoclusters.

When noble metal nanoclusters react with foreign ligands, they undergo a transformation that leads to three types of ligand-exchange products. These products can result in the nanocluster with (i) retention of its structure and composition upon exchange, (ii) alteration in geometry while retaining its composition, or (iii) alteration in both structure and composition.

The initial reports on ligand-exchange reactions indicate that structure and composition of the nanocluster remain unaltered in the process. Murray *et al.* extensively studied the ligand-exchange reactions on $\text{Au}_{25}(\text{PET})_{18}$ with different SR (where, R = Ph-CH₃, Ph-F, *etc.*), which resulted in $\text{Au}_{25}(\text{SR})_{18-x}(\text{SR}')_x$ series ($x = 1-12$).^{200,202,203} Partial ligand exchange was observed during the reaction of *p*-BBT (BBT = bromobenzenethiol) with $\text{Au}_{102}(\text{p-MBA})_{44}$ and $\text{Au}_{25}(\text{PET})_{18}$ which led to the formation of $\text{Au}_{102}(\text{p-MBA})_{40}(\text{p-BBT})_4$ and $\text{Au}_{25}(\text{PET})_{16}(\text{p-BBT})_2$, respectively.^{204,205} In 2014, Abdulhalim *et al.* reported the ligand exchange on $\text{Ag}_{44}(\text{4-FTP})_{30}$ (FTP = fluorothiophenol) with various other aryl thiols such as MNBA (5-mercapto-2-nitrobenzoic acid), 4-NTP (NTP = nitrothiophe-

no), and 2-NT (NT = naphthalenethiol) which resulted in the formation of $\text{Ag}_{44}(\text{SR})_{30}$ (where SR = MNBA/4-NTP/2-NT).²⁰⁶ A second type of ligand exchange, referred to as ligand-induced isomerization, was reported in 2016 by Jin *et al.* upon the reaction of $\text{Au}_{28}(\text{CHT})_{20}$ (CHT = cyclohexanethiol) with TBBT ligand (4-*tert*-butylbenzenethiol), in which the structure of the nanocluster changed while the composition remained unchanged.²⁰⁷

In 2008, Shibu *et al.* came up with the first report on post-synthetic modification of atomically precise Au_{25} nanoclusters *via* ligand exchange reaction.¹⁹⁵ Performing a ligand exchange with functionalized glutathione on the $\text{Au}_{25}(\text{SG})_{18}$ nanocluster altered its optical and photoluminescence properties. These reactions have since found widespread application for modifying the chemical and other properties of nanoclusters through the introduction of new ligands to the parent clusters. Recently, ligand-exchange-induced structure transformation (LEIST) has become a rapidly developing technique in nanoclusters. In such reactions, when a foreign ligand is introduced, it can cause significant distortion of the core, resulting in both structural and compositional changes within the nanocluster. In 2013, Jin *et al.* introduced the term LEIST when they observed the transformation of $\text{Au}_{38}(\text{SR})_{24}$ to $\text{Au}_{36}(\text{SR}')_{24}$ nanocluster through a ligand-exchange reaction. Jin *et al.* performed the ligand-exchange reaction on $\text{Au}_{38}(\text{PET})_{24}$ with excess TBBT (TBBT = 4-*tert*-butylbenzenethiol) under thermal conditions, resulting in molecularly pure $\text{Au}_{36}(\text{TBBT})_{24}$ in excellent yield.²⁰⁸ The process of ligand exchange brings about a change in the structure of biicosahedral $\text{Au}_{38}(\text{PET})_{24}$, transforming it into a truncated tetrahedral $\text{Au}_{36}(\text{TBBT})_{24}$ with an FCC kernel. Interestingly, one of the first examples of an FCC-structured $\text{Au}_n(\text{SR})_m$ nanocluster is $\text{Au}_{36}(\text{TBBT})_{24}$. Zeng *et al.* established the universality of the LEIST method by reacting $\text{Au}_{25}(\text{PET})_{18}$ with TBBT under thermal conditions, which led to the formation of $\text{Au}_{28}(\text{TBBT})_{20}$.¹⁵⁶ The Jin group's discovery of the LEIST method led to the synthesis of numerous new nanoclusters.²⁰⁹ Following this work, a large number of transformations was studied by different groups, such as conversions of $\text{Au}_{11}(\text{PPh}_3)_7\text{Cl}_3$ to $[\text{Au}_{25}(\text{SR})_5(\text{PPh}_3)_{10}\text{X}_2]^{2+}$,²¹⁰ $\text{Au}_{15}(\text{SG})_{13}$ to $\text{Au}_{16}(\text{S-Adm})_{12}$,²¹¹ $\text{Au}_{18}(\text{S-C-C}_6\text{H}_{11})_{14}$ to $\text{Au}_{21}(\text{S-Adm})_{15}$,²¹² *etc.*, which proved the method to be versatile for making new structures. Furthermore, similar structural changes were observed in silver nanoclusters, and the mechanisms underlying these changes were investigated in detail. Bakr *et al.* showed the reversible conversion between $\text{Ag}_{25}(\text{2,4-DMBT})_{18}$ (DMBT = dimethylbenzenethiol) and $\text{Ag}_{44}(\text{4-FTP})_{30}$ (FTP = fluorothiophenol).²¹³ Upon reaction with 2,4-DMBT, $\text{Ag}_{44}(\text{4-FTP})_{30}$ underwent a disproportionation reaction to form smaller sized $\text{Ag}_{25}(\text{4-FTP})_1(\text{2,4-DMBT})_{17}$ and bigger sized $\text{Ag}_{46-50}(\text{4-FTP})_{4-9}(\text{2,4-DMBT})_{21-26}$. After complete ligand exchange, other less stable nanoclusters transformed to more stable $\text{Ag}_{25}(\text{2,4-DMBT})_{18}$. On the other hand, the conversion of $\text{Ag}_{25}(\text{2,4-DMBT})_{18}$ to $\text{Ag}_{44}(\text{4-FTP})_{30}$ occurred *via* dimerization of $\text{Ag}_{25}(\text{2,4-DMBT})_{18}$ followed by a rearrangement pathway. A similar mechanism was observed during the conversion of $\text{Ag}_{35}(\text{SG})_{18}$ to $\text{Ag}_{44}(\text{4-FTP})_{30}$.²¹⁴ Khatun *et al.* showed a distinctly

different mechanistic pathway during the transformation of $\text{Ag}_{59}(\text{2,5-DCBT})_{32}$ (DCBT = dichlorobenzenethiol) to $\text{Ag}_{44}(\text{2,4-DCBT})_{30}$, $\text{Ag}_{25}(\text{2,4-DMBT})_{18}$ and $\text{Ag}_{29}(\text{1,3-BDT})_{12}(\text{PPh}_3)_4$ (BDT = benzenedithiol) upon reaction with 2,4-DCBT, 2,4-DMBT and 1,3-BDT/ PPh_3 , respectively (Fig. 3).²¹⁵ In the presence of incoming thiol ligands, $\text{Ag}_{59}(\text{2,5-DCBT})_{32}$ dissociated completely into smaller nanoclusters and thiolates instead of ligand exchange. Then, these smaller nanoclusters and thiolates recombined and rearranged to form the final product. The nature of the thiolate ligand plays an important role in determining the structure and composition of the product nanoclusters. Khatun *et al.* also reported the synthesis of $\text{MgAg}_{28}(\text{1,3-BDT})_{12}(\text{PPh}_3)_4$ from $\text{MgAg}_{24}(\text{2,4-DMBT})_{18}$ via the LEIST method. Recently, a phosphine-protected nanocluster $\text{Ag}_{18}(\text{PPh}_3)_{10}\text{H}_{16}$ synthesized by Bakr *et al.* was observed as a very good precursor for the LEIST reaction (Fig. 4).²¹⁶ Bodiuzzaman *et al.* synthesized two new nanoclusters, $\text{Ag}_{46}(\text{DMBT})_{24}(\text{PPh}_3)_8$ and $\text{Ag}_{40}(\text{DMBT})_{24}(\text{PPh}_3)_8$ via the LEIST method, using $\text{Ag}_{18}(\text{PPh}_3)_{10}\text{H}_{16}$.²¹⁷ Manju *et al.* synthesized NIR-emitting $[\text{Ag}_{34}\text{S}_3(\text{SBB})_{20}(\text{CF}_3\text{COO})_6]^{2+}$ nanocluster from $\text{Ag}_{18}(\text{PPh}_3)_{10}\text{H}_{16}$ upon reacting it with tertiary-butylbenzylthiol (SBB).²¹⁸ Upon reacting $\text{Ag}_{18}(\text{PPh}_3)_{10}\text{H}_{16}$ with 2-pyrene imine thiol (2-PIT), Jana *et al.* synthesized a new dual-emitting nanocluster, $[\text{Ag}_{35}(\text{2-PIT})_7(\text{PPh}_3)_7@(\text{H}_2\text{O})]^{3+}$.²¹⁹ Kang and Zhu published an extensive review on the evolution of the LEIST methodology and its application.²²⁰

Ligand exchange is an effective strategy to improve the physical and chemical properties of nanoclusters. The method has largely been used to enhance the emission quantum yield (QY) of several non-luminescent or feebly luminescent nano-

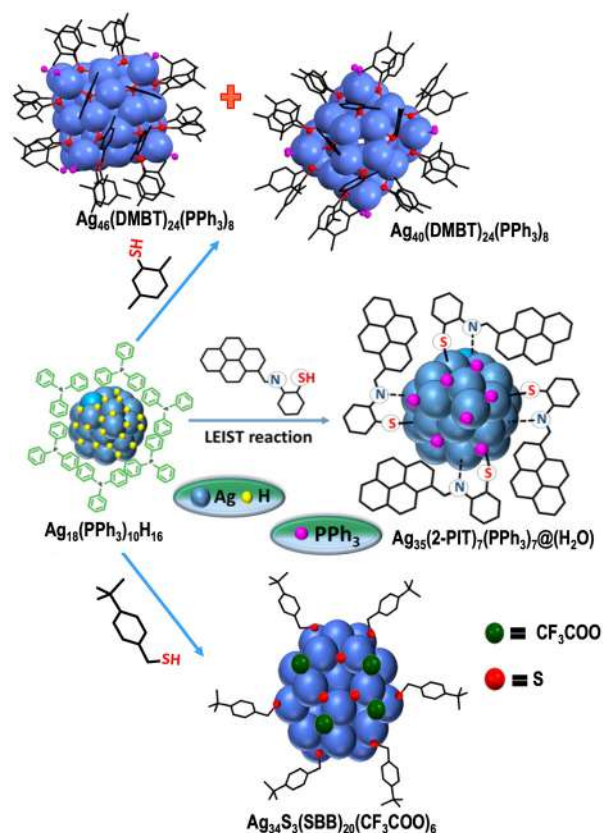


Fig. 4 Formation of $[\text{Ag}_{34}\text{S}_3(\text{SBB})_{20}(\text{CF}_3\text{COO})_6]^{2+}$, $[\text{Ag}_{35}(\text{2-PIT})_7(\text{PPh}_3)_7@(\text{H}_2\text{O})]^{3+}$, $\text{Ag}_{46}(\text{DMBT})_{24}(\text{PPh}_3)_8$ and $\text{Ag}_{40}(\text{DMBT})_{24}(\text{PPh}_3)_8$ from $\text{Ag}_{18}(\text{PPh}_3)_{10}\text{H}_{16}$ via LEIST method. Adapted from ref. 217. Copyright 2019 John Wiley and Sons.

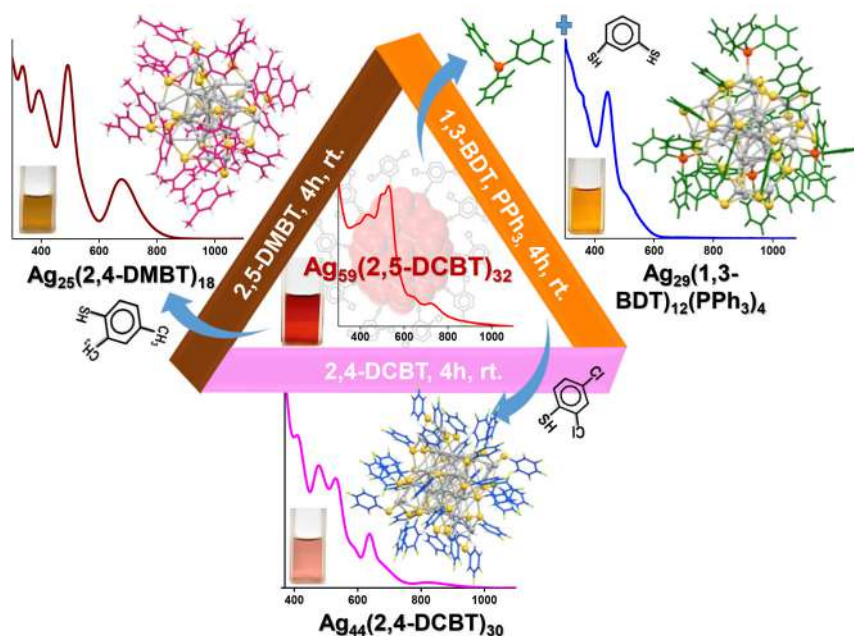


Fig. 3 Schematic representation of ligand exchange-induced conversion of $\text{Ag}_{59}(\text{2,5-DCBT})_{32}$ to $\text{Ag}_{44}(\text{2,4-DCBT})_{30}$, $\text{Ag}_{25}(\text{2,4-DMBT})_{18}$ and $\text{Ag}_{29}(\text{1,3-BDT})_{12}(\text{PPh}_3)_4$ after the reaction with 2,4-DCBT, 2,4-DMBT and 1,3-BDT/ PPh_3 , respectively, under ambient conditions. Adapted from ref. 215. Copyright 2017 Royal Society of Chemistry.

clusters. Jin *et al.* showed an improvement in photoluminescence (PL) intensity while preserving the composition of $\text{Au}_{25}(\text{SR})_{18}$.²²¹ They found higher QY for $\text{Au}_{25}(\text{PET})_{18}$ (PET = 2-phenylethanethiol) than for $\text{Au}_{25}(\text{DDT})_{18}$ (DDT = dodecanethiol) and $\text{Au}_{25}(\text{HT})_{18}$ (HT = hexanethiol). Later on, the PL intensity of $\text{Au}_{25}(\text{PET})_{18}$ enhanced 6.5 fold on using NAP (NAP = 2-(naphthalen-2-yl)ethanethiolate) ligand instead of PET.²²² Kim *et al.* showed enhancement in PL intensity of $\text{Au}_{36}(\text{TBBT})_{24}$ (TBBT = *tert*-butylbenzenethiol) by partial ligand exchange using CPT (CPT = cyclopentanethiol) ligand.²²³ Similar to gold nanoclusters, ligand engineering in silver nanoclusters also led to the enhancement of the PL QY. Khatun *et al.* found structure-conserved ligand exchange in $\text{Ag}_{29}(\text{BDT})_{12}(\text{PPh}_3)_4$ (BDT = 1,3-benzenedithiol) using various diphosphine ligands such as DPPM (1,1-bis(diphosphino)methane), DPPE (1,2-bis(diphosphino)ethane) and DPPP (1,3-bis(diphosphino)propane) which resulted in the increment of PL QY, as shown in Fig. 5.²²⁴ Among these nanoclusters, $\text{Ag}_{29}(\text{BDT})_{12}(\text{DPPP})_4$ exhibited highest PL QY which is 30 fold higher than that of $\text{Ag}_{29}(\text{BDT})_{12}(\text{PPh}_3)_4$. The PL intensity can also be modified by the structure, transformed due to ligands. Such an example is the conversion of $\text{Pt}_1\text{Ag}_{24}(\text{SR})_{18}$ to $\text{Pt}_1\text{Ag}_{28}(\text{SAdm})_{18}(\text{PPh}_3)_4$ (SAdm = adamantanethiol) which displayed 50-fold higher PL QY than the parent nanocluster.²²⁵ Other properties such as chirality is introduced in nanoclusters using the ligand exchange method.^{226,227} Bürgi *et al.* introduced chirality in $\text{Au}_{38}(\text{PET})_{24}$ nanocluster by partial ligand exchange using chiral bidentate thiol, BINAS (BINAS = 1,1'-binaphthyl-2,2-dithiol).²²⁸

3.2. Reactions with metal ions

The interaction of a metal ion with the noble metal nanocluster is reflected in the changes observed in the absorption and emission spectra of the nanocluster. Some metal nanoclusters are known to be highly fluorescent compared to their

bulk counterparts. Also, the post-synthetic metal-exchange reactions with noble metal nanoclusters are an important method for the preparation of alloy nanoclusters. Of all the known metal-exchange methods, galvanic reduction is one of the most efficient approaches for the preparation of multimetallic alloy nanoclusters.

Metal ion-induced alteration in the fluorescence of nanoclusters is one of the most used strategies for sensing heavy metal ions, like Hg^{2+} , Cu^{2+} , As^{3+} , Cr^{3+} , Pb^{2+} , *etc.*⁷⁵ In 2007, Habeeb *et al.* were the first to report the reactivity of $\text{Au}_{25}\text{SG}_{18}$ nanocluster to AuCl_4^- .²²⁹ The $\text{Au}_{25}\text{SG}_{18}$ nanocluster underwent an instantaneous decomposition in the presence of AuCl_4^- ions to form an insoluble gold-glutathione coordination polymer (Au_nSG_m). The characteristic absorption features of $\text{Au}_{25}\text{SG}_{18}$ nanocluster get quenched immediately after addition of AuCl_4^- ions due to the formation of Au(I) – glutathione complex. Upon reaction with other metal ions, such as Ag^+ , Fe^{3+} , Cu^{2+} , Ni^{2+} , Cd^{2+} , Zn^{2+} and Sr^{2+} , the $\text{Au}_{25}\text{SG}_{18}$ nanocluster decomposes but at a slower rate. The net reaction of $\text{Au}_{25}\text{SG}_{18}$ nanocluster – Au^{3+} ion can be represented as an electron-transfer process where the electrons from the nanocluster core reduce AuCl_4^- to AuCl_2^- ions.

Mercury (Hg) is one of the most toxic heavy metals. Bootharaju and Pradeep reported that the $\text{Ag}_{7,8}(\text{MSA})_{7,8}$ nanocluster (MSA = mercaptosuccinic acid) can act as a Hg and other heavy metal scavenger.²³⁰ In the reaction medium, the silver nanocluster interacts preferentially through its core and the carboxylate group of mercaptosuccinic acid (MSA) ligand depending upon the concentration of Hg^{2+} ion. The $\text{Ag}_{7,8}(\text{MSA})_{7,8}$ nanocluster undergoes luminescence quenching as it interacts with Hg^{2+} . To understand the scavenging property of the $\text{Ag}_{7,8}(\text{MSA})_{7,8}$ nanocluster, it is important to note that the redox potentials of Ag^+/Ag^0 decrease with the particle size compared with the bulk metal, which is +0.79 V, whereas it is +0.8 V for the interacting metal ion ($\text{Hg}^{2+}/\text{Hg}^0$). The net cell electromotive force (*emf*) for the reduction of Hg^{2+} by the silver nanocluster is positive. The alumina-loaded $\text{Ag}_{7,8}(\text{MSA})_{7,8}@\text{Al}_2\text{O}_3$ nanocluster can be used quantitatively for Hg^{2+} removal from contaminated water. Later on, from the same group, Chakraborty *et al.* went ahead to report the selective reaction of $\text{Ag}_{25}\text{SG}_{18}$ nanocluster with Hg^{2+} ion. The chemical interaction of $\text{Ag}_{25}\text{SG}_{18}$ nanocluster and Hg^{2+} ion resulted in the formation of Ag_3Hg_2 alloy (*parascachnerite* with an orthorhombic crystal structure), as observed with the appearance of new blue-shifted features in the optical absorption spectra (Fig. 6). XPS studies show that the $\text{Ag}_{25}\text{SG}_{18}$ nanocluster – Hg^{2+} ion reaction is a redox process which involves oxidation of Ag^0 to Ag^+ and reduction of Hg^{2+} to Hg^0 . The luminescent $\text{Ag}_{25}\text{SG}_{18}$ nanocluster can act as a sensing material, as it undergoes fluorescence quenching upon interaction with Hg^{2+} ions with a limit of detection of 1 ppb.

Another heavy metal present in drinking water is Cu^{2+} , which has a permissible limit of 1.3 ppm in drinking water as set by the U.S. Environmental Protection Agency (EPA). Glutathione (GSH) is a natural tripeptide in amino acids, such as cysteine, glutamic acid, and glycine. GS-protected gold

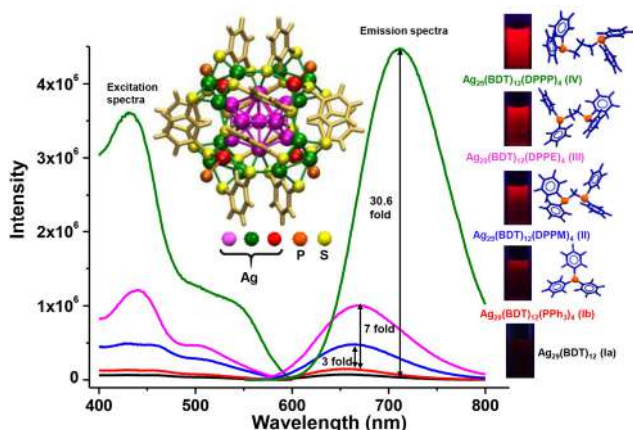


Fig. 5 Excitation and emission spectra of $\text{Ag}_{29}(\text{BDT})_{12}$ and $\text{Ag}_{29}(\text{BDT})_{12}(\text{P})_4$ where P = PPh_3 , DPPM, DPPE, DPPP. A systematic enhancement of PL intensity is observed. Photographs of nanoclusters under UV light are also shown. Reproduced from ref. 224. Copyright 2018 Royal Society of Chemistry.

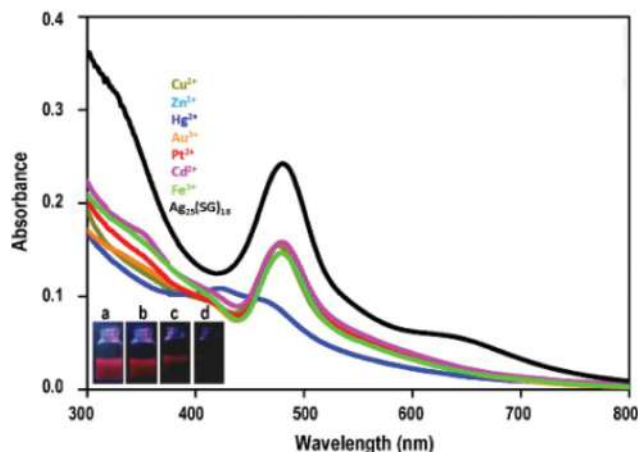


Fig. 6 Optical absorption spectra of the $\text{Ag}_{25}\text{SG}_{18}$ nanocluster solution on addition of different metal ions. Under UV excitation, images corresponding to fluorescence quenching of (a) phase transferred nanocluster and on the addition of (b) 1 ppm, (c) 2 ppm, and (d) 10 ppm of Hg^{2+} . Adapted from ref. 290. Copyright 2012 Elsevier.

nanoclusters are biocompatible and have strong near-IR fluorescence emission compared with other non-aqueous $\text{Au}_n(\text{SR})_m$, making them a popular candidate for developing biological and heavy metal sensors. Back in 2009, fluorescent Au@GS NPs made a debut as a highly selective Cu^{2+} sensor, which is a classic example of aggregation-induced fluorescence quenching.²³¹ Later on, efforts were undertaken by George *et al.* for sensing Cu^{2+} ions using thiolate-protected gold nanoclusters.³⁴ This work involved a GS-protected Au_{15} nanocluster encapsulated in cyclodextrin (CD) cavities (denoted by $\text{Au}_{15}@\text{CD}$). The sensor material is prepared by loading the $\text{Au}_{15}@\text{CD}$ nanocluster onto a freestanding film of chitosan. This nanocluster composite material is a bright luminescent film under UV light. Upon exposing the nanocluster composite material to Cu^{2+} ions, luminescence quenching happens which is selective to Cu^{2+} ion concentration. A change in emission maximum was observed in the PL spectra of the material before and after its exposure to Cu^{2+} ions. The sensing specificity of the nanocluster composite material towards Cu^{2+} ion was studied using XPS analysis, which suggested a reduction of Cu^{2+} to $\text{Cu}^{1+}/\text{Cu}^0$ by the glutathione ligand or the Au_{15} core. The reported limit of detection of the GS-protected- $\text{Au}_{15}@\text{CD}$ nanocluster composite material is 1 ppm of Cu^{2+} ion present in the medium. Zhang *et al.* reported the application of water-soluble GS-protected gold nanoclusters in Cu^{2+} sensing with a limit of detection of 86 nM.⁷² The quenching of the fluorescence is attributed to the carboxylic group in GSH-ligand, which is a chelating agent with a high affinity and selectively towards Cu^{2+} ion over other metal ions, like Hg^{2+} and Pb^{2+} , present in the medium. Krishnadas *et al.* reported a highly luminescent MSA-protected Ag-Au bimetallic nanocluster (denoted as AgAu@MSA) material as a Cu^{2+} sensor. Initially, the preparation of the AgAu@MSA nanocluster involved a galvanic reduction of polydispersed Ag NPs by Au^{I} -MSA thiolates.

A methanolic solution of the AgAu@MSA nanocluster undergoes immediate luminescence quenching selectively upon interaction with Cu^{2+} even in the presence of other metal ions. The mechanism of metal-induced fluorescence quenching of the nanocluster was investigated using XPS, and it was concluded that the Cu^{2+} ion interacts with the AgAu metal core of the nanocluster. The nanocluster-metal ion interaction is a redox process; the AgAu metal core reduces the Cu^{2+} ion to $\text{Cu}^{1+}/\text{Cu}^0$, while it gets oxidized in the process.

In the following part, we will focus on the metal-exchange reactions of noble metal nanoclusters resulting in alloy nanoclusters. As per the galvanic theory, the metal ion with a higher reduction potential replaces another metal with a lower reduction potential, and subsequently, it gets reduced (Fig. 7A). The reduction potential of metals in decreasing order is $\text{Fe}^{2+} > \text{Cd}^{2+} > \text{Co}^{2+} > \text{Ni}^{2+} > [\text{Au NCS}] > \text{Cu}^{2+} > \text{Hg}^{2+} > \text{Ag}^{1+} > \text{Pd}^{2+} > \text{Pt}^{2+} > \text{Au}^{1+}$.^{232,233} Using the galvanic replacement method, various multimetallic noble metal alloy nanoclusters are formed. One such example is the Au-incorporated $\text{Ag}_{24}\text{Au}(\text{DMBT})_{18}$ nanocluster derived from $\text{Ag}_{25}(\text{DMBT})_{18}$ studied by Bootharaju *et al.*, where the reduction potentials of Ag^+/Ag and Au^+/Au are 0.080 and 1.69 V, respectively (Fig. 7C(a)).²³⁴ The structure of the bimetallic $\text{Ag}_{24}\text{Au}(\text{DMBT})_{18}$ nanocluster is analogous to its monometallic counterpart with enhanced stability and photoluminescence. The reaction of $\text{PdAg}_{24}(\text{SR})_{18}$ and Au-salt was found to proceed *via* trimetallic $\text{PdAuAg}_{23}(\text{SR})_{18}$ nanocluster intermediate and finally resulting in a replacement product, the $\text{AuAg}_{24}(\text{SR})_{18}$ nanocluster. But the Au ionic reaction with the structurally equivalent $\text{PtAg}_{24}(\text{SR})_{18}$ nanocluster led to the formation of $\text{Au}_2\text{PtAg}_{22}(\text{SR})_{18}$ nanocluster. Later, Kang *et al.* reported dopant-dependent shape-controlled galvanic exchange reactions.²³⁵ The Au-doping in a $\text{PtAg}_{24}(\text{DMBT})_{18}$ nanocluster with the precursors Au-DMBT and AuBrPPh_3 resulted in the formation of trimetallic nanoclusters with shape-unaltered $\text{PtAu}_x\text{Ag}_{24-x}(\text{DMBT})_{18}$ and altered $\text{Pt}_2\text{Au}_{10}\text{Ag}_{13}(\text{PPh}_3)_{10}\text{Br}_7$ nanoclusters, respectively (Fig. 7C(b)). Similarly, multimetallic $\text{PtCu}_x\text{Ag}_{28-x}(\text{BDT})_{12}(\text{PPh}_3)_4$ and $\text{Pt}_1\text{Ag}_{12}\text{Cu}_{12}\text{Au}_4(\text{S-Adm})_{18}(\text{PPh}_3)_4$ nanoclusters were prepared using the galvanic exchange method.²³⁶ Bootharaju *et al.* studied the metal-exchange reaction between $\text{MAg}_{24}(\text{SR})_{18}$ ($\text{M} = \text{Pd}/\text{Pt}$) and AuPPh_3Cl salt, using mass spectrometry (Fig. 7C(c)).²³⁷ Likewise, using the templated galvanic metal-exchange route, a highly stable $\text{Au}_{5.34}\text{Ag}_{44.66}(\text{Dppm})_6(\text{TBBM})_{30}$ ($\text{Dppm} = \text{bis}(\text{diphenylphosphino})\text{methane}$ and $\text{TBBM} = 4\text{-tert-butylbenzyl mercaptan}$) nanocluster was prepared from $\text{Ag}_{50}(\text{Dppm})_6(\text{TBBM})_{30}$ (Fig. 7C(d)).²³⁸

An anti-galvanic reaction (AGR) defies the classical galvanic reduction (GR) as the metal ions get reduced by the less reactive (or more noble) metal (Fig. 7B). The driving force for an anti-galvanic reaction can be explained in terms of the difference in the redox potential of the participating entities. In 1985, Plieth proposed a theory on the relationship between the electrode potential of metal nanoparticles and their particle diameter.²³⁹ Theoretically, bulk metals (M_{bulk}) can be transformed into small metal particles (M_{NP}) by dissolving into metal ions (M^+) and then redepositing as particles. The

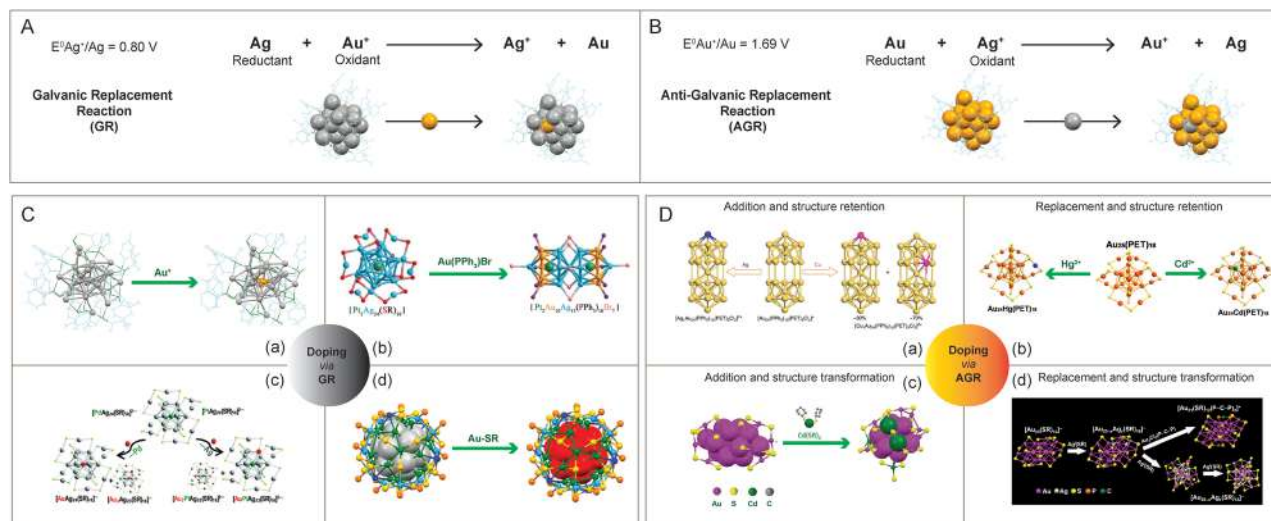
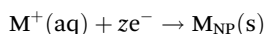


Fig. 7 Schematic representation of (A) galvanic replacement and (B) anti-galvanic replacement reaction from the context of doping in $\text{Ag}_{25}(\text{SR})_{18}$ and $\text{Au}_{25}(\text{SR})_{18}$, respectively. Examples showing the preparation of alloy nanoclusters using (C) galvanic and (D) anti-galvanic reaction routes. Reproduced with permission from ref. C-a,²³⁴ b,²³⁶ c,²³⁷ and d,²³⁸ and D-a,²⁴⁶ b,²⁴⁸ c,²⁵¹ and d.²⁴⁹ Copyright 2015 and 2017 American Chemical Society. Copyright 2016 and 2018 John Wiley and Sons. Copyright 2016 Royal Society of Chemistry. Copyright 2017, Springer Nature Group. Copyright 2019 National Academy of Sciences.

reduction of bulk metal (M_{bulk}) into metal nanoparticles (M_{NP}) can be described by the electrochemical cell reaction,²³⁹



Plieth states that the standard reduction potential of a small metal particle undergoes a negative shift, as expressed in the following equation,²³⁹

$$\mu_d = \mu_b - \left(\frac{2M}{zF} \right) \frac{\gamma}{r}$$

where, μ_d and μ_b are the reduction potentials of metal NP and electrode of the same metal, respectively. The other terms are molar mass (M), specific mass (ρ), number of electrons (z), Faraday's constant (F), surface free energy (γ), and NP radius (r). Later, Zamborini *et al.* and Henglein *et al.* experimentally demonstrated a significant negative shift in the electrode potentials of Ag^{87} and Au NPs²⁴⁰ having sizes below 4 nm.

The ultrasmall-sized noble metals nanoclusters have been recently emerging as interesting candidates for anti-galvanic reactions.^{232,241} The anti-galvanic reaction route provides a more facile and milder method towards alloying with a better control over the composition, structure, and properties of the nanoclusters. Choi *et al.* reported the first anti-galvanic reaction in nanoclusters with the alloying of $[\text{Au}_{25}(\text{PET})_{18}]$ nanocluster.²⁴² The $[\text{Au}_{25}(\text{PET})_{18}]^-$ nanocluster upon reaction with Ag^+ ion resulted in a bimetallic $[\text{Au}_{24}\text{Ag}(\text{PET})_{18}]^-$ nanocluster. From the electrochemical series, it is known that Au is less reactive than Ag, and it was anticipated that the reduction of Au(III) by Ag metal is facile in the ambient conditions but the opposite is not. In 2012, Wu studied the reaction of $\text{Au}_{25}(\text{PET})_{18}$ with Ag^+ and Cu^{2+} ions resulting in bimetallic pro-

ducts as characterized using matrix-assisted laser desorption/ionization time of flight mass spectrometry (MALDI-TOF MS) and XPS.²³² Ag^+ ions failed to react with 2–3 nm Au NPs, thereby establishing $\text{Au}_{25}(\text{PET})_{18}$ nanoclusters as a unique candidate towards anti-galvanic reaction. The thiolate ($-\text{SR}$) ligand coverage on the nanocluster surface plays a pivotal role in the anti-galvanic reactions. As the ligand attaches to the metal surface, it gains a partial negative charge which further assists in the reduction of less noble ions, like, Ag^+ and Cu^{2+} . Here, the anti-galvanic reaction is catalyzed by the highly reactive metal atom on the nanocluster surface. The AGR products are influenced by monolayers on the nanocluster surface. For instance, Wu *et al.* demonstrated that when exposed to silver ion precursors (such as AgNO_3 , Ag-PET, Ag-EDTA, and Ag-DTZ; where EDTA stands for ethylenediamine tetraacetic acid disodium salt and DTZ for dithiazone), $\text{Au}_{25}(\text{PET})_{18}$ reacts and forms various Ag–Au alloy nanoclusters.²⁴³ However, $\text{Au}_{25}(\text{SG})_{18}$ does not exhibit any reaction with Ag^+ ions.²⁴⁴

Using anti-galvanic reaction routes, gold nanoclusters can be alloyed by a heteroatom addition or replacement that also involves a retention or an alteration of the structural framework.²⁴¹

Here are a few examples of heteroatom addition with retention of the initial nanocluster structural framework. The reaction between $\text{Au}_{25}(\text{PET})_{18}$ and AgNO_3 in acetonitrile results in the formation of $\text{Au}_{25}\text{Ag}_2(\text{PET})_{18}$ nanocluster as a major product.²⁴⁵ The incoming Ag-atoms, instead of replacing Au-atoms, get added to the $\text{Au}_{25}(\text{PET})_{18}$ nanocluster structure. Upon comparison with the $\text{Au}_{25}(\text{PET})_{18}$ nanocluster, the Ag-added species, $\text{Au}_{25}\text{Ag}_2(\text{PET})_{18}$, has a ~3.5-fold enhancement in QY while no change was seen in the Ag-replaced species, $\text{Au}_{25-x}\text{Ag}_x(\text{PET})_{18}$ ($x \sim 3$). Wang *et al.* observed that a foreign Ag-atom can squeeze into the hollow site of the $\text{Au}_{24}(\text{PPh}_3)_{10}(\text{PET})_5\text{Cl}_2$ nanocluster without altering its compo-

sition or structure (Fig. 7D(a)).²⁴⁶ Other popular examples of metallic replacement with the retention of starting nanocluster structure are Ag, Pt, and Pd-doped Au₃₈(PET)₂₄, Ag-doped Au₃₆(TBBT)₂₄, Cu and Ag-doped Au₁₄₄(PET)₆₀.²⁴⁷ In 2015, Liao *et al.* synthesized Au₂₅Hg₁(PET)₁₈ and Au₂₅Cd₁(PET)₁₈ from Au₂₅(PET)₁₈ using an anti-galvanic reaction (Fig. 7D(b)).²⁴⁸ The single-crystal X-ray diffraction of Au₂₅Hg₁(PET)₁₈ revealed the structural similarity with Au₂₅(PET)₁₈ where one of the outer-shell Au-atoms is replaced by a Hg-atom, while for the Au₂₅Cd₁(PET)₁₈ structure, the Cd-atom replaces the Au-atom to occupy the central position (Fig. 7B).

Jin *et al.* pioneered alloying methods where the heteroatomic replacement initiates a structural transformation. Li *et al.* studied the Ag-doping-induced transformation of the Au₂₃(CHT)₁₆ (CHT = cyclohexanethiolate) nanocluster into Au_{25-x}Ag_x(CHT)₁₈ (Fig. 7D(d)).²⁴⁹ The alloying reaction between Au₂₃(CHT)₁₆ and Ag(I)-CHT proceeds through a two-step metal-exchange route: (i) Au₂₃(CHT)₁₆ is initially converted to a Au_{23-x}Ag_x(CHT)₁₆ ($x \sim 1$) intermediate, and (ii) then it is allowed to grow into Au_{25-x}Ag_x(CHT)₁₆ ($x \sim 4$), with Ag sitting at the icosahedral inner shell.²⁵⁰ Zhu *et al.* reported another method of synthesis of the bimetallic nanocluster involving a non-replacement of the heteroatom along with a structural transformation. The Au₂₀Cd₄(SH)(CHT)₁₉ nanocluster was prepared from Au₂₃(SR)₁₆ using the anti-galvanic reaction (Fig. 7D(c)).²⁵¹ The starting Au₂₃(SR)₁₆ nanocluster is known to have an Au₁₅ bi-capped cuboctahedron-based kernel, protected by two Au₃(SR)₄ trimeric and Au(SR)₂ monomeric staples along with four simple bridge -SR- ligands.²⁵² Structural similarity of Au₂₅ and Au₂₀Cd₄(SH)(CHT)₁₉ nanocluster system was found to be composed of a centered icosahedral Au₁₃ and Au₁₁Cd₂ kernel, respectively. The introduction of two Cd-atoms distorts the Au₁₃ kernel of Au₂₅. The resulting nanocluster structure consists of a distorted central icosahedral Au₁₁Cd₂ kernel with the capping of two non-equivalent trimeric staples, one dimeric staple, two monomeric staples, four bridging thiolates (-SR-), and one CdSH unit. Li *et al.* reported Cd-addition to the Au₂₂(SAdm)₁₆ (SAdm = 1-adamantanethiol) nanocluster (biocuboctahedral Au₁₀ kernel), which resulted in a structurally transformed Au₂₂Cd₁(SAdm)₁₆ nanocluster (cuboctahedral Au₁₂Cd₁ kernel).²⁵³ Using the reaction between Cl@Ag₁₄ and AgClO, Hau *et al.* introduced the metal core enlargement in nanoclusters, leading to the formation of bigger Cl₆Ag₈@Ag₃₀.¹¹⁶ Recent investigations have shown that carboxylate ligands on the surface of Ag nanoclusters provide ligand-shell flexibility, inducing structural modifications in the NCs due to differential coordination of Ag between carboxylate and thiol/alkyl moieties.^{254,255} For example, monocarboxylate and dicarboxylate ligand triggers structural transformations Mo₆O₂₂@Ag₄₄ → Mo₈O₂₈@Ag₅₀ (ref. 254) and Ag₅₄ → Ag₂₈, (ref. 255) respectively.

3.3. Reactions with halocarbons

The studies of the reaction of halocarbons with noble metal NPs opened up a new direction in nanocluster chemistry. Nair and Pradeep reported that citrate-capped Ag and Au NPs

possess catalytic property for the destruction of halocarbons, resulting in the formation of metal halides and amorphous carbon. This was the first time such properties had been reported.²⁵⁶ The halocarbon, CCl₄, upon reaction with an alcoholic solution of Ag and Au NPs resulted in the formation of AgCl and AuCl₃, respectively, along with an amorphous carbon residue. This reaction was able to completely mineralize halocarbons like chloro, fluoro, and bromocarbons. Later, Bootharaju and Pradeep identified a pesticide degradation pathway using the citrate-capped Ag and Au NPs.²⁵⁷ Here, chlorpyrifos (CP), an organophosphorothioate pesticide, was used as the model pesticide. After reacting with CP, optical absorption spectroscopy showed a red shift in the surface plasmon of Ag NP, and transmission electron microscopic (TEM) analysis revealed aggregation. Upon reaction with the unsupported and alumina-supported Ag and Au NP, the CP degrades into less toxic by-products like 3,5,6-trichloro-2-pyridinol (TCP) and diethyl thiophosphate (DETP), which was established using mass spectrometric studies. The proposed mechanisms involve steps like: (i) first, the CP binds to the NP surface through an Ag⁺ ← S bond, (ii) P-O cleavage, (iii) nucleophilic H₂O attack at the electrophilic P site, and (iv) finally, electron withdrawal from Ag⁺ ← N and Ag⁺ ← S bonds resulting the formation of stable TCP and DETP compounds. The Ag NPs were found to have better catalytic performance over Au NPs. When reacting with CP, the unsupported Ag@citrate NPs tend to aggregate, while the alumina-supported Ag NPs do not. This makes the latter more efficient for water purification, and reusable.

In 2013, Bootharaju *et al.* reported the degradation of halocarbons like CCl₄, C₆H₅CH₂Cl, and CHCl₃, using atomically precise Ag₉MSA₇ nanoclusters.²⁵⁸ The reaction products, AgCl, CCl₃COOH, amorphous carbon, and acetone, were characterized using XRD, Raman, infrared, optical absorption, X-ray photoelectron spectroscopy, and mass spectrometry. To increase the miscibility of halocarbons like CCl₄ in the reaction mixture, isopropyl alcohol (IPA) was used. The precipitate is amorphous carbonaceous material with a graphitic structure, while the supernatant contains acetone from oxidation of IPA. The proposed mechanism (Fig. 8) involves an initial adsorption of IPA and CCl₄ on the nanocluster surface, which in turn catalyses the oxidation of IPA into acetone and activation of the C-Cl bond of the CCl₄. The surface activities initiate a series of electron transfer reactions like release of H⁺ and Cl⁻ ions to the medium, making it acidic, Cl⁻ ions replacing the MSA ligands, oxidation of Ag⁰ to Ag⁺, and finally, mineralization of CCl₄.

3.4 Supramolecular chemistry of metal nanoclusters

The supramolecular chemistry of nanoclusters is an emerging area of research which also highlights the molecular nature of atomically precise nanoclusters. The organic ligands protecting the metal core of the nanocluster can interact with suitable molecules by weak supramolecular interactions. Such interactions include π - π , C-H... π , van der Waals and electrostatic interactions. Moreover, metallophilic interactions of the nano-

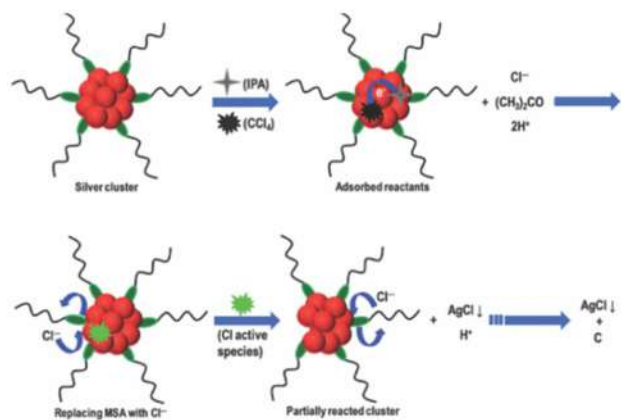


Fig. 8 Schematic representation of the proposed mechanism for degradation of halocarbons, like CCl₄, by Ag nanocluster. Adapted from ref. 258. Copyright 2013 Royal Society of Chemistry.

cluster core also play an active role in controlling the interactions. Such interactions have been the major driving force in controlling the crystal packing of the nanoclusters. Recently, such interactions have also been explored with other molecules. Mathew *et al.* reported interaction between Au₂₅SBB₁₈ (SBB = 4-(*t*-butyl)benzyl mercaptan) and cyclodextrins (CDs), which showed that the SBB ligands were encapsulated in the cavity of CDs, forming inclusion complexes of the nanocluster with CDs.²⁵⁹ Chakraborty *et al.* reported host–guest complexes

of nanoclusters and fullerenes.²⁶⁰ Such interactions were largely dependent on the geometrical compatibility of the two molecules for forming the adducts and further assisted by weak supramolecular interactions. A range of such complexes can be made depending on the structure of the nanoclusters. Ag₂₉(BDT)₁₂ nanocluster can capture C₆₀ molecules on its surfaces, forming adducts such as [Ag₂₉(BDT)₁₂(C₆₀)_{*n*}]^{3−} (*n* = 1–9). Structures of [Ag₂₉(BDT)₁₂(C₆₀)₄]^{3−} and [Ag₂₉(BDT)₁₂(C₆₀)₈]^{3−} are presented in Fig. 9A(a), which reveals that C₆₀ molecules are captured on tetrahedral sites on the nanocluster surface, assisted by interactions with the BDT ligands. Similarly, Ag₂₅(DMBT)₁₈[−] and Au₂₅(PET)₁₈[−] nanoclusters also formed adducts with fullerenes.²⁶¹ Due to a different geometrical structure of M₂₅(SR)₁₈[−] nanoclusters compared with that of [Ag₂₉(BDT)₁₂]^{3−} nanocluster, the nature of the host–guest adducts with fullerenes were also different in the two cases. Ag₂₅(DMBT)₁₈[−] and Au₂₅(PET)₁₈[−] nanoclusters formed aggregates with fullerenes as shown in Fig. 9A(b), and these aggregates were actually dimeric, trimeric, or polymeric adducts of the nanoclusters. Supramolecular interactions of nanoclusters with crown ethers have also been observed, and such complexes were crystallized.²⁶² Crown ethers were captured in the crystal lattice of Ag₂₉ nanoclusters, forming lattice inclusion compounds, as shown in Fig. 9B. Such interactions also resulted in a change in the emission properties compared to the crystals of parent nanocluster. The chemical reactivity of the nanoclusters with other molecules also leads to the emer-

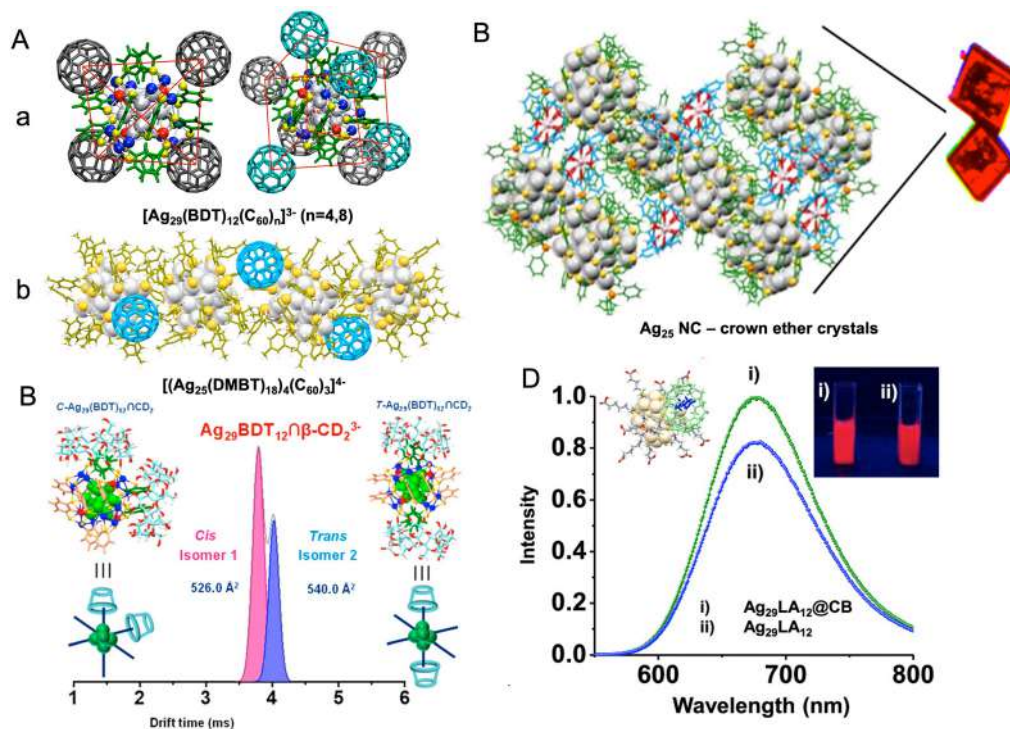


Fig. 9 (A) Host–guest complexes of (a) Ag₂₉(BDT)₁₂^{3−} and (b) Ag₂₅(DMBT)₁₈[−] nanocluster with C₆₀. (B) crystal packing of Ag₂₉(BDT)₁₂(TPP)₄^{3−} nanocluster with 18-crown-6-ether, (C) separation of isomers of the inclusion complex, [Ag₂₉(BDT)₁₂(β-CD)₂]^{3−} by ion mobility mass spectrometry, (D) enhancement in emission of Ag₂₉LA₁₂@CB complexes compared with that of Ag₂₉LA₁₂ nanocluster alone. Reproduced with permission from ref. A-a,²⁶⁰ b,²⁶¹ B,²⁶² C,²⁶³ and D.²⁶⁴ Copyright 2018, 2019, and 2020 American Chemical Society.

gence of new properties in the host-guest complexes. Nag *et al.* reported inclusion complexes of $\text{Ag}_{29}(\text{BDT})_{12}^{3-}$ nanocluster with CDs.²⁶³ Such complexes showed isomerism due to the different binding possibilities of CDs on the nanocluster surface, as presented in Fig. 9C. About six CD attachments to the nanocluster were observed and the geometry of the supramolecular adducts resulted in isomerism similar to the octahedral coordination complexes of metals. Water-soluble and red luminescent $\text{Ag}_{29}(\text{LA})_{12}$ (LA is lipoic acid) nanocluster also formed host-guest complexes with cucurbiturils and CDs which resulted in an enhancement in luminescence of the nanoclusters, as shown in Fig. 9D.²⁶⁴ Such luminescent complexes were used for dopamine sensing. Pillar[5]arene-protected nanoclusters, $\text{Ag}_{29}(\text{LA-P5})_{12}(\text{TPP})_2$, were reported by Muhammed *et al.* which formed spherical assemblies with enhanced luminescence.²⁶⁵ The reactivity of the nanoclusters was also reflected in their interaction with nanostructures like Au nanorods and Te nanorods to form a variety of self-assembled hybrid nanostructures (to be discussed later in detail). Recently, Sheng *et al.* reported the first supramolecular polymorphs of high-nuclearity Ag_{48} NCs encapsulated in an anionic template *via* solvent mediation.²⁶⁶

3.5 Intercluster reactions

Nanoclusters that undergo chemical reactions with one another, also known as intercluster reactions, are a rapidly developing field in nanoscience. Intercluster reactions are now utilized as tools to generate novel hybrid nanoclusters. It is crucial to have an atomic-level understanding of the chemical transformations of nanoclusters in such reactions. In this section, we will be discussing a few such examples of intercluster reactions and their associated mechanisms.

3.5.1. Diversity of reactions. In 2016, Krishnadas *et al.* reported the reaction between structurally and compositionally different $\text{Au}_{25}(\text{PET})_{18}$ and $\text{Ag}_{44}(\text{FTP})_{30}$ nanoclusters.⁵⁴ The intercluster reactions proceed through multiple intersystem exchanges involving both the metal and ligand to form alloy nanoclusters as the reaction product. The ESI mass spectra of the $\text{Au}_{25}(\text{PET})_{18}$ and $\text{Ag}_{44}(\text{FTP})_{30}$, and the reaction products, are shown in Fig. 10A. The mass spectrum shows a series of intercluster reaction products, like alloy nanoclusters formed from $\text{Au}_{25}(\text{PET})_{18}$ by exchange of metal atoms (Au–Ag exchange), ligands (PET–FTP exchange) and metal–ligand fragments (Au–PET with Ag–FTP exchange). Similarly, the Au atoms, PET ligands and Au–PET fragments are also exchanged with $\text{Ag}_{44}(\text{FTP})_{30}$, resulting in the formation of Ag-rich alloy nanoclusters. The total number of metal atoms, ligands, the overall structural features and the charge states of the nanoclusters are preserved in this reaction. Intercluster reaction was then studied for two structurally and compositionally analogous nanoclusters, $\text{Au}_{25}(\text{PET})_{18}$ and $\text{Ag}_{25}(\text{DMBT})_{18}$.⁵⁵ In this case, both interacting nanoclusters possess common structural features, like M_{13} (Ag/Au) icosahedral core and $\text{M}_2(\text{SR})_3$ staple motifs. As shown in Fig. 10B, the ESI mass spectra of these two nanoclusters and the alloy nanoclusters formed as a reaction product were observed. Similarly, these nanoclusters also

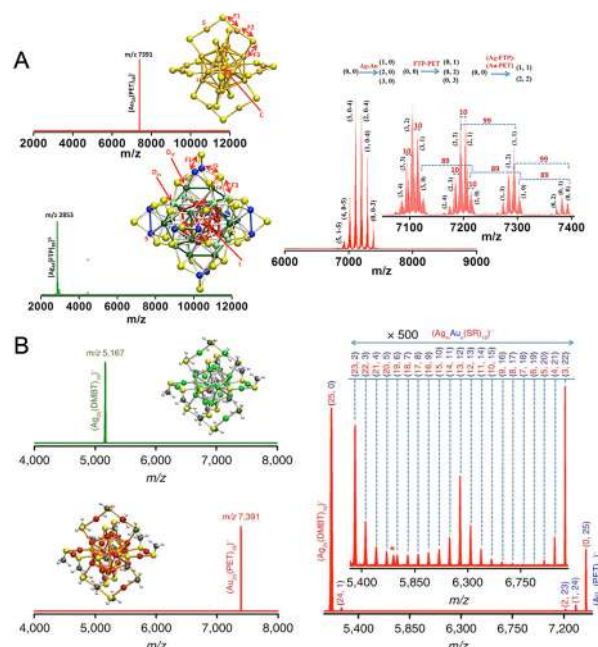


Fig. 10 Intercluster reaction of structurally and compositionally (A) different, $\text{Au}_{25}(\text{PET})_{18}$ and $\text{Ag}_{44}(\text{FTP})_{30}$, and (B) analogous $\text{Au}_{25}(\text{PET})_{18}$ and $\text{Ag}_{25}(\text{DMBT})_{18}$ nanoclusters. Adapted from ref. A,⁵⁴ and B.⁵⁵ Copyright 2016 American Chemical Society and Springer Nature Group.

exchange their metal atoms, ligands and metal–ligand fragments (Au–PET with Ag–DMBT exchange) to form alloy nanoclusters. Unlike the previous example, metal exchange (Ag–Au exchange) was only detected, and other exchanges, such as ligand (PET–DMBT exchange) and metal–ligand fragment (PET–DMBT exchange) were not detected in mass spectral measurements as the molecular masses of PET and DMBT ligands are equal. The mass spectrum collected after 2 min of reaction shows an entire range of alloy nanoclusters of $\text{M}_{25}(\text{SR})_{18}$ composition as formed in the solution. Also, most importantly, in the course of reaction, the overall structure and charge of the nanocluster are conserved.

Several questions arise, such as (i) how two negatively charged nanoclusters interact despite the electrostatic repulsion and steric hindrance offered by the ligands, (ii) whether the reaction is driven by the entire nanocluster entity or any metal–thiolate fragments, and (iii) whether the reaction involves any intermediate or adduct species. In the next section, we will be discussing answers to a few of the questions, while a few remain unanswered.

3.5.2. Mechanism of intercluster reactions. To address the dynamics involved in the intercluster reactions in terms of atomic events, a systematic structural model is needed. Recent experiments suggest that the origin of any intercluster reactivity is the dynamic structure of nanoclusters in the solution. Of all the reported models, the Borromean ring model or *aspicule* (Greek meaning of “aspis” is the *shield*, with “molecule”) model, wherein these nanoclusters are viewed as interlocked rings of metal thiolates (Fig. 11A), explains the intercluster

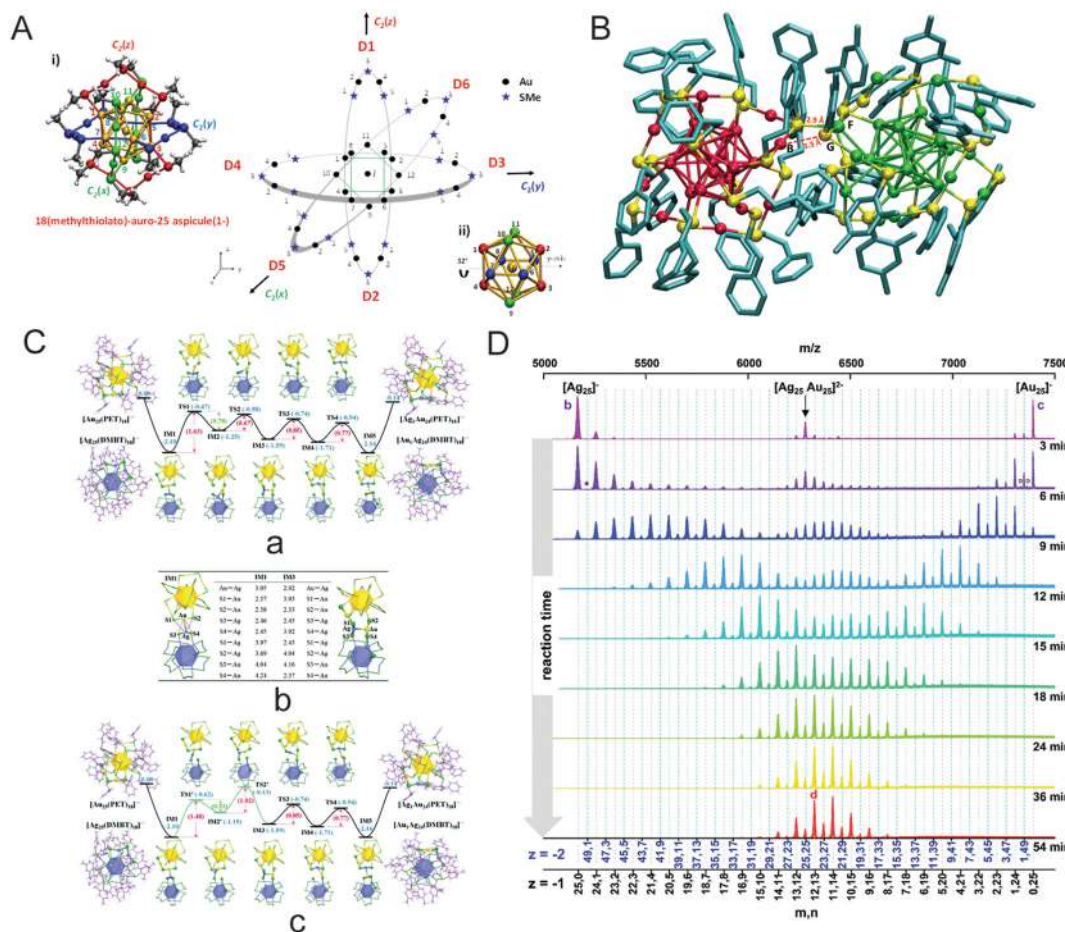


Fig. 11 (A) Borromean rings diagram of $\text{Au}_{25}(\text{SMe})_{18}$, (B) DFT-optimization of the structure of $[\text{Ag}_{25}\text{Au}_{25}(\text{DMBT})_{18}(\text{PET})_{18}]^{2-}$ adduct (with Ag_{25} on the left and Au_{25} on the right) as obtained from a force-field-based molecular docking simulation, (C) energy profiles of the metal exchange reaction between the $[\text{Au}_{25}(\text{PET})_{18}]^{-}$ and $[\text{Ag}_{25}(\text{DMBT})_{18}]^{-}$ nanoclusters; (a) path 1 initiated by Au-S_{PET} bond breaking, (b) DFT optimized metal-metal and metal-S bond lengths (in Angstrom) (c) path 2 initiated by $\text{Ag-S}_{\text{DMBT}}$ bond breaking, and (D) time-dependent mass spectra of a 1 : 1 mixture of $[\text{Au}_{25}(\text{PET})_{18}]^{-}$ and $[\text{Ag}_{25}(\text{DMBT})_{18}]^{-}$. Reproduced with permissions from ref. A–B,¹⁶⁶ C,²⁷⁰ and D.²⁷¹ Copyright 2015 and 2021 American Chemical Society. Copyright 2016, The Royal Chemical Society.

reaction better.¹⁶⁶ As per this model, an $\text{M}_{25}(\text{SR})_{18}$ ($\text{M} = \text{Ag}/\text{Au}$) is composed of three interlocked $\text{M}_8(\text{SR})_6$ rings around the central metal atom, M , where, the $\text{M}_{25}(\text{SR})_{18}$ can be represented as $\text{M}@\text{[M}_8(\text{SR})_6\text{]}_3$. The most important aspect of this *aspicule* model lies in the fact that the metal atoms (excluding the central metal) belong to a single structural unit, that is, metal-thiolate oligomeric rings, contrary to the *divide and protect* model, where the metal atoms belong to two distinct structural units, namely the innermost M_{13} icosahedron and the six outer $\text{M}_2(\text{SR})_3$ staple units. The Borromean ring construction of the nanocluster suggests that in the event of metal-sulfur bond cleavage from any of the rings, the nanocluster can be reorganised as the entire cluster can be separated. This makes it possible for rapid metal exchange, as observed experimentally. In short, the Borromean ring model addresses the intercluster reactions in terms of the structural dynamics of the interlocked rings.

To study the mechanism of intercluster reactions, one needs to understand the role played by the metal-ligand inter-

face in such reactions. The intercluster reaction is a redox-like reaction triggered by the difference in oxidation states of the metal atoms present in the core and staple. For example, let us consider the intercluster reaction between $\text{Ag}_{25}(\text{SR})_{18}$ and $\text{Au}_{25}(\text{SR})_{18}$.⁵⁵ Here, an $\text{Ag}_{25}(\text{SR})_{18}$ molecule reacts with the $\text{Au}_2(\text{SR})_3$ staples of $\text{Au}_{25}(\text{SR})_{18}$, wherein Au in the $\text{Au}_2(\text{SR})_3$ staples is in the +1 oxidation state. Similarly, an $\text{Au}_{25}(\text{SR})_{18}$ molecule reacts with the $\text{Ag}_2(\text{SR})_3$ staples of $\text{Ag}_{25}(\text{SR})_{18}$, wherein Ag from the $\text{Ag}_2(\text{SR})_3$ staple is in the +1 oxidation state. Such redox reactions between $\text{M}_{25}(\text{SR})_{18}$ and $\text{M}(\text{I})$ thiolates, where $\text{M} = \text{Ag}/\text{Au}$, are well studied,^{267,268} although it is still unclear how this difference in oxidation states contributes to the chemical reaction. Next, the intercluster reaction was studied for two entirely different nanoclusters, $\text{Au}_{25}(\text{SR})_{18}$ and $\text{Ag}_{44}(\text{SR})_{30}$, that resulted in the formation of reactive fragments like $\text{Ag}(\text{SR})_2^-$, which further reacts with the $\text{Au}_2(\text{SR})_3$ staples of $\text{Au}_{25}(\text{SR})_{18}$, resulting in an exchange of metal atoms, ligands, and metal-ligand fragments.⁵⁴ In conclusion, the stability and chemical reactivity of these nanoclusters are characteristics of

the nature of the ligand and the bonding present in the metal–ligand oligomeric units.⁵⁸

New insights into the intercluster reactions of $\text{Au}_{25}(\text{PET})_{18}$ and $\text{Ag}_{25}(\text{DMBT})_{18}$ came up with the detection of $[\text{Ag}_{25}\text{Au}_{25}(\text{DMBT})_{18}(\text{PET})_{18}]^{2-}$ adduct species.⁵⁵ Detection of such species indicates a possible pathway involving the formation of an adduct intermediate when two intact nanoclusters participate in these ‘bimolecular’ reactions. Using density functional theory (DFT), the Ag–S bond between the staples of the nanoclusters is observed in an optimized adduct structure (Fig. 11B). Computational studies suggest an interaction at the metal–ligand interface for the reacting nanoclusters at the early stages of the reaction. Furthermore, no metallic exchange was detected when nanoclusters, $\text{Ag}_x\text{Au}_{38-x}(\text{SR})_{24}$ and $\text{Au}_{38}(\text{SR})_{24}$, were separated by a dialysis membrane, and that suggests an intercluster collision as the origin of such reactions.²⁶⁹

In this section, some more mechanistic insights into the intercluster reactions are presented. More studies are needed to understand how two negatively charged nanoclusters collide, overcoming the electrostatic repulsion. One possible explanation for this could be coming from the fact that the anionic nanoclusters are not point charges; the overall negative charge is diffused over the entire nanocluster entity. At the early stages of the reaction, the intercluster interaction could lead to collisions, electron transfer, *etc.*, resulting in nanocluster destabilization. The destabilization of the nanocluster eventually may lead to ring opening (refer to the Borromean ring model) followed by it taking up a flexible elongated conformation, allowing atoms to interact freely with other nanoclusters. At this stage, the nanoclusters with open rings can interact more easily and undergo metal, ligand, and metal–ligand fragment exchanges. The Borromean ring model of $\text{Au}_{25}(\text{SR})_{18}$ suggests the spontaneous inclusion of Ag-atom in

the nanocluster core as it is not sterically hindered. Theoretical calculations were performed by Huang *et al.* to understand the intercluster exchange reaction mechanism between $\text{Au}_{25}(\text{SR})_{18}$ and $\text{Ag}_{25}(\text{SR})_{18}$ (Fig. 11C).²⁷⁰ As per calculations, the intercluster reactions are a two-step mechanism: (i) dianionic adduct $[\text{Au}_{25}\text{Ag}_{25}(\text{PET})_{18}(\text{DMBT})_{18}]^{2-}$ intermediate formation followed by metal–ligand staple rearranges to facilitate metal exchange, and (ii) then the heterometal atom in the staple swaps with the metal atom present in the icosahedral M_{13} -kernel. Recently, Neumaier *et al.* reported a detailed experimental and computational study of the intercluster reaction kinetics of $\text{Au}_{25}(\text{PET})_{18}$ and $\text{Ag}_{25}(\text{DMBT})_{18}$ at room temperature.²⁷¹ During the reaction, the participation of both nanocluster monomer and dimers were observed in mass spectral and collision-induced dissociation (CID) measurements. For an equimolar concentration of nanoclusters, time-dependent mass spectra show a sufficient abundance of both monomers and dimers along with continuous change in overall Ag: Au compositions until a dynamic equilibrium is achieved (Fig. 11D). The kinetic model suggested a three-step reaction route involving dimerization of monomers, metal atom exchange in the transient dimer, and dimer dissociation.

Chakraborty *et al.* reported isotopic metal exchanges in nanoclusters, which provided further insights into the mechanism of atom transfer in NPs. Two isotopic $\text{Ag}_{25}(\text{DMBT})_{18}^-$ nanoclusters, made from ^{107}Ag and ^{109}Ag , reacted spontaneously in solution to form an isotopically mixed nanocluster (Fig. 12A).²⁷² Such isotopic exchanges were similar to isotopic exchanges in $\text{H}_2\text{O}/\text{D}_2\text{O}$, further supporting the molecular nature of the nanoclusters. The exchange was rapid and occurred within seconds after mixing the solutions at room temperature. The exchange could be controlled by controlling the temperature. The exchange kinetics was better studied

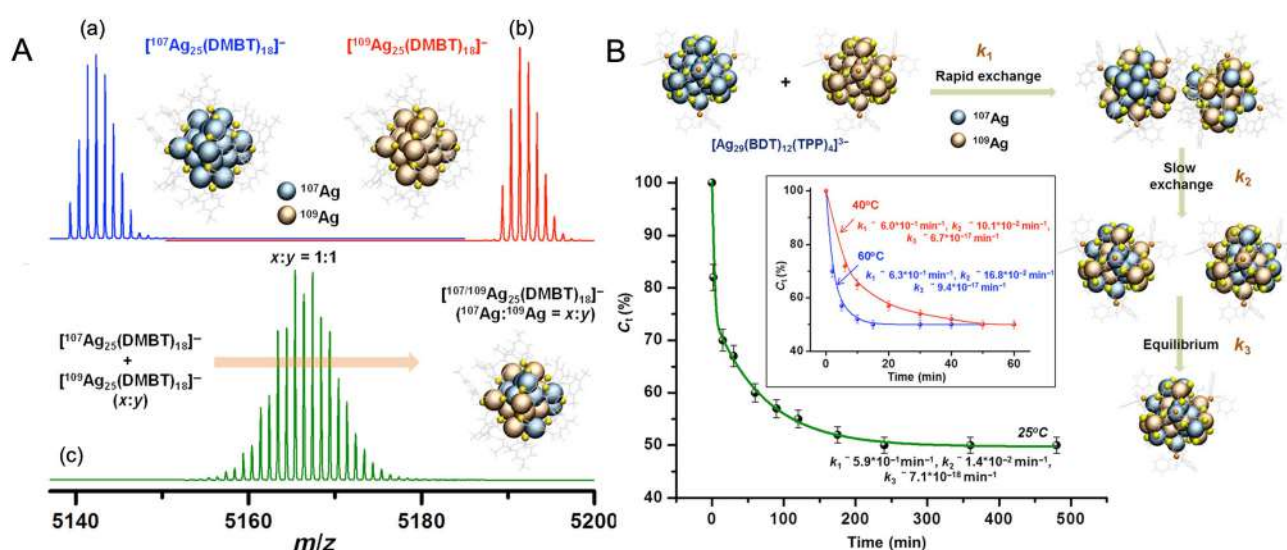


Fig. 12 (A) ESI MS of (a) $^{107}\text{Ag}_{25}(\text{DMBT})_{18}^-$, (b) $^{109}\text{Ag}_{25}(\text{DMBT})_{18}^-$, and (c) isotopically mixed $[\text{Ag}_{25}(\text{DMBT})_{18}]^-$ nanocluster with $^{107}\text{Ag} : ^{109}\text{Ag}$ ratio of 1 : 1. (B) Kinetics of isotopic Ag atom exchange in $[\text{Ag}_{25}(\text{BDT})_{12}(\text{TPP})_4]^{3-}$ nanocluster. Adapted from ref. 272. Copyright 2019 American Association for the Advancement of Science.

using a more rigid nanocluster system, $\text{Ag}_{29}(\text{BDT})_{12}(\text{TPP})_4^{3-}$, which exhibited slower exchange rates. Similar isotopic $^{107}\text{Ag}/^{109}\text{Ag}$ atom exchange was also observed in this case, and a time-resolved study revealed that the process involved an initial fast reaction rate, probably arising from atom exchanges in the staples, followed by a slow reaction rate arising from the diffusion of atoms from staple to core and a final state where the exchanged atoms rearrange until they attain the thermodynamic equilibrium state (Fig. 12B). Such an exchange process was driven by the entropy of mixing. These results suggested the dynamic nature of the metal atom transfer in nanoclusters in solution. The dynamic nature of the ligand monolayers was also reported in a study by Salassa *et al.*²⁷³ The metal–ligand interface also plays an important role in controlling atom transfer and intercluster reactions of nanoclusters.

3.6. Interparticle reactions: reactions with higher dimension materials

In 2014, Ghosh *et al.* made the first attempt to study the chemical interactions between atomically precise nanoclusters with other nanomaterials.²⁷⁴ In this study, graphene reacted with $\text{Au}_{25}(\text{PET})_{18}$, resulting in the formation of a larger nanocluster, $\text{Au}_{135}(\text{PET})_{57}$. The conversion of $\text{Au}_{25}(\text{PET})_{18}$ nanocluster was monitored using time-dependent matrix-assisted laser desorption/ionization mass spectrometry (MALDI MS) (Fig. 13A). As the reaction progressed, the nanocluster peak at m/z 7391 due to $\text{Au}_{25}(\text{PET})_{18}$ gradually disappeared with the simultaneous evolution of the peak at m/z 34.4 kDa corresponding to $\text{Au}_{135}(\text{PET})_{57}$. This conversion process is driven by an overall energy gain of the system due to the entrapment of smaller nanoclusters at the local valleys of the graphenic surface resulting in the reduction in surface curvature and, finally, leading to coalescence. This study gave insights into the utility of surface as a reactive substrate for the chemical transformations of ligand-protected metal nanoclusters.

Unique reactivity of water-soluble $\text{Ag}_{32}\text{SG}_{19}$ nanocluster to Te nanowires (NWs) was reported by Som *et al.*²⁷⁵ This reaction results in the formation Ag–Te hybrid NWs with the growth of nodule-shaped Ag NPs on the NW surface (Fig. 13B). Structural analysis of the modified Te NWs using HRTEM-EDS and XRD confirmed the presence of Ag as nodules with Te NW retaining its inherent (001) hexagonal structure. Furthermore, on heating the Ag-decorated Te NWs, the morphology evolves into nano dumbbell-shaped Ag–Te–Ag NWs with Ag NPs specifically located at the tips (Fig. 13B). The ultrasmall size of the $\text{Ag}_{32}\text{SG}_{19}$ nanocluster provides an increased surface free energy, thereby inducing a tendency of intercluster coalescence, resulting in bigger particles.

Ligand-protected metal nanoclusters make excellent building blocks to create self-assembled hierarchical frameworks.^{192,276,277} An interesting phenomenon of self-assembly arises in Te NWs when the surface is modified with $\text{Ag}_{44}(p\text{-MBA})_{30}$ nanocluster. The $p\text{-MBA}$ ligand shells initiate a H-bonding interaction among themselves, leading to the formation of a bilayer assembly of NWs oriented at an angle of 81° w.r.t. each other (Fig. 14A).²⁷⁸ Nonappa *et al.* reported the

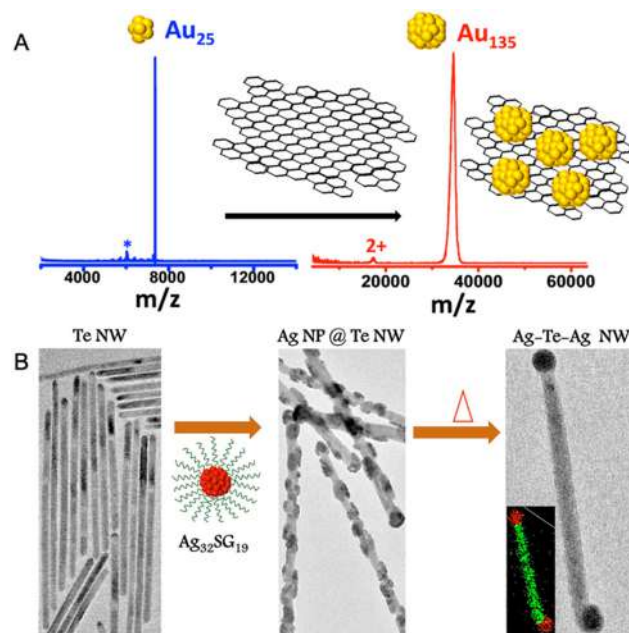


Fig. 13 (A) MALDI MS study for the conversion of $\text{Au}_{25}(\text{PET})_{18}$ to $\text{Au}_{135}(\text{PET})_{57}$ entrapped on the graphene surface upon reaction with graphene. (B) HRTEM images and corresponding schematic representation of pure Te NW upon reaction with $\text{Ag}_{32}\text{SG}_{19}$ and upon further heating yielding Ag nodule-decorated Te NW and dumbbell-shaped Ag–Te–Ag NWs, respectively. Adapted from ref. 274 and 275 for A and B, respectively. Copyright 2014 American Chemical Society.

unique ability of $p\text{-MBA}$ -protected gold nanoclusters to undergo intercluster H-bonding resulting in monolayer-thick 2D nanosheets and spherical capsids.^{276,279} Som *et al.* showed that the $\text{Na}_4\text{Ag}_{44}p\text{MBA}_{30}$ nanoclusters can be self-assembled into a large-area freestanding elastic membrane *via* entrapping them in a transient solvent layer at the air–water interface.²⁸⁰ The patchy distribution of ligands around the metal core facilitates symmetry breaking and eventually directs a preferential interlayer H-bonding between the carboxylic acid groups of the $p\text{-MBA}$ ligands.^{276,277,279} Chakraborty *et al.* showed hydrogen bonding-induced chemical interaction between the $\text{Ag}_{44}(p\text{-MBA})_{30}$ nanocluster and a plasmonic gold nanorod (GNR), leading to the encapsulation of the latter (Fig. 14B), here denoted as $\text{GNR}@p\text{-MBA}$.²⁸¹ The nanocage-like hybrid material was found to have an octahedral morphology as studied using a series of highly sophisticated microscopes, like transmission electron microscopy (TEM), scanning transmission electron microscopy (STEM), and 3D reconstruction using electron tomography. The anisotropic growth was credited to the preferential anchoring of the nanoclusters to Au $\langle 110 \rangle$ over Au $\langle 100 \rangle$ facet of $\text{GNR}@p\text{-MBA}$. $\text{Ag}_{25}(\text{DMBT})_{18}$ nanocluster-mediated site-selective etching of anisotropic planar gold nanotriangles (NTs) was reported.²⁸² Due to differential surface energies, the Au NTs interacting with the nanocluster underwent metallic etching at the edges and doping at the tips while the core remained unaltered. Roy *et al.* reported a polydispersed CuO NP and $\text{Au}_{25}(\text{PET})_{18}$ reaction-mediated formation of spherical-

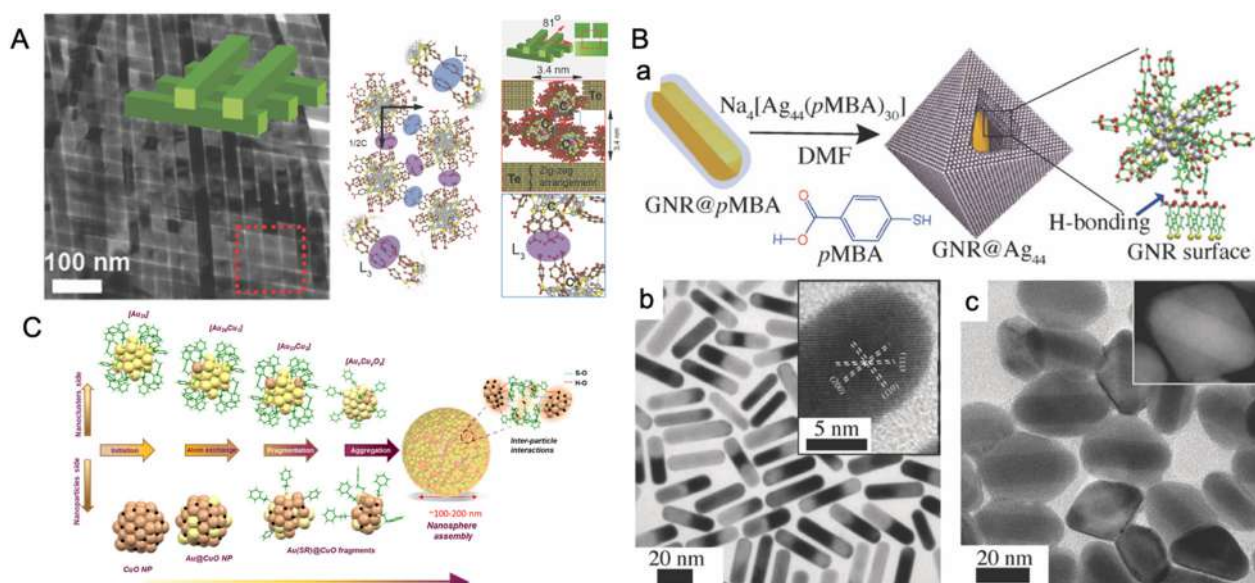


Fig. 14 (A) Composite $\text{Ag}_{44}@\text{Te}$ NW bilayer oriented at an 81° angle w.r.t to each other and (B) its corresponding packing driven by the intercluster H-bonding. (C) Schematic representation and HRTEM micrographs illustrating the assembly of Ag_{44} on the GNR. Adapted from ref. A,²⁷⁸ B,²⁸¹ and C.²⁸³ Copyright 2014 and 2018, John Wiley and Sons. Copyright 2023, The Royal Society of Chemistry.

shaped nanoaggregates of Cu-doped-Au-nanoclusters (Fig. 14C).²⁸³ The reaction involved an NP–NC atom transfer reaction route. Rival *et al.* recently demonstrated that the thiolated azobenzene-protected Au_{25} nanoclusters form reversible assemblies triggered by light.²⁸⁴ With the right choice of nanocluster system, such hybrid nanomaterials having extraordinary stability at room temperature can significantly improve the limit of detection of nanocluster-based sensors.

Bose *et al.* extended the interparticle chemistry to the reactions involving isotropic Ag NPs.²⁸⁵ A spontaneous reaction between $\text{Au}_{25}(\text{PET})_{18}$ nanocluster and polydispersed Ag NPs

with a core diameter of 4.4 ± 2.3 nm, protected with 2-phenylethanthiol (PET), resulted in monodispersed alloy NPs with a core diameter of 3.4 ± 1.2 nm under ambient conditions. The resulting NPs also underwent a spontaneous self-assembly to form a 2D superlattice which was analysed using HRTEM. Using STEM-EDS analysis, the reacted NPs were found to be Ag–Au alloy NPs. A 3D reconstruction of the 2D assembly using electron tomography further revealed that the assembly was composed of reacted alloy NPs arranged in a hexagonal close-packed (hcp) lattice with an interparticle distance of ~ 4.5 nm (Fig. 15A). The mechanism involved an interparticle

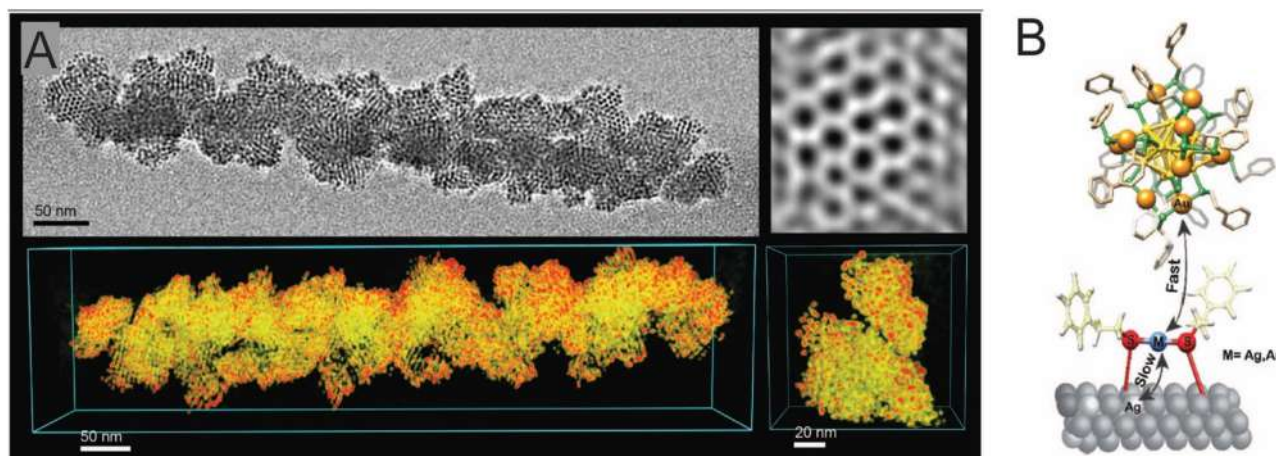


Fig. 15 (A) TEM micrograph, its corresponding 3D reconstruction, and inverse fast Fourier transform image of 2D superlattice assembly (hcp) of the Au–Ag alloy NP resulting from the NP–nanocluster reaction. (B) The number of Ag-doped Au nanocluster versus time plot for the nanocluster–Ag surface reaction and the schematic representation of metal–ligand exchange at the metal–ligand interface in the bulk surface. Reproduced with permission A²⁸⁵ and B.²⁸⁸ Copyright 2020 Royal Society of Chemistry. Copyright 2008 American Chemical Society.

atomic exchange (metal–ligand species), and the metal–ligand interface was found to be crucial in controlling the reaction. Systematic analysis using time-dependent ESI MS showed that the reaction proceeds through a transient $\text{Au}_{25-x}\text{Ag}_x(\text{PET})_{18}$ ($x = 1, 2, 3, \dots$) species along with other alloy nanocluster intermediates. Similar reactions were performed for $\text{Au}_{25}(\text{PET})_{18}$ nanocluster with differently sized Ag@PET NPs, in which the interparticle reactivity was enhanced upon decreasing the size of NPs. The nanocluster–NP reactions can thereby open up an entirely new way of generating alloy NPs in the solution phase with better control over the NP size distribution.

As we move from noble metal nanosystems to their bulk counterparts, chemical properties are altered due to changes in energy levels. Bakshi *et al.* explored the glucose-mediated extraction of Ag from bulk silver surfaces otherwise considered inert.²⁸⁶ Later, Nag *et al.* reported the solution phase synthesis of Ag nanoclusters from bulk metallic silver in the presence of carbohydrate and glutathione followed by chemical reduction.²⁸⁷ Kazan *et al.* utilized the bulk thiolated silver surface to understand intercluster reaction as an interfacial phenomenon of metal–ligand exchange.²⁸⁸ The study involved $\text{Au}_{25}(\text{PET})_{18}$ and $\text{Au}_{38}(\text{PET})_{24}$ nanoclusters, and pure silver foil as model systems. MALDI MS and XPS characterization techniques were used to study the effect of reaction on the nanocluster and foil, respectively. Upon time-dependent monitoring of the $\text{Au}_{25}(\text{PET})_{18}$ and PET-monolayered Ag foil, $\text{Au}_{25-x}\text{Ag}_x(\text{PET})_{18}$ ($x = 1-4$) appeared just after 2 min and a higher Ag-doping was detected for a longer reaction time. With the neat Ag foil, the reaction was found to be slow, as $\text{Au}_{24}\text{Ag}(\text{PET})_{18}$ appeared only after 3 h. Hence, the kinetics of pre-adsorbed and neat silver foils are very different. The average number of doped Ag plotted as a function of time shows that the substitution follows a 2-phase kinetics (initially fast followed by slower exchange) and a sigmoidal trend (initially delayed followed by faster exchange) in preadsorbed and neat foils, respectively. This sigmoidal kinetics can be related to the autocatalytic reactions where the starting 3 h is an induction period for the thiolate, here acting as a catalyst, to deposit on the surface. As the time progressed, thiolate deposition happened, and this is reflected with an increased reaction rate. The mechanism behind the 2-phase kinetics in an atomic exchange reaction was explained using the scheme in which thiolated-Ag on the surface exchanges faster in the early stages of the reaction (Fig. 15B). At the later stages of the reaction, kinetics become slower due to less availability of exchangeable sites on the Ag foil surface. XPS measurements of the reacted Ag foil surface showed the presence of the metallic Au. Similar trends were observed when the $\text{Au}_{38}(\text{PET})_{18}$ nanocluster reacts with both the pre-adsorbed and neat Ag surfaces. XPS measurements of the reacted pre-adsorbed thiolated and neat foils also confirmed the presence of metallic Au. The $\text{Au}_{25}(\text{PET})_{18}$ and $\text{Au}_{38}(\text{PET})_{18}$ reaction was also explored with pre-adsorbed and free surface of other metals like Cd and Cu. This study concluded that for a feasible Au doping in the Ag nanocluster, thiol plays a key role. Recently, Chakraborty *et al.* reported the dynamics of isotopic exchange reactions of iso-

pically pure Ag nanocluster with different dimensions of metallic Ag, like nanoclusters, plasmonic NPs, and bulk.²⁸⁹ Isotopically pure $^{107}\text{Ag}_{25}(\text{DMBT})_{18}$ and $^{108}\text{Ag}_{25}(\text{DMBT})_{18}$ was reacted with different sizes of Ag@DMBT NPs (naturally abundant Ag). With the increase in the NP size, the rate of atomic exchange was reduced. The exchange rate further decreased when the nanocluster was reacted with bulk Ag samples, such as foil and micron-sized powder. The kinetics of isotopic exchange, *i.e.*, reaction timescales, was analyzed by fitting the reactant concentration as a function of time to a reaction model. Under similar reaction conditions, the reaction timescale was longer for the nanocluster–NP reactions compared with intercluster reactions. This suggests that such reactions can be controlled by careful engineering the reacting nanostructures.

4. Insights from nanocluster chemistry

From the results presented, we list below the factors determining the feasibility of reactions of nanoclusters.

- (1) The metal–ligand interface primarily controls the atomic exchange reactions and their feasibility.
- (2) The geometry and stereochemistry of the protecting groups play crucial roles in the intercluster and interparticle reactions.
- (3) Thermodynamics drives the interparticle and isotopic exchange reactions.
- (4) Entropy of mixing drives the isotopic metal exchange in intercluster reactions.
- (5) Nanoclusters exhibit redox-like reactions triggered by the difference in oxidation states of the metal atoms present in the core and staple.
- (6) The core–shell geometry of a nanocluster influences the nanocluster–analyte reaction primarily *via* weak interactions, such as metallophilic and supramolecular interactions.
- (7) Supramolecular interactions like C–H $\cdots\pi$, $\pi\cdots\pi$, van der Waals, hydrogen bonding, and electrostatic interactions guide the formation of the nanocluster assemblies.
- (8) Reactive intermediates, such as adducts and fragments, vary depending on the reacting species.
- (9) LEIST, a method to prepare new nanoclusters, is a ligand-controlled phenomenon. The rate of ligand exchange depends also on the electron-donating or withdrawing nature of the ligand.
- (10) Chemical reactions occur between atomically precise nanoclusters and a range of systems such as ions, clusters, NPs, and bulk metals, and therefore we may suggest that nanoclusters are reactive to the whole range of chemical systems.
- (11) The chemistry is highly sensitive to reaction conditions such as concentration, time, and temperature, and is expected to be influenced by other factors such as the medium, ionic strength, *etc.*

5. Conclusions and future perspectives

Nanoclusters, with their inherent molecule-like properties, show a wide range of chemical reactions with counterparts such as metal ions, clusters, NPs and bulk metals. These chemical reactions yield well-defined alloys which may be nanoclusters, NPs or bulk materials, depending on the systems involved. Such reactions also lead to ligand exchange. The processes yield supramolecular interactions forming assemblies and superstructures. Thermodynamics and kinetics govern the chemistry, and the underlying processes can be modelled with greater accuracy. The chemistry is sensitive to various process conditions such as concentration, temperature, solvent, *etc.*, as typical of molecular events. The products formed and their kinetics and dynamics confirm their molecular nature. In the coming years, such cluster chemistry of atomically precise metal nanoclusters will be explored with oxides, sulfides, and others in the form of clusters, NPs, and bulk materials, yielding new materials. Similar science will be possible between materials of different size regimes of oxides and sulfides themselves, expanding the diversity of the area. The science presented will be greatly influenced by the experimental and computational methodologies used, which can reveal the intricate details of the processes involved. The science at this stage has provided us with many insights into the phenomena at the nanoscale as revealed by the fast isotopic exchange between NPs. Applications of such science are still at infancy.

Author contributions

All authors contributed equally.

Conflicts of interest

There are no conflicts to declare.

Acknowledgements

We acknowledge the Department of Science and Technology (DST), Government of India, and Centre of Excellence program of the Indian Institute of Technology Madras, on the theme of Molecular Materials and Functions, under the Institutions of Eminence of Ministry of Education, India, for supporting our research.

References

- 1 R. Feynman, *Feynman And Computation*, CRC Press, 2002.
- 2 F. A. Cotton and J. T. Mague, *Inorg. Chem.*, 1964, **3**, 1094–1098.
- 3 F. A. Cotton, *Inorg. Chem.*, 1964, **3**, 1217–1220.

- 4 R. W. Murray, *Chem. Rev.*, 2008, **108**, 2688–2720.
- 5 G. Chen, J. Seo, C. Yang and P. N. Prasad, *Chem. Soc. Rev.*, 2013, **42**, 8304–8338.
- 6 H. Zhu, Y. Yang and T. Lian, *Acc. Chem. Res.*, 2013, **46**, 1270–1279.
- 7 R. Jin, C. Zeng, M. Zhou and Y. Chen, *Chem. Rev.*, 2016, **116**, 10346–10413.
- 8 Y. Du, H. Sheng, D. Astruc and M. Zhu, *Chem. Rev.*, 2020, **120**, 526–622.
- 9 T. Tsukuda and H. Hakkinen, *Protected Metal Clusters: From Fundamentals to Applications*, 2013, vol. 53.
- 10 A. Ghosh, O. F. Mohammed and O. M. Bakr, *Acc. Chem. Res.*, 2018, **51**, 3094–3103.
- 11 I. Chakraborty and T. Pradeep, *Chem. Rev.*, 2017, **117**, 8208–8271.
- 12 R. Jin, *Nanoscale*, 2010, **2**, 343–362.
- 13 V. G. Albano, P. L. Bellon, M. Manassero and M. Sansoni, *J. Chem. Soc. D*, 1970, 1210–1211.
- 14 C. E. Briant, B. R. C. Theobald, J. W. White, L. K. Bell, D. M. P. Mingos and A. J. Welch, *J. Chem. Soc., Chem. Commun.*, 1981, 201–202.
- 15 *Atomically precise metal clusters*, ed. T. Pradeep, Elsevier, 1st edn, 2023.
- 16 S. S. Narayanan and S. K. Pal, *J. Phys. Chem. C*, 2008, **112**, 4874–4879.
- 17 J. Xie, Y. Zheng and J. Y. Ying, *J. Am. Chem. Soc.*, 2009, **131**, 888–889.
- 18 J. Yu, S. Choi and R. M. Dickson, *Angew. Chem., Int. Ed.*, 2009, **48**, 318–320.
- 19 P. L. Xavier, K. Chaudhari, A. Baksi and T. Pradeep, *Nano Rev.*, 2012, **3**, 14767.
- 20 X. Wen, P. Yu, Y. R. Toh, A. C. Hsu, Y. C. Lee and J. Tang, *J. Phys. Chem. C*, 2012, **116**, 19032–19038.
- 21 D. M. Chevrier, V. D. Thanthirige, Z. Luo, S. Driscoll, P. Cho, M. A. MacDonald, Q. Yao, R. Guda, J. Xie, E. R. Johnson, A. Chatt, N. Zheng and P. Zhang, *Chem. Sci.*, 2018, **9**, 2782–2790.
- 22 T. Vosch, Y. Antoku, J. C. Hsiang, C. I. Richards, J. I. Gonzalez and R. M. Dickson, *Proc. Natl. Acad. Sci. U. S. A.*, 2007, **104**, 12616–12621.
- 23 H. C. Yeh, J. Sharma, J. J. Han, J. S. Martinez and J. H. Werner, *Nano Lett.*, 2010, **10**, 3106–3110.
- 24 J. T. Petty, B. Sengupta, S. P. Story and N. N. Degtyareva, *Anal. Chem.*, 2011, **83**, 5957–5964.
- 25 J. Sharma, H. C. Yeh, H. Yoo, J. H. Werner and J. S. Martinez, *Chem. Commun.*, 2011, **47**, 2294–2296.
- 26 E. Gwinn, D. Schultz, S. M. Copp and S. Swasey, *Nanomaterials*, 2015, **5**, 180–207.
- 27 D. J. E. Huard, A. Demissie, D. Kim, D. Lewis, R. M. Dickson, J. T. Petty and R. L. Lieberman, *J. Am. Chem. Soc.*, 2019, **141**, 11465–11470.
- 28 L. A. Peyser, A. E. Vinson, A. P. Bartko and R. M. Dickson, *Science*, 2001, **291**, 103–106.
- 29 L. A. Peyser, T. H. Lee and R. M. Dickson, *J. Phys. Chem. B*, 2002, **106**, 7725–7728.

- 30 J. Zheng and R. M. Dickson, *J. Am. Chem. Soc.*, 2002, **124**, 13982–13983.
- 31 J. Zheng, C. Zhang and R. M. Dickson, *Phys. Rev. Lett.*, 2004, **93**, 077402, 8AD.
- 32 M. C. Paa, C. K. Lo, X. Yang and M. M. F. Choi, *J. Phys. Chem. C*, 2010, **114**, 15995–16003.
- 33 E. S. Shibu and T. Pradeep, *Chem. Mater.*, 2011, **23**, 989–999.
- 34 A. George, E. S. Shibu, S. M. Maliyekkal, M. S. Bootharaju and T. Pradeep, *ACS Appl. Mater. Interfaces*, 2012, **4**, 639–644.
- 35 M. Mayer, M. Rohdenburg, V. van Lessen, M. C. Nierstenhöfer, E. Aprà, S. Grabowsky, K. R. Asmis, C. Jenne and J. Warneke, *Chem. Commun.*, 2020, **56**, 4591–4594.
- 36 H. W. Kroto, J. R. Heath, S. C. O'Brien, R. F. Curl and R. E. Smalley, *Nature*, 1985, **318**, 162–163.
- 37 H. W. Kroto, A. W. Allaf and S. P. Balm, *Chem. Rev.*, 1991, **91**, 1213–1235.
- 38 J. Almutlaq, J. Yin, O. F. Mohammed and O. M. Bakr, *J. Phys. Chem. Lett.*, 2018, **9**, 4131–4138.
- 39 Y. Yan, J. Gong, J. Chen, Z. Zeng, W. Huang, K. Pu, J. Liu and P. Chen, *Adv. Mater.*, 2019, **31**, 1808283.
- 40 R. B. Wyrwas, M. M. Alvarez, J. T. Khoury, R. C. Price, T. G. Schaaff and R. L. Whetten, *Eur. Phys. J. D*, 2007, **43**, 91–95.
- 41 H. Häkkinen, *Chem. Soc. Rev.*, 2008, **37**, 1847–1859.
- 42 Y. Negishi, T. Iwai and M. Ide, *Chem. Commun.*, 2010, **46**, 4713–4715.
- 43 C. M. Aikens, *J. Phys. Chem. Lett.*, 2011, **2**, 99–104.
- 44 O. Lopez-Acevedo, H. Tsunoyama, T. Tsukuda, H. Häkkinen and C. M. Aikens, *J. Am. Chem. Soc.*, 2010, **132**, 8210–8218.
- 45 R. Jin, *Nanoscale*, 2015, **7**, 1549–1565.
- 46 C. M. Aikens, *Acc. Chem. Res.*, 2018, **51**, 3065–3073.
- 47 Q. Tang, G. Hu, V. Fung and D. Jiang, *Acc. Chem. Res.*, 2018, **51**, 2793–2802.
- 48 R. S. Ingram, M. J. Hostetler, R. W. Murray, T. G. Schaaff, J. T. Khoury, R. L. Whetten, T. P. Bigioni, D. K. Guthrie and P. N. First, *J. Am. Chem. Soc.*, 1997, **119**, 9279–9280.
- 49 D. Lee, R. L. Donkers, J. M. DeSimone and R. W. Murray, *J. Am. Chem. Soc.*, 2003, **125**, 1182–1183.
- 50 M. Zhu, C. M. Aikens, F. J. Hollander, G. C. Schatz and R. Jin, *J. Am. Chem. Soc.*, 2008, **130**, 5883–5885.
- 51 D. Jiang, M. L. Tiago, W. Luo and S. Dai, *J. Am. Chem. Soc.*, 2008, **130**, 2777–2779.
- 52 P. Yu, X. Wen, Y.-R. Toh, X. Ma and J. Tang, *Part. Part. Syst. Charact.*, 2015, **32**, 142–163.
- 53 S. Chen, R. S. Ingram, M. J. Hostetler, J. J. Pietron, R. W. Murray, T. G. Schaaff, J. T. Khoury, M. M. Alvarez and R. L. Whetten, *Science*, 1998, **280**, 2098–2101.
- 54 K. R. Krishnadas, A. Ghosh, A. Baksi, I. Chakraborty, G. Natarajan and T. Pradeep, *J. Am. Chem. Soc.*, 2016, **138**, 140–148.
- 55 K. R. Krishnadas, A. Baksi, A. Ghosh, G. Natarajan and T. Pradeep, *Nat. Commun.*, 2016, **7**, 13447.
- 56 K. R. Krishnadas, A. Baksi, A. Ghosh, G. Natarajan, A. Som and T. Pradeep, *Acc. Chem. Res.*, 2017, **50**, 1988–1996.
- 57 S. Hossain, Y. Niihori, L. V. Nair, B. Kumar, W. Kurashige and Y. Negishi, *Acc. Chem. Res.*, 2018, **51**, 3114–3124.
- 58 K. R. Krishnadas, G. Natarajan, A. Baksi, A. Ghosh, E. Khatun and T. Pradeep, *Langmuir*, 2019, **35**, 11243–11254.
- 59 T. Kawawaki, A. Ebina, Y. Hosokawa, S. Ozaki, D. Suzuki, S. Hossain and Y. Negishi, *Small*, 2021, **17**, 2005328.
- 60 N. Goswami, Q. Yao, Z. Luo, J. Li, T. Chen and J. Xie, *J. Phys. Chem. Lett.*, 2016, **7**, 962–975.
- 61 X. Kang and M. Zhu, *Chem. Soc. Rev.*, 2019, **48**, 2422–2457.
- 62 S. Biswas, A. K. Das and S. Mandal, *Acc. Chem. Res.*, 2023, **56**, 1838–1849.
- 63 Y. Xiao, Z. Wu, Q. Yao and J. Xie, *Aggregate*, 2021, **2**, 114–132.
- 64 Y. Negishi, H. Tsunoyama, M. Suzuki, N. Kawamura, M. M. Matsushita, K. Maruyama, T. Sugawara, T. Yokoyama and T. Tsukuda, *J. Am. Chem. Soc.*, 2006, **128**, 12034–12035.
- 65 M. Zhu, C. M. Aikens, M. P. Hendrich, R. Gupta, H. Qian, G. C. Schatz and R. Jin, *J. Am. Chem. Soc.*, 2009, **131**, 2490–2492.
- 66 S. Antonello, N. V. Perera, M. Ruzzi, J. A. Gascón and F. Maran, *J. Am. Chem. Soc.*, 2013, **135**, 15585–15594.
- 67 M. Agrachev, S. Antonello, T. Dainese, J. A. Gascón, F. Pan, K. Rissanen, M. Ruzzi, A. Venzo, A. Zoleo and F. Maran, *Chem. Sci.*, 2016, **7**, 6910–6918.
- 68 M. Agrachev, S. Antonello, T. Dainese, M. Ruzzi, A. Zoleo, E. Aprà, N. Govind, A. Fortunelli, L. Sementa and F. Maran, *ACS Omega*, 2017, **2**, 2607–2617.
- 69 M. Agrachev, M. Ruzzi, A. Venzo and F. Maran, *Acc. Chem. Res.*, 2019, **52**, 44–52.
- 70 M. Galchenko, A. Black, L. Heymann and C. Klinke, *Adv. Mater.*, 2019, **31**, 1–6.
- 71 P. Yuan, R. Zhang, E. Selenius, P. Ruan, Y. Yao, Y. Zhou, S. Malola, H. Häkkinen, B. K. Teo, Y. Cao and N. Zheng, *Nat. Commun.*, 2020, **11**, 2229.
- 72 G. Zhang, Y. Li, J. Xu, C. Zhang, S. Shuang, C. Dong and M. M. F. Choi, *Sens. Actuators, B*, 2013, **183**, 583–588.
- 73 X. Yuan, Y. Tay, X. Dou, Z. Luo, D. T. Leong and J. Xie, *Anal. Chem.*, 2013, **85**, 1913–1919.
- 74 X. Chen, J. B. Essner and G. A. Baker, *Nanoscale*, 2014, **6**, 9594–9598.
- 75 A. Mathew and T. Pradeep, *Part. Part. Syst. Charact.*, 2014, **31**, 1017–1053.
- 76 G. Schmid, *Chem. Soc. Rev.*, 2008, **37**, 1909–1930.
- 77 L. Shang, S. Dong and G. U. Nienhaus, *Nano Today*, 2011, **6**, 401–418.
- 78 S. Choi, R. M. Dickson and J. Yu, *Chem. Soc. Rev.*, 2012, **41**, 1867–1891.
- 79 X. R. Song, N. Goswami, H. H. Yang and J. Xie, *Analyst*, 2016, **141**, 3126–3140.
- 80 L. Zhang and E. Wang, *Nano Today*, 2014, **9**, 132–157.

- 81 S. Yamazoe, K. Koyasu and T. Tsukuda, *Acc. Chem. Res.*, 2014, **47**, 816–824.
- 82 P. Liu, R. Qin, G. Fu and N. Zheng, *J. Am. Chem. Soc.*, 2017, **139**, 2122–2131.
- 83 L. Liu and A. Corma, *Chem. Rev.*, 2018, **118**, 4981–5079.
- 84 W. Jing, H. Shen, R. Qin, Q. Wu, K. Liu and N. Zheng, *Chem. Rev.*, 2023, **123**, 5948–6002.
- 85 A. Henglein, *J. Phys. Chem.*, 1979, **83**, 2209–2216.
- 86 A. Henglein and R. Tausch-Treml, *J. Colloid Interface Sci.*, 1981, **80**, 84–93.
- 87 A. Henglein, *J. Phys. Chem.*, 1993, **97**, 5457–5471.
- 88 A. Henglein, *Chem. Rev.*, 1989, **89**, 1861–1873.
- 89 M. Haruta, N. Yamada, T. Kobayashi and S. Iijima, *J. Catal.*, 1989, **115**, 301–309.
- 90 P. Gruene, D. M. Rayner, B. Redlich, A. F. G. van der Meer, J. T. Lyon, G. Meijer and A. Fielicke, *Science*, 2008, **321**, 674–676.
- 91 P. Chakraborty and T. Pradeep, *NPG Asia Mater.*, 2019, **11**, 48.
- 92 W. D. Knight, K. Clemenger, W. A. de Heer, W. A. Saunders, M. Y. Chou and M. L. Cohen, *Phys. Rev. Lett.*, 1984, **52**, 2141–2143.
- 93 R. E. Leuchtner, A. C. Harms and A. W. Castleman Jr., *J. Chem. Phys.*, 1989, **91**, 2753–2754.
- 94 D. E. Bergeron, A. W. Castleman, T. Morisato and S. N. Khanna, *Science*, 2004, **304**, 84–87.
- 95 S. N. Khanna and P. Jena, *Phys. Rev. B: Condens. Matter Mater. Phys.*, 1995, **51**, 13705–13716.
- 96 T. P. Martin, *Phys. Rep.*, 1996, **273**, 199–241.
- 97 S. Gilb, P. Weis, F. Furche, R. Ahlrichs and M. M. Kappes, *J. Chem. Phys.*, 2002, **116**, 4094–4101.
- 98 F. Furche, R. Ahlrichs, P. Weis, C. Jacob, S. Gilb, T. Bierweiler and M. M. Kappes, *J. Chem. Phys.*, 2002, **117**, 6982–6990.
- 99 A. Lechtken, C. Neiss, M. M. Kappes and D. Schooss, *Phys. Chem. Chem. Phys.*, 2009, **11**, 4344–4350.
- 100 B. Yoon, H. Häkkinen, U. Landman, A. S. Wörz, J.-M. Antonietti, S. Abbet, K. Judai and U. Heiz, *Science*, 2005, **307**, 403.
- 101 Z. Li, H. Y. T. Chen, K. Schouteden, T. Picot, T. W. Liao, A. Seliverstov, C. Van Haesendonck, G. Pacchioni, E. Janssens and P. Lievens, *Sci. Adv.*, 2020, **6**, eaay4289.
- 102 M. Brust, M. Walker, D. Bethell, D. J. Schiffrin and R. Whyman, *J. Chem. Soc., Chem. Commun.*, 1994, 801–802.
- 103 M. McPartlin, R. Mason and L. Malatesta, *J. Chem. Soc. D*, 1969, 334–334.
- 104 B. K. Teo, X. Shi and H. Zhang, *J. Am. Chem. Soc.*, 1992, **114**, 2743–2745.
- 105 G. Schmid, R. Pfeil, R. Boese, F. Bandermann, S. Meyer, G. H. M. Calis and J. W. A. van der Velden, *Chem. Ber.*, 1981, **114**, 3634–3642.
- 106 N. Jian, C. Stapelfeldt, K. J. Hu, M. Fröba and R. E. Palmer, *Nanoscale*, 2015, **7**, 885–888.
- 107 T. G. M. M. Kappen, P. P. J. Schlebos, J. J. Bour, W. P. Bosman, J. M. M. Smits, P. T. Beurskens and J. J. Steggerda, *Inorg. Chem.*, 1994, **33**, 754–758.
- 108 M. Bodiuzzaman and T. Pradeep, in *Atomically Precise Metal Nanoclusters*, ed. T. Pradeep, Elsevier, 2023, pp. 271–298.
- 109 R. L. Whetten, J. T. Khoury, M. M. Alvarez, S. Murthy, I. Vezmar, Z. L. Wang, P. W. Stephens, C. L. Cleveland, W. D. Luedtke and U. Landman, *Adv. Mater.*, 1996, **8**, 428–433.
- 110 Y. Shichibu, Y. Negishi, T. Tsukuda and T. Teranishi, *J. Am. Chem. Soc.*, 2005, **127**, 13464–13465.
- 111 D. Lee, R. L. Donkers, G. Wang, A. S. Harper and R. W. Murray, *J. Am. Chem. Soc.*, 2004, **126**, 6193–6199.
- 112 T. Carducci and R. Murray, in *Nanoelectrochemistry*, ed. S. A. Michael and V. Mirkin, CRC Press, Boca Raton, 2015, pp. 73–124.
- 113 Y. Negishi, K. Nobusada and T. Tsukuda, *J. Am. Chem. Soc.*, 2005, **127**, 5261–5270.
- 114 H. Häkkinen, M. Walter and H. Grönbeck, *J. Phys. Chem. B*, 2006, **110**, 9927–9931.
- 115 Y. Shichibu, Y. Negishi, T. Watanabe, N. K. Chaki, H. Kawaguchi and T. Tsukuda, *J. Phys. Chem. C*, 2007, **111**, 7845–7847.
- 116 S. C. K. Hau, P.-S. Cheng and T. C. W. Mak, *J. Am. Chem. Soc.*, 2012, **134**, 2922–2925.
- 117 Z. Wang, H. F. Su, X. P. Wang, Q. Q. Zhao, C. H. Tung, D. Sun and L. S. Zheng, *Chem. – Eur. J.*, 2018, **24**, 1640–1650.
- 118 Z. Wang, J. W. Liu, H. F. Su, Q. Q. Zhao, M. Kurmoo, X. P. Wang, C. H. Tung, D. Sun and L. S. Zheng, *J. Am. Chem. Soc.*, 2019, **141**, 17884–17890.
- 119 Z. Wang, Y. J. Zhu, Y. Z. Li, G. L. Zhuang, K. P. Song, Z. Y. Gao, J. M. Dou, M. Kurmoo, C. H. Tung and D. Sun, *Nat. Commun.*, 2022, **13**, 1802.
- 120 Z. G. Jiang, K. Shi, Y. M. Lin and Q. M. Wang, *Chem. Commun.*, 2014, **50**, 2353–2355.
- 121 S. Wang, Q. Li, X. Kang and M. Zhu, *Acc. Chem. Res.*, 2018, **51**, 2784.
- 122 K. M. Harkness, D. E. Cliffl and J. A. McLean, *Analyst*, 2010, **135**, 868–874.
- 123 T. Chen, Q. Yao, R. R. Nasaruddin and J. Xie, *Angew. Chem., Int. Ed.*, 2019, **58**, 11967–11977.
- 124 B. L. Nannenga and T. Gonen, *Emerging Top. Life Sci.*, 2018, **2**, 1–8.
- 125 S. Vergara, D. A. Lukes, M. W. Martynowycz, U. Santiago, G. Plascencia-Villa, S. C. Weiss, M. J. de la Cruz, D. M. Black, M. M. Alvarez, X. López-Lozano, C. O. Barnes, G. Lin, H. C. Weissker, R. L. Whetten, T. Gonen, M. J. Yacaman and G. Calero, *J. Phys. Chem. Lett.*, 2017, **8**, 5523–5530.
- 126 C. M. Aikens, *J. Phys. Chem. C*, 2008, **112**, 19797–19800.
- 127 J. Enkovaara, C. Rostgaard, J. J. Mortensen, J. Chen, M. Dulák, L. Ferrighi, J. Gavnholt, C. Glinsvad, V. Haikola, H. A. Hansen, H. H. Kristoffersen, M. Kuisma, A. H. Larsen, L. Lehtovaara, M. Ljungberg, O. Lopez-Acevedo, P. G. Moses, J. Ojanen, T. Olsen, V. Petzold, N. A. Romero, J. Stausholm-Møller, M. Strange, G. A. Tritsarlis, M. Vanin, M. Walter, B. Hammer, H. Häkkinen, G. K. H. Madsen, R. M. Nieminen,

- J. K. Nørskov, M. Puska, T. T. Rantala, J. Schiøtz, K. S. Thygesen and K. W. Jacobsen, *J. Phys.: Condens. Matter*, 2010, **22**, 253202.
- 128 K. L. D. M. Weerawardene and C. M. Aikens, *J. Am. Chem. Soc.*, 2016, **138**, 11202–11210.
- 129 P. Bose, G. Natarajan and T. Pradeep, *Atomically Precise Metal Nanoclusters*, Elsevier, 2023, pp. 313–343.
- 130 M. Walter, J. Akola, O. Lopez-Acevedo, P. D. Jadzinsky, G. Calero, C. J. Ackerson, R. L. Whetten, H. Grönbeck and H. Häkkinen, *Proc. Natl. Acad. Sci. U. S. A.*, 2008, **105**, 9157–9162.
- 131 P. D. Jadzinsky, G. Calero, C. J. Ackerson, D. A. Bushnell and R. D. Kornberg, *Science*, 2007, **318**, 430–433.
- 132 X. Kang, H. Chong and M. Zhu, *Nanoscale*, 2018, **10**, 10758–10834.
- 133 J. Akola, M. Walter, R. L. Whetten, H. Häkkinen and H. Grönbeck, *J. Am. Chem. Soc.*, 2008, **130**, 3756–3757.
- 134 M. W. Heaven, A. Dass, P. S. White, K. M. Holt and R. W. Murray, *J. Am. Chem. Soc.*, 2008, **130**, 3754–3755.
- 135 N. A. Sakthivel, S. Theivendran, V. Ganeshraj, A. G. Oliver and A. Dass, *J. Am. Chem. Soc.*, 2017, **139**, 15450–15459.
- 136 N. A. Sakthivel, M. Stener, L. Sementa, A. Fortunelli, G. Ramakrishna and A. Dass, *J. Phys. Chem. Lett.*, 2018, **9**, 1295–1300.
- 137 C. Kumara, X. Zuo, J. Ilavsky, D. Cullen and A. Dass, *J. Phys. Chem. C*, 2015, **119**, 11260–11266.
- 138 S. K. Eswaramoorthy, N. A. Sakthivel and A. Dass, *J. Phys. Chem. C*, 2019, **123**, 9634–9639.
- 139 H. Yang, Y. Wang, X. Chen, X. Zhao, L. Gu, H. Huang, J. Yan, C. Xu, G. Li and J. Wu, *Nat. Commun.*, 2016, **7**, 12809.
- 140 H. Qian, Y. Zhu and R. Jin, *Proc. Natl. Acad. Sci. U. S. A.*, 2012, **109**, 696.
- 141 C. Zeng, Y. Chen, K. Kirschbaum, K. J. Lambright and R. Jin, *Science*, 2016, **354**, 1580.
- 142 S. Vergara, U. Santiago, C. Kumara, D. Alducin, R. L. Whetten, M. J. Yacaman, A. Dass and A. Ponce, *J. Phys. Chem. C*, 2018, **122**, 26733–26738.
- 143 C. Kumara, M. M. Hoque, X. Zuo, D. A. Cullen, R. L. Whetten and A. Dass, *J. Phys. Chem. Lett.*, 2018, **9**, 6825–6832.
- 144 J. H. Beynon, *Microchim. Acta*, 1956, **44**, 437–453.
- 145 E. McDaniel, D. Martin and W. Barnes, *Rev. Sci. Instrum.*, 1962, **33**, 2–7.
- 146 F. W. McLafferty and T. A. Bryce, *Chem. Commun.*, 1967, 1215–1217.
- 147 A. Baksi, P. Chakraborty, A. Nag, D. Ghosh, S. Bhat and T. Pradeep, *Anal. Chem.*, 2018, **90**, 11351–11357.
- 148 Z. Luo, V. Nachammai, B. Zhang, N. Yan, D. T. Leong, D. E. Jiang and J. Xie, *J. Am. Chem. Soc.*, 2014, **136**, 10577–10580.
- 149 A. Baksi, P. Chakraborty, S. Bhat, G. Natarajan and T. Pradeep, *Chem. Commun.*, 2016, **52**, 8397–8400.
- 150 A. Baksi, A. Ghosh, S. K. Mudedla, P. Chakraborty, S. Bhat, B. Mondal, K. Krishnadas, V. Subramanian and T. Pradeep, *J. Phys. Chem. C*, 2017, **121**, 13421–13427.
- 151 P. Chakraborty, A. Baksi, S. K. Mudedla, A. Nag, G. Paramasivam, V. Subramanian and T. Pradeep, *Phys. Chem. Chem. Phys.*, 2018, **20**, 7593–7603.
- 152 P. Chakraborty, S. Malola, M. Neumaier, P. Weis, H. Häkkinen and M. M. Kappes, *Angew. Chem.*, 2023, e202305836.
- 153 P. Chakraborty, M. Neumaier, P. Weis and M. M. Kappes, *J. Am. Soc. Mass Spectrom.*, 2023, **34**, 676–684.
- 154 R. Yost and C. Enke, *J. Am. Chem. Soc.*, 1978, **100**, 2274–2275.
- 155 F. W. McLafferty, *Acc. Chem. Res.*, 1980, **13**, 33–39.
- 156 C. Zeng, T. Li, A. Das, N. L. Rosi and R. Jin, *J. Am. Chem. Soc.*, 2013, **135**, 10011–10013.
- 157 H. Qian, W. T. Eckenhoff, Y. Zhu, T. Pintauer and R. Jin, *J. Am. Chem. Soc.*, 2010, **132**, 8280–8281.
- 158 S. Malola, L. Lehtovaara, S. Knoppe, K.-J. Hu, R. E. Palmer, T. Bürgi and H. Häkkinen, *J. Am. Chem. Soc.*, 2012, **134**, 19560–19563.
- 159 C. Zeng, Y. Chen, C. Liu, K. Nobusada, N. L. Rosi and R. Jin, *Sci. Adv.*, 2015, **1**, e1500425.
- 160 C. Zeng, C. Liu, Y. Chen, N. L. Rosi and R. Jin, *J. Am. Chem. Soc.*, 2016, **138**, 8710–8713.
- 161 A. Dass, S. Theivendran, P. R. Nimmala, C. Kumara, V. R. Jupally, A. Fortunelli, L. Sementa, G. Barcaro, X. Zuo and B. C. Noll, *J. Am. Chem. Soc.*, 2015, **137**, 4610–4613.
- 162 A. Desiredy, B. E. Conn, J. Guo, B. Yoon, R. N. Barnett, B. M. Monahan, K. Kirschbaum, W. P. Griffith, R. L. Whetten and U. Landman, *Nature*, 2013, **501**, 399–402.
- 163 C. P. Joshi, M. S. Bootharaju, M. J. Alhilaly and O. M. Bakr, *J. Am. Chem. Soc.*, 2015, **137**, 11578–11581.
- 164 L. G. AbdulHalim, M. S. Bootharaju, Q. Tang, S. D. Gobbo, R. G. AbdulHalim, M. Eddaoudi, D. E. Jiang and O. M. Bakr, *J. Am. Chem. Soc.*, 2015, **137**, 11970–11975.
- 165 L. Cheng, Y. Yuan, X. Zhang and J. Yang, *Angew. Chem., Int. Ed.*, 2013, **52**, 9035–9039.
- 166 G. Natarajan, A. Mathew, Y. Negishi, R. L. Whetten and T. Pradeep, *J. Phys. Chem. C*, 2015, **119**, 27768–27785.
- 167 W. W. Xu, B. Zhu, X. C. Zeng and Y. Gao, *Nat. Commun.*, 2016, **7**, 13574.
- 168 H. Qian, Y. Zhu and R. Jin, *ACS Nano*, 2009, **3**, 3795–3803.
- 169 Y. Negishi, K. Munakata, W. Ohgake and K. Nobusada, *J. Phys. Chem. Lett.*, 2012, **3**, 2209–2214.
- 170 D. R. Kauffman, D. Alfonso, C. Matranga, H. Qian and R. Jin, *J. Phys. Chem. C*, 2013, **117**, 7914–7923.
- 171 K. Kwak, Q. Tang, M. Kim, D. Jiang and D. Lee, *J. Am. Chem. Soc.*, 2015, **137**, 10833–10840.
- 172 K. Kwak, V. D. Thanthirige, K. Pyo, D. Lee and G. Ramakrishna, *J. Phys. Chem. Lett.*, 2017, **8**, 4898.
- 173 K. Kwak and D. Lee, *Acc. Chem. Res.*, 2019, **52**, 12–22.
- 174 J. P. Wilcoxon, J. E. Martin, F. Parsapour, B. Wiedenman and D. F. Kelley, *J. Chem. Phys.*, 1998, **108**, 9137–9143.
- 175 Z. Wu and R. Jin, *ACS Nano*, 2009, **3**, 2036–2042.
- 176 H. Qian, M. Zhu, C. Gayathri, R. R. Gil and R. Jin, *ACS Nano*, 2011, **5**, 8935–8942.

- 177 T. G. Schaaff and R. L. Whetten, *J. Phys. Chem. B*, 2000, **104**, 2630–2641.
- 178 I. Dolamic, S. Knoppe, A. Dass and T. Bürgi, *Nat. Commun.*, 2012, **3**, 798.
- 179 S. Tian, Y. Z. Li, M. B. Li, J. Yuan, J. Yang, Z. Wu and R. Jin, *Nat. Commun.*, 2015, **6**, 8667.
- 180 I. Dolamic, B. Varnholt and T. Bürgi, *Phys. Chem. Chem. Phys.*, 2013, **15**, 19561–19565.
- 181 B. Varnholt, P. Oulevey, S. Lubner, C. Kumara, A. Dass and T. Bürgi, *J. Phys. Chem. C*, 2014, **118**, 9604–9611.
- 182 E. Khatun, P. Chakraborty, B. R. Jacob, G. Paramasivam, M. Bodiuzzaman, W. A. Dar and T. Pradeep, *Chem. Mater.*, 2020, **32**, 611–619.
- 183 Y. Negishi, W. Kurashige and U. Kamimura, *Langmuir*, 2011, **27**, 12289–12292.
- 184 W. Kurashige, S. Yamazoe, K. Kanehira, T. Tsukuda and Y. Negishi, *J. Phys. Chem. Lett.*, 2013, **4**, 3181–3185.
- 185 Q. Xu, S. Wang, Z. Liu, G. Xu, X. Meng and M. Zhu, *Nanoscale*, 2013, **5**, 1176–1182.
- 186 I. Chakraborty, W. Kurashige, K. Kanehira, L. Gell, H. Häkkinen, Y. Negishi and T. Pradeep, *J. Phys. Chem. Lett.*, 2013, **4**, 3351–3355.
- 187 D. M. Chevrier, X. Meng, Q. Tang, D. Jiang, M. Zhu, A. Chatt and P. Zhang, *J. Phys. Chem. C*, 2014, **118**, 21730–21737.
- 188 P. Maity, S. Takano, S. Yamazoe, T. Wakabayashi and T. Tsukuda, *J. Am. Chem. Soc.*, 2013, **135**, 9450–9457.
- 189 Z. Lei, X. K. Wan, S. F. Yuan, J. Q. Wang and Q. M. Wang, *Dalton Trans.*, 2017, **46**, 3427–3434.
- 190 M. R. Narouz, K. M. Osten, P. J. Unsworth, R. W. Y. Man, K. Salorinne, S. Takano, R. Tomihara, S. Kaappa, S. Malola, C.-T. Dinh, J. D. Padmos, K. Ayoo, P. J. Garrett, M. Nambo, J. H. Horton, E. H. Sargent, H. Häkkinen, T. Tsukuda and C. M. Crudden, *Nat. Chem.*, 2019, **11**, 419–425.
- 191 C. M. Aikens, *Acc. Chem. Res.*, 2018, **51**, 3065–3073.
- 192 V. Linko, H. Zhang, Nonappa, M. A. Kostianen and O. Ikkala, *Acc. Chem. Res.*, 2022, **55**, 1785–1795.
- 193 X. Kang, Y. Li, M. Zhu and R. Jin, *Chem. Soc. Rev.*, 2020, **49**, 6443–6514.
- 194 X. Kang and M. Zhu, *Chem. Soc. Rev.*, 2019, **48**, 2422–2457.
- 195 E. S. Shibu, M. A. H. Muhammed, T. Tsukuda and T. Pradeep, *J. Phys. Chem. C*, 2008, **112**, 12168–12176.
- 196 M. J. Hostetler, S. J. Green, J. J. Stokes and R. W. Murray, *J. Am. Chem. Soc.*, 1996, **118**, 4212.
- 197 Y. Song, T. Huang and R. W. Murray, *J. Am. Chem. Soc.*, 2003, **125**, 11694–11701.
- 198 R. Guo and R. W. Murray, *J. Am. Chem. Soc.*, 2005, **127**, 12140–12143.
- 199 J. F. Parker, J. E. F. Weaver, F. McCallum, C. A. Fields-Zinna and R. W. Murray, *Langmuir*, 2010, **26**, 13650–13654.
- 200 R. Guo, Y. Song, G. Wang and R. W. Murray, *J. Am. Chem. Soc.*, 2005, **127**, 2752–2757.
- 201 C. Zeng, C. Liu, Y. Pei and R. Jin, *ACS Nano*, 2013, **7**, 6138–6145.
- 202 A. Dass, A. Stevenson, G. R. Dubay, J. B. Tracy and R. W. Murray, *J. Am. Chem. Soc.*, 2008, **130**, 5940–5946.
- 203 A. C. Templeton, W. P. Wuelfing and R. W. Murray, *Acc. Chem. Res.*, 2000, **33**, 27–36.
- 204 C. L. Heinecke, T. W. Ni, S. Malola, V. Mäkinen, O. A. Wong, H. Häkkinen and C. J. Ackerson, *J. Am. Chem. Soc.*, 2012, **134**, 13316–13322.
- 205 T. W. Ni, M. A. Tofanelli, B. D. Phillips and C. J. Ackerson, *Inorg. Chem.*, 2014, **53**, 6500–6502.
- 206 L. G. Abdulhalim, N. Kothalawala, L. Sinatra, A. Dass and O. M. Bakr, *J. Am. Chem. Soc.*, 2014, **136**, 15865–15868.
- 207 Y. Chen, M. Zhou, Q. Li, H. Gronlund and R. Jin, *Chem. Sci.*, 2020, **11**, 8176–8183.
- 208 C. Zeng, H. Qian, T. Li, G. Li, N. L. Rosi, B. Yoon, R. N. Barnett, R. L. Whetten, U. Landman and R. Jin, *Angew. Chem., Int. Ed.*, 2012, **51**, 13114–13118.
- 209 C. Zeng, Y. Chen, A. Das and R. Jin, *J. Phys. Chem. Lett.*, 2015, **6**, 2976–2986.
- 210 L. C. McKenzie, T. O. Zaikova and J. E. Hutchison, *J. Am. Chem. Soc.*, 2014, **136**, 13426–13435.
- 211 S. Yang, S. Chen, L. Xiong, C. Liu, H. Yu, S. Wang, N. L. Rosi, Y. Pei and M. Zhu, *J. Am. Chem. Soc.*, 2018, **140**, 10988–10994.
- 212 A. Das, T. Li, G. Li, K. Nobusada, C. Zeng, N. L. Rosi and R. Jin, *Nanoscale*, 2014, **6**, 6458–6462.
- 213 M. S. Bootharaju, C. P. Joshi, M. J. Alhilaly and O. M. Bakr, *Chem. Mater.*, 2016, **28**, 3292–3297.
- 214 M. S. Bootharaju, V. M. Burlakov, T. M. D. Besong, C. P. Joshi, L. G. AbdulHalim, D. M. Black, R. L. Whetten, A. Goriely and O. M. Bakr, *Chem. Mater.*, 2015, **27**, 4289–4297.
- 215 E. Khatun, A. Ghosh, D. Ghosh, P. Chakraborty, A. Nag, B. Mondal, S. Chennu and T. Pradeep, *Nanoscale*, 2017, **9**, 8240–8248.
- 216 M. S. Bootharaju, R. Dey, L. E. Gevers, M. N. Hedhili, J.-M. Basset and O. M. Bakr, *J. Am. Chem. Soc.*, 2016, **138**, 13770–13773.
- 217 M. Bodiuzzaman, A. Ghosh, K. S. Sugi, A. Nag, E. Khatun, B. Varghese, G. Paramasivam, S. Antharjanam, G. Natarajan and T. Pradeep, *Angew. Chem., Int. Ed.*, 2019, **58**, 189–194.
- 218 C. K. Manju, D. Ghosh, M. Bodiuzzaman and T. Pradeep, *Dalton Trans.*, 2019, **48**, 8664–8670.
- 219 A. Jana, P. Chakraborty, W. A. Dar, S. Chandra, E. Khatun, M. P. Kannan, R. H. A. Ras and T. Pradeep, *Chem. Commun.*, 2020, **56**, 12550–12553.
- 220 X. Kang and M. Zhu, *Chem. Mater.*, 2019, **31**, 9939–9969.
- 221 Z. Wu and R. Jin, *Nano Lett.*, 2010, **10**, 2568–2573.
- 222 S. Wang, X. Zhu, T. Cao and M. Zhu, *Nanoscale*, 2014, **6**, 5777–5781.
- 223 A. Kim, C. Zeng, M. Zhou and R. Jin, *Part. Part. Syst. Charact.*, 2017, **34**, 1600388.
- 224 E. Khatun, A. Ghosh, P. Chakraborty, P. Singh, M. Bodiuzzaman, P. Ganesan, G. Natarajan, J. Ghosh, S. K. Pal and T. Pradeep, *Nanoscale*, 2018, **10**, 20033–20042.

- 225 X. Kang, M. Zhou, S. Wang, S. Jin, G. Sun, M. Zhu and R. Jin, *Chem. Sci.*, 2017, **8**, 2581–2587.
- 226 E. Reyes, R. Madueño, M. Blázquez and T. Pineda, *J. Phys. Chem. C*, 2010, **114**, 15955–15962.
- 227 S. Knoppe, A. C. Dharmaratne, E. Schreiner, A. Dass and T. Bürgi, *J. Am. Chem. Soc.*, 2010, **132**, 16783–16789.
- 228 S. Knoppe, R. Azoulay, A. Dass and T. Bürgi, *J. Am. Chem. Soc.*, 2012, **134**, 20302–20305.
- 229 M. A. Habeeb Muhammed and T. Pradeep, *Chem. Phys. Lett.*, 2007, **449**, 186–190.
- 230 M. S. Bootharaju and T. Pradeep, *Langmuir*, 2011, **27**, 8134–8143.
- 231 W. Chen, X. Tu and X. Guo, *Chem. Commun.*, 2009, 1736–1738.
- 232 Z. Wu, *Angew. Chem., Int. Ed.*, 2012, **51**, 2934–2938.
- 233 J. Sun, H. Wu and Y. Jin, *Nanoscale*, 2014, **6**, 5449–5457.
- 234 M. S. Bootharaju, C. P. Joshi, M. R. Parida, O. F. Mohammed and O. M. Bakr, *Angew. Chem., Int. Ed.*, 2016, **55**, 922–926.
- 235 X. Kang, L. Xiong, S. Wang, H. Yu, S. Jin, Y. Song, T. Chen, L. Zheng, C. Pan, Y. Pei and M. Zhu, *Chem. – Eur. J.*, 2016, **22**, 17145–17150.
- 236 X. Kang, X. Wei, S. Jin, Q. Yuan, X. Luan, Y. Pei, S. Wang, M. Zhu and R. Jin, *Proc. Natl. Acad. Sci. U. S. A.*, 2019, **116**, 18834–18840.
- 237 M. S. Bootharaju, L. Sinatra and O. M. Bakr, *Nanoscale*, 2016, **8**, 17333–17339.
- 238 W. Du, S. Jin, L. Xiong, M. Chen, J. Zhang, X. Zou, Y. Pei, S. Wang and M. Zhu, *J. Am. Chem. Soc.*, 2017, **139**, 1618–1624.
- 239 W. J. Plieth, *Surf. Sci.*, 1985, **156**, 530–535.
- 240 R. A. Masitas and F. P. Zamborini, *J. Am. Chem. Soc.*, 2012, **134**, 5014–5017.
- 241 Z. Gan, N. Xia and Z. Wu, *Acc. Chem. Res.*, 2018, **51**, 2774–2783.
- 242 J. P. Choi, C. A. Fields-Zinna, R. L. Stiles, R. Balasubramanian, A. D. Douglas, M. C. Crowe and R. W. Murray, *J. Phys. Chem. C*, 2010, **114**, 15890–15896.
- 243 S. Tian, C. Yao, L. Liao, N. Xia and Z. Wu, *Chem. Commun.*, 2015, **51**, 11773–11776.
- 244 Z. Wu, M. Wang, J. Yang, X. Zheng, W. Cai, G. Meng, H. Qian, H. Wang and R. Jin, *Small*, 2012, **8**, 2028–2035.
- 245 C. Yao, J. Chen, M.-B. Li, L. Liu, J. Yang and Z. Wu, *Nano Lett.*, 2015, **15**, 1281–1287.
- 246 S. Wang, H. Abroshan, C. Liu, T.-Y. Luo, M. Zhu, H. J. Kim, N. L. Rosi and R. Jin, *Nat. Commun.*, 2017, **8**, 848.
- 247 X. Yuan, X. Dou, K. Zheng and J. Xie, *Part. Part. Syst. Charact.*, 2015, **32**, 613–629.
- 248 L. Liao, S. Zhou, Y. Dai, L. Liu, C. Yao, C. Fu, J. Yang and Z. Wu, *J. Am. Chem. Soc.*, 2015, **137**, 9511–9514.
- 249 Q. Li, S. Wang, K. Kirschbaum, K. J. Lambright, A. Das and R. Jin, *Chem. Commun.*, 2016, **52**, 5194–5197.
- 250 Q. Li, T. Y. Luo, M. G. Taylor, S. Wang, X. Zhu, Y. Song, G. Mpourmpakis, N. L. Rosi and R. Jin, *Sci. Adv.*, 2017, **3**, e1603193.
- 251 M. Zhu, P. Wang, N. Yan, X. Chai, L. He, Y. Zhao, N. Xia, C. Yao, J. Li, H. Deng, Y. Zhu, Y. Pei and Z. Wu, *Angew. Chem., Int. Ed.*, 2018, **57**, 4500–4504.
- 252 A. Das, T. Li, K. Nobusada, C. Zeng, N. L. Rosi and R. Jin, *J. Am. Chem. Soc.*, 2013, **135**, 18264–18267.
- 253 Y. Li, M. J. Cowan, M. Zhou, T.-Y. Luo, Y. Song, H. Wang, N. L. Rosi, G. Mpourmpakis and R. Jin, *J. Am. Chem. Soc.*, 2020, **142**, 20426–20433.
- 254 A. Fernando and C. M. Aikens, *J. Phys. Chem. C*, 2016, **120**, 14948.
- 255 Z. Wang, R. K. Gupta, F. Alkan, B.-L. Han, L. Feng, X.-Q. Huang, Z.-Y. Gao, C.-H. Tung and D. Sun, *J. Am. Chem. Soc.*, 2023, **145**, 19523–19532.
- 256 A. Sreekumaran Nair and T. Pradeep, *Curr. Sci.*, 2003, **84**, 1560–1564.
- 257 M. S. Bootharaju and T. Pradeep, *Langmuir*, 2012, **28**, 2671–2679.
- 258 M. S. Bootharaju, G. K. Deepesh, T. Udayabhaskararao and T. Pradeep, *J. Mater. Chem. A*, 2013, **1**, 611–620.
- 259 A. Mathew, G. Natarajan, L. Lehtovaara, H. Häkkinen, R. M. Kumar, V. Subramanian, A. Jaleel and T. Pradeep, *ACS Nano*, 2014, **8**, 139–152.
- 260 P. Chakraborty, A. Nag, G. Paramasivam, G. Natarajan and T. Pradeep, *ACS Nano*, 2018, **12**, 2415–2425.
- 261 P. Chakraborty, A. Nag, B. Mondal, E. Khatun, G. Paramasivam and T. Pradeep, *J. Phys. Chem. C*, 2020, **124**, 14891–14900.
- 262 P. Chakraborty, A. Nag, K. S. Sugi, T. Ahuja, B. Varghese and T. Pradeep, *ACS Mater. Lett.*, 2019, **1**, 534–540.
- 263 A. Nag, P. Chakraborty, G. Paramasivam, M. Bodiuzzaman, G. Natarajan and T. Pradeep, *J. Am. Chem. Soc.*, 2018, **140**, 13590–13593.
- 264 A. Nag, P. Chakraborty, A. Thacharon, G. Paramasivam, B. Mondal, M. Bodiuzzaman and T. Pradeep, *J. Phys. Chem. C*, 2020, **124**, 22298–22303.
- 265 M. A. H. Muhammed, L. K. Cruz, A. H. Emwas, A. M. El-Zohry, B. Moosa, O. F. Mohammed and N. M. Khashab, *Angew. Chem., Int. Ed.*, 2019, **58**, 15665–15670.
- 266 K. Sheng, Z. Wang, L. Li, Z. Y. Gao, C. H. Tung and D. Sun, *J. Am. Chem. Soc.*, 2023, **145**, 10595–10603.
- 267 S. Wang, Y. Song, S. Jin, X. Liu, J. Zhang, Y. Pei, X. Meng, M. Chen, P. Li and M. Zhu, *J. Am. Chem. Soc.*, 2015, **137**, 4018–4021.
- 268 K. R. Krishnadas, T. Udayabhaskararao, S. Choudhury, N. Goswami, S. K. Pal and T. Pradeep, *Eur. J. Inorg. Chem.*, 2014, **2014**, 908–916.
- 269 B. Zhang, G. Salassa and T. Bürgi, *Chem. Commun.*, 2016, **52**, 9205–9207.
- 270 B. Huang and Y. Pei, *J. Mater. Chem. A*, 2020, **8**, 10242–10251.
- 271 M. Neumaier, A. Baksi, P. Weis, E. K. Schneider, P. Chakraborty, H. Hahn, T. Pradeep and M. M. Kappes, *J. Am. Chem. Soc.*, 2021, **143**, 6969–6980.
- 272 P. Chakraborty, A. Nag, G. Natarajan, N. Bandyopadhyay, G. Paramasivam, M. K. Panwar, J. Chakrabarti and T. Pradeep, *Sci. Adv.*, 2019, **5**, eaau7555.

- 273 G. Salassa, A. Sels, F. Mancin and T. Bürgi, *ACS Nano*, 2017, **11**, 12609–12614.
- 274 A. Ghosh, T. Pradeep and J. Chakrabarti, *J. Phys. Chem. C*, 2014, **118**, 13959–13964.
- 275 A. Som, A. K. Samal, T. Udayabhaskararao, M. S. Bootharaju and T. Pradeep, *Chem. Mater.*, 2014, **26**, 3049–3056.
- 276 Nonappa and O. Ikkala, *Adv. Funct. Mater.*, 2018, **28**, 1704328.
- 277 Nonappa, *Chem. Commun.*, 2023, **59**, 13800–13819.
- 278 A. Som, I. Chakraborty, T. A. Maark, S. Bhat and T. Pradeep, *Adv. Mater.*, 2016, **28**, 2827–2833.
- 279 Nonappa, T. Lahtinen, J. S. Haataja, T. R. Tero, H. Häkkinen and O. Ikkala, *Angew. Chem., Int. Ed.*, 2016, **55**, 16035–16038.
- 280 A. Som, A. Griffo, I. Chakraborty, H. Hähl, B. Mondal, A. Chakraborty, K. Jacobs, P. Laaksonen, O. Ikkala, T. Pradeep and Nonappa, *Small*, 2022, **18**, 2201707.
- 281 A. Chakraborty, A. C. Fernandez, A. Som, B. Mondal, G. Natarajan, G. Paramasivam, T. Lahtinen, H. Häkkinen, Nonappa and T. Pradeep, *Angew. Chem., Int. Ed.*, 2018, **57**, 6522–6526.
- 282 A. Chakraborty, M. M. Stanley, B. Mondal, Nonappa, M. Bodiuzzaman, P. Chakraborty, M. P. Kannan and T. Pradeep, *Nanoscale*, 2023, **15**, 2690–2699.
- 283 J. Roy, B. Mondal, G. Vishwakarma, Nonappa, N. V. Sridharan, P. Krishnamurthi and T. Pradeep, *Nanoscale*, 2023, **15**, 8225–8234.
- 284 J. V. Rival, Nonappa and E. S. Shibu, *ACS Appl. Mater. Interfaces*, 2020, **12**, 14569–14577.
- 285 P. Bose, P. Chakraborty, J. S. Mohanty, Nonappa, A. Ray Chowdhuri, E. Khatun, T. Ahuja, A. Mahendranath and T. Pradeep, *Nanoscale*, 2020, **12**, 22116–22128.
- 286 A. Baksi, M. Gandhi, S. Chaudhari, S. Bag, S. S. Gupta and T. Pradeep, *Angew. Chem., Int. Ed.*, 2016, **55**, 7777–7781.
- 287 A. Nag, A. Baksi, K. C. Krishnapriya, S. S. Gupta, B. Mondal, P. Chakraborty and T. Pradeep, *Eur. J. Inorg. Chem.*, 2017, **2017**, 3072–3079.
- 288 R. Kazan, U. Muller and T. Burgi, *Nanoscale*, 2019, **11**, 2938–2945.
- 289 P. Chakraborty, P. Bose, J. Roy, A. Nag, B. Mondal, A. Chakraborty and T. Pradeep, *J. Phys. Chem. C*, 2021, **125**, 16110–16117.
- 290 I. Chakraborty, T. Udayabhaskararao and T. Pradeep, *J. Hazard. Mater.*, 2012, **211–212**, 396–403.
- 291 H. Yang, Y. Wang, H. Huang, L. Gell, L. Lehtovaara, S. Malola, H. Häkkinen and N. Zheng, *Nat. Commun.*, 2013, **4**, 2422.
- 292 H. Qian, W. T. Eckenhoff, Y. Zhu, T. Pintauer and R. Jin, *J. Am. Chem. Soc.*, 2010, **132**, 8280–8281.

Vacuum Ultraviolet Photolysis of Condensed Methyl Chloride in Interstellar Model Conditions and Trapping of Intermediates at Intergrain Interfaces

Bijesh K. Malla, Gaurav Vishwakarma, Soham Chowdhury, and Thalappil Pradeep*



Cite This: *J. Phys. Chem. C* 2023, 127, 24149–24157



Read Online

ACCESS |



Metrics & More

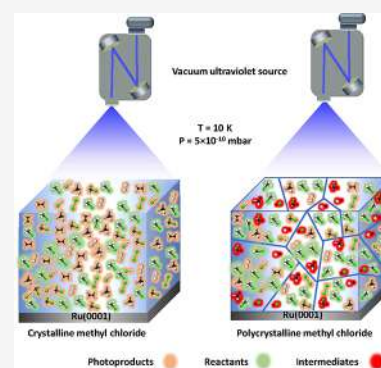


Article Recommendations



Supporting Information

ABSTRACT: Photochemistry can generate chemical complexity in an interstellar space. This may occur due to photolysis and associated events that can happen in condensed molecular solids under the prevailing temperature and pressure conditions. In the present study, using reflection absorption infrared spectroscopy (RAIRS), three different condensed phases of methyl chloride ice, namely, amorphous, crystalline, and polycrystalline, were detected in ultrahigh vacuum (UHV) ($p = 5 \times 10^{-10}$ mbar) and cryogenic conditions ($T = 10$ – 90 K). Upon vacuum ultraviolet (VUV) photoirradiation, crystalline methyl chloride formed more photoproducts than amorphous and polycrystalline forms. This unusual finding is attributed to the rapid diffusion and reaction of photochemical intermediates in a crystalline matrix, whereas the intermediates are trapped at grain boundaries in the polycrystalline solid. Normally, the intermediate diffusion is high in the case of the amorphous phase as compared with the crystalline phase. During long-term irradiation, discontinuity in the polycrystalline phase is removed, resulting in enhancement in the formation of photoproducts in the matrix, which was observed by the intensified desorption of photoproducts in temperature-programmed desorption mass spectrometry (TPD-MS). Further, all major and minor neutral photoproducts were detected by highly surface-sensitive Cs^+ ion-based secondary ion mass spectrometry (SIMS).



INTRODUCTION

The fate of molecules in the interstellar medium is largely governed by photochemistry and radiation chemistry.^{1,2} The diversity of such chemistry has contributed to the richness of the interstellar medium (ISM), which is now known to be composed of over 270 species, including simple and complex organic molecules (such as ethylene glycol, benzene, indene, and fullerenes).^{3–6} Such complex molecules are proposed to be formed through radical chemistry in icy grain mantles.⁷ Two of the recent additions to the chemical soup of ISM are methyl chloride (CH_3Cl) and methyl fluoride (CH_3F), which appear to have been formed through photochemistry.⁸ Intriguingly, methyl chloride and other chlorine-bearing organic molecules have also been identified on Mars via the Curiosity rover.⁹ On Earth, the genesis of organohalogens involves geological and biological mechanisms, rendering them potential biomarkers for exoplanets.¹⁰ Despite the evident importance of organohalogens on terrestrial and in extraterrestrial environments, there are no experimental spectroscopic data available on pure and photoirradiated condensed methyl chloride in view of the temperature and pressure conditions prevailing on ISM. Photochemistry of the system will be relevant in affecting the chemical diversity of ISM.

While it is well-known that the amorphous phase of molecules in ISM may undergo a structural change upon annealing to higher temperatures to form their stable

crystalline structures, it is unknown if the crystalline phase is of long-range order or polycrystalline in nature. To the best of our knowledge, there is no report on the phases (crystalline and polycrystalline) of methyl chloride ice based on its IR spectra and no report exists on the analysis of the photoproducts formed by these different ices in ISM conditions. We note that in this literature, ice is a term used for all condensed molecular solids.

In this study, we present a combined infrared and mass spectrometric investigation of the vacuum ultraviolet (VUV) photochemical transformation of condensed methyl chloride ices in its amorphous, crystalline, and polycrystalline phases. A 1958 study reported the vibrational spectrum of methyl chloride crystallites along with other methyl halides,¹⁴ and several studies reported the IR spectra of amorphous and crystalline methyl chloride.^{11–13} However, the nature of crystallinity, long-range or short-range, is unclear. Here, we characterized the three distinct phases of methyl chloride ice created by three different paths by RAIR spectroscopy and

Received: August 31, 2023

Revised: November 14, 2023

Accepted: November 14, 2023

Published: December 8, 2023



performed a detailed study of the photochemistry of these solids. Upon VUV irradiation with deuterium continuum of 115–400 nm wavelength (Lyman- α), with a peak flux of 6×10^{12} photons $\text{cm}^{-2} \text{s}^{-1}$, condensed methyl chloride ice produces methane (CH_4), ethane (C_2H_6), hydrogen chloride (HCl), dichloromethane (CH_2Cl_2), ethylene (C_2H_4), acetylene (C_2H_2), and ethyl chloride ($\text{CH}_3\text{CH}_2\text{Cl}$). Surprisingly, we found that this photochemical transformation is more facile in the crystalline phase than in the expected amorphous phase. Notably, the concentration of photoproducts is in the order crystalline \geq amorphous $>$ polycrystalline phases. We interpreted the results in view of the rapid diffusion of the intermediates (radicals) of photolysis through the crystalline matrix and the localization of these intermediates at the crystallite grain interfaces in the case of the polycrystalline phase. The consequence of the product accumulation in the crystalline lattice was studied by TPD-MS.

EXPERIMENTAL SECTION

Experimental Setup. In this study, all experiments were carried out in an ultrahigh vacuum (UHV) instrument (with a base pressure of $\sim 5 \times 10^{-10}$ mbar) discussed in detail in our previous literature.^{14,15} The instrument consists of three UHV chambers (namely, ionization, octupole, and scattering) and is equipped with reflection absorption infrared spectroscopy (RAIRS), low energy ion scattering (LEIS), temperature-programmed desorption (TPD) mass spectrometry, and Cs^+ ion-based secondary ion mass spectrometry (SIMS), along with a vacuum ultraviolet (VUV) lamp (Figure 1). Six turbomolecular pumps maintain the vacuum chambers' base pressure, which are supplemented by several oil-free diaphragm

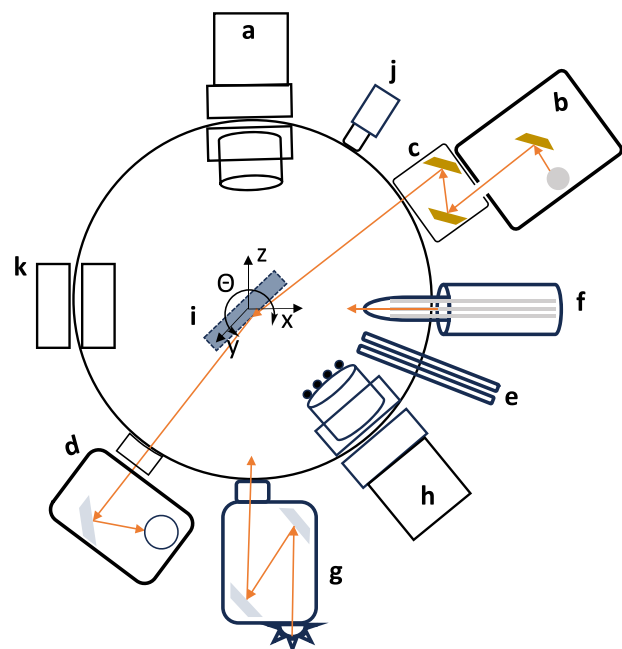


Figure 1. Simplified schematic diagram of experimental setup. (a) Quadrupole mass analyzer. (b) Fourier transmission infrared (FTIR) source. (c) Mirror box. (d) Mercury cadmium telluride (MCT) liquid nitrogen cooled detector. (e) Two sample inlet lines. (f) Low energy alkali ion gun (Cs^+). (g) Deuterium lamp. (h) TPD probe fitted with ionizer and quadrupole mass analyzer and detector. (i) Ru(0001) substrate. (j) Bayard–Alpert (BA) gauge. (k) Low energy ion scattering MS (not used in this study).

pumps. The chamber pressure is monitored by a Bayard–Alpert gauge, controlled by a MaxiGauge vacuum gauge controller (Pfeiffer, Model TPG 256 A).

A highly polished Ru(0001) single crystal was used as the substrate to create thin ice films that was mounted on a copper holder. It was connected to a helium cryostat (Cold Edge technology), which could maintain a temperature as low as 8 K. A resistive heater (25 Ω), controlled by a temperature controller (Lakeshore 336), was used to heat the substrate to 1000 K. The substrate temperature was measured with a K-type thermocouple sensor that has ± 0.5 K accuracy. Repeated heating to 400 K before each vapor deposition ensured a clean surface suitable for the current study. It is worth noting that the surface has a negligible role in the current study, as our experiments were on multilayer ice films (63 monolayer (ML)).

RAIRS and TPD-MS Setup. In this study, the thermal processing of vapor-deposited ice samples was monitored using RAIRS (reflection–absorption infrared spectroscopy) and TPD-MS (temperature-programmed desorption-mass spectrometry). The RAIRS data was collected in the 4000–550 cm^{-1} range with a spectral resolution of 2 cm^{-1} , using a Bruker FT-IR spectrometer called Vertex 70. The ice sample was exposed to an incident angle of $80^\circ \pm 7^\circ$ by focusing the IR beam through a ZnSe viewport. The reflected IR beam from the sample was detected by using a liquid N_2 -cooled mercury cadmium telluride (MCT) detector. To prevent absorption by atmospheric moisture, the IR beam outside the vacuum chamber was purged with dry N_2 . Each RAIR spectrum was obtained by averaging over 512 scans to improve the signal-to-noise ratio. An Extrel quadrupole mass spectrometer was used for TPD-MS in an out-of-sight configuration.

SIMS Setup. The Cs^+ ion-based secondary ion mass spectrometry (SIMS) technique can molecularly identify and monitor the reactions occurring on the surfaces. Cs^+ ($m/z = 133$) was chosen for the ion scattering due to its high depth resolution of 1 bilayer and the ability to monitor neutral chemicals on the CH_3Cl ice surface. We conducted reactive ion scattering experiments with Cs^+ of 60 eV kinetic energy generated by a low-energy alkali gun. The Cs^+ ion collides on the ice surface, adducts with neutral molecules on the surface, and drags them from the surface along its outgoing trajectory, which is known as the RIS (reactive ion scattering) process. The Cs^+ ion adducts with the neutral molecules are driven by an ion-neutral dipole interaction. The mass of the Cs^+ ion adduct was determined with a quadrupole mass analyzer. The mass of the neutral product formed on methyl chloride ice due to photolysis can be identified by subtracting the mass of Cs^+ ($m/z = 133$) from that of the Cs^+ ion adduct.

VUV Source. A deuterium lamp (McPherson, Model 634, with MgF_2 window, 30 W) of vacuum ultraviolet (VUV) range 115–400 nm with a spectral bandwidth of 0.8 nm (shown in Figure S1) was used as the UV light source. The VUV lamp was differentially pumped and attached to the UHV chamber through the MgF_2 window (with a cutoff at ~ 114 nm (10.87 eV)). This design allows the source to effectively emit light at incredibly short wavelengths, reaching as far down as 115 nm. The UV lamp flux was determined by applying the widely used ozone method ($\text{O}_2 \rightarrow \text{O}_3$ conversion), where solid O_2 was VUV photolyzed at 10 K. The average photon flux reaching the ice sample was estimated to be $\sim 6 \times 10^{12}$ photons $\text{cm}^{-2} \text{s}^{-1}$.

Materials and Sample preparation. As received, methyl chloride (Akkaran gas and energy, 99.9% purity) and argon

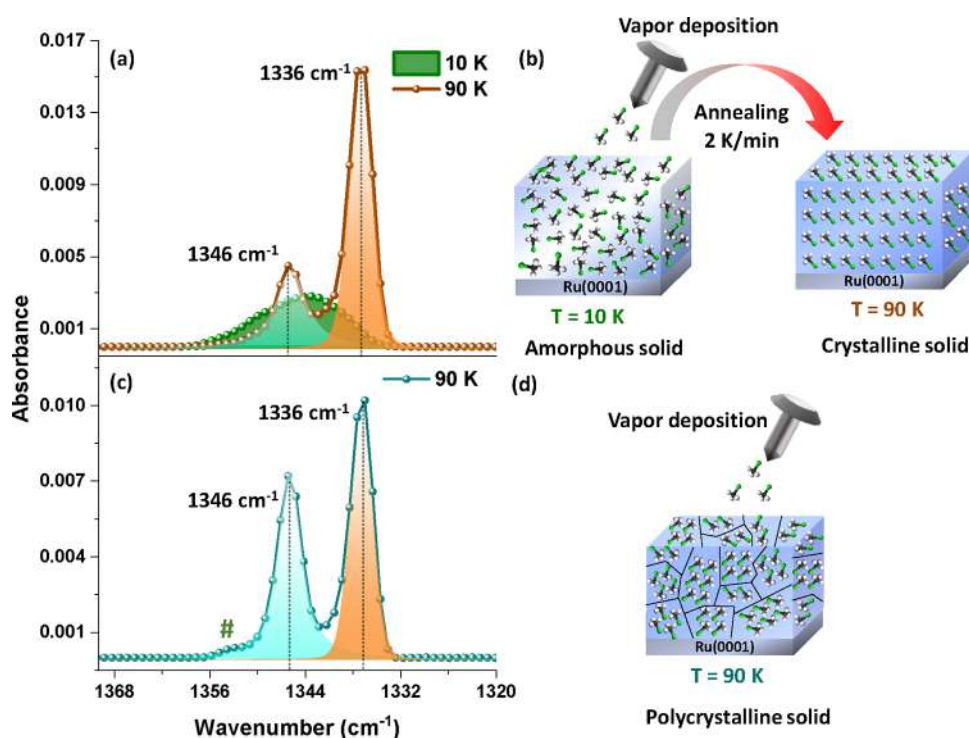


Figure 2. RAIR spectra of amorphous, crystalline, and polycrystalline methyl chloride ice. (a) RAIR spectra of 63 ML of methyl chloride ice at 10 and 90 K in the C–H symmetric mode. For this, methyl chloride vapor was deposited at 10 K on a Ru(0001) substrate and annealed to 90 K with a ramping rate of 2 K/min. (b) Schematic illustration of the phase transition of amorphous to crystalline methyl chloride ice upon annealing. (c) RAIR spectra of 63 ML of methyl chloride ice at 90 K in the C–H symmetric bending mode. For this, methyl chloride vapor was directly deposited at 90 K on the Ru(0001) substrate. (d) Schematic illustration of the formation of polycrystalline methyl chloride ice at 90 K.

(Ar) (Rana industrial gases and products, 99.9% purity) gases were connected to the main chamber through sample inlet lines controlled by high-precision metal leak valves. Millipore water (H_2O of 18.2 M Ω resistivity) was taken in a vacuum-sealed test tube (with a glass-to-metal seal) and was further purified by several freeze–pump–thaw cycles. A source of water vapor was connected to the main chamber through the sample inlet line. It is worth noting that we have two sample inlet lines that were connected to specific gas/liquid in accordance with the distinct experimental requirements.

Methyl chloride ice of 63 ML was prepared by vapor deposition on Ru(0001) at 10 K. The vapor deposition coverage in the case of N_2 (ion gauge sensitivity factor ~ 1) was expressed in ML, assuming 1.33×10^{-6} mbar s = 1 ML, which was estimated to contain $\sim 1.1 \times 10^{15}$ molecules cm^{-2} , as adopted in other reports.^{16–18} Methyl chloride has an ion gauge sensitivity factor of 2.4. To deposit 63 ML of methyl chloride ice, we backfilled the chamber at a pressure of 5×10^{-7} mbar pressure for 5 min. For higher temperature deposition, the Ru(0001) substrate was heated to 90 K with a heating rate of 2 K/min, and methyl chloride was deposited at 90 K. The vacuum gauge was calibrated with nitrogen, and the methyl chloride coverage may be slightly different in view of this uncorrected pressure reading.

For 160 ML of a 2:1 mixture of methyl chloride and water, the chamber was backfilled to a pressure of 4×10^{-7} mbar for methyl chloride and 1×10^{-7} mbar for water for 10 min. For a separate deposition step involving 100 ML of argon (Ar), the chamber was backfilled to a pressure of 5×10^{-7} mbar. This backfilling process was carried out for 4 min and 20 s. Throughout each molecular deposition process, special attention was paid to the ion gauge sensitivity factor to ensure

accurate measurements and control over the deposition. Mass spectra were taken simultaneously during vapor deposition to check the purity and ratio of the deposited molecules. The as-prepared sample was irradiated by a deuterium lamp (McPherson, Model 634, with MgF_2 window, 30 W) in the VUV range of 115–400 nm.

RESULTS AND DISCUSSION

RAIRS Study of Amorphous, Crystalline, and Polycrystalline Methyl Chloride Ice. In this study, we created condensed methyl chloride ice in UHV under cryogenic conditions, as in the interstellar medium, via three different paths, as mentioned above. Figure 2a,c shows the RAIR spectra of 63 ML of methyl chloride ice in the C–H symmetric bending region. In Figure 2a, the broad green spectrum represents the amorphous methyl chloride obtained by vapor deposition at 10 K. Slow annealing of this ice from 10 to 90 K at a rate of 2 K/min causes the rise of two sharp peaks 1346 and 1336 cm^{-1} (cyan and brown color filled, respectively in Figure 2a). This band splitting occurs due to intermolecular coupling within the newly formed crystalline lattice. However, the peak intensity is different.^{19,20} These two split peaks are also observed when methyl chloride is directly deposited at 90 K, as shown in Figure 2c. Further, a tiny peak (marked #) near 1355 cm^{-1} represents methyl chloride gas trapped in the matrix.¹⁹ It is not surprising that a small amount of methyl chloride gas can be trapped in the crystal grains during the direct deposition at 90 K.

However, the peak intensity ratio differs in Figure 2a,c, which may be attributed to the degree of irregularities or random orientations in the crystal lattice. This raises the question if the two nonamorphous solids are identical in their

crystallinity. To resolve this, control experiments were carried out to determine how the intensity of the higher wavenumber peak (or peak ratio) changes with the crystallinity of methyl chloride ice. This is shown by two separate control experiments. One is the annealing rate, a crucial factor in UHV chemistry,^{21,22} and another is the addition of impurities, such as water, in this case. In the first experiment, we deposited 63 ML of methyl chloride ice at 10 K and annealed it to 90 K with a higher annealing rate of 10 K/min. We observed the RAIR spectra of the resulting solid (shown in Figure S2) resemble the spectra observed in the case of direct deposition at 90 K (Figure 2c), including the presence of the gas phase peak (marked by #); however, interestingly, it is absent when slow-annealed (Figure 2a). An increased annealing rate increases the mobility of molecules, so the amorphous solid did not get enough time to form the extended crystal lattice. Next, we deposited 160 ML of 2:1 methyl chloride and water on Ru(0001) and annealed the sample to 90 K with a slow annealing rate of 2 K/min; the obtained IR spectrum (Figure S3) of solid methyl chloride resembles the IR spectra obtained from the randomly oriented crystalline solid (Figure 2c). Here, it is evident that the water impurity within the methyl chloride ice matrix disturbs the extended range of crystallinity. A similar effect is already shown in the dichloromethane case.²⁰ Here, it is concluded that a more ordered crystalline solid can be formed only by slow annealing of the pure ice sample. It is established that the polycrystalline nature of a substance increases upon (a) increasing the annealing rate and (b) introducing an impurity in the sample. We propose that the peak intensities in the C–H symmetric bending mode can be correlated with the extent of the crystalline nature of the methyl chloride solid. Control experiments supported this suggestion. Based on this, we noted that with increased polycrystallinity (irregularities in crystalline), the intensity of the 1346 cm^{−1} peak increases.

Dows has reported the IR spectra for solid methyl chloride and found that the crystallites are randomly oriented, with the intensity ratio of 1.46¹⁹ for the peaks of 1336 and 1346 cm^{−1}. In our study, we found a ratio of 1.42 for the directly deposited thin film, which supports the polycrystalline nature of methyl chloride. Notably, this ratio is comparable to the ratios of 1.73 and 1.22 in the case of the ice formed via quick annealing and with an impurity, as shown in Figures S4 and S5, respectively. However, the ice formed by slow annealing (Figure 2c exhibits a higher ratio (~3.4), suggestive of a highly crystalline nature (less polycrystalline). A comparison of RAIR spectra of four condensed methyl chloride samples created by four different methods in the C–H symmetric bending region is shown in Figure S4. The annealed sample may be described as a low-polycrystalline or long-range crystalline ice, as depicted in Figure 2b. Thus, the relatively higher intensity of the 1346 cm^{−1} peak represents the randomness in the crystal lattice. Although our study is not supported by diffraction data, to the best of our knowledge, this is the first report of this nature. We suggest crystalline (less polycrystalline) methyl chloride formation is possible upon slow annealing in a homogeneous environment.

Additionally, the evolution of the C–H stretching and C–H antisymmetric bending modes with increasing temperature for the crystalline solid is shown in Figure S5a,b. In the C–H stretching region, we observed that the broad amorphous peak splits into two peaks at 2961 and 2952 cm^{−1}, while in the C–H antisymmetric bending region, the broad (due to the

amorphous phase) peak splits into 1443 and 1437 cm^{−1}. For the polycrystalline ice, three peaks were observed at 2961, 2955, and 2952 cm^{−1} in the C–H stretching and 1445, 1441, and 1437 cm^{−1} in the C–H antisymmetric bending regions (Figure S6). In this experiment, an additional peak appeared in the C–H stretching (2955 cm^{−1}), and the C–H bending regions (1441, 1445 cm^{−1} peaks were observed in place of 1443 cm^{−1}), which may indicate high irregularities (Figure S6). This may be attributed to molecular interactions between two crystallites in the methyl chloride solid. All the IR peaks for amorphous, crystalline, and polycrystalline methyl chloride ice and gas phases are assigned in Table S1.^{19,23–26}

Photochemistry of Amorphous Methyl Chloride. Such diverse crystallinity can significantly affect the photochemistry in ISM. Photochemical pathways are a succession of photodissociation, radical–radical interactions, and subsequent rearrangements that culminate in the formation of complex organic compounds in ISM.⁷ Therefore, we undertook an investigation of the kinetics of photoproducts formed in these phases of ice. At the outset, we subjected the amorphous methyl chloride ice to VUV light irradiation at 10 K and subsequently analyzed the products using RAIR, SIMS, and TPD-MS.

Figure 3 shows the RAIR spectra of 63 ML of amorphous methyl chloride before and after 60 min of VUV irradiation in

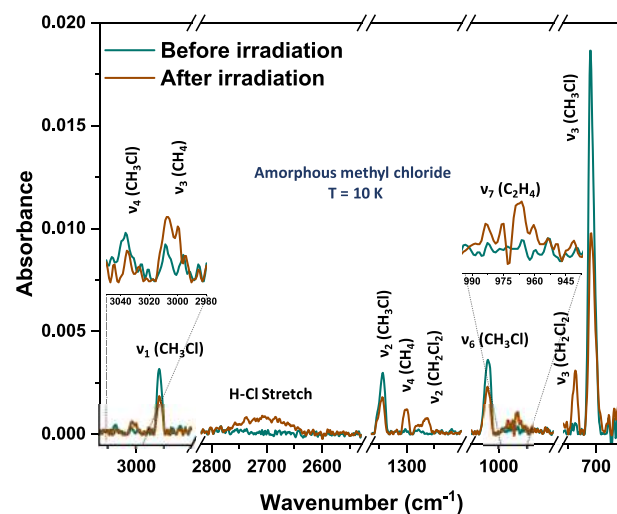


Figure 3. RAIR spectra of 63 ML of methyl chloride before and after irradiation with VUV light at 10 K in the mid-infrared region. Zoomed views of weaker peaks are shown as insets. Methyl chloride vapor was deposited at 10 K on a Ru(0001) substrate and the amorphous methyl chloride ice was photoirradiated for 60 min.

the mid-infrared region. In the IR spectrum shown, methyl chloride is identified by the C–H antisymmetric stretching (ν_4 , 3036 cm^{−1}), C–H symmetric stretching (ν_1 , 2958 cm^{−1}), C–H symmetric bending (ν_2 , 1343 cm^{−1}), C–Cl rocking (ν_6 , 1018 cm^{−1}), and C–Cl stretching (ν_3 , 710 cm^{−1}) modes.^{13,27} New IR peaks arise after 60 min of VUV irradiation due to the formation of new species in the ice matrix. Four major photoproducts were identified by their prominent IR peaks. Methane was identified by C–H antisymmetric stretch (ν_3 , 3009 cm^{−1}) and C–H symmetric stretch (ν_4 , 1302 cm^{−1}); dichloromethane was identified by the C–H symmetric bending (ν_2 , 1263 cm^{−1}), and C–Cl symmetric stretch (ν_3 , 737 cm^{−1}); hydrogen chloride was identified by the H–Cl

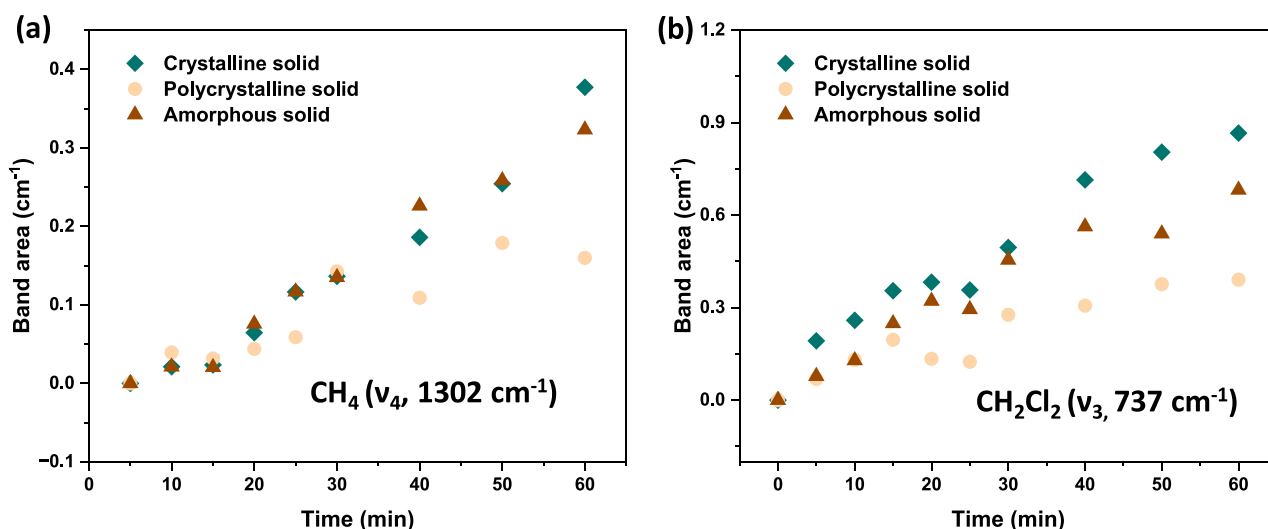


Figure 6. (a) Normalized integrated area of the ν_4 band of methane as a function of irradiation time. (b) Normalized integrated area of the ν_3 band of dichloromethane with irradiation time. Three phases of ice were irradiated for 60 min, and IR spectra were taken at 5 min intervals.

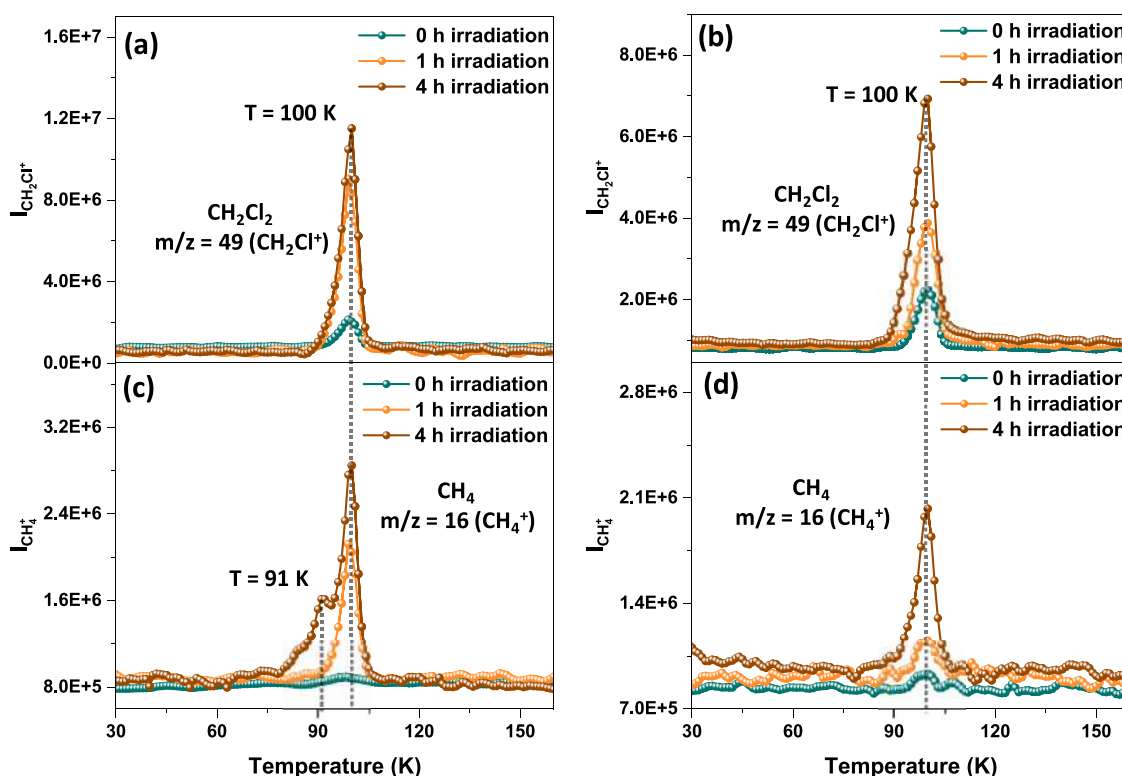


Figure 7. TPD-MS spectra of the photoproducts (CH_4 , CH_2Cl_2) formed by the irradiation of 63 ML of crystalline (a, c) and polycrystalline (b, d) methyl chloride for 0, 1, and 4 h. The sublimation profiles using integrated ion counts in (a, b) at $m/z = 49$ (CH_2Cl^+ due to CH_2Cl_2) and (c, d) at $m/z = 16$ (CH_4^+) are plotted.

enables the observation of sublimed products by TPD. Figure S9 shows the TPD mass spectrum for the major photoproducts hydrogen chloride ($m/z = 36$), dichloromethane ($m/z = 49$), and methane ($m/z = 16$). All the molecules desorb at 99 K, along with methyl chloride

Comparison of Photoproducts Formation and Trapping of Intermediates. We compared the efficiency of photoproduct formation in three distinct solids of methyl chloride, namely, amorphous, crystalline, and polycrystalline. Photoirradiation was performed on these solids at 10 K for a duration of 60 min, with RAIR spectra being recorded at 5 min

intervals. Figure 6 compares the formation of methane and dichloromethane, the major photoproducts resulting from the radical association (shown in Figure 3) within these three condensed phases. Abundances were calculated by integrating the band areas corresponding to methane (ν_4 , 1302 cm^{-1}) and dichloromethane (ν_3 , 737 cm^{-1}). The time-dependent areas due to methane and dichloromethane were calculated and subsequently normalized with respect to the C–Cl rocking (ν_6 , 1018 cm^{-1}) band of methyl chloride. For this normalization, the area under the curve (ν_6 , 1018 cm^{-1} band) for methyl chloride in the three solid phases was considered to be 1 cm^{-1}

before the radiation process. After normalization, the band areas of products of different types of ice versus time of irradiation are shown in Figure 6. Amorphous solids offer a conducive environment for enhanced product formation, primarily attributed to the augmented diffusion and tunneling of radicals within the porous matrix, a phenomenon not possible in crystalline solids.^{41–44} Here, a carefully created crystalline solid shows an equal or larger quantity of photoproducts than those in its amorphous and polycrystalline state. In the astrochemical model, the kinetics of reactions are influenced by reaction barriers and diffusion barriers. When there are no reaction barriers and the reactants are well-aligned, reactions are assumed to occur with high efficiency.⁷ This assumption is commonly applied to radical–radical reactions. The higher methane and dichloromethane production in crystalline than polycrystalline materials could be because radical migration is feasible in periodic crystalline materials. However, polycrystalline solids are composed of crystal domains with existing crystalline grain boundaries, and these grain-bound molecules play a vital role in the process of photolysis.⁴⁵ The presence of a thermal energy barrier on these boundaries is crucial, as it hinders radicals from moving between different crystalline grains. Consequently, the diffusion of intermediates is impeded, leading to the entrapment of all of the radicals within the boundaries themselves.

The phenomenon of extended irradiation leading to the conversion of crystalline solids into their amorphous analog has been widely established in the literature.^{46,47} A long-term irradiation experiment was carried out to investigate the consequences of the intermediates upon the amorphization of crystalline and polycrystalline solids. In this experiment, we irradiated the crystalline and polycrystalline ice for 4 h and compared it with the sample of 1 h irradiation using TPD-MS. Figure 7a,c shows the mass spectra of desorbed dichloromethane and methane before and after the irradiation of crystalline methyl chloride for 1 and 4 h. It is worth noting that the peak at 100 K for m/z 49 (Figure 7a,b) in the before irradiation spectrum represents the mass fragment from the methyl chloride reactant. In the spectrum collected after 1 h of irradiation, the desorption peaks of dichloromethane and methane at 100 K coincide with that of methyl chloride, and this is due to the small amount of photoproduct, which is trapped in the methyl chloride ice matrix. In Figure 7a, no specific changes have been detected other than an increase in dichloromethane. In the case of methane (Figure 7c), molecular volcano-like peaks were observed at 91 K in the 4 h irradiation experiment.^{48,49} Here, methane formation increased in the crystalline solid, which accumulated in specific locations. It is obvious that molecular mobility will be high prior to the desorption temperature in methyl chloride from its solid. Due to this high mobility, the accumulated methane molecules desorb earlier than methyl chloride as the methane desorption temperature is lower than that of methyl chloride.

Surprisingly, more intriguing results were observed when polycrystalline methyl chloride was irradiated for 4 h. The formation of dichloromethane (as shown in Figure 7b) increased by approximately 2 times, while methane (as shown in Figure 7d) increased by approximately 3 times when the irradiation time was extended from 1 to 4 h. This difference in product formation can be attributed to the transition of polycrystalline to the amorphous nature of methyl chloride during long-term irradiation, which removes the grain boundaries in the ice matrix. Consequently, the trapped

intermediates at the crystallite boundaries in the polycrystalline solid diffuse through the matrix and facilitate the formation of photoproducts. These results demonstrate strong agreement with our previous claim regarding the intermediate entrapment in polycrystalline solids.

This study presents a new direction in our understanding of molecular materials in space and their fate upon photoirradiation. Such photochemistry in molecular solids could make each of the distinct phases of any molecular solid an admixture of different species. In the course of time, an increase in the number of reaction products leads to the collapse of the crystallites, leading to an amorphous matrix. Therefore, photochemistry becomes an important factor in affecting the morphology of interstellar organics.

CONCLUSIONS

This study provides evidence for the formation of amorphous, crystalline, and polycrystalline methyl chloride via three different paths, using RAIRS in UHV ($\sim 5 \times 10^{-10}$ mbar) at low temperature (10–90 K), conditions analogous to ISM. The photochemistry of the methyl chloride solid was studied using a deuterium lamp (VUV source). The photoproducts were detected by RAIRS and SIMS in the solid state and by TPD-MS in the gas phase. The result of irradiation of three solid phases found that the formation of photoproducts is most facile for crystalline solid than for amorphous followed by polycrystalline. This is due to the feasibility of diffusion of the reactants and intermediates in crystalline solid compared to the amorphous and polycrystalline solids. Due to the existence of crystalline boundaries in polycrystalline solids, the intermediates are trapped at the interfaces of grains. However, long-term irradiation leads to the removal of discontinuity in the polycrystalline solid, which leads to the increased concentration of photoproducts accumulating in the ice matrix. This phenomenon becomes evident through the amplified desorption of photoproducts in TPD-MS. This study adds fresh spectroscopic data in the photochemistry of condensed methyl chloride molecules in ISM and provides a possible mechanistic interpretation that provides a scope for future investigations.

ASSOCIATED CONTENT

Supporting Information

The Supporting Information is available free of charge at <https://pubs.acs.org/doi/10.1021/acs.jpcc.3c05889>.

Temperature and time-dependent RAIRS, TPD-MS spectra, and SIMS spectrum of condensed methyl chloride (PDF)

AUTHOR INFORMATION

Corresponding Author

Thalappil Pradeep – Department of Science and Technology Unit of Nanoscience (DST UNS) and Thematic Unit of Excellence (TUE), Department of Chemistry, Indian Institute of Technology Madras, Chennai 600036, India; International Centre for Clean Water, IITM Research Park, Chennai 600113, India; orcid.org/0000-0003-3174-534X; Email: pradeep@iitm.ac.in

Authors

Bijesh K. Malla – Department of Science and Technology Unit of Nanoscience (DST UNS) and Thematic Unit of Excellence

(TUE), Department of Chemistry, Indian Institute of Technology Madras, Chennai 600036, India

Gaurav Vishwakarma – Department of Science and Technology Unit of Nanoscience (DST UNS) and Thematic Unit of Excellence (TUE), Department of Chemistry, Indian Institute of Technology Madras, Chennai 600036, India

Soham Chowdhury – Department of Science and Technology Unit of Nanoscience (DST UNS) and Thematic Unit of Excellence (TUE), Department of Chemistry, Indian Institute of Technology Madras, Chennai 600036, India

Complete contact information is available at:
<https://pubs.acs.org/10.1021/acs.jpcc.3c05889>

Author Contributions

B.K.M. and T.P. designed the experiments, B.K.M, G.V., and S.C. performed the experiments and analyzed the results. T.P. proposed the project and supervised the progress. The manuscript was written with the contributions of all authors.

Notes

The authors declare no competing financial interest.

ACKNOWLEDGMENTS

We acknowledge the Science and Engineering Research Board (SERB), Department of Science and Technology (DST), and Government of India for support. T.P. acknowledges funding from the Centre of Excellence on Molecular Materials and Functions under the Institution of Eminence scheme of IIT Madras. B.K.M. thanks the Council of Scientific and Industrial Research (CSIR) for his research fellowship. G.V. and S.C. thanks IITM for their research fellowships.

REFERENCES

- (1) Arumainayagam, C. R.; Garrod, R. T.; Boyer, M. C.; Hay, A. K.; Bao, S. T.; Campbell, J. S.; Wang, J.; Nowak, C. M.; Arumainayagam, M. R.; Hodge, P. J. Extraterrestrial Prebiotic Molecules: Photochemistry vs. Radiation Chemistry of Interstellar Ices. *Chem. Soc. Rev.* **2019**, *48* (8), 2293–2314.
- (2) Hama, T.; Watanabe, N. Surface Processes on Interstellar Amorphous Solid Water: Adsorption, Diffusion, Tunneling Reactions, and Nuclear-Spin Conversion. *Chem. Rev.* **2013**, *113* (12), 8783–8839.
- (3) Hollis, J. M.; Lovas, F. J.; Jewell, P. R.; Coudert, L. H. Interstellar Antifreeze: Ethylene Glycol. *Astrophys. J.* **2002**, *571* (1), L59–L62.
- (4) Cernicharo, J.; Heras, A. M.; Tielens, A. G. G. M.; Pardo, J. R.; Herpin, F.; Guélin, M.; Waters, L. B. F. M. Infrared Space Observatory's Discovery Of C₄H₂C₆H₂ And Benzene in Crl 618. *Astrophys. J.* **2001**, *546* (2), L123–L126.
- (5) Cami, J.; Bernard-Salas, J.; Peeters, E.; Malek, S. E. Detection of C₆₀ and C₇₀ in a Young Planetary Nebula. *Science* (80-) **2010**, *329* (5996), 1180–1182.
- (6) Cernicharo, J.; Agúndez, M.; Cabezas, C.; Tercero, B.; Marcelino, N.; Pardo, J. R.; De Vicente, P. Pure Hydrocarbon Cycles in TMC-1: Discovery of Ethynyl Cyclopropenyldiene, Cyclopentadiene, and Indene. *Astron. Astrophys.* **2021**, *649*, L15.
- (7) Öberg, K. I. Photochemistry and Astrochemistry: Photochemical Pathways to Interstellar Complex Organic Molecules. *Chem. Rev.* **2016**, *14*, 9631–9663.
- (8) Fayolle, E. C.; Öberg, K. I.; Jørgensen, J. K.; Altwegg, K.; Calcutt, H.; Müller, H. S. P.; Rubin, M.; van der Wiel, M. H. D.; Bjerkeli, P.; Bourke, T. L.; Coutens, A.; van Dishoeck, E. F.; Drozdovskaya, M. N.; Garrod, R. T.; Ligterink, N. F. W.; Persson, M. V.; Wampfler, S. F.; Balsiger, H.; Berthelier, J. J.; De Keyser, J.; Fiethe, B.; Fuselier, S. A.; Gasc, S.; Gombosi, T. I.; Sémon, T.; Tzou, C. Y.; et al. Protostellar and Cometary Detections of Organohalogens. *Nat. Astron.* **2017**, *1* (10), 703–708.
- (9) Keppler, F.; Harper, D. B.; Greule, M.; Ott, U.; Sattler, T.; Schöler, H. F.; Hamilton, J. T. G. Chloromethane Release from Carbonaceous Meteorite Affords New Insight into Mars Lander Findings. *Sci. Rep.* **2014**, *4* (1), 1–11.
- (10) Segura, A.; Kasting, J. F.; Meadows, V.; Cohen, M.; Scalo, J.; Crisp, D.; Butler, R. A. H.; Tinetti, G. Biosignatures from Earth-like Planets around M Dwarfs. *Astrobiology* **2005**, *5* (6), 706–725.
- (11) Nalezinski, R.; Bradshaw, A. M.; Knorr, K. A Vibrational Spectroscopy Study of the Orientational Ordering in CH₃Cl Monolayers Physisorbed on Graphite. *Surf. Sci.* **1997**, *393* (1–3), 222–230.
- (12) Burbank, R. D. The Crystal Structure of Methyl Chloride At-12501. *J. Am. Chem. Soc.* **1953**, *75*, 1211–1214, DOI: [10.1021/ja01101a059](https://doi.org/10.1021/ja01101a059).
- (13) Stoppa, P.; Pietropolli Charmet, A.; De Lorenzi, A.; Tamassia, F.; Melosso, M.; Cané, E.; Dore, L.; Pizzarini, C. High Resolution FTIR Study of the ν_5 , ν_6 , and ν_9 Fundamental Bands of CH₂D³⁷Cl. *J. Quant. Spectrosc. Radiat. Transfer* **2021**, *270*, No. 107719.
- (14) Bag, S.; Bhui, R. G.; Methikkalam, R. R. J.; Pradeep, T.; Kephart, L.; Walker, J.; Kuchta, K.; Martin, D.; Wei, J. Development of Ultralow Energy (1–10 eV) Ion Scattering Spectrometry Coupled with Reflection Absorption Infrared Spectroscopy and Temperature Programmed Desorption for the Investigation of Molecular Solids. *Rev. Sci. Instruments* **2014**, *85* (1), 1–7.
- (15) Vishwakarma, G.; Ghosh, J.; Pradeep, T. Desorption-Induced Evolution of Cubic and Hexagonal Ices in an Ultrahigh Vacuum and Cryogenic Temperatures. *Phys. Chem. Chem. Phys.* **2021**, *23* (41), 24052–24060.
- (16) Bartmess, J. E.; Georgiadis, R. M. Empirical Methods for Determination of Ionization Gauge Relative Sensitivities for Different Gases. *Vacuum* **1983**, *33* (3), 149–153.
- (17) Vishwakarma, G.; Malla, B. K.; Chowdhury, S.; Khandare, S. P.; Pradeep, T. Existence of Acetaldehyde Clathrate Hydrate and Its Dissociation Leading to Cubic Ice under Ultrahigh Vacuum and Cryogenic Conditions. *J. Phys. Chem. Lett.* **2023**, *14*, 5328–5334.
- (18) Lee, D. H.; Kang, H. Acid-Promoted Crystallization of Amorphous Solid Water. *J. Phys. Chem. C* **2018**, *122* (42), 24164–24170.
- (19) Dows, D. A. Vibrational Spectra of the Crystalline Methyl Halides. *J. Chem. Phys.* **1958**, *29* (3), 484–489.
- (20) Gobinda Bhui, R.; Rajan, R.; Methikkalam, J.; Bag, S.; Pradeep, T. Diffusion and Crystallization of Dichloromethane within the Pores of Amorphous Solid Water. *J. Phys. Chem. C* **2016**, *120* (25), 13474–13484, DOI: [10.1021/acs.jpcc.6b00436](https://doi.org/10.1021/acs.jpcc.6b00436).
- (21) Nesheva, D.; Bineva, I.; Levi, Z.; Aneva, Z.; Merdzhanova, T.; Pivin, J. C. Composition, Structure and Annealing-Induced Phase Separation in SiO_x Films Produced by Thermal Evaporation of SiO in Vacuum. *Vacuum* **2002**, *68* (1), 1–9.
- (22) Philip, J.; Gnanaprakash, G.; Panneerselvam, G.; Antony, M. P.; Jayakumar, T.; Raj, B. Effect of Thermal Annealing under Vacuum on the Crystal Structure, Size, and Magnetic Properties of ZnFe₂O₄ Nanoparticles. *J. Appl. Phys.* **2007**, *102* (5), 54305.
- (23) Lilach, Y.; Asscher, M. Compression and Caging of CD₃Cl by H₂O Layers on Ru(0001). *J. Chem. Phys.* **2002**, *117* (14), 6730–6736.
- (24) Makino, T.; Zulaehah, S.; Gueriba, J. S.; Diño, W. A.; Okada, M. CH₃Cl/Cu(410): Interaction and Adsorption Geometry. *J. Phys. Chem. C* **2018**, *122* (22), 11825–11831.
- (25) Takeuchi, H.; Harada, I.; Shimanouchi, T. Anomalous Splitting Pattern of the ν_3 Vibrational Band of Crystalline Methyl Chloride: Chlorine Isotopic Effects. *Chem. Phys. Lett.* **1976**, *43* (3), 516–519.
- (26) Duncan, J. L.; McKean, D. C.; Mallinson, P. D.; McCulloch, R. D. Infrared Spectra of CHD₂Cl and CHD₂CCH and the Geometries of Methyl Chloride and Propyne. *J. Mol. Spectrosc.* **1973**, *46* (2), 232–239.
- (27) Lin, M.-Y.; Huang, T.-P.; Wu, P.-Z.; Chin, C.-H.; Wu, Y.-J. Formation of Halogen-Bearing Species. II. Irradiation of Chloromethane in Carbon Monoxide Ice with VUV Light and Electrons. *Astrophys. J.* **2020**, *888* (1), 39.

- (28) Morrison, A. M.; Flynn, S. D.; Liang, T.; Doublerly, G. E. Infrared Spectroscopy of (HCl)_m(H₂O)_n Clusters in Helium Nanodroplets: Definitive Assignments in the HCl Stretch Region. *J. Phys. Chem. A* **2010**, *114* (31), 8090–8098.
- (29) Öberg, K. I.; Garrod, R. T.; Van Dishoeck, E. F.; Linnartz, H. Formation Rates of Complex Organics in UV Irradiated CH₃OH-Rich Ices - I. Experiments. *Astron. Astrophys.* **2009**, *504* (3), 891–913.
- (30) Lin, J. J.; Chen, Y.; Lee, Y. Y.; Lee, Y. T.; Yang, X. Photodissociation Dynamics of CH₃Cl at 157.6 nm: Evidence For. *Chem. Phys. Lett.* **2002**, *361* (5–6), 374–382.
- (31) Matsumi, Y.; Tonokura, K.; Kawasaki, M.; Inoue, G.; Satyapal, S.; Bersohn, R. Erratum: Fine Structure Branching Ratios and Doppler Spectroscopy of Chlorine Atoms from the Photodissociation of Alkyl Chlorides and Chlorofluoromethanes at 157 and 193 nm [*J. Chem. Phys.* **94**, 2669 (1991)]. *J. Chem. Phys.* **1992**, *97* (7), 5261.
- (32) Kawasaki, M.; Kasatani, K.; Sato, H.; Shinohara, H.; Nishi, N. Photodissociation of Molecular Beams of Halogenated Hydrocarbons at 193 nm. *Chem. Phys.* **1984**, *88* (1), 135–142.
- (33) Brownsword, R. A.; Hillenkamp, M.; Laurent, T.; Vatsa, R. K.; Volpp, H. R.; Wolfrum, J. Photodissociation Dynamics of the Chloromethanes at the Lyman- α Wavelength (121.6 nm). *J. Chem. Phys.* **1997**, *106* (4), 1359.
- (34) Amaral, G.; Xu, K.; Zhang, J. H-Atom Product Channels in the Photodissociation of CH₃Cl, CH₃Br, and CH₃I at 121.6 nm. *J. Phys. Chem. A* **2001**, *105* (7), 1115–1120, DOI: 10.1021/jp0028507.
- (35) Lilach, Y.; Asscher, M. Photochemistry of Caged Molecules: CD₃Cl@Ice. *J. Chem. Phys.* **2003**, *119* (1), 407–412.
- (36) Ayoub, Y.; Asscher, M. Photochemistry of Ethyl Chloride Caged in Amorphous Solid Water. *Phys. Chem. Chem. Phys.* **2008**, *10* (32), 6486–6491.
- (37) Gilton, T. L.; Dehnhostel, C. P.; Cowin, J. P. Electron Transmission through Layers of H₂O and Xe in the Ultrahigh Vacuum Photoreduction of CH₃Cl on Ni(111). *J. Chem. Phys.* **1989**, *91* (3), 1937–1938.
- (38) Kang, H. Chemistry of Ice Surfaces. Elementary Reaction Steps on Ice Studied by Reactive Ion Scattering. *Acc. Chem. Res.* **2005**, *38* (12), 893–900.
- (39) Park, S. C.; Maeng, K. W.; Pradeep, T.; Kang, H. Reactive Ion Scattering from Pure and Mixed HCl, NH₃ and D₂O Surfaces. *Nucl. Instruments Methods Phys. Res. Sect. B Beam Interact. with Mater. Atoms* **2001**, *182* (1–4), 193–199.
- (40) Kim, Y.; Moon, E.; Shin, S.; Kang, H. Acidic Water Monolayer on Ruthenium(0001). *Angew. Chem.* **2012**, *124* (51), 12978–12981.
- (41) Andersson, S.; Al-Halabi, A.; Kroes, G. J.; van Dishoeck, E. F. Molecular-Dynamics Study of Photodissociation of Water in Crystalline and Amorphous Ices. *J. Chem. Phys.* **2006**, *124* (6), 64715.
- (42) Yabushita, A.; Inoue, Y.; Senga, T.; Kawasaki, M.; Sato, S. Photodissociation of Chlorine Molecules Adsorbed on Amorphous and Crystalline Water Ice Films. *J. Phys. Chem. B* **2002**, *106* (12), 3151–3159.
- (43) Yabushita, A.; Hama, T.; Iida, D.; Kawasaki, M. Hydrogen Peroxide Formation Following the Vacuum Ultraviolet Photodissociation of Water Ice Films at 90 K. *J. Chem. Phys.* **2008**, *129* (1), 14709.
- (44) Noble, J. A.; Michoulier, E.; Aupetit, C.; Mascetti, J. Influence of Ice Structure on the Soft UV Photochemistry of PAHs Embedded in Solid Water. *Astron. Astrophys.* **2020**, *644*, A22.
- (45) Watanabe, N. Behaviour of Radicals on Interstellar Dust Analogues. *Proc. Int. Astron. Union* **2019**, *15* (S350), 116–122.
- (46) Kouchi, A.; Kuroda, T. Amorphization of Cubic Ice by Ultraviolet Irradiation. *Nat.* **1990**, *344* (6262), 134–135.
- (47) Tachibana, S.; Kouchi, A.; Hama, T.; Oba, Y.; Piani, L.; Sugawara, I.; Endo, Y.; Hidaka, H.; Kimura, Y.; Murata, K.-I.; et al. Liquid-like Behavior of UV-Irradiated Interstellar Ice Analog at Low Temperatures. *Sci. Adv.* **2017**, *3* (9), No. eaao2538, DOI: 10.1126/sciadv.aao2538.
- (48) Malla, B. K.; Vishwakarma, G.; Chowdhury, S.; Selvarajan, P.; Pradeep, T. Formation of Ethane Clathrate Hydrate in Ultrahigh Vacuum by Thermal Annealing. *J. Phys. Chem. C* **2022**, *2022*, 17983–17989.
- (49) Ramakrishnan, S.; Sagi, R.; Mahapatra, N.; Asscher, M. Effect of Coadsorbed Oxygen on the Photochemistry of Methane Embedded in Amorphous Solid Water. *J. Phys. Chem. C* **2018**, *122* (27), 15287–15296.

Vacuum Ultraviolet Photolysis of Condensed Methyl Chloride in Interstellar Model Conditions and Trapping of Intermediates at Intergrain Interfaces

Bijesh K. Malla¹, Gaurav Vishwakarma¹, Soham Chowdhury¹, and Thalappil Pradeep^{1,2}*

¹Department of Science and Technology Unit of Nanoscience (DST UNS) and Thematic Unit of Excellence (TUE), Department of Chemistry, Indian Institute of Technology Madras, Chennai 600036, India.

²International Centre for Clean Water, IITM Research Park, Chennai 600113, India.

Corresponding author

***Email:** pradeep@iitm.ac.in

This PDF file includes:

Figure S1 to S9 (pages S2-S9)

Table 1 (page S6)

Reference (pages S9)

Supporting information 1:

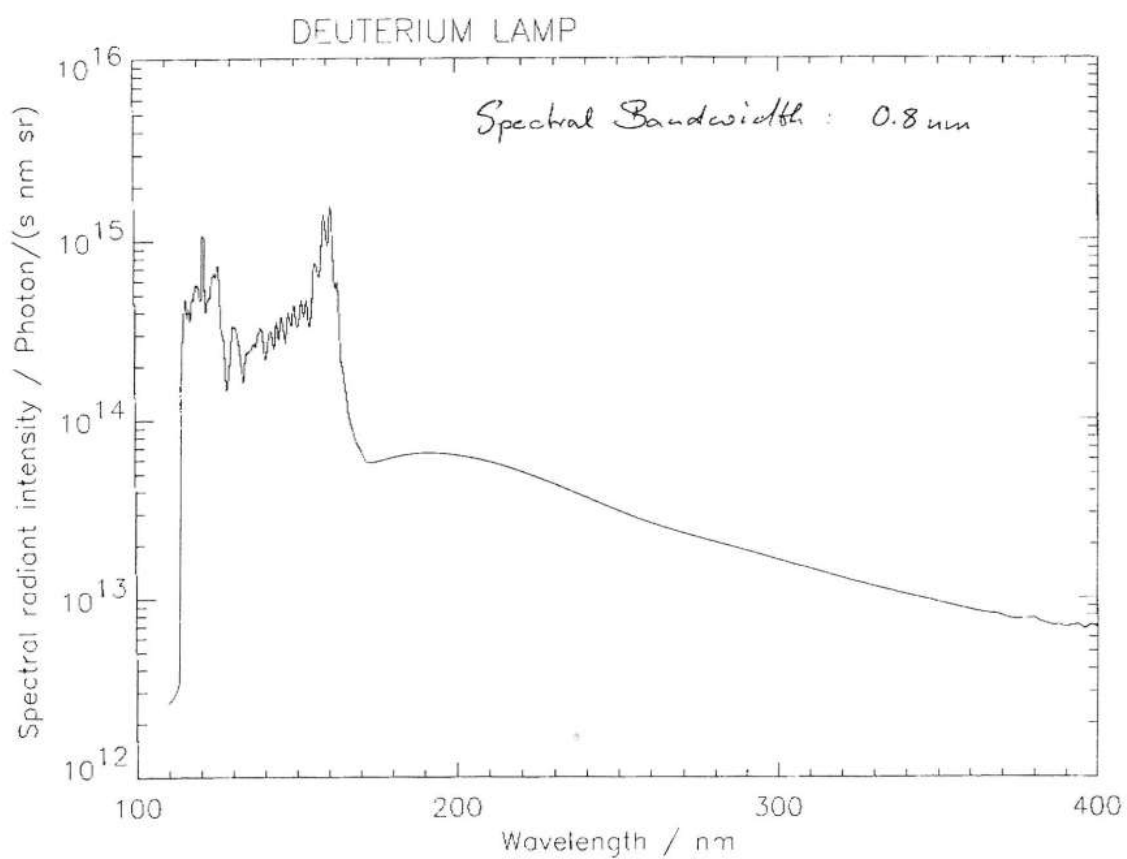


Figure S1. Emission spectrum of Model 634 Deuterium lamp, provided by the McPherson.

Supporting information 2:

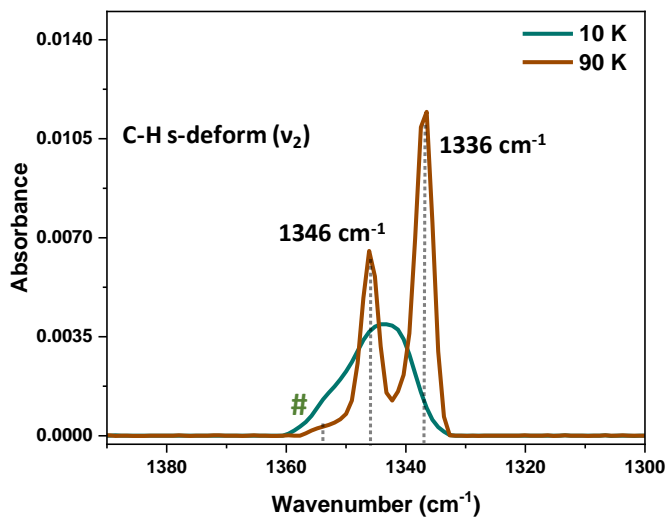


Figure S2. RAIR spectra of 63 ML of methyl chloride in C-H symmetric bending region. The pure methyl chloride was vapor-deposited on Ru(0001) substrate at 10 K and further annealed to 90 K with a ramping rate of 10 K/min, and it was waited for 2 hours.

Supporting information 3:

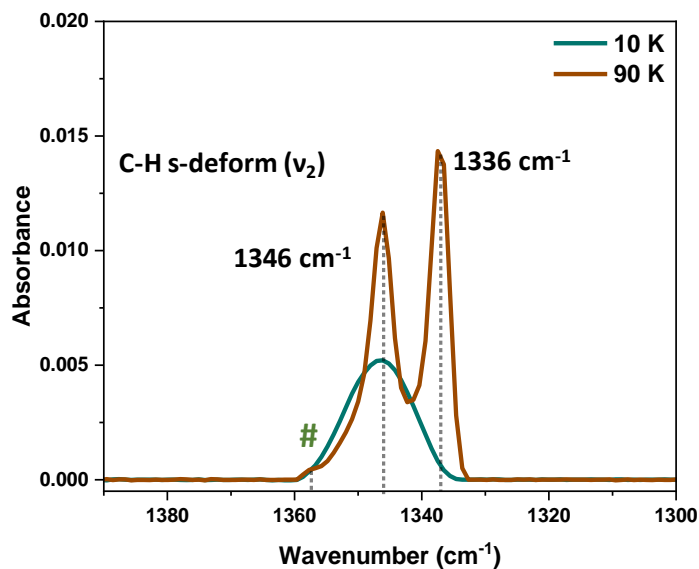


Figure S3. RAIR spectra of 160 ML of methyl chloride:water (2:1) in C-H symmetric bending region. The 160 ML of methyl chloride:water (2:1) was vapor-deposited on Ru(0001) substrate at 10 K and further annealed to 90 K with a ramping rate of 2 K/min.

Supporting information 4:

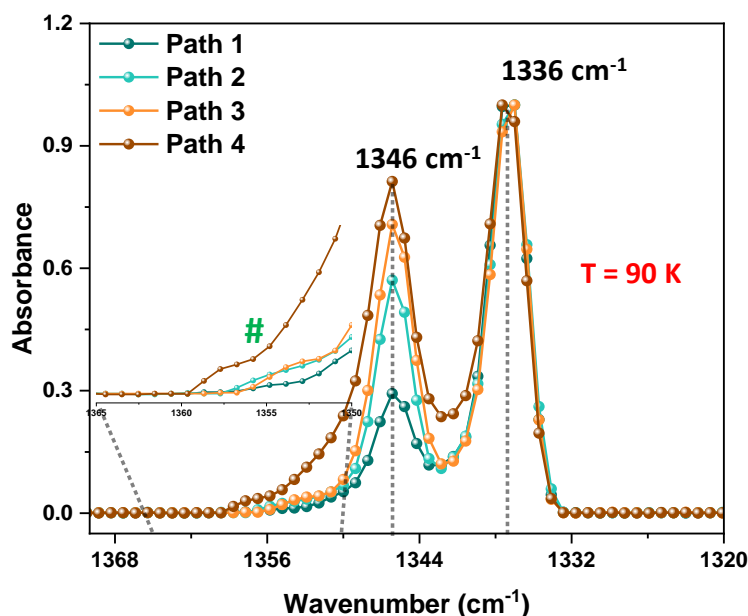


Figure S4. Normalized RAIR spectra of condensed methyl chloride ice in the C-H symmetric bending region at 90 K created by four different paths. In path 1 and path 2, 63 ML of methyl chloride vapor was deposited on Ru(0001) at 10 K substrate and slowly annealed to 90 K at an annealing rate of 2 K/min and 10 K/min, respectively. In path 3, methyl chloride directly vapor deposited on Ru(0001) substrate at 90 K. In path 4, 160 ML of methyl chloride:water (2:1) co-deposited on Ru(0001) substrate at 10 K and slowly annealed to 90 K at an annealing rate of 2 K/min. The enlarged spectra in the inset show a hump around 1354 cm⁻¹ (denoted by #), representing the gas phase methyl chloride.

Supporting information 5:

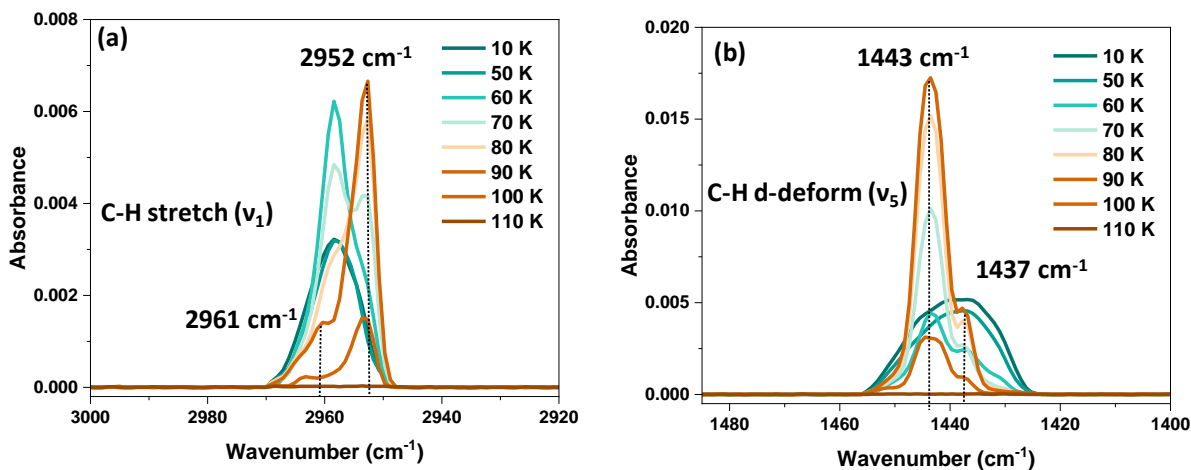


Figure S5. Temperature-dependent RAIR spectra of 63 ML of methyl chloride in (a) C-H stretching region, (b) C-H antisymmetric bending region. The pure methyl chloride was vapor-deposited on Ru(0001) substrate at 10 K and further annealed to 90 K with a ramping rate of 2 K/min.

Supporting information 6:

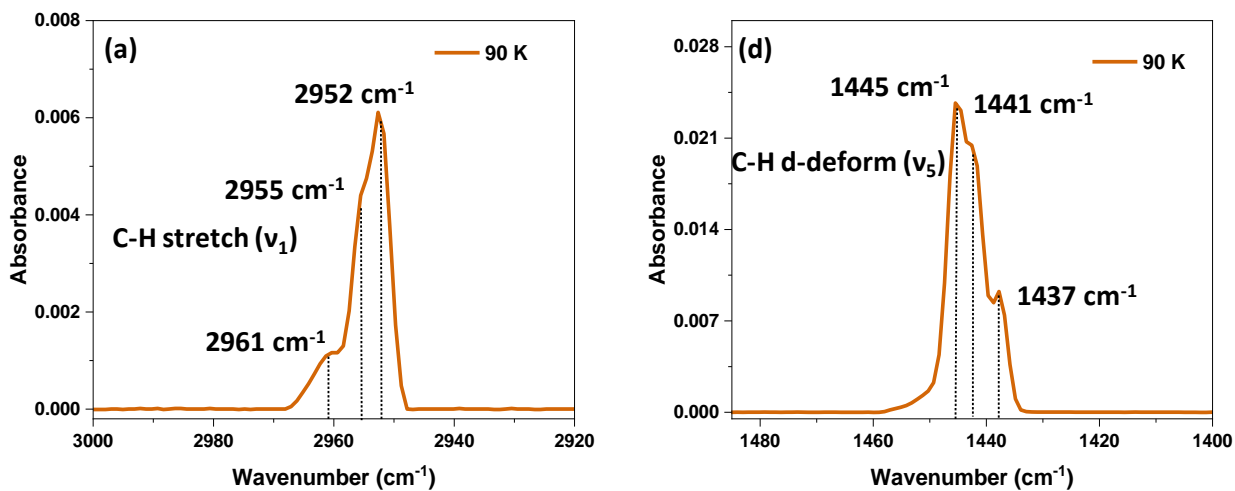


Figure S6. RAIR spectrum of 63 ML of methyl chloride in (a) C-H stretching region, (b) C-H antisymmetric bending region. The pure methyl chloride was vapor-deposited on Ru(0001) substrate at 90 K.

Supporting information 7:

Table S1. Vibrational frequencies of methyl chloride in amorphous, crystalline, polycrystalline, and gas phases.¹

Mode	Amorphous (cm ⁻¹)	Crystalline (cm ⁻¹)	Polycrystalline (cm ⁻¹)	Gas (cm ⁻¹)
C-Cl stretching (ν_3)	710	704, 700, 695	705, 700, 695	732
C-Cl rocking (ν_6)	1019	1022	1022	1015
C-H symmetric bending (ν_2)	1343	1336, 1346	1336, 1346	1354
C-H antisymmetric bending (ν_5)	1438	1443, 1437	1445, 1441, 1437	1454
C-H symmetric stretching (ν_1)	2958	2952, 2961	2952, 2955, 2961	2966

Supporting information 8:

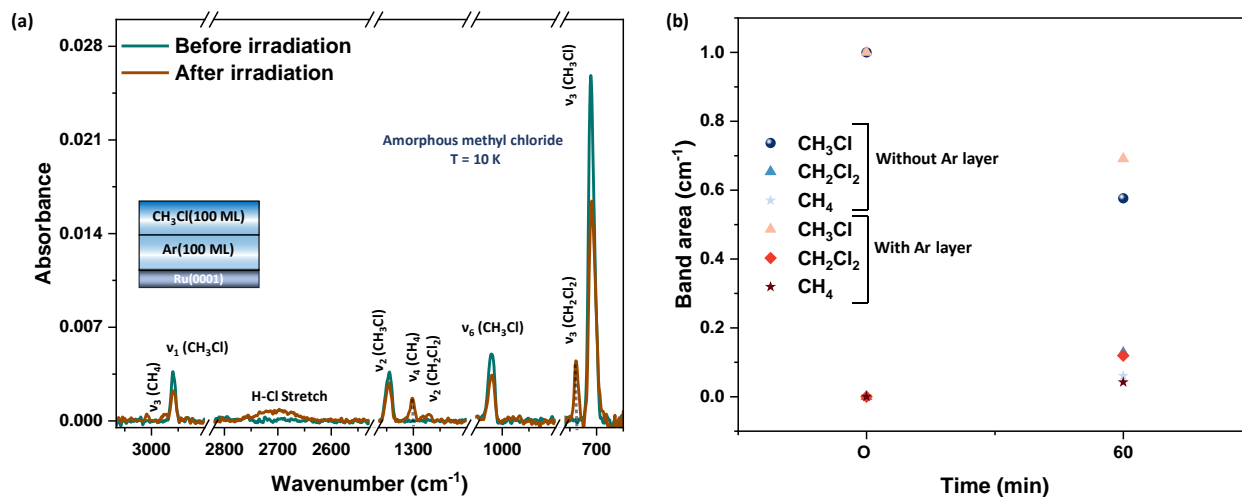


Figure S7. (a) RAIR spectra of 100 ML of methyl chloride before and after irradiation with VUV light at 10 K in the mid-infrared region. At first, 100 ML of Ar vapor was deposited on Ru(0001) substrate, followed by methyl chloride vapor deposited on top of that. The amorphous methyl chloride ice was photo-irradiated for 60 minutes. (b) Normalized band area of methyl chloride, dichloromethane, and methane before and after 60 min irradiation. Two systems were taken: in the first system, 63 ML of methyl chloride was directly vapor deposited on Ru(0001) substrate, and in the second system, 100 ML of methyl chloride was deposited on the top of 100 ML of Ar matrix on Ru(0001) substrate.

Supporting information 9:

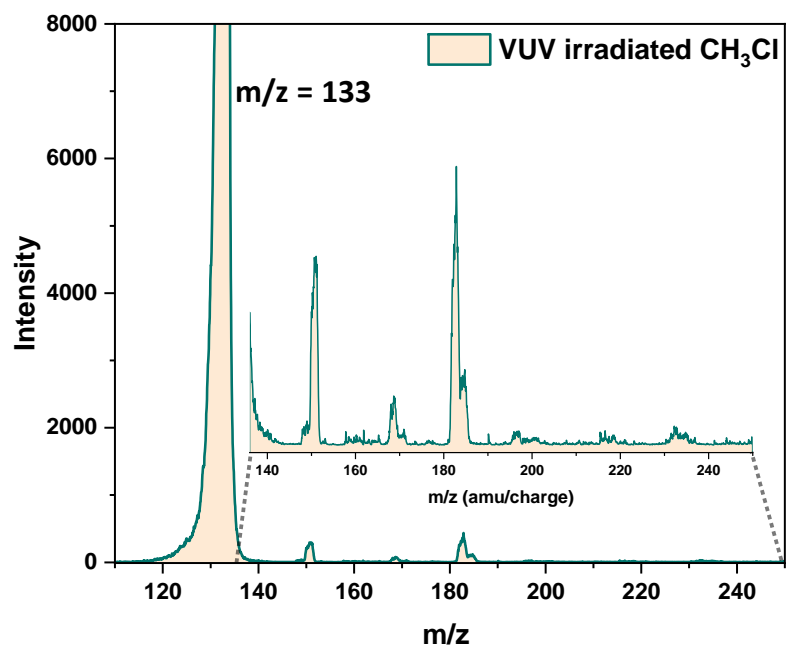


Figure S8. Reactive ion scattering mass spectrum obtained on 60 minutes VUV irradiated amorphous methyl chloride ice at 10 K.

Supporting information 10:

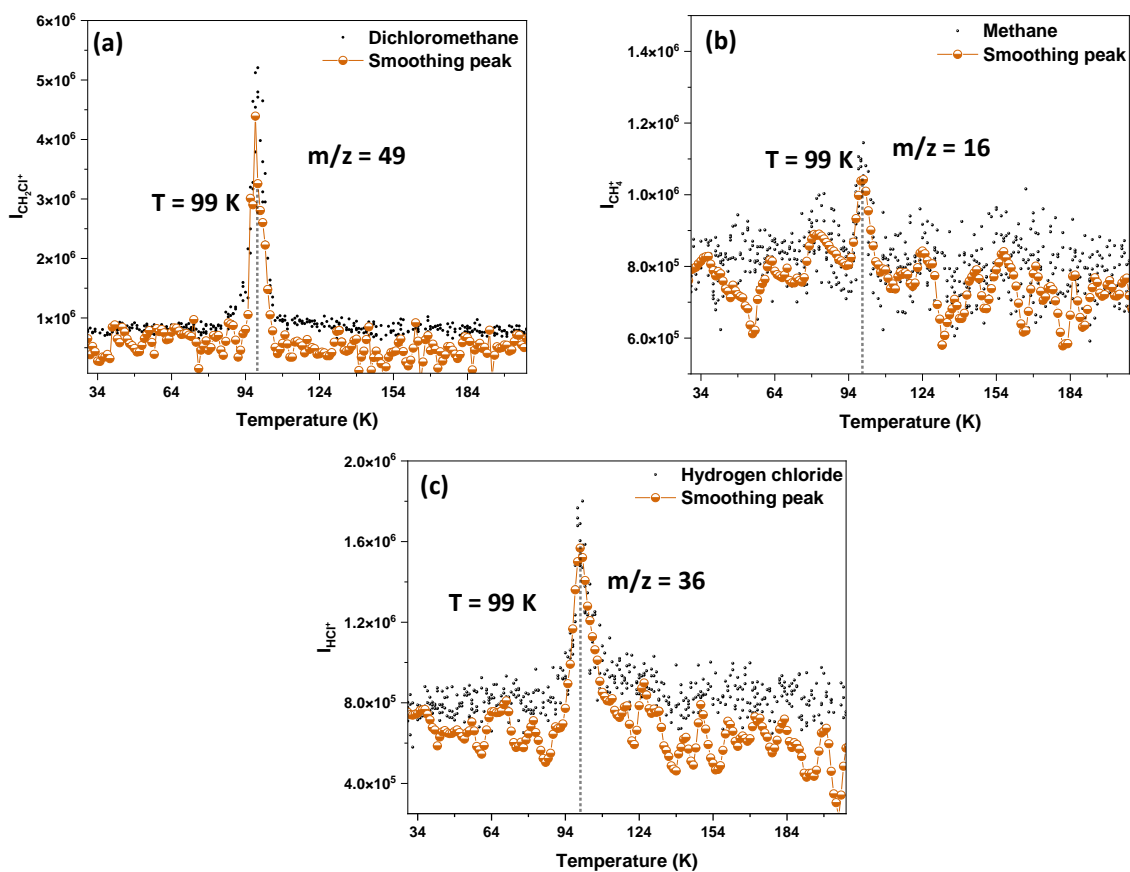


Figure S9. Sublimation profile of integrated ion counts in (a) at $m/z = 49$ (CH_2Cl_2) in (b) at $m/z = 16$ (CH_4) in (c) at $m/z = 36$ (HCl) recorded by quadrupole mass spectrometer. 63 ML of pure methyl chloride was deposited on Ru(0001) substrate, followed by 60 min of VUV light irradiation. The irradiated sample was annealed to 200 K with a 10 K/min ramping rate; subsequently, mass spectra were taken.

REFERENCES

- (1) Dows, D. A. Vibrational Spectra of the Crystalline Methyl Halides. *J. Chem. Phys.* **1958**, 29 (3), 484. <https://doi.org/10.1063/1.1744528>.

Publications with other groups

Gold Au(I)_6 Clusters with Ligand-Derived Atomic Steric Locking: Multifunctional Optoelectrical Properties and Quantum Coherence


Sourov Chandra,* Alice Sciortino, Susobhan Das, Faisal Ahmed, Arijit Jana, Jayoti Roy, Diao Li, Ville Liljeström, Hua Jiang, Leena-Sisko Johansson, Xi Chen,* Nonappa, Marco Cannas, Thalappil Pradeep, Bo Peng, Robin H. A. Ras, Zhipei Sun, Olli Ikkala,* and Fabrizio Messina*

An atomically precise ultrasmall Au(I)_6 nanocluster where the six gold atoms are complexed by three sterically interlocking stabilizing ligands is reported, allowing a unique combination of efficient third harmonic generation (THG), intense photoluminescence quantum yield (35%), ultrafast quantum coherence, and electron accepting properties. The reaction of 6-(dibutylamino)-1,3,5-triazine-2,4-dithiol (TRZ) with HAuCl_4 leads to complexation by thiolation. However, intriguingly, another reduction step is needed to form the centrosymmetric $\text{Au(I)}_6\text{TRZ}_3$ clusters with the multifunctional properties. Here, ascorbic acid is employed as a mild reducing agent, in contrast to the classic reducing agents, like NaBH_4 and NaBH_3CN , which often produce mixtures of clusters or gold nanoparticles. Such Au(I)_6 nanocluster films produce very strong THG response, never observed for nanoclusters. The clusters also produce brilliant single and multiphoton luminescence with exceptional stability. Density functional theory calculations and femtosecond transient absorption studies suggest ultrafast ligand-to-metal charge transfer, quantum coherence with long decoherence time 200–300 fs, and fast propagation of excitation from the core to the surrounding solvent. Finally, novel electron-accepting ground state properties allow *p*-doping of 2D field-effect transistor devices. Summarizing, the potential of ultrasmall sterically interlocked Au(I) clusters, i.e., complexes allowed by the new sequential reduction protocol, towards multifunctional devices, fast photoswitches, and quantum colloidal devices is shown.

1. Introduction

Gold nanoclusters and small gold complexes have attracted considerable attention due to their fundamental properties and application potential upon bridging the functional gap between molecules and larger plasmonic nanoparticles.^[1] Atomically precise ultrasmall gold nanoclusters (GNCs) typically have contained an exact number of $\approx 10 - 300$ gold atoms aiming at well-defined particle sizes. They are stabilized by protecting ligands, whereupon their binding typically leads to outer metal surfaces with different valence than that of the inner metal core.^[2] Their photo-physics is more complex than that of small molecules and larger quantum dots, leading to both challenges and suggesting novel application possibilities. GNCs allow several relevant properties, such as luminescence with promoted photostability combining biocompatibility.^[3–7] Unlike larger plasmonic nanoparticles, GNCs display molecule-like electronic spectra, as their electronic structure is

S. Chandra, X. Chen, B. Peng, R. H. A. Ras, O. Ikkala
Department of Applied Physics
Aalto University
P. O. Box 15100, Espoo, Aalto FI-00076, Finland
E-mail: sourov.chandra@aalto.fi; xi.6.chen@aalto.fi; olli.ikkala@aalto.fi
A. Sciortino, M. Cannas, F. Messina
Dipartimento di Fisica e Chimica – Emilio Segrè
Università degli Studi di Palermo
Via Archirafi 36, Palermo 90123, Italy
E-mail: fabrizio.messina@unipa.it
A. Sciortino, F. Messina
CHAB – ATeN Center
Università degli studi di Palermo
Viale delle Scienze, Edificio 18, Palermo 90128, Italy

 The ORCID identification number(s) for the author(s) of this article can be found under <https://doi.org/10.1002/adom.202202649>.

DOI: 10.1002/adom.202202649

S. Das, F. Ahmed, D. Li, Z. Sun
Department of Electronics and Nanoengineering
Aalto University
Maarintie 13, Espoo 02150, Finland
A. Jana, J. Roy, T. Pradeep
Department of Chemistry
DST Unit of Nanoscience (DST UNS) and Thematic Unit of Excellence (TUE)
Indian Institute of Technology Madras
Chennai 600036, India
V. Liljeström, H. Jiang
Nanoscience Center
OtaNano
Aalto University
Aalto FI-00076, Finland
L.-S. Johansson
Department of Bioproducts and Biosystems
Aalto University
Vuorimiehentie 1, Espoo FI-00076, Finland

dominated by delocalized states spread over a relatively large Au core. Beyond that, there is a scientific interest toward in-depth understanding of GNC photocycle.^[8–17] In particular, studies using relatively large Au₁₃ and Au₂₅ clusters, often modeled within the “superatom” theoretical framework, suggest that the optically active electronic states are localized within the gold cores.^[8,16–19] Recent theoretical calculations suggest that all excited states may arise from core-based superatomic orbitals.^[16] Importantly, the protecting ligands also play a role in the electronic response of the GNCs through ligand-to-metal charge transfer (LMCT) transitions^[10,14,15] or by so-called semi-ring states.^[11] Still, recently questions have been posed whether the knowledge accumulated on classical GNCs such as Au₂₅, containing both Au(0) and Au(I) atoms, can directly apply to ultrasmall GNCs containing less than ten Au atoms where all atoms are in Au(I) state due to the ligand binding, also related to new properties. Such GNC structures have recently also been specifically denoted as Au(I) complexes.^[1]

Regarding to optical applications, a materials platform allowing tunably multifunctionality would be highly desired. For optical nonlinearities, the basis for all-optical devices employs self-phase modulation, optical bistability, regenerative oscillations, and four-wave mixing.^[20] Due to their applications in imaging, medicine, communication, and industry, the present demand for devices motivates the assessment of the nonlinear optical (NLO) properties of materials in visible and near-infrared region.^[21,22] Traditional bulk NLO materials, such as β -BaB₂O₄ and LiNbO₃, suffer from low conversion efficiency and poor NLO susceptibility.^[23] Two-dimensional (2D) nanomaterials such as graphene, hexagonal boron nitride, transition-metal dichalcogenides, and GeAs show strong second and third-harmonic generation (SHG and THG) stemming from their crystal noncentrosymmetry.^[21,24–26] However, they do not display combined strong photoluminescence (PL), robust harmonic generation, or electric doping, thus they have not shown multifunctionality so far.

Therefore, one can foresee a need to develop materials having both advanced linear and nonlinear optical properties with high conversion efficiency and high nonlinear susceptibility, as well as electric functionality. Therein, developing biocompatible molecular level clusters below 1 nm would offer potential applications not only in devices but also in medicine as such particles can readily cross the blood-brain barrier.^[27,28] Gold nanoparticles have been investigated for NLO properties.^[29] THG has been reported for isolated gold nanorods and nanoparticles of specific shapes and sizes using highly sophisticated designs for plasmonic nanoparticles.^[29] Nevertheless, plasmonic nanoparticles typically involve polydispersity, therefore, achieving THG is a fundamental challenge. Recent experimental and theoretical studies have shown that gold and

silver nanoclusters also exhibit SHG.^[30] However, multifunctional ultrasmall GNCs displaying THG have not been reported, even more to combine with luminescence. Also, showing GNC-dependent doping of semiconductor devices could allow new modular approaches, not shown before.

Herein, we report the synthesis and optoelectronic properties of 6-(dibutylamino)-1,3,5-triazine-2,4-dithiol (TRZ) stabilized GNCs containing a metal core of six gold atoms Au(I)₆, i.e., where all gold atoms are in the Au(I) state and the vibration of the atoms is locked by the TRZ ligands via dual thiolate bindings. This is done by a novel two-step chemical reduction. The experimental data along with density functional theory (DFT) calculations suggest that the Au(I)₆ core has an octahedral geometry, resulting in a triclinic crystal lattice in solid state. The centrosymmetric Au-core produces an intense THG under infrared laser excitations. The particles exhibit a strong third-order susceptibility. They also display strong PL with high quantum efficiency and peculiar photophysical behavior unlike larger nanoclusters. The photocycle is controlled by ligand-to-metal charge transfer transitions without intermediates. Moreover, we show that the energy cascade from the initially excited state proceeds through a coherent pathway, involving the generation of core vibrational wave packets damped through successive relaxation. As a result, GNCs induce a controllable *p*-type (hole dominant) doping effect to the 2D multilayer WSe₂ field effect transistors (FETs) through a charge transfer mechanism.

2. Results and Discussion

2.1. Synthesis and Characterizations

The reaction of 6-(dibutylamino)-1,3,5-triazine-2,4-dithiol (TRZ) with HAuCl₄ leads to complexation and gold reduction by thiolation, but results in uncontrolled fibrillar aggregates (Figure S1, Supporting Information). To achieve spherical well-controlled nanoclusters of TRZ-stabilized GNCs, another reduction step by preferably ascorbic acid (denoted as GNC-1) or alternatively by NaBH₄ (denoted as GNC-2) was required (Figure 1a). The scanning transmission electron microscopy (STEM) images of GNC-1 and GNC-2 are presented in Figure 1b,c respectively, suggesting uniform distribution of clusters with a size of ~1 nm. The resulting GNCs exhibit intense yellow-green emission under exposure to UV light (inset in Figure 1b). The energy-dispersive X-ray (Figure S2, Supporting Information) and the X-ray photoelectron spectra (XPS) (Figure S3, Supporting Information) confirm the elements Au, S, C, O, and N. While C 1s, N 1s, and S 2p spectra further approve the C–C, C–H, C–N, –C≡N–C, ≡N–C≡, and Au–S bonds (Figure S4, Supporting Information), the Au 4f doublet at 85.0 and 88.7 eV confirms the existence of Au(I) atoms in both GNC-1 and GNC-2 (Figure 1d). Finally, electrospray ionization mass spectra (ESI-MS) in both negative and positive ion modes confirm the composition as Au(I)₆(TRZ)₃ (Figure 1e and Figure S5, Supporting Information). The results indicate the coexistence of both -2 and +1 states of the GNCs and that they are in equilibrium. The collision energy-dependent studies show the fragmentation of the clusters (Figure S6, Supporting

Nonappa
Faculty of Engineering and Natural Sciences
Tampere University
Korkeakoulunkatu 6, P. O. Box 541, Tampere FI-33101, Finland
Z. Sun
QTF Centre of Excellence
Department of Applied Physics
Aalto University
Aalto FI-00076, Finland

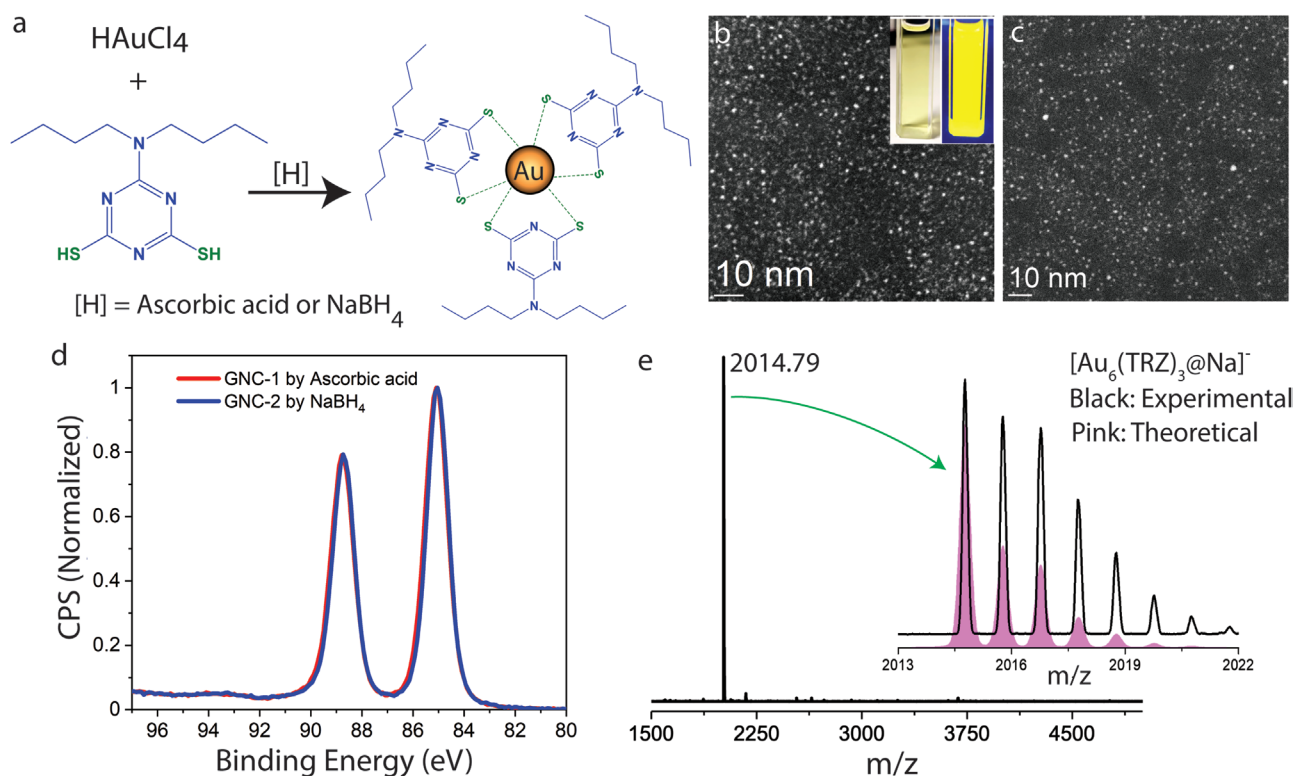


Figure 1. a) Schematic representation for the synthesis of GNCs. STEM images of b) GNC-1 and c) GNC-2. Inset in (b) shows the dichloromethane (DCM) solution of GNCs under ambient light (left) and exposure to UV light (right). d) Au 4f XPS spectra of GNCs. e) Electrospray ionization mass spectrum of GNC-1, suggesting a composition $\text{Au}(\text{I})_6(\text{TRZ})_3$ based on experiment and modeling.

Information). The ^1H NMR spectra of the free TRZ-ligand and the GNCs (Figures S7 and S8, Supporting Information) further support their compositions and nature of fast protonation and deprotonation.

2.2. DFT Calculations and Mapping of Electronic Transitions

Based on ESI-MS, the atomic models of $[\text{Au}(\text{I})_6(\text{TRZ})_3]^{2-}$ and $[\text{Au}(\text{I})_6(\text{TRZ})_3]^+$ GNCs are created using DFT with GPAW code.^[31] Two possible isomers of $[\text{Au}(\text{I})_6(\text{TRZ})_3]^{2-}$ NCs are produced (Figure 2a,b), wherein the latter one shows the most stable structure consisting of an octahedral $\text{Au}(\text{I})_6$ core surrounded by three TRZ ligands. The average Au–Au and Au–S bond lengths are 2.84 and 2.38 Å, respectively. The HOMO–LUMO energy gap of the cluster is 1.43 eV; the HOMO states have contributions both from the ligands and Au atoms, while the electrons in the Au atoms dominate the LUMO states (Figure 2c). The time-dependent DFT^[32] simulated optical absorption (OA) spectrum from the octahedral $[\text{Au}(\text{I})_6(\text{TRZ})_3]^{2-}$ GNC displays two distinct peaks at 413 and 318 nm (Figure 2d). The computed spectral patterns are close to the experimental OA with a slight red shift.^[33] To get insight into electron-hole transitions responsible for the absorption ≈ 400 nm, we analyzed the transitions at 3.0 eV (413 nm) using the transition contribution map (TCM) method.^[34] The TCM in Figure 2e demonstrates the Kohn–Sham (KS) absorption decomposition weight at a fixed energy ω in the two-dimensional (ϵ_0 ,

ϵ_u)- plane, where ϵ_0 and ϵ_u are the energies of the occupied and unoccupied states, respectively. The corresponding projected density of states (PDOS) are plotted on the top and right side of the TCM, respectively. It implies that the most significant contribution for the OA at 413 nm is due to the electronic transitions from the occupied states at -1.14 eV to the unoccupied states ≈ 1.78 eV (Fermi level is set to 0 eV). Figure 2f shows the wave functions at -1.14 eV and 1.78 eV, in which the ligands significantly contribute to the occupied states while the Au atoms dominate the unoccupied states, i.e., the OA at ≈ 400 nm is due to the ligand to metal electron-hole or charge transfer transitions. Regarding $[\text{Au}(\text{I})_6(\text{TRZ})_3]^+$, one proton is added to each ligand, which changes the cluster's charge from -2 to $+1$ (Figure S9, Supporting Information). The calculated OA spectra of deprotonated $[\text{Au}(\text{I})_6(\text{TRZ})_3]^{2-}$ and protonated $[\text{Au}(\text{I})_6(\text{TRZ})_3]^+$ NCs are quite similar (Figure S10, Supporting Information), indicating the analogous electron-hole transitions in these two systems.

The small angle X-ray diffraction pattern of the GNC-1 and pure ligand are shown in Figure S11a,b, Supporting Information, respectively. The diffraction pattern (Figure 2g) is calculated by including the octahedral gold core of the nanocluster to the best-fitting crystal lattice. Ligand molecules are not included in the model. The theoretical diffraction pattern corresponds to the triclinic crystal structure (space group P1, number 1) with unit cell dimensions $a = 11.85$ Å, $b = 9.81$ Å, $c = 8.37$ Å, and unit cell angles $\alpha = 85.7^\circ$, $\beta = 85.3^\circ$, $\gamma = 98.2^\circ$ (Figure 2h). The volume of the unit cell is 956.1 Å³.

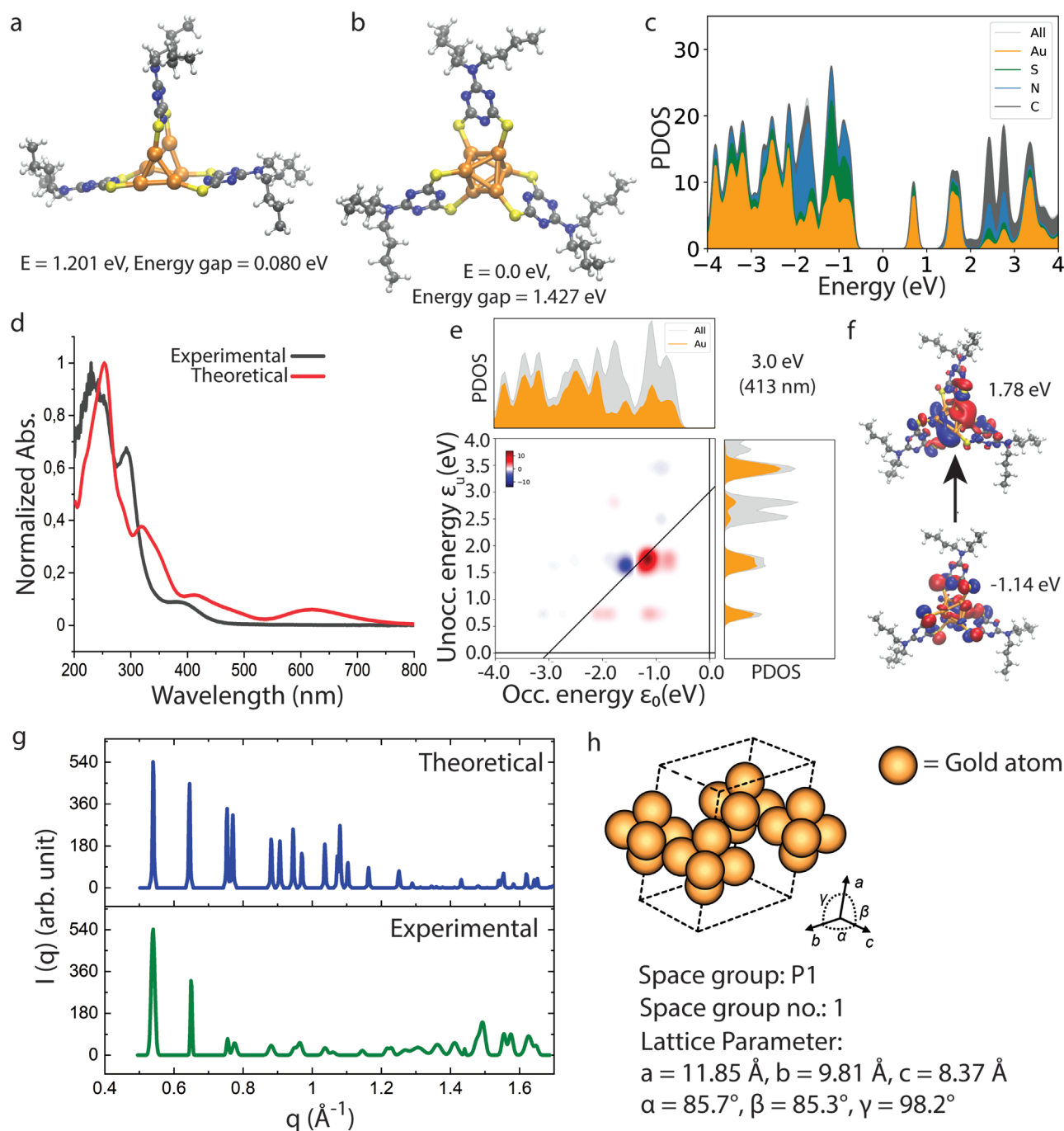


Figure 2. a,b) The atomic structures for two different isomers of $[\text{Au}(\text{I})_6(\text{TRZ})_3]^{2-}$ optimized by DFT, where (b) shows the lowest energy structure with octahedral $\text{Au}(\text{I})_6$ core. c) The projected density of states of the most stabilized octahedral core of the cluster, shown in (b). d) Experimental and theoretical OA spectra of GNC-1. e) The TCM map and PDOS of the cluster at 3.0 eV (413 nm). f) The highest contribution of OA from the occupied state at -1.14 eV to the unoccupied state at 1.78 eV , assuming the Fermi level at 0 eV . g) Calculated diffraction peaks and the theoretical diffractogram based on the triclinic crystal structure. h) The unit cell of the proposed triclinic crystal structure (ligands are excluded in the model).

2.3. Linear and Nonlinear Optical Responses

The photoluminescence (PL) spectra of GNC-1 and GNC-2 are quite similar, with broad emissions centered at $\approx 540 \text{ nm}$ (Figure 3a). The photoluminescence excitation (PLE) spectrum

of the 540 nm emission displays two peaks at 327 and 400 nm for both GNCs. When exciting in the LMCT state at 400 nm , the emission peak at 540 nm with absolute quantum yield of $\approx 35\%$ and decay over a few microseconds (Figure 3b) are observed, almost identically in GNC-1 and GNC-2 (Figure S12

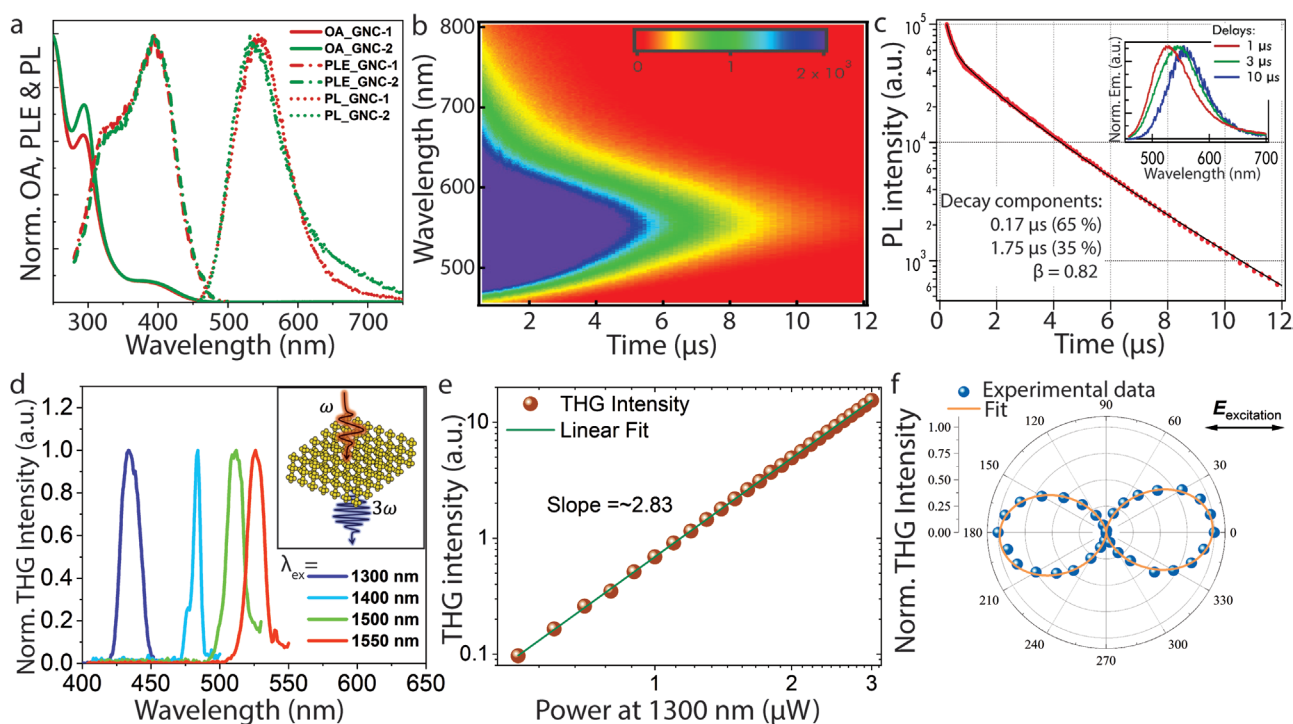


Figure 3. a) Optical absorption (OA), steady-state PL ($\lambda_{\text{ex}} = 400$ nm), and PLE ($\lambda_{\text{em}} = 540$ nm) spectra of GNC-1 and GNC-2 in DCM. b) Time-resolved PL spectra of GNC-1 at 410 nm excitation. c) Decay kinetics of the spectrally integrated PL signal. The data are fitted by a biexponential decay function, that is: $I = A \exp[-t/\tau_1] + B \exp[-(t/\tau_2)^b]$. The stretching factor b in the slower exponential is a typical feature of disordered systems, consistent with the progressive shift of the emission during decay shown the figure in its inset. Inset: Normalized PL spectra at various delays after photoexcitation. d) THG emissions from the thin film of GNC-1 at 1300, 1400, 1500, and 1550 nm excitations. Inset: Schematic diagram of THG process in $\text{Au}(\text{I})_6$ NCs. The top and bottom waves indicate the excitation beam (ω) and the generated THG signal (3ω), respectively. e) Excitation power dependency of THG signal of the GNC film at 1300 nm excitation. f) THG response as a function of excitation polarization.

Supporting Information). The emission decay is bi-exponential ($0.17 \mu\text{s} + 1.75 \mu\text{s}$) (Figure 3c), revealing two quasi-degenerate emitting states, most likely due to the coexistence of two different charge states of the NC: $[\text{Au}(\text{I})_6(\text{TRZ})_3]^+$ and $[\text{Au}(\text{I})_6(\text{TRZ})_3]^{2-}$. Besides, an appreciable redshift of the band during decay (inset of Figure 3c) suggests a further statistical distribution of lifetimes. The observed microsecond lifetimes imply a weakly allowed emissive transition. The PL is strongly Stokes shifted (>150 nm) and lacks mirror symmetry from the lowest-energy absorption band. Therefore, the emissive state is presumably characterized by a significant triplet character, i.e., the emission stems from a $^3\text{LMCT}$ state populated indirectly from the $^1\text{LMCT}$ state excited at 400 nm through an intersystem crossing process (ISC) (Figure S13, Supporting Information).

Interestingly, the GNCs show a strong nonlinear optical effect, particularly for THG (depicted in Figure 3d). The lack of even-order harmonics along with such intense THG can be explained by an inversion symmetry in the molecular structure of these octahedral $[\text{Au}(\text{I})_6(\text{TRZ})_3]^{2-}$ nanoclusters. When illuminated by ultrafast infrared lasers at variable wavelengths, GNC-1 produces strong THG signals at ≈ 433 , 470, 500, and 520 nm, corresponding to frequency tripling by the excitation beams at 1300, 1400, 1500, and 1550 nm, respectively. In addition to the narrow THG peaks, we also observe a broadband signal between 520 to 700 nm, indicating PL caused by three-photon absorption (Figure S14, Supporting Information). The emission band shape is identical when produced by single-,

two-, or three-photon absorption. The power-dependent THG measurements under 1300 nm excitation (Figure 3e) demonstrate that the THG signal intensity ($I_{3\omega}$) is large and increases with incident intensity (I_ω) as $I_{3\omega} = (I_\omega)^\alpha$ with $\alpha = 2.83$, close to the value of 3 expected for a nonlinear THG process. The polarization of the generated THG is highly dependent on the incident polarization (Figure 3f). With the horizontal polarization of excitation, the THG signal intensity is maximum along the direction of the excitation and minimum at the cross-polarization. The mathematical fit shows a sinusoidal behavior of the generated THG signal with the polarization angle of the detection polarizer. The third-order nonlinear susceptibility is calculated with the formula given as:

$$\chi^{(3)} = \frac{4\epsilon_0 c^2}{3\omega d} \sqrt{n_\omega^3 n_{3\omega} \frac{I_{3\omega}}{I_\omega^3}} \quad (1)$$

where ϵ_0 , c , and d are the permittivity of vacuum, speed of light in vacuum, and sample thickness respectively. n_ω ($n_{3\omega}$) and I_ω ($I_{3\omega}$) are the refractive index at frequency ω (3ω) and pump (THG) intensity respectively.^[35] Based on this, we obtain the third-order susceptibility of GNCs, $\chi^{(3)} = 9.73 \times 10^{-19} \text{ m}^2 \text{ V}^{-2}$ (see details in Supporting Information).

Femtosecond transient absorption (TA) measurements indicate energy cascade initiated by 400 nm absorption (Figure 4a and Figure S15, Supporting Information). Immediately after photoexcitation, the TA signal displays a negative sign, being

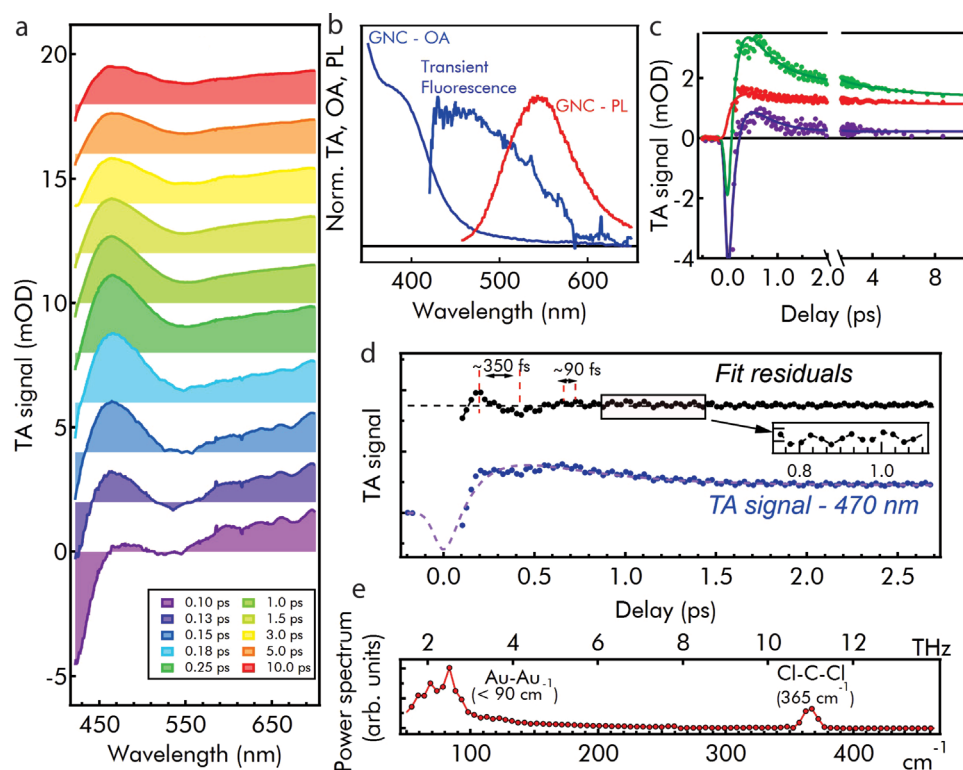


Figure 4. a) Pump-probe transient absorption (TA) spectra recorded at variable delays from femtosecond excitation at 400 nm. b) Transient fluorescence from the electronic state initially excited at 400 nm, isolated as the difference TA (0.18 ps) – TA (0.13 ps), and compared to steady-state OA and PL. c) Kinetic traces of the TA signal, fitted with a three-exponential function convoluted with the Gaussian instrumental response of the TA instrument. d) TA signal at 470 nm (blue dots), fitted by a multi-exponential function describing ISC and further relaxations. The fit residuals (black dots, vertically shifted for the sake of clarity) show coherent oscillations at two different frequencies. e) Fourier transform of the fit residuals at 470 nm.

dominated by ground-state bleaching from the initially excited ¹LMCT state and fluorescence, detected in TA as stimulated emission.^[36,37] The disappearance of these negative components within ca. 300 fs provides the direct signature of the depopulation of ¹LMCT state via ISC, in favor of the ³LMCT. The extremely short-lived ¹LMCT fluorescence can be isolated by taking the difference between two TA spectra at successive times. Indeed, this difference signal is a broad band at ≈450 nm, approximately mirror symmetric to the OA at 400 nm (Figure 4b). The TA signal observed at $t > 0.25$ ps, i.e., after the ultrafast singlet-to-triplet cascade, appears as a broad positive TA signal with a peak at 470 nm, providing a spectral fingerprint of the ³LMCT manifold. The multi-exponential fit of the kinetic traces reveals that these dynamics are described by 0.15 ps, 0.45 ps, and 3.9 ps timescales (Figure 4c). While the fastest one is the time scale of ISC, the longer scales represent relaxation and thermalization within the emissive ³LMCT manifold. Similar trends are observed by TA measurements on GNC-2 (Figure S16, Supporting Information).

Closer analysis of TA data reveals a role of quantum coherent effects in the photocycle, visible as a regular modulation of the TA signal persisting for several ps (Figure 4d). In general, these oscillations in TA are due to the motion of coherent vibrational or excitonic wave packets initiated by ultrashort pulses. The Fourier transform of the residuals calculated from a multi-exponential fit (Figure 4e) pinpoints two main frequencies of ≈90 and 365 cm⁻¹. The latter can be attributed to the Cl–C–Cl

deformation mode of dichloromethane (DCM) in which GNCs are dispersed, while the vibration at 90 cm⁻¹ is in the expected range for Au–Au oscillations of the GNC core.^[9,14] Thereby, we infer that Au core is impulsively brought out of equilibrium by the additional electron projected inside it by ¹LMCT photoexcitation, triggering the onset of Au–Au oscillations. Thereafter, as clearly seen in Figure 4d, this oscillation is damped within 200–300 fs, because the excess vibrational energy is redistributed over the entire GNCs, and finally to the solvent, during the ISC process. Further details can be obtained by time-frequency analysis of the fit residuals (Figure S17, Supporting Information). This analysis confirms an instantaneous activation of the Au–Au oscillation, the damping of which is accompanied by the growth of solvent oscillations. Most importantly, the Cl–C–Cl oscillation (365 cm⁻¹) appears progressively growing in amplitude and upshifting in frequency until it is fully established after a delay of ≈300 fs, that is about twice the time scale of ISC. Such a delayed activation of solvent oscillations reports the arrival of the perturbation to the nearest solvent molecules in contact with the ligands, reaching as far as ≈1 nm from the Au core within an extremely short (200–300 fs) time scale. Indeed, we conclude that the whole relaxation cascade of this ultras-small NC proceeds through a fully coherent pathway, favoring the exceedingly fast propagation of energy throughout the system.^[38–40]

GNCs are relatively stable in powder form or thin film under UV exposure. Notably, a small photobleaching has

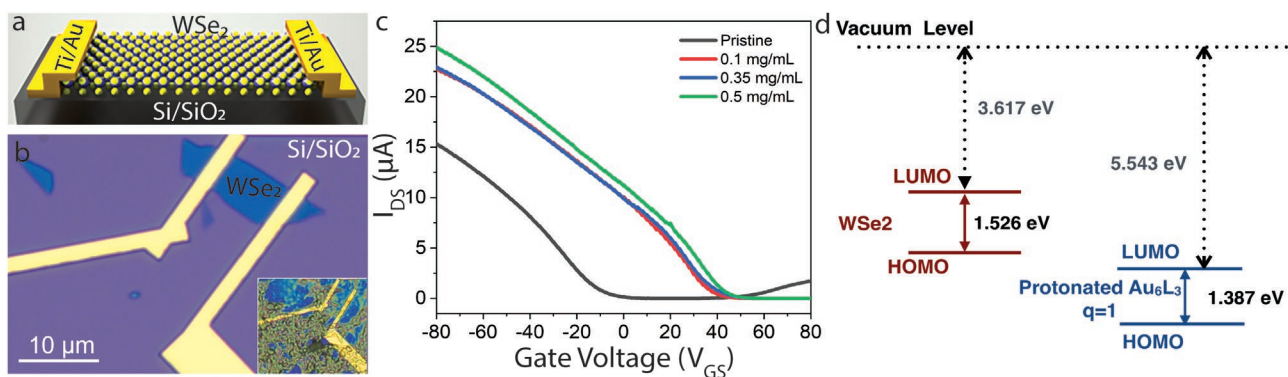


Figure 5. a) The schematic diagram and b) optical microscope image of the back gated WSe₂ field effect transistor. Inset: optical micrograph of WSe₂ device after deposition of GNCs. c) Transfer plots (*I*_{DS}-*V*_{GS}) obtained from the multilayer WSe₂ device before and after deposition of different concentration of GNCs at *V*_{SD} = 0.5 V. d) Theoretical calculations for the HOMO-LUMO states of [Au(I)₆(TRZ)₃]⁺ and multilayer WSe₂.

been observed during continuous UV exposure up to 14 h in our experiment (Figure S18, Supporting Information). Such extremely high photostability of the NCs is probably associated with the strong metal-ligand bonding and the compact structure of the ligand. In addition, the Au(I) states in these ultrasmall NCs could highly influence a strong LMCT transition characterized by high QY and excellent photostability. Furthermore, the NCs are highly stable at high temperature up to 150 °C and emit brilliant green-yellowish light even after treating at 100 °C for 1 h (Figure S19, Supporting Information).

2.4. GNCs as Dopants in Field-Effect Transistors

We fabricated a back-gated multilayer WSe₂ device, schematically represented in Figure 5a. The multilayer WSe₂ device (Figure 5b) has been characterized by measuring the drain-source current (*I*_{DS}) while sweeping the gate-source voltage (*V*_{GS}) in the range of ±80 V at a fixed drain-source voltage (*V*_{DS}) of 0.5 V at room temperature. The WSe₂ channel is ≈8 nm in thick, indicating 11–12 layers (Figure S20, Supporting Information).^[41] The device depicts a *p*-dominant characteristic with relatively small electron current along positive *V*_{GS} (Figure 5c), suggesting that the Fermi level is inclined towards the valence band edge of WSe₂. With the further application of positive (negative) *V*_{GS}, the Fermi level is pushed towards the conduction band (valence band), respectively, thus injecting electrons (holes) in WSe₂. Interestingly, we found that the deposition of GNCs over WSe₂ significantly enhances the hole-current in this device, while electron-current is suppressed. Moreover, the threshold voltage (= *V*_{GS}), which is needed to turn on the device and extracted from the intercept of *I*_{DS}-*V*_{GS} plot, is shifted towards positive *V*_{GS}. More specifically, with 0.1 mg mL⁻¹ solution of GNC-1 in DCM, threshold voltage has significantly shifted from -5 V to +42 V. The result suggests that WSe₂ device contains more positively charged carriers after deposition of GNCs, i.e., a non-degenerate *p*-doping is realized in WSe₂ in contact with the GNCs. With increasing the concentration of GNCs up to a certain extent, the *I*_{DS} continuously increases, and the threshold voltage shifts towards more positive *V*_{GS} values. This is due to the close proximity (0.4 eV) in between

the valence band (HOMO) of WSe₂ and the LUMO state of the protonated [Au(I)₆(TRZ)₃]⁺ (Figure 5d), which allows the former as a donor and the GNCs as an acceptor.

3. Conclusion

We report for the first time atomically precise ultrasmall gold nanoclusters where all atoms are in the same valence state Au(I) and where they are sterically locked by specific dual ligand thiolate interactions to suppress vibrations to allow multifunctional electro-optical and quantum coherent behaviors. In particular, we report Au(I)₆ nanoclusters with steric locking of each atom by 6-(dibutylamino)-1,3,5-triazine-2,4-dithiol ligands, where a two-step chemical reaction was required to allow centrosymmetric octahedral structure. The underlying films produce a very strong THG response, very close to the high magnitude of the 2D monolayer metal dichalcogenide nanosheets, never observed before for gold nanoclusters. They also produce brilliant single and multiphoton luminescence response with exceptional stability. DFT calculations and femtosecond transient absorption studies suggest an ultrafast ligand-to-metal charge transfer with ultra-efficient intersystem crossing and demonstrate the role of quantum coherent effects in the photocycle. The quantum coherent behavior and relatively long decoherence time (200–300 fs) of the photoexcited GNCs allow extremely fast propagation of excitation from the core to the surrounding solvent. Finally, the Au(I) cores display marked electron-accepting properties also in the ground state, as we show in a proof-of-principle application as a *p*-dopant in 2D FET devices. In summary, these ultrasmall GNCs with interlocked 6 Au(I) atoms provide key insight for future applications as ultrafast photoswitches, or in emerging technologies such as quantum computing, since decoherence sets the maximum timeframe for the fully quantum operation of a device.

Supporting Information

Supporting Information is available from the Wiley Online Library or from the author.

Acknowledgements

This work was supported by the ERC Advanced grant (DRIVEN, ERC-2016-AdG-742829), the ERC grant (834742), the EU H2020-MSCA-RISE-872049 (IPN-Bio), the Academy of Finland's Centre of Excellence in Molecular Engineering of Biosynthetic Hybrid Materials Research (HYBER, 2014–2019), and Life-Inspired Hybrid Materials (LIBER, 346108), Academy of Finland project fundings (No. 352900, 314810, 333982, 336144, 352780, 352930 and 353364), FinnCERES and Photonics Research and Innovation (PREIN) flagship programs. The authors acknowledge the provision of facilities and technical support by Aalto University OtaNano – Nanomicroscopy Center (Aalto-NMC).

Conflict of Interest

The authors declare no conflict of interest.

Data Availability Statement

The data that support the findings of this study are available from the corresponding author upon reasonable request.

Keywords

field effect transistors, quantum coherence, nanoclusters, photoluminescence, third-harmonic generation

Received: November 7, 2022

Revised: January 14, 2023

Published online:

- [1] M. Zhou, C. Zeng, Q. Li, T. Higaki, R. Jin, *Nanomaterials* **2019**, *9*, 933.
- [2] W. D. Si, Y. Z. Li, S. S. Zhang, S. Wang, L. Feng, Z. Y. Gao, C. H. Tung, D. Sun, *ACS Nano* **2021**, *15*, 16019.
- [3] R. Jin, C. Zeng, M. Zhou, Y. Chen, *Chem. Rev.* **2016**, *116*, 10346.
- [4] S. Chandra, Nonappa, G. Beaune, A. Som, S. Zhou, J. Lahtinen, H. Jiang, J. V. I. Timonen, O. Ikkala, R. H. A. Ras, *Adv. Opt. Mater.* **2019**, *7*, 1900620.
- [5] V. Hynninen, S. Chandra, S. Das, M. Amini, Y. Dai, S. Lepikko, P. Mohammadi, S. Hietala, R. H. A. Ras, Z. Sun, O. Ikkala, Nonappa, *Small* **2021**, *17*, 2005205.
- [6] I. Chakraborty, T. Pradeep, *Chem. Rev.* **2017**, *117*, 8208.
- [7] S. Chandra, A. Sciortino, S. Shandilya, L. Fang, X. Chen, Nonappa, H. Jiang, L.-S. Johansson, M. Cannas, J. Ruokolainen, R. H. A. Ras, F. Messina, B. Peng, O. Ikkala, *Adv. Opt. Mater.* **2023**, *11*, 2201901.
- [8] M. Zhu, C. M. Aikens, F. J. Hollander, G. C. Schatz, R. Jin, *J. Am. Chem. Soc.* **2008**, *130*, 5883.
- [9] S. A. Miller, J. M. Womick, J. F. Parker, R. W. Murray, A. M. Moran, *J. Phys. Chem. C* **2009**, *113*, 9440.
- [10] Z. Wu, R. Jin, *Nano Lett.* **2010**, *10*, 2568.
- [11] M. S. Devadas, J. Kim, E. Sinn, D. Lee, T. Goodson, G. Ramakrishna, *J. Phys. Chem. C* **2010**, *114*, 22417.
- [12] M. Zhou, C. Zeng, M. Y. Sfeir, M. Cotlet, K. Iida, K. Nobusada, R. Jin, *J. Phys. Chem. Lett.* **2017**, *8*, 4023.
- [13] M. Y. Sfeir, H. Qian, K. Nobusada, R. Jin, *J. Phys. Chem. C* **2011**, *115*, 6200.
- [14] T. D. Green, C. Yi, C. Zeng, R. Jin, S. McGill, K. L. Knappenberger, *J. Phys. Chem. A* **2014**, *118*, 10611.
- [15] X. Kang, S. Wang, Y. Song, S. Jin, G. Sun, H. Yu, M. Zhu, *Angew. Chem., Int. Ed.* **2016**, *55*, 3611.
- [16] K. L. D. M. Weerawardene, C. M. Aikens, *J. Am. Chem. Soc.* **2016**, *138*, 11202.
- [17] K. L. D. M. Weerawardene, P. Pandeya, M. Zhou, Y. Chen, R. Jin, C. M. Aikens, *J. Am. Chem. Soc.* **2019**, *141*, 18715.
- [18] Y. Song, J. Zhong, S. Yang, S. Wang, T. Cao, J. Zhang, P. Li, D. Hu, Y. Pei, M. Zhu, *Nanoscale* **2014**, *6*, 13977.
- [19] S. S. Zhang, L. Feng, R. D. Senanayake, C. M. Aikens, X. P. Wang, Q. Q. Zhao, C. H. Tung, D. Sun, *Chem. Sci.* **2018**, *9*, 1251.
- [20] N. Vermeulen, D. Castelló-Lurbe, M. Khoder, I. Pasternak, A. Krajewska, T. Ciuk, W. Strupinski, J. L. Cheng, H. Thienpont, J. Van Erps, *Nat. Commun.* **2018**, *9*, 2675.
- [21] A. Taghizadeh, K. S. Thygesen, T. G. Pedersen, *ACS Nano* **2021**, *15*, 7155.
- [22] A. Krasnok, M. Tymchenko, A. Alù, *Mater. Today* **2018**, *21*, 8.
- [23] D. Nikogosyan, *Nonlinear Optical Crystals: A Complete Survey*, Springer, New York **2005**.
- [24] G. Soavi, G. Wang, H. Rostami, D. G. Purdie, D. De Fazio, T. Ma, B. Luo, J. Wang, A. K. Ott, D. Yoon, S. A. Bourelle, J. E. Muench, I. Goykhman, S. Dal Conte, M. Celebrano, A. Tomadin, M. Polini, G. Cerullo, A. C. Ferrari, *Nat. Nanotechnol.* **2018**, *13*, 583.
- [25] A. Autere, H. Jussila, Y. Dai, Y. Wang, H. Lipsanen, Z. Sun, *Adv. Mater.* **2018**, *30*, 1705963.
- [26] Y. Cheng, H. Hong, H. Zhao, C. Wu, Y. Pan, C. Liu, Y. Zuo, Z. Zhang, J. Xie, J. Wang, D. Yu, Y. Ye, S. Meng, K. Liu, *Nano Lett.* **2020**, *20*, 8053.
- [27] Z. Yu, B. Musnier, K. D. Wegner, M. Henry, B. Chovelon, A. Desroches-Castan, A. Fertin, U. Resch-Genger, S. Bailly, J. L. Coll, Y. Usson, V. Josserand, X. L. Guérol, *ACS Nano* **2020**, *14*, 4973.
- [28] L. Xiao, F. Wei, Y. Zhou, G. J. Anderson, D. M. Frazer, Y. C. Lim, T. Liu, Y. Xiao, *Nano Lett.* **2020**, *20*, 478.
- [29] M. Lippitz, M. A. Van Dijk, M. Orrit, *Nano Lett.* **2005**, *5*, 799.
- [30] R. Barbosa-Silva, M. L. Silva-Neto, D. Bain, L. Modesto-Costa, T. Andrade-Filho, V. Manzoni, A. Patra, C. B. De Araújo, *J. Phys. Chem. C* **2020**, *124*, 15440.
- [31] J. Enkovaara, C. Rostgaard, J. J. Mortensen, J. Chen, M. Dufak, L. Ferrighi, J. Gavnholt, C. Glinsvad, V. Haikola, H. A. Hansen, H. H. Kristoffersen, M. Kuisma, A. H. Larsen, L. Lehtovaara, M. Ljungberg, O. Lopez-Acevedo, P. G. Moses, J. Ojanen, T. Olsen, V. Petzold, N. A. Romero, J. Stausholm-Møller, M. Strange, G. A. Tritsarlis, M. Vanin, M. Walter, B. Hammer, H. Häkkinen, G. K. H. Madsen, R. M. Nieminen, et al., *J. Phys. Condens. Matter* **2010**, *22*, 253202.
- [32] M. Kuisma, A. Sakko, T. P. Rossi, A. H. Larsen, J. Enkovaara, L. Lehtovaara, T. T. Rantala, *Phys. Rev. B Condens. Matter Mater. Phys.* **2015**, *91*, 115431.
- [33] E. Makkonen, T. P. Rossi, A. H. Larsen, O. Lopez-Acevedo, P. Rinke, M. Kuisma, X. Chen, *J. Chem. Phys.* **2021**, *154*, 114102.
- [34] T. P. Rossi, M. Kuisma, M. J. Puska, R. M. Nieminen, P. Erhart, *J. Chem. Theory Comput.* **2017**, *13*, 4779.
- [35] L. Du, Y. Zhao, L. Wu, X. Hu, L. Yao, Y. Wang, X. Bai, Y. Dai, J. Qiao, M. G. Uddin, X. Li, J. Lahtinen, X. Bai, G. Zhang, W. Ji, Z. Sun, *Nat. Commun.* **2021**, *12*, 4822.
- [36] C. Ruckebusch, M. Sliwa, P. Pernot, A. de Juan, R. Tauler, *J. Photochem. Photobiol. C: Photochem. Rev.* **2012**, *13*, 1.
- [37] A. Sciortino, F. Ferrante, N. Mauro, G. Buscarino, L. Sciortino, G. Giammona, M. Cannas, D. Duca, F. Messina, *Carbon* **2021**, *173*, 454.
- [38] R. Monni, G. Capano, G. Auböck, H. B. Gray, A. Vlček, I. Tavernelli, M. Chergui, *Proc. Natl. Acad. Sci. USA* **2018**, *115*, E6396.
- [39] S. Rafiq, G. D. Scholes, *J. Phys. Chem. A* **2016**, *120*, 6792.
- [40] Q. Bian, F. Ma, S. Chen, Q. Wei, X. Su, I. A. Buyanova, W. M. Chen, C. S. Ponseca, M. Linares, K. J. Karki, A. Yartsev, O. Inganäs, *Nat. Commun.* **2020**, *11*, 617.
- [41] P. R. Pudasaini, A. Oyedele, C. Zhang, M. G. Stanford, N. Cross, A. T. Wong, A. N. Hoffman, K. Xiao, G. Duscher, D. G. Mandrus, T. Z. Ward, P. D. Rack, *Nano Res.* **2018**, *11*, 722.

Supporting Information

for *Adv. Optical Mater.*, DOI: 10.1002/adom.202202649

Gold Au(I)₆ Clusters with Ligand-Derived Atomic Steric Locking: Multifunctional Optoelectrical Properties and Quantum Coherence

Sourov Chandra, Alice Sciortino, Susobhan Das, Faisal Ahmed, Arijit Jana, Jayoti Roy, Diao Li, Ville Liljeström, Hua Jiang, Leena-Sisko Johansson, Xi Chen,* Nonappa, Marco Cannas, Thalappil Pradeep, Bo Peng, Robin H. A. Ras, Zhipei Sun, Olli Ikkala,* and Fabrizio Messina**

Supporting Information

Gold Au(I)₆ clusters with ligand-derived atomic steric locking: Multifunctional optoelectrical properties and quantum coherence

Sourov Chandra^{1*}, Alice Sciortino^{2,3}, Susobhan Das⁴, Faisal Ahmed⁴, Arijit Jana⁵, Jayoti Roy⁵, Diao Li⁴, Ville Liljeström⁶, Hua Jiang^{1,6}, Leena-Sisko Johansson⁷, Xi Chen^{1*}, Nonappa⁸, Marco Cannas², Thalappil Pradeep⁵, Bo Peng¹, Robin H. A. Ras¹, Zhipei Sun^{4,9}, Olli Ikkala^{1*} and Fabrizio Messina^{2,3*}

¹ Department of Applied Physics, Aalto University, P. O. Box 15100, Espoo, FI-00076 Aalto, Finland.

² Dipartimento di Fisica e Chimica - Emilio Segrè. Università degli Studi di Palermo. Via Archirafi 36, 90123 Palermo, Italy.

³ CHAB - ATeN Center, Università degli studi di Palermo, viale delle scienze, Edificio 18, 90128, Palermo, Italy.

⁴ Department of Electronics and Nanoengineering, Aalto University, FI-00076 Aalto, Finland.

⁵ Department of Chemistry, DST Unit of Nanoscience (DST UNS) and Thematic Unit of Excellence (TUE), Indian Institute of Technology Madras, Chennai 600036, India.

⁶ Nanomicroscopy Center, OtaNano, Aalto University, FI-00076 Aalto, Finland.

⁷ Department of Bioproducts and Biosystems, School of Chemical Engineering, Aalto University, FI-00076 Aalto, Finland.

⁸ Faculty of Engineering and Natural Sciences, Tampere University, P. O. Box 541, Tampere, FI-33101 Finland.

⁹ QTF Centre of Excellence, Department of Applied Physics, Aalto University, FI-00076 Aalto, Finland.

EXPERIMENTAL SECTION

Materials

HAuCl₄·3H₂O, methanol, ethanol, dichloromethane (DCM), ascorbic acid, sodium borohydride (NaBH₄), DCM-d₂ and sodium acetate were purchased from Sigma-Aldrich and used as received. The ligand, 6-(Dibutylamino)-1,3,5-triazine-2,4-dithiol was acquired from TCI Europe N.V. Ultrapure Milli-Q water (18 Ω) was used in our experiments.

Synthesis of gold nanoclusters

The synthesis of GNCs were performed using HAuCl₄ and 6-(Dibutylamino)-1,3,5-triazine-2,4-dithiol (TRZ) as the precursors. Briefly, 20 mg of HAuCl₄ was dissolved in 5 mL of methanol in a closed glass vial (20 mL) at room temperature (~22 °C). To the mixture, 7 mL of DCM was added. A solution containing 23.5 mg of TRZ ligand in 2 mL of DCM was added to the above mixture with vigorous stirring. The pale-yellow solution of HAuCl₄ was immediately turned to bright red in colour. After few minutes (~10-15 minutes) of stirring the colour of the solution gradually transformed to yellow. Then the reducing agents, either ascorbic acid (45 mg in 1 mL of water) or NaBH₄ (2 mg in 1 mL of water) was added to the solution. The reaction mixture was stirred for 12 hours at room temperature (~22 °C). The solvent was removed under reduced pressure using a rotary evaporator at 30 °C. The residue was washed with ethanol to remove the excess ligand and the reducing agent. Finally, the product was separated by centrifugation at 5000 rpm for 30 mins and dried in air after discarding the ethanol. The clusters were stored in a refrigerator at 4 °C for further use.

X-ray photoelectron spectroscopy (XPS)

X-ray photoelectron spectroscopy was performed in Kratos Axis Ultra ESCA X-ray photoemission spectrometer using AlK α irradiation at low power (100 W) and under neutralization. The X-ray source was operated at 8 mA and 12.5 kV and the analyzer pass energy was 20 eV for high resolution scans and 80 eV for the survey spectra. The pressure in the analysis chamber was about 8×10^{-8} Pa during the measurements. The binding energy (BE) scale was referenced to 284.8 eV as determined by the location of the maximum peak on the C1s spectra, associated with adventitious carbon. The accuracy of the BE determined with respect to this standard value was within ± 0.1 eV.

STEM analysis

STEM images were captured by using JEM-2200FS Double Cs-corrected transmission electron microscope. The instrument was operated at an acceleration voltage of 200 kV with field-emission guns. Specimen for STEM analyses were prepared by drop-casting from the solution of GNCs in DCM over the ultrathin-carbon (<10 nm thickness) coated copper grids. The samples were incubated for 1 min, after which the excess material was removed by washing with ethanol.

ESI Mass spectroscopy

High resolution mass spectrum was carried out using SYNAPT G2-Si High Definition MS (HDMS) system. It is equipped with an electrospray ionization source, step wave ion transfer optics and a quadrupole mass filter. Sodium acetate is used as an ionization enhancer during the measurement. The spectrum was collected in negative and positive ion mode following an optimized condition of flow rate 20 μ L/ml, capillary voltage 2.5 - 3 kV, spray current 100 - 120 nA, cone voltage 0 V, source voltage 70-100 $^{\circ}$ C. The collision energy-dependent fragmentation studies were performed after selecting the molecular ion (at $m/z = 2025.28$) trapped inside the ion mobility cell.

^1H -NMR Spectroscopy

^1H -NMR spectra were recorded using Bruker AV III 400 spectrometer operating at 400 MHz for ^1H . For sample preparation, dried GNC-1 and TRZ ligand were dissolved in dichloromethane- d_2 .

Measurement of refractive index

Refractive index measurements were performed using J. A. Woollam M-2000UI spectroscopic ellipsometer. Thin layer of the samples was prepared by spin coating over a silicon wafer.

Absolute quantum yield measurement

The absolute PL quantum yield was measured using a C9920-03G system equipped with a 150W xenon lamp (Hamamatsu Photonics Co. Ltd., Japan).

Small angle X-ray scattering (SAXS) measurements

X-ray diffraction measurements were performed to complement the structural characterization of the nanoclusters. The measurements were carried out from dried samples. The gold nanocluster-DCM solution was dried to form a powder, which was confined between thin Kapton films. The

X-ray diffraction measurement was carried out in perpendicular transmission geometry with the Xenocs Xeuss 3.0 system using Cu K- α radiation (multilayer monochromator, $\lambda=1.542$ Å, parallel beam collimation). The samples were measured in a vacuum and the background scattering from the Kapton films was subtracted. The final model was calculated using Powder Cell software^[1]. The diffraction peaks of the NCs have been analyzed by comparing the plausible structure factors (lattices) and calculating a full diffraction pattern.

Steady-state optical measurements

Steady-state absorption measurements were carried out on GNCs dispersed in dichloromethane within a 1 cm quartz cuvette, using a double beam spectrophotometer (JASCO V-560) in the 220–700 nm range.

Steady-state emission

The emission spectra have been collected on diluted suspensions of GNCs in dichloromethane (absorption < 0.2 OD at the excitation wavelength) by a JASCO FP-6500 spectrofluorometer in a 1 cm cuvette with a 3 nm resolution bandwidth.

Nanosecond time-resolved fluorescence

The emission decay kinetics were recorded by exciting the samples by laser pulses of 0.1–0.3 mJ energy and 5 ns duration, obtained from a tunable laser (410-700 nm), and dispersing their photoluminescence on an intensified CCD camera. The camera was triggered to acquire spectra within windows of variable widths (0.5 ns – 0.5 ms) and delays from the laser pulse. Decay kinetics were obtained by spectrally integrating the photoluminescence signal and analysing it as a function of delay time. The decay curves were fitted by a bi-exponential kinetics in the form: $A \exp[-t/t_1] + B \exp[-(t/t_2)^b]$. In this expression, b is a stretching parameter (estimated to be 0.8 by the fit), that we find necessary to satisfactorily reproduce the experimental data, suggestive of the presence of a statistical distribution of different lifetimes around t_2 .

Femtosecond transient absorption (TA)

TA measurements in a pump/probe geometry were carried out on a home-built setup, described in previous publication^[2]. The setup is pumped by a 5 kHz Ti:sapphire femtosecond amplifier (Spectra Physics Solstice-Ace), which produces 50 fs pulses peaking at 800 nm (FWHM = 30 nm) with 350 mJ energy per pulse. The fundamental beam is split 80%/20% by a beam splitter to

generate the pump and the probe, respectively. The pump at 400 nm was obtained by frequency-doubling the fundamental in an ultrathin β -BBO crystal (250 μm) in order to create a 400 nm beam (20% efficiency), which is isolated from the fundamental by a Schott BG40 filter. The typical pump intensity was 50-100 nJ/pulse. This beam was chopped at 500 Hz and focused on the sample by a parabolic beam with $f = 150$ mm, while its polarization is controlled by a waveplate.

On the second arm, white light is generated focusing the 800 nm beam in a 1 mm quartz cuvette containing D_2O , generating a broadband pulse extending from 400 to 750 nm. The probe is focused on the sample by the same parabolic mirror used to focus the pump. The pump–probe delay is controlled by a motorized delay stage. The probe and the pump overlap within the sample, which continuously flows in a 0.2 mm thick flow cell. After the sample, the probe beam is dispersed by a home-built monochromator (resolution = 3 nm) onto a camera detector system with 1024 pixels (Glaz Linescan-I) with single-shot capability. A typical signal is obtained by averaging 5000 pumped and 5000 unpumped spectra for each delay and scanning over the pump–probe delay 10–20 times. The measurements were carried out under magic angle detection conditions. The data presented in the paper were subjected to standard correction procedures, which eliminate the effects of cross-phase modulation and group velocity dispersion (GVD). The temporal resolution is about 70 fs for measurements pumped at 400 nm.

TA kinetics at different wavelengths were initially fitted by multi-exponential decay kinetics convoluted to a Gaussian instrumental response function, obtaining the fits shown in Figure 4c and Figure 4d. The fit residuals were processed by FFT in order to analyse the oscillatory behaviour of the TA signal. The time-frequency analysis of the fit residuals was obtained by calculating the short-time Fourier transform within a Hann moving window with 800 fs width (that is, about twice the period of Au-Au oscillations).

Third harmonic generation experiment and setup

The dry GNC-1 powder was dispersed in dichloromethane. The transparent films were then prepared by drop-casting the dispersion over a clean glass slide and allowed to dry under ambient conditions. The thin film over the glass slide has been analysed as the sample for non-linear optical responses. We use an ultrafast laser for the measurement. An optical parametric amplifier (Spectra-Physics, TOPAS) with a repetition rate of 2 kHz is used to generate the light pulses. The wavelength range of the light beam comes from the optical parametric amplifier, which is tuneable from 0.8 μm to 1.6 μm . The pulse width of light pulses is ~ 230 fs. The beam is focused onto the

sample with an objective (NA=0.75, 40X). The spot sizes of the Gaussian beam (FWHM) over the samples are $\sim 2.5 \mu\text{m}$. The reflected light is separated from the input light using filters and measured with a photo multiplier tube following a monochromator (Andor 328i). The THG signal has been measured under ambient temperature ($\sim 25^\circ\text{C}$) with an average incident power of $\sim 1 \mu\text{W}$ (28.84 GW/cm^2 intensity).

Device Fabrication

The device preparation started with mechanically exfoliating WSe_2 flakes using standard scotch-tape technique from a commercial bulk source (2D Semiconductors) over *p*-doped silicon substrate ($0.001 - 0.005 \Omega\cdot\text{cm}$) covered with a 285 nm thick SiO_2 . The electron beams sensitive polymer (PMMA A4.5) was spin coated, and the electrodes were patterned *via* electron beam lithography (EBL Vistec, EPBG5000pES) over targeted flakes in desired geometry. The metallization of 5 nm Ti adhesion layer followed by 50 nm thick Au was carried out by electron beam evaporator (MASA IM-9912) at $\sim 10^{-7}$ torr chamber pressure. The electrical measurements were performed with a custom-built setup based on a Linkam LN600-P probe station with the source-measure unit (Keithley 2400) and multiplexing/voltage measurement unit (Keithley 2700). GNC-1 dispersions in DCM with concentration 0.1, 0.37 and 0.5 mg/mL were drop-casted over WSe_2 in such a way that the device is fully covered by the solution.

Atomic force microscopy (AFM)

The topographic image and thickness of WSe_2 flakes were collected by Bruker, Dimension Icon atomic force microscope.

DFT and TDDFT simulations

In this work, the GPAW software package^[3] was applied to do all the calculations. The structure optimizations were done using the GPAW grid mode with the real-spacing $h=0.2 \text{ \AA}$. The $\text{Au(I)}_6(\text{TRZ})_3$ clusters was placed into a cubic unit cell with a vacuum size 6 \AA added to the cluster's edge at each dimension. The geometry was considered to be converged when the maximum residual force was below 0.05 eV/\AA . A hexagonal unit cell of WSe_2 from [materialproject.org](https://doi.org/10.17188/1192989) (DOI:10.17188/1192989) was repeated 4 times in *z* direction to build an 8-layer model for the WSe_2 simulation. Periodic conditions were applied in *x* and *y* directions, while the

8 Å vacuum was added to both sides of the surface in z direction. 8*8*1 K-points were used for the simulation.

Perdew-Burke-Ernzerhof (PBE) functional was used for the exchange-correlation energy^[4], and the van der Waals interactions were described by the Tkatchenko-Scheffler model^[5]. Per atom, the electronic configuration of valence electrons is H(1s¹) C(2s²2p²), S(3s²3p⁴), N(2s²2p⁵) and Au (5d¹⁰6s¹). The remaining electrons were treated as a frozen core. The default PAW dataset package 0.9.20000 was used for all the atoms.

The optical absorption spectrum were computed by the real-time-propagation time-dependent density functional theory (RT-TDDFT) implemented in GPAW with PBE functionals and LCAO (Linear Combination of Atomic Orbitals) mode^[6]. In the LCAO mode, the default GPAW double-zeta polarized (dzp) basis sets were used for C, H, N, S, while the optimized double-zeta basis set (so- called "p-valence" basis set) was picked for Au atoms. In the RT-TDDFT simulation, the propagation was carried out up to T=30.0 fs in steps of 5.0 as. The real-spacing h=0.3 and vacuum size 8 Å were chosen for the RT-TDDFT calculations. The work-function of the clusters are calculated based on the method elsewhere^[7].

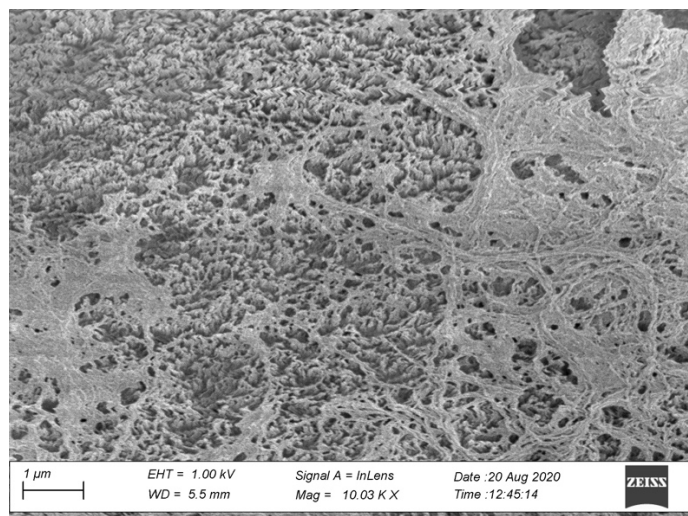


Figure S1. The reaction of 6-(dibutylamino)-1,3,5-triazine-2,4-dithiol (TRZ) with HAuCl_4 leads to complexation with fibrillar poorly defined assemblies, demanding another second reduction step by ascorbic acid to allow the final ultrasmall well defined nanoclusters.

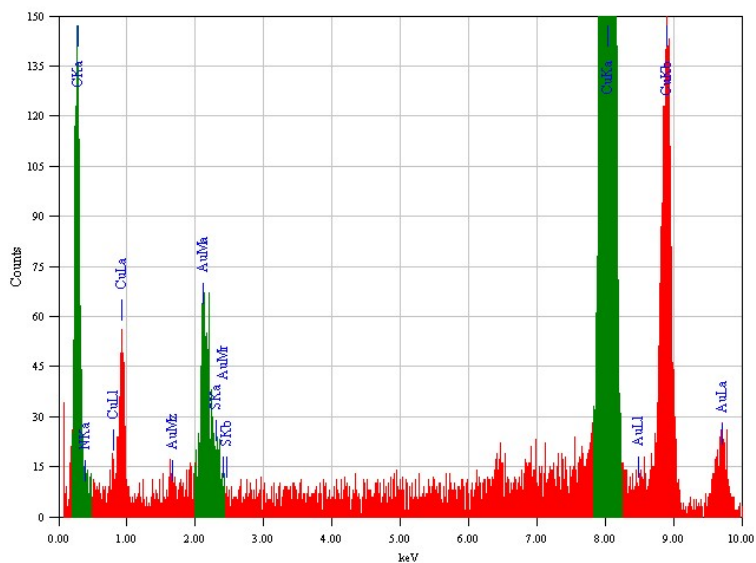


Figure S2. EDX spectrum of GNC-1.

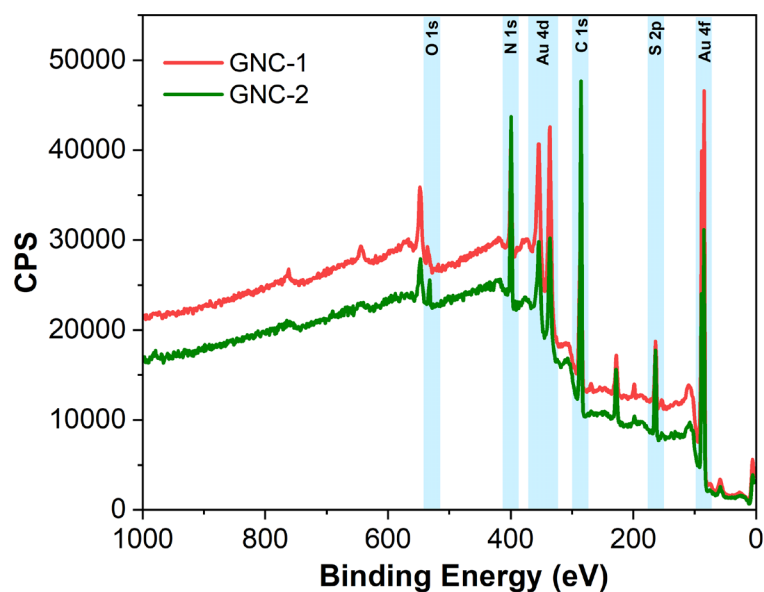


Figure S3. Full-width XPS spectra of GNC-1 and GNC-2.

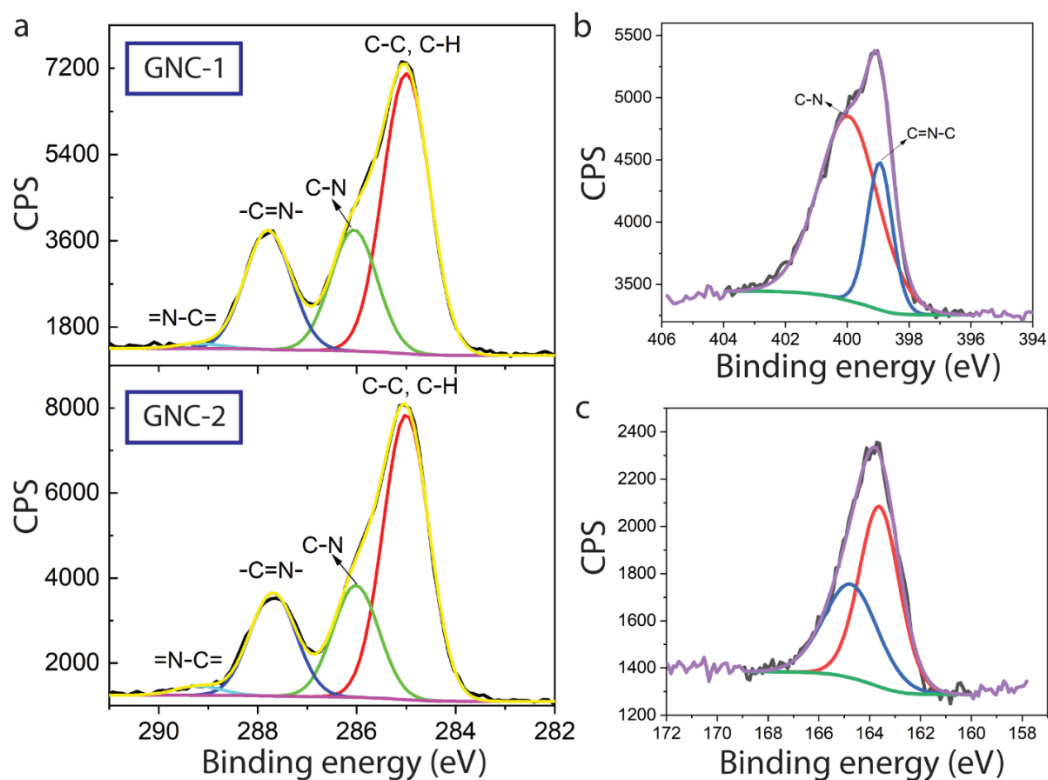


Figure S4. (a) C1s XPS spectrum of GNC-1 and GNC-2. (b) N1s and (c) S2p XPS spectrum of GNC-1.

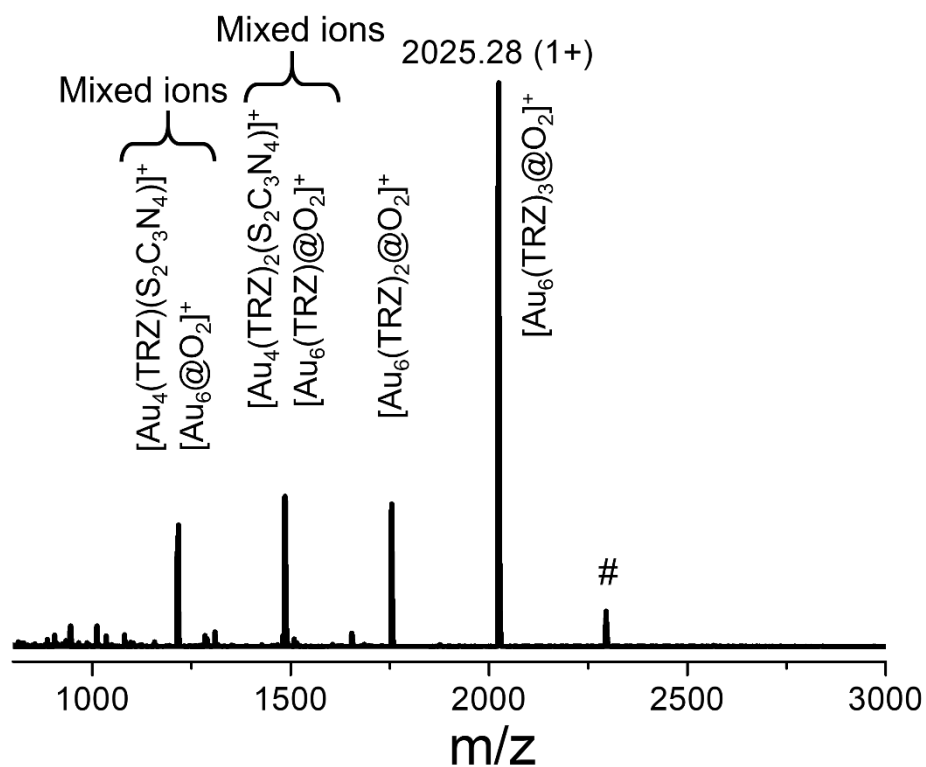


Figure S5. Full range ESI-MS spectrum of GNC-1 in positive ion mode. TRZ fragmentations were observed from the parent ion peak. The fragmentation of Au_6 core was also observed. The peak ‘#’ indicates one TRZ attachment with the parent peak.

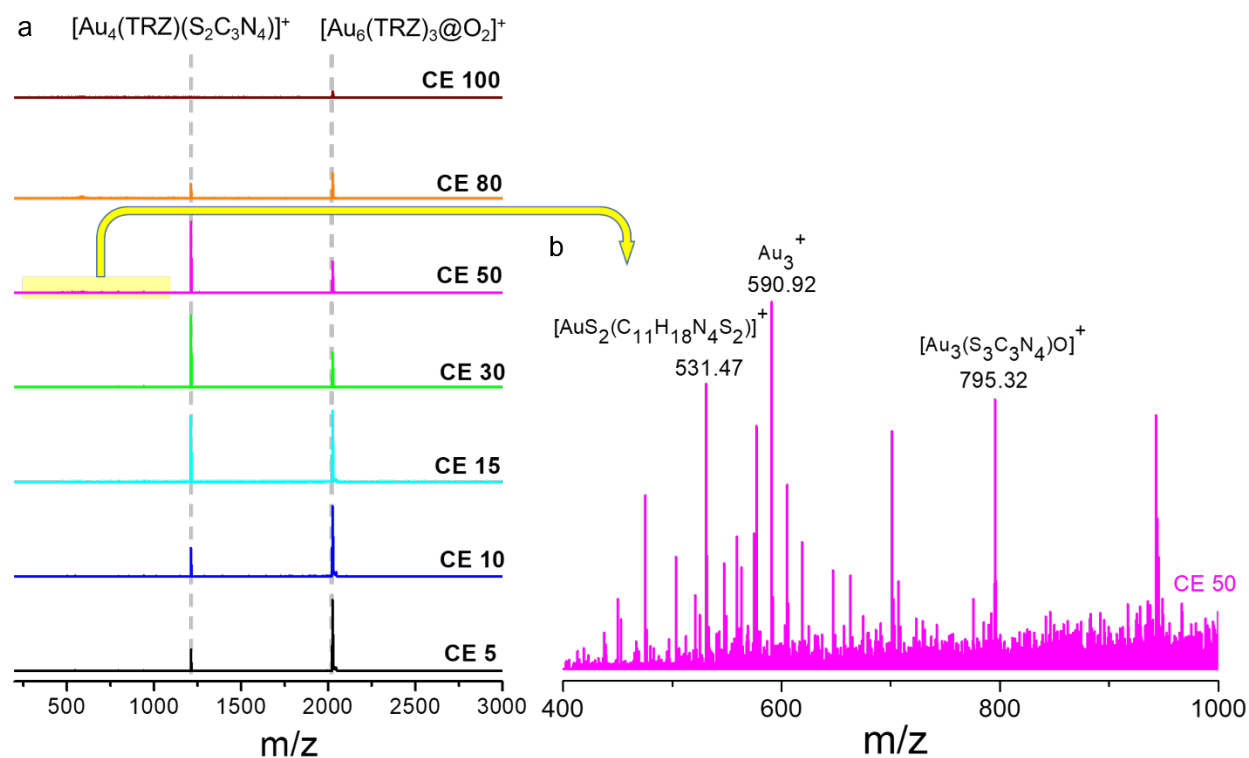


Figure S6. (a) The collision energy dependent fragmentation studies shows the formation of $[\text{Au}_4(\text{TRZ})(\text{S}_2\text{C}_3\text{N}_4)]^+$ fragments from the parent cluster. (b) Expanded view of the lower spectral region shows other fragmented peaks.

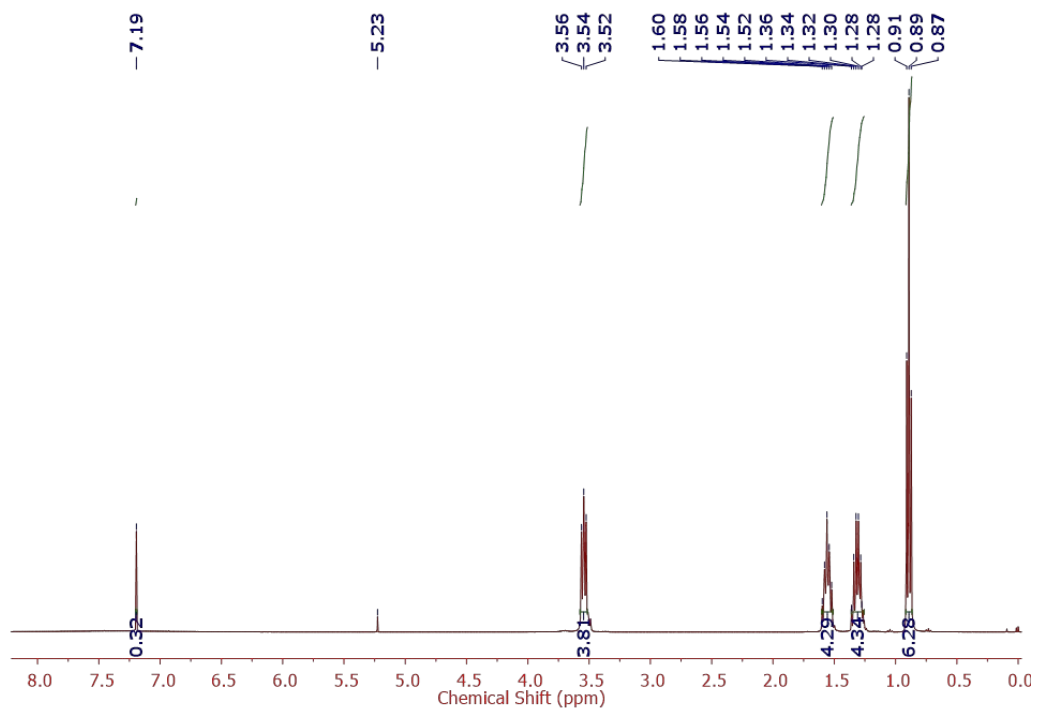


Figure S7. ¹H-NMR spectrum of the isolated TRZ ligand.

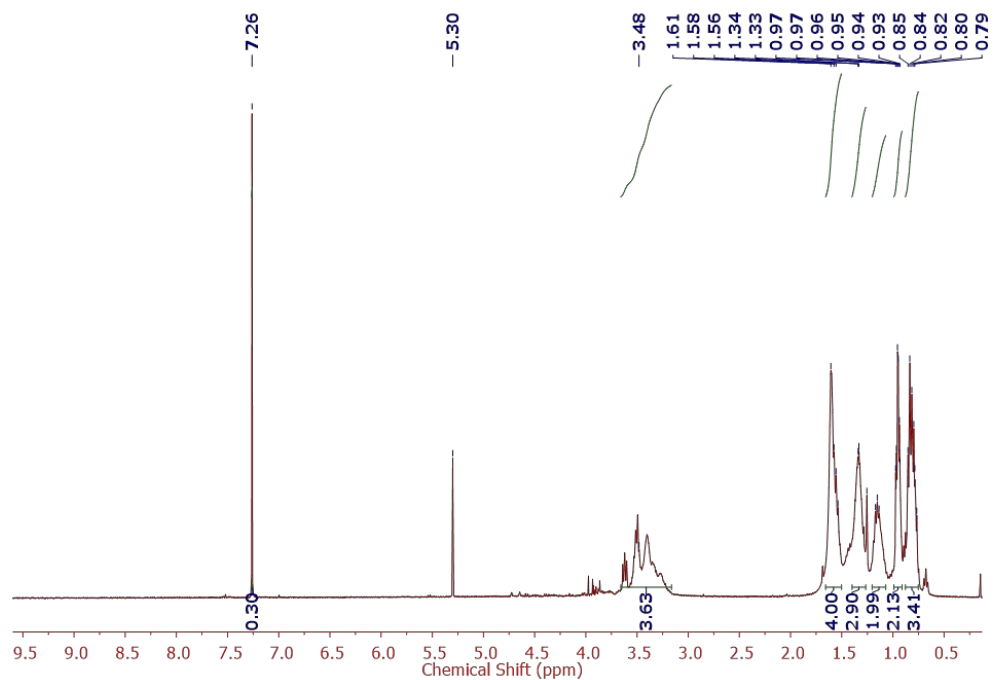


Figure S8. ¹H-NMR spectrum of the GNC-1.

The ^1H NMR spectrum of the ligand shows a peak at 7.19 ppm, probably due to the NH^+ proton. The absence of ^1H resonance signals between 2-3 ppm region, indicates deprotonation from the -SH group (i.e., the same proton is bound to nitrogen atoms). Upon binding the ligands with the Au_6 core, peak broadening was not observed for the NH^+ peak. However, broadening of the peaks corresponding to butyl protons was observed due to electron dense Au atoms. Direct covalent bonding of the butyl chains through the nitrogen center strongly influences the easy delocalization of electrons to these hydrogens.

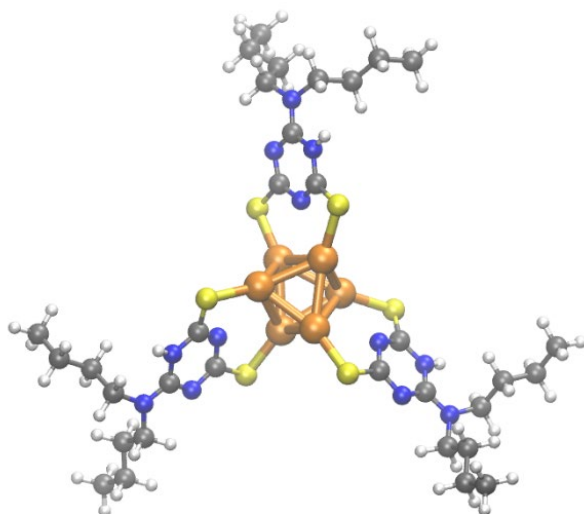


Figure S9. The atomic structure of $[\text{Au}_6(\text{TRZ})_3]^+$ optimized by DFT.

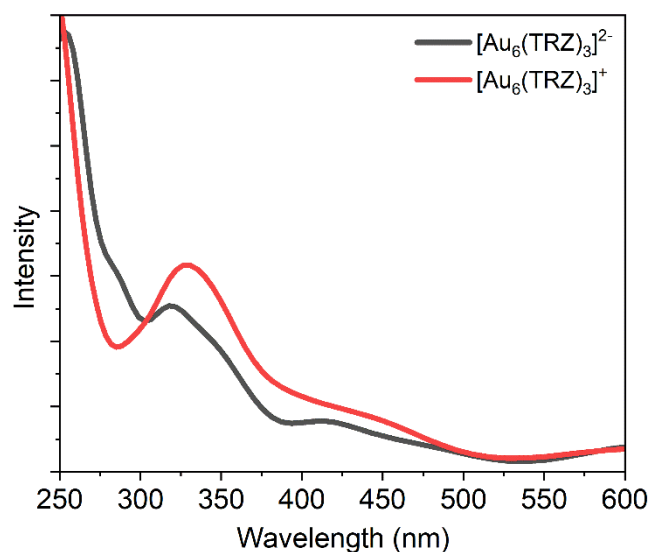


Figure S10. The TDDFT calculated optical absorption spectra of $[\text{Au}(\text{I})_6(\text{TRZ})_3]^{2-}$ and its protonated $[\text{Au}(\text{I})_6(\text{TRZ})_3]^+$ nanoclusters.

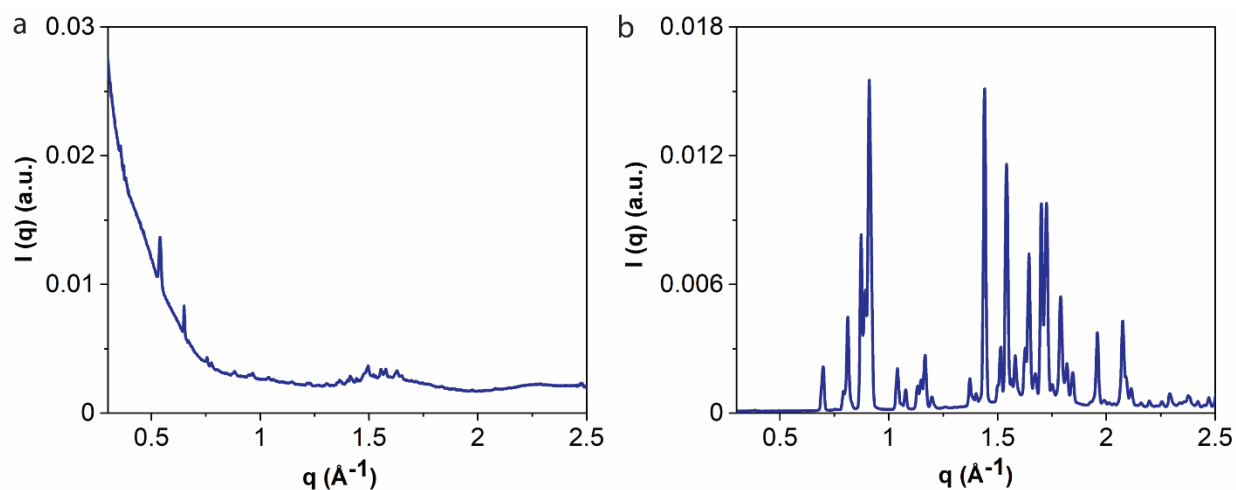


Figure S11. Small angle X-ray diffraction (SAXS) pattern of (a) GNC-1 and (b) isolated TRZ ligand.

The small angle X-ray diffraction (SAXS) of NCs produced distinct diffraction peaks in the range 0.5 to 2 \AA^{-1} on a baseline with broad maxima and shoulders. The SAXS results support the octahedral structure of $\text{Au}(\text{I})_6$ NCs (Figure S11a). The baseline shape cannot be unambiguously correlated with any specific structure, and it reflects the less ordered fraction that results from the rapid drying of DCM. The comparison of the SAXS pattern of pure ligand without gold (Figure

S11b) confirms that the diffraction peaks from the nanocluster sample are not arising from excess starting components.

The input parameters for diffraction pattern calculation:

Unit cell dimension: $a = 11.85 \text{ \AA}$, $b = 9.81 \text{ \AA}$, $c = 8.37 \text{ \AA}$

Unit cell angles: $\alpha = 85.700 \text{ deg.}$, $\beta = 85.300 \text{ deg.}$, $\gamma = 98.200 \text{ deg.}$

Atom	N	a coordinate	b coordinate	c coordinate
Au1	79	0.3305	0.0000	0.0000
Au2	79	0.6695	0.0000	0.0000
Au3	79	0.5061	0.1287	0.1707
Au4	79	0.4715	0.8362	0.1707
Au5	79	0.5285	0.1638	0.8293
Au6	79	0.4939	0.8713	0.8293
RGNR	1			

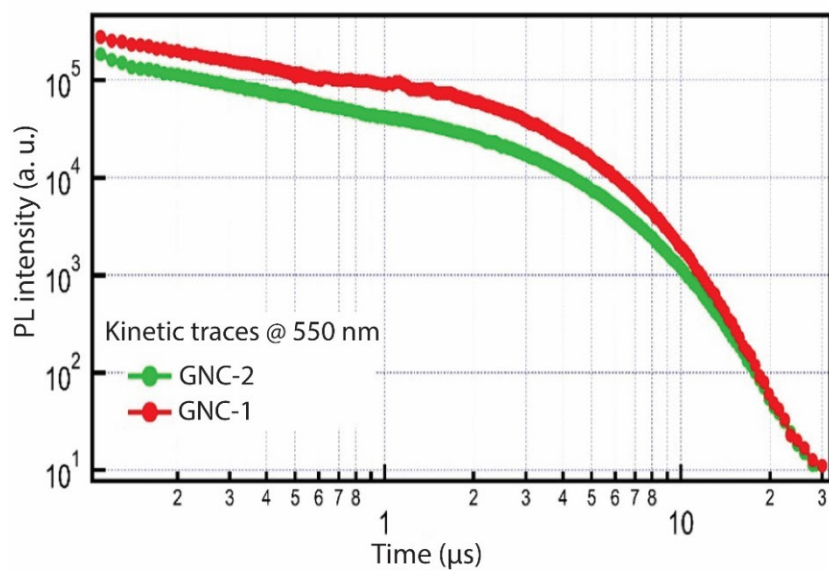


Figure S12. Decay kinetics of the spectrally integrated PL signal of GNC-1 (red line) and GNC-2 (green line).

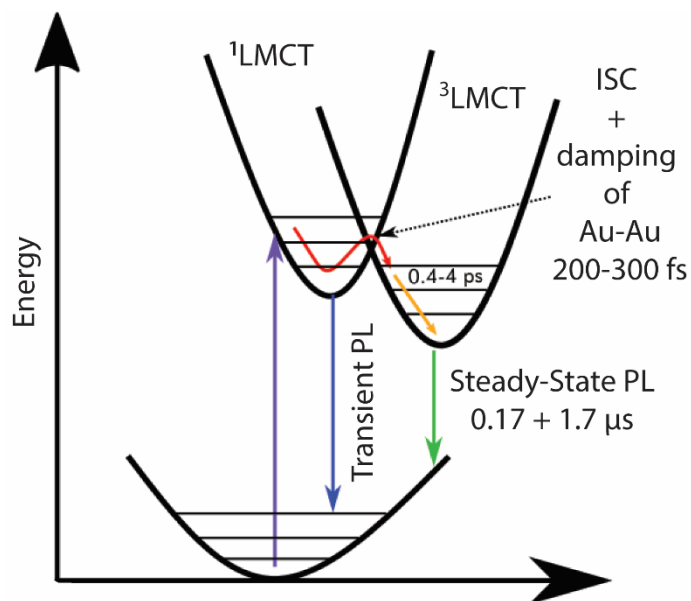


Figure S13. Photocycle of GNCs.

Calculation of third order nonlinear susceptibility:

The third order nonlinear susceptibility is calculated at 1300 nm wavelength with the formula given as:

$$\chi^{(3)} = \frac{4\varepsilon_0 c^2}{3\omega d} \sqrt{n_\omega^3 n_{3\omega} \frac{I_{3\omega}}{I_\omega^3}}$$

Where ε_0 , c and d are the permittivity of vacuum, speed of light in vacuum, and sample thickness respectively. n_ω ($n_{3\omega}$) and I_ω ($I_{3\omega}$) are the refractive index at frequency ω (3ω) and pump (THG) intensity respectively. The values are as follows:

$$\varepsilon_0 = 8.845 \times 10^{-12} \text{ F/m}$$

$$c = 3 \times 10^8 \text{ m/s}$$

$$n_\omega = 1.908$$

$$n_{3\omega} = 2.1684$$

$$I_\omega = 28.84 \text{ GW/cm}^2$$

$$I_{3\omega} = 7.02 \text{ KW/cm}^2$$

$$d = 5 \text{ nm}$$

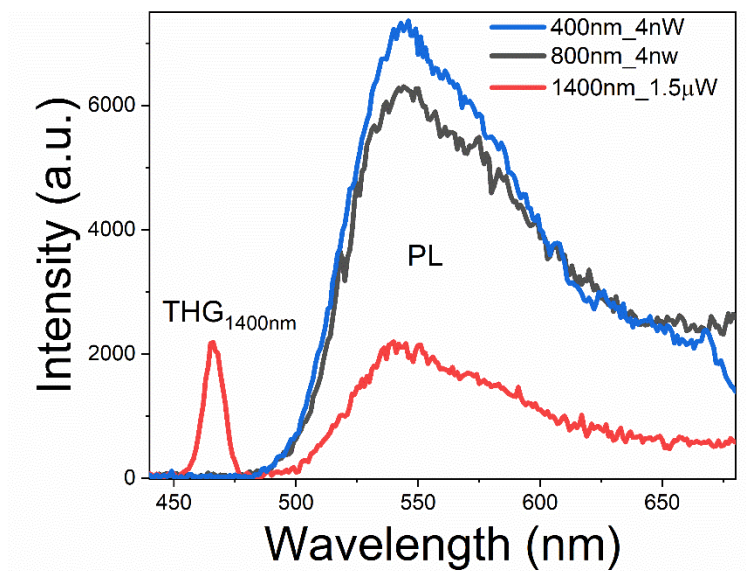


Figure S14. Multiphoton PL response of the thin film GNCs from pulsed laser of different wavelengths of excitation.

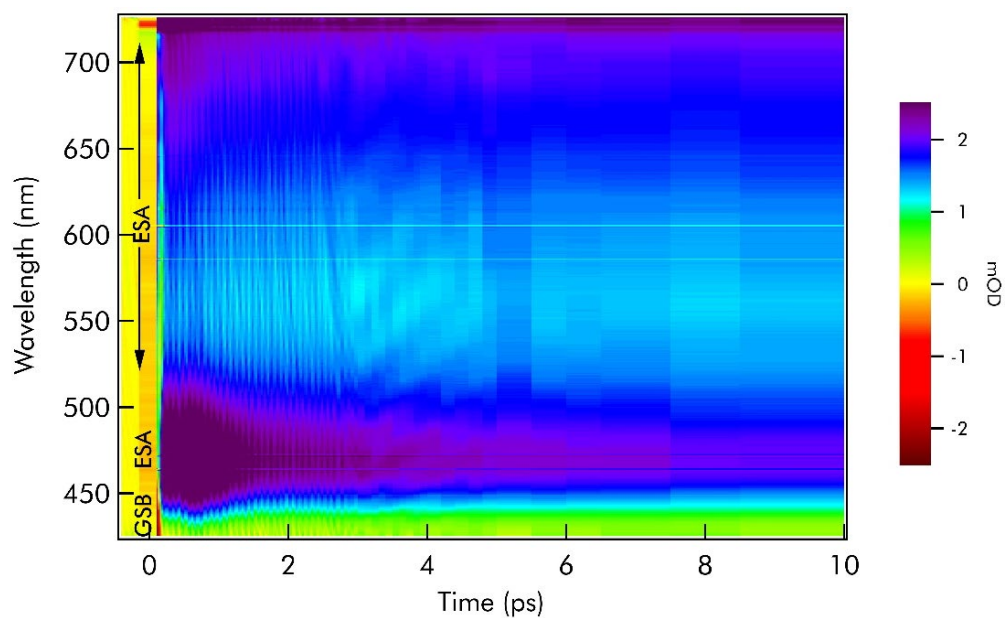


Figure S15. Time-wavelength contour plot of the TA signal of GNC-1 excited at 400 nm, shown in the first 5 ps.

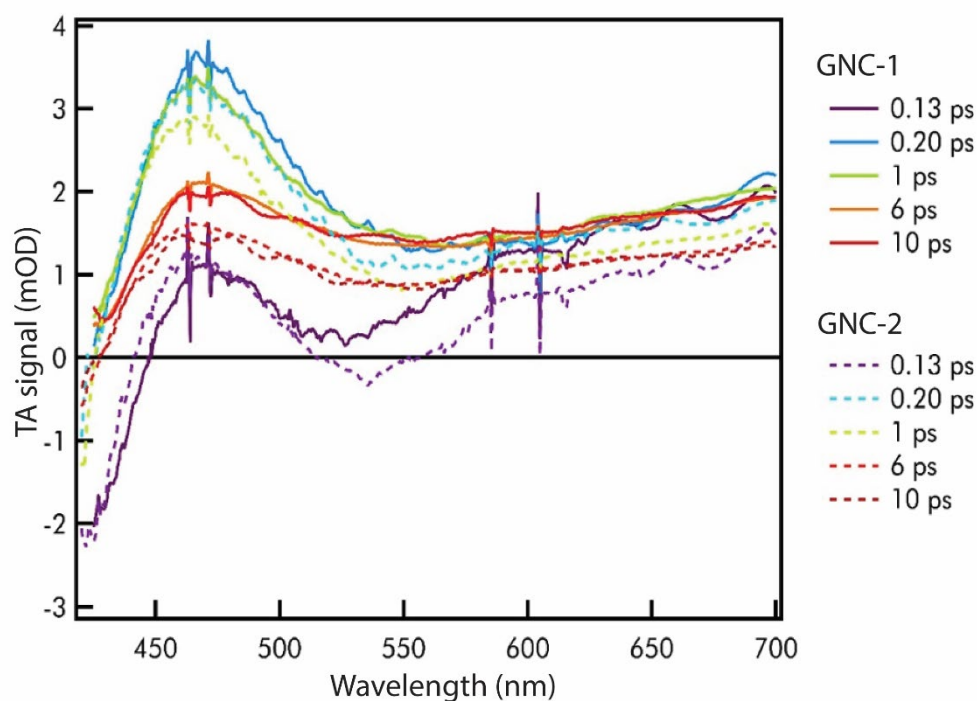


Figure S16. TA spectra at different pump-probe delays of GNC-1 (continuous lines) and GNC-2 (dashed lines).

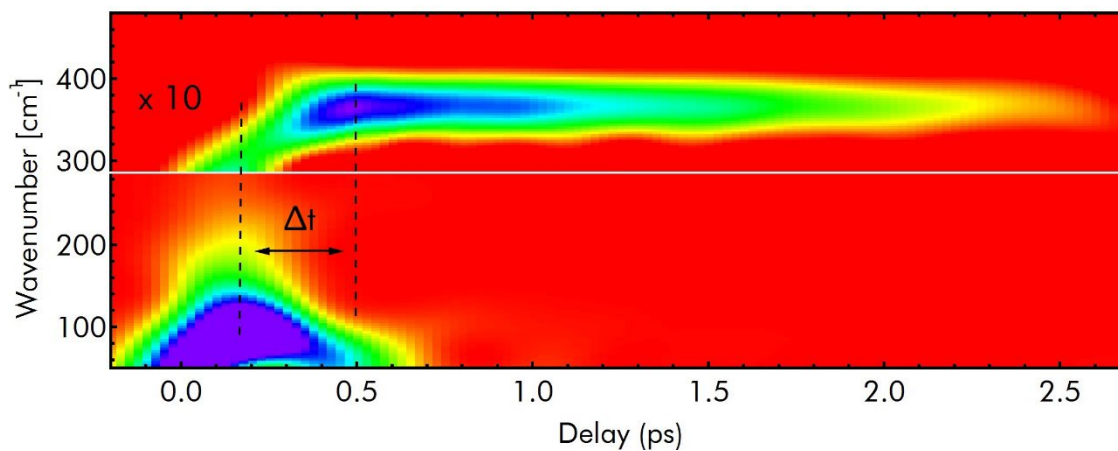


Figure S17. Time-frequency analysis of the fit residuals plotted in Figure 4d of the main paper, calculated as a short-time Fourier transform within a Hann moving window with 800 fs width (about twice the period of Au-Au oscillations).

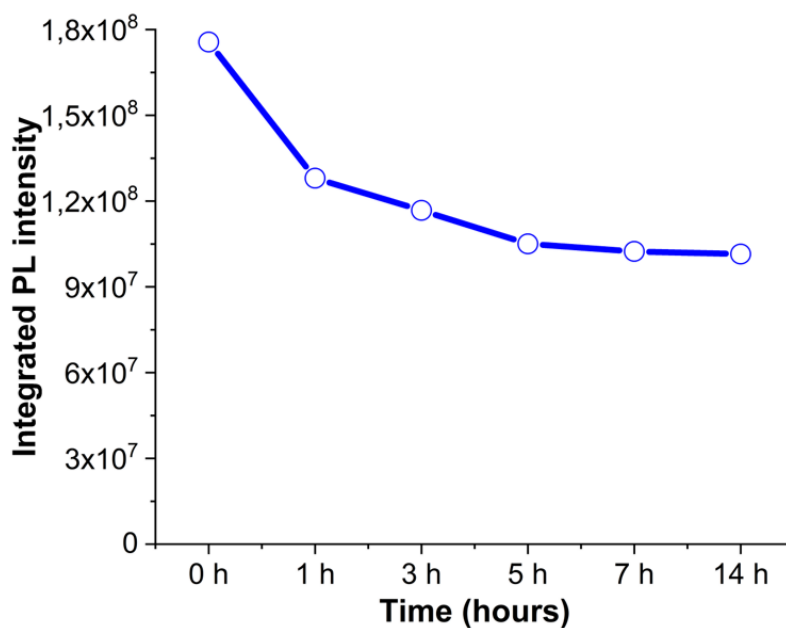


Figure S18. Photostability of GNC-1 under continuous exposure of UV light.

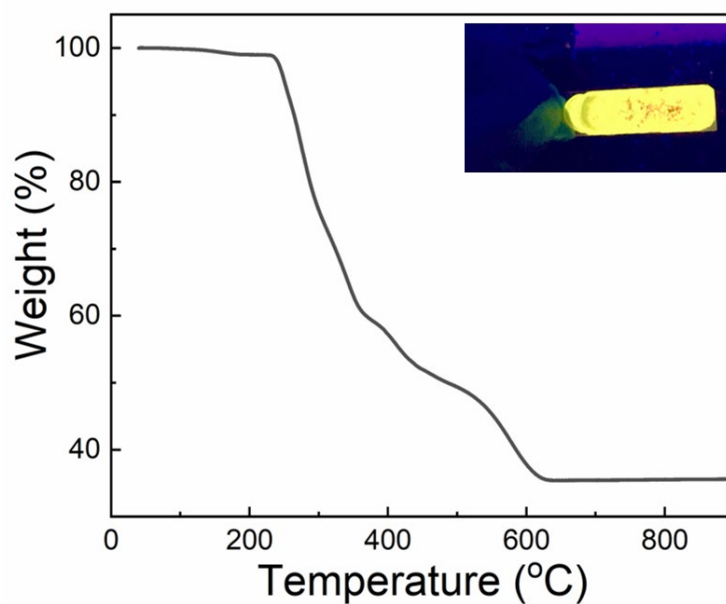


Figure S19. Thermogravimetric analysis (TGA) of GNC-1. Inset shows the GNC-1 film under UV exposure after treatment at 100 °C for 1 hour.

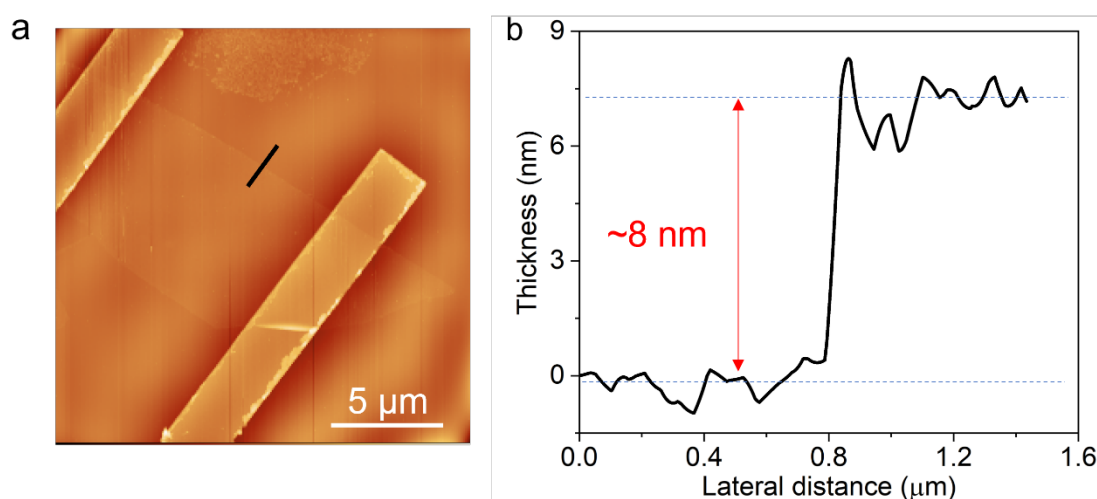


Figure S20. Thickness extraction of WSe₂ flakes. (a) Topographic image of pristine WSe₂ devices obtained by atomic force microscope. (b) Height profile of WSe₂ flake collected across black line indicated in (a).

References:

- [1] W. Kraus, G. Nolze, *J. Appl. Crystallogr.* **1996**, 29, 301–303.
- [2] A. Sciortino, F. Ferrante, N. Mauro, G. Buscarino, L. Sciortino, G. Giammona, M. Cannas, D. Duca, F. Messina, *Carbon N. Y.* **2021**, 173, 454–461.
- [3] J. Enkovaara, C. Rostgaard, J. J. Mortensen, J. Chen, M. Dułak, L. Ferrighi, J. Gavnholt, C. Glinsvad, V. Haikola, H. A. Hansen, H. H. Kristoffersen, M. Kuisma, A. H. Larsen, L. Lehtovaara, M. Ljungberg, O. Lopez-Acevedo, P. G. Moses, J. Ojanen, T. Olsen, V. Petzold, N. A. Romero, J. Stausholm-Møller, M. Strange, G. A. Tritsarlis, M. Vanin, M. Walter, B. Hammer, H. Häkkinen, G. K. H. Madsen, R. M. Nieminen, J. K. Nørskov, M. Puska, T. T. Rantala, J. Schiøtz, K. S. Thygesen, K. W. Jacobsen, *J. Phys. Condens. Matter* **2010**, 22, 253202.
- [4] J. P. Perdew, K. Burke, M. Ernzerhof, *Phys. Rev. Lett.* **1996**, 77, 3865–3868.
- [5] A. Tkatchenko, M. Scheffler, *Phys. Rev. Lett.* **2009**, 102, 6–9.
- [6] M. Kuisma, A. Sakko, T. P. Rossi, A. H. Larsen, J. Enkovaara, L. Lehtovaara, T. T. Rantala, *Phys. Rev. B - Condens. Matter Mater. Phys.* **2015**, 91, 115431.
- [7] E. Kalered, N. Brenning, I. Pilch, L. Caillault, T. Minéa, L. Ojamäe, *Phys. Plasmas* **2017**, 24, 013702.

RESEARCH ARTICLE

Endangered indigenous rice varieties as a source of B vitamins for the undernourished population

Priyabrata Roy^{1,2}  | Debal Deb¹  | Arunan Suganya³  | Brindaban Roy⁴ |
Thalappil Pradeep³  | Tanima Saha² 

¹Basudha Laboratory for Conservation, Centre for Interdisciplinary Studies, Kolkata, India

²Department of Molecular Biology and Biotechnology, University of Kalyani, Kalyani, India

³DST Unit of Nanoscience, Thematic Unit of Excellence (TUE), Department of Chemistry, Indian Institute of Technology Madras, Chennai, India

⁴Department of Chemistry, University of Kalyani, Kalyani, India

Correspondence

Priyabrata Roy, Debal Deb, and Tanima Saha, Basudha Laboratory for Conservation, Centre for Interdisciplinary Studies, Kolkata 700099, India.

Email: proyrice@gmail.com, priyabratroy2009@gmail.com, debdeb@gmail.com and sahatanima@yahoo.co.in

Funding information

Indian Council of Medical Research, Grant/Award Number: 2019-6997

Abstract

Background and Objectives: Rice is a staple food for half of the world's population and plays an important role to deliver several micronutrients including B vitamins to humans. The present investigation was carried out to detect some B vitamins and estimate their concentrations in 309 traditional indica rice landraces, compared with three modern rice varieties predominantly available in the Indian market.

Findings: Liquid chromatographic examination of the rice samples demonstrated that a large number of traditional rice landraces contained considerable amounts of different B vitamins. In the landraces examined, vitamin B1 (thiamine) was recorded to be present in the range of 0.01–10.55 mg/100 g, vitamin B2 (riboflavin) 0.01–2.63 mg/100 g, vitamin B3 (niacin) 0.20–4.52 mg/100 g, vitamin B5 (pantothenic acid) 0.01–18.55 mg/100 g, vitamin B6 (pyridoxine) 0.01–0.86 mg/100 g, and vitamin B7 (biotin) 0.01–5.90 mg/100 g in different rice landraces.

Conclusion: Compared with traditional rice, modern rice cultivars seem to have substantially lower B vitamin levels. It appears that these vitamin-rich traditional rice landraces if incorporated into daily diet, may serve to attain nutritional security of the poor.

Significance and Novelty: Our results show that many traditional rice landraces are nutritionally superior to any modern rice cultivar, even though traditional rice landraces are normally not in priority for agronomic research and development. This study shows how native rice landraces may be leveraged to constitute novel nutritious diet that could enhance human health.

KEYWORDS

B vitamins, HPLC, landrace, nutrition, traditional rice

1 | INTRODUCTION

Rice (*Oryza sativa* L.) is an important part of the human diet because it contains a large amount of carbohydrates, and small quantities of protein, fatty acids, dietary fibers,

B vitamins, and minerals. B vitamins are critically important vitamin groups, as they help keep the nervous system (Calderón-Ospina & Nava-Mesa, 2020), skin and eyes (Shabbir et al., 2020), liver (Khan et al., 2009), brain function (Klenner, 2005), and gastrointestinal tract

(Tappenden & Deutsch, 2007) healthy and functional. These vitamins concerted work to promote metabolism, facilitate adequate oxygen supply to cells, detoxify organs, stabilize nervous system functions, prevent vision problems (Gonçalves & Portari, 2021), and also to treat debilitating conditions (Tice, 2010).

B-vitamin deficiencies have diverse aetiologies, including inadequate intake, increased needs at different life history stages, malabsorption, drug-nutrient interactions, and other factors like hereditary diseases or health conditions (Porter et al., 2016). In many developing countries, vitamin B inadequacies are very common, particularly in those with diets that are low in animal products, fruits, and vegetables, and where cereal grains are milled before consumption. The most vulnerable groups to vitamin B deficiency are newborns, adolescents as well as pregnant and lactating women (Ashley, 2016). Infantile beriberi, a potentially fatal condition brought on by thiamine deficiency, is widely believed to be a sickness of the past in regions of the world where milled white rice consumption is the norm. Recent case reports, however, have demonstrated that thiamine deficiency is still a contributing factor in infant mortality in South and Southeast Asia. In the United States and UK, riboflavin deficiency is uncommon, but prevalent in developing countries in Asia and Africa. Niacin deficiency in the diet is usually common during periods of the food crisis, and frequent in Africa and Asia's maize-eating regions. Pyridoxine deficiency mostly occurs when the body has low levels of other B vitamins, especially vitamin B12 and folic acid, which is common in South Asia (Harding et al., 2018).

Fortification of rice with different vitamins and minerals is considered to be an important step toward addressing endemic malnutrition in rice-growing countries. While rice endosperm is virtually devoid of micro-nutrients, brown rice is known to contain several vitamins and minerals (Deb et al., 2015; Mondal et al., 2021; Rezaei et al., 2022; Roy et al., 2021). Knowledge of vitamin contents of specific rice landraces is important for strategizing the nutritional security of populations through the public distribution of vitamin-rich rices, as a viable and cheaper alternative to rice fortification programs. However, there is very limited information on the presence of B vitamins in rice landraces in its brown, or polished form. Liquid chromatographic method has evolved as one of the best methods for the identification and quantitative determination of B vitamins in food matrixes (Nguyen et al., 2021; Rezaei et al., 2022). Thiamine, riboflavin, nicotinic acid, biotin, pantothenic acid, and so forth have been reported by liquid chromatographic methods in a small number of *indica* rice landraces (Cho et al., 2020; Deepa et al., 2008; Priya

et al., 2019; Roy et al., 2021; Sumczynski, et al., 2018). Vitamin B12 is reported to be absent in the plant system (Watanabe, 2007), although vitamin B12 derived from microbial biosynthesis is rarely found in some processed plant foods (Jedut et al., 2021). On a larger scale, there is a research gap on the profiling of B vitamins and their concentrations in diverse rice (*O. sativa* ssp. *indica*) landraces. In this study, we report the results of a quantitative analysis of seven crucial B vitamins in 309 *indica* rice landraces, compared to three modern rice cultivars, and discuss the compositional diversity to address nutritional security.

2 | MATERIALS AND METHODS

2.1 | Samples

Freshly harvested grains of 309 traditional rice landraces were collected in 2019 from the Centre for Inter-disciplinary Study's conservation farm Basudha (<http://www.cintdis.org/basudha>), located in Rayagada district of Odisha (19° 42' 32.0"N, 83° 28' 8.4"E) where all the rice landraces are cultivated with zero external input. The farm is situated in the northern Eastern Ghat, characterized by hot subhumid eco-region with annual rainfall ranging from 1030.21 mm to 1569.50 mm. Samples of three modern varieties, namely, IR36, IR64, and BPT5204, were examined for comparison. Samples of the first two were collected from Chinsurah Rice Research Station, Hooghly, India, and BPT5204 was procured from Rajendranagar market, Hyderabad, India. All rice samples were decorticated manually in the laboratory by rubbing against a pumice stone, keeping the rice germ and bran layer intact, and ground to a fine powder using mortar and pestle, and stored at -20°C for vitamin analysis.

2.2 | Chemicals

Thiamine hydrochloride (B1), riboflavin (B2), nicotinic acid (B3), D-pantothenic acid calcium salt (B5), pyridoxine HCl (B6), and biotin (B7) and cyanocobalamin (B12) standards were purchased from Sigma-Aldrich. Methanol, chromatography-grade water and analytical-grade hydrochloric acid were obtained from Merck.

2.3 | Preparation of stock solution

Stock solutions of thiamine hydrochloride, pyridoxine HCl, cyanocobalamin, nicotinic acid, and D-pantothenic

acid calcium salt were prepared by dissolving 10 mg of the respective compound in 10 mL of deionized water (1 mg/mL), and stock solutions of riboflavin, and biotin were prepared by dissolving 10 mg of the respective compound in 10 mL of 0.1 mol/L NaOH (1 mg/mL). Stock solutions were prepared afresh before each analysis.

2.4 | Extraction of B vitamins

Extraction was carried out following the methods described in Puwastien et al. (2011) with slight modification, and detailed in Roy et al. (2021).

2.5 | Chromatographic procedure

High-performance liquid chromatography (HPLC) was used for the analysis of all B vitamins from the extracted rice samples. The reverse-phase-HPLC (RP-HPLC) method, reported by Heudi et al. (2005) was adopted for standardization, with slight modification. A gradient elution method was employed to get the baseline separation of the B vitamins (Roy et al., 2021). Briefly, gradient of two mobile phases were: methanol (A) and water with 0.02% aqueous H_3PO_4 (B) were set at: 0% A + 100% B for 3 min; 10% A + 90% B for 10 min; 30% A + 70% B for 15 min and 30% A + 70% B for 35 min. The injection volume was 20 μ L. The flow rate was kept at 1 mL/min and analytes were scanned at 210 nm wavelength. The peaks were identified by comparing the relative retention time with proper peak integration, co-chromatography with standard, and calibration against absorption spectra obtained from the analytical standards. Considering the large number of samples and quick completion of the analysis, we have carried out the experiments using three different liquid chromatographic machines. However, the method was identical for B complex vitamin analyses in all the instruments. The instrumental details are (i) Shimadzu Prominence Analytical HPLC System attached with Zorbax SB-C18 column (4.6 mm \times 150 mm, 3.5 micron, Agilent) with Photo Diode Array Detector; (ii) Waters HPLC attached with Atlantis dC18 column (100 Å, 5 μ m, 3.9 mm \times 150 mm) and UV-Vis detector, and (iii) Shimadzu Prominence UFLC (Ultra-Fast Liquid Chromatography), attached with Zorbax SB-C18 column (4.6 mm \times 150 mm, 3.5 μ m, Agilent, USA) with dual-channel UV-Vis detector. In all these cases, the separated peaks were calculated by comparing the relative retention time with the right peak integration, standard co-chromatography, and absorption spectra calibration obtained from the authentic standard.

2.6 | Detection of B vitamins and chromatographic separation

Following the recent understanding (Sasaki et al., 2020) that all B vitamins can be spectrophotometrically detected at 210 nm. We used 210 nm wavelength to detect the presence of all seven B vitamins (Supplementary Figure S1) in our experiment. The chromatographic separation of seven B vitamins in the mixture of standard solution using the gradient elution method is shown in Supplementary Figure S2 (I). The elution order was vitamin B1 (thiamine), B3 (niacin), B6 (pyridoxin), B5 (pantothenic acid), B7 (biotin), B12 (cyanocobalamin), and B2 (riboflavin). Supplementary Figure S2 (II) shows the chromatographic separation of B vitamins from an extracted rice sample G37. All seven B vitamins were separated to the baseline and eluted as sharp peaks within 20 min. The reproducibility of the retention time was checked three times over, and only after getting an acceptable standard deviation value the method was adopted. By combining the stock solutions in the proper proportions and diluting them with mobile phase, the analytical solutions were used for assessing the linearity, range, LOD, and LOQ. Peak areas were plotted against five comparable concentrations (μ g/mL) of each vitamin B molecule to develop calibration curves. Using the outcomes of these analyses, the linearity (with $R^2 > 0.998$), range, LOD, and LOQ were estimated (Table 1). The concentrations at which vitamin B compound peaks could be identified without being interfered with by baseline noise were used to determine LOD and LOQ. All vitamins were quantified by using the standard validation method and finally, the amounts of the analytes were expressed as mg/100 g. Results below the LOD were considered as not detected (ND) in case of all B vitamins.

2.7 | Statistical analysis

Data are presented as the mean of three replications. Pearson's correlation and principal component analysis (PCA) were performed using R statistical software (v4.2.2; R Core Team 2022). Considering replications ($df = 2$), the confidence limit was set at $p < .05$. Using the same data sets, bidirectional heatmap clustering was performed.

3 | RESULTS AND DISCUSSIONS

3.1 | Analysis of B vitamins in rice samples

The concentrations of different B vitamins in 309 rice landraces and three modern rice cultivars examined

TABLE 1 LOD and LOQ of B vitamins in chromatographic detection and variation of B vitamins across rice lines achieving recommended daily intake.

Name of B vitamins	LOQ (ppm)	LOD (ppm)	Variations B vitamins in rice landraces (mg/100 g)	Average recommended Daily Intake ^a for an adult (19-60 years)	A few recommended rice lines with high amount of B vitamins
Thiamine	0.04	0.05	0.01–10.55	1.2 (mg)	C09, DD16, G43, TT16, B24
Riboflavin	0.07	0.01	0.01–2.63	1.3 (mg)	B38, M04, M33, K71
Nicotinic acid	0.02	0.008	0.20–4.52	16 (mg)	SS04, M51, S54, G12
Pantothenic acid	0.03	0.005	0.01–18.55	5 (mg)	A10, DD18, S61, T01
Pyridoxine	0.02	0.01	0.01–0.86	1.3 (mg)	C12, B21, S54, G12
Biotin	0.03	0.008	0.01–5.90	30 (μg)	SS02, SH06, SH04, M33
Cyanocobalamin	0.01	0.006	N.D.	2.4 (μg)	---

Abbreviations: LOD, Limit of detection; LOQ, limit of quantitation; N.D., not detected.

^aTaken from Kennedy (2016).

here are given in Supplementary Tables S1 and S2, respectively. Vitamin B1 (thiamine) was present in the range of 0.01–10.55 mg/100 g, vitamin B2 (riboflavin) 0.01–2.63 mg/100 g, vitamin B3 (nicotinic acid) 0.20–4.52 mg/100 g, vitamin B5 (D-pantothenic acid calcium salt) 0.01–18.55 mg/100 g, vitamin B6 (pyridoxine hydrochloride) 0.01–0.86 mg/100 g, and vitamin B7 (biotin) 0.01–5.90 mg/100 g in different rice landraces. In comparison with several traditional rice landraces, the modern rice cultivars IR36, IR64, and BPT5204 contained much lower quantities of B vitamins in their grains (Supplementary Table S2). In contrast, among the 309 landraces studied here, there were several landraces containing remarkably high levels of different B vitamins in their grains (Figure 1), implying that their consumption could meet the recommended daily intake (RDI) of these vitamins (Table 1). There was no strong correlation among the levels of different B vitamins in the rice landraces examined here (Supplementary Figure S3).

The association between the rice landraces was investigated using important B vitamins to determine suitable rice landraces for future studies. The outcomes of the heat-map analysis of the rice landraces are shown in Supplementary Figure S4. The efficacy of applied methodologies in identifying rice landraces based on phenotypic data is highlighted in the heatmap, which clearly classifies 309 landraces into five main clusters and 12 sub-clusters. Our PCA failed to detect any distinctive group among our rice samples Supplementary Figure S5. However, separation was visible in the first two main components, which collectively account for 54.7% of variation. The principal component 1 (Dim-1, 36.2%) score and loading indicated that the rice

lines had greater concentrations of B1, B2, B3, B5, and B6 with high and positive relations among each other. On the other hand, the level of B7 was higher in the PC2 loading (Dim2, 18.5%) plot and score than those in PC1. These findings, however, do not indicate that the concentrations of any B vitamin had any influence on the presence of other B vitamins in the rice grains. It is likely that edaphoclimatic diversity of origin of the landraces and different agronomic factors (Choi et al., 2012)—in addition to the varietal genotype—may independently influence the B vitamin contents in these rice landraces.

3.1.1 | Vitamin B1 (thiamine)

Almost 96% of the rice landraces examined here contained much greater than 0.1 mg/100 g of thiamine in their grains (Figure 1). The higher contents of thiamine were found especially in DD16, C09, G43, and TT16 samples, in a range between 9.03 and 10.55 mg/100 g. As Supplementary Table S1 shows, traditional rice landraces are a rich source of thiamine. The major forms of this vitamin in cells are free thiamine, thiamine monophosphate, and thiamine pyrophosphate, which are one of the cofactors for the enzymes of basic metabolic pathways like glycolysis, pentose phosphate pathway, and tricarboxylic acid pathway, amino acid and acetyl Co-A biosynthesis pathways (Rapala-Kozik, 2011). Deficiency of thiamine leads to beriberi, which affects cardiovascular and nervous systems (Lonsdale, 2006). Our finding suggests that RDI may be attained by consuming whole grain (unpolished) rice in a daily diet (Table 1).

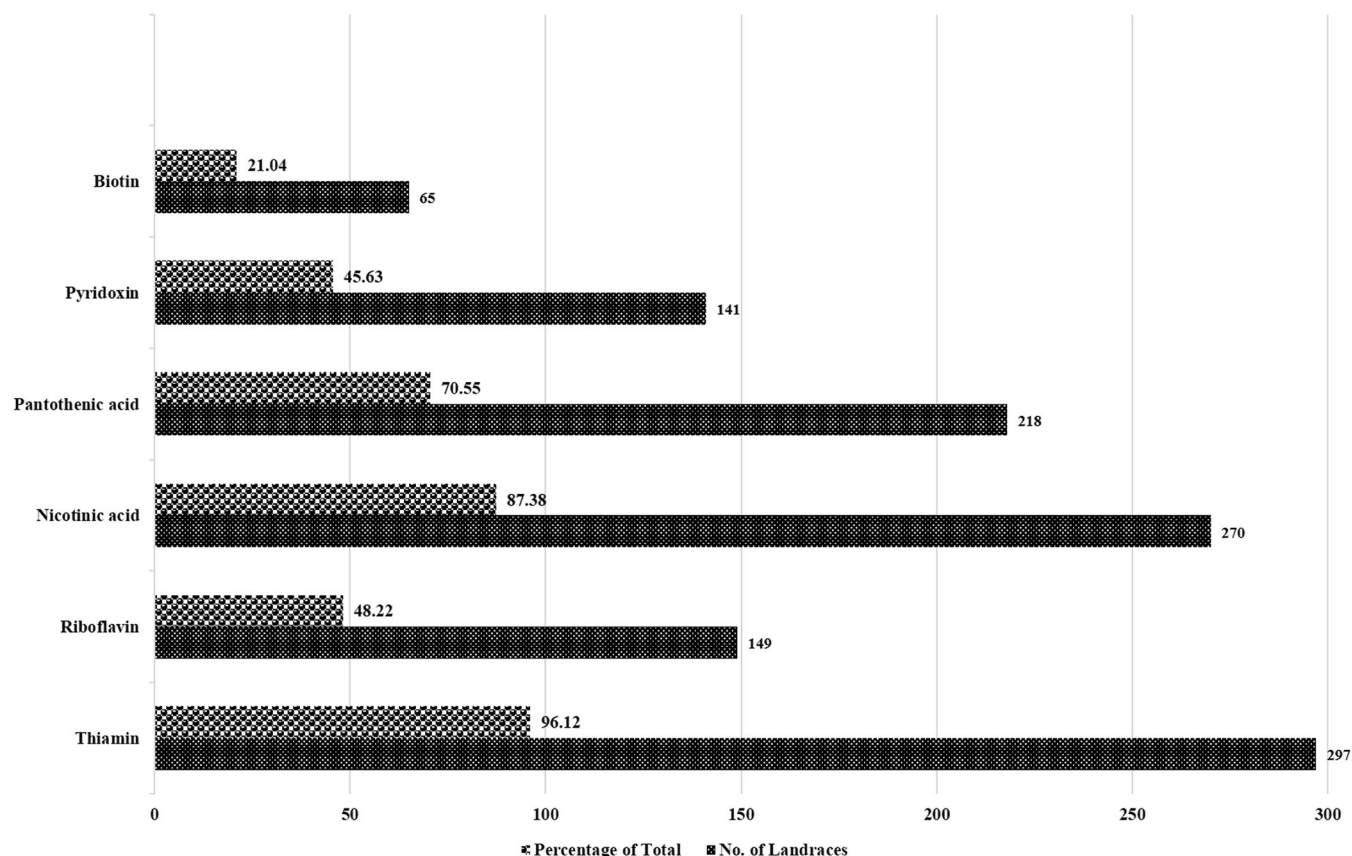


FIGURE 1 The number of landraces (dotted bars) and their proportions (bubble bars), Containing > 100 µg of different B complex vitamins in 100 g of sample. Figures beside the bubble bars indicate the % of $N = 309$ landraces examined.

3.1.2 | Vitamin B2 (riboflavin)

Considerably high riboflavin levels were found in M04 (2.63 mg/100 g) and B38 (1.05 mg/100 g) rice landraces. Riboflavin is a precursor of various redox-active coenzymes associated with different proteins, which act as cofactors in different metabolic enzymes (Giancaspero et al., 2013). Deficiency of vitamin B2 in the diet leads to anemia, neurological, and developmental disorders (Powers, 2003). Our study indicates that RDI may be achieved by consuming some traditional rice landraces, which were a good source of vitamin B2 and could be recommended to patients suffering from ariboflavinosis (Table 1).

3.1.3 | Vitamin B3 (nicotinic acid)

The higher contents of niacin were found in SS04 (4.52 mg/100 g), M51 (4.05 mg/100 g), S54 (3.86 mg/100 g), and so forth rice landraces. However, 87.38% of the rice landraces examined here contained more than 0.1 mg/100 g in their grains (Figure 1, Supplementary Table S1). Niacin is a precursor of pyridine alkaloids

(Noctor, 2006) and helps to metabolize macronutrients, resulting in the healthy functioning of the nervous system. Severe deficiency of niacin in the diet causes pellagra, poor concentration, anxiety, depression, and so forth (Penberthy & Kirkland, 2020). Consuming the rice varieties examined here may not meet the need of RDI of vitamin B3 in diet (Table 1), but a moderate amount of niacin present in rice landraces could be helpful for people who are suffering from vitamin B3 deficiency.

3.1.4 | Vitamin B5 (D-pantothenic acid calcium salt)

The higher contents of pantothenic acid were found in 70.55% of rice landraces. Pantothenic acid (B5) is commonly available among other B vitamins and could be found in both animal and plant-based food items. It is the precursor of coenzyme A which is essential for fatty acid metabolism. It is also responsible for the secondary metabolite synthesis pathway (Coxon et al., 2005). Pantothenic acid deficiency in humans is extremely rare and has received less attention. The RDI for vitamin B5 could

be easily achieved by consuming traditional rice landraces, which are an excellent source of pantothenic acid as our data suggest (Table 1).

3.1.5 | Vitamin B6 (pyridoxin hydrochloride)

The higher contents of pyridoxine (B6) were found in 45.63% of the total rice landraces (Figure 1). Vitamin B6 is a potent antioxidant that helps to metabolize sugars and fatty acids and acts as a cofactor in different enzymatic reactions (Drewke & Leistner, 2001). Deficiency of vitamin B6 leads to depression, lower immunity, kidney diseases, rheumatoid arthritis, and so forth (Sharifzadeh et al., 2018). Vitamin B6 may lower the risk of cancer (Mocellin et al., 2017), help with brain function by lowering levels of homocysteine (Rutjes et al., 2018), and prevent cardiovascular diseases. Our results suggest that a good number of traditional rice landraces contain this vitamin in moderate amounts.

3.1.6 | Vitamin B7 (biotin)

An adequate amount of biotin was found in 21% of the rice landraces examined here (Figure 1), which are capable to meet the RDI (Table 1). Plants, most bacteria, and some fungi can synthesize biotin, whereas animals and some other fungi must obtain biotin from their diet because they are unable to synthesize it. Biotin operates as a cofactor for enzymes that are required in many biological functions (Knowles, 1989). Deficiency of vitamin B7 leads to brittle and thin fingernails, conjunctivitis, red rash on the face, and neurological symptoms such as depression, lethargy, hallucination, and so forth (Penberthy & Kirkland, 2020).

There are some recent reports of a few traditional rice landraces containing B vitamins. Specifically, Njavara from Kerala and Jyothi from Karnataka are reported to contain thiamine (0.35–0.52 mg/100 g), riboflavin (0.053–0.071 mg/100 g), niacin (7.15–7.32 mg/1100 g), and folic acid (0.05 mg/100 g) (Deepa et al., 2008). Similarly, 32 folk rice varieties from Meghalaya are reported to contain thiamine (0.17–0.38 mg/100 g), riboflavin (0.03–0.09 mg/100 g), nicotinic acid (1.43–3.87 mg/100 g), pantothenic acid (0.36–3.10 mg/100 g), and pyridoxine (0.03–0.17 mg/100 g) (Longvah et al., 2020). Roy et al. (2021) also reported different B vitamins, namely, thiamine (0.11–1.38 mg/100 g), riboflavin (0.01–0.56 mg/100 g), niacin (0.17–0.80 mg/100 g), pantothenic acid (0.81–2.9 mg/100 g), pyridoxine (0.1–0.2 mg/100 g), and biotin (0.01–0.24 mg/100 g) in a few selected rice

landraces, also included in our present study of 309 rice landraces. In this study, we detected an outstandingly high concentration of thiamine in some landraces, to the extent of more than 9 mg/100 g. In addition to thiamine, the concentrations of pantothenic acid, pyridoxine, niacin, biotin in these folk rice grains are much greater than in the three modern high-yielding rice cultivars (Supplementary Tables S1 and S2). In fact, most of the B vitamins are not yet reported in any modern high-yielding rice cultivars (Deepa et al., 2008; Roy et al., 2021). In this study, the richness of B vitamins in the grains of some traditional rice landraces implies a robust solution to the problem of vitamin B deficiency, especially in rice-eating cultures. We suggest that the recommended daily dietary requirement of many B vitamins may adequately be fulfilled by a large number of traditional rice landraces (Table 1), most of which are not yet adequately examined.

This research indicates how indigenous rice landraces might be utilized into a nutritious rice-based product that is high in vitamins or used as a component in novel functional foods that could improve human health (Itagi et al., 2023). While folk rice landraces are typically not high on the priority list for agronomic research and development, our findings indicate that a large number of rice landraces are nutritionally superior to any modern rice cultivar.

4 | CONCLUSION

The present work is the first quantitative study of several B vitamins in fresh decorticated grains of a large number (309) of *indica* rice landraces, compared to 3 modern rice cultivars. Most of the landraces examined here have almost disappeared from rice farms as a result of preferences for modern HYVs. The extinction of these landraces from rice farms indicates a substantial loss of a wealth of indigenous rice genetic diversity, with their great potential to ensure nutritional security for the poor. One apparent policy recommendation is to conserve and promote the cultivation and consumption of traditional rice landraces. Widespread cultivation and consumption would be a viable means to assuring nutritional security for the poor and marginal sections of the country's population.

AUTHOR CONTRIBUTIONS

Debal Deb and Priyabrata Roy conceived the presented idea. Debal Deb designed the analyses and selected the rice cultivars, Tanima Saha and Thalappil Pradeep verified the analytical methods. Debal Deb, Brindaban Roy, Tanima Saha, and Thalappil Pradeep enlisted

Priyabrata Roy and Arunan Suganya to investigate all the analyses, statistical computations, provided the access and instrumental facilities for all analyses and supervised the entire work. Priyabrata Roy and Tanima Saha prepared the first draft of manuscript. All authors contributed to the final manuscript.

ACKNOWLEDGMENTS

We are thankful to Central Instrumentation Facility at the Indian Institute of Chemical Biology, Kolkata for the HPLC analyses of B vitamins in 200 rice samples; to Debdulal Bhattacharjee for providing us the pure lines of rice landraces from Basudha farm, Odisha. No institutional funding support was received for the conservation, characterization, and cultivation of the rice landraces on Basudha farm. P.R. acknowledges the infrastructural and fellowship support from Indian Council for Medical Research, Govt. of India (IRIS No. 2019-6997) and University of Kalyani, Kalyani. S.A & T.P. acknowledge the financial assistance from Department of Science & Technology, Govt. of India.

CONFLICT OF INTEREST STATEMENT

The authors declare no conflict of interest.

ORCID

Priyabrata Roy  <http://orcid.org/0000-0002-0953-6528>

Debal Deb  <http://orcid.org/0000-0002-7230-659X>

Arunan Suganya  <http://orcid.org/0000-0002-2990-1916>

Thalappil Pradeep  <http://orcid.org/0000-0003-3174-534X>

Tanima Saha  <http://orcid.org/0000-0002-9529-160X>

REFERENCES

- Ashley, J. M. (2016). *Food security in the developing world*. Academic Press.
- Calderón-Ospina, C. A., & Nava-Mesa, M. O. (2020). B vitamins in the nervous system: Current knowledge of the biochemical modes of action and synergies of thiamine, pyridoxine, and cobalamin. *CNS Neuroscience & Therapeutics*, 26(1), 5–13. <https://doi.org/10.1111/cns.13207>
- Cho, J. J., Hong, S. J., Boo, C. G., & Shin, E. C. (2020). Investigation of Water-Soluble vitamin (B 1, B 2, and B 3) contents in rice, noodles, and sauces. *Journal of Food Hygiene and Safety*, 35(4), 398–410.
- Choi, H., Moon, J.-K., Park, B.-S., Park, H.-W., Park, S.-Y., Kim, T.-S., Kim, D.-H., Ryu, T.-H., Kweon, S.-J., & Kim, J.-H. (2012). Comparative nutritional analysis for genetically modified rice, Iksan483 and Milyang204, and nontransgenic counterparts. *Journal of the Korean Society for Applied Biological Chemistry*, 55(1), 19–26. <https://doi.org/10.1007/s13765-012-0004-5>
- Coxon, K. M., Chakauya, E., Ottenhof, H. H., Whitney, H. M., Blundell, T. L., Abell, C., & Smith, A. G. (2005). Pantothenate biosynthesis in higher plants. *Biochemical Society Transactions*, 33(4), 743–746. <https://doi.org/10.1042/BST0330743>
- Deb, D., Sen Gupta, S., & Pradeep, T. (2015). A profile of heavy metals in rice (*Oryza sativa* ssp. *indica*) landraces. *Current Science*, 109(3), 407–409.
- Deepa, G., Singh, V., & Naidu, K. A. (2008). Nutrient composition and physicochemical properties of Indian medicinal rice–njavara. *Food Chemistry*, 106(1), 165–171. <https://doi.org/10.1016/j.foodchem.2007.05.062>
- Drewke, C., & Leistner, E. (2001). Biosynthesis of vitamin B6 and structurally related derivatives. *Vitamins and Hormones*, 61, 121–155. [https://doi.org/10.1016/S0083-6729\(01\)61004-5](https://doi.org/10.1016/S0083-6729(01)61004-5)
- Giancaspero, T. A., Busco, G., Panebianco, C., Carmone, C., Miccolis, A., Liuzzi, G. M., Colella, M., & Barile, M. (2013). FAD synthesis and degradation in the nucleus create a local flavin cofactor pool. *Journal of Biological Chemistry*, 288(40), 29069–29080. <https://doi.org/10.1074/jbc.M113.500066>
- Gonçalves, A. C., & Portari, G. V. (2021). The B-complex vitamins related to energy metabolism and their role in exercise performance: A narrative review. *Science & Sports*, 36(6), 433–440.
- Harding, K. L., Aguayo, V. M., & Webb, P. (2018). Hidden hunger in South Asia: A review of recent trends and persistent challenges. *Public Health Nutrition*, 21(4), 785–795. <https://doi.org/10.1017/S1368980017003202>
- Heudi, O., Kilinç, T., & Fontannaz, P. (2005). Separation of water-soluble vitamins by reversed-phase high performance liquid chromatography with ultra-violet detection: Application to polyvitaminated premixes. *Journal of Chromatography A*, 1070(1–2), 49–56. <https://doi.org/10.1016/j.chroma.2005.02.033>
- Itagi, H., Sartagoda, K. J. D., Pratap, V., Roy, P., Tiozon, R. N., Regina, A., & Sreenivasulu, N. (2023). Popped rice with distinct nutraceutical properties. *LWT*, 173, 114346. <https://doi.org/10.1016/j.lwt.2022.114346>
- Jedut, P., Sz wajgier, D., Glibowski, P., & Hlowiecka, K. (2021). Some plant food products present on the Polish market are a source of vitamin B12. *Applied Sciences*, 11(8), 3601. <https://doi.org/10.3390/app11083601>
- Kennedy, D. (2016). B vitamins and the brain: Mechanisms, dose and Efficacy--A review. *Nutrients*, 8(2), 68. <https://doi.org/10.3390/nu8020068>
- Khan, M., Mostofa, M., Jahan, M., Sayed, M., & Hossain, M. (2009). Effect of garlic and vitamin B-complex in lead acetate induced toxicities in mice. *Bangladesh Journal of Veterinary Medicine*, 6(2), 203–210. <https://doi.org/10.3329/bjvm.v6i2.2337>
- Klenner, F. R. (2005). Response of peripheral and central nerve pathology to mega-doses of the vitamin B-complex and other metabolites. *Townsend Letter for Doctors and Patients*, (269), 99+. <https://link.gale.com/apps/doc/A139602817/AONE?u=anon-cc9925b9&sid=googleScholar&xid=b439d274>
- Knowles, J. R. (1989). The mechanism of biotin-dependent enzymes. *Annual Review of Biochemistry*, 58, 195–221. <https://doi.org/10.1146/annurev.bi.58.070189.001211>
- Longvah, T., Vooradi Sathya Sai, P., Rajendran, A., Kharkhonger, G. C., & Rangad, C. (2020). In situ nutrient variability in rice landraces from Garo Hills, Meghalaya in North East India. *Journal of Food Composition and Analysis*, 92, 103543. <https://doi.org/10.1016/j.jfca.2020.103543>
- Lonsdale, D. (2006). A review of the biochemistry, metabolism and clinical benefits of thiamin(e) and its derivatives. *Evidence-*

- Based Complementary and Alternative Medicine, 3(1), 49–59. <https://doi.org/10.1093/ecam/nek009>
- Mocellin, S., Briarava, M., & Pilati, P. (2017). Vitamin B6 and cancer risk: a field synopsis and meta-analysis. *Journal of the National Cancer Institute*, 109, djw230. <https://doi.org/10.1093/jnci/djw230>
- Mondal, P., Datta, S., & Deb, D. (2021). Agronomic and nutraceutical properties of indigenous rice varieties. In: D. Sinha, (Ed.), *A handbook of agriculture and plant sciences* (pp. 71–91). ABS Publishers.
- Nguyen, Q. H., Hoang, A. Q., Truong, T. M. H., Dinh, T. D., Le, T. T., Luu, T. H. T., Dinh, V. C., Nguyen, T. M. T., Vu, T. T., & Nguyen, T. A. H. (2021). Development of simple analytical method for B-group vitamins in nutritional products: Enzymatic digestion and UPLC-MS/MS quantification. *Journal of Analytical Methods in Chemistry*, 2021, 1–10. <https://doi.org/10.1155/2021/5526882>
- Noctor, G. (2006). NAD (P) synthesis and pyridine nucleotide cycling in plants and their potential importance in stress conditions. *Journal of Experimental Botany*, 57(8), 1603–1620. <https://doi.org/10.1093/jxb/erj202>
- Penberthy, W. T., & Kirkland, J. B. (2020). Chapter 12 - Niacin. In B. P. Marriott, D. F. Birt, V. A. Stallings, & A. A. Yates (Eds.), *Present knowledge in nutrition* (11th ed., pp. 209–224). Academic Press (Elsevier). <https://doi.org/10.1016/B978-0-323-66162-1.00012-3>
- Porter, K., Hoey, L., Hughes, C., Ward, M., & McNulty, H. (2016). Causes, consequences and public health implications of low B-vitamin status in ageing. *Nutrients*, 8(11), 725. <https://doi.org/10.3390/nu8110725>
- Powers, H. J. (2003). Riboflavin (vitamin B-2) and health. *The American Journal of Clinical Nutrition*, 77(6), 1352–1360. <https://doi.org/10.1093/ajcn/77.6.1352>
- Puwastien, P., Siong, T. E., Kantasubrata, J., Caven, G., Felicionoand, R. R., & Judprasong, K. (2011). ASEAN Manual of Food Analysis. Regional centre of ASEAN Network of Food Data System. Institute of Nutrition, Mahidol University Thailand, 1–190.
- Rapala-Kozik, M. (2011). Vitamin B1 (Thiamine): A cofactor for enzymes involved in the main metabolic pathways and an environmental stress protectant. *Advances in Botanical Research*, 58, 37–91. <https://doi.org/10.1016/B978-0-12-386479-6.00004-4>
- Rathna Priya, T. S., Eliazar Nelson, A. R. L., Ravichandran, K., & Antony, U. (2019). Nutritional and functional properties of coloured rice varieties of South India: A review. *Journal of Ethnic Foods*, 6(1), 11. <https://doi.org/10.1186/s42779-019-0017-3>
- Rezaei, M., Alizadeh Sani, M., Amini, M., Shariatifar, N., Alikord, M., Arabameri, M., Chalipour, A., & Hazrati Reziabad, R. (2022). Influence of cooking process on the content of water-soluble B vitamins in rice marketed in Iran. *Food Science & Nutrition*, 10(2), 460–469. <https://doi.org/10.1002/fsn3.2690>
- Roy, P., Deb, D., Pradeep, T., Talai-Mukhopadhyay, S., Sinha, A. K., & Saha, T. (2021). Comparative analyses of the nutraceutical potentialities of selected Indian traditional black rice (*Oryza sativa* L.) landraces. *Oryza*, 58(2), 295–309. <https://doi.org/10.35709/ory.2021.58.2.6>
- Rutjes, A. W., Denton, D. A., Di Nisio, M., Chong, L.-Y., Abraham, R. P., Al-Assaf, A. S., Anderson, J. L., Malik, M. A., Vernooij, R. W., Martinez, G., Tabet, N., & McCleery, J. (2018). Vitamin and mineral supplementation for maintaining cognitive function in cognitively healthy people in mid and late life. *Cochrane Database of Systematic Reviews*, 2019, 1–156. <https://doi.org/10.1002/14651858.CD011906.pub2>
- Sasaki, K., Hatate, H., & Tanaka, R. (2020). Determination of 13 vitamin B and the related compounds using HPLC with UV detection and application to food supplements. *Chromatographia*, 83(7), 839–851. <https://doi.org/10.1007/s10337-020-03902-2>
- Shabbir, H., Shabbir, I., Aslam, M., Sarwar, M. F., Sarwar, M. H., & Sarwar, M. (2020). Fundamental aspects of vitamin B complex in human nourishment and fitness. *American Journal of Food Science and Health*, 6(4), 109–118.
- Sharifzadeh, F., Kashanian, M., Koohpayehzadeh, J., Rezaian, F., Sheikhsari, N., & Eshraghi, N. (2018). A comparison between the effects of ginger, pyridoxine (vitamin B6) and placebo for the treatment of the first trimester nausea and vomiting of pregnancy (NVP). *The Journal of Maternal-Fetal & Neonatal Medicine*, 31(19), 2509–2514. <https://doi.org/10.1080/14767058.2017.1344965>
- Sumczynski, D., Koubová, E., Šenkárová, L., & Orsavová, J. (2018). Rice flakes produced from commercial wild rice: Chemical compositions, vitamin B compounds, mineral and trace element contents and their dietary intake evaluation. *Food Chemistry*, 264, 386–392. <https://doi.org/10.1016/j.foodchem.2018.05.061>
- Tappenden, K. A., & Deutsch, A. S. (2007). The physiological relevance of the intestinal microbiota-contributions to human health. *Journal of the American College of Nutrition*, 26(6), 679S–683S. <https://doi.org/10.1080/07315724.2007.10719647>
- Tice, J. A. (2010). The vital amines: Too much of a good thing? Comment on “effects of lowering homocysteine levels with B vitamins on cardiovascular disease, cancer, and cause-specific mortality”. *Archives of Internal Medicine*, 170(18), 1631–1633. <https://doi.org/10.1001/archinternmed.2010.338>
- Watanabe, F. (2007). Vitamin B12 sources and bioavailability. *Experimental Biology and Medicine*, 232(10), 1266–1274. <https://doi.org/10.3181/0703-MR-67>

SUPPORTING INFORMATION

Additional supporting information can be found online in the Supporting Information section at the end of this article.

How to cite this article: Roy, P., Deb, D., Suganya, A., Roy, B., Pradeep, T., & Saha, T. (2023). Endangered indigenous rice varieties as a source of B vitamins for the undernourished population. *Cereal Chemistry*, 1–8. <https://doi.org/10.1002/cche.10668>

Endangered indigenous rice varieties as a source of B vitamins for the undernourished population.

Priyabrata Roy^{a,b,*}, Debal Deb^{a,*}, Suganya Arunan^c, Brindaban Roy^d, Thalappil Pradeep^c, Tanima Saha^{b,*}

Supplementary table 1: Concentrations of seven B complex vitamins in 309 traditional rice landraces.

Sl. No.	Sample	Landrace Name	B ₁ (mg/100g)	B ₂ (mg/100g)	B ₃ (mg/100g)	B ₅ (mg/100g)	B ₆ (mg/100g)	B ₇ (mg/100g)	B ₁₂ (mg/100g)
1	AA03	Aash	1.17	0.31	1.09	2.88	0.15	0.06	N.D.
2	AA24	Abor Xali	0.11	0.16	1.82	1.87	0.15	0.06	N.D.
3	A13	Ahana	0.38	0.05	0.21	0.06	0.03	0.02	N.D.
4	AA08	Ajipa	1.54	0.28	1.37	2.32	0.10	0.05	N.D.
5	A01	Akshay Rani	1.42	N.D.	0.43	0.06	0.04	0.01	N.D.
6	AA16	Alta Pati	0.38	0.06	0.25	0.05	0.03	0.04	N.D.
7	A02	Amar-Sal	0.43	N.D.	1.13	0.06	0.01	0.01	N.D.
8	A08	Amit	0.58	0.12	0.86	1.08	0.05	0.01	N.D.
9	AA26	Ampakhi Bora	2.71	0.26	0.50	4.11	0.13	0.07	N.D.
10	AA23	Anandi	0.12	0.15	1.90	1.80	0.11	0.09	N.D.
11	AA21	Anandur Sanna	3.49	0.31	0.43	2.91	0.14	0.10	N.D.
12	A11	Artharayi	0.48	N.D.	N.D.	0.06	0.01	0.05	N.D.
13	A10	Arunurvadllu	3.67	N.D.	1.35	18.55	0.54	0.04	N.D.
14	AA31	Aryan	4.45	N.D.	1.13	1.36	0.07	N.D.	N.D.
15	AA01	Asanleya	1.09	0.32	1.26	0.48	0.10	0.05	N.D.
16	AA10	Ashphal	0.63	0.14	0.68	1.51	0.04	0.04	N.D.
17	AA05	Ashwin Jharia (P)	0.39	N.D.	0.25	0.16	0.02	0.02	N.D.
18	A04	Athi Karaya	0.50	0.01	0.46	0.07	0.02	0.01	N.D.
19	AA19	Aurar	1.64	0.47	3.00	1.49	0.29	0.04	N.D.
20	AA07	Ausha Bonkata	0.42	0.06	0.24	0.06	0.01	0.02	N.D.
21	B100	Bada Dhan	0.41	N.D.	0.90	0.06	0.02	0.02	N.D.
22	B22	Badabona	4.95	0.01	0.85	1.67	0.14	N.D.	N.D.

Sl. No.	Sample	Landrace Name	B ₁ (mg/100g)	B ₂ (mg/100g)	B ₃ (mg/100g)	B ₅ (mg/100g)	B ₆ (mg/100g)	B ₇ (mg/100g)	B ₁₂ (mg/100g)
23	B06	Bagh Jhapta	1.14	0.05	1.90	1.54	0.24	0.04	N.D.
24	B09	Baid Dhusuri	1.19	0.12	1.29	1.30	0.19	0.03	N.D.
25	B10	Baid Dulah	1.40	0.63	2.89	7.43	0.42	0.21	N.D.
26	B05	Baid Kalamkathi	0.53	0.08	0.62	0.47	0.06	0.01	N.D.
27	B14	Baidras	0.23	0.06	0.82	0.47	0.07	N.D.	N.D.
28	B21	Bakul Phool	0.01	0.02	N.D.	3.60	0.86	1.38	N.D.
29	B55	Balaram-Sal	1.14	0.15	1.51	1.32	0.16	0.03	N.D.
30	B02	Bank Chur	1.36	0.32	1.46	2.59	0.08	0.04	N.D.
31	B40	Bankui	0.64	0.29	0.94	3.13	0.10	0.08	N.D.
32	B65	Bankuli	3.56	0.34	0.48	3.54	0.13	0.12	N.D.
33	B49	Banmae Jo	1.46	0.17	1.96	1.19	0.14	0.01	N.D.
34	B38	Bansh Mugur	0.95	1.05	0.80	1.86	0.05	0.05	N.D.
35	B07	Bansh Pati	0.55	N.D.	0.25	0.13	0.03	0.03	N.D.
36	B24	Bansh Tara	8.32	0.09	0.94	3.13	0.13	0.11	N.D.
37	B60	Banya-Sal	0.28	N.D.	0.38	0.04	0.04	0.03	N.D.
38	B71	Basan Kayal	5.53	0.02	0.57	1.05	0.08	0.02	N.D.
39	B04	Basumati	1.23	N.D.	2.88	0.04	0.38	N.D.	N.D.
40	B81	Baya Gunda	1.12	0.25	1.88	1.07	0.14	0.02	N.D.
41	B30	Belgam Sanna	1.06	0.32	1.23	3.96	0.15	0.04	N.D.
42	B26	Benajhuri	0.39	0.02	0.72	0.05	0.03	0.03	N.D.
43	V25	Bhaboli Joha	0.42	0.06	N.D.	0.02	0.04	N.D.	N.D.
44	V04	Bhalki	1.26	N.D.	0.39	0.05	0.08	N.D.	N.D.
45	V10	Bhasa Kalmi	0.40	N.D.	N.D.	0.16	0.11	N.D.	N.D.
46	V13	Bheral	0.67	0.24	0.32	0.15	0.08	N.D.	N.D.
47	V27	Bhog Dhan	0.39	N.D.	N.D.	0.04	0.17	N.D.	N.D.
48	V19	Bhoglaya	0.84	0.31	2.86	1.51	0.29	0.03	N.D.
49	V07	Bhuri	1.34	0.08	1.12	0.99	0.05	0.03	N.D.
50	V23	Bhusihara	1.99	N.D.	1.14	0.03	0.07	N.D.	N.D.

Sl. No.	Sample	Landrace Name	B ₁ (mg/100g)	B ₂ (mg/100g)	B ₃ (mg/100g)	B ₅ (mg/100g)	B ₆ (mg/100g)	B ₇ (mg/100g)	B ₁₂ (mg/100g)
51	V20	Bhutta Churi	0.84	0.31	2.86	1.51	0.29	0.03	N.D.
52	B101	Biti Kaberi	1.04	0.27	1.34	4.42	0.18	0.06	N.D.
53	B75	Biti Dhadi Budda	2.75	0.19	2.49	0.42	0.30	0.04	N.D.
54	B57	Boddimani	1.14	0.15	1.51	1.32	0.16	0.03	N.D.
55	B90	Bogi Xali	1.91	0.18	1.08	1.16	0.11	0.01	N.D.
56	B20	Bokra	0.89	N.D.	2.84	0.03	0.44	N.D.	N.D.
57	B68	Boloi Genti	1.86	N.D.	0.70	0.05	0.03	0.02	N.D.
58	B87	Bor Jahingia	2.12	0.14	0.54	1.49	0.05	0.10	N.D.
59	B33	Bora	1.76	0.02	0.23	1.13	0.03	0.26	N.D.
60	B69	Bou Bhog	0.94	0.26	1.16	2.03	0.05	0.04	N.D.
61	B72A	Burma Black-A	2.75	0.19	2.49	0.42	0.30	0.04	N.D.
62	C34	Chakhaw Poireiton	0.40	N.D.	0.20	0.21	0.02	0.09	N.D.
63	C02	Chakramala	1.26	N.D.	0.43	0.05	0.01	0.05	N.D.
64	C14	Champa	0.70	N.D.	0.26	3.28	0.09	0.02	N.D.
65	C12	Chandrakanta	3.94	0.01	1.30	1.07	0.86	0.13	N.D.
66	C13	Cheena Kamini	0.97	0.18	1.32	1.16	0.12	0.05	N.D.
67	C06	Chenga	2.10	0.10	1.46	1.93	0.30	0.43	N.D.
68	C19	Chenga Rang	2.04	0.16	1.07	1.10	0.10	0.01	N.D.
69	C31	Chengeeran	0.26	N.D.	N.D.	0.05	0.02	0.10	N.D.
70	C07	Cheng-Sal	1.26	N.D.	0.45	0.07	N.D.	0.04	N.D.
71	C26	Chennellu	0.65	0.13	0.72	2.55	0.09	0.04	N.D.
72	CH03	Chhota	2.17	0.15	0.79	1.16	0.10	0.01	N.D.
73	CH01	Chhoto Nuniya	0.77	0.27	1.22	3.32	0.16	0.03	N.D.
74	C24	Chittiga	1.83	0.12	0.85	1.55	0.05	0.03	N.D.
75	C20	Chila Meteh	2.38	0.01	1.90	2.44	0.26	0.33	N.D.
76	C18	Chila Patnai	2.83	0.02	0.63	1.40	0.19	0.03	N.D.
77	C21	Chinna Poni	1.17	0.33	1.81	1.92	0.19	0.14	N.D.
78	C28	Choura Goda	1.29	0.01	3.05	4.02	0.42	N.D.	N.D.

Sl. No.	Sample	Landrace Name	B ₁ (mg/100g)	B ₂ (mg/100g)	B ₃ (mg/100g)	B ₅ (mg/100g)	B ₆ (mg/100g)	B ₇ (mg/100g)	B ₁₂ (mg/100g)
79	C09	Chumokathi	9.43	0.22	1.39	3.75	0.13	0.38	N.D.
80	D05	Dambar Salé	1.19	0.39	1.52	3.69	0.13	0.05	N.D.
81	DD02	Darka-Sal	4.82	N.D.	2.18	1.96	0.08	0.02	N.D.
82	DD06	Dar-Sal	1.07	0.19	1.57	1.75	0.17	0.01	N.D.
83	DD18	Dashra Mathiya	0.82	N.D.	0.32	16.89	0.14	0.01	N.D.
84	DD04	Dayal Madina	1.55	0.30	1.62	3.77	0.10	0.03	N.D.
85	DD05	Dehradun	1.22	0.02	1.56	2.94	0.33	0.07	N.D.
86	DD13	Dehradun-Bas	5.51	0.06	1.46	4.12	0.27	0.54	N.D.
87	DD10	Deulabhog	3.00	0.35	0.53	4.47	0.12	0.09	N.D.
88	D08	Dewri Baw	1.23	N.D.	0.40	0.03	0.02	0.05	N.D.
89	DH02	Dhanashree	0.77	N.D.	N.D.	0.04	0.02	0.11	N.D.
90	DX01	Dhankadi Deepa	3.21	0.46	0.62	3.70	0.15	0.08	N.D.
91	DH05	Dhowa-Sal	1.34	0.34	1.42	3.69	0.15	0.05	N.D.
92	DH04	Dhula Dhusuri	2.37	0.17	1.16	1.83	0.14	0.02	N.D.
93	DH01	Dhusuri	0.70	0.08	1.71	0.96	0.08	0.02	N.D.
94	DD30	Dodda Vallya	0.41	N.D.	1.34	0.04	0.03	0.02	N.D.
95	D10	Dokra Mesa	0.41	N.D.	0.50	0.05	0.02	0.02	N.D.
96	D06	Dopeh	0.81	0.24	0.96	3.17	0.10	0.03	N.D.
97	DD19	Dorangi	1.90	0.02	3.21	3.04	0.39	0.13	N.D.
98	DD16	Dudhe Bolta	10.55	0.05	1.56	4.24	0.26	0.50	N.D.
99	DD21	Dukhi Darbar	3.41	N.D.	0.55	3.30	0.11	N.D.	N.D.
100	DD26	Durga Sundari	1.43	0.13	0.32	0.84	0.04	0.03	N.D.
101	E04	Elchir	0.97	0.34	1.44	1.40	0.15	0.04	N.D.
102	G37	Gaada Dhan	0.97	0.20	1.98	1.32	0.14	0.02	N.D.
103	G19	Gandheswari	1.08	0.05	1.04	0.34	0.05	0.01	N.D.
104	G15	Garia	0.55	N.D.	N.D.	0.05	0.03	0.03	N.D.
105	G02	Garib-Sal	0.41	0.02	0.95	N.D.	N.D.	1.37	N.D.
106	G20	Garjo Joha	0.86	0.14	1.05	0.46	0.06	0.01	N.D.

Sl. No.	Sample	Landrace Name	B ₁ (mg/100g)	B ₂ (mg/100g)	B ₃ (mg/100g)	B ₅ (mg/100g)	B ₆ (mg/100g)	B ₇ (mg/100g)	B ₁₂ (mg/100g)
107	G06	Gentu	1.00	N.D.	0.30	0.07	0.03	0.29	N.D.
108	W03	Ghaiya	0.62	0.13	1.45	0.77	0.08	0.03	N.D.
109	W01	Ghasraiz	0.73	0.30	1.40	1.07	0.12	0.04	N.D.
110	W02	Ghasraji	0.73	0.30	1.40	1.07	0.12	0.04	N.D.
111	W05	Ghoi Bir	1.41	N.D.	0.36	1.33	0.06	N.D.	N.D.
112	W07	Ghunsi	1.02	0.38	2.79	0.56	0.20	0.03	N.D.
113	G32	Gidda Batha	1.00	0.24	1.05	1.90	0.08	0.04	N.D.
114	G43	Gidda Gowri	9.21	0.03	1.60	3.25	0.27	0.12	N.D.
115	G39	Gidhan Dhan	0.59	N.D.	2.84	0.02	0.40	N.D.	N.D.
116	G17	Gita	0.81	0.27	0.97	2.13	0.07	0.03	N.D.
117	G11	Gochari Patnai	0.92	0.22	1.14	1.75	0.06	0.23	N.D.
118	G12	Gopalbhog	1.65	0.87	3.70	9.45	0.56	0.25	N.D.
119	G35	Government Churi	0.62	0.07	0.66	0.25	0.06	0.01	N.D.
120	G44	Gulvady Sanna	1.19	0.15	1.43	0.97	0.14	0.06	N.D.
121	H07	Hagmuni	0.53	0.01	2.12	4.69	0.32	N.D.	N.D.
122	H14	Haldi Guri	0.11	0.51	2.16	4.50	0.29	0.06	N.D.
123	H10	Hanseswari	1.71	N.D.	0.22	0.01	0.04	0.03	N.D.
124	H27	Harfoni = Salpuna	1.03	0.17	0.93	0.23	0.09	0.01	N.D.
125	H04	Hari Shankar	1.25	0.06	1.55	3.74	0.35	0.26	N.D.
126	H21	Hati Dhan	0.81	0.08	0.84	0.61	0.04	0.01	N.D.
127	H18	Heerai Joha	0.45	N.D.	0.21	0.14	0.02	0.03	N.D.
128	H33	Hende Baba	0.40	N.D.	0.37	0.14	0.03	0.02	N.D.
129	H38	Hettalu Mnje	0.50	0.22	1.30	0.17	0.02	0.04	N.D.
130	H05	Hinche Saroo	2.61	0.02	1.55	0.81	0.29	0.08	N.D.
131	H22	Hudar	1.31	0.39	1.69	3.16	0.16	0.05	N.D.
132	J12	Jabra = Bor Dhan	0.02	0.32	1.97	2.60	0.21	0.05	N.D.
133	J18	Jagannath Bhog	1.15	N.D.	0.25	0.07	0.02	0.03	N.D.
134	J26	Jahingia	2.30	0.33	1.20	5.95	0.11	0.11	N.D.

Sl. No.	Sample	Landrace Name	B ₁ (mg/100g)	B ₂ (mg/100g)	B ₃ (mg/100g)	B ₅ (mg/100g)	B ₆ (mg/100g)	B ₇ (mg/100g)	B ₁₂ (mg/100g)
135	J30	Jarhan Baihar	0.38	N.D.	N.D.	0.05	0.03	0.06	N.D.
136	J15	Jata Leta-Sal	1.31	0.46	2.42	2.82	0.08	0.04	N.D.
137	Z10	Jhanti	1.34	0.19	0.80	0.56	0.04	0.01	N.D.
138	Z04	Jhuli (N)	1.30	N.D.	0.69	0.04	0.03	N.D.	N.D.
139	Z02	Jhuloor	1.62	0.11	0.44	0.74	0.05	0.02	N.D.
140	Z16	Jhulpo	3.65	0.17	0.55	1.63	0.12	0.06	N.D.
141	Z17	Jhumpuri	0.97	0.30	1.16	1.40	0.15	0.01	N.D.
142	Y02	Jugal	1.42	N.D.	N.D.	0.03	0.01	0.99	N.D.
143	J37	Juna Kolam	0.38	N.D.	0.27	0.05	0.01	0.02	N.D.
144	K136	Kaberi	0.71	N.D.	N.D.	0.06	0.16	0.02	N.D.
145	K50	Kabiraj-Sal	1.18	0.31	1.83	1.56	0.21	0.08	N.D.
146	K79	Kadaliya	0.07	0.72	2.22	2.46	0.19	0.03	N.D.
147	K87	Kaggi Salla	0.43	N.D.	0.39	0.07	0.03	0.02	N.D.
148	K43	Kajal Kathi	0.75	0.19	0.79	0.47	0.09	0.02	N.D.
149	K103	Kala Malli	0.03	0.09	1.21	1.07	0.10	0.02	N.D.
150	K126	Kala Namak	1.23	0.16	1.19	0.69	0.13	0.02	N.D.
151	K105	Kalam Dani	2.21	0.20	0.57	0.54	0.13	0.01	N.D.
152	K28	Kalam Kathi	0.25	0.07	0.62	0.79	0.04	0.01	N.D.
153	K144	Kaleswar	1.24	0.03	0.78	0.80	0.05	0.03	N.D.
154	K68	Kali Jira	0.88	0.10	1.15	0.68	0.09	0.02	N.D.
155	K13	Kali Komad	0.03	0.48	2.07	1.75	0.13	0.08	N.D.
156	K39	Kalishankar	1.06	0.21	0.78	0.54	0.10	0.02	N.D.
157	K71	Kalo Dhepa	1.28	0.89	3.20	4.80	0.35	2.10	N.D.
158	K49	Kalo Meteh	0.35	0.12	1.17	0.34	0.07	0.01	N.D.
159	K34	Kalo Nuniya	1.26	0.09	1.30	1.06	0.11	0.02	N.D.
160	K140	Kalo Tulsi	4.16	0.16	0.82	1.46	0.07	0.03	N.D.
161	K21	Kankhiri	0.57	N.D.	N.D.	0.53	0.01	0.06	N.D.
162	K45	Kankhria	0.89	0.15	1.44	0.85	0.08	0.05	N.D.

Sl. No.	Sample	Landrace Name	B ₁ (mg/100g)	B ₂ (mg/100g)	B ₃ (mg/100g)	B ₅ (mg/100g)	B ₆ (mg/100g)	B ₇ (mg/100g)	B ₁₂ (mg/100g)
163	K92	Kariga Javeli	1.26	N.D.	N.D.	0.03	0.03	0.15	N.D.
164	K77	Karni	0.63	0.22	0.80	2.11	0.10	0.10	N.D.
165	K33	Kartik-Sal	0.65	0.12	0.73	0.36	0.04	0.01	N.D.
166	K112	Kashi Phool (J)	1.42	N.D.	0.96	0.06	0.03	0.02	N.D.
167	K73	Kata Raini	1.44	0.17	0.59	0.49	0.03	0.01	N.D.
168	K100	Kba Lyngkot	1.02	0.16	1.94	0.93	0.11	0.04	N.D.
169	K94	Kempu Purigo Nelli	0.56	N.D.	0.22	0.07	0.02	0.12	N.D.
170	K31	Keshab-Sal	0.80	N.D.	0.21	0.09	0.02	0.06	N.D.
171	K151	Ketsari	0.03	0.42	2.43	2.34	0.13	0.05	N.D.
172	Q09	Kharisha Bhog	1.79	0.25	1.54	1.06	0.12	0.01	N.D.
173	Q06	Khatia Tika	2.07	N.D.	0.62	0.09	N.D.	0.05	N.D.
174	K115	Kokua Baw	0.37	0.61	N.D.	0.07	0.04	0.20	N.D.
175	K101	Kola Amona Baw	1.38	0.25	2.03	2.39	0.18	0.01	N.D.
176	K96	Koliya Lengri	1.18	N.D.	0.38	0.11	0.02	0.15	N.D.
177	K119	Kona Musori	1.31	N.D.	0.33	0.08	0.07	0.05	N.D.
178	K98	Koshi Kamon	1.65	0.20	0.57	0.28	0.06	0.02	N.D.
179	K147	Kotpe	0.58	N.D.	0.61	0.05	0.03	0.04	N.D.
180	K65	Kulthi Kayame	0.40	N.D.	0.50	0.08	0.02	0.02	N.D.
181	K24	Kumrogorh	0.65	0.32	0.82	2.70	0.11	0.09	N.D.
182	K131	Kundapullan	0.93	0.32	1.29	3.27	0.09	0.04	N.D.
183	K10	Kurai	1.02	0.16	1.94	0.93	0.11	0.04	N.D.
184	L43	Ladari	5.88	N.D.	1.92	3.78	0.17	N.D.	N.D.
185	L18	Lakshmi Chura	1.03	0.17	1.45	1.28	0.15	0.04	N.D.
186	L39	Lakshmi Kajal	0.51	N.D.	0.46	0.12	0.01	0.03	N.D.
187	L31	Lal Bahal	6.47	N.D.	2.40	0.02	N.D.	N.D.	N.D.
188	L50	Lal Dhan Patla	N.D.	N.D.	1.66	0.14	0.01	0.02	N.D.
189	L27	Lal Gobindabhog	1.17	0.31	1.92	1.91	0.21	0.14	N.D.
190	L02	Lal Jhulur	1.52	N.D.	N.D.	0.17	0.01	0.07	N.D.

Sl. No.	Sample	Landrace Name	B ₁ (mg/100g)	B ₂ (mg/100g)	B ₃ (mg/100g)	B ₅ (mg/100g)	B ₆ (mg/100g)	B ₇ (mg/100g)	B ₁₂ (mg/100g)
191	L34	Lal Kamal	0.39	N.D.	N.D.	0.05	0.01	0.06	N.D.
192	L24	Lal Kamini	0.90	0.08	1.61	4.83	0.10	N.D.	N.D.
193	L47	Lalu Dhan	0.57	N.D.	N.D.	0.05	0.01	0.01	N.D.
194	L45	Langka	0.82	N.D.	0.29	0.29	0.02	0.04	N.D.
195	L59	Lankeswari	1.42	N.D.	0.37	0.08	0.01	0.01	N.D.
196	L53	Laser	0.64	N.D.	N.D.	0.07	0.01	0.08	N.D.
197	L16	Lata-Sal	1.17	0.35	1.79	1.69	0.10	0.03	N.D.
198	L12	Lebu-Sal	0.64	0.17	1.62	1.00	0.08	0.04	N.D.
199	L09	Lohajangi	0.49	0.13	1.50	0.83	0.07	0.01	N.D.
200	L01	Lugdhi-Sal	0.89	N.D.	0.28	0.02	0.01	1.38	N.D.
201	M30	Maadu	0.40	N.D.	N.D.	0.04	0.02	0.02	N.D.
202	M09	Madhumita	3.68	0.34	0.45	2.88	0.14	0.11	N.D.
203	M38	Madhuri	0.42	0.10	0.94	0.33	0.02	0.01	N.D.
204	M17	Madraraj	0.43	0.07	0.87	0.50	0.02	0.02	N.D.
205	M02	Mahadi	0.57	0.23	2.11	0.51	0.11	0.02	N.D.
206	M04	Mala	0.33	2.63	1.26	2.25	0.18	0.07	N.D.
207	M36	Malabati	0.44	0.05	0.52	0.34	0.02	0.01	N.D.
208	M03	Malgudia Kalam	0.35	0.10	0.96	0.25	0.04	0.01	N.D.
209	M15	Mallika	0.13	0.33	1.29	2.00	0.15	0.05	N.D.
210	M82	Mami Dhan	0.76	N.D.	1.36	0.03	0.02	0.02	N.D.
211	M95	Mangu Gadi	0.38	N.D.	N.D.	0.15	0.02	0.02	N.D.
212	M74	Manipura Batta	1.10	0.31	2.38	1.07	0.19	N.D.	N.D.
213	M06	Marich Mukul	0.40	N.D.	N.D.	0.15	0.04	0.04	N.D.
214	M75	Maskati	1.06	0.36	2.31	2.70	0.16	0.01	N.D.
215	M33	Mathallaga	1.11	0.90	1.92	5.53	0.21	2.95	N.D.
216	M84	Mavilon	1.37	N.D.	0.36	0.23	0.01	0.03	N.D.
217	M63	Maw Thlen	0.83	N.D.	0.31	0.31	0.06	0.02	N.D.
218	M77	Meese Batta	2.01	0.19	0.35	1.11	0.03	0.03	N.D.

Sl. No.	Sample	Landrace Name	B ₁ (mg/100g)	B ₂ (mg/100g)	B ₃ (mg/100g)	B ₅ (mg/100g)	B ₆ (mg/100g)	B ₇ (mg/100g)	B ₁₂ (mg/100g)
219	M49	Mehdi	1.85	0.25	0.93	1.91	0.11	0.07	N.D.
220	M52	Melhitte	2.00	0.26	1.21	0.87	0.18	0.01	N.D.
221	M21	Mohanbhog	0.19	0.23	1.49	2.11	0.16	0.38	N.D.
222	M44	Mohannala	0.45	0.10	1.05	0.86	0.09	0.01	N.D.
223	M13	Mohanras	0.19	0.25	1.23	1.58	0.11	0.02	N.D.
224	M51	Moynaguri	1.02	0.28	4.05	1.50	0.19	0.02	N.D.
225	M59	Muttu Gulla	0.09.	N.D.	0.06	0.31	0.09	0.03	N.D.
226	N21	Nagaland Kalo	1.64	0.30	2.73	1.65	0.19	0.02	N.D.
227	N07	Nagra	1.45	0.21	3.69	1.23	0.18	0.06	N.D.
228	N14	Najirma	0.38	N.D.	0.45	0.27	0.02	0.02	N.D.
229	N42	Nalwa	0.46	N.D.	N.D.	0.16	0.01	0.20	N.D.
230	N18	Narahasoi	1.08	0.39	3.15	0.71	0.27	0.04	N.D.
231	N36	Nekera	1.07	0.23	1.88	0.98	0.24	0.01	N.D.
232	N32	Nellur Pisthal	0.23	N.D.	0.89	0.12	0.02	0.02	N.D.
233	N12	Nona	0.54	N.D.	1.23	0.17	0.01	0.22	N.D.
234	N29	Nona Khirish	1.50	0.33	1.59	1.27	0.15	0.03	N.D.
235	N19	Nona-Sal	2.02	0.38	1.64	1.31	0.15	0.02	N.D.
236	O01	Olee	0.39	N.D.	N.D.	0.28	0.02	N.D.	N.D.
237	O02	Orah	1.26	N.D.	N.D.	0.16	0.02	0.03	N.D.
238	P32	Paloi Thopa	2.20	N.D.	0.60	0.09	0.01	0.09	N.D.
239	P21	Panati	5.73	0.05	0.70	0.34	0.17	0.03	N.D.
240	P12	Panirui	0.57	N.D.	0.36	0.09	0.01	0.08	N.D.
241	P24	Paramita	1.81	0.17	0.70	1.61	0.05	0.01	N.D.
242	P29	Pateni	0.73	0.15	0.87	0.51	0.10	N.D.	N.D.
243	F02	Phul Mugri	1.40	N.D.	0.26	0.06	0.03	0.27	N.D.
244	P35	Pittasalé	0.43	0.05	N.D.	0.06	N.D.	0.05	N.D.
245	P40	Pusa Badh	0.99	0.25	1.26	0.73	0.14	0.03	N.D.
246	P05	Putikali	0.57	0.12	0.63	0.15	0.01	0.03	N.D.

Sl. No.	Sample	Landrace Name	B ₁ (mg/100g)	B ₂ (mg/100g)	B ₃ (mg/100g)	B ₅ (mg/100g)	B ₆ (mg/100g)	B ₇ (mg/100g)	B ₁₂ (mg/100g)
247	R14	Raban-Sal	1.40	N.D.	0.67	0.01	0.01	0.03	N.D.
248	R53	Radha Jugal	0.39	N.D.	N.D.	0.07	0.02	0.03	N.D.
249	R07	Radhuni Pagal	1.31	N.D.	0.26	0.06	0.12	N.D.	N.D.
250	R41	Raj Bako	0.49	N.D.	N.D.	0.06	0.02	0.05	N.D.
251	R02	Raj Jhinga	0.38	N.D.	N.D.	0.08	0.01	0.07	N.D.
252	R34	Raj Kamal	0.41	N.D.	0.87	0.02	0.01	0.27	N.D.
253	R31	Ramigali	0.39	N.D.	0.21	0.03	0.02	0.17	N.D.
254	R60	Ranga Dhan	0.40	N.D.	N.D.	0.04	0.04	0.75	N.D.
255	R25	Rani Akand	0.38	N.D.	N.D.	0.03	0.06	0.22	N.D.
256	R56	Rani Siyali	0.43	N.D.	N.D.	0.06	0.02	0.65	N.D.
257	R22	Rani-51	1.08	N.D.	0.56	0.04	0.09	0.52	N.D.
258	R48	Rassi	1.34	0.21	2.06	4.90	0.43	0.14	N.D.
259	R19	Ratnachuri	1.85	N.D.	0.28	0.02	0.01	0.23	N.D.
260	R29	Reda Dhan	0.12	0.56	1.95	2.94	0.20	0.10	N.D.
261	R28	Riso Nano Veronese	1.87	0.58	2.61	5.80	0.33	0.19	N.D.
262	S05	Sada Chenga	1.32	N.D.	0.70	0.05	0.06	0.02	N.D.
263	S21	Sada Dhan	0.87	0.24	0.81	0.50	0.05	N.D.	N.D.
264	S23	Sada Dhepa	1.42	0.28	1.56	1.53	0.10	0.03	N.D.
265	S43	Sada Jabra	0.52	N.D.	N.D.	0.04	0.03	0.86	N.D.
266	S01	Sada Kaya	1.92	0.23	1.02	1.24	0.10	0.02	N.D.
267	S39	Sada Meteh	5.34	0.14	0.32	2.63	0.14	0.32	N.D.
268	S36	Sada Mota	0.38	N.D.	N.D.	0.05	0.03	1.08	N.D.
269	S61	Salaer	5.18	0.01	1.08	17.17	0.21	N.D.	N.D.
270	S53	Sanna Bhatta	0.37	0.06	0.65	0.42	0.03	0.01	N.D.
271	S54	Sanna Vallya	0.02	N.D.	3.86	2.76	0.60	N.D.	N.D.
272	S76	Sarasbhog	0.38	N.D.	0.34	0.04	0.03	0.14	N.D.
273	S33	Saroo Gurguri	0.42	N.D.	0.60	0.02	0.05	0.51	N.D.
274	S16	Sateen	0.39	N.D.	1.35	0.01	0.01	0.66	N.D.

Sl. No.	Sample	Landrace Name	B ₁ (mg/100g)	B ₂ (mg/100g)	B ₃ (mg/100g)	B ₅ (mg/100g)	B ₆ (mg/100g)	B ₇ (mg/100g)	B ₁₂ (mg/100g)
275	SH08	Sesh Phal	0.51	0.16	1.24	0.56	0.05	0.01	N.D.
276	SH19	Shamla	2.65	0.21	0.90	0.90	0.10	0.04	N.D.
277	SH14	Shankari Komal	2.68	0.07	0.35	1.39	0.05	N.D.	N.D.
278	SS02	Shati Jeleh	0.43	N.D.	0.26	0.05	0.05	5.90	N.D.
279	SS04	Shatia Bhadoi	1.01	N.D.	4.52	0.07	0.05	0.27	N.D.
280	SH01	Shishaphal	1.83	N.D.	N.D.	0.04	0.03	0.07	N.D.
281	SH02	Shiuli	0.69	0.15	0.82	0.71	0.04	N.D.	N.D.
282	SH15	Shivappu Kuzhiadichan	0.61	0.57	0.75	4.05	0.11	0.14	N.D.
283	SH04	Shiyal Raj	0.38	N.D.	N.D.	0.04	0.03	4.09	N.D.
284	SH06	Shua Kalma	0.05	N.D.	N.D.	0.05	0.05	4.20	N.D.
285	S82	Sona Pan	0.46	0.02	0.24	0.05	0.02	0.26	N.D.
286	S15	Sonajhuli	0.77	0.26	1.80	1.31	0.16	0.02	N.D.
287	S47	Soorakurvai	0.40	N.D.	N.D.	0.03	0.06	0.07	N.D.
288	SH10	Srabanti-Sal	1.96	0.20	1.03	0.81	0.15	0.01	N.D.
289	S11	Subasita	1.13	0.12	0.40	0.67	0.01	0.01	N.D.
290	S09	Sundar Mukhi	0.08	N.D.	0.91	0.07	0.01	0.17	N.D.
291	S58	Supari	0.38	0.15	N.D.	0.03	0.09	0.14	N.D.
292	T01	Tangra Patnai	0.77	N.D.	0.30	13.57	0.12	0.02	N.D.
293	T08	Teloshing	0.39	N.D.	0.30	0.04	0.05	N.D.	N.D.
294	TX01	Thakur-Sal	0.39	N.D.	0.45	0.03	0.07	0.20	N.D.
295	TT15	Thavala Kannan	1.50	0.28	1.42	1.57	0.24	0.04	N.D.
296	TH04	Thevürti Lha	0.99	0.17	0.99	0.42	0.07	0.01	N.D.
297	TH05	Thonnuran	1.47	0.27	1.65	1.43	0.21	0.04	N.D.
298	TH07	Thonnuran Thondi	1.38	0.30	1.39	0.81	0.12	0.03	N.D.
299	TH03	Thupa Bora	2.68	N.D.	0.70	3.41	0.19	0.07	N.D.
300	TH01	Thupi-Sal	2.01	N.D.	0.23	0.03	0.06	N.D.	N.D.
301	T11	Tike Churi	0.11	0.20	2.19	0.64	0.09	0.03	N.D.

Sl. No.	Sample	Landrace Name	B ₁ (mg/100g)	B ₂ (mg/100g)	B ₃ (mg/100g)	B ₅ (mg/100g)	B ₆ (mg/100g)	B ₇ (mg/100g)	B ₁₂ (mg/100g)
302	T03	Tikia Patnai	0.81	N.D.	1.41	0.05	0.07	N.D.	N.D.
303	TT19	Tsorinyü	1.11	0.18	0.63	0.30	0.10	0.02	N.D.
304	TT16	Tulasi Xali	9.03	0.10	0.59	3.72	0.26	0.08	N.D.
305	TT09	Tulo Pajoy	1.92	N.D.	0.27	0.02	0.14	N.D.	N.D.
306	TT07	Tulsibhog	0.49	N.D.	1.95	0.03	0.05	N.D.	N.D.
307	V21	Vella Thondi	6.65	0.01	0.65	5.78	0.10	0.10	N.D.
308	B36	Vishnu Bhog	6.85	N.D.	2.29	0.01	N.D.	N.D.	N.D.
309	Y04	Yella Salli	0.80	0.24	1.67	1.21	0.15	0.02	N.D.

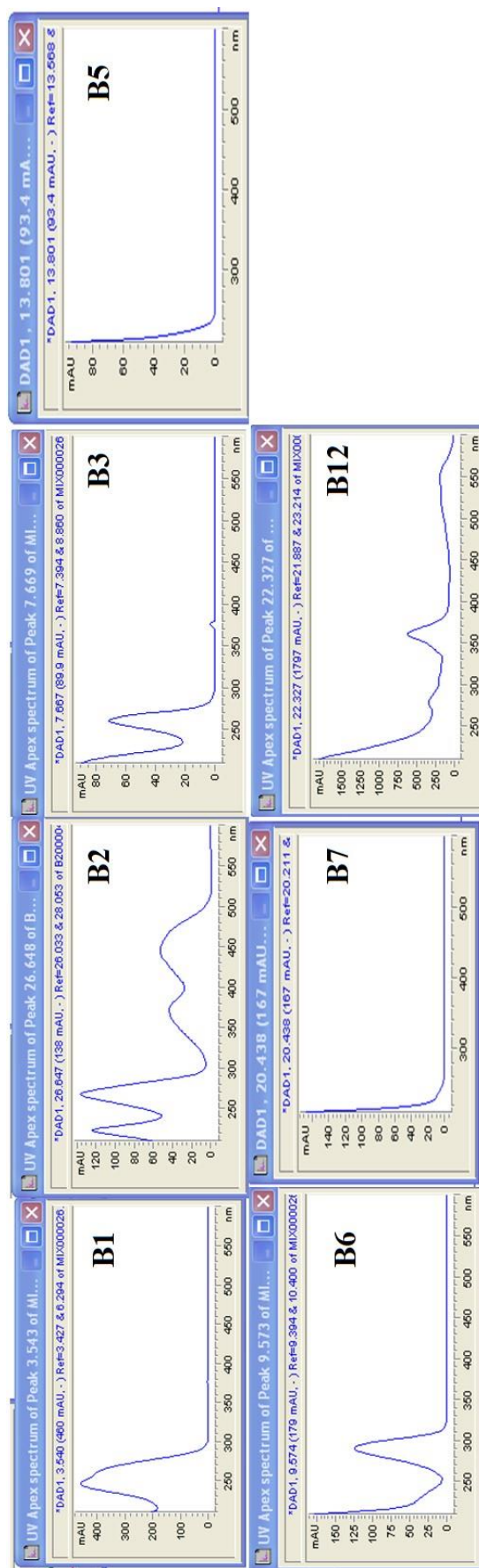
* Values are the mean of three determinations. N.D. Not detected.

Supplementary table 2: Concentrations of Seven B vitamins in 3 modern rice cultivars.

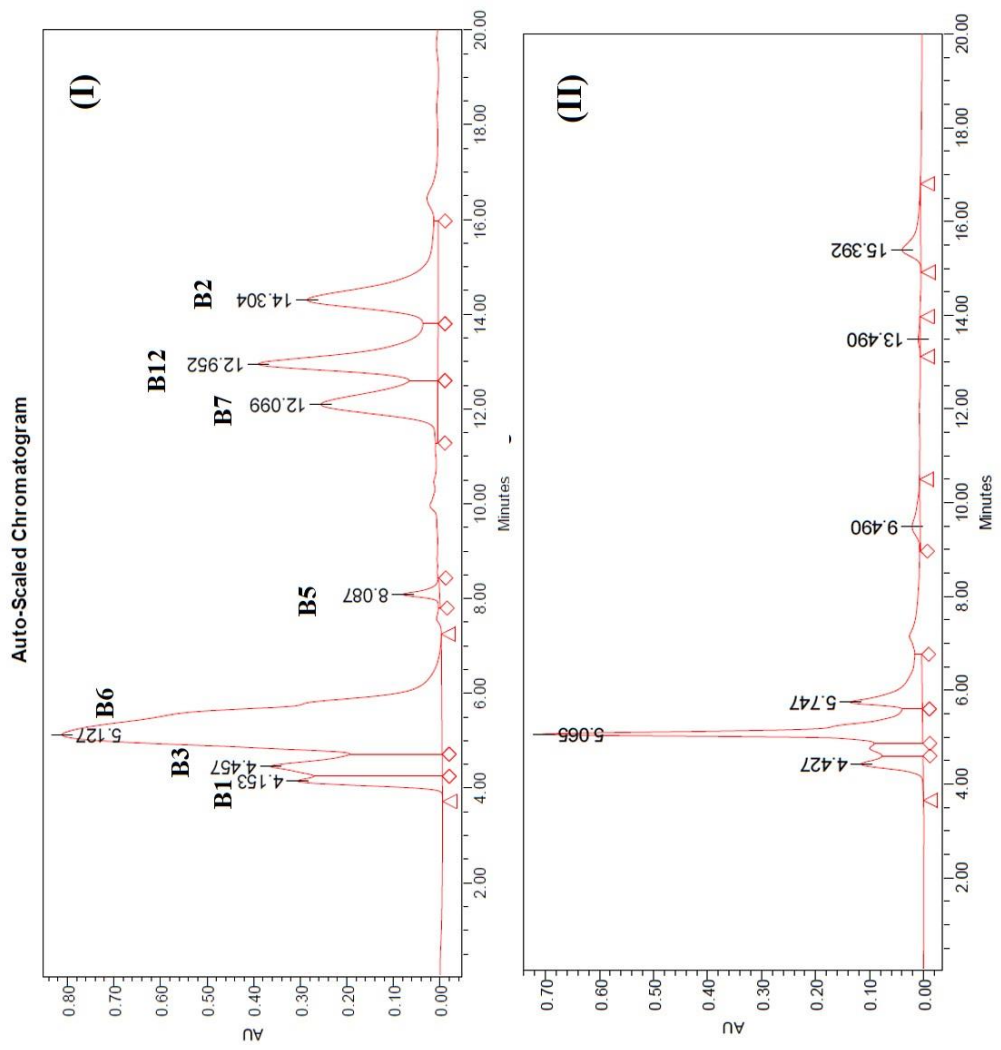
Sl. No.	Sample	Rice cultivars	B1 (mg/100g)	B2 (mg/100g)	B3 (mg/100g)	B5 (mg/100g)	B6 (mg/100g)	B7 (mg/100g)	B12 (mg/100g)
310	BPT5204	BPT5204	0.37	0.02	0.50	N.D.	N.D.	0.01	N.D.
311	IR36	IR 36	3.50	0.25	2.10	1.50	N.D.	0.30	N.D.
312	IR64	IR 64	0.41	0.08	2.90	N.D.	0.09	N.D.	N.D.

* Values are the mean of three determinations. N.D. Not detected.

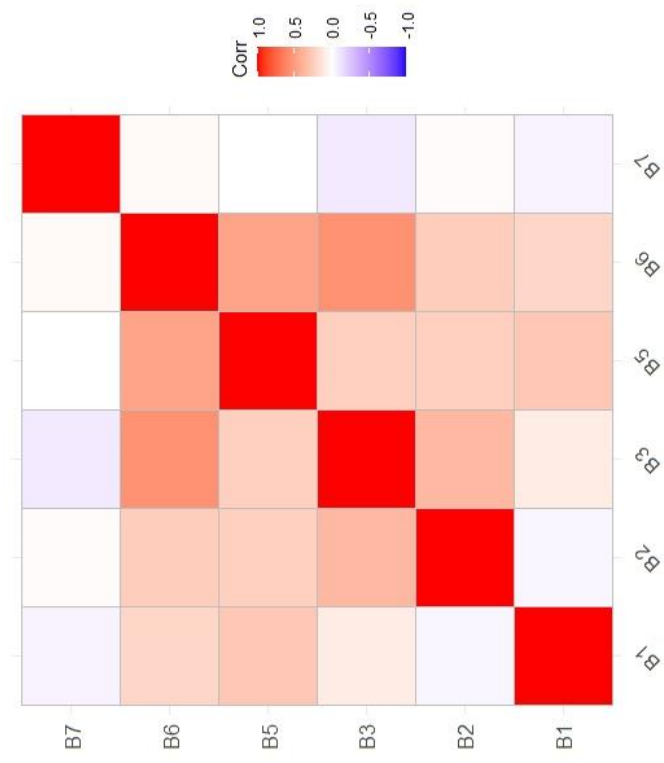
Supplementary figure 1: The UV spectrum of seven B vitamins was used to identify the individual vitamins from sample chromatograms.



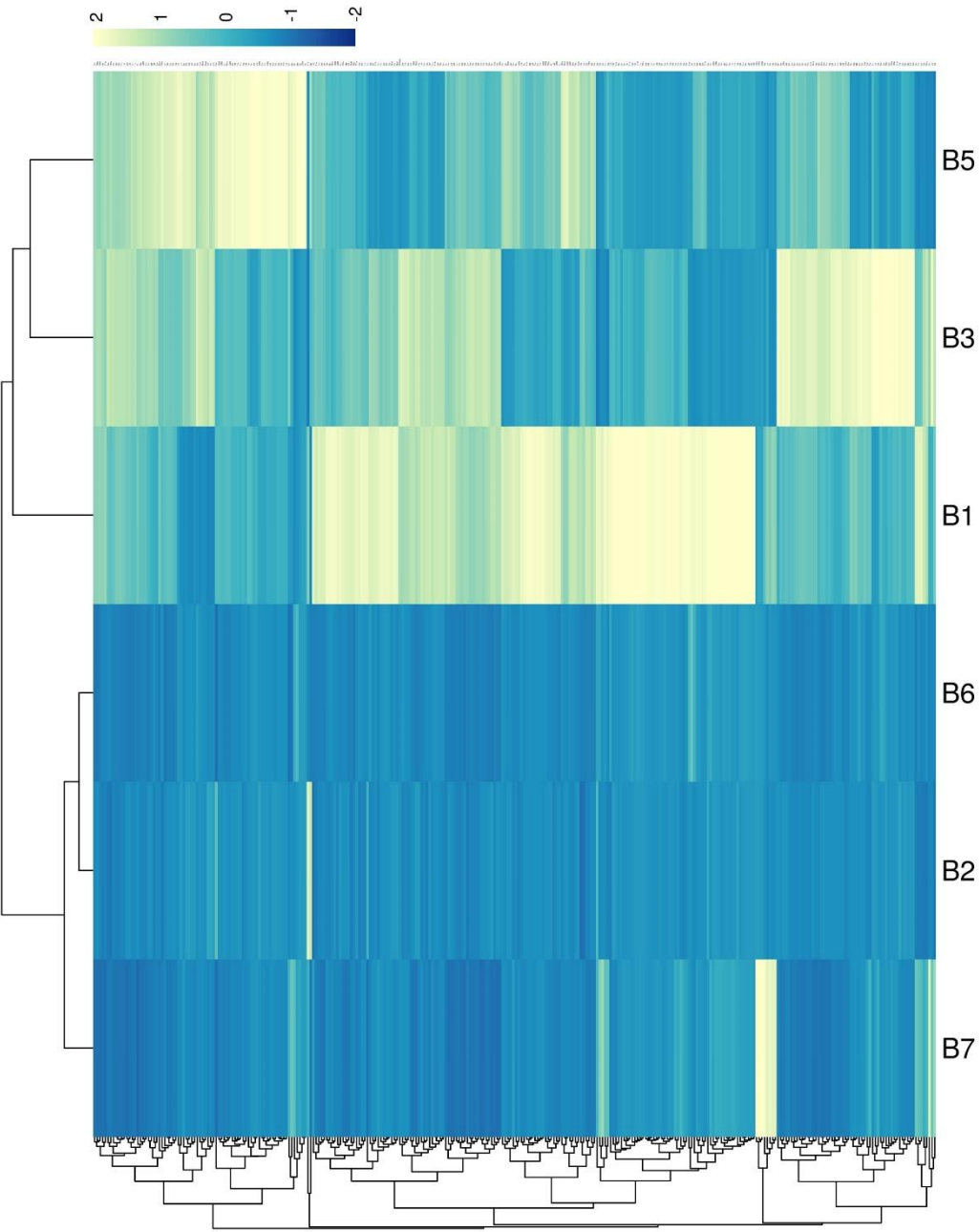
Supplementary figure 2: (I): The baseline separation of seven B vitamins by RP - HPLC and (II): the chromatographic separation of extracted B vitamins from G37 rice sample. RP - HPLC, reverse - phase - high - performance liquid chromatography.



Supplementary figure 3: Correlation heatmap plot of B vitamins among 309 traditional rice landraces.



Supplementary figure 4: The bidirectional heat - map analysis of the rice landraces based on phenotypic data of B vitamins.



Macropolyhedral $\text{syn-B}_{18}\text{H}_{22}$, the “Forgotten” IsomerDeepak Kumar Patel,[⊥] B. S. Sooraj,[⊥] Kaplan Kirakci, Jan Macháček, Monika Kučeráková, Jonathan Bould, Michal Dušek, Martha Frey, Christof Neumann, Sundargopal Ghosh,* Andrey Turchanin,* Thalappil Pradeep,* and Tomas Base*Cite This: <https://doi.org/10.1021/jacs.3c05530>

Read Online

ACCESS |



Metrics & More

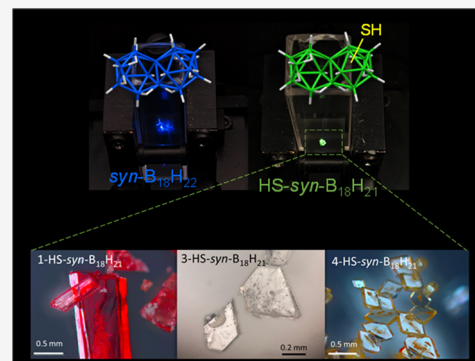


Article Recommendations



Supporting Information

ABSTRACT: The chemistry and physics of macropolyhedral $\text{B}_{18}\text{H}_{22}$ clusters have attracted significant attention due to the interesting photophysical properties of *anti-B* $_{18}\text{H}_{22}$ (blue emission, laser properties) and related potential applications. We have focused our attention on the “forgotten” *syn-B* $_{18}\text{H}_{22}$ isomer, which has received very little attention since its discovery compared to its *anti-B* $_{18}\text{H}_{22}$ isomer, presumably because numerous studies have reported this isomer as non-luminescent. In our study, we show that in crystalline form, *syn-B* $_{18}\text{H}_{22}$ exhibits blue fluorescence and becomes phosphorescent when substituted at various positions on the cluster, associated with peculiar microstructural-dependent effects. This work is a combined theoretical and experimental investigation that includes the synthesis, separation, structural characterization, and first elucidation of the photophysical properties of three different monothiol-substituted cluster isomers, [1-HS-*syn-B* $_{18}\text{H}_{21}$] **1**, [3-HS-*syn-B* $_{18}\text{H}_{21}$] **3**, and [4-HS-*syn-B* $_{18}\text{H}_{21}$] **4**, of which isomers **1** and **4** have been proved to exist in two different polymorphic forms. All of these newly substituted macropolyhedral cluster derivatives (**1**, **3**, and **4**) have been fully characterized by NMR spectroscopy, mass spectrometry, single-crystal X-ray diffraction, IR spectroscopy, and luminescence spectroscopy. This study also presents the first report on the mechanochromic shift in the luminescence of a borane cluster and generally enriches the area of rather rare boron-based luminescent materials. In addition, we present the first results proving that they are useful constituents of carbon-free self-assembled monolayers.



INTRODUCTION

As the search for new and unusual molecules and materials in various fields intensifies, boron hydrides emerge as fascinating candidates with properties substantially different from those of organic molecules.^{1–7} Among the boron hydrides, the structural motif of the deltahedron is the most common. A prominent position belongs to the icosahedron due to the exceptional stability and geometry of the $[\text{B}_{12}\text{H}_{12}]^{2-}$ dianion and its heteroatomic analogues, e.g., the 12-vertex carborane $[\text{C}_2\text{B}_{10}\text{H}_{12}]$.^{8,9} Most boron hydride molecules with a number of boron atoms fewer than 12 take the form of a simple convex deltahedron or its open fragment, and they can thus be viewed as analogues of cyclic hydrocarbons.¹⁰ For boron hydrides with more than 12 skeletal atoms, the structures of the so-called macropolyhedral boranes are formed by the fusion of two or more polyhedra or polyhedral fragments, analogous to polycyclic hydrocarbons.¹¹ Two of the largest known macropolyhedral boranes are the isomeric docosahydrooctadecaboranes $\text{B}_{18}\text{H}_{22}$.^{12,13} They exhibit a unique molecular structure with two open faces and six acidic bridging hydrogen atoms ($\mu\text{H-BB}$).^{14–16} Their structural and chemical properties, together with their interaction with light, make $\text{B}_{18}\text{H}_{22}$ a promising candidate for a wide range of applications, from energy storage,^{1,3} semiconductor doping,^{4,17–20} to nano- and optoelectronic devices.^{21–23} The molecular structure of $\text{B}_{18}\text{H}_{22}$ can be

viewed as two decaborane molecules condensed together, with each subcluster sharing atoms B(5) and B(6) in the decaborane numbering system, in common (Figure 1B,C). The isomer *syn-B* $_{18}\text{H}_{22}$ on which this study focuses is a much less-studied (“forgotten”) system compared to its *anti-B* $_{18}\text{H}_{22}$ isomer, and it has a 2-fold symmetry axis due to the fusion of two {B10} units sharing the B(5)–B(6) edge so that B(5)≡B(5′) and B(6)≡B(6′) (Figure 1B); in the *anti-B* $_{18}\text{H}_{22}$ isomer, B(5)≡B(6′) and B(6)≡B(5′), which results in the inversion symmetry (Figure 1C).^{15,16,24} What has stimulated most of the recent interest in *anti-B* $_{18}\text{H}_{22}$ and its substituted derivatives has mainly been their luminescence properties.^{25–38} Our interest in the “forgotten”, nonluminescent isomer, *syn-B* $_{18}\text{H}_{22}$, has been stimulated mainly by its unique geometry and size with respect to its use as constituents of purely borane, carbon-free self-assembled monolayers and its further use toward 2-dimensional membranes³⁹ with thickness below 1 nm and with a 3D-aromatic

Received: May 26, 2023

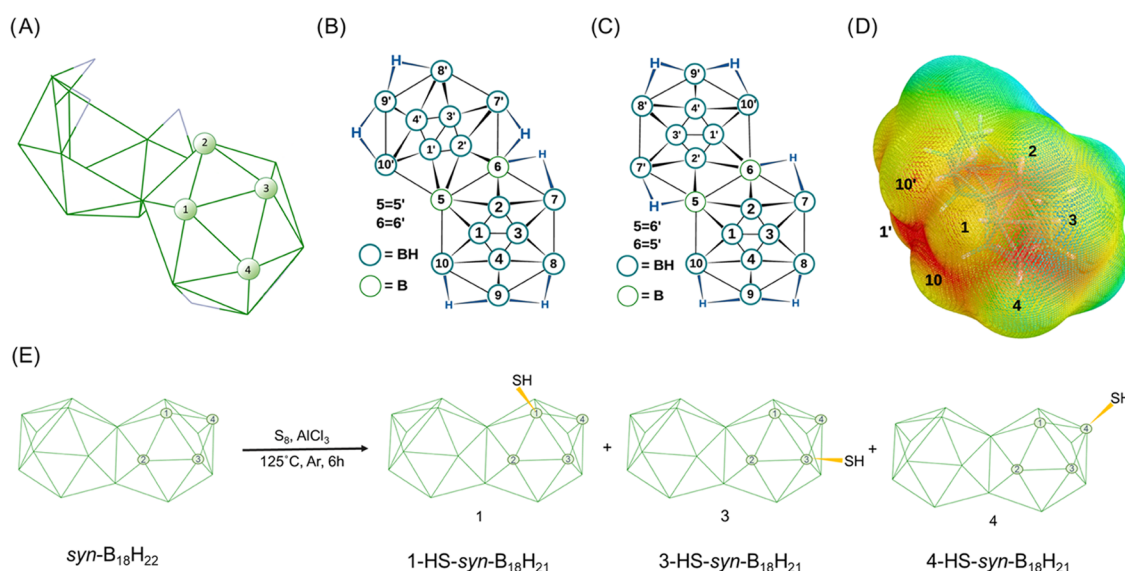


Figure 1. (A) Schematic of *syn*-B₁₈H₂₂ with partial numbering on one of the two subclusters. (B, C) Complete numbering systems of *syn*-B₁₈H₂₂ and *anti*-B₁₈H₂₂, respectively, in their net-like representation. (D) Electrostatic potential map of *syn*-B₁₈H₂₂ with selected BH vertices numbered. On the color scale, red shows areas with the highest negative potential, localized mainly in between vertices 1, 3, and 4. The red part in between the vertices 1', 10, and 10' represents the negative pole of the molecule. (E) Schematic of the synthesis of the three HS-*syn*-B₁₈H₂₁ isomers of *syn*-B₁₈H₂₂.

character, as well as capping ligands of atomically precise metal nanoclusters, a newly emerging class of materials with adjustable geometry, size, and properties.^{40,41}

Previously, we reported the thiol derivatives of decaborane (*nido*-B₁₀H₁₄), specifically [1-HS-*nido*-B₁₀H₁₃], [2-HS-*nido*-B₁₀H₁₃], and [1,2-(HS)₂-*nido*-B₁₀H₁₂] as reactive building blocks for self-assembled monolayers (SAMs).^{42,43} Although the macropolyhedral cluster *anti*-B₁₈H₂₂ has been extensively explored over the last decade, for various applications including lasers⁷ and semiconductor dopants,^{4,18,19} the *syn*-B₁₈H₂₂ isomer has remained relatively unexplored, perhaps due to its supposed lack of luminescence. For numerous reasons mentioned foregoing, we have synthesized three new monothiol-substituted derivatives: [1-HS-*syn*-B₁₈H₂₁] **1**, [3-HS-*syn*-B₁₈H₂₁] **3**, and [4-HS-*syn*-B₁₈H₂₁] **4**. We have found interesting interactions in the supramolecular structures, observed the changes in the molecular structure caused by substitution at different vertices, and, surprisingly and interestingly, observed luminescence not only in the novel thiol derivatives but also in the parent *syn*-B₁₈H₂₂ molecule, which, until now, has been presented in various reports^{7,26} as the nonluminescent isomer of *anti*-B₁₈H₂₂. Also, we have observed that substitution affects its photophysical properties extensively. The *syn*-B₁₈H₂₂ cluster functionalization thus promises new directions for novel materials with a range of properties and uses.

Boron hydrides as functional molecules, going beyond alkanethiols in their structural diversity for self-assembled monolayers (SAMs), are potentially very interesting and stable 2D materials for filtration technology due to their symmetry, limited conformational flexibility, well-defined, and different to-carbon-chemistries and other unique aspects such as thickness, and porosity adjusted in the subnanometer range or extraordinary thermal and chemical stability.^{42–48} These engineered cage molecules may interact in different ways to provide control over surface interactions.^{44,49} The advantage of boron hydrides as building blocks of SAMs over many linear chain systems is that simple cage molecules do not exhibit domain boundaries caused by the orientation of molecular tilt,

with respect to the surface normal.^{42,45,47} The first boron cage, Cs₂[B₁₂H₁₁SH], was employed to study SAMs on gold surfaces in 1998.⁴⁷ Mercapto-functionalized cage molecules provided great control over surface responses, a higher order of supramolecular assembly, and eventually a precise three-dimensional assembly over a surface.^{42,45,47} However, the SAMs of boron hydrides still remain much less explored than those of alkanethiol derivatives, and macropolyhedral borane derivatives assembled on metal or other substrate surfaces have not been investigated yet. Keeping all of this in mind, we delved into the world of macropolyhedral boron hydrides, explored the HS functionalization of *syn*-octadecaborane, and investigated the impact of these modifications on its physical and chemical properties, together with the first preliminary view of these molecules as building blocks of carbon-free SAMs on a flat metal surface.

RESULTS AND DISCUSSION

Three thiol isomers of the octadecaborane cluster [1-HS-*syn*-B₁₈H₂₁] **1** (two polymorphic structures labeled as PM1a and PM1b), [3-HS-*syn*-B₁₈H₂₁] **3**, and [4-HS-*syn*-B₁₈H₂₁] **4** (two polymorphs labeled PM4a and PM4b) were synthesized directly from *syn*-B₁₈H₂₂ by heating it with sulfur in the presence of anhydrous aluminum trichloride for 6 h at 125 °C under an Ar atmosphere. The crude product contained a mixture of monothiolated isomers and unreacted *syn*-B₁₈H₂₂, and these were all separated using standard chromatography on a silica gel column with diethyl ether as the eluent. The separated products were crystalline, with many single crystals suitable for X-ray diffraction. Three isomers were structurally resolved by X-ray diffraction (Figure 2), with two of the isomers found to be in two polymorphic structures. All of these results gave us a very good possibility to look at the effect of substitution on the parent *syn*-B₁₈H₂₂ molecular structure as well as to investigate the molecular packing of these isomers in order to set a basis for further investigation toward the origin of their luminescent properties.

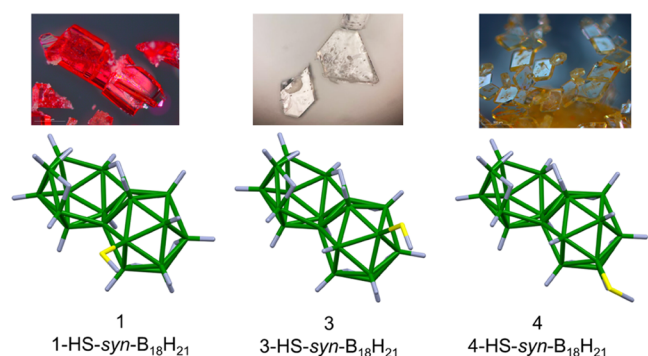


Figure 2. X-ray determined structures of three synthesized thiol isomers of *syn*-B₁₈H₂₂.

Molecular Structure, the Effect of a Substituent. All of the three isomers **1**, **3**, and **4** were prepared in quantities ranging from a few tens to hundreds of milligrams. Isomer **4** was dominating the crude product, but chromatography and crystallization from diethyl ether yielded many well-developed single crystals of all three and two of them in two polymorphic forms. Crystallization experiments from diethyl ether yielded all three isomers pure, and they were further characterized using ¹H and ¹¹B NMR, MS, IR, and X-ray studies. Computational analysis of the electrostatic potential map suggests that the thiol (HS-) group might substitute positions B1, B2, B3, and B4 of the *syn*-B₁₈H₂₂ cluster due to the relatively high negative charge localization in that part of the molecule (Figure 1D). Conformational analysis and mutual comparison of the respective energies of all four isomers and their most stable conformers also do not show significant differences, and isomer 3-*HS-syn*-B₁₈H₂₁ seems to be even more stable than isomer 4-*HS-syn*-B₁₈H₂₁ (Figure 3). Experimentally, we have found that thiol substitution follows the order B4 > B1 ≅ B3, and, interestingly, we have not observed the 2-*HS-syn*-B₁₈H₂₁ isomer.

The molecular composition of the thiol derivatives was confirmed by the positive ion mode ESI-MS analysis. The monocationic species with the mass value centered at *m/z* 248.3152 was identified as HS-B₁₈H₂₁, while the *m/z* value at 216.3422 corresponds to B₁₈H₂₁, which can be attributed to the loss of an HS fragment (Figure S28). The introduction of a thiol

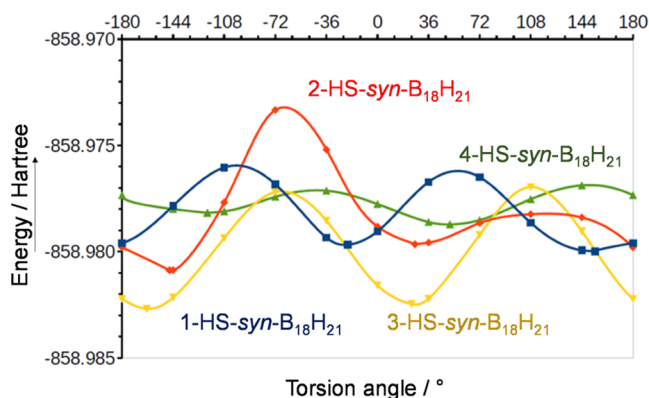


Figure 3. Plot of energies of various HS-rotamers for all four computationally analyzed HS-*syn*-B₁₈H₂₁ isomers. Torsion angles were defined as positive in the B(1)-B(2)-B(3)-B(4) direction, between atoms B(2)-B(1)-S(1)-H(S) for isomer **1**, B(6)-B(2)-S(2)-H(S) for the experimentally unobtained isomer **2**, B(2)-B(3)-S(3)-H(S) for **3**, and B(1)-B(4)-S(4)-H(S) for **4**.

(HS-) group to B₁₈H₂₂ breaks the twofold symmetry as manifested in its ¹¹B{¹H} NMR spectra by the splitting of the peaks that had intensity 2 in the parent compound. The resonance of the substituted boron atom is easily identifiable in comparison to the decoupled ¹¹B{¹H} spectrum⁵⁰ with the simple coupled ¹¹B one as a third singlet in addition to the peaks of boron vertices 5 and 6. The thiol group causes a deshielding of the substituted atom and moves its peak around 10 ppm downfield; the effect of the substitution on other boron atoms is weaker and more complex (Figure 4). Unsurprisingly, the NMR signals of the atoms of the unsubstituted subunit (numbers with prime) are, in general, less affected than those of the substituted subunit (labeled by simple numbers), often observed at positions almost unchanged from the parent borane. One remarkable exception is position 2, which is very little affected by the substitution in all our compounds, where in **3** the peak of 2' is shifted upfield more than that of position 2. The calculation of the NMR spectra at the DFT level (Table S2) reproduces well only the most prominent features of the spectra, often failing to capture the more sophisticated ones, and several times even the relative positions of the peak of an atom of the substituted subunit (*n*) with respect to its symmetry counterpart from the unsubstituted subunit (*n'*) differ between the calculation and the experiment (Figures S11, S17, and S24). Additionally, FT-IR spectroscopy corroborates the structure of isomers **1**, **3**, and **4** (Figure S29). A strong band at ~2560 cm⁻¹ can be attributed to the terminal B-H and SH stretching vibrations. Another strong band at about 1490 cm⁻¹ is characteristic of the bridging μ-BHB vibrations.

Single-crystal X-ray diffraction (SC-XRD) investigation of all five thiol isomers/polymorphs of HS-*syn*-B₁₈H₂₁, structures **1** (PM1a and PM1b), **3**, and **4** (PM4a and PM4b), reveal the positions of all of the heavier elements (B and S) in the compound. After refining the heavier atoms anisotropically, the remaining electron-density map reveals all of the hydrogen atoms in the cluster. After isotropic hydrogen atom refinement, the maximum electron-density peak for the thiol hydrogen atoms was near the sulfur atom; however, the final refinement was done with a riding model. Both the [1-*HS-syn*-B₁₈H₂₁] **1** and [4-*HS-syn*-B₁₈H₂₁] **4** isomers were found to exist in two polymorphic structures PM1a, PM1b and PM4a, PM4b, respectively. Although the 18-vertex cage structure of the parent *syn*-B₁₈H₂₂ remains intact after thiolation, a more detailed comparative analysis of the interatomic distances and angles of all six single-crystal structures, **1** (PM1a, PM1b), **3**, and **4** (PM4a, PM4b), and the parent *syn*-B₁₈H₂₂ demonstrates that the presence of the thiol substituent produces an obvious effect on the clusters' geometry (see Table 1). This effect is difficult to spot if we look at a local vertex to adjacent vertex distances in close proximity to the substitution. However, as shown in Figure 5, we here selected geometrical parameters that cover the accumulation of small changes across the whole molecules, such as the *d*(B₉-B₉) distance, or related angles that reflect the changes in mutual orientation of the two 10-vertex subclusters, and we can thus demonstrate and evaluate the substituents' effect on the molecular structure. The substitution at position 3 of *syn*-B₁₈H₂₂ has a significant effect on isomer 3-*HS-syn*-B₁₈H₂₁ **3**. The distances between the respective centroids, *c*₁-*c*₂, as well as between the vertices from opposite ends of the molecule, B(9)-B(9'), increased compared to the parent *syn*-B₁₈H₂₂. Intramolecular angles α and β, specified in Figure 5, also showed expansion as the direct consequence of the substitution (for detail, see Figure S35), causing a change in the cage geometry,

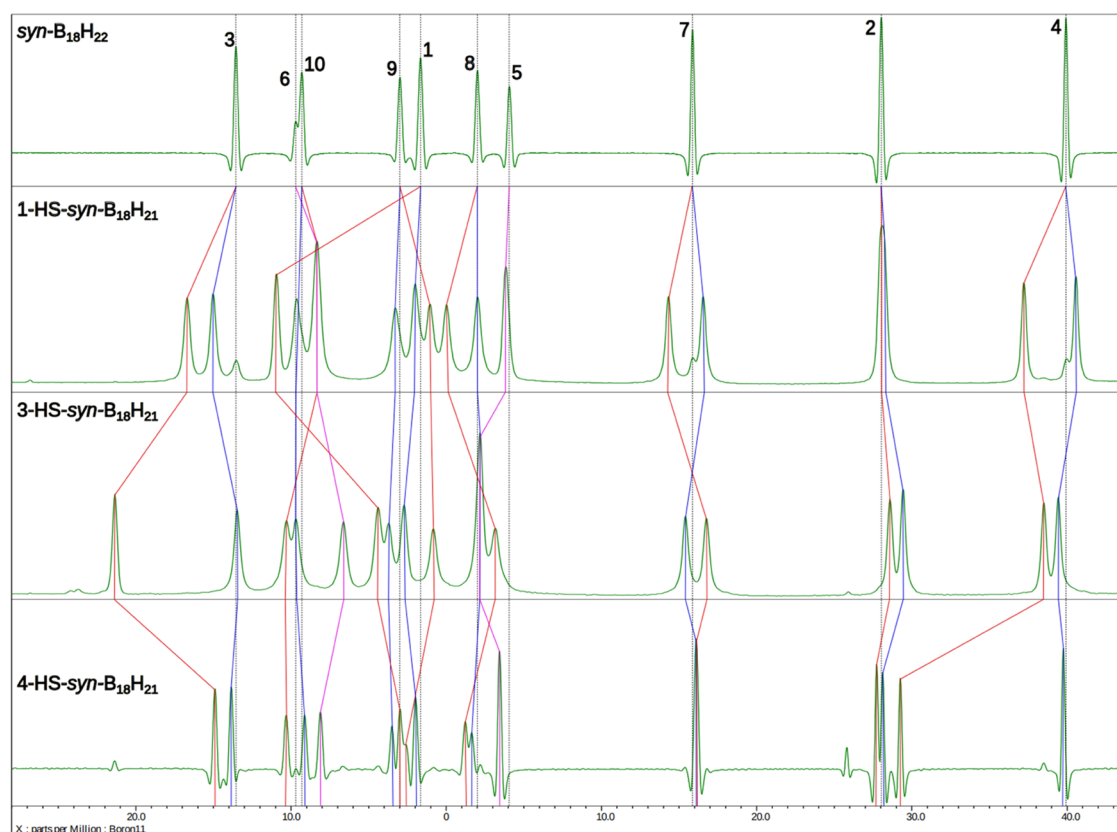


Figure 4. Experimentally decoupled $^{11}\text{B}\{^1\text{H}\}$ NMR spectra of *syn*- $\text{B}_{18}\text{H}_{22}$ and HS-*syn*- $\text{B}_{18}\text{H}_{21}$ isomers.

Table 1. Selected Centroid Distance [\AA] (c_1 : Centroid of 10 B Atoms Representing One Subcluster of the *syn*- $\text{B}_{18}\text{H}_{22}$ Cage, c_2 : Centroid of 10 B Atoms of Another Fused Borane Cage), Intracage $d(\text{B}_9\cdots\text{B}_{9'})$ Bond Distance [\AA], and Bond Angle for [1-HS-*syn*- $\text{B}_{18}\text{H}_{21}$] 1 (PM1a and PM1b), [3-HS-*syn*- $\text{B}_{18}\text{H}_{21}$] 3, and [4-HS-*syn*- $\text{B}_{18}\text{H}_{21}$] 4 (PM4a and PM4b) with Comparison Data of *syn*- $\text{B}_{18}\text{H}_{22}$

isomers/PMs	$d(c_1\cdots c_2)$		$d(\text{B}_9\cdots\text{B}_{9'})$		$\alpha(\text{B}_{10}\text{B}_5\text{B}_{10'})$		$\beta(\text{B}_9\text{B}_6\text{B}_9')$	
	expt.	cal.	expt.	cal.	expt.	cal.	expt.	cal.
<i>syn</i> - $\text{B}_{18}\text{H}_{22}$	3.332	3.312	6.343	6.298	126.02	127.50	125.97	127.07
1-HS- <i>syn</i> - $\text{B}_{18}\text{H}_{21}$ (PM1a)	3.342	3.318	6.370	6.299	129.53	128.50	128.52	127.64
1-HS- <i>syn</i> - $\text{B}_{18}\text{H}_{21}$ (PM1b)	3.334	3.318	6.348	6.299	127.85	128.50	126.78	127.64
3-HS- <i>syn</i> - $\text{B}_{18}\text{H}_{21}$	3.452	3.314	6.383	6.301	130.18	127.73	128.96	127.18
4-HS- <i>syn</i> - $\text{B}_{18}\text{H}_{21}$ (PM4a)	3.330	3.314	6.345	6.300	128.44	127.40	128.20	127.14
4-HS- <i>syn</i> - $\text{B}_{18}\text{H}_{21}$ (PM4b)	3.330	3.314	6.356	6.300	127.94	127.40	127.57	127.14

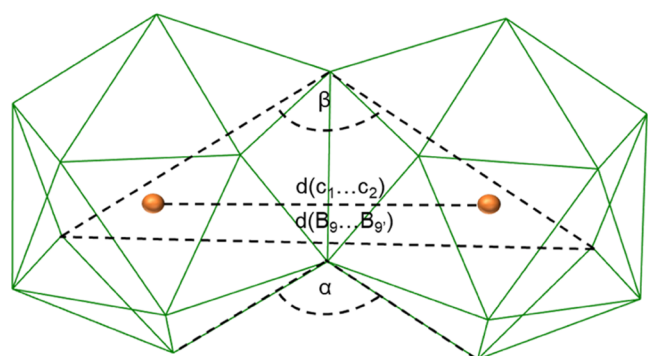


Figure 5. Schematic illustration of selected distances and bond angles of *syn*- $\text{B}_{18}\text{H}_{22}$ and its thiol derivatives.

which may be disadvantageous for the stability of the cluster and responsible for the lower yields of isomers 1 and 3 compared to

that of isomer 4 (Table 1). All of the above changes in distance between centroid c_1 – c_2 , intracage $\text{B}(9)$ – $\text{B}(9')$, and intracage cage angle (α and β) are due to the accumulation of small changes in the B–B bond length of the cage (for more detail, see Table S5).

Supramolecular Structure. The successful X-ray diffraction analysis of five different single crystals provided sufficient data for the investigation of intermolecular interactions. In all of the synthesized thiol isomers, the respective sulfur atoms bear high electron densities and show interactions with the acidic bridging hydrogen atoms, μ -BHB, which manifest their presence by strong bands at about 1490 cm^{-1} in the IR spectra. In addition to their acidic nature, *i.e.*, the bridging hydrogen atom bearing a relatively high positive charge, it was interesting to see the supramolecular structures and how this interaction influences the orientation of the clusters. Figure 6 shows four out of five of the analyzed structures, and in all of them, the $-\text{S}(\text{H})\cdots\mu\text{-BHB}$ interaction dominates the packing forces. In the

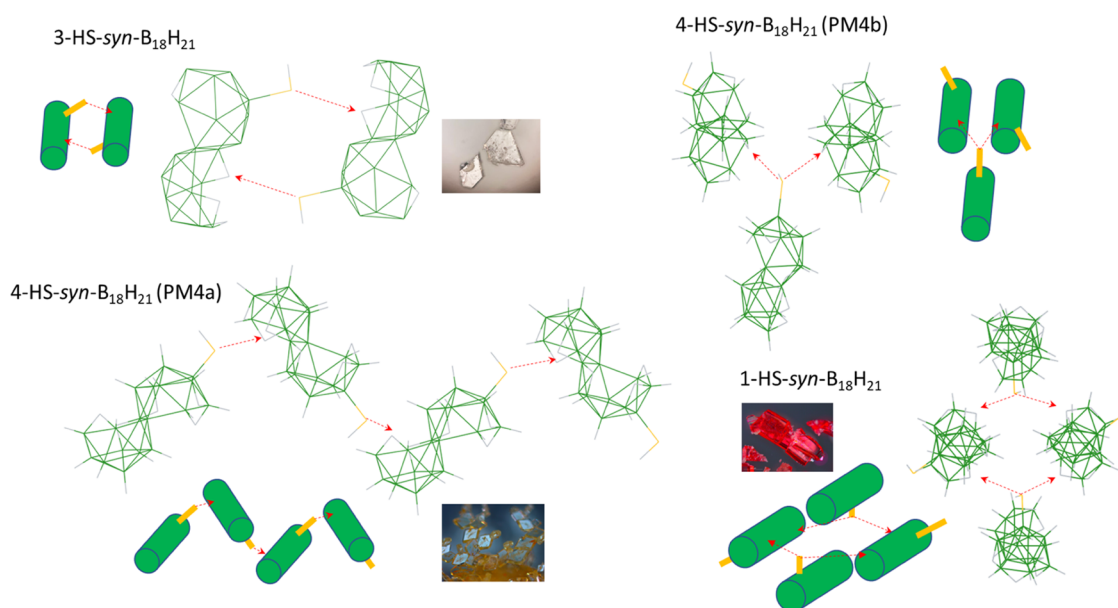


Figure 6. $-S(H)\cdots\mu H-BHB$ interaction observed in the supramolecular structures of $HS-syn-B_{18}H_{21}$ isomers/polymorphs.

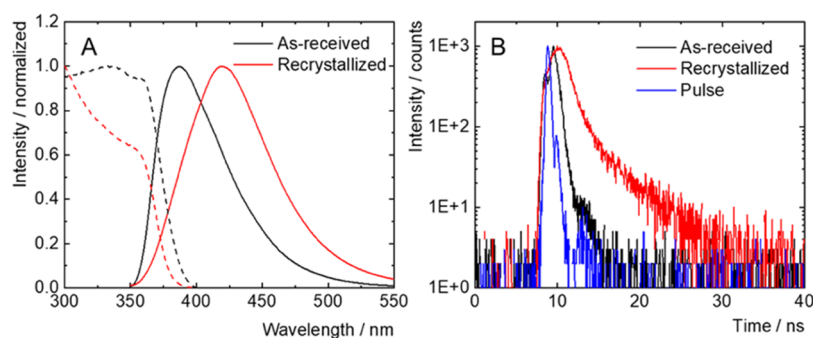


Figure 7. Normalized emission spectra (plain lines) of as-received $syn-B_{18}H_{22}$ (black) and recrystallized $syn-B_{18}H_{22}$ (red) excited at 380 nm in the air atmosphere; normalized excitation spectra (dashed lines) recorded at the maximum of emission (A). Fluorescence decay kinetics of $syn-B_{18}H_{22}$ in the air atmosphere, excited at 402 nm, recorded at the maximum of emission (B).

single-crystal supramolecular structure of isomer 3- $HS-syn-B_{18}H_{21}$ **3**, this interaction leads to a pair of molecules directly connected by two such interactions. The sulfur atom of the substituted subcluster shows an interaction with the bridging hydrogen atoms of the unsubstituted subcluster of another molecule. This isomer was found only in one polymorphic form. In comparison, the most preferred isomer 4- $HS-syn-B_{18}H_{21}$ **4** exhibits a similar interaction in which the sulfur atom of one molecule interacts with the bridging hydrogen atoms of another molecule to form a zigzag chain or, in a second polymorph of this isomer, the sulfur atom shows an interaction with the bridging hydrogen atoms of two other molecules, leading to a fork-like arrangement. Both supramolecular structures are easy to distinguish. The last isomer, 1- $HS-syn-B_{18}H_{21}$ **1**, shows two very similar polymorphic structures in which the sulfur atom also interacts with the bridging hydrogen atoms of two other molecules in such a way that it resembles wooden logs. The existence of different polymorphic structures can therefore be rationalized as a result of this specific interaction, $-S(H)\cdots\mu-BHB$, between sulfur and some of the six similar bridging hydrogen atoms per molecule of each isomer. In addition to influencing the packing of molecules in their respective SC supramolecular structures, this interaction also explains the difference between the parent $syn-B_{18}H_{22}$ and all three thiolated

isomers in the differential thermal analysis (Figure S30). While the parent $syn-B_{18}H_{22}$ shows complete loss of mass due to sublimation, all three thiol isomers sublime off at slightly higher temperature and only partly, 20–40%. The remaining 60–80% of the starting material turns into highly involatile blackish material. The lower volatility of the thiolated isomers compared to $syn-B_{18}H_{22}$ can be attributed particularly to this $-S(H)\cdots\mu-BHB$ interaction. One related issue is the HS -hydrogen atom and its orientation, as the hydrogen is not directly involved in this structure-determining interaction between the sulfur of the HS group and the bridging hydrogen, $\mu-BHB$, and is left to either exhibit a weak interaction with terminal BH vertices or be left to free conformation, which corresponds to computationally optimized minima.

Luminescence Properties. Borane compounds possess fascinating photophysical properties such as stimulated emission, thermochromism, or singlet oxygen photosensitization.^{7,25,28,33,34,36,51} We were therefore tempted to investigate the photophysical properties of the prepared borane compounds. In contrast to the remarkable fluorescence efficiency of *anti*- $B_{18}H_{22}$ in hexane ($\phi_L \sim 1$), its $syn-B_{18}H_{22}$ isomer has been reported to be nonemissive in solution.²⁹ However, our measurement of the as-received powder of $syn-B_{18}H_{22}$, precursor to the thiolated boranes, showed an intense fluorescence in the

solid state with a maximum at 385 nm, a quantum yield of 0.17, and an amplitude average lifetime of 0.4 ns (Figure 7 and Table 2). Interestingly, the recrystallization of *syn*-B₁₈H₂₂ from a

Table 2. Photophysical Properties of *syn*-B₁₈H₂₂ and *anti*-B₁₈H₂₂ in the Solid State at Room Temperature^a

sample	λ_L (nm)	ϕ_L	τ_L (ns)
<i>syn</i> -B ₁₈ H ₂₂ ^b	385	0.17	0.4
<i>syn</i> -B ₁₈ H ₂₂ ^c	420	0.20	1.6
<i>anti</i> -B ₁₈ H ₂₂ ^c	420	0.78	6.5

^a λ_L , luminescence maximum ($\lambda_{exc} = 340$ nm); τ_L , amplitude average lifetimes ($\lambda_{exc} = 402$ nm) measured at 420 nm; ϕ_L , luminescence quantum yields ($\lambda_{exc} = 340$ nm, experimental error of ϕ_L is ± 0.01).

^bAs-received. ^cRecrystallized diethyl ether/hexane mixture.

diethyl ether/hexane mixture provided homostructural single crystals that displayed fluorescence with a maximum at 420 nm, a quantum yield of 0.20, and an amplitude average lifetime of 1.6 ns (Figure 7 and Table 2). For both samples, the excitation spectra were characterized by broad absorption bands in the UV-A region (Figure 7A). Thus, *syn*-B₁₈H₂₂ displays aggregation-induced fluorescence, and its photophysical parameters are microstructure-dependent. For comparison, solid *anti*-B₁₈H₂₂, recrystallized from a diethyl ether/hexane mixture, displayed a fluorescence band with maximum at 420 nm, an emission quantum yield of 0.78, and a lifetime of 6.5 ns, significantly higher than for *syn*-B₁₈H₂₂ (Figure S33 and Table 2).

Single crystals of the thiolated boranes were measured on a single-crystal X-ray diffractometer to ensure their crystallographic purity, and they were then used for photophysical characterizations, the results of which are summarized in Table 3. Upon excitation at 380 nm, single crystals of 1, 3, and 4

Table 3. Photophysical Properties of Crystals of the Thiolated Boranes at Room Temperature^a

sample	λ_L (nm)	ϕ_L	τ_L (μ s)
1-HS- <i>syn</i> -B ₁₈ H ₂₁	582, 465 ^b		14, 5.2 ^b
3-HS- <i>syn</i> -B ₁₈ H ₂₁	535		8.8
4-HS- <i>syn</i> -B ₁₈ H ₂₁	570	0.06	40
4-HS- <i>syn</i> -B ₁₈ H ₂₁ ^c	490	0.02	2.2

^a λ_L , luminescence maximum ($\lambda_{exc} = 380$ nm); τ_L , amplitude average lifetimes ($\lambda_{exc} = 380$ nm) measured at the maximum of emission; ϕ_L , luminescence quantum yields ($\lambda_{exc} = 380$ nm, experimental error of ϕ_L is ± 0.01). ^bShoulder. ^cAfter grinding.

displayed broad luminescence bands in the green/yellow region, with the respective maxima at 582, 535, and 570 nm (Figure 8). Interestingly, isomer 1 possessed a shoulder near its main emission band located in the blue region, which might be caused by additional emissive excited states. The excitation spectra recorded at the maximum of emission revealed broad absorption bands in the UV-A region (Figure 8A). Analysis of the luminescence decay kinetics recorded at the emission maximum evidenced amplitude average lifetimes of 14, 8.8, and 40 μ s for isomers 1, 3, and 4, respectively (Figure 8B). Thus, the thiolation of *syn*-B₁₈H₂₂ causes a bathochromic shift of the emission maximum and a decrease in luminescence efficiency. In addition, it leads to a switch from fluorescence to phosphorescence due to an increased intersystem crossing from singlet excited to triplet excited states, as already reported for iodinated or thiolated *anti*-B₁₈H₂₂ (Figure 8).^{37,52}

Isomer 4 was obtained in sufficient quantity and crystallographic purity (Figure S38) to allow for a complete study of the luminescent properties as single crystals and the powdered sample resulting after grinding. Upon the grinding of the single crystals, a hypsochromic shift of the emission band was observed, with a shift of the luminescence maximum from 570 to 490 nm (Figure 9A). The corresponding emission quantum yield decreased from 0.06 to 0.02, and the emission amplitude average lifetime decreased from 40 to 2.2 μ s (Figure 9B). Passing a flow of argon or oxygen through the powdered sample did not affect the emission lifetime, indicating the absence of quenching of the emissive triplet states by oxygen, a process often observed for phosphorescent dyes (Figure S31). It should be noted that this is the first report of a mechanochromic shift of the luminescence band of a borane cluster. Such a phenomenon has already been observed for phosphorescent copper-iodide complexes of the cubane-type, and it was attributed to a relaxation of the intramolecular distances upon grinding, thereby affecting the luminescent properties.⁵² In our case, the mechanochromic shift probably has a similar origin, as it is well known that the luminescent properties of borane compounds are dependent on their structure, which is affected by their environment.⁵² Finally, the luminescent properties of *syn*-B₁₈H₂₂ and the thiolated boranes were studied in hexane, where they showed very weak fluorescence ($\phi_L < 0.01$), with maxima spanning from UV-A up to the green region of the spectrum and with a lifetime in the low nanosecond range (Table S4 and Figure S32). Overall, the strong dependency of the luminescent properties of these boranes on their environment allows for

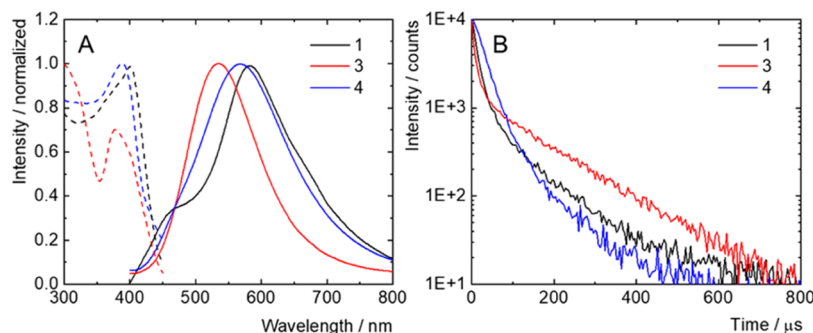


Figure 8. Normalized emission spectra (plain lines) of single crystals of 1, 3, and 4 excited at 380 nm in the air atmosphere; normalized excitation spectra (dashed lines) recorded at the maximum of emission (A). Phosphorescence decay kinetics of single crystals of 1, 3, and 4 in the air atmosphere, excited at 380 nm, recorded at the maximum of emission (B).

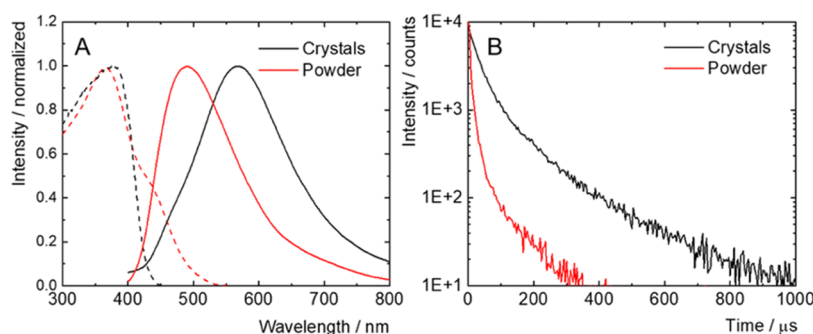


Figure 9. Normalized emission spectra (plain lines) of single crystals (black) and powder (red) of **4**, excited at 380 nm in an air atmosphere; normalized excitation spectra (dashed lines) recorded at the maximum of emission (A). Phosphorescence decay kinetics of single crystals (black) and powder (red) of **4** in an air atmosphere, excited at 380 nm, recorded at the maximum of emission (B).

peculiar behaviors, which may further deepen the interest in this class of photoactive compounds.

Self-Assembled Monolayers on Silver Surfaces, XPS

Analysis. Self-assembled monolayers (SAMs) of the isomer [4-*HS-syn-B₁₈H₂₁*] **4** on silver substrates were prepared by vapor deposition in ultra-high vacuum (UHV). The successful formation of these carbon-free SAMs was investigated using X-ray photoelectron spectroscopy (XPS). Figure 10A shows the

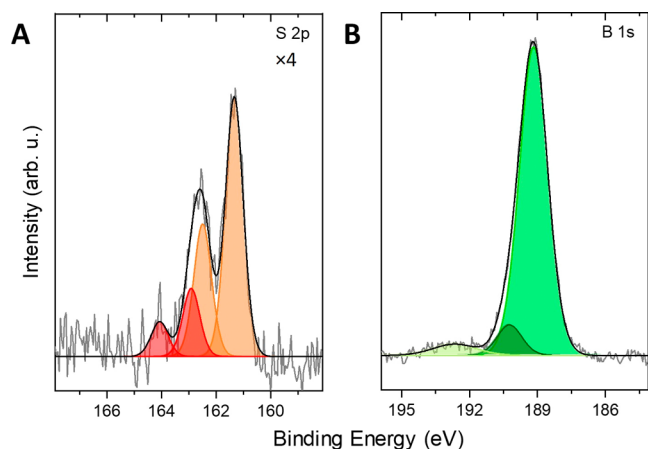


Figure 10. High-resolution S 2p (A) and B 1s (B) X-ray photoelectron spectra of the SAM formed by vacuum vapor deposition of isomer [4-*HS-syn-B₁₈H₂₁*] **4** on a Ag substrate. For better visualization, the S 2p spectrum is multiplied by a factor of 4.

high-resolution S 2p spectrum consisting of a main doublet (orange) with the binding energy (BE) of the S 2p_{3/2} and S 2p_{1/2} components at 161.3 and 162.5 eV, respectively, due to the formation of thiulates. The signal is accompanied by another doublet at the BE values of S 2p_{3/2} and S 2p_{1/2} at 162.9 and 164.1 eV, respectively (red). The formation of this additional sulfur signal can be attributed to the partial formation of disulfides during the self-assembly or to the presence of some physisorbed thiol molecules integrated into the monolayer *via* hydrogen bridge bonds. Both signals are shifted by ~0.5 eV to lower BE values in comparison to the published values for boron-bound thiulates (typical values of S 2p_{3/2} at about 161.7 eV) and disulfides, or thiols, with the typical values of S 2p_{3/2} electrons at 163.0 eV.^{53,54} This indicates higher electron density on sulfur in [4-*HS-syn-B₁₈H₂₁*] **4**, as also evidenced by the value of the ¹H NMR chemical shift at about 1.4 ppm and indirectly also from the above-reported short-contact interactions with the acidic bridging hydrogen atoms.

In the B 1s spectrum, the main component (green) is found at a BE value of 189.1 eV with the full width at half-maximum of 1.5 eV, which corresponds to B–B bonds in the cluster (Figure 10B). This peak is accompanied by a shoulder at a BE of 190.2 eV (dark green), which we assign to the boron atom attached directly to sulfur in the B–S bonds. At 192.6 eV, a broad low-intensity peak due to aromatic shake-ups is visible. No other XP signals, with the exception of the metallic Ag substrate, were detected (see Figure S34) in the samples. Especially the absence of carbon and oxygen confirms the formation of high-quality, carbon-free SAM on the silver surface. The thickness was calculated to be 7 ± 2 Å and the B/S ratio to 19 ± 1:1, matching very well to the molecular structure and nominal stoichiometry of the isomer [4-*HS-syn-B₁₈H₂₁*] **4**. Figure 11 further shows the steric requirements (both lateral and longitudinal) of all three synthesized isomers and shows the theoretically enabled range in the subnanometer thickness of the respective SAMs.

CONCLUSIONS

We have investigated the *syn-B₁₈H₂₂* isomer, the “forgotten” isomer of the long-established *B₁₈H₂₂* molecule.^{12,15,24} The more intensely studied *anti-B₁₈H₂₂* isomer has been recently recognized for its lasing properties.⁷ Several previous studies^{7,26} stated that the *syn*-isomer is nonluminescent, and thus comparatively little attention has been paid to it over the last decade compared to *anti-B₁₈H₂₂* boron hydride. In this study, we have demonstrated that not only does the parent compound have luminescence properties in its crystalline form but also that the HS-substituted isomers, (1-*HS-syn-B₁₈H₂₁*) **1**, (3-*HS-syn-B₁₈H₂₁*) **3**, and (4-*HS-syn-B₁₈H₂₁*) **4**, show luminescence both in their crystalline form and in solution. Within our systematic investigation of the HS-derivatives of *syn-B₁₈H₂₂*, we have aimed to use this molecule to reach our goal for the preparation of carbon-free self-assembled monolayers. Additionally, we have focused on monothiolated isomers of *syn-B₁₈H₂₂* as constituents that enable us to adjust SAM thicknesses below 1 nm, depending on which vertex bears the HS group. In total, we have prepared five new crystal structures, as two of the isomers, isomers 1-*HS-syn-B₁₈H₂₁* and 4-*HS-syn-B₁₈H₂₁*, were found to exist as two polymorphs. The packing of the molecules in the respective supramolecular structures of all of the isomers was commonly found to exhibit *-S(H)⋯μBHB-* interactions, and these give rise to the existence of different crystal polymorphs. We have also observed the substituent effect on the structure in comparison with the parent *syn-B₁₈H₂₂* molecule. Changes of interboron distances adjacent to the substituent are too subtle to be

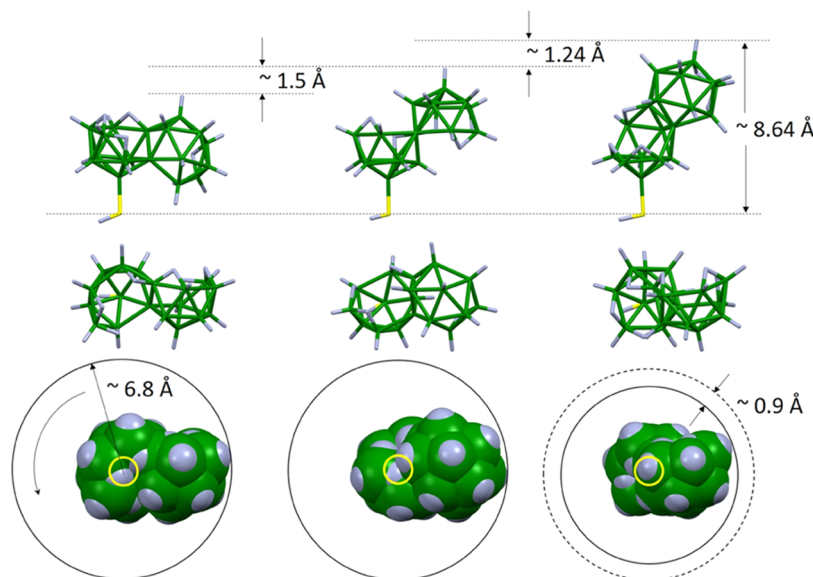


Figure 11. All three isomers are oriented with the HS group downward (top row), the respective top view (middle), and the space-filling projections (also top view). The yellow circle represents the position of the sulfur atom. Circles around the space-filling models show the lateral space requirement of the molecules rotating along their B–S axis.

apparent, but they become more obvious when we measure the effect on geometrical parameters effectively encompassing the whole molecule, as a whole, *i.e.*, on the distance between the centroids of the two subclusters of *syn*-B₁₈H₂₂, or on the distance between vertices from the opposite ends of the molecule, such as B(9)–B(9′). Such substituent metrics have also been estimated in terms of the overall cluster volume,^{28,32} and it is anticipated that *syn*-B₁₈H₂₂ with other substituents should also modify the photophysical properties. This study lays a solid foundation for further work in this direction.

EXPERIMENTAL SECTION

General Procedure and Instrumentation. All of the experiments were performed under an inert (argon, Ar) atmosphere using the standard Schlenk-line vacuum technique. Prior to use, all of the solvents were dried with sodium-benzophenone ketyl and distilled under an Ar atmosphere. Chloroform-*d* was purchased from ACROS Organic (Thermo Scientific Chemicals). Starting *syn*-B₁₈H₂₂ was purchased from Katchem s.r.o., Czech Republic, and used as received. Other chemicals, such as anhydrous aluminum trichloride and sulfur, were purchased from Fluka. The chromatographic separations were performed using a silica gel column. NMR spectra were recorded on a 600 MHz JEOL NMR spectrometer. Chemical shifts were analyzed with reference to the solvent (δ = 7.26 ppm, CDCl₃, 600 MHz, 295K) and boron (δ = 0 ppm, relative to BF₃(OEt)₂) in CDCl₃, 192.6 MHz, 295 K for the ¹H and ¹¹B{¹H} NMR spectra, respectively. Mass spectrometry measurements were performed on a Thermo Scientific LCQ Fleet Ion Trap instrument using ESI with helium (5.0 Messer) as a collision gas in the ion trap. The sample was dissolved in acetonitrile (concentration ~100 ng/ml) and introduced through a fused-silica sample tube of 0.100 mm (inner S-9 diameter) × 0.19 mm (outer diameter) to the ion source from a Hamilton syringe using infusion at 15 μ L/min, a source voltage of 5.47 kV, a tube lens voltage of −44.71 V, a capillary voltage of −23.06 V, a capillary temperature of 165.01 °C, and N₂ (isolated from air in NitroGen N1118LA, Peak Scientific) as a nebulizing sheath gas (flow rate 14.97 p.d.u.). Only negative ions of the respective molecular peaks were detected. IR spectra in the region from 4000 to 400 cm^{−1} (with a resolution of 4 cm^{−1}) were measured using the Nexus 670 FT-IR firmy Thermo Electron Corporation with an ATR Smart iTX equipped with a diamond crystal. Total number of scans: 192, spectrometer detector: DTGS KBr, beam splitter: KBr. The

thermal analysis of the samples was performed using Setsys Evolution 1750 (Setaram) equipped with an MS detector QMG 422 (Pfeiffer).

Compound Synthesis. [1-*HS-syn*-B₁₈H₂₁] **1** (PM1a and PM1b), [3-*HS-syn*-B₁₈H₂₁] **3**, and [4-*HS-syn*-B₁₈H₂₁] **4** (PM4a and PM4b). Under an inert atmosphere of Ar, *syn*-B₁₈H₂₂ (4.4 g, 20 mmol), sulfur (1.25 g, 39 mmol), and AlCl₃ (3.8 g, 29 mmol) were placed in a 500 mL round-bottom flask and heated with stirring to 125 °C. After 15 minutes of heating, the reaction mixture melted to form a brown liquid. The stirring continued for 6 h. The reaction mixture was then left to cool to room temperature, 250 mL of hexane was added, and then it was kept under an Ar atmosphere overnight. The reaction mixture was then cooled in an ice bath, and 50 mL of distilled water was added dropwise into the reaction mixture, followed by 10 mL of hydrochloric acid (10% v/v). The product was then gently stirred using a glass rod. The solution turned orange, with brownish solid particles at the bottom of the flask. The solution was filtered, and the filtrate was extracted with hexane (4 × 100 mL). The collected hexane fractions (slightly orange solution) were dried with MgSO₄ and filtered, and the solvent was evaporated under reduced pressure on a rotary evaporator. All three isomers were then separated using column chromatography on silica gel with diethyl ether as the eluent. The yield was ~50 mg of isomer 1-*HS-syn*-B₁₈H₂₂ **1**, ~30 mg of 3-*HS-syn*-B₁₈H₂₂ **3**, and ~230 mg 4-*HS-syn*-B₁₈H₂₂ **4**.

MS (ESI⁺). *m/z* calculated for HS-B₁₈H₂₁ monocationic species: 248.3148 experimentally found 248.3152.

NMR for [1-*HS-syn*-B₁₈H₂₁] **1.** ¹¹B{¹H} NMR (192.6 MHz, 295 K, CDCl₃): B3 (16.7 ppm) > B3′ (15.0 ppm) > B1 (10.9 ppm) > B10′ (9.6 ppm) > B10 (8.3 ppm, according to the B10–B5 cross peak 8.6 ppm) > B6 (8.3 ppm, according to the B6–B2, B2′ cross peak 8.3 ppm) > B9′ (3.3 ppm) > B1′ (2.0 ppm) > B9 (1.0 ppm) > B8 (0.0 ppm) > B8′ (−2.0 ppm) > B5 (−3.8 ppm) > B7 (−14.3 ppm) > B7′ (−16.6 ppm) > B2 (−28.1 ppm, according to the B2–B1 and B2–B3 cross peaks: −28.0 ppm on the *x*-axis, −27.9 on the *y*-axis) > B2′ (−28.1 ppm, according to the B2′–B3′ and B1′–B2′ cross peaks: −28.4 ppm on the *x*-axis, −28.3 on the *y*-axis) > B4 (−37.2 ppm) > B4′ (−40.6 ppm).

Crystal Data for PM1a. Empirical formula = B₁₈H₂₂S₁, *M*_r = 248.8, monoclinic, space group P21/c, *a* = 10.0437 (6) Å, *b* = 11.3556 (6) Å, *c* = 13.8050 (8) Å, α = 90°, β = 108.575 (5)°, γ = 90°, *V* = 1492.47 (15) Å³, *Z* = 4, ρ_{calc} = 1.1073 g/cm³, μ = 1.536 mm^{−1}, *F*(000) = 512, *R*₁ = 0.0452, *wR*₂ = 0.0944, 2952 independent reflections and 238 parameters (for more detail, see Table S8).

Crystal Data for PM1b. Empirical formula = B₁₈H₂₂S₁, *M*_r = 248.8, monoclinic, space group P21/n, *a* = 10.0415(7) Å, *b* = 11.6578(8) Å, *c* = 13.4184(9) Å, α = 90°, β = 110.018(6)°, γ = 90°, *V* = 1475.88(18) Å³, *Z*

= 4, $\rho_{\text{calc.}} = 1.1198 \text{ g/cm}^3$, $\mu = 1.553 \text{ mm}^{-1}$, $F(000) = 512$, $R1 = 0.0451$, $wR2 = 0.1115$, 2867 independent reflections and 238 parameters (for more detail, see Table S9).

NMR for [3-HS-*syn*-B₁₈H₂₁] 3. $^{11}\text{B}\{^1\text{H}\}$ NMR (192.6 MHz, 295 K CDCl₃): B3 (21.4 ppm) > B3' (13.5 ppm) > B10 (10.3 ppm) > B10' (9.7 ppm) > B6 (6.6 ppm) > B1 (4.4 ppm) > B9' (3.7 ppm) > B1' (2.7 ppm) > B9 (0.8 ppm) > B8' (-2.0 ppm according to COSY) > B5 (-2.2 ppm) > B8 (-3.2 ppm) > B7' (-15.4 ppm) > B7 (-16.8 ppm) > B2 (-28.6 ppm) > B2' (-29.4 ppm) > B4 (-38.5 ppm) > B4' (-39.4 ppm).

Crystal Data. Empirical formula = B₁₈H₂₂S₁, $M_r = 248.8$, monoclinic, space group $P2_1/c$, $a = 12.264(2) \text{ \AA}$, $b = 6.659(2) \text{ \AA}$, $c = 19.098(4) \text{ \AA}$, $\alpha = 90^\circ$, $\beta = 107.06(3)^\circ$, $\gamma = 90^\circ$, $V = 1491.0(6) \text{ \AA}^3$, $Z = 4$, $\rho_{\text{calc.}} = 1.1084 \text{ g cm}^{-3}$, $\mu = 1.538 \text{ mm}^{-1}$, $F(000) = 512$, $R1 = 0.0356$, $wR2 = 0.0804$, 2891 independent reflections and 238 parameters (for more detail, see Table S10).

NMR for [4-HS-*syn*-B₁₈H₂₁] 4. $^{11}\text{B}\{^1\text{H}\}$ NMR (192.6 MHz, 295 K, CDCl₃): B3 (14.9 ppm) > B3' (13.8 ppm) > B10 (10.3 ppm) > B10' (9.1 ppm) > B6 (8.1 ppm) > B9' (3.5 ppm) > B1 (3.0 ppm) > B9 (2.6 ppm) > B1' (2.0 ppm) > B8 (-1.2 ppm) > B8' (-1.6 ppm) > B5 (-3.4 ppm) > B7' (-16.1 ppm) > B7 (-16.2 ppm) > B2 (-27.7 ppm) > B2' (-28.1 ppm) > B4 (-29.2 ppm) > B4' (-39.8 ppm).

Crystal Data for PM4a. Empirical formula = B₁₈H₂₂S₁, $M_r = 248.8$, orthorhombic, space group $Pbca$, $a = 14.4249(5) \text{ \AA}$, $b = 11.9778(4) \text{ \AA}$, $c = 17.8595(6) \text{ \AA}$, $\alpha = 90^\circ$, $\beta = 90^\circ$, $\gamma = 90^\circ$, $V = 3085.74(18) \text{ \AA}^3$, $Z = 8$, $\rho_{\text{calc.}} = 1.0712 \text{ g cm}^{-3}$, $\mu = 1.486 \text{ mm}^{-1}$, $F(000) = 1024$, $R1 = 0.0300$, $wR2 = 0.0720$, 2994 independent reflections and 238 parameters (for more details, see Table S11).

Crystal Data for PM4b. Empirical formula = B₁₈H₂₂S₁, $M_r = 248.8$, monoclinic, space group $P2_1/n$, $a = 10.453(2) \text{ \AA}$, $b = 12.585(3) \text{ \AA}$, $c = 11.985(2) \text{ \AA}$, $\alpha = 90^\circ$, $\beta = 91.29(3)^\circ$, $\gamma = 90^\circ$, $V = 1576.2(5) \text{ \AA}^3$, $Z = 4$, $\rho_{\text{calc.}} = 1.0485 \text{ g cm}^{-3}$, $\mu = 1.454 \text{ mm}^{-1}$, $F(000) = 512$, $R1 = 0.0355$, $wR2 = 0.0781$, 3109 independent reflections and 238 parameters (for more details, see Table S13).

Computational Study. Quantum chemistry calculations were performed with the Gaussian 16 package. The geometries were optimized by means of the density functional theory with the long-range-corrected functional wB97XD from Head-Gordon and co-workers, which includes empirical dispersion,⁵⁵ using Ahlrichs' triple-zeta set with polarization functions def2-TZVPP.⁵⁶ A series of optimizations were performed in internal coordinates with the torsion angle between the thiol hydrogen atom and a selected neighbor of the substituted boron (2 for 1 and 3, 6 for 2, and 1 for 4) kept fixed at values reflecting the pentagonal arrangement around the substituted boron: 36, 108, 180, 252, and 324° (hydrogen between two neighboring borons) as well as 0, 72, 144, 216, and 288° (hydrogen above a neighboring boron); then the angle was relaxed, and a full optimization to a local minimum was conducted without constraints. NMR shielding was then calculated at the same level of theory using the GIAO method⁵⁷ for the minima found (only two for each isomer), and their weighted averages with Boltzmann factors at 300 K for the weights were used to calculate the ^{11}B chemical shifts, based on the shielding of diborane (chemical shift $\delta(^{11}\text{B}) + 16.6$) calculated at the same level of theory in geometry optimized at the same level. Computationally obtained dipole moment values are summarized in the supporting information (Table S14 and Figure S47). The excited states were calculated within the frame of the time-dependent DFT (TD-DFT); the results are provided in the Supporting information file (Table S15 and Figures S48–S55).

Single-Crystal X-ray Diffraction Analysis. Single crystals suitable for X-ray diffraction analysis of all three isomers were grown by slow evaporation of diethyl ether solutions at room temperature (18 °C). The X-ray diffraction data of the samples were collected with a Rigaku OD Supernova using an Atlas S2 CCD detector and a mirror-collimated Cu K α ($\lambda = 1.54184 \text{ \AA}$) from a microfocused sealed X-ray tube. The samples were cooled to 95 K during the measurement. Integration of the CCD images, absorption correction, and scaling were done by the program CrysAlisPro 1.171.41.123a (Rigaku Oxford Diffraction, 2022). Crystal structures were solved by charge-flipping with the program SUPERFLIP⁵⁸ and refined with the Jana2020

program package⁵⁹ by full-matrix least-squares technique on F^2 . The crystal data collection and analysis details are reported in more detail in the Supporting Information.

Luminescence Properties. Luminescence properties were analyzed on an FLS1000 spectrometer (Edinburgh Instruments, U.K.) using a cooled PMT-900 photon detection module (Edinburgh Instruments, U.K.). The FLS1000 spectrometer was also used for time-resolved luminescence measurements using, for excitation, a microsecond flash lamp (for 1, 3, and 4) or a 402 nm EPL Series laser diode (for *syn*-B₁₈H₂₂). The recorded decay curves were fitted to exponential functions using the Fluoracle software (v. 2.13.2, Edinburgh Instruments, U.K.). Luminescence quantum yields were recorded using a Quantaaurus QY C11347-1 spectrometer (Hamamatsu, Japan).

Formation of Self-Assembled Monolayers (SAMs). SAMs of [4-HS-*syn*-B₁₈H₂₁] 4 were prepared by evaporation in a UHV Multiprobe system ($<2 \times 10^{-10}$ mbar, Scienta Omicron) using a molecular evaporator (Kentax). The molecules were evaporated at 80 °C for 1 h on 300 nm silver on mica substrates (Georg Albert PVD), which were held at room temperature. The substrates were cleaned before by repeated sputtering with argon ions (1 keV, 10 mA, FDG15, Focus) and annealing at 370 °C.

X-ray Photoelectron Spectroscopy (XPS). XPS was measured in the same UHV system used for SAM formation with a monochromatic X-ray source (Al K α , 1486.7 eV) and an electron analyzer (Argus CU) with a spectral energy resolution of 0.6 eV. The XP spectra were calibrated by referencing the binding energy of the Ag 3d_{5/2} signal at 368.2 eV and fitted using Voigt functions (30:70) after linear background subtraction. Calculations of stoichiometry were performed with the software CasaXPS using the relative sensitivity factors of 1.68 (S 2p) and 0.49 (B 1s); the layer thickness was calculated using the Lambert–Beer equation. A mean free path of 27 Å was used for electrons that were released from the silver substrate and reached the detector through the SAM.⁶⁰

■ ASSOCIATED CONTENT

Supporting Information

The Supporting Information is available free of charge at <https://pubs.acs.org/doi/10.1021/jacs.3c05530>.

Supporting information provides complete information on the NMR spectra (both experimental and computational), IR spectra, ESI mass spectra, results from thermal differential analysis, tables with structural data for all X-ray diffraction-determined isomers and polymorphs, analysis of supramolecular arrangement, more data on photo-physical properties, X-ray photoelectron spectra of the respective SAM, and further computational data (PDF)

Optimized structure 1 (XYZ)

Optimized structure 2 (XYZ)

Optimized structure 3 (XYZ)

Optimized structure 4 (XYZ)

Optimized structure 5 (XYZ)

Accession Codes

CCDC 2262294, 2262296, 2262299, 2262306–2262308, 2265132, and 2265136 contain the supplementary crystallographic data for this paper. These data can be obtained free of charge via www.ccdc.cam.ac.uk/data_request/cif, or by emailing data_request@ccdc.cam.ac.uk, or by contacting The Cambridge Crystallographic Data Centre, 12 Union Road, Cambridge CB2 1EZ, UK; fax: +44 1223 336033.

■ AUTHOR INFORMATION

Corresponding Authors

Sundargopal Ghosh – DST Unit of Nanoscience (DST UNS) and Thematic Unit of Excellence (TUE), Department of

Chemistry, Indian Institute of Technology, Madras, Chennai 600036, India; orcid.org/0000-0001-6089-8244; Email: sghosh@iitm.ac.in

Andrey Turchanin – Institute of Physical Chemistry Friedrich Schiller University Jena, 07743 Jena, Germany; orcid.org/0000-0003-2388-1042; Email: andrey.turchanin@uni-jena.de

Thalappil Pradeep – DST Unit of Nanoscience (DST UNS) and Thematic Unit of Excellence (TUE), Department of Chemistry, Indian Institute of Technology, Madras, Chennai 600036, India; orcid.org/0000-0003-3174-534X; Email: pradeep@iitm.ac.in

Tomas Base – Institute of Inorganic Chemistry, The Czech Academy of Science, 25068 Rez, Czech Republic; orcid.org/0000-0003-2533-8705; Email: tbase@iic.cas.cz

Authors

Deepak Kumar Patel – DST Unit of Nanoscience (DST UNS) and Thematic Unit of Excellence (TUE), Department of Chemistry, Indian Institute of Technology, Madras, Chennai 600036, India; Institute of Inorganic Chemistry, The Czech Academy of Science, 25068 Rez, Czech Republic

B. S. Sooraj – DST Unit of Nanoscience (DST UNS) and Thematic Unit of Excellence (TUE), Department of Chemistry, Indian Institute of Technology, Madras, Chennai 600036, India; Institute of Inorganic Chemistry, The Czech Academy of Science, 25068 Rez, Czech Republic; orcid.org/0000-0002-6963-6491

Kaplan Kirakci – Institute of Inorganic Chemistry, The Czech Academy of Science, 25068 Rez, Czech Republic; orcid.org/0000-0002-1068-5133

Jan Macháček – Institute of Inorganic Chemistry, The Czech Academy of Science, 25068 Rez, Czech Republic; orcid.org/0000-0003-4723-0789

Monika Kučeráková – Institute of Physics, The Czech Academy of Science, 182 21 Prague 8, Czech Republic

Jonathan Bould – Institute of Inorganic Chemistry, The Czech Academy of Science, 25068 Rez, Czech Republic; orcid.org/0000-0003-3615-1938

Michal Dušek – Institute of Physics, The Czech Academy of Science, 182 21 Prague 8, Czech Republic; orcid.org/0000-0001-9797-2559

Martha Frey – Institute of Physical Chemistry Friedrich Schiller University Jena, 07743 Jena, Germany

Christof Neumann – Institute of Physical Chemistry Friedrich Schiller University Jena, 07743 Jena, Germany; orcid.org/0000-0002-3598-7656

Complete contact information is available at: <https://pubs.acs.org/10.1021/jacs.3c05530>

Author Contributions

[†]D.K.P. and B.S.S. contributed equally to this work.

Notes

The authors declare no competing financial interest.

ACKNOWLEDGMENTS

The authors thank and acknowledge the support of the Ministry of Education, Youth and Sports (MEYS) of Czech Republic and the Department of Science and Technology (DST), Govt. of India, for their financial support to the bilateral research program Inter-Excellence, subprogram Inter-Action, grants #LTAIN19152 and DST/INT/Czech/P-16/2020, respectively,

for financial support to the collaboration between T.B. and T.P. D.K.P. thanks the Ministry of Human Resource Development (MHRD) for the Prime Minister's Research Fellows (PMRF) research grant #SB22230356CYPMRF008224, and B.S.S. thanks the Council of Scientific and Industrial Research (CSIR) for his fellowship. The authors would like to thank Dr. Dmytro Baval for MS analysis and Pavla Kurhajcova for IR and DTA measurements. Computational resources were provided by the e-INFRA CZ project (ID:90140), supported by the Ministry of Education, Youth and Sports of the Czech Republic. The crystallographic part was supported by MGML (mgml.eu) infrastructure within the program of Czech Research Infrastructures (grant #LM2023065). M.F., C.N., and A.T. acknowledge Deutsche Forschungsgemeinschaft (DFG) for funding—Projekt Nummer 364549901—TRR 234 [Projects B7 and Z2]. T.P. acknowledges funding from the Centre of Excellence on Molecular Materials and Functions under the Institution of Eminence scheme of IIT Madras. This project is a part of collaborations between the research groups of T.B., T.P., and A.T., aimed at investigating a new class of hybrid metal and boron nanocluster molecules and new 2-dimensional borane materials.

REFERENCES

- (1) Huang, Z.; Wang, S.; Dewhurst, R. D.; Ignat'ev, N. V.; Finze, M.; Braunschweig, H. Boron: Its Role in Energy-Related Processes and Applications. *Angew. Chem., Int. Ed.* **2020**, *59*, 8800–8816.
- (2) Ochi, J.; Tanaka, K.; Chujo, Y. Recent Progress in the Development of Solid-State Luminescent *o*-Carboranes with Stimuli Responsivity. *Angew. Chem., Int. Ed.* **2020**, *59*, 9841–9855.
- (3) Mukherjee, S.; Thilagar, P. Boron Clusters in Luminescent Materials. *Chem. Commun.* **2016**, *52*, 1070–1093.
- (4) Horsky, T. N.; Hahto, S. K.; McIntyre, E. K.; Sacco, G. P.; Matsuo, J.; Kase, M.; Aoki, T.; Seki, T. *N- and P-Type Cluster Source; Kyoto, (Japan)* 2011, 452–455 DOI: [10.1063/1.3548447](https://doi.org/10.1063/1.3548447).
- (5) Dash, B. P.; Satapathy, R.; Maguire, J. A.; Hosmane, N. S. Polyhedral Boron Clusters in Materials Science. *New J. Chem.* **2011**, *35*, 1955.
- (6) Messina, M. S.; Axtell, J. C.; Wang, Y.; Chong, P.; Wixtrom, A. I.; Kirlikovali, K. O.; Upton, B. M.; Hunter, B. M.; Shafaat, O. S.; Khan, S. I.; Winkler, J. R.; Gray, H. B.; Alexandrova, A. N.; Maynard, H. D.; Spokoiny, A. M. Visible-Light-Induced Olefin Activation Using 3D Aromatic Boron-Rich Cluster Photooxidants. *J. Am. Chem. Soc.* **2016**, *138*, 6952–6955.
- (7) Cerdán, L.; Braborec, J.; Garcia-Moreno, I.; Costela, A.; Londeborough, M. G. S. A Borane Laser. *Nat. Commun.* **2015**, *6*, No. 5958.
- (8) Sivaev, I. B.; Bregadze, V. I.; Sjöberg, S. Chemistry of Closododecaborate Anion [B₁₂H₁₂]²⁻: A Review. *Collect. Czech. Chem. Commun.* **2002**, *67*, 679–727.
- (9) Wunderlich, J. A.; Lipscomb, W. N. Structure of B₁₂H₁₂²⁻ Ion. *J. Am. Chem. Soc.* **1960**, *82*, 4427–4428.
- (10) King, R. B. Three-Dimensional Aromaticity in Polyhedral Boranes and Related Molecules. *Chem. Rev.* **2001**, *101*, 1119–1152.
- (11) Jemmis, E. D.; Balakrishnarajan, M. M.; Pancharatna, P. D. Electronic Requirements for Macropolyhedral Boranes. *Chem. Rev.* **2002**, *102*, 93–144.
- (12) Pitochelli, A. R.; Hawthorne, M. F. The Preparation of a New Boron Hydride B₁₈H₂₂. *J. Am. Chem. Soc.* **1962**, *84*, 3218.
- (13) Li, Y.; Sneddon, L. G. Improved Synthetic Route to *n*-B₁₈H₂₂. *Inorg. Chem.* **2006**, *45*, 470–471.
- (14) Simpson, P. G.; Lipscomb, W. N. Molecular, Crystal, and Valence Structures of B₁₈H₂₂. *J. Chem. Phys.* **1963**, *39*, 26–34.
- (15) Olsen, F. P.; Vasavada, R. C.; Hawthorne, M. F. The Chemistry of *n*-B₁₈H₂₂ and *i*-B₁₈H₂₂. *J. Am. Chem. Soc.* **1968**, *90*, 3946–3951.
- (16) Simpson, P. G.; Lipscomb, W. N. Molecular Structure of B₁₈H₂₂. *Proc. Natl. Acad. Sci. U.S.A.* **1962**, *48*, 1490–1491.

- (17) Henke, D.; Jakubowski, F.; Deichler, J.; Venezia, V. C.; Ameen, M. S.; Harris, M. A. P-Type Gate Electrode Formation Using $B_{18}H_{22}$ Ion Implantation. *AIP Conf. Proc.*, AIP: Marseille (France), 2006; 866, 202–205.
- (18) Heo, S.; Lee, D.; Cho, H. T.; Krull, W. A.; Hwang, H. Ultrashallow P+/n Junction Formed by $B_{18}H_{22}$ Ion Implantation and Excimer Laser Annealing. In *AIP Conference Proceedings*, AIP: Marseille (France), 2006; pp 171–173.
- (19) Kawasaki, Y.; Kuroi, T.; Yamashita, T.; Horita, K.; Hayashi, T.; Ishibashi, M.; Togawa, M.; Ohno, Y.; Yoneda, M.; Horsky, T.; Jacobson, D.; Krull, W. Ultra-Shallow Junction Formation by $B_{18}H_{22}$ Ion Implantation. *Nucl. Instrum. Methods Phys. Res. Sect. B Beam Interact. Mater. At.* **2005**, 237, 25–29.
- (20) Marqués, L. A.; Pelaz, L.; Santos, I. Molecular Dynamics Study of $B_{18}H_{22}$ Cluster Implantation into Silicon. *Nucl. Instrum. Methods Phys. Res. Sect. B Beam Interact. Mater. At.* **2007**, 255, 242–246.
- (21) Harris, M. A.; Rubin, L.; Tieger, D.; Venezia, V.; Hsieh, T. J.; Miranda, J.; Jacobson, D. Dose Retention Effects in Atomic Boron and ClusterBoron ($B_{18}H_{22}$) Implant Processes, In *AIP Conf. Proc.*, AIP: Marseille (France), 2006; pp 155–158.
- (22) Lee, J.; Choi, J.; An, J.; Ryu, S.; Lee, K. W.; Kim, J.; Ra, G. J.; Kim, S.; Cho, H. T.; Seebauer, E. G.; Felch, S. B.; Jain, A.; Kondratenko, Y. V. Investigation of PMOS Device Matching and Characteristics Using $B_{18}H_{22}$ Implantation. In *AIP Conf. Proc.*, AIP: Monterey (California), 2008; pp 438–441.
- (23) John, A.; Bolte, M.; Lerner, H.-W.; Meng, G.; Wang, S.; Peng, T.; Wagner, M. Doubly Boron-Doped Pentacenes as Emitters for OLEDs. *J. Mater. Chem. C* **2018**, 6, 10881–10887.
- (24) Simpson, P. G.; Lipscomb, W. N. Molecular, Crystal, and Valence Structures of $B_{18}H_{22}$. *J. Chem. Phys.* **1963**, 39, 26–34.
- (25) Londesborough, M. G. S.; Dolanský, J.; Jelínek, T.; Kennedy, J. D.; Císařová, I.; Kennedy, R. D.; Roca-Sanjuán, D.; Francés-Monerris, A.; Lang, K.; Clegg, W. Substitution of the Laser Borane *anti*- $B_{18}H_{22}$ with Pyridine: A Structural and Photophysical Study of Some Unusually Structured Macropolyhedral Boron Hydrides. *Dalton Trans.* **2018**, 47, 1709–1725.
- (26) Anderson, K. P.; Waddington, M. A.; Balaich, G. J.; Stauber, J. M.; Bernier, N. A.; Caram, J. R.; Djurovich, P. I.; Spokoiny, A. M. A Molecular Boron Cluster-Based Chromophore with Dual Emission. *Dalton Trans.* **2020**, 49, 16245–16251.
- (27) Kolská, Z.; Matoušek, J.; Čapková, P.; Braborec, J.; Benkocká, M.; Černá, H.; Londesborough, M. G. S. A New Luminescent Montmorillonite/Borane Nanocomposite. *Appl. Clay Sci.* **2015**, 118, 295–300.
- (28) Bould, J.; Lang, K.; Kirakci, K.; Cerdán, L.; Roca-Sanjuán, D.; Francés-Monerris, A.; Clegg, W.; Waddell, P. G.; Fuciman, M.; Polívka, T.; Londesborough, M. G. S. A Series of Ultra-Efficient Blue Borane Fluorophores. *Inorg. Chem.* **2020**, 59, 17058–17070.
- (29) Londesborough, M. G. S.; Hnyk, D.; Bould, J.; Serrano-Andrés, L.; Sauri, V.; Oliva, J. M.; Kubát, P.; Polívka, T.; Lang, K. Distinct Photophysics of the Isomers of $B_{18}H_{22}$ Explained. *Inorg. Chem.* **2012**, 51, 1471–1479.
- (30) Londesborough, M. G. S.; Dolanský, J.; Bould, J.; Braborec, J.; Kirakci, K.; Lang, K.; Císařová, I.; Kubát, P.; Roca-Sanjuán, D.; Francés-Monerris, A.; Slušná, L.; Noslavská, E.; Lorenc, D. Effect of Iodination on the Photophysics of the Laser Borane *anti*- $B_{18}H_{22}$: Generation of Efficient Photosensitizers of Oxygen. *Inorg. Chem.* **2019**, 58, 10248–10259.
- (31) Anderson, K. P.; Hua, A. S.; Plumley, J. B.; Ready, A. D.; Rheingold, A. L.; Peng, T. L.; Djurovich, P. I.; Kerestes, C.; Snyder, N. A.; Andrews, A.; Caram, J. R.; Spokoiny, A. M. Benchmarking the Dynamic Luminescence Properties and UV Stability of $B_{18}H_{22}$ -Based Materials. *Dalton Trans.* **2022**, 51, 9223–9228.
- (32) Londesborough, M. G. S.; Lang, K.; Clegg, W.; Waddell, P. G.; Bould, J. Swollen Polyhedral Volume of the *anti*- $B_{18}H_{22}$ Cluster via Extensive Methylation: *anti*- $B_{18}H_8Cl_2Me_{12}$. *Inorg. Chem.* **2020**, 59, 2651–2654.
- (33) Anderson, K. P.; Rheingold, A. L.; Djurovich, P. I.; Soman, O.; Spokoiny, A. M. Synthesis and Luminescence of Monohalogenated $B_{18}H_{22}$ Clusters. *Polyhedron* **2022**, 227, No. 116099.
- (34) Chen, J.; Xiong, L.; Zhang, L.; Huang, X.; Meng, H.; Tan, C. Synthesis, Aggregation-Induced Emission of a New *anti*- $B_{18}H_{22}$ -Isoquinoline Hybrid. *Chem. Phys. Lett.* **2020**, 747, No. 137328.
- (35) Ševčík, J.; Urbánek, P.; Hanulíková, B.; Čapková, T.; Urbánek, M.; Antoš, J.; Londesborough, M. G. S.; Bould, J.; Ghasemi, B.; Petřkovský, L.; Kuřitka, I. The Photostability of Novel Boron Hydride Blue Emitters in Solution and Polystyrene Matrix. *Materials* **2021**, 14, 589.
- (36) Londesborough, M. G. S.; Dolanský, J.; Cerdán, L.; Lang, K.; Jelínek, T.; Oliva, J. M.; Hnyk, D.; Roca-Sanjuán, D.; Francés-Monerris, A.; Martinčík, J.; Nikl, M.; Kennedy, J. D. Thermochromic Fluorescence from $B_{18}H_{20}(NC_5H_5)_2$: An Inorganic-Organic Composite Luminescent Compound with an Unusual Molecular Geometry. *Adv. Opt. Mater.* **2017**, 5, No. 1600694.
- (37) Sauri, V.; Oliva, J. M.; Hnyk, D.; Bould, J.; Braborec, J.; Merchán, M.; Kubát, P.; Císařová, I.; Lang, K.; Londesborough, M. G. S. Tuning the Photophysical Properties of *anti*- $B_{18}H_{22}$: Efficient Intersystem Crossing between Excited Singlet and Triplet States in New 4,4'-(HS) $_2$ -*anti*- $B_{18}H_{20}$. *Inorg. Chem.* **2013**, 52, 9266–9274.
- (38) Cerdán, L.; Francés-Monerris, A.; Roca-Sanjuán, D.; Bould, J.; Dolanský, J.; Fuciman, M.; Londesborough, M. G. S. Unveiling the Role of Upper Excited Electronic States in the Photochemistry and Laser Performance of *anti*- $B_{18}H_{22}$. *J. Mater. Chem. C* **2020**, 8, 12806–12818.
- (39) Richard-Lacroix, M.; Küllmer, M.; Gaus, A.; Neumann, C.; Tontsch, C.; Delius, M.; Deckert, V.; Turchanin, A. Synthesis and Nanoscale Characterization of Hierarchically Assembled Molecular Nanosheets. *Adv. Mater. Interfaces* **2022**, 9, No. 2102389.
- (40) Jana, A.; Jash, M.; Poonia, A. K.; Paramasivam, G.; Islam, M. R.; Chakraborty, P.; Antharjanam, S.; Machacek, J.; Ghosh, S.; Adarsh, K. N. V. D.; Base, T.; Pradeep, T. Light-Activated Intercluster Conversion of an Atomically Precise Silver Nanocluster. *ACS Nano* **2021**, 15, 15781–15793.
- (41) Jana, A.; Jash, M.; Dar, W. A.; Roy, J.; Chakraborty, P.; Paramasivam, G.; Lebedkin, S.; Kirakci, K.; Manna, S.; Antharjanam, S.; Machacek, J.; Kucerakova, M.; Ghosh, S.; Lang, K.; Kappes, M. M.; Base, T.; Pradeep, T. Carborane-Thiol Protected Copper Nanoclusters: Stimuli-Responsive Materials with Tunable Phosphorescence. *Chem. Sci.* **2023**, 14, 1613–1626.
- (42) Bould, J.; Macháček, J.; Londesborough, M. G. S.; Macías, R.; Kennedy, J. D.; Bastl, Z.; Rupper, P.; Baše, T. Decaborane Thiols as Building Blocks for Self-Assembled Monolayers on Metal Surfaces. *Inorg. Chem.* **2012**, 51, 1685–1694.
- (43) Wang, S.; Goronzy, D. P.; Young, T. D.; Wattanatorn, N.; Stewart, L.; Baše, T.; Weiss, P. S. Formation of Highly Ordered Terminal Alkyne Self-Assembled Monolayers on the Au{111} Surface through Substitution of 1-Decaboranethiolate. *J. Phys. Chem. C* **2019**, 123, 1348–1353.
- (44) Claridge, S. A.; Liao, W.-S.; Thomas, J. C.; Zhao, Y.; Cao, H. H.; Cheunkar, S.; Serino, A. C.; Andrews, A. M.; Weiss, P. S. From the Bottom up: Dimensional Control and Characterization in Molecular Monolayers. *Chem. Soc. Rev.* **2013**, 42, 2725–2745.
- (45) Baše, T.; Bastl, Z.; Havránek, V.; Macháček, J.; Langecker, J.; Malina, V. Carboranedithiols: Building Blocks for Self-Assembled Monolayers on Copper Surfaces. *Langmuir* **2012**, 28, 12518–12526.
- (46) Mills, H. A.; Jones, C. G.; Anderson, K. P.; Ready, A. D.; Djurovich, P. I.; Khan, S. I.; Hohman, J. N.; Nelson, H. M.; Spokoiny, A. M. Sterically Invariant Carborane-Based Ligands for the Morphological and Electronic Control of Metal–Organic Chalcogenolate Assemblies. *Chem. Mater.* **2022**, 34, 6933–6943.
- (47) Yeager, L. J.; Saeki, F.; Shelly, K.; Hawthorne, M. F.; Garrell, R. L. A New Class of Self-Assembled Monolayers: *closo*- $B_{12}H_{11}S^3^-$ on Gold. *J. Am. Chem. Soc.* **1998**, 120, 9961–9962.
- (48) Hohman, J. N.; Claridge, S. A.; Kim, M.; Weiss, P. S. Cage Molecules for Self-Assembly. *Mater. Sci. Eng. R Rep.* **2010**, 70, 188–208.
- (49) Kristiansen, K.; Stock, P.; Baimpos, T.; Raman, S.; Harada, J. K.; Israelachvili, J. N.; Valtiner, M. Influence of Molecular Dipole

Orientations on Long-Range Exponential Interaction Forces at Hydrophobic Contacts in Aqueous Solutions. *ACS Nano* **2014**, *8*, 10870–10877.

(50) Todd, L. J.; Siedle, A. R. NMR Studies of Boranes, Carboranes and Hetero-Atom Boranes. *Prog. Nucl. Magn. Reson. Spectrosc.* **1979**, *13*, 87–176.

(51) Braunschweig, H.; Herbst, T.; Rais, D.; Ghosh, S.; Kupfer, T.; Radacki, K.; Crawford, A. G.; Ward, R. M.; Marder, T. B.; Fernández, I.; Frenking, G. Borylene-Based Direct Functionalization of Organic Substrates: Synthesis, Characterization, and Photophysical Properties of Novel π -Conjugated Borirenes. *J. Am. Chem. Soc.* **2009**, *131*, 8989–8999.

(52) Benito, Q.; Le Goff, X. F.; Maron, S.; Fargues, A.; Garcia, A.; Martineau, C.; Taulelle, F.; Kahlal, S.; Gacoin, T.; Boilot, J.-P.; Perruchas, S. Polymorphic Copper Iodide Clusters: Insights into the Mechanochromic Luminescence Properties. *J. Am. Chem. Soc.* **2014**, *136*, 11311–11320.

(53) Neumann, C.; Szwed, M.; Frey, M.; Tang, Z.; Koziel, K.; Cyganik, P.; Turchanin, A. Preparation of Carbon Nanomembranes without Chemically Active Groups. *ACS Appl. Mater. Interfaces* **2019**, *11*, 31176–31181.

(54) Thomas, J. C.; Goronzy, D. P.; Serino, A. C.; Auluck, H. S.; Irving, O. R.; Jimenez-Izal, E.; Deirmenjian, J. M.; Macháček, J.; Sautet, P.; Alexandrova, A. N.; Baše, T.; Weiss, P. S. Acid–Base Control of Valency within Carboranedithiol Self-Assembled Monolayers: Molecules Do the Can-Can. *ACS Nano* **2018**, *12*, 2211–2221.

(55) Chai, J.-D.; Head-Gordon, M. Long-Range Corrected Hybrid Density Functionals with Damped Atom–Atom Dispersion Corrections. *Phys. Chem. Chem. Phys.* **2008**, *10*, 6615.

(56) Weigend, F.; Ahlrichs, R. Balanced Basis Sets of Split Valence, Triple Zeta Valence and Quadruple Zeta Valence Quality for H to Rn: Design and Assessment of Accuracy. *Phys. Chem. Chem. Phys.* **2005**, *7*, 3297.

(57) Cheeseman, J. R.; Trucks, G. W.; Keith, T. A.; Frisch, M. J. A Comparison of Models for Calculating Nuclear Magnetic Resonance Shielding Tensors. *J. Chem. Phys.* **1996**, *104*, 5497–5509.

(58) Palatinus, L.; Chapuis, G. *SUPERFLIP* – a Computer Program for the Solution of Crystal Structures by Charge Flipping in Arbitrary Dimensions. *J. Appl. Crystallogr.* **2007**, *40*, 786–790.

(59) Petříček, V.; Palatinus, L.; Plášil, J.; Dušek, M. Jana2020 – a New Version of the Crystallographic Computing System Jana. *Z. Krist. - Cryst. Mater.* **2023**, *00* DOI: 10.1515/zkri-2023-0005.

(60) Lamont, C. L. A.; Wilkes, J. Attenuation Length of Electrons in Self-Assembled Monolayers of *n*-Alkanethiols on Gold. *Langmuir* **1999**, *15*, 2037–2042.

SUPPORTING INFORMATION

Macropolyhedral $\text{syn-B}_{18}\text{H}_{22}$, the “Forgotten” Isomer

Deepak Kumar Patel ^{a,b}, B. S. Sooraj ^{a,b}, Kaplan Kirakci^b, Jan Macháček ^b, Monika Kučeráková ^c, Jonathan Bould ^b, Michal Dušek ^c, Martha Frey ^d, Christof Neumann ^d, Sundargopal Ghosh ^{a*}, Andrey Turchanin ^{d*}, Thalappil Pradeep ^{a*}, and Tomas Base ^{b*}

^a*DST Unit of Nanoscience (DST UNS) and Thematic Unit of Excellence (TUE), Department of Chemistry, Indian Institute of Technology, Madras, Chennai – 600036, India. E-mail: pradeep@iitm.ac.in, sghosh@iitm.ac.in*

^b*Institute of Inorganic Chemistry, The Czech Academy of Science, 25068 Rez, Czech Republic. E-mail: tbase@iic.cas.cz*

^c*Institute of Physics, The Czech Academy of Science, 182 21 Prague 8, Czech Republic.*

^d*Institute of Physical Chemistry Friedrich Schiller University Jena, 07743 Jena, Germany. E-mail: andrey.turchanin@uni-jena.de*

Keywords: Macropolyhedral, Boron hydride, $\text{syn-B}_{18}\text{H}_{22}$, Cluster, Luminescence, Phosphorescence, Self-assembled monolayers, Polymorphs

Contents

NMR

Figure S1. Experimental Stack plot of $^{11}\text{B}\{^1\text{H}\}$ decoupled spectra of *syn*- $\text{B}_{18}\text{H}_{22}$, 1-HS-*syn*- $\text{B}_{18}\text{H}_{21}$, 3-HS-*syn*- $\text{B}_{18}\text{H}_{21}$, and 4-HS-*syn*- $\text{B}_{18}\text{H}_{21}$.

Figure S2. Correlation of experimental coupled and decoupled $^{11}\text{B}\{^1\text{H}\}$ spectra of *syn*- $\text{B}_{18}\text{H}_{22}$, 1-HS-*syn*- $\text{B}_{18}\text{H}_{21}$, 3-HS-*syn*- $\text{B}_{18}\text{H}_{21}$, and 4-HS-*syn*- $\text{B}_{18}\text{H}_{21}$.

Figure S3. Experimental decoupled (top) and coupled (bottom) ^{11}B NMR spectra of *syn*- $\text{B}_{18}\text{H}_{22}$ with integrals normalised to 1 atom = 10 units.

Figure S4. Correlation between the (top) experimental and (bottom) computational ^{11}B NMR spectra of *syn*- $\text{B}_{18}\text{H}_{22}$. Ratio of the boron signal intensity of experimental ^{11}B NMR: 2:1:2:2:2:2:1:2:2:2.

Figure S5. 2-D [^{11}B - ^{11}B]-COSY- $\{^1\text{H}\}$ NMR spectrum of *syn*- $\text{B}_{18}\text{H}_{22}$ with the 1D spectra aligned along its edges.

Figure S6. *syn*- $\text{B}_{18}\text{H}_{22}$ connections deduced from ^{11}B -COSY NMR

Figure S7. *syn*- $\text{B}_{18}\text{H}_{22}$ connections deduced from ^{11}B COSY NMR: a) augmented with hydrogen bridges found in ^{11}B - ^1H HMQC NMR; b) expanded to the full formula.

Figure S8. 2-D [^1H - ^{11}B]-HMQC NMR spectrum of *syn*- $\text{B}_{18}\text{H}_{22}$ with the 1D spectra aligned along its edges.

Figure S9. $^1\text{H}\{\text{B}\}$ decoupled (top) and coupled (bottom) proton NMR spectra of *syn*- $\text{B}_{18}\text{H}_{22}$

Figure S10. Experimental decoupled (top) and coupled (bottom) ^{11}B NMR spectra of 1-HS-*syn*- $\text{B}_{18}\text{H}_{21}$ (**1**).

Figure S11. Correlation between the (top) experimental and (bottom) computational ^{11}B NMR spectra of 1-HS-*syn*- $\text{B}_{18}\text{H}_{21}$ (**1**). Ratio of the boron signal intensity of experimental ^{11}B NMR: 1:1:1:1:2:1:1:1:1:1:1:2:1:1

Figure S12. 2-D [^{11}B - ^{11}B]-COSY- $\{^1\text{H}\}$ NMR spectrum of 1-HS-*syn*- $\text{B}_{18}\text{H}_{21}$ (**1**).

Figure S13: ^{11}B COSY NMR spectrum of 1-HS-*syn*- $\text{B}_{18}\text{H}_{21}$ treated to see as many cross peaks as possible.

Figure S14. 2-D [^1H - ^{11}B]-HMQC NMR spectrum of 1-HS-*syn*- $\text{B}_{18}\text{H}_{21}$ (**1**).

Figure S15. $^1\text{H}\{\text{B}\}$ decoupled (top) and coupled (bottom) proton NMR spectra of 1-HS-*syn*- $\text{B}_{18}\text{H}_{21}$ (**1**)

Figure S16. Experimental decoupled (top) and coupled (bottom) ^{11}B NMR spectra of 3-HS-*syn*- $\text{B}_{18}\text{H}_{21}$ (**3**).

Figure S17. Correlation between the (top) experimental and (bottom) computational ^{11}B NMR spectra of 3-HS-*syn*- $\text{B}_{18}\text{H}_{21}$ (**3**). Ratio of the boron signal intensity of experimental ^{11}B NMR: 1:1:1:1:1:1:2:1:1:1:1:1:1:1:1.

Figure S18. 2-D [^{11}B - ^{11}B]-COSY- $\{^1\text{H}\}$ NMR spectrum of 3-HS-*syn*- $\text{B}_{18}\text{H}_{21}$ (**3**).

Figure S19. 2-D [^1H - ^{11}B]-HMQC NMR spectrum of 3-HS-*syn*- $\text{B}_{18}\text{H}_{21}$ (**3**).

Figure S20. $^1\text{H}\{\text{B}\}$ decoupled (top) and coupled (bottom) proton NMR spectra of 3-HS-*syn*- $\text{B}_{18}\text{H}_{21}$ (**3**).

Figure S21: ^1H - ^{11}B HMQC NMR spectrum of 3-HS-*syn*- $\text{B}_{18}\text{H}_{21}$ treated to resolve the cross peaks of B(2) with H(2) and B(2') with H(2')

Figure S22. Experimental decoupled (top) and coupled (bottom) ^{11}B NMR spectra of 4-HS-*syn*- $\text{B}_{18}\text{H}_{21}$.

Figure S23: ^1H decoupled ^{11}B NMR spectrum of 4-HS-*syn*- $\text{B}_{18}\text{H}_{21}$ superimposed on the non-decoupled one, transformation of the FID fine-tuned to get lines narrow enough for discriminating all the signals.

Figure S24. Correlation between the (top) experimental and (bottom) computational ^{11}B NMR spectra of 4-HS-*syn*- $\text{B}_{18}\text{H}_{21}$ (**4**). Ratio of the boron signal intensity of experimental ^{11}B NMR: 1:1:1:1:1:1:2:1:2:1:2:1:1:1:1

Figure S25. 2-D [^{11}B - ^{11}B]-COSY- $\{^1\text{H}\}$ NMR spectrum of 4-HS-*syn*- $\text{B}_{18}\text{H}_{21}$ (**4**)

Figure S26. 2-D [^1H - ^{11}B]-HMQC NMR spectrum of 4-HS-*syn*- $\text{B}_{18}\text{H}_{21}$ (**4**)

Figure S27. Decoupled (top) $^1\text{H}\{\text{B}\}$ and coupled (bottom) proton NMR spectra of 4-HS-*syn*- $\text{B}_{18}\text{H}_{21}$ (**4**).

Table S1: NMR chemical shifts of ^{11}B and ^1H in *syn*- $\text{B}_{18}\text{H}_{22}$

Table S2. Calculated chemical shift in ppm

Table S3. Experimental chemical shift in ppm

MS

Figure S28. Positive ion mode MS ESI spectra of HS- $\text{B}_{18}\text{H}_{21}$. (Top) full range m/z spectrum and (bottom) corresponding experimental and theoretical matching of different fragments.

IR

Figure S29. FTIR of HS-*syn*- $\text{B}_{18}\text{H}_{21}$ isomers and *syn*- $\text{B}_{18}\text{H}_{22}$.

TGA

Figure S30. DT analysis showing the volatility of HS-*syn*- $\text{B}_{18}\text{H}_{21}$ isomers.

Photophysical Properties

Figure S31. Phosphorescence decay kinetics of powder of 4-HS-*syn*- $\text{B}_{18}\text{H}_{21}$ in air atmosphere (black), argon atmosphere (red) or oxygen atmosphere (blue) excited at 380 nm, recorded at 470 nm.

Figure S32. Normalized emission spectra of *syn*- $\text{B}_{18}\text{H}_{22}$, **1**, **3**, and **4** in air-saturated hexane, excited at 330 nm; normalized excitation spectra (dashed lines) recorded at the maximum of emission, apart for *syn*- $\text{B}_{18}\text{H}_{22}$ recorded at 420 nm (A). Fluorescence decay kinetics of *syn*- $\text{B}_{18}\text{H}_{22}$, **1**, **3**, and **4** in air-saturated hexane, excited at 402 nm, recorded at the maximum of emission, apart for *syn*- $\text{B}_{18}\text{H}_{22}$ recorded at 420 nm (B).

Figure S33. Normalized emission spectra (plain lines) of *anti*- $\text{B}_{18}\text{H}_{22}$ excited at 340 nm in air atmosphere; normalized excitation spectra (dashed lines) recorded at the maximum of emission (A). Fluorescence decay kinetics of *anti*- $\text{B}_{18}\text{H}_{22}$ in air atmosphere, excited at 402 nm, recorded at 420 nm (B).

Table S4. Photophysical properties of *syn*- $\text{B}_{18}\text{H}_{22}$ and the thiolated boranes in hexane at room temperature.^a

XPS

Figure S34. Overview X-ray photoelectron spectrum (A) as well as high-resolution C 1s (B) and O 1s (C) spectra of the formed [4-HS-*syn*- $\text{B}_{18}\text{H}_{21}$] **4** SAM on Ag. The data clearly show only the presence of boron, sulfur and silver signals in the sample. No carbon or oxygen signals are detected demonstrating a high quality of the formed SAM.

X-ray diffraction analysis

Figure S35. B-B-B angle, bond and centroid(c1-c2) distance of *syn*- $\text{B}_{18}\text{H}_{22}$, **1**, **3**, and **4** isomers polymorphs (A, B, C, D, E, and F respectively).

Figure S36. Rietveld refinement of the powdered sample of *syn*- $\text{B}_{18}\text{H}_{22}$.

Figure S37. Rietveld refinement of the powdered sample of 1-HS-*syn*- $\text{B}_{18}\text{H}_{21}$ (PM1b) and *syn*- $\text{B}_{18}\text{H}_{22}$.

Figure S38. Rietveld refinement of the powdered sample of 4-HS-*syn*- $\text{B}_{18}\text{H}_{21}$ (PM4a).

Figure S39. Rietveld refinement of the powdered sample of 4-HS-*syn*- $\text{B}_{18}\text{H}_{21}$ (PM4a and PM4b) and *syn*- $\text{B}_{18}\text{H}_{22}$.

Figure 40. Powder X-ray diffraction pattern (PXRD) of *anti*- $\text{B}_{18}\text{H}_{22}$ (obtained at room temperature using a PANalytical Empyrean diffractometer equipped with a conventional Cu X-ray tube and PIXcel detector). The data were processed using the HighScore Plus program from PANalytical, and the obtained diffraction pattern fits perfectly to the single-crystal simulated one.

Figure S41. ORTEP structure of *syn*- $\text{B}_{18}\text{H}_{22}$ isomer having 50% thermal ellipsoid probability.

Figure S42. ORTEP structure of 1-HS-*syn*-B₁₈H₂₁ PM1a isomer having 50% thermal ellipsoid probability.

Figure S43. ORTEP structure of 1-HS-*syn*-B₁₈H₂₁ PM1b isomer having 50% thermal ellipsoid probability.

Figure S44. ORTEP structure of 3-HS-*syn*-B₁₈H₂₁ isomer having 50% thermal ellipsoid probability.

Figure S45. ORTEP structure of 4-HS-*syn*-B₁₈H₂₁ PM4a isomer having 50% thermal ellipsoid probability.

Figure S46. ORTEP structure of 4-HS-*syn*-B₁₈H₂₁ PM4b isomer having 50% thermal ellipsoid probability.

Table S5. Bond distance comparison of all the isomers with *syn*-B₁₈H₂₂

Table S6. Crystallographic collection and refinement data for *syn*-B₁₈H₂₂ measured at 95 K.

Table S7. Crystallographic collection and refinement data for *syn*-B₁₈H₂₂ measured at room temperature.

Table S8. Crystallographic collection and refinement data for 1-HS-*syn*-B₁₈H₂₁ (PM1a).

Table S9. Crystallographic collection and refinement data for 1-HS-*syn*-B₁₈H₂₁ (PM1b).

Table S10. Crystallographic collection and refinement data for 3-HS-*syn*-B₁₈H₂₁.

Table S11. Crystallographic collection and refinement data for 4-HS-*syn*-B₁₈H₂₁ (PM 4a).

Table S12. Crystallographic collection and refinement data for PM4a measured at room temperature.

Table S13. Crystallographic collection and refinement data for 4-HS-*syn*-B₁₈H₂₁ (PM4b).

Dipole moment

Figure S47. Graphical projection of the dipole moment vectors in the SH-B₁₈H₂₁ isomers as well as in the parent *syn*-B₁₈H₂₂ and *anti*-B₁₈H₂₂.

Table S14. Table of the computationally obtained dipole moment values of all isomers and the parent *syn*-B₁₈H₂₂.

TD-DFT

Figure S48: Simulated spectra (A, D), excited states (B, E) and excited states in the relaxed geometry of S1 (C, F) of *anti* (A-C) and *syn* (D-F) B₁₈H₂₂; in the excited states diagrams, singlets are depicted yellow, triplets orange, and the length of the yellow lines on the left side, with scale labels in nm, represents the relative oscillator strengths of the singlet excited states.

Figure S49: Simulated spectra (A), excited states (B) and excited states in the relaxed geometry of S1 (C) of 1-HS-*syn*-B₁₈H₂₁.

Figure S50: Simulated spectra (A), excited states (B) and excited states in the relaxed geometry of S1 (C) of 2-HS-*syn*-B₁₈H₂₁.

Figure S51: Simulated spectra (A), excited states (B) and excited states in the relaxed geometry of S1 (C) of 3-HS-*syn*-B₁₈H₂₁.

Figure S52: Simulated spectra (A), excited states (B) and excited states in the relaxed geometry of S1 (C) of 4-HS-*syn*-B₁₈H₂₁.

Figure S53: Optimized geometries of *anti*-B₁₈H₂₂: the ground state (A) and the first excited singlet (B).

Figure S54: Optimized geometries of *syn*-B₁₈H₂₂: the ground state (A) and the first excited singlet (B).

Figure S55: Natural Transition Orbitals (bottom hole, top electron) for the absorption of *syn*-B₁₈H₂₂ to the first excited singlet in the ground state geometry (left) and its luminescence from the relaxed geometry of S1 (right).

Table S15: Excitation energies (E_{exc}) and the associated wavelengths (λ) of the first (S1) and second (S2) excited states in the ground state geometry, and that of the first singlet excited state in its optimised geometry (S1/S1)

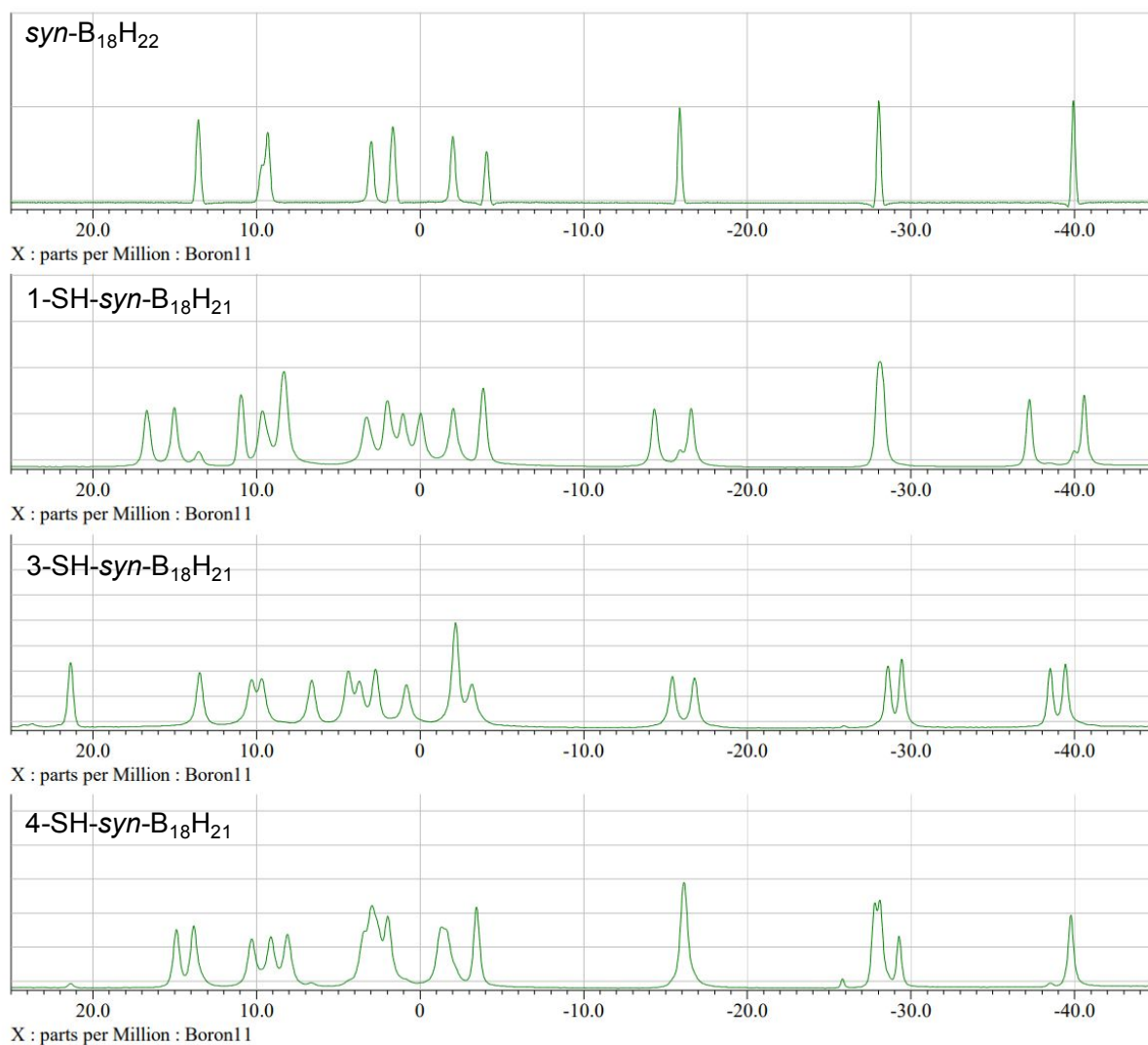


Figure S1. Experimental Stack plot of ¹¹B{¹H} decoupled spectra of *syn*-B₁₈H₂₂, 1-HS-*syn*-B₁₈H₂₁, 3-HS-*syn*-B₁₈H₂₁, and 4-HS-*syn*-B₁₈H₂₁.

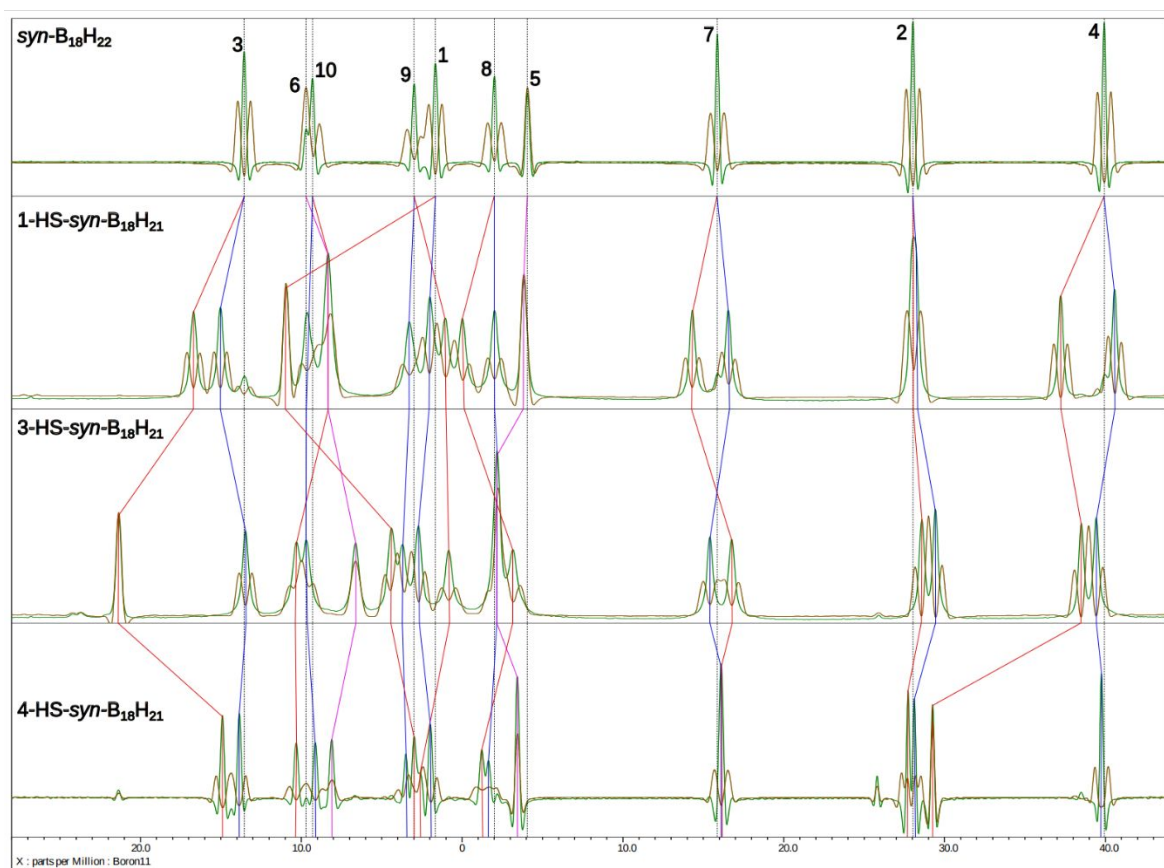


Figure S2. Correlation of experimental coupled and decoupled $^{11}\text{B}\{^1\text{H}\}$ spectra of $\text{syn-B}_{18}\text{H}_{22}$, $1\text{-HS-syn-B}_{18}\text{H}_{21}$, $3\text{-HS-syn-B}_{18}\text{H}_{21}$, and $4\text{-HS-syn-B}_{18}\text{H}_{21}$.

$\text{syn-B}_{18}\text{H}_{21}$ ^{11}B NMR assignment

In the ^{11}B NMR spectrum of $\text{syn-B}_{18}\text{H}_{22}$ (Figure S3) we see ten peaks: 13.5 ppm (a), 9.7 ppm (b), 9.3 ppm (c), 3.0 ppm (d), 1.7 ppm (e), -2.0 ppm (f), -4.1 ppm (g), -15.9 (h), -28.0 (i), and -40.0 (j); b and g are singlets of intensity 1, and all others doublets of intensity 2, so b and g evidently belong to the two common atoms of the two decaborane subunits, 5 and 6.

The ^{11}B COSY NMR spectrum (Figure S5) allows to deduce information on the connectivity of the boron atoms represented by individual signals. The signal a has cross peaks with e, f, h, i, and j; b with i, and possibly a weak one with h; c with e, g, and j; d only with j; e with a, c, g, i, and j; f with a, h, and j; g with c, e, and i; h with a, f, i, and possibly b; i with a, b, e, g, and h; and j with a, c, d, e, and f. So a will be a neighbour of e, and they will have two common neighbours, i and j, which suggests the arrangement of two triangles a-e-i and a-e-j with a-e for a common edge; a and i have h for another common neighbour besides e, a and j form another triangle with f, e

and i with g, and e and j with c, while h and f also interact with one another, and so do c and g; we can connect d on the basis of the COSY only to j, and b to i with a possible but uncertain completion of a triangle with h (Figure S6).

The ^{11}B - ^1H HMQC spectrum (Figure S8) allows assignment of protons to borons. To identify the correct position of our connection diagram in the schematic structure of *syn*- $\text{B}_{18}\text{H}_{22}$ (Figure 1B), we will need, especially for the bridging hydrogens, the information which pairs of boron atoms are connected by them. Among our ^{11}B signals, a has a cross peak with ^1H at 3.8 ppm, b at 1.3 ppm, and we know for two reasons that this is a bridging hydrogen: b is a singlet, so it has no terminal hydrogen, and the hydrogen at 1.3 has another cross peak with h; at the same time, h has another cross peak with ^1H , its terminal hydrogen, at 2.6 ppm. For c, there is a cross peak with -0.9 ppm with another bridging hydrogen that interacts with d as well, and a weak cross peak with its terminal ^1H at 3.8 ppm. The cross peak with the terminal ^1H of d is at 3.4 ppm, and there is one more cross peak of d with one more bridging hydrogen at -2.5 ppm; that bridging hydrogen interacts with f. That boron has the cross peak with its terminal hydrogen at 3.1 ppm, while e has it at 3.6 ppm, i at -0.2 ppm, j at 0.6 ppm, and g, the second singlet in ^{11}B spectrum, has none. The important part for ^{11}B NMR assignment are the three bridging hydrogens that connect b with h, c with d, and d with f: when we add these hydrogen bridges to our connection diagram, we can finally fit it on the *syn*- $\text{B}_{18}\text{H}_{22}$ structure unequivocally (Figure S7).

From the comparison of Figure S7 and Figure 1B follows that a (13.5 ppm) = 3, 3'; b (9.7 ppm) = 6 (= 6'); c (9.3 ppm) = 10, 10'; d (3.0 ppm) = 9, 9'; e (1.7 ppm) = 1, 1'; f (-2.0 ppm) = 8, 8'; g (-4.1 ppm) = 5 (= 5'); h (-15.9 ppm) = 7, 7'; i (-28.0 ppm) = 2, 2'; and j (-40.0 ppm) = 4, 4'.

Table S1: NMR chemical shifts of ^{11}B and ^1H in *syn*- $\text{B}_{18}\text{H}_{22}$

positions	1, 1'	2, 2'	3, 3'	4, 4'	5 = 5'	6 = 6'	7, 7'	8, 8'	9, 9'	10, 10'	$\mu(6, 7)$	$\mu(8, 9)$	$\mu(9, 10)$
$\delta(^{11}\text{B})/\text{ppm}$	1.7	-28.0	13.5	-40.0	-4.1	9.7	-15.9	-2.0	3.0	9.3	X	X	X
$\delta(^1\text{H})/\text{ppm}$	3.6	-0.2	3.8	0.6	X	X	2.6	3.1	3.4	3.8	1.3	-2.5	-0.9

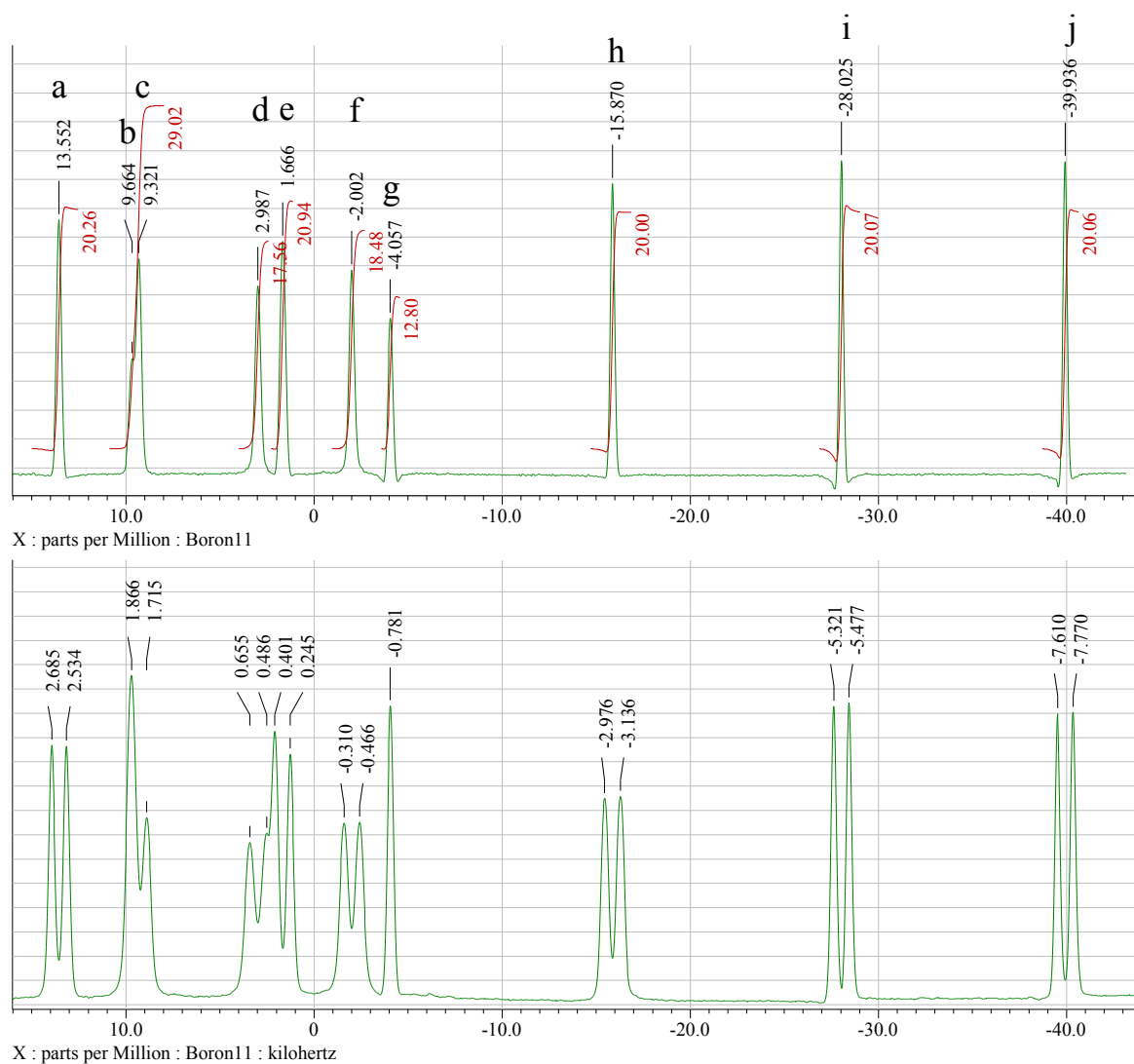


Figure S3. Experimental decoupled (top) and coupled (bottom) ^{11}B NMR spectra of *syn*- $\text{B}_{18}\text{H}_{22}$ with integrals normalised to 1 atom = 10 units.

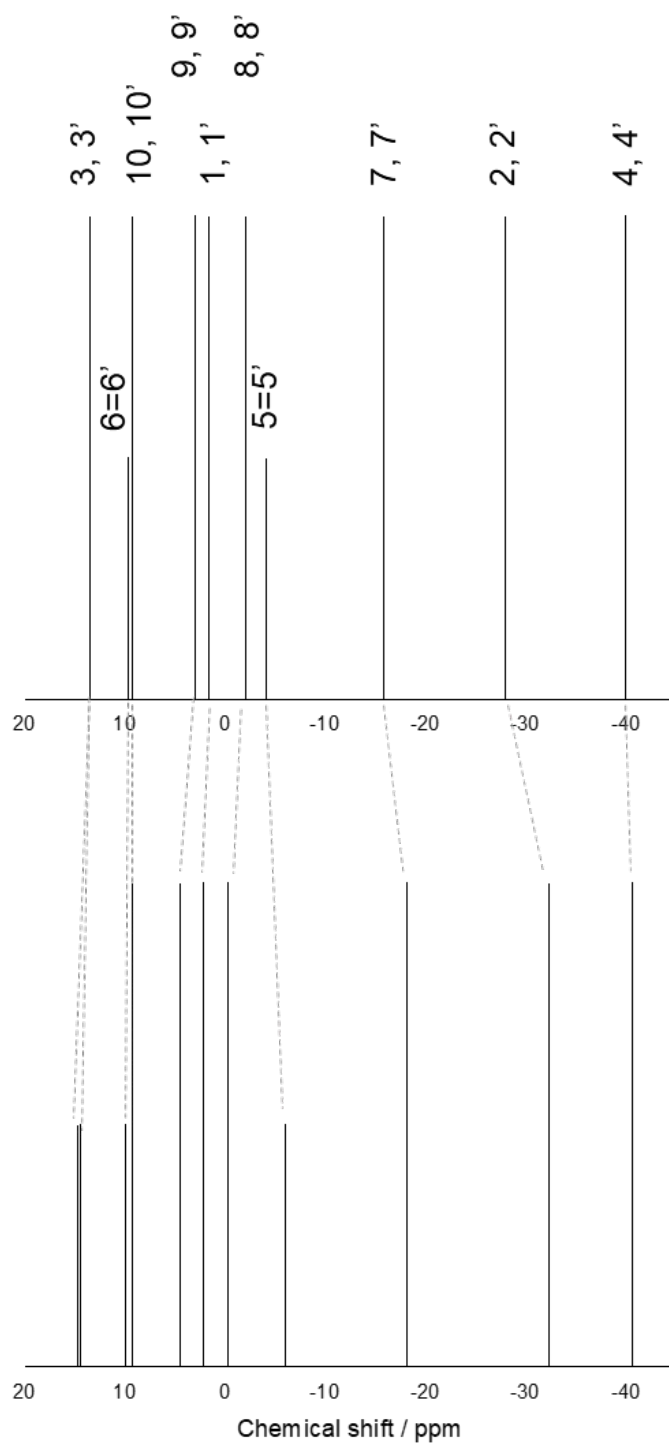


Figure S4. Correlation between the (top) experimental and (bottom) computational ^{11}B NMR spectra of *syn*- $\text{B}_{18}\text{H}_{22}$. Ratio of the boron signal intensity of experimental ^{11}B NMR: 2:1:2:2:2:2:1:2:2:2.

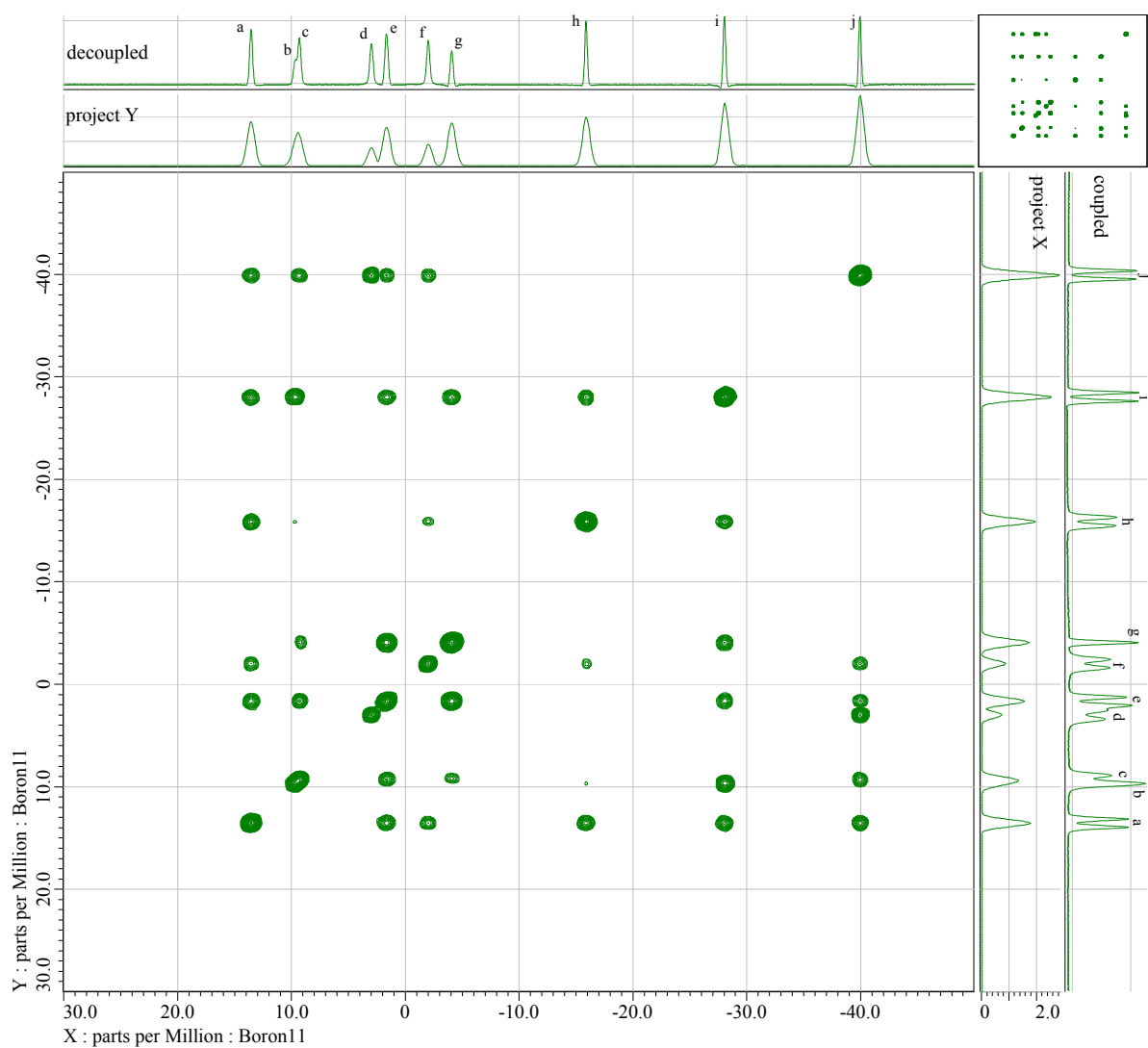


Figure S5. 2-D $[^{11}\text{B}-^{11}\text{B}]\text{-COSY-}\{^1\text{H}\}$ NMR spectrum of *syn*- $\text{B}_{18}\text{H}_{22}$ with the 1D spectra aligned along its edges.

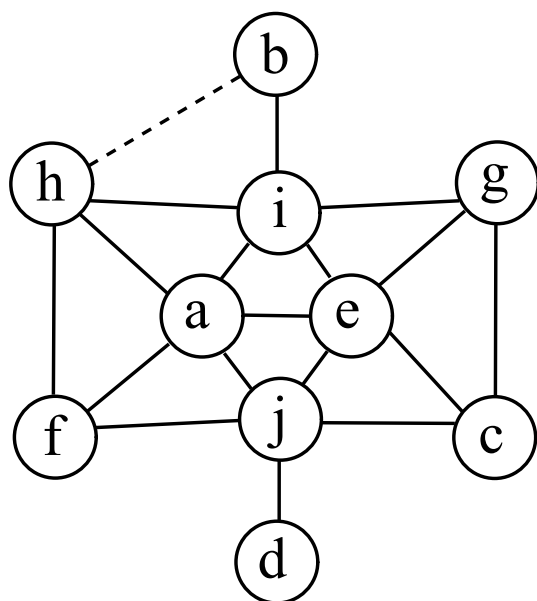


Figure S6. *syn*-B₁₈H₂₂ connections deduced from ¹¹B-COSY NMR

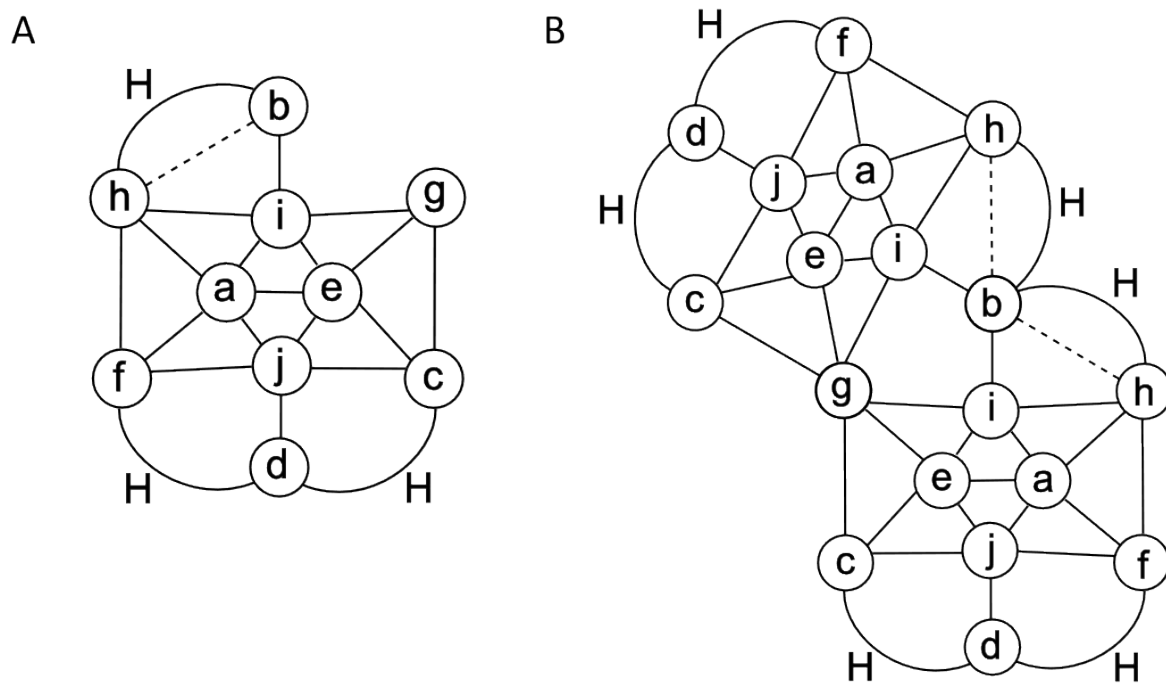


Figure S7. *syn*-B₁₈H₂₂ connections deduced from ¹¹B COSY NMR: (A) augmented with hydrogen bridges found in ¹¹B-¹H HMQC NMR; (B) expanded to the full formula.

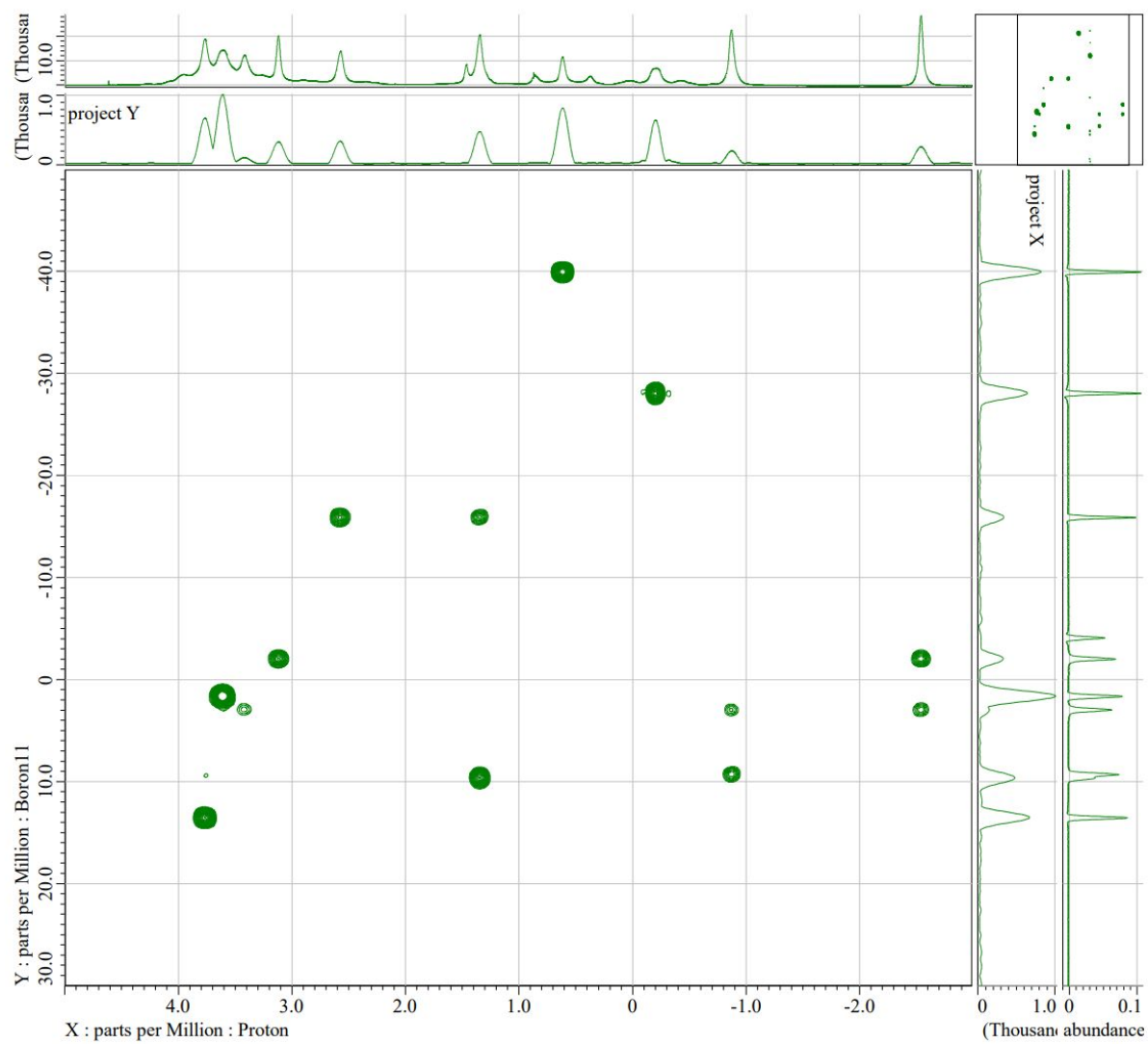


Figure S8. 2-D $[^1\text{H}-^{11}\text{B}]$ -HMQC NMR spectrum of *syn*- $\text{B}_{18}\text{H}_{22}$ with the 1D spectra aligned along its edges.

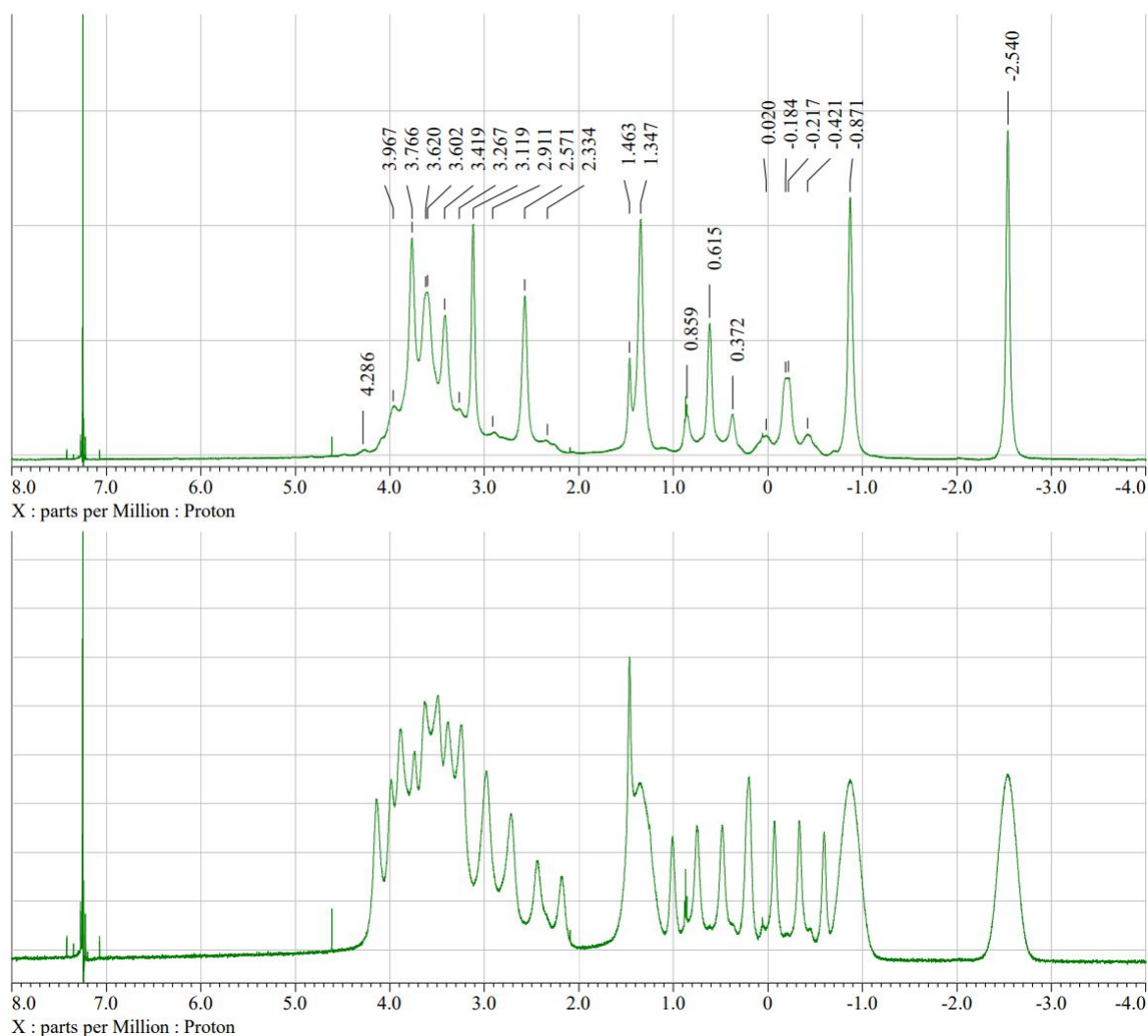


Figure S9. $^1\text{H}\{\text{B}\}$ decoupled (top) and coupled (bottom) proton NMR spectra of *syn*- $\text{B}_{18}\text{H}_{22}$

1-HS-*syn*- $\text{B}_{18}\text{H}_{21}$ ^{11}B NMR assignment

In the ^{11}B NMR spectra of monosubstituted *syn*- $\text{B}_{18}\text{H}_{22}$ derivatives we can expect three singlets: the peaks of B(5) and B(6), and that of the substituted atom. In the spectra of 1-HS-*syn*- $\text{B}_{18}\text{H}_{21}$ (Figure S10) we see clearly two singlets at 11.0 ppm and -3.8 ppm, altogether 16 major peaks, and three smaller peaks of a major impurity (10–20 molar %) that correspond to three peaks (of intensity 2) of the parent *syn*- $\text{B}_{18}\text{H}_{22}$. The peaks at 8.3 ppm and -28.1 ppm have integrated intensity two times larger than the other 14, and that at 8.3 ppm contains the third singlet, coinciding with a doublet. Comparing the spectra of the derivative with those of the parent borane, we can tentatively assign the pair of peaks in the lowest field, at 16.7 ppm and 15.0 ppm, to the boron atoms 3 and 3', that in the highest field, at -37.2 and -40.6 ppm, to the borons 4 and 4', the peaks coinciding at -28.0 ppm to 2 and 2', and the pair of peaks at -14.3 and -15.6 ppm to 7 and 7'. If we did not know from the X-ray structure that the compound is 1-HS-*syn*- $\text{B}_{18}\text{H}_{21}$, we could have deduced it from our chemical expectation that the substitution would occur in one of the four positions 1, 2, 3, and 4, and the fact that all the peaks in the areas around those of the borons 3, 4, and 2 of the parent borane are doublets here. We can expect that the singlet at the highest field, that at -3.8 ppm, will belong to the boron 5 (-4.1 ppm in the parent), while choosing between the assignment of 6 (9.7 ppm in the parent) and 1 (1.7 in the parent) to the singlets at 11.0 ppm and 8.3 ppm is trickier, as the ^{11}B COSY shows.

In the ^{11}B - ^{11}B COSY (Figure S12), we may not see all the cross peaks we could expect according to what we have seen in the COSY of the parent, but after the analysis of the spectrum we were able to fine tune its transformation so that we can find at least tentative traces of most, keeping still the occurrence of noise and artefacts at an acceptable level (Figure S13). For 5, we expect cross peaks with 1, 1', 2, 2', and 10, 10', for 6 with 2, and 2' only, and for 1 with 2, 3, 4, 5, and 10, and no one with any atom of the unsubstituted subunit. The singlet at -3.8 ppm has a strong cross peak with that at 11.0 ppm, one more strong one at 2.0 ppm, a weaker one with the peak of 2, 2', and a weak one at 8.6 ppm, with one of the peaks coinciding at 8.3 ppm in the 1D spectrum. That is in accord with the assignment of -3.8 ppm to the boron 5, and points to the singlet at 11.0 ppm belonging to the boron 1, not 6. This is confirmed by the singlet at 11.0 ppm having multiple cross peaks besides that with 5: also with 16.7 ppm (so it is 3, and 15.0 ppm will be 3'), -37.2 ppm (4, and -40.6 ppm will be 4'), -28.0 ppm (2, coinciding with 2'), and with one of the peaks coinciding at 8.3 ppm — only 10 remains to be assigned, and this position corresponds to the cross peak of 5 at 8.6 ppm, the exact position of which is possibly affected there by the neighbouring strong cross peak of 5 with 1. There is another cross peak of the coinciding pair of signals at 8.3 ppm with 2, 2' around [8.3 ppm, -28.0 ppm], and even one uncertain weak one with 4 at [8.3 ppm, -37.2 ppm], so as those signals coinciding at 8.3 ppm should be those of the borons 6 and 10, for 6 we expect the only cross peak with 2, 2', and for 10 those with 1, 4, and 5, we should assign the chemical shift of 8.3 ppm to both borons 6 and 10, their coincidence exact within the error of our measurement.

As the boron 3 in the parent borane has cross peaks with 1, 2, 4, 7, and 8, we can, after the assignment of 11.0 ppm to 1, and consequently 16.7 ppm to 3 and -37.2 ppm to 4 follow the cross peaks of 3 (16.7 ppm) and 3' (15.0 ppm), confirm the assignment of -37.2 ppm to 4 and -40.6 ppm to 4', assign -28.0 ppm to 2 and -28.4 ppm to 2', -14.3 ppm to 7 and -16.6 to 7', and 2.0 ppm to 1', and end up assigning the weak cross peaks at 0.0 ppm to 3 with 8, and at -2.0 ppm to 3' with 8'; we can verify this assignment by looking up other weak cross peaks of 8 with 7, 8' with 7', and 8' with 4', that of 8 with 4 possibly present as well, but hidden by the vicinity of a much stronger cross peak. The assignment of 2.0 ppm to 1' is confirmed by its cross peaks with 5, 2', and 4', the last unassigned of them at 9.7 ppm thus belonging necessarily to 10'. Boron 4 in the parent borane interacts with 1, 3, 8, 9, and 10, here we see cross peaks of 4 with 1 and 3, have already discussed the weak one with 10 and apparent absence of that with 8, so the last one, strong enough, at 1.1 ppm remains for 9; analogically we have already assigned the strong cross peaks of 4' with 1' and 3', as well as the weak ones with 10' and 8', so the last unassigned strong cross peak 3.3 ppm must correspond to 9'.

We thus get the observed ^{11}B NMR (192.6 MHz, 295K, CDCl_3) signals of 1-HS-*syn*- $\text{B}_{18}\text{H}_{22}$ assigned in the sequence:: B3 (16.7 ppm) > B3' (15.0 ppm) > B1 (10.9 ppm) > B10' (9.6 ppm) > B10 (8.3 ppm, according to the B10–B5 cross peak 8.6 ppm) > B6 (8.3 ppm, according to the B6–B2,B2' cross peak 8.3 ppm) > B 9' (3.3 ppm) > B1' (2.0 ppm) > B9 (1.0 ppm) > B8 (0.0 ppm) > B8' (-2.0 ppm) > B 5 (-3.8 ppm) > B7 (-14.3 ppm) > B7' (-16.6 ppm) > B2 (-28.1 ppm, according to the B2–B1 and B2–B3 cross peaks: -28.0 ppm on the x-axis, -27.9 on the y-axis) > B2' (-28.1 ppm, according to the B2'–B3' and B1'–B2' cross peaks: -28.4 ppm on the x-axis, -28.3 on the y-axis) > B4 (-37.2 ppm) > B4' (-40.6 ppm).

The cross peaks we see in the ^{11}B - ^1H HMQC NMR spectrum (Figure S14) do not allow us to assign ^1H NMR shifts to all the hydrogen atoms in the molecule. Looking up the cross peaks of the boron atoms from 3 (16.7 ppm) to 4' (-40.6 ppm), we find the ^1H chemical shifts 4.2 ppm for 3, and 3.9 ppm for 3'. The substituted boron 1 has no terminal hydrogen, but 10' does, and we see only its cross peak with the bridging hydrogen 10'–9' at -1.0 ppm anyway. The case of 10 and 6 is identical, $\mu\text{H}(10, 9)$ has the chemical shift -0.4 ppm, and $\mu\text{H}(6, 7)$ 1.7 ppm; even the expected cross peak of B(6) with $\mu\text{H}(6, 7')$ is absent. The boron 9' has, besides its cross peak with $\mu\text{H}(10', 9')$ that with $\mu\text{H}(9', 8')$ at -2.5 ppm, but again none with a terminal hydrogen, only for 1' we see the cross peak with H(1') at 3.7 ppm. $\mu\text{H}(9, 8)$ has chemical shift -2.5 ppm but only B(8') has also a visible cross peak with its terminal hydrogen at 3.1 ppm. For the boron 5 we do not expect contact with any hydrogen but at the borons 7 and 7' we again have expected cross peaks missing, 7 only having on with $\mu\text{H}(6, 7)$, and 7' in contrast with H(7') at 2.6 ppm. According to the only cross peak of the coinciding signals of B(2) and B(2'), H(2) and H(2') probably have the same chemical shift -0.2 ppm, and the cross peaks of the borons 4 and 4' show the chemical shifts of H(4) as 0.7 ppm and of H(4') as 0.6 ppm. At least the five bridging hydrogens identified of the expected six confirm our assignment of the ^{11}B spectrum.

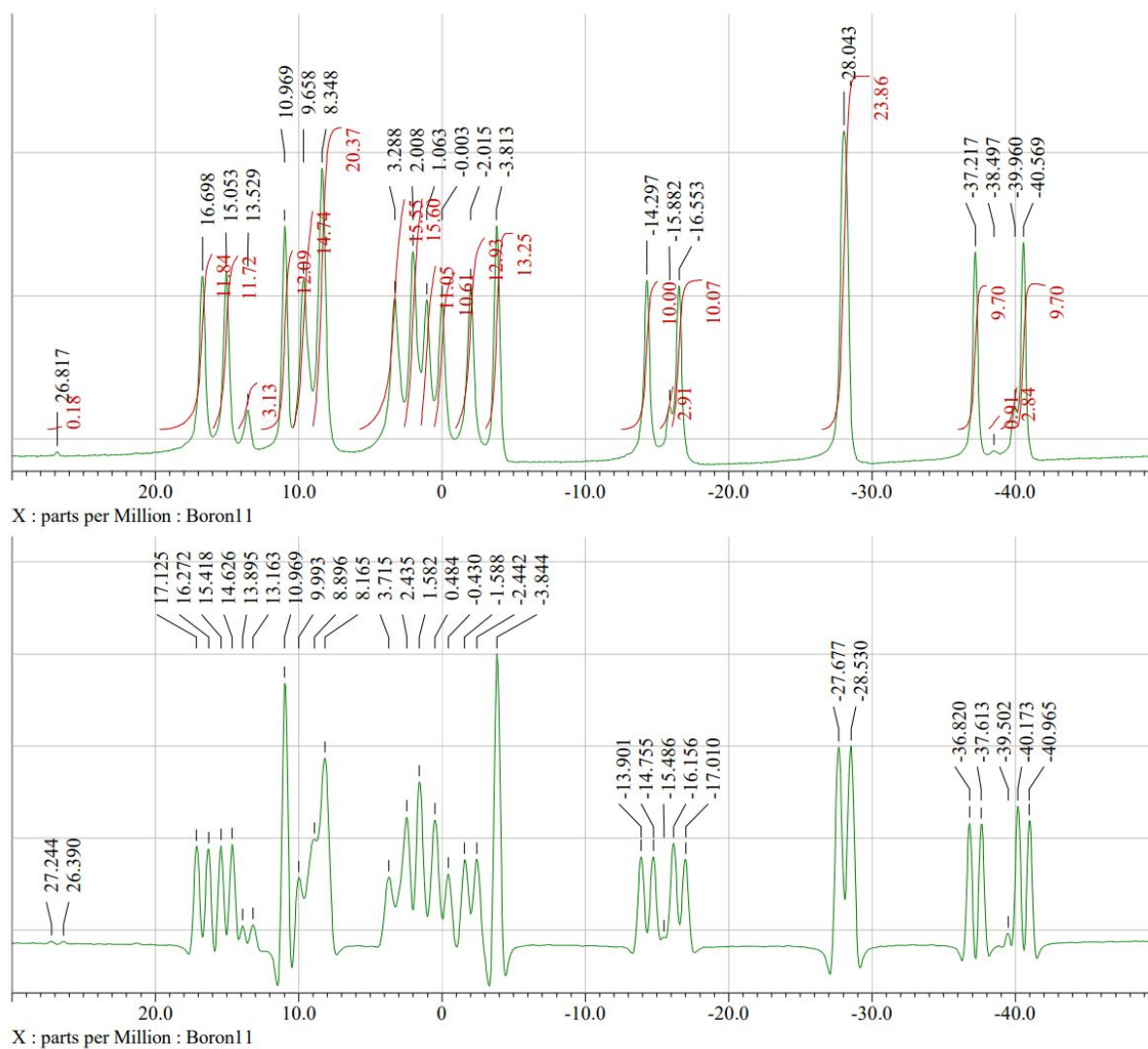


Figure S10. Experimental decoupled (top) and coupled (bottom) ^{11}B NMR spectra of 1-HS-syn- $\text{B}_{18}\text{H}_{21}$ (**1**).

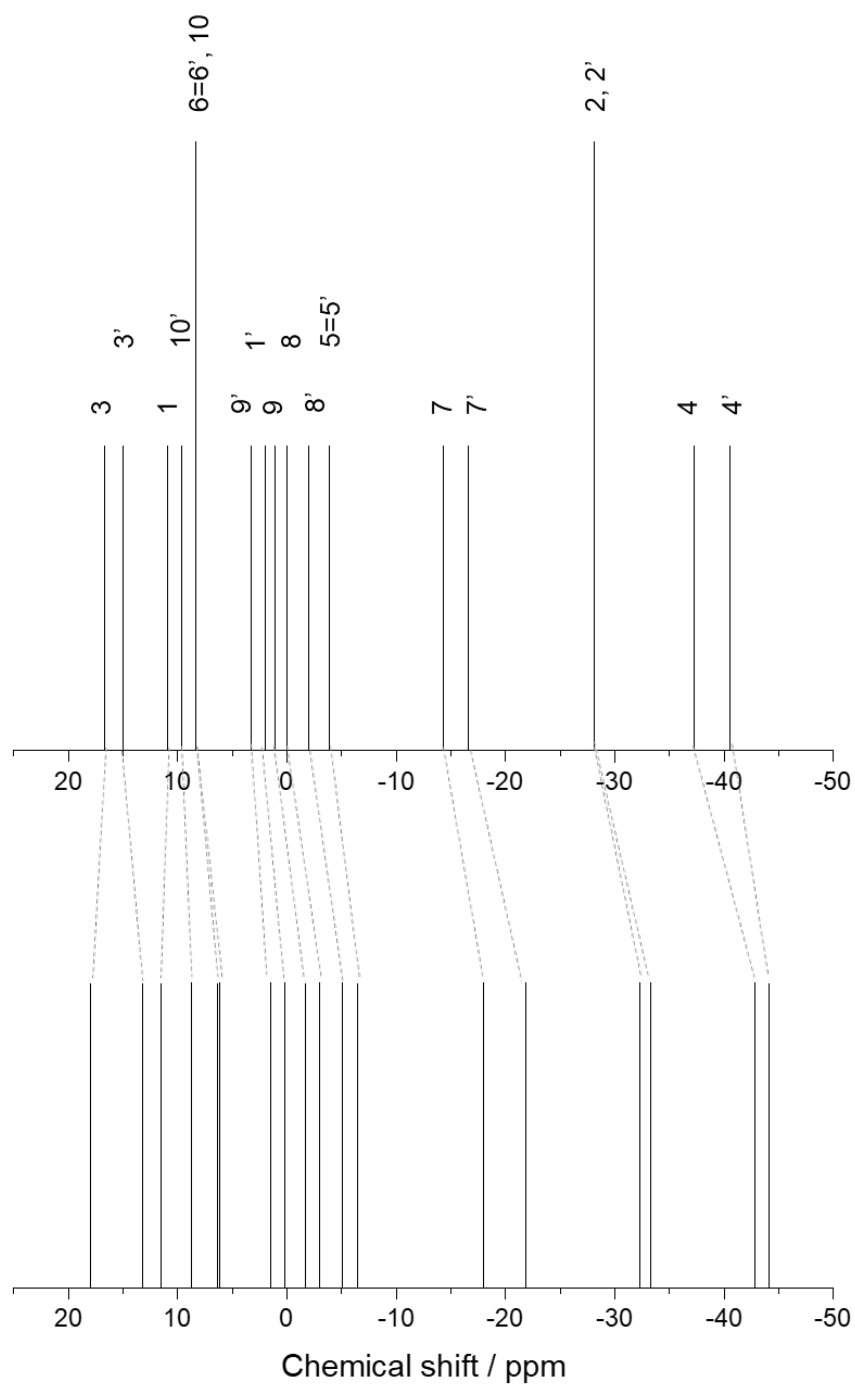


Figure S11. Correlation between the (top) experimental and (bottom) computational ^{11}B NMR spectra of 1-HS-syn-B₁₈H₂₁ (**1**). Ratio of the boron signal intensity of experimental ^{11}B NMR: 1:1:1:1:2:1:1:1:1:1:1:1:2:1:1

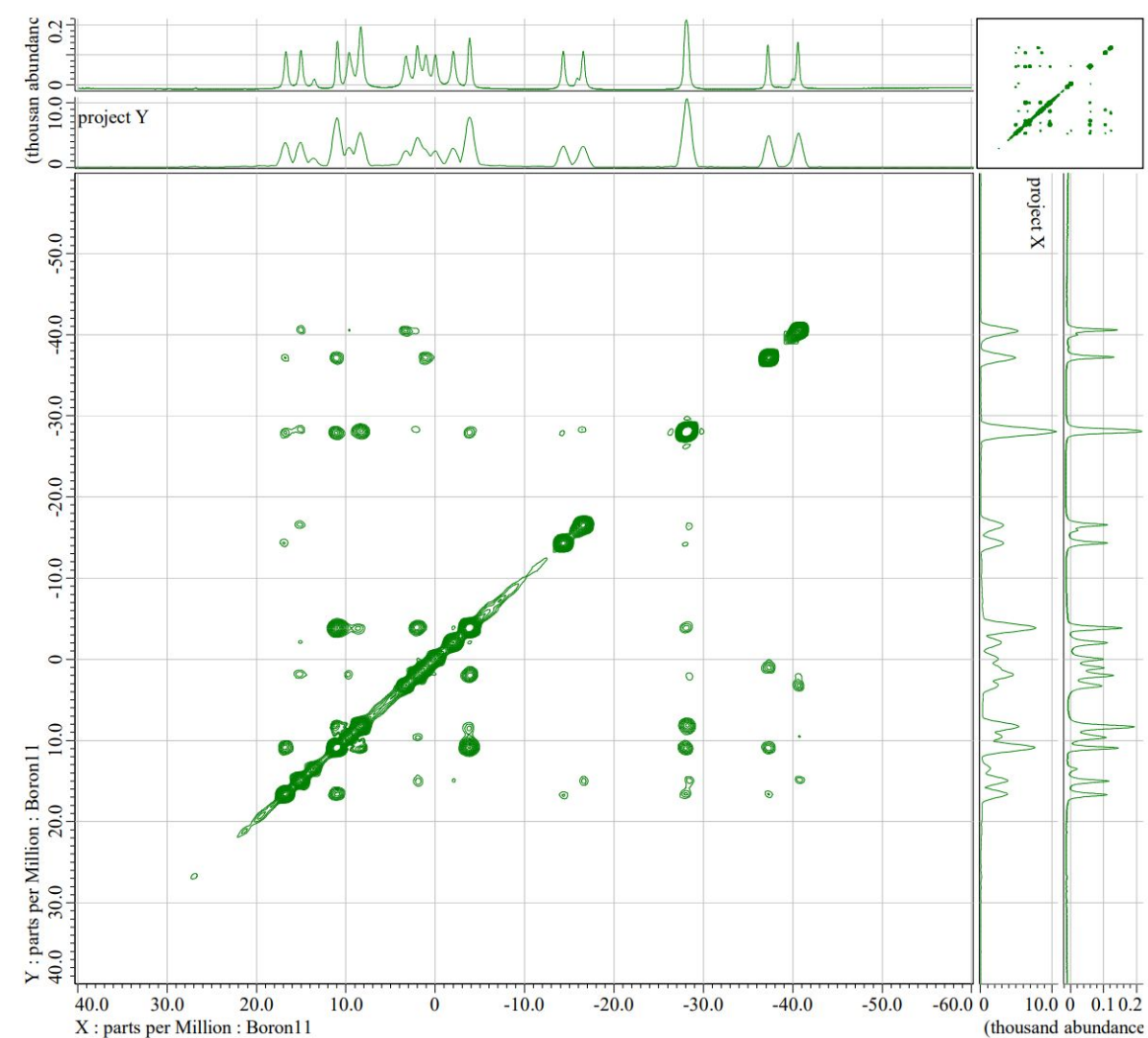


Figure S12. 2-D $[^{11}\text{B}-^{11}\text{B}]\text{-COSY-}\{^1\text{H}\}$ NMR spectrum of 1-HS-*syn*- $\text{B}_{18}\text{H}_{21}$ (**1**).

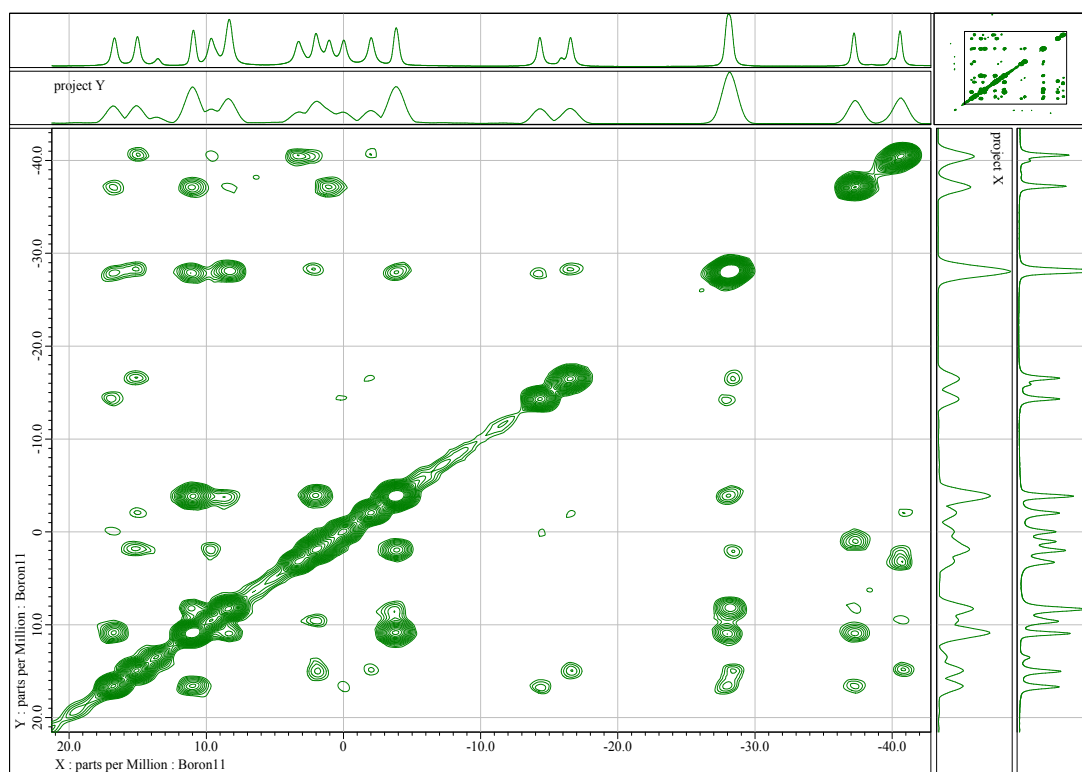


Figure S13: ^{11}B COSY NMR spectrum of 1-HS-syn- $\text{B}_{18}\text{H}_{21}$ treated to see as many cross peaks as possible.

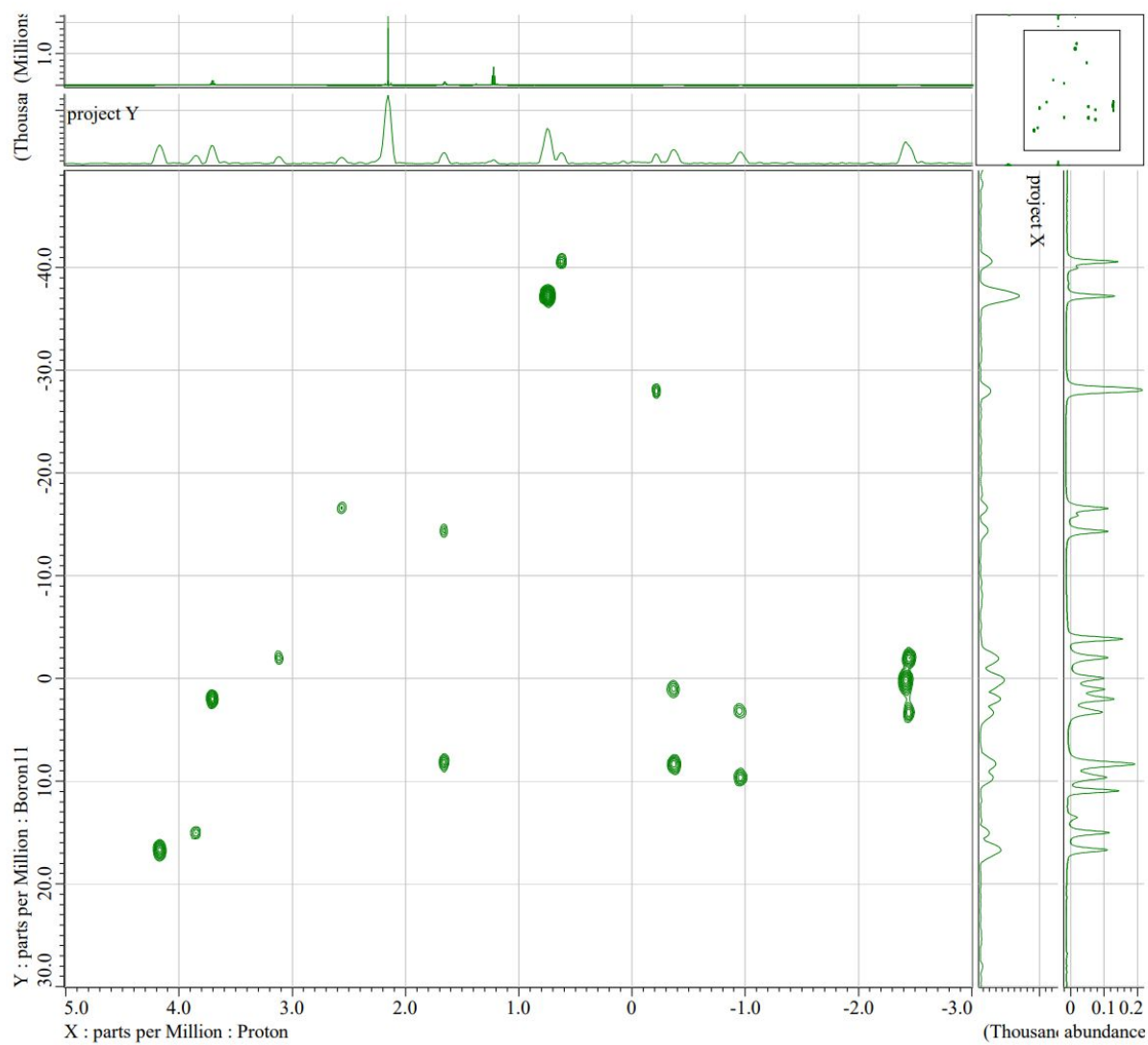


Figure S14. 2-D $[^1\text{H}-^{11}\text{B}]$ -HMQC NMR spectrum of 1-HS-*syn*- $\text{B}_{18}\text{H}_{21}$ (**1**).

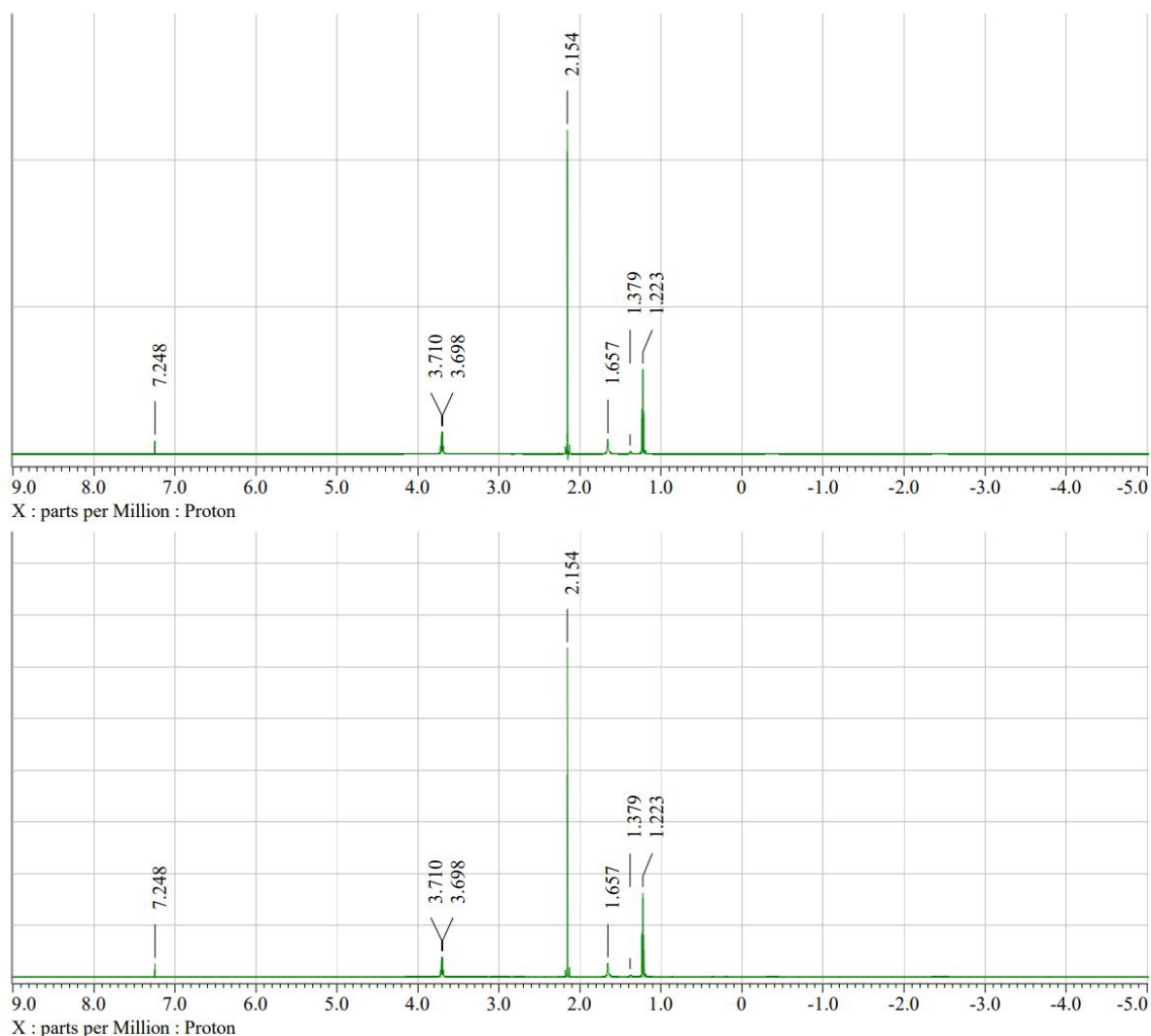


Figure S15. $^1\text{H}\{\text{B}\}$ decoupled (top) and coupled (bottom) proton NMR spectra of 1-HS-*syn*- $\text{B}_{18}\text{H}_{21}$ (**1**)

3-HS-*syn*- $\text{B}_{18}\text{H}_{21}$ ^{11}B NMR assignment

In the comparison of ^1H decoupled and simple (coupled) ^{11}B NMR spectra of 3-HS-*syn*- $\text{B}_{18}\text{H}_{21}$ (Figure S16) we see immediately three singlets, that we can on the basis of the parent borane spectrum assign to the substituted position 3 (21.4 ppm) and the two borons common to both subunits, that have no terminal hydrogens, 6 (6.6 ppm) and 5 (-2.2 ppm). The decoupled spectrum contains 17 peaks, in one of them the singlet of B(5) coincides with a doublet of another boron atoms, and all the signals of the other 16 boron atoms are individually resolved. Still by the analogy with the spectra of the parent we can assign 15.0 ppm to 3' and tell that the three pairs in the upfield part of the spectrum belong -15.4 ppm and -16.8 ppm to 7 and 7', -28.6 ppm and -29.4 ppm to 2 and 2', and -38.5 ppm and -39.4 ppm to 4 and 4'.

Again, we verify and complete the assignment by interpreting the ^{11}B - ^{11}B COSY NMR spectrum (Figure S18). Cross peaks of 3 and 3' allow us to assign -38.5 ppm to 4 and -39.4 ppm to 4', -28.6 ppm to 2 and -29.4 ppm to 2', -29.4 ppm to 7 and -28.6 ppm to 7', and 4.4 ppm to 1 and 2.7 ppm to 1', and -3.2 ppm to 8, and -2.0 ppm to 8', in the 1D spectrum coinciding with 5 at -2.2 ppm. As we expect for 5 cross peaks with 1, 1', 2, 2', 10, and 10', for 8'

with 3', 4', and 7', and for 1' with 2', 3', 4', 5, and 10', our assignment is verified by the cross peaks at [-2.2 ppm, 4.4 ppm] and [-2.2 ppm, 2.6 ppm] that can only belong to 5-1 and 5-1' because 8 and 8' cannot have cross peaks with 5, nor with 1'. We do not see the cross peaks of 5 with 10 and 10' but 1 has a weak cross peak with 10 at 10.3 ppm, and 1' has similar with 10' at 9.7 ppm. Even though we do not see all the expected cross peaks for 4 and 4', there are strong enough cross peaks of 4 with 9 at 0.8 ppm and 4' with 9' at 9.7 ppm. The assignment of the ^{11}B spectrum is thus complete, and other visible cross peaks like those of 5 with 2 and 2' of 6 with 2 and 2' or those of 1 with 2 and 1' with 2' corroborate it.

The sequence of the observed ^{11}B NMR signals of 3-HS-*syn*- $\text{B}_{18}\text{H}_{22}$ is: 3 (21.4 ppm) > 3' (13.5 ppm) > 10 (10.3 ppm) > 10' (9.7 ppm) > 6 (6.6 ppm) > 1 (4.4 ppm) > 9' (3.7 ppm) > 1' (2.7 ppm) > 9 (0.8 ppm) > 8' (-2.0 ppm) > 5 (-2.2 ppm) > 8 (-3.2 ppm) > 7' (-15.4 ppm) > 7 (-16.8 ppm) > 2 (-28.6 ppm) > 2' (-29.4 ppm) > 4 (-38.5 ppm) > 4' (-39.4 ppm).

An interesting feature in the ^{11}B - ^1H HMQC spectrum of 3-HS-*syn*- $\text{B}_{18}\text{H}_{21}$ (Figure S19) is the cross peak of the substituted B(3) at 1.4 ppm — with the thiol group hydrogen, in the ^1H NMR spectrum decoupled by ^{11}B represented by a very sharp peak, and without decoupling only slightly broadened (Figure S20). 3' has a cross peak with its terminal hydrogen at 3.8 ppm. For 10 and 10' we have detected cross peaks only with their bridging hydrogens with B(9) and B(9'); the chemical shifts of those hydrogens are -0.9 ppm, identical within our experimental error, even though $\mu\text{H}(9, 10)$ is visibly upfield of $\mu\text{H}(9', 10')$. B(6) has strong cross peaks with its bridging hydrogens, $\mu\text{H}(6, 7)$ at 1.9 ppm, downfield from $\mu\text{H}(6, 7')$ at 1.1 ppm. According to the cross peaks of 1 and 1', H(1) has chemical shift 4.0 ppm, and H(1') 3.6 ppm. For borons 9 and 9' we see only their cross peaks with their bridging hydrogens, besides $\mu\text{H}(9, 10)$ and $\mu\text{H}(9', 10')$, there are $\mu\text{H}(8, 9)$ at -2.1 ppm and $\mu\text{H}(8', 9')$ at -2.5 ppm. As B(5) is not connected to any hydrogen atom, it does not interfere with the assignment of the chemical shift 3.5 ppm to H(8'), while H(8) has 3.1 ppm, according to a weak cross peak. The borons 7 and 7' have, besides their cross peaks with $\mu\text{H}(6, 7)$ and $\mu\text{H}(6, 7')$ those with their terminal hydrogens too, even though that of B(7) with H(7) at 2.6 ppm is weaker than that of B(7') with H(7') at 2.7 ppm, just like that of B(8) with H(8) in comparison to that of B(8') with H(8'). According to their cross peaks with B(4) and B(4'), H(4) has chemical shift 0.7 ppm and H(4') 0.6 ppm. For B(2) and B(2'), we had to adjust the parameters of the transformation of the spectrum to resolve their cross peaks with H(2) and H(2') at the expense of others (Figure S21): follows that H(2) is slightly upfield of H(2') but within our experimental error their chemical shifts are identical, -0.2 ppm.

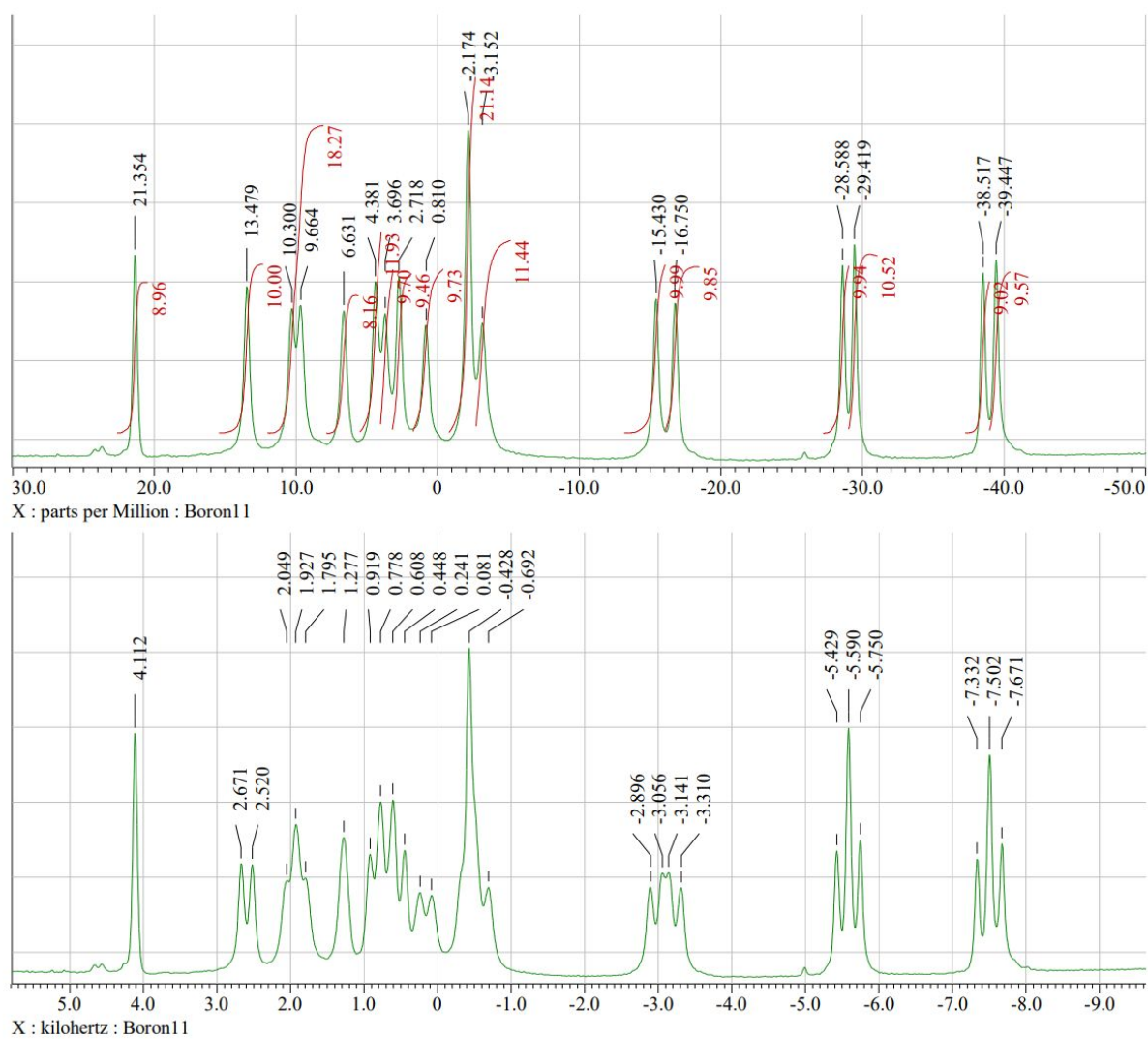


Figure S16. Experimental decoupled (top) and coupled (bottom) ^{11}B NMR spectra of 3-HS-syn- $\text{B}_{18}\text{H}_{21}$ (**3**).

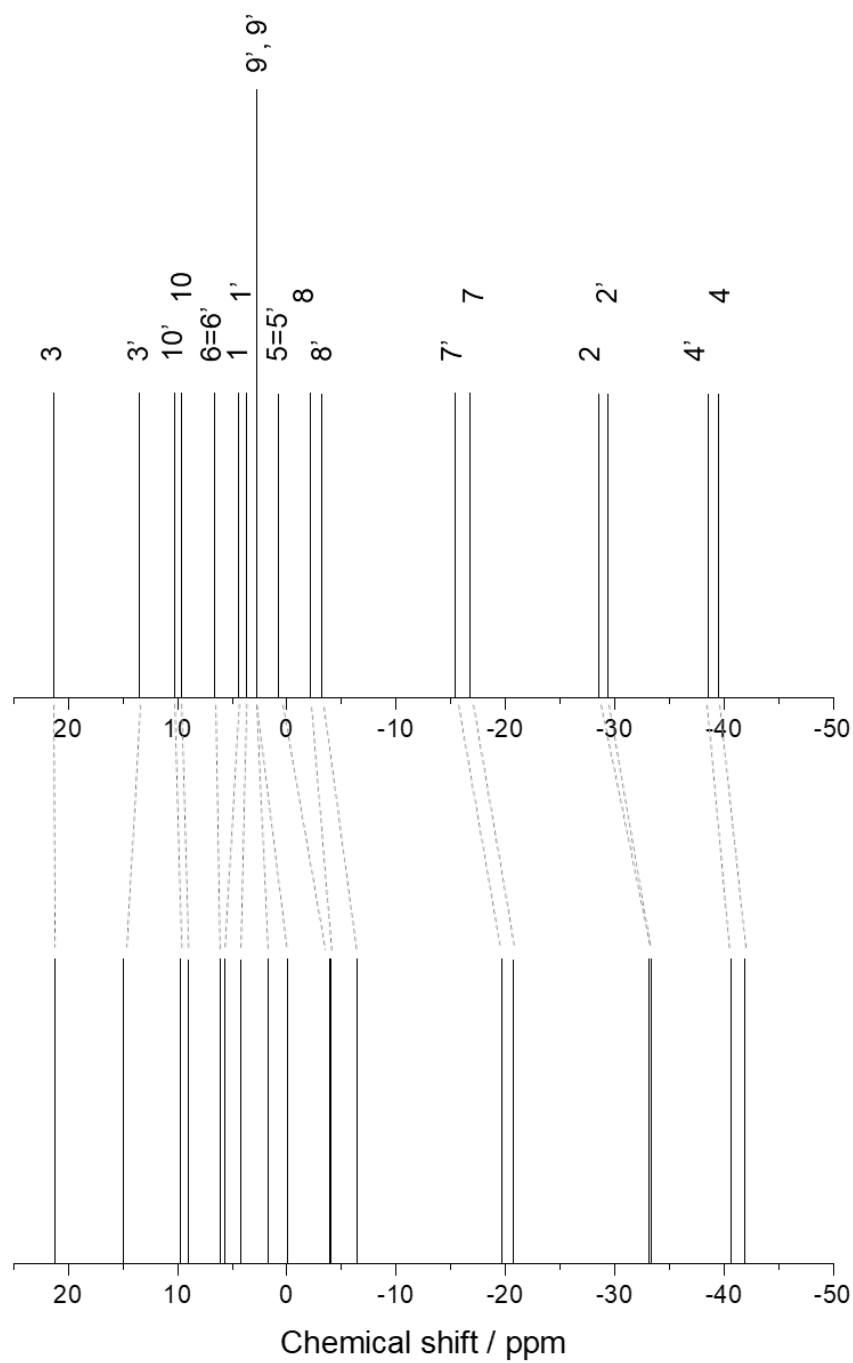


Figure S17. Correlation between the (top) experimental and (bottom) computational ^{11}B NMR spectra of 3-HS-*syn*- $\text{B}_{18}\text{H}_{21}$ (**3**). Ratio of the boron signal intensity of experimental ^{11}B NMR: 1:1:1:1:1:1:1:2:1:1:1:1:1:1:1.

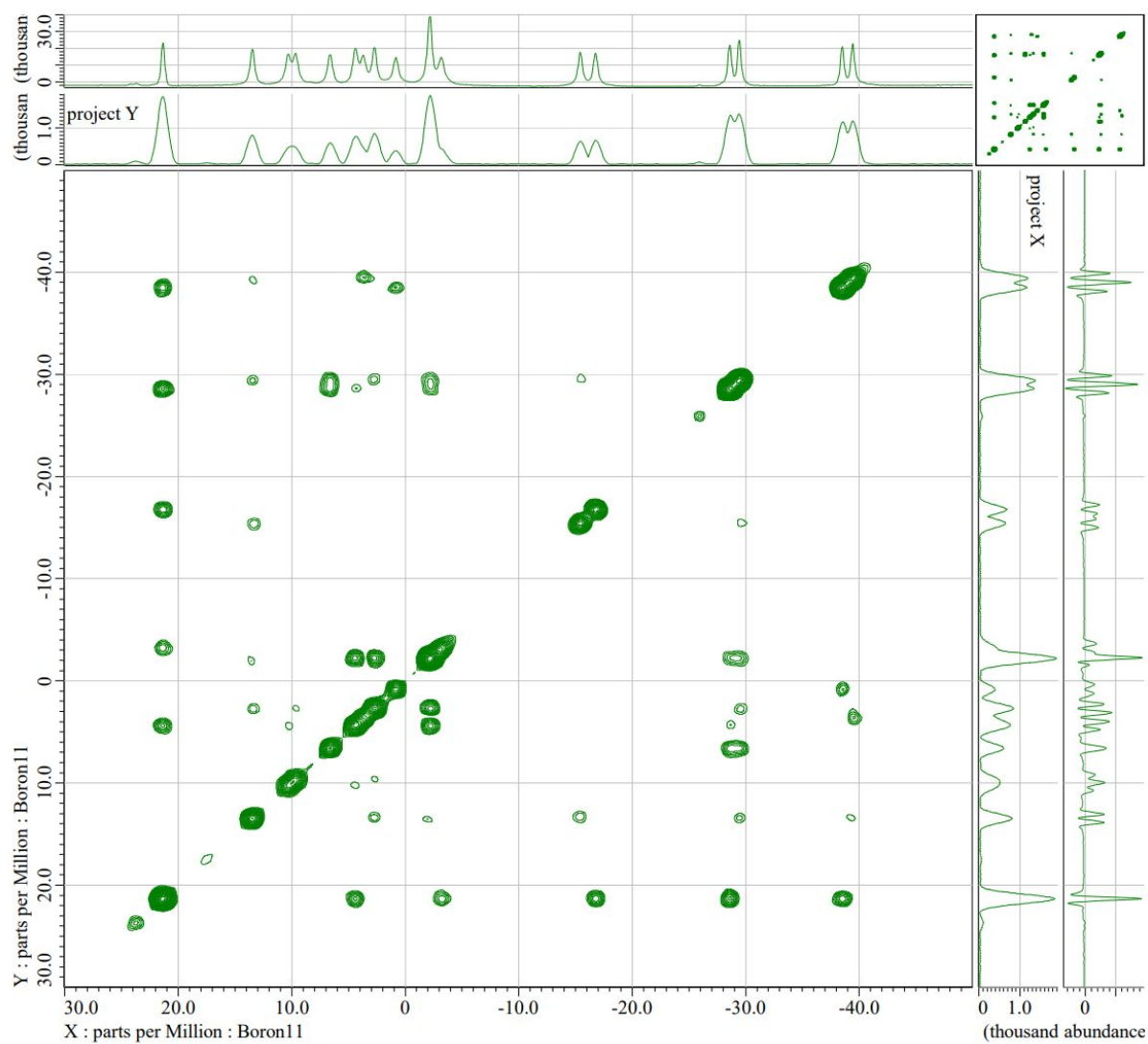


Figure S18. 2-D $[^{11}\text{B}-^{11}\text{B}]\text{-COSY-}\{^1\text{H}\}$ NMR spectrum of 3-HS-*syn*- $\text{B}_{18}\text{H}_{21}$ (**3**).

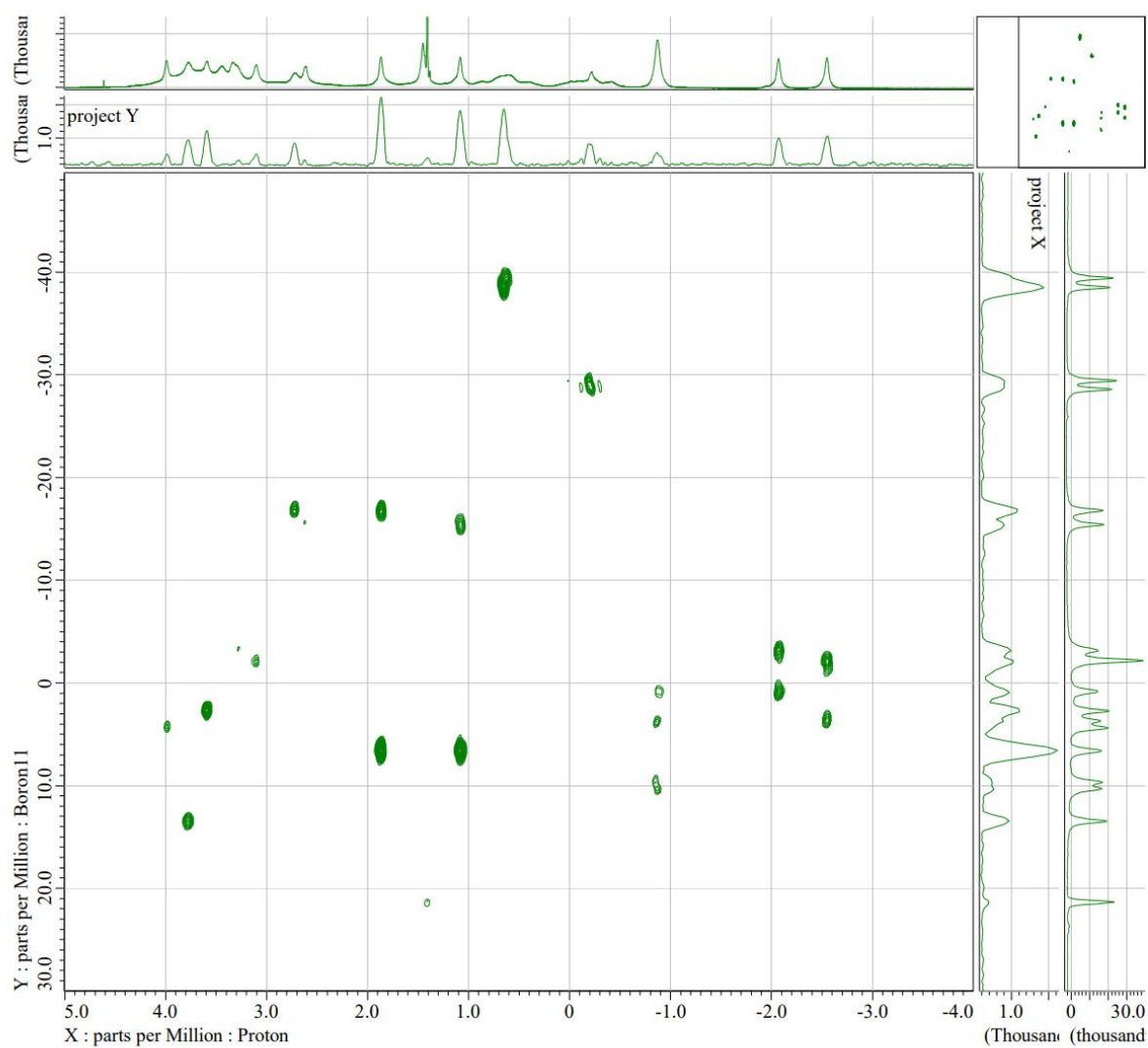


Figure S19. 2-D $[^1\text{H}-^{11}\text{B}]$ -HMQC NMR spectrum of 3-HS-*syn*- $\text{B}_{18}\text{H}_{21}$ (**3**).

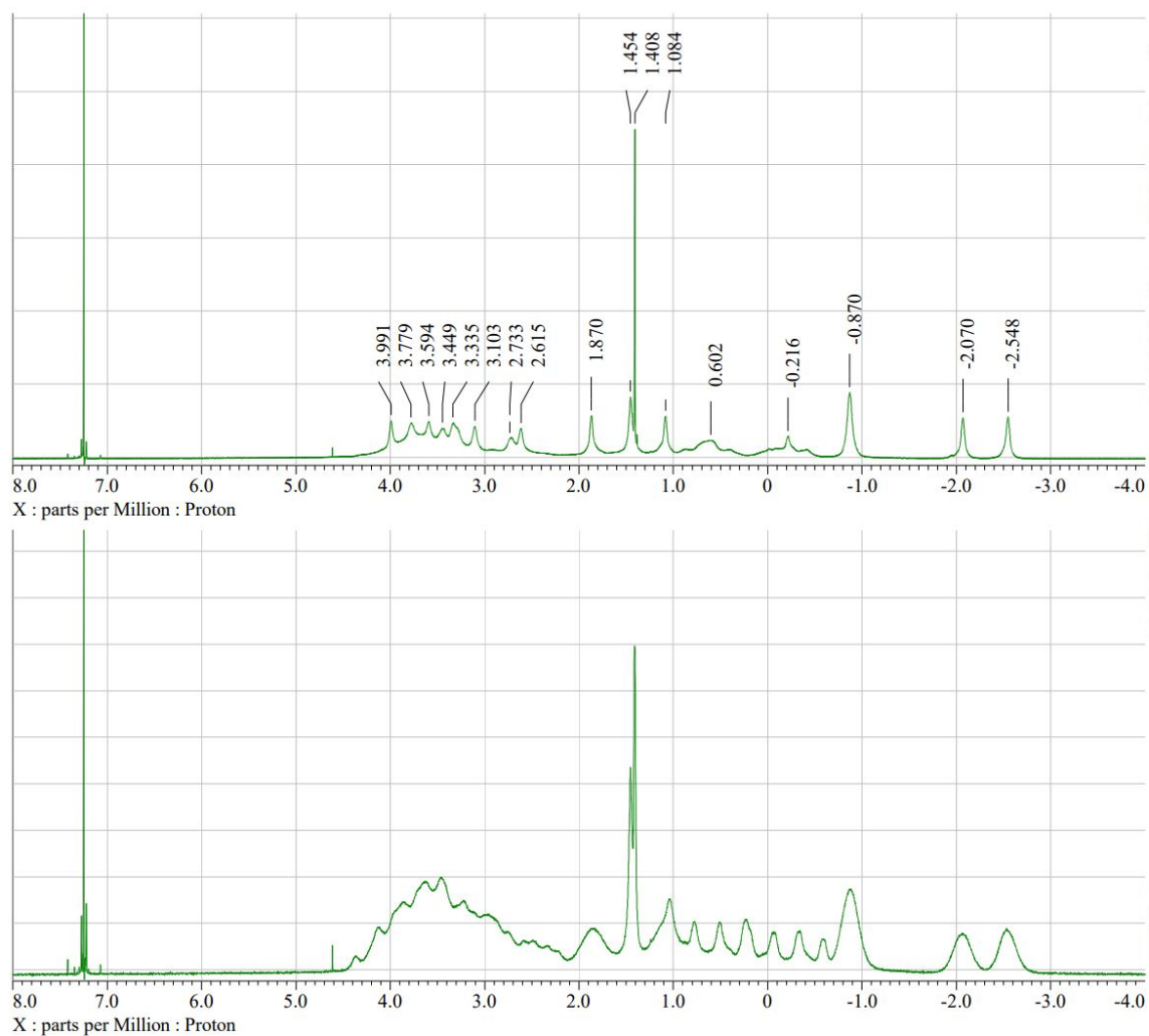


Figure S20. $^1\text{H}\{\text{B}\}$ decoupled (top) and coupled (bottom) proton NMR spectra of 3-HS-syn- $\text{B}_{18}\text{H}_{21}$ (**3**).

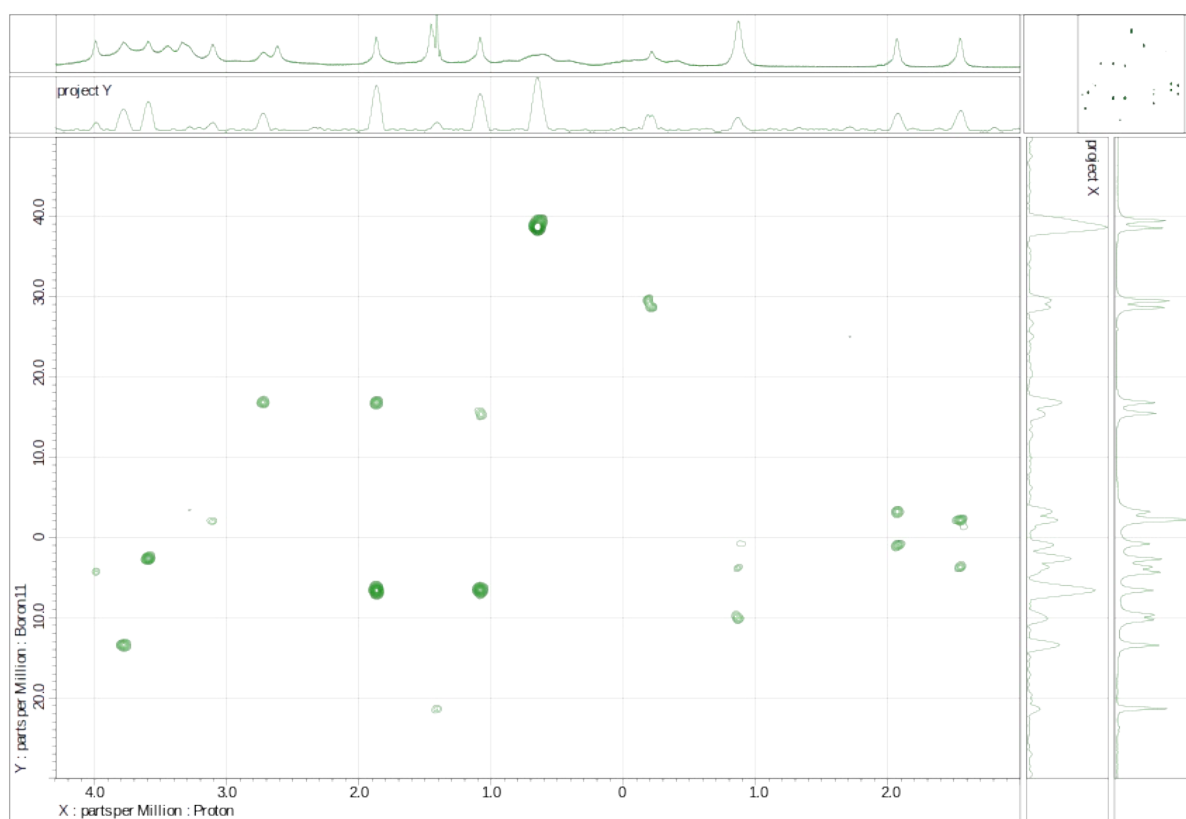


Figure S21: ^1H - ^{11}B HMQC NMR spectrum of 3-HS-*syn*- $\text{B}_{18}\text{H}_{21}$ treated to resolve the cross peaks of B(2) with H(2) and B(2') with H(2')

4-HS-*syn*- $\text{B}_{18}\text{H}_{21}$ ^{11}B NMR assignment

4-HS-*syn*- $\text{B}_{18}\text{H}_{21}$ has many ^{11}B NMR signals (Figure S22) very close together, especially the group 1, 1', 9, 9'; 8 and 8' almost coincide, and 7, 7' do not differ at all. Nevertheless, a strong line narrowing transformation (Gaussian window on the FID before the Fourier transform 42 Hz wide and shifted 13 ms for the ^1H decoupled spectrum and 50 Hz shifted 10 ms for the coupled one) allows to differentiate all the peaks (Figure S23). Interestingly, there is at -25.8 ppm, in the typical area of 2, 2' signals, a singlet, so likely a signal of a substituted B(2), which suggests that even the 2-HS isomer that we have not obtained in pure form may have been formed at least as a very minor product, and present as an impurity.

Singlets at 8.1 ppm, -3.4 ppm, and -29.2 ppm can be assigned to B(6), B(5), and B(4) respectively just on the comparison with the spectra of the parent and the other isomers: 8.1 ppm is upfield of B(6) of the parent, slightly more than in 1-HS and less than in 3-HS, -3.4 ppm is downfield of B(5) in the parent, again more than in 1-HS but less than in 3-HS, and -29.2 ppm is a singlet downfield of B(4) peaks at the upfield end of *syn*- $\text{B}_{18}\text{H}_{22}$ derivatives spectra, shifted from the parent towards the B(2) region, but must belong to the substituted B(4), even if we did not know from the X-ray that this is the 4-HS isomer, because there are two doublets close to one another at -27.7 ppm and -28.1 ppm, evidently B(2) and B(2') (we only have to find out which is which), and only one doublet of B(4') is left at -39.8 ppm, downfield of 4, 4' of the parent but less than B(4') of 3-HS.

In ^{11}B - ^{11}B COSY, B(4) of *syn*- $\text{B}_{18}\text{H}_{22}$ (Figure S5) has cross peaks with 1, 2, 3, 8, 10, and 9. In the COSY of 4-HS-*syn*- $\text{B}_{18}\text{H}_{21}$ (Figure S25), no 4'-2' or 4-2 cross peak is seen. There are four cross peaks of 4 (or 5 if there are two at 3.0 and 2.6 ppm fused together), and four of 4', so besides those with 2 and 2', one more must be missing, at least for 4', perhaps that with 8', based on our experience with 1-HS and 3-HS. Assignment of 14.9 ppm to 3 and 13.8

ppm to 3' is easy, both downfield of the parent, 3 about as much as 3' in 1-HS, 3' less. Similarly, 10.3 ppm will be B(10), downfield of the parent about as much as in 3-HS, and 9.1 ppm B(10'), slightly upfield of the parent, but less than B(10) in 1-HS. 4' has a strong cross peak with 3.5 ppm and weaker with 2.0 ppm, 4 has a strong one with 2.6 ppm, and possibly a weaker one with 3.0 ppm, fused with the stronger one. We can assign them, along with 2 and 2', based on the cross peaks of 2 and 2', as this is the area of borons 1 and 9, and in the parent borane, 9 has a cross peak only with 4 (and can hardly have one with 2, not even hypothetically), while 1 has cross peaks with both 4 and 2 (and 3, 5, and 10). The signal at -28.1 ppm has a cross peak with 2.0 ppm, which has a cross peak with 4', so 2.0 ppm is 1', and -28.1 ppm is 2'. It leaves 2 to assign to -27.7 ppm, and its cross peak with 3.0 ppm, that may, with some uncertainty, have one with 4 as well, make 3.0 ppm B(1). Subsequently 3.5 ppm must belong to B(9'), and 2.6 ppm to B(9). The remaining cross peak of B(4) at -1.2 ppm allows us to assign -1.2 ppm to B(8), and consequently -1.6 ppm, even without cross peaks detected, to B(8'). The cross peaks of 1 with 3 and 10, and of 1' with 3' and 10', corroborate this assignment, as do the cross peaks of 3 with 2 and 3' with 2', borons 5 and 6 having cross peaks with both 2 and 2'. The peak at -16.1 ppm that belongs to borons 7 and 7', has cross peaks only with 3 and 3'; those allow to differentiate a bit, albeit around the level of experimental error, between B(7) and B(7'), and to assign -16.1 ppm to 7', and -16.2 ppm to 7. We thus have the signals in the ^{11}B (^1H decoupled) NMR spectrum of 4-HS-*syn*-B₁₈H₂₁ assigned as: 3 (14.9 ppm) > 3' (13.8 ppm) > 10 (10.3 ppm) > 10' (9.1 ppm) > 6 (8.1 ppm) > 9' (3.5 ppm) > 1 (3.0 ppm) > 9 (2.6 ppm) > 1' (2.0 ppm) > 8 (-1.2 ppm) > 8' (-1.6 ppm) > 5 (-3.4 ppm) > 7' (-16.1 ppm) > 7 (-16.2 ppm) > 2 (-27.7 ppm) > 2' (-28.1 ppm) > 4 (-29.2 ppm) > 4' (-39.8 ppm).

From the cross peaks in the ^1H - ^{11}B HMQC spectrum (Figure S26) we see that H(3) has chemical shift 4.0 ppm, H(3') 3.8 ppm, $\mu\text{H}(9, 10)$ -0.3 ppm, $\mu\text{H}(9', 10')$ -0.9 ppm, $\mu\text{H}(6, 7')$ 1.2 ppm, $\mu\text{H}(6, 7)$ 1.4 ppm, $\mu\text{H}(8', 9')$ -2.5 ppm, $\mu\text{H}(8, 9)$ -1.9 ppm, the cross peaks of the terminal hydrogens at the positions 10 and 10' are not detected, H(1) has chemical shift 3.8 ppm, H(1') 3.7 ppm, H(8) 3.4 ppm, H(8') 3.1 ppm, H(7') 2.5 ppm, H(7) 2.7 ppm, H(2) -0.1 ppm, H(2') -0.3 ppm, and H(4') 0.6 ppm. The cross peaks of the bridging hydrogens confirm our assignment of the ^{11}B spectrum.

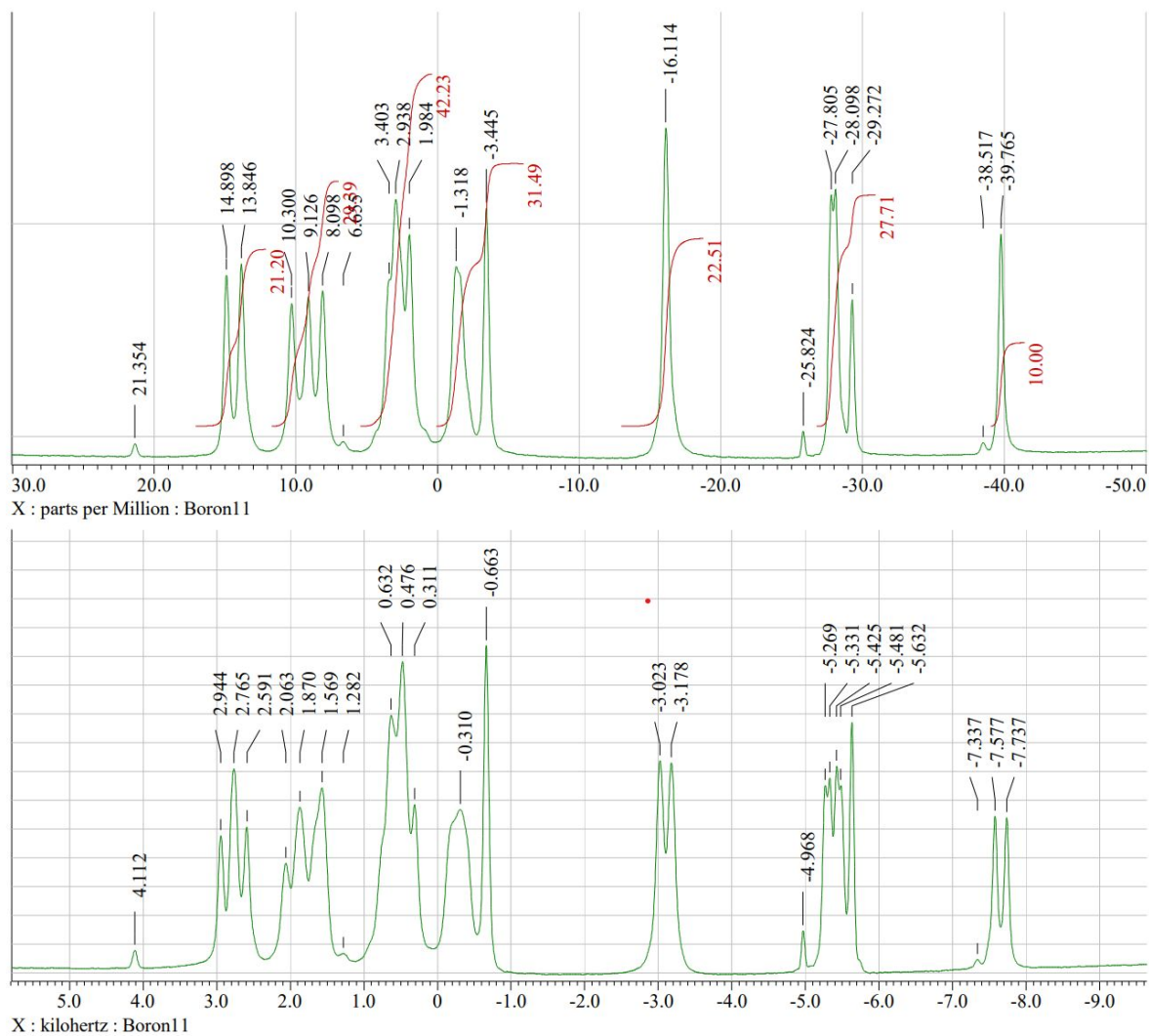


Figure S22. Experimental decoupled (top) and coupled (bottom) ^{11}B NMR spectra of 4-HS-syn- $\text{B}_{18}\text{H}_{21}$.

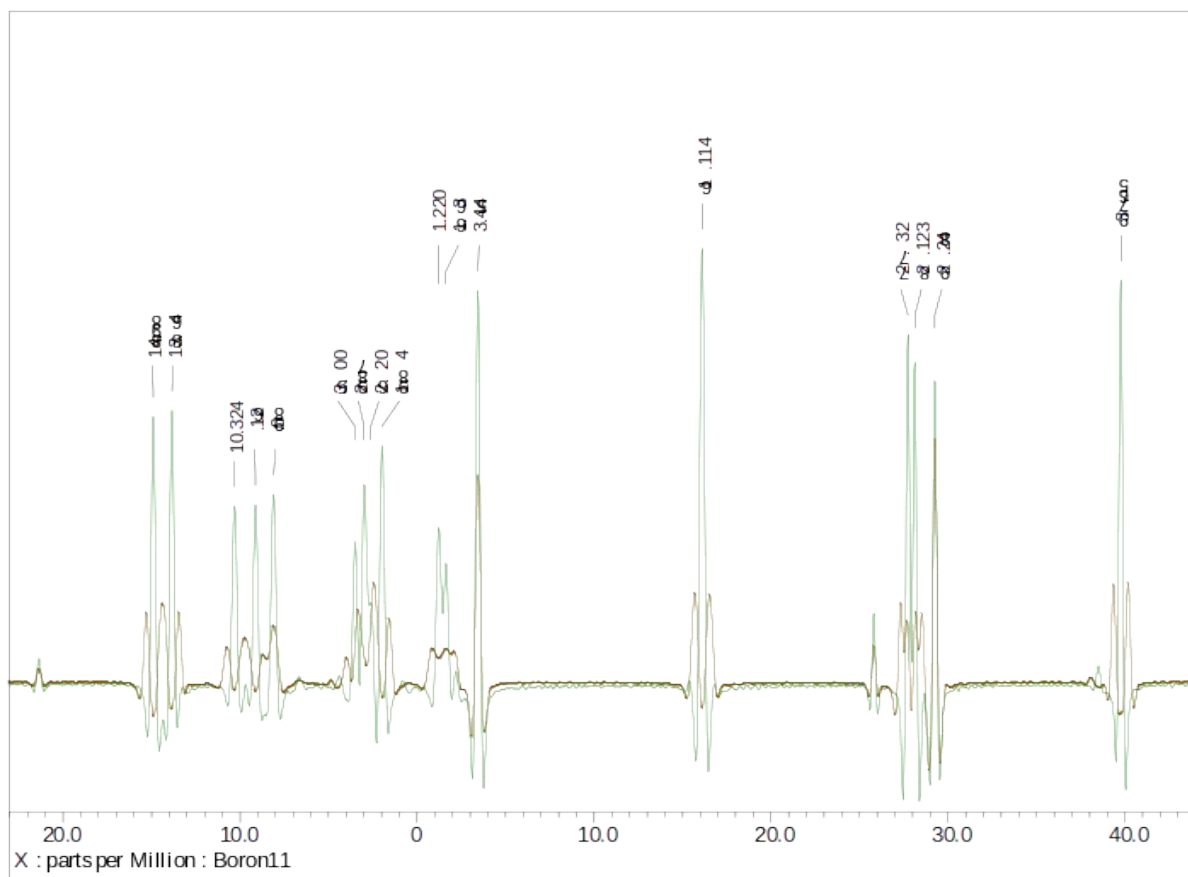


Figure S23: ^1H decoupled ^{11}B NMR spectrum of 4-HS-syn- $\text{B}_{18}\text{H}_{21}$ superimposed on the non-decoupled one, transformation of the FID fine-tuned to get lines narrow enough for discriminating all the signals.

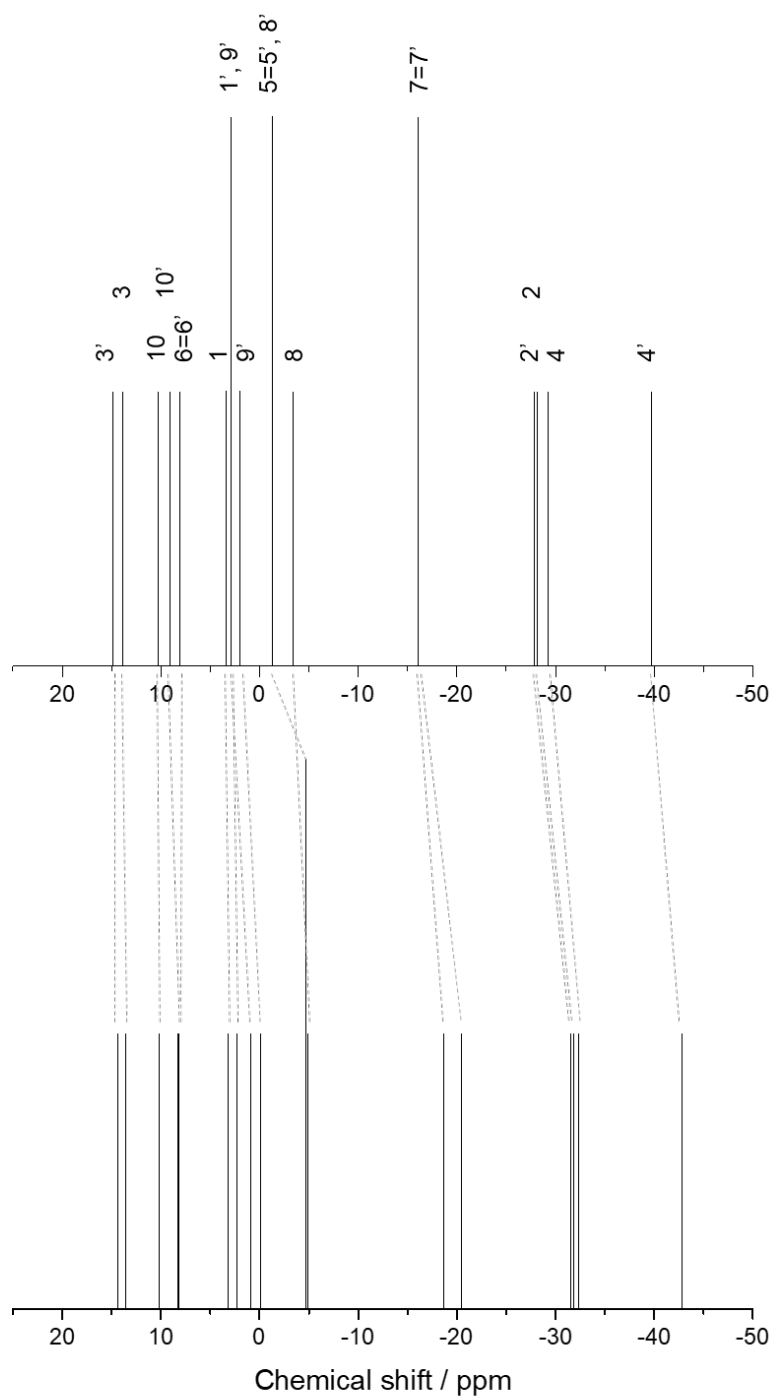


Figure S24. Correlation between the (top) experimental and (bottom) computational ^{11}B NMR spectra of 4-HS-*syn*- $\text{B}_{18}\text{H}_{21}$ (**4**). Ratio of the boron signal intensity of experimental ^{11}B NMR: 1:1:1:1:1:1:2:1:2:1:2:1:1:1:1

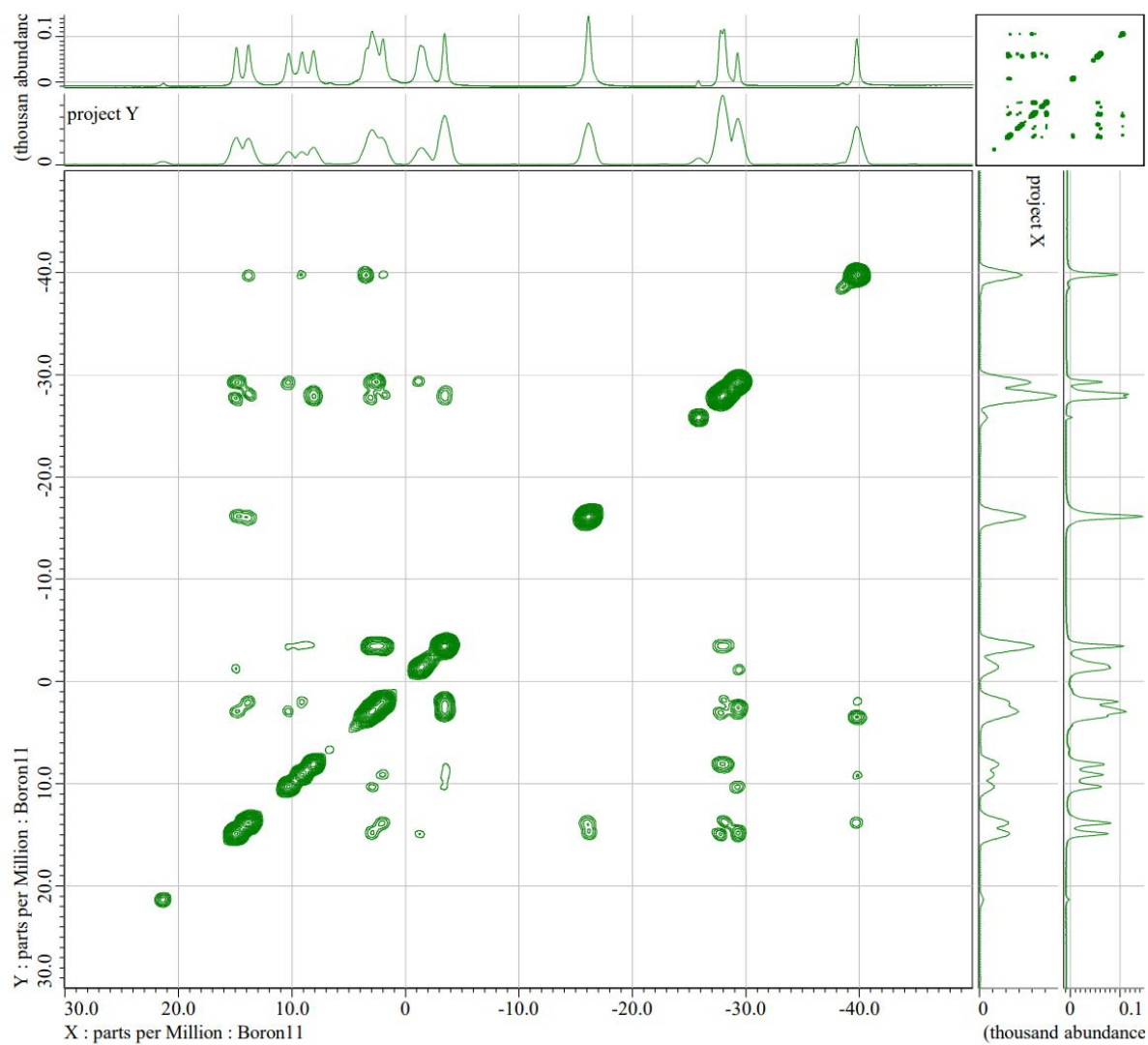


Figure S25. 2-D $[^{11}\text{B}-^{11}\text{B}]\text{-COSY-}\{^1\text{H}\}$ NMR spectrum of 4-HS-*syn*- $\text{B}_{18}\text{H}_{21}$ (**4**)

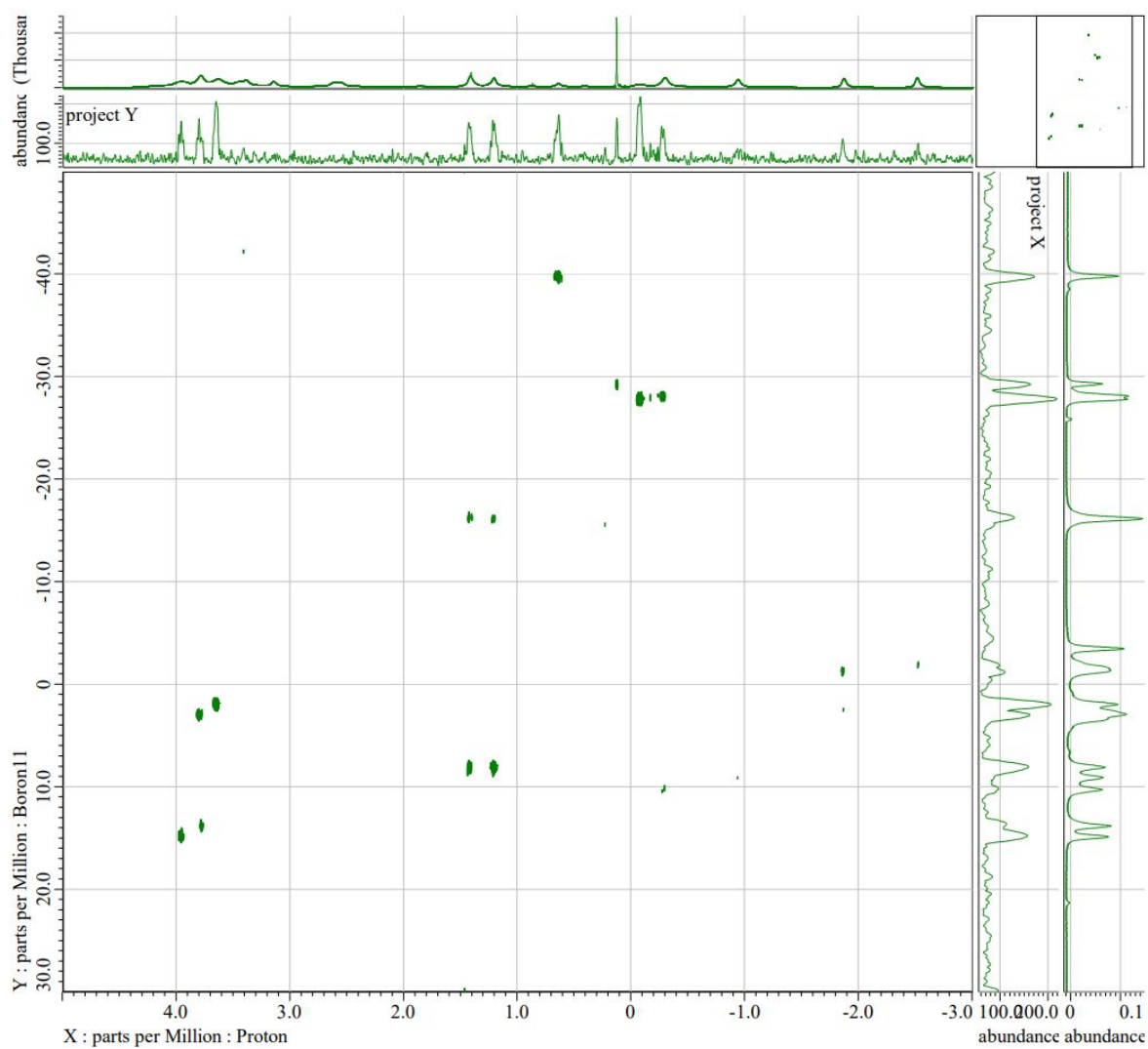


Figure S26. 2-D $[^1\text{H}-^{11}\text{B}]$ -HMQC NMR spectrum of 4-HS-*syn*- $\text{B}_{18}\text{H}_{21}$ (**4**)

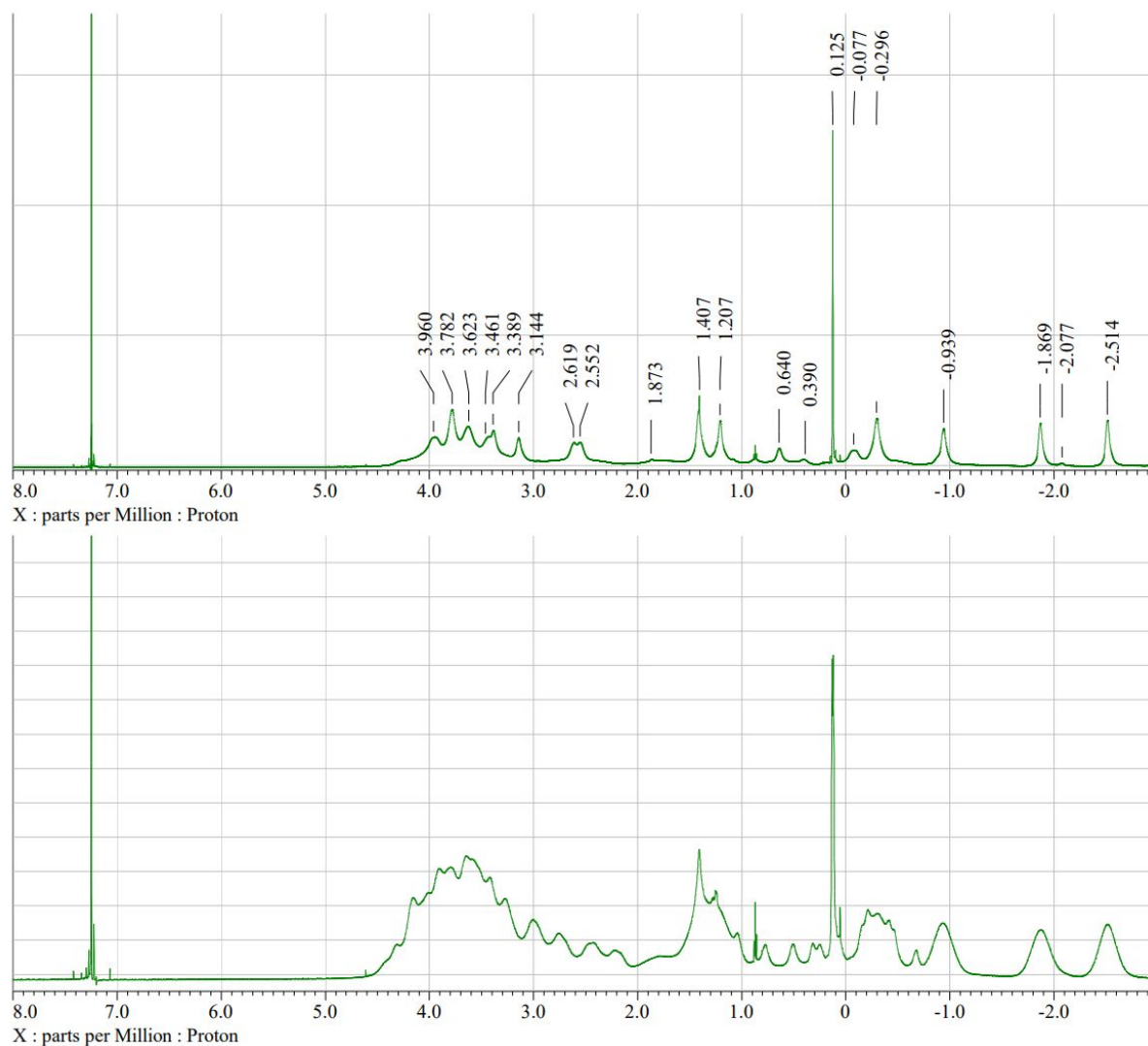


Figure S27. Decoupled (top) $^1\text{H}\{\text{B}\}$ and coupled (bottom) proton NMR spectra of 4-HS-*syn*- $\text{B}_{18}\text{H}_{21}$ (**4**).

Table S2. Calculated chemical shift in ppm

Atom (Position)	<i>syn</i> - $\text{B}_{18}\text{H}_{22}$	1-HS- <i>syn</i> - $\text{B}_{18}\text{H}_{21}$	2-HS- <i>syn</i> - $\text{B}_{18}\text{H}_{21}$	3-HS- <i>syn</i> - $\text{B}_{18}\text{H}_{21}$	4-HS- <i>syn</i> - $\text{B}_{18}\text{H}_{21}$
B(1)	2.15	11.57	3.49	5.70	3.18
B(2)	-32.27	-33.26	-27.29	-33.15	-32.37
B(3)	14.76	17.93	16.04	21.23	13.57
B(4)	-40.64	-42.84	-42.36	-41.86	-31.81
B(5=5')	-6.03	-5.04	-4.60	-3.94	-4.67
B(6=6')	9.93	6.13	7.63	6.08	8.13
B(7)	-18.12	-18.00	-20.19	-20.67	-20.43
B(8)	-0.28	-2.99	-5.89	-4.01	-4.88
B(9)	4.44	-1.74	-2.17	-0.04	-0.13
B(10)	9.32	6.31	7.78	8.96	10.15
B(1')	2.15	1.50	3.77	4.17	2.27
B(2')	-32.27	-32.29	30.72	-33.34	-31.57
B(3')	14.46	13.24	10.71	15.00	14.38
B(4')	-40.64	-44.07	-37.88	-40.66	-42.81
B(7')	-18.12	-21.84	-18.52	-19.68	-18.66
B(8')	-0.28	-6.42	-7.57	-6.42	-4.67
B(9')	4.44	0.19	5.75	1.73	0.87
B(10')	9.32	8.75	3.32	9.72	8.23

Table S3. Experimental chemical shift in ppm

<i>syn</i> -B ₁₈ H ₂₂	Intensity Ratio	1-HS- <i>syn</i> -B ₁₈ H ₂₁	Intensity Ratio	3-HS- <i>syn</i> -B ₁₈ H ₂₁	Intensity Ratio	4-HS- <i>syn</i> -B ₁₈ H ₂₁	Intensity Ratio
13.552	2	16.698	1	21.354	1	14.898	1
9.664	1	15.022	1	13.479	1	13.846	1
9.321	2	10.938	1	10.300	1	10.3	1
2.987	2	9.628	1	9.664	1	9.126	1
1.666	2	8.348	2	6.631	1	8.098	1
-2.002	2	3.288	1	4.381	1	3.403	1
-4.057	1	2.008	1	3.696	1	2.938	2
-15.870	2	1.063	1	2.718	2	1.984	1
-28.025	2	-0.003	1	0.810	1	-1.318	2
-39.936	2	-2.015	1	-2.174	1	-3.445	1
		-3.844	1	-3.152	1	-16.114	2
		-14.328	1	-15.430	1	-27.805	1
		-16.553	1	-16.750	1	-28.098	1
		-28.073	2	-28.588	1	-29.272	1
		-37.217	1	-29.419	1	-39.765	1
		-40.569	1	-38.517	1		
				-39.447	1		

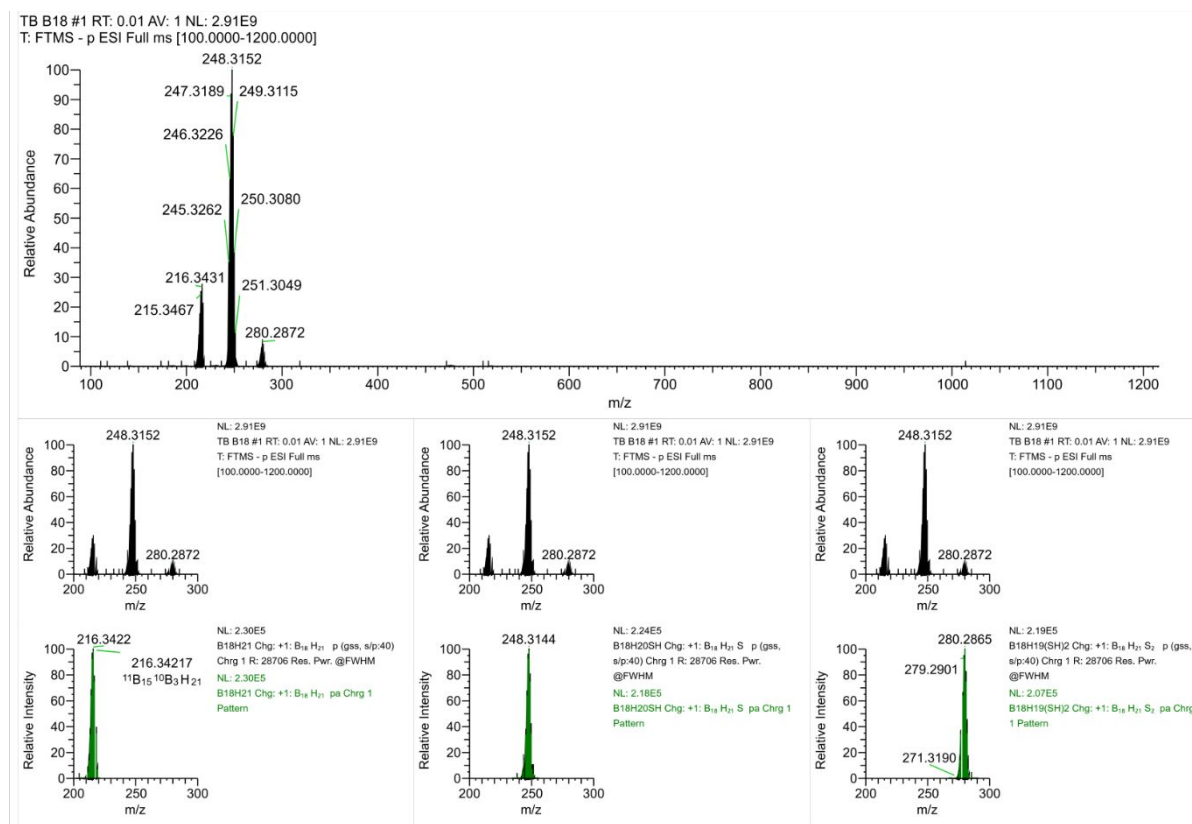


Figure S28. Positive ion mode MS ESI spectra of HS-B₁₈H₂₁. (Top) full range m/z spectrum and (bottom) corresponding experimental and theoretical matching of different fragments.

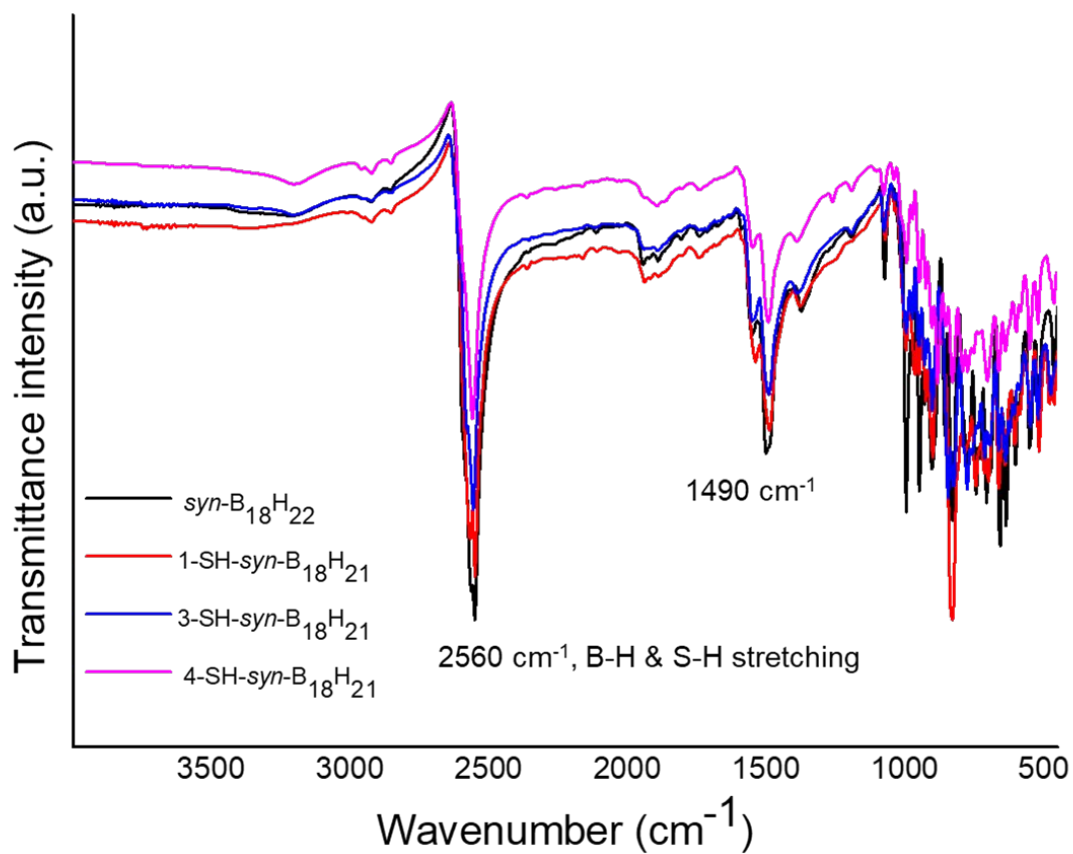


Figure S29. FTIR of HS- $\text{syn-B}_{18}\text{H}_{21}$ isomers and $\text{syn-B}_{18}\text{H}_{22}$.

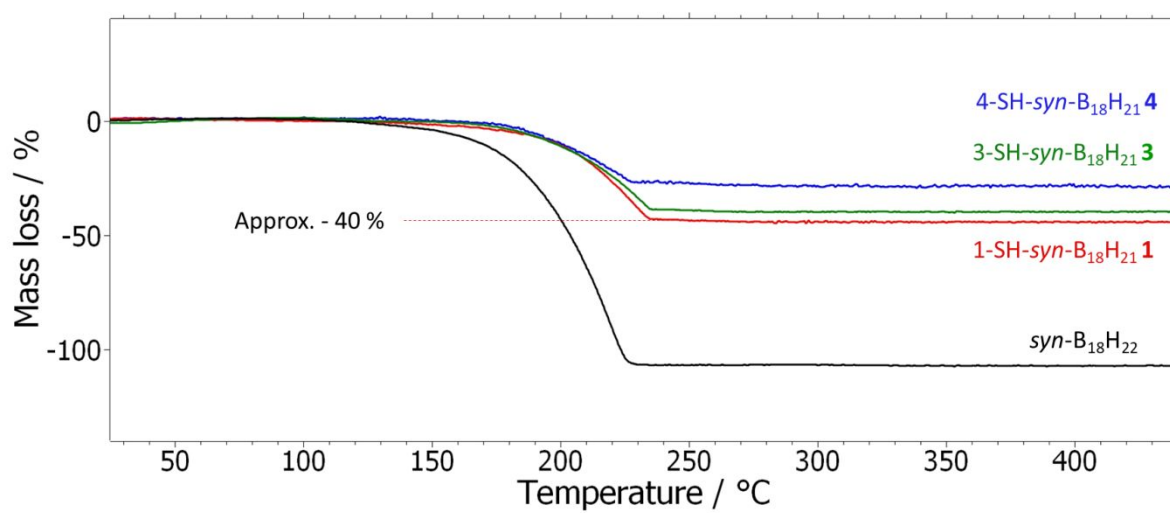


Figure S30. DT analysis showing the volatility of HS- $\text{syn-B}_{18}\text{H}_{21}$ isomers and $\text{syn-B}_{18}\text{H}_{22}$.

Luminescence properties

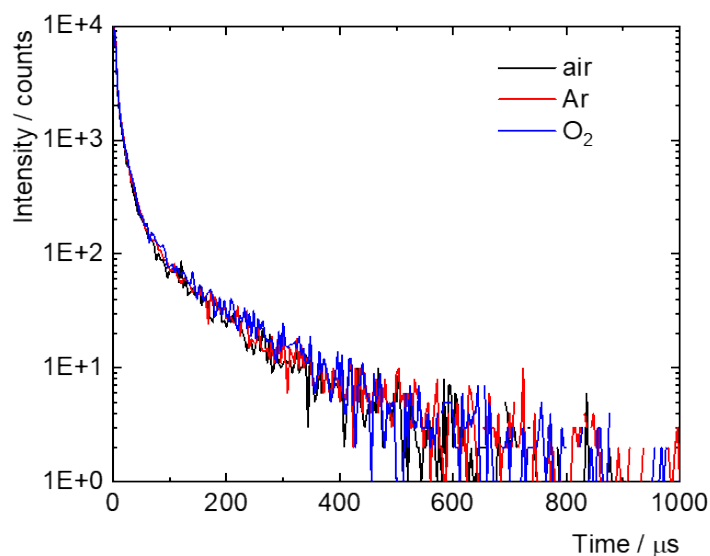


Figure S31. Phosphorescence decay kinetics of powder of 4-HS-*syn*-B₁₈H₂₁ in air atmosphere (black), argon atmosphere (red) or oxygen atmosphere (blue) excited at 380 nm, recorded at 470 nm.

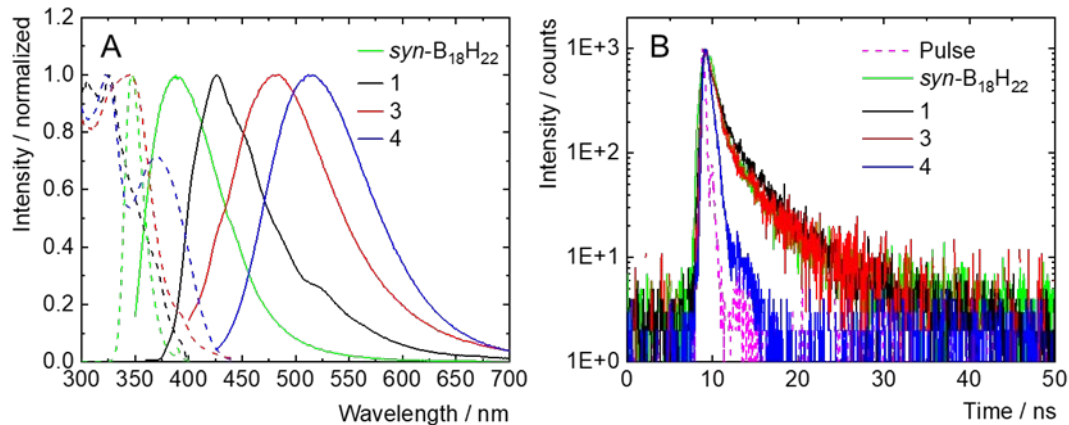


Figure S32. Normalized emission spectra of *syn*-B₁₈H₂₂, **1**, **3**, and **4** in air-saturated hexane, excited at 330 nm; normalized excitation spectra (dashed lines) recorded at the maximum of emission, apart for *syn*-B₁₈H₂₂ recorded at 420 nm (A). Fluorescence decay kinetics of *syn*-B₁₈H₂₂, **1**, **3**, and **4** in air-saturated hexane, excited at 402 nm, recorded at the maximum of emission, apart for *syn*-B₁₈H₂₂ recorded at 420 nm (B).

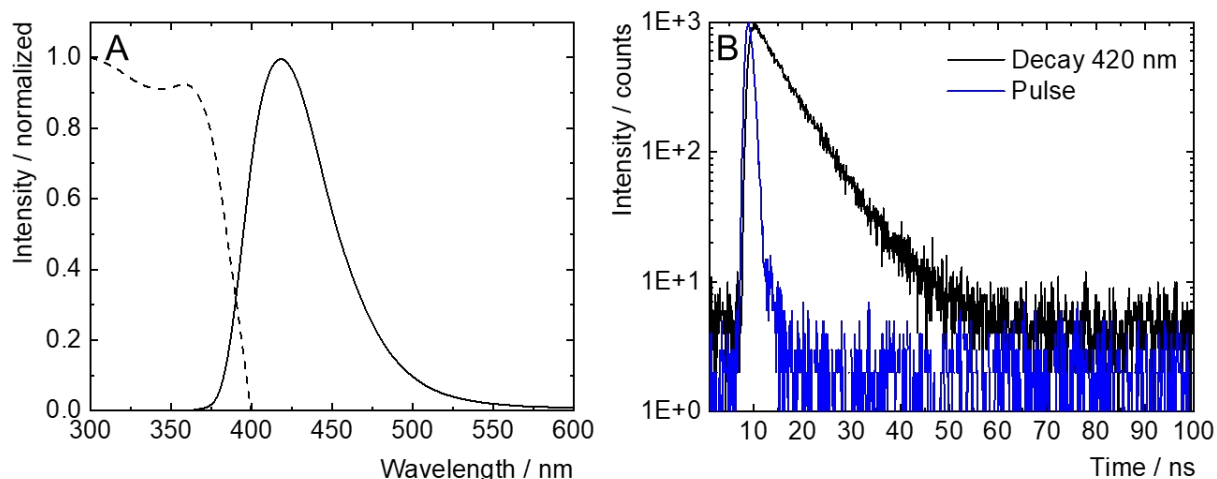


Figure S33. Normalized emission spectra (plain lines) of *anti*-B₁₈H₂₂ excited at 340 nm in air atmosphere; normalized excitation spectra (dashed lines) recorded at the maximum of emission **(A)**. Fluorescence decay kinetics of *anti*-B₁₈H₂₂ in air atmosphere, excited at 402 nm, recorded at 420 nm **(B)**.

Table S4. Photophysical properties of *syn*-B₁₈H₂₂ and the thiolated boranes in hexane at room temperature.^a

Sample	λ_L / nm	ϕ_L	τ_L / ns
Syn-B ₁₈ H ₂₂	390	<0.01	1.1
1	426	<0.01	1.4
3	483	<0.01	1.0
4	515	<0.01	0.3

^a λ_L - luminescence maximum ($\lambda_{exc} = 380$ nm); τ_L - amplitude average lifetimes ($\lambda_{exc} = 380$ nm) measured at the maximum of emission; ϕ_L luminescence quantum yields ($\lambda_{exc} = 380$ nm, experimental error of ϕ_L is ± 0.01); ^b shoulder; ^c after grinding

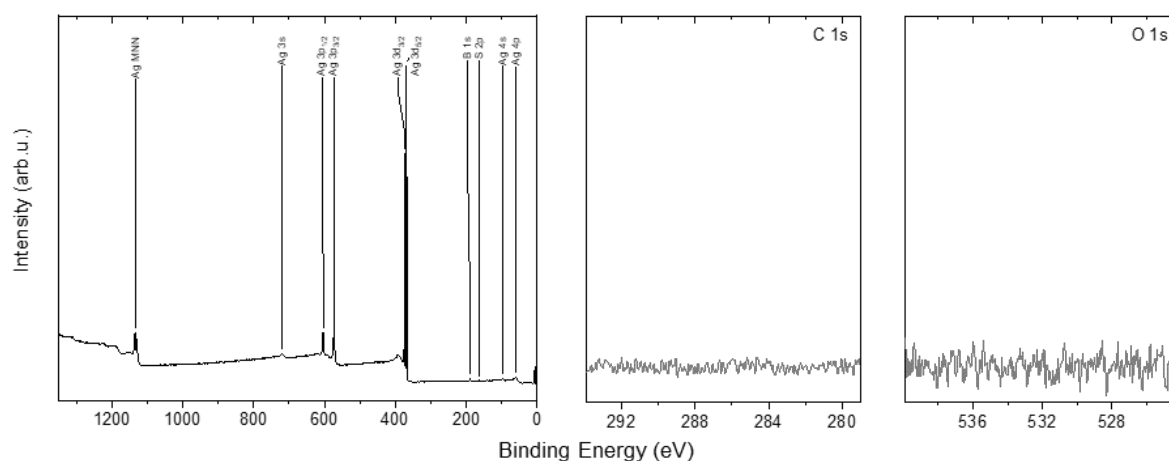


Figure S34. Overview X-ray photoelectron spectrum (A) as well as high-resolution C 1s (B) and O 1s (C) spectra of the formed [4-HS-syn-B₁₈H₂₁] **4** SAM on Ag. The data clearly show only the presence of boron, sulfur and silver signals in the sample. No carbon or oxygen signals are detected demonstrating a high quality of the formed SAM.

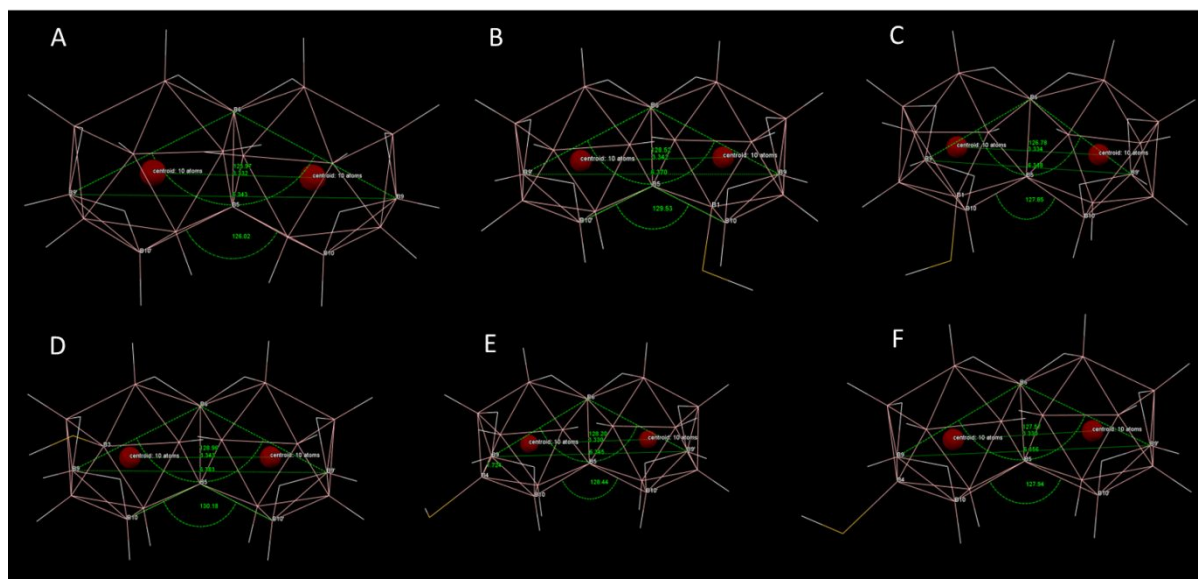


Figure S35. B-B-B angle, bond and centroid(c1-c2) distance of syn-B₁₈H₂₂, **1**, **3**, and **4** isomers polymorphs (A, B, C, D, E, and F respectively).

Table S5. Bond distance comparison of all the isomers with syn-B₁₈H₂₂

Atom1	Atom2	syn-B ₁₈ H ₂₂	1-HS-syn-B ₁₈ H ₂₁ PM1a	1-HS-syn-B ₁₈ H ₂₁ PM1b	1-HS-syn-B ₁₈ H ₂₁	4-HS-syn-B ₁₈ H ₂₁ PM4a	4-HS-syn-B ₁₈ H ₂₁ PM4b
B6	B5	1.810(2)	1.808(3)	1.815(3)	1.810(3)	1.803(2)	1.799(2)
B6	B2'	1.735(2)	1.734(3)	1.735(4)	1.741(3)	1.737(2)	1.737(2)
B6	B7	1.789(2)	1.783(3)	1.793(4)	1.795(2)	1.797(2)	1.785(2)
B6	B2	1.729(2)	1.737(4)	1.736(4)	1.740(3)	1.743(2)	1.737(3)

B6	B7'	1.792(2)	1.798(3)	1.796(5)	1.796(3)	1.781(2)	1.783(2)
B6	H1b0607'	1.28(2)	1.21(2)	1.23(3)	1.27(2)	1.30(1)	1.29(2)
B6	H1b0607	1.28(1)	1.30(2)	1.28(3)	1.30(2)	1.28(1)	1.30(2)
B5	B1'	1.777(2)	1.768(3)	1.776(4)	1.768(2)	1.775(2)	1.775(2)
B5	B2'	1.837(2)	1.834(4)	1.841(4)	1.829(2)	1.830(2)	1.833(3)
B5	B10	1.985(2)	1.980(3)	1.973(4)	1.995(3)	1.991(2)	1.973(2)
B5	B1	1.771(2)	1.793(4)	1.778(4)	1.771(2)	1.775(2)	1.779(2)
B5	B2	1.843(2)	1.840(3)	1.841(4)	1.831(2)	1.834(2)	1.839(2)
B5	B10'	1.981(2)	1.988(3)	1.977(4)	1.990(2)	1.976(2)	1.976(2)
B1'	B2'	1.788(2)	1.791(3)	1.793(3)	1.793(3)	1.793(2)	1.791(2)
B1'	B10'	1.749(2)	1.746(4)	1.747(3)	1.749(3)	1.754(2)	1.745(3)
B1'	B3'	1.789(2)	1.787(3)	1.792(4)	1.786(3)	1.790(2)	1.785(2)
B1'	B4'	1.797(2)	1.796(3)	1.792(4)	1.794(3)	1.796(2)	1.795(2)
B1'	H1b1'	1.05(2)	1.05(2)	1.09(2)	1.06(2)	1.05(1)	1.06(2)
B2'	B3'	1.763(2)	1.757(3)	1.758(5)	1.765(2)	1.762(2)	1.764(2)
B2'	B7'	1.803(2)	1.794(3)	1.793(4)	1.801(3)	1.793(2)	1.796(2)
B2'	H1b2'	1.05(1)	1.05(2)	1.10(3)	1.05(2)	1.07(1)	1.06(2)
B10	B1	1.746(2)	1.760(4)	1.761(3)	1.754(3)	1.744(2)	1.752(2)
B10	B9	1.781(2)	1.784(3)	1.778(4)	1.781(2)	1.791(2)	1.786(3)
B10	B4	1.792(2)	1.793(4)	1.792(5)	1.787(2)	1.788(2)	1.789(3)
B10	H1b0910	1.25(2)	1.27(3)	1.26(3)	1.31(2)	1.26(1)	1.24(2)
B10	H1b10	1.08(2)	1.09(3)	1.07(4)	1.06(2)	1.05(1)	1.07(2)
B7	B8	1.953(2)	1.949(3)	1.953(4)	1.923(3)	1.946(2)	1.951(2)
B7	B2	1.796(2)	1.793(3)	1.796(3)	1.801(3)	1.796(2)	1.799(3)
B7	B3	1.758(2)	1.758(4)	1.761(4)	1.770(3)	1.760(2)	1.760(3)
B7	H1b7	1.05(2)	1.03(3)	1.09(4)	1.10(2)	1.08(1)	1.09(2)
B7	H1b0607	1.26(2)	1.22(3)	1.20(3)	1.22(2)	1.22(1)	1.22(2)
B1	B2	1.787(2)	1.798(3)	1.794(4)	1.796(3)	1.790(2)	1.793(2)
B1	B4	1.798(2)	1.797(3)	1.800(4)	1.805(3)	1.805(2)	1.795(2)
B1	B3	1.787(2)	1.794(3)	1.795(4)	1.790(2)	1.795(2)	1.791(2)
B1	H1b1	1.08(2)			1.07(2)	1.07(1)	1.08(2)
B8	B9	1.800(2)	1.798(3)	1.803(4)	1.802(3)	1.805(2)	1.812(3)
B8	B4	1.808(2)	1.804(4)	1.804(4)	1.808(3)	1.813(2)	1.809(3)
B8	B3	1.763(2)	1.761(4)	1.769(4)	1.774(3)	1.767(2)	1.762(3)
B8	H1b8	1.08(2)	1.04(2)	1.07(3)	1.07(2)	1.07(1)	1.07(2)
B8	H1b0809	1.23(2)	1.26(3)	1.26(4)	1.24(2)	1.25(1)	1.23(2)
B9	B4	1.726(2)	1.721(4)	1.727(5)	1.729(3)	1.724(2)	1.725(3)
B9	H1b0910	1.27(2)	1.27(3)	1.21(4)	1.19(2)	1.24(1)	1.26(2)
B9	H1b9	1.07(1)	1.05(3)	1.07(3)	1.02(2)	1.05(2)	1.09(2)
B9	H1b0809	1.27(2)	1.34(3)	1.32(4)	1.27(2)	1.27(2)	1.27(2)
B2	B3	1.763(2)	1.767(3)	1.767(5)	1.756(2)	1.761(2)	1.756(2)
B2	H1b2	1.05(1)	1.05(2)	1.11(2)	1.05(2)	1.07(1)	1.04(2)
B10'	B4'	1.786(2)	1.782(5)	1.779(4)	1.783(3)	1.785(2)	1.785(3)
B10'	B9'	1.783(2)	1.788(4)	1.778(4)	1.788(3)	1.784(2)	1.785(2)
B10'	H1b10'	1.09(2)	1.06(3)	1.02(2)	1.04(2)	1.10(1)	1.07(2)
B10'	H1b0910'	1.27(2)	1.28(3)	1.27(3)	1.21(2)	1.25(1)	1.27(2)
B4	B3	1.782(2)	1.785(3)	1.789(3)	1.771(3)	1.775(2)	1.787(2)
B4	H1b4	1.03(2)	1.08(3)	1.03(4)	1.06(2)		
B3'	B7'	1.762(2)	1.762(3)	1.759(4)	1.761(2)	1.761(2)	1.762(2)
B3'	B4'	1.780(2)	1.774(4)	1.775(3)	1.778(3)	1.780(2)	1.774(3)
B3'	B8'	1.767(2)	1.759(3)	1.760(3)	1.761(3)	1.765(2)	1.761(2)
B3'	H1b3'	1.07(2)	1.04(3)	1.01(4)	1.07(2)	1.09(1)	1.08(2)
B7'	B8'	1.959(2)	1.950(3)	1.965(4)	1.954(2)	1.952(2)	1.956(2)
B7'	H1b7'	1.07(2)	1.03(3)	1.05(3)	1.08(2)	1.07(1)	1.08(2)
B7'	H1b0607'	1.23(2)	1.22(3)	1.22(3)	1.22(2)	1.23(1)	1.23(2)
B3	H1b3	1.05(2)	1.13(3)	1.13(3)		1.08(1)	1.07(2)
B4'	B8'	1.811(2)	1.802(3)	1.800(3)	1.810(3)	1.804(2)	1.801(2)
B4'	B9'	1.725(2)	1.724(4)	1.729(3)	1.727(3)	1.727(2)	1.723(3)
B4'	H1b4'	1.05(2)	1.27(3)	1.05(3)	1.06(2)	1.09(1)	1.15(2)

B8'	B9'	1.806(2)	1.796(4)	1.798(3)	1.796(3)	1.794(2)	1.794(3)
B8'	H1b8'	1.08(2)	1.08(3)	1.02(3)	1.03(2)	1.06(2)	1.03(2)
B8'	H1b0809'	1.26(2)	1.20(3)	1.24(4)	1.28(2)	1.25(1)	1.26(2)
B9'	H1b9'	1.07(1)	1.02(2)	1.09(3)	1.08(2)	1.07(2)	1.05(2)
B9'	H1b0809'	1.29(2)	1.29(2)	1.30(3)	1.30(2)	1.30(2)	1.26(2)
B9'	H1b0910'	1.25(2)	1.23(3)	1.23(4)	1.18(2)	1.23(1)	1.24(2)

Powder X-ray diffraction and Rietveld refinement

XRPD was investigated on a SmartLab Rigaku powder diffractometer with a rotating Cu anode at room temperature using a HyPix-3000 detector. It was confirmed that no phase of HS-*syn*-B₁₈H₂₁ was missed. The data were processed using the HighScore Plus program from PANalytical. The results of the phase analysis are in following Figures S36 to S40.

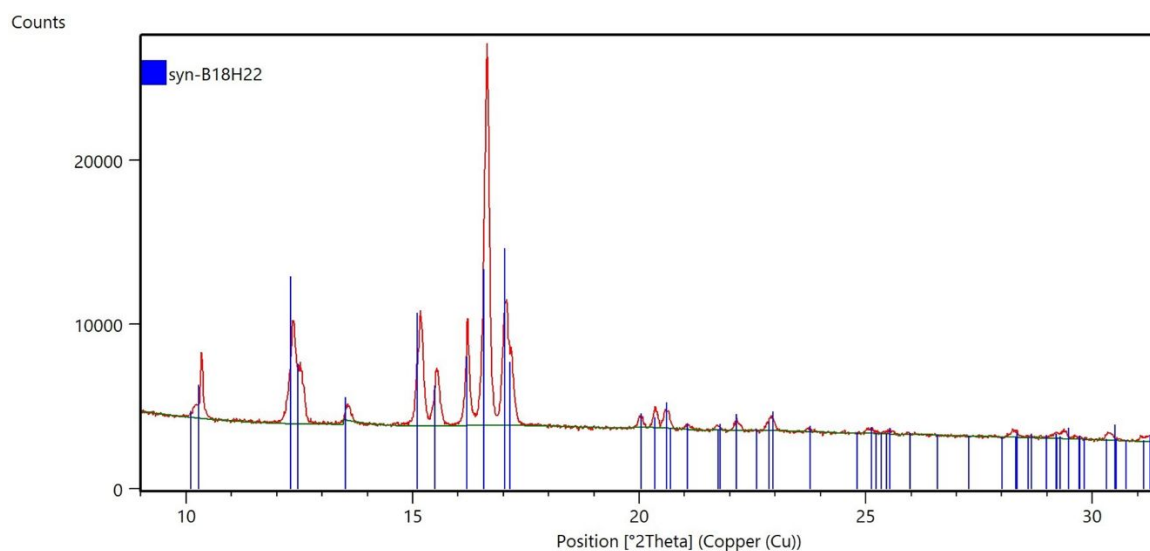


Figure S36. Rietveld refinement of the powdered sample of *syn*-B₁₈H₂₂.

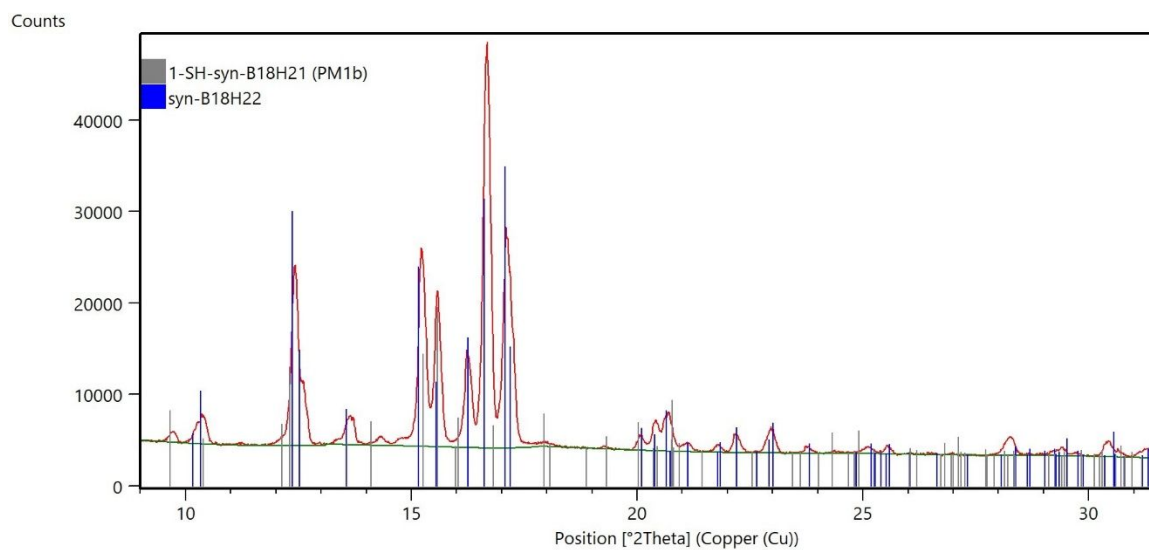


Figure S37. Rietveld refinement of the powdered sample of 1-HS-*syn*-B₁₈H₂₁ (PM1b) and *syn*-B₁₈H₂₂.

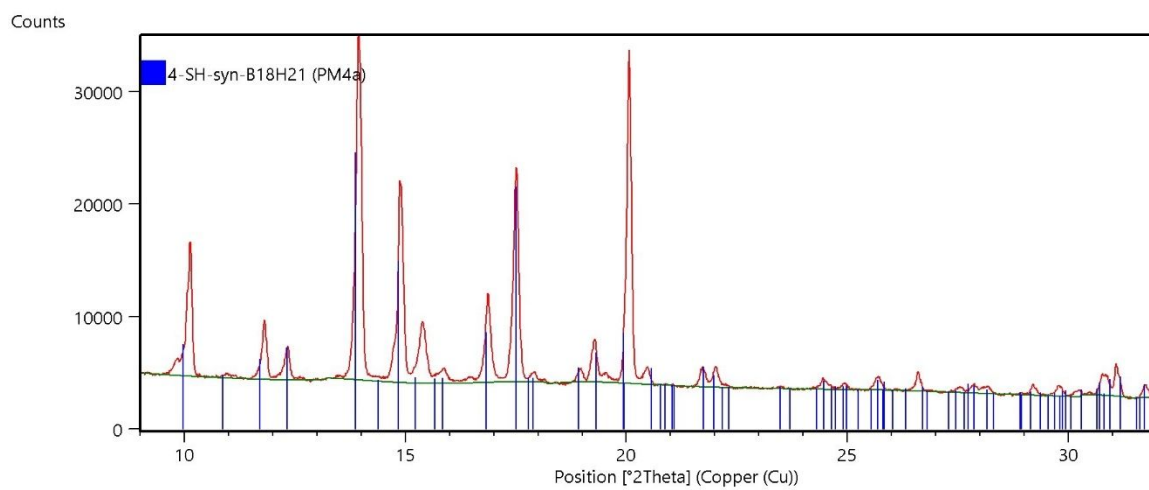


Figure S38. Rietveld refinement of the powdered sample of 4-HS-*syn*-B₁₈H₂₁ (PM4a).

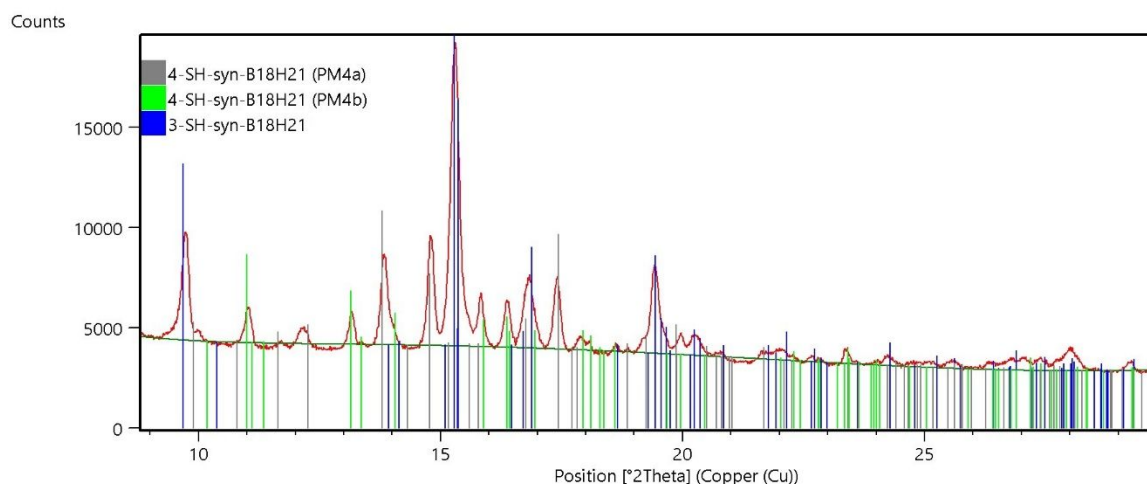


Figure S39. Rietveld refinement of the powdered sample of 4-HS-syn-B₁₈H₂₁ (PM4a and PM4b) and syn-B₁₈H₂₂.

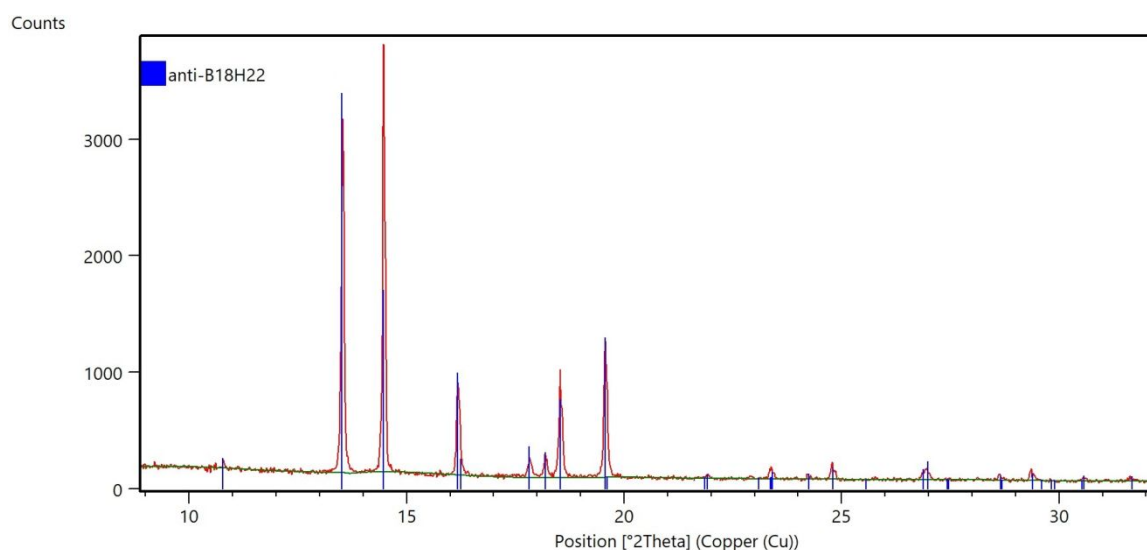


Figure 40. Powder X-ray diffraction pattern (PXRD) of *anti*-B₁₈H₂₂ (obtained at room temperature using a PANalytical Empyrean diffractometer equipped with a conventional Cu X-ray tube and PIXcel detector). The data were processed using the HighScore Plus program from PANalytical, and the obtained diffraction pattern fits perfectly to the single-crystal simulated one (CCDC number 602765).

Single crystal X-ray analysis

The X-ray diffraction data of samples were collected with Rigaku OD Supernova using Atlas S2 CCD detector and mirror collimated Cu-K α ($\lambda = 1.54184 \text{ \AA}$) from micro-focused sealed X-ray tube. The samples were cooled to 95 K during the measurement. Integration of the CCD images, absorption correction and scaling were done by program CrysAlisPro 1.171.41.123a (Rigaku Oxford Diffraction, 2022). Crystal structures were solved by charge flipping with program SUPERFLIP and refined with the Jana2020 program package by full-matrix least-squares technique on F^2 . All hydrogen atoms were visible in difference Fourier maps and positions of all of them were

refined freely. The isotropic atomic displacement parameters of hydrogen atoms were evaluated as 1.2Ueq of the parent atom. ORTEP diagrams (Figure S41 to S46) were made in Diamond 4.5.1. Obtained crystallographic data are in Tables S6 to S13

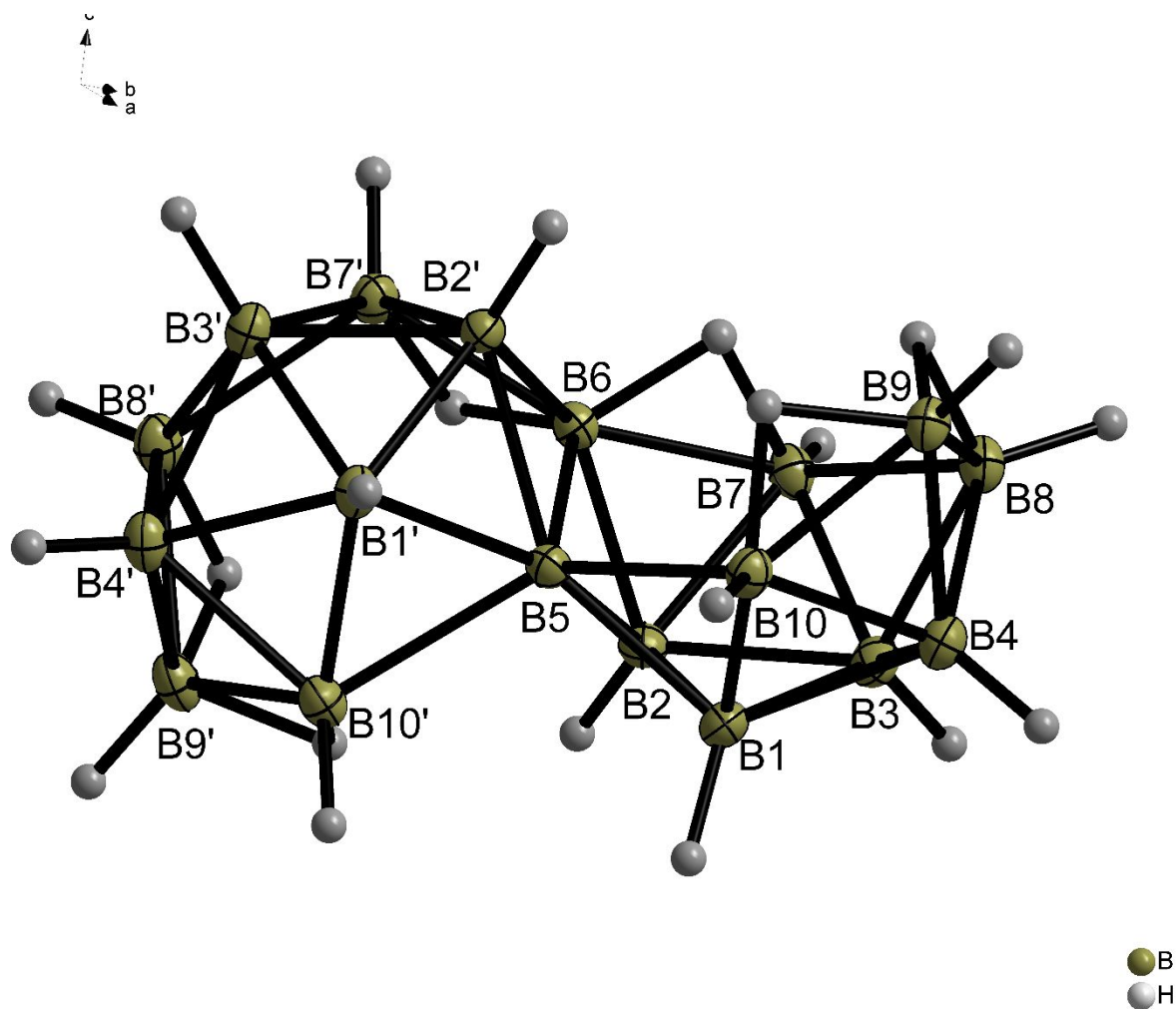


Figure S41. ORTEP structure of *syn*-B₁₈H₂₂ isomer having 50% thermal ellipsoid probability.

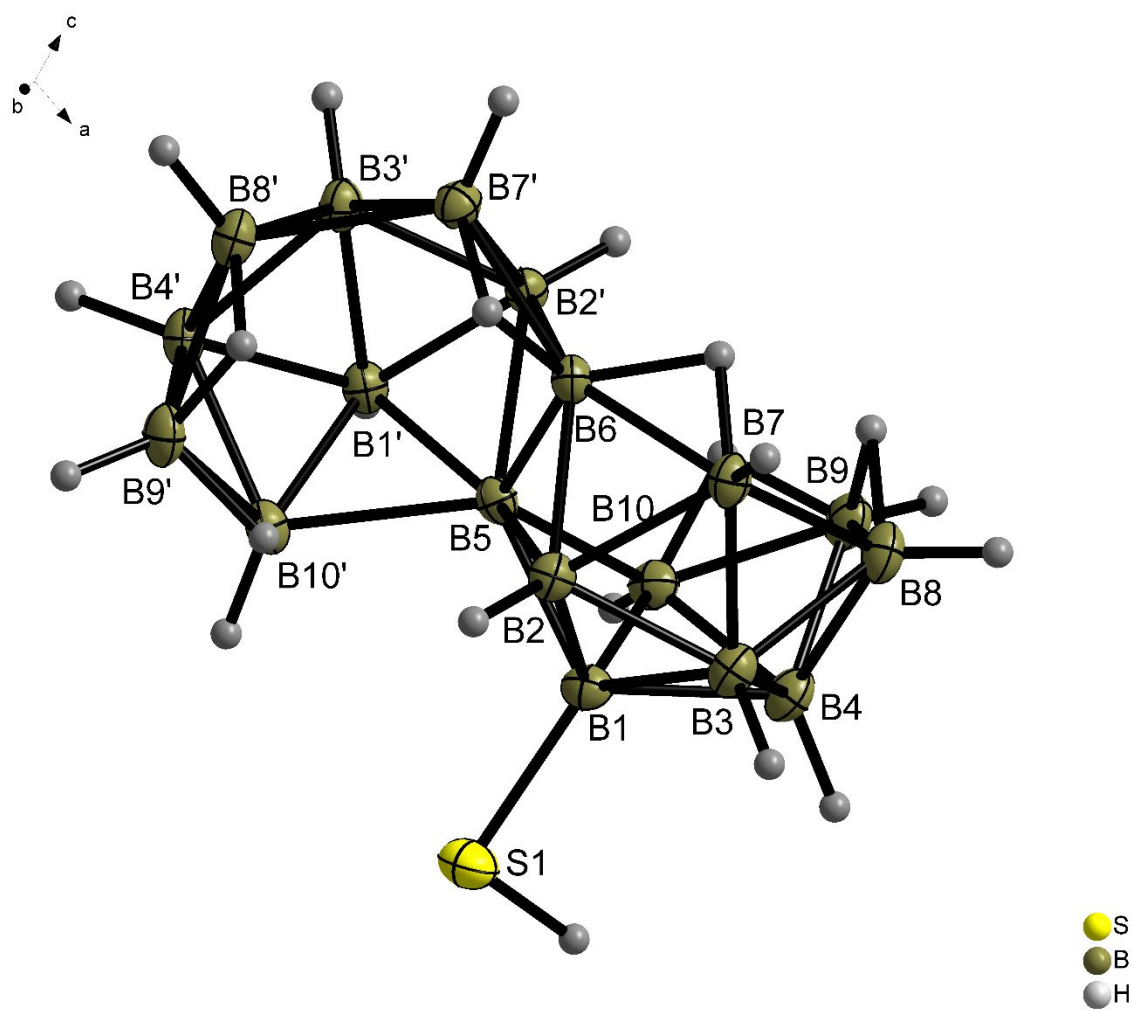


Figure S42. ORTEP structure of 1-HS-*syn*-B₁₈H₂₁ PM1a isomer having 50% thermal ellipsoid probability.

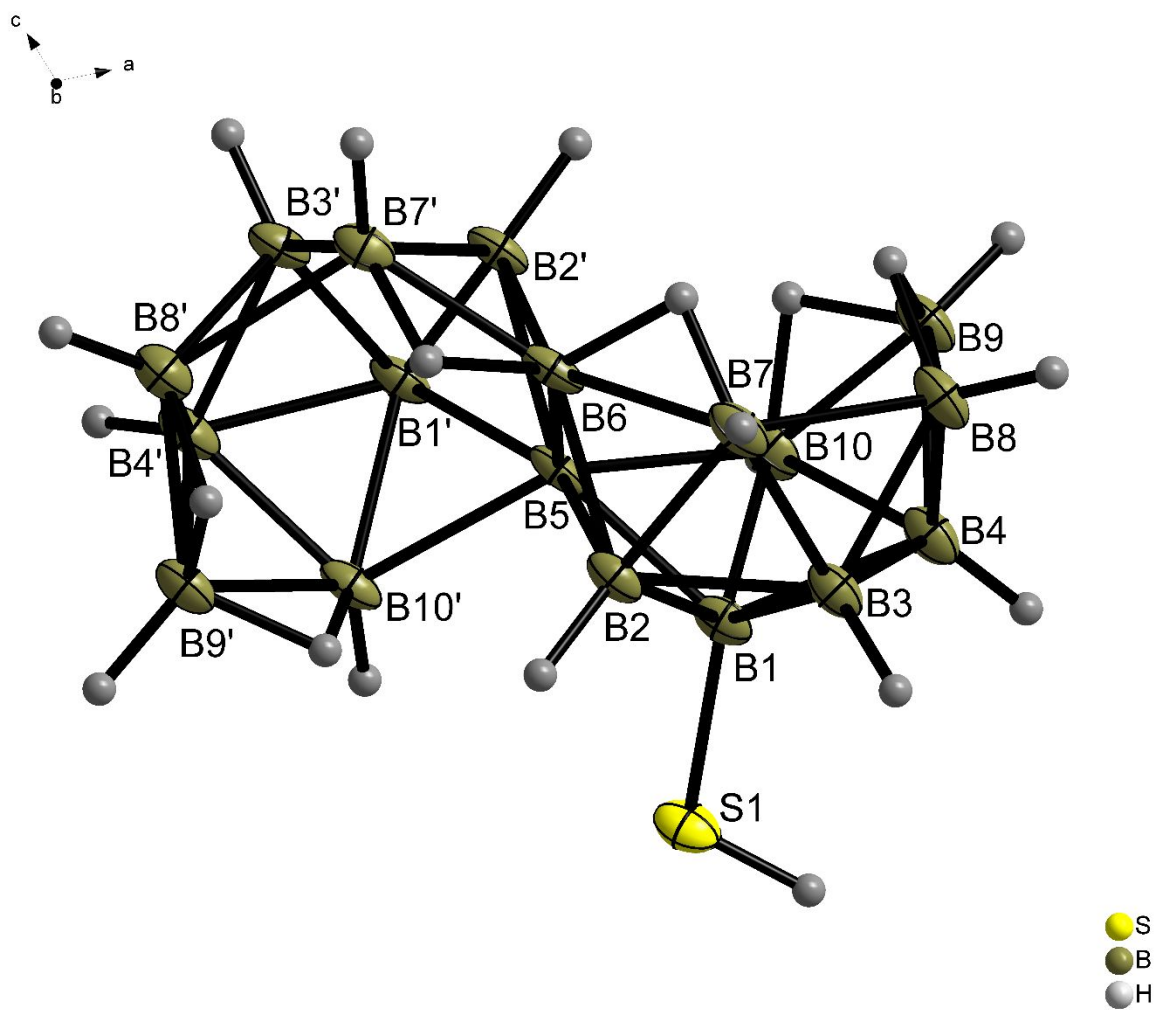


Figure S43. ORTEP structure of 1-HS-*syn*-B₁₈H₂₁ PM1b isomer having 50% thermal ellipsoid probability.

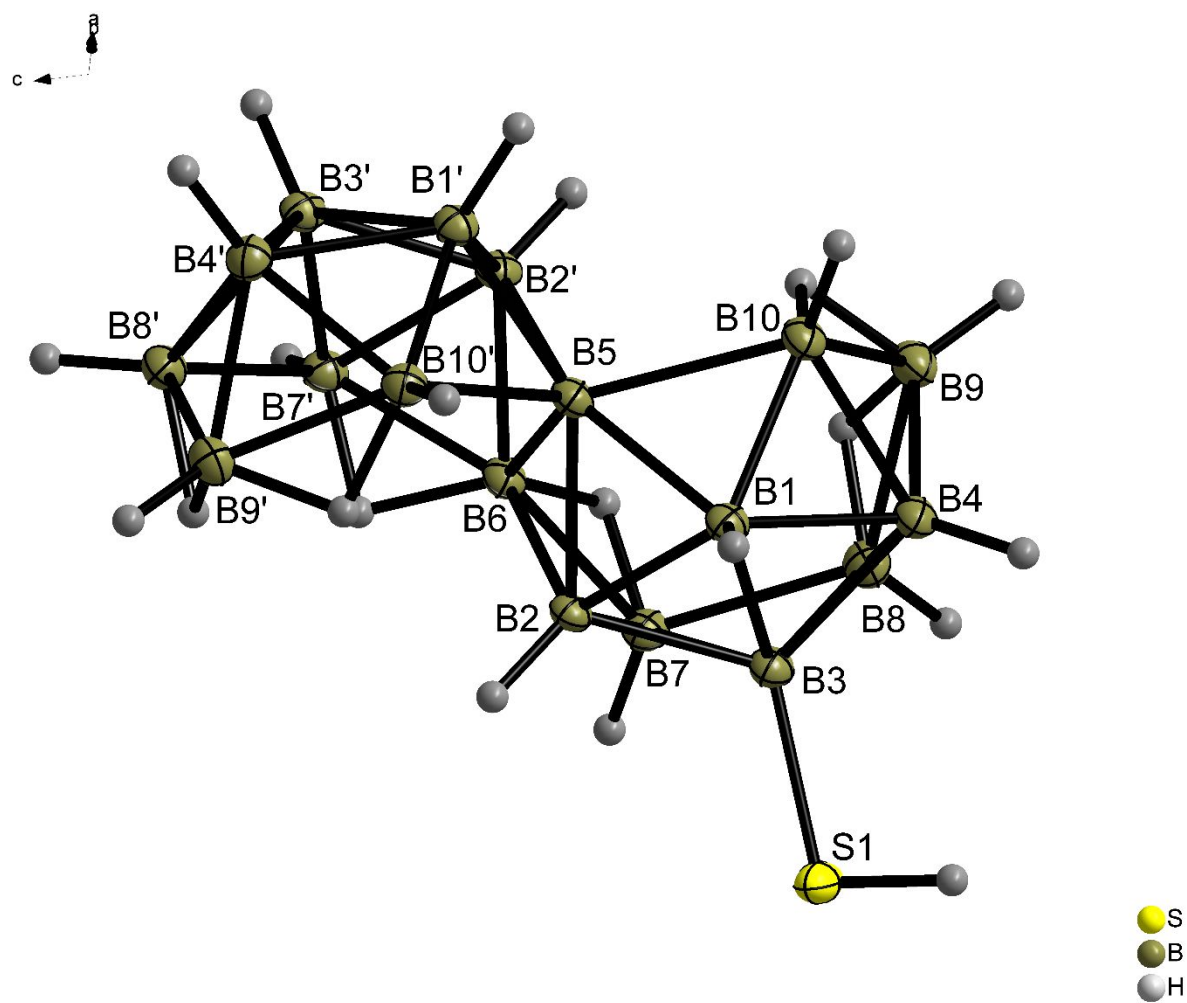


Figure S44. ORTEP structure of 3-HS-*syn*-B₁₈H₂₁ isomer having 50% thermal ellipsoid probability.

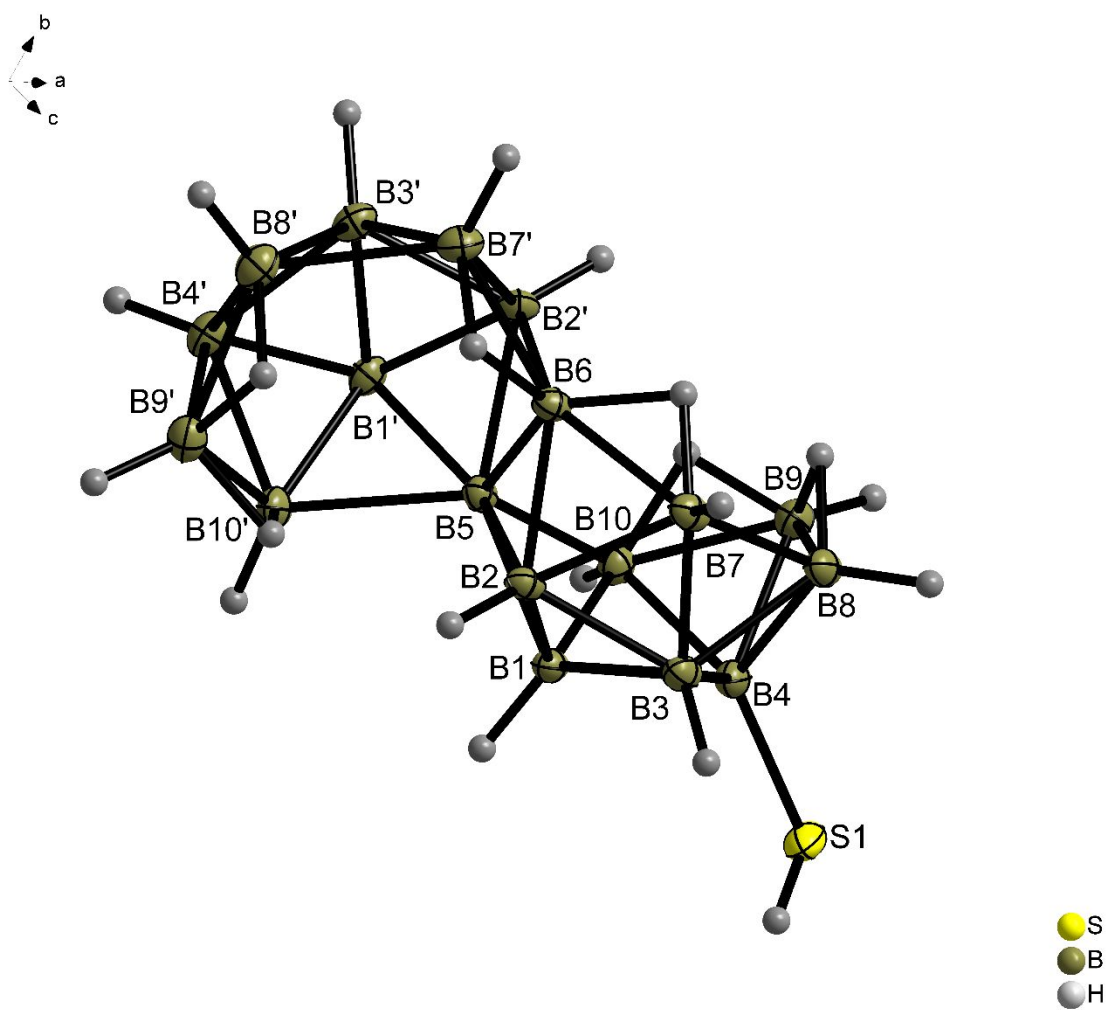


Figure S45. ORTEP structure of 4-HS-*syn*-B₁₈H₂₁ PM4a isomer having 50% thermal ellipsoid probability.

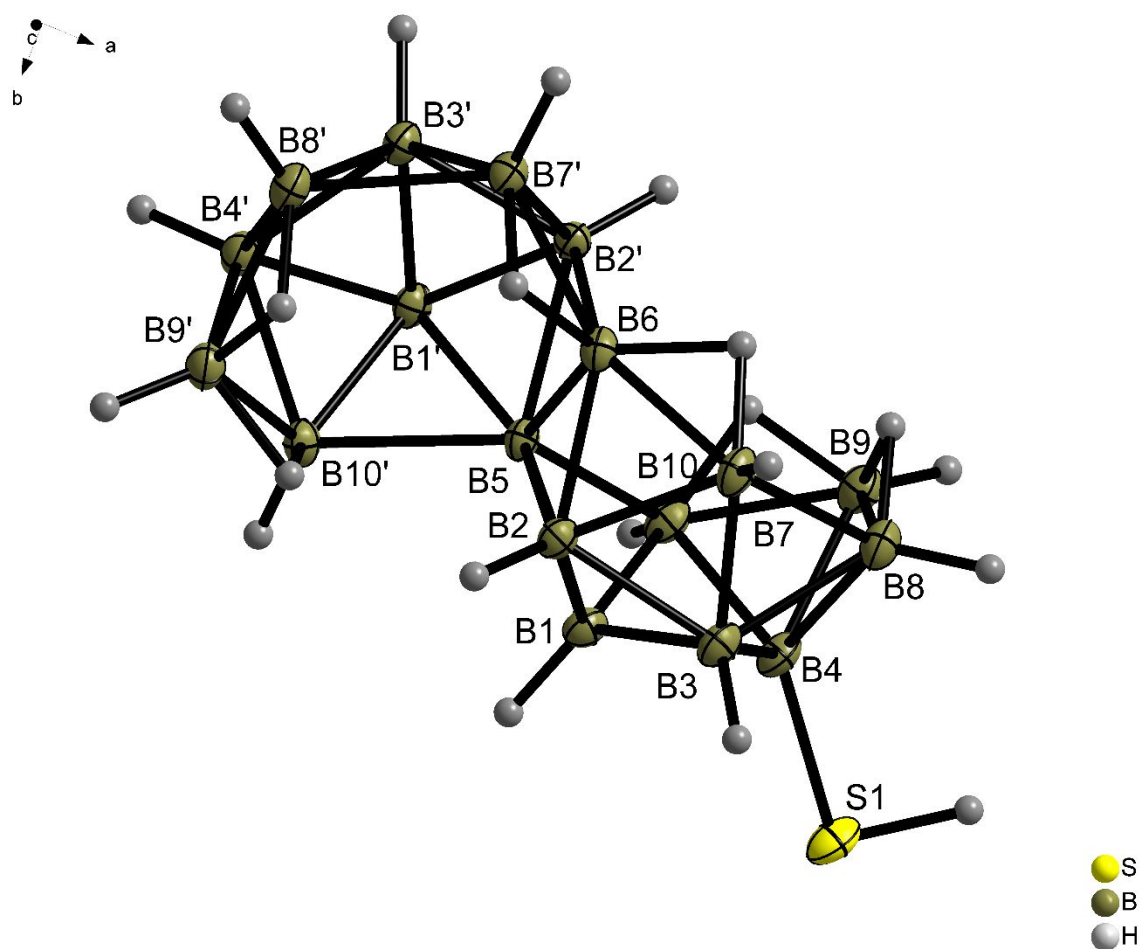


Figure S46. ORTEP structure of 4-HS-*syn*-B₁₈H₂₁ PM4b isomer having 50% thermal ellipsoid probability.

Table S6. Crystallographic collection and refinement data for *syn*-B₁₈H₂₂ measured at 95 K.

	<i>syn</i> -B ₁₈ H ₂₂ – at 95 K.
CCDC	2262308
Empirical formula	B ₁₈ H ₂₂
Diffractometer	four-cycle diffractometer Cryostream, AtlasS2, Rigaku OD Supernova
M_r /g mol ⁻¹	216.8 (formula weight)

	<i>syn</i> -B ₁₈ H ₂₂ – at 95 K.
<i>T</i> /K	95
Wavelength / Å	1.54184
Crystal system	monoclinic
Space group	P2 ₁ /c
<i>a</i> /Å	9.108(2)
<i>b</i> /Å	13.050(3)
<i>c</i> /Å	12.432(2)
α /deg	90
β /deg	109.94(3)
γ /deg	90
<i>V</i> /Å ³	1389.1(6)
<i>Z</i>	4
Calc. density/g cm ⁻³	1.0364
μ mm ⁻¹	0.219
F(000)	448
Crystal size /mm ³	0.090 x 0.080 x 0.040
θ range /°	5.1 – 73.0
Index ranges / <i>hkl</i>	-10, 11, -16, 16, -15, 8
Reflections collected (<i>R</i> _{int})	7784 (0.042)
Independent reflections	2740

	<i>syn</i> -B ₁₈ H ₂₂ – at 95 K.
Completeness /% to θ /°	98, 73.53
Absorption correction	multiscan
Max. and min. transmission	0.76, 1
Data / restraints / constraints / parameters	2740 / 0 / 22 / 229
Goodness-of-fit on F ²	1.51 ⁽¹⁾
R1, wR2 [I>3 σ (I)]	0.0397, 0.0857
R1, wR2 (all data)	0.0573, 0.0920
Largest diff. peak and hole, eÅ ⁻³	0.15, -0.15

Table S7. Crystallographic collection and refinement data for *syn*-B₁₈H₂₂ measured at room temperature.

	<i>syn</i> -B ₁₈ H ₂₂ – at RT.
CCDC	2265132
Empirical formula	B ₁₈ H ₂₂
Diffractometer	four-cycle diffractometer Cryostream, AtlasS2, Rigaku OD Supernova
M_r /g mol ⁻¹	216.8 (formula weight)
T /K	300
Wavelength / Å	0.71073

	<i>syn</i> -B ₁₈ H ₂₂ – at RT.
Crystal system	monoclinic
Space group	P2 ₁ /c
<i>a</i> /Å	9.1929(11)
<i>b</i> /Å	13.1716(14)
<i>c</i> /Å	12.5191(14)
α /deg	90
β /deg	109.759(11)
γ /deg	90
<i>V</i> /Å ³	1426.63
<i>Z</i>	4
Calc. density/g cm ⁻³	1.009
μ mm ⁻¹	0.04
F(000)	448
Crystal size /mm ³	0.21 × 0.12 × 0.07
θ range /°	2.8 – 25.5
Index ranges / <i>hkl</i>	-9, 12, -18, 13, -16, 14
Reflections collected (<i>R</i> _{int})	6140 (0.035)
Independent reflections	3293
Completeness /% to θ /°	98, 26.86
Absorption correction	multiscan

	<i>syn</i> -B ₁₈ H ₂₂ – at RT.
Max. and min. transmission	0.69, 1
Data / restraints / constraints / parameters	3293/ 0 / 22 / 229
Goodness-of-fit on F ²	1.31 ⁽¹⁾
<i>R</i> 1, <i>wR</i> 2 [<i>I</i> >3σ(<i>I</i>)]	0.0585, 0.1231
<i>R</i> 1, <i>wR</i> 2 (all data)	0.1146, 0.1472
Largest diff. peak and hole, eÅ ⁻³	0.13, -0.12

Table S8. Crystallographic collection and refinement data for 1-HS-*syn*-B₁₈H₂₁ (PM1a).

POLYMORPH	1-HS- <i>syn</i> -B ₁₈ H ₂₁ (PM1a)
CCDC	2262296
Empirical formula	B ₁₈ H ₂₂ S ₁
Diffractometer	four-cycle diffractometer Cryostream, AtlasS2, Rigaku OD Supernova
<i>M</i> _r /g mol ⁻¹	248.8 (formula weight)
<i>T</i> /K	95
Wavelength / Å	1.54184
Crystal system	monoclinic
Space group	P2 ₁ /c
<i>a</i> /Å	10.0437 (6)

POLYMORPH	1-HS- <i>syn</i> -B ₁₈ H ₂₁ (PM1a)
<i>b</i> /Å	11.3556 (6)
<i>c</i> /Å	13.8050 (8)
α /deg	90
β /deg	108.575 (5)
γ /deg	90
<i>V</i> /Å ³	1492.47 (15)
<i>Z</i>	4
Calc. density/g cm ⁻³	1.1073
μ mm ⁻¹	1.536
F(000)	512
Crystal size /mm ³	0.050 x 0.042 x 0.020
θ range /°	4.6 – 73.3
Index ranges / <i>hkl</i>	-12, 12, -11, 14, -16, 16
Reflections collected (<i>R</i> _{int})	10154 (0.072)
Independent reflections	2952
Completeness /% to θ /°	99, 66.97
Absorption correction	multiscan
Max. and min. transmission	0.164, 1
Data / restraints / constraints	2891 / 0 / 22 / 238
/ parameters	
Goodness-of-fit on <i>F</i> ²	1.26 ⁽¹⁾

POLYMORPH	1-HS- <i>syn</i> -B ₁₈ H ₂₁ (PM1a)
<i>R</i> 1, <i>wR</i> 2 [<i>I</i> >3σ(<i>I</i>)]	0.0452, 0.0944
<i>R</i> 1, <i>wR</i> 2 (all data)	0.0744, 0.1057
Largest diff. peak and hole, eÅ ⁻³	0.25, -0.31

Table S9. Crystallographic collection and refinement data for 1-HS-*syn*-B₁₈H₂₁ (PM1b).

	1-HS- <i>syn</i> -B ₁₈ H ₂₁ (PM1b)
CCDC	2262299
Empirical formula	B ₁₈ H ₂₂ S ₁
Diffractometer	four-cycle diffractometer Cryostream, AtlasS2, Rigaku OD Supernova
<i>M</i> _r /g mol ⁻¹	248.8 (formula weight)
<i>T</i> /K	95
Wavelength / Å	1.54184
Crystal system	monoclinic
Space group	P2 ₁ /n
<i>a</i> /Å	10.0415(7)
<i>b</i> /Å	11.6578(8)
<i>c</i> /Å	13.4184(9)
α/deg	90

	1-HS- <i>syn</i> -B ₁₈ H ₂₁ (PM1b)
β /deg	110.018(6)
γ /deg	90
$V/\text{\AA}^3$	1475.88(18)
Z	4
Calc. density/g cm ⁻³	1.1198
μ mm ⁻¹	1.553
F(000)	512
Crystal size /mm ³	0.068 x 0.047 x 0.032
θ range /°	4.80 – 72.87
Index ranges / hkl	-12, 11, -8, 13, -14, 16
Reflections collected (R_{int})	8326 (0.0651)
Independent reflections	2867
Completeness /% to θ /°	99, 66.49
Absorption correction	multiscan
Max. and min. transmission	0.621, 1
Data / restraints / constraints / parameters	2867 / 0 / 22 / 238
Goodness-of-fit on F^2	1.54 ⁽¹⁾
$R1, wR2$ [$I > 3\sigma(I)$]	0.0451, 0.1115
$R1, wR2$ (all data)	0.0674, 0.1189

	1-HS- <i>syn</i> -B ₁₈ H ₂₁ (PM1b)
Largest diff. peak and hole, eÅ ⁻³	0.28, -0.35

Table S10. Crystallographic collection and refinement data for 3-HS-*syn*-B₁₈H₂₁.

	3-HS- <i>syn</i> -B ₁₈ H ₂₁
CCDC	2262294
Empirical formula	B ₁₈ H ₂₂ S ₁
Diffractometer	four-cycle diffractometer Cryostream, AtlasS2, Rigaku OD Supernova
<i>M_r</i> /g mol ⁻¹	248.8 (formula weight)
<i>T</i> /K	95
Wavelength / Å	1.54184
Crystal system	monoclinic
Space group	P2 ₁ /c
<i>a</i> /Å	12.264(2)
<i>b</i> /Å	6.659(2)
<i>c</i> /Å	19.098(4)
α/deg	90
β/deg	107.06(3)

	3-HS- <i>syn</i> -B ₁₈ H ₂₁
γ/deg	90
$V/\text{\AA}^3$	1491.0(6)
Z	4
Calc. density/ g cm^{-3}	1.1084
$\mu \text{ mm}^{-1}$	1.538
$F(000)$	512
Crystal size / mm^3	0.070 x 0.046 x 0.027
θ range / $^\circ$	7.1 – 72.5
Index ranges / hkl	-13, 15, -8, 8, -23, 23
Reflections collected (R_{int})	8518 (0.038)
Independent reflections	2891
Completeness /% to θ / $^\circ$	99, 66.49
Absorption correction	multiscan
Max. and min. transmission	0.471, 1
Data / restraints / constraints / parameters	2891 / 0 / 22 / 238
Goodness-of-fit on F^2	1.52 ⁽¹⁾
$R1, wR2$ [$I > 3\sigma(I)$]	0.0356, 0.0804
$R1, wR2$ (all data)	0.0469, 0.0846
Largest diff. peak and hole, e\AA^{-3}	0.24, -0.24
3	

Table S11. Crystallographic collection and refinement data for 4-HS-*syn*-B₁₈H₂₁ (PM 4a).

POLYMORPH	4-HS- <i>syn</i> -B ₁₈ H ₂₁ (PM 4a)
CCDC	2262307
Empirical formula	B ₁₈ H ₂₂ S ₁
Diffractometer	four-cycle diffractometer Cryostream, AtlasS2, Rigaku OD Supernova
M_r /g mol ⁻¹	248.8 (formula weight)
T /K	95
Wavelength / Å	1.54184
Crystal system	orthorhombic
Space group	Pbca
a /Å	14.4249 (5)
b /Å	11.9778 (4)
c /Å	17.8595 (6)
α /deg	90
β /deg	90
γ /deg	90
V /Å ³	3085.74 (18)
Z	8
Calc. density/g cm ⁻³	1.0712

POLYMORPH	4-HS- <i>syn</i> -B ₁₈ H ₂₁ (PM 4a)
μ mm ⁻¹	1.486
F(000)	1024
Crystal size /mm ³	0.074 x 0.044 x 0.019
θ range /°	4.9 – 72.9
Index ranges / <i>hkl</i>	-15, 17, -7, 14, -21, 18
Reflections collected (R _{int})	6528 (0.022)
Independent reflections	2994
Completeness /% to θ /°	99, 66.97
Absorption correction	multiscan
Max. and min. transmission	0.81, 1
Data / restraints / constraints / parameters	2994 / 0 / 22 / 238
Goodness-of-fit on F ²	1.69 ⁽¹⁾
R1, wR2 [I>3 σ (I)]	0.0300, 0.0720
R1, wR2 (all data)	0.0361, 0.0743
Largest diff. peak and hole, eÅ ⁻³	0.18, -0.20

Table S12. Crystallographic collection and refinement data for PM4a measured at room temperature.

	PM4a – at RT.
CCDC	2265136
Empirical formula	SB ₁₈ H ₂₂
Diffractometer	four-cycle diffractometer Cryostream, AtlasS2, Rigaku OD Supernova
M_r /g mol ⁻¹	248.8 (formula weight)
T /K	300
Wavelength / Å	1.54184
Crystal system	orthorhombic
Space group	Pbca
a /Å	17.9237 (10)
b /Å	14.6363 (8)
c /Å	12.0552 (7)
α /deg	90
β /deg	90
γ /deg	90
V /Å ³	3162.5 (3)
Z	8
Calc. density/g cm ⁻³	1.045
μ mm ⁻¹	1.45
F(000)	1024

	PM4a – at RT.
Crystal size /mm ³	0.14 × 0.09 × 0.05
θ range /°	4.9 – 72.9
Index ranges /hkl	-21, 1, -17, 17, -4, 14
Reflections collected (R _{int})	6766 (0.028)
Independent reflections	3053
Completeness /% to θ /°	98, 71.21
Absorption correction	multiscan
Max. and min. transmission	0.79, 1
Data / restraints / constraints / parameters	3053/ 0 / 22 / 238
Goodness-of-fit on F ²	1.75 ⁽¹⁾
R1, wR2 [I>3σ(I)]	0.0486, 0.1271
R1, wR2 (all data)	0.0686, 0.1388
Largest diff. peak and hole, eÅ ⁻³	0.18, -0.16

Table S13. Crystallographic collection and refinement data for 4-HS-*syn*-B₁₈H₂₁ (PM4b).

	4-HS- <i>syn</i> -B ₁₈ H ₂₁ (PM4b)
CCDC	2262306

	4-HS- <i>syn</i> -B ₁₈ H ₂₁ (PM4b)
Empirical formula	B ₁₈ H ₂₂ S ₁
Diffractometer	four-cycle diffractometer Cryostream, AtlasS2, Rigaku OD Supernova
M_r /g mol ⁻¹	248.8 (formula weight)
T /K	95
Wavelength / Å	1.54184
Crystal system	monoclinic
Space group	P2 ₁ /n
a /Å	10.453 (2)
b /Å	12.585 (3)
c /Å	11.985 (2)
α /deg	90
β /deg	91.29 (3)
γ /deg	90
V /Å ³	1576.2(5)
Z	4
Calc. density/g cm ⁻³	1.0485
μ mm ⁻¹	1.454
$F(000)$	512
Crystal size /mm ³	0.130 x 0.068 x 0.037

	4-HS- <i>syn</i> -B ₁₈ H ₂₁ (PM4b)
θ range /°	5.1 – 73.4
Index ranges / <i>hkl</i>	-11, 12, -15, 15, -14, 11
Reflections collected (<i>R</i> _{int})	9348 (0.0486)
Independent reflections	3109
Completeness /% to θ /°	99, 66.97
Absorption correction	multiscan
Max. and min. transmission	0.235, 1
Data / restraints / constraints / parameters	3109 / 0 / 22 / 238
Goodness-of-fit on <i>F</i> ²	1.35 ⁽¹⁾
<i>R</i> 1, <i>wR</i> 2 [<i>I</i> >3 σ (<i>I</i>)]	0.0355, 0.0781
<i>R</i> 1, <i>wR</i> 2 (all data)	0.0515, 0.0843
Largest diff. peak and hole, eÅ ⁻³	0.19, -0.20

⁽¹⁾ The refinement program Jana2020 does not refine the weighting scheme. Therefore, GOF is usually fairly above one, especially for strongly diffracting crystals.

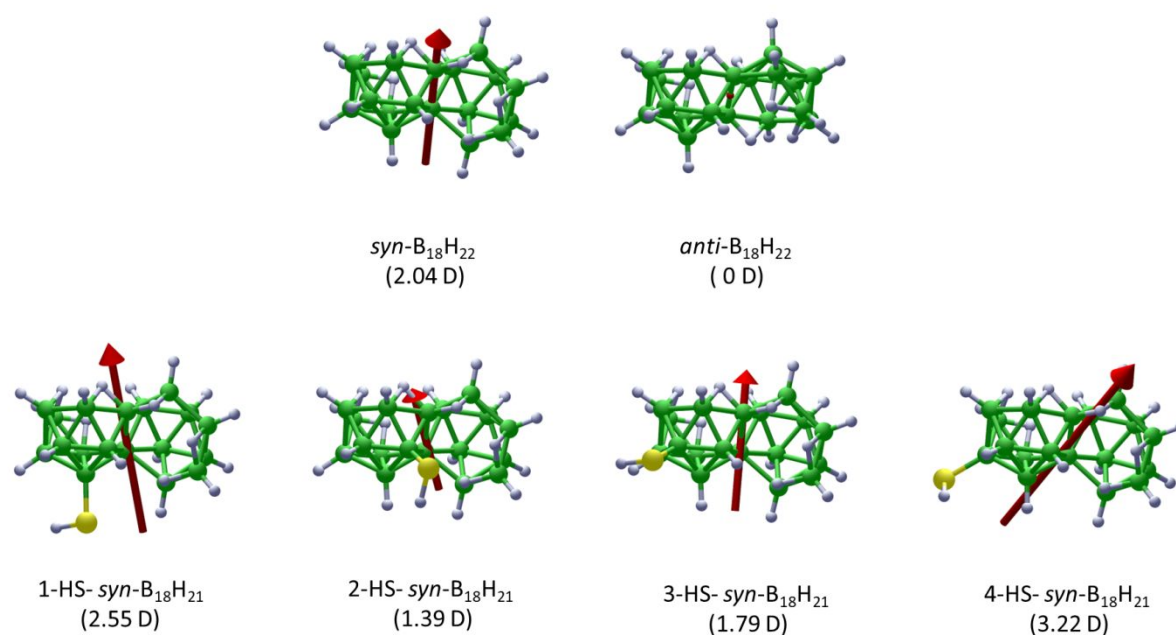


Figure S47. Graphical projection of the dipole moment vectors in the SH-B₁₈H₂₁ isomers as well as in the parent *syn*-B₁₈H₂₂ and *anti*-B₁₈H₂₂.

Table S14. Table of the computationally obtained dipole moment values of all isomers and the parent *syn*-B₁₈H₂₂.

Isomer	Dipole moment (Debye)
<i>syn</i> -B ₁₈ H ₂₂	2.0361
<i>anti</i> -B ₁₈ H ₂₂	0
1-HS- <i>syn</i> -B ₁₈ H ₂₁	2.5538
2-HS- <i>syn</i> -B ₁₈ H ₂₁	1.3852
3-HS- <i>syn</i> -B ₁₈ H ₂₁	1.7931
4-HS- <i>syn</i> -B ₁₈ H ₂₁	3.2160

TD-DFT

The results of the Time Dependent Density Functional Theory (TD-DFT) calculations are summarised in the Table S. Simulated spectra and calculated excited states energies of *anti*- and *syn*-B₁₈H₂₂ are compared in the Figure S48, those of 1-, 2-, 3-, and 4-HS-*syn*-B₁₈H₂₁ follow in Figure S49 to Figure S52.

Table S15: Excitation energies (E_{exc}) and the associated wavelengths (λ) of the first ((S1) and second (S2) excited states in the ground state geometry, and that of the first singlet excited state in its optimised geometry (S1/S1)

	$E_{\text{exc}}(\text{S1})/\text{eV}$	$\lambda(\text{S1})/\text{nm}$	$E_{\text{exc}}(\text{S2})/\text{eV}$	$\lambda(\text{S2})/\text{nm}$	$E_{\text{exc}}(\text{S1/S1})/\text{eV}$	$\lambda(\text{S1/S1})/\text{nm}$
<i>anti</i> -B ₁₈ H ₂₂	4.2328	292.91	5.1265	241.85	3.3196	373.49
<i>syn</i> -B ₁₈ H ₂₂	4.5570	272.07	4.7794	259.41	3.6805	336.87
1-HS- <i>syn</i> -B ₁₈ H ₂₁	4.0143	308.85	4.6626	265.91	2.7267	454.70
2-HS- <i>syn</i> -B ₁₈ H ₂₁	4.1112	301.58	4.6108	268.90	2.7203	455.77
3-HS- <i>syn</i> -B ₁₈ H ₂₁	4.2357	292.71	4.5551	272.19	2.7193	455.94
4-HS- <i>syn</i> -B ₁₈ H ₂₁	3.6743	337.44	4.5487	272.57	2.5432	487.52

Upon optimisation of the first excited singlet geometry on the TD-DFT level of theory, the calculated energy of the first excited singlet of *syn*-B₁₈H₂₂ above the ground state lowers from 4.56 eV only to 3.68 eV, the S1 thus remains in its relaxed geometry even a bit higher above the ground state than that of *anti*-B₁₈H₂₂. The differences between the optimized geometry of the ground state, and that of the first excited singlet, are for both *anti*-B₁₈H₂₂ (Figure S53) and *syn*-B₁₈H₂₂ (Figure S54) almost imperceptible. There is no indication in our TD-DFT results pointing to the existence of an easily accessible conical intersection of the first excited singlet with the ground state, claimed as responsible for the observed absence of luminescence in the solution of *syn*-B₁₈H₂₂ at the CASPT2/CASSCF level of theoryⁱ. For a correct description of the excited states of *syn*-B₁₈H₂₂, extensive theoretical studies at higher levels of theory are probably necessary. Also, the calculated luminescence wavelengths $\lambda(\text{S1/S1})$ of *syn*-B₁₈H₂₂ and all its thiol derivatives investigated are too short compared to those measured experimentally in the solid state. Similarly, the longest calculated absorption wavelength, the weak line at 337 nm of 4-HS-*syn*-B₁₈H₂₁ (Table S15, Figure S52), lies still in the ultraviolet range, although the species forms intensively pink crystals. These observations clearly suggest that the spectroscopic properties of these species in solid state are predominantly determined by their supramolecular crystalline structure, and their further theoretical analysis is beyond the scope of the basic DFT calculations of isolated molecules.

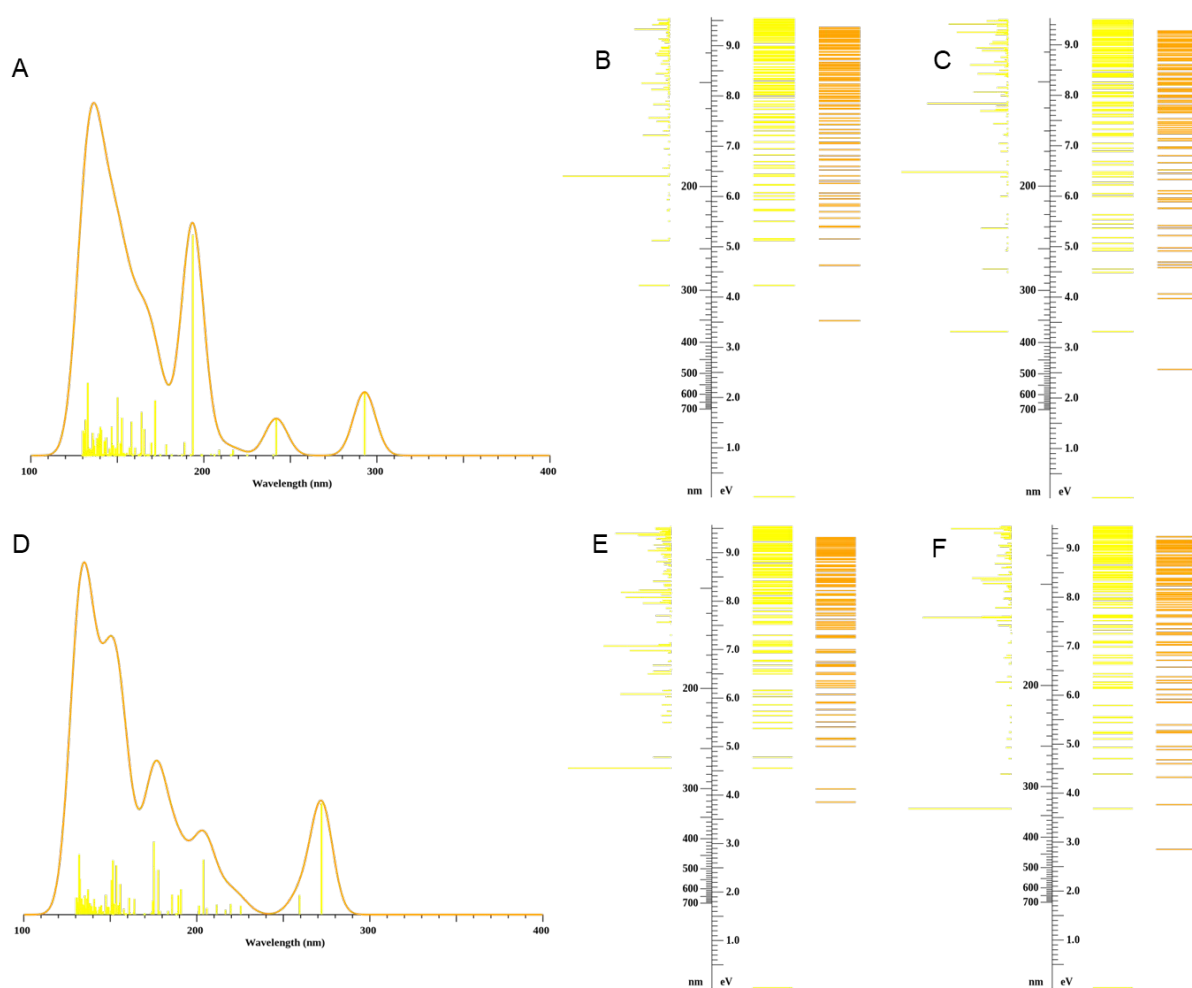


Figure S48: Simulated spectra (A, D), excited states (B, E) and excited states in the relaxed geometry of S1 (C, F) of *anti* (A-C) and *syn* (D-F) B₁₈H₂₂; in the excited states diagrams, singlets are depicted yellow, triplets orange, and the length of the yellow lines on the left side, with scale labels in nm, represents the relative oscillator strengths of the singlet excited states.

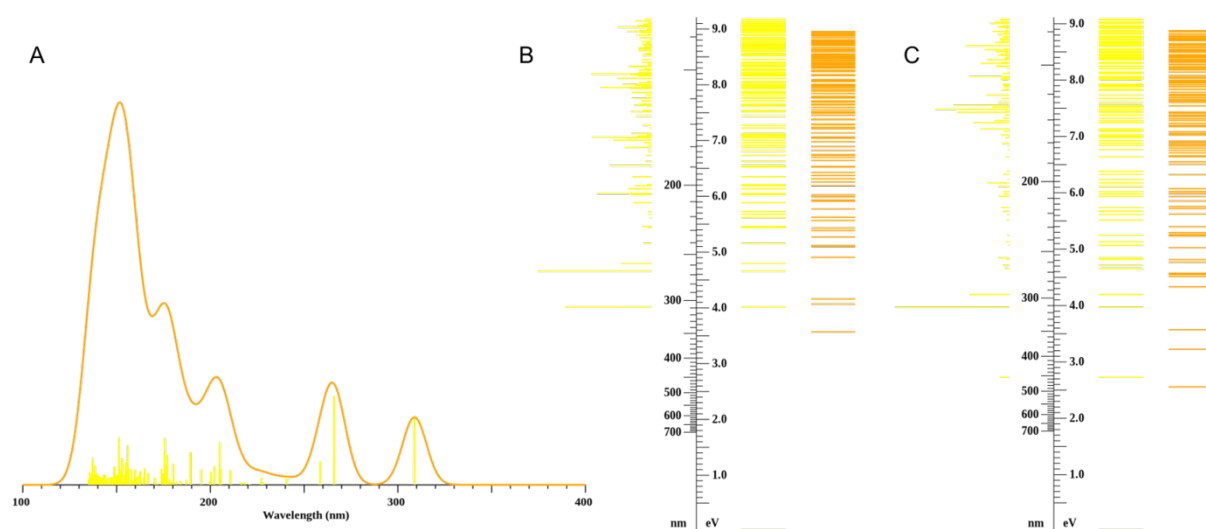


Figure S49: Simulated spectra (A), excited states (B) and excited states in the relaxed geometry of S1 (C) of 1-HS-syn-B₁₈H₂₁.

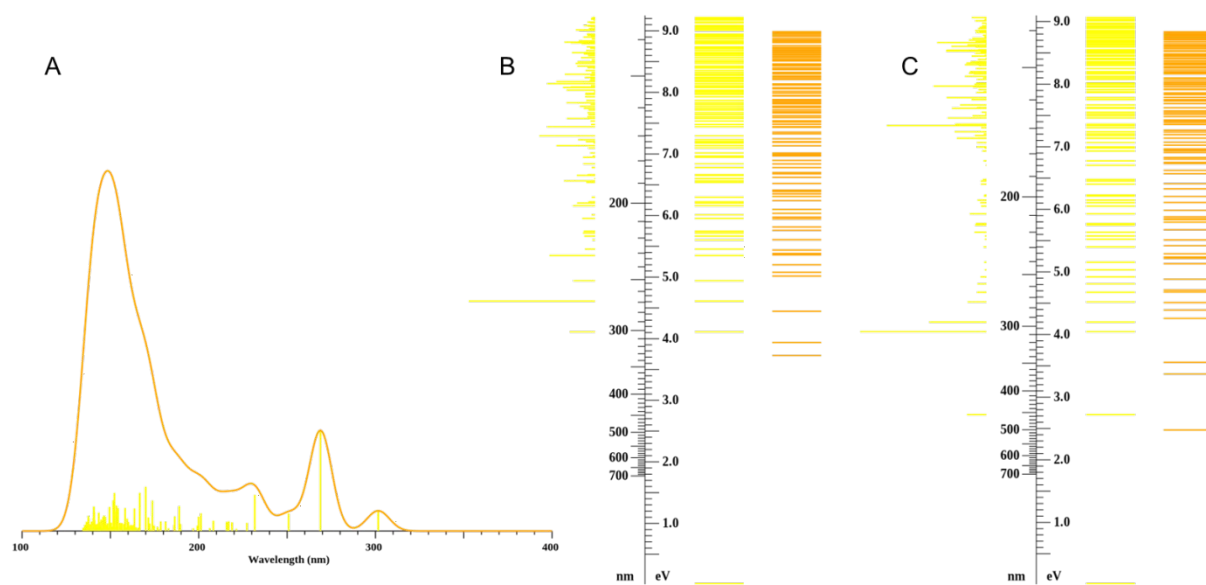


Figure S50: Simulated spectra (A), excited states (B) and excited states in the relaxed geometry of S1 (C) of 2-HS-syn-B₁₈H₂₁.

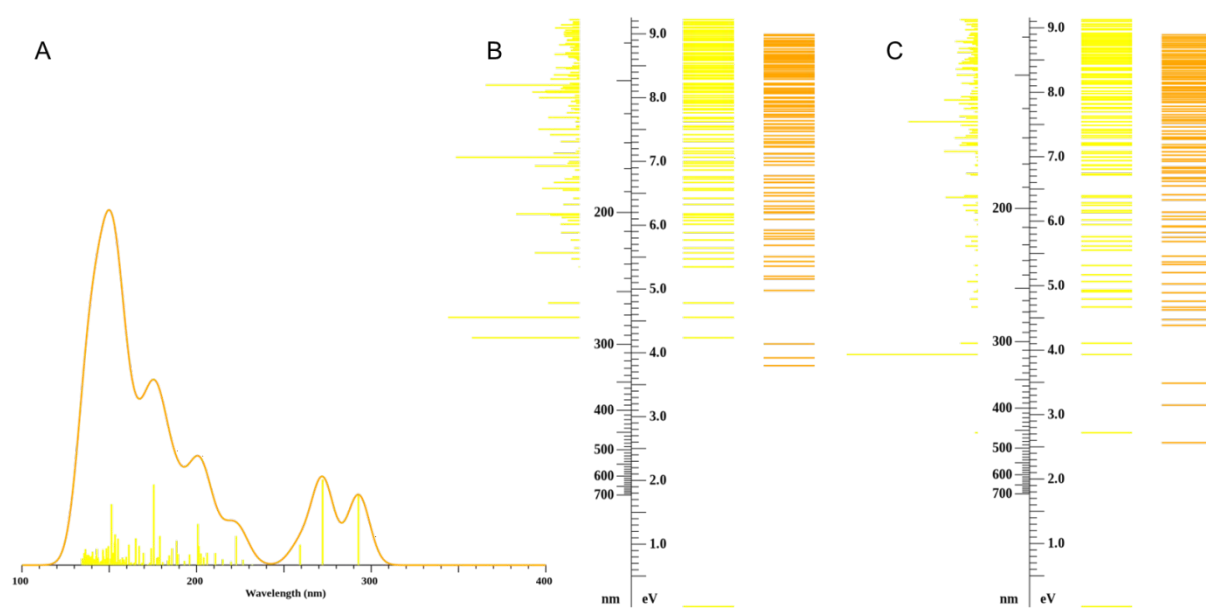


Figure S51: Simulated spectra (A), excited states (B) and excited states in the relaxed geometry of S1 (C) of 3-HS-syn-B₁₈H₂₁.

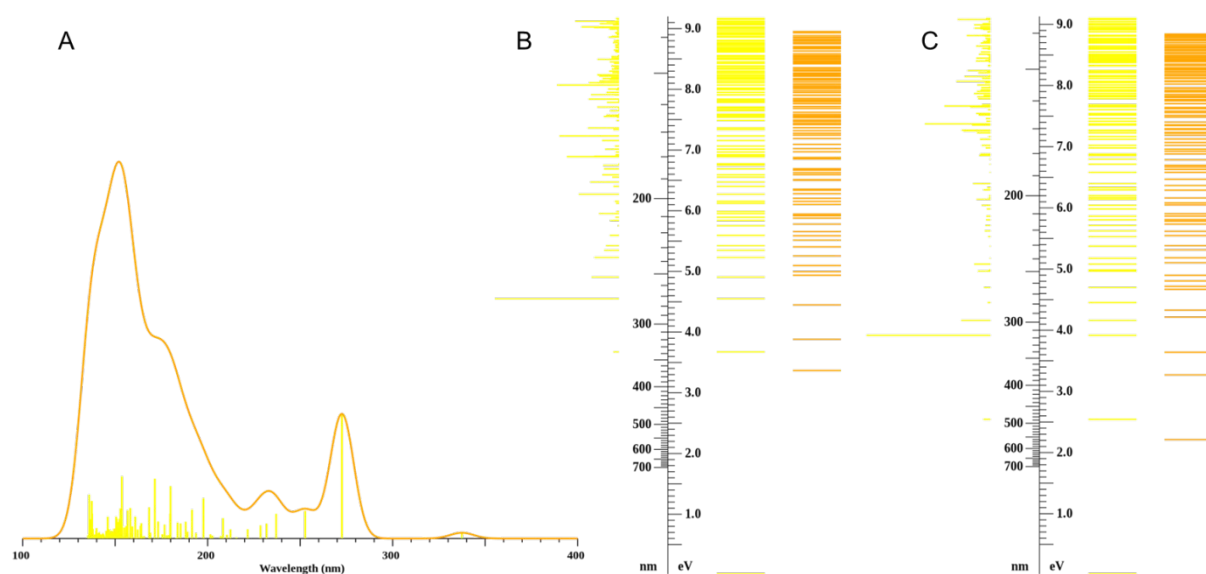


Figure S52: Simulated spectra (A), excited states (B) and excited states in the relaxed geometry of S1 (C) of 4-HS-syn-B₁₈H₂₁.

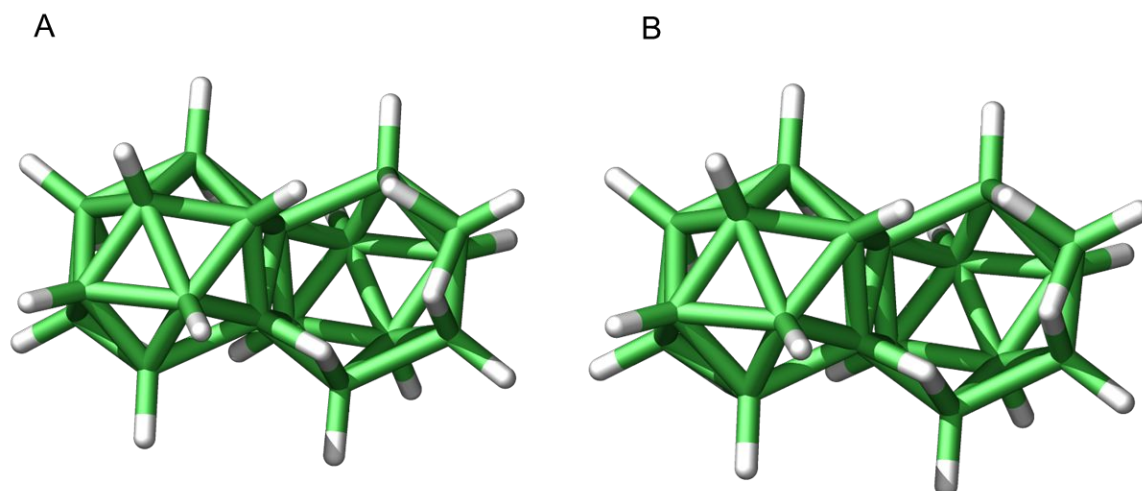


Figure S53: Optimized geometries of *anti*-B₁₈H₂₂: the ground state (A) and the first excited singlet (B).

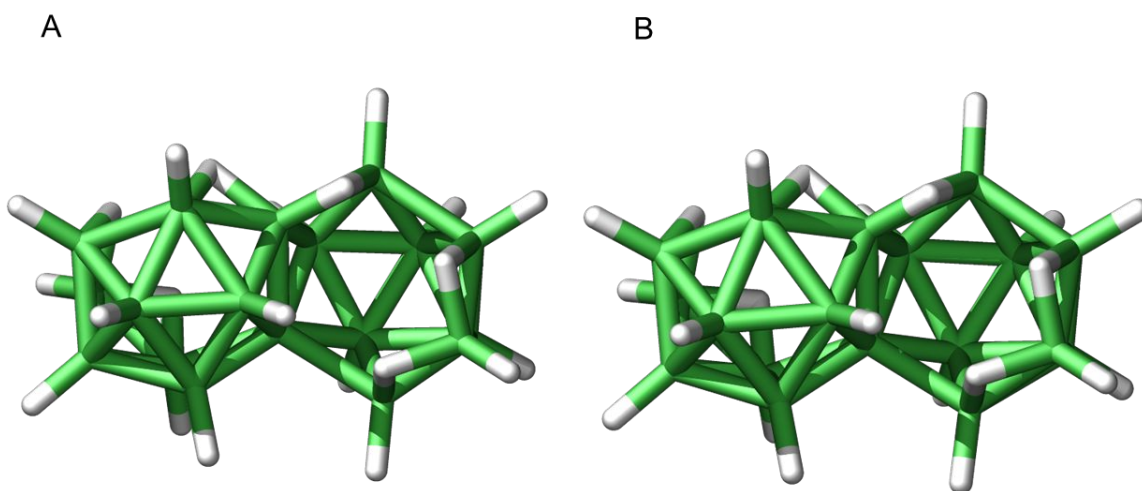


Figure S54: Optimized geometries of *syn*-B₁₈H₂₂: the ground state (A) and the first excited singlet (B).

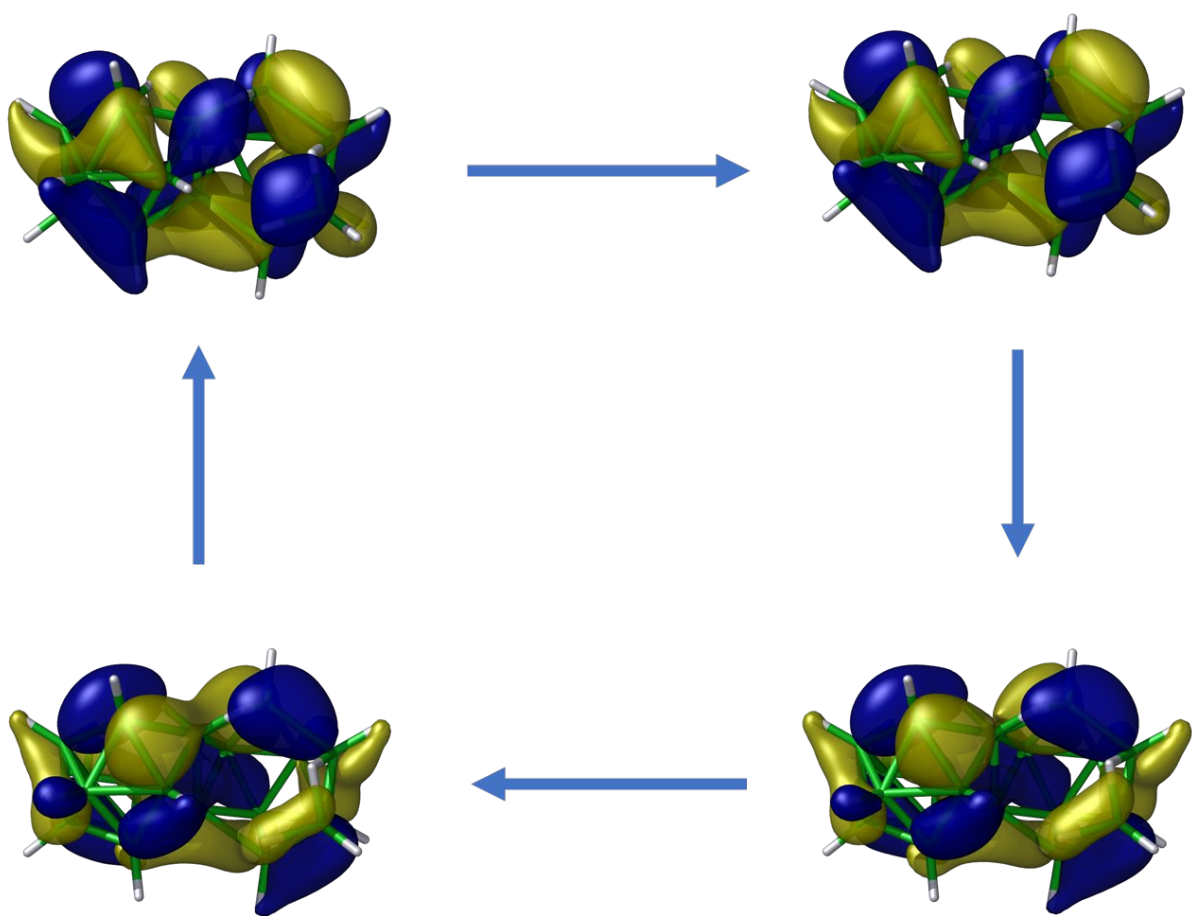


Figure S55: Natural Transition Orbitals (bottom hole, top electron) for the absorption of *syn*-B₁₈H₂₂ to the first excited singlet in the ground state geometry (left) and its luminescence from the relaxed geometry of S1 (right).

- i Londesborough, M. G. S.; Hnyk, D.; Bould, J.; Serrano-Andrés, L.; Sauri, V.; Oliva, J. M.; Kubát, P.; Polívka, T.; Lang, K.: Distinct Photophysics of the Isomers of B₁₈H₂₂ Explained, *Inorg. Chem.* **2012**, *51*, 1471–1479. [dx.doi.org/10.1021/ic201726k](https://doi.org/10.1021/ic201726k)

Editorials

The frontiers of water and sanitation

Anna M. Michalak, Jun Xia, Damir Brdjanovic, Aimée-Noël Mbiyozo, David Sedlak, Thalappil Pradeep, Upmanu Lall, Nitya Rao & Joyeeta Gupta

 Check for updates

The way in which human society uses water is continuously evolving. The present challenges related to clean water availability require the development of sustainable technologies and infrastructure. Furthermore, a stronger and wider appreciation of water inequalities and injustice demand an adequate transformation of water governance at local and global scale. We have asked nine experts in various sectors of water-related research to share their views on how water and sanitation science, technology and governance must evolve to meet the requirements of a healthier relationship between water and society.

Anna M. Michalak: Safeguarding the planet's water quality in the face of climate change

'Water, water, every where, nor any drop to drink.' This line from Samuel Taylor Coleridge's *The Rime of the Ancient Mariner* is spoken by a sailor adrift at sea. But it could equally well be a person whose water supply is contaminated and basement is flooded following a hurricane supercharged by climate change.

Human welfare and ecosystem health are inextricably linked to water. Water sustainability, in turn, is predicated on the availability of the right amount of water (not too much, not too little!) of the right quality. The 'right' quantity and quality depend on whether you are a fish, a tree, a basement, or a human being. But, regardless of who you are, both the quantity and quality of water are changing and will continue to do so.

A rich and growing literature has quantified how the amount of water available is changing in response to global change¹. More nascent literature is working to do the same for water quality^{2,3} for the world's lakes, reservoirs, estuaries, rivers, aquifers and coastal zones. Understanding the impacts of global change on water quality across a broad set of systems is challenging because water quality outcomes

are the result of a complex interplay between human action at scales ranging from the local (for example, land management, water treatment) to the global (that is, climate change)⁴. This means that both impacts and solutions may occur across a cascade of scales.

In addition, long-term in situ water quality monitoring has been limited and heterogeneous. Some systems have been studied extensively, but water quality in most water bodies around the world is not regularly monitored. Also, whereas satellite observations are effective at augmenting in situ observations for parameters such as precipitation, the same is less true for metrics of water quality beyond basic characteristics based on colour⁵.

Quantifying impacts across systems globally will necessarily come at the expense of the level of detail and site specificity; however, perhaps counterintuitively this should be embraced rather than avoided. For example, while understanding phytoplankton population dynamics may be possible for systems that have benefited from long-term monitoring and research, deriving general principles across entire regions or continents will necessarily require a focus on large-scale emergent properties.

Climate affects water quality both because it impacts the water bodies themselves (for example, water temperature, and stratification) and because it impacts upstream land (for example, precipitation and temperature impacts on nutrient runoff). The relative roles of these two primary pathways are poorly understood. For example, the National Lakes Assessment⁶ monitored nutrient concentrations in thousands of lakes in the United States; these concentrations result from a multitude of climate-sensitive processes within and upstream of each lake.

More broadly, we know very little about how global change is impacting the co-variability of water quantity and quality outcomes. For example, in some systems drought can reduce the intensity of harmful algal blooms, while in others it can exacerbate them, amplifying the challenge to sustainability. Documenting historical co-variability between trends and extremes in quantity and quality is a necessary first step, followed by their attribution to key drivers.

Designing effective strategies for water quality management in the face of global change will also require us to move beyond pitting the environment against economic activity. For example, much of the increases in nutrient pollution in the United States over the past 30 years are due primarily to climate variability rather than land use intensification, but the leverage we have to tackle this problem may nevertheless be predicated on rethinking land management.

Lastly, just as both quantity and quality must be considered to understand water sustainability, potential trade-offs between water security, food security, energy security, and climate change mitigation must also be recognized⁷. The idea of taking a systems approach to environmental impacts is not new, but the scope and scale of the systems that we need to consider are growing. In doing so, we need to remember that win-win solutions are often possible and we should not shy away from the challenge.

Jun Xia: Toward water systems science and technology

Water security is one of the major challenges in our society. Water stress and its effect on water supply, extreme climate events like floods and droughts, poor water quality due to increasing pollution and loss of biodiversity are all interconnected problems that require sustainable solutions^{8,9}. To find such solutions, water scientists and practitioners must operate along two fronts. First, it is essential to understand the complex behaviour of water systems at all scales, from global to regional and even urban and how these systems are affected by natural and social processes. Second, it is necessary to develop new ways, through science and technology, to manage water resources.

To understand how water resources are affected by natural and social phenomena in a changing environment, hydrological science must evolve from traditional physical hydrology centred on natural water cycles to a new water systems science and technology that blends natural hydrology, social hydrology and systems science¹⁰. Studies on the mechanisms of coupled human–water systems evolution will facilitate better planning,

water exploitation, and managing water for climate, environment, economy, and society. The application of systems science to water systems entails understanding the interactions and feedback between hydrology and society, building advanced multi-source monitoring and information systems, developing integrated modelling systems, and facilitating systematic decision-making for integrated water planning and management. For example, based on water systems science and applied technology, China is developing the Yangtze River Simulator, which aims to achieve smart management of the Yangtze River through an integrated system that provides multi-dimensional strategies for water utilization, biodiversity and eco-environment protection, climate change adaptation and sustainable development¹¹.

A systematic multi-source and multi-scale monitoring network is essential to better understand the spatiotemporal dynamics of water systems and to further assist decision-making. Current monitoring approaches primarily include manual sampling, laboratory time-decoupled analysis and sensor-based monitoring. New monitoring techniques have emerged with the development of satellite systems and advanced artificial intelligence technology. The latest monitoring systems cover air-based, space-based, and ground-based networks, with the ability to sense water systems at multiple spatiotemporal scales. High-resolution remote sensing, drone technology and ground sensors (for example, radar, thermal infrared and video) allow for real-time acquisition of spatiotemporal data, extending the scope and accuracy of monitoring. Going forward we can also expect that mobile communication, the Internet of Things, multi-source heterogeneous data fusion and artificial intelligence will enable automatic processing as well as real-time transmission and visualization of data.

Integrated modelling of water systems should decipher and represent both the natural and societal hydrological processes, focusing on the dynamic links and feedback between hydrology and society at the watershed scale. Since the last century, researchers have developed many models, from simple structure-based lumped models to component-based spatially-distributed models. However, hydrological modelling of the interactions between connected systems has mainly been conducted by considering each system separately. As a result, the complex water systems' behaviours have not been well captured. The next-generation water systems



models are expected to provide a platform for simulating natural–societal water cycling processes based on data from the systematic monitoring network. Such models would then help to better understand the co-evolving characteristics of interconnected natural–societal processes and to project the changes in hydrology and society under future climate scenarios.

To support regional sustainable development, watershed planning and management will rely heavily on intelligent technologies capable of processing massive information from monitoring, simulations and optimization phases. Previous studies show that the correlations between sustainable development levels and environmental footprints (for example, water, carbon and ecological footprints) satisfy the Environmental Kuznets Curve¹², which explores the potential inflection points of resources consumption along with the structural transformation of economies. For sustainable watershed planning and management, these relationships should be integrated into the water–environment–economy systems. This will increase our ability to build a smart framework, that is, instrumented, interconnected, intelligent and capable of tackling all the complexities of different nature discussed above. Digital twins, intelligent water affairs and other innovative technologies may also be integrated into a general social–hydrology scheme for holistic monitoring, processing massive information, analyzing the current situation, predicting future changes, enabling quick responses and optimizing troubleshooting solutions.

Damir Brdjanovic: The rise of non-sewered sanitation

For more than a century, urban sanitation research has been dominated by sewer-based approaches, carried out by research groups from high-income industrialized countries, embracing chemistry, microbiology, physical and bioprocess engineering, mathematics and modelling¹³. Such a situation has led to remarkable technological advances in activated sludge sewage treatment which, in turn, has facilitated environmental protection, closing cycles and the recovery and reuse of energy, water and chemicals^{14,15}. However, the launch of the United Nation's Millennium (and later Sustainable) Development Goals drew attention to the fact that more than half of the people on Earth do not have access to safely managed sanitation, with the vast majority of these living in low- and middle-income countries (LMICs) where sewer-based sanitation is unfeasible, impractical, or simply too expensive¹⁶.

Partly due to this, since the turn of this century, we have seen a change in attitude towards non-sewered sanitation research, which has become highly relevant, and necessary and has started to be published in scientific journals. The decision by the Bill & Melinda Gates Foundation to invest in non-conventional approaches to sanitation (for example, The Reinvent the Toilet Challenge) has also been instrumental in increasing the visibility of non-sewer-based sanitation research; it has triggered the curiosity of many research groups and mobilized the scientific community to

BOX 1

The contributors

Anna M. Michalak is the Director of the Department of Global Ecology at the Carnegie Institution for Science and a Professor (By courtesy) in the Departments of Earth System Science and of Biology at Stanford University. Her research interests focus on the interplay between climate change and water quality and on characterizing feedbacks between the global carbon cycle and climate. She is the lead author of the U.S. Carbon Cycle Science Plan and a member of the National Academies of Sciences, Engineering, and Medicine Committee on Earth Sciences and Applications from Space.

Jun Xia is an Academician of Chinese Academy of Sciences (CAS) on hydrology, and Chair Professor & Director of the Research Institute for Water Security (RIWS) and State Key Laboratory of Water Resources and Hydropower Engineering Science, Wuhan University, China. His research focused on nonlinear hydrological theory and integrated water system management as an engine for sustainable social and economic development in the world. He has served in various leadership positions, such as being the President of International Water Resources Association (IWRA, 2009–2012).

Damir Brdjanovic is a Professor and Head of the Citywide Inclusive Sanitation research group at IHE Delft Institute for Water Education, The Netherlands. He is an Endowed Professor at Delft University of Technology and Director of the Global Sanitation Graduate School. His research interests cover many aspects of urban

sanitation. In 2018, he received the IWA Publishing Award, in 2021 the IWA Water and Development Award, and in 2022, he was co-awarded the IWAP Best Scientific Book Prize.

Aimée-Noël Mbiyozo is a Senior Migration Researcher with the Institute for Security Studies, Africa. Over the past decade, she researches the intersection of migration with other prevailing issues such as climate change, gender, asylum law, human smuggling, violent extremism and citizenship. Her work has focused on high-risk and fragile environments in Africa and across west, central and south Asia. She has authored dozens of intelligence, policy-oriented and research reports and participates in multiple forums and networks to inform migration policies and enhance understanding of complex migration themes.

David Sedlak is the Plato Malozemoff Professor in the Department of Civil & Environmental Engineering at the University of California, Berkeley, USA. He is also the Director of the Berkeley Water Center and the Lead Cartographer for the US Department of Energy's National Alliance for Water Innovation (NAWI).

Thalappil Pradeep is an Institute Professor and Professor of Chemistry at the Indian Institute of Technology Madras, Chennai 600036, India. He works on affordable clean water using advanced materials and several of his technologies have been commercialised. He conceptualised and built the International Centre for Clean Water. For his work on water, he was awarded one of the VinFuture Prizes of 2022.

Upmanu Lall is the Alan & Carol Silberstein Professor of Engineering, and the Director of the Columbia Water Center, at Columbia University in the City of New York, USA. He has broad interests in hydrology, climate dynamics, water resource systems analysis, risk management and sustainability. He is motivated by challenging questions at the intersection of these fields, especially where they have relevance to societal outcomes or to the advancement of science towards innovative application.

Nitya Rao is Professor Gender and Development at the School of International Development, University of East Anglia, Norwich, UK. Her research interests include fine-grained gender analyses of agrarian relations and livelihoods in the context of climatic variability and economic precarity. She is Director of the Norwich Institute for Sustainable Development, a Member of the Steering Group of the High Level Panel of Experts to the Committee on World Food Security and Commissioner, EAT-lancet 2.0.

Joyeeta Gupta is a professor of Environment and Development at the University of Amsterdam and IHE-Delft Institute for Water Education, co-chaired UNEP's Global Environment Outlook-6 (2016-2021), is presently co-chair of the Earth Commission (2019-2022), and is a Commissioner in the Global Commission on Water Economics. In 2022, she was awarded the 2022 Piers Sellers Prize for her climate research and impact; and won in 2021 a European Research Council Advanced Grant.

engage more actively. Non-sewered sanitation has become the topic of specialized faecal sludge management conferences and dedicated scientific journals, and innovations for onsite sanitation have started appearing, as well as global network alliances and education and research programs and scholarships. The recently introduced Citywide Inclusive Sanitation (CWIS) approach¹⁷, which embraces both sewer and non-sewered sanitation,

and focuses on public services in an equitable, well-planned, properly managed, safe, sustainable, responsible, accountable and inclusive manner, is also gaining popularity among researchers from different disciplines, realizing that technical solutions alone are in principle insufficient to address sanitation challenges, in particular in LMICs.

During the last few years, leading research groups on wastewater and sludge

management have started showing interest in non-sewered sanitation and, in particular, in faecal sludge management. Besides the traditionally well-established global north-south collaboration between research groups, south-south cooperation is also steadily becoming more prominent. This in turn has facilitated the transfer of knowledge from more than a century of experience with activated sludge-based sewage treatment to a

rather juvenile domain of non-sewered sanitation, and to some extent vice versa. It has also clarified that we cannot simply adopt solutions from centralized, sewer-based treatment, or assume that sewage or urban wastewater characteristics are similar to those of faecal or septic sludge¹⁸.

One of the forthcoming research areas in non-sewered sanitation is the prediction of the characteristics and quantities of accumulated faecal sludge, understanding the correlations to source populations, and eventually building a reliable database of faecal sludge characteristics. This also includes further development and verification of methods for faecal sludge analysis, as well as standardization of the experimental procedures used in faecal sludge research. Another focal area is a better understanding of the microbial and physico-chemical processes taking place in onsite sanitation containment and treatment systems to predict the characteristics and degradation of faecal sludge. In addition, the research on pathogen inactivation and destruction, reduction of volume of faecal sludge, safe reuse of end products, and treatment in the context of the circular economy and sustainability will continue to attract the interest of researchers in the coming years.

Future research will combine smart sanitation technologies and medical research, resulting in crossover innovations, such as medical toilets, that could revolutionize the public health sector in both high-income countries (for example, preventive cancer detection) and LMICs (for example, pre-diagnosis of tropical diseases) by longitudinal monitoring of users' health and early detection of epidemics¹⁹. Furthermore, the recent COVID-19 pandemic revealed the potential of data mining from sewage to monitor and predict the spreading of the virus. This approach could be used to expand the public health-relevant data collection to non-sewered sanitation areas (via, for example, medical toilets) as a step towards the development of a community-wide system for early detection of epidemics. Finally, more research into emergency sanitation will be necessary to support humanitarian WASH (water, sanitation and hygiene) activities.

We should also remember that onsite sanitation services provision is closely related to the necessities of the users, arguably more than is the case for sewer-based sanitation. Advancing this field will therefore require substantial consideration of social aspects, gender-based aspects of sanitation and in particular the needs of women, behavioural



change and advocacy, cultural and religious aspects as well as business and financial aspects. Undoubtedly, non-sewered sanitation allows for a wide spectrum of both inter- and trans-disciplinary research and it is expected that the most impactful results will be obtained from unconventional combinations of expertise and skills.

Aimée-Noël Mbiyozo: Water is at the heart of climate mobility

The amount of available water – whether too little or too much – is a core driver of forced displacement and immobility, particularly among vulnerable groups in fragile communities and countries. Locally-driven water solutions to avert, minimize or address forced displacement and immobility among vulnerable groups are extremely important but often overlooked.

Water scarcity is a primary factor driving climate mobility and immobility in Africa. High water stress affects about 250 million people²⁰. These numbers are projected to increase with population growth combined with rising temperatures, longer and recurrent drought periods, and diminished river flows. Flood-related disasters also cause high levels of displacement; however, water scarcity pushes five times more migration.

Like climate change, lack of water is a fragility amplifier that intersects with socio-economic stressors and exacerbates existing vulnerabilities. Marginalized people are more vulnerable because they have less access to

the financial and social assets needed to cope, such as land tenure, social and legal services, political participation, paid livelihoods, governance, and infrastructure. This includes gender inequality. For example, in Sub-Saharan Africa, women are responsible for 80% of food production, and more than 60% of all employed women work in agriculture, yet they rarely own the land²¹. Similarly, water-related challenges disproportionately affect women due to gender inequalities in roles and responsibilities²². Women carry a disproportionate unpaid work burden and rely more on natural resources and water-sensitive sectors for their livelihoods. Water access forms a core element of daily activities and household labour, including cooking, washing, and caring for the ill, children and elderly. Globally, women and girls spend almost 200 million hours daily collecting water²³. In water-scarce situations, girls and women must travel further to find it. This restricts their access to education, livelihoods and safety and exposes them to increased risks of violence, including sexual violence²⁴. Travelling longer distances also increases exposure to potential water contamination.

Many poor people who depend on climate-vulnerable resources such as agriculture or aquaculture are at risk of involuntary immobility. The most vulnerable people have the fewest human, financial and social capital required to migrate as an adaptation strategy. As water scarcity reduces crop yields, they face diminishing returns, their resources deplete further, and they become even less mobile.

This is a dangerous cycle. Some of the most vulnerable people will be left behind in ‘the poverty trap.’ In many cases, working-aged men are the first to depart and leave behind women, children, the elderly, and the disabled.

Water availability also impacts other fragile situations, such as transhumance and urban settings. Changes in seasonal rain patterns and droughts affect access to arable land and grazing, altering traditional patterns and timing and even causing conflict. Water scarcity in cities impacts sanitation, access to drinking water, and the provision of essential social services and healthcare systems²⁵. Unplanned urbanization can prevent proper draining and cause floods, particularly in informal settings.

Water interventions and infrastructure play a crucial role in helping to prevent or minimize forced displacement or immobility and in preparing areas to receive climate migrants. Solutions should be context-specific, flexible, adaptable and engage local leaders and community members in their design. Projects that provide water and sanitation, livelihoods and economic development, and protective climate-resilient water infrastructure and alternatives, such as nature-based solutions, are necessary and should factor in mobility and immobility considerations.

David L. Sedlak: The next stage of the reverse osmosis revolution

Over the past three decades, reverse osmosis (RO) has become one of the most attractive ways to overcome water scarcity. Each day about 60 million cubic meters of seawater is turned into drinking water in coastal cities while thousands of smaller communities use RO technology to desalinate brackish groundwater²⁶. Early adopters, like Singapore and Orange County, California use RO to turn another million cubic meters per day of municipal wastewater into drinking water. The impact of RO extends beyond wealthy, water-stressed places: small-scale systems are being used by people in low-income countries to purify tap water that otherwise would be unsafe to drink. If current trends continue, over half a billion people may be consuming RO-treated drinking water by 2030.

Despite such positive developments, numerous challenges remain. Research is needed to understand and reduce the potential risks that RO and related desalination technologies might pose to human health and the environment. Further technological advancements also are needed to lower costs and make

advanced water technologies accessible to more people²⁷.

The main human health concern of RO is related to the fact that RO-treated water is essentially free of any ions, including some that have health benefits. In recognition of the tendency of ion-free (‘aggressive’) water to damage infrastructure, calcium hydroxide (that is, lime) is usually added back into RO-treated water at the end of the desalination process. Although the addition of calcium and pH adjustment helps, the near absence of other ions can lead to the mobilization of geogenic toxins like arsenic when aquifers are recharged with RO-treated water²⁸. Furthermore, without careful management, the chemical composition of RO-treated water could alter minerals in water distribution systems, enhancing the release of toxic metals like lead or creating conditions that are conducive to the colonization of pipes by undesirable microbes. Finally, the near absence of beneficial ions that people would normally obtain from their water supply, such as magnesium and fluoride in RO-treated water, may contribute to health problems²⁹. Beyond the assessment of the risks associated with the use of RO-treated water, there is a need for research that leads to cost-effective technologies for adding key ions back to water at the end of the treatment process.

The main risk to the environment from RO treatment is related to the waste produced when ions are removed from water. In the case of seawater and brackish water desalination, the waste is a salty brine. RO treatment of wastewater also produces a salty waste, referred to as concentrate, that contains relatively high concentrations of nutrients, metals and organic chemicals. Until recently, engineers assumed that dilution of brine and concentrate by mixing wastes into seawater would be sufficient to protect the environment. However, it is becoming clear that in regions where multiple desalination plants discharge brine into shallow coastal waters, salinity can approach levels of concern. Furthermore, the discharge of RO concentrate could contribute to hypoxia, ocean acidification and compromise the health of aquatic organisms. For these reasons, it may become necessary to treat concentrates from wastewater recycling projects prior to discharge or avoid the discharges altogether³⁰. For RO plants lacking coastal access, the current generation of brine and concentrate management technologies, such as deep well injection, evaporation ponds, zero liquid discharge (ZLD) or near zero-liquid discharge (NZLD)

greatly increase the overall cost of water purification. To enable further spread of RO technologies, research is needed to lower the costs of selectively removing trace constituents and dewatering brine and concentrate to decrease the volume of liquid produced.

Innovations in materials science and process engineering could lower the cost and energy consumed by ZLD and NZLD systems, but the current approaches for managing residual salts (for example, landfill disposal) are not sustainable. Valorization of the solid or highly saline wastes produced in these processes could result in the production of useful products like sulfuric acid, caustic, gypsum and other commodity chemicals from desalination brines. With more selective separations, it also could be possible to develop cost-effective approaches to recover nutrients, metals and organic matter from concentrate from brines created by water reuse²⁷. Thus, wastes generated from RO treatment could provide a means of supporting a more circular economy.

If researchers can resolve some of the issues identified above, desalination and water reuse – technologies that already are seeing large investments in a handful of wealthy, water-stressed locations – could play a much greater role in humanity’s efforts to overcome water scarcity.

Thalappil Pradeep: Circularity in water and the role of nanotechnology

Circularity in water has emerged as a response to the unsustainable linear water model of ‘harvest, use, and waste’. In a robust circular water (CW) economy, the entire cycle of water harvest and recovery can be repeated endlessly without the loss of water, and the contamination caused in the process can act as raw material or fuel for other valuable purposes. Historically, ‘circular economy’ was introduced in 1990 (ref. ³¹), and it was later extended to multiple sectors including water and waste management, food production, and sustainable design and construction.

Incremental innovations to improve treatment efficiencies, long-distance conveyance of freshwater, and resource-intensive seawater desalination are unlikely to move towards a carbon-neutral CW ecosystem. Thus, there’s a dire need to augment the existing water flow networks with disruptive water-reuse technologies to maximize circularity. It is possible to evaluate the circular and non-circular water footprints individually and focus on minimizing the non-circular portion. We may assume



that circular water consumption has negligible environmental impacts, or the extent of the impact may be considered as a deviation from circularity. Given the rapid evolution of nanoscience around clean water challenges in the past two decades, it is natural to wonder what role can nanotechnology play in the transformation from a linear to a circular water economy.

It is possible to approach CW by adopting nine strategies: rethink, avoid, reduce, replace, reuse, recycle, cascade, store and recover³². The loop of CW has several entry points (surface water and groundwater extraction, rainwater and humidity harvesting and desalination), and exit points (wastewater discharge, leakage, evaporation and overflows from storage tanks). Points, where water is returned to the hydrological cycle, are not covered in the strategies, as they do not retain water in the CW loop.

The sustainability of any technology is usually assessed by estimating its environmental, social, and economic performance. Sustainable nanomaterials are required to cross thresholds in the aspects of safety, stability, regeneration, reuse, and disposal. Sustainability metrics, such as mass intensity, solvent or water intensity, carbon footprint, and life cycle assessment, and tools like GUIDEnano-tool, LICARA nanoSCAN, and Fuzzy-Delphi method may be applied to assess the sustainability of materials and technologies³³. Moreover, large-scale deployment of IoT-enabled nanosensors, data analytics, machine learning, and artificial intelligence, with the support of governments and industries will

contribute to the transition of the emerging technologies into a CW ecosystem at a global level. This is essential as water is also a global resource, just like air. Measurement becomes central to sustainability as global warming reminds us.

The strategies followed to achieve CW may be supported by the implementation and adoption of emerging water treatment technologies. Among such technologies, those based on nanomaterials are attractive for their potential in several ways. For example, nano-enabled filters and membrane separators, the use of nano-catalysts as a replacement for metal catalysts, the development of advanced reverse osmosis membranes for desalination and nanostructured atmospheric water harvesters can all contribute to increasing water availability. In terms of water delivery and consumption, nanofluids could replace freshwater in geothermal operations and hydraulic fracturing, self-healing nano-coatings could be used to prevent leakages in distribution networks and to realize water-efficient cooling technologies for thermoelectric power generation. Finally, the development and deployment of affordable nanosensors can ensure real-time water quality monitoring to tackle potential challenges related to water management. For instance, nanotubes and nanowires with large surface area-to-volume ratio could produce enhanced signal-to-noise ratios for ultra-trace detection.

Naturally, beyond the development of advanced water technologies, a complete transition to a CW economy will require support from the local governments, tailoring

the existing norms, and availability of easy-to-implement technologies which are compliant with the existing water infrastructure as well as appropriate policy guidelines.

Upmanu Lall: The future of America's water security

America's water infrastructure – dams, levees, conveyance, and treatment systems – set the global standard in the 20th century for mitigating drought and flood risk, and providing water and wastewater services. Today, America is challenged by a deteriorating water infrastructure due to decades of deferred maintenance and under-investment. It faces climate change, fragmented governance, socio-economic inequity, and environmental impacts from failing infrastructure. Similar challenges are experienced worldwide.

Recognizing the impacts of lead in water in Flint, Michigan, and PFAS contamination elsewhere, President Biden and the US Congress approved US\$15 billion for lead pipe replacement and US\$5 billion to address PFAS contamination. However, whether this is the best way to address the projected US\$1 to US\$2 trillion needed for failing water infrastructure, recognized but not addressed by four previous administrations, remains to be seen.

Public health concerns focus on contamination and motivate responses like Biden's. However, conveyance and storage account for 70–80% of the costs of traditional designs. The USA experiences over 300,000 main pipe failures per year, up from 850 in the 1950s. Each incident is accompanied by a boil water notice, service disruption, and potential pathogen exposure. The USA has over 90,000 dams with a median age of 67 years (beyond the nominal design life)³⁴. The condition of most dams owned by municipalities is unknown or poor. Decadal droughts in the Western USA have led to empty reservoirs, depleting groundwater and supply restrictions.

Investment is needed in water systems that minimize climate and pollution risks, and are affordable, efficient, reliable, and suited to local demographic, physiographic, economic, ecological, and climate conditions. The traditional approach led to large (often oversized), centralized treatment and conveyance infrastructure. As it aged, it was difficult to maintain and expensive to replace.

The lead-in-water example for Flint highlights a different problem. Water quality at the treatment plant may meet standards, but not water delivered at the tap, as it is not regularly tested. Worse, the list of contaminants is



ever-growing, and concern over higher treatment costs has blocked efforts to add more contaminants to the regulated list. Exposure to drinking and cooking is a primary concern. This is a very small fraction of urban water use. Increasing drinking water quality violations³⁵ have driven an increase in bottled water sales³⁶.

Perhaps point-of-use treatment systems and sensors could be used to assure the quality of water for these uses, thus enabling a decentralized architecture³⁷ that integrates water supply, stormwater, and wastewater control and reuse. Digital architecture would provide system control even in areas with limited technical and financial capacity. The reduction in storage and conveyance costs would pay for higher treatment and digital water quantity and quality monitoring costs. Managed aquifer recharge with treated wastewater and stormwater would provide storage and address groundwater depletion. Infrastructure could be integrated with neighbourhood parks and green spaces to limit land requirements. The 'optimal' economic scale of decentralization would be determined by local factors, such as population/building density, soils, climate, roads, and condition of existing infrastructure, and offer dramatic cost reductions^{38,39}.

Water treatment research has focused largely on a one-contaminant-at-a-time strategy. Given the plethora of man-made and geogenic contaminants and pathogens, this is challenging. Today, membrane filtration and electrochemical technologies can complement biological treatment methods to achieve dramatic reductions in a broad spectrum of contaminants, while providing materials and energy resource recovery. The rapid growth and reduction in the cost of point-of-use filtration devices demonstrate growing consumer adoption. Point of use water quality assurance is still an open question.

The financial, technical, and social conditions are ripe for a water transformation. Climate change and ageing, failing infrastructure can be accelerants to a resilient future, especially for underserved populations that currently face the biggest challenges.

Nitya Rao: Water is a gendered human right

Water is critical for life on Earth. For humans, water security is essential for food and nutrition security⁴⁰. The Sustainable Development Goal (SDG) 6 provides a framework for ensuring water and sanitation availability and sustainable management but it does not explicitly recognise how power and wealth imbalances

mediate access and rights to water. Water scarcity is not just physical, but also experienced through socio-political processes of inclusion and exclusion⁴¹. It does not address issues like why it is acceptable for rural women to wait several hours or walk long distances to access water, for the urban poor to be deprived of legal connections, or for one state to deny another its share of water.

Equity and justice are central to researching water access, distribution and use, and are indicators of resource-sharing at different scales, from the household and communities to markets and states. Patterns of socio-economic inequalities shape the mechanisms through which not just overconsumption by some and under-consumption by others are justified, but also how different uses of water are prioritised. Intensification of these inequalities often leads to conflicts.

Gender relations and the intersecting identities of class, race, ethnicity, marital status and age underpin the unequal power relations that set up false dichotomies between the uses of water for production or domestic purposes, associating men with the former and women with the latter⁴². Not just does reproduction underpin the productive economy⁴³, but in a majority of small landholder households, water-related divisions of labour overlap due to the interlinkages between ecology (land use), embeddedness of food production and consumption systems within these ecologies, and the gendered labour use patterns therein. Women usually play central roles in farming and irrigation, alongside household reproduction. By ignoring women's work, both 'productive' and 'reproductive', costs of labour are shifted from the paid to the unpaid economy, and the inequities that reproduce male privilege are further strengthened.

In a context of persistent drought and climate variability, gendered labour relations impact health and wellbeing. In pastoralist Kenya, men are moving further away from their homes in search of pastures and water⁴⁴, and those without cattle migrate to nearby cities and towns to diversify household livelihoods. Women, though differentiated by their marital status, land ownership and the number of cattle owned, acutely feel the impact of water scarcity, most confronting trade-offs between water costs, time availability for collection and the health impacts of the same. Shortages imply either purchasing or walking long distances for safe water. As the responsibility for accessing water and ensuring water quality is privatized and placed on individual households and women within them⁴⁵, these

trade-offs get sharper, leading to declines in consumption alongside a rise in workloads. Where these cannot be managed one finds an increase in water-borne diseases, poor health and nutrition, and rising mortality. Economic advantages and disadvantages are bound to social and cultural advantages and disadvantages in relation to the value attributed to different activities⁴⁶, with women denied decision-making and control in water management institutions.

Water research needs integration of women and gender issues into mainstream agendas to ensure material wellbeing but also the transformation of these agendas to reflect strategic gender interests related to increased say in decision-making, recognition of reproductive needs as legitimate, and an equal share of benefits. Water, like land, is both a physical asset and a source of meaning, so correcting the invisibility of gendered power relations here can also contribute to the larger goal of gender equality.

Joyeeta Gupta: Water Justice is essential for life within the planetary boundaries

The current water crises related to poor water access, over-abstraction, pollution and extreme weather events – result from inequitable, unsustainable and failing governance. If justice is not central to direct and indirect water policy at all levels, it will be impossible to live within the water, climate and nutrient planetary boundaries.

There are three main issues related to water justice. First, scholars propose water boundaries to maintain water system stability, which require drastic reductions in water use, constraining water supply. Even without this constraint, many cities are reaching ‘day zero’ (or when there is no fresh water available for city consumption) and many basins are ‘closed’ (as demand exceeds supply and no more water can be extracted from the basin). Water shortage raises the price of water beyond the reach of the poor affecting and exacerbating existing problems of water, sanitation and hygiene (WASH) access, and shifts water from uses with low but necessary (for example, drinking water) to high, but not quite so necessary, returns on investment (for example, golf courses, biofuels). This requires redistributing water.

Second, declining water quality, whether because of sewage, pharmaceutical, plastic, nutrient, or pesticide pollution results from the ability of users to externalize pollution. This raises issues such as who is polluting, how,

where, in relation to production for whom, or questions of liability (who is liable) and redistribution (how can pollution be reduced by restructuring production, distribution and consumption processes).

Third, extreme weather events (droughts, floods, cyclones) affect lives, livelihoods, infrastructure, and redistribute risks in society, especially in the global South. Such events are in line with climate models and will rise in the future. Sadly, the costs of such damages are not fairly distributed. To put things in context, we should consider that Hurricane Ian caused more than US\$75 billion worth of damage to Florida⁴⁷, while only US\$100 billion was promised annually to the entire developing world for adaptation, much of which is not being provided or provided as commercial loans⁴⁸. Although at COP27, countries came to an agreement to finance loss and damage already caused to other countries, given the history of climate change finance, it is likely that this will be no more than a symbolic gesture. Damage caused to other countries, to the extent caused by greenhouse gas emissions should in principle be borne by those who emitted those gases⁴⁹. However, if finance is provided through loans it may lead to a spiralling debt crisis in the developing world.

All three issues raise distributive and corrective justice points. Challenges to redistributive justice include a) past (colonial) and institutionalized inequitable water property rights and quasi-property rights in permits/concessions and contracts that cannot easily be expropriated without compensation⁵⁰; b) the direct link between water use and GDP encouraging water use to enhance GDP and the Jevon’s paradox where increased water efficiency ironically leads to higher water use; c) water overuse and ‘water grabbing’ by rich people and investment funds⁵¹; d) the externalization of local to global pollution (for example, Coca Cola sells 200,000 plastic bottles a minute, much of which ends up as plastic soup, that is, plastic pollution in the ocean⁵²; e) the unwillingness to take responsibility for damage caused and pay compensation; f) the fact that some companies that use large quantities of water, directly or indirectly, avoid paying taxes (for example, Starbucks⁵³) which reduces country revenues for reinvesting in public goods.

Proposed solutions often institutionalize or exacerbate existing inequities. In the market-based system, the rich (whether countries, companies or people) benefit from actual and virtual water uses while externalising

damage⁵⁴, they create rules that favour them, and prevent, avoid or evade rules that regulate them or require them to pay taxes. The poor pay the final bill as their water resources are expropriated (for example, indigenous populations^{55,56}) and often polluted (for example, communities near dams and mines), and cannot afford rising water prices for drinking or irrigation or the bankable loans to adapt to extreme weather events. The situation can be summarized by considering that as of 2021, 2.3 billion people live in water-stressed areas, 1.8 billion drink polluted water, and 2.8 billion people suffered from floods between 2001–2018.

The question is: Is water justice needed to live within water boundaries? I would argue that further denying the poor drinking water and sanitation services will only exacerbate health problems with spillover effects on society, and denying them adaptation services will expose them to extreme weather events that will displace millions beyond borders; all of which will have repercussions on the Earth we share. If we want to live within planetary boundaries, we have to engage in redistributive justice.

Anna M. Michalak¹✉, Jun Xia²✉, Damir Brdjanovic³✉, Aimée-Noël Mbiyozo⁴✉, David Sedlak⁵✉, Thalappil Pradeep⁶✉, Upmanu Lall⁷✉, Nitya Rao⁸✉ & Joyeeta Gupta⁹✉

¹Department of Global Ecology, Carnegie Institution for Science, and Department of Earth System Science, Stanford University, Stanford, California, USA. ²The Research Institute for Water Security (RIWS), and State Key Laboratory of Water Resources and Hydropower Engineering Science, Wuhan University, Wuhan, China. ³HE Delft Institute for Water Education, Delft, The Netherlands.

⁴Institute for Security Studies Africa, Pretoria, South Africa. ⁵Department of Civil and Environmental Engineering, University of California, Berkeley, CA, USA. ⁶Indian Institute of Technology Madras, Chennai, India. ⁷Columbia University, New York, NY, USA. ⁸School of International Development, University of East Anglia, Norwich, UK.

⁹Faculty of Social and Behavioural Sciences, University of Amsterdam, Amsterdam, Netherlands.

✉ e-mail: michalak@carnegiescience.edu; xiajun666@whu.edu.cn; d.brdjanovic@un-ihe.org; ambiyozo@issafrica.org; sedlak@berkeley.edu; pradeep@iitm.ac.in; ula2@columbia.edu; N.Rao@uea.ac.uk; J.Gupta@uva.nl

Published online: 19 January 2023

References

- Caretta, M.A. et al. in *Climate Change 2022: Impacts, Adaptation and Vulnerability* (eds Pörtner, H.-O. et al.) (Cambridge Univ. Press, 2022); <https://research.birmingham.ac.uk/en/publications/water-in-climate-change-2022-impacts-adaptation-and-vulnerability>
- Gobler, C. J. *Harmful Algae* **91**, 101731 (2020).
- Whitehead, P. G., Wilby, R. L., Battarbee, R. W., Kernan, M. & Wade, A. J. *Hydrol. Sci. J* **54**, 101–123 (2009).
- Michalak, A. *Nature* **535**, 349–350 (2016).
- Gholizadeh, M. H., Melesse, A. M. & Reddi, L. *Sensors* **16**, 1298 (2016).
- National Aquatic Resource Surveys* (EPA, 2017); <http://www.epa.gov/national-aquatic-resource-surveys/data-national-aquatic-resource-surveys>.
- IPCC Climate change 2018: Summary for Policymakers (eds Masson-Delmotte, V., P. et al.) (Cambridge Univ. Press, 2018).
- Braga, B. et al. *Water and the Future of Humanity: Revisiting Water Security* (Springer Press, 2014)
- Vörösmarty, C. J. et al. *Nature* **467**, 555–561 (2010).
- McMillan, H. et al. *Hydrol. Sci. J* **61**, 1174–1191 (2016).
- Xia, J. et al. *Geosci. Lett.* **8**, 18–29 (2021).
- Wiedmann, T. & Allen, C. *Nat. Commun.* **12**, 3758 (2021).
- Chen, G.-H. et al. *Biological wastewater treatment: principles, modelling and design* 2nd edition (IWA Publishing, 2020).
- Van Loosdrecht, M. C. M. & Brdjanovic, D. *Science* **344**, 1452–1453 (2014).
- Brdjanovic D. in *Government Gazette* (October 2015); https://issuu.com/government.gazette/docs/government_gazette
- Ferré, A. et al. *Methods for Faecal Sludge Analysis* (eds Velkushanova, K. et al.) (IWA Publishing, 2021).
- Schrecongost, A., Pedi, D., Rosenboom, J. W., Shrestha, R. & Ban, R. *Front. Environ. Sci.* **8**, 19 (2020).
- Strande, L., Ronteltap, M. & Brdjanovic, D. *Faecal Sludge Management: System Approach for Implementation and Operation* (IWA Publishing, 2018).
- Brdjanovic, D. *Nat. Biomed. Eng.* **4**, 581–582 (2020).
- State of the Climate in Africa* (WMO, 2021); <https://public.wmo.int/en/our-mandate/climate/wmo-statement-state-of-global-climate/Africa>
- Schalatek, L. *Gender and Climate Finance* (Heinrich-Böll-Stiftung, 2022); <https://climatefundsupdate.org/wp-content/uploads/2022/03/CFF10-Gender-and-CF-ENG-2021.pdf>
- Outlook on Migration, Environment and Climate Change, Brief 13: A Gender Approach to Environmental Migration* (IOM, 2015); <https://www.iom.int/sites/g/files/tmzbd1486/files/about-iom/gender/Gender-Approach-to-Environmental-Migration.pdf>
- Farley, M. How long does it take to get water? For Aysha, eight hours a day. *UNICEF USA* <https://www.unicefusa.org/stories/how-long-does-it-take-to-get-water-aysha-eight-hours-a-day/30776> (2018).
- Aamer, F. Water Crisis in the MENA region: Women, Water, and Migration. *Stimson Women and Water Security Project* <https://www.stimson.org/2021/water-crisis-in-the-mena-region/> (2021).
- McFee, E. et al. *Desk Review: Climate Change, Water Scarcity and Migration* (ISS, 2022); <https://issafrica.s3.amazonaws.com/site/uploads/pb-178.pdf>
- Jones, E., Qadir, M., van Vliet, M. T. H., Smakhtin, V. & Kang, S. M. *Sci. Total Environ.* **657**, 1343–1356 (2019).
- Sedlak, D. L. et al. *National Alliance for Water Innovation* (NAWI, 2021).
- Fakhreddine, S., Prommer, H., Gorelick, S. M., Dadakis, J. & Fendorf, S. *Environ. Sci. Technol.* **54**, 8728–8738 (2020).
- Sedlak, D. L. *Environ. Sci. Technol.* **53**, 3999–4000 (2019).
- Scholes, R. C., Stiegler, A. N., Anderson, C. W. & Sedlak, D. L. *ACS Environ. Au* **1**, 7–17 (2021).
- Pearce, D. W. & Turner, R. K. *Economics of Natural Resources and the Environment* (Johns Hopkins University Press, 1990).
- Morseletto, P., Mooren, C. E. & Munaretto, S. *Circ. Econ. Sustain* **2**, 1463–1477 (2022).
- Mukherjee, S., Shantha Kumar, J., Nagar, A. & Pradeep, T. *J. Am. Chem. Soc.* **16**, 625–657 (2022).
- Ho, M. et al. *Wat. Resour. Res.* **53**, 982–998 (2017).
- Allaire, M., Wu, H. & Lall, U. *Proc. Natl Acad. Sci. USA* **115**, 2078–2083 (2018).
- Allaire, M., Mackay, T., Zheng, S. & Lall, U. *Proc. Natl Acad. Sci. USA* **116**, 20917–20922 (2019).
- Daigger, G. T., Voutchkov, N., Lall, U. & Sarni, W. *Nature* **504**, 657 (2019).
- Schwetschenau, S. E. et al. *ACS EST Engg.* **3**, 1–14 (2023).
- Kavvada, O., Nelson, K. L. & Horvath, A. *Environ. Res. Lett.* **13**, 064001 (2018).
- Water for food security and nutrition* (HLPE, 2015); <http://www.fao.org/3/a-av045e.pdf>
- Mehta, L. *World Dev.* **59**, 59–69 (2014).
- Rao, N., Lawson, E. T., Raditloaneng, W. N., Solomon, D. & Angula, M. N. *Clim. Dev.* **11**, 14–26 (2014).
- Crow, B. & Sultana, F. *Soc. Nat. Resour.* **15**, 709–724 (2002).
- Elson, D. *New Left Rev.* **1**, 172 (1988).
- Rao, N., Lawson, E. T., Raditloaneng, N., Solomon, D. & Angula, M. *Clim. Dev.* **11**, 14–26 (2017).
- Bakker, K. *Antipode* **39**, 430–455 (2007).
- Kabeer, N. *IDS Bull.* **31**, 83–97 (2000).
- Hurricane Ian a wake-up call for insurers as losses forecast to hit \$75bn. *Financial Times* (16 October 2022).
- Timperley, J. *Nature* **598**, 400–402 (2021).
- Caney, S. in *Global basic rights* (eds Beitz, C & Goodin, R.) 227–247 (Oxford University Press, 2009).
- Bosch, H. J. & Gupta, J. *Rev. Eur. Community Int. Environ. Law* **31**, 295–316 (2022).
- Dell'Angelo, J., Rulli, M. C. & D'Odorico, P. *Ecol. Econ.* **143**, 276–285 (2018).
- Starbucks: Social responsibility and tax avoidance, Coca-Cola Broken Promises on Plastic Bottles - Plastic Soup Foundation* (Plastic Soup Foundation, 2022); <https://www.plasticsoupfoundation.org/en/2022/02/is-coca-colas-latest-promise-really-a-step-forward/>
- Campbell, K. & Helleloid, D. *J. Account. Educ.* **37**, 38–60 (2016).
- Gupta, J. & Lebel, L. *Int. Environ. Agreement Polit. Law Econ.* **20**, 393–410 (2020).
- Hartwig, L. D., Jackson, S., Markham, F. & Osborne, N. *Int. J. Water Resour. Dev.* **38**, 30–63 (2022).

Competing interests

The authors declare no competing interests.

Selected Media Reports

IIT-Madras ties up with Israeli government for water security

The Hindu Bureau
CHENNAI

The Indian Institute of Technology, Madras has partnered with the Israeli government to ensure water security in the country.

The India-Israel Centre of Water Technology (CoWT) that will come up on the institute campus, will customise Israeli technologies for Indian requirements and pilot sustainable technologies in the country. IIT-M Director V. Kamakoti and Secretary in the Union Ministry of Housing and Urban Affairs Manoj Joshi signed a letter of intent in New Delhi last week.

The MoHUA will collaborate with Israel's agency for International Development Cooperation Mashav.

To help Amrut mission

The new centre will help the Ministry's Amrut mission besides pursuing joint activities to implement technological solutions through separate agreements.

Lior Asaf, water attache, Embassy of Israel, said the new state-of-the-art Israeli technology and know-how would be introduced.

Mr. Kamakoti said the collaboration will work on conservation and proper use of water.

India and Israel will work closely to enhance capacity building of Indian water professionals at all



The India-Israel Centre of Water Technology will come up on the IIT-M premises.

levels and demonstrate latest technologies besides holding exhibitions of Israeli water companies.

IIT-Madras Professor T. Pradeep said water security in India depended on implementing advanced and affordable technologies besides efficiently managing resources. "There is much to learn from Israel, a leader in the area, under the guidance of Amrut Mission," he said.

Specific projects related to integrated water resources management, urban water supply and non-revenue water, water and sewage recycling, IoT solution and online monitoring, water harvesting, smart data management and AI, were on the anvil.

Israel was represented by Naor Gilon, Israel's Ambassador to India. External Affairs Minister S. Jaishankar and his Israeli counterpart Eli Cohen were present at the event.

IIT Madras, Israel government join hands to establish ‘India – Israel Center of Water Technology

As per the agreement, the MoHUA will collaborate with MASHAV, Israel's Agency for International Development Cooperation, to establish this new centre, which will be located at IIT Madras campus.



The agreement was signed in presence of Shri. S. Jaishankar (C) & Mr. Eli Cohen (2nd L), Hon'ble External Affairs Ministers of India & Israel. (Photo source: IIT Madras)

The [Indian Institute of Technology \(IIT\), Madras](#) has joined hands with the government of Israel to establish an ‘India – Israel Center of Water Technology’ (CoWT) in Water Resources Management and Water Technologies at IIT Madras campus.

A letter of Intent was signed at New Delhi on May 9 by Manoj Joshi, Secretary, Ministry of Housing and Urban Affairs (MoHUA), Government of India, Prof. V. Kamakoti, Director, IIT Madras and Naor Gilon, Ambassador of Israel to India. This letter was signed in presence of S. Jaishankar and Eli Cohen, Hon'ble External Affairs Ministers of India and Israel, respectively, in the presence of Prof. T. Pradeep, Institute Professor, IIT Madras.



THE NEW
INDIAN EXPRESS

[NATION](#)[WORLD](#)[STATES](#)[CITIES](#)[OPINIONS](#)[BUSINESS](#)[SPORT](#)[GOOD NEWS](#)[MOVIES](#)[PHOTOS](#)[VIDEOS](#)

[Home](#) > [States](#) > [Tamil Nadu](#)

IIT-M professor T Pradeep secures Eni Award

Professor in the department of Chemistry, Pradeep has been recognised for his work on affordable clean water using advanced materials.

Published: 18th July 2023 06:59 AM | Last Updated: 18th July 2023 06:59 AM

| [A+](#) [A](#) [A-](#)



Indian Institute of Technology Madras (IIT-M) professor T Pradeep

Education Minister Dharmendra Pradhan launches books on science and technology written by IIT Madras faculty, alumnus



Two books written by distinguished faculty members of IIT Madras and alumnus have been launched by Education Minister Dharmendra Pradhan on July 30. The books published by the Indian Academy of Sciences and is part of the IIT Madras Alumni Association's (IITMAA) thought leadership activities were released at Bharat Mandapam in New Delhi.



Events Innovation and Research Oil & Gas Energy production

Eni Award 2023: Eni's scientific research awards awarded

🕒 October 18, 2023

🕒 Reading time: 6 minutes

[Facebook](#) [X](#) [LinkedIn](#) [Share via Email](#) [Print](#)



📷 Group photo of young researchers and entrepreneurs who won the Eni Award 2023.

It took place on Monday 16 October at the Palazzo del Quirinale, in the presence of the President of the Republic Sergio Mattarella, the President of the Board of Directors of [Eni](#) Giuseppe Zafarana and the CEO of Eni Claudio Descalzi, the award ceremony for the Eni Award 2023.

Patents

Indian Patents (Granted)

- (1) A selective and efficient process for the extraction of noble metal ions from complex mixtures, Thalappil Pradeep, Md Rabiul Islam and Tanmayaa Nayak, application no. 202241026274, May 5, 2022, issued as patent no. 417781, dated January 12, 2023.
- (2) Method for colocalization of plasmonic nanoparticles and biomolecules with plasmonic and Raman scattering microspectroscopy, T. Pradeep and Kamalesh Choudhari, application no. 1864/CHE/2015, dated April 09, 2015, issued as patent no. 419154, dated January 24, 2023.
- (3) Method of fabricating a conducting cloth based breath humidity sensor and applications thereof, T. Pradeep, Pillalamarri Srikrishnarka, Dasi Raaga Madhuri, Sourav Kanti Jana and Bobby George, application no. 202241008331, dated February 17, 2022, issued as patent no. 480519, dated December 12, 2023.
- (4) Method for accumulation of silver by rice and possible metal extraction by agriculture, T. Pradeep, Soujit Sengupta, Ananya Baksi and Debal Deb, application no. 6846/CHE/2014, dated December 31, 2014; full specification filed on December 28, 2015, issued as patent no. 416654, dated January 3, 2023.
- (5) A method for facile, rapid and industrially scalable preparation of metal hydroxide composition, Hydromaterials Private Limited & Indian Institute of Technology Madras (IIT Madras), ^[1] application no. 201941054546, dated December 30, 2019, issued as patent no. 429730 dated April 24, 2023.
- (6) Methods for selective visual detection of TNT, T. Pradeep, Ammu Mathew and P. R. Sajanlal, application no. 3150/CHE/2012, dated August 1, 2012, issued as patent no. 442508, dated August 2, 2023.
- (7) An electrode system based on differential oxidant response for the detection of free chlorine, Thalappil Pradeep, Kamalesh Chaudhari, Tullio Servida, Vishnu Kannan and Spoorthi Bhat, application no. 202141031970, TEMP/E-1/42985/2021-CHE, dated July 15, 2021, issued as patent no. 443964, dated August 9, 2023.

- (8) Reactivation of silver metal particle-based antimicrobial compositions, T. Pradeep, Sahaja Aigal, Amrita Chaudhary, M. Udhaya Sankar and Anshup, application no. 4300/CHE/2011, dated December 9, 2011, issued as patent no. 462074, dated October 26, 2023.
- (9) A compact, modular and scalable continuous-flow greywater sink for potable and non-potable uses, Pradeep and Ankit Nagar, application no. 202141054715, dated November 26, 2021, issued as patent no. 462091, dated October 26, 2023.
- (10) Vertically aligned nanoplates of atomically precise Co₆S₈ cluster for practical arsenic sensing, T. Pradeep, Anagha Jose, Arijit Jana, Tanvi Gupte, Keerthana Unni, Ankit Nagar, Amoghavarsha R. Kini and B.K. Spoorthi, application no. 202241076581, dated December 29, 2022, issued as patent no. 465466, dated November 3, 2023.
- (11) A method for environmental arsenic detection and public awareness using human cells, Thalappil Pradeep and Tanvi Gupte, application no. 202241049077, dated August 28, 2022, issued as patent no. 484281, dated December 18, 2023.
- (12) A point-of-care (POC) amperometric device for selective arsenic sensing, Thalappil Pradeep, Sourav Kanti Jana and Kamalesh Choudhuri, application no. 202041023576, dated June 5, 2020, issued as patent no. 490895, dated December 28, 2023.

Patents Applied

- (1) A method of identifying authenticity of ayurvedic preparations using hand-held Raman spectroscopy, Thalappil Pradeep, Ajaya Kumar Barik, Mithun N, Anish R Nath, Jijo Lukose and Santhosh Chidangil, Application no: 202341048917, dated July 20, 2023.

PCT Applied

- (1) A selective and efficient process for the extraction of noble metal ions from complex mixtures, Thalappil Pradeep, Md Rabiul Islam and Tanmayaa Nayak, application no. PCT/IN2023/050401, dated April 24, 2023.
- (2) A method to transform crystalline minerals to nanoparticles by microdroplets, Thalappil Pradeep, B. K. Spoorthi and Pallab Basuri, application no. PCT/IN2023/050649, dated July 4, 2023.

- (3) Material and method for sustainable and affordable atmospheric water harvesting, Thalappil Pradeep, Ankit Nagar and Sonali Seth, application no. PCT/IN2023/050808, dated August 27, 2023.
- (4) Vertically aligned nanoplates of atomically precise Co_6S_8 cluster for practical arsenic sensing, Thalappil Pradeep, Anagha Jose, Arijit Jana, Tanvi Gupte, Keerthana Unni, Ankit Nagar, Amoghavarsha R. Kini and B. K. Spoorthi. Application no. PCT/IN2023/050856, dated September 12, 2023.

AUGUST 15, 2023

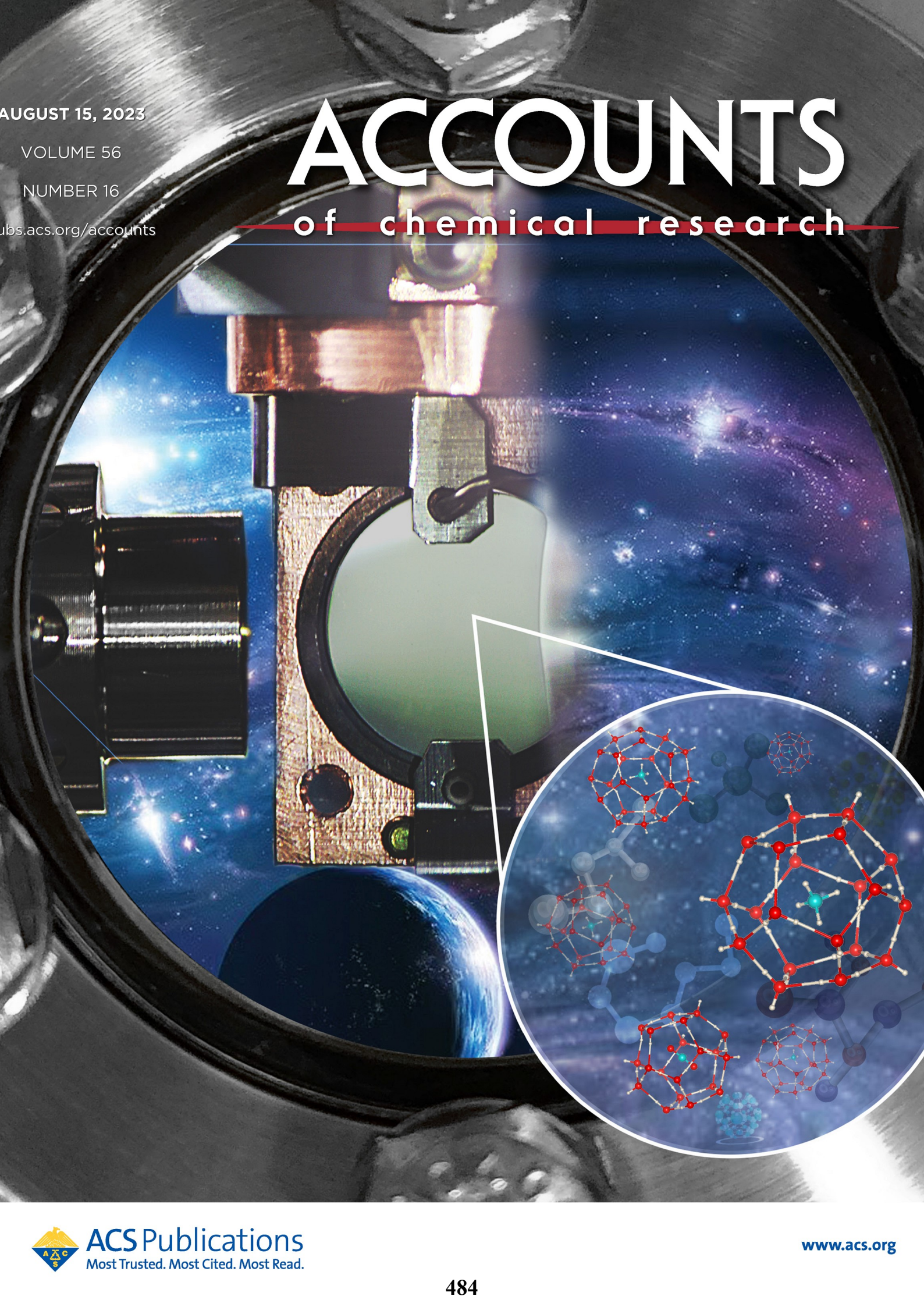
VOLUME 56

NUMBER 16

pubs.acs.org/accounts

ACCOUNTS

of chemical research



ACS Publications
Most Trusted. Most Cited. Most Read.

www.acs.org

Pradeep Research Group



Current group as on December 30, 2023



Acknowledgement



Students
and
Collaborators

Funding

